SEPTEMBER 1986

analytical chemistry

EASTERN ANALYTICAL SYMPOSIUM CELEBRATES ITS SILVER ANNIVERSARY

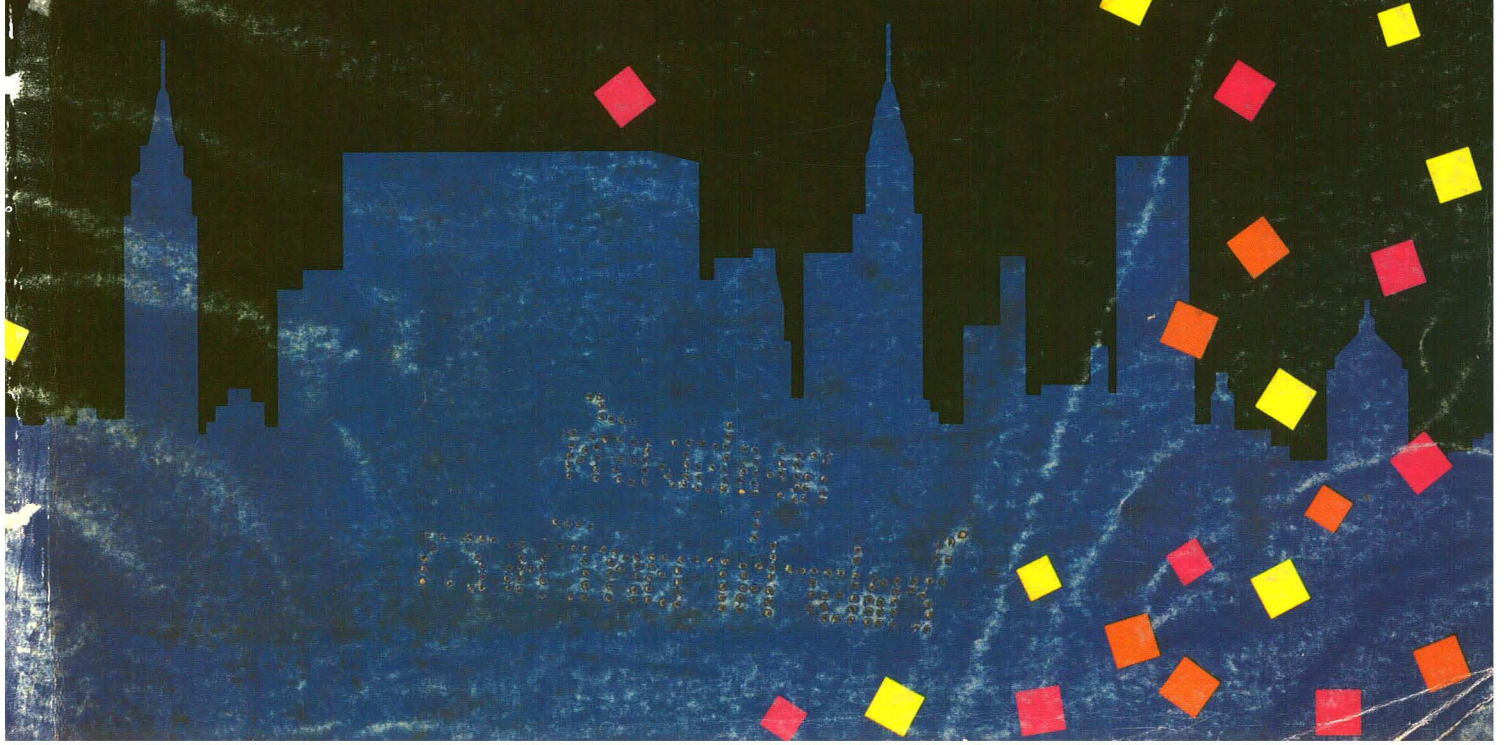

ACE™

MULTICHANNEL ANALYZER

EG&G ORTEC

NEW! Optional Software Available

Features: Peak Search, Nuclide Identification, Autocycling, and MUCH more.

SPECTROSCOPISTS: DEAL YOURSELF AN ACE

The EG & G ORTEC ACE™ transforms your IBM PC (or compatible) into a friendly, advanced, economical MCA.

Based on ORTEC's concept of Advanced Data Collection and Management, the ACE™ consists of a card and emulation software for your PC to produce a fully featured MCA. The result is performance usually found only in much more costly instruments. The PC is entirely free for other tasks during data acquisition.

Features:

- 2048 (optional 4096) channel ADC and memory
- 25μs fixed conversion time ADC
- Up to 4 ADCs per MCA
- Multiple Regions of Interest
- Net/Gross Area (with statistical error)
- Peak Centroid/Shape
- Smooth
- Energy Calibrate
- Constant Stripping
- Compare
- Storage of spectra and presets on disk
- Multiple preset types
- Fast data storage/retrieval from disk
- Optional Color Display
- Graphics Printing

To find out more, write or call, and we will show you our cards.

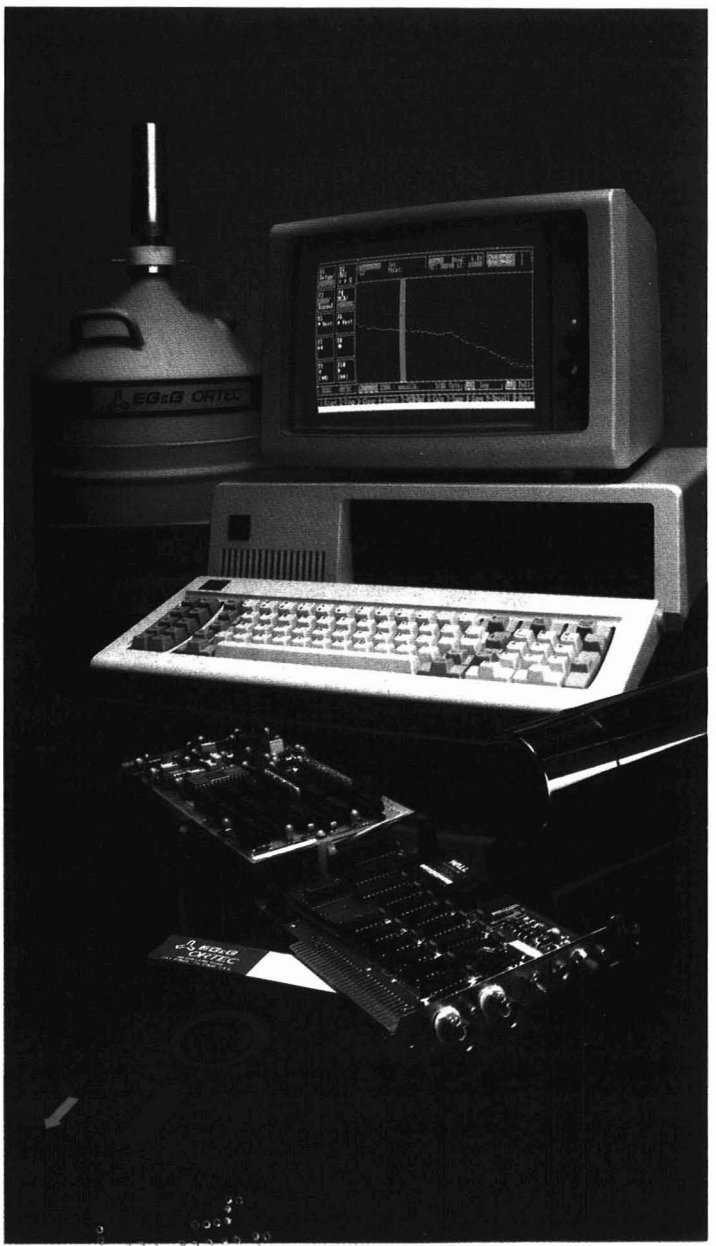

EG&G ORTEC

100 Midland Road, Oak Ridge, TN 37830
Hotline: (800) 251-9750 (In USA)
(615) 482-4411

CIRCLE 48 ON READER SERVICE CARD

NEW ACE™ Multichannel Demonstration Disks are now available.
Call or write for your FREE copy.

Call Amy Larabee at (800) 251-9750 or your local EG&G ORTEC sales representative.

FREEDOM!

Gilson programmable samplers give you all the freedom you need to successfully automate quality control procedures, rare product conditioning, liquid sample preparation before analysis.

In flame photometry or atomic absorption, in ICP Spectrometry, in HPLC, in RIA, in turbidimetry ... 24 hours a day, Gilson programmable samplers take charge... saving you hours for more productive work.

GILSON AUTO-SAMPLERS

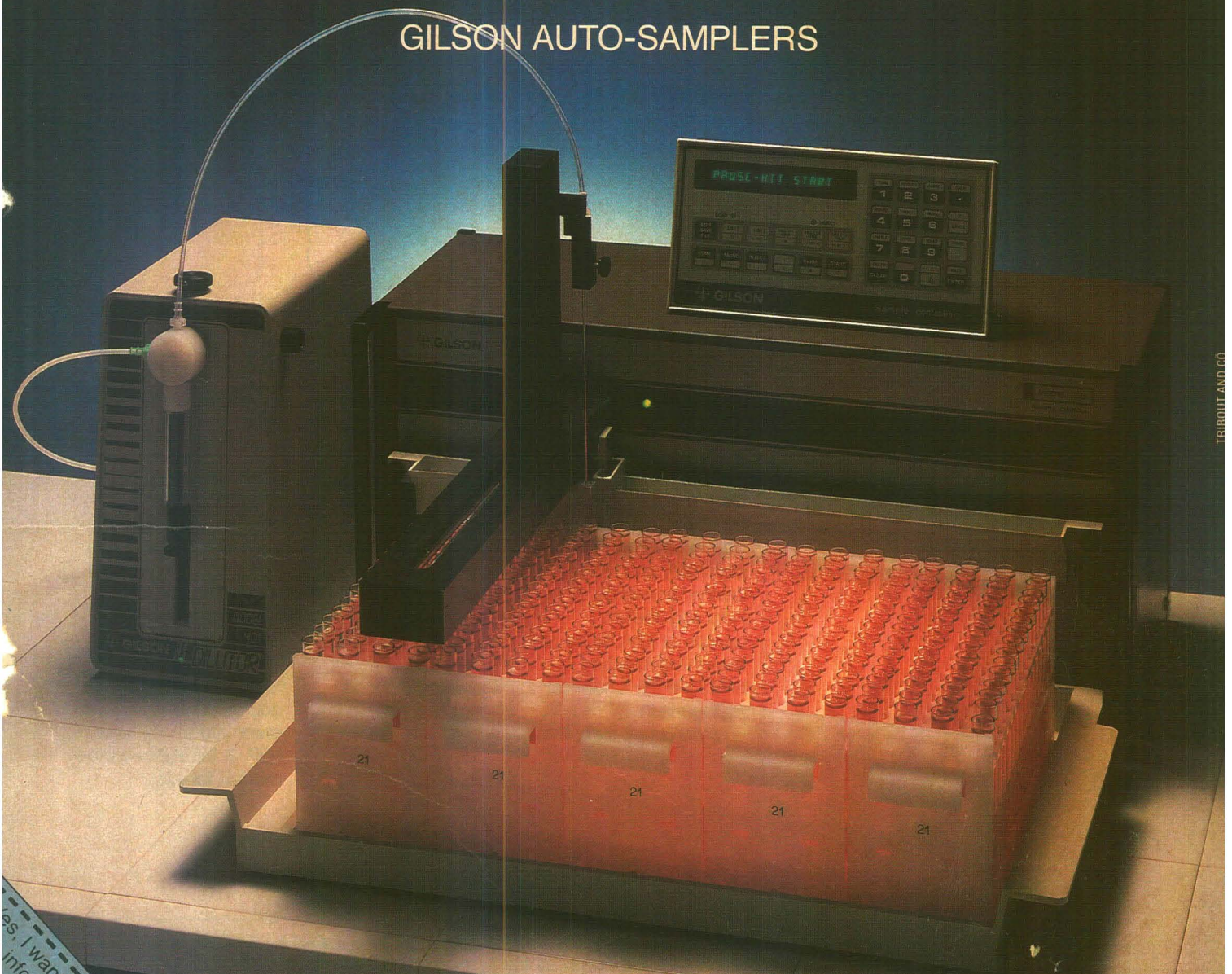

Yes, I want to gain time and improve quality. Send me more information about Gilson programmable samplers.

Name
Position
Company
Address
Tel.

GILSON
INTERNATIONAL

France : B.P. 45, F-95400 Villiers-le-Bel.
Tel. : (1) 39 90 54 41. Telex : 696 682 F
USA : Box 27, 3000 W. Beltline, Middleton, Wisc. 53562.
Tel. : (608) 836 1551. Telex : 26.5478 MTWI

CIRCLE 64 ON READER SERVICE CARD

analytical chemistry

SEPTEMBER 1986

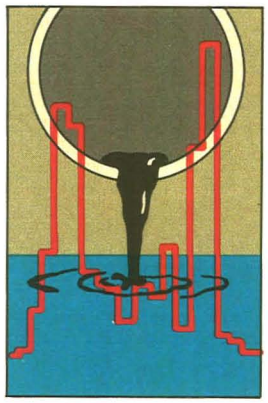

REPORT

Bioassay-directed chemical analysis combines methods from analytical chemistry and biology. Dennis Schuetzle of Ford and Joellen Lewtas of EPA describe how this procedure helps identify chemical mutagens in environmental samples

1060 A

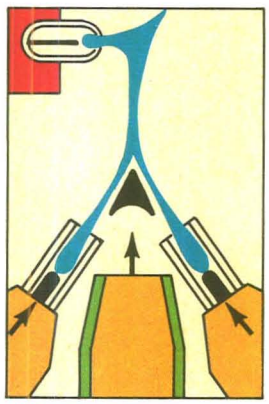

INSTRUMENTATION

Atomic emission sources for solution spectrochemistry. Andrew T. Zander of Perkin-Elmer provides a comparison of inductively coupled plasma, direct-current plasma, and microwave-induced plasma sources

1139 A

FOCUS

Chromatographic–spectroscopic combinations: Milton Lee of Brigham Young University reviews this year's Division of Analytical Chemistry Summer Symposium. ▶ **Cell separations:** two-phase partitioning, countercurrent chromatography, and FFF. ▶ **Instrumentation market forecast**

1076 A

Volume 58, No. 11
September 1986
ANCHAM
58(11) 1039A–1152A
2113–2352 (1986)
ISSN 0003 2700

Registered in U.S. Patent and Trademark Office; Copyright 1986 by the American Chemical Society

ANALYTICAL CHEMISTRY (ISSN 0003-2700) is published monthly except semimonthly in April and August by the American Chemical Society at 1155 16th St., N.W., Washington, D.C. 20036. Editorial offices are located at the same ACS address (202-872-4600; TDD 202-872-8733). Second-class postage paid at Washington, D.C., and additional mailing offices. Postmaster: Send address changes to ANALYTICAL CHEMISTRY Membership & Subscription Services, P.O. Box 3337, Columbus, Ohio 43210.

Claims for missing numbers will not be allowed if loss was due to failure of notice of change of address to be received in the time specified; if claim is dated (a) North America: more than 90 days beyond issue date, (b) all other foreign: more than one year beyond issue date, or if the reason given is "missing from files."

Copyright Permission: An individual may make a single reprographic copy of an article in this publication for personal use. Reprographic copying beyond that permitted by Section 107 or 108 of the U.S. Copyright Law is allowed, provided that the appropriate per-copy fee is paid through the Copyright Clearance Center, Inc., 27 Congress St., Salem, Mass. 01970. For reprint permission, write Copyright Administrator, B&J Division, ACS, 1155 16th St., N.W., Washington, D.C. 20036.

Registered names and trademarks, etc., used in this publication, even without specific indication thereof, are not to be considered unprotected by law.

Advertising Management: Centcom, Ltd., 25 Sylvan Road South, Westport, Conn. 06881 (203) 226-7131

Technical Contents/Briefs . . . . . 1046 A
For Your Information . . . . . 1114 A
Call for Papers . . . . . 1114 A
Meetings . . . . . 1116 A
Short Courses . . . . . 1116 A
New Products . . . . . 1122 A
Software . . . . . 1126 A
Manufacturers' Literature . . . . . 1128 A
Advertising Index . . . . . 1150 A
Author Index, Future Articles . . . . . Inside back cover

COVER FEATURE





NEWS

Eastern Analytical Symposium: The Silver Jubilee EAS will be held in New York City in October. ▶ **Division of Analytical Chemistry** fellowship winners. ▶ **Fred Lytle** wins Chemical Instrumentation Award. ▶ **Joel Harris** wins Coblentz Award. ▶ **Henry Freiser** wins Anachem Award

1095 A

BOOKS

Critical reviews. Books on Fourier transform infrared spectrometry and liquid chromatography in pharmaceutical analysis are reviewed by Stephen Lowry and Roger Gilpin

1132 A

EDITORIAL

"Big Three." Lecture series to honor Furman and Kolthoff, like the one established at the University of Michigan for Willard, would be appropriate tributes to these pioneers who shaped modern analytical chemistry and influenced generations of students

2113

1986 subscription rates include air delivery outside the U.S., Canada, and Mexico

	1 yr	2 yr
Members		
Domestic	22	37
Canada and Mexico	43	79
Europe	68	129
All Other Countries	91	175
Nonmembers		
Domestic	33	56
Canada and Mexico	54	98
Europe	111	202
All Other Countries	134	248

Three-year and other rates contact: Membership & Subscription Services, ACS, P.O. Box 3337, Columbus, Ohio 43210, (614) 421-3776.

Subscription orders by phone may be charged to Visa, MasterCard, Barclay card, Access, or American Express. Call toll free at (800) 424-6747 from anywhere in the continental U.S.; from Washington, D.C., call 872-8065. Mail orders for new and renewal subscriptions should be sent with payment to the Business Management Division, ACS, P.O. Box 57136, West End Station, Washington, D.C. 20037.

Subscription service inquiries and changes of address (include both old and new addresses with ZIP code and *recent mailing label*) should be directed to the ACS Columbus address noted above. Please allow six weeks for change of address to become effective.

ACS membership information: Bebe Olsen, Washington address.

Single issues, current year, $8.00 except review issue and LabGuide, $9.00; **back issues and volumes and microform editions** available by single volume or back issue collection. For information or to order, call (800) 424-6747 or write the Sales Department at the Washington address.

Nonmember rates in Japan: Rates at left do not apply to nonmember subscribers in Japan, who must enter subscription orders with Maruzen Company Ltd., 3–10 Nihonbashi 2-chome, Chuo-ku, Tokyo 103, Japan. Tel: (03) 272-7211.

ห้องสมุดกรมวิทยาศาสตร์บริการ
17 ก.ค. 2529

"Before the Carlo Erba MEGA, capillary GCs couldn't reach their peak."

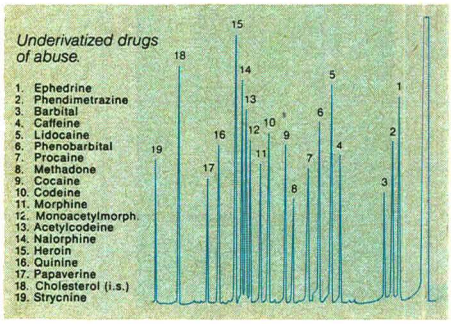

Either they suffered from thermal peak splitting, or their ability to quantify high molecular weight components was limited.

The Carlo Erba MEGA GC's oven was specifically designed for high-resolution, fused silica columns, so its superior temperature stability eliminates the "Christmas tree" effect.

A patented on-column injection system, with primary cooling of the injection block and secondary cooling of the column, eliminates peak discrimination.

The MEGA also allows fast detector exchange (FID to ECD in 30 seconds), series multidetector configurations, and the addition of a full range of accessories, including an on-column autosampler and headspace unit.

For more information about the Carlo Erba MEGA HRGC, call or write:
Haake Buchler Instruments, Inc.,
Analytical Instruments Division
244 Saddle River Road,
Saddle Brook, NJ 07662-6001.
201-843-2330 or 1-800-631-1369

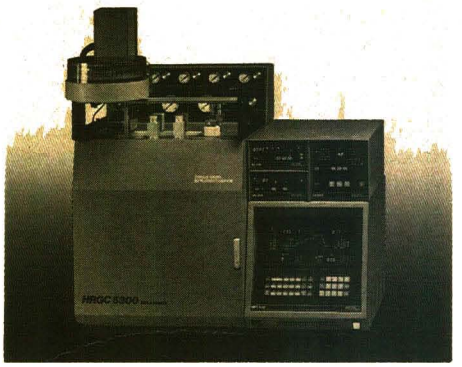

MEGA applications include environmental analysis, polymers, paints, micro-organisms, solvent residue analysis, flavors and foods, fragrances, pharmaceuticals, and petrochemicals.

CARLO ERBA INSTRUMENTS

HBI

HAAKE BUCHLER INSTRUMENTS, INC.

CIRCLE 103 ON READER SERVICE CARD

"Before the Carlo Erba VEGA, a low-cost GC was just a low-cost GC."

Today this low-cost GC is a lot more. It's ease of operation. It's full-scale automation. It's microprocessor control and flexible data processing. It's full networking capability and graphic display of run conditions. And Carlo Erba's pedigree guarantees unsurpassed injector and capillary and packed column technology. That's complete versatility. It's analytical power unrivalled in a routine GC of moderate price and compact size.

In other words, what was optional in yesterday's low-cost GC is standard in today's VEGA. Find out why the VEGA 6000 makes yesterday's low-cost GC a thing of the past.

For more information, contact:
Haake Buchler Instruments, Inc.
244 Saddle River Road
Saddle Brook, NJ 07662-6001.
201-843-2320 or 1-800-631-1369



This automated low-cost GC speaks your language: the VEGA 6000 boasts an "Intelligent Control Unit."

CARLO ERBA INSTRUMENTS

HBI

HAAKE BUCHLER INSTRUMENTS, INC.

CIRCLE 104 ON READER SERVICE CARD

Briefs

Characterization of High Molecular Weight Polycyclic Aromatic Hydrocarbons by Charge Exchange Chemical Ionization Mass Spectrometry **2114**

Thermally stable capillary columns are prepared to separate large PAHs. The (CE/CI) MS working range is expanded by increasing the ion source pressure.

William J. Simonsick, Jr., and Ronald A. Hites*, School of Public and Environmental Affairs and Department of Chemistry, Indiana University, Bloomington, Ind. 47405

Anal. Chem., 58 (1986)

Substituent Effects in Charge Exchange Chemical Ionization Mass Spectrometry **2121**

A linear Hammett relationship is observed for a series of monosubstituted benzenes and naphthalenes. Substituted aromatic compounds not distinguished by electron impact MS are predictively resolved.

William J. Simonsick, Jr., and Ronald A. Hites*, School of Public and Environmental Affairs and Department of Chemistry, Indiana University, Bloomington, Ind. 47405

Anal. Chem., 58 (1986)

Application of Particle Desorption Mass Spectrometry to the Characterization of Minerals **2126**

Four mineral specimens are analyzed by PDMS using californium-252 as the primary ion source. Qualitative results are validated by XPS, EMP, and SIMS.

W. R. Summers and E. A. Schweikert*, Center for Chemical Characterization & Analysis, Texas A&M University, College Station, Tex. 77843-3144 *Anal. Chem., 58 (1986)*

Multidimensional, Laser-Based Instrument for the Characterization of Environmental Samples for Polycyclic Aromatic Compounds **2129**

Laser–analyte interaction products are simultaneously monitored for GC eluents "on-the-fly." Absolute detection limits for 21 PACs are in the low-picogram range with a linear dynamic range of 4 decades.

R.L.M. Dobson, A. P. D'Silva, S. J. Weeks, and V. A. Fassel*, Ames Laboratory—USDOE and Department of Chemistry, Iowa State University, Ames, Iowa 50011 *Anal Chem., 58 (1986)*

Detection of Nonvolatile Species by Laser Desorption Atmospheric Pressure Mass Spectrometry **2137**

Various drugs, vitamins, amino acids, nucleosides, and catecholamines are examined, and an ultimate detection limit of approximately 0.3 ng is estimated for imipramine and chlorpromazine.

Leonidas Kolaitis and David M. Lubman*, Department of Chemistry, The University of Michigan, Ann Arbor, Mich. 48109

Anal. Chem., 58 (1986)

Photoionization in Air with Ion Mobility Spectrometry Using a Hydrogen Discharge Lamp **2142**

Simple spectra with one to three peaks are obtained for 10 organic compounds. Detection limits in PI–IMS range from 0.1 to 50 ppb without sample preconcentration.

C. S. Leasure, M. E. Fleischer, G. K. Anderson, and G. A. Eiceman*, Department of Chemistry, New Mexico State University, Las Cruces, N.M. 88003 *Anal. Chem., 58 (1986)*

Measurement of the Laser-Induced Ionization Yield for Lithium in an Air–Acetylene Flame **2147**

Two pulsed, tunable dye lasers simultaneously pumped by an excimer laser are used to measure the ionization yield of lithium atoms in an air–acetylene flame. Both single-step and two-step excitation followed by collisional ionization are reported.

B. W. Smith, L. P. Hart, and Nicoló Omenetto*, Joint Research Centre, Chemistry Division, Ispra (Varese), Italy

Anal. Chem., 58 (1986)

High-Temperature Pulsed Nozzle for Supersonic Jet Spectrometry and Its Application to Gas Chromatography **2152**

The electrically controlled pulsed nozzle has a minimum pulse width of 1.3 ms and can be operated up to 300 °C. It is applied to GC determination of aromatic hydrocarbons.

Totaro Imasaka, Takeshi Okamura, and Nobuhiko Ishibasi*, Faculty of Engineering, Kyushu University, Hakozaki, Fukuoka 812, Japan *Anal. Chem., 58 (1986)*

Theoretical Optimization of Parameter Selection in Constant Energy Synchronous Luminescence Spectrometry **2156**

Mathematical relationships are derived for peak wavelength maximum, intensity maximum, and peak bandwidth, defining their dependence on the luminescence excitation and emission spectral characteristics and the selected scan path.

Eugene L. Inman, Leigh Ann Files, and James D. Winefordner*, Department of Chemistry, University of Florida, Gainesville, Fla. 32611 *Anal. Chem., 58 (1986)*

* Corresponding author

The VG TS-250...
Not just a New Mass Spectrometer but a New Technology

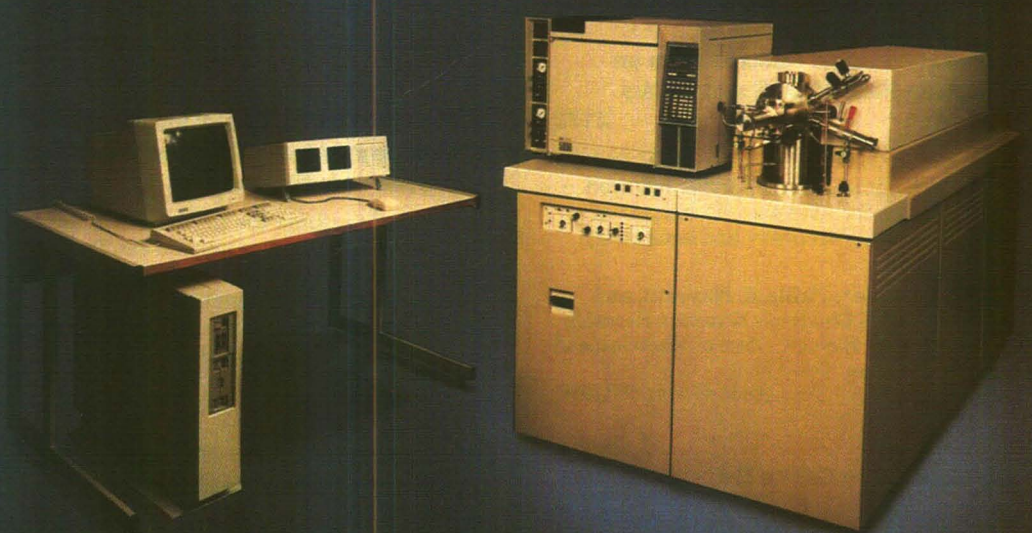

TS-250 triple-sector technology starts at the magnet. Its unique, fast, hysteresis-free design gives the extremely rapid scanning usually associated with quadrupoles. In addition, the high scanning accuracy eliminates the need for magnet calibration in all ionization modes.

Other VG advances that make the TS-250 a whole new concept in mass spectrometry are electronically selectable mass resolution directly programmable from the microprocessor keyboard and a unique source changeover system that goes from EI to FAB in under 30 seconds!

And . . . we've made it a simple push-button operation.

Put an entirely new MS technology at your command. Contact VG Instruments for more details on the TS-250.

VG INSTRUMENTS

VG Instruments, Inc./300 Broad Street/Stamford, CT 06901/(203) 322-4546

Mass Spectrometers • Gas Analysis MS • Isotope Ratio MS • LC-MS • MBE • ICP-MS • Ion Beam Lithography

CIRCLE 219 ON READER SERVICE CARD

Briefs

Metal Chelate Fluorescence Enhanced by Nonionic Micelles: Surfactant and Auxiliary Ligand Nature Influence on the Niobium–Lumogallion Complex **2161**

The limit of detection for fluorometric determination of Nb(V) is 0.007 ppm. The role of nonionic surfactants on metal chelate micellar fluorometry is discussed.

Alfredo Sanz-Medel* and M. M. Fernandez Perez, Department of Analytical Chemistry, Faculty of Chemistry, University of Oviedo, Oviedo, Spain, and **Miguel De La Guardia Cirugeda and J. L. Carrion Dominguez,** Department of Analytical Chemistry, Faculty of Chemistry, University of Valencia, Valencia, Spain
Anal. Chem., 58 (1986)

Synchrotron X-ray Fluorescence: Diffraction Interference **2167**

X-ray diffraction represents a significant interference in synchrotron X-ray fluorescence analyses. The probability of detecting a diffraction peak in a quartz EDS spectrum is estimated to be near unity for continuum excitation.

S. R. Sutton*, M. L. Rivers, and J. V. Smith, Department of the Geophysical Sciences, University of Chicago, Chicago, Ill. 60637
Anal. Chem., 58 (1986)

Measurement of $^{13}CO_2/^{12}CO_2$ Abundance by Nondispersive Infrared Heterodyne Ratiometry as an Alternative to Gas Isotope Ratio Mass Spectrometry **2172**

The instrument response in volts varied from −0.51 to 1.22 over the range of −85 to +329‰. Nondispersive infrared heterodyne ratiometry can determine the ^{13}C content of respiratory CO_2 with acceptable accuracy and sensitivity for clinical studies.

Charles S. Irving, Peter D. Klein*, Philip R. Navratil, and Thomas W. Boutton, USDA/ARS Children's Nutrition Research Center, Department of Pediatrics, Baylor College of Medicine, and Texas Children's Hospital, Houston, Tex. 77030
Anal. Chem., 58 (1986)

Effect of Absorbing Matrices on Diffuse Reflectance Infrared Spectra **2179**

Explanations for the quantitative behavior of diffuse-reflectance IR spectra of analytes are offered. The results of this study are important in the interpretation of spectra of adsorbates on absorbing substrates.

Paul J. Brimmer and Peter R. Griffiths*, Department of Chemistry, University of California, Riverside, Calif. 92521
Anal. Chem., 58 (1986)

Continuous Recording of Reflection–Absorbance Fourier Transform Infrared Spectra of the Effluent of a Microbore Liquid Chromatograph **2184**

The effluent from a high-performance liquid chromatograph is deposited onto a rotating disk that has a reflective surface, and the resulting record of the chromatographic experiment continuously analyzed by recording reflectance–absorbance spectra with an FT–IR spectrometer.

John J. Gagel and Klaus Biemann*, Department of Chemistry, Massachusetts Institute of Technology, Cambridge, Mass. 02139
Anal. Chem., 58 (1986)

Rapid Nontarget Screening of Environmental Extracts by Directly Linked Gas Chromatography/Fourier Transform Infrared/Mass Spectrometry **2189**

Even with a small FT–IR data base, this system doubles the chemical information obtainable from either single detector. Six complex environmental extracts are analyzed, confirming 20 identifications and 24 compound class assignments.

Donald F. Gurka*, U.S. Environmental Protection Agency, Office of Research and Development, Environmental Monitoring Systems Laboratory, Las Vegas, Nev. 89114, and **Richard Titus,** Chemistry Department, University of Nevada at Las Vegas, Las Vegas, Nev. 89109
Anal. Chem., 58 (1986)

Maximum Absorbance Algorithm for Reconstruction of Gas Chromatograms from Gas Chromatography/Infrared Spectrometry Data **2195**

The maximum absorbance algorithm is compared with both the integrated absorbance method and the Gram–Schmidt reconstruction technique. The maximum absorbance reconstruction is more sensitive than the integrated absorbance method for selective detection reconstruction.

Ian C. Bowater, Robert S. Brown, John R. Cooper, and Charles L. Wilkins*, Department of Chemistry, University of California, Riverside, Calif. 92521
Anal. Chem., 58 (1986)

Probability Distributions of the Number of Chromatographically Resolved Peaks and Resolvable Components in Mixtures **2200**

A model describing the probability distribution of resolved peaks and sample components can be calculated for simple as well as complex mixtures from readily accessible chromatographic parameters.

Michel Martin*, David P. Herman, and Georges Guiochon, Ecole Polytechnique, Laboratoire de Chimie Analytique Physique, 91128 Palaiseau, France
Anal. Chem., 58 (1986)

Physical Model for Gas–Solid Chromatography with Volatile and Nonvolatile Modifiers **2207**

The scaled-particle adsorption theory is used to model the behavior of solutes adsorbed on graphitized carbon black. An equation is derived to describe the retention of infinitely dilute solutes in the presence of coadsorbed species.

Jon F. Parcher*, Ping J. Lin, and David M. Johnson, Chemistry Department, University of Mississippi, University, Miss. 38677
Anal. Chem., 58 (1966)

Carbon Hollow Tubes as Collectors in Thermal Desorption/Gas Chromatographic Analysis of Atmospheric Organic Compounds **2213**

A linear response is obtained from 3 to 770 ng/sample. The collector's capacity is found to range from 0.4 to 2.6 μmol depending on the compound being adsorbed.

George P. Cobb and Robert S. Braman*, Department of Chemistry, University of South Florida, Tampa, Fla. 33610, and **Ke Min Hua,** Southwest Institute for National Minorities, Chengdu, The People's Republic of China
Anal. Chem., 58 (1986)

VICI

Valco Instruments Co. Inc.
P.O. Box 55603 Houston, Texas 77255
(713) 688-9345
TWX 910-881-5550 Telex 79-0033.

Valco Switzerland
Tannenberg P.O. Box 13 CH-6214 Schenkon
(045) 216868
Telex 72609 vici ch

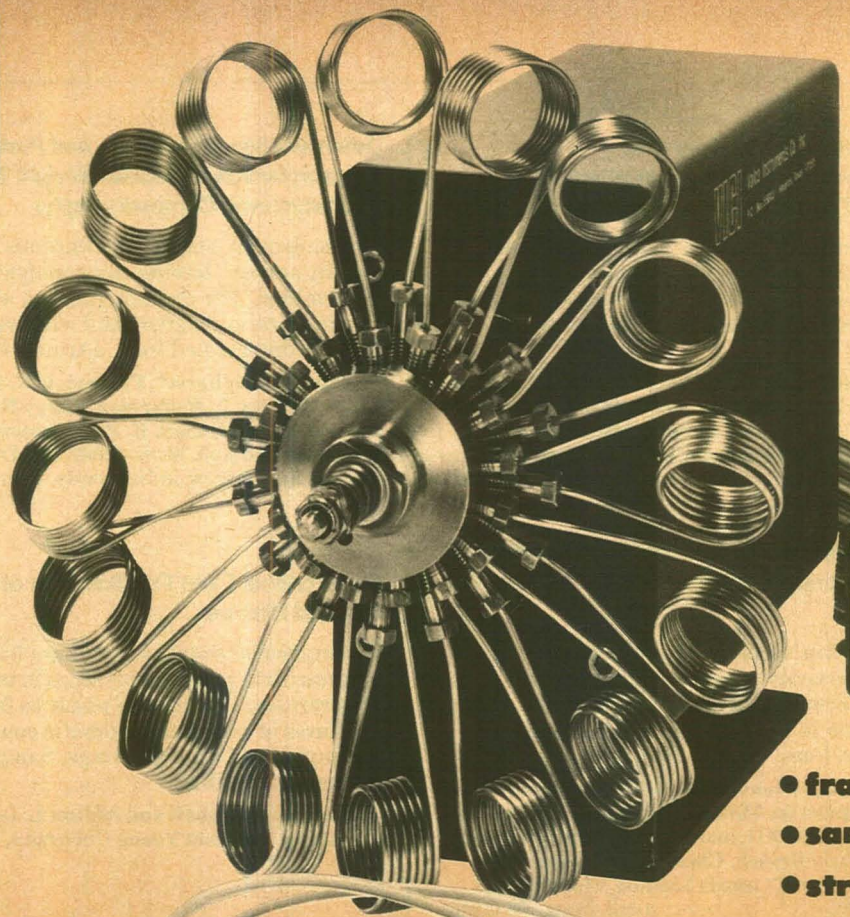



Electric actuation with complete computer interfacing shown

- **fraction collection**
- **sample injection**
- **stream selection**
- **reactor selection**
- **column selection**

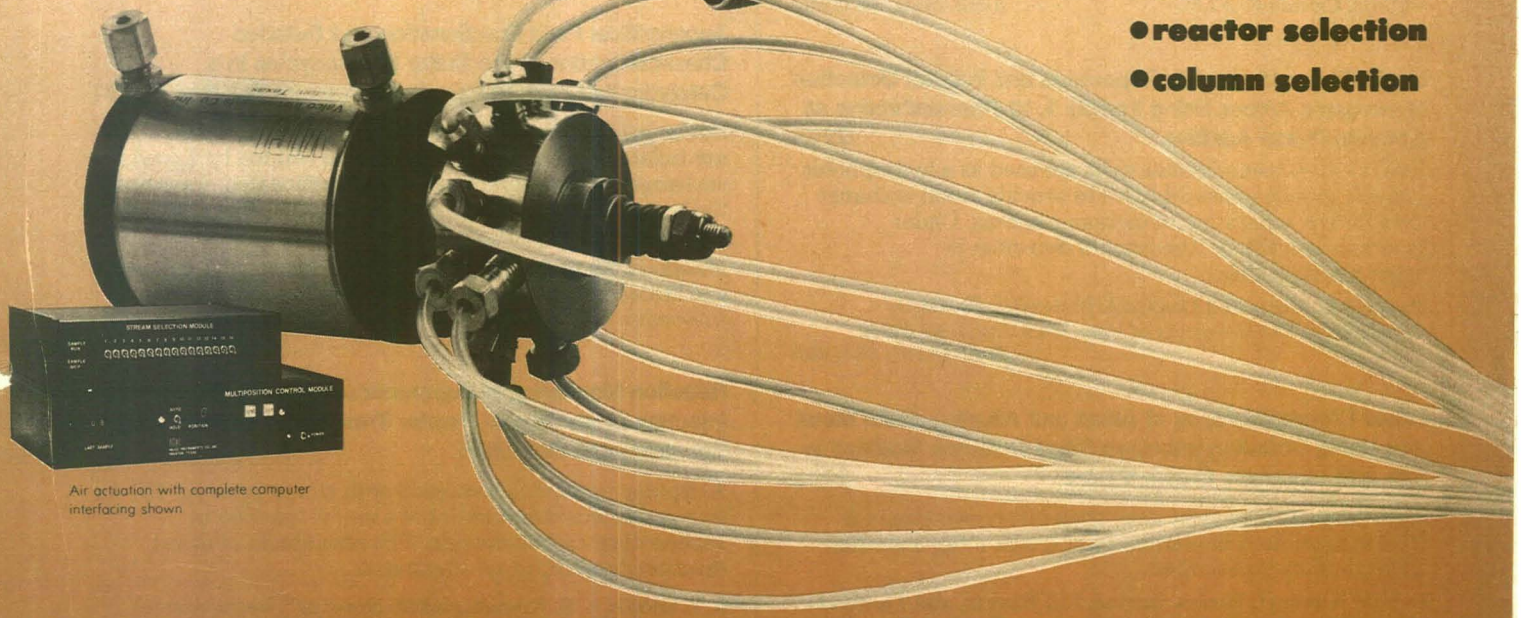

Air actuation with complete computer interfacing shown

POWERFUL NEW TOOLS

FOR RESEARCH AND PROCESS CONTROL

Valco multiposition switching / sampling valves present a world of possibilities.

SD Type Flowpath
Inputs dead-ended, flow when selected, or input to multiple selected outputs.

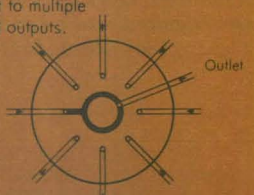

SC Type Flowpath
All inputs to a common outlet except selected one.



SF Type Flowpath
Each input flows to individual outlet except selected one which is diverted.

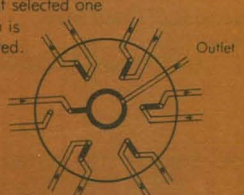

ST Type Flowpath
Used for multi-column, multi-sampling, or multi trap selection.

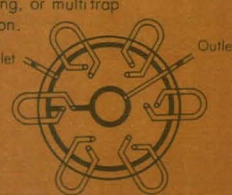

CIRCLE 218 ON READER SERVICE CARD

Determination of Nicotine *N*-Oxide by Gas Chromatography following Thermal Conversion to 2-Methyl-6-(3-pyridyl)tetrahydro-1,2-oxazine 2218

A method for determining nicotine-*N*-oxide in smokers' urine using 5-methylnicotine *N*-oxide as an internal standard is described. A correlation of 0.99 is obtained for a set of samples analyzed by both capillary and packed-column GC.

Peyton Jacob, III*, Neal L. Benowitz, Lisa Yu, and Alexander T. Shulgin, Division of Clinical Pharmacology of the Department of Medicine, University of California, Building 100, Room 235, San Francisco General Hospital Medical Center, San Francisco, Calif. 94110 *Anal. Chem., 58 (1986)*

Dynamic Chromatographic Systems for the Determination of Rare Earths and Thorium in Samples from Uranium Ore Refining Processes 2222

Optimization of the effective capacity of the dynamic ion exchanger and the selectivity of postcolumn reaction detection permits determination down to 0.1 μg/mL of the rare earths and yttrium in the presence of U, Th, and a number of other metal ions.

D. J. Barkley* and Marcia Blanchette, Mineral Sciences Laboratories, Canada Centre for Mineral and Energy Technology, Ottawa, Ontario, Canada K1A 0G1, and **R. M. Cassidy and Steve Elchuk,** General Chemistry Branch, Chalk River Nuclear Laboratories, Atomic Energy of Canada Limited, Chalk River, Ontario, Canada K0J 1J0 *Anal. Chem., 58 (1986)*

Liquid Chromatographic Separation and Indirect Detection of Inorganic Anions Using Iron(II) 1,10-Phenanthroline as a Mobile Phase Additive 2226

Fe(II) 1,10-phenanthroline salts are used as a hydrophobic cationic mobile phase additive to provide anion exchange sites for the separation of inorganic anions. Under favorable conditions, the limit of detection is approximately 1 ng.

Pantelis G. Rigas and Donald J. Pietrzyk*, Chemistry Department, The University of Iowa, Iowa City, Iowa 52242 *Anal. Chem., 58 (1986)*

Liquid Chromatography of Alkali and Alkaline-Earth Metal Ions Using Octadecylsilanized Silica Columns Modified in Situ with Lipophilic Crown Ethers 2233

Simultaneous coating of more than one crown ether on ODS is possible. The durability of crown-ether-modified ODS columns is described.

Keiichi Kimura*, Hiroya Harino, Eiji Hayata, and Toshiyuki Shono*, Department of Applied Chemistry, Faculty of Engineering, Osaka University, Yamada-oka, Suita Osaka 565, Japan *Anal. Chem., 58 (1986)*

Mechanism of the Reversed-Phase High-Performance Liquid Chromatographic Separation of D- and L-Valine Using Copper(II) and L-Aspartyl-L-phenylalanine Methyl Ester 2237

Solution equilibrium constants for ternary mixtures of Cu(II), aspartame, and D- or L-valine are determined. A model is proposed that satisfactorily accounts for the chromatographic retention times and separation of D- and L-valine when using a Cu–aspartame eluent phase.

J. M. Broge and D. L. Leussing*, Department of Chemistry, The Ohio State University, Columbus, Ohio 43210 *Anal. Chem., 58 (1986)*

Determination of Nonionic and Partially Hydrolyzed Polyacrylamide Molecular Weight Distributions Using Hydrodynamic Chromatography 2242

The molecular weight distributions of ultrahigh molecular weight polyacrylamide and copolymers of acrylic acid are determined. The characterization is independent of composition and agrees well with weight-average molecular weights determined from intrinsic viscosity.

Martin A. Langhorst*, Frederick W. Stanley, Jr., Sergio S. Cutié, Jeffrey H. Sugarman, Larry R. Wilson, David A. Hoagland, and Robert K. Prud'homme, The Dow Chemical Company, Midland, Mich. 48667, and Department of Chemical Engineering, Princeton University, Princeton, N.J. 08544 *Anal. Chem., 58 (1986)*

Supercritical Fluid Fractionation of Petroleum- and Coal-Derived Mixtures 2247

An aminosilane stationary phase bonded on an intermediate particle size silica is used in conjunction with supercritical CO_2 mobile phase to fractionate complex mixtures of polycyclic aromatic compounds according to the number of aromatic rings. Sample capacities up to 20 mg are possible.

Robert M. Campbell and Milton L. Lee*, Department of Chemistry, Brigham Young University, Provo, Utah 84602 *Anal. Chem., 58 (1986)*

Supercritical Fluid Fractionation and Detailed Characterization of the Sulfur Heterocycles in a Catalytically Cracked Petroleum Vacuum Residue 2251

Sulfur heterocycles containing three to five aromatic rings are isolated from a petroleum vacuum residue by ligand exchange chromatography and are fractionated according to the number of aromatic rings using SFF. The PAHs in each fraction are identified using GC/MS.

Masaharu Nishioka, David G. Whiting, Robert M. Campbell, and Milton L. Lee*, Department of Chemistry, Brigham Young University, Provo, Utah 84602 *Anal. Chem., 58 (1986)*

Reaction Monitoring in Supercritical Fluids by Flow Injection Analysis with Fourier Transform Infrared Spectrometric Detection 2256

A capillary system is combined with a high-pressure FT–IR flow cell to monitor kinetics of a model reaction in supercritical carbon dioxide. The advantages of direct reaction monitoring are illustrated.

S. V. Olesik, S. B. French, and M. Novotny*, Department of Chemistry, Indiana University, Bloomington, Ind. 47405 *Anal. Chem., 58 (1986)*

Versatile Automatic Development System for Flow Injection Analysis 2258

The apparatus allows variation of flow rates, pH, and reagent concentration in one or more sample or carrier streams. The system software, written in BASIC, is menu driven and interactive.

D. Betteridge*, Timothy J. Sly, and Adrian P. Wade, Department of Chemistry, University College of Swansea, Singleton Park, Swansea SA2 8PP, United Kingdom, and **Derrick G. Porter,** Department of Trade and Industry, Laboratory of the Government Chemist, Cornwall House, Stamford Street, London SE1 9NQ, United Kingdom *Anal. Chem., 58 (1986)*



Ohaus: Experience The Difference...

EXPERIENCE TRUE PERFORMANCE

Your laboratory is no place to experiment with the performance of your electronic balance. So, before you invest in just any analytical—test out our GALAXY® G160D, G160 and G110 models. Experience our design breakthroughs that promise to boost productivity, heighten security and simplify operation!

Here's just a sampling of what you'll see! Larger, clearer, more stable display digits for mistake-proof reading from any angle. Our innovative one-step calibration system, with a unique removable security key (on the GALAXY® G160 and G110 models) for eliminating unwanted access to the mode. Clearly marked, individually placed operating controls. Plus, planned flexibility with programmable operating parameters and bi-directional interface.

EXPERIENCE REAL VALUE

Ohaus brings to its GALAXY® Balance Series over 75 years of experience in the precision weighing field. Which means greater performance at a greater cost savings to you. All three GALAXY® analytical models are available for hundreds of dollars less than any comparable electronic balances on the market today! But, see for yourself.

Free

Test and compare our GALAXY® balances. And when you do, we'll present you with an elegant gold Cross™ pencil. For experiencing the Ohaus difference *and* investing in any GALAXY® analytical balance, we'll thank you with the matching gold Cross™ pen.

So, call us today, toll free at 800-672-7722.

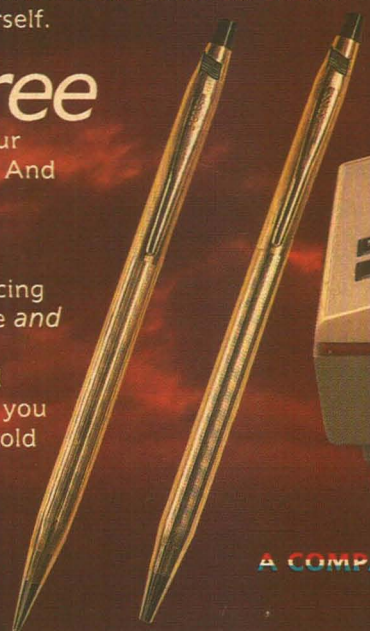

OHAUS Scale Corporation
29 Hanover Rd.
Florham Park, N.J. 07932

© Ohaus Scale Corporation 1986.

OHAUS
A COMPANY BORN IN THE U.S.A.

CIRCLE 156 ON READER SERVICE CARD

Briefs

Indirect Atomic Absorption Determination of Anionic Surfactants in Wastewaters by Flow Injection Continuous Liquid–Liquid Extraction 2265

A selective method for determining the overall concentration of the anionic surfactants using a two-phase FIA system is described. Under optimum experimental conditions, the range of detection for detergents is 0.1–5.0 μg/mL.

Mercedes Gallego, Manuel Silva, and Miguel Valcárcel*, Department of Analytical Chemistry, Faculty of Sciences, University of Córdoba, Córdoba, Spain *Anal. Chem., 58 (1986)*

Solvent Extraction Studies of Lanthanum(III) and Neodymium(III) with Ionizable Macrocyclic Ligands and Thenoyltrifluoroacetone 2269

TTA is used as an extractant in the presence of 1,7-diaza-4,10,13-trioxacyclopentadecane-*N*,*N*′-diacetic acid and 1,10-diaza-4,7,13,16-tetraoxacyclooctadecane-*N*,*N*′-diacetic acid as macrocyclic ionophores at high and low pH.

V. K. Manchanda and C. Allen Chang*, Department of Chemistry, University of Texas at El Paso, El Paso, Tex. 79968-0513 *Anal. Chem., 58 (1986)*

Determination of Sub-Part-per-Trillion Amounts of Cobalt by Extraction and Photoacoustic Spectroscopy 2275

Ultratrace amounts of cobalt at parts-per-trillion levels are extracted into *m*-xylene from aqueous solution as nitrosonaphthol chelates and determined colorimetrically using PAS.

Takehiko Kitamori*, Kazumichi Suzuki, Tsuguo Sawada, Yohichi Gohshi, and Kenji Motojima, Energy Research Laboratory, Hitachi, Ltd., 1168 Moriyama, Hitachi, Ibaraki 316, Japan, and Department of Industrial Chemistry, Faculty of Engineering, University of Tokyo, 7-3-1 Hongo, Bunkyo, Tokyo 113, Japan *Anal. Chem., 58 (1986)*

Electrochemistry in the Gas Phase. Use of Ultramicroelectrodes for the Analysis of Electroactive Species in Gas Mixtures 2278

Ultramicroelectrodes are demonstrated to be sensitive and selective detectors for analytes in the gas phase. For some analytes, they are 4–6 orders of magnitude more sensitive than thermal conductivity detectors.

Jamal Ghoroghchian, Fereshteh Sarfarazi, Timothy Dibble, John Cassidy, Jerry J. Smith, Andrea Russell, Gordon Dunmore, Martin Fleischmann, and Stanley Pons*, Department of Chemistry, University of Utah, Salt Lake City, Utah 84112 *Anal. Chem., 58 (1986)*

Neutral Carrier Based Ca^{2+}-Selective Electrode with Detection Limit in the Sub-Nanomolar Range 2282

Ca^{2+}-selective liquid membrane electrodes based on the synthetic neutral carrier ETH 129 show a Na^+ and K^+ rejection by a factor of $10^{7.4}$ and 10^8, respectively. The detection limit in an intracellular ion background is approximately 100 pM Ca^{2+}.

Urs Schefer, Daniel Ammann, Ernö Pretsch, Urs Oesch, and Wilhelm Simon*, Department of Organic Chemistry, Swiss Federal Institute of Technology (ETH), Universitätstrasse 16, CH-8092 Zürich, Switzerland *Anal. Chem., 58 (1986)*

Design of Neutral Hydrogen Ion Carriers for Solvent Polymeric Membrane Electrodes of Selected pH Range 2285

The dynamic pH range is directly related to the acidity constant of the active site on the ionophore. Further features for designing an SPM-based pH electrode are discussed.

Urs Oesch, Zbigniew Brzózka, Aipig Xu, Bruno Rusterholz, Gabriela Suter, Hùng Viet Pham, Dieter H. Welti, Daniel Ammann, Ernö Pretsch, and Wilhelm Simon*, Department of Organic Chemistry, Swiss Federal Institute of Technology (ETH), Universitätstrasse 16, CH-8092 Zürich, Switzerland *Anal. Chem., 58 (1986)*

Predicting Standard pH Values for Reference Buffer Solutions in Solvent Mixtures with Water 2290

Standard pH values for aqueous organic solvent mixtures of moderate to high dielectric constants can be predicted using temperature, composition, dielectric constant, and transfer activity coefficient.

Paolo Longhi, Torquato Mussini*, and Sandra Rondinini, Department of Physical Chemistry and Electrochemistry, University of Milan, Via Golgi 19, I-20133 Milano, Italy *Anal. Chem., 58 (1986)*

On-Line Differential Pulse Polarographic Detection of Carboplatin in Biological Samples after Chromatographic Separation 2293

Increased sensitivity is achieved with a pulse amplitude of −250 mV at a potential of −1.6 V. The detection limits are 0.1 μM carboplatin in plasma ultrafiltrate and 1 μM in urine.

Frits Elferink*, Wim J. F. van der Vijgh, and Herbert M. Pinedo, Free University Hospital, Department of Oncology, De Boelelaan 1117, 1081 HV Amsterdam, The Netherlands *Anal. Chem., 58 (1986)*

Convolution: A General Electrochemical Procedure Implemented by a Universal Algorithm 2296

Concentrations at an electrode surface can be calculated from the faradaic current for a variety of geometric and kinetic conditions. A convolution algorithm is derived that applies equally to all situations.

Keith B. Oldham, Department of Chemistry, Trent University, Peterborough, Ontario K9J 7B8, Canada *Anal. Chem., 58 (1986)*

Ion Intensity and Image Resolution in Secondary Ion Mass Spectrometry 2300

Multivariate statistical methods are developed for resolving ion intensity data from secondary ion mass spectra and ion images into chemically meaningful compounds.

Margaret E. Kargacin and Bruce R. Kowalski*, Laboratory for Chemometrics, Department of Chemistry, BG-10, University of Washington, Seattle, Wash. 98195 *Anal. Chem., 58 (1986)*



A Pledge To Our Customers...For Now, And The Future.

For over sixty years, Matheson Gas Products has been committed to service, quality, safety and innovation. We've provided you with the best. And, we renew our commitment for the next sixty years.

Service: We'll Help You Solve Application Problems
Have a question regarding a new or difficult application? Matheson employees are committed to helping you find an answer. Every Matheson location has technical specialists — recognized as authorities in the scientific community — specifically available to work with you. As a Matheson customer, you can expect this service. And, if we do not have an appropriate product to answer your need, we are prepared to develop one.

Quality: An Unbending Commitment To Excellence
Matheson became the world leader by selling our products and services to customers who insisted on the best. We know that good quality control adds to the cost, but we'll never compromise our commitment to quality by shipping a product that does not meet specifications. Our commitment to quality demands excellence.

Safety: We Remain Devoted To A Safer Workplace
Matheson made a commitment to safety education long before it became popular. Today, we still believe information is the key to safety. We routinely give safety seminars to our customers to help them educate their employees. And, Matheson's unique reference books are known worldwide as invaluable information sources for anyone using compressed gases.

Innovation: A Continuous Effort To Bring You The Most Progressive New Products
Here, at Matheson, we apply the most advanced technical resources to provide you with innovative new products. Whatever you require: a purer gas, a custom gas mixture, a special pressure regulator or a complete gas handling system. Talk to Matheson. We have the answer to your current needs.

Matheson®
Gas Products
World Leader in Specialty Gases & Equipment
30 Seaview Drive, Secaucus, NJ 07094

CIRCLE 136 ON READER SERVICE CARD

Driving Lessons Included!

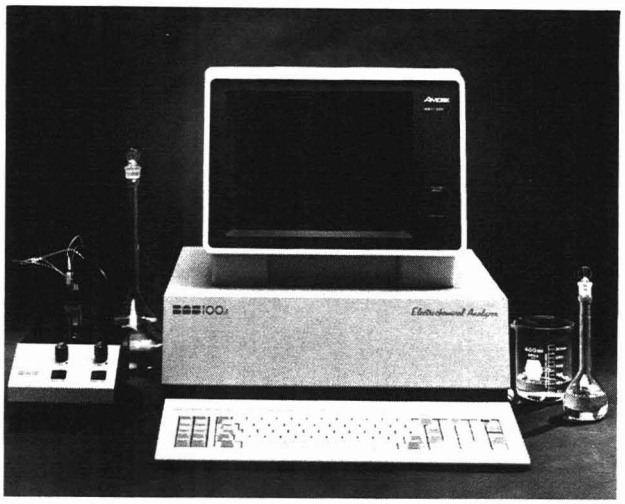

What do the new BAS-100A Electrochemical Analyzer and an Italian sports car have in common? Both are fast, sleek, powerful, fully loaded, and ready for action! The BAS-100A has more ways of reaching the answer to an electroanalytical problem than any other "vehicle" on the road, and it makes the going fun!

New programs and system architecture facilitate the techniques of chronoamperometry, hydrodynamic voltammetry, hydrodynamic modulation voltammetry, hydrodynamic amperometry, AC impedance, and many other pulse and D.C. waveforms. The BAS-100A features improved iR compensation and expanded data handling and storage. New "micro" voltammetric electrodes can now be accommodated! An external computer (the BASpc™) develops methods files for transfer to the BAS-100A and further massages collected data.

Give us a call for a test drive.

P.S. One big difference: you can buy four BAS-100A Analyzers with all the options for the price of one Ferrari, and you won't get a ticket for speeding.



BAS

Bioanalytical Systems, Inc

2701 Kent Ave
West Lafayette
Indiana 47906

Telex: 276141
(317) 463-4527

CIRCLE 17 ON READER SERVICE CARD

Briefs

Evaluation of Multipoint Kinetic Methods for Immunoassays: Kinetic Quantitation of Immunoglobulin G **2306**

Stopped-flow mixing with nephelometric measurements is used to monitor the time of the reaction. A variety of kinetic parameters are evaluated for the quantitation of IgG.

John W. Skoug and Harry L. Pardue*, Department of Chemistry, Purdue University, West Lafayette, Ind. 47906

Anal. Chem., 58 (1986)

Two-Method Verification of Hydrogen Peroxide Determinations in Natural Waters **2312**

An iodometric titration method using amperometric end-point detection is described with detection limits of 0.02 μM. In field tests, the method confirms data obtained by a sensitive fluorometric method.

R. J. Kieber* and G. R. Helz, Department of Chemistry and Biochemistry, University of Maryland, College Park, Md. 20742

Anal. Chem., 58 (1986)

Unattended, Robotic Drug-Release Testing of Enterically Coated Aspirin **2316**

A robotic drug release testing system is developed that is capable of performing multiple, unattended dissolution runs. The performance of the system has been validated by comparison with an HPLC method, drug release manual data, and the analysis of USP calibrator tablets.

R. J. Eckstein and G. D. Owens*, The Procter and Gamble Company, Miami Valley Labs, P.O. Box 39175, Cincinnati, Ohio 45247, and **M. A. Baim and D. A. Hudson,** The Procter and Gamble Company, Sharon Woods Technical Center, 11511 Reed Hartman Highway, Cincinnati, Ohio 45241

Anal. Chem., 58 (1986)

Digital Simulation of the Measured Electrochemical Response of Reversible Redox Couples at Microelectrode Arrays: Consequences Arising from Closely Spaced Ultramicroelectrodes **2321**

A collection efficiency of 93% is observed for reoxidation of $Ru(NH_3)_6^{2+}$ generated at a central microelectrode 0.2 μm from two flanking collector microelectrodes.

Allen J. Bard*, Joseph A. Crayston, Gregg P. Kittlesen, Theresa Varco Shea, and Mark S. Wrighton*, Department of Chemistry, Massachusetts Institute of Technology, Cambridge, Mass. 02139, and Department of Chemistry, University of Texas, Austin, Tex. 78712

Anal. Chem., 58 (1986)

Correspondence

Charge Exchange in Binary Mixtures of Polycyclic Aromatic Hydrocarbons Using Photoionization–Ion Mobility Spectrometry **2331**

G. A. Eiceman* and V. J. Vandiver, Department of Chemistry, New Mexico State University, Las Cruces, N.M. 88003

Anal. Chem., 58 (1986)

FOXY matches fractions to your chromatogram.

Not to the clock.

Microprocessor control. Program your collection by absorbance peaks, timed intervals, or counted drops. You can even enter fraction size directly in ml if you have a WIZ peristaltic pump. FOXY rejects void volume before collection begins, and changes racks and volumes according to peaks or time.

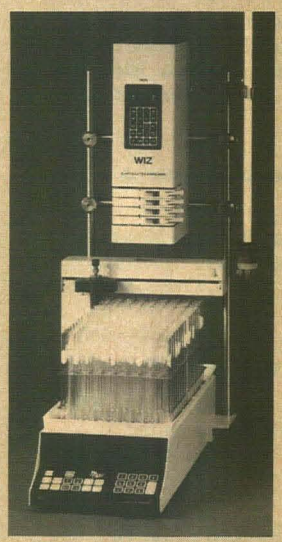

Eleven outputs allow valves, pumps, or other automation components to be turned on and off by the FOXY program. For HPLC, collect successive injections without resetting the program and changing racks, or overlay repeated injections of the same sample to collect identical peaks in the same tubes. FOXY does everything upon one signal from your chromatograph.

Isolate peaks in separate tubes. Identify peaks by elution times or with an Isco slope-detecting peak separator. Collect only desired peaks in one rack; put baseline effluent with unwanted peaks in another container or divert it to waste.

Holds up to 288 tubes. FOXY holds practically any size test tube, 28 mm scintillation vials, even 500 ml bottles. A preparative adapter lets you collect up to 72 fractions of unlimited size.

Even though FOXY is by far the most capable fraction collector you can buy, it still costs a lot less than the competition. Call toll-free [**800**] **228-4250**. Or write Isco, P.O. Box 5347, Lincoln, NE 68505.

ISCO



Circle 105 for literature. Circle 106 to have a technical representative telephone.



The Series 580 Isothermal Gas Chromatograph NEW from GOW-MAC Instrument Co.

- User friendly
- Sophisticated, yet compact
- Easily customized
- Supports micro organic techniques

GOW-MAC presents the Series 580 Isothermal Gas Chromatograph offering advanced technology in GC instrumentation for today's advanced laboratories.

Pertinent for trace gas analysis, the Series 580 is easily customized; it is the best application dedicated GC money can buy. . . Especially for routine analytical investigation in industrial QC laboratories, research laboratories or academic settings.

GOW-MAC is the largest manufacturer of chromatography detectors, and the 580 Series has an optimized detector for increased performance.

Compare the features; you will agree that now, more than ever, GOW-MAC belongs in your laboratory . . . Your work is worth it.

Send for your free Series 580 Brochure containing prices and specifications immediately.

GOW-MAC INSTRUMENT CO.

P.O. Box 32, Bound Brook, NJ 08805-0032
Telephone: 1-210-560-0600, Telex: 833174

CIRCLE 63 ON READER SERVICE CARD

Briefs

Excited Triplet State Infrared Spectrometry as an Analytical Technique 2335

David E. Bugay and Willem R. Leenstra*, Department of Chemistry, University of Vermont, Burlington, Vt. 05405 *Anal. Chem., 58 (1986)*

Indirect Electrochemical Detection in Liquid Chromatography 2337

Jiannong Ye and Richard P. Baldwin*, Department of Chemistry, University of Louisville, Louisville, Ky. 40292, and **K. Ravichandran,** Department of Chemistry, University of Georgia, Athens, Ga. 30602 *Anal. Chem., 58 (1986)*

Aids for Analytical Chemists

Digestion of Biological Materials for Mineral Analyses Using a Combination of Wet and Dry Ashing 2340

A. D. Hill*, K. Y. Patterson, C. Veillon, and E. R. Morris, U.S. Department of Agriculture, Agricultural Research Service, Beltsville Human Nutrition Research Center, Beltsville, Md. 20705 *Anal. Chem., 58 (1986)*

Generation of a Helium Inductively Coupled Plasma in a Low-Gas-Flow Torch 2342

Shi-Kit Chan, Raymond L. Van Hoven, and Akbar Montaser*, Department of Chemistry. The George Washington University, Washington, D.C. 20052 *Anal. Chem. 58 (1986)*

Modifying the Gaussian Peak Shape with More Than One Time Constant 2344

Roland Delley, Central Research, CIBA-GEIGY, Limited, CH-4002 Basel, Switzerland *Anal. Chem., 58 (1986)*

Mechanical Removal of the Central Sample Zone To Avoid Air Bubbles in Monosegmented Continuous Flow Analysis 2346

Célio Pasquini, Instituto de Química, Universidade Estadual de Campinas, 13081 Campinas, São Paulo, Brazil *Anal. Chem., 58 (1986)*

Multifunction Valve for Flow Injection Analysis 2348

Jun-ichi Toei* and Nobuyuki Baba, Development Department, Scientific Instrument Division, Toyo Soda Manufacturing Company, Ltd., 2743-1 Hayakawa, Ayase-shi, Kanagawa 252, Japan *Anal. Chem., 58 (1986)*

Rapid Headspace Analysis in Sealed Drug Vials by Multichannel Raman Spectrometry 2350

Laura Porter Powell*, American Cyanamid Company, Chemical Research Division, 1937 West Main Street, Stamford, Conn. 06904, and **Alan Campion,** Department of Chemistry, University of Texas, Austin, Tex. 78712 *Anal. Chem., 58 (1986)*

The NMR evolution continues:

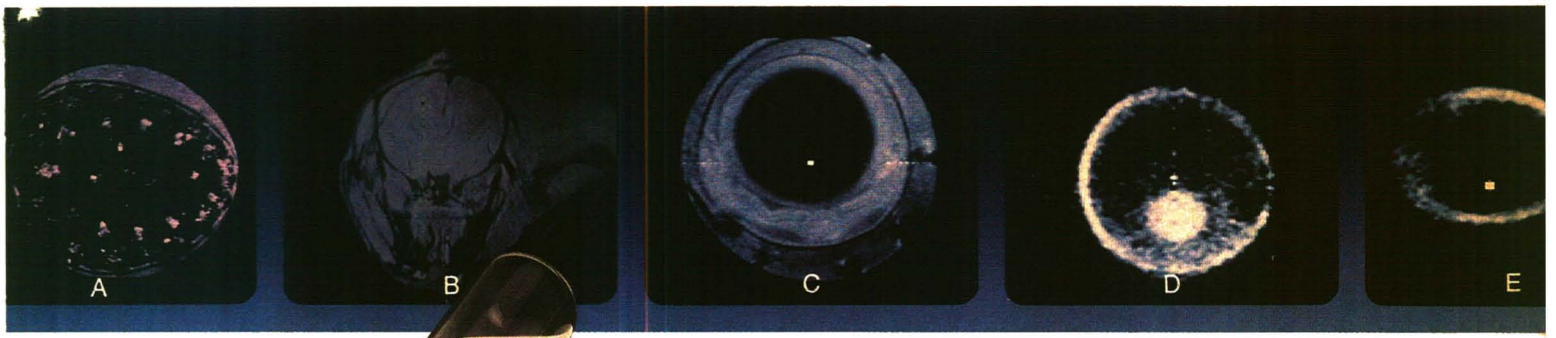

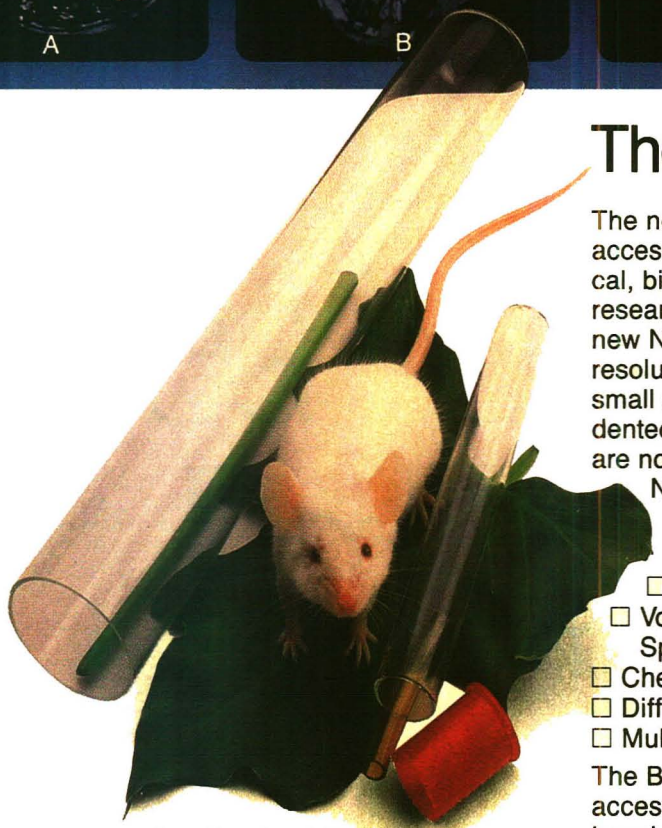

New visions through NMR microscopy.

The NMR microscope, at last.

The new Bruker microscopy accessory provides the medical, biological and materials researcher with an exciting new NMR capability: very high resolution NMR imaging on small samples. An unprecedented variety of experiments are now possible using the NMR microscope.

- ☐ T_1/T_2 Imaging
- ☐ Multi-Echo
- ☐ Multi-Slice
- ☐ Volume Selective Spectroscopy
- ☐ Chemical Shift Imaging
- ☐ Diffusion Imaging
- ☐ Multi-Nuclear Imaging

The Bruker NMR microscope accessory comes as a comprehensive package, requires virtually no modification of the standard spectrometer, and includes software and image processor.

Designed to work on both Bruker wide-bore AM and MSL systems, this versatile new accessory redefines the limits of spatial resolution.

The power of this technique is illustrated by the images shown above, which were obtained using an AM-400WB spectrometer with 9.4 Tesla operating field strength.

Fig. A: Cross sectional image of a philodendron stem. Resolution 19μ x 19μ x 300μ.
Fig. B: Cross sectional image of a mouse brain tumor. Resolution 100μ x 100μ x 500μ.
Fig. C: A cross sectional image of a mouse eye, 3 mm in diameter. Resolution 20μ x 20μ x 250μ.
Fig. D: Image of an ovum from laevis (frog egg). Resolution 10μ x 10μ x 250μ.
Fig. E: Diffusion of water through a piece of nylon. Resolution 50μ x 50μ x 1000μ.

Explore the potential of this technology. Ask your nearest Bruker representative for more details on the new microscope or other NMR products.

Bruker Instruments, Inc.
Manning Park, Billerica, MA 01821
In Europe: Bruker Analytische Messtechnik GmbH, Silberstreifen, D-7512 Rheinstetten 4, W. Germany

BRUKER *NMR systems designed to solve problems.*

CIRCLE 22 ON READER SERVICE CARD

The next time someone says, "It's just as good as J.T. Baker," see how they stand up to a few pointed questions.

For starters, ask them about consistent purity.

In laboratory reagents, purity is critical.

But consistent purity is everything!

To that end, no one (repeat, *no one*) requires more purity tests or has tighter specifications than J. T. Baker.

From selection of raw materials to finished products, Baker standards and testing capabilities go as far as the most advanced analytical instrumentation can take us. Not for just one container or reagent, or for one lot, but consistently, lot after lot . . . today and next year.

Proof of Consistent Purity

As proof of purity, long ago J. T. Baker pioneered printing the actual lot analysis on the labels of every 'BAKER ANALYZED'® Reagent. (Even today, there are still manufacturers who don't provide that information.) But the real proof is in comparing the actual lot analysis of the same 'BAKER ANALYZED' Reagent from two or three different lots. There's proof of purity. Consistent purity. And no one else can match us.



How about their hazard communication system?

Chances are they have none.

J. T. Baker can provide you with a Hazard Communication System which is built around an integrated 4-part program of product labels, Material Safety Data Sheets, training materials, and a Written Hazard Communication Program. It's unparalleled in reinforcing employee safety and facilitating compliance with Federal Hazard Communication requirements. And it should be. It was developed through Baker's eight years of experience in training over 50,000 safety and laboratory professionals. Best of all, the entire system could be yours, FREE!

What about service?

Our nationwide network of distributors is backed by Baker's ultra-modern distribution center in Jackson, Tennessee. The Jackson facility combines prompt replenishment of distributor stocks with a 24-hour drop-shipment service to ensure our distributors meet emergency requirements.

Our distributors have invested millions of dollars in inventory of Baker products, and they are dedicated to providing the best service in the industry.

When you order a 'BAKER ANALYZED' Reagent from one of our distributors, you can be confident that it will be delivered to your lab or stockroom—on time.

Now ask yourself this question:

Who should be your reagents supplier? Half-hearted imitators? Or J. T. Baker, the genuine innovator who for over 80 years has led the reagent industry in technology, quality, safety and service?

Even the imitators tell you the answer. After all, they wouldn't say, "It's just as good as J. T. Baker," if J. T. Baker weren't the best.

Call us today for a list of J. T. Baker distributors or to learn more about how we can help you implement an effective Hazard Communication Program.

It's toll free at 1-800-JTBAKER (in NJ 201-859-5411).

J.T.Baker®

They wouldn't say, "It's just as good as J. T. Baker," if J. T. Baker weren't the best.

222 Red School Lane • Phillipsburg, NJ 08865

CIRCLE 21 ON READER SERVICE CARD



Bioassay-Directed Chemical Analysis in Environmental Reseach

The identification of specific chemical compounds that can produce human health or ecological effects is a major research objective in environmental and health sciences. The impact of environmental pollution on human health, including mutagenic and carcinogenic effects, is a primary concern. Cancer is a generic term for various neoplastic diseases that can occur many years after exposure to a carcinogenic substance. The best means of eliminating cancer is to define precisely the nature of the carcinogenic chemical, mixture of chemicals, or enhancing factors in the environment that produce the cancer (*1*). Bioassay studies in the early 1960s showed that environmental mixtures such as cigarette smoke and ambient air particulates can cause cancer in animals. Extensive studies were undertaken to determine the chemical components that could be responsible for such an effect. It was found that most environmental samples were chemically complex and comprised of thousands of chemical compounds (*2*, *3*). Identification of the most biologically active compounds presented an enormous if not an impossible task.

During the mid-1970s several microbial tests were developed that were simple, cheap, rapid, and above all genetically very well defined (*4*). The bacterial reverse mutation test battery in *Salmonella* as developed by Ames et al. (*5*) provided a vast body of information on the presence of genotoxic activity not only in defined industrial chemicals, pesticides, and cosmetics but also in complex mixtures such as air, water, and other complex sources of pollutants. Although this test, and others like it, were used to determine the relative mutagenic potency for a wide variety of environmental samples, such studies did not yield infor-

0003-2700/86/A358-1060$01.50/0
© 1986 American Chemical Society

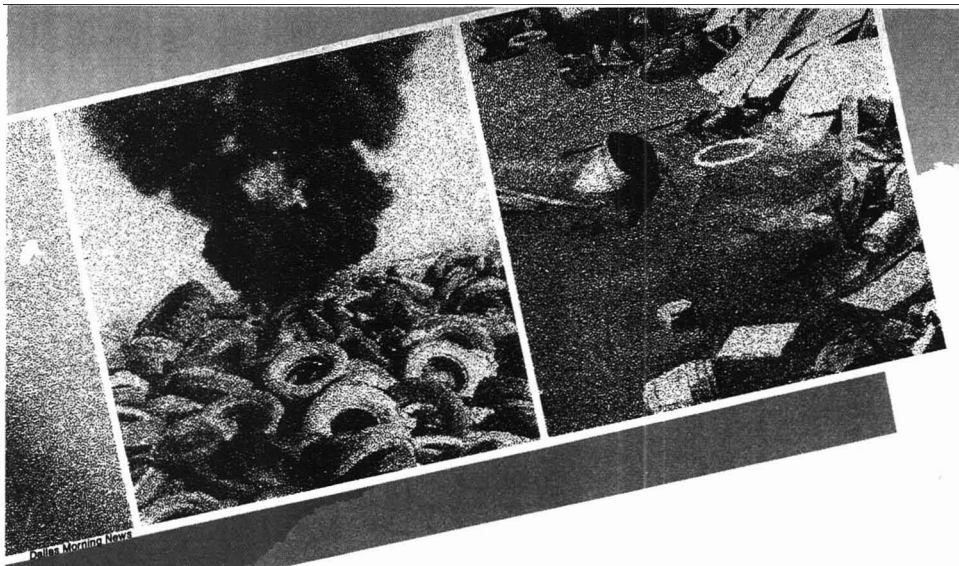

Report

Dennis Schuetzle

Research Staff
Ford Motor Company
Dearborn, Mich. 48121

Joellen Lewtas

U.S. Environmental Protection Agency
Research Triangle Park, N.C. 27711

mation on which specific compounds were primarily responsible for this activity.

The Ames tester strains were selected so that types of mutations (e.g., frame shift vs. base pair substitutions) can be distinguished. This information, together with differential responses (e.g., with and without microsomal activation), can be used to provide information about the general classes of chemicals causing the response. More recently, new tester strains that are sensitive to certain classes of chemical mutagens have been developed. For instance, strain TA98NR (Rosenkranz nitroreductase strain) is deficient in nitroreductase enzymes and therefore gives a reduced response to certain nitrated PAH compounds. The magnitude of results varies depending on the type of assay used, as shown for diesel particles in Table I. In addition, the contribution of an individual compound to total fraction mutagenicity is dependent on the type of bacteria used in the assay. These differences make it possible to apply these strains in a diagnostic way. Because strain TA98 has been used most frequently for assays of environmental samples, we will limit our discussion to its use in this REPORT.

Table I. Direct-Acting Mutagenicity of Diesel Particulate Extract (NBS SRM 1650)

Bacterial strain	Mutagenicity (rev/μg)
TA98	5.0
TA98NR	1.5
TA100	5.5
TA104	17.0

It became apparent in the late 1970s that these bioassays could be used in combination with chemical fractionation to greatly simplify the process of identifying significant mutagens in complex environmental samples, such as diesel particles, petroleum and petroleum substitutes, chemicals in drinking water (*6*), and commercial products (*7*). The use of short-term bioassays in conjunction with analytical measurements constitutes a powerful tool for identifying environmental contaminants. We have coined the term "bioassay-directed chemical analysis" to best describe this marriage of analytical chemistry and biology. The objective of this methodology is to identify key compounds in various types of air pollutant samples. Once that task is completed, studies on metabolism, sources, environmental exposure, and atmospheric chemistry can be undertaken.

The protocol for bioassay-directed chemical analysis illustrated in Figure 1 was developed originally in our laboratories during the late 1970s (*8*, *9*) to identify chemical mutagens in diesel particulate extracts. At about the same time similar techniques for the identification of chemical mutagens in synthetic fuels were reported by Guerin et al. (*10*) and Wilson et al. (*11*) and in drinking water by Tabor et al. (*12*). More recently, these techniques have been used in a rigorous manner for the identification of mutagens in other types of air pollution samples, such as ambient air particulates, diesel particulates, and wood smoke (*13*–*15*), and in water pollution samples such as river water (*16*). Most of our work has been directed toward the characterization of ambient air and diesel particulates. We will use these examples to illustrate the analytical logic used in identifying the mutagenic components of complex mixtures.

Proper sampling, storage, and extraction of an environmental sample are crucial parts of the analysis. If the sample is not qualitatively and quantitatively representative of what is present in the environment, results obtained from the bioassay-directed chemical analyses are of little value in assessing environmental risk. However, it is not necessary to use a representative sample to develop methods. Some selected large samples collected in early studies were used for methods development. Since that time, the National Bureau of Standards (NBS) has made available a number of environmentally related reference materials that are useful in developing bioassay-directed chemical analysis techniques. These materials were not meant to be representative samples from which conclusions could be made concerning their origin or environmental risk. The major advantage of this approach is that a common and representative material is available to many laboratories for intercomparison of results. Two materials that have been used most widely for this purpose are NBS SRM 1650 (heavy-duty diesel particulates) and NBS SRM 1649 (ambient

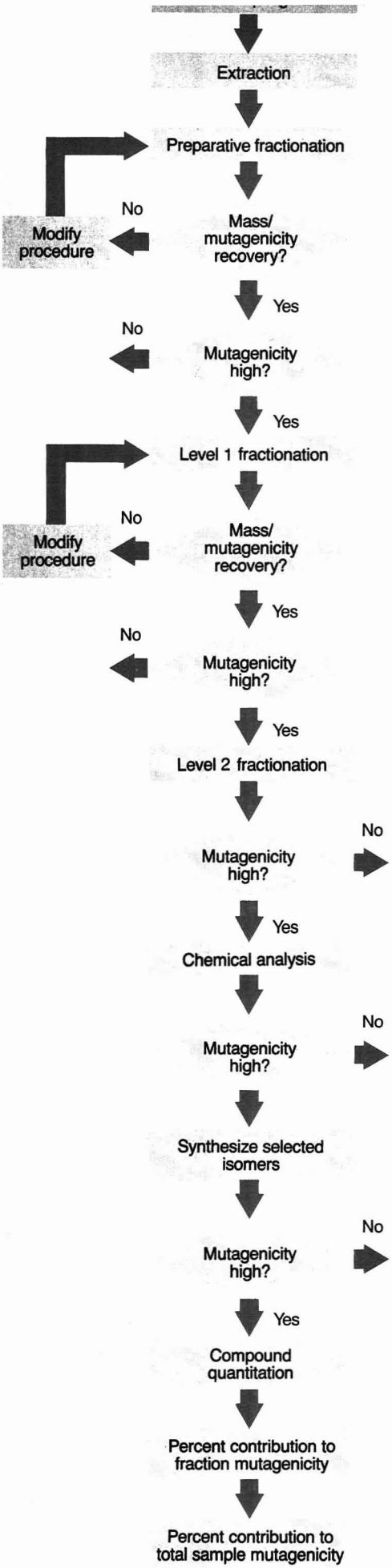

Figure 1. Protocol for bioassay-directed chemical analysis

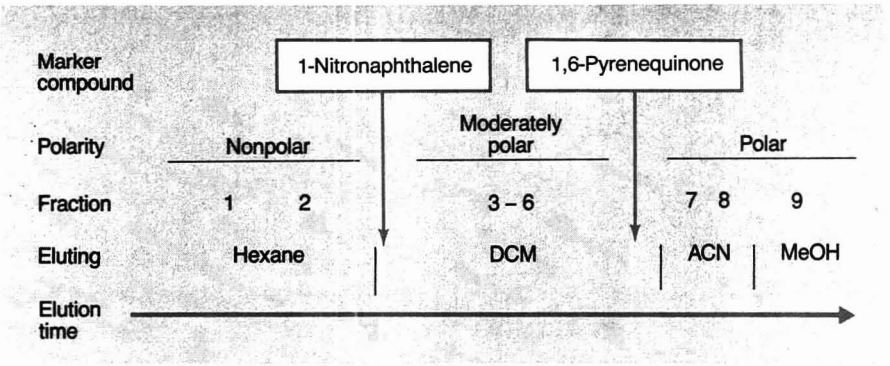

Figure 2. Designation of nonpolar, moderately polar, and polar fractions using normal-phase HPLC in the level 1 fractionation scheme

air particulate matter collected in Washington, D.C.).

Extraction

Sequential extraction with increasingly polar solvents, binary solvents, and supercritical fluid extraction are used to separate organic material from particulates and other types of solid environmental samples. A two-step extraction process using methylene chloride followed by methanol is effective for efficient recovery of mutagenicity and mass for several types of combustion emission samples. Liquid–liquid extraction using dichloromethane and diethyl ether is suitable for extraction of mutagenic material from heavily polluted waters. Adsorption of pollutants on resins followed by solvent elution is effective for concentrating organics that are present in low concentrations (*17*).

Preparative fractionation

A number of prefractionation and preseparation techniques have been developed to help simplify the analysis of environmental samples. They are usually applied on a preparative or semipreparative scale to yield gram to milligram quantities, respectively, of samples. The two most widely used techniques are chromatography on an open normal-phase silica column to separate groups of compounds on the basis of polarity and separation of compounds into acidic, basic, and neutral fractions.

Early attempts to chemically characterize the trace components in sample fractions proved to be extremely difficult, and it was estimated that hundreds of compounds were present. However, bioassay analysis helped researchers decide which fractions should be studied in more detail (Figure 1).

One of the concerns of the early work in the late 1970s was the potential loss and formation of mutagenic substances during analysis. The procedural recovery of mass and mutagenicity is determined by combining the individual fractions to produce a reconstituted sample. The mass and mutagenicity of this sample are then compared with that of the unfractionated sample. Another test is to determine if the biological activity of the unfractionated sample equals the sum of the activities of the individual fractions. If they are unequal, the mutagenicity may be due to synergistic or toxic effects or to the fact that cell killing was not taken into account. If the separation removes highly toxic components from the mutagenic components, the additivity of the fraction mutagenicities may be greater than 100%. Any bioassay that has enough sensitivity to obtain good quantitative results (*6*, *13*) on small (microgram) quantities of material can be used in the bioassay-directed chemical analysis technique.

Level 1 fractionation

Normal-phase high-performance liquid chromatography (HPLC) is a highly reproducible technique that separates environmental samples into chemical fractions of increasing polarity using hexane, dichloromethane (DCM), acetonitrile (ACN), and methanol (MeOH) as eluents (*8*). The reference materials 1-nitronaphthalene and 1,6-pyrenequinone may be used as chemical markers to designate the separation of samples into nonpolar (1–2), moderately polar (3–6), and polar (7–9) fractions (Figure 2). Results from a number of laboratories using slightly different fractionation procedures can be compared using this definition of polarity (*18*). It was found that the nonpolar fractions accounted for less than 2–3% of the total extract mutagenicity and that the distribution of moderately polar and polar materials was dependent on the sample source (Figure 3).

Table II gives the distribution of mass and mutagenicity for nonpolar, moderately polar, and polar fractions of NBS SRM 1650. Although 54% of the recovered mutagenicity is associated with polar compounds (fractions 7–9), the additivity of mass (94%) and mutagenicity (79%) is good. Diesel

Those small LC columns need a better filter.

So Rheodyne made one.

We're talking about those 1-mm or 2-mm microbore columns and short high-speed columns.

Like larger conventional columns, they should have an inlet filter to protect them from particle contamination. Unlike conventional columns, they are highly sensitive to sample dispersion within this filter. Filter sample dispersion that has little effect on the resolution of a conventional column can seriously reduce the resolution of a small column.

To remedy this situation, Rheodyne made two low-dispersion filters designed especially to preserve the resolution of small columns. The Rheodyne 7315 for microbore columns. And the Rheodyne 7335 for short high-speed columns. They're identical except for a tiny internal filter element.

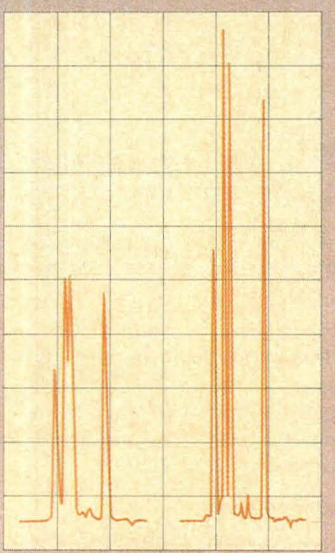

LEFT: Conventional filter with 1 mm x 300 mm column.
RIGHT: Rheodyne 7315 low-dispersion filter with 1 mm x 300 mm column.

The accompanying chromatograms show the dramatic improvement in resolution that occurs when a new low-dispersion filter is used in place of a conventional filter.

For more about these new column inlet filters—plus our Tech Note 6 describing the experimental effect of filters on resolution—contact Rheodyne, Inc., P.O. Box 996, Cotati, California 94928, U.S.A. Phone (707) 664-9050.

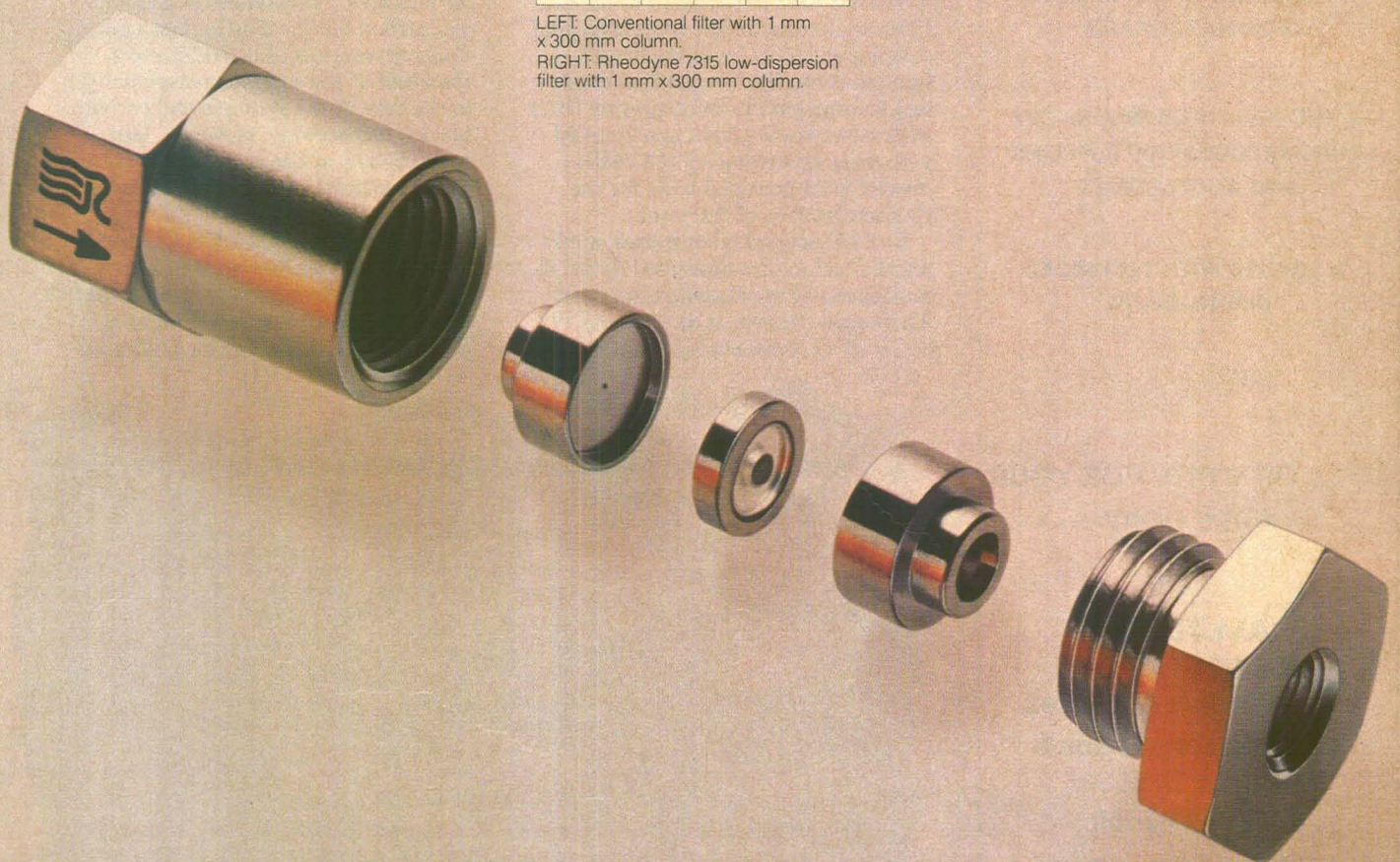

RHEODYNE

THE LC CONNECTION COMPANY

CIRCLE 182 ON READER SERVICE CARD

FREE



CHROMATOGRAPHY CATALOG

★ HUNDREDS OF REFERENCE CHROMATOGRAMS

★ THOUSANDS OF INNOVATIVE CHROMATOGRAPHIC SUPPLIES AND ACCESSORIES

★ LOADED WITH TECHNICAL INFORMATION

CALL OR WRITE FOR YOUR FREE COPY

ALLTECH ASSOCIATES
APPLIED SCIENCE LABS
2051 Waukegan Road
Deerfield, Il. 60015
(312) 948-8600

CHROMATOGRAPHY

CIRCLE 4 ON READER SERVICE CARD

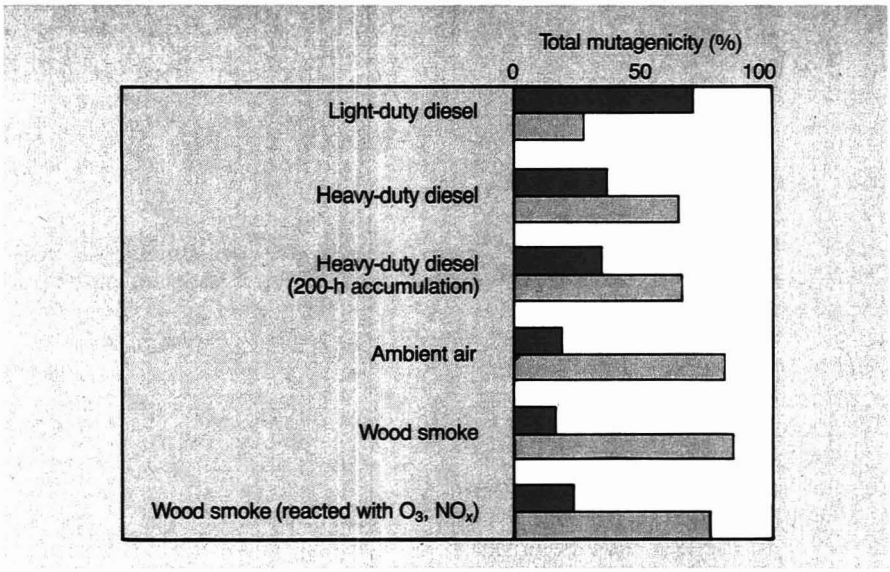

Figure 3. Distribution of mutagenicity (direct-acting TA98) between the moderately polar (green) and polar (blue) mutagenic fractions for six air particulate samples

particulate extract samples usually yield mass and mutagenicity additivities of greater than 90% and 70%, respectively, and mass and mutagenicity recoveries of better than 90%.

Chemical analysis

Studies were undertaken in the late 1970s to determine the composition of samples collected from the level 1 fractionation. High-resolution capillary column gas chromatography (GC) with selective detectors and coupled with mass spectrometry (GC/MS) proved to be powerful tools for the characterization of fractions.

By 1980 several laboratories, applying the techniques described so far, simultaneously made some important discoveries. Guerin et al. (*10*) and Wilson et al. (*11*) discovered the presence of highly mutagenic polynuclear aromatic amines (PAH–NH_2) in synfuels; Schuetzle et al. (*8*) found a significant mutagen, 1-nitropyrene, in diesel particles; and Lofroth et al. (*19*) and Rosenkranz et al. (*20*) identified 1,3-, 1,6-, and 1,8-dinitropyrenes as the major mutagenic substances in commercial carbon blacks. The amines and dinitropyrenes accounted for more than half of the sample mutagenicity in the case of the synfuels and carbon blacks, respectively. However, less than 25–30% of the mutagenicity of diesel particles could be accounted for by the 1-nitropyrene.

In the case of SRM 1650, GC and GC/MS analysis showed that hundreds of compounds were still present in each fraction. Figure 4 depicts a portion of a chromatogram generated

Table II. Mass and Mutagenicity Distribution (TA98, Direct Acting) for NBS SRM 1650[a]

Fraction	Distribution of mass (%)	Distribution of mutagenicity (%)
Nonpolar		
1	0.6	0
2	0.7	0
Moderately polar		
3	1.3	0
4	2.6	19
5	2.4	10
6	1.3	7
Polar		
7	3.7	24
8	41.6	9
9	39.9	10
Percent recovered	94.0	79

[a] Data from Reference 18

Brownlee Takes the Mystery Out of Supercritical Fluid Chromatography (SFC).

Think of SFC as an extension of gas chromatography. An extension into molecular weight ranges which would require an oven temperature of over 400°C by conventional GC. Because SFC is really dense gas chromatography, it allows you to separate high molecular weight or thermally labile compounds at oven temperatures below 200°C.

Now think about what you really need for SFC. You need a GC, a special pumping system and controller, column restrictor and SFC software. You need the Brownlee SFC System One, complete with the Hewlett-Packard Model 5890 GC and our MicroGradient System.

The heart of SFC is the pump. Our MicroGradient System is the only pumping system for SFC with a proven three-year history and over 400 installed units. The built-in microprocessor comes with SFC software, ready to run. You don't need an external computer. Our pumping system automatically refills with liquefied gas (such as CO_2). There is no need to cool the pump or the supply line.

With the Brownlee SFC System One, anyone experienced in capillary GC can be doing SFC within a day. We'll install it in your lab and train your staff. Our applications scientists will be happy to share their experience with you.

Contact Brownlee Labs today for a copy of our Technical Note 925, "Supercritical Fluid Chromatography (SFC): Bridging the Gap Between GC and HPLC." And find out how easy it is to get started in SFC.

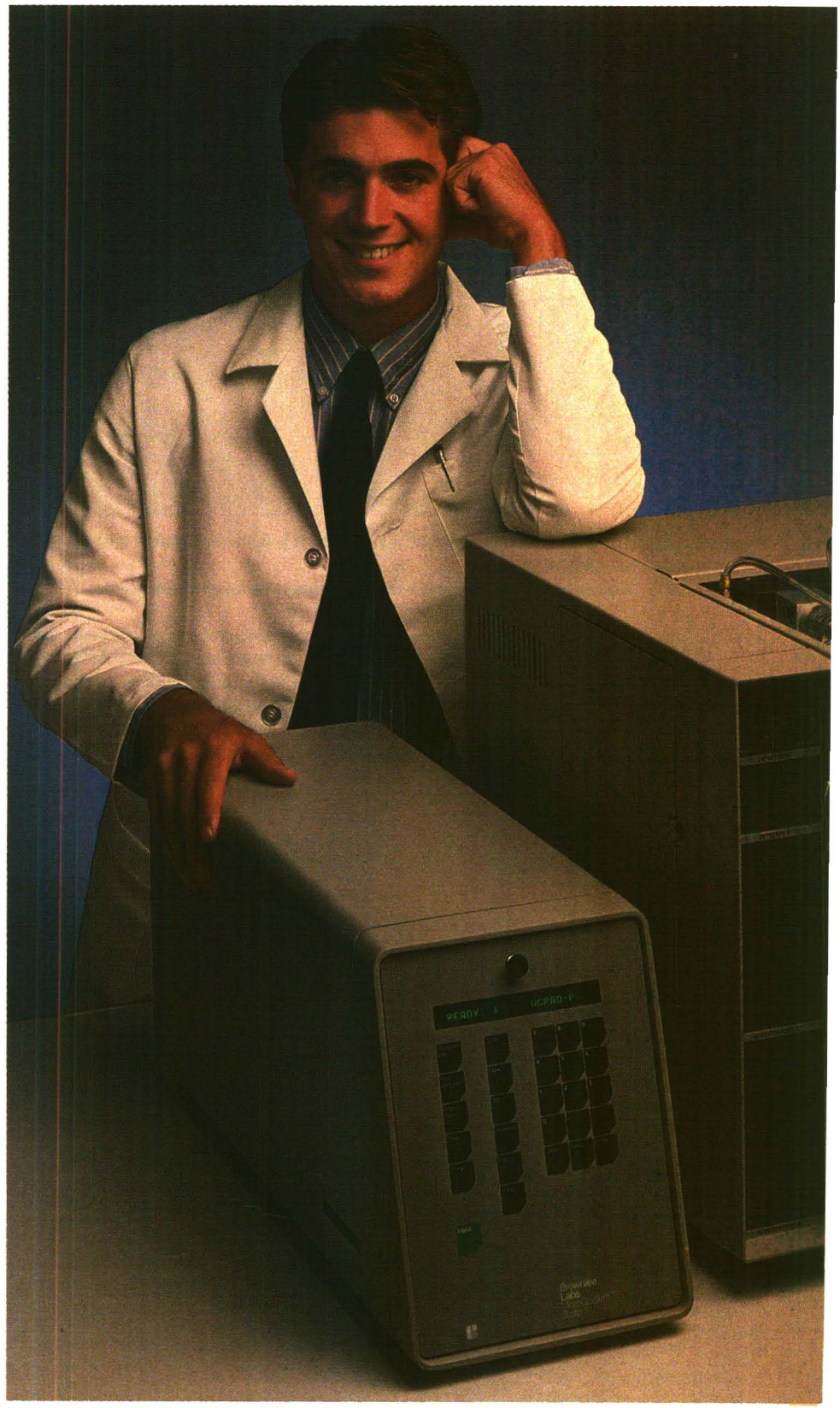

Brownlee Labs

A Division of Applied Biosystems, Inc.

2045 Martin Avenue Santa Clara, CA 95050 408/727-1346 800/231-4038

CIRCLE 20 ON READER SERVICE CARD

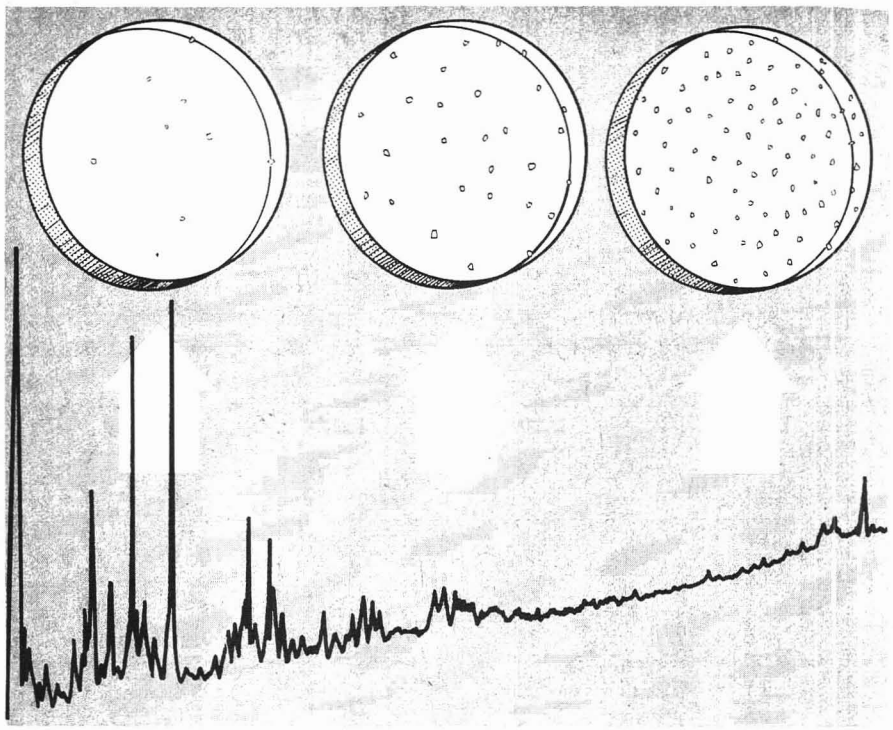

Figure 4. Capillary gas chromatogram of fraction 5 of a light-duty diesel sample with nitrogen-selective detection

Petri dishes at top illustrate results of Ames assays of subfractions of the diesel sample fraction

from the capillary column GC analysis of fraction No. 5 of a light-duty diesel sample using a nitrogen-selective detector. Scores of nitrogen compounds were found to be present in this fraction. GC/MS analysis verified that most of the nitrogen-containing compounds were nitrated polynuclear aromatic hydrocarbons (nitro PAHs). Ames assays of subfractions of fraction No. 5 showed that most of the mutagenicity was associated with compounds that eluted in the last one-third of the chromatogram.

Further analysis was made using direct-probe high-resolution mass spectrometry, high-resolution GC/high-resolution MS, and mass spectrometry/mass spectrometry (MS/MS). An important finding in these studies was that the moderately polar chemical fractions primarily consisted of substituted PAH compounds with ring sizes of 2–6 and the substituents consisted of hydroxy, aldehyde, anhydride, nitro, ketone, dinitro, and quinone functional groups (*8*). A potentially important group of mutagens, the nitrohydroxypyrenes, was identified in these studies (*21*).

Although a multitude of compounds were identified or tentatively identified, it was obvious that such fractions were still too complex to allow identification of chemical mutagens and that further separation of each fraction into subfractions would be necessary.

Level 2 fractionation

Further developments in HPLC, high-performance thin-layer chromatography (HPTLC) (*22*), and mutagenicity testing (*23*) have contributed to a much finer tuning of this combined chemical and biological approach to the characterization of mutagens in environmental samples. HPLC can generate scores of fractions, each of which is tested for mutagenicity. We refer to this resulting relationship of fraction mutagenicity to

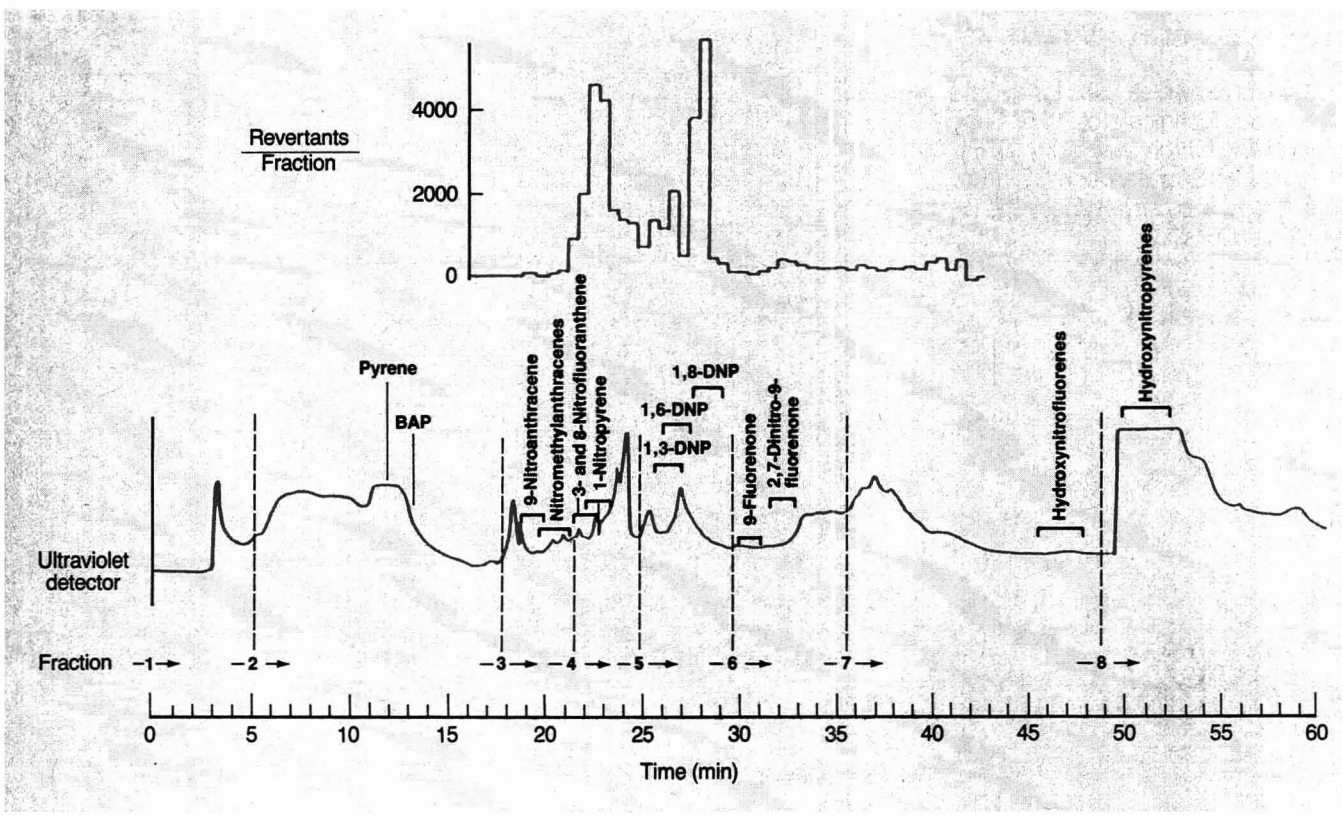

Figure 5. Ames assay chromatogram (TA98, without activation) and HPLC–UV analysis of a light-duty diesel particulate extract (level 1 fractionation)

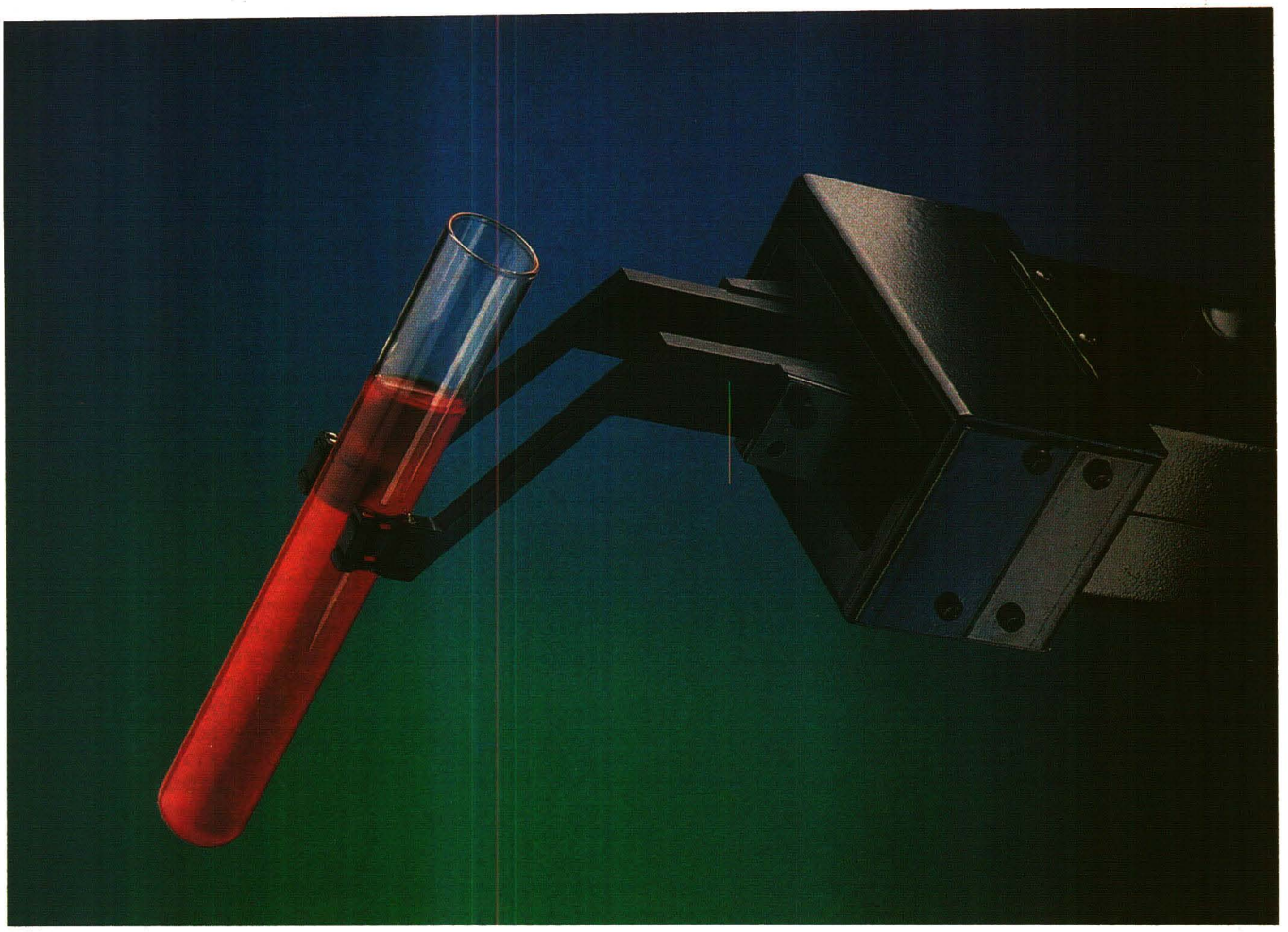

We made this hand so you could work with your head.

Analytical chemistry requires you to use your head. And your hands. With our MasterLab™ Robotics System you can use your mind more. And your hands less.

Over and over again.

It's like having an assistant who doesn't mind doing repetitive, routine, or potentially hazardous sample preparation while you focus your energies on such things as methods development, planning, scheduling, evaluating, reviewing—the things that you can do, but the robot can't.

You'll save valuable hours while the robot carries out its tasks. And you'll be free of the worry that fatigue, oversight or operator variability might threaten the repeatability of your results. Every repetitive procedure is performed precisely the same every time.

Because the MasterLab System interfaces with such a broad range of lab equipment, instrumentation and computers, its versatility is almost limitless. Today, MasterLab Systems are working around the clock—and around the world—with materials as diverse as cancer drugs and plutonium. Cigarette filters and shampoos.

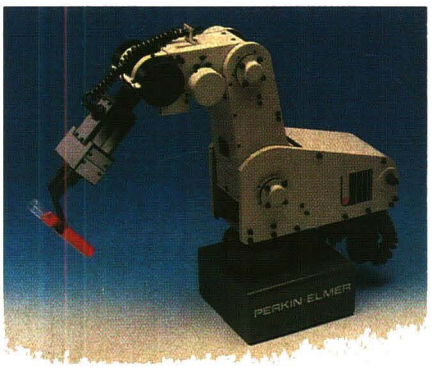

We're with you every step of the way.

The MasterLab System is supported by an experienced field staff to help you determine how best to use the system, program it and develop new uses for the system. We even have a special robot hotline to answer any questions you might have.

Get the full story today. Contact your local Perkin-Elmer representative. Or in the U.S., use the hotline and give us a call at: 1-800-ROBOT-PE.

Perkin-Elmer Corp., 761 Main Ave., Norwalk, CT 06859-0012 U.S.A. Tel: (203) 762-1000. Telex 965-954.

Bodenseewerk Perkin-Elmer & Co., GmbH, Postfach 1120, 7770 Ueberlingen, Federal Republic of Germany. Tel: (07551) 810.

Perkin-Elmer Ltd., Post Office Lane, Beaconsfield, Bucks HP9 1QA, England. Tel: Beaconsfield (049 46) 6161.

PERKIN-ELMER

CIRCLE 167 ON READER SERVICE CARD

Table III. Distribution of Mutagenicity and Mass for Acid, Base, and Neutral Subfractions of Polar Fractions 7, 8, and 9[a]

Subfraction	% distribution of mutagenicity (mass)		
	7	8	9
Acid	4 (27)	22 (39)	39 (70)
Base	19 (28)	14 (7)	4 (4)
Neutral	66 (59)	84 (41)	162 (26)
Total recovery	89 (114)	120 (87)	205 (100)

[a] Jensen, T.; Ball, J. Presented at the Symposium on the Chemical Characterization of Diesel Exhaust Emissions Workshop II, Coordinating Research Council, Dearborn, Mich., March 4–6, 1985.

fraction elution time as a bioassay chromatogram or an Ames assay chromatogram in cases in which the Ames test is used (*24*). A bioassay chromatogram for a diesel particulate sample is illustrated in Figure 5. The lower portion of the figure shows the corresponding HPLC chromatogram using a UV detector. The most mutagenic fractions have elution times that approximately coincide with 1-nitropyrene, 3-nitrofluoranthene, 8-nitrofluoranthene, 1,3-dinitropyrene, 1,6-dinitropyrene, 1,8-dinitropyrene, and 2,7-dinitro-9-fluorenone reference compounds.

GC/MS is a powerful technique for quantitative analysis of these trace constituents. Deuterated standards are added to the extracts before sample analysis, and quantitative results are readily obtained by comparing the signals from the eluting native and deuterated compounds. On the basis of such analysis it was found that 30–40% of the total recovered extract mutagenicity of SRM 1650 was attributable to the seven moderately polar nitro PAHs. The remainder of the mutagenicity (10–15%) was attributable to the presence of an unidentified compound or compounds eluting between 23 and 26 min; 30–35% was recovered in the polar fractions, and 5–10% was distributed about equally among the remaining fractions.

Although separation of the sample into acid, base, and neutral fractions is usually done in the early stages of sample preparation, this procedure can be used to further simplify the polar fractions. As an example, some preliminary data on the distribution of mutagenicity for the acid, base, and neutral fractions 7, 8, and 9 of SRM 1650 are given in Table III. This analysis shows that the most mutagenic compounds in the diesel sample are neutral in character. The additive mutagenicity for the acid, base, and neutral fractions is close to that of the unfractionated fraction 7. However, the additive mutagenicity for fractions 8 and 9 exceeded 100%. It is postulated that these high recoveries are indicative of chemical changes that may have occurred during acid–base extraction or separation of toxic compounds from these fractions. High-resolution mass spectrometric analysis of fractions 8 and 9 shows that organic esters and acids of PAHs and aliphatic compounds are major components. Acid or base hydrolysis of PAH esters could account for increased mutagenicity.

The specific fractionation scheme that most effectively separates the mutagens from the nonmutagens while minimizing the destruction or creation of mutagens varies with the types of complex mixture being analyzed. Diesel emissions from different sources will vary in the amount of specific components but the general composition is sufficiently consistent to develop one approach to the bioassay-directed chemical analysis, although several may be equally effective.

The scheme used to identify mutagens in synfuels has concentrated on preparative separative techniques because large quantities of materials were needed for extensive biological and chemical characterization studies. A relatively high level of mutagenic activity was found in an 800–850 °F distillation fraction of a synfuel sample (*10*). Nitrogen-containing compounds were separated on an alumina column using $CHCl_3$/ethanol. Level 1 fractionation was accomplished on a silicic acid column. GC/MS was used to identify PAH-amines as the major mutagenic species in the synfuels.

Ambient air particulates contain more chemical components than most other types of environmental samples. For this reason, the identification of mutagenic species in ambient air particulates has been more difficult than in diesel emissions. However, bioassay-directed chemical analysis procedures are being used to single out some potential candidate compounds.

LC and HPLC fractionation used in combination with acid–base–neutral separation appears to be an effective protocol for this purpose, as illustrated in Figure 6 (*25*). Good recovery of mass (98%) and mutagenicity (86%) for an extract of the NBS SRM 1649 air particulate sample was obtained by elution of five fractions on silica gel using hexane, hexane–benzene, methylene chloride, methanol, and acidic methanol (*26*).

SRM 1649 was used to develop the

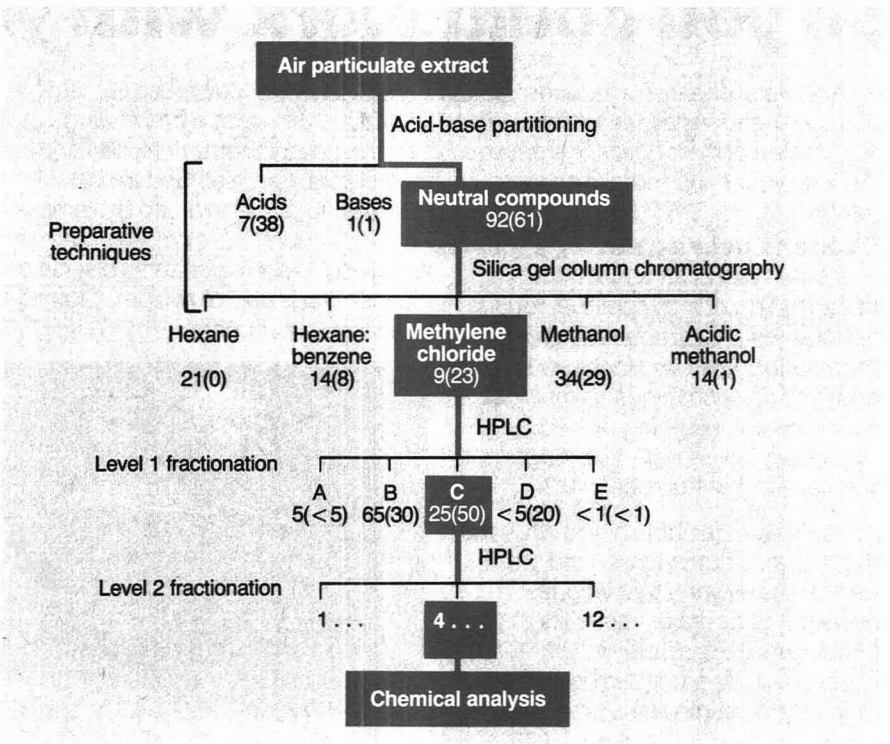

Figure 6. Bioassay-directed chemical analysis scheme for the analysis of NBS SRM 1649 (air particulate matter)

The numbers under each fraction represent the percentage distribution of mass and mutagenicity (in parentheses)

No Comparison.



Finally, a GC/FTIR designed for chromatographers.

The new HP 5965A IR detector makes capillary GC/FTIR an affordable, routine technique in the chromatography lab.

Not only does this new system give you the structural information you need, it's also more sensitive than most general-purpose FTIR instruments — including systems that cost two to three times as much. And it takes up a lot less space. (The detector itself is only eight inches wide.)

The IRD is the first system that lets you display and compare GC/FTIR and GC/MS data side by side on the same screen and in the same report. It'll even integrate library search results and produce a ranking of probable IDs based on hit quality and common matches.

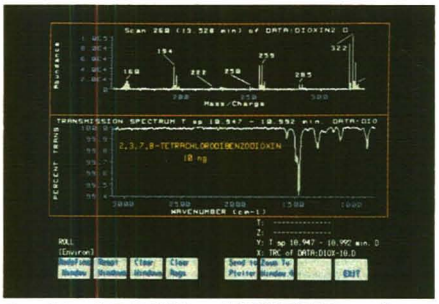

Combined GC/MS and GC/FTIR results on the IRD ChemStation screen.

It's easy to set up. Easy to operate. And easy to maintain. You don't need a special bench for it, and you don't have to tiptoe around it.

For more information, call the HP office listed in your telephone directory white pages and ask for an analytical product representative. Or write Hewlett-Packard Analytical Group, 1820 Embarcadero Road, Palo Alto, CA 94303.

HEWLETT PACKARD

AG04602

Circle 98 for literature. Circle 99 to have an HP representative call.

methodology for the ambient air samples. Once this methodology was developed, it was applied to fine air particles (<1.7 μm in diameter) collected in Philadelphia. The three fractions of greatest interest were the acid, methylene chloride, and methanol fractions, which produced 38%, 23%, and 29%, respectively, of the recovered mutagenicity (Figure 6). Because the methylene chloride fraction was more amenable to subfractionation by existing HPLC methods, this fraction was chosen for further fractionation. Normal-phase HPLC was used to fractionate the methylene chloride fraction (*26*).

The first HPLC subfractionation resulted in one fraction, methylene chloride-C, which contained nearly 50% of the mutagenicity in 25% of the mass. Analysis of this fraction by both electron impact and negative chemical ionization high-resolution (HR) GC/MS techniques indicated that the complexity of the sample was not reduced sufficiently to identify individual components. Subfraction C was further fractionated by normal-phase HPLC into 12 fractions for bioassay.

As we proceeded to higher levels of subfractionation, less and less mass was available for bioassay. In this study, the first-level fractions obtained from the preparative techniques were bioassayed in triplicate at seven doses with and without activation so that we could quantitate the distribution and recovery of mutagens. At the first and second levels of fractionation, fewer doses and plates were used for the bioassay until nearly the entire fraction was used for a single plate. Therefore, the ability to quantitate the recovery of both mass and mutagenicity decreases as we subfractionate. The bioassay chromatogram showed peaks of relatively higher mutagenicity in fractions 4 and 11 with 29 and 37 rev/μg, respectively. Mass spectral analysis of peak 4 demonstrated that the goal of sequential fractionation had been achieved such that individual components could be resolved and quantified using HRGC/MS. The major mutagenic compounds identified in the methylene chloride-C-4 fraction were hydroxy-nitro-substituted fluoranthenes (OH-NO_2-PAH) (*26*); work is continuing to synthesize and identify the specific isomers. This class of compounds (i.e., the hydroxynitropyrenes) also has been identified in diesel particulates (*21*, *27*).

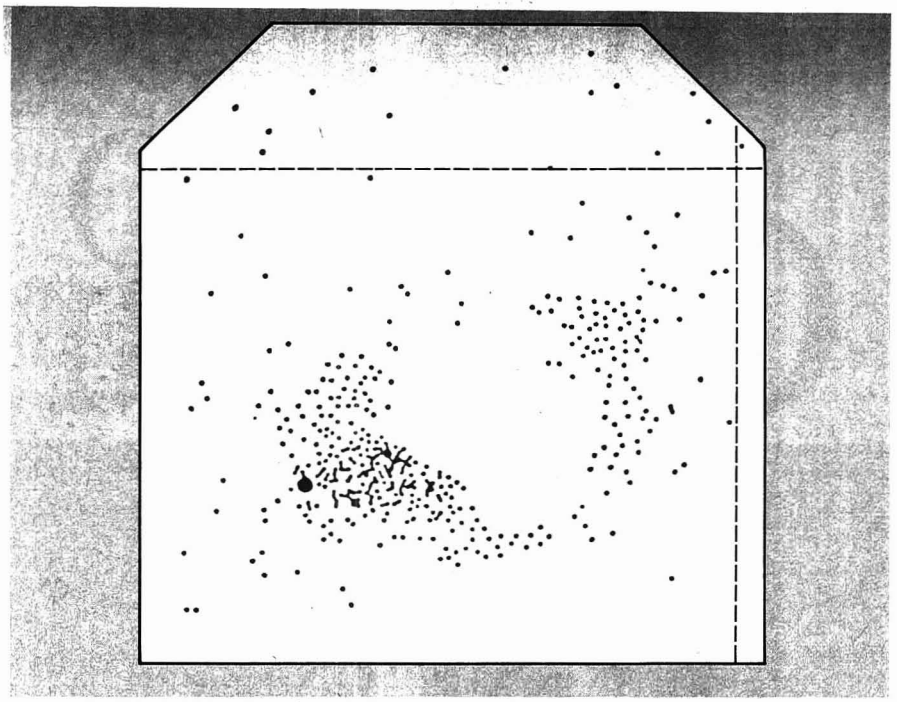

Figure 7. Distribution of mutagenicity for a combined Ames assay–HPTLC analysis of an ambient air particulate extract

Reprinted with permission from Reference 36. Copyright 1982, American Association for the Advancement of Science

Development of new analytical techniques

Despite the considerable progress that has been made in determining moderately polar organics in environmental samples, there remain classes of compounds that have not yet been identified because of limitations in the analytical methods and detection systems.

There has been much less success with the determination of labile compounds (e.g., organic peroxides) and polar organic species. To date, only a limited number of compounds have been identified or tentatively identified as potentially important mutagenic species in the polar fractions of particulate extracts. This lack of information is the result of problems associated with determining polar PAH derivatives, including sample loss from physical adsorption, chemical interactions among components, and sample decomposition. Several laboratories are now developing and applying new methodologies for the determination of polar chemical mutagens.

Direct-insertion probe distillation coupled with HRMS of whole extracts can be used as a survey technique to determine the types of compounds present or in some cases to identify groups of isomeric compounds (e.g., nitropyrenes and nitrofluoranthenes) (*8*, *28*). This technique is also useful for thermally labile organics.

MS/MS coupled with direct-insertion probe introduction of sample yields a higher level of specificity than can be obtained with the HRMS technique (*29*). Although this method does not readily yield specific isomer information, it is a valuable screening tool with a high degree of compound specificity. Secondary ion mass spectrometry (SIMS) using ion and neutral atom beams also may be useful for determination of polar and nonvolatile organic substances in environmental samples (*18*).

The above techniques are good for screening analyses. However, chromatographic separation is needed for positive identification of specific isomers in highly complex fractions. The poor recoveries GC and GC/MS achieve in the identification of polar compounds illustrate the limitations of GC techniques. One of the most promising analytical techniques for the determination of polar PAH derivatives appears to be supercritical fluid chromatography (*30*) and HPLC coupled with mass spectrometry (*31*).

New micromutagenesis methodologies that permit the quantitation of mutagenic activity on microgram quantities of material can now be used together with analytical-scale reversed-phase HPLC. The micro-forward mutation assay, which measures both mutagenicity and survival (toxicity), provides potentially more quantitation of a single-fraction mutagenicity (*32*, *33*), whereas the micro-reverse suspension assay (*34*) uses the standard Ames and Rosenkranz strains. We have successfully coupled these assays to analytical reversed-phase HPLC separation and analysis of polar mammalian metabolites of nitropyrene. This approach shows great promise in helping to identify the polar mutagens in complex environmental samples.

Recently, techniques have been developed to couple liquid chromatography directly with bioassay analysis (*35*, *36*). Duplicate (HPTLC) plates are used to fractionate organic matter.

The Ultimate FT-IR Spectroscopy Research System

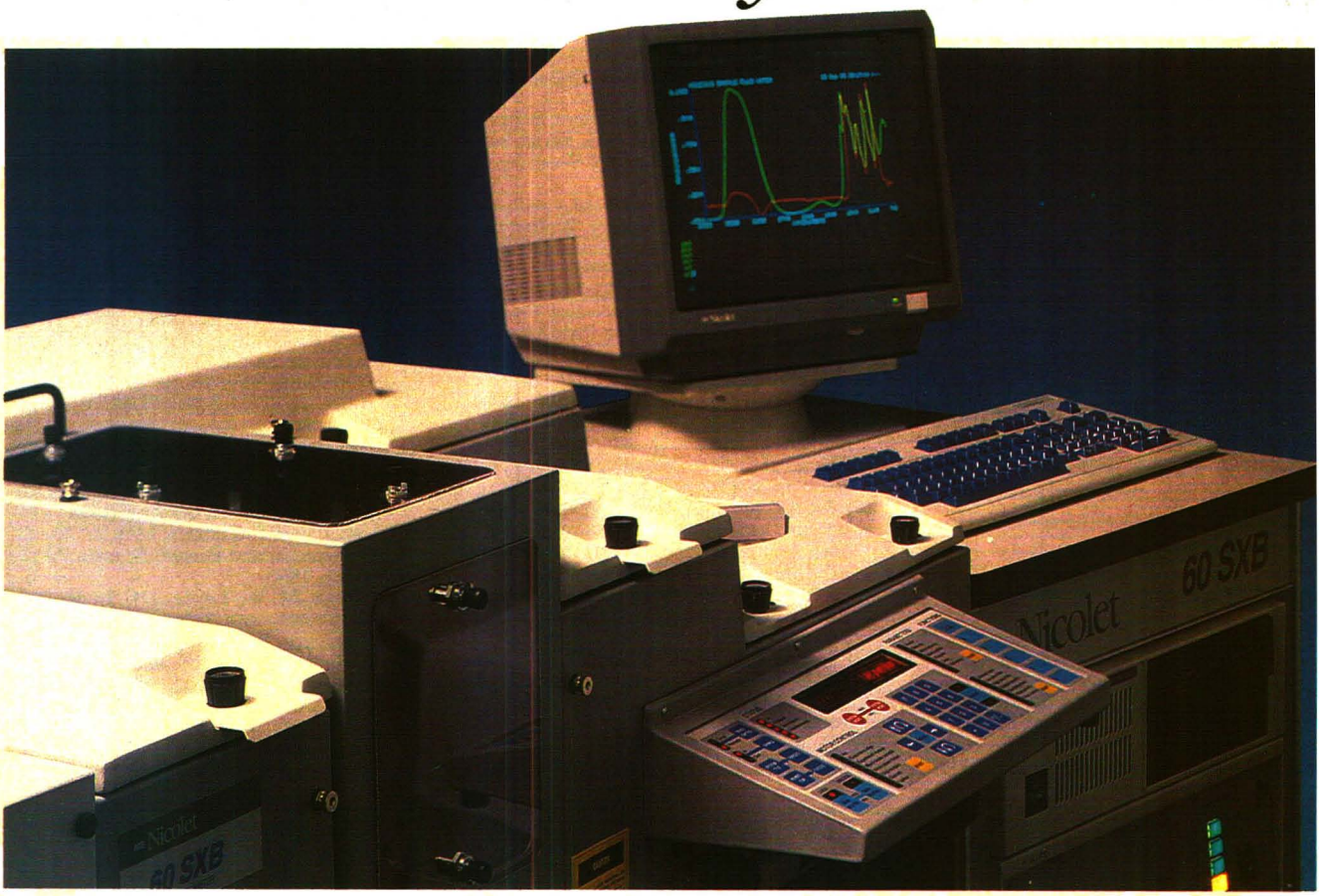

With its capability to rapidly produce superior information for any infrared spectroscopy application, its versatility in quickly adapting to a wide range of experiments, and its extensive automation and real-time capabilities, the 60SXB clearly stands in a class all its own.

The 60SXB performs the full range of today's FT-IR experiments—and adapts to experiments not yet devised. With the 60SXB, you can obtain superb results for any FT-IR spectroscopy experiment, and you can rapidly switch from one technique to another with minimal set-up time. The 60SXB easily adapts to your research needs—no other FT-IR available can match the versatility and convenience of the 60SXB.

Proven performance, productivity, technical innovation. The 60SXB builds upon field-proven performance and productivity, while offering important new refinements and extended capabilities.

- A new-generation interferometer with enhanced performance, stability, and real-time capabilities.
- New NICOS real-time multitasking operating system optimized for the demands of spectroscopy applications.
- New NIC-SIS (Spectroscopic Information System) relational data base management software is provided as standard.
- Comprehensive NIC-COM communications with VAX/VMS operating system, including direct linking of quantitative data into the VAX LIMS/SM environment.*
- A new GC-IR interface and software system provides ease-of-use and performance in analyzing complex mixtures.
- The unique capability to collect and store 60 complete individual FT-IR spectra per second for chemical kinetics studies.
- Unmatched microanalysis capabilities with superb optical efficiency and experimental versatility, including micro-ATR of surfaces, automated spatial mapping, and sample profiling.
- Spectral range capabilities from 25,000 to 10 cm^{-1}.

60SXB: A cost-effective investment. The 60SXB is unmatched in its productivity, versatility, and ease-of-use. The 60SXB user further benefits from the well-established Nicolet tradition of excellence and innovation, the network of qualified and responsive Nicolet service personnel, and the research and applications support Nicolet provides.

Call or write for our new 32-page brochure describing the 60SXB—the FT-IR system for scientists who demand the best.

*VAX, VMS, and VAX LIMS/SM are registered trademarks of Digital Equipment Corporation.

Nicolet

The FT Spectroscopy People

5225-1 Verona Rd. Madison, WI 53711
608/271-3333 / Telex: 910-286-2736

CIRCLE 150 ON READER SERVICE CARD

One plate is used for chemical class tests and the second plate is used for an in situ Ames bioassay. This system has revealed some surprising and interesting differences among particulate matter samples from different cities. Figure 7 shows the distribution of mutagenicity for a combined Ames assay–HPTLC analysis of an ambient air particulate extract. Although the compounds responsible for the concentrated areas of mutagenicity are not known, it is envisioned that future advances in chemical analysis will help this effort. One such aid would be direct chemical analysis of the HPTLC plates using ESCA or SIMS to generate spatial chemical maps of the surface, which could be correlated with the pattern of mutagenicity.

In the future, a substantial effort will be needed to determine the compounds responsible for the mutagenicity of air and water pollutants. Bioassay-directed chemical analysis will continue to be a valuable tool for this purpose.

Acknowledgment

We gratefully acknowledge the helpful comments of I. Alfheim, E. Chess, H. Hertz, R. Gray, T. Jensen, G. Lofroth, W. Pierson, H. Rosenkranz, I. Salmeen, and W. May.

The research described in this article was reviewed by the EPA and approved for publication. Approval does not signify that the contents necessarily reflect the views and policy of the agency.

References

(1) *Chemical Carcinogens*, 2nd ed.; Searle, C. E., Ed.; ACS Monograph 173; American Chemical Society: Washington, D.C., 1984.

(2) *Monitoring Toxic Substances;* Schuetzle, D., Ed.; ACS Symposium Series 94; American Chemical Society: Washington, D.C., 1979.

(3) Schuetzle, D. In *Biomedical Applications of Mass Spectrometry;* Waller, G.; Dermer, O., Eds.; John Wiley and Sons: New York, 1980; pp. 969–1005.

(4) Zimmermann, F. K. In *Mutagenic Testing and Related Analytical Techniques*, Proceedings of the 10th Annual Symposium on the Analytical Chemistry of Pollutants, May 28–30, 1980; Gordon and Breach Science Pub.: London, 1980.

(5) Ames, B. N. In *Monitoring Toxic Substances;* Schuetzle, D., Ed.; American Chemical Society: Washington, D.C., 1979; pp. 1–11.

(6) *Mutagenic Testing and Related Analytical Techniques*, Proceedings of the 10th Annual Symposium on the Analytical Chemistry of Pollutants, May 28–30, 1980; Frei, R. W.; Brinkman, U.A.Th., Eds.; Gordon and Breach Science Pub.: London, 1980.

(7) Rosenkranz, H. S.; McCoy, E. C.; Sanders, D. R.; Butler, M.; Kiriazides, D. K.; Mermelstein, R. *Science* **1980,** *209,* 1039–43.

(8) Schuetzle, D.; Lee, F. S.-C.; Prater, T. J.; Tejada, S. B. In *Mutagenic Testing and Related Analytical Techniques*, Proceedings of the 10th Annual Symposium on the Analytical Chemistry of Pollutants, May 28–30, 1980; Frei, R. W.; Brinkmann, U.A.Th., Eds.; Gordon and Breach Science Pub.: London, 1980; pp. 193–244.

(9) Huisingh, J.; Bradow, R.; Jungers, R.; Claxton, L.; Zweidinger, R.; Tejada, S.; Bumgarner, J.; Duffield, F.; Waters, M.; Simmon, V. F.; Hare, C.; Rodriquez, C.; Snow, L. *Application of Bioassay to the Characterization of Diesel Particle Emissions, Part I and Part II*, Symposium on Application of Short-Term Bioassays in the Fractionation and Analysis of Complex Environmental Mixtures, Williamsburg, Va., 1978; U.S. Environmental Protection Agency: Washington, D.C., 1978.

(10) Guerin, M. R.; Ho, C.-H.; Rao, T. K.; Clark, B. R.; Epler, J. L. In *Mutagenic Testing and Related Analytical Techniques*, Proceedings of the 10th Annual Symposium on the Analytical Chemistry of Pollutants, May 28–30, 1980; Gordon and Breach Science Pub.: London, 1980; pp. 183–91.

(11) Wilson, B. W.; Pelroy, R. A. In *Mutagenic Testing and Related Analytical Techniques*, Proceedings of the 10th Annual Symposium on the Analytical Chemistry of Pollutants, May 28–30, 1980; Gordon and Breach Science Pub.: London, 1980.

(12) Tabor, M. W.; Loper, J. C. In *Mutagenic Testing and Related Analytical Techniques*, Proceedings of the 10th Annual Symposium on the Analytical Chemistry of Pollutants, May 28–30, 1980; Gordon and Breach Science Pub.: London, 1980; pp. 139–59.

(*continued on p. 1075 A*)

MN again enlarges HPLC programme

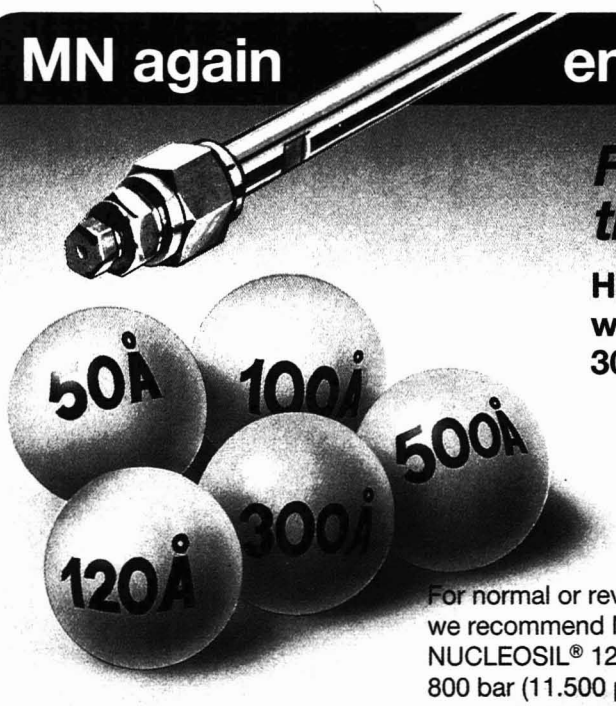

For every separation problem the right NUCLEOSIL®

HPLC packings with average pore diameters of 50, 100, 120, 300, 500, 1000 or 4000 Å, respectively

- spherically shaped silica gel, totally porous
- narrow particle size distribution: 3, 5, 7 and 10 µm
- wide range of chemically bonded phases

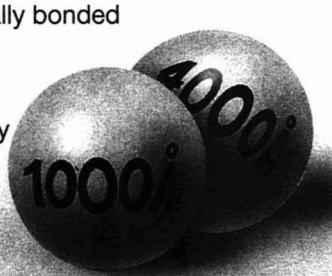

For normal or reversed-phase chromatography we recommend NUCLEOSIL® 50, 100 or 120. NUCLEOSIL® 120 is pressure stable up to 800 bar (11.500 psi).

Wide-pore packings are especially suitable for the separation of macromolecules such as proteins and other biological compounds and in addition they can be used for SEC (Size Exclusion Chromatography)

Please request your free copy of our HPLC Catalogue today from

MACHEREY-NAGEL GmbH & Co. KG · P.O. Box 307
D-5160 Düren · West Germany · Tel. 0 24 21 / 6 10 71 · Telex 83 38 [illegible]

MACHEREY-NAGEL · DÜREN

MN

Switzerland: MACHEREY-NAGEL AG · P.O. Box 46 · CH-4702 Oensingen · Tel. (062) 76 20 66

CIRCLE 135 ON READER SERVICE CARD

Cole-Parmer's New Catalog 1987-88

Nearly 20,000 items for science, research and development, education and industry.

Ask for it...it's free

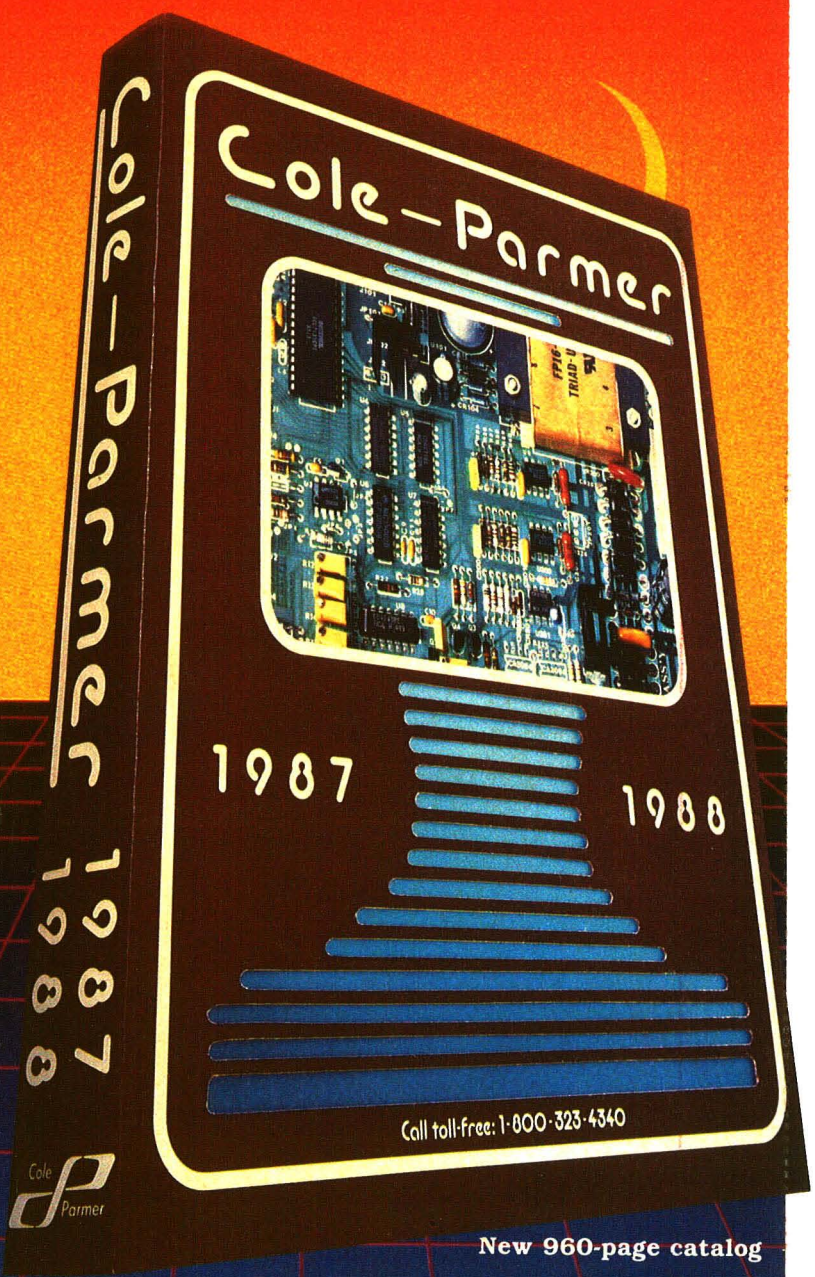

New 960-page catalog

Cole-Parmer . . . THE Research Catalog Company

Cole Parmer

Circle reader service No. 32

Return this card for your FREE '87-88 Catalog today! 32

Please print or type

Name

Title/Department/Mail Stop

Firm/Institution

Address

City

State Zip

☐ Yes, I am currently on your mailing list. Please send me the new catalog as soon as possible.

☐ No, I am not on your mailing list. Please add my name and send me the new catalog.

Field of Activity **Please print or type**

Please check box and fill in specific field

☐ Chemistry_____

☐ Biology_____

☐ Engineering_____

☐ Health Science_____

☐ Other_____

Type of organization (specify)

☐ Manufacturing_____

☐ Educational_____

☐ Research_____

☐ Health Care_____

☐ Government_____

Return this card for your FREE '87-88 Catalog today! 32

Please print or type

Name

Title/Department/Mail Stop

Firm/Institution

Address

City

State Zip

☐ Yes, I am currently on your mailing list. Please send me the new catalog as soon as possible.

☐ No, I am not on your mailing list. Please add my name and send me the new catalog.

Field of Activity **Please print or type**

Please check box and fill in specific field

☐ Chemistry_____

☐ Biology_____

☐ Engineering_____

☐ Health Science_____

☐ Other_____

Type of organization (specify)

☐ Manufacturing_____

☐ Educational_____

☐ Research_____

☐ Health Care_____

☐ Government_____

Use the attached cards to reserve your Cole-Parmer '87-88 Catalog

Get a personal copy of our entire product line. 960 pages of the products you need. This edition is easier-to-use, easier-to-read, fully illustrated in color, clearly indexed, and complete with accurate specifications and ordering information.

Here're just a few of the thousands of new products for '87-88 . . . bio-technology products . . . more pumps—one of the largest selections available. . . sophisticated instrumentation including balances, thermometry, pH, conductivity, dissolved oxygen . . . process control instrumentation . . . computer interfaces and data acquisition equipment. See the rest soon!



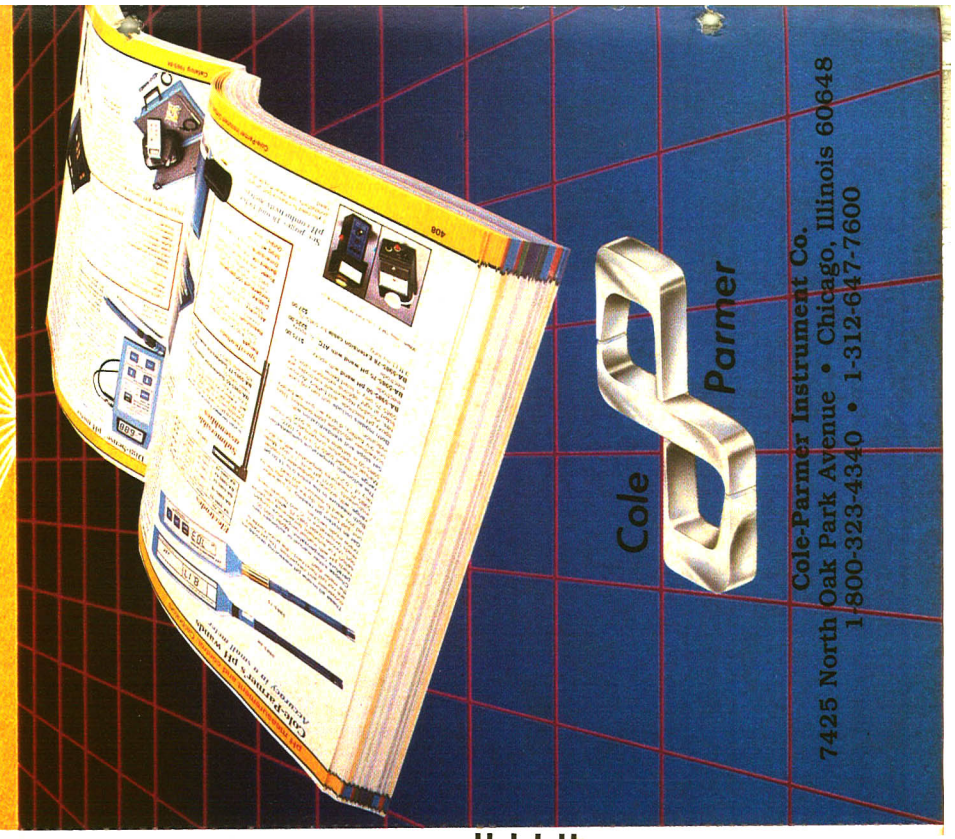

No postage necessary if mailed in the United States

BUSINESS REPLY MAIL
FIRST CLASS MAIL PERMIT NO. 49678 CHICAGO, IL

POSTAGE WILL BE PAID BY ADDRESSEE

Cole-Parmer Instrument Co.
7425 North Oak Park Avenue
Chicago, Illinois 60648-9930

No postage necessary if mailed in the United States

BUSINESS REPLY MAIL
FIRST CLASS MAIL PERMIT NO. 49678 CHICAGO, IL

POSTAGE WILL BE PAID BY ADDRESSEE

Cole-Parmer Instrument Co.
7425 North Oak Park Avenue
Chicago, Illinois 60648-9930

(13) *Proceedings of the Workshop on Genotoxic Air Pollutants*, April 24–27, 1984; Lewtas, J.; Alfheim, I.; Ball, L. M.; Gustafsson, J.-A., Eds.; Environment International: Raleigh, N.C., 1985; p. 11.
(14) Pederson, T.; Siak, J-S. *J. Appl. Toxicol.* **1981,** *1*, 54.
(15) Pitts, J. N., Jr.; Lokensgard, D. M.; Harger, W.; Fisher, T. S.; Mejia, V.; Schuler, J. J.; Scorziell, G. M.; Katzenstein, Y. A. *Mutat. Res.* **1982,** *103*, 241.
(16) West, W. R.; Smith, P. A.; Booth, G. M.; Wise, S. A.; Lee, M. L. *Arch. Environ. Contam. Toxicol.* **1986,** *15*.
(17) Van Kreijl, C. F.; Verlaan-deVries, M; Van Kranen, H. J.; deGreef, E. *Mutat. Res.* **1983,** *113*, 313–14.
(18) Schuetzle, D.; Jensen, T. E.; Ball, J. C. *Environ. Int. J.* **1985,** *11*, 169.
(19) Lofroth, G.; Hefner, E.; Alfheim, I.; Moller, M. *Science* **1980,** *209*, 1037.
(20) Rosenkranz, H. S.; McCoy, E. C.; Sanders, D. R.; Butler, M.; Kiriazides, D. K.; Mermelstein, R. *Science* **1980,** *209*, 1039.
(21) Schuetzle, D. *Environ. Health Perspect.* **1983,** *47*, 65.
(22) Alfheim, I.; Bjorseth, A.; Moller, M. "Characterization of Microbial Mutagens in Complex Samples—Methodology and Application," *Critical Reviews in Environmental Control;* CRC Press: Boca Raton, Fla., 1984; Vol. 14.
(23) Epler, J. L. In *Chemical Mutagens: Principles and Methods for Their Detection*; deSerres, F. J.; Hollander, A., Eds.; Plenum: New York, 1983; Vol. 6, pp. 239–70.
(24) Salmeen, I. T.; Pero, A. M.; Zator, R.; Schuetzle, D.; Riley, T. L. *Environ. Sci. Technol.* **1984,** *18*, 375.
(25) Peterson, B. A.; Chuang, C. C. In *Toxicological Effects of Emissions from Diesel Engines;* Lewtas, J., Ed.; Elsevier Biomedical: Amsterdam, 1982; p. 51.
(26) Nishioka, M. G.; Chuang, C. C.; Petersen, B. A.; Austin, A.; Lewtas, J. *Environ. Int.* **1985,** *11*, 137.
(27) Manabe, Y.; Kinouchi, T.; Ohnishi, Y. *Mutat. Res.* **1985,** *158*, 3.
(28) Xu, X. B.; Nachtman, J. P.; Jin, Z. L.; Wei, E. T.; Rappaport, S. W. *Anal. Chim. Acta* **1982,** *136*, 163.
(29) Schuetzle, D.; Prater, T. J.; Riley, T.; Harvey, T. M.; Hunt, D. *Anal. Chem.* **1982,** *54*, 265.
(30) West, W. R.; Lee, M. L., *J.H.R.C./C.C.* **1986,** *9*, 161.
(31) Blakely, C. R.; Vestal, M. L. *Anal. Chem.* **1983,** *55*, 750.
(32) Thilly, W. G.; Longwell, J.; Andon, B. M. *Environ. Health Perspectives* **1983,** *8*, 129.
(33) Goto, S.; Williams, K.; Claxton, L. D.; Lewtas, J., submitted for publication in *Mutat. Res.*
(34) Kado, N.; Langlely, D.; Eisenstadt, E. *Mutat. Res.* **1985,** *121*, 25.
(35) Butler, J. P.; Kneip, T. J.; Daisey, J. M., submitted for publication in *Atmos. Environ.*
(36) Bjorseth, A.; Eidsa, G.; Gether, J.; Landmark, L.; Moller, M. *Science* **1982,** *215*, 87.

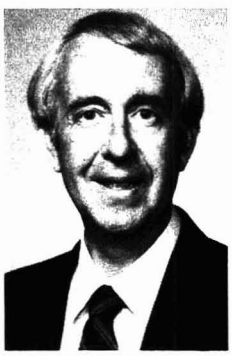

Dennis Schuetzle is a principal research scientist and head of the chemical research department of Ford Motor Company. He received his B.S. degree in chemistry in 1965 and interdisciplinary Ph.D.s in analytical chemistry and environmental engineering at the University of Washington. His primary research interests include environmental analytical chemistry, surface analysis, and process analytical chemistry.



Joellen Lewtas is chief of the genetic bioassay branch at the Environmental Protection Agency's Health Effects Research Laboratory. She received a B.S. degree in chemistry in 1966 and a Ph.D. in biochemistry from North Carolina State University in 1973. Her research has included evaluation of the mutagenicity and carcinogenicity of diesel and gasoline exhaust emissions and identification of mutagenically active components in these emissions.

VOLTAMMETRIC ANALYSES



Environmental Analyses— A New Perspective!

Hexavalent chrome or cyanide in waste water... formaldehyde in particle board...ultra-trace heavy metals in sea water...a multitude of pesticides in soil...these are just a few of the environmental applications for voltammetry.

Voltammetry is equally successful in applications as diverse as plating bath, cosmetics, food, beverage and pharmaceutical analyses, to name a few.

***EG&G** Princeton Applied Research* can determine if your analytical problems have a voltammetric solution *and* we can provide you with the highest performance instrumentation you can buy.



Discuss your requirements with our Applications Group or arrange for a feasibility study. See how we can give *your* analyses a new perspective. Call *today*: **(609) 895-0100.**

EG&G PRINCETON APPLIED RESEARCH
Electrochemical Instruments Division
CN 5206 • Princeton NJ 08543 USA • (609) 895-0100 • TELEX: 843409

JO1007E

CIRCLE 52 ON READER SERVICE CARD

Milton L. Lee

Department of Chemistry
Brigham Young University
Provo, Utah 84602

Chromatographic-Spectroscopic Combinations

This year's American Chemical Society Division of Analytical Chemistry Summer Symposium on Chromatographic–Spectroscopic Combinations was held in June at the University of Utah campus, situated in the foothills of the Wasatch Mountains. This location proved to be very fitting for such a meeting; the magnificent backdrop of the towering mountain range resembled the three-dimensional countour profiles characteristic of graphical data representations from chromatographic–spectroscopic combinations. There were 180 attendees at this year's Summer Symposium.

The meeting was organized under the direction of Harold McNair (Virginia Tech), with local arrangements made by Joel Harris (University of Utah). Session organizers and chairmen were Milton Lee (supercritical fluid chromatography/spectroscopy), Larry Taylor (liquid chromatography/Fourier transform infrared spectrometry), and Harold McNair (liquid chromatography/mass spectrometry, in addition to sessions on new spectroscopic detectors, multidimensional chromatography, and the handling of high-resolution chromatographic–spectroscopic data).

The generation of analytical data in two dimensions provides considerably more information than data displayed along a single axis. J. Calvin Giddings (University of Utah) discussed the advantages and disadvantages of coupled systems in general, with emphasis on the relative merits of separation/separation combinations as compared with separation/spectroscopic techniques.

Statistical calculations reveal a large potential for overlap of chromatographic peaks (even in high-resolution separations), and often these overlapped peaks cannot be unambiguously resolved by spectroscopy in the second dimension. Joel Harris described approaches to analyzing data from components that are severely overlapped chromatographically and spectrally. His iterative least-squares method, which has been applied to both gas chromatography/mass spectrometry and liquid chromatography/UV data, has successfully resolved fused peaks containing up to seven components.

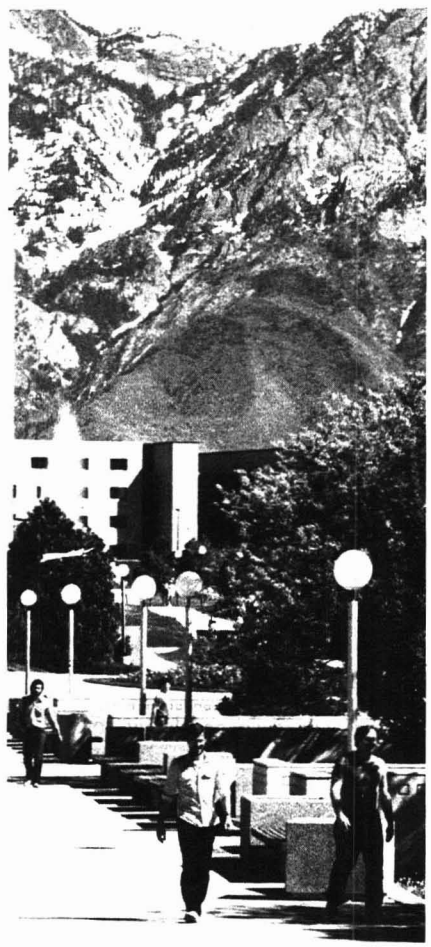

University of Utah campus with the Wasatch Mountains in the background

During the meeting, considerable attention was focused on the coupling of liquid chromatography (LC) with Fourier transform infrared spectrometry (FT–IR). A number of improvements have been made in conventional flow cell detection, such as improved flow cell design and segmented flow extraction with immiscible solvents before detection, as described by Larry Taylor (Virginia Tech). However, there are still two basic limitations with conventional flow cells: relatively poor sensitivity and solvent restrictions. Much more promising is elimination of the solvent after deposition of the eluant on a solid surface, followed by diffuse-reflectance FT–IR. Several approaches were presented by Peter Griffiths (University of California, Riverside), Kathryn Kalasinsky (Mississippi State University), and Kiyokatsu Jinno (Toyohashi University). Using these techniques, detection limits in the mid- to low-nanogram range have been attained.

The coupling of mass spectrometry (MS) with LC has received much attention in the past several years, and this was a major topic at the symposium. Jack Henion (Cornell University) gave an excellent overview of the various approaches to LC/MS, whereas subsequent speakers concentrated primarily on the popular thermospray interface. It became obvious in discussions that a current limitation to LC/MS is the lack of structural information in acquired mass spectra. It was a general feeling among symposium participants that LC coupled with triple-quadrupole instrumentation would be an increasingly important combination in the future.

The use of capillary columns (both tubular and packed) in LC and supercritical fluid chromatography (SFC) places stringent requirements on detection systems, necessitating submicroliter detector volumes to preserve chromatographic efficiency. Laser-

0003-2700/86/A358-1076$01.50/0
© 1986 American Chemical Society

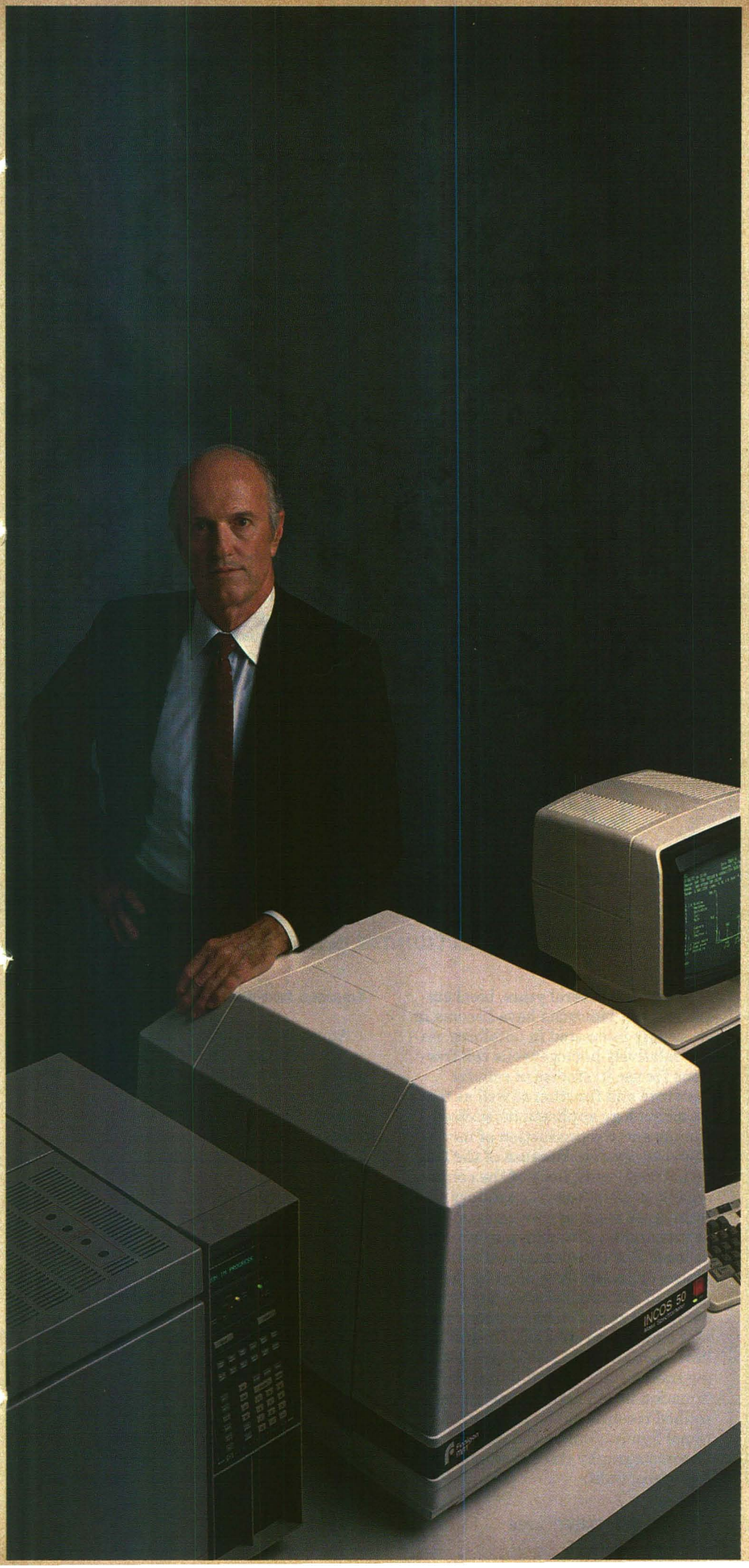

The new INCOS™ 50 GC/MS means business.

Whether you run a commercial lab or an analytical department, you can't afford to be without the INCOS 50. It's a small investment in big performance.

Big GC/MS performance begins with the best GC for you. The INCOS 50 interfaces with all leading GCs. We've made it compatible with capillary, wide-bore and packed columns.

The INCOS 50 quadrupole mass spectrometer gives you EI or CI with positive or negative ion detection. Use it with GC, desorption or other solids probes. The advanced controls guarantee easy, stable and reproducible tuning. The result: highest analytical flexibility, highest data quality, highest throughput... every day.

Multiply your productivity with the 4th generation data system. True foreground/background. Large internal memory. Print spooling. Communications with the whole world... PCs, LIMS, mainframes. You name it.

Of course the INCOS 50 incorporates the industry-standard Incos™ software and is compatible with EPA protocols. Bob Finnigan wouldn't have it any other way.

Your investment? Minimal bench space and a remarkably low price. Contact your Finnigan MAT representative today, and let's talk business.

Finnigan MAT did it. Again.

Finnigan MAT

U.S.A., 355 River Oaks Parkway, San Jose, CA 95134. (408) 433-4800
Germany, Postfach 14 40 62, D-2800 Bremen 14. (0421) 54 93-0
U.K., Paradise, Hemel Hempstead, Herts HP2 4TG. (0442) 4 04 91
France, 69 rue de Paris, F-91400, Orsay. (1) 69 28 52 53
Benelux, Landjuweel 7, 3905 PE Veenendaal. 08385 27266
Italy, Via Valadier, 37B, 00193 Rome. (06) 316 000
Japan, Shiozaki Bldg., 2-7-1 Hirakawa-cho, Chiyoda-ku, Tokyo 102. (03) 221-1001

Circle 58 for literature.
Circle 59 to have a representative call.

Fundamentals and Applications of Chemical Sensors

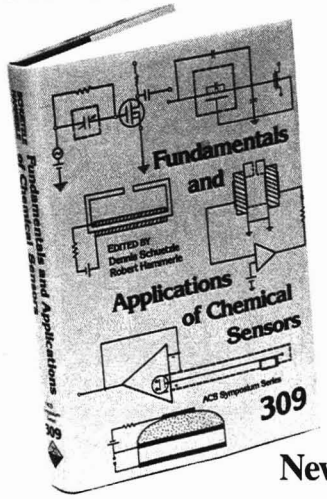

New!

Dennis Schuetzle and Robert Hammerle, *Editors*
Ford Motor Company

Presents the first comprehensive collection of articles on the fundamentals and applications of a wide variety of chemical sensors. Discusses a range of topics from the development of new sensor concepts to improvements in sensors that have been mass produced for several years. Specific types of sensors discussed include oxygen, electrochemical, microbial, drug, and glucose sensors.

CONTENTS
Chemically Sensitive Electronic Devices • Gas Sensors in Japan • Tin Oxide Microsensors • Tin(IV) Oxide Gas Sensors • Perovskite-Type Oxides • Zirconium Oxide Oxygen Sensors • Microsensor Vapor Detectors • Chemical Microsensors • Solid State Gas Sensors • Amperometric Proton-Conductor Sensors • Atmospheric Gas Composition Determinations • Chemically Modified Electrode Sensors • Coated-Wire Ion-Selective Electrodes • Chemical Sensing • Detection of Airborne Chemicals • Amidoxime-Functionalized Coatings • Optical Waveguide Devices • Microbial Sensors • Stabilized Lipid Membranes • Design of Sensitive Drug Sensors • Subcutaneous-Type Glucose Sensors

Developed from a symposium presented at the Congress of Pacific Basin Societies, Honolulu, Hawaii

ACS Symposium Series No. 309
395 pages (1986) Clothbound
LC 86-86-3518 ISBN 0-8412-0973-1
US & Canada **$74.95** Export **$89.95**

Order From:
American Chemical Society
Distribution Office Dept. 16
1155 Sixteenth St., N.W.
Washington, DC 20036
or CALL TOLL FREE 800-424-6747
and use your credit card!

based detectors have great potential in this area, as discussed by Ed Yeung (Iowa State University) and Milos Novotny (Indiana University). Yeung described the use of indirect detection methods in which one probes the environment of the species rather than the species itself. In polarimetry, for example, the signal-to-noise ratio of the background is sufficiently high that very sensitive measurements can be made. Because fluorescence detection is already highly sensitive and selective, derivatization of nonfluorescing solute molecules with fluorescing moieties is another approach to achieving sensitivity. In this way, the solute is modified to suit the detection system; usually it is the detection system that is modified to suit the solutes of interest.

Because of the current interest in the newly emerging technology of SFC, several papers were given on the interfacing of SFC with spectroscopy. Dick Smith (Battelle Pacific Northwest Laboratory) described in detail the problems associated with restriction and decompression at the SFC column outlet. Jack Henion described the modification of a bench-top mass spectrometer for SFC/MS. For FT–IR detection, deposition of the effluent on a solid surface (a moving ZnSe window, for example) before detection provides the same sensitivity advantages as noted previously for LC/FT–IR. Steven Goates (Brigham Young University) presented recent results obtained from introducing the SFC column effluent into a supersonic jet for fluorescence measurements. The narrow-line fluorescence spectra obtained as a result of rotational cooling in the jet expansion region offer great improvement in the selectivity of coupled SFC/fluorescence spectroscopy.

Development of modern analytical measurement techniques is driven by the desire to improve detection limits and to increase the information content of measurements. This year's Summer Symposium primarily addressed the second of these two goals. With the current interest in chromatography–spectroscopy combinations and with the rapid advancements being made in this area, there is every reason to expect that this topic will again be the central focus of a Summer Symposium in the not-too-distant future.

Cell Separations

Aqueous two-phase partitioning, countercurrent chromatography, and field flow fractionation can be used to fractionate cell populations

In the past several years, biochemists and cell biologists have become increasingly interested in obtaining viable, relatively homogeneous cell fractions for use in studies of cellular structure and function as well as for biotechnology applications, such as cloning and the production of monoclonal antibodies. Because of the fragile nature of cells, none of the common organic-solvent-based separatory techniques (such as solvent extraction or preparative chromatography) can be used. But three analytical techniques originally developed for separation of macromolecules—aqueous two-phase partitioning, countercurrent chromatography (CCC), and field flow fractionation (FFF)—are now being successfully applied to the fractionation of cell populations, as described recently at the 10th International Symposium on Column Liquid Chromatography (HPLC '86) in San Francisco, Calif.

Aqueous two-phase partitioning

Aqueous solutions of dextran (Dx) and polyethylene glycol (PEG), when mixed above certain concentrations, form immiscible liquid two-phase systems consisting of a PEG-rich top layer and a Dx-rich bottom layer. These aqueous polymer systems have been found useful not only for fractionation of proteins and nucleic acids, but also for fractionation of cells, as described at the symposium by Harry Walter of the Veterans Administration Medical Center in Long Beach, Calif.

"Particles usually partition between one of the phases and the interface (unlike soluble materials, which partition between the bulk phases)," Walter explains. "The normal position of cells in a two-phase polymer system is at the interface, so whenever you see partitioning it indicates that something is acting on the cells to pull them out of the interface and into one

More GCs prefer our ITD.™ More than any other mass spec detector.

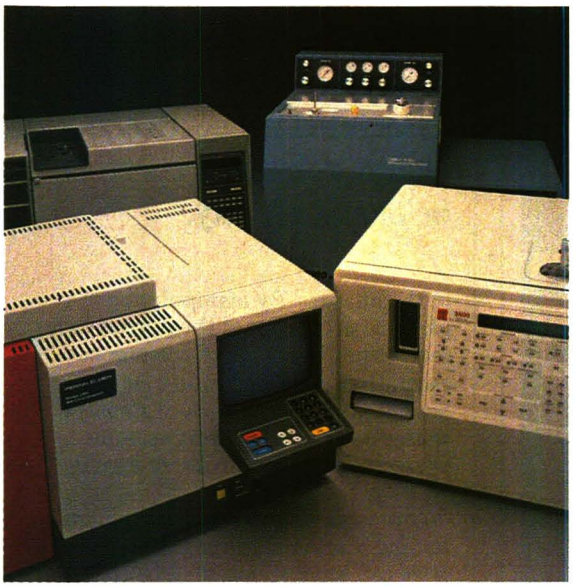

And laboratories everywhere are putting it to work—analyzing pharmaceuticals, environmental pollutants, food and flavors, forensic samples...

The GCs like the ITD because it complements them. Just plug it in, and it's ready to go.

Results come easily and quickly. Library searches take seconds, not minutes. The IBM® PC/XT opens the door to other popular laboratory software. And the price is right.

The Finnigan MAT Ion Trap Detector™ (ITD). Call or write today, and find out how hundreds of GCs are experiencing a new level of analytical power and productivity.

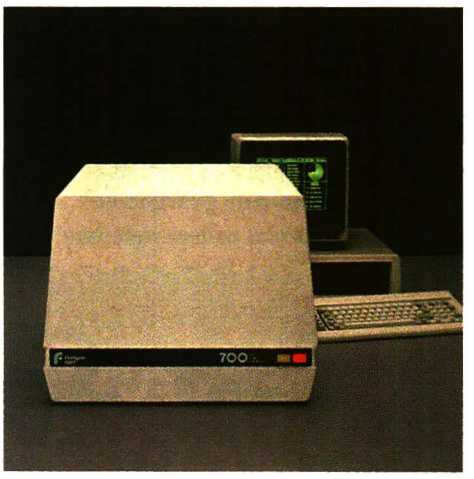

355 River Oaks Parkway, San Jose, CA 95134-1991, USA (408) 433-4800.
Postfach 14 40 62, D-2800 Bremen 14, FRG (0421) 54-93-0.
Paradise, Hemel Hempstead, Herts HP2 4TG, UK (0442) 4 04 91.
69, rue de Paris, F-91400 Orsay, France (1) 69 28 52 53.
Landjuweel 7, 3905 PE Veenendaal, The Netherlands 08385 27266.
Via Valadier, 37B, 00193 Rome, Italy (06) 316000.
Shiozaki Building, 2-7-1 Hirakawa-cho, Chiyoda-ku, Tokyo 102, Japan (03) 221-1001.

Finnigan MAT

Circle 60 for literature. Circle 61 to have a representative contact you.

Print, Plot, Graph, Record, Monitor

KIPP&ZONEN BD70/71 high-resolution printer/plotters provide hard copy for personal computers, laboratory work stations and industrial control

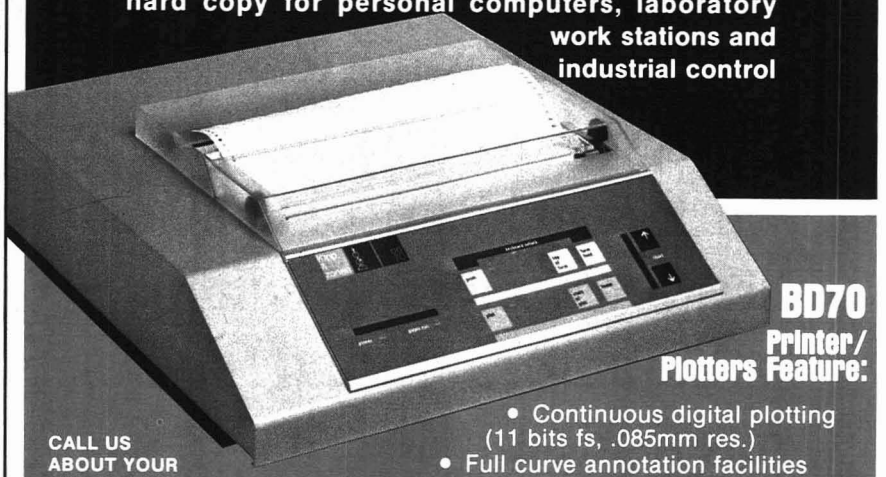

BD70 Printer/Plotters Feature:

- Continuous digital plotting (11 bits fs, .085mm res.)
- Full curve annotation facilities
- Epson compatible text and graphics
- Fast, silent thermal printing
- 12 function keyboard w/4 LED's
- Centronics parallel interface
- Optional A/D converter, RS232/20mA interface
- Dual channel BD71 and OEM models available

CALL US ABOUT YOUR APPLICATION TODAY!

KIPP & ZONEN

div. of ENRAF-NONIUS

390 Central Ave., Bohemia, NY 11716 / 516-589-2885 / Telex: 96-0250

CIRCLE 122 ON READER SERVICE CARD

JANUS Laboratories, Inc.

Special Team for Spectrophotometer Cells

- Want to discover the ultimate in optical technology?
- Research quality products-unconditionally guaranteed!
- OEM/Special orders welcome!



CALL COLLECT FOR FREE CATALOG

JANUS Laboratories Inc.
P.O. BOX 1406, Orangevale, CA 95662
TEL: (916) 988-1181 TELEX: 797063

CIRCLE 114 ON READER SERVICE CARD

By manipulating the physical properties of the polymer system, cells can be separated on the basis of surface-charge-associated properties, non-charge-related properties, or ligand affinity.

of the phases." By manipulating the physical properties of the polymer system, either by choice of polymer concentration, salts, or ligands, cells can be separated on the basis of surface-charge-associated properties, non-charge-related properties, or ligand affinity.

Although aqueous two-phase partitioning is often used for actual preparative cell separations, it can also be used as an analytical tool to trace subtle differences in cell surface characteristics that occur as a function of normal in vivo processes or in vitro treatments. "Because the parameters that determine the partition coefficient (K) are exponentially, rather than linearly, related to the K value," says Walter, "partitioning often yields separation and information on physical properties of biomaterials that are not readily obtained by other means." For example, Walter has been able to detect charge-associated surface differences between red blood cells that are indiscernible by electrophoresis. He has also been able to establish the heterogeneity of certain cell populations where other methods have shown only homogeneous populations.

In addition to Walter's work with red blood cells, two-phase partitioning has been used to separate other types of mammalian cells, plant cells, bacterial cells, and viruses and phages. It has also been used to study red blood cells from individuals with diseases in which red blood cell surface alterations have been reported or are suspected, such as chronic alcoholism and multiple sclerosis. (See Walter's recent review article, *Anal. Biochem.* **1986,** *155*, 215–42, for a detailed description of partitioning in aqueous two-phase systems.)

Countercurrent chromatography

Countercurrent chromatography (CCC) is a form of liquid–liquid chromatography that uses low-speed centrifugation to hold one phase of an im-

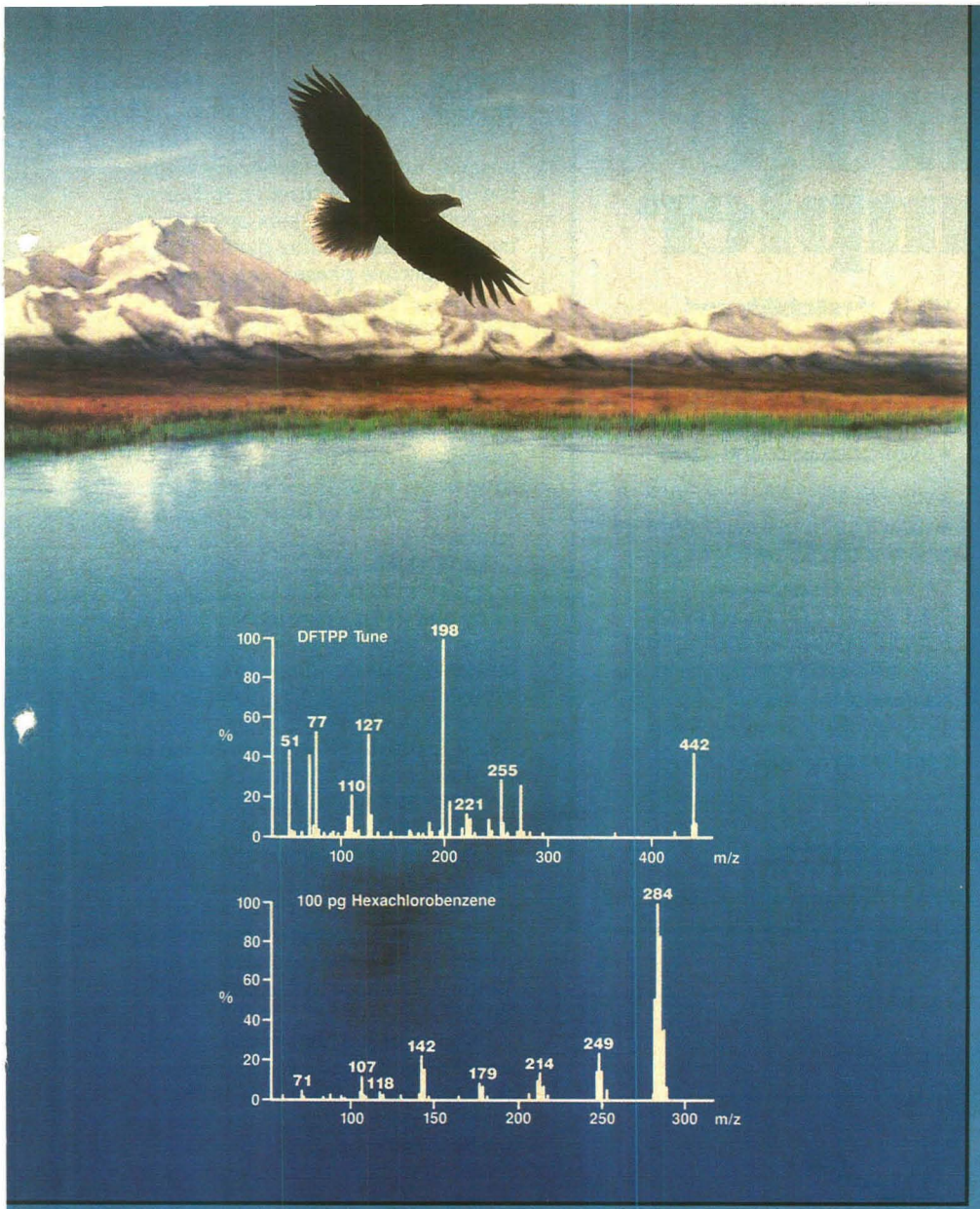



The MS25RFA is in tune with your needs.

Eliminate costly reruns and expensive, time-consuming recalibration.

The MS25RFA offers you...

- Compliance to strict criteria for DFTPP runs to EPA standards. (Methods 624/625)
- Faster calibration than any other system — as fast as 10 minutes from start to TUNE.
- Calibration achieved at full sensitivity, assuring the widest dynamic range of detection.
- Greater stability of calibration for the day's work — once achieved, calibration remains the same.
- Purge and trap concentrator for qualitative and quantitative results.

No other analytical instrument provides so much flexibility, sensitivity and guaranteed compliance to stringent test criteria . . . all in a reliable, easy-to-use package.

Turn your environmental problems into solutions now. Contact Kratos Analytical for literature and a demonstration. 170 Williams Drive, Ramsey, NJ 07446. **1-201-934-9000.**

KRATOS
ANALYTICAL
a division of SPECTROS

Turn Environmental Problems into Solutions...

CIRCLE 123 ON READER SERVICE CARD

New HPLC Autosampler



Highest reliability and precision

- RS-232-C standard
- Requires no auxiliary gas
- Works with any HPLC system
- Interfaces with any valve

Micromeritics' new Model 728 Autosampler uses a patented positive displacement sampling technique to eliminate the need for an auxiliary gas supply. It provides the highest reliability and precision on the market at the lowest cost, using state-of-the-art microcomputer technology.

micromeritics®

One Micromeritics Drive, Norcross, GA 30093-1877, Telephone: (404) 662-3669

CIRCLE 140 ON READER SERVICE CARD



CIRCLE 26 ON READER SERVICE CARD

miscible liquid pair stationary while the other is eluted through it. Epicyclic rotation of a coil sets up alternating mixing and settling bands of the two immiscible phases, and these bands then travel through the coil, giving up to 50,000 partitioning steps per hour. Sample material is usually injected with the mobile phase using a conventional liquid chromatographic sample loop; sample components that partition toward the mobile phase will elute early, while those favoring the stationary phase or interface will be retained.

Applications of CCC, including purification of natural products, peptides, and drugs, have mainly concentrated on aqueous–organic phase systems using the multilayer coil planet centrifuge developed by Yoichiro Ito of the National Heart, Lung, and Blood Institute. (For a description of the development of this technique, see Ito's REPORT in the April 1984 issue of ANALYTICAL CHEMISTRY.) This process has now been extended for use with double aqueous-phase systems similar to those used for two-phase partitioning, as reported by Ian Sutherland of the National Institute for Medical Research in London at HPLC '86.

Because of the high-viscosity and low-density differences of aqueous polymer phases, the methods developed for use with the Ito machine cannot be directly applied. "The multilayer coil works very well with aqueous/organic phase systems," says Sutherland, "but with aqueous/aqueous phase systems, the interfacial tension is too low and the phases emulsify." Consequently, special toroidally wound coils that enhance retention of the viscous polymer phases must be used for aqueous two-phase CCC.

Sutherland has used the toroidal coil machines with PEG–Dx polymer systems to fractionate rat liver organelles and for an affinity-based purification of Torpedo electroplax membranes enriched in nicotinic cholinergic receptors. These particles are relatively small (less than a micrometer) and separate well using the toroidal coil system. But larger particles, such as bacterial cells, require an extremely complicated version of the Ito machine, the nonsynchronous coil planet centrifuge. Although Sutherland has used this technique to separate red blood cells, he doesn't believe that the results necessarily justify the sort of effort required to achieve such separations.

CCC has a number of potential advantages for cell separations, including very rapid separations and suit-

THE USERS OF BOMEM'S DA3 AND DA2 SERIES FTIR SYSTEMS ARE A SELECT GROUP. THEY WORK AT SOME OF THE WORLD'S MOST RENOWNED SPECTROSCOPY LABS, SOLVING SOME OF THE TOUGHEST SCIENTIFIC PROBLEMS ENCOUNTERED.

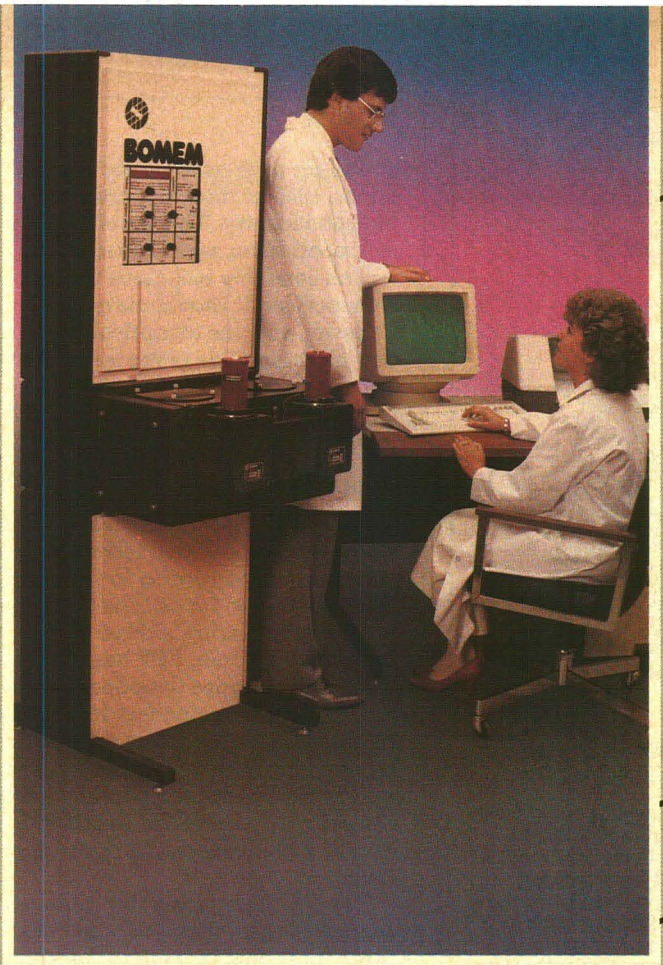

Here are some examples:

AT & T Bell Labs
Atomic Energy of Canada
Chinese Academy of Sciences
Department of National Defense
DOW Chemical Corp.
ETH Centrum
General Electric
General Motors
Hughes Aircraft
IBM Research Labs
Jet Propulsion Labs
Martin Marietta
Max Planck Institüt
NASA, Ames Research Labs
National Bureau of Standards
National Research Council of Canada
National Tsing Hua University
National University of Singapore
Naval Research Lab.
NIES Japan
Nippon Tel. Co.
Princeton University
Université de Paris
Universita di Roma
Universität Bern
University of California
Seoul National University
Stockholm Universitet
Yale University

GET ON THE FTIR SMART LIST

"DA3 — THE FULL PICTURE"

Multitasking

Solving tough scientific problems requires team work! Many of our users chose the DA3 for the 5 experiment positions on one spectrometer. They also liked our Multi-Tasking software based on Digital Equipment's RSX-11M or MicroVMS operating systems.

Performance

Tough problems require high performance instruments. Bomem's DA3 has the widest spectral range available (5 to 50,000 cm-1) and the widest range of selectable resolutions (64 to .002 cm-1). And the DA3 is evacuable, so they get superior performance in Far IR and UV regions.

Obsolescence?

Not with Bomem. Superior scientists are always coming up with new challenges. Recently they have inspired us to introduce an interface for Raman spectroscopy so they can operate in the Near IR to eliminate fluorescence problems. Others required a polarizing interferometer for direct circular dichroism studies, we provided it. From the start, Bomem designed its instruments for upgradability. That's why we chose to use a universally accepted host computer (Digital Equipment Corp), and we have matched that technology with the fastest array processor available for FTIR. It makes fast work out of heavy computing like needed for GCIR or high resolution.

Special requirements

A lot of our Users have special needs which can't be met with standard accessories so we keep a strong engineering team available to design special optical interfaces, data processing techniques, and experimental routines. That can give you an edge when those tough problems need to be solved.

DA2 — SKY'S THE LIMIT

Field Studies

Sometimes the tough problems won't come to the lab. Bomem's DA2 Field Portable FTIR goes to the problem! They've been used in high altitude aircraft, in battlefield testing sites and in remote, ground-based air pollution monitoring. The DA2 Users will testify, it goes where you need it, and with performance up to laboratory standards!

So join the growing number of oustanding professionals who use Bomem FTIR. Call us today at one of our 3 sales offices. We have reps worldwide.

BOMEM
ELEGANT FT-IR

Canada
625 rue Marais
Vanier, Québec
G1M 2Y2
Tél (418) 683-1707
Télex 051-3438
Fax 418.683.9344

USA
4 New Casho Mill Road
Newark, Delaware
19711
Tél (302) 366-8260
Télex 650-270-2430
Fax 302.366.8260

Europe
Bizonspoor 6007
3605 Lv Maarssen
The Netherlands
Tél 034.656.2773
Télex 40835
Fax 034.656.3998

CIRCLE 18 ON READER SERVICE CARD

Computer Applications in the Polymer Laboratory

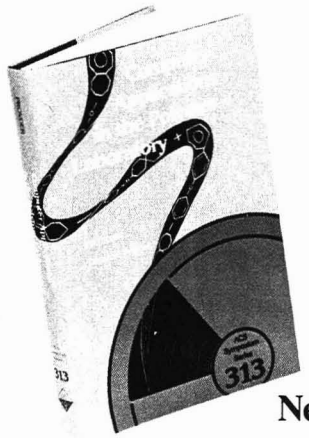

New!

Theodore Provder, *Editor*
Glidden Coatings and Resins

Reports on the impact the technological revolution is having on the research worker in polymer chemistry. Reviews the impact of computer technology in the polymer laboratory, and speculates on future trends in task automation. Concentrates on three important areas: Laboratory information generation, management, and analysis tools; instrument automation for polymer characterization; and polymerization cure process modeling and control. Helps bridge the gap between technical and office tools for all scientists and technologists working in the field of polymer research.

CONTENTS
Laboratory Automation: A New Perspective • Economic Considerations of LIMS • Applications of Computer Data Base Management • Advances in Scientific Software Packages • Computer-Assisted Polymer Design • Silicone Acrylate Copolymers • Constrained Mixture-Design Formulations • Analysis of Isochronal Mechanical Relaxation Scans • Automated Rheology Laboratory: Part I • Automated Rheology Laboratory: Part II • Automated Analyses for the Tensile Tester • Data Collection for a Size-Exclusion Liquid Chromatograph • X-ray Pole Figure Studies of Polymers • Computers and the Optical Microscope • Simulation Activities in a R&D Laboratory for Coatings • Flexible Control of Laboratory Polymer Reactors • Control of a Polystyrene Reactor • The Modeling of Polymerization Kinetics • Mathematical Modeling of Emulsion Polymerization Reactors • Kinetics Analysis of Consecutive Reactions • Optimization of Bake Conditions for Thermoset Coatings • An Anhydride-Cured Epoxy Polymerization • Investigation of Self-Condensation of 2,4-Dimethyol-0-cresol

Developed from a symposium sponsored by the Division of Polymeric Materials Science and Engineering of the American Chemical Society

ACS Symposium Series No. 313
321 pages (1986) Clothbound
LC 86-10831 ISBN 0-8412-0977-4
US & Canada **$69.95** Export **$83.95**

Order from:
American Chemical Society
Distribution Office Dept. 20
1155 Sixteenth St., N.W.
Washington, DC 20036
or CALL TOLL FREE 800-424-6747
and use your credit card!

ability for preparative-scale fractionations, such as those required in the biotech industry. The use of CCC for cell separations, says Sutherland, is still an emerging technique that is far from perfect. It should move forward, however, with the identification of new biocompatible phase systems that are more appropriate for use with CCC than the current aqueous polymer systems.

Field flow fractionation

Steric field flow fractionation (steric FFF), an elution-based technique that sorts particles according to their size, can also be used for cell fractionation, according to Karin Caldwell of the University of Utah. FFF has a large fractionation range (baseline separation of a seven-component mixture of polystyrene latex spheres with diameters ranging from 2 to 45 μm has been performed in less than 5 min), making it particularly useful for fractionation of cells with diameters in the 1–20-μm range.

The fractionator is a thin ribbon-shaped channel that is exposed to a centrifugal field perpendicular to the major walls. Sample particles settle at one of the channel walls, and the flow of carrier forces the particles to move downstream at rates proportional to their size. This is a highly efficient process, and separations can be accomplished in a matter of minutes.

One advantage of FFF, says Caldwell, is that the choice of carrier has little influence on the separation, allowing use of a carrier with maximum compatibility with the cells, such as aqueous buffers or growth medium. "Generally, when you work with live materials such as cells, the less bizarre an environment they are exposed to, the better off you are," she explains. "If cells are separated in a polymer phase, then you have to move them very carefully from the polymer medium to a growth medium so as to avoid osmotic and other shocks. But because FFF can be performed directly in the growth medium, no such transfers are necessary."

This carrier flexibility, combined with the short separation times, makes FFF particularly suitable for handling cell samples in which viability following separation is important. Hela cells, neurons, and glial cells have all shown good growth in tissue culture after passage through a sedimentation-based steric FFF system.

Like the aqueous polymer-based techniques, FFF can be used to detect small differences in cell populations (although in the case of FFF, these are differences in size rather than in cell surface characteristics), as well as for preparative separations. For example, retention differences can be seen between cells of the same type from different species and between cells of the same line grown in different environments. FFF can also be used to separate cells for use in cloning and production of monoclonal antibodies and to obtain growth-synchronized cell populations. *M.D.W.*

Instrumentation Growth Areas

Environment, process control, and biotechnology are seen driving the market

Although the worldwide analytical instrument industry is currently estimated to be generating more than $3 billion in annual revenues, it has never enjoyed high visibility among investment analysts. This lack of visibility probably has something to do with the title of a recently published analysis of the industry by Nancy E. Pfund of Hambrecht & Quist Inc. (San Francisco, Calif.): "The Quiet Revolution: Analytical Instrumentation Extends Its Reach." For, despite the fact that revolutionary advances have been made in analytical instrumentation over the past decade, this revolution has heretofore obtained little recognition on Wall Street.

Investment analyses of Perkin-Elmer Corporation, for example, frequently focus on the company's semiconductor chip-making equipment, despite the fact that analytical instrumentation constitutes a larger segment of Perkin-Elmer's gross revenues. Recognition of the scientific instrument industry as a quintessentially high-technology enterprise has developed slowly, which makes increased attention to the industry by an invest-

Simultaneous Elemental Analysis

Introducing the Spectrace 6000 — a low cost, easy to use energy dispersive X-ray fluorescense system for process monitoring environments.

- Single pushbutton, non-destructive elemental analysis with minimum or no sample preparation
- Low ppm to 100% concentrations of Na-U may be determined in solids, powders or liquids
- X-ray tube source sample excitation
- High resolution, maintenance free, thermoelectrically cooled, solid state X-ray detector
- IBM PC XT or AT data processor
- Extensive software library provides quantitative analysis for sample types ranging from a relatively simple hydrocarbon matrix to more complex mineral and alloy matrices

Tracor Xray

TEL. 415/967-0350

CIRCLE 203 ON READER SERVICE CARD

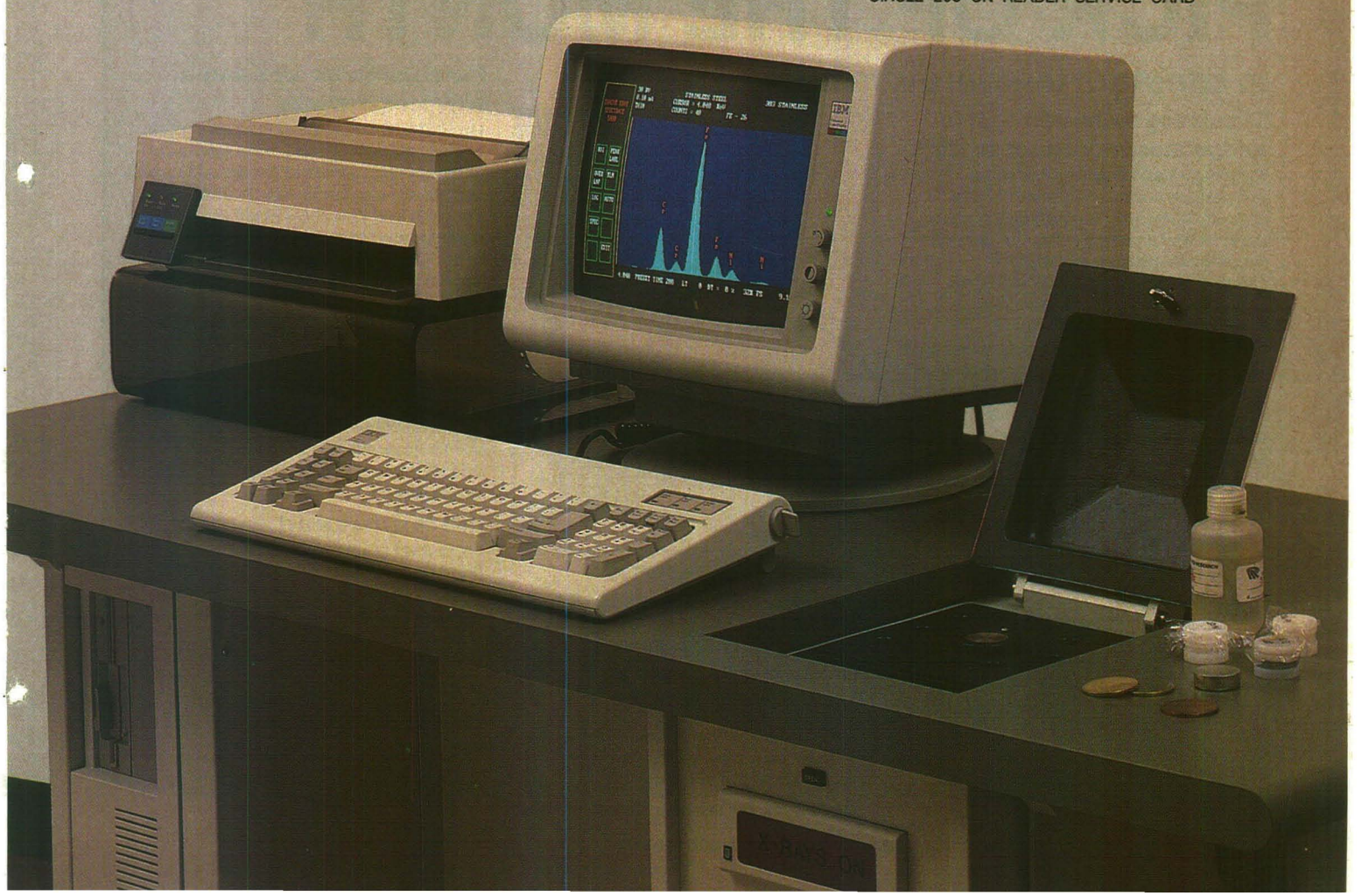

ment firm of the caliber of Hambrecht & Quist a development of some importance.

The Hambrecht & Quist study presents an interesting brief on three major forces shaping contemporary demand for analytical instrumentation—environmental concerns, process control needs, and biotechnology.

Environment. According to the report, about 5% of the total federal funding allocation for Superfund (the program designed to identify and clean up chemical hazards at abandoned waste sites across the country) will go toward analytical testing. As of this writing, Superfund has not yet been reauthorized by Congress, but proposals for five-year appropriations for Superfund go as high as $10 billion, which would set the analytical component at as much as $500 million. The Resource Conservation and Recovery Act, which extends coverage to all current and future toxic waste problems, will also generate considerable revenue for analytical testing.

The way in which environmental concerns can translate into demands for analytical services is exemplified by a 1985 California incident in which widespread contamination of watermelons by the pesticide aldicarb resulted in the destruction of tons of watermelons. The aldicarb incident focused attention on the need for greater financial support of the California Department of Food and Agriculture's analytical laboratories. This led to an increase in the annual departmental budget of $1.5 million, about half of which is being allocated to an instrumentation replacement program. According to a spokesman at the department, this year's funding increase is supporting the purchase of eight gas chromatographs and four liquid chromatographs (plus associated detectors and accessories), to be used by departmental analytical laboratories in Berkeley, Fresno, Anaheim, and Sacramento. The purchase was in the procurement stage this past July.

The Hambrecht & Quist study is the latest instance of what seems to be a growing interest among investment analysts in the analytical instrument industry.

Additional expenditures for analytical equipment purchases have stemmed from corporate concerns about potential liability relating to inadvertent releases of toxic substances. The report explains that "the long-term trend will be toward self-monitoring, given the social and legal costs of rectifying problems once they occur. This trend will drive demand for both lab-based and real-time measuring capabilities."

Process monitoring and control represents a second area of growth for analytical instrumentation. The Hambrecht & Quist report sees 25–30% annual growth for various instruments used in process monitoring and control, such as high-performance liquid chromatographs and ion chromatographs. "Corporations wanting to improve efficiency in the face of increas-

PICK OF THE MONTH

in constant temperature baths

Circulating Baths with built-in refrigerators work down to -35°C

Eight high-performance circulating refrigerated baths—5-liter and 12-liter capacity baths with built-in refrigeration systems and a choice of four immersion circulators—provide you with the capability of selecting a cost-effective combination that will best suit your application.

The baths feature heat-removal rates up to 360 watts, pump capacities to 10 liters per minute, operating ranges down to -35°C, microprocessor programming capability, temperature presets, and digital control and display.

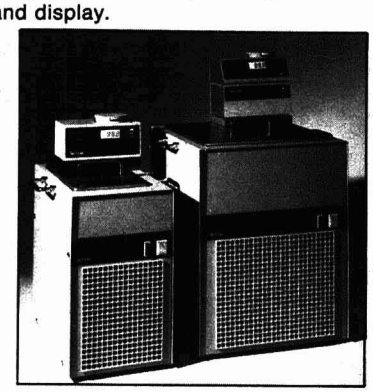

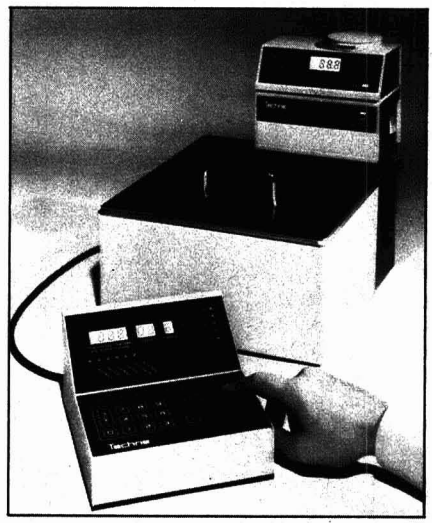

Set your own program for automatic heating and cooling

Up to 119,880 consecutive temperature changes (15 "rise," "fall" or "hold" segments per program—each for a specified time period: 8 programs per cycle; 999 cycle repeats) can be programmed into the Tecam® TP-16. The TP-16 can be used with any controller accepting an input of 5mV/°C.

Fluidized Solids for safety at high temperatures

Up to 600°C Tecam® lab fluidized baths provide the safety and convenience you need but find difficult to get with other high temperature systems. Dry fluidized solids circulate and flow like a liquid but have no melting point or boiling point. No fumes or evaporation. Ideal for reaction experiments, heat treatment, distillation, etc.

Free pack of insulating balls with your bath

With each Tecam® bath you order, you get a free pack of insulating balls. It's our way of saying thank you for your order and introducing you to a unique and very effective way of reducing heat loss and evaporation from your bath.

Call or write today!

If you want to upgrade your lab with a bath that has the features you are looking for, at a price that will surprise you (pleasantly!) and is backed up by nationwide distribution and service, request more details now! Send for complete details to Techne Incorporated, 3700 Brunswick Pike, Princeton, NJ 08540-6192. Or call (609) 452-9275.

Techne CELEBRATING OUR 25TH ANNIVERSARY

CIRCLE 201 ON READER SERVICE CARD

Karl Fischer's idea has undergone optimum development by Metrohm

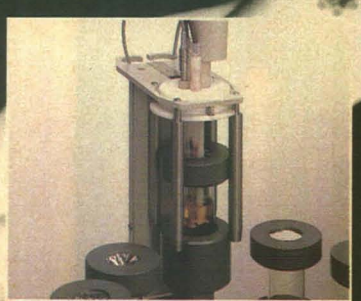

KF Sample Changer

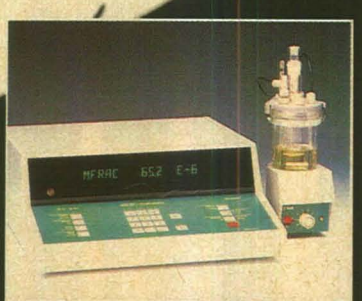

KF-Coulometer

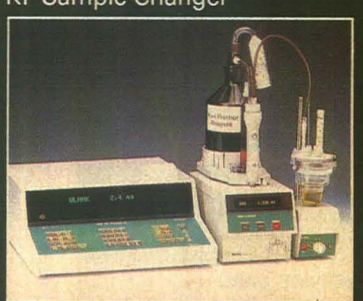

KF-Processor 658

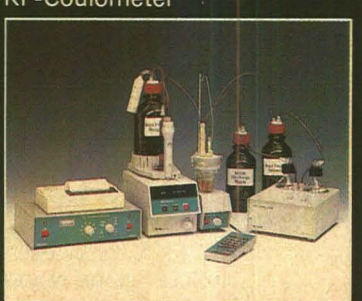

KF-Automat 633

The appropriate solution for every application

For sample series
The new KF Sample Changer with 678 EP/KF Processor for automated water determination from 1–100%. Ideal for routine laboratory work. With options for balance and LIMS.

For trace water
Over 1 ppm water content rapidly and precisely with the KF Coulometer. Factor setting unnecessary, many analyses in one reagent vessel possible. Ideal for trace amounts and liquid samples.

KF at budget prices
The 633 KF Automat is a modular system constructed from economical components. Measure automatically even on a tight budget.

For direct and back titration
For the universal determination of single samples, the 658 KF Processor is available. With options for balance, computer, second Dosimat, KF Oven and Pump Unit, it can be adapted to every problem.

Metrohm
Measurement in Chemistry
Worldwide with Metrohm

METROHM Ltd.
CH-9100 HERISAU Switzerland
Phone 071 / 53 11 33
Telefax 071 / 52 11 14
Telex 77267 metro ch

Brinkmann
INSTRUMENTS CO.
Cantiague Road, Westbury, New York 11590
Phone: (516) 334-7500, TWX: 510 222 8524

CIRCLE 141 ON READER SERVICE CARD

Eckhauer + Schoch ASW

ing international competition will fine-tune their manufacturing processes with analytical instrument-based monitoring of critical compounds," says the report.

In the vanguard of developments in this area has been the Center for Process Analytical Chemistry (CPAC), a cooperative academic–industrial enterprise founded by Bruce Kowalski, James Callis, and their colleagues at the University of Washington (*Anal. Chem.* **1984,** *56*[1], 36 A). These researchers recognized a trend that has already seen integrated-circuit manufacturers instituting on-line chromatographic sampling systems to detect chip impurities and biotechnology companies installing analytical sensors and spectrometers to monitor input and product concentrations in fermentation vats.

Of course, recognition of the tremendous potential of process analytical chemistry predates the establishment of CPAC by many years. For example, Sidney Siggia (then of Olin Mathieson, later to join the faculty at the University of Massachusetts) explained back in 1964 that "the signal from the analytical device can be used to activate computing and/or controlling mechanisms so that the chemical process can be automatically kept within the desired limits. . . . In the application of analytical approaches for in-line process analysis, we have seen great advances. Almost any analytical tool is now available in an on-stream form; i.e., infrared and ultraviolet, mass spectrometry, gas chromatography, titration, colorimeters, . . . and many others" (*J. Chem. Ed.* **1964,** *41*, 329–30). However, process analytical chemistry has become considerably more important over the past few years as companies have had to produce more efficiently to compete in global markets, comply with increasingly complex government regulations, and deal with burgeoning financial exposures from high-award liability suits.

Biotechnology is a third major area of potential growth for the analytical instrument industry, a fact exemplified by recent events such as the acquisition of Brownlee Labs by Applied Biosystems Inc. and the establishment of joint ventures such as Perkin-Elmer Cetus Instruments and HP Genenchem. The significance of the biotechnology–analytical chemistry interface has been frequently noted in ANALYTICAL CHEMISTRY (see, for example, Warren, Doris C. **1984,** *56*[14], 1528–44 A; **1984,** *56*[14], 1548–54 A; and Glajch, Joseph L. **1986,** *58*[3], 385–94 A.

The Hambrecht & Quist study is the latest instance of what seems to be a growing interest among investment analysts in the analytical instrument industry. (Companies such as Alex. Brown & Sons of Baltimore, Md., and L. F. Rothschild, Unterberg, Towbin of New York City have also followed the industry closely for the past few years.) This increased visibility has been helped along by the evident success of recent start-ups such as Mattson Instruments, Zymark Corporation, and Nelson Analytical, by the advent of the first newsletter ("Analytical Instrument Industry Report") to cover the industry in a comprehensive fashion, and by investment seminars sponsored by organizations such as the Scientific Apparatus Makers Association. It is hoped that this increased attention to the industry by the investment community will attract more resources to analytical instrumentation development and, thus, ultimately redound to the benefit of the analytical chemistry community. *S.A.B.*

CONSTANT

LOW TEMPERATURE FREEZERS THAT ASSURE PERFORMANCE WHEN THE HEAT IS ON.



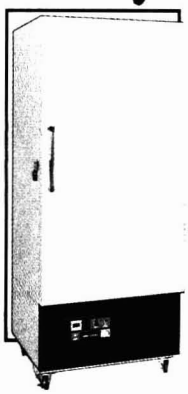

Whether it's sample or specimen storage, or applications processing, Puffer-Hubbard offers a no-nonsense alternative to your freezer shopping. Our freezers assure -90°C in work environments of up to +90°F. Puffer-Hubbard cools your budget too with prices that buy good reliable performance – and nothing less!

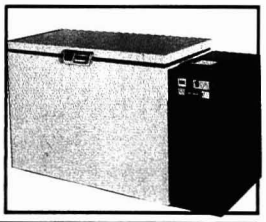

puffer hubbard

Write or call for more information on Puffer-Hubbard Laboratory Appliances, a name you can trust.

350 Park Ave., 11th Floor
New York, N.Y. 10022-6022
1-800-521-8004

CIRCLE 168 ON READER SERVICE CARD

eenie, meenie, miney, mo.



One of these bottles contains a hazardous chemical. Without proper labels, choosing the right bottle becomes a dangerous guessing game. Our new catalog features over 15 pages of chemical labels, including "In Plant" labelling systems that meet the latest "Right-to-Know" requirements.

For your free 200 page safety equipment catalog call (1-800-356-0783) or circle the reader service card number.

LAB SAFETY SUPPLY

A division of Science Related Materials, Inc.
P.O. Box 1368, Janesville, WI 53547-1368

CIRCLE 125 ON READER SERVICE CARD

RESEARCH-SENSITIVE FT-IR UNDER $40,000

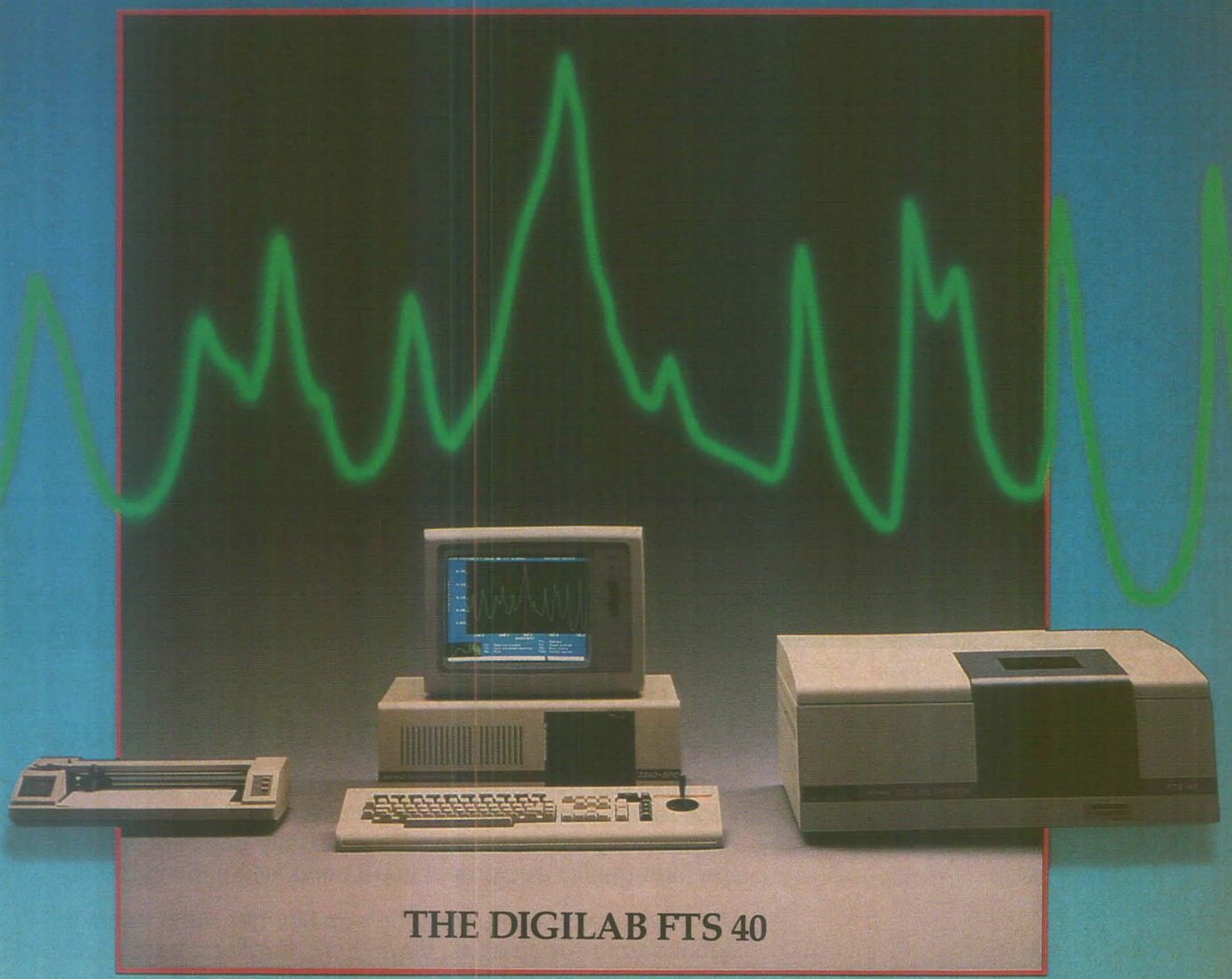

THE DIGILAB FTS 40

If you want an FT-IR spectrometer powerful enough for tomorrow's problems as well as today's, we built our new FTS 40 just for you.

The FTS 40 has the same sensitivity as our higher priced FTS spectrometers, allowing you to do GC/IR, microscopy, ATR, photoacoustic studies and other research level techniques, on difficult samples, over a range of 10,000 cm^{-1} to 220 cm^{-1}, at a resolution of 0.5 cm^{-1}.

And with its new desktop 3240 data system, the FTS 40 has the computing power for GC/IR, rapid searching of large Sadtler libraries, multi-component analysis and other applications far beyond the capabilities of other modestly priced spectrometers.

Available with accessories and full support. Starting at $39,500, it's the best value in FT-IR today.

Please write for literature to Bio-Rad Digilab Division, 237 Putnam Avenue, Cambridge, MA 02139. Or call (800) 225-1248, ext. 150.



BIO-RAD Digilab Division

CIRCLE 23 ON READER SERVICE CARD

Specialty Gases plus...

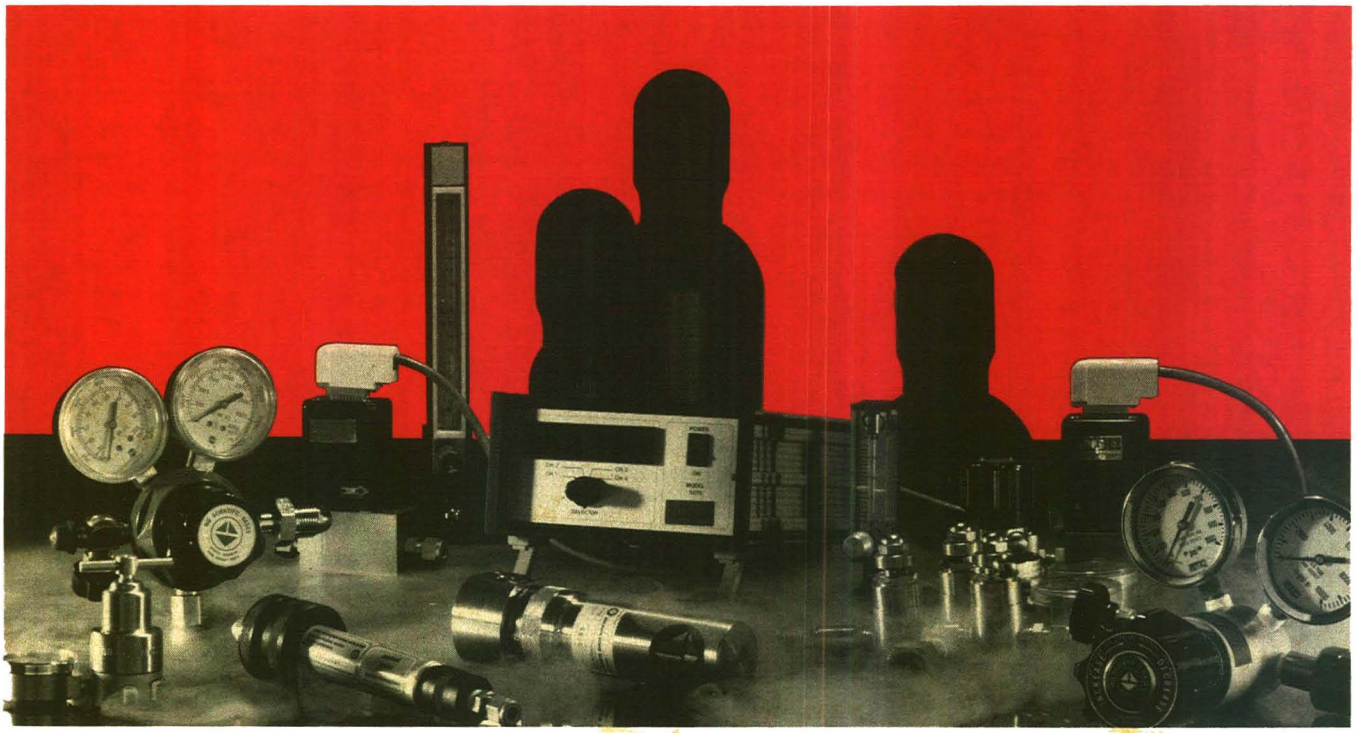

...all the high quality gas handling equipment you need.

We offer you not only a full range of high purity gases for a wide range of applications, and more Grade 6 gases (99.9999% pure) than any other specialty gas supplier, but all the high-quality equipment you'll need for handling them.

We have over 250 separate high-quality hardware items to choose from—regulators, flowmeters, purifiers, purge systems, filters, accessories, and related components. For any purity level of toxic and non-toxic, corrosive and non-corrosive gases.

NEW

And now we make top-quality Gas Cabinets, too—engineered for safety, designed for convenience. All with the quality you demand and at prices you'll like!

Call or write for the facts.
MG Industries/Gas Products Division
P.O. Box 945, Valley Forge, PA 19482. (215) 630-5400.

MG Industries™
Gas Products

Circle 133 for Gas Cabinet information. Circle 134 for Gas Handling Equipment information.

CIRCLE 95 ON READER SERVICE CARD →

0.2 ... 200 mg

Multifunctional CHN, CN, N or O analyzer

Heraeus Elemental Analyzer CHN-O-Rapid

Range of sample weights
For solid and liquid substances from 0.2 to 200 mg, depending on the element content.

Analysis of inhomogenous substances, such as coal, soil samples, agricultural products, fine chemicals, etc.

Optimum substance decomposition up to 1150 °C.

Optional O determination with modern non-dispersive IR photometer in only 4 to 6 min.



Ee

Heraeus W.C. Heraeus GmbH · Produktbereich Elektrowärme
Postfach 1553 · D-6450 Hanau 1 · Telephone (06181) 35-1

Elemental Analyzer CHN-O-Rapid

Characteristics

Sample weights:

from 0.2 to 200 mg, depending on substance (e.g., samples of nitroaniline from 0.2 to 25 mg).

Sample feed:

automatic feed, 49 samples; adjustable from continuous to single feed.

Working temperatures:

combustion tube O: 1140 °C
reduction tube CHN: 550 – 700 °C

Duration of combustion:

variable from 0.1 to 9.9 min; recommended: 1.5 min.

Indication of measured values:

with computer: automatic print-out in %;
with printer (optional): automatic print-out of integrals.

Standard deviation:

0.1 % for nitroaniline.

Absolute deviation:

generally 0.2 %.

Gas consumption per analysis:

1 to 1.5 l of He and 40 to 100 ml of O_2 for one simultaneous CHN determination.
280 to 450 ml of forming gas for one O determination.

Required consumable reagents and gases:

commercially available reagents for analyses.

Advantages

- Multifunctional analyzer with four different operational modes: CHN, CH, N and O (optional); uncomplicated conversion to O determination in just about 5 min.
- CHN determination: suited for all organic and inorganic substances which decompose at 1050 °C in an oxygen stream.
  O determination: suited for organic substances which are cracked at 1145 °C.
- Large sample weights reduce demands on homogeneity.
- Uncomplicated, automatic sample feed via a vertical combustion furnace.
  Sample feeder loading possible any time during the analysis.
- Combustion temperature and tube filling may be adapted readily to each measuring problem: hence complete decomposition without additives.
- The integrator will start each desorption process only after total integration of the preceding gas component has been achieved. This feature permits measurement of radically different quantities of CHN.

Duration of analysis:

Simultaneous CHN determinations:
9 to 14 min.
CN determinations: 6 to 9 min.
N determinations: 6 to 9 min.
O determinations: 4 to 6 min.

Computer-controlled analysis program: hence regular, automatic monitoring of the calibrating factors, the reduction tube filling, and the mechanical analysis. Automatic transfer of the weighing data.

Measuring ranges:
– N: 1 x 10^{-3} mg absolute
– C: 5 x 10^{-4} mg absolute
– H: 1 x 10^{-4} mg absolute
– O: 1 x 10^{-3} mg absolute

Design featuring easy service and handling (advantageous for leak tests, tube changes, etc.).

Inexpensive disposable tin boats or capsules for liquid samples.

Applications

- Polymers, including those containing halogens, phosphorus, sulphur and similar substances (also Teflon®, for example).
- Petroleum products, such as diesel oils, gasolines, lubricants, oil additives and fuel oil.
- Refinery catalysts, carbon determination.
- All types of coal, from anthracite to lignite.
- Oil shale, crude as well as processed.
- Synthetic oils and gasolines in liquid and solid form.
- All shorts of petrochemicals and chemicals in liquid (weighed and burned in tin capsules) and solid form.
- Coal liquefaction products.
- Pharmaceutical products.
- Ocean and river bottom sediments.
- Soil samples.
- Synthetics and rubber products.
- Plants, wood, food products, fruit.
- Hardly combustible substances, such as graphite/carbon. (Graphite was found to contain from 99.6 to 99.9 % carbon).

Examples: Complex Substances

Substance	Range of sample weights (mg)	% C	% H	% N
Plastics	10 – 30	12.81	3.05	2.35
Heavy oil	4 – 10	85.30	10.80	0.28
Soil	30 – 200	2.79	0.40	0.17
Anthracite	3 – 10	75.50	4.92	1.44
Lignite coke	4 – 10	98.40	0.30	0.30
Lignite briquettes (free from water and ashes)	6 – 10	71.50	4.93	0.77

Request for Information

Please send the following:

- ☐ Brochure PEW-F 1.1 Elemental Analyzer CHN-O-Rapid
- ☐ Detailed Offer on CHN-O-Rapid
- ☐ Flask-Type Combustion Apparatus acc. to Schöniger

From:

Name _____
Company/Institution _____
Dept., Lab. _____
Street/P.O. Box _____
City _____ ZIP Code _____

Heraeus
W.C. Heraeus GmbH
Produktbereich Elektrowärme
P.O. Box 1553
D-6450 Hanau 1
Telephone (0 61 81) 35-1

e/17

Direct racemic separation



Now you can directly resolve racemic amines, acids and many other compounds without any preceding preparations of derivatives. Use the new EnantioPac HPLC cartridge column from LKB. It outdates every other known separation technique with a completely novel and patented approach. EnantioPac is based on the immobilized plasma protein α, -acid glycoprotein, which shows high enantioselectivity for a wide range of pharmaceuticals and other chiral substances. Lets you screen for optical purity very fast, very simply and very reliably.

Substances separated with EnantioPac

Substance	α		α		α		α
Atropine	1.64	Dimethindene	1.53	Methadone	1.59	Phenmetrazine	1.57
Bromdiphen-hydramine	1.17	Diperodone	1.47	Methorphan	2.54	Phenoxy-benzamine	1.37
Brompheniramine	1.50	Disopyramide	2.70	Methylatropine	1.27	Promethazine	1.25
Bupivacaine	1.41	Doxylamine	1.37	Methylhom-atropine	4.2	Pronethalol	1.26
Butorphanol	1.99	Ephedrine	1.83	Methylphenidate	1.70	Propoxyphene	2.3
Carbinoxamine	1.33	Ephedrine, pseudo-	1.34	Metoprolol	1.64	Propranolol	1.13
Chlorpheniramine	2.26	Homatropine	1.63	Nadolol A	3.98	Terbutaline	1.22
Clidinium	1.21	Labetalol A	2.10	Nadolol B	3.03	Tocainide	1.44
Cocaine	1.46	Labetalol B	1.36	Oxyphencyclimine	1.42	Tridihexethyl	1.64
Cyclopentolate	3.86	Mepensolate	1.32	Oxprenolol	1.25	Trimeprazine	1.11
		Mepivicaine	1.25				

This list is published by the kind permission of Göran Schill, Thomas D. Doyle and Irving W. Wainer, Division of Drug Chemistry, Food and Drug Administration, Washington DC.

Applications and references

You'll find these in our latest brochure. Together with detailed technical information about this revolutionary new column. Get in touch with LKB. We'll send you all the facts. Fast!

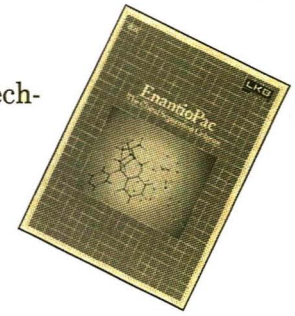

LKB
BROMMA

LKB-Produkter AB, Box 305, S-161 26 Bromma, Sweden. Tel. +46 (8) 98 00 40, telex 10492

Antwerp (03) 218 93 35 · **Athens-Middle East** +30 (1) 894 73 96 · **Copenhagen** (01) 29 50 44 · **Hongkong** (852) 5-555555
London (01) 657 88 22 · **Lucerne** (041) 57 44 57 · **Madras** (044) 45 28 74 · **Moscow** (095) 256-9002 · **Munich** (089) 85 830
Paris (06) 928 65 07 · **Rome** (06) 39 90 33 · **Stockholm** (08) 98 00 40 · **Tokyo** (03) 293-5141 · **Turku** (021) 678 111
Vienna +43 (222) 92 16 07 · **Washington** (301) 963 3200 · **Zoetermeer** (079) 31 92 01
Over 60 qualified representatives throughout the world.

356

CIRCLE 127 ON READER SERVICE CARD

PHOTON ENGINEERING '87

A Workshop for Instrument Manufacturers Their Engineers and Product Designers

PITTSBURGH CONFERENCE • ATLANTIC CITY • MARCH 9–13, 1987

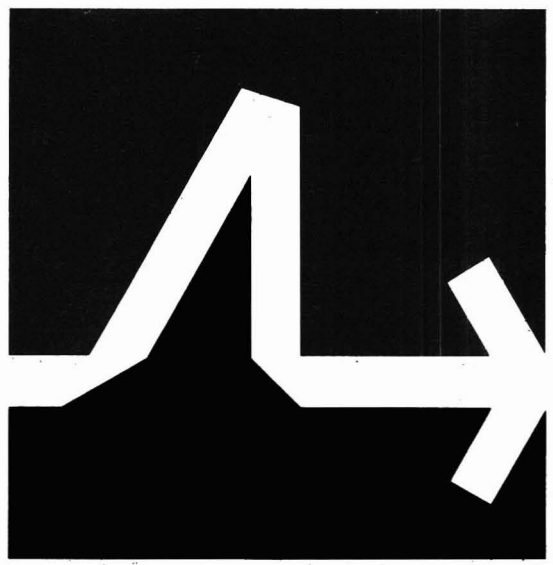

If you're involved in the design or development of light-sensitive instruments, plan now to attend Hamamatsu's fourth annual Photonic Workshop. Hamamatsu's senior engineers for vacuum detectors, solid state detectors and scientific light sources will review latest technology available for your instruments. They'll also provide trouble-shooting assistance to help you solve problems. If you require special specifications, ask about custom selection or product modification possibilities.

The workshops will be in continuous sessions at 3 tables during the Pittsburgh Conference. You will have the full attention of Hamamatsu's engineers responsible for each product line discussed during a private session at the tables you select.

There is no charge and you may request a session at each of the tables. But, we need to hear from you now to reserve time for your appointment.

Learn how new technology can enhance your instruments' performance at Photon Engineering '87.

TABLE 1.

DETECTORS Learn about a new fast response PMT for fluorescent life time studies, a new red sensitive fiberoptic faceplace PMT, a hollow cathode PMT, plus the world's smallest and world's largest photomultiplier tubes and many others.

TABLE 2.

SCIENTIFIC LIGHT SOURCES A new mercury xenon lamp, a continuous and a flash xenon lamp will be demonstrated. New zinc, cadmium and mercury lamps also will be shown along with Hamamatsu's high performance deuterium and hollow cathode lamps.

TABLE 3.

SOLID STATE DETECTORS Investigate the advantages of plasma coupled devices, self-scan arrays, intensified multi-dimensional arrays, silicon, gallium arsenide, germanium and other precision solid state detectors.

Instrument Manufacturers Call Now For an Appointment at Photon '87.

800-524-0504.

In New Jersey call 201-231-0960.

HAMAMATSU

HAMAMATSU CORPORATION • 360 FOOTHILL ROAD, P.O. BOX 6910, BRIDGEWATER, NJ 08807 • PHONE 201/231-0960

UNITED KINGDOM: Hakuto International (UK) Ltd. (phone: 0992-769090) • FRANCE: Hamamatsu Photonics France (phone: 46 55 47 58)
ITALY: Hess S.P.A. (phone: [02] 34.92.679) • W. GERMANY: Dr. R. Seitner, Mess-U, Regeltechnik (phone: 08152-3021)
SWEDEN NORWAY, FINLAND, DENMARK: Lambda Electronics AB (phone: 08-620610)

CIRCLE 101 ON READER SERVICE CARD

October 20-24

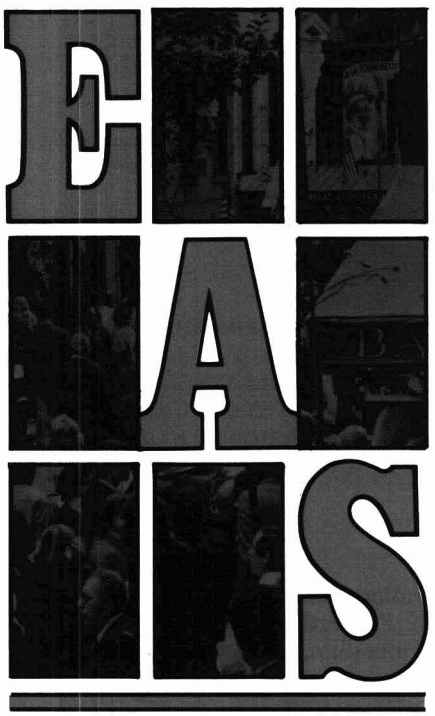

New York City

The Silver Jubilee Eastern Analytical Symposium (EAS) will be held at the New York Hilton in New York City, Oct. 20–24. The meeting is sponsored by the North Jersey and New York Sections of the American Chemical Society; the Delaware Valley, New England, and New York Sections of the Society for Applied Spectroscopy; and the American Microchemical Society.

Sixty technical sessions including poster sessions are scheduled. Session topics include

- advances in environmental analysis
- advances and future trends in microbore column technology
- frontiers in toxicology and therapeutic drug monitoring
- new directions in chemometrics
- thermal analysis for pharmaceutical application
- investigative characterizations of new and commercial polymers
- twenty-five years of NMR spectroscopy
- frontiers for sample introduction in atomic emission spectroscopy
- the ubiquitous PC
- advances in pharmaceutical and biomedical analysis
- LIMS: Starting up and keeping them up-to-date

Four symposia will be held to honor this year's award recipients. Paul Lauterbur will receive the New York Society for Applied Spectroscopy Gold Medal at a symposium on Wednesday, Oct. 22. George H. Morrison, Editor of ANALYTICAL CHEMISTRY, will receive the first EAS Award for Outstanding Achievements in Analytical Chemistry at a symposium on Thursday, Oct. 23. Wilhelm Simon will be presented the American Microchemical Society's Benedetti–Pichler Memorial Award at a symposium on Friday, Oct. 24. Finally, the EAS Award in Chromatography will be presented to Csaba Horvath at a symposium on Friday, Oct. 24.

An exposition of scientific instruments will also take place in the New York Hilton. In addition, there will be 12 workshops sponsored by the exhibitors. Workshops consisting of lectures and demonstrations will be offered on the following topics: capillary and headspace GC, PCs in the laboratory, X-ray diffraction and fluorescence, NMR, polymer characterization, HPLC detectors and columns, IR accessories, polymer flow studies, LIMS, MS, FT–IR, and robotics. Those interested in preregistering should use the form on p. 1097 A. For further information on the workshops, contact Robert Vetrecin, EAS Workshops Chairman, Ethicon, Route 22, Sommerville, N.J. 08876 (201-218-3051).

The American Chemical Society will sponsor six short courses, Oct. 18–19, in conjunction with EAS: Effective Management of Chemical Analysis Laboratories, Quality Assurance of Chemical Measurements, Special Topics in Liquid Chromatography, Capillary Gas Chromatography, The Electronic Laboratory: Tutorials and Case Histories in Laboratory Automation, and Gas Chromatography/Mass Spectrometry. For additional information, see p. 1116 A of this issue or contact the Department of Educational Materials, American Chemical Society, 1155 16th St., N.W., Washington, D.C. 20036 (202-872-4508).

Four EAS-sponsored short courses will also be offered: Near-IR Analysis: An Industrial Tool (Oct. 18–19), Fundamental Principles and Applications of 2D NMR (Oct. 20), Advanced HPLC for the Practicing Chromatographer (Oct. 21), and An Introduction to Laboratory Microcomputers (Oct. 22). Further information on these courses can be obtained from Gwendolyn Chmurny, EAS Short Course Chairman, NCI-Frederick Cancer Research Facility, P.O. Box B, Frederick, Md. 21701 (301-698-1226).

The form on page 1097 A can be used for preregistration.

In addition, a short course will be offered for undergraduate chemistry majors. It is designed to educate students about careers as analytical chemists in industry. The course is complimentary and limited to 35 students. Preregistration is necessary. For more information, contact Alan Ullman at 513-659-6445.

An employment service will be available during the meeting. For details, contact Karl Bratin, EAS Employment Chairman, Pfizer, Central Research, Box 25, Groton, Conn. 06340 (203-441-4910).

The Symposium dinner reception will be held on Wednesday, Oct. 22, in the Grand Ballroom of the New York Hilton Hotel. It is complimentary and open to all regular registrants, exhibitors, and speakers.

The EAS has reserved a block of rooms for conferees at the New York Hilton Hotel. To obtain special convention rates, rooms must be reserved through the EAS. Reservation forms can be obtained from Ken Fleischer, EAS Housing Chairman, R.D. No. 3, Box 730, Valatie, N.Y. 12184 (518-758-6431) or from Hal Ferrari (914-623-3019).

Preregistration may be completed by filling out the form on p. 1097 A and sending it to Hercules Felder, EAS Registration Chairman, P.O. Box 213, Middlesex, N.J. 08846. Preregistrations must be postmarked by Sept. 12. For further information on the symposium, contact S. David Klein, EAS Publicity, 642 Cranbury Cross Rd., North Brunswick, N.J. 08902 (201-846-1582).

Symposium Officers

General Chairman: *Walton Caldwell*, Berlex Laboratories
Chairman-Elect: *S. David Klein*, Merck & Company
Past Chairman: *Hal Ferrari*, Lederle Laboratories
Secretary: *Richard Soltero*, Berlex Laboratories
Treasurer: *Harvey Gold*, E.I. du Pont de Nemours & Company
Archives Chairman: *Louis Brancone*
Arrangements Chairman: *J. P. Luongo*, AT&T Bell Laboratories
Audit Chairman: *S. David Klein*, Merck & Company
Budget Chairman: *S. David Klein*, Merck & Company
Employment Chairman: *Karl Bratin*, Pfizer
Exhibit Manager: *Norman Gardner*
Exposition Chairman: *William Grossman*, Hunter College
Housing Chairman: *Kenneth Fleischer*
Legal Chairman: *Thomas Kashuba*
Long-Range Planning Chairman: *S. David Klein*, Merck & Company
Message Center Chairman: *David Nash*, AT&T Bell Laboratories
Parlimentarian: *Kenneth Fleischer*
Printing and Direct-Mail Chairman: *S. David Klein*, Merck & Company
Program Chairman: *Concetta Paralusz*, Permacel/Avery International
Publicity Chairman: *Waldemar Palaitis*, Merck & Company
Registration Chairman: *Hercules Felder*, Permacel/Avery International
Short Courses Chairman: *Gwendolyn Chmurny*, NCI—Frederick
Student Awards Chairman: *Mary Lynn Grayeski*, Seton Hall University
Technical Films Chairman: *James McDivitt*, Ethicon
Workshops Chairman: *Robert Vetrecin*, Ethicon

Program

Monday Morning

Advances in Environmental Analysis—I Isolation, Detection, and Evaluation of Toxic Chemicals in Water

Chaired by F. C. Kopfler, U.S. EPA

9:00 Biological Testing/Chemical Interface. **V. L. Cunningham**, R. E. Hannah, and J. B. Johnston, Smith Kline and French Laboratories

9:40 Evaluation of XAD Resins for the Preparation of Samples of Drinking Water for the Ames Test. **H. P. Ringhand** and F. C. Kopfler, U.S. EPA

10:40 Evaluation of Continuous Liquid–Liquid Extractor for the Preparation of Samples of Drinking Water for the Ames Test. **I. H. Suffet,** R. Baker, L. Lippincott, and T. Atashroo, Drexel U

11:20 The Health Effects–Analytical Chemistry Interface at Water Treatment Plants. **J. Mallevialle** and L. Cognet, Lyonnaise Des Eaux, France

General Analytical Chemistry and Computers in Chemistry

Chaired by V. V. Berry, Salem State College

9:00 Analytical Laboratory Data Acquisition and Management with a Shared Resource Management Network. **E. R. Fluck,** J. A. Knowles, T. R. Brunner, and J. A. Hofmann, Wyeth Laboratories

9:20 Automated-System Suitability Using Interactive Instrument Control. **S. D. Frans,** C. W. Crandell, J. M. Nelson, and Y. Liang, Spectra Physics

9:40 Merging Third-Party Software into an Integrated Laboratory Data Management Network. **J. A. Hofmann,** T. R. Brunner, J. A. Knowles, E. R. Fluck, Wyeth Laboratories

10:00 New Design for Chromatography Automation. **P. G. Berthrong,** Beckman Instruments

10:40 Telephone Bugged? Send Spectral Data Anyway—With Safety! **D. A. Burns.** Technicon Science Center

11:00 Review of Eluent Gradients in Microbore LC—Techniques and Applications. **V. V. Berry,** Salem State College; H. E. Schwartz, Brownlee Laboratories

11:20 Science and the Preservation of Art. **J. D. Portell,** Sculpture Conservation

11:40 The Forensic Scientist in the Courtroom. **A. A. Porro, Jr.,** U of Baltimore

Advances and Future Trends in Microbore Column Technology—GC/HPLC

Chaired by F. J. Yang, Varian Instrument Group

9:00 Introduction. **F. J. Yang,** Varian Instrument Group

9:05 Microbore Column Chromatography: A Review of Current Technology and Future Trends. **S. P. Cram** and F. J. Yang, Varian Associates

9:45 Methodical and Instrumental Advances in Analytical High-Resolution GC. **G. Schomburg,** Max Planck Institut für Kohlenforschung, F.R.G.

10:40 Capillary Zone Electrophoresis of Biopolymers. **J. W. Jorgenson,** J. S. Green, D. Rose, Y. Walbroehl, and M. Bushey, U of North Carolina

11:20 Column Stability in Capillary Supercritical Fluid Chromatography. **K. E. Markides,** C. L. Woolley, J. S. Bradshaw, and M. L. Lee, Brigham Young U

Laser Excitation in Analytical Spectroscopy

Chaired by J. D. Winefordner, U of Florida

9:00 Analytical Limits of Laser-Excited Spectroscopy. **J. D. Winefordner,** U of Florida

9:30 Laser-Induced Ionization Spectroscopy of Small Biological Precursors in Supersonic Beam–Mass Spectrometry. **D. M. Lubman,** U of Michigan

10:20 Laser-Excited Atomic Fluorescence Spectrometry (LEAFS) in a Carbon Tube Furnace with Zeeman Background Correction. **R. G. Michel,** F. Preli, and J. P. Dougherty, U of Connecticut

10:50 Laser-Induced Molecular Fluorescence. **M. J. Sepaniak,** U of Tennessee

11:20 Analytical Applications of Nonlinear Optics Including Phase Conjugation. **J. M. Ramsey,** Oak Ridge National Laboratory

Preregistration

Eastern Analytical Symposium
October 20–24, 1986

Make checks payable to "Treasurer, EAS" and mail with this form to Hercules Felder, EAS Registration Chairman, P.O. Box 213, Middlesex, N.J. 08846.

Deadline for preregistration is Sept. 12, 1986

Preregistrations postmarked after Sept. 12, 1986, will be charged the full at-meeting rates.

Fees:	Preregistration	At-Meeting
Regular	$ 40	$ 55
Student	$ 10	$ 15
Workshop*	$ 40	$ 55
1-Day EAS Short Course**	$250	$250
2-Day EAS Short Course**	$400	$400

*Fee for workshops is in addition to the registration fee.
**Fee for short courses includes registration fee.

Name _____
Last First Initial

Address _____

City _____ State _____ Zip _____

Business phone _____

Check applicable: ☐ This is my first EAS
☐ Note change of address.

Check one: Mailing address is ☐ Home ☐ Business

Check the appropriate box and indicate the fee in blank spaces:

Registration: Regular ☐ Student ☐ ..... $ _____

Workshops:

GC: Capillary and Headspace (Oct. 21 A.M.) ..... $ _____

PCs in the Laboratory (Oct. 21 A.M.) ..... $ _____

X-ray Diffraction and Fluorescence (Oct. 21 P.M.) ..... $ _____

NMR (Oct. 21 P.M.) ..... $ _____

Polymer Characterization (Oct. 22 A.M.) ..... $ _____

HPLC Detectors and Columns (Oct. 22 A.M.) ..... $ _____

IR Accessories (Oct. 22 P.M.) ..... $ _____

Polymer Flow Studies (Oct. 22 P.M.) ..... $ _____

LIMS (Oct. 23 A.M.) ..... $ _____

Mass Spectrometry (Oct. 23 A.M.) ..... $ _____

FT–IR (Oct. 23 P.M.) ..... $ _____

Robotics (Oct. 23 P.M.) ..... $ _____

EAS Short Courses:

Near-Infrared Analysis (Oct. 18–19) ..... $ _____

2D NMR (Oct. 20) ..... $ _____

Advanced HPLC (Oct. 21) ..... $ _____

Lab Microcomputers (Oct. 22) ..... $ _____

Total Amount Enclosed ..... $ _____

Payment must accompany preregistration form.

Frontiers in Toxicology and Therapeutic Drug Monitoring

Chaired by S.H.Y. Wong, U of Connecticut

9:00 Alcohol Measurement in Blood and Breath: Current Status. **K. M. Dubowski,** U of Oklahoma

9:40 Micellar Chromatography for Therapeutic Drug Monitoring and Toxicology: Direct-Sample-Injection Drug Analysis by HPLC. **L. J. Cline Love** and J. Fett, Seton Hall U

10:40 HPLC UV–Photodiode Array Detection for Toxicological Drug Analysis. **D. Hill** and K. Langner, U of Connecticut

11:20 Microbore HPLC for Therapeutic Drug Monitoring and Toxicology: Assessment for Neonatal and Pediatric Drug Monitoring. **S.H.Y. Wong,** U of Connecticut

New Directions in Chemometrics

Chaired by S. D. Brown, U of Delaware

9:00 Higher Order Tensor-Based Calibration. **B. R. Kowalski,** U of Washington

9:40 Methods for Identifying the Factors Responsible for Chemical Data. **E. R. Malinowski,** Stevens Institute of Technology

10:40 Artificial Intelligence and Real-Time Optimization. **C. Wong,** Lawrence Livermore National Laboratory

11:20 New Uses of Adaptive Kalman Filtering. **S. D. Brown,** U of Delaware

Poster Session Nuclear Magnetic Resonance

Monday Afternoon

Advances in Environmental Analysis—II. Detection and Evaluation of Hazardous Wastes

Chaired by I. H. Suffet, Drexel U

1:30 EMSL–LV FT–IR and FT–IR/MS Research Program. **D. F. Gurka,** U.S. EPA

2:10 On-Line GC/FT–IR, HPLC/FT–IR, and SFC/FT–IR of Toxic Substances. **P. R. Griffiths,** A. W. Haefner, D.J.J. Fraser, and S. L. Pentoney, Jr., U of California, Riverside

3:10 GC/MS/IR for Hazardous Waste Analysis: FT–MS and Quadrupole MS. J. R. Cooper and **C. L. Wilkins,** U of California, Riverside

3:50 Thermal Evolution and Multidimensional GC Ion Trap Detection Analysis of Organic Contaminants in Residues. **T. Bridle** and M. Antonic, Environmental Protection Service, Canada

Thermal Analysis for Pharmaceutical Application

Chaired by A. Melveger, Ethicon

1:30 Application of Thermal Analysis to Analytical and Process Research in the Pharmaceutical Industry. **J. A. McCauley,** Merck & Co.

2:05 Use of Thermal Analysis To Study Solid-State Degradation and Transitions. **A. P. Simonelli,** U of Connecticut

3:00 Thermal Analysis of Phase Transitions of Molecular Organic Solids. **A. R. Mlodozenic,** U of Kentucky

3:35 Absolute Purity Determination of Thermally Unstable Compounds. **A. Ramsland,** Hoffmann La Roche

Near-Infrared Spectroscopy

Organized by T. Hirschfeld, Lawrence Livermore National Laboratory
Chaired by E. Stark, KES Analysis

1:30 Recent Applications of Near-IR Spectroscopy. **D. A. Burns,** Technicon Science Center

2:05 Near-IR Software: State of the Art. **E. Stark,** KES Analysis

3:00 Applications of Near-IR Learning Approaches to NMR. **D. E. Honigs** and J. B. Callis, U of Washington

3:35 Evaluation of Near-IR Algorithms. **J. Workman,** Technicon Instrument

4:10 On-Line Process Control Measurements Using Near-IR Spectroscopy. **I. Landa,** LTI Industries

Investigative Characterizations of New and Commercial Polymers: Spectroscopic Characterization

Chaired by J. R. McDivitt, Ethicon

1:30 Raman Spectra of Polymer Fibers. **B. J. Bulkin,** F. De Blase, J. Kim, and M. Lewis, Polytechnic U

2:10 Raman Investigation of the Solution Properties of Polymers. **J. A. Larabee** and D. N. Schultz, Exxon Research Center

3:10 FT–IR Studies of Polymers Subjected to Pressure and Stress. **R. J. Jakobsen,** F. Wasacz, Mattson Institute for Spectroscopic Research

3:50 Artificial Intelligence Application to Materials Characterization. **S. A. Liebman,** U.S. Army Ballistics Research Laboratory

Recent Advances in Sample Preparation Using Microwave Technology

Chaired by H. M. Kingston and L. B. Jassie, NBS

1:30 Guidelines for Developing Microwave Dissolution Methods for Geological and Metallurgical Samples. **S. Matthes,** U.S. Department of Interior

2:00 Open-Vessel and Reflux Vessel Development for Microwave Digestion of Botanical, Biological, and Food Samples for Elemental Analysis by Automated FIA/ICP. **R. T. White, Jr.,** R. J. Reynolds Tobacco

2:30 Remote Operation of Microwave Systems for Solids Content Analysis and Chemical Dissolution in Highly Radioactive Environments. **E. Sturcken,** Du Pont; T. Floyd and D. Manchester, CEM

3:20 Kjeldahl–Nitrogen Determination Using a Microwave System. Z. Zakaria-Meehan and **E. Neas,** CEM

3:50 Closed-Vessel Microwave Acid Decomposition: Monitoring and Predicting Conditions. **H. M. Kingston** and L. B. Jassie, NBS

Advances in Detection for Liquid Chromatography

Chaired by R. Weinberger, Kratos Analytical

1:30 Laser Fluorescence Detection in LC. **V. L. McGuffin,** Michigan State U

If you are planning to buy a liquid chromatograph, and you haven't considered the BAS 200...

Don't Let Your Boss See This Ad!

MULTI-ELECTRODE LCEC DETECTOR
all new LCEC cell; easily interchangeable electrodes; adjustable volume, microbore capability; numerous electrode materials and geometries, suitable for LCEC gradients!

MULTI-CHANNEL VARIABLE WAVELENGTH UV/VIS DETECTOR
unsurpassed sensitivity; unique beam splitter provides high energy throughput; cells for microbore or conventional LC

PROGRAMMABLE DETECTOR CONTROLS
change potential or wavelength up to 8 times during a single chromatographic run, programmable gain and automatic baseline zero

SOLVENT DEOXYGENATION
all stainless steel fluid handling combines with rigorous deoxygenation and heating to permit determination of unstable compounds and reductive LCEC

ADVANCED TEMPERATURE CONTROL
forced air oven accommodates most column formats as well as detector cells and injector; better precision, lower baseline drift and improved symmetry; independent control of built-in LCEC detectors

MANAGEMENT BY A SINGLE KEYBOARD
control of all systems from autosampling through data reduction with the keyboard of either the System Director™ or BASpc™ Scientific Workstation; no unnecessary duplication of controls.

REFRIGERATED MICRO-VOLUME AUTOSAMPLING
add on the optional, programmable autosampler and handle sample volumes from 1 microliter at temperatures from 0° to 40° C. and with very low dead volume.

DATA REDUCTION
handles up to 4 channels; 2 built-in A/D converters allow access to data reduction package from external detectors; add on detectors already in your laboratory.

NEW 3 μm ODS CARTRIDGE COLUMNS
new PHASE-2™ system provides excellent speed, resolution and symmetry in a format that is easy to use and economical too.

A TERNARY GRADIENT PUMP YOU CAN LIVE WITH!
unsurpassed seal life; operates without a pulse damper; maintenance and troubleshooting accomplished in seconds without elaborate tools; superior performance; interchangeable pump heads, and more!

TOTAL FLEXIBILITY
configure the BAS 200 to your immediate needs and budget; every option is user-upgradeable so you can add on as your requirements expand.

BIG PERFORMANCE, SMALL PACKAGE
only 21 inches wide; requires less real estate on your shrinking lab bench.

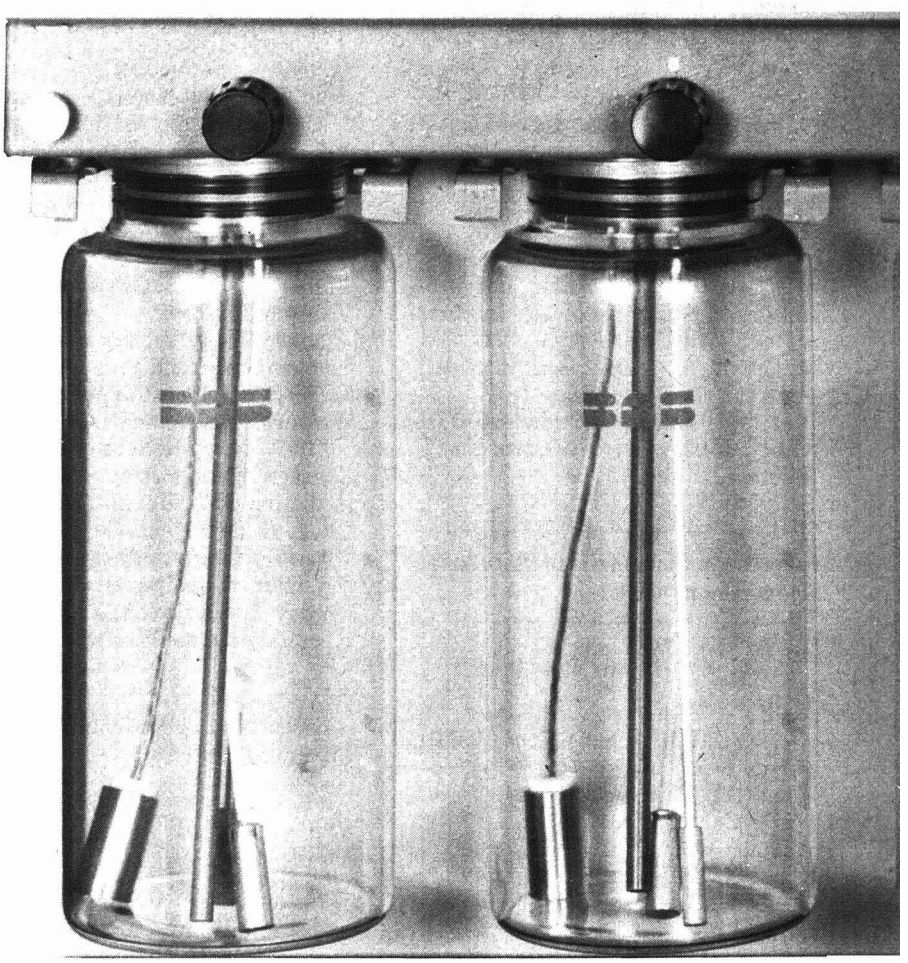

(P.S. If the boss DID see the ad, we'll be happy to send additional information by overnight mail, or offer a demonstration of the BAS 200. Call today!)

BAS
Bioanalytical Systems, Inc

2701 Kent Ave
West Lafayette
Indiana 47906

Telex: 276141
(317) 463-4527

CIRCLE 16 ON READER SERVICE CARD

2:10 On-Column Voltammetric Detection in Open-Tubular LC. **J. W. Jorgenson,** J. G. White, R. L. St. Clair III, and R. Kennedy, U of North Carolina

3:10 New Perspectives in Computer-Aided Multichannel HPLC Detection. **A. F. Fell,** B. Clark, J. Gordon, D. Marr, and G. Seaton, U of Bradford, U.K.

3:50 Singlet Oxygen Sensitization as a Chemical Amplification Technique in HPLC Detection. **J. W. Birks** and C. Shellum, U of Colorado

Tuesday Morning

Progress in Analytical Luminescence—I

Chaired by D. Eastwood, U.S. Army Corps of Engineers

9:00 Optimization of Fluorescence Measurements. **I. M. Warner,** G. Patonay, M. Rollie, and G. Nelson, Emory U

9:40 Expert Systems and Digital Techniques in Total Luminescence. **A. F. Fell** and B. Clark, U of Bradford, U.K.; K. Milne and M. Williams, Heriot-Watt U, U.K.

10:40 Multicomponent Determination of Polycyclic Aromatic Hydrocarbons by Phase-Resolved Fluorometry with HPLC Separation. **L. B. McGown,** W. T. Cobb, and K. Nithipapikom, Oklahoma State U

11:20 Photochemical Reaction Detection in HPLC. **J. W. Birks,** U of Colorado

Progress in Computerized Vibrational Spectroscopy—I

Chaired by G. L. McClure, Perkin-Elmer

9:00 Multivariate Calibration by Partial Least Squares (PLS) Regression. **H. A. Martens,** Norwegian Computing Center, Norway

9:40 Quantitative Analysis of Glasses by FT–IR. **D. M. Haaland** and E. V. Thomas, Sandia National Laboratories

10:40 Analyzing Near-IR Spectral Data To Provide Quantitative Analyses. **K. H. Norris** and W. Hruschka, Beltsville Agricultural Research Center

11:20 New Uses for Raman Measurements through Numerical Methods. **C. K. Mann** and T. J. Vickers, Florida State U

Twenty-Five Years of NMR Spectroscopy: Past, Present, and Future

Chaired by F.A.L. Anet, U of California, Los Angeles

9:00 Past, Present, and Future of High-Field NMR Spectroscopy. **F.A.L. Anet,** U of California, Los Angeles

9:40 Past, Present, and Future of Theoretical Calculations. **C. Jameson,** U of Illinois

10:40 Past, Present, and Future of NMR Software. **G. Levy,** Syracuse U

11:20 Past, Present, and Future of Quadrupolar Nuclei in Solid State. **E. Oldfield,** U of Illinois

X-ray Analysis of Polymer Structure

Chaired by J. Blackwell, Case Western Reserve U

9:00 Introduction.

9:05 Simultaneous X-ray and DSC Studies of Polymer Structure. **J. T. Koberstein** and A. F. Galambos, U of Connecticut; T. P. Russell, IBM Almaden Research Center

9:40 X-ray Studies of Molecular Organization in PMDA/ODA Polyimide Films. **K. H. Gardner** and L. E. Manring, Du Pont

10:30 X-ray Techniques for Treating Complexed and Free-Solvent Molecules in Polymer Complexes. **W. T. Winter,** Polytechnic U

11:05 New Methods of Polymer Characterization Using Synchrotron Radiation. **P. J. Harget,** D. P. Karim, and C. K. Saw, Celanese Research

11:40 X-ray Analysis of Liquid Crystalline Copolyesters and Copolyamides. **J. Blackwell,** A. Biswas, R. A. Cageo, Case Western Reserve U

Advances in Supercritical Fluid Chromatography

Chaired by K. E. Markides, Brigham Young U

9:00 New Detection Techniques and Application Strategies for Capillary SFC. **M. V. Novotny,** Indiana U

9:35 SFC and SFC–MS of Nonvolatile Materials. **R. D. Smith,** B. W. Wright, R. W. Gale, C. R. Yonker, H. R. Udseth, and H. T. Kalinoski, Pacific Northwest Laboratories

10:30 SFC/FT–IR with Mobile-Phase Elimination. **P. R. Griffiths,** S. L. Pentoney, Jr., and G. L. Pariente, U of California, Riverside

11:00 Industrial Applications of SFC. **T. L. Chester,** D. P. Innis, G. D. Owens, Leisa J. Burkes, and J. D. Pinkston, Procter & Gamble

11:30 Pesticide and Drug Analysis by Capillary SFC. **B. E. Richter,** D. E. Knowles, M. Andersen, and D. W. Later, Lee Scientific

Frontiers for Sample Introduction in Atomic Emission Spectroscopy

Chaired by R. F. Browner, Georgia Institute of Technology

9:00 Sample Introduction—A Key to New Developments in AES. **R. F. Browner,** Georgia Institute of Technology

9:40 Advanced Nebulization Techniques for Atomic Spectroscopy. **M. B. Denton** and T. R. Smith, U of Arizona; J. S. Babis, Beckman Instruments

10:40 Chromatographic Sample Introduction with Plasma Emission Detection. **J. A. Caruso,** U of Cincinnati

11:20 Survey of Solid Sample Introduction for ICP–AES. **M. W. Routh** and M. W. Tikkanen, Applied Research Laboratories

Poster Session
General Analytical Chemistry, Electrochemistry, and LIMS

Tuesday Afternoon

Progress in Analytical Luminescence—II

Chaired by L. J. Cline Love, Seton Hall U

2:00 Resolution of D,L-Amino Acids by Capillary Zone Electrophoresis Using Chiral Support Electrolytes. **R. N. Zare** and P. Gozel, Stanford U

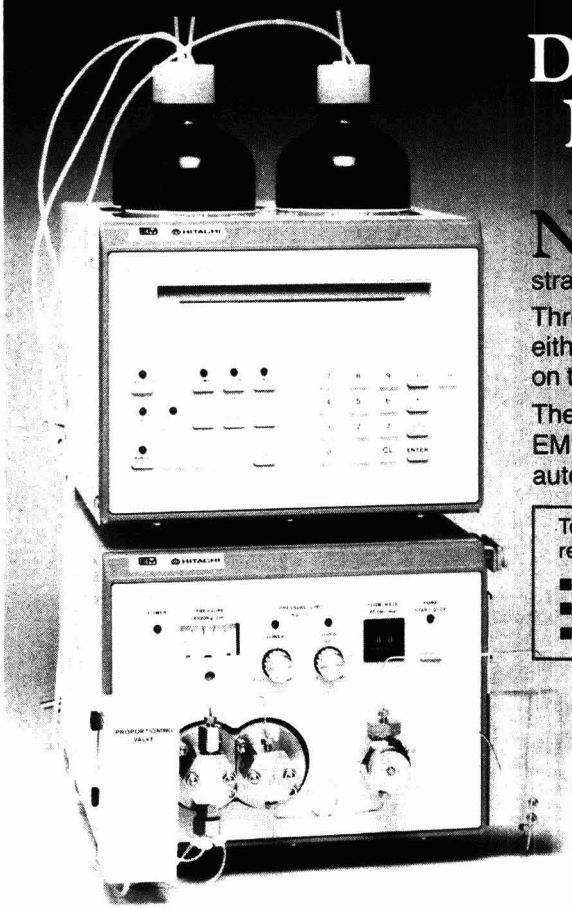

Do HPLC Gradient Systems Need To Be Complicated?

No! The new EM SCIENCE/Hitachi* Model L-5000 LC Controller makes gradient generation a simple and straight forward procedure.

Through the use of an interactive LCD, the L-5000 can be used in either low-pressure or high-pressure gradient formation depending on the analytical requirements.

The Model L-5000 can also be used in concert with other EM SCIENCE/Hitachi components to form an interactive automated HPLC system.

To complete your modular EM SCIENCE/Hitachi HPLC Systems, request additional information on:

- Pumps
- UV Detectors
- Semi-Micro Systems
- Fluorescence Detectors
- Autosamplers
- Column Ovens
- Columns
- High Purity Solvents/ Reagents

For additional information on the L-5000 or to arrange for a demonstration, call or write:

EM™
EM SCIENCE
A Division of EM Industries, Inc

111 Woodcrest Rd.
Cherry Hill, NJ 08034-0395
(609) 354-9200
(800) 222-0342
Associate of E. Merck; Darmstadt, Germany

*Reg. TM Hitachi, Ltd., Japan

Circle RS #50 for literature. Circle RS #51 for a demonstration.

Specialty Gases & Chemicals

- Calibration Gas Standards
- High Purity Gases
- Electronic Gases
- Silanes
- Clinical Gases
- Emission Gases
- Fluorocarbons
- Sterilizing Gases
- Research Gases

We offer a full range of high-purity gases and mixtures. Whether you require specialty gases in small quantities for laboratory work, or in production volumes, Liquid Carbonic can meet your needs.

Liquid has established a network of specialty gas laboratories and stocking depots throughout North America. Our laboratories are equipped with sophisticated analytical instruments and staffed by chemists and engineers ready to meet your needs for specialty gases and solve your problems.

If quality and service are what you expect from a supplier, why not write to Liquid Carbonic for further information and a catalog.

Liquid®

LIQUID CARBONIC
SPECIALTY GAS CORPORATION
135 SOUTH LA SALLE STREET • CHICAGO, ILLINOIS 60603-4282

Send me your catalog and information on:

☐ Calibration Gases ☐ Emission Gases ☐ Equipment
☐ Electronic Gases ☐ Clinical Gases ☐ Sterilizing Gases

Name_____
Title _____ Phone (___) _____
Company_____
Address_____
City_____ State_____ Zip_____
☐ Have your local representative contact me.

AL

CIRCLE 129 ON READER SERVICE CARD

2:40 Fluorescence Properties of Polycyclic Aromatic Carcinogen–Nuclei Acid Adducts. **N. E. Geacintov,** New York U

3:40 Enhancement of Aqueous Peroxyoxalate Chemiluminescence by Organized Media: Application to Analysis of Fluorophor–Protein Complexes. **M. L. Grayeski,** E. J. Woolf, and M. L. Lau, Seton Hall U

4:20 Fluorometric Determination of Water Activity in Mixed Aqueous–Organic Solvents. **S. G. Shulman** and R. N. Kelly, U of Florida

Progress in Computerized Vibrational Spectroscopy—II

Chaired by D. M. Haaland, Sandia National Laboratories

2:00 Comparison of Regression Approaches for the Analysis of IR and Near-IR Spectra, **D. W. Osten,** 3M

2:40 Intercomparison of Linear Regression and PLS Data Treatments. **D. E. Honigs,** B. Buchanan, K. Bebe, and B. Kowalski, U of Washington

3:40 Quantitative Analysis of Unknown Mixtures of Unknown Components by Factor Analysis. R. Leon and **E. Malinowski,** Stevens Institute of Technology

4:20 Application of Factor Analysis to IR Quantitative Analysis. **R. W. Hannah,** Perkin-Elmer; R. A. Spragg, Perkin-Elmer, U.K.

New Frontiers in Applications of NMR Spectroscopy

Chaired by R. Bible, G. D. Searle

2:00 Application of Two-Dimensional NMR to Structural Elucidation of Complex Organic Molecules. **W. F. Reynolds,** U of Toronto, Canada

2:40 Applications of NMR in Pharmaceutical Analysis. **G. S. Slomp,** Upjohn

3:40 Application of NMR to Ecological Recognition. **D. Lynn,** U of Chicago

4:20 Structure Determination of Desertomycin by Means of Two-Dimensional NMR Techniques. **A. Bax,** NIH; A. Aszalos, FDA

5:30 Teaching the New NMR: A Multimedia Presentation of Density Matrix Treatment. **G. Mateescu,** Case Western Reserve U

The Ubiquitous PC

Chaired by A. Bober, Carltech Associates

2:00 The Ubiquitous Computer in a Small College Chemistry Laboratory. **D. E. Jones,** Western Maryland College

2:40 Shifting the Equilibrium Point. **B. L. Pollock,** Carltech Associates

3:20 The PC as an Extension of the Laboratory. **E. F. Frees** and R. G. Marquart, Fein-Marquart Associates

3:40 Statistics and Process Control with a PC. **J. K. Hurwitz,** consultant

4:20 Development of PC Tools for the Laboratory. **R. A. Vogel,** Perkin-Elmer

Chiral Separations in Chromatography

Chaired by D. W. Armstrong, Texas Tech U

2:00 Introduction. **D. W. Armstrong,** Texas Tech U

2:05 High-Level Enantioselectivity from a Mechanistically Well-Defined Chiral Stationary Phase. T. C. Pochapsky, G. S. Mahler, and **W. H. Pirkle,** U of Illinois

2:40 Theory and Use of Cyclodextrin Bonded Phases in Chiral Separations. **W. L. Hinze,** Wake Forest U

3:30 Theory and Use of Chiral Polymer Phases for the LC Separation of Enantiomers. **M. Yoshikane,** T. Shibata, Y. Yuki, K. Tachibana, A. Ichida, H. Nishimura, M. Kawabe, T. Sei, H. Namikoshi, and Y. Toga, Daicel Chemical Industries, Japan

4:00 Comparison of Chiral Stationary Phases. D. W. Armstrong, Texas Tech U

4:35 Separation of Peptides and Nitrososamines on β-Cyclodextrin and Reversed-Phase Media. **H. J. Issaq,** Program Resources, NCI—Frederick

Inductively Coupled Plasma–Mass Spectrometry

Chaired by G. M. Hieftje, Indiana U

2:00 ICP–MS: Is It the Answer? **G. Horlick,** M. A. Vaughn, S. H. Tan, and J. Lam, U of Alberta, Canada

2:40 Applications of ICP–MS to Biological and Environmental Samples. **R. M. Barnes,** U of Massachusetts

3:40 Sampling Ions from the ICP for Quadrupole MS. **D. J. Douglas,** SCIEX, Canada

4:20 New Systems for Plasma Source MS. **G. M. Hieftje,** D. A. Wilson, and G. H. Vickers, Indiana U

Wednesday Morning

Advances in Pharmaceutical and Biomedical Analysis—I

Chaired by A. F. Fell, U of Bradford, U.K.

9:00 Present and Future Perspectives in Analytical Research and Development. **L. A. Sternson,** Smith Kline and French

9:40 Current Status of Standardization in TLC and HPLC in Pharmaceutical Development. **J. Kirschbaum,** Squibb Institute for Medical Research

10:40 Principles and Practice of Microcolumn LC Separations in Pharmaceutical Analysis. **P. Kucera,** Lederle Laboratories

11:20 Lasers for Ultrahigh Sensitivity Detection in Biomedical Analysis. **M. V. Novotny,** Indiana U

Current State of Atomic Spectrometry Research

Chaired by A. T. Zander, Perkin-Elmer

9:00 State-of-the-Art Graphite Furnace AAS. **W. A. Slavin,** Perkin-Elmer

9:40 Simultaneous, Multielement Zeeman AA Spectrometer Utilizing Phase-Sensitive Detection and Encoding Techniques. **T. Hadeishi,** Lawrence Berkeley Laboratory

10:30 Possibilities of Totally Pyrolytic Graphite as a Tube Material in Electrothermal Atomization AAS. **M.T.C. deLoos-Vollebregt** and L. deGalan, Delft U of Technology, the Netherlands

11:00 Coherent Forward Scattering—An Alternative to AA Analysis? **C. A. Monnig** and G. M. Hieftje, Indiana U

11:30 Additional Chemical Information from Time and Spatial Data from Graphite Furnace AA. **J. Holcombe,** U of Texas

Modern Methods of Thin-Film and Surface Analysis

Chaired by R. J. Colton, Naval Research Laboratories

9:00 Recent Developments in Surface Analysis by X-ray Photoelectron Spectroscopy (XPS or ESCA). **C. J. Powell,** NBS

9:40 Surface Analysis Using Auger Electron and Ion Milling Techniques. **C. C. Chang,** Bell Communications Research

10:40 Ion Scattering and IR Analysis of Organic and Polymeric Surfaces. **J. A. Gardella, Jr.,** SUNY at Buffalo

11:20 Secondary Ion Mass Spectrometry: Theory, Technique, and Application. **R. J. Colton,** Naval Research Laboratory

Progress in Infrared Microspectroscopy

Chaired by R. Messerschmidt, Spectra-Tech

9:00 Applications of Molecular Microspectroscopy to Paper Chemistry. **G. E. Pacey,** A. J. Sommer, P. L. Lang, and J. E. Katon, Miami U

9:30 Micro FT–IR Applications in Pharmaceutical Research. **J. A. Reffner,** American Cyanamid

10:20 Polymers and Contaminants by IR Microspectroscopy. **H. Humecki,** McCrone Associates

10:50 IR Ultramicrospectroscopic Studies—Probing the "Near Field." **R. Messerschmidt,** Spectra-Tech

11:20 Transmission, Reflection–Absorption, Diffuse Reflection, and Diffuse Transmission by FT–IR Microscopy. **P. R. Griffiths,** U of California, Riverside

Advances in High-Resolution NMR Spectroscopy

Chaired by G. N. Chmurny, NCI—Frederick

9:00 Performance Envelopes in the Design of NMR Experiments. **R. E. Santini,** Purdue U

9:40 Two-Dimensional NMR Studies of Polysaccharides. **R. A. Byrd,** W. Egan, and M. F. Summers, NIH

10:40 Structural and Conformational Studies of Biologically Active Peptides in H_2O. **J. A. Ferretti,** D. G. Davis, and K. S. Gallagher, NIH

11:20 New Pulse Techniques in Two-Dimensional NMR. **O. W. Sorensen** and R. R. Ernst, ETH-Zentrum, Switzerland

Advances in Chromatography

Chaired by K. Bratin, Pfizer

9:00 Elemental Microanalysis in Chromatography by Plasma Spectral Emission Detection. **P. C. Uden,** U of Massachusetts

9:20 Optimization and Automated Confirmation of Peak Purity and Identification Using an HPLC Photodiode Array Detector. **T. Alfredson,** J. Robinson, T. Sheehan, and J. L. Excoffier, Varian Associates

HELLMA®

D² LAMPS

From Original Hanau.

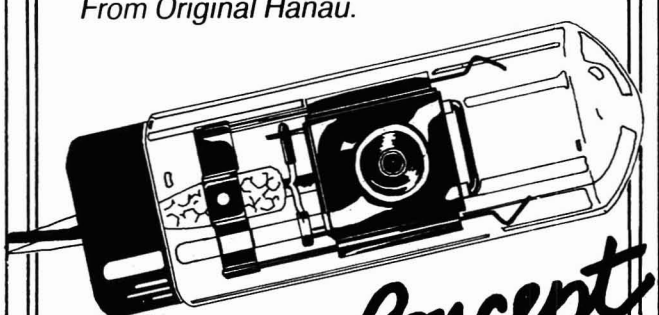

The new Concept

UV light sources for all major spectrophotometers and detectors. Also inquire about our large variety of stock and custom cells.

For over 20 years...
HELLMA® Quality you can trust.
Box 544, Borough Hall Station, Jamaica, N.Y. 11424
Telephone (718) 544-9534 or (718) 544-9166.

CIRCLE 96 ON READER SERVICE CARD

Separate and Equal

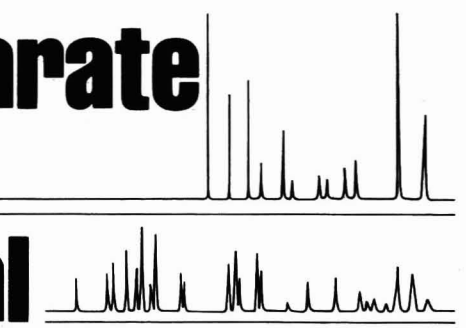

Chrompack's Exclusive BFU Lets Packed, Capillary GC Columns Share the Same Instrument.

In just five minutes you can go from standard packed columns to true high-resolution fused silica capillaries — or back again — with the Chrompack Basic Flow Unit conversion kit. The low-cost BFU doubles the utility of any chromatograph. A metal diaphragm pressure regulator eliminates oxygen contamination.

Only from Chrompack, the single source for standard and custom GC and HPLC columns, glass column systems, instruments, and accessories.

CHROMPACK, INC.
1130 Route 202, Raritan, NJ 08869
Tel.: 800-526-3687 or NJ 201-722-8930

CIRCLE 34 ON READER SERVICE CARD

9:40 Reversed-Phase HPLC with Indirect Photometric Detection. **S. Scypinski** and P. Metz, Varian Instrument Group

10:00 Windowless Microvolume Mixing Chamber and Flow Cell. **R. J. Miller** and J. D. Ingle, Jr., Oregon State U

10:40 Investigations into the Use of Modifiers in Supercritical Fluid Chromatography. **J. M. Levy** and W. M. Ritchey, Standard Oil

11:00 Minimization of System Variance for LC/GC and LC/LC Separations. **T. Raglione,** J. Troskosky, and R. Hartwick, Rutgers U

11:20 Effect of Gradient Rate on HPLC Column Efficiency. **A. Nohl,** Spectra Physics

11:40 Affecting Cation Chromatographic Selectivity. **D. P. Lee** and A. D. Lord, Hamilton

Poster Session
Chromatography

Wednesday Afternoon

New York SAS Award Symposium: NMR Imaging Science—Parents and Offspring

Chaired by V. S. Venturella, Anaquest BOC Technical Center

2:00 Introduction: NMR Imaging. **V. S. Venturella,** Anaquest BOC Technical Center

2:05 Applications of Magnetic Relaxation and Spectroscopy. **R. G. Bryant,** U of Rochester

2:45 NMR Imaging in Solids. J. B. Miller and **A. N. Garroway,** Naval Research Laboratory

3:40 Ultrahigh Resolution NMR Microscopy. **T. R. Brown,** Fox Chase Cancer Center

4:20 Presentation of the Award to Paul C. Lauterbur

4:30 The Complete Resonator: NMR Pictures and Spectra of Molecules and Men. **P. C. Lauterbur,** U of Illinois

TRIM Investigations: Chromatospectroscopy's Greatest Hits

Chaired by G. L. McClure, Perkin-Elmer

2:00 To be announced

2:40 Direct Interpretation of GC–IR Interferograms. **T. L. Isenhour** and W. E. Greene, Utah State U

3:40 When Pure Peaks Aren't Pure: An Application for Principal-Component Analysis of Spectroscopic–Chromatographic Data. **P. J. Gemperline,** East Carolina U

4:20 Resolution of IR Spectra of Chromatographic Mixtures by Self-Modeling Curve Resolution. **D. M. Mauro** and M. F. Delaney, Boston U

Advances in Pharmaceutical and Biomedical Analysis—II

Chaired by M. V. Novotny, U of Indiana

2:00 The Impact of LC/MS on Pharmaceutical Research and Development. **F. Erni** and K. Schellenberg, Sandoz, Switzerland

2:40 Concepts for Standardization of Diode Array Spectrometry for Analytical Research and Development. **D. G. Jones,** Tracor Northern

3:40 Biomedical Applications of Total Luminescence Spectroscopy Using a Linear Photodiode Array Detector. **L. J. Cline Love,** S. Zibas, and C. Cruz, Seton Hall U

4:20 Current Trends in Computer-Aided Methods for Analytical Research and Development. **A. F. Fell,** U of Bradford, U.K.

Recent Advances in Plasma Emission Spectrometry

Chaired by R. M. Barnes, U of Massachusetts

2:00 Solid Sample Analysis by Slurry Atomization—Plasma Emission Spectrometry. **L. Ebdon,** Plymouth Polytechnic, U.K.

2:40 Direct Current Plasma Spectroscopic Ultratrace Metal Determination in Effluent Waters. **H. Griffin,** G. Olear, and A. Savolainen, Texas Instruments

3:30 Trace Elements Analysis of Refractory Metallurgical Materials—A Critical Evaluation of Internal References and High-Resolution Spectrometers. **I. B. Brenner,** and S. Erlich, Geological Survey of Israel, Israel

4:00 Potentials and Limitations of Helium ICPs for Element Analysis: A Comparison with Argon ICPs and Molecular-Gas Discharges. **A. Montaser,** George Washington U

4:30 Considerations in Practical ICP–Fourier Transform Spectrometry. **M. W. Routh,** M. W. Tikkanen, and J. E. Goulter, ARL

Applications and Techniques in Light Microscopy

Chaired by W. C. McCrone, McCrone Research Institute

2:00 Detecting Problems with a Microscope. **A. Coates,** Polaroid

2:40 Digital Restoration of Spectra. **J. G. Dodd** and L. K. DeNoyer, Colgate U

3:40 Understanding Photographic Sensitivity. **M. Scott,** Eastman Kodak

4:20 The Failure of Analytical Chemistry. **W. C. McCrone,** McCrone Research Institute

Molecular Spectroscopy: What's Exciting?

Chaired by W. Fateley, Kansas State U

2:00 Bistable Fiber-Optic Sensors. **D. Honigs** and B. Tenge, U of Washington

2:40 New Horizons in FT Spectroscopy. **B. Chase,** Du Pont

3:40 A Tribute to Tomas. **W. Fateley,** Kansas State U

4:20 The "Rest" of FT. **W. Fateley,** Kansas State U

Thursday Morning

Silver Jubilee Award Symposium: Recent Advances in Analytical Chemistry—I

Chaired by T. Isenhour, Utah State U

9:00 Presentation of the Award to George H. Morrison

9:10 Trace Elements: Back to the Future. **G. H. Morrison,** Cornell U

9:50 Use of Lasers in Analytical Spectroscopy. **F. E. Lytle,** Purdue U

10:45 Tandem Mass Spectrometry. **F. W. McLafferty,** Cornell U

11:25 Recent Developments in Preparative Scale Chromatography. **G. Guiochon,** Georgetown U

Electroanalytical Chemistry

Chaired by W. S. Selig, Lawrence Livermore National Laboratory

9:00 Ascending Water Electrode Studies of Metal Extractants. **H. Freiser,** U of Arizona

9:40 Twenty-Five Years of Analytical Controlled Potential Coulometry. **J. E. Harrar,** Lawrence Livermore National Laboratory

10:40 State-of-the-Art Voltammetric Electrodes. **J. Jordan,** Pennsylvania State U; A. Robbat, Jr., Tufts U; M. Gross, Universite Louis Pasteur, France

11:20 Applications of Pulse Voltammetry. **J. G. Osteryoung,** SUNY at Buffalo

Solid-State NMR Spectroscopy

Chaired by P. M. Henrichs, Eastman Kodak

9:00 Multinuclear NMR Studies of Protein Dynamics in Solids. **D. A. Torchia,** Y. Hiyama, and S. W. Sparks, NIH

9:40 ^{13}C Solid-State NMR of Small Molecules Adsorbed on Supported Metal Catalysts. **K. W. Zilm,** G. Webb, and D. Simonsen, Yale U

10:40 Structural Characterization of Solid Synthetic Polymers with NMR Spectroscopy. **P. M. Henrichs** and J. M. Hewitt, Eastman Kodak

11:20 Mixing in Magnetic Resonance. H. Seidel, R. D. Kendrick, P.-K. Wang, and **C. S. Yannoni,** IBM Almaden Research Center; M. E. Galvin, AT&T Bell Laboratories; R. A. Wind, Colorado State U

Expert Systems in Chromatography

Chaired by L. R. Snyder, LC Resources

9:00 Expert Systems for Experimental Design. **S. N. Deming,** U of Houston

9:35 Small Expert Systems for LC Troubleshooting. **B. Buglio** and T. Jupille, Pi Technologies

10:30 Foundations of an Expert System for HPLC. **S. A. Tomellini,** U of New Hampshire

11:00 Expert System for HPLC Method Development. **S. R. Abbott,** S. Williams, J. Karnicky, and J.-L. Excoffier, Varian Associates

11:30 The Drylab Program: Personal Computer Modules for Simulating HPLC Runs. **L. R. Snyder** and J. W. Dolan, LC Resources

Developing Methods for Clinical Chemistry

Chaired by H. L. Pardue, Purdue U

9:00 Emerging Analytical Developments for Clinical Chemistry. **J. Savory,** U of Virginia Medical Center

9:40 Viral Detection via a Nonisotopic Assay. **G. J. Buffone,** C. M. Schimbor, G. J. Demmler, D. R. Wilson, and G. J. Darlington, Baylor College of Medicine and Texas Children's Hospital

10:40 Flexible Approach to Clinical Laboratory Automation—Robotics. **G. Hawk** and P. Volk, Zymark;

NEW SAFE-FRIT™ FUNNELS

SAFE-LAB, INC. introduces its NEW fritted glass funnel. The SAFE-FRIT™ funnel features a threaded removable unbreakable polypropylene stem just below the fritted glass disc. This unique design eliminates the danger of broken glass funnel tips and allows *easy* and *safe* cleaning from both sides. The removable stem permits you to set the funnel top, with the filtered product, on bench top or directly inside an oven or desiccator for drying, without the danger of tipping or spilling. SAFE-FRIT™ funnels provide *safety* and *economy* in the laboratory.

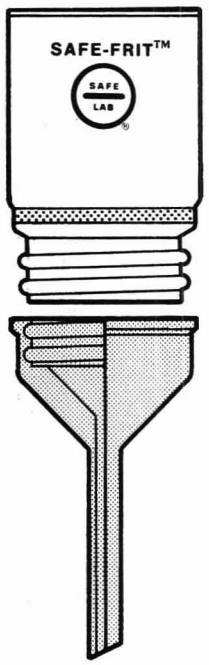

SAFE LAB®

Call or write for a FREE catalog.
Safe-Lab, Inc., P.O. Box 1290,
Santee, CA 92071
(619)448-9100

CIRCLE 190 ON READER SERVICE CARD

Separate from the Rest



Chrompack's Exclusive GC Columns for Light Hydrocarbons, Permanent Gases, Optical Isomers

The Tailor-made series of fused-silica capillary columns separate challenging materials with unmatched resolution. A whole range of unique columns are available, including gasoline, fatty acids, amines, and FAME (Fatty Acid Methyl Esters). And all can be used on *any* chromatograph with Chrompack's Basic Flow Unit.

Only from Chrompack, the single source for standard and custom GC and HPLC columns, glass column systems, instruments, and accessories.

CHROMPACK, INC.
1130 Route 202, Raritan, NJ 08869
Tel.: 800-526-3687 or NJ 201-722-8930

CIRCLE 35 ON READER SERVICE CARD

C. E. Pippenger, Cleveland Clinic Foundation

11:20 Novel Instrumental Approaches for Clinical Determinations. **H. L. Pardue,** Purdue U

Advances and New Trends in FT-IR

Chaired by J. P. Coates, Spectra Tech

9:00 New Trends in FT-IR: An Overview. **J. A. deHaseth,** U of Georgia

9:25 Automated FT-IR Methods—Macro Programming Makes It Easier. **J. W. Rydzak,** Colgate-Palmolive

9:50 Bringing the Spectrometer to the Sample: New Developments in Automated Batch and Process Measurement. **W. M. Doyle** and B. C. McIntosh, Analect Instruments

10:35 New Approaches to User/Sample/FT-IR. **C. Friedman,** L. A. Finger, J. D'Agostino, and J. P. Coates, Spectra-Tech

11:00 New Developments in Integrated Data Bases for FT-IR. **J. F. Sprouse,** Sprouse Scientific Systems

11:25 Reliability and Performance Aspects of a New Industrial-Grade FT-IR Spectrometer. **F. L. Baudais,** Bomem, Canada

Poster Session
Atomic and Molecular Spectrometry

Thursday Afternoon

Silver Jubilee Award Symposium: Recent Advances in Analytical Chemistry—II

Chaired by T. Kashuba

2:00 Ion Beams, Lasers, and X-rays!: Some Aspects of the Current Renaissance in Surface Science. **N. Winograd,** Pennsylvania State U

2:40 Electroanalytical Chemistry: Past Successes and Future Promises. **A. J. Bard,** U of Texas

3:40 Computer-Generated Robot Control for the Analytical Laboratory. **T. L. Isenhour,** W. A. Schliper, P. B. Harrington, and S. E. Eckert, Utah State U

4:20 Electronic Publishing in Chemistry. **D.H.M. Bowen,** American Chemical Society

Clinical Applications in Mass Spectrometry

Chaired by S. P. Markey, NIMH

2:00 Application of Mass Spectrometric Techniques to Guide Treatment Strategies in Metabolic Disease. **D. S. Millington,** Duke U Medical Center

2:40 Direct Measurement of Fractional Absorption Using Stable Isotopic Tracers. **A. L. Yergey,** N. E. Vieira, and D. G. Covell, NIH

3:40 Analytical Needs for Measuring Stable Isotope Tracers in Human Metabolic Studies. **D. Matthews,** Washington U School of Medicine

4:20 Mass Spectrometry in Medicine and Pharmacology: Current Uses and Future Trends. **S. P. Markey,** NIMH

Optical and Electrochemical Sensors

Chaired by W. S. Selig, Lawrence Livermore National laboratory

2:00 Protein-Coated Piezoelectric Crystal Detectors. **G. G. Guilbault,** J. Jordan, J. Ngeh-Ngwainbi, and P. Foley, U of New Orleans

2:40 Potentiometric Sensors for Ionic and Gaseous Analytes. **J. F. Coetzee,** U of Pittsburgh

3:40 Potentiometric Gas Sensors for Electrically Neutral Molecules. **J. Janata** and M. Josowicz, U of Utah

4:20 Design and Use of Ion Sensors. M. Huser, U. Wuthier, H. V. Pham, U. Oesch, D. Ammann, E. Pretsch, and **W. Simon,** ETH-Zentrum, Switzerland

NMR Spectroscopy and Imaging in Biological Systems

Chaired by R. S. Balaban, NIH

2:00 To be announced. **R. S. Balaban,** NIH

2:40 To be announced. **R. G. Shulman,** Yale U

3:40 Tissue Oxygen Determination by ^{31}P NMR. **B. Chance,** J. S. Leigh, Jr., D. Smith, S. Nioka, and B. J. Clark, U of Pennsylvania

4:20 Metabolism and Blood Flow: Concomitant Quantification by in Vivo NMR Spectroscopy. **J. J. Ackerman,** Washington U

Forty Years of Chromatography: Perspectives and Future Trends—I

Chaired by H. J. Issaq, NCI—Frederick

2:00 Introduction: The 1946 Conference on Chromatography. **H. J. Issaq,** NCI—Frederick

2:05 Two-Dimensional Separations: Future Prospects. **J. C. Giddings,** U of Utah

2:30 TLC: Advances and Future Trends. **D. Jaenchen,** Camag, Switzerland

3:05 New Developments in Stationary Phases and Supports for HPLC. **R. A. Hartwick,** Rutgers U

3:45 Critical Concepts in the Effective Practice of HPLC. **L. Snyder,** LC Resources

4:15 Trace Analysis of Sugars in Wine by HPLC by Postcolumn Detection. **H. Engelhardt** and P. Ohs, Universitat des Saarlands, F.R.G.

4:35 Gas Chromatography: Past, Present, and Future. **H. McNair,** Virginia Polytechnic Institute and State U

Trace Evidence Analysis

Chaired by S. Palenik, McCrone Associates

2:00 Setting Up a Trace Evidence Section. **S. M. Ryan,** Suffolk County Crime Laboratory

2:30 CBS Homicides—A Case for Trace. **N. Petraco,** New York City Police Laboratory

3:20 Effects of Exposure on Hair. **P. DeForest,** John Jay College of Criminal Justice

3:50 Microtechniques for the Examination of Drug Samples. **J. Koles,** Drug Enforcement Administration

4:20 Evidential Value of Cotton Fibers. **S. Palenik,** McCrone Associates

Friday Morning

American Microchemical Society—Benedetti-Pichler Award Symposium

Chaired by P. N. Keliher, Villanova U

9:00 Microchemical Separation Techniques. **M. V. Novotny,** Indiana U

9:40 Potentiotitrimetry of Anions Using Quaternary Ammonium Halides. **W. S. Selig,** Lawrence Livermore National Laboratory

10:40 Electroanalytical and Optical Methods in the Study of Analytically Important Reactions. **P. Zuman,** Clarkson U

11:20 Presentation of the Award to Wilhelm Simon

11:25 Microsensors in Microchemistry. A. Manz, D. Ammann, W. E. Morf, and **W. Simon,** ETH-Zentrum, Switzerland

LIMS: Expectancies vs. Experience

Chaired by G. Gibbon, U.S. Department of Energy

9:00 Tailoring LIMS for a Contract Analytical Laboratory. **A. Bridge,** Multiware

9:40 Laboratory Data Management Systems Specification, Compromise, and Result. **L. M. Caudill,** F. T. Green, and V. L. Turner, Du Pont

10:40 Implementation of a Data Management System in an Environmental Laboratory Using an IBM PC Network. **K. Hausknect,** A. Schkuta, L. Leonard, and D. Farnsworth, Cambridge Analytical Associates

11:20 User Perspective on the Beckman LIMS. **R. Gifford,** Smith Kline Chemicals

Chromatography Award Symposium Forty Years of Chromatography: Perspectives and Future Trends—II

Chaired by I. Halasz, Universitat des Saarlands, F.R.G.

9:00 People, Ideas and Instruments: Reflections on the Formative Years of GC and HPLC. **I. Halasz,** Universitat des Saarlands, F.R.G.

9:30 Multichromatography Using Selectivity Tuning of Serially Connected Capillary Columns. **L. S. Ettre** and J. V. Hinshaw, Jr., Perkin-Elmer

9:55 Recent Advances in Capillary Column Chromatography. **S. Lipski,** Yale U

10:30 Presentation of the Award to Csaba Horvath

10:35 Trials and Triumphs of Instrumentation in Chromatography. **C. Horvath,** Yale U

11:05 High-Resolution Approaches to the Separation of Biological Samples. **B. Karger,** Northeastern U

11:35 Impact of HPLC on Modern Biochemistry. **F. Regnier,** Purdue U

Applications of Robotics in Chromatography and the Pharmaceutical Industry

Chaired by G. D. Owens, Procter & Gamble

9:00 Robotic Assay for Fermentation Products. **S. Hamilton,** Eli Lilly

9:40 Robotic Sample Preparation for High-Volume HPLC Analysis: A Case Study. **W. Sonnefeld,** R. Newcomb, and M. Sprengart, Eastman Kodak

10:40 Robotic Automation for the Analytical Laboratory: A Two-Vendor Comparison from the Users' Point of View. **R. B. Kirsch,** American Cyanamid

11:20 Robotic Drug Extractions from Plasma To Support Pharmacokinetic Studies. **R. L. Schoenhard,** M. S. Chang, L. A. Kosobud, and R. E. Schmidt, G. D. Searle

Intelligent Systems

Chaired by S. N. Deming, U of Houston

9:00 History of Intelligent Systems in Analytical Chemistry. **W. E. Baitinger,** Purdue U

9:40 Learning Algorithms. **D. A. Burns,** Technicon Science Center

10:40 Fuzzy Sets, Desirability Functions, and Analytical Chemistry. **S. Deming,** U of Houston

11:20 Expert Systems for the Analytical Laboratory. **T. Isenhour,** Utah State; J. C. Marshall, St. Olaf College

Multidisciplinary Approaches to Materials Analysis

Chaired by W. Boyko, Villanova U

9:00 Procedural Optimization Based on Pattern Analysis: Isolation of the Petroporphyrins from Crude Oil. **D. H. Freeman** and R. M. Angeles, U of Maryland

9:20 Compositional Analysis of Urethanes and Polyesters via Hydrolysis/Chromatography. **J. Belisle** and V. Bunnelle, 3M

9:40 Comparison of Isocratic and Gradient Elution Modes for Reversed-Phase HPLC Characterization of Purified Proteins. **R. M. Riggin,** Eli Lilly

SUPER-QUIET XENON LAMPS FOR PHOTOMETRIC INSTRUMENTS

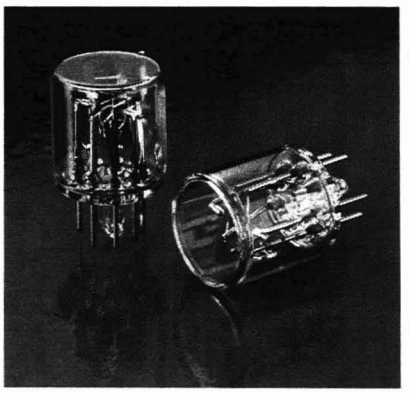

Outstanding luminance from UV to IR

Hamamatsu flash mode Super-Quiet Xenon Lamps provide a minimum of 10^9 flashes! Arc stability is 5 times higher, service life 10 times longer than conventional lamps. Available in three sizes for:

- Stroboscopes
- Chromatographs
- Photoacoustic Spectroscopes
- Strobe Cameras
- Photomasking Devices
- Fluorospectrophotometers
- Color and SO_2 Analyzers
- Other light-sensitive instruments

For Application Information, Call
1-800-524-0504
1-201-231-0960 in New Jersey

HAMAMATSU

HAMAMATSU CORPORATION
360 FOOTHILL ROAD
P. O. BOX 6910
BRIDGEWATER, NJ 08807
PHONE: 201/231-0960
International Offices in Major Countries of Europe and Asia.

© Hamamatsu Photonics, 1986

CIRCLE 102 ON READER SERVICE CARD

10:00 Fast Protein Separations by High-Performance Hydrophobic Interaction Chromatography. **T. S. Reid** and D. J. Gisch, Supelco

10:40 Improvements in the Analysis of Biopolymers by Pyrolysis GC. **T. P. Wampler** and E. J. Levy, Chemical Data Systems

11:00 Time-Dependent Structure of a Polymer Surface as Observed by ESCA. **R. J. Kostyla,** K. Stolt, and S. Wheeler, Polaroid

11:20 X-ray Fluorescence Tissue Analysis during Tumor Growth. **A. S. Frank,** M. K. Schauble, I. L. Preiss, and T. Ptak, Veterans Administration Medical Center and Rensselaer Polytechnic Institute

11:40 Compatibility of Plastics with Explosives. **T. H. Chen** and C. Campbell, ARDC

Friday Afternoon

American Microchemical Society—Benedetti-Pichler Award Symposium

Chaired by W. S. Selig, Lawrence Livermore National Laboratory

1:30 Lipemia in Biological Measurements: The Problem—A Simple Solution. **B. Zak** and J. D. Artiss, Wayne State U

2:10 New Microchemical Approach to Amperometric Analysis. **J. Jordan** and J. Talbott, Pennsylvania State U

3:10 Microchemical Methods Based upon Capillary Gas Chromatography for the Study of Vapor Liquid Equilibria. **P. W. Carr,** A. Hussam, J. H. Park, and P. Cousanon, U of Minnesota

3:50 A New Instrument for Dual-Wavelength X-ray Absorption Edge Spectrometry. **P. Lott** and R. W. Morton, U of Missouri

Emerging Analytical Techniques

Organized by T. Hirschfeld, Lawrence Livermore National laboratory
Chaired by J. Callas, U of Washington

1:30 TLC/Electrophoresis with SIMS Detection. **K. L. Busch** and G. C. DiDonato, Indiana U

2:00 On-Line Analytical Chemistry. **J. Callas,** U of Washington

2:30 Frequency-Based Fluorescence Spectra. **F. V. Bright** and G. M. Hieftje, Indiana U

3:20 Gas-Phase Ionization Microsensors. T. Hirschfeld, Lawrence Livermore National Laboratory; **J. Callas,** U of Washington

3:50 Laplace Transform Near-IR Spectroscopy. **D. E. Honigs** and J. Perkins, U of Washington

LIMS : Starting Up and Keeping Them Up to Date

Chaired by E. L. Schneider, Gemini Information Systems

1:30 LIMS: A Tool to Meet the Challenge of the Eighties. **A. E. Cibulas,** Calgon

2:10 Developing an Analytical Data Network. **R. Kobrin,** Mobil Research and Development

3:10 Managing To Change: Observations on Surviving in a Large Laboratory. **R. Ferguson,** Travenol Laboratories

3:50 LIMS Development in a Fourth-Generation Language Environment. **R. Kantz,** Hazelton Laboratories

Applications of HPLC in Biopolymers Separations

Chaired by F. E. Regnier, Purdue U

1:30 Large-Scale Purification of Biologically Active Peptides. **T. Lambrose,** Hoffmann La Roche

2:10 New Techniques for Amino Acid Analysis. **N. Meltzer,** G. Taus, S. Grover, and S. Stein, Schering-Plough

3:10 High-Performance Ion Exchange Chromatography of Lens Crystalline Proteins. **E. Kaplan** and R. Sizen, Massachusetts Institute of Technology

3:50 Purifications and Characterizations of Recombinant Human Calcitonin and Human Growth Hormone Releasing Factors. **G. Gillitan,** B. W. Jones, S. Young, and A. Bertelsen, Unigen Laboratories

Robotics

Chaired by L. J. Kostek, Pfizer

1:30 Analysis of Drugs in Biological Fluids: Manual vs. Robotic Assays. **H. G. Fouda** and R. P. Schneider, Pfizer

2:10 Robotic Experiences in a Public Health Laboratory. **B. L. Therrell,** Texas Department of Health

3:10 To be announced. **J. B. Cross,** Phillips Petroleum

3:50 Increased Productivity and Repeatability through Laboratory Robotics. **T. Hight,** Radian

Environmental and Biomedical Analysis

Chaired by V. S. Venturella, Anaquest BOC Technical Center

1:30 Evaluation of a Mass-Selective Detector for the Analysis of Halogenated Dioxins and Furans in Incinerator Emissions. **K. M. Aldous,** D. R. Hilker, P. W. O'Keefe, R. M. Smith, and S. Connor, New York State Department of Health

1:50 Comprehensive Analysis of Environmental Samples for Chlorinated Dioxins, Dibenzofurans, and Potential Precursors. **D. R. Hilker,** K. M. Aldous, H. Valente, R. M. Smith, P. W. O'Keefe, S. Connor, J. Jurusik, D. Kinney, and D. Spink, New York State Department of Health

2:10 Application of an Expert System to the Interpretation of IR Spectra of Hazardous Waste. **S. A. Tomellini,** U of New Hampshire; M. A. Puskar and S. P. Levine, U of Michigan; S. R. Lowry, Nicolet Instrument

2:30 Convenient Way To Chlorinate Aromatic Compounds for Use as Reference Standards in Analysis of Environmental Contaminants. **E. R. Barnhart,** D. G. Patterson, Jr., D. L. Ashley, V. L. Maggio, J. A. MacBride, and C. C. Alley, U.S. Department of Health and Human Services

3:10 System Suitability Tests for Immunoassays. **E. C. Rickard,** S. Sittampalam, W. C. Smith, and J. K. Frischmann, Lilly Research Laboratories

3:30 Effect of Subambient Temperatures on Resolution of Steroids by HPLC. **J. C. Touchstone** and S. U. Sheikh, U of Pennsylvania

3:50 Optimization of Multimodal Chromatographic Separations by Column Diameter Scaling. **N. Sagliano, Jr.,** and R. A. Hartwick, Rutgers U

4:10 Stability of Short Aliphatic Silane Stationary Phases Under Acidic pH Conditions. **T. R. Floyd** and R. A. Hartwick, Rutgers U

INTRODUCING THE **MODEL 5000** AUTOMATIC DESORBER

for Volatile Organic Studies

FROM

Tekmar®

the world's leader in Purge and Trap Technology

The Model 5000 is designed for automatic thermal desorption and cryofocused GC injection of samples from 5/8" or 1/4" O.D. adsorbent traps.

APPLICATIONS INCLUDE:

- Ambient air analysis
- Indoor air monitoring
- Hazardous waste incineration emissions
- Industrial hygiene analysis
- Outgassing of VOCs from solid materials
- Low level thermal degradation studies
- Cryofocusing direct injections of gas samples



CALL TEKMAR NOW

Toll Free **800-543-4461** In Ohio, Canada call collect **513-761-0633** Telex No. 21-4221

Tekmar Company / P.O. Box 371856 / Cincinnati, OH 45222-1856

CIRCLE 202 ON READER SERVICE CARD

UNION GIKEN



Stopped Flow Rapid Scan Spectrophotometer

- Minimum dead time — 500 μsec
- 16 spectra measured every 1 msec sequentially
- Simple and robust mixing system without syringe
- Fluorescence, T-jump and flash accessories.

Please write to:

ATAGO BUSSAN CO., LTD.

7-23, 5-chome Shimbashi, Minato-ku, Tokyo 105

Telex: 28421 Phone: (03) 432-8741

CIRCLE 1 ON READER SERVICE CARD

Division of Analytical Chemistry Announces Fellowship Winners

The Fellowship Committee of the ACS Division of Analytical Chemistry has announced the 1986–87 winners of two $8500 full-year graduate fellowships and five $2500 summer fellowships. According to Margaret V. Merritt of Wellesley College, chairman of the committee, the purpose of the fellowship program is to encourage basic research in the field of analytical chemistry through the support of outstanding graduate students. Financial support for the 1986–87 awards has been provided by the Perkin-Elmer Corporation, the Procter & Gamble Company, the Dow Chemical Company, and the Society for Analytical Chemists of Pittsburgh (SACP).

Recipient of the full-year fellowship sponsored by Perkin-Elmer is Kurt L. Haller of Northwestern University, who has been working with Richard P. Van Duyne on spatially resolved surface laser spectroscopy. Haller has shown the technique of spatially resolved surface-enhanced Raman scattering to have a calculated mass detection limit of 10^5 molecules.

Karen Sentell of the University of Florida has received the full-year fellowship sponsored by Procter & Gamble. She is investigating the structure and conformation of bonded-phase chromatography packings with the goal of achieving a better understanding of retention mechanisms in reversed-phase liquid chromatography. Her thesis work may reveal new information about the solubility of small molecules in interphases such as micelles, vesicles, and lipid bilayer membranes. Last year, Sentell was a recipient of one of the summer fellowship awards.

This year four summer fellowships were sponsored by SACP:

- Stephen L. Pentoney, Jr., of the University of California, Riverside, has interfaced a supercritical fluid chromatograph to a Fourier transform infrared spectrometer and is investigating the use of this system for environmental analyses. Pentoney is working under the direction of Peter R. Griffiths.
- At the University of Rhode Island, Steven Donahue is developing techniques for processing data from chemical instrumentation. The algorithms he has developed have been used for multicomponent analysis in IR and UV–vis spectroscopy. Donahue's thesis adviser is Chris W. Brown.

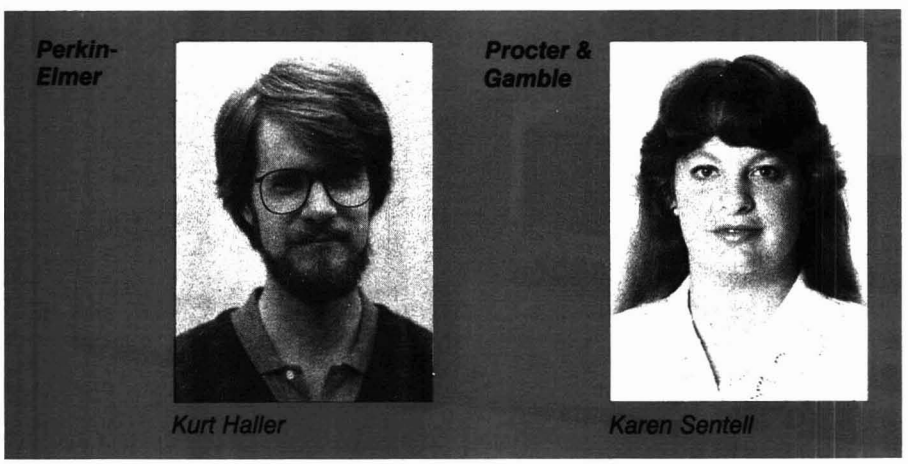

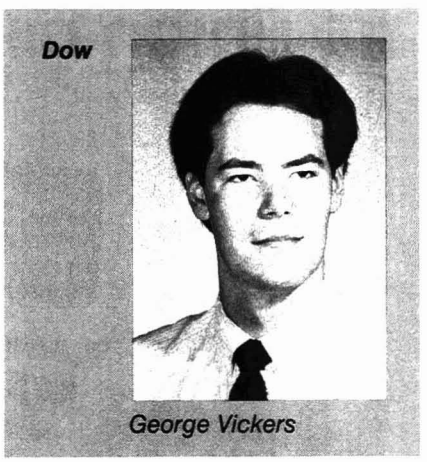

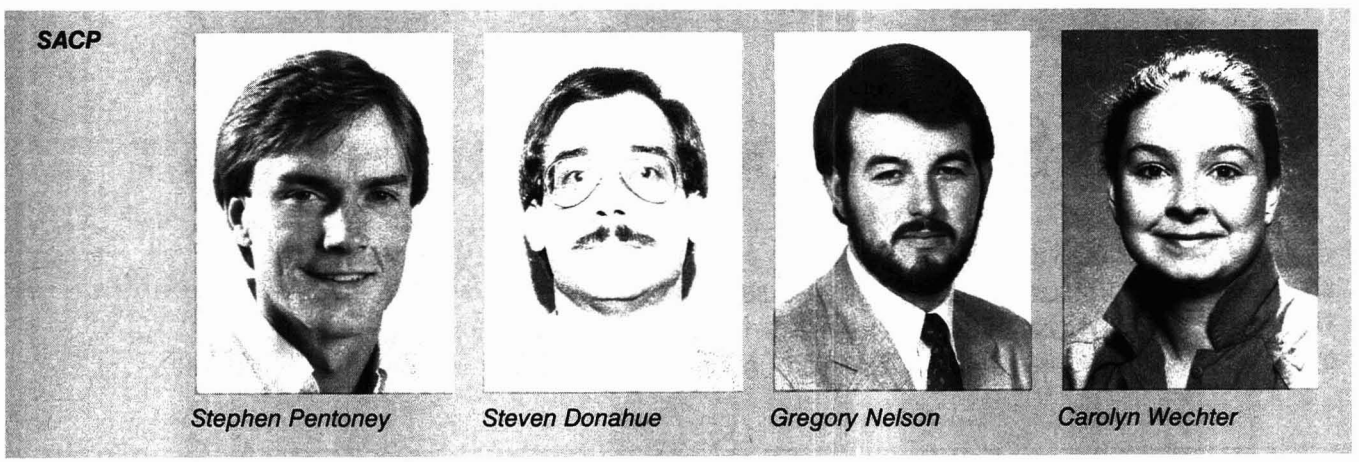

• Gregory W. Nelson is exploring the use of fluorescence lifetimes to study interactions of cyclodextrins with selected fluorophores as part of his research under the direction of Isiah M. Warner at Emory University.

• Carolyn Wechter is completing her thesis research under the direction of Janet Osteryoung at the State Unversity of New York at Buffalo. She is investigating the characteristics of glassy carbon electrodes modified by the deposition of thin metallic films and their use in anodic stripping voltammetry and flow injection analysis.

Recipient of a fifth summer award, this one sponsored by Dow Chemical, is George H. Vickers of Indiana University. Working under the direction of Gary M. Hieftje, Vickers is pursuing studies aimed at understanding ion extraction in inductively coupled plasma/mass spectrometry.

The following students received honorable mention: Jennifer Brodbelt of Purdue University; Roger J. Carlson of the University of Wisconsin, Madison; Joseph P. Dougherty of the University of Connecticut; Lawrence E. Fosdick of the University of Georgia; and Kevin McKenna of the University of Florida.

Fred Lytle Wins Chemical Instrumentation Award

Winner of the 1986 ACS Division of Analytical Chemistry Award in Chemical Instrumentation is Fred E. Lytle, professor of chemistry at Purdue University and an Associate Editor of ANALYTICAL CHEMISTRY.

The Chemical Instrumentation Award is sponsored by the Dow Chemical Company and consists of a



plaque and a stipend of $4000. It will be presented at a symposium to be held at the spring 1987 ACS national meeting in Denver, Colo.

The award was established to recognize and encourage significant achievements in the origination or improvement of instrumentation for analytical chemistry. Lytle was cited for pioneering work in introducing the laser as a light source for analytical spectroscopy: "His greatest impact has been in the fields of time-resolved fluorescence, Raman, and two-photon spectroscopies. The instrumentation and methodology developed in these areas have established the state of the art in temporal resolution, sensitivity, and measurement strategy. His contributions in pulsed laser design, high-speed detection and signal processing, and nonlinear spectroscopy have played a significant role in bringing revolutionary measurement concepts into analytical practice."

Lytle received a B.S. in chemistry from Juniata College in 1964 and earned a Ph.D. in analytical chemistry at the Massachusetts Institute of Technology in 1968. He joined the faculty at Purdue University that same year and was promoted to associate professor in 1974 and professor in 1979. He was the head of the analytical chemistry division in Purdue's Department of Chemistry from 1979 to 1984.

His research interests include the theory and application of absorption, fluorescence, and phosphorescence spectroscopy; time-resolved fluorescence and Raman spectroscopy; and two-photon spectroscopy. Lytle has received the Merck Company Faculty Development Award, he was voted outstanding teacher in the Purdue School of Science in 1979, and he won the Amoco Undergraduate Teaching Award in 1985. He was appointed an Associate Editor of ANALYTICAL CHEMISTRY in 1985.

Coblentz Award to Joel Harris

Joel M. Harris of the University of Utah has won the 1986 Coblentz Award. This award is sponsored by the Coblentz Society and is given each year to a young researcher who has made significant contributions to molecular spectroscopy. Harris received the award at the 41st Symposium on Molecular Spectroscopy, held in June at Ohio State University in Columbus, Ohio.

Harris did undergraduate research at Duke University on solute–solvent interactions in gas chromatography under the supervision of Charles H. Lochmüller. His graduate research under Fred E. Lytle at Purdue University on the development of laser-based instrumentation for time-resolved fluorimetry helped earn Harris a Ph.D. degree in 1976. In that same year, Harris was appointed to an assistant professorship in the Department of Chemistry at the University of Utah, where he was promoted to associate professor in 1981 and to professor in 1985. He also holds an adjunct appointment in Utah's Department of Bioengineering.

Harris's research activities have concentrated on the application of lasers to analytical spectroscopy, partic-



ularly in the areas of photothermal absorbance measurements, trace level chemical detection, and time-resolved fluorescence. In the latter area, he has initiated research on multiple-component data analysis and on the spectroscopy of the liquid–solid interface. Harris is a member of ANALYTICAL CHEMISTRY's Instrumentation Advisory Panel and is an Alfred P. Sloan fellow.

Anachem Award to Henry Freiser

Henry Freiser of the University of Arizona has been selected as the 1986 recipient of the Anachem Award for his "numerous and profound contributions to the field of analytical chemistry." The award will be presented, as part of a full-day symposium in his honor, at the 1986 national meeting of the Federation of Analytical Chemistry and Spectroscopy Societies in St. Louis on Oct. 1.

The Anachem Award has been presented annually by the Association of Analytical Chemists (Detroit, Mich.) since 1953. Previous recipients have included H. H. Willard, P. J. Elving, I. M. Kolthoff, A. A. Benedetti–Pichler, V. A. Fassel, J. J. Kirkland, J. D. Winefordner, G. M. Hieftje, and F. W. McLafferty.

Freiser earned his B.S. degree from City College (New York) in 1941 and M.S. and Ph.D. degrees in 1942 and 1944, respectively, from Duke University. He was chairman of the Department of Physical and Analytical

Chemistry at North Dakota State University (1944–45) prior to spending a year as a research fellow at the Mellon Institute. He served on the faculty of the University of Pittsburgh from 1946–58 and has been at the University of Arizona since 1958.



His research activities have included work on metal chelation, solvent extraction, the determination of fundamental constants, reaction kinetics, nonaqueous chemistry, novel ion-selective electrodes, and innovative approaches to chromatography. He and his wife have raised three children: daughters Debbie and Manny, who are both artists, and son Ben, a professor of analytical chemistry at Purdue University.

ACIL Requests Uniform Accreditation Procedure

The American Council of Independent Laboratories Inc. (ACIL) has published a white paper appealing for a uniform national system of accreditation for independent, for-profit laboratories to replace the more than 100 accreditation programs currently operating across the country. ACIL defines laboratory accreditation as "verification by a competent, disinterested third party that a laboratory possesses the capability to provide accurate test data and that it can be relied upon in its day-to-day operations to maintain high standards of performance."

In most states, laboratories testing the safety of drinking water are accredited by state agencies, such as public health departments or environmental resource departments, under the oversight of the U.S. Environmental Protection Agency (EPA). Under these programs, each laboratory must demonstrate proficiency on an annual basis by successfully analyzing samples supplied by EPA and by undergoing periodic on-site inspections. Similar accreditation programs, but with different testing requirements, obtain for laboratories that do wastewater, groundwater, and hazardous waste testing. ACIL contends that these separate state accreditation programs have created great difficulties for laboratories, especially those operating in regional or national markets. The council argues that the plethora of state and federal accreditation programs is overly costly in terms of both money and time and that this inefficiency ultimately hurts the consumer of these services—the general public.

"Because the goal is common and because the same testing laboratory community is the object of all programs, why cannot the many regulators begin to work together rather than in isolation?" asks the white paper. ACIL is urging EPA and state environmental officials to address themselves to the possibility of rationalizing the laboratory accreditation system.

"The obvious goal," according to ACIL, "is a single, uniform, national accreditation program; a program technically sound, so as to satisfy the high standards appropriate for environmental data, and flexible enough to meet the specific requirements of the various agencies and the different areas of environmental regulation." ACIL is recommending a "discipline" or "field-of-testing" approach, in which laboratories are accredited on the basis of their ability to perform testing in certain disciplines, such as analytical chemistry, as opposed to a "product/standard approach" that assesses a laboratory's ability to perform tests on particular substrates.

Copies of the ACIL white paper, entitled "Accreditation of Environmental Testing Laboratories: An Independent Laboratory Perspective," are available free of charge from ACIL, 1725 K St. N.W., Washington D.C. 20006 (202-887-5872).

DOE Announces Small Business Awards

The Department of Energy (DOE) has selected 101 proposals from small high-technology firms for funding under its Small Business Innovation Research (SBIR) program. Thirteen of the winning projects involve analytical chemistry. The proposals were chosen on the basis of technical merit from almost 700 applications.

The purpose of the SBIR program (*Anal. Chem.* **1985,** *57,* 1130 A) is to increase the participation of small, innovative firms in areas of federally funded R&D. The 101 Phase-I awards announced by DOE will support attempts by the winning companies to demonstrate the feasibility of their project proposals. After that, each will be eligible to compete for Phase-II funding, which involves grants of up to $500,000 for two years. Normally about half of the original contracts are continued into the second phase.

The analytical-chemistry-related projects in this year's Phase-I contracts are as follows:

- ADA Technologies, Aurora, Colo., development of a total peroxy detector for flame and combustion measurements
- Catalytica Associates, Mountain View, Calif., development of reliable SO_2 and NO_x sensors and an integrated in-situ analyzer for combustion flue gas monitoring
- Jonas Inc., Wilmington, Del., in-line monitoring of particulates in gas streams
- OptiChem Technologies, Raleigh, N.C., dosimetry and monitoring of aromatic amines
- FWG Associates, Tullahoma, Tenn., electret for analysis of dry constituents of acid precipitation
- QE Technology, Tampa, Fla., frequency-stabilized dual-wavelength CO_2 laser system for remote sensing of trace gases
- Atom Science, Oak Ridge, Tenn., method of groundwater characterization based on Kr-81 and Kr-85 atom counting, and isotopically selective single-atom counting of noble gases (two contracts)
- EIC Laboratories, Norwood, Mass., remote fiber-optic surface-enhanced Raman spectroscopy of organic pollutants in ground and surface water
- Enzyme Technology Research Group, Durham, N.C., enzyme immobilization on gold surfaces for determination of low levels of environmentally released compounds
- Ohmicron Corporation, Pennington, N.J., differential microcalorimetric biosensor for enzymatic assays
- ORD Inc., Nahant, Mass., portable readout device for fiber-optic sensors (optrodes)
- Ionwerks, Houston, Tex., application of direct recoil spectroscopy for surface analysis of Li, H, and D on fusion materials

DOE's fiscal year 1987 SBIR program solicitation was issued in August 1986, with a due date for proposals of Nov. 3, 1986. Copies of the solicitation may be obtained by writing to SBIR Program Manager, U.S. DOE, Washington, D.C. 20545.

This year's National Science Foundation SBIR awards were announced earlier, in the July 1986 issue of ANALYTICAL CHEMISTRY (*58,* 904 A).

ELEMENTAL ANALYSIS

- **Rapid, Quantitative Analysis of Difficult Samples**
- **With Little Sample Preparation**
- **Simply**
- **At Low, Low Cost**

Too good to be true? Look at ASOMA's new model 8620 X-Ray Fluorescence Analyzer:

DIRECT Analysis of solids, liquids, powders, foams, coatings, suspensions, film thickness . . . means less time spent in sample preparation.

Less Sample Preparation . . . means fewer workup errors, more samples per day, closer product quality control.

Rapid, Simple Operation . . . means at-the-site analysis. No waiting for laboratory results. Automatic readout, too!

Low Cost . . . means early payback, less cost per analysis. If you've ever priced XRF analyzers, you'll be amazed at the price of the ASOMA Model 8620. The ASOMA Model 8620 is a reliable, high precision tool . . . automatic, easy to use . . . Why not let it do your difficult analyses?

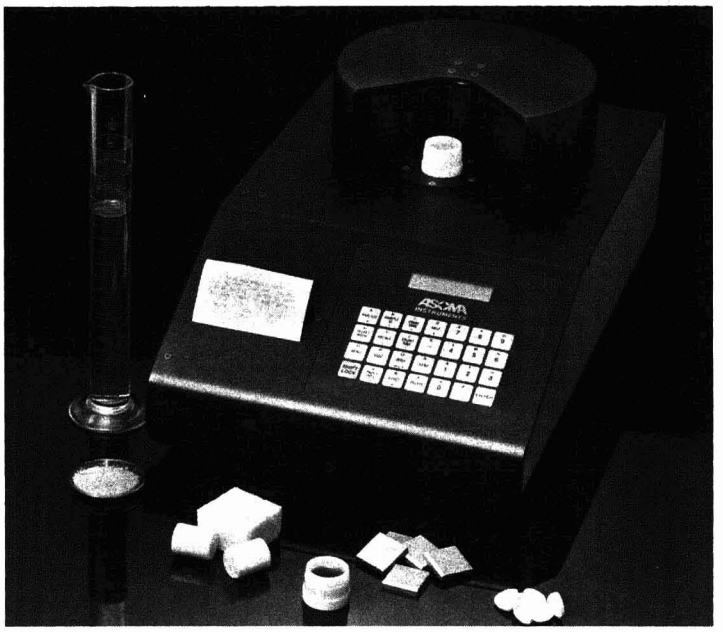

ASOMA INSTRUMENTS

12741 Research Blvd., Suite 501
Austin, Texas 78759
Phone (512) 258-6608 • Telex 76-7177

CIRCLE 3 ON READER SERVICE CARD

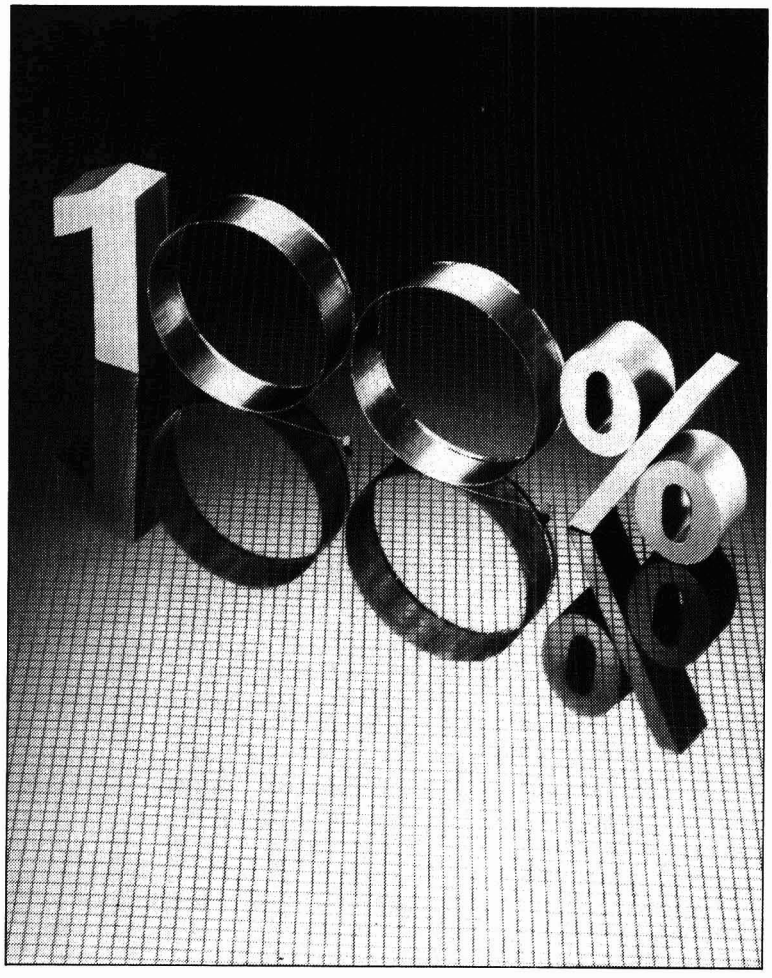

You'll find that all Chrompack columns are 100% excellent. Firstly, because we control production from start to finish. And secondly, because every column is quality checked to guarantee 100% consistency.

We are never complacent in our excellence. Our research and development programme continues to augment a range that is already the largest in the world. Two recent, and highly effective, additions are:

► The TAP column, tailor-made for the analysis of triglycerides.

► The wide bore Al_2O_3/KCl PLOT column for the analysis of light hydrocarbons.

EXCELLENCE

Free Chrompack application notes add to this effectiveness. And, it goes without saying, that you'll find our service and back-up excellently reliable.

Your passport to excellence is a Chrompack Capillary Column Brochure, obtainable from your nearest Chrompack dealer. Naturally, it's 100% free.

CHROMPACK
FROM CHROMATOGRAPHERS
FOR CHROMATOGRAPHERS

CHROMPACK INTERNATIONAL B.V.
P.O. Box 8033, 4330 E A Middelburg, The Netherlands
Tel:01180-27352 Telex: 37852

CIRCLE 37 ON READER SERVICE CARD

For Your Information

Rohm & Haas Company has announced its intention to acquire Supelco Inc., a manufacturer of chromatographic chemicals, columns, and accessories. According to Al Levantin, vice-president for corporate development, the acquisition complements Rohm & Haas's existing strengths in the separations market. "Our businesses in enhanced ion exchange resins, ultrafiltration systems, and reverse osmosis membranes allow us to provide a wide range of sophisticated technologies for fluid process applications," he said. Supelco, located in Bellefonte, Pa., employs more than 300 people and reported sales in excess of $20 million for the 1986 fiscal year.

Strategic Directions International Inc. (9841 Airport Blvd., Suite 806, Los Angeles, Calif. 90045, 213-641-4982) has completed a **report on high-performance liquid chromatography** ($1995) that estimates the worldwide market for 1985 at $480 million. This figure includes sales of all systems, components, data systems associated with HPLC, autosamplers, and related supplies. According to the researchers, although the HPLC market continues to grow rapidly (about 10% per year in real terms), this is not as rapid as during the previous 10 years, when growth was closer to 15% annually. The report notes that "the dominant player in the market is, and will continue to be, Waters Chromatography Division of Millipore Corporation, which holds about 35% of the market." Other strong contenders include Shimadzu, Perkin-Elmer, Hewlett-Packard, Varian, Beckman, Spectra-Physics, Philips, and LDC/Milton Roy.

Waters Chromatography Division of Millipore Corporation has begun construction on an addition to its headquarters facility in Milford, Mass. The design of the addition complements the existing building and will include laboratory and office space, a new main visitors' entry and lobby, and additional parking.

Business Communications Company Inc. (9 Viaduct Rd., Stamford, Conn. 06906, 203-325-2208) has published a study on the growing field of **immobilized-enzyme technology** entitled "New Immobilization Technology: Commercial Opportunities for Reagents, Catalysts, and Biocatalysts" (C-066, July 1986, $1950). According to the report, diagnostic kits and analytical chemistry instrumentation will use increasing amounts of immobilized-biocatalyst technology. Factors stimulating this growth include a 15% annual increase in sales of diagnostic kits used in homes and doctors' offices.

NUS Corporation (Gaithersburg, Md.) reports on the advantages of **soil gas analysis** as a preliminary survey technique in field testing **for the detection of underground organic pollutants** in the June issue of its publication *NUS Breaks*. Soil gas contains contaminants in groundwater that have volatilized and then escaped into pore spaces in the soil. In soil gas analysis, a stainless steel probe is driven into the ground, a gas sample is withdrawn, and the sample is either analyzed directly on a field gas chromatograph or concentrated on Tenax or charcoal for subsequent GC analysis. From concentrations of volatile organic compounds found in the soil gas, investigators can estimate contaminant concentrations in groundwater more quickly and efficiently than by traditional drilling techniques.

A new type of analytical technique for **measurement of chemical and thermal reactions** has been licensed for commercial development to Autoclave Engineers of Erie, Pa., by Research Corporation, a nonprofit foundation based in Tucson, Ariz. The patented technique, called thermocentrifugometric analysis (TCA), was developed by Jin Y. Park, a chemical engineering professor at the University of Idaho. According to Research Corporation, "Unlike the conventional technique of thermogravimetric analysis, TCA is capable of stable weight measurement at high gas velocities, high pressures, and high temperatures."

Harry B. Gray, Arnold O. Beckman Professor of Chemistry at the California Institute of Technology, **has been appointed director of Cal Tech's Beckman Institute.** The institute was established in June 1986 with a gift of $50 million from the Arnold and Mabel Beckman Foundation. Its major objective is to attack problems at the interface of biology and chemistry that require multidisciplinary approaches.

Sievers Research of Boulder, Colo., was recently awarded a research grant from the National Science Foundation under Phase II of the Small Business Innovation Research program (*Anal. Chem.* **1985,** *57*[11], 1130 A). The grant, totaling $190,000, will support research on new detectors for gas and liquid chromatography and on the fundamental chemistry of gold-catalyzed reactions of oxides of nitrogen. Sievers Research was also recently awarded a research contract by the U.S. Air Force to develop new methods for the analysis of high-density jet fuels.

The Credentialing Commission of the International Society for Clinical Laboratory Technology has established a **new certification category for physician office laboratory technicians.** Officials at the Centers for Disease Control in Atlanta estimated that in 1985 about 50% of all diagnostic tests in the United States were being performed in approximately 40,000 physician office laboratories.

Francis T. Coyle, manager of analytical chemistry and quality assurance at Cabot Corporation in Boyerstown, Pa., **and Rudolph Dyck,** engineering manager, materials analysis department, GTE Products Corporation (Towanda, Pa.) **are 1986 recipients of American Society for Testing and Materials (ASTM) Awards of Merit.** Coyle is being honored for 21 years of exceptional technical and administrative contributions to ASTM Committee E-3, Chemical Analysis of Metals. Dyck was honored for outstanding contributions to ASTM Committee E-2, Emission Spectroscopy, including the establishment of methodology for testing refractory metals and the development of reference materials.

Analytical Abstracts Online is now available via Orbit Search Services (formerly SDC) under the file names ANALYTICA or ANABS. The file runs from 1980 to date and currently contains almost 80,000 references spanning the complete field of analytical chemistry worldwide. AA Online is also available via Data-Star and Pergamon Infoline. For further information, contact the host system of your choice or Helen Whitehead, Royal Society of Chemistry, The University, Nottingham NG7 2RD, United Kingdom (telephone 0602-507411).

Call for Papers

2nd International Symposium of Quantitative Luminescence Spectrometry in Biomedical Sciences

ARL has a new source of excitement.



DC Plasma, for complex matrices, nasty samples and tight budgets.

Meet our new plasma. ARL is now your exclusive source for SpectraSpan DC Plasma Spectrometers. But we warn you. You may find their performance, and price irresistible.

To begin with, the SpectraSpan DCP is famous for its ruggedness and reliability. It tackles high solids, organic solvents, viscous samples, and complex matrices as a matter of course. Plus, its Echelle Spectrometer covers a broad 190 nm to 800 nm range, with extremely high resolution.

Operation is easy. And so is the price, with a single element sequential for less than $25,000 and a 20-element simultaneous unit for about $75,000.

Exciting? Yes. Perfect for everyone? No. Which is why ARL offers more elemental analysis choices than anyone else. We have written a paper to help you decide which technology... AA, ICP or DCP... is right for you. Send or call for your copy today.

ARL

Applied Research Laboratories, Inc.

9545 Wentworth Street, P.O. Box 129, Sunland, California 91040

For more sales and marketing information, call ARL toll-free at: 800-551-8741 Interstate and 800-631-6841 in California.

CIRCLE 6 ON READER SERVICE CARD

Ghent, Belgium. May 11–14, 1987. The symposium will cover current research on all aspects of luminescence analysis. The scientific program will consist of plenary and invited lectures and submitted research papers and posters. Abstracts should be submitted before Dec. 31, 1986, to W. Baeyens, Symposium Chairman, Laboratory of Pharmaceutical Chemistry and Drug Analysis, State University of Ghent, Harelbekestraat 72, B-9000-Ghent, Belgium.

Meetings

The following meetings are newly listed in ANALYTICAL CHEMISTRY. Other 1986 meetings are listed in the January through August issues.

1986

■ **Physiological NMR Spectroscopy—From Isolated Cells to Man.** Sept. 24–26. New York, N.Y. *Contact: New York Academy of Sciences, Conference Dept., 2 East 63rd St., New York, N.Y. 10021*

■ **10th International Congress for Instrumentation and Automation (INTERKAMA '86)** Oct. 6–11. Dusseldorf, F.R.G. *Contact: INTERKAMA '86, Dusseldorf Messegesellschaft mbh NOWEA, Postfach 32 02 03, D-4000 Dusseldorf, F.R.G.*

■ **5th International Symposium on New Spectroscopic Methods for Biomedical Research.** Oct. 7–9. Seattle, Wash. *Contact: Mady Lund, 206-545-1229*

■ **6th International Conference on Instrumentation/Automation in the Paper, Rubber, and Plastics Industries.** Oct. 27–29. Akron, Ohio. *Contact: A. Kaya, Department of Mechanical Engineering, University of Akron, Akron, Ohio 44325*

1987

■ **Laser Applications to Chemical Analysis.** Jan. 26–29. Incline Village, Nev. *Contact: Optical Society of America, Laser Applications Meeting, 1816 Jefferson Pl., N.W., Washington, D.C. 20036*

■ **193rd ACS National Meeting.** April 5–10. Denver, Colo. Contact: Barbara Hodsdon, *1155 16th St., N.W., Washington, D.C. 20036*

■ **International Symposium on Analysis of Neurotransmitters.** April 7–10. Stockholm, Sweden. *Contact: Swedish Academy of Pharmaceutical Sciences, P.O. B. 1136, S-111 81 Stockholm, Sweden*

■ **Ion-Ex '87.** April 13–16. Wrexham, Clwyd, U.K. *Contact: P.A. Williams, Research Division, The North East Wales Institute, Deeside, Clwyd CH5 4BR, U.K.*

■ **9th Australian Symposium on Analytical Chemistry.** April 27–May 1. Sydney, Australia. *Contact: J. Eames. 9 AC Secretary, P.O. Box 137, North Ryde, N.S.W. 2113, Australia*

■ **International GPC Symposium '87.** May 11–13. Chicago, Ill. *Contact: Mary Ellen Goffredo, Waters Chromatography Division of Millipore Corp., 34 Maple St., Milford, Mass. 01757*

■ **2nd International Symposium on Quantitative Luminescence Spectrometry in Biomedical Sciences.** May 11–14. Ghent, Belgium. *Contact: W. Baeyens. Symposium Chairman, Laboratory of Pharmaceutical Chemistry and Drug Analysis, State University of Ghent, Harelbekestraat 72, B-9000-Ghent, Belgium*

■ **Scientific Computing and Automation 1987.** May 13–15. Amsterdam, the Netherlands. *Contact: Keith Foley, Elsevier Science Publishers, P.O. Box 330, 1000 AH Amsterdam, the Netherlands*

■ **31st Educational Conference and Annual Meeting of the American Association of Bioanalysts.** May 18–22. Grand Traverse Village, Mich. *Contact: AAB, Suite 918, 818 Olive St., St. Louis, Mo. 63101*

■ **Euro Food Chem IV.** June 1–4. Loen, Norway. *Contact: Euro Food Chem IV, Conference Secretariat, Norwegian Food Research Institute. P.O. Box 50, N-1432 Ås-NLH Norway*

■ **Colloquium Spectroscopicum Internationale XXV.** June 21–26. Toronto, Canada. *Contact: L. Forget, Conference Services Office, National Research Council of Canada, Ottawa K1A 0R6, Canada*

■ **11th International Symposium on Column Liquid Chromatography.** June 28–July 4. Amsterdam, the Netherlands. *Contact: Organisatie Bureau Amsterdam bv, Europaplein, 1078 GZ Amsterdam, the Netherlands*

■ **6th International Conference on Fourier Transform Spectroscopy.** Aug. 24–28. Vienna, Austria. *Contact: INTERCONVENTION, P.O. Box 80, A-1107 Vienna, Austria*

■ **194th ACS National Meeting.** Aug. 30–Sept. 4. New Orleans, La. *Contact: Barbara Hodsdon, 1155 16th St., N.W., Washington, D.C. 20036*

■ **Euroanalysis VI.** Sept. 7–11. Paris, France. *Contact: GAMS, 88 Boulevard Malesherbes, 75008 Paris, France*

■ **101st AOAC Annual International Meeting and Exhibition.** Sept. 14–17. San Francisco, Calif. *Contact: Margaret Ridgell, AOAC, 1111 N. 19th St., Suite 210, Arlington, Va. 22209*

■ **Symposium on Accuracy in Trace Analysis—Accomplishments, Goals, Challenges.** Sept. 28–Oct 1. Gaithersburg, Md. *Contact: Kathy Stang, National Bureau of Standards, A353 Physics Bldg., Gaithersburg, Md. 20899*

■ **European Conference on Applications of Surface and Interface Analysis.** Oct. 19–23. Fellbach, F.R.G. *Contact: U. Nagorny, Max Planck Institut für Metallforschung, Institut für Werkstoffwissenschaften, Seestr. 92, D-7000 Stuttgart 1, F.R.G.*

Short Courses

ACS Short Courses. These new courses will be listed only once. For information on other ACS courses, see back issues and contact the Department of Educational Materials, American Chemical Society, 1155 16th St., N.W., Washington, D.C. 20036 (202-872-4508).

The following courses are offered in conjunction with the EAS meeting in New York, Oct. 20–24.

Special Topics in Liquid Chromatography. Oct. 18–19. Lloyd Snyder, J. J. Kirkland, and John Dolan. $495, ACS members; $575, nonmembers

The Electronic Laboratory: Tutorials and Case Histories in Lab Automation. Oct. 18–19. Raymond Dessy. $495, ACS members; $575, nonmembers

Effective Management of Chemical Analysis Labs. Oct. 18–19. Mary McKown and John H. Taylor, Jr. $495, ACS members; $575, nonmembers

Capillary Gas Chromatography. Oct. 18–19. Stuart Cram and Milos Novotny. $495, ACS members; $575, nonmembers

Quality Assurance of Chemical Measurements. Oct. 18–19. John K. Taylor. $495, ACS members; $575, nonmembers

Gas Chromatography/Mass Spectrometry. Oct. 18–19. J. Throck Watson and O. David Sparkman. $495, ACS members; $575, nonmembers

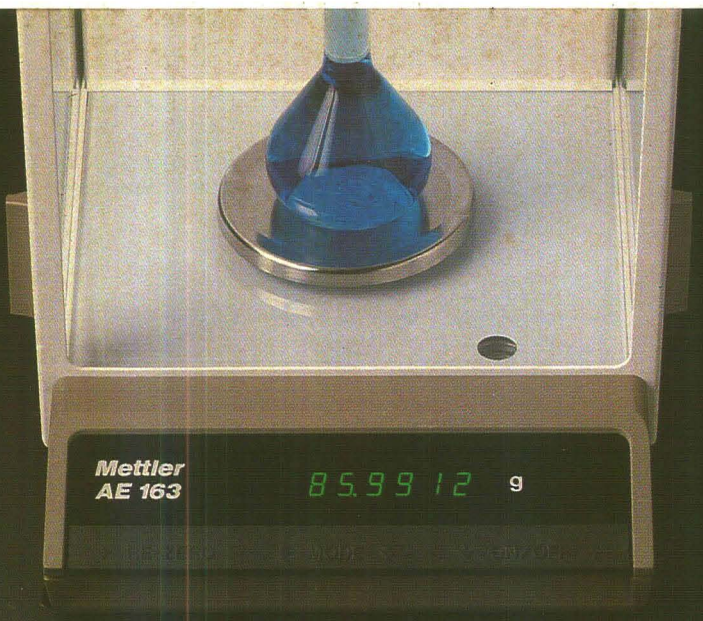

Do you know what's behind every Mettler AE?


Mettler
AE 200
Mettler
AE 163
85.9912 g



Success.

Mettler analytical balances have passed the toughest test of all. The test of time.

Mettler. Proven in thousands of laboratories.

The Mettler electronic AE that revolutionized analytical weighing has become the balance of choice in laboratories around the world. Earning acclaim not only for its accuracy and ease of use, but also for its endurance on the job.

The initial appeal of the AE is apparent. The design is sleek and highly functional. The pan is set close to the bench for easy access. A single control bar puts weighing technology at your fingertips. Results are bright and clear, readable in any light. And Mettler applications are virtually limitless, from connecting printers to interfacing with computers; from routine software programs to advanced robotic systems.

But it is the consistent performance in real laboratories that has made the Mettler AE a success. Scientists who use AEs know that after tens of thousands of weighings their balance will still give them accurate, reproducible results. That's why a Mettler AE is the balance of choice, worldwide.

For information and a copy of our booklet, The History of the Analytical Balance, contact Mettler Instrument Corporation, Box 71, Hightstown, NJ 08520, Tel. 1-800-257-9535.

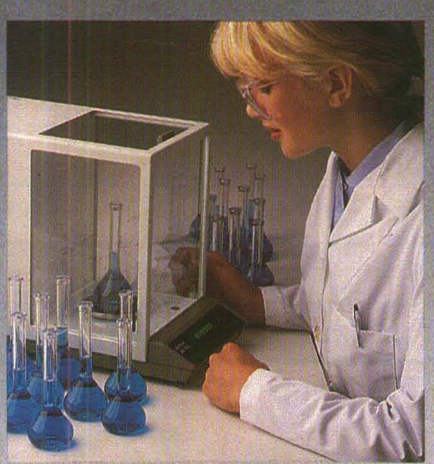

☐ Send me your **free** booklet, The History of the Analytical Balance

☐ Send me complete information on the Mettler AE

☐ Please arrange a demonstration

Name _____

Company _____

Address _____

City _____

State _____ Zip _____

Phone _____
(Area Code) (Number)

Mettler®

Analytical and Precision Balances ☐ Industrial Precision Scales ☐ Thermal, Titration and Density Instruments ☐ Nationwide Service

CIRCLE NO. 142 ON READER SERVICE CARD

Mettler Electronic Analytical Balances

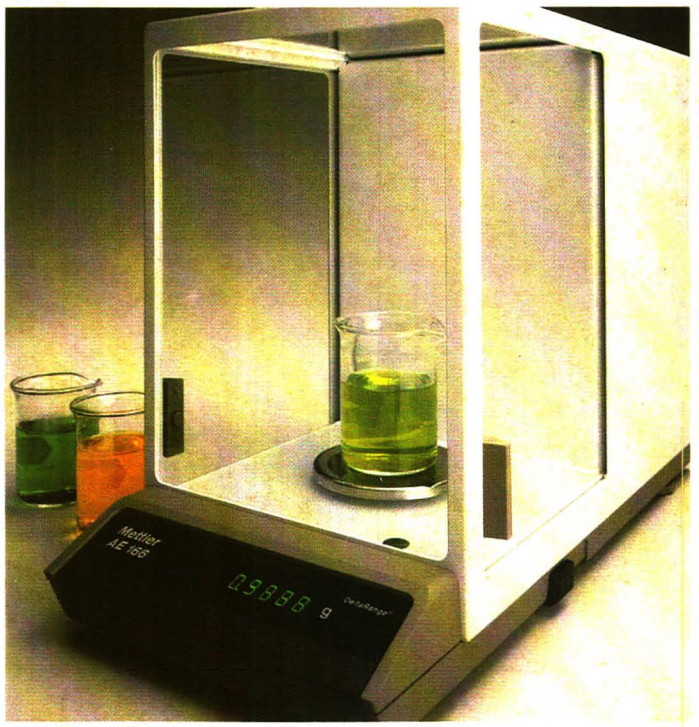

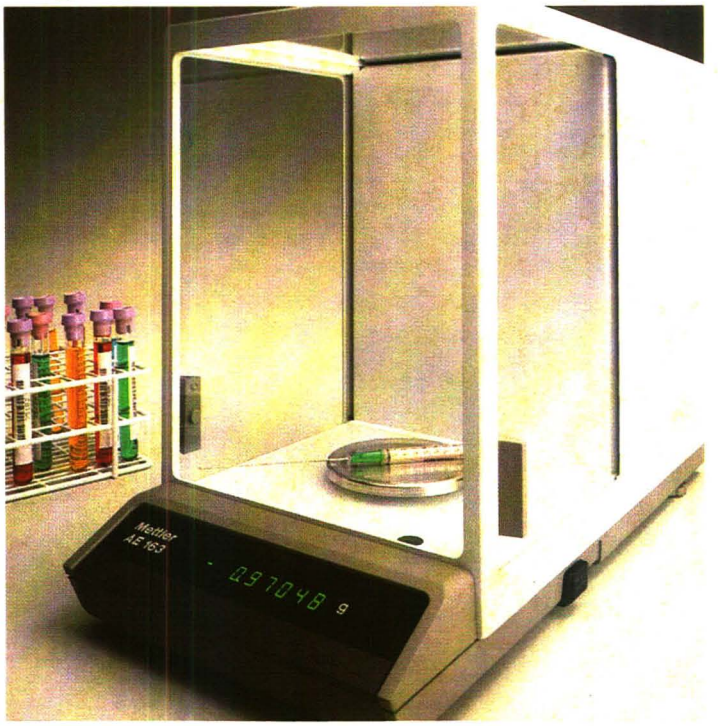

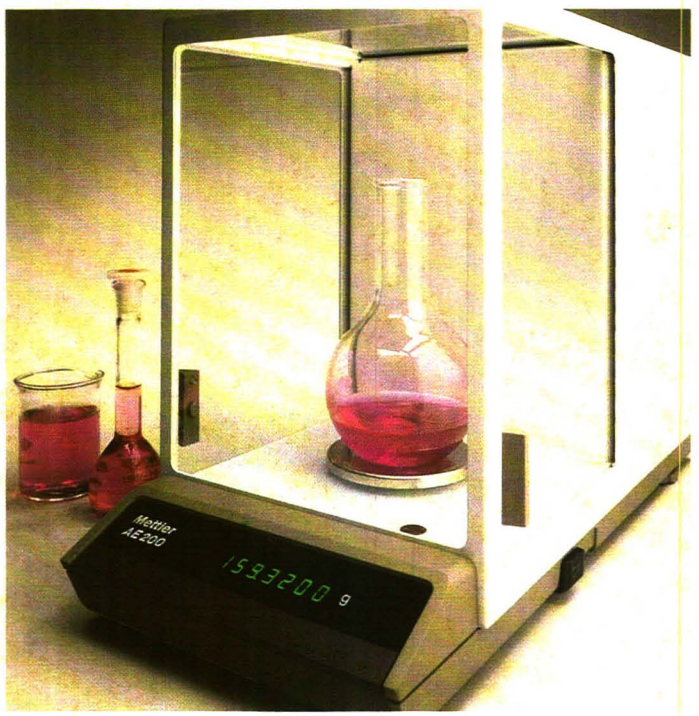

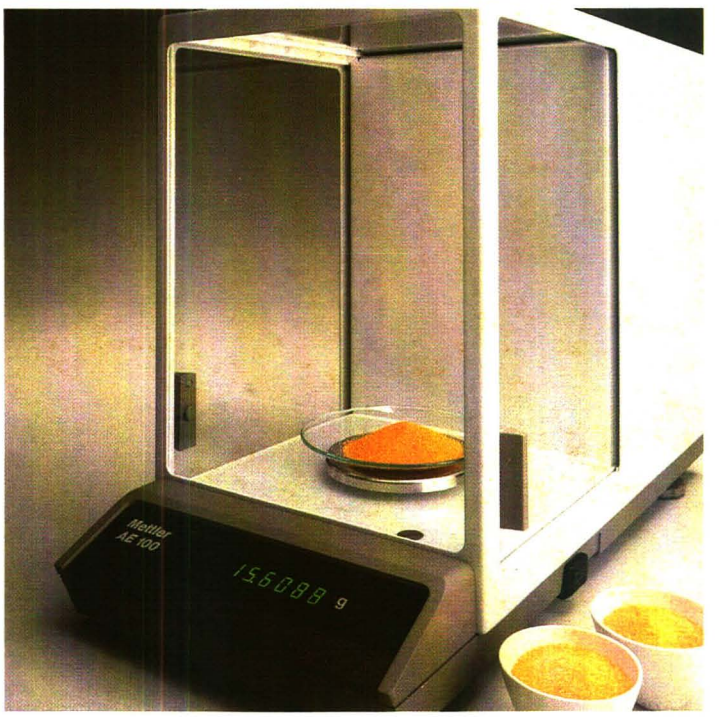

Model	Read-ability	Weighing Range	Reproducibility (standard deviation)	Weighing Pan	Balance Housing Width x Depth x Height
AE163 Macro Semimicro	0.1 mg 0.01 mg	0...162 g 0...31 g	0.02 mg 0.1 mg	3 ¼ in dia.	8 x 16 ¼ x 11 ½ in.
AE50	0.1 mg	0...55 g	0.1 mg	3 ¼ in dia.	8 x 16 ¼ x 11 ½ in.
AE100	0.1 mg	0...109 g	0.1 mg	3 ¼ in dia.	8 x 16 ¼ x 11 ½ in.
AE200	0.1 mg	0...205 g	0.1 mg	3 ¼ in dia.	8 x 16 ¼ x 11 ½ in.
AE166 Mettler DeltaRange	1 mg 0.1 mg	0...162 g 0...60 g	0.5 mg 0.1 mg	3 ¼ in dia.	8 x 16 ¼ x 11 ½ in.

AE Balances are available with the following data output/interface options 011 (CL/RS232C) unidirectional, 012 (CL/RS232C) bidirectional, 013 (IEEE HP-IB)

Mettler®

CIRCLE NO. 142 ON READER SERVICE CARD

For Over Six Decades...



The Leader in the Field.

Few endeavors depend more on a constant flow of new advances and breakthroughs than does the field of analytical chemistry. Keeping pace with these changes has continued to make Analytical Chemistry the pinnacle of publications in the field . . . for over 6 decades.

Call now for your own personal subscription to a publication you don't want to be without—Analytical Chemistry.

American Chemical Society
1155 16th St., NW
Washington, DC 20036

New Products

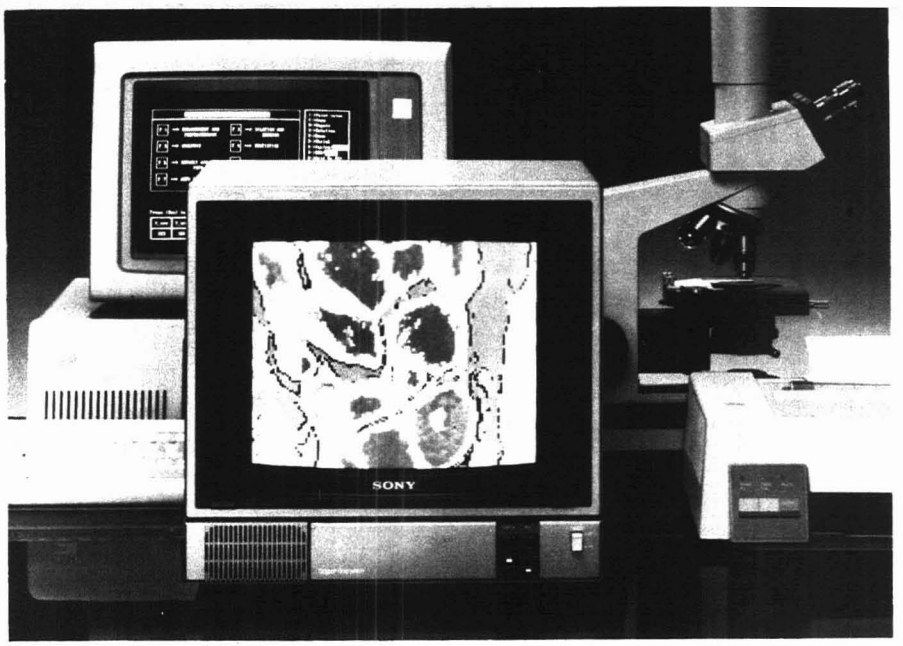

Cue 2 image analyzer uses IBM PC-based instrumentation to acquire specimen images and subject them to rapid processing, enhancement, and analysis. Applications range from cell, tissue, and particle measurement and analysis to materials testing of metals, ceramics, and polymers. Olympus **401**

Membrane filtration

MegaFlow PM-600 pilot plant filtration system features tangential flow across the filter membranes to inhibit macromolecule or particle buildup by continuous action of the turbulent stream. A polypropylene channel plate provides unimpeded process flow and consistent hydrodynamics across the membrane. New Brunswick Scientific **406**

Microdialysis probe

CMA/10 microdialysis probe consists of two concentric steel cannulas covered at the tip by a dialyzing membrane. It can be used to recover low-molecular-weight substances present in the extracellular space, such as neurotransmitters or drugs, and to introduce substances into the tissue. The probe can be easily sterilized, and the molecular weight cutoff can be varied by choice of membrane. Carnegie Medicin **407**

Carbon monoxide detector

Dead/Stop indicator badge changes color when the level of CO in the breathing area is approaching or exceeds the maximum allowable concentration under federal regulations. The badge is good for 30 days and will change back to its original color when flushed with clean air for 2–3 h during the 30-day period. Tracor Atlas **408**



Pulse ChemiSorb 2700 chemisorption analyzer can be used to obtain a detailed analysis of the catalytic activity of samples as well as to determine surface area, total pore volume, and adsorption–desorption isotherms. Samples can be prepared and analyzed without exposure to ambient contamination. Micromeritics **402**

Infrared spectrophotometers

800 series ratio recording IR spectrophotometers feature fast scanning and a monochrome video display. Standard data-handling routines include stored methods, quantitative analysis, interactive difference, spectral memories, graphics, data formatting, and data manipulation. An RS-232 interface is provided for communication with external computers. Perkin-Elmer **409**

Grazing-angle FT–IR

Model FT-80 specular-reflectance accessory for grazing-angle studies mounts directly in the sample compartment of all commercially available FT–IR instruments with minimal alignment. It uses gold-coated mirrors to produce a fixed 80° angle of incidence and is suitable for analysis of thin films on surfaces, especially from metal substrates such as magnetic disks and silicon wafers. Spectra-Tech **410**

Microvolume cuvette

Micro-Leader UV–vis package includes a microvolume cuvette and cell holder for the DU-50 series spectrophotometer and a software package for automating procedures and calculations involved in the measurement of DNA purity. Spectra can be obtained on sample volumes of less than 50 μL, and the cell can be easily cleaned to avoid cross-contamination of samples. Beckman **413**

Gas analyzer

Dycor MA100/MA200 quadrupole gas analyzer, intended for applications in gas analysis, process monitoring, leak detection, and vacuum evaluation, features 1–100 amu range, dual filaments, Faraday cup detector, an RS-232 computer interface, and a 9-in. high-resolution display with choice of graphic or tabular format. Ametek **412**

Gel scanning

Model 1312 gel scanner accessory converts a Model 228 or UA-5 absorbance detector into a transmission densitometer for scanning slab gels or film. Six interchangeable filters from 470 to 620 nm permit a high signal-to-noise ratio for all popular stains, and an IR reference beam minimizes the effects of gel cracks, bubbles, or thickness variations. Isco **414**

Pumping system

MicroFeed, a dual-syringe pump system for microscale pilot reactors, can handle any fluid with a viscosity below 2.2 cP at room temperature, including mercury, volatile organic fluids, and liquified gases. It has a flow rate range of 1–1000 μL/min and can be controlled by a built-in programmable microprocessor or by an external computer via an RS-232C interface. Brownlee Labs **416**

For more information on listed items, circle the appropriate numbers on one of our Readers' Service Cards

THE LATEST GREATEST PLATE IS OURS



Diamond Series TLC Plate. All New and Readily Available to Meet Today's Laboratory Needs.

The Whatman technologically advanced Diamond Series is the latest plate on the market. Yet, it already promises to make all others obsolete.

In laboratory tests, it has shown the no-nonsense characteristics you've been waiting for ... like a superior hard and reflective surface, a quality organic binder, and uniform particle size and distribution.

So what you end up with, of course, is a great plate. One that doesn't flake, can be easily written on, gives off less background noise, isn't reactive towards reagents, is highly efficient and offers fast development time.

And, just as great, a plate that can be delivered in the quantities you want ... where you want them ... when you want them.

Why not put our "latest and greatest" claim to the test today. For more information on the Diamond Series Plate, contact the Analytical Specialists at Anspec: offering tomorrow's technology today, for all your laboratory needs. (800) 521-1720 In Michigan, (800) 482-3452 In Canada, (800) 237-1017.

The Analytical Specialists

ANSPEC

The Anspec Company, Inc.

CIRCLE 230 ON READER SERVICE CARD

CAN YOUR MANTLE PASS THESE TESTS?

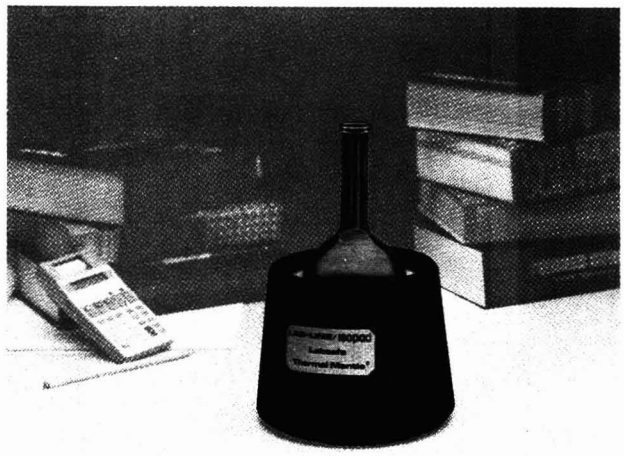

EXCLUSIVE 5 YEAR WARRANTY:
We're so confident in our heating mantles' ability to withstand all your working conditions, with unmatched safety, durability and performance, WE PROVIDE A 5 YEAR WARRANTY!

EXCLUSIVE SEALED CONSTRUCTION PROVIDES PROTECTION FROM SPILLS
The totally encapsulated molded ceramic construction and special coating protects all electrical components from exposure to spillage.

SAFETY FROM BARE HEATING ELEMENTS:
The unique molded construction keeps personnel safe from exposed heating elements.

WELL INSULATED:
The low outside shell surface temperature reduces the risk of burns.

RESISTS CHEMICAL DAMAGE:
The ceramic surface is rugged, fireproof and resists most chemicals.

COMPLETELY WATERPROOF:
Encapsulated electrical connections and heating element make this mantle so safe it is tested under water!

EASY TO CLEAN:
The special innovative surface coating insures that should spillage occur, the mantle can easily be washed out and re-used.

RAPID HEAT UP:
Our powerful heating elements and thermal insulation give you unprecedented rapid heat up.

RECOVERY OF SPILLS:
If spillage should occur, an exclusive drain hole allows for the collection of rare, expensive or corrosive materials.

Seven models, sizes 50ml to 3L.

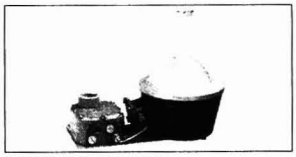

EXPLOSION PROOF
Explosion proof mantles are constructed for use in hazardous areas. Nine explosion proof models are available in sizes ranging from 500 ml to 20L.

LAB-LINE

Lab-Line® Instruments, Inc.
15th & Bloomingdale
Melrose Park, IL 60160
Phone: (312)450-2600
TWX: 6871028 LBLIN UW
Cable: LABLINE

OURS CAN!

PATENT PENDING

CIRCLE 128 ON READER SERVICE CARD

New Products

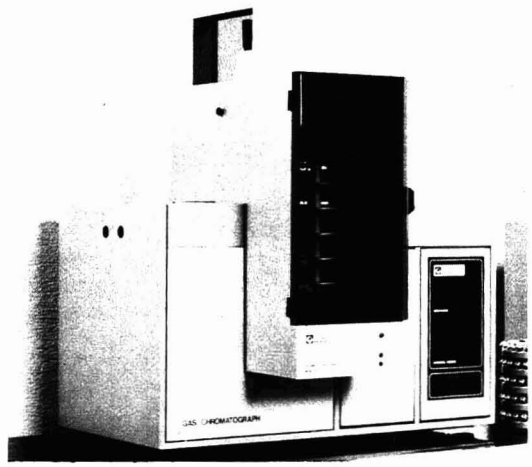

Model 910 and 911 automatic liquid samplers for GC can inject up to 110 samples. The Model 910 injects only into the injection port above which it is mounted, whereas the Model 911 features software-controlled selection of the desired injection port. Packard **404**

AAS sample cleanup

Automated preconcentration system for graphite furnace AA uses a broad-range ion exchange column to retain trace metals and eliminate matrix interferences. Thirty-five samples can be automatically processed in 105 min. Control Equipment Corporation **411**

LC detector

UV-M ultraviolet detector for high-performance and standard LC combines multiwavelength capability with a computer-designed flow cell to provide enhanced sensitivity, long bulb life, and a low signal-to-noise ratio. Pharmacia **415**

LC pump

Model 222 single-piston, rapid-refill pump features a compressibility compensation control for adjustment of flow with compressible solvents, a wide dynamic range pulse damper, and convenient prime–purge valve and luer-type drain port. It is capable of external control and can be upgraded to gradient operation by addition of a compatible gradient controller. Scientific Systems **418**

Slurry packer

PC-50D and PC-100D high-pressure slurry packing systems for on-site LC column packing use air-actuated, pressure amplifier pumps to generate high solvent flows and pressures. The PC-50D is designed for 4.6-mm to 20-mm-i.d. columns, whereas the PC-100D can pack 4.6-mm to 100-mm-i.d. columns. All necessary tubes, valves, and fittings are included. YMC **419**

GAS FACTS

published periodically for analytical chemists

Safety in the laboratory

Someone once described a laboratory as an accident waiting to happen. Actually, analytical chemists have good safety records and also have a unique appreciation for the potency of chemical species at very low concentrations.





Both new and experienced bench workers can benefit from a Scott gas safety training workshop.

Suppliers of specialty gases have been in the forefront of laboratory safety programs. They have actively cooperated with educators, industrial hygienists and safety personnel in setting up and maintaining high standards in the laboratory. The Scott catalog, for example, provides lists of threshold limit values (TLV's) for hazardous materials, safety checks, illustrations and descriptions of CGA valve outlets and connections. Reprints of papers discussing safety in handling compressed and liquefied gases are also made available by Scott. And safety training workshops can be held in your own laboratory to inculcate good practices into newly recruited personnel and review them for experienced bench workers. All of these materials and activities are provided by Scott without charge.

Information when you need it—fast!

Did you know that Scott also has an information hotline? If you have questions about the compatibility of equipment and tubing with certain gases—if the valve outlet on a cylinder doesn't mate with the inlet of a regulator—if you want to know OSHA limits for a gas—call Scott toll-free for guidance. There is no obligation. And remember too, that you can use the same number to order the highest quality calibration mixtures, pure gases and gas handling equipment. (If you don't have your personal copy of the Scott catalog, request it today.)

INFORMATION HOTLINE:
800-331-4953
8:00AM-5:00PM Eastern time
In PA: 215-766-8861

Scott
Specialty Gases
Plumsteadville, PA • Troy, MI •
San Bernadino, CA • Houston, TX

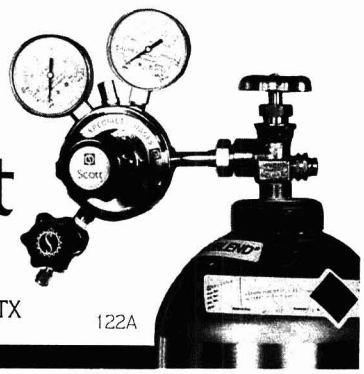

CIRCLE 191 ON READER SERVICE CARD

PRA INTERNATIONAL INC.
ANNOUNCES A UNIQUE

ICP SPECTROMETER SYSTEM

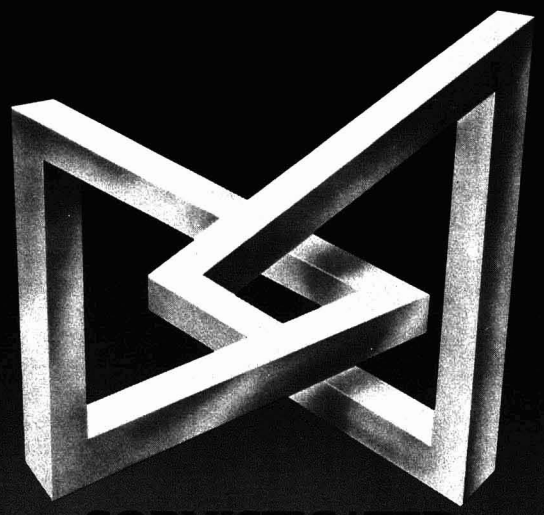

SOPHISTICATED SIMULTANEOUS MULTIELEMENT ANALYSIS

- UNPARALLELED FLEXIBILITY
  Freedom to update sets of analytical lines in seconds
- HIGH RESOLUTION
  Echelle based spectrometer design
- TRUE BACKGROUND CORRECTION
  Only multichannel detection permits simultaneous background correction
- COMPLETE SPECTRAL PICTURE
- STABILITY

PRA International Inc.

45 Meg Drive
London, Ontario
Canada N6E 2V2

100 Tulsa Road
Oak Ridge, Tennessee
USA 37830

1-800-265-1226
VISIT PRA AT FACSS
Booth 205 - 207

CIRCLE 165 ON READER SERVICE CARD



CONJURE UP ALL THE DATA YOU NEED

If you need information about laboratory instruments, equipment, apparatus, or supplies, you've come to the right one-stop genie: *Analytical Chemistry.*

Here, you'll find ads from just about everyone you need product data from. And most of the ads have a key number at the bottom.

Simply circle on one of our reader service reply cards those key numbers that pertain to the advertised products on which you need more information.

And, presto. Like magic, the data you need will be spirited to you at no charge or obligation.

analytical chemistry

New Products

Software

NMR

PCNMR work station program performs off-line post-acquisition processing of NMR spectra on a PC AT. It can be easily operated with standard DISNMR commands or mouse-driven pull-down menus and provides full peak picking routines along with on-screen and plotted annotation of peaks and normalized integrals. Other features include semi-automatic phase correction and an on-screen axis with tic marks. IBM **422**

Graphics

Grapher, a scientific graphics package for the IBM PC family and compatibles, is designed for illustrating large volumes of complex data. Data can be loaded into the worksheet from the keyboard or from external data files generated by Lotus 1-2-3, dBase, or a user-written program. Graph types include linear–linear, log–linear, log–log, triangular, and high–close–low, and data can be represented by five types of regression curves and four types of error bars. Golden Software **423**

Data entry

Balance and Barcode, two software programs for use with the series 3000 IBM PC-compatible chromatography work station, allow automatic entry of balance and bar code data. Balance reads weights from a Mettler AE163 balance equipped with an RS-232 communications option; Barcode prints bar-coded labels for subsequent reading in conjunction with data base management programs for data entry and sample tracking. Nelson Analytical **426**

Electrochemistry

MiCES electrochemistry software for the Apple II automates cyclic voltammetry, double-step chronocoulometry, differential-pulse voltammetry, and measurements of cell resistance. The system is menu controlled, and the program is written in machine language for rapid execution of operator commands. Interactive Microware **424**

Molecular structure

Molecular Graphics allows full-color display and interactive manipulation of complex molecules using either wire frame, stick and ball, or space-filling models. Hardware requirements include an IBM PC with a minimum of 512K memory, DOS 2.1 or higher, a math coprocessor, EGA card with 256 K memory, and an enhanced graphics monitor. COMPress **425**

Quality control

EQUIS, a laboratory data management system for use with the IBM PC-AT, can be used for automated sample entry, work list generation, information reporting, and data archiving. A quality control template procedure allows automatic assignment of blanks, duplicates, spikes, and standards in work lists, and standard reports include results printed by test or sample, sample status, quality control plots with control and target limits, and invoices. Perkin-Elmer **427**



Delsa laser-based particle electrophoresis analyzer measures electrophoretic mobility distribution, zeta potential, and specific conductance of charged particles in liquid suspensions. Four separate detectors provide simultaneous measurements at four different scatter angles. Coulter Electronics **403**

Let the new 8000 Series GC's show you the way — to a peak of perfection!

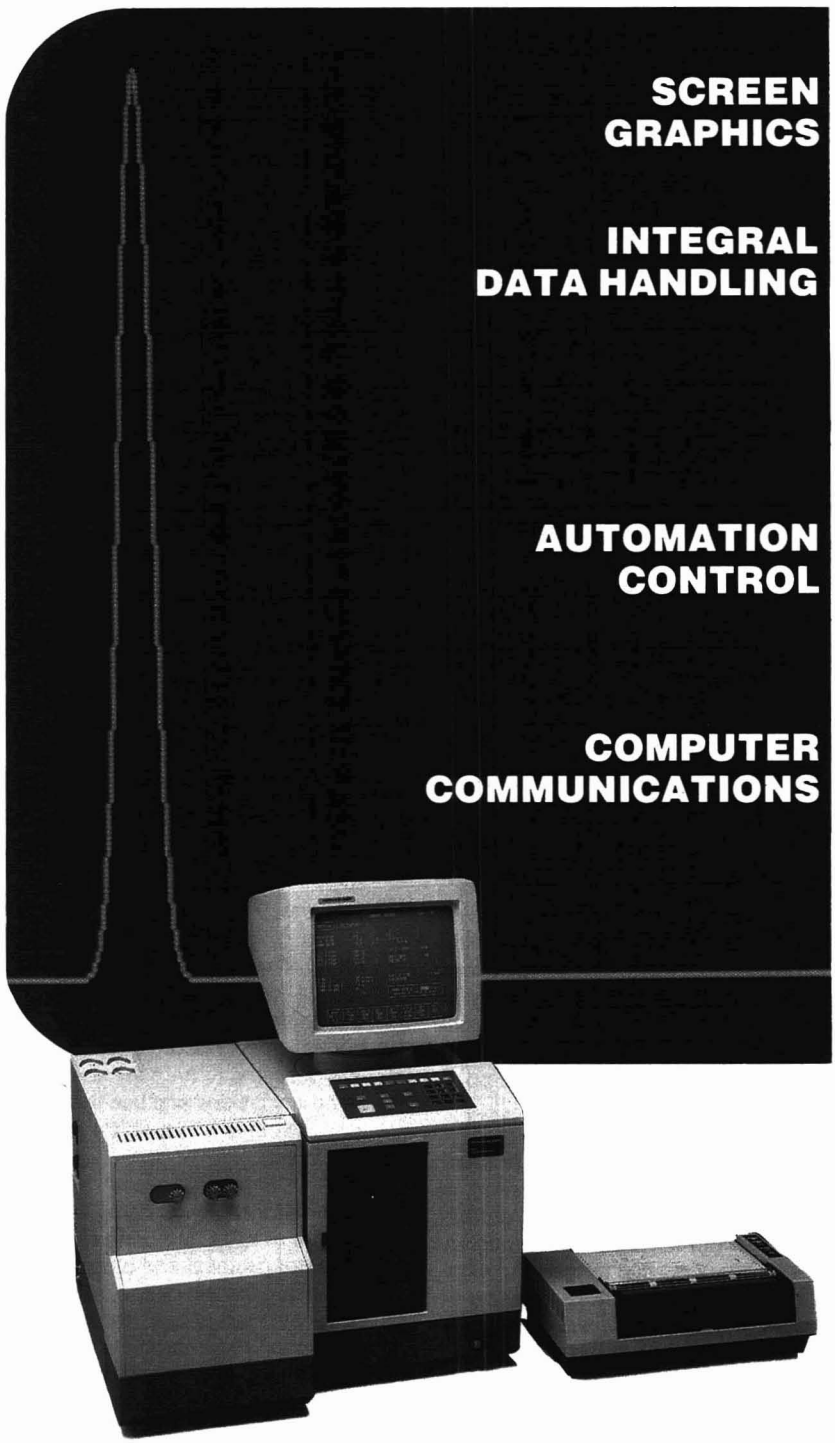

Whether your requirement is for a single or dual detector gas chromatograph, only an 8000 Series instrument can offer you:

Screen Graphics to display your chromatogram in real time *and* at the end of a run to replot and examine all or part of it. Combine this unique feature with .....

Integral Data Handling and you have the ultimate in self-contained gas chromatographs, presenting each chromatogram with overlaid component names and all the required integration data. The optional reintegration facility saves valuable time in method development and, when the day just isn't long enough .....

Automation Control can integrate the AS-8300 autosampler with the 8000 Series instrument control to handle the analysis of up to 100 samples in a completely unattended mode of operation. Finally, via RS232-C, ...

Computer Communications the 8000 Series system can be linked to a wide range of computer systems including Perkin-Elmer's Chromatography Laboratory Automation System (CLAS), to provide the most powerful instrumentation for today's fully automated laboratory.

The 8000 Series – *the peak of perfection!*

For further information please contact:
Perkin-Elmer Corp., Analytical Instruments, Main Ave. Norwalk, CT 06859-0012 U.S.A. Tel: (203) 762-1000.
Perkin-Elmer Ltd., Post Office Lane, Beaconsfield, Bucks HP9 1QA, England. Tel: Beaconsfield (049 46) 6161
Bodenseewerk Perkin-Elmer & Co., GmbH, Postfach 1120, 7770 Ueberlingen, Federal Republic of Germany. Tel: (07551) 811.

PERKIN-ELMER

CIRCLE 166 ON READER SERVICE CARD

Manufacturers' Literature

Bioanalyzer. Brochure describes Multipurpose Bioanalyzer, which uses an enzyme electrode to detect a wide variety of biochemicals in complex mixtures. The instrument includes a sensor probe; electronics; a starter kit for determination of glucose, lactose, lactic acid, and ethanol; and a blank gel matrix for user-provided enzymes. 6 pp. Provesta **430**

LC selection. HPLC system selection guide offers information about gradient and isocratic systems and instructions on configuring an LC system to meet user-specific separation goals. 24 pp. Gilson Medical Electronics **431**

Chromatography workstation. Literature features the Maxima chromatography work station, which can interactively control up to four complete chromatography systems, including pumps, valves, autosamplers, and detectors. Individual work stations can be linked in a network to provide larger labs with central computer power. 6 pp. Dynamic Solutions **432**

Matrix isolation GC/FT-IR. Technical information kit describes the Cryolect matrix isolation GC/FT-IR system for detection of trace levels of organic compounds and explains how it can be used to solve problems in petrochemical research, flavor and fragrance chemistry, pharmaceuticals, specialty and agricultural chemicals, and environmental monitoring and control. Mattson Instruments **433**

GPC applications note. *Polymer Notes* is a new series of applications briefs on the use of gel permeation chromatography for the compositional analysis of polymers and additives. The first issue describes the analysis of polyolefin additives; future issues will describe various techniques for spectroscopic characterization of polymers as well as applied uses of GPC to solve manufacturing and process problems. Waters Associates **434**

Electrochemical detectors. Literature discusses the principles and operation of electrochemical detectors for LC and describes the various configurations of detectors available. 4 pp. Bioanalytical Systems **436**

GC. Brochure describes the 6000 Vega series of six high-performance gas chromatographs, including detailed specifications for column oven, control system, injection systems, gas flow system, and detectors. Ordering information is given for each unit in the series. Carlo Erba **435**

LC pump. Brochure features two dual-piston pumps, one using conventional stainless steel components and the other using titanium technology with all wetted parts made of either titanium, sapphire, ruby, or inert polymers. The titanium pump is corrosion resistant and requires only minor maintenance, making it particularly suitable for biochemical applications. LKB **437**

GC columns. Brochure describes the DB-624 megabore column for analyzing purgeable organics as specified by EPA methods and shows chromatograms of a wide variety of volatile hydrocarbons obtained with various thick-film (3 and 5 μm) columns. Also included are chromatograms of alkaloids, amphetamines, barbiturates, anticonvulsants, and other drugs obtained with a single 30-m DB-1 megabore column. 8 pp. J & W Scientific **438**

Electrophoresis. Brochure highlights the GE-2/4LS vertical electrophoresis system for 2D electrophoresis, Disc-PAGE, or SDS-PAGE. Associated accessories, including a power supply, a gel destainer, and a slab drier, are also described. Pharmacia **439**

LC systems. Bulletin 5920A describes the series 340 gradient, micro-gradient, and isocratic HPLC systems, including pumps, data system–controller, integrator, autosampler, and detector. Applications include proteins, substituted aromatics, oligodeoxynucleotides, and pharmaceutical formulations. 12 pp. Beckman **440**

Syringe pumps. Literature describes three high-pressure, high-precision, syringe pumps, which feature no detectable pulsation or flow noise throughout their entire operating ranges. Applications include LC with flow-sensitive detectors, microbore LC, supercritical fluid chromatography, and rock core flooding. 6 pp. Isco **441**

LC/MS wall chart. Educational wall chart illustrates the principles of LC/MS, describing the two analysis techniques and how they are linked. A visual description of the thermospray interface is included. Kratos Analytical **442**

Catalogs

Drug standards. Catalog lists more than 300 abused drugs and therapeutic drug standards, including many metabolites. Also included are tips on determination of drugs by GC and HPLC. Alltech Associates **445**

Microfiltration. Silver membranes, microporous ceramic filters and crucibles, prefilters, membrane holders, and filter forceps are featured. A guide to filter holder selection is also included. 13 pp. Poretics **446**

Diffraction gratings. Plane, standard and special, holographic plane, blazed holographic, concave, echelle, and large astronomical certified-precision diffraction gratings are included. Dye- and molecular-laser-tuning gratings are also featured. Milton Roy **447**

Chromatography. Products for HPLC, GC, and TLC, including columns, packings, ion pair reagents, derivatization reagents, septa, reaction vials, syringes, flow meters, and fittings, are featured. Several books on chromatography are also included. 47 pp. Regis **448**

Amino acids. Catalog features amino acids and their salts, amino acid derivatives, reagents for peptide synthesis, peptides, amino acid analogues, and sugars and their derivatives. 24 pp. Degussa **449**

Electrodes. A complete line of pH, reference, combination pH, ion-selective, and oxidation reduction potential electrodes is described. Technical information designed to help the user understand electrodes and use them for problem solving is included. 24 pp. Gam Rad West **450**

Chromatography. Catalog features a full line of HPLC supports for determination of proteins and other biochemicals using ion exchange, steric-exclusion, reversed-phase, and hydrophobic interaction chromatography. Guard columns and peptide standards are also featured. 16 pp. SynChrom **451**

For more information on listed items, circle the appropriate numbers on one of our Readers' Service Cards

XR200/300

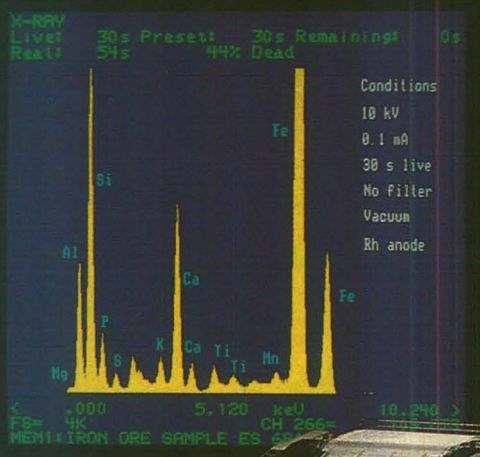

The world's most flexible ENERGY DISPERSIVE X-RAY FLUORESCENCE SPECTROMETER



Only elemental analysis using the Link Systems XR200/300 spectrometer EDXRF provides:

Extreme versatility

- Simultaneous multielement analysis facilitated by energy dispersive XRF technology.
- Full dynamic range from low ppm to high wt% without dilution.
- Superb qualitative identification of all elements from Na to U in periodic table.

Fast operation

- Fully automatic analysis of up to 16 samples using computer controlled carousel.
- Minimal sample preparation.
- Accurate quantitative analysis with minimal calibration.

Integrated systems with safety and reliability

- Powerful on-line data processing utilizing dedicated computer.
- Totally non-destructive technique ensures safety for valuable works of art or preservation of vital evidence/samples.
- Full backing of Link worldwide sales and service.

LINK SYSTEMS

LINK SYSTEMS LIMITED,
HALIFAX ROAD,
HIGH WYCOMBE,
BUCKS HP12 3SE,
ENGLAND.
TEL: 0494 442255
TELEX: 837542LINK HWG
FAX: 0494 24129

LINK SYSTEMS (FRANCE),
LE MAZIERE,
RUE DES MAZIERES,
91033 EVRY CEDEX,
TEL: (1) 6078 10 20
TELEX: 691884F

LINK ANALYTICAL,
240 TWIN DOLPHIN DRIVE,
SUITE B,
REDWOOD CITY,
CALIFORNIA 94065 USA
TEL: (415) 595-5465
FAX: (415) 595 5589

LINK NORDISKA, AB
BOX 153,
181 22 LINDINGOE,
SWEDEN.
TEL: 08-767 9170
TELEX: 12645 SPECTAB

CIRCLE 131 ON READER SERVICE CARD

HOW WE MAKE SURE YOU GET PRECISELY WHAT YOU PAY FOR.

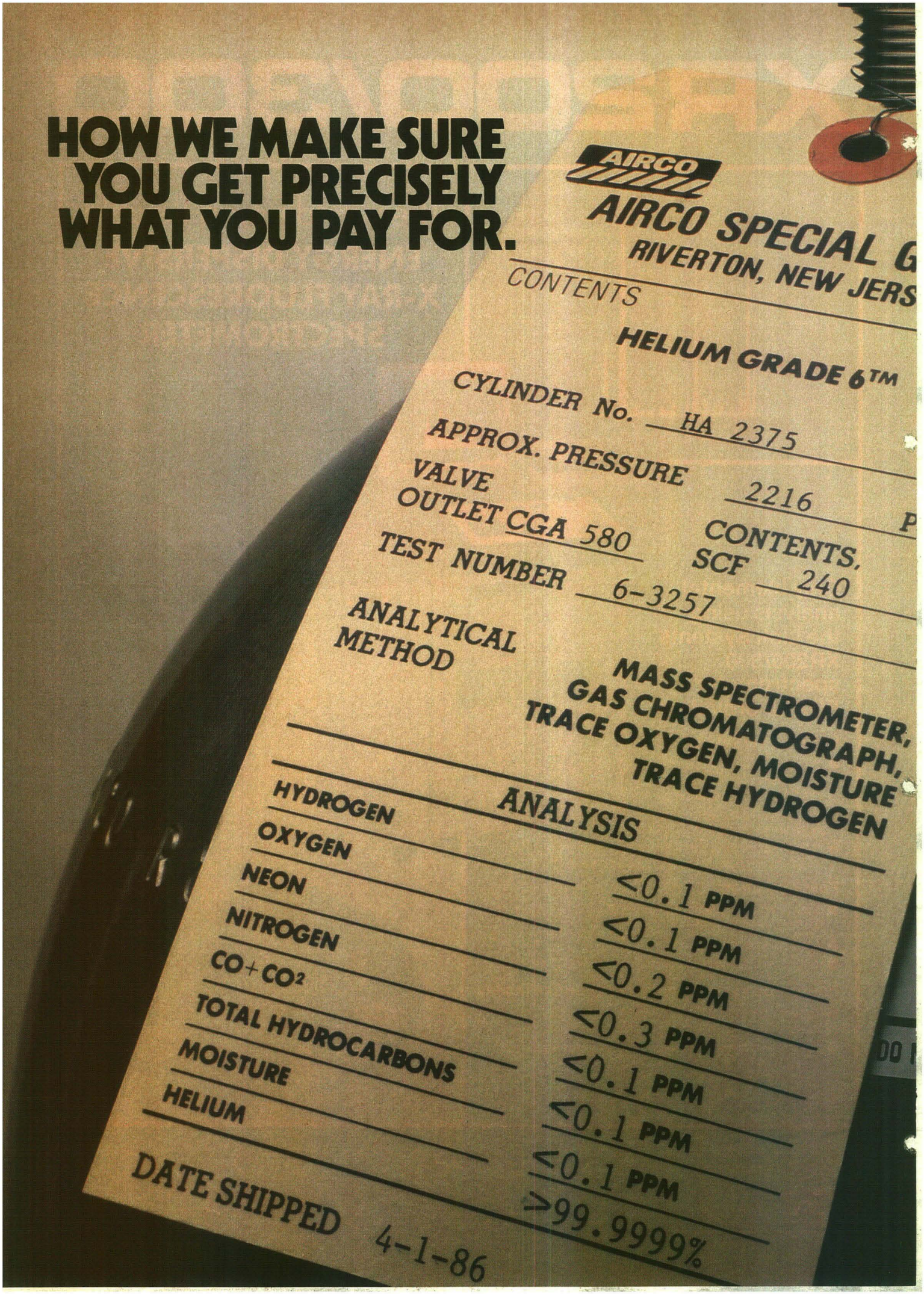

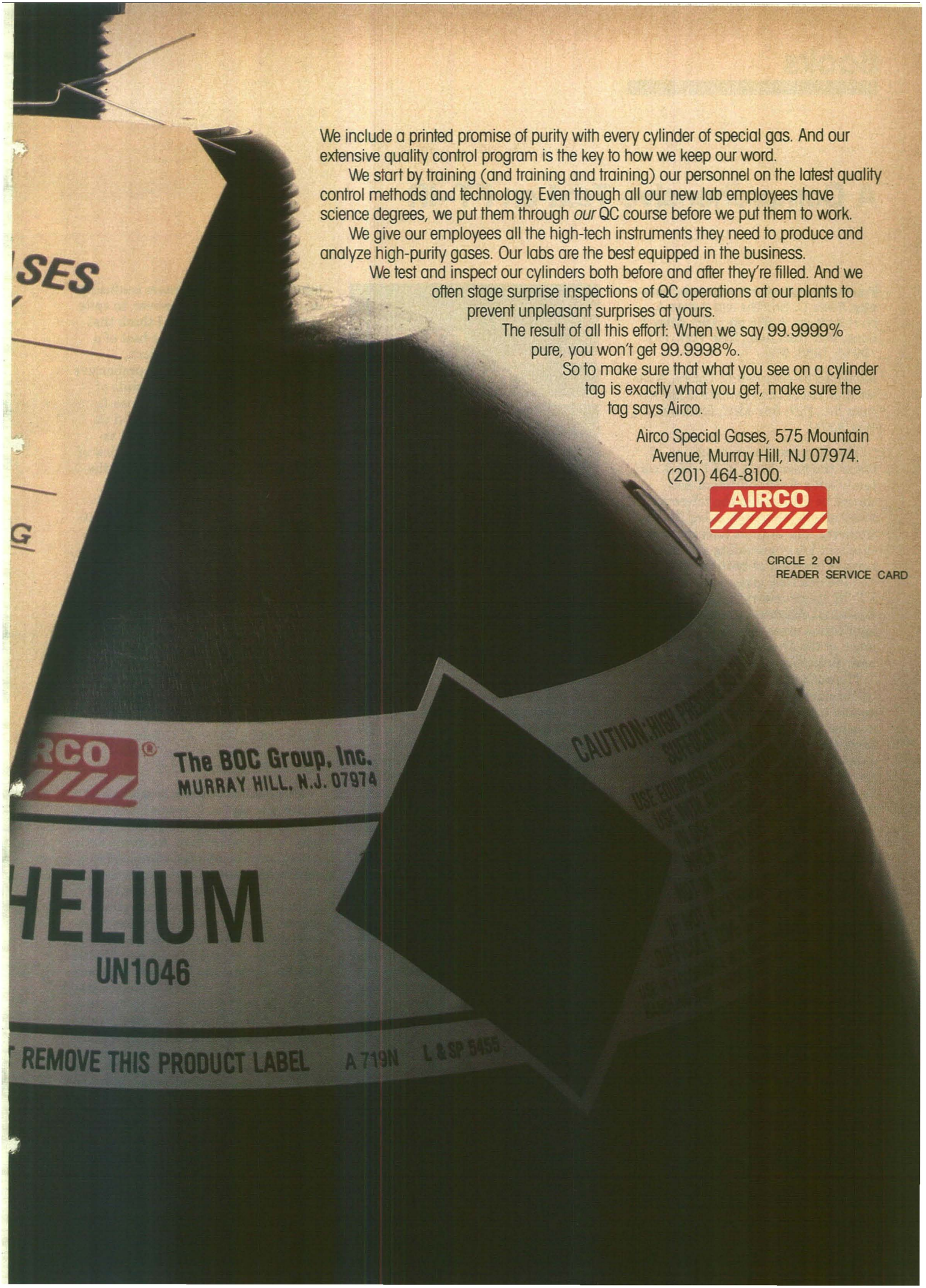

We include a printed promise of purity with every cylinder of special gas. And our extensive quality control program is the key to how we keep our word.

We start by training (and training and training) our personnel on the latest quality control methods and technology. Even though all our new lab employees have science degrees, we put them through *our* QC course before we put them to work.

We give our employees all the high-tech instruments they need to produce and analyze high-purity gases. Our labs are the best equipped in the business.

We test and inspect our cylinders both before and after they're filled. And we often stage surprise inspections of QC operations at our plants to prevent unpleasant surprises at yours.

The result of all this effort: When we say 99.9999% pure, you won't get 99.9998%.

So to make sure that what you see on a cylinder tag is exactly what you get, make sure the tag says Airco.

Airco Special Gases, 575 Mountain Avenue, Murray Hill, NJ 07974. (201) 464-8100.

AIRCO

CIRCLE 2 ON READER SERVICE CARD

A Comprehensive Text on FT–IR

Fourier Transform Infrared Spectrometry. Peter D. Griffiths and James A. de Haseth. xv + 656 pp. John Wiley & Sons, 605 Third Ave., New York, N.Y. 10016. 1986. $75

Reviewed by Stephen R. Lowry, Nicolet Analytical Instruments, 5225 Verona Rd., P.O. Box 4508, Madison, Wis. 53711

This long-awaited new edition of one of the basic texts in FT–IR is certainly not a disappointment and should be included in the reference library of any laboratory using IR spectrometry. The authors have done an excellent job of providing a comprehensive overview of both the theory and the practical aspects of modern FT–IR spectrometry. They have added several chapters on some of the new application areas and have enhanced much of the original discussion of the basic principles of FT–IR.

The authors claim that this should be considered a new text rather than a second edition, and I would agree. The number of pages has doubled, and there are 11 new chapters. Some of the areas that are covered in depth are photoacoustic spectrometry (Chapter 9), matrix isolation and related techniques (Chapter 15) GC/FT–IR (Chapter 18), HPLC/FT–IR (Chapter 19), and time-dependent measurements, including time-resolved spectrometry (Chapter 12). The authors have also included several chapters on specific application areas, including surface analysis, polymer applications, and biological spectrometric techniques.

One chapter that is very interesting but does not really fit into the scope of this monograph covers the use of Fourier transform techniques for atomic emission spectrometry in the visible and ultraviolet regions. Although this chapter is well written and summarizes the work performed in this area I do not feel that it contributes to this text.

Two areas that are not covered sufficiently are quantitative analysis and computerized spectral searching. Although I admit to a bias toward these applications I think that there has been a significant increase in both new

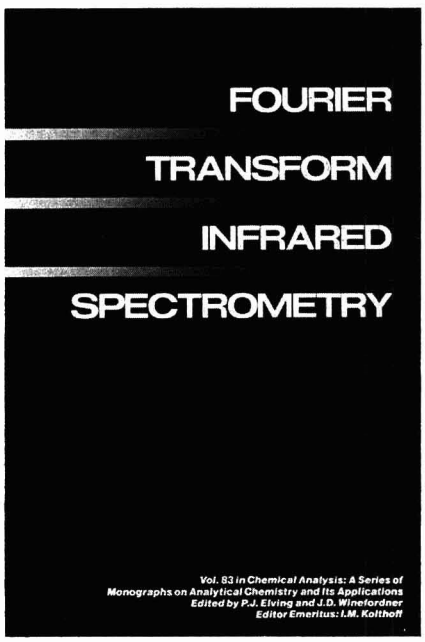

methods and user interest in these fields. A chapter is included on quantitative analysis (10), but much of the discussion involves spectral subtraction and factor analysis, which are not actually quantitative analysis techniques. Spectral searching receives a brief mention in the chapter on GC/FT–IR. The subject of performing either of these techniques on the original interferograms is not discussed.

The only general criticism I have of this book is perhaps its overall organization. Although the authors have done a good job of describing the many accessories and also some of the application areas where FT–IR is used today, they should have chosen either to focus on the accessories and techniques by providing examples of applications or to concentrate on the application areas and describe how certain techniques are used. By including chapters emphasizing both techniques and applications, the authors are a bit redundant, and I found myself flipping back and forth when they alluded to techniques described in a previous chapter or to see how a technique might be applied to one of the application areas. I also found the discussion of hardware components, basic theory, and mathematical calculations contained in the early chapters confusing in several instances. However, in spite of these minor problems I think that the authors have made the best of a large and complicated subject.

In summary, this is a comprehensive text that covers the major points of FT–IR extremely well. The book is well written and provides a good explanation of many of the subtle aspects of FT–IR. The basic overview of instrumental design and some of the trade-offs in those designs should prove invaluable to users of FT–IR spectrometers and to anyone interested in the field. Even someone who already has the original book would certainly find enough new information in this completely updated version to justify the cost.

Liquid Chromatography in Pharmaceutical Development. Irving W. Wainer, Ed. x + 496 pp. Aster Publishing Corporation, 320 North A St., Springfield, Ore. 97477. 1985. $97.50

Reviewed by Roger K. Gilpin, Department of Chemistry, Kent State University, Kent, Ohio 44242

This book provides a broad look at a number of topics. It is subdivided into five major categories: fundamental aspects of the separation, isolation, and detection of compounds; preparative separations; automated coupled-column techniques; quality control and methods validation; and emerging trends. Specific subjects include column design, mobile-phase optimization, advances in detection and identification, compound isolation, pharmacological testing, interlaboratory comparisons, and column standardization.

The book is much more comprehensive than the title indicates, especially in the first major subdivision, which comprises over half of the text. Most chapters emphasize basic concepts and principles rather than citing applications only. The book is more of a general treatise than one devoted simply to pharmaceutical analysis. Coverage tends to be less comprehensive in the later chapters. The fourth section, which deals with quality control and methods validation, emphasizes a

Molecular Weight Determinations Without Standards or Calibrations

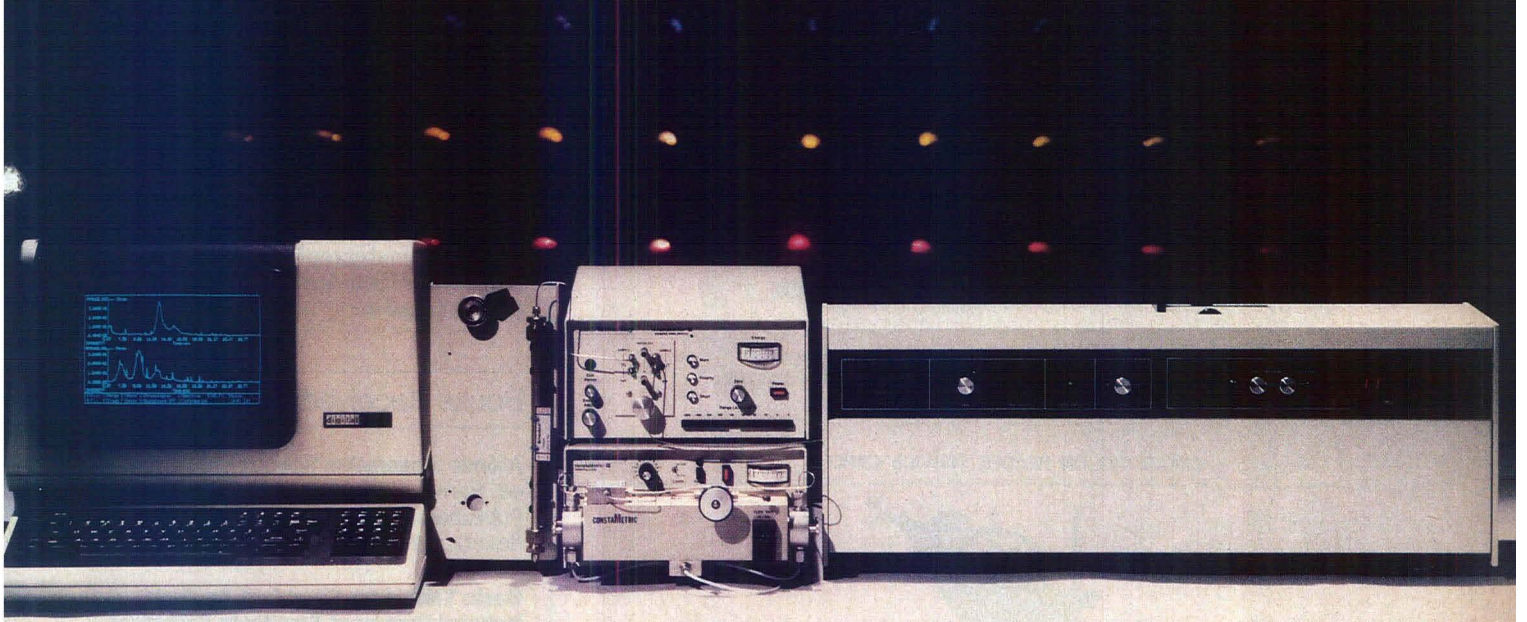

Absolute Molecular Weight Distribution

Coupled with your existing chromatograph, the CMX-100 polymer analyzer provides absolute weight distribution without using standards or calibrations.

Polymer Branching

The CMX-100 easily detects branching; information impossible to obtain with linear standards.

Gel Formation

The CMX-100 is inherently sensitive to high molecular weight species such as gels. These species frequently have concentrations too low for detectors such as UV or DRI.

For more information contact . . .

LDC/Milton Roy

U.S. HEADQUARTERS, P.O. Box 10235, Riviera Beach, FL 33404 Toll-free: 800-327-6182, In Florida: (305) 844-5241 Telex: 441098
UNITED KINGDOM, LDC UK, Milton Roy House, 52 High Street, Stone, Staffordshire ST15 8AR England Telephone: (0) 785-81-3542 Telex: 36623
FRANCE, LDC S.A., 15 rue Guyton de Morveau, Paris 75013, France Telephone: 588-2800 Telex: 205331
WEST GERMANY, Milton Roy (Deutschland) GMBH Jahnstrasse 22-24 6467 Hasselroth 2, West Germany Telephone: (0) 6055-3366 (2031) Telex: 4184357
JAPAN, Milton Roy K.K., Takanawa Dai-Ichi Building 21-41, Takanawa 2-Chome, Minato-Ku, Tokyo 108, Japan Telephone: (03) 473-3181 Telex: 242-4296

CIRCLE 130 ON READER SERVICE CARD

WARM TO THE IDEA

THIN FILM COLUMN HEATING

A Technological Step Ahead of Blocks, Baths and Ovens:
More Accurate and Convenient • Faster Heating and Cooling
• Requires No System Alteration • Adds No Dead Volume
• Compatible with All Columns, from Prep. to Microbore
. . . And Less Expensive

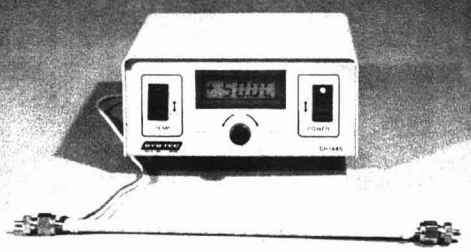

GOLDENFOIL™
COLUMN TEMPERATURE CONTROL SYSTEM

SYSTEC INC
3816 Chandler Drive
Minneapolis, MN 55421
(612) 788-9701

INNOVATORS IN LABORATORY CONTROL

CIRCLE 192 ON READER SERVICE CARD

For automatic mixing in separatory funnels, 500 ml to 2,000 ml capacity...

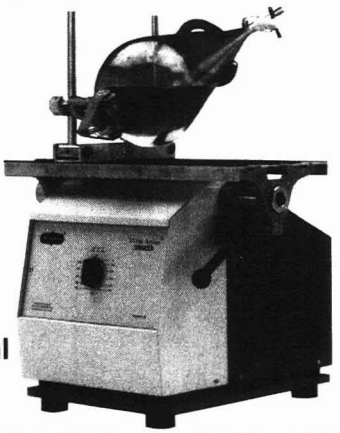

BURRELL WRIST-ACTION® SHAKER

Attach the Separatory Funnel Support's base to the top platform of the Burrell Shaker and handle BIG funnels with ease! Adjustable clamps hold funnels at the angle and height you require. Swirling's consistent, and time and agitation speed can be set, so you can accurately repeat all mixing operations.

And the Burrell Build-Up® System lets you increase capacity by adding side-arms and clamps for Erlenmeyer flasks and other containers.

Write or call for information on Separatory Funnel Supports used on the *only* Wrist-Action® Shaker available.

BURRELL

BURRELL CORPORATION
2223 Fifth Avenue, Pittsburgh, PA 15219
Telephone: (412) 471-2527

CIRCLE 19 ON READER SERVICE CARD

Books

number of points that are not always apparent to those not involved in regulatory aspects of analysis. This section was a good idea; however, it could have been expanded.

Many of the chapters are written by recognized experts in their respective areas. There are a few marginal chapters, but as a whole coverage ranges from good to very good. For example, the chapter on resolution of optical isomers is extremely well developed and leads one through the fundamental aspects of stereochemistry to the separation of important compounds, such as amino acids and pharmaceutically active enantiomeric amines. There are numerous illustrations throughout the book that are well-chosen to clarify important points.

In summary, despite a few deficiencies, this book's positive points far outweigh its negative features. It will make a beneficial addition to the practicing chromatographer's library, especially for those involved in pharmaceutical analysis.

Books Received

Atomic Absorption Spectrometry. 2nd ed. Bernhard Welz. xii + 506 pp. VCH Publishers, 303 N.W. 12th Ave., Deerfield Beach, Fla. 33442. 1985. $40

Basic Tables for Chemical Analysis. National Bureau of Standards Technical Note 1096. Thomas J. Bruno and Paris D. N. Svoronos. 240 pp. U.S. Government Printing Office, Washington, D.C. 20402. 1986. $11

Chromatography and Separation Chemistry: Advances and Developments. Satinder Ahuja, Ed. viii + 304 pp. American Chemical Society, 1155 16th St., N.W., Washington, D.C. 20036. 1986. $54.95

Artificial Intelligence Applications in Chemistry. Thomas H. Pierce and Bruce A. Hohne, Eds. x + 395 pp. American Chemical Society, 1155 16th St., N.W., Washington, D.C. 20036. 1986. $59.95

Topics in Organic Electrochemistry. Albert J. Fry and Wayne E. Britton, Eds. xiv + 296 pp. Plenum Press, 233 Spring St., New York, N.Y. 10013. 1986. $49.50

Instrumentation for Environmental Monitoring. 2nd ed. Vol. 2: Water. Lawrence Berkeley Laboratory Environmental Instrumentation Survey. xxx + 982 pp. John Wiley & Sons, 605 Third Ave., New York, N.Y. 10016. 1986. $190

New Books From Wiley Examine 15 Days Free

ANALYTICAL APPLICATIONS OF LASERS
Edward Piepmeier, Editor
A thorough and complete overview of the contemporary laser technology. Contributions by twenty-two experts provide the analytical chemist with a valuable reference on uses of the laser as an investigative or analytical tool in a wide variety of ways.
approx. 670 pp. (1-87023-4) **Aug. 1986** $89.95

TRACE ANALYSIS
Spectroscopic Methods For Molecules
Edited by Gary Christian & James B. Callis
An up-to-the-minute volume on all aspects of modern methods for molecules utilizing spectroscopic methods, both in the research laboratory and in industry. *Vol. 84 in the Wiley Chemical Analysis Series.*
approx. 400 pp. (1-87583-X) **Sept. 1986** $55.00

ULTRATRACE ANALYSIS OF PHARMACEUTICALS AND OTHER COMPOUNDS OF INTEREST
Edited by S. Ahuja
Describes ultratrace analysis and how it is used in solving complex scientific problems related to drugs, food safety, pharmaceuticals, air, food, water, and the environment. Covers methodologies and forensics. Suggests best methods for determining mechanism of action, disposition, and toxic properties of chemicals.
384 pp. (1-82673-1) **July 1986** $59.95

APPLIED GEOCHEMICAL ANALYSIS
C. O. Ingamells and F. F. Pitard
A treatise on practical inorganic analytical chemistry. Includes not only classical, but also most newly developed determinative techniques: XRF, ICP, AA, etc. Chapters on Sampling, the art of chemical analysis, classical analysis, the elements, rapid methods, chemical calculations, and geochemical standards. Vol. 88 in the Wiley *Chemical Analysis Series.*
approx. 700 pp. (1-83279-0) **Nov. 1986** In Press

ORGANIC CARCINOGENS IN DRINKING WATER
Detection, Treatment and Risk Assessment
Edited by Neil M. Ram, Edward Calabrese, and Russell F. Christman
Comprehensive coverage of environmental concerns, issues, findings, and recommendations concerning the presence of organic micropollutants in drinking water.
approx. 540 pp. (1-80959-4) **Oct. 1986** $65.00

MASS SPECTROMETRY
Applications in Science and Engineering
Frederick A. White & George M. Wood
An overview of mass spectrometry, its instrumentation and applications in the sciences. Organized to afford use by R&D scientists, in seminars and courses, or in independent study. Emphasis is interdisciplinary for both scientific and engineering applications.
approx. 780 pp. (1-09236-3) **Sept. 1986** $72.50

SECONDARY ION MASS SPECTROMETRY
Basic Concepts, Instrumental Aspects, Applications and Trends
A Benninghoven, F. G. Rüdenauer, and H. W. Werner
An attempt to provide a comprehensive work on developments in the last decade in Secondary Ion Mass Spectrometry (SIMS). Provides a rapid survey of basic concepts, applications, and a comprehensive and systematic presentation of the entire field. Vol. 86 in the Wiley *Chemical Analysis Series.*
approx. 1,000 pp. (1-01056-1) **Dec. 1986** In Press

COAL SCIENCE
An Introduction to Chemistry, Technology and Utilization
Rita K. Hessley, John W. Reasoner & John T. Riley
269 pp. (1-81225-0) **1986** $35.00

CHEMOMETRICS
Muhmmad A. Sharaf, Deborah L. Illman & Bruce R. Kowalski
Describes the new disciplines, Chemometrics, which has evolved from the widespread use of computers, the explosion of data coming out of chemical laboratories and methods which have been developed to collect and interpret such data. *Vol. 82 in the Wiley Chemical Analysis Series.*
352 pp. (1-83106-9) **1986** $49.95

PHOTOMETRIC DETERMINATION OF TRACES OF METALS, 4th Ed., Pt. 2A
Hiroshi Onishi
This work introduces Part 2 of a two-part work. Part 2 will deal with all metals from aluminum to zirconium. This work, Part 2A, covers aluminum to lithium. Part 2B, to follow later, will cover magnesium to zirconium. *Vol. 3 in the Wiley Chemical Analysis Series.*
885 pp. (1-86139-1) **1986** $139.95

DETECTORS FOR LIQUID CHROMATOGRAPHY
Edited by Edward S. Yeung
A comprehensive work on the subject of detectors in liquid chromatography. Nine chapters deal with the pursuit of new detection techniques and recent improvements in well-known detection principles. Vol. 89 in the Wiley *Chemical Analysis Series.*
approx. 400 pp. (1-82169-1) **Oct. 1986** In Press

INFRARED AND RAMAN SPECTRA OF INORGANIC AND COORDINATION COMPOUNDS, 4th Ed.
Kazuo Nakamoto
Describes fundamental theories of vibrational spectroscopy in a condensed form. Illustrates their applications to inorganic, coordination, organometallic, and bioinorganic compounds, using typical examples. New Fourth Edition introduces covereage of metal isotope spectroscopy and bioinorganic compounds.
approx. 480 pp. (1-01066-9) **Aug. 1986** $55.00

COMPUTER SOFTWARE APPLICATIONS IN CHEMISTRY
Peter C. Jurs
Focuses on use of software (in numerical calculations and abstract information processing) in chemistry. Coverage in introductory, with advanced material in selected sections.
approx. 240 pp. (1-84735-6) **Oct. 1986** $34.95

FOURIER TRANSFORM INFRARED SPECTROMETRY
Peter R. Griffiths & James A. deHaseth
672 pp. (1-09902-3) **1986** $75.00

THERMAL ANALYSIS, 3rd Ed.
Wesley W. Wendlandt
814 pp. (1-88477-4) **1986** $89.95

THE ANALYSIS OF EXTRATERRESTRIAL MATERIALS
Isadore Adler
346 pp. (1-87880-4) **1986** $55.00

ORGANIC ELECTRONIC SPECTRAL DATA
Volume 22 — 1980
J.P. Phillips, Dallas Bates, Henry Feuer & B.S. Thyagarajan
Latest volume in a series providing chemists with special interests in spectrophotometry with a page-by-page search of the major chemical journals for the year 1980.
approx. 1,050 pp. (1-83816-0) **Aug. 1986** $120.00

INSTRUMENTATION FOR ENVIRONMENTAL MONITORING, 2nd Ed. (2-Volume Set)
Lawrence Berkeley Laboratory
Presents all currently available data on environmental monitoring instruments.
Volume 1: Radiation ($179.50)
Volume 2: Water ($190.00)
2-Volume Set: (1-85615-0) **1983/1986** $345.00

Visit the Wiley Exhibit at the Fall 1986 American Chemical Society Exposition September 8-10, Anaheim Booth Numbers 801-811

Order through your bookstore or write to Jules Kazimir, Dept. 6-0666.

TO ORDER FOR 15-DAY FREE EXAM CALL TOLL FREE

1 800 526-5368

In New Jersey, call collect (201) 342-6707 Order Code #6-0666.

WILEY-INTERSCIENCE
a division of John Wiley & Sons, Inc.
605 Third Avenue, New York, N.Y. 10158

In Canada: 22 Worcester Road, Rexdale, Ontario M9W 1L1
Prices subject to change and higher in Canada

092-6-0666

CIRCLE 231 ON READER SERVICE CARD

Spotlighting

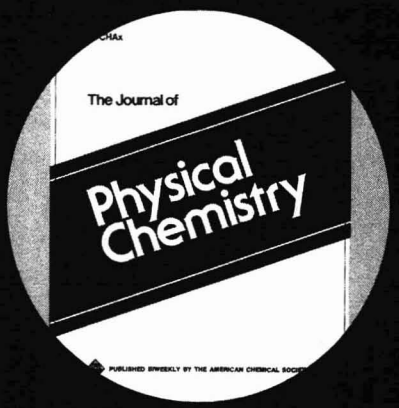

The Journal of Physical Chemistry

reporting the most recent experimental and theoretical research in fundamental aspects of physical chemistry and chemical physics.

Over forty papers of original research by the world's leading physical chemists in each biweekly issue keep you up-to-date in this dynamic field.

Plus an expanded format now includes—

- *Letters*—Each issue begins with this section of short articles where findings that deserve rapid dissemination are reported. Letters are handled expeditiously by the Editors and publication staff.
- *Feature Articles*—Leading scientists are invited to contribute critique articles in specialized areas of research, with emphasis on his own contributions. These are written for physical chemists who are not necessarily in the author's research area.
- *Articles*—Peer-reviewed research in print for the first time covering all areas of physical chemistry and contributed by scientists around the world.
- *Symposia Issues*—Special issues include the publishing of significant selected symposia.

Join the thousands of physical chemists who have already put *The Journal of Physical Chemistry* on their list of mandatory reading and have found JPC to be a comprehensive and authoritative source of important findings in physical chemistry and chemical physics.

1986	U.S.	Canada & Mexico	Europe Air Service Included	All Other Countries Air Service Included
ACS Members	$ 62	$ 93	$121	$151
Nonmembers	$369	$400	$428	$458

Mostafa El-Sayed, EDITOR
University of California, Los Angeles

Associate Editors
D. Herschbach, *Harvard Univ.*
M.F. Nicol, *Univ. of California, Los Angeles*
W.A. Steele, *The Pennsylvania State Univ.*
A.H. Zewail, *California Inst. of Tech.*

Advisory Board
J.L. Beauchamp
B.J. Berne
R.B. Bernstein
J.A. Beswick
J.I. Brauman
A.W. Castleman, Jr.
E.R. Davidson
I.R. Epstein
G.E. Ewing
G.R. Fleming
A. Heller
D. Henderson
R.M. Hochstrasser
M. Ito
G.A. Kenney-Wallace
J.L. Kinsey
R. Kopelman
E.K.C. Lee
Y.T. Lee
S.R. Leone
R.D. Levine
R.J. Madix
N. Mataga
H. Metiu
W.H. Miller
C.B. Moore
M.D. Newton
C.S. Parmenter
E.W. Schlag
G. Scoles
J.K. Thomas
D.G. Truhlar
R.P. Van Duyne
J.M. White
D.G. Whitten
B. Widom
C. Wittig
R.H. Wood
J.T. Yates

Call Toll Free 800-424-6747

Cable Address: JIECHEM **Telex:** 440159 ACSPUI or 892582 ACSPUBS

American Chemical Society • 1155 16th Street, N.W. • Washington, D.C. 20036

SPEED AND SAFETY TOGETHER

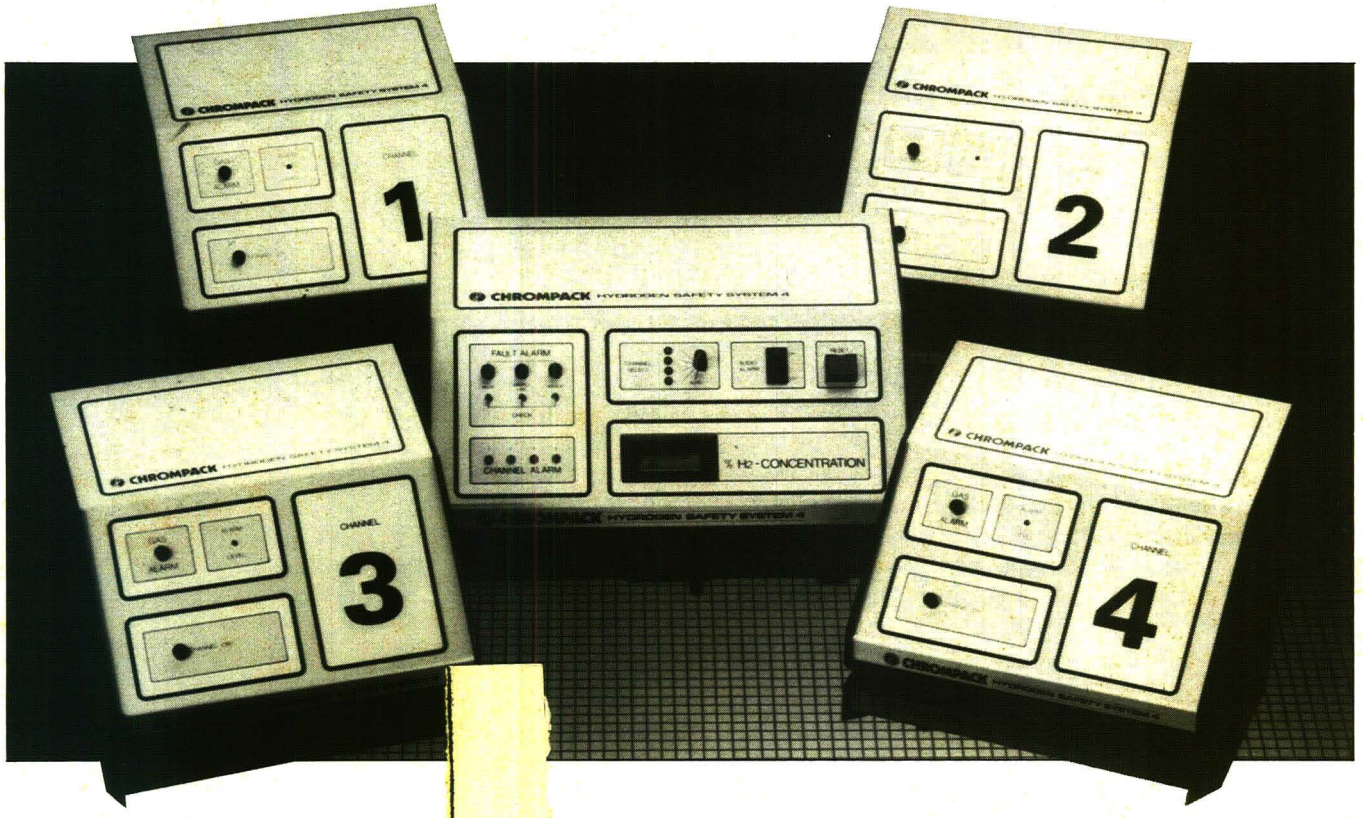

WITH CHROMPACK'S HYDROGEN SAFETY SYSTEMS

As chromatographers speaking to chromatographers, we don't have to tell you that hydrogen is a fast, cost-effective carrier gas. You know that already. But perhaps you didn't know that with Chrompack's Hydrogen Safety Systems (HSS) safety is as certain as speed.

There are a variety of HSS Systems to suit set-ups of one to four GCs. All sample the GC atmosphere constantly, and display digital read-outs of the hydrogen level in real time. No delay means no risk.



If the hydrogen level rises to a pre-set alarm level, the GC is turned off and an audible alarm sounds. Double-safe options include a flashing amber light and a 3/2 way valve for purging the column with an inert gas.

Why continue wasting money on expensive, slower systems? Switch to hydrogen and the HSS - speed and safety together.

CHROMPACK

FROM CHROMATOGRAPHERS
FOR CHROMATOGRAPHERS

Chrompack International B.V.
PO Box 8033, 4330 E A Middelburg,
The Netherlands.

Tel: 01 180-27352 Telex: 37852

CIRCLE 38 ON READER SERVICE CARD

Philips Analytical

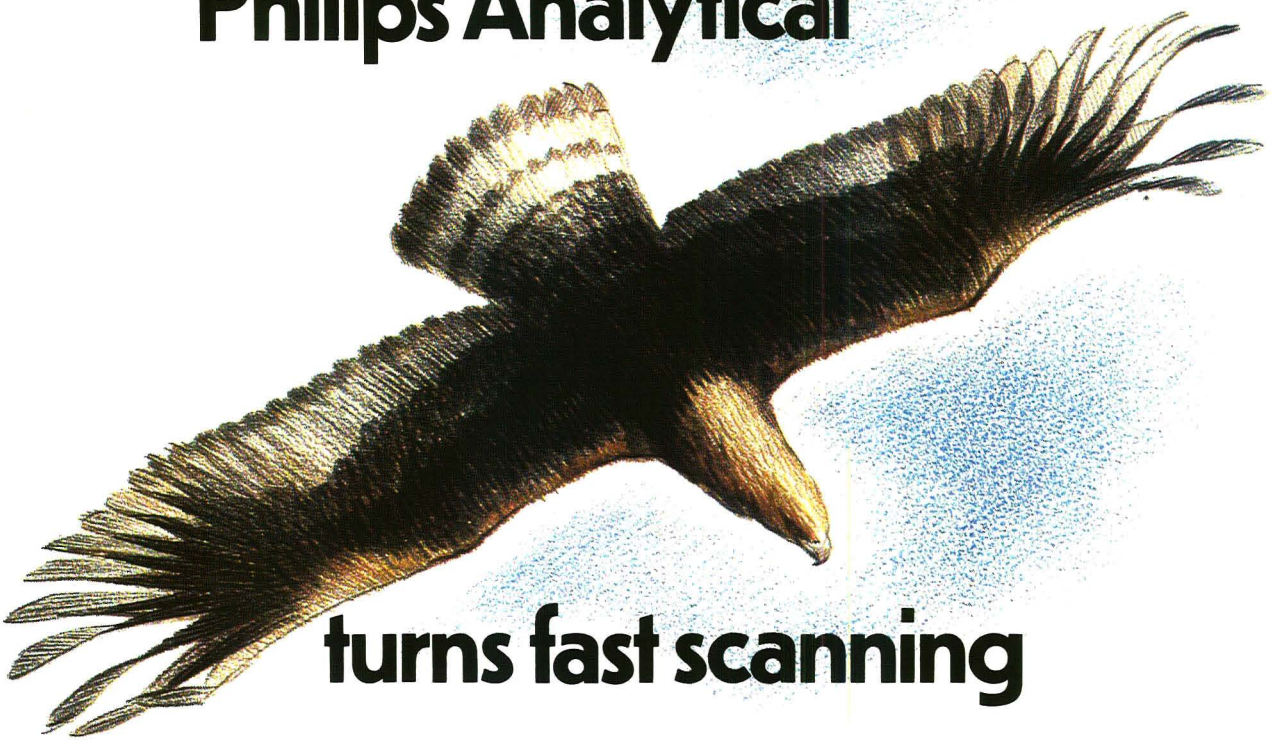

turns fast scanning

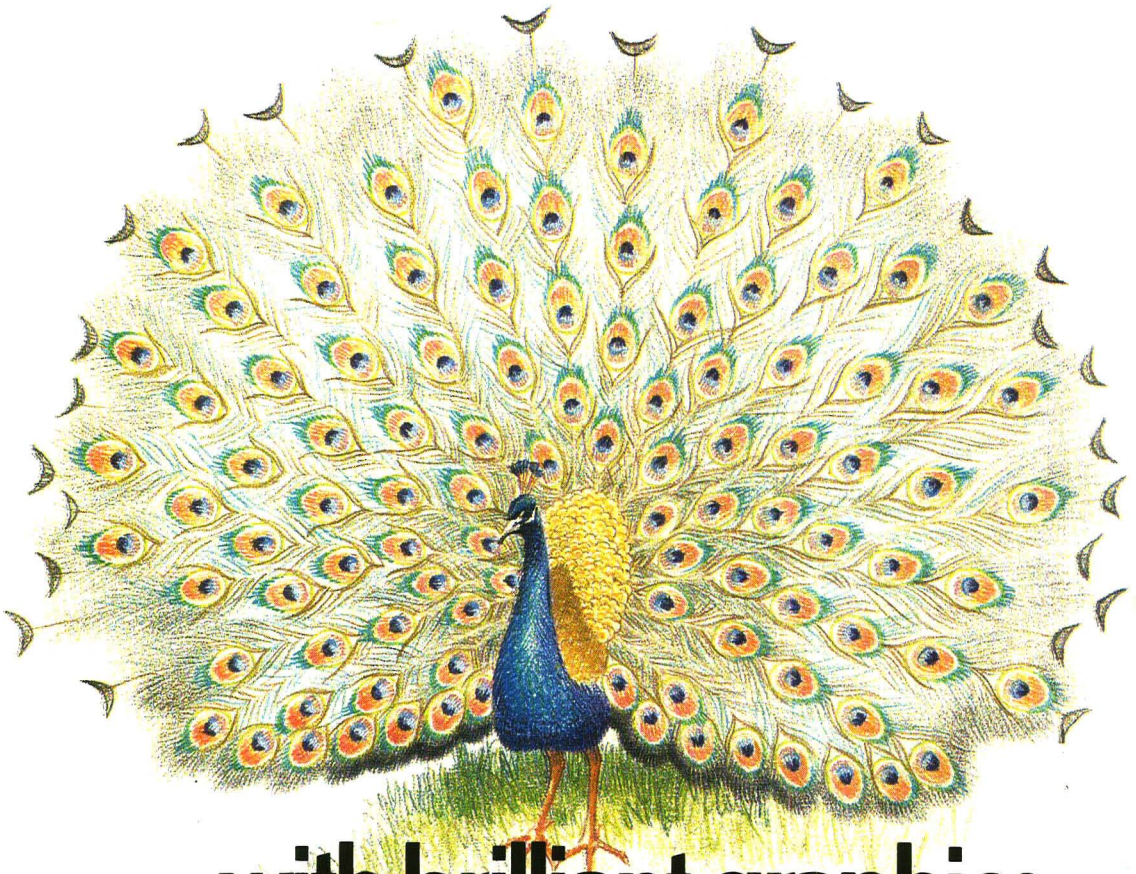

with brilliant graphics

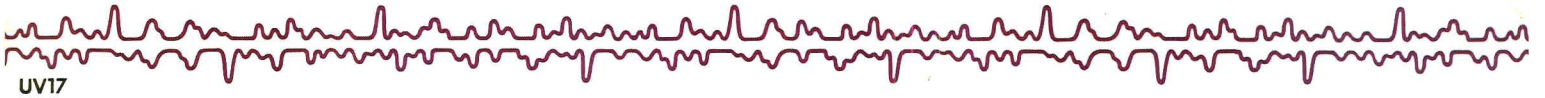

UV17

PHILIPS
Scientific and
Analytical Equipment



into child's play.

Whether UV expert or absolute beginner, irrespective of your application, the remarkable new PU8700 Series will provide you with high quality, no compromise answers in seconds.

You will enjoy the experience so much, you will positively look forward to your next analytical problem.

Sounds far fetched?
Look at the instrument.
Check out the features.
Ask the price.
Please call or write for further details.

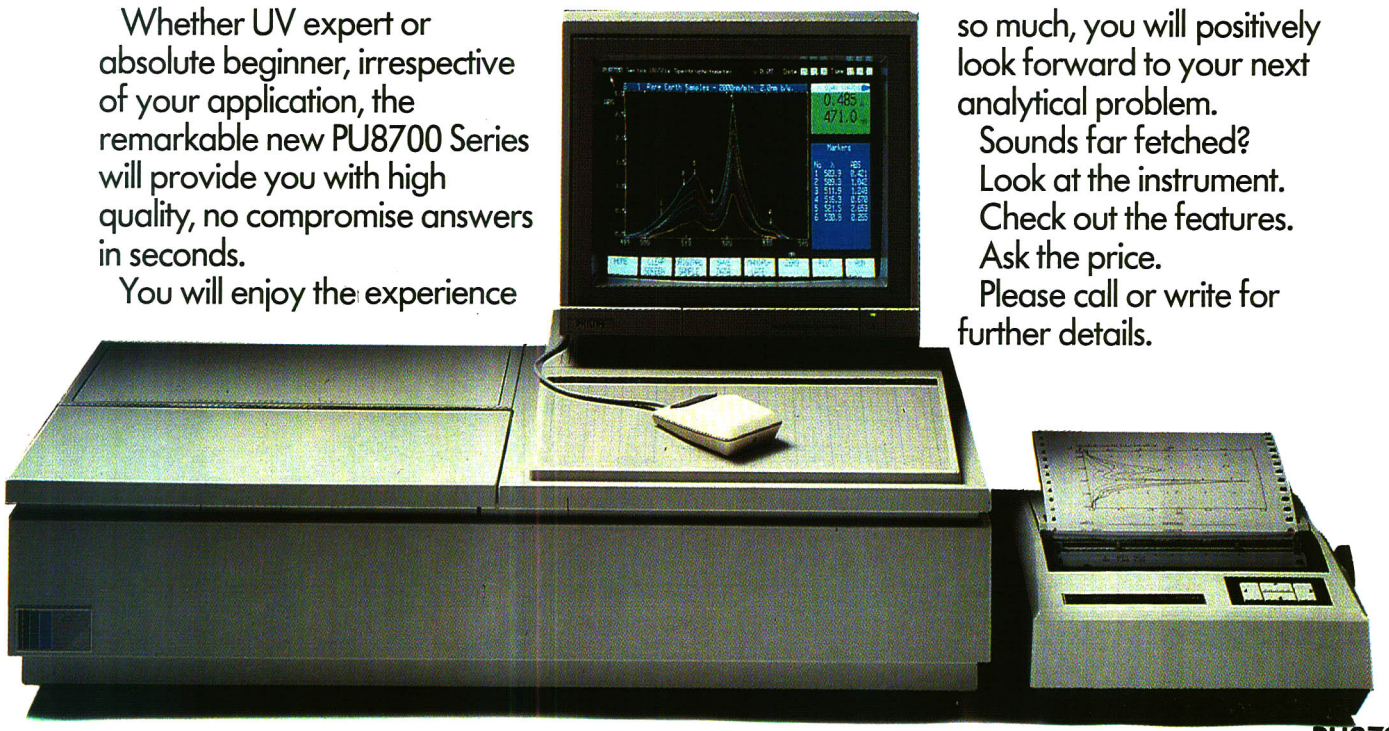

PU8700

New, low cost UV/Vis scanners.

Bigger ideas for better analysis.

Pye Unicam Ltd York Street Cambridge Great Britain CB1 2PX Telephone (0223) 358866 Telex 817331

PHILIPS

CIRCLE 80 ON READER SERVICE CARD

What in the world isn't chemical

— and how do you keep up with it all?

You keep current with developments by subscribing to the timely, authoritative, comprehensive journals published by the American Chemical Society.

Langmuir
Analytical Chemistry
Chemical & Engineering News
CHEMTECH
Environmental Science and Technology
Accounts of Chemical Research
Biochemistry
Chemical Reviews
Industrial & Engineering Chemistry –Process Design and Development
Industrial & Engineering Chemistry –Product R&D
Industrial and Engineering Chemistry –Fundamentals
Inorganic Chemistry
Journal of Agricultural & Food Chemistry
Journal of the American Chemical Society
Journal of Chemical & Engineering Data
Journal of Chemical Information and Computer Sciences
Macromolecules
Journal of Medicinal Chemistry
The Journal of Organic Chemistry
Organometallics
The Journal of Physical Chemistry
ACS Single Article Announcement
Journal of Physical and Chemical Reference Data

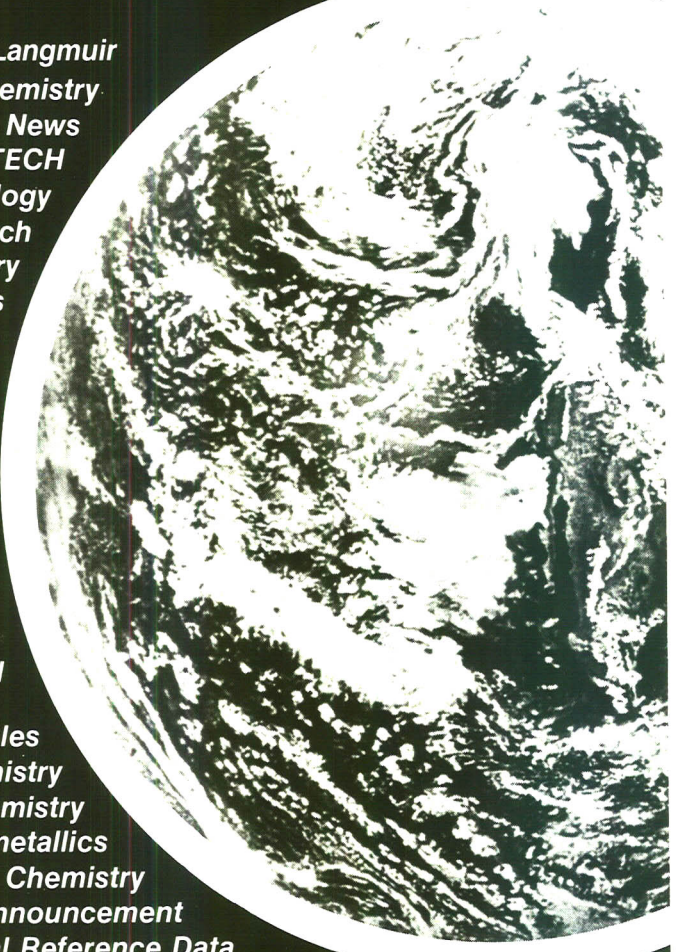

TOLL FREE: U.S. New Orders Only (800) 424-6747
Cable Address: JIECHEM — Telex: 440159 ACSP UI or 892582 ACSPUBS

AMERICAN CHEMICAL SOCIETY PUBLICATIONS
1155 Sixteenth Street, N.W., Washington, D.C. 20036 U.S.A.

We've had lots of bright ideas since you last checked Philips Analytical.

Quite a few of them appear in our new PU 9700 IR Series.

Here is a range of spectrophotometers especially suited to educational and quality control requirements that combine low cost with ease of use and flair.

Just look at what's on offer:

- **Superb ratio recording performance including an ultra-fast 1 minute scan.**
- **Proven reliability with excellent after-sales service for peace of mind.**
- **The opportunity to link to the new Philips Analytical Data Station based on the IBM PC environment.**



PU9700

New low-cost I.R.

IR06

Bigger ideas for better analysis.

Pye Unicam Ltd. York Street, Cambridge CB1 2PX Gt. Britain. Telephone (0223) 358866 Telex 817331

PHILIPS **Scientific and Analytical Equipment**

CIRCLE 83 ON READER SERVICE CARD

PHILIPS

The Reaction is Purely Chemical

Subscribe to these outstanding AMERICAN CHEMICAL SOCIETY publications. Choose from 23 different titles.

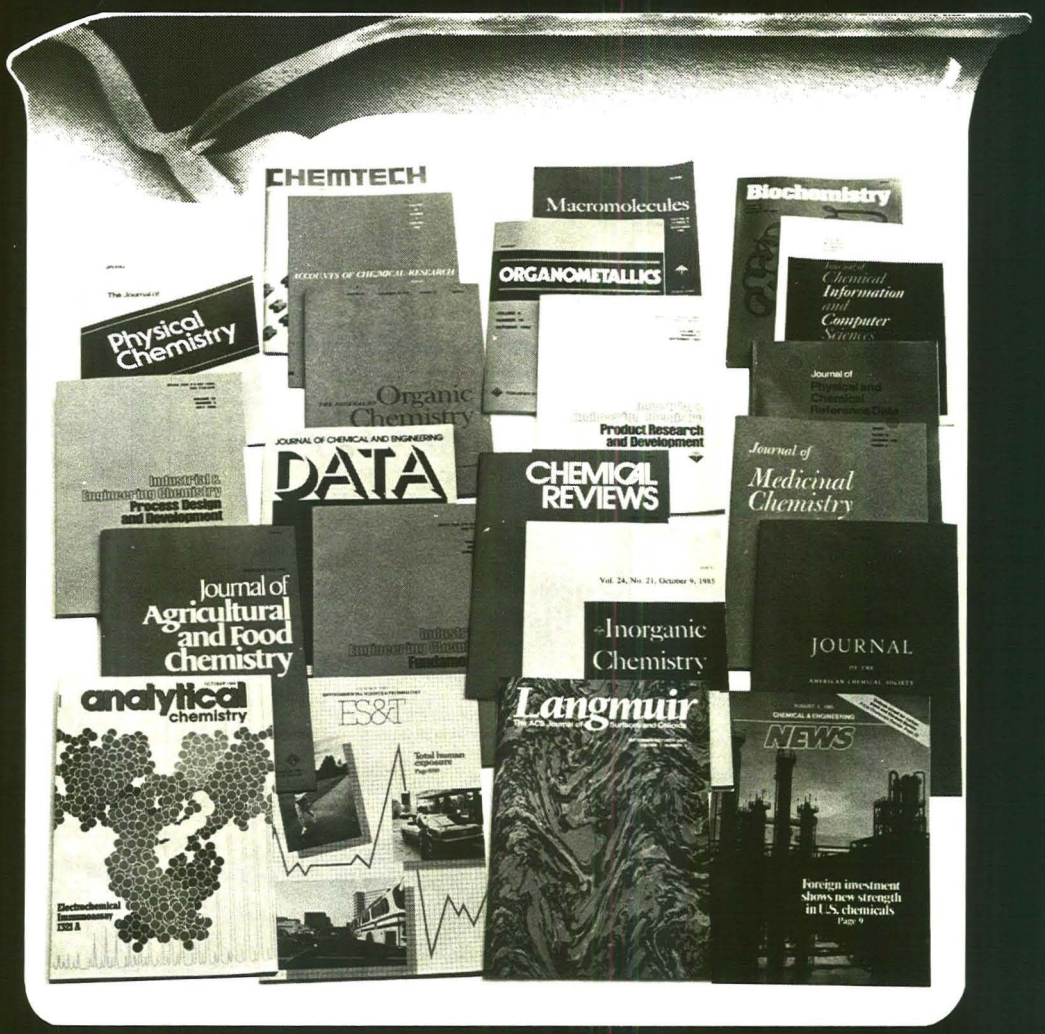

ACS publications are designed for you. They're timely, authoritative, comprehensive. They give you the latest in research, news, and commentary — everything you need to know to keep you on top of every aspect of your professional life.

- Analytical Chemistry
- Chemical & Engineering News
- CHEMTECH
- Environmental Science & Technology
- Accounts of Chemical Research
- Biochemistry
- Chemical Reviews
- Industrial & Engineering Chemistry — Process Design and Development
- Industrial & Engineering Chemistry — Product R&D
- Industrial & Engineering Chemistry — Fundamentals
- Inorganic Chemistry

CALL TOLL FREE 800-424-6747
Cable Address: JIECHEM
Telex: 440159 ACSP UI or 892582 ACSPUBS

AMERICAN CHEMICAL SOCIETY PUBLICATIONS
1155 Sixteenth Street, N.W.
Washington, D.C. 20036 U.S.A.

- Journal of Agricultural & Food Chemistry
- Journal of the American Chemical Society
- Journal of Chemical & Engineering Data
- Journal of Chemical Information and Computer Sciences
- Macromolecules
- Journal of Medicinal Chemistry
- The Journal of Organic Chemistry
- The Journal of Physical Chemistry
- ACS Single Article Announcement
- Journal of Physical and Chemical Reference Data
- Organometallics
- Langmuir

Philips Analytical crossed a squirrel with an elephant.



Combine the infallible memory of an elephant (dual disk-drive) with the storage and retrieval abilities of a squirrel (over 100 spectra per disk) and you have just two of the features of Philips' brilliant new PU 9550 series spectrophotometer. And that's not all PU 9550 has to offer...

- **Superb ratio recording performance including an excellent 1 minute scan.**
- **256K IBM environment computer is a standard item.**
- **Full range of spectral manipulation routines.**

And as well as that it's a real pleasure to use.



PU9550

New disk storage IR

IR07/1

Bigger ideas for better analysis.

Pye Unicam Ltd. York Street, Cambridge CB1 2PX Gt. Britain. Telephone (0223) 358866 Telex 817331

PHILIPS **Scientific and Analytical Equipment**

CIRCLE 82 ON READER SERVICE CARD

PHILIPS

An Invitation to Submit Manuscripts and Subscribe to

Langmuir

The ACS Journal of Surfaces and Colloids

Arthur Adamson, ***Editor***
Arthur Hubbard, ***Associate Editor***



This journal published by the American Chemical Society fills the void existing in current literature available today—*Langmuir's* broad coverage brings together authoritative papers from all aspects of this major field of chemistry!

Scope

Langmuir includes fundamental and applied papers covering ultra-high vacuum surface chemistry and spectroscopy, heterogeneous catalysis, all aspects of interface chemistry involving fluids, and disperse systems.

Specifically, *Langmuir* publishes peer-reviewed research in

- **'Wet' Surface Chemistry**
  surface tension • spread monolayers • wetting and contact angle • adsorption from solution • nucleation • fundamental aspects of flotation, detergency, emulsions, foams, lubrication, etc.
- **'UHV' Surface Chemistry**
  solid surfaces in ultra-high vacuum including surface structure, composition and spectroscopy • and fundamental papers in heterogeneous cataysis
- **Disperse Systems**
  colloidal suspension including aerosols • microemulsions • biological and polymeric colloids and membrane systems
- **Electrochemistry**
  related to interfacial structure and processes

Bimonthly issues of *Langmuir* feature experimental and theroetical original papers, letters to the editor, and book reviews, as well as some selected symposium collections. Papers having applied aspects are included.

The editors of the journal welcome research papers in all areas of surface and colloid chemistry, and are establishing the journal as a unifying influence on research in this field.

Langmuir does not have page charges.

Editorial Advisory Board

N.R. Armstrong, *University of Arizona*
G.T. Barnes, *University of Queensland, AUSTRALIA*
P. Biloen, *University of Pittsburgh*
K.S. Birdi, *Technical University of Denmark, DENMARK*
A.M. Bond, *Deakin University, AUSTRALIA*
B.V. Derjaguin, *Moscow University, USSR*
D.D. Eley, *University of Nottingham, ENGLAND*
G. Ertl, *Technical University of Munich, WEST GERMANY*
J. Fendler, *Syracuse University*
T. Fort, Jr., *California Polytechnic State University*
G. Gaines, Jr., *General Electric Corporate R&D*
W.A. Goddard, III, *California Institute of Technology*
R.S. Hansen, *Iowa State University*
J. Lyklema, *Agricultural University, THE NETHERLANDS*
R.J. Madix, *Stanford University*
J.A. Mann, Jr., *Case Western Reserve University*
P. Mukerjee, *University of Wisconsin*
K.J. Mysels, *Research Consulting*
A.W. Neumann, *University of Toronto, CANADA*
R. Ottewill, *University of Bristol, ENGLAND*
H. Reiss, *University of California at Los Angeles*
H.A. Resing, *Naval Research Laboratory*
T. Rhodin, *Cornell University*
S. Ross, *Rensselaer Polytechnic University*
J. Rouquerol, *Centre de Thermodynamique et de Microcalorimetrie du CNRS, FRANCE*
R.L. Rowell, *University of Massachusetts*
R. Rye, *Sandia National Laboratory*
H. Seki, *IBM*
K. Shinoda, *Yokohama National University, JAPAN*
G.A. Somorjai, *University of California at Berkeley*
W.A. Steele, *Pennsylvania State University*

General Information for Authors

Manuscript instructions are available in "Handbook for Authors of Papers in American Chemical Society Publications" (1978).
Manuscripts should be submitted to either:

Dr. Arthur Adamson, Editor
Department of Chemistry
University of Southern California
Los Angeles, CA 90089

Dr. Arthur T. Hubbard, Associate Editor
Department of Chemistry
University of California at Santa Barbara
Santa Barbara, CA 93106

Subscription Information

Langmuir
Published Bimonthly

American Chemical Society
1155 Sixteenth St., N.W.
Washington, D.C. 20036

One Volume Issued Per Year
Volume 2 1986
ISSN: 0743-7463

1986 Subscription Information

	*Personal	Institutional
U.S.	$55	$329
Canada & Mexico	$64	$338
Europe**	$65	$339
All Other Countries**	$70	$344

*Subscriptions at ACS member rates are for personal use only.
**Includes Air Service

To subscribe, call ***Toll Free (800)-424-6747***

KONTRON INSTRUMENTS

your partner in science and health



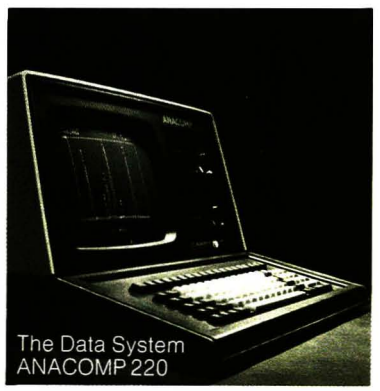

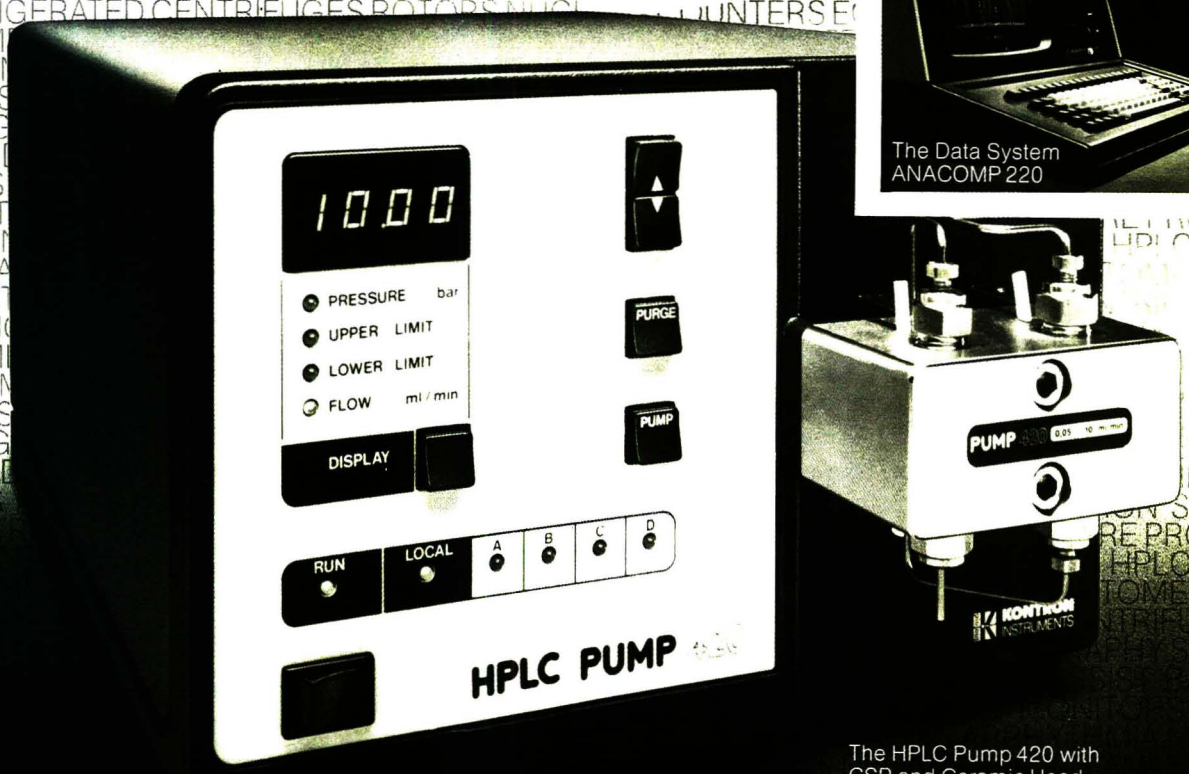

The HPLC Pump 420 with
CSP and Ceramic Head

Your partner in science and health

KONTRON INSTRUMENTS

For further information please contact your local Kontron Company

Austria (Vienna)	(0222) 692531	Japan (Tokyo)	(03) 2634801
France (Montigny le Br.)	(1) 30438152	Scandinavia (Stockholm)	(08) 7567330
West Germany (Munich)	(08165) 6060	Spain (Madrid)	(01) 729 11 55
Great Britain (Watford)	(0923) 45991	Switzerland (Zurich)	(01) 435 41 11
Italy (Milan)	(02) 50721	USA (Everett/Mass.)	(617) 389-6400

International Business Management, KONTRON AG, Bernstrasse Süd 169, 8010 Zurich/Switzerland, Telephone (01) 435 41 11, Telex 822 191

CIRCLE 121 ON READER SERVICE CARD

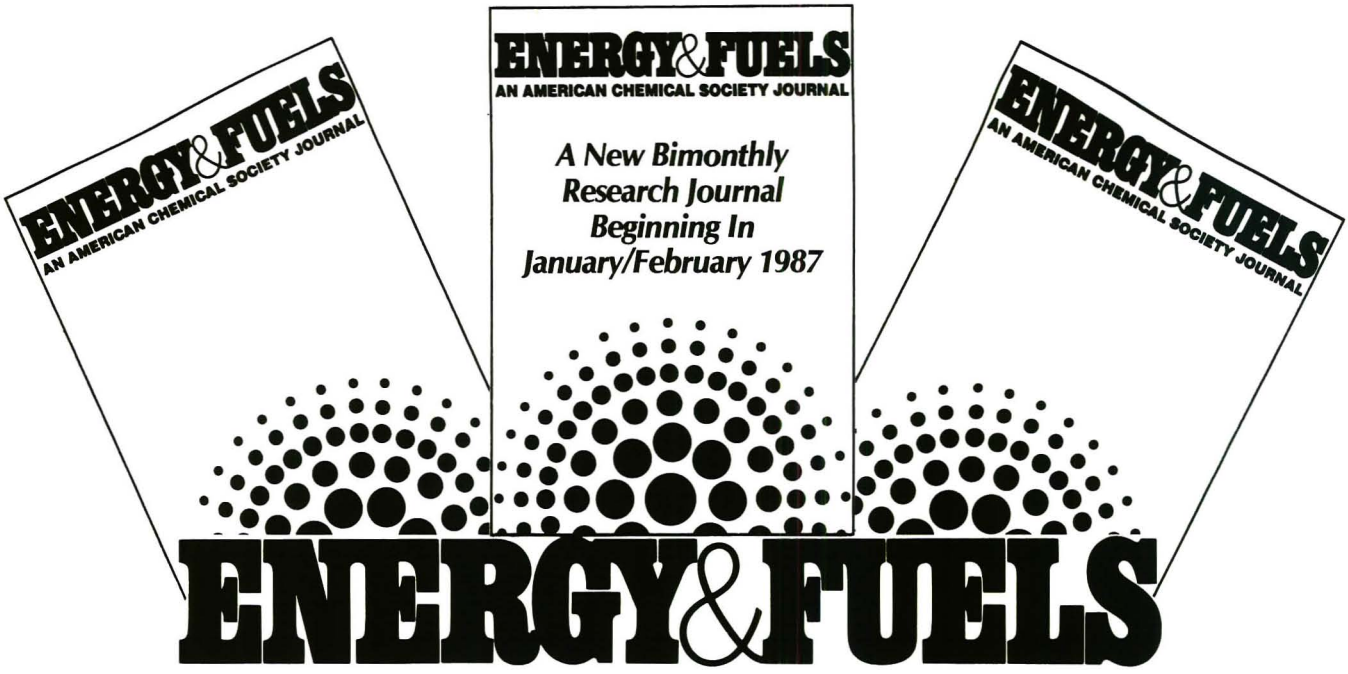

ENERGY&FUELS

AN AMERICAN CHEMICAL SOCIETY JOURNAL

Published Bimonthly Beginning In January/February 1987

Editor: John W. Larsen, Lehigh University
Associate Editor: Thomas R. Hughes, Chevron Research Company

A New Home for Research in the Chemistry of Non-Nuclear Energy Sources

ENERGY & FUELS, the latest ACS Journal, promises a unique and unified treatment of the chemistry of non-nuclear energy sources. The Journal will address a broad spectrum of topics from natural gas through biomass; origin through production; structure and composition through process and utilization; analysis through catalysis. ENERGY & FUELS will publish more than research papers. Communications, book reviews, and invited reviews, complete each bimonthly issue.

Contributing Authors! Look to ENERGY & FUELS for Rapid Publication

The Editors are working toward a timely turnaround of papers—about 6 months from submission to publication, if significant revision is not required. This will assure that ENERGY & FUELS is at the forefront of developments in the field.

Guiding ENERGY & FUELS in Its First Year
1987 Editorial Advisory Board

Tom Aczel, Exxon
M.M. Boduszynski, Chevron
Alan K. Burnham, Lawrence Livermore
Blaine Cecil, U.S.G.S.
Clarence D. Chang, Mobil
Peter Griffiths, Univ. of Calif., Riverside
Csaba Horvath, Yale
Jack Howard, MIT
Leszek Ignasiak, Alberta Research Council
Michael Lewan, Amoco
Ron Liotta, Exxon
Om Mahajan, Amoco
John McKay, Western Research Ctr.
Henk Meuzelaar, Biomaterials Profiling Ctr.
Marvin Poutsma, O.R.N.L.
Y. Sanada, Hokkaido Univ.
John H. Shinn, Chevron
Mike Siskin, Exxon
Leon Stock, Univ. of Chicago
Irving Wender, Univ. of Pittsburgh
D.D. Whitehurst, Mobil

For further information on how to submit your manuscripts write: John Larsen, Editor, ENERGY & FUELS, Department of Chemistry, Lehigh University, Bethlehem, PA 18015. Or call (215) 861-3489.

1987 Subscription Information

1987 Volume 1 (6 Issues Per Year) **ISSN: 0887-0624** **CODEN: ENFUEM**

	U.S.	Canada & Mexico	Europe Air Service Included	All Other Countries Air Service Included
*ACS Members	$ 46.00	$ 56.00	$ 57.00	$ 63.00
Nonmembers	242.00	252.00	253.00	259.00
(Special nonmember price for orders received before 12/31/86)				
Nonmembers (After 1/1/87)	269.00	279.00	280.00	286.00

*Member rates are for personal use only.
Foreign payment must be made in U.S. Currency, by international money order, UNESCO coupons, U.S. bank draft, or order through your subscription agent.
Above rates do not apply in Japan. Contact Maruzen Co., Ltd.
Call Toll Free (800) 424-6747 or write American Chemical Society, 1155 16th St. N.W., Washington DC 20036.

Our line-splitting ICP breaks all the rules

How can the new PU 7450 offer high-resolution bench-top ICP, when a conventional spectrometer needs a focal length in excess of a metre? To cut a long story short, it breaks the rules.

Instead of a conventional spectrometer the PU 7450 has an echelle grating monochromator which provides the line-splitting resolution so important for critical applications in such fields as geology and metallurgy. Yet it also allows the instrument to become a bench-top reality.

Accurate results are achieved with fixed optics and a moving on-peak detection system using stored computer co-ordinates for speed and reliability.

With the addition of sequential ICP, Philips now offers total capability in elemental analysis. So find out how well we fit into your laboratory by contacting us for more details today.

Pye Unicam Ltd,
York Street, Cambridge
Great Britain CB1 2PX
Tel (0223) 358866 Telex 817331

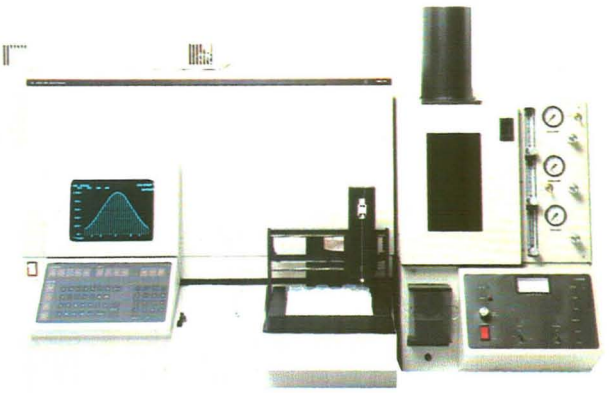

The new Philips PU 7450 – more nanometres from fewer centimetres

PHILIPS Scientific & Analytical Equipment

PHILIPS

CIRCLE 81 ON READER SERVICE CARD

AA14

DURAN® Why settle for less?

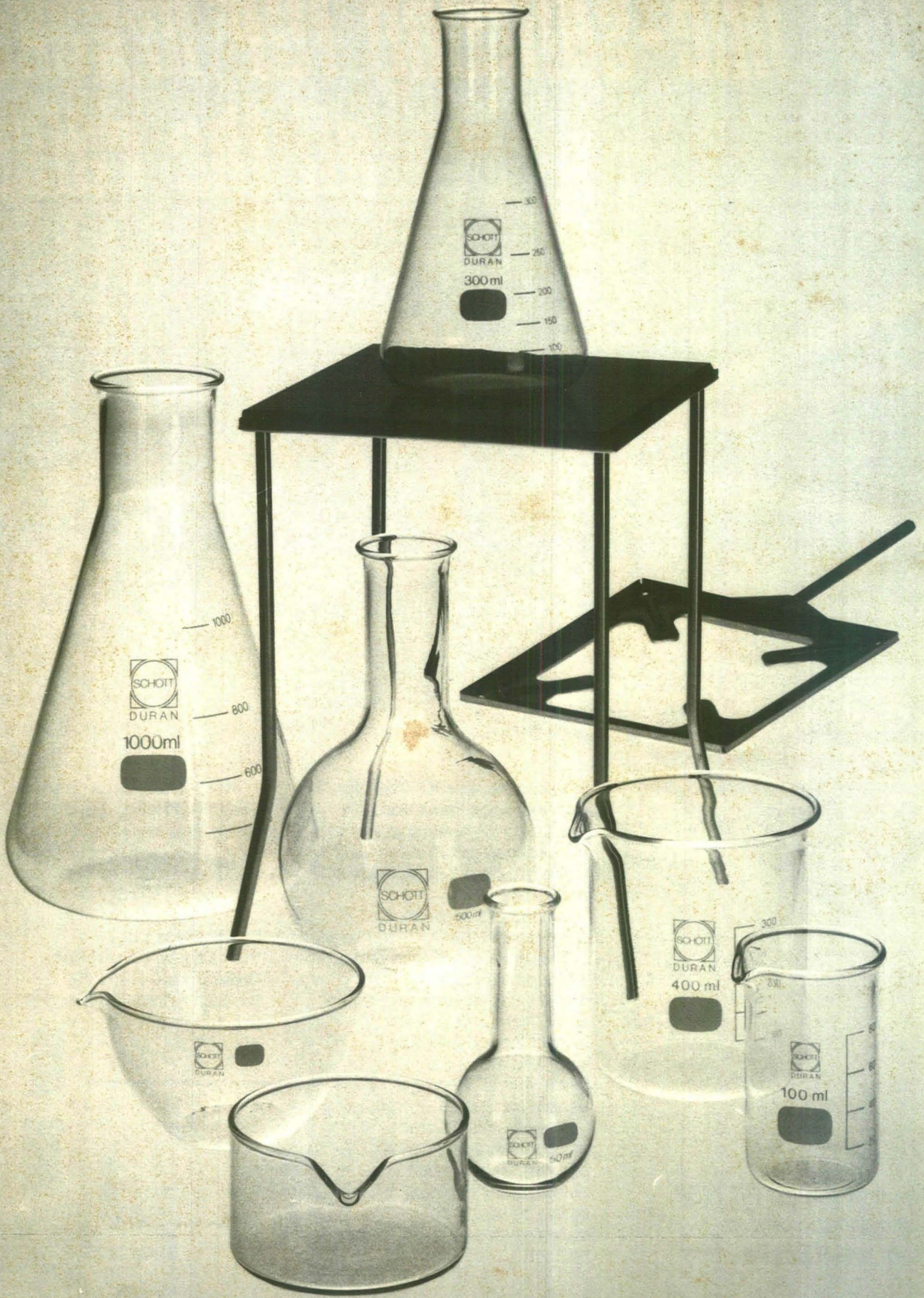

SCHOTT SCHOTT

DURAN® laboratory glassware is available through leading laboratory suppliers.

SCHOTT GLASWERKE, Chemical Division
Laboratory Glassware Product Group, D-6500 Mainz (West Germany)
Hattenbergstr. 10, Tel. (0 61 31) 6 60, Telex 41 879 230 smd

Circle Reader Service Card No. 189

SCHOTT GROUP

516/84e

Don't let tough samples interfere with your AA results.

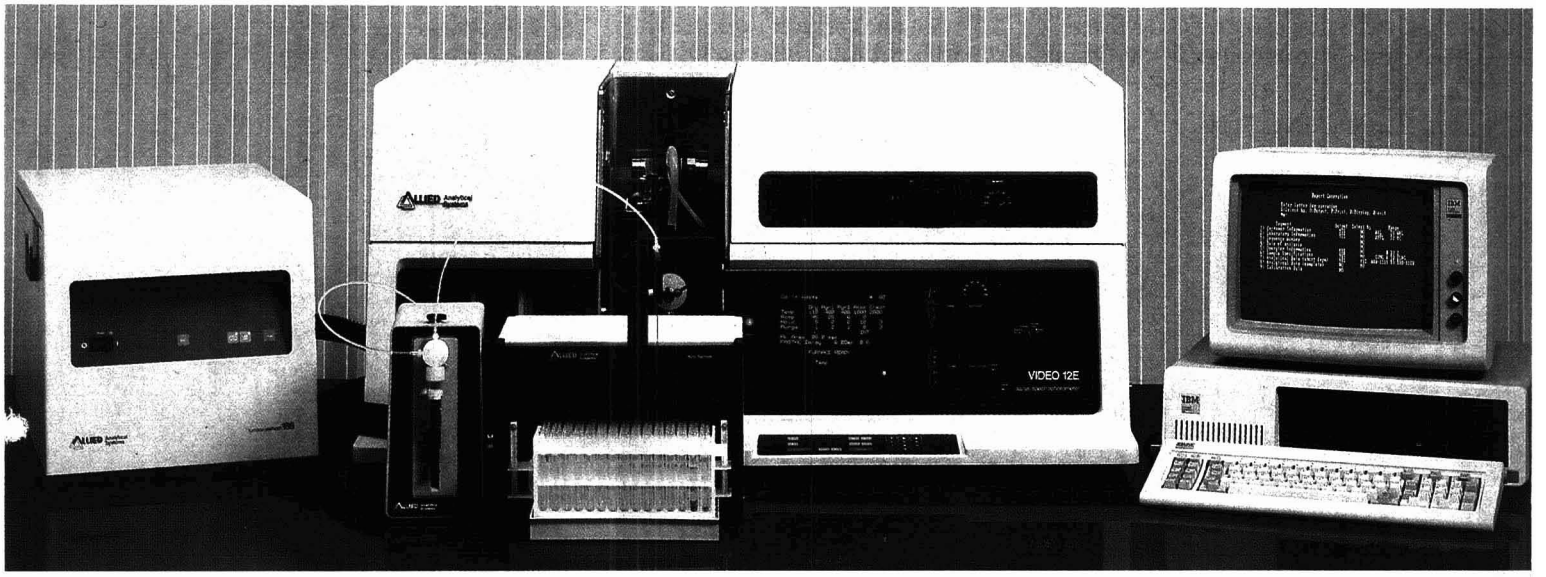

See our new Video™ E/CTF™ 188 Flame/Furnace AA Spectrophotometer System.

We've developed an analytical instrument for the most demanding applications. For samples which present serious matrix problems. And for laboratories where even novice users handle large volumes of samples.

It's our Video E/CTF 188 Furnace/Flame AA Spectrophotometer System. And it consists of:

- a single or double beam AA spectrophotometer
- the new fully automatic CTF 188 Furnace Atomizer
- an autosampler with a sample preparation accessory and
- the ADS-200™ Data Station (IBM PC/XT) with dot matrix printer.

Here's a small sampling of what our new AA system offers to the serious user.

No Background Interference

The Smith-Heiftje technique gives accurate corrections for structured background at any wavelength.

No Vapor Phase Interferences

Our Delayed Atomization Cuvette (DAC) virtually eliminates vapor phase interferences by atomizing into a hotter temperature environment.

No Solid Phase Interferences

The patented FASTAC® aerosol sampling device minimizes crystal occlusion of analytes by applying a fine aerosol of the sample to the cuvette surface instead of a large droplet.

Reproducible Pyrolysis And Atomization

Exact temperature control through direct feedback from the InAs optical sensor eliminates variability in the furnace temperature and in the results.

Easy To Use

Method development and storage, run initiation, display and printing of results are completely menu-driven, and can be learned, easily, by a non-technical operator.

Add the Autosampler with its sample preparation accessory, and up to 80 samples can be prepared and run unattended.

Add the ADS-200 Data Station (IBM PC/XT) to provide a powerful, versatile desktop data system for laboratory data storage and analysis.

For an appointment to see our new AA in operation or to get literature, call (800) 225-8711 (in Massachusetts, call (617) 890-4300). Or write Allied Analytical Systems, 590 Lincoln Street, Waltham, MA 02254.

CIRCLE 5 ON READER SERVICE CARD

ALLIED Analytical Systems

Have you ever had an idea that could change the world, only to have someone else beat you to it? After months of painstaking research, there's nothing more frustrating than reinventing the wheel. Again.

DIALOG® is the online information system that can give you a flying head start on your competition. Dialog goes right to the source, with 10 to 15 years of data on every subject, from aerospace to zoology. Even if you're in a specialized area of research, you never know when you'll need something from another field. With Dialog, it's all available instantly.

Anyone can learn to use Dialog, too. In fact, Dialog is so useful if it didn't already exist, you'd just have to invent it.

To find out about Dialog now, call 800-3-DIALOG. Or write: Dialog, Dept. 30, 3460 Hillview Ave., Palo Alto, CA 94304.

DIALOG® *Find out about it.*

A subsidiary of Lockheed Corp.

©Dialog Information Services, Inc. 1985

Guess who didn't use Dialog.



CIRCLE 43 ON READER SERVICE CARD

CALL 800-3-DIALOG TODAY.

Andrew T. Zander

Perkin-Elmer Corporation
North American Instrument Division
761 Main Ave.
Norwalk, Conn. 06859-0905

Atomic Emission Sources for Solution Spectrochemistry

Atomic emission spectrometry (AES) is used for elemental determinations in a variety of sample types. Solution samples, or solid samples that have been prepared for analysis as solutions, comprise a significant portion of the analytical demand met by AES. A solution sample presents a more homogeneous matrix for the elements being sought. As a result, it is somewhat easier to prepare standards, and fewer different standards are required. Consequently, a substantial amount of effort has been expended on the development of spectrometric instrumentation that preferentially uses solution sample input.

There are many components and subsystems in a modern atomic spectrochemical analysis system. All of their performances have been improved markedly with recent technical advances. "Holographically" produced diffraction gratings and the increased use of high-capability, low-cost microprocessors are key examples. The single most important development in atomic spectrochemical equipment in the past 10 to 15 years, however, has been the development of the inert gas, electrical discharge plasma excitation source. Unlike other electrical discharges that have been optimized principally for solid or powdered samples, the inert gas plasma has been developed specifically for solution sample types. In this regard it is a replacement for the flame excitation source. Besides being a replacement, the inert gas plasma has performance advantages so significant that it has rejuvenated the atomic spectrochemical instrumentation market. The market growth for plasma emission instrumentation far exceeds that of any other type of atomic analysis equipment

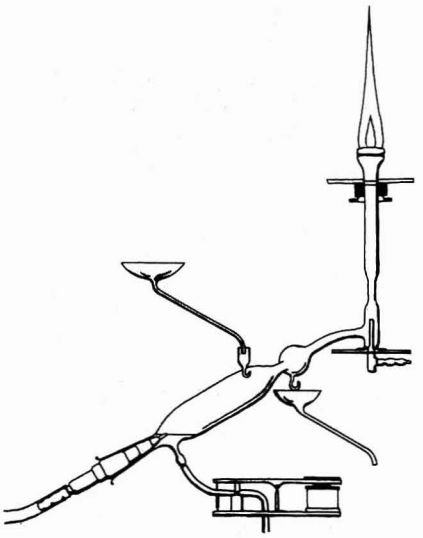

and is expected to continue to do so for a number of years.

The inert gas electrical discharge plasma, commonly using argon, comes in a few different configurations. In order of market preference and associated research activity, the principal versions are the inductively coupled plasma (ICP), the direct current plasma (DCP), and the microwave-induced plasma (MIP). Other excitation sources are popular for AES, of course. None, however, have received the market acceptance of the ICP and DCP or the level of research activity of the MIP. Or they may be principally associated with analysis of solid samples, such as the Grimm discharge or the hollow-cathode discharge devices. It is evident that, at least for the short term, no other device will be able to compete successfully for the interest garnered by the more popular and more prevalent plasmas.

The following is a comparison, sometimes somewhat subjective, of the ICP, the DCP, and the MIP. However, it is less a comparison of performance figures of merit, which can be found in any number of review articles, than an identification of the ways in which the devices are similar and dissimilar. In that regard, this comparison should shed light on the relative "usefulness" of the devices, and their consequent commercial acceptance. On the basis of commercial acceptance, it might be argued that the MIP does not belong in the comparison. It has held and still does hold, however, a prominent position of interest within the atomic analysis research community, certainly far greater than for the DCP, and is included for that reason.

Table I presents a list of device characteristics and operational parameters for the DCP, ICP, and MIP. With this information as a basis, we can compare and contrast the analytically relevant features of these plasmas.

Operating parameters

Operating frequency. The DCP operates at dc and the inductive plasmas operate at radio or microwave frequencies. Direct current power supplies of comparable output power to ac supplies are smaller, may have fewer components, and are generally less expensive (for equivalently stable output power).

The ICP and MIP do not operate at arbitrary frequencies. The Federal Communications Commission has regulated the use of the electromagnetic spectrum to well above 30 GHz (a wavelength of about 1000 μm). Certain narrow bands have been set aside for industrial, scientific, and medical (ISM) uses. The ICP typically operates at 27.12 MHz or 40.68 MHz. The

0003-2700/86/A358-1139$01.50/0
© 1986 American Chemical Society

Table I. Component identification and comparison

Parameter	Direct-current plasma (DCP)	Inductively coupled plasma (ICP)	Microwave-induced plasma (MIP)
Operating frequency	dc	27.12 MHz, 40.68 MHz (ISM)	915 MHz, 2450 MHz (ISM)
Discharge structure	Multiple electrode set Anodes: Pyrolytic graphite Cathodes: Thoriated tungsten Cooled by carrier gas	RF coil and ceramic torch Coil: Protected copper Cooled by water Torch: Quartz or ceramic, carrier-gas-cooled	Microwave structure and torch Structure: Protected copper Cooled by gas or water Torch: Quartz or alumina, carrier-gas-cooled
Discharge type	Flowing, thermally pinched, transferred dc arc plume	Flowing, electrodeless discharge plume	Flowing, electrodeless discharge
Carrier gas	Argon, 99.995% or better	Argon, 99.995% or better	Helium, 99.9995% or better Argon, 99.995% or better
Gas consumption (total)	About 10 L/min	10 to 20 L/min	0.05 to 1.5 L/min
Operating pressure	Atmospheric (1.013 kPa)	Atmospheric (1.013 kPa)	Moderate vacuum to atmospheric (0.133–1.013 kPa)
Power required	110 V, 60 Hz, single phase, 20 A	220 V, 60 Hz, single phase, 25–30 A	110 V, 60 Hz, single phase, 15 A
Applied power	0.5–0.75 kW	0.5–2.5 kW	0.02–0.5 kW
Generated plasma volume	0.2–0.3 cm^3	3–4 cm^3	0.07–0.18 cm^3
Power density (power input zone only)	0.93–2.5 kW/cm^3	0.13–0.63 kW/cm^3	0.11–2.8 kW/cm^3
Viewing zone size	About 8 mm^2	20–60 mm^2	0.8–7 mm^2
Gas temperature	4000–6000 K stratified	4000–6000 K stratified	Possibly as high as 3000 K
Electron density (N_e)	10^{14}–10^{15} cm^{-3}	10^{14}–10^{15} cm^{-3}	10^{14} cm^{-3}

MIP typically operates at 2450 MHz, the frequency of microwave ovens; 915 MHz is not as popularly used.

Table II lists the ISM frequencies and their bandwidths. The 461-MHz band is not consistently listed on all charts as an ISM frequency. What should be noted is the very narrow width of the allowed band across the center frequencies. The impact of this is that equipment designed for operation at these frequencies is complex because of the stringent requirements for radio frequency (rf) shielding of the generators. Shielding requirements are much less severe at microwave frequencies, where even a few sheets of aluminum foil are generally sufficient to minimize extraneous radiation surrounding a plasma device. Shielding at lower rf is very difficult to implement properly.

Discharge structure. The mechanical configuration that contains or supports the plasmas is quite different for each of the discharges. The DCP (Figure 1) uses a multiple electrode set: two pyrolytic graphite anodes and one thoriated tungsten cathode. It should be noted that the three-electrode DCP has four electrical poles: two anodes and two cathodes. It uses two power supplies. The single cathode connects to the negative pole of both power supplies. Each electrode is efficiently cooled by flowing argon. The electrode set tends to lock the generated plasma volume in position, which provides much of the stability

Table II. ISM frequencies and bandwidths

Frequency (MHz)	Bandwidth limit	
	Frequency (MHz)	%
13.56	±0.07	±0.05
27.12	±0.16	±0.6
40.68	±0.02	±0.05
461.04	±0.92	±0.2
915	±13	±1.4
2450	±50	±2.0
5800	±75	±1.3
24125	±125	±0.5

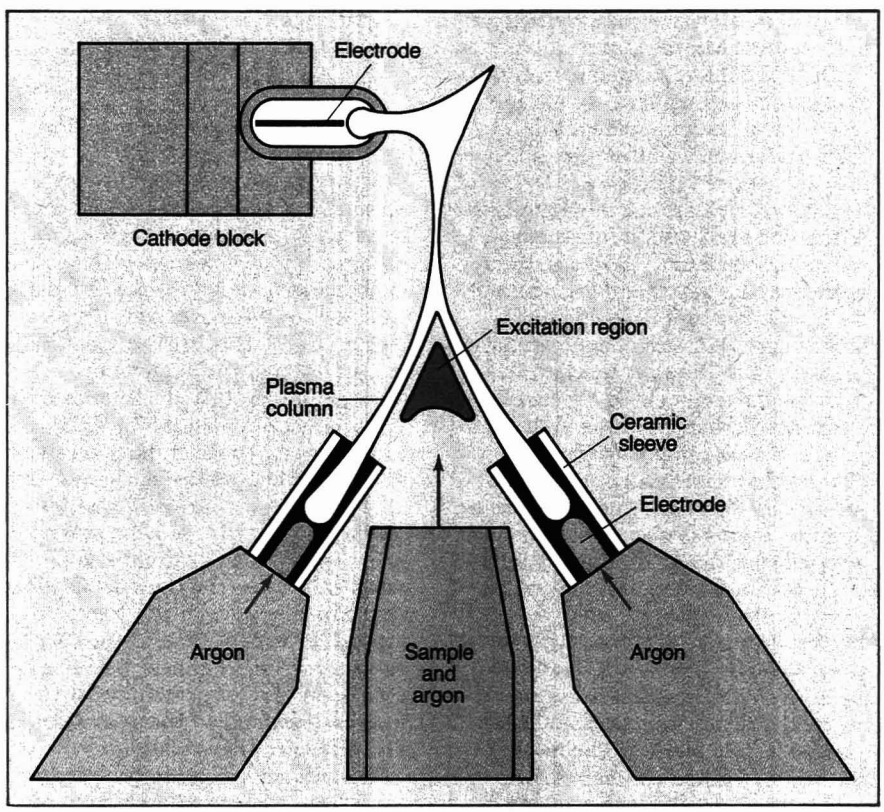

Figure 1. Schematic diagram of a three-electrode DCP

Linking Value to Performance.

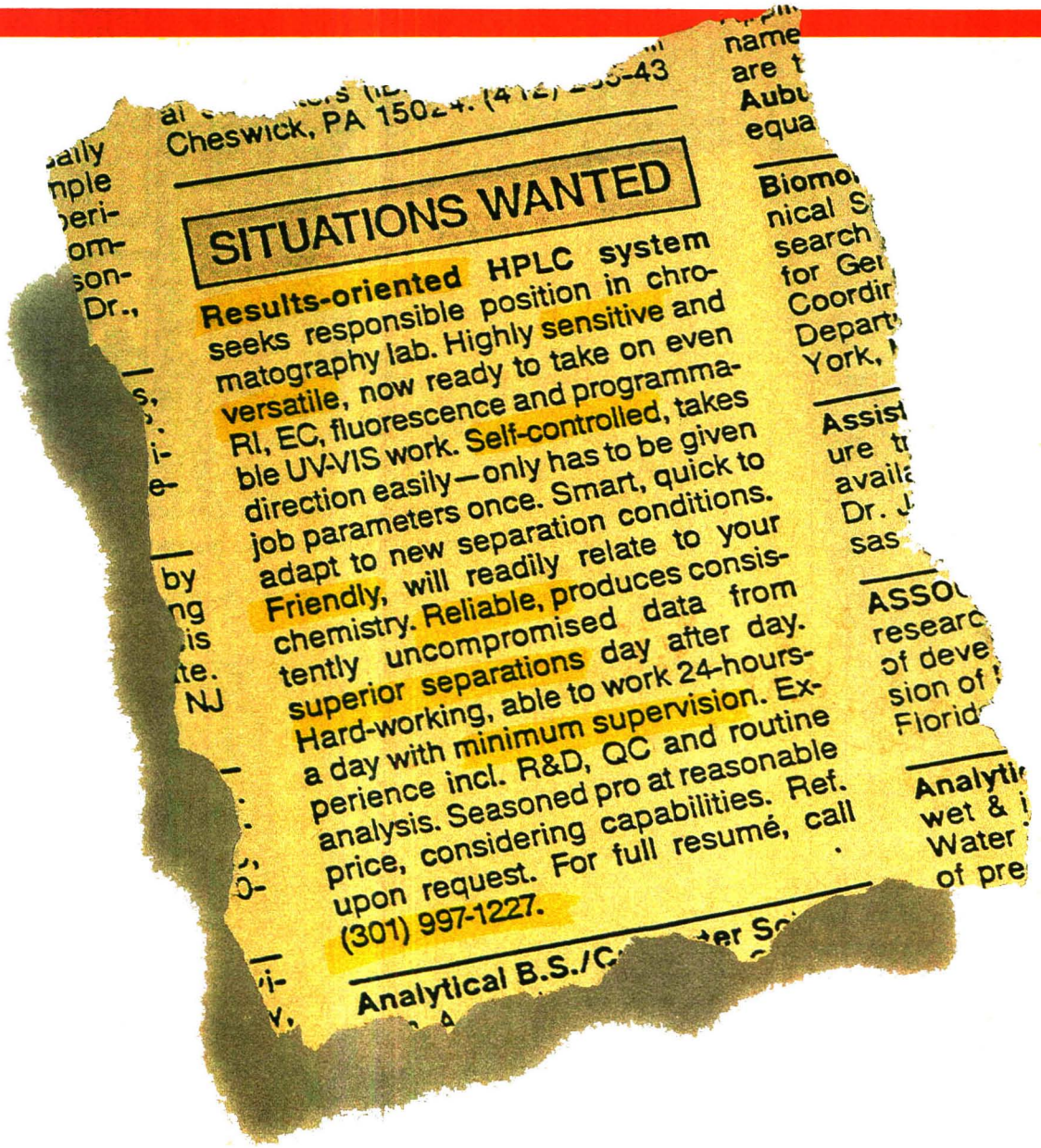

The LC-6A HPLC from Shimadzu: give it a job in your lab and watch the results.



Call or write today for a full resumé on the LC-6A modular HPLC system with its new RI, EC, and fluorescence detectors as well as post column reaction ovens.

Shimadzu Scientific Instruments, Inc.,
7102 Riverwood Drive, Columbia, MD 21046,
(301) 997-1227

SHIMADZU

Shimadzu Corporation International Marketing Div.: Shinjuku-Mitsui Building, 1-1, Nishishinjuku 2-chome, Shinjuku-ku, Tokyo 160, Japan. Tel: Tokyo 03-346-5641 Telex: 0232-3291 SHMDT J.
Shimadzu (Europa) GmbH: Acker Strasse 111, 4000 Düsseldorf, F.R. Germany. Tel: (0211) 666371 Telex: 08586839

Circle 187 for literature. Circle 188 to have a representative call.

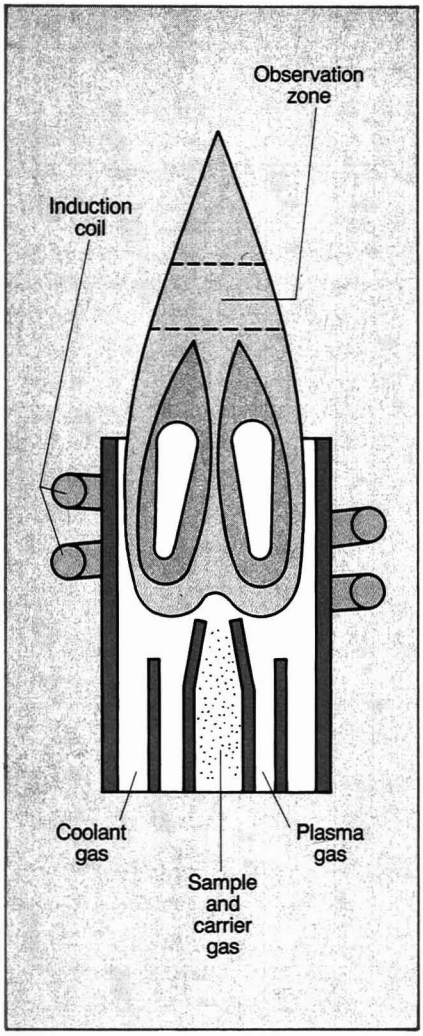

Figure 2. Schematic diagram of an argon ICP

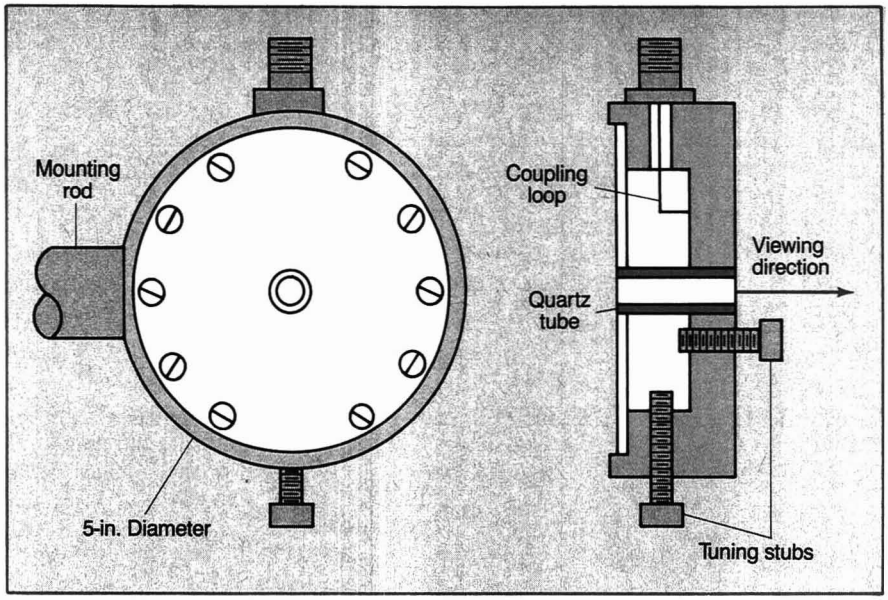

Figure 3. Schematic diagram of a 2450-MHz TM_{010} resonant MIP cavity (the Beenakker cavity)
A face view is shown at the left, a cross-sectional side view at the right

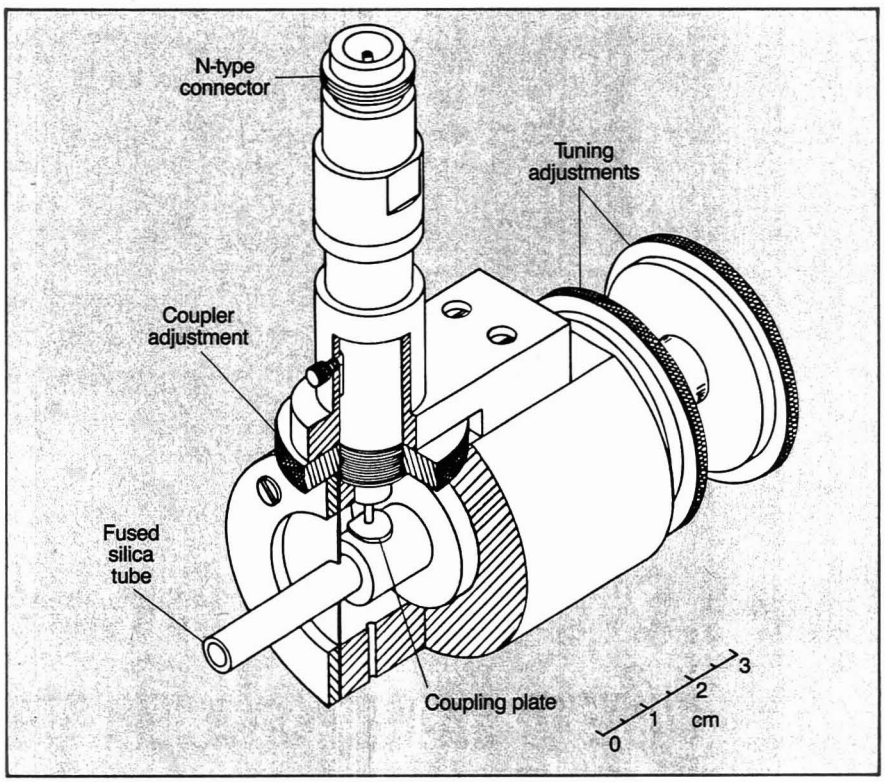

Figure 4. Schematic diagram of a microwave surface wave launcher (the "surfatron")

of the generated signals.

The rf ICP uses a radio frequency coil antenna surrounding a ceramic, flow-controlling torch (Figure 2). Usually, the coil is made of copper, is protected from oxidation and corrosion in some manner, and is water-cooled. The torch, generally a concentric arrangement of quartz tubes, is efficiently cooled by flowing argon. The pneumatic arrangement tends to hold the generated plasma volume in position, but not nearly as well as a set of electrodes does. The trade-off, of course, is that there is no electrode material present in the ICP discharge. This cannot be considered very much of an advantage, though, since the electrode material present in the DCP is carbon. The amount of carbon that can be found in a DCP discharge is so small that it has virtually no influence on the background structure. Carbon is quantitated so poorly by plasma AES of any sort that it is rarely considered an analyte.

The MIP uses some form of short circuit or open circuit for transmission of microwave radiation, or it uses a device to confine the microwave field. The resonant cavity, Figure 3, or electromagnetic field launcher, Figure 4, can be made of anything having a sufficiently shallow skin depth at the operating frequency. Pure copper works well but is hard to machine. Brass and aluminum work best if they are silver-coated. Gold flashing helps significantly. The microwave structure can be gas- or water-cooled, depending on the applied power. Usually water cooling is needed above 200–300 W. The MIP is contained in a quartz or ceramic tube, which is cooled by the flowing carrier gas. Concentric tube torches and devices to swirl the carrier gas are used quite successfully.

Obviously, the hardware requirements for each of the plasmas are markedly different. It is not possible to switch between plasma types in the same way that it is possible to switch flame types on the same burner system.

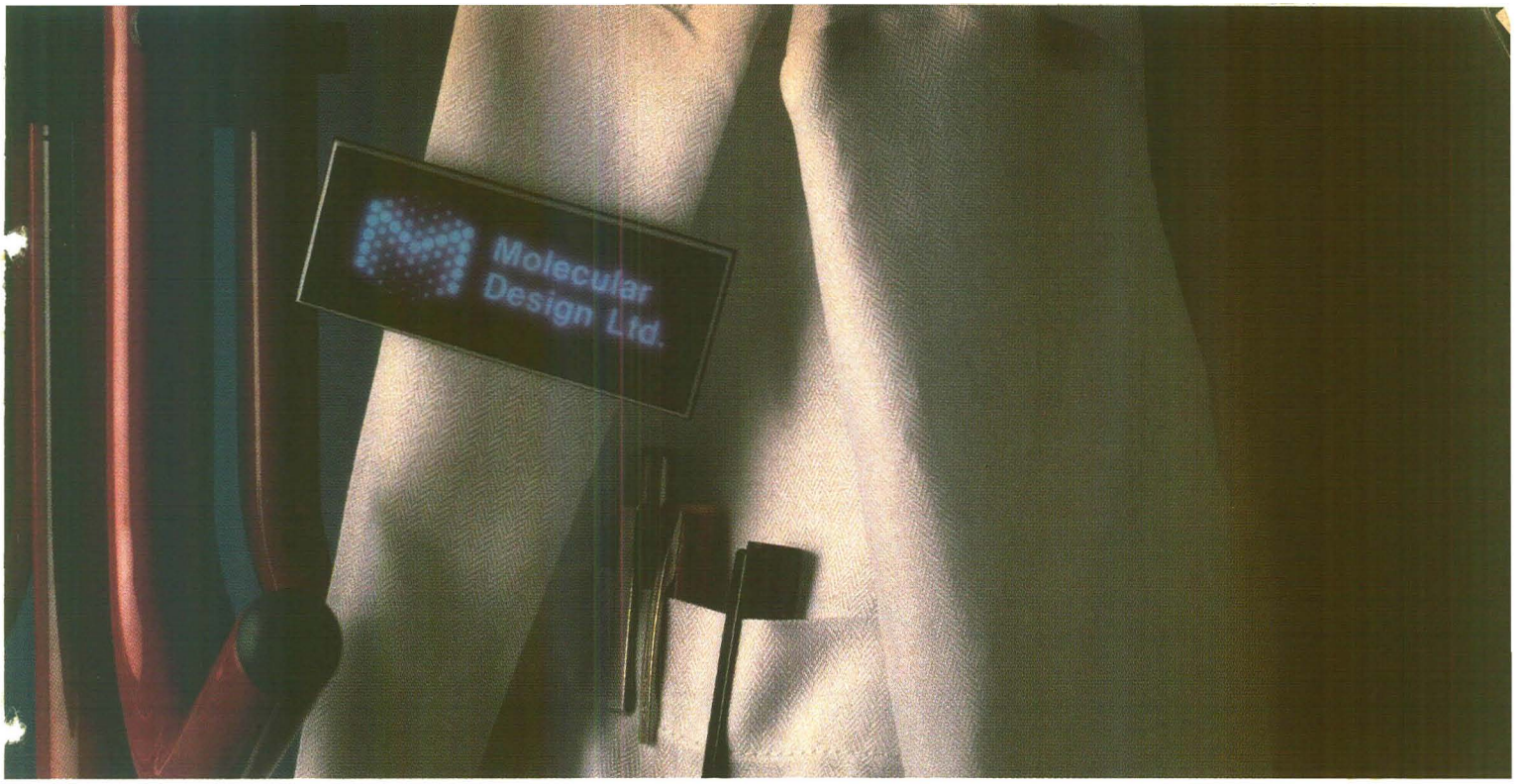

HIRE A LAB ASSISTANT WITH 728 YEARS OF EXPERIENCE.

ChemBase.™ The personal database manager for chemists. Created by a team of chemists who, collectively, represent over 728 years of lab experience.

Chemists who realize that a chemist's place is in the lab. Not hunting through files.

That's why ChemBase works the way you think. Graphically. With structures.

Let's say you need to find a specific group of related compounds. Normally that might take hours searching through files and notebooks. But ChemBase can store all that data on any of the IBM family of personal computers.

And it understands chemistry. Bonds. All 103 elements. Isotopes. Valence. Even reaction transformations. In seconds, it races through your data. Recognizes what you want. And displays the results. In customized forms and tables.

And ChemBase is just one of our family of chemistry software tools. Used by thousands of chemists worldwide. Making us the leading supplier of chemistry software.

For details about ChemBase, write or call Molecular Design Limited, 2132 Farallon Drive, San Leandro, CA 94577, (415) 895-1313.

Because every chemist needs experienced help around the lab.

Molecular Design Ltd

IBM is a registered trademark of International Business Machines Corporation

CIRCLE 138 ON READER SERVICE CARD

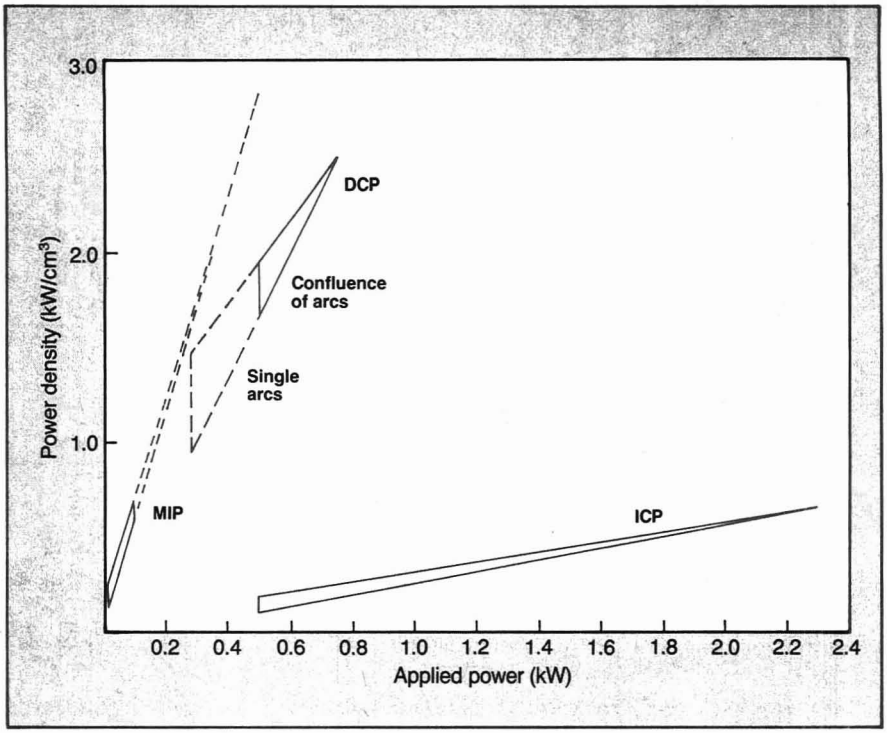

Figure 5. Power density in the generated plasma volume of different analytical plasmas

Carrier gas requirements. Each device is continually regenerated because of its flowing character. Consequently, memory effects from prior samples are negligible. The argon carrier gas for the DCP and ICP should be at least 99.995% pure. When funding allows, liquid argon is recommended as the reservoir. The tank boil-off is used, resulting in effectively purer argon. The MIP typically uses argon, but newer cavities and launchers allow atmospheric pressure operation with helium. Quite high-purity He is required due to the high excitation capabilities of the He MIP, which makes impurity spectra quite intense.

The DCP uses nearly 10 L/min of argon, with the bulk of that going to the single type of nebulizer developed for it. Most ICPs use between 10–20 L/min of argon, with the bulk of that going to the gas that cools the quartz torch. Newer low-flow versions use as little as 5 L/min. The same gas also supplies the fireball, but it is directed first to provide primary cooling. The MIP uses very little carrier gas, 50 mL/min to a few liters per minute. It goes predominantly to the discharge. The more popular versions of MIP use more expensive helium, which greatly offsets its reduced gas consumption.

Power requirements. External service to the plasma generators is most similar for the DCP and MIP. Standard 110–120-V, 20-A power is sufficient. Quite frequently, the stability of this supply is inadequate. It is always wise to use a power regulator between the plasma line and the power source. The ICP requires more power capacity since it generally uses more power: 220-V, 20–30-A, single-phase service is typical.

The generation of a DCP within a 3-electrode set requires two 7-A arcs at 40–50 V. Consequently, about 0.75 kW (max.) can be applied to the discharge. The ICP is generated from about 2.5 kW or less radiated power at a coil antenna. Rf current and voltage are rarely monitored by the operator. The MIP is generated from a few watts to a few hundred watts of radiated power within a confinement structure. Microwave current and voltage also are not monitored.

Power density. The power density in the volume of power input (the generated plasma volume) is quite different for each discharge. This can be seen more clearly in Figure 5. It is apparent that the larger the generated plasma volume, the lower will be the power density at a particular power level. The low levels for the ICP are the result of the large size of the fireball. Note that there are no regions of power density overlap among these plasmas. That is, each plasma source has its own characteristic range of *useful power.*

More important, the rate of change of power density with applied power is quite different for each plasma. For the MIP, there is a very steep rate of change of power density with applied power. This can partially account for both the poorer signal precision obtained from the MIP and the large fluctuation of background signal upon sample introduction. Sample injection into the MIP, at all but the very lowest injection rates, causes an alteration of the power transfer efficiency to the plasma and consequent power density fluctuations. As a result, sample introduction into an MIP with retention of power stability, and thereby, signal stability, is quite difficult. Even with MIPs operated at relatively high power, the small size of the plasma and the viewing of the plasma itself make sample introduction a complicated task.

The DCP has a larger generated plasma volume, the confines of which are mostly controlled by laminar-flowing hot argon. The device, though, is *current controlled*, not power controlled. Consequently, the power density can fluctuate if the resistance of the material in the electrical gap changes measurably. High concentrations of easily ionized matrix elements, for example, can alter the ohmic heating zones of the discharge. The resultant swelling of the generated plasma volume results in reduced power density; the consequent temperature drop of the discharge under these conditions has been verified. This sensitivity of the power density does not directly lead to reduced signal stability, though, since the viewing zone of the DCP is the plume exhaust of the thermally pinched arcs, not the arcs themselves. But some disturbance to the signal can occur, since the temperature and electron density gradients defining the plume are altered.

The ICP has a relatively constant power density over its typical operating range. This is very much the result of the large size of the ICP, in which power or volume fluctuations that would be significant in the smaller MIP or DCP cause very little alteration of the ICP power density. That is, the useful power in the ICP is very nearly always the same. The exhaust plume used for observation will be even less affected. This can partially account for the exceptional short-, medium-, and long-term precision seen with ICPs.

Viewing zone size. A result of the size of the generated plasma volume is the size of the viewing zone for spectroanalytical observation. The DCP viewing zone is a volume confined between two pinched arcs. The cross-sectional area imaged on the spectrometer slit block containing the most useful emission is about 8 mm^2. In the ICP, analyte emission can be viewed in a tall, narrow region above the load coil. The total viewing zone is tens of square millimeters. The MIP discharge itself is used for analyte emission viewing. The containment tubes are 1 mm to 3 or 4 mm in diameter, leading to a very small total viewing zone. Unfortunately, the discharge is often heterogeneously distributed

Optimal Moisture Measurement System



CA-05 Moisture Meter
VA-05 Water Vaporizer

Accuracy, cost-efficiency and application versatility from MCI.

Our CA-05 Moisture Meter/VA-05 Water Vaporizer system delivers advanced fully automatic performance. Microprocessor control assures exceptional speed, accuracy and operational ease with coulometric Karl Fischer titration. Applications range from plastics, oils and chemicals to diverse other samples. Features include an airtight titration cell, 16-digit display, built-in printer and automatic calendar.

The KF-05 Karl Fischer Titrator is another high accuracy, fully automatic choice from MCI. Contact your nearest MCI dealer for details.



KF-05 Karl Fischer Titrator

MITSUBISHI CHEMICAL INDUSTRIES LIMITED

Instruments Dept., Mitsubishi Bldg., 5-2, Marunouchi 2-chome, Chiyoda-ku, Tokyo 100, Japan.
Tel: (03) 455-4220. Telex: MCIINS J34480. Cable Address: MBISHICHEMICAL TOKYO.

☐ **North America** **U.S.A.** COSA Instrument Corp. (201) 767 6600. **Canada** Mandel Scientific Co., Ltd. (519) 856 9566.

☐ **Europe** **U.K.** Anachem Ltd. 0582-456666. **Germany** ABIMED (0211) 21 80 04. **France** SIDERCOM 572 44 00. **Netherlands** Charles Goffin 03408-87717. **Belgium** Ankersmit (02) 374 91 10. **Ireland** AGB Scientific Ltd. 309533. **Denmark** CLAUS KETTEL (02) 98 44 11. **Switzerland** Synmedic AG (01) 463 69 90. **Spain** Comercial Rafer 976 237400. **Norway** Houm & Co. (02) 15 92 50. **Finland** PPM-systems Oy 90-803 7588.

☐ **Asia & Oceania** **India** Toshniwal Brothers Private Ltd. 446 448. **Korea** Sam Jin Commercial Co., Ltd. 778-3151. **Singapore** SPECTRUM Supplies & Services 265 7766. **Taiwan** PAN-YA Instrument Co., Ltd. 07-241-6003. **Australia** FSE Scientific (02) 745 3377.

CIRCLE 137 ON READER SERVICE CARD

across the viewed area, making the useful viewed area quite a bit smaller still.

Gas temperature. One of the leading features of inert gas electrical discharges for atomic emission is their high thermal temperatures. That is, they are convenient means to obtain much hotter reservoirs of hot gas than combustion flames, furnaces, arcs, and sparks. Comparisons would be much simpler if they were truly thermal sources in equilibrium, but they are not. Accurate gas temperatures of the ICP, DCP, and MIP are not available. The ICP and DCP have almost equivalent kinetic temperatures, with the MIP generally accepted to be thermally cooler.

A temperature comparison at best can only tell whether progress over earlier excitation sources for AES has been achieved. This is easily seen if inert gas electrical discharges alleviate most of the classical chemical interferences in emission analyses and provide more intense analyte emission. Both of these features have been documented extensively, and so it can be assumed they are "hotter" than previous emission sources.

Electron density. Inert gas discharges in thermodynamic equilibrium will have electron densities on the order of 10^{16} cm^{-3} or above. The electron density of the plasmas and their N_e gradients can provide some insight into the excitation mechanisms dominant in them.

The DCP and ICP only barely approach the level of N_e associated with equilibrium discharges. In some limited instances, LTE (local thermodynamic equilibrium) might be invoked; but, in general, the DCP and ICP cannot be assumed to be equilibrium discharges. As a result, clear, uncomplicated models of their fundamental operation leading to analyte excitation will be developed only slowly, if at all.

The MIP exhibits electron density characteristics that definitely place it in the nonequilibrium discharge category. Only for low-pressure MIPs might a complete description of excitation be possible.

Commercial availability of systems

A mundane but essential concern about these plasmas is their availability. Availability means much more than the presence in the marketplace of the various major components of the plasma devices. It means the presence of complete, turnkey systems, or as close to that as possible. In effect, such commercial availability is an indicator of the level of development of the device. It is certainly an indicator of its acceptance.

The ICP is available worldwide as a complete atomic emission analysis system from a dozen or more companies. Another dozen companies sell just the plasma generator and torch. Buying an ICP system is much like buying a Chevrolet: Lots of people have them; parts are available when needed; and experienced service personnel can be found relatively easily.

The DCP is available worldwide as a complete AES system from just one company. A number of electronic houses sell an acceptable power supply for the DCP; but there is no second source for the plasma device itself. This does not mean the DCP system is undeveloped or poorly accepted. The DCP has been commercially successful for more than a dozen years. Well over 1000 units have been sold. At least to mid-1983, the DCP systems commanded 20–30% of the plasma emission marketplace. The absence of development of the DCP by instrument companies other than SpectraMetrics (now Beckman) is probably explainable; suffice it to say, it did not occur. To continue the automobile analogy, buying a DCP might be like buying a Land Rover: They can be found all over the world; a lot of them are in distinctly inhospitable locations; and in ownership one is consoled by their remarkable durability.

Optimal Chromatography

MICRO TO MACRO

TOTAL FLOW RANGE

1µl-30ml

Only one HPLC system gives you full micro to analytical to preparative performance with little more than the flick of a switch.

The Beckman 344 gradient HPLC system. The new definition of high performance.

It shows in our 421A controller. A powerful multi-window workstation that lets you tackle very complex gradient analyses. Even change parameters in real-time without interrupting ongoing runs.

The 344 also delivers four times the repeatability of its nearest competitors. Thanks to compressibility feedback circuitry in our 114M pumps. Their high torque, direct drive design produce on-demand precision flow, 0.001 to 30 mL/min. With guaranteed seal life. And smoother solvent delivery than any geared system.

The MIP is available as an emission system only in the form of a multichannel chromatographic detector. There are no AES systems built around the MIP or its variants. A number of companies sell acceptable microwave generators, transmission line components, resonant cavities, or launchers. All these pieces can be configured on a spectrometer system designed to use ICPs or DCPs, but no instrument company provides a system. Thus, having an MIP is much like owning an Indianapolis race car: It can perform in some really amazing ways; a lot of its parts look like other race car parts; but the device is only what the operator decides to make of it.

Detection limits

DCPs, ICPs, and MIPs do not perform in exactly the same manner, as can be seen from just one of the more common performance figures of merit. Table III lists detection limits obtained from each plasma type for 10 frequently determined analytes. The plasmas were operated on spectrometer systems or instrument systems of reasonably equal quality. That is, the data are not biased for one plasma or the other due to the use of superior signal retrieval and conditioning equipment. Data for all three plasmas on the same instrumental system were available only for Ni.

Table III. Detection limits (μg/L)

Element	DCP	ICP	MIP
Fe	5	3	1
Cu	1	2	0.04
Pb	13	12	1
Ca	0.5	0.05	0.2
Zn	4	0.5	0.04
Na	2	9	0.001
Mg	0.1	0.08	0.05
Ni	1	7	80
Cr	1	4	1
K	13	30	—

The MIP has better detection limits for 7 of the 10 elements. In addition, the MIP has the capability of exciting the halogens well enough that they can be quantitated at the μg/mL level at their UV and visible lines, not their vacuum UV (VUV) lines. The DCP and ICP excite the halogen VUV lines only with great difficulty.

Of course, one figure of merit cannot be paramount. Too often, though, it is only the detection limits that are discussed in the context of acceptable performance. Researchers must realize that the MIP routinely requires more extensive sample pretreatment, or a complicated sample introduction technique, or a nonstandard one-of-a-kind approach to sample injection for these kinds of detection limits to be seen. Were we to normalize the sample introduction systems to that used for the conventional ICP, the MIP would be, in the words of one prominent developer, "a mediocre performer." The principal point is that the performances of each of these plasmas must be considered on a sample-by-sample, even analyte-by-analyte basis.

A subjective measure of relative performance

A broader list of performances has been created for the comparison of these plasmas. Using current research literature and reviews describing the use of DCPs, ICPs, and MIPs, a list of operational parameters most frequently commented upon has been compiled (Table IV). With the diversity of systems involved, and the diversity of experience supporting the literature, a nonquantitative but nonetheless informative means of comparing these parameters was used. Each plasma is given a score of from 1 to 10 for each of the points of comparison. This is done as much to keep track of the device with the better performance in the description of each parameter, as it is to actually rate the devices

No. 11 IN A SERIES

PERFORMANCE



And you won't find faster real-time scanning than our 165 UV-Vis detector. It's so sensitive you see peaks stop-flow and diode array detectors can't catch. Plus simultaneously monitor or ratio any two wavelengths.

So if you're after the ultimate in micro to macro performance, it's called the Beckman 344 HPLC system. For the full story call your local Beckman office: In the U.S. (800) 742-2345. Or write Beckman Instruments, Inc., Altex Division, 2350 Camino Ramon, San Ramon, CA 94583. Telephone (415) 866-0511. Offices in major cities worldwide.

BECKMAN

CIRCLE 24 ON READER SERVICE CARD

© 1986 Beckman Instruments Inc. AX 86-8036

Table IV. Subjective performance comparisons (scale: 1–10, 10 = best)

Parameter	DCP	ICP	MIP
Sample form			
Solids	4	3	1
Liquids			
Aqueous	10	10	7
Organic	10	9–10	2
Saline	10	9	5
Slurry	10	4	1
Gases	10	10	10
Linearity	10	10	6
Tolerance to matrix effects			
Chemical	9	10	4
Physical	10	9	5
Interelement	6	9	3
Precision	8–9	10	5–6
Operational costs	8	7	9
Instrumental complexity	9	7	7
Cost of plasma	10	5	9
Commercial availability	2	10	1
Data base size	1–2	10	2–3
Level of development			
Plasma			
Theoretical	1	8	1–2
Practical	3	8	1–2
Sample introduction	4–5	8	4–5
Potential for development			
Plasma			
Theoretical	10	8	9
Practical	8–9	2–3	4–5
Sample introduction	7–8	2–3	8–9

against each other. No one has yet provided a particularly reliable measure with which to do that; this is not an attempt to do so. Some of the comparisons will be explained in detail.

Sample form. The ability of a plasma to provide acceptable results when the sample is in the listed state is compared with this parameter. All of the plasmas do poorly with solid sample introduction. They are not as robust as dc arcs and graphite atomizers. (Laser vaporization of solids is not considered here.) The DCP and ICP were specifically developed for solution analyses. The MIP does not perform as well for solution analyses. This is often the result of the sample introduction being improperly matched to the material input rate limitations of the MIP. Organic liquids are handled nearly equally well by DCPs and ICPs. The ICP requires slightly more fine adjustment than the DCP, although the newer free-running ICPs are more durable.

Organics rapidly extinguish the MIP at all but the very lowest of input rates or at the highest of applied powers. Saline matrices have a tendency to clog ICP sample input tubes faster than DCP components. MIPs can only just manage a saline sample. The simplified sample introduction device and the geometric rigidity of the DCP allow slurry samples to be run reasonably well. Except for use with some versions of the Babington nebulizer, conventional ICPs have difficulty with very high total-dissolved-solids samples. MIPs cannot handle slurries. All of the plasmas perform well when the sample is gaseous or completely vaporized prior to entering the excitation volume. Separation of sample introduction, vaporization, and excitation steps is clearly an advantageous route. But it has been offset traditionally by the greater instrument system complexity in this approach.

Linearity. Linearity refers to the range of concentration over which signal response is linearly predictable to within experimental error. The wide range and linearity of ICP standard curves have been commented upon repeatedly. The DCP provides equivalent linearity, but few publications have described this, and, more importantly, in the first versions of DCP–AES systems, instrument electronics did not permit unhindered use of the inherent linearity, so that it was commonly assumed the DCP source did not possess this feature. The latest version of the DCP–AES system does allow use of the total DCP linear range. The MIP shows shorter linear dynamic ranges. In many cases, the material rate limit of the MIP is reached before the standard curve becomes nonlinear. The small size of the MIP is the cause of this limitation.

Precision. Routinely obtained short-term and long-term precision is better with an ICP than with a DCP, according to most of the published reports. The DCP can be shown to be as precise as the ICP; there is no fundamental reason why it should be less so. However, the unsophisticated sample introduction system may be the cause. Further development would be helpful. The MIP suffers poor precision because the injected sample causes a disruption of the generation of the plasma itself.

Instrumental complexity. The number of adjustable variables required for normal operation is greatest for the ICP. The MIP, depending on the control of the device desired, will have quite a few adjustments. Unfortunately, they are usually interdependent to a large extent. A large number of papers have been published describing the numerous parameter trade-offs involved in obtaining various levels of optimized operation for ICPs and MIPs. For the DCP, only infrequently will more than the viewing height have to be adjusted. The operator does not have access to the power supply beyond the on/off switch.

Cost of the plasma device. DCP sources could retail for approximately $7500, but it is not certain that they are available outside of total instrument systems. An ICP source costs two or three times more than a DCP. The MIP probably can be configured for as low as about $2000, but more likely would be around $5000 or more. Its effective cost would be even more, since what is purchased is not turnkey and the purchaser is required to supply further components.

The total cost of an atomic emission system, of course, is significantly greater than just that of the plasma. By the time an appropriate spectrometer, detector, electronics subsystem, control computer, and adequate software are incorporated into the instrument array, the fact that an ICP might cost two to three times more than a DCP is not quite as significant. Other considerations, such as the volume of the DCP power supply being less than 10% of that of an ICP power supply, begin to come into play.

Data base size. The most quantitative parameter listed in Table IV is data base size. It is the number of research publications produced over the previous four years, as documented in

the ANALYTICAL CHEMISTRY biannual reviews. Taking the ICP citations as the base, there are only 20–30% that many MIP papers, and only 10–20% that many DCP papers. The number of DCP papers is as high as it is as a result of the recently established biennial Winter Plasma Conference. The size of the data base is an indication that more people know more about ICPs than MIPs and DCPs combined.

Level of development. The DCP has been commercially available for a longer period of time than the ICP. A dc plasma jet was available in the early 1950s. Even the most recent version of DCP has been around longer than most of the ICPs. As characterized by the data base material, however, the ICP has been described more extensively at a fundamental level. There are numerous papers describing microwave devices, but very few report on any single, specific configuration. Consequently, the theoretical development of the MIP is still fragmented. The theoretical treatment of the DCP is only now starting to appear. Some recent DCP papers have examined the DCP in the sort of detail with which the ICP has always been reported.

From a practical point of view, characterized by the type of tinkering that results in physical alterations to the source or its power supply, not much has been done with the DCP. This is probably because there is only one version available. Without a second or third variation on the theme, very little curiosity has been shown about how the device might be rearranged. Further, the DCP provides little to be adjusted in normal operation. So the device does not lend itself to inventive tweaking that might indicate the diversity of modifications from which it could benefit. The ICP has evolved through many stages of development; it continues to do so. Some of the latest practical developments involve lower power, lower argon usage, and different support gases. The MIP probably offers the greatest opportunity for configuration development. Except for the TM_{010} cavity, no single variation of MIP has become widely accepted.

With regard to sample introduction, there are more versions of sample input device for the ICP than for DCPs and MIPs. The MIP is interfaced best to a capillary column gas chromatograph; it requires quite a bit of development for direct solution input. The sample introduction device used on the DCP is reasonably effective considering it wasn't developed for that purpose originally. The DCP sample introduction scheme could use much more development.

The MIP has yet to find a consistent need in plasma AES. It is an answer looking for a problem. Even for the halogen detection with which it does so well, adequate demand does not exist to warrant commercial development of an MIP system at this time.

The DCP provides a less expensive, more operationally forgiving source for plasma AES. It is easy to run and maintain. And it is an exceptionally clever optical match to the echelle spectrometer to which it has always been mated. It suffers from lack of a wider interest base among the publishing research community and its unwarranted connection to dc arc technology.

The ICP is the de facto standard source of plasma AES. It may not be the best. But there are more of them around. And all the latest, hottest work is being done with them.

Suggested reading

Inductively coupled plasmas

Fassel, V. A. *Science* **1978,** *202*(13), 183.

Barnes, R. M. *CRC Crit. Rev. Anal. Chem.* **1978,** *7*.

Thompson, M.; Walsh, J. N. *A Handbook of Inductively Coupled Plasma Spectrometry*; Chapman and Hall: New York, 1984.

Direct current plasmas

Miller, M. H.; Eastwood, D.; Schulz-Hendrick, M. *Spectrochim. Acta* **1984,** *39B*, 13.

Zander, A. T.; Miller, M. H. *Spectrochim. Acta* **1985,** *40B*, 1023.

Miller, M. H.; Zander, A. T. *Spectrochim. Acta* **1986,** *41B*, 453.

Microwave-induced plasmas

Zander, A. T.; Hieftje, G. M. *Appl. Spectrosc.* **1981,** *35*(4), 357.

Matousek, J. P.; Orr, B. J.; Selby, M. *Prog. Analyt. Atom. Spectrosc.* **1984,** *7*, 275.



Andrew T. Zander is a senior staff engineer at Perkin-Elmer, working in analytical instrumentation development. He holds a B.S. degree in chemistry from the University of Illinois and received a Ph.D. in analytical chemistry in 1976 from the University of Maryland. He held a postdoctoral appointment at Indiana University, spent two years on the faculty at Cleveland State University, and was an application engineer with SpectraMetrics, Inc., prior to his present position. His research interests center on radiation sources for atomic spectrometry, diffraction devices, and signal detection and processing schemes.

The Egg™

A formula editor you can be using in minutes

In just a few minutes after reading The Egg's tutorial you can be creating and editing both chemical formulas and mathematical expressions. Now, with The Egg's Chemistry Enhancement, you can utilize 500 of the most frequently used preformed Chemical structures. The Egg can produce typeset camera-ready output **quickly, easily,** and very **cost-effectively.**

Whether you are preparing text or tests, papers or proposals, journals or just producing on paper the formulae in your mind, The Egg will address your needs. With an IBM-PC (or compatible) and most dot-matrix and laser printers, you are minutes away from utilizing a WYSIWYG (what you see is what you get) technical editing package, which comes equipped with several standard word-processing capabilities.

With the Chemistry Enhancement package you'll see an immediate time-savings. A benzene ring, for example, can be produced with two key-strokes and a backspace.

For a limited time, The Egg and Chemistry Enhancement may be purchased for **$375.00** (includes shipping.) The retail price of these packages is $625.00; by ordering *now* **you save 40%.**

To order The Egg and and Chemistry Enhancement call:

800-621-0851 Ext. 204

To place your order, we accept your purchase order, American Express, Visa or MasterCard.

If you're still not sure about ordering The Egg, call and order the Egg Demonstration Package. The cost is $20 and is refundable when you purchase the full package.

If you would like to write—please address correspondence to: THOMAS CUTLER-Peregrine Falcon Company, 2330 Marinship Way, Suite 307, Sausalito, CA 94965.

CIRCLE 170 ON READER SERVICE CARD

LABORATORY SERVICE CENTER

Acetonedicarboxylic Acid & esters • p-Aminohippuric Acid • Biuret
tert-Butyl Chloride • Chloranil • Chromotropic Acid, Disodium Salt
Glucose-1-Phosphate, Di K & DiNa Salts • Glutaric Acid & Anhydride
Histamine Diphosphate • INT • Maltose • 4-(4-Nitrobenzyl)pyridine
Potassium Hydrogen Phthalate • Potassium & Sodium-m-Periodates
Protocatechuic Aldehyde • Pyruvic Acid & Na Salt • Sodium Dithionate
Suberic Acid • dl-Tartaric Acid • Tetrabutylammonium Iodide • Thoron
Triethyl Citrate • Tryptamine • Veratraldehyde • Xylose • Xylitol

Write for our Products List of over 3000 chemicals

Tel: 516-273-0900 • TOLL FREE: 800-645-5566 TWX: 510-227-6230

EASTERN CHEMICAL
A Division of UNITED-GUARDIAN, INC.
P. O. Box 2500
DEPT. AC
SMITHTOWN, N. Y. 11787

SHRADER ANALYTICAL & CONSULTING LABORATORIES, INC.
• Mass Spectrometry • GC/MS • High Resolution/MS
• Chemical Ionization • High Resolution GC/MS • FAB
• GC/MS/SIM • Purge & Trap GC/MS • Pyrolysis GC/MS
• Gas Chromatography • Capillary GC/MS • Consulting
3814 VINEWOOD, DETROIT, MI 48208 • (313) 894-4440

Polymeric GPC/HPLC Columns
• GPC & HPLC Resin Columns
• Solvent of Your Choice
• HPLC Column Heaters
• Column Repacking

JORDI ASSOCIATES, INC.
26 Pearl Street, Bellingham, MA 02019 (617) 966-1301

DELSEN
Testing Laboratories, Inc.
• Thermal Analysis • HPLC GPC
• Electrical & Mechanical Properties • Flammability
• Many other capabilities
1024 Grand Central Ave.
Glendale, CA 91201
(213) 245-8517
(818) 247-4106

FREE DATA, FAST
To quickly amass data on all of the products you need, consult the Lab Data Service section on our *Analytical Chemistry* reader reply card insert.

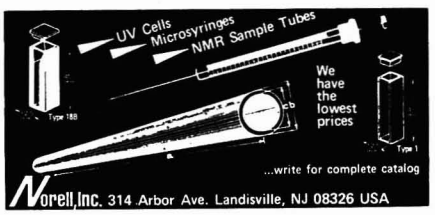

Use Laboratory Service Center

INDEX TO ADVERTISERS IN THIS ISSUE

CIRCLE INQUIRY NO.	ADVERTISERS	PAGE NO.
2	*Airco Special Gases (Hammond Farrell, Inc.)	1130A–1131A
5	*Allied Analytical Systems	1137A
4	*Alltech Associates, Inc. (Chromad)	1064A
230	The Anspec Company, Inc. (Whatman Communications)	1123A
6	Applied Research Laboratories (ICE Communications, Inc.)	1115A
3	Asoma Instruments	1113A
1	*Atago Bussan Company, Ltd. (Echo Japan Corporation)	1109A
21	J.T. Baker Chemical Company (Steigler, Wells & Brunswick, Inc.)	1058A–1059A
24	Beckman Instruments (Cochrane, Chase, Livingston & Company)	1146A–1147A
16–17	Bioanalytical Systems (Kissinger Advertising Associates)	1054A, 1099A
23, 26	*Bio-Rad Digilab Division	1082A, 1089A
18	*Bomem, Inc.	1083A
20	*Brownlee Labs, Inc. (Lena Chow, Inc.)	1065A
22	*Bruker Instruments, Inc. (Techmarketing, Inc.)	1057A
19	Burrell Corporation (David J. Westhead Company)	1134A
39	*Cambridge Isotope Laboratories, Inc.	1091A
34–35	Chrompack, Inc. (Sardi & Bleeker)	1103A, 1105A
37	Chrompack International B.V. (Centrum, Ltd.)	1113A
38	**Chrompack International B.V. (Centrum, Ltd.)	1136B
32	Cole-Parmer Instrument Company (C-P Advertising)	1073A–1074A
43	Dialog Information Services (Humpal, Leftwich, Lauk & Sinn, Inc.)	1138A
48	EG&G Ortec	IFC
52	EG&G Princeton Applied Research (Jackson & O'Malley)	1075A
50–51	EM Science (G & C Advertising & Marketing, Inc.)	1101A
58–61	Finnigan MAT Corporation (Lena Chow, Inc.)	1077A, 1079A
64	*Gilson Medical Electronics, Inc.	1041A
63	Gow-Mac Instrument Company (Kenyon Hoag Associates)	1056A
101–102	Hamamatsu Corporation (Mandabach & Simms, Inc.)	1094A, 1107A
103–104	*HBI/Haake Buchler Instruments (Techmarketing, Inc.)	1044A–1045A
96	*Helma Cells, Inc. (Dansco Advertising)	1103A
95	**W.C. Heraeus GmbH (Amann Werbung)	1092B–1092C

INDEX TO ADVERTISERS IN THIS ISSUE

CIRCLE INQUIRY NO.	ADVERTISERS	PAGE NO.
98–99	*Hewlett-Packard Company Pinné, Garvin, Herbers & Hock, Inc.	1069A
105–106	*Isco, Inc. Farneaux Associates	1055A
114	Janus Laboratories, Inc. Sky Corporation	1080A
122	Kipp & Zonen	1080A
121	**Kontron, Ltd. Promotion Kontron AG	1136J
123	*Kratos Analytical Hogan Gazzara Associates	1081A
128	*Lab-Line Instruments, Inc.	1124A
125	*Lab Safety Supply Company Janesville Ad Agency	1088A
130	*LDC/Milton Roy HRS Communications	1133A
126	*Leco Corporation	OBC
131	*Link Systems U.S.A., Inc.	1129A
129	Liquid Carbonic Corporation	1101A
127	LKB-Produkter AB Media Services	1093A
135	Macherey-Nagel GmbH & Co. KG Werbeagentur Beier	1072A
136	Matheson Gas Products Kenyon Hoag Associates	1053A
141	Metrohm AG Ecknauer & Schoch Werbeagentur	1087A
142	*Mettler Instrument Corporation McKinney, Inc.	1117A–1120A
133–134	MG Industries Techmarketing, Inc.	1090A
140	Micromeritics Instrument Corporation Fahlgren, Swink & Nucifora	1082A
137	*Mitsubishi Chemical Industries, Ltd. Global Advertising Company, Ltd.	1145A
138	Molecular Design, Ltd.	1143A
150	*Nicolet Corporation Technical Communications	1071A
156	Ohaus Scale Corporation Libra Associates	1051A
170	Peregrine Falcon Company	1149A
166–167	*Perkin-Elmer Corporation AC&R Advertising	1067A, 1127A
169	*PolyScience Corporation	1039A
165	P.R.A. International, Inc. Design Associates	1125A
168	Puffer Hubbard	1088A
80–83	**Pye Unicam, Ltd. Connors Publicity, Ltd.	1136C–1136D, 1136F, 1136H, 1136L
182	*Rheodyne, Inc. Bonfield Associates	1063A
190	Safe-Lab, Inc.	1105A
189	**Schott Glaswerke Werbeagentur Frenz	1136M
191	Scott Specialty Gases The Matlin Company, Inc.	1125A
187–188	*Shimadzu Scientific Instruments, Inc. Techmarketing, Inc.	1141A
192	Systec, Inc.	1134A
201	*Techne, Inc. Brunswick Advertising	1086A
202	Tekmar Kenyon Hoag Associates	1109A
203	Tracor Xray	1085A
218	*Valco Instruments Company, Inc. Technical Advertising Associates	1049A
219	VG Instruments Barbeau-Hutchings Advertising	1047A
231	Wiley-Interscience/Division of John Wiley & Sons, Inc.	1135A

** See ad in ACS Laboratory Guide.*

*** Company so marked has advertisement in Foreign Regional edition only.*

Advertising Management for the American Chemical Society Publications

CENTCOM, LTD

President

Thomas N. J. Koerwer

Executive Vice President *Senior Vice President*

James A. Byrne **Benjamin W. Jones**

Alfred L. Gregory, *Vice President*
Clay S. Holden, *Vice President*
Robert L. Voepel, *Vice President*
Joseph P. Stenza, *Production Director*

25 Sylvan Rd. South
P.O. Box 231
Westport, Connecticut 06881
(Area Code 203) 226-7131
Telex No. 643310

ADVERTISING SALES MANAGER
James A. Byrne, VP

ASSISTANT ADVERTISING SALES MANAGER
Bruce E. Poorman

ADVERTISING PRODUCTION MANAGER
Jane F. Gatenby

SALES REPRESENTATIVES

Philadelphia, PA . . . Patricia O'Donnell, CENTCOM, LTD., GSB Building, Suite 725, 1 Belmont Avenue, Bala Cynwyd, Pa. 19004. Telephone: 215-667-9666

New York, NY . . . Dean A. Baldwin, CENTCOM, LTD., 60 East 42nd St., New York, N.Y. 10165. Telephone: 212-972-9660

Westport, CT . . . Edward M. Black, CENTCOM, LTD., 25 Sylvan Rd. South, P.O. Box 231, Westport, Ct. 06881. Telephone: 203-226-7131, Telex 643310

Cleveland, OH . . . Bruce E. Poorman, John C. Guyot, CENTCOM, LTD., 325 Front St., Suite 2, Berea, Ohio 44017. Telephone: 216-234-1333

Chicago, IL . . . Michael J. Pak, CENTCOM, LTD., 540 Frontage Rd., Northfield, Ill. 60093. Telephone: 312-441-6383

Houston, TX . . . Michael J. Pak, CENTCOM, LTD. Telephone: 312-441-6383

San Francisco, CA . . . Paul M. Butts, CENTCOM, LTD., Suite 1070, 2672 Bayshore Frontage Road, Mountain View, CA 94043. Telephone: 415-969-4604

Los Angeles, CA . . . Clay S. Holden, CENTCOM, LTD., Newton Pacific Center, 3142 Pacific Coast Highway, Suite 200, Torrance, CA 90505. Telephone: 213-325-1903

Boston, MA . . . Edward M. Black, CENTCOM, LTD. Telephone: 203-226-7131

Atlanta, GA . . . Edward M. Black, CENTCOM, LTD. Telephone: 203-226-7131

Denver, CO . . . Paul M. Butts, CENTCOM, LTD. Telephone: 415-969-4604

United Kingdom

Reading, England . . . Malcolm Thiele, Technomedia Ltd., Wood Cottage, Shurlock Row, Reading RG10 OQE. Berkshire, England. Telephone: 073-434-3302, Telex #848800

Lancashire, England . . . Technomedia Ltd., c/o Meconomics Ltd., Meconomics House, 31 Old Street, Ashton Under Lyne, Lancashire, England. Telephone: 061-308-3025

Continental Europe . . . Andre Jamar, International Communications, Inc., Rue Mallar 1, 4800 Verviers, Belgium. Telephone: (087) 22-53-85, Telex #49263

Tokyo, Japan . . . Shuji Tanaka, International Media Representatives Ltd., 2-29 Toranomon, 1-Chome Minato-ku Tokyo 105 Japan. Telephone: 502-0656, Telex #22633

New and Improved!



A "must" for beginners—indispensable for those wanting to learn more about this important analytical tool!

INTERPRETATION OF INFRARED SPECTRA, SECOND EDITION

An Audio Course Produced by the American Chemical Society

This updated edition of the ACS bestseller audio course sets the standard in teaching the basics of IR interpretation! Learn how to successfully interpret IR spectra of organic compounds and master the basic theory you need to understand how electromagnetic radiation interacts with molecules. Study the important vibrational principles behind IR absorption.

Sharpen your technical knowledge of the fundamentals of instrumentation, sample preparation, and current techniques. Focus on interpretation of the spectra with particular emphasis on the nature of the vibrations involved. Investigate quantitative analysis and concentrate on group frequencies of many common function groups.

This course is useful to anyone who uses infrared spectroscopy to solve a wide variety of chemical problems. Although no experience with IR interpretation is necessary, a basic knowledge of organic chemistry and elementary physics would be helpful to fully benefit from this course.

Special feature! This new edition provides you with a separate appendex that includes 75 unknown spectra for analysis.

Brief Course Contents

Basic Theory: electromagnetic spectrum; molecular vibrations; infrared absorption; dipole moment change; anaharmonicity; oscillators; overtone, combination, and difference bands; Fermi resonance; Raman effect. **Instrumentation and Sample Preparation:** grating monochromator; interferometer; IR transmitting materials; liquid cells; mulls and KBr discs; Internal reflection. **Quantitative Analysis:** Beer's Law; ratio methods; multicomponent analysis. **Vibrational Interactions:** diatomic vibrations; Stretching-stretching interactions; bending interactions. **Group Frequency Analysis:** CH_2 and CH_3 groups; C=C groups; triple bonds and cumulated double bonds; benzene rings; OH and C—O groups; C=O groups; nitrogen containing groups; sulfur and phosphorous groups containing groups.

About the Instructor

Norman B. Colthup holds a B.S. degree from Antioch College and an honorary Doctor of Science degree from Fisk University. He is author of numerous publications in the field of infrared spectroscopy, including his widely distributed chart of IR spectra-chemical structure correlation tables. He is also author of the textbook *Introduction to Infrared and Raman Spectroscopy,* which he coauthored with L.H. Daly and S.E. Wiberly. He has lectured widely and has conducted the popular ACS Short Course on infrared spectroscopy. In 1979 he was given the Williams-Wright Award from the Colblentz Society.

Unit and Price (Catalog No. 83)

Four cassettes (4.3 hours playing time) and a 152-page manual: U.S. & Canada **$340.00;** Export **$408.00.** Additional manuals: U.S. & Canada **$21.00** each; Export **$26.00** each.

No-Risk Guarantee

All ACS Audio Courses come to you with a money-back guarantee. If you are not completely satisfied, return the course within ten days for a full refund or cancellation of invoice.

To place your order, use the coupon below or CALL TOLL FREE 800-424-6747 and use your credit card or purchase order number. To help us serve you better, please quote Department 526 when you place your order.

American Chemical Society, Distribution Office, Department 526, 1155 Sixteenth Street, N.W., Washington, DC 20036

Yes! Please send me the following:

Qty. **Total**

_____ Complete course(s), *Interpretation of IR Spectra, Second Edition,* at $340.00 each (U.S. & Canada) or $408.00 each (export). Catalog No. 83 $ _____

_____ Additional manuals at $21.00 each (U.S. & Canada) or $26.00 each (export) $ _____

TOTAL $ _____

☐ Payment enclosed (make checks payable to American Chemical Society)

☐ Purchase order enclosed P.O. # _____

Charge my ☐ MasterCard ☐ VISA ☐ American Express ☐ Diners Club/Carte Blanche ☐ ACCESS ☐ Barclaycard

Account # _____

Expires _____ Interbank # _____ (MC and ACCESS only)

Name of cardholder _____

Signature _____

Ship to:

Name _____

Title _____

Organization _____

Address _____

City, State, Zip _____

analytical chemistry

EDITOR: **GEORGE H. MORRISON**

ASSOCIATE EDITORS: **Klaus Biemann, Georges Gulochon, Theodore Kuwana, Fred Lytle**

EDITORIAL HEADQUARTERS
1155 Sixteenth St., N.W.
Washington, D.C. 20036
Phone: 202-872-4570 Teletype: 710-8220 151

Executive Editor: Josephine M. Petruzzi
Associate Editors: Stuart A. Borman, Rani A. George, Louise Voress
Assistant Editor: Mary D. Warner
Editorial Assistant: Grace K. Lee
Production Manager: Leroy L. Corcoran
Art Director: Alan Kahan
Designer: Sharon Harris Wolfgang
Production Editor: Gail M. Mortenson
Circulation: Cynthia G. Smith
Editorial Assistant, LabGuide: Joanne Mullican

Journals Dept., Columbus, Ohio
Associate Head: Marianne Brogan
Associate Editor: Rodney L. Temos

Advisory Board: Shier S. Berman, Brian S. Bidlingmeyer, Henry N. Blount, Gary D. Christian, Harry V. Drushel, Larry R. Faulkner, William R. Heineman, Harry S. Hertz, Gary M. Hieftje, Atsushi Mizuike, Erno Pungor, Melvin W. Redmond, Jr., Martin A. Rudat, Dennis Schuetzle, Charles L. Wilkins, Nicholas Winograd

Instrumentation Advisory Panel: Howard G. Barth, Richard F. Browner, Richard S. Danchik, Thomas C. Farrar, Joel M. Harris, John F. Holland, F. James Holler, Peter N. Keliher, D. Warren Vidrine.

The Analytical Approach Advisory Panel: Edward C. Dunlop, Robert A. Hofstader, Wilbur D. Shults

Published by the
AMERICAN CHEMICAL SOCIETY
1155 16th Street, N.W.
Washington, D.C. 20036

Books and Journals Division
Director: D. H. Michael Bowen
Journals: Charles R. Bertsch
Research and Development: Lorrin R. Garson

Manuscript requirements are published in the January 1986 issue, page 267. Manuscripts for publication (4 copies) should be submitted to ANALYTICAL CHEMISTRY at the ACS Washington address.

The American Chemical Society and its editors assume no responsibility for the statements and opinions advanced by contributors. Views expressed in the editorials are those of the editors and do not necessarily represent the official position of the American Chemical Society.

The Big Three in Analytical Chemistry

Those of us who are privileged to be involved in the graduate education of analytical chemists derive great pleasure in following the professional careers of our former students. These careers have been pursued in academe, government, and industry, and we take great pride in the accomplishments of successive generations of graduates who have contributed to the remarkable progress of our discipline.

Although it is rewarding to examine the progress of the current generations of graduates, it is important to periodically review the impact of our antecedents who have made it all possible. In particular, it is important to review the first half of this century and to recognize the tremendous contributions of earlier pioneers to the development of modern analytical chemistry. We should all be reminded of three educators who were particularly responsible for the shaping of our discipline in the United States. They are N. Howell Furman (1893–1965) of Princeton University, Izaak Maurits Kolthoff (1894–) of the University of Minnesota, and Hobart H. Willard (1881–1974) of the University of Michigan.

Although these "Big Three" (who incidentally were collaborators in text writing and were great friends) played a dominant role in shaping the analytical research of the first half of this century, perhaps their most important contribution to science is the lasting and growing influence of generations of students and postdoctorals. Many of today's leaders in the field can trace their lineage to these giants who collectively were responsible for the supervision of 120 Ph.D.s (Furman—26 between 1933 and 1960; Kolthoff—51 between 1932 and 1960; Willard—43 between 1917 and 1951).

A very effective method for ensuring that subsequent generations of scientists remember these leaders is the establishment of a lecture series in their honor, and one such series already exists at the University of Michigan. The Hobart H. Willard Lectureship in Analytical Chemistry was established in 1976 through donations in memory of the late Professor Willard from former students, colleagues, friends, and relatives. In alternate years, an outstanding analytical chemist is invited to present the lecture at the University of Michigan. It would be most fitting to set up a national lecture program to honor the memory of more of the early leaders of our discipline.

G. H. Morrison

Characterization of High Molecular Weight Polycyclic Aromatic Hydrocarbons by Charge Exchange Chemical Ionization Mass Spectrometry

William J. Simonsick, Jr.,[1] and Ronald A. Hites*

School of Public and Environmental Affairs and Department of Chemistry, Indiana University, Bloomington, Indiana 47405

Charge exchange chemical ionization mass spectrometry (CE/CI)MS has been used to analyze high molecular weight polycyclic aromatic hydrocarbons (PAH) isolated from a carbon black. Thermally stable capillary columns were prepared to separate these large PAH. The (CE/CI)MS working range was expanded by increasing the ion source pressure. Reliable ionization potentials (IP) were obtained by semiempirical molecular orbital calculations using the MNDO method. On the basis of the ratio of the $(M + H)^+$ ion to the M^+ ion and on the calculated IP, high molecular weight PAH were predictively distinguished. The (CE/CI)MS technique, coupled with high-resolution GC, permitted the rejection of several isomeric PAH as possible components in the extract. The method also revealed that many isomers present in a carbon black have not been documented in the literature.

Polycyclic aromatic hydrocarbons (PAH) currently represent the largest class of chemical carcinogens known to man. Because of their carcinogenic behavior PAH have been the subject of numerous research investigations (*1*, *2*). The majority of these studies have concentrated on PAH containing from two to six rings although the existence of higher molecular weight (>300) carcinogenic PAH have been documented (*3*). Limited solubilities, low vapor pressures, the absence of standard references compounds, and the lack of analytical techniques that allow isomer elucidation are the reasons for the scarcity of information on large PAH.

McKay used gel permeation chromatography coupled with fluorescence spectroscopy detection to identify large PAH in petroleum distillates (*4*). PAH of molecular weights 300–402 were detected in airborne particulate matter by GC/MS (*5*). These high molecular weight PAH were characterized by electron impact mass spectrometry, which does not distinguish among isomeric PAH. High-performance liquid chromatography (HPLC) (*6*) and more recently microcolumn (capillary) LC (*7*, *8*) have been the most successful methods for large PAH analysis. Unfortunately, unless one has standard compounds or reference spectra available, only molecular weights (*5*) or representative structures for an isomeric group typically are measurable (*7*, *8*). This is unfortunate because the exact structure is important since only certain structural isomers are carcinogenic.

Charge exchange chemical ionization mass spectrometry (CE/CI)MS was sucessfully employed to differentiate isomeric PAH in the absence of standard compounds (*9*). This is of particular interest for high molecular weight PAH of which there are few commercially available standards. Recent advances in the preparation of thermally stable capillary column stationary phases have extended the upper temperature limit for gas chromatography (*10*, *11*). Cross-linked phases are stable to operating temperatures of 400 °C, which facilitate the analysis of PAH possessing molecular weights in excess of 400 (*11*). We have prepared these columns in our laboratory and coupled them to a mass spectrometer operated in the CE/CI mode to be able to analyze high molecular weight PAH with isomeric specificity.

Under (CE/CI)MS conditions, $(M + H)^+$ ions of PAH are formed by proton transfer with $C_2H_5^+$, and M^+ ions are generated by charge exchange with Ar^+; these reagent ions are generated by using a mixture of argon and methane in an ion source operating at about 1 torr. On the basis of the ratio of the MH^+ to M^+ ions [$(M + H)^+/M^+$ ratio] and on the measured first ionization potential (IP), isomeric PAH are predictively differentiated (*9*). Unfortunately, experimental IP's are not available for many four to six ring PAH and for most greater than seven ring PAH. Therefore, we have selected a semiempirical method, modified neglect of diatomic overlap (MNDO) (*12*), for the calculation of IP's. The MNDO method has been previously demonstrated to yield calculated molecular parameters in accord with experimental results for PAH (*13–15*).

EXPERIMENTAL SECTION

Chemicals and Reagents. Most of the PAH used in this study were obtained in pure form from Analabs (New Haven, CT). Several of the PAH that are not commercially available were furnished by M. L. Lee and G. R. West (Brigham Young University, Provo, UT) and Chevron research (*16*). Methylene chloride (MCB, Cincinnati, OH) solutions containing approximately 20 ng/μL of each compound were prepared. The high molecular weight PAH required slow heating of the solution to solubilize these chemicals. If we were unable to dissolve these compounds in warm methylene chloride, the PAH were dissolved in hot anisole (MCB, Cincinnati, OH).

A 10-g aliquot of 260 nm particle size carbon black (Cabot Corp., Boston, MA) was Soxhlet extracted for 24 h with 400 mL of methylene chloride. The extract was reduced to a volume of approximately 5 mL and analyzed directly by (CE/CI)MS.

Molecular Orbital Calculations. All MO computations were carried out by use of an enlarged version of Dewar and Thiel's MNDO program (*12*) operating on Indiana University's CDC Cyber 170/855. The program was modified in order to accommodate PAH with molecular weights in excess of 400. Several arrays were enlarged to facilitate these calculations according to the method described by Thiel (*17*).

At the start of the calculation, the PAH molecules were assumed to be planar with uniform bond lengths and angles. The aromatic C–C bonds were input as 1.4 Å and the C–H bonds were 1.1 Å. All planar bond angles were 120° except the five-membered rings where a value of 105° was used. The initial geometry was optimized by minimizing the total energy with respect to the planar bond lengths and angles using the Davidson–Fletcher–Powell (DFP) algorithm, which is incorporated into the MNDO program (*18*).

Capillary Column Preparation. Thermally stable capillary columns were prepared in the following manner: Approximately 50 m of new 0.25 mm i.d. fused silica capillary tubing (Spectran Corp., Surbridge, MA) was purged overnight with helium at 100 °C. The tubing was then rinsed with 10 mL of filtered (0.47 μm) methylene chloride. The stationary phase employed was a methylphenylpolysiloxane containing 70% phenyl and 4% vinyl

[1] Current address: E. I. du Pont de Nemours & Co., Marshall R&D Laboratory, Philadelphia, PA 19146.

0003-2700/86/0358-2114$01.50/0 © 1986 American Chemical Society

groups; it was obtained from M. L. Lee and G. W. West (Brigham Young University, Provo, UT). A small amount (0.2 mg) of the stationary phase was dissolved in equal portions of methylene chloride and *n*-pentane (10 mL each) and subsequently filtered (0.2 μm). The capillary tubing was then filled with the solution and a vacuum pulled to remove the solvent. The stationary phase (0.12-μm film thickenss) was cross-linked by purging the column with azo-*t*-butane (Alfa Products, Danvers, MA). Once the column was saturated with azo-*t*-butane vapors both ends were sealed. The column was then placed in a GC oven and heated from 40 °C to 225 °C at 4 deg/min and held at 225 °C for 1 h. The column was then washed with 10 mL of methylene chloride and purged with helium.

Conditioning of the column proceeded in the following manner: The column was installed in a GC oven that had been modified to accommodate a nitrogen purge line. A low flow of helium (about 1 mL/min) was passed through the column as it was heated from 100 °C up to 400 °C at 4 °C/min. The final temperature was held for 12 h under a low purge of nitrogen. The column was evaluated by use of *n*-alkane standards.

All GC retention data for PAH were acquired on a Carlo Erba 4160 gas chromatograph (Carlo Erba Strumentazione, Milan, Italy) equipped with an on-column injector and an FID detector. Retention index measurements of standards were accomplished by on-column injection of approximately 0.1–0.2 μL solutions of each PAH. Hydrogen was employed as the carrier gas at a head pressure of 2 kg/cm^2. The GC was temperature programmed from 80 °C to 400 °C at 4 °C/min. The FID signal was output to a Hewlett-Packard 3392A integrator (Palo Alto, CA) from which retention indexes were calculated.

Mass Spectrometry. The (CE/CI)MS epxeriments were all performed on a Hewlett Packard 5985B GC/MS system. The reagent gas, a 15% mixture of methane in argon (Linde Co., New York), was introduced to the ion source through a transfer line (*19*) that had been further modified to facilitate capillary column interchange. The ion source pressure was measured by a Baratron capacitance manometer (MKS Instruments, Burlington, MA) mounted outside the manifold housing. A stainless steel tube extending from the ion source block through a vacuum lock into the manometer provided the path for an accurate and rapid ion source pressure measurement. The ion source pressure was set with an automatic pressure controller (Granville Phillips Co., Boulder, CO) at approximately 0.8 torr. The CI gas flow was adjusted to achieve a $(M + H)^+/M^+$ ratio of 1.5 for 1,2,3,5-tetrafluorobenzene (TFB) (Aldrich, Milwaukee, WI). The ion source temperature was set at 250 °C and measured by a thermocouple located in the ion source body.

The mass spectrometer was tuned prior to each set of experiments using binary mixtures of perfluorotributylamine (PFTBA) (PCR Research Chemicals, Inc., Gainesville, FL) and TFB. A complete mass spectrum (100–500 amu) was then obtained for each compound. All subsequent mass spectral data were collected by use of selected ion monitoring. A dwell time of 10 ms was used. The software examined the complete M^+ and $(M + H)^+$ mass spectral peak profiles of each compound analyzed. This was accomplished by stepping across the M^+ and $(M + H)^+$ peaks at 0.1 dalton intervals followed by integration ±0.2 amu from the peak maxima. All $(M + H)^+/M^+$ ratios were corrected for the natural abundance of carbon-13.

RESULTS AND DISCUSSION

Validity of the MNDO Method for IP Calculations of PAH. Semiempirical molecular orbital calculations can provide accurate and reliable information where experimental data are not available. The MNDO method (*12*) with optimization of geometry has been used in this laboratory to calculate the first ionization potential (IP) of over 200 PAH. The IP calculations with optimization of planar geometry take at least an order of magnitude more computer time than a single point calculation (*12*). Nevertheless, we chose to optimize the planar geometry because we found that the calculated IP's obtained by geometric optimization were significantly better ($p < 0.01$) when compared to experimental values ($r^2 = 0.98$, $N = 8$) than those obtained from a single-point calculation ($r^2 = 0.90$, $N = 8$). The calculated IP's, in most cases, were higher than experimental values (see Table I), but an excellent linear correlation was observed ($r^2 = 0.959$, $n = 60$). We concluded that the IP's calculated by the MNDO method are reliable for our work, and we elected to use these values even when experimental values were available.

Ion Source Pressure. As the PAH increase in size, the difference in ionization potentials between isomers decreases because larger π systems permit increased delocalization of the charge on radical ions (*21*). Therefore when larger PAH are analyzed, it is important to have a large change in $(M + H)^+/M^+$ for small changes in IP. From our earlier work (*9*), it was found that lowering the ion source temperature, increasing the percent methane in argon, or raising the ion source pressure caused larger $(M + H)^+/M^+$ differences for small IP changes. Because the ion source pressure has the most pronounced effect on the $(M + H)^+/M^+$ ratios of PAH (*9*) and because it is the easiest parameter to vary, we chose to increase the ion source pressure in order to expand the (CE/CI)MS working range.

The working range of (CE/CI)MS was increased by adjusting the flow of reagent gas to achieve an $(M + H)^+/M^+$ of 1.5 for our internal standard, TFB. With conditions adjusted to TFB approximately 1.0 (*9*), naphthalene and anthanthrene differed by 1.8 ratio units, but at TFB = 1.5 this difference is expanded to 3.1 ratio units. The precision for the $(M + H)^+/M^+$ ratios obtained at the higher source pressure is quite good, averaging about 3% relative standard deviation (see Table II).

Correlations with Calculated Molecular Parameters. The experimental $(M + H)^+/M^+$ ratios of PAH seem to correlate well with the experimental ionization potentials (IP) (*9*). Therefore, a high correlation is expected between the MNDO IP's and the experimental $(M + H)^+/M^+$ ratios because of the agreement between the experimental and calculated IP's. However, before use of the MNDO IP as the definitive predictor of the $(M + H)^+/M^+$ ratio, other possible predictors were investigated. In addition to the first IP, the MNDO program gave us the energies of the frontier orbitals, the HOMO (highest occupied molecular orbital) and the LUMO (lowest unoccupied molecular orbital), which are important properties of PAH. Although a statistically significant ($p < 0.01$) correlation exists ($r^2 = 0.75$, $N = 53$) between the LUMO energy and the $(M + H)^+/M^+$ ratios obtained at TFB = 1.5, the LUMO energy is not a better predictor of the $(M + H)^+/M^+$ behavior than the IP. Combining the IP and LUMO energy data for PAH and regressing on the $(M + H)^+/M^+$ ratios did not yield a better correlation than that obtained by using only the IP.

Clar and Schmidt found that the second IP (IP_2) was a better indicator of chemical reactivity than only the first IP (*22*). Thus, we investigated the possibility that either IP_2 or the difference between the first and second IP's could be used to predict the (CE/CI)MS response of PAH; unfortunately, no correlation was observed. Additionally, we observed no higher correlation when we classified PAH according to structural type.

We found the best predictor of $(M + H)^+/M^+$ behavior is simply the MNDO calculated IP. Therefore, (CE/CI)MS allows one to predictively assign specific structures to isomeric PAH based on a calculated IP and an experimentally determined $(M + H)^+/M^+$ ratio.

Table II lists the calculated MNDO IP's, the $(M + H)^+/M^+$ ratios acquired at TFB = 1.5 and the experimental error for 53 PAH studied in this laboratory. It is obvious that an increase in the IP will be reflected by a corresponding increase in the $(M + H)^+/M^+$ ratio. The equation that best relates the $(M + H)^+/M^+$ ratio and the calculated IP is

$$\log [(M + H)^+/M^+] = 15.64 \log [IP(MNDO)] - 14.16$$

Table I. Comparison between MNDO Calculated IP and Experimental Values

compound	mol wt	ionization potential, eV exptl[a]	ionization potential, eV calcd[b]	compound	mol wt	ionization potential, eV exptl[a]	ionization potential, eV calcd[b]
benzene	78	9.24	9.386	benzo[*b*]picene	328	7.18	8.009
acenaphthylene	152	8.22	8.778	benzo[*c*]pentaphene	328	7.17	8.066
indene	116	8.15	8.759	benzo[*ghi*]perylene	276	7.16	7.944
naphthalene	128	8.15	8.575	naphtho[2,3-*g*]chrysene	328	7.15	8.051
fluoranthene	202	7.95	8.466	dibenzo[*b,pqr*]perylene	326	7.12	7.959
fluorene	166	7.91	8.609	naphtho[1,2,3,4-*rst*]pentaphene	352	7.09	7.869
phenanthrene	178	7.90	8.479	benzo[*a*]coronene	350	7.08	7.936
triphenylene	228	7.87	8.505	benzo[*rst*]pentaphene	302	7.07	7.817
acenaphthene	154	7.79	8.525	benzo[*a*]naphthacene	278	7.06	7.797
benzo[*c*]phenanthrene	228	7.61	8.327	tetracene	228	7.01	7.722
chrysene	228	7.60	8.261	dibenzo[*a,j*]naphthacene	328	7.00	7.861
picene	278	7.52	8.239	benzo[*p*]naphtho[1,8,7-*ghi*]chrysene	352	7.00	7.940
dibenzo[*c,g*]phenanthrene	278	7.50	8.243	dibenzo[*b,ghi*]perylene	326	6.99	7.904
benz[*a*]anthracene	228	7.46	8.112	dibenzo[*b,k*]chrysene	328	6.98	7.831
pyrene	202	7.43	8.029	dibenzo[*a,c*]naphthacene	328	6.97	7.846
azulene	128	7.43	8.072	hexaphene	328	6.97	7.784
anthracene	178	7.42	8.049	naphtho[1,2,3,4-*ghi*]perylene	326	6.96	7.803
benzo[*b*]triphenylene	278	7.41	8.172	benzo[*pqr*]naphtho[8,1,2-*bcd*]perylene	350	6.92	7.699
dibenzo[*de,qr*]naphthacene	302	7.41	8.163	anthanthrene	276	6.92	7.621
dibenzo[*fg,op*]naphthacene	302	7.40	8.198	benzo[*b*]perylene	302	6.89	7.826
dibenz[*a,j*]anthracene	278	7.40	8.175	naphtho[8,1,2-*bcd*]perylene	326	6.82	7.621
naphtho[1,2–*b*]triphenylene	328	7.38	8.222	dibenzo[*cd,lm*]perylene	326	6.74	7.571
dibenzo[*a,h*]anthracene	278	7.38	8.148	benzo[*a*]perylene	302	6.71	7.567
coronene	300	7.36	8.077	pentacene	278	6.66	7.496
benzo[*h*]pentaphene	328	7.33	8.184	dibenzo[*a,l*]pentacene	378	6.66	7.634
pentaphene	278	7.29	8.116	benzo[*a*]pentacene	328	6.66	7.565
benzo[*c*]picene	328	7.28	8.149	dibenzo[*bc,ef*]coronene	374	6.50	7.417
benzo[*b*]chrysene	278	7.23	7.971	dibenzo[*bc,kl*]coronene	374	6.42	7.230
dibenzo[*g,p*]chrysene	328	7.19	8.161	hexacene	328	6.40	7.201
naphtho[1,2-*b*]chrysene	328	7.19	8.044	phenanthro[1,10,9,8-*opqra*]perylene	350	6.30	7.251

[a] All values taken from ref 20. [b] Calculated by MNDO method with optimization of planar geometry (*12*).

This equation gives a very high correlation between the MNDO IP and the $(M + H)^+/M^+$ ratio obtained at TFB = 1.5 ($r^2 = 0.959$, $N = 53$). Therefore, we conclude that many authentic standards are not necessary to characterize the (CE/CI)MS behavior of isomeric PAH, and we can reliably predict the $(M + H)^+/M^+$ response of isomeric PAH using the MNDO IP.

Application to a Carbon Black Extract. The successful preparation of thermally stable capillary GC columns will facilitate the separation of large PAH, and (CE/CI)MS detection will permit the differentiation of high molecular weight PAH. The following paragraphs present an example of this approach.

The demonstration sample we selected was an experimental, 260-nm carbon black from Cabot Corp. We selected this particular sample for our investigations because this sample is well-known for its high concentration of high molecular weight, adsorbed PAH and because it has been the subject of several other studies (*6, 7, 23*). Recently, microcolumn LC was used to separate the large PAH in this sample; unfortunately, no positive identification of any of the constituents was made (*7*). In an earlier investigation of the same mixture, HPLC was used to separate many large PAH and detection was accomplished by electron impact MS and by spectrofluorometry (*6*). Two $C_{28}H_{14}$ PAH, benzo[*cd*]naphtho-[3,2,1,8-*pqr,a*]perylene [350(4)] and benzo[*pqr*]naphtho-[8,1,2-*bcd*]perylene [350(6)], were positively identified as components in the extract by comparison to known UV spectra (*6*). However, only tentative identifications of the remaining $C_{28}H_{14}$ isomers and for two $C_{30}H_{14}$ isomers were suggested based on molecular weight information (*6*).

Figure 1 shows a portion of the total ion chromatogram of the carbon black extract run under CE/CI conditions adjusted such that TFB = 1.5, and Table III gives the data for each peak. The experimental $(M + H)^+/M^+$ ratios for PAH of

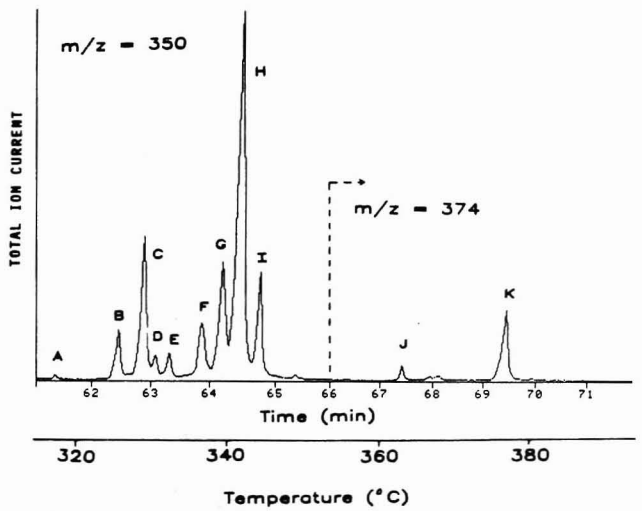

Figure 1. Partial (CE/CI)MS total ion chromatogram of high molecular weight PAH isolated from a carbon black. MS conditions were adjusted to TFB = 1.5 (see text). GC conditions were as follows: 20 m × 0.25 mm i.d., 0.12 mm film thickness (methylphenylpolysiloxane phase), helium carrier gas, 11 psi head pressure.

molecular weights 350 and 374 found in this carbon black extract span a range of 0.637 ratio units as compared to only 0.383 ratio units when working such that TFB = 1.0.

Most of the isomeric $C_{28}H_{14}$ and $C_{30}H_{14}$ PAH are not commercially available; although some large PAH compounds have been synthesized. Our laboratory has recently acquired four of these large PAH, and Table IV summarizes the analytical information of importance for these compounds.

Figure 2 lists the structures of all the isomeric $C_{28}H_{14}$ (m/z 350) PAH for which the IP's were calculated in this laboratory. The eight PAH containing only fused six-membered rings (PAH6) [350(1–8)] represent all the possible PAH6 structures

Table II. Selected PAH with Their Calculated Ionization Potentials and Their Measured $(M + H)^+/M^+$ Ratios

compound	mol wt	IP (MNDO)[a]	$(M + H)^+/M^+$ ratio[b] TFB = 1.5	std dev[c]	N	compound	mol wt	IP (MNDO)[a]	$(M + H)^+/M^+$ ratio[b] TFB = 1.5	std dev[c]	N
dibenzo[*bc,ef*]coronene	374	7.417	0.316	0.020	2	benzo[*ghi*]perylene	276	7.944	0.683	0.027	8
tribenzo[*de,kl,rst*]pentaphene	376	7.452	0.250	0.013	2	dibenzo[*b,g*]phenanthrene	278	8.001	0.832	0.018	5
						indeno[1,2,3-*cd*]pyrene	276	8.024	0.932	0.017	8
pyranthene	376	7.544	0.410	0.018	4	dibenzo[*a,e*]fluoranthene	302	8.028	1.104	0.018	4
dibenzo[*cd,lm*]perylene	326	7.571	0.327	0.005	4	pyrene	202	8.029	1.019	0.048	8
anthanthrene	276	7.621	0.416	0.018	6	anthracene	178	8.049	1.042	0.031	8
naphtho[8,1,2-*bcd*]perylene	326	7.621	0.476	0.022	4	coronene	300	8.077	0.832	0.016	8
						benz[*a*]anthracene	228	8.112	1.227	0.047	8
dibenzo[*a,l*]pentacene	378	7.634	0.434	0.035	2	pentaphene	278	8.116	1.300	0.049	4
dibenzo[*b,def*]chrysene	302	7.644	0.440	0.023	7	benzo[*e*]pyrene	252	8.137	1.225	0.034	7
naphtho[2,1,8-*qra*]naphthacene	302	7.689	0.472	0.010	3	cyclopenta[*cd*]pyrene	226	8.145	1.417	0.048	6
						dibenz[*a,h*]anthracene	278	8.148	1.288	0.052	7
benzo[*pqr*]naphtho[8,1,2-*bcd*]perylene	350	7.699	0.497	0.032	4	benzo[*k*]fluoranthene	252	8.167	1.435	0.039	8
						benzo[*b*]triphenylene	278	8.172	1.587	0.037	7
						benzo[*j*]fluoranthene	252	8.207	1.274	0.018	6
naphtho[8,1,2-*abc*]coronene	374	7.709	0.511	0.014	7	picene	278	8.239	2.062	0.051	6
						chrysene	228	8.261	2.035	0.072	8
tetracene	228	7.722	0.537	0.024	8	benzo[*a*]fluorene	216	8.309	1.571	0.049	7
benzo[*a*]naphthacene	278	7.797	0.622	0.042	4	benzo[*c*]phenanthrene	228	8.327	1.855	0.048	7
dibenzo[*h,rst*]pentaphene	352	7.799	0.719	0.022	3	benzo[*b*]fluorene	216	8.390	1.984	0.081	6
						benzo[*b*]fluoranthene	252	8.410	2.396	0.057	6
naphtho[1,2,3,4-*ghi*]perylene	326	7.803	0.631	0.039	5	4*H*-cyclopenta[*def*]phenanthrene	190	8.436	2.243	0.066	7
benzo[*rst*]pentaphene	302	7.817	0.570	0.026	6	fluoranthene	202	8.466	2.654	0.082	7
benzo[*b*]perylene	302	7.826	0.515	0.001	3	phenanthrene	178	8.479	2.671	0.053	8
benzo[*a*]pyrene	252	7.830	0.683	0.043	6	triphenylene	228	8.505	2.777	0.079	8
perylene	252	7.846	0.497	0.005	7	benzo[*ghi*]fluoranthene	226	8.507	2.617	0.032	5
diindeno[1,2,3-*cd*:1′,2′,3′-*lm*]perylene	400	7.874	0.632	0.042	3	naphthalene	128	8.575	3.467	0.155	5
						fluorene	166	8.609	2.447	0.057	5
benzo[*a*]coronene	350	7.936	0.698	0.020	5	indene	116	8.759	3.403	0.042	4
naphtho[1,2,3,4-*def*]chrysene	302	7.943	0.820	0.034	7	acenaphthylene	152	8.778	3.023	0.063	7
						benzene	78	9.386	7.596	0.154	3

[a] Obtained using MNDO with planar optimization of geometry. [b] All ratios are corrected for natural abundance of carbon-13. The ratios were measured such that the internal standard, 1,2,3,5-tetrafluorobenzene (TFB), gave an $(M + H)^+/M^+$ ratio of 1.5 (TFB = 1.5). [c] Standard deviation of an individual measurement.

Table III. Summary of Results for Isomer $C_{28}H_{14}$ and $C_{30}H_{14}$ PAH Isolated from 260-nm Carbon Black Extract[a]

peak[b]	mol wt	retention index[c]	$(M + H)^+/M^+$[d]
A	350	616.70 ± 0.71 (3)	1.025 ± 0.097 (3)
B	350	624.57 ± 0.44 (9)	0.832 ± 0.037 (5)
C	350	627.60 ± 0.49 (9)	0.753 ± 0.028 (5)
C	350	629.26 ± 0.56 (4)	0.708 ± 0.029 (5)
E	350	631.10 ± 0.62 (3)	0.470 ± 0.007 (5)
F	350	635.22 ± 0.53 (7)	0.720 ± 0.034 (5)
G	350	637.46 ± 0.63 (7)	0.388 ± 0.022 (5)
H	350	639.29 ± 0.70 (7)	0.593 ± 0.012 (5)
I	350	641.63 ± 0.64 (8)	0.431 ± 0.018 (5)
J	374	663.56 ± 0.59 (9)	0.917 ± 0.019 (5)
K	374	678.08 ± 0.78 (9)	0.521 ± 0.027 (5)

[a] Numbers in parentheses refer to number of determinations. [b] See Figure 1. [c] Retention index based on extrapolation of chrysene = 400.00 and picene = 500.00 interval. [d] Conditions adjusted to $(M + H)^+/M^+$ of TFB = 1.5; all ratios corrected for natural abundance of carbon-13.

possessing the molecular formula $C_{28}H_{14}$ as defined by Dias (*24*). We used the MNDO method and computed the IP's of two additional PAH [350(9–10)] which were listed in *Chemical Abstracts*. One of these compounds, diindeno[1,2,3-*cd*:1′,2′,3′-*jk*]pyrene [350(9)] was reported, although not confirmed, to be present in this carbon black (*6*).

The following discussion illustrates how the (CE/CI)MS method is used for the analysis of high molecular weight PAH in complex mixtures. Figure 3 displays the $(M + H)^+/M^+$ ratios (from Table III) obtained from the (CE/CI)MS analysis of the $C_{28}H_{14}$ (m/z 350) isomers found in the carbon black. The experimental $(M + H)^+/M^+$ ratios are designated by the lettered vertical lines (corresponding to peaks A to I) which overlay the range bars that represent the 90% confidence limits of the $(M + H)^+/M^+$ ratios estimated using the above equation. The two standards that we possess, benzo[*pqr*]naphtho[8,1,2-*bcd*]perylene [350(6)] and benzo[*a*]coronene [350(8)], are designated by asterisks.

Inspection of this figure reveals that neither phenanthro[1,10,9,8-*opqra*]perylene [350(1)], perinaphthacenonaphthacene [350(2)], benzo[*cd*]naphtho[3,2,1,8-*pqra*]perylene [350(3)], or acenaphtho[1,2-*k*]cyclopenta[*cd*]fluranthene [350(10)] are constituents of this carbon black because no $(M + H)^+/M^+$ (vertical bar) is within the 90% confidence limits

Table IV. GC Retention Data and (CE/CI)MS Behavior of Four High Molecular Weight PAH Standards[a]

compound	compd no	GC retention index[b]	$(M + H)^+/M^+$[c]
benzo[*a*]coronene	350(8)	635.16 ± 0.27 (4)	0.689 ± 0.020 (5)
benzo[*pqr*]naphtho[8,1,2-*bcd*]perylene	350(6)	638.91 ± 0.49 (3)	0.497 ± 0.032 (4)
naphtho[8,1,2-*abc*]coronene	374(4)	678.60 ± 0.44 (4)	0.511 ± 0.014 (5)
dibenzo[*bc,ef*]coronene	374(3)	683.62 ± 0.17 (3)	0.316 ± 0.020 (4)

[a] Numbers in parentheses refer to number of determinations. [b] Calculated by extrapolation of chrysene (RI = 400.00) to picene (RI = 500.00) interval. [c] Conditions adjusted such that TFB = 1.5; all ratios corrected for natural abundance of carbon-13.

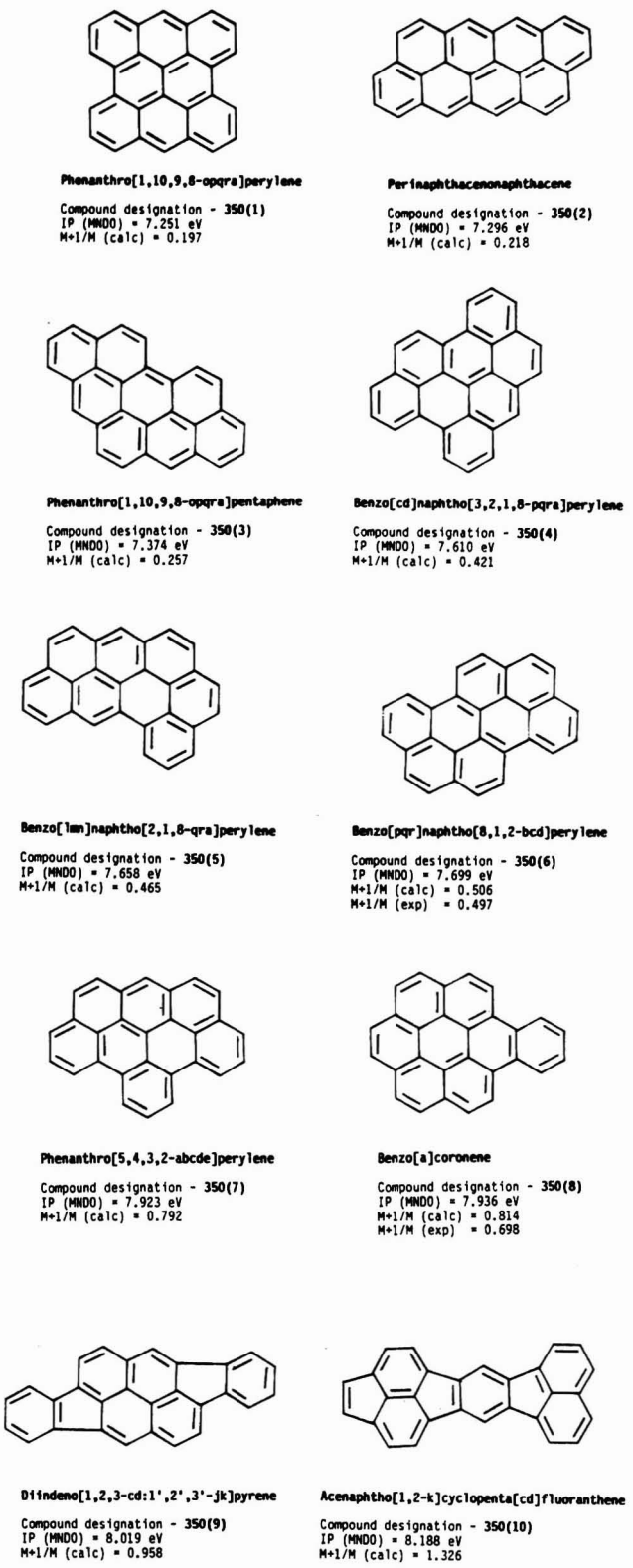

Figure 2. Structures of isomeric $C_{28}H_{14}$ PAH (mol wt 350) studied in this laboratory.

for these PAH. These compounds were not found in this mixture in an earlier investigation either (*6*).

Peak A gave an $(M + H)^+/M^+$ of 1.025. This value falls within the 90% confidence limits (Figure 3) of diindeno-[1,2,3-*cd*:1′,2′,3′-*jk*]pyrene [350(9)], which has been suggested, but not confirmed, to be in this mixture (*6*). From the compounds available in our data set, we concluded that peak A was diindeno[1,2,3-*cd*:1′,2′,3′-*jk*]pyrene [350(9)].

Peak B gave an $(M + H)^+/M^+$ ratio of 0.832. This falls within the 90% confidence limits (Figure 3) of both phenanthro[5,4,3,2-*abcde*]perylene [350(7)] and benzo[*a*]coronene

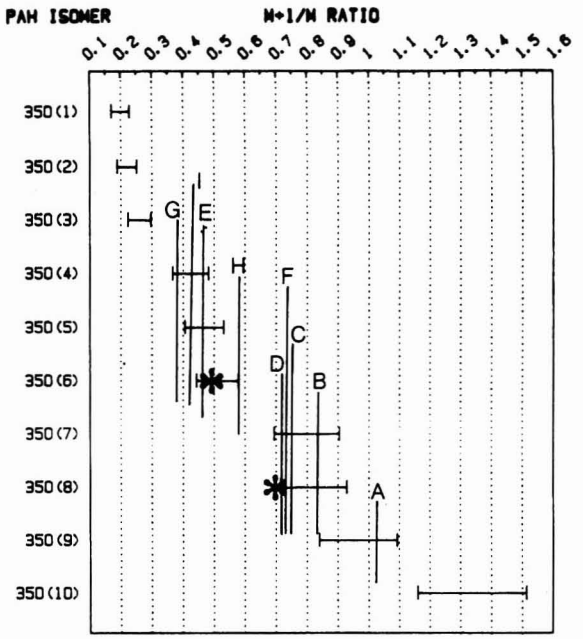

Figure 3. Range chart illustrating the resolving power of the (CE/CI)MS technique for the compounds given in Figure 2 with the experimental $(M + H)^+/M^+$ ratios of $C_{28}H_{14}$ PAH from the carbon black superimposed. The letters refer to the peaks in Figure 1.

[350(8)]. Fortunately, we possess a standard of benzo[*a*]-coronene, and we can eliminate this as a possiblity because its GC retention index 635.16 ± 0.27 is significantly different from the index for peak B, 624.57 ± 0.44. Therefore, in conjunction with a standard, the CE/CI model predicts that peak B (Figure 3) is phenanthro[5,4,3,2-*abcde*]perylene [350(7)]. This PAH was previously suggested, although not confirmed, to be a component in this carbon black (*6*).

Peak C gave an $(M + H)^+/M^+$ ratio of 0.753, which also falls within the 90% confidence interval of both phenanthro-[5,4,3,2-*abcde*]perylene [350(7)] and benzo[*a*]coronene [350(8)]. We rejected benzo[*a*]coronene [350(8)] as a possibility because its retention index was different (635.16 ± 0.27) than the index for peak C (627.60 ± 0.49). Hence, the CE/CI model predicts that peak C (Figure 3) is also phenanthro-[5,4,3,2-*abcde*]perylene [350(7)]. This inconsistency will be explained later.

Peak D yields an $(M + H)^+/M^+$ of 0.708 which also suggests that this peak is benzo[*a*]coronene [350(8)] or phenanthro-[5,4,3,2-*abcde*]perylene [350(7)]. Once again benzo[*a*]coronene may be eliminated as a candidate using retention index measurements, 629.26 ± 0.56 (Table III) vs. 635.16 ± 0.27 (Table IV). Thus, the model predicts peak D as being phenanthro[5,4,3,2-*abcde*]perylene [350(7)].

The reason for this impossible prediction is as follows: We have limited out data set of $C_{28}H_{14}$ PAH to only those listed in *Chemical Abstracts*, and we have concentrated primarily on PAH6 compounds because their occurrence in the environment is more prevalent than PAH containing five-membered rings. The number of PAH6 isomers for a given molecular formula has been fully enumerated (*25–27*) whereas PAH containing five-membered rings have not. This is no trivial task. Dias predicts that the maximum number of five-membered rings that a PAH of molecular formula $C_{28}H_{14}$ can possess is six (*27*). When one considers all the possible PAH structures of molecular formula $C_{28}H_{14}$ containing from one to six pentagonal rings, the number of possible structures becomes overwhelming. Even when considering PAH containing only one or two pentagonal rings, the situation is still a complicated one. Therefore, we have performed molecular orbital calculations only on compounds that were found in *Chemical Abstracts*. Since we have not calculated (M +

$H)^+/M^+$ ratios for all isomers, some GC peak may not have a match with our model. Thus, of peaks B, C, and D, which all seem to be compound 350(7), at least two are compounds for which we have not calculated $(M + H)^+/M^+$ ratios.

Peak E gave an $(M + H)^+/M^+$ ratio of 0.470. This falls within the confidence limits of three $C_{28}H_{14}$ PAH, namely, benzo[*cd*]naphtho[3,2,1,8-*pqr*,*a*]perylene [350(4)], benzo[*lmn*]naphtho[2,1,8-*qr*,*a*]perylene [350(5)], and benzo[*pqr*]naphtho[8,1,2-*bcd*]perylene [350(6)]. We can eliminate benzo[*pqr*]naphtho[8,1,2-*bcd*]perylene [350(6)] as a possiblity because we have a standard of this compound, and its retention index is 638.91 ± 0.49 as compared to 631.10 ± 0.62 for peak E. Therefore, peak E is predicted to be either benzo[*cd*]naphtho[3,2,1,8-*pqra*]perylene [350(4)] or benzo[*lmn*]naphtho[2,1,8-*gra*]perylene [350(5)].

Peak F was confirmed to be benzo[*a*]coronene [350(8)]. The retention index for the standard was 635.16 ± 0.27, and for peak F, a value of 635.22 ± 0.53 was measured. The experimental $(M + H)^+/M^+$ ratio for the authentic compound was 0.689 ± 0.020 while that of peak F was 0.720 ± 0.034. This isomer has been suggested to be in this mixture by Peaden et al. (*6*).

Peak G gave an $(M + H)^+/M^+$ of 0.388. Consulting Figure 3, we predict that this peak consists of benzo[*cd*]naphtho[3,2,1,8-*pqra*]perylene [350(4)]. This compound has been previously confirmed to be a constituent of this mixture (*6*).

As discussed previously, we proposed peak E to be either benzo[*cd*]naphtho[3,2,1,8-*pqra*]perylene [350(4)] or benzo[*lmn*]naphtho[2,1,8-*qra*]perylene [350(5)]. We now have assigned benzo[*cd*]naphtho[3,2,1,8-*pqra*]perylene [350(4)] to peak G. Therefore, we predict that peak E is benzo[*lmn*]naphtho[2,1,8-*qra*]perylene [350(5)]. However, the experimental $(M + H)^+/M^+$ ratio for peak I is 0.431, which the (CE/CI)MS model predicts to be either benzo[*lmn*]naphtho[3,2,1,8-*pqra*]perylene [350(4)] or benzo[*lmn*]naphtho[2,1,8-*qra*]perylene [350(5)]. We can eliminate benzo[*cd*]naphtho[3,2,1,8-*pqra*]perylene [350(4)] as a possibility because we have assigned this isomer to peak G, but we encounter a similar situation as before. We conclude that either peak E or peak I is benzo[*lmn*]naphtho[2,1,8-*qra*]perylene [350(5)]; the other peak is an isomer that has not appeared in the literature, and thus we have not calculated its IP.

(CE/CI)MS allows one to conclude that a given peak may contain more components than thought. This is the case of peak H. The retention index of this peak, 639.29 ± 0.70, agrees with the retention index, 638.91 ± 0.49, of benzo[*pqr*]naphtho[8,1,2-*bcd*]perylene [see Figure 3; 350(6)]; however, the observed $(M + H)^+/M^+$ of peak H is 0.593 ± 0.012 (Table III) in contrast to 0.497 ± 0.032 measured for the pure standard. It is reasonable to postulate that peak H contains compound 350(6) and at least one other compound. For this specific case where a standard was available, (CE/CI)MS provided the analytical information that led to the conclusion that peak H was multicomponent.

The eluting GC peaks were assumed to contain only one component unless it was obvious that the peak was multicomponent (broadened or shoulders). Therefore, we assumed that the measured $(M + H)^+/M^+$ ratio originated from only one species. This was not always the case (for example, peak H). We did not have a method for determining how many isomers were present under an eluting GC peak because retention indexes have not been published and pure standards are not available for large PAH. The following example illustrates this potential problem. If an eluting peak was composed for equal amounts of perinaphthacenonaphthacene, [350(2)], and phenanthro[5,4,3,1-*abcde*]perylene, [350(7)], an $(M + H)^+/M^+$ ratio of about 0.5 would be predicted. Because we might not have any indication that the eluting peak was

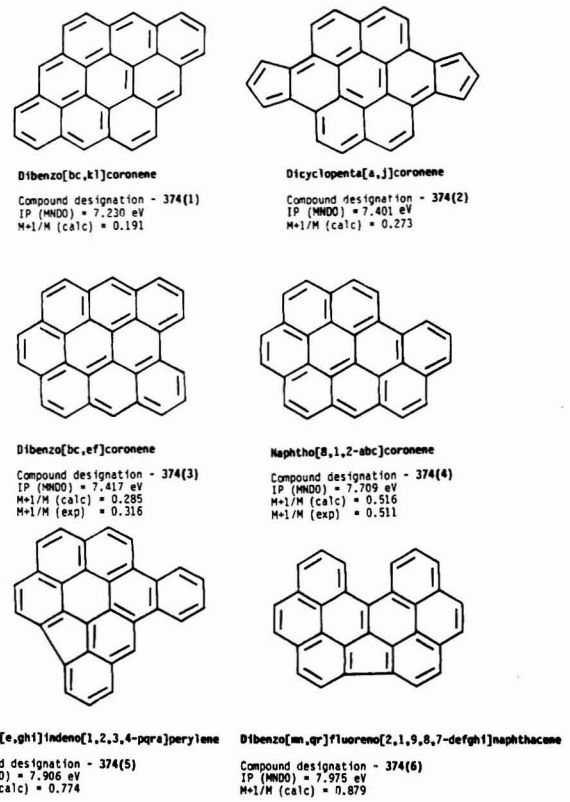

Figure 4. Structures of isomeric $C_{30}H_{14}$ PAH (mol wt = 374) studied in this laboratory.

a binary mixture, erroneous conclusions could be reached. Both perinaphthacenonaphthacene [350(2)] and phenanthro[5,4,3,2-*abcde*]perylene [350(7)] would be rejected as possible structures since the 90% conficence limits on an observed ratio of approximately 0.5 (see Figure 3) fall outside the 90% confidence limits for either of the two compounds. This limitation can, of course, be diminished by improvements in the chromatographic separation of PAH.

The largest molecular weight isomer set we investigated was the $C_{30}H_{14}$ group, which has a molecular weight of 374. Again, we only present those PAH that were listed in *Chemical Abstracts*. The three PAH6 listed in Figure 4 [374(1,3,4)] are all the possible PAH in this isomer class containing only fused six-membered rings (*24*). However, the maximum number of pentagonal rings this molecular formula can have is eight; we did not consider any of these possibilities. Rather, we restricted our MNDO calculations to those compounds listed in *Chemical Abstracts*. Of the compounds listed in Figure 4, structures 374(4) and 374(5) have been suggested to be in this carbon black (*6*). Consulting Figure 5 shows that these two compounds are fully resolved by the (CE/CI)MS method.

Figure 5 shows the $(M + H)^+/M^+$ ratios obtained from the (CE/CI)MS analysis of the $C_{30}H_{14}$ (m/z) 374) isomers present in the carbon black; these ratios are shown by the lettered vertical bars as described before. The two standards we have, dibenzo[*bc*,*ef*]coronene [374(3)] and naphtho[8,1,2-*abc*]coronene [374(4)], are represented by asterisks. Examination of Figure 5 suggests that only naphtho[8,1,2-*abc*]coronene [374(4)] and dibenzo[*mn*,*qr*]flureno[2,1,9,8,7-*defghi*]naphthacene [374(6)] are present in the mixture. Peak J crosses only the range bar corresponding to dibenzo[*mn*,*qr*]-fluoreno[2,1,9,8,7-*defghi*]naphthacene [374(6)], and peak K intersects only the range bar for naphtho[8,1,2-*abc*]coronene [374(4)].

Peak K was confirmed to be naphtho[8,1,2-*abc*]coronene [374(4)] by a retention index comparison: 678.60 ± 0.44 for the standard compared to 678.08 ± 0.78 for peak K. Additionally, the experimental $(M + H)^+/M^+$ ratio of naphtho-

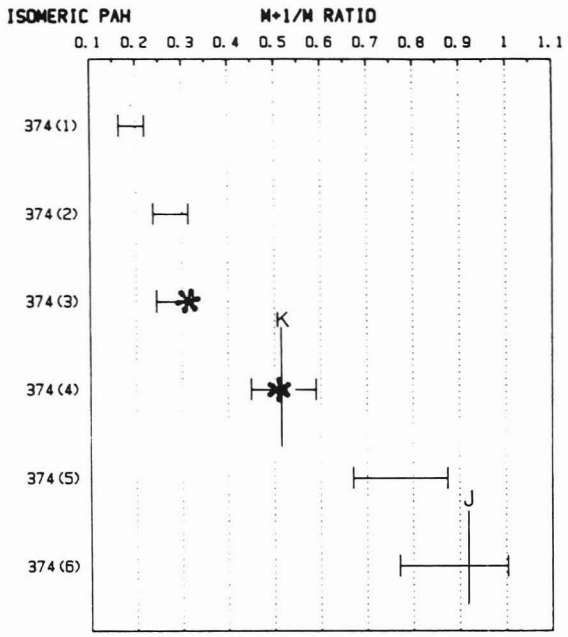

Figure 5. Range chart illustrating the resolving power of the (CE/CI)MS technique for the compounds given in Figure 4 with the experimental $(M + H)^+/M^+$ ratios of $C_{30}H_{14}$ PAH from the carbon black superimposed. The letters refer to the peaks in Figure 1.

[8,1,2-*abc*]coronene [374(4)] is 0.511 as compared to 0.521 for peak J. This is good agreement.

Dibenzo[*bc*,*ef*]coronene [374(3)] was probably absent or below the (CE/CI)MS detection limits because no GC peak had a molecular ion of 374 daltons and gave an $(M + H)^+/M^+$ within the range of 0.244 to 0.324 ratio units (see Figure 5). A retention index measurement confirmed our hypothesis. The retention index of compound 374(3) was 683.62 ± 0.17 (Table III-4), and there were no peaks observed within that GC interval. Additionally dibenzo[*bc*,*kl*]coronene [374(1)] and dicyclopenta[*a*,*j*]coronene [374(2)] were rejected as possible components in the extract based on the predicted $(M + H)^+/M^+$ values. Dibenzo[*e*,*ghi*]indeno[1,2,3,4-*pqra*]perylene [374(5)] has been reported to be in the carbon black (*6*), but our calculated $(M + H)^+/M^+$ ratio does not support this. The experimental $(M + H)^+/M^+$ ratios of 0.521 and 0.917 fall outside the 90% confidence interval (Figure 5) for dibenzo[*e*,*ghi*]indeno[1,2,3,4-*pqra*]perylene [374(5)].

A summary of our data obtained for this carbon black is presented in Table V. Using thermally stable capillary columns with (CE/CI)MS detection, we were able to reject many compounds as components in this mixture, tell if a given peak contained more than a single component (provided we had a standard), and predict the exact structure of certain high molecular weight isomeric PAH.

CONCLUSION

We have shown that the IP's of PAH calculated by the MNDO method compare well with those obtained by experimental methods. A high correlation was found between the $(M + H)^+/M^+$ ratio of PAH and these calculated IP's. Fused silica capillary columns with a thermally stable stationary phase were successfully prepared in this laboratory. These columns facilitated the characterization of PAH containing up to nine rings. The resolving power of (CE/CI)MS for large PAH was evaluated for the $C_{28}H_{14}$ and the $C_{30}H_{14}$ isomeric series. The (CE/CI)MS method reliably predicts the mass spectral behavior of large isomeric PAH. The method was successfully employed for the analysis of high molecular weight PAH extracted from a carbon black. The method allowed us to reject several isomeric species as constituents of this mixture. We were also able to deduce that one GC peak had more than one component, and we were able to assign specific structures to certain isomeric PAH without possessing standards.

Table V. Summary of Structure Assignments of $C_{28}H_{14}$ and $C_{30}H_{14}$ PAH Isolated from a Carbon Black

peak[a]	mol wt	$(M + H)^+/M^+$[b]	predicted compd	calcd[c] $(M + H)^+/M^+$
A	350	1.025	350(9)	0.958
B	350	0.832	350(7)	0.792
C	350	0.750	350(7)	0.792
D	350	0.708	350(7)	0.792
E	350	0.470	350(5)	0.465
F	350	0.720	350(8)	0.814
G	350	0.388	350(4)	0.421
H	350	0.593	350(6)	0.506
I	350	0.431	350(5)	0.465
J	374	0.917	374(6)	0.879
K	374	0.521	374(4)	0.516

[a] See Figure 1. [b] Corrected for natural abundance of carbon-13. [c] Refer to Figures 2 and 4.

The major limitations of the model were revealed. The first drawback is a result of the insufficient number of isomers documented in the literature. Although a full enumeration of PAH6 has been presented, the PAH containing one or two pentagonal fused rings have not. This results in the assignment of more than one GC peak to the same compound. Additionally, the method is hampered by the GC separations. Erroneous conclusions can be drawn if an eluting GC peak is multicomponent, and this may go unrecognized. However, the (CE/CI)MS technique still provides the most information available for the analysis of isomeric PAH.

ACKNOWLEDGMENT

The authors are grateful to M. L. Lee of Brigham Young University and John Fetzer of Chevron Research for supplying many of the large PAH used in this study. We also thank Indiana University's Bloomington Academic Computing Services for the use of their computing facilities.

Registry No. Benzo[*cd*]naphtho[3,2,1,8-*pqra*]perylene, 6208-20-4; benzo[*lmn*]naphtho[2,1,8-*qra*]perylene, 75449-94-4; benzo[*pqr*]naphtho[8,1,2-*bcd*]perylene, 190-71-6; phenanthro[5,4,3,2-*abcde*]perylene, 75449-92-2; benzo[*a*]coronene, 190-70-5; diindeno[1,2,3-*cd*:1′,2′,3′-*jk*]pyrene, 191-23-1; naphtho[8,1,2-*abc*]coronene, 6596-38-9; dibenzo[*mn*,*qr*]fluoreno[2,1,9,8,7-*defghi*]naphthacene, 76759-99-4; dibenzo[*bc*,*ef*]coronene, 190-31-8; tribenzo[*de*,*kl*,*rst*]pentaphene, 188-72-7; pyranthene, 191-13-9; dibenzo[*cd*,*lm*]perylene, 188-96-5; anthanthrene, 191-26-4; naphtho[8,1,2-*bcd*]perylene, 188-89-6; dibenzo[*a*,*l*]pentacene, 227-09-8; dibenzo[*b*,*def*]chrysene, 189-64-0; naphtho[2,1,8-*qra*]naphthacene, 196-42-9; tetracene, 92-24-0; benzo[*a*]naphthacene, 226-88-0; dibenzo[*h*,*rst*]pentaphene, 192-47-2; naphtho[1,2,3,4-*ghi*]perylene, 190-84-1; benzo[*rst*]pentaphene, 189-55-9; benzo[*b*]perylene, 197-70-6; benzo[*a*]pyrene, 50-32-8; perylene, 198-55-0; naphtho[1,2,3,4-*def*]chrysene, 192-65-4; benzo[*ghi*]perylene, 191-24-2; dibenzo[*b*,*g*]phenanthrene, 195-06-2; indeno[1,2,3-*cd*]pyrene, 193-39-5; dibenzo[*a*,*e*]fluoranthene, 5385-75-1; pyrene, 129-00-0; anthracene, 120-12-7; coronene, 191-07-1; benz[*a*]anthracene, 56-55-3; pentaphene, 222-93-5; benzo[*e*]pyrene, 192-97-2; cyclopenta[*cd*]pyrene, 27208-37-3; dibenz[*a*,*h*]anthracene, 53-70-3; benzo[*k*]fluoranthene, 207-08-9; benzo[*b*]triphenylene, 215-58-7; benzo[*j*]fluoranthene, 205-82-3; picene, 213-46-7; chrysene, 218-01-9; benzo[*a*]fluorene, 30777-18-5; benzo[*c*]phenanthrene, 195-19-7; benzo[*b*]fluorene, 30777-19-6; benzo[*b*]fluoranthene, 205-99-2; 4*H*-cyclopenta[*def*]phenanthrene, 203-64-5; fluoranthene, 206-44-0; phenanthrene, 85-01-8; triphenylene, 217-59-4; benzo[*ghi*]fluoranthene, 203-12-3; naphthalene, 91-20-3; fluorene, 86-73-7; indene, 95-13-6; acenaphthylene, 208-96-8; benzene, 71-43-2; phenanthro[1,10,9,8-*opqra*]perylene, 190-39-6; perinaphthacenonaphthacene, 188-50-1; phenanthro[1,10,9,8-*opqra*]pentaphene, 4552-79-8; dibenzo[*bc*,*kl*)coronene, 190-55-6; dicyclopenta[*a*,*j*]coronene, 90207-46-8;

dibenzo[*bc*,*ef*]coronene, 190-31-8; dibenzo[*e*,*ghi*]indeno[1,2,3,4-*pqra*]perylene, 75449-96-6; acenaphtho[1,2-*k*]cyclopenta[*cd*]-fluoranthene, 30909-04-7.

LITERATURE CITED

(1) Lee, M. L.; Novotny, M. V.; Bartle, K. D. *Analytical Chemistry of Polycyclic Aromatic Compounds*; Academic Press: New York, 1981.
(2) Bjorseth, A. *Handbook of Polycyclic Aromatic Hydrocarbons*; Marcel Dekker: New York, 1983.
(3) Lacassagne, A.; Buu-Hoi, N. P.; Zajdela, F.; Saint-Ruf, G. *C. R. Acad. Sci. Paris, Ser. D.* **1968**, *226*, 301–304.
(4) McKay, J. F.; Latham. D. R. *Anal. Chem.* **1973**, *45*, 1050–1055.
(5) Romanowski, T.; Funke, W.; Grossman, I.; Konig, J.; Balfanz, E. *HRC CC, J. High Res. Chromatogr. Chromatogr. Commun.* **1981**, *4*, 209–214.
(6) Peaden, P. A.; Lee, M. L.; Hirata, Y.; Novotny, M. *Anal. Chem.* **1980**, *52*, 2268–2271.
(7) Hirosa, A.; Wiesler, D.; Novotny, M. *Chromatographia* **1984**, *18*, 239–242.
(8) Hirosa, A.; Wiesler, D.; Novotny, M. *Anal. Chem.* **1984**, *56*, 1243–1248.
(9) Simonsick, W. J., Jr.; Hites, R. A. *Anal. Chem.* **1984**, *56*, 2749–2754.
(10) Peaden, P. A.; Wright, B. W.; Lee, M. L. *Chromatographia* **1982**, *15*, 335–340.
(11) Stenberg, V.; Alsberg, T.; Blomberg, L.; Wannman, T. In *Polynuclear Aromatic Hydrocarbons*; eds. Jones, P. W., Leber, P., *Eds.*; Ann Arbor Science: Ann Arbor, MI, 1979; pp 313–326.
(12) Dewar, M. J. S.; Thiel, W. *J. Am. Chem. Soc.* **1977**, *99*, 4899–4907.
(13) Dewar, M. J. S.; Thiel, W. *J. Am. Chem. Soc.* **1977**, *99*, 4907–4917.
(14) Ford, G. P.; Scribner, J. D. *J. Am. Chem. Soc.* **1981**, *103*, 4281–4291.
(15) Mirek, J.; Buda, A. *Z. Naturforsch., A* **198**, *39a*, 386–390.
(16) Fetzer, J. C.; Biggs, W. R. *J. Chromatogr.* **1984**, *295*, 161–169.
(17) Thiel, W. In *Quantum Chemistry Program Exchange No. 438*; Indiana University: Bloomington, IN 1983.
(18) Fletcher, R.; Powell, M. J. D. *Comput. J.* **1963**, *6*, 163–168.
(19) Jensen, T.; Kaminsky, R.; McVeety, B.; Wozniak, T.; Hites, R. A. *Anal. Chem.* **1982**, *54*, 2388–2390.
(20) Levin, R. D.; Lias, S. G. *Natl. Stand. Ref. Data Ser. (U.S., Natl. Bur. Stand.) No. 71*, **1982**.
(21) Moet-Ner, M. *J. Phys. Chem.* **1980**, *84*, 2716–2723.
(22) Clar, E.; Schmidt, W. *Tetrahedron* **1979**, *35*, 2673–2680.
(23) Lee, M. L.; Hites, R. A. *Anal. Chem.* **1976**, *48*, 1890–1893.
(24) Dias, J. R. *Nouv. J. Chim.* **1985**, *9*, 125–134.
(25) Dias, J. R. *J. Chem. Inf. Comput. Sci.* **1984**, *24*, 124–135.
(26) Dias, J. R. *J. Chem. Inf. Comput. Sci.* **1982**, *22*, 15–22.
(27) Dias, J. R. *J. Chem. Inf. Comput. Sci.* **1982**, *22*, 139–152.

RECEIVED for review February 4, 1986. Accepted April 16, 1986. Supported by the U.S. Department of Energy (Grant No. 80EV-10449).

Substituent Effects in Charge Exchange Chemical Ionization Mass Spectrometry

William J. Simonsick, Jr.,[1] and Ronald A. Hites*

School of Public and Environmental Affairs and Department of Chemistry, Indiana University, Bloomington, Indiana 47405

We examined substituent effects in charge exchange chemical ionization mass spectrometry. A linear Hammett relationship was observed for a series of monosubstituted benzenes and naphthalenes. Substituted aromatic compounds not distinguished by electron impact mass spectrometry can be predictively resolved by charge exchange chemical ionization mass spectrometry.

Charge exchange chemical ionization mass spectrometry (CE/CI)MS has been shown to be a valuable tool for the analysis of unsubstituted polycyclic aromatic hydrocarbons (PAH) (*1*). Using a 15% mixture of methane in argon, (CE/CI)MS yields abundant M^+, $(M + H)^+$, and $(M + C_2H_5)^+$ ions from PAH with minimal fragmentation. Molecular ions (M^+) are formed by charge exchange reactions with the ionized argon, and protonated molecular ions $[(M + H)^+]$ result from proton transfer between the analyte and $C_2H_5^+$. Based on the ratio of the $(M + H)^+$ to the M^+ ion currents and on the ionization potential (IP), this technique differentiates, in a predictable manner, isomeric structures of unsubstituted PAH (see preceding paper in this journal).

Slight modifications in molecular structure, such as the addition of an alkyl group on a ring, can either enhance or diminish the carcinogenic properties of a compound. In the methylchrysene series, for example, only the 5-methyl isomer is a potent carcinogen while the others only show marginal activity (*2*). In the same fashion, the addition of a substituent to a parent PAH can dramatically affect its mutagenic activity. For example, aminopyrenes have been identified in the mutagenic fraction of a coal-derived heavy distillate (*3*), and nitropyrenes have been reported to be the most mutagenic chemicals known, although pyrene itself shows no biological activity (*4*). Given the significant biological effects of certain substituted aromatic compounds, we thought it would be important to investigate the effect of substituents on the $(M + H)^+/M^+$ behavior for a series of substituted aromatic compounds.

The ion/molecule reactions that occur in chemical ionization mass spectrometry are in many cases analogous to those that occur in solution chemistry (*5*, *6*). Therefore, the rules governing solution chemistry should be applicable in (CE/CI)MS. For example, the application of the Hammett equation (*7*) is a well-known, useful way of correlating the effects of substituents upon reaction rates or equilibrium constants (*8*).

The list is too long to cite all the applications of the Hammett equation for explaining substituent effects in mass spectrometry, but a few of the most important studies will be presented. Bursey used the Hammett equation to explain substituent effects observed under electron ionization (EI) conditions (*9*). Field studied the effect of substituents in chemical ionization mass spectrometry and has observed correlations between the rates of reactions of several substituted benzyl acetates and the substituent constants (σ^+) (*10*). Linear correlations exist between the ionization potential and σ^+ values for substituted benzenes (*11*). Recently substituent effects related to the Hammett constant (σ) were used to explain trends observed in the newly developed technique of resonant two photon ionization spectroscopy (*12*). Based

[1] Current address: E. I. du Pont de Nemours & Co., Marshall R&D Laboratory, Philadelphia, PA 19146.

0003-2700/86/0358-2121$01.50/0 © 1986 American Chemical Society

on this history of use, was have used Hammett constants to correlate our (CE/CI)MS data. We will also demonstrate that the (CE/CI)MS behavior of substituted PAH is predictable based upon ionization potentials obtained from molecular orbital calculations.

EXPERIMENTAL SECTION

Mass spectra were acquired on a Hewlett-Packard 5985B GC/MS system equipped with a dual ionization source (EI and CI). The mixed reagent gas (15% or 10% methane in argon) (Linde Co., Indianapolis, IN) was introduced into the ion source through a modified transfer line (*13*). The electron energy for the (CE/CI)MS experiments was set at 230 eV. The fluorinated benzenes were studied by use of a 10% mixture of methane in argon at an ion source pressure of 0.4 torr (capacitance manometer). All other investigations utilized a 15% mixture of methane in argon. The flow of the mixed reagent gas was increased until an $(M + H)^+/M^+$ ratio of approximately 1.0 was achieved for the internal standard, 1,2,3,5-tetrafluorobenzene (TFB) (Aldrich, Milwaukee, WI). This corresponded to an ion source pressure of about 0.6 torr. For this study, an ion source temperature of 250 °C was used. The ion source temperature was measured by a thermocouple located in the ion source body.

One-microliter methylene chloride (MCB, Cincinnati, OH) solutions, containing approximately 20 ng/μL of each standard (Aldrich, Milwaukee, WI), were loaded in the splitless mode (injector temperature) 280 °C) for 0.7 min onto a 30-m (0.25-μm film thickness) DB-5 capillary column (J and W Scientific Inc., Ranchero, CA) employing helium as the carrier gas at a head pressure of 11 psi. The temperature program was adjusted according to the compounds being analyzed.

The mass spectrometer was tuned prior to each set of experiments using a binary mixture of perfluorotributylamine (PFTBA) (PCB Research Chemicals, Inc., Gainesville, FL) and TFB. A complete mass spectrum (50–300 daltons) was then obtained for each compound. All subsequent mass spectral data were collected by using selected ion monitoring. The complete M^+ and $(M + H)^+$ mass spectral peak profiles of each compound were examined by use of selected ion monitoring software. This was accomplished by stepping across the M^+ and $(M + H)^+$ peaks at 0.1-dalton intervals followed by integration ±0.2 daltons from the peak maxima. The $(M + H)^+/M^+$ ratios were corrected for the natural abundance of carbon-13.

All molecular orbital calculations reported here were carried out as follows. Input geometrics of PAH were entered into the next editor of Indiana University's CDC Cyber 170/855. The calculations were performed with an enlarged version of Dewar and Thiel's MNDO program (*14*). At the start of the calculation, the carbon skeleton and adjacent hydrogens were assumed to be completely planar (except methyl hydrogens) with uniform bond lengths and angles. The aromatic C–C bonds were input as 1.4 Å, the aromatic aliphatic C–C as 1.5 Å, C–O as 1.4 Å, C–N as 1.4 Å, C–Cl as 1.7 Å, C–F as 1.3 Å, C=O as 1.2 Å, C≡N as 1.2 Å, N–O as 1.2 Å, O–H as 1.0 Å, and C–H as 1.1 Å. All planar bond angles were 120°. The initial carbon skeleton geometry was then optimized by minimizing the total energy with respect to the planar bond lengths and angles using the Davidson–Fletcher–Powell (DFP) algorithm, which is incorporated into the MNDO program (*15*). In addition to the optimization listed above, the substituent groups were also optimized with respect to the dihedral angle.

RESULTS AND DISCUSSION

The mass spectra of most substituted PAH obtained under electron impact (EI) and chemical ionization (CI) conditions are simple consisting of either a molecular ion or a protonated molecular ion with little fragmentation. For example, Figure 1 shows the mass spectra of 1-cyanonaphthalene analyzed by four different types of ionization. The EI mass spectrum (Figure 1a) is dominated by the molecular ion m/z 153 and a loss of HCN is observed (m/z *126*). The argon CI mass spectrum (Figure 1b) is similar to the EI mass spectrum; both spectra display intense molecular ions with corresponding losses of HCN. This finding is not surprising because Hunt and Gale found that nitrogen, another charge exchange gas,

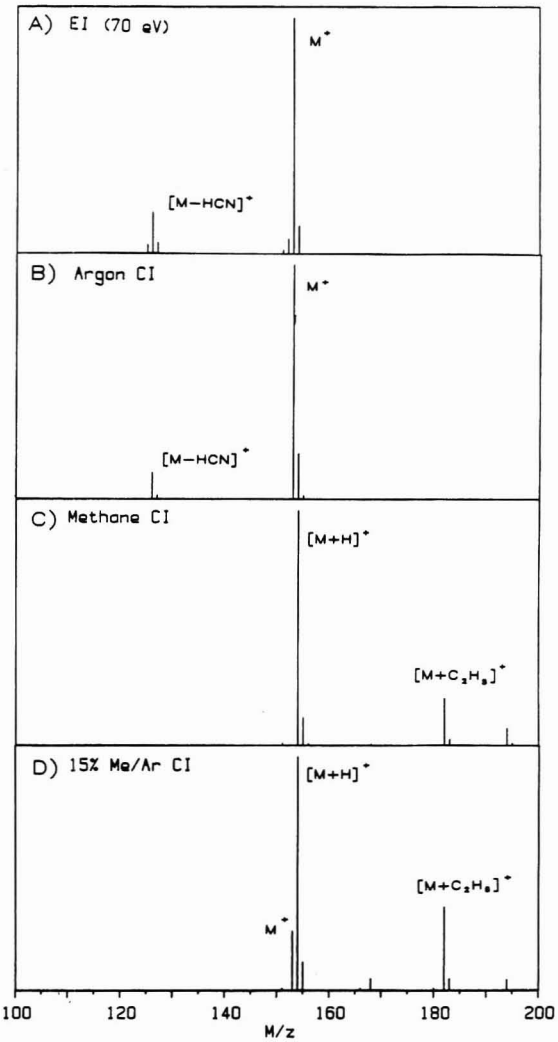

Figure 1. Mass spectra of 1-cyanonaphthalene analyzed by different ionizing methods. All spectra were obtained at an ion source tempertaure of 250 °C; the CIMS spectra were acquired at an ion source pressure of 0.6 torr.

gave mass spectra similar to electron impact (*16*). The methane CI mass spectrum (Figure 1c) is dominated by the protonated molecular ion and has adduct ions at masses 168, 182, and 194 corresponding to $[M + CH_3]^+$, $[M + C_2H_5]^+$, and $[M + C_3H_5]^+$. No fragmentation is observed. The (CE/CI) mass spectrum (Figure 1d) has a characteristic of both the argon and methane CI spectra. Molecular, protonated molecular, and adduct ions are all observed. Therefore, in a single experiment one obtains both EI and CI information.

The mixed reagent gas mass spectra of the remaining substituted naphthalenes had characteristics similar to that of 1-cyanonaphthalene. The majority of the ion current (>90%) was concentrated in the M^+, $(M + H)^+$, and $(M + C_2H_5)^+$ ions. The monobrominated and mononitrated compounds behaved differently. The monobrominated naphthalenes gave a base peak at m/z 156 corresponding to $[M - Br + C_2H_5]^+$. The base peak of the mononitronaphthalenes was $[M - 30]^+$, which we attribute to a loss of NO. The bond strengths of the bromo and nitro groups bonded to an aromatic ring are lower by at least 15 kcal/mol when compared to the other substituents (*17*). This may be the reason for the observed anomalies.

Single Substituents. The σ^+ constants of Brown and Okamoto (*18*) yield higher correlations with experimental IP's than do the normal Hammett constants (*9*). Since the (CE/CI)MS technique is very sensitive to the IP of a particular compound (*1*), we selected to use these modified constants. If a Hammett type relationship exists under (CE/CI)MS

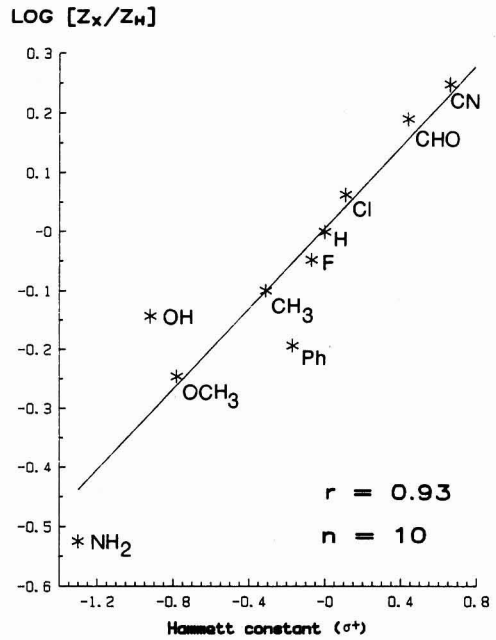

Figure 2. Hammett plot for 1-substituted naphthalenes. All σ^+ values were taken from ref 8 except for CHO, which was taken from ref 20. Z_H and Z_x refer to the $(M + H)^+/M^+$ ratios of the unsubstituted and substituted naphthalenes, respectively.

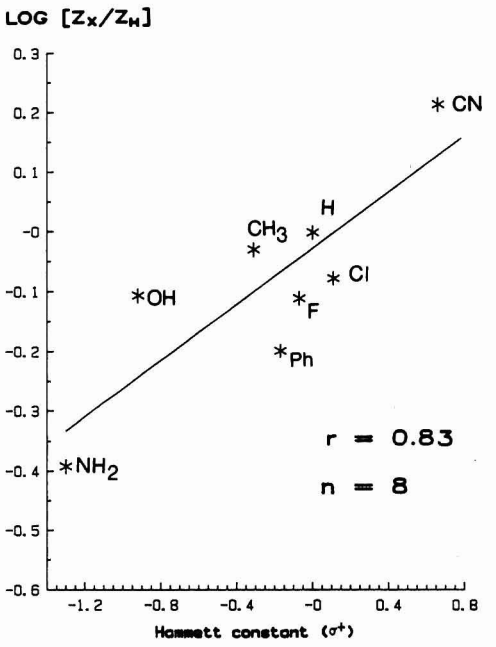

Figure 3. Hammett plot for monosubstituted benzenes. All σ^+ values were taken from ref 8 except for CHO, which was taken from ref 20. Z_H and Z_x refer to the $(M + H)^+/M^+$ ratios of the unsubstituted and substituted benzenes, respectively.

conditions, then a plot of the following equation should be linear:

$$\log (Z_x/Z_H) = \rho\sigma^+$$

where Z_H and Z_x are the experimentally determined $(M + H)^+/M^+$ ratios of the unsubstituted and substituted compounds, respectively, σ^+ is the Hammett σ^+ value of the substituent, and ρ is the reaction constant, which indicates the magnitude of an effect that a substituent exerts on the particular reaction.

Figure 2 shows a plot of this equation for a series of ten 1-substituted naphthalenes. Neither 1-bromonaphthalene nor 1-nitronaphthalene were included in this plot for the reasons discussed above. The linear correlation coefficient (r) is 0.93,

Table I. IP and $(M + H)^+/M^+$ Data for Fluorinated Benzenes

compound	mol wt	ionization potential, eV exptl[a]	ionization potential, eV MNDO	$(M + H)^+/M^+$[b]	std dev[c]	N[d]
fluorobenzene	96	9.23	9.467	2.308	0.008	3
1,4-difluorobenzene	114	9.26	9.557	1.357	0.002	3
1,2-difluorobenzene	114	9.40	9.688	1.413	0.002	3
1,3-difluorobenzene	114	9.42	9.728	1.690	0.035	3
1,2,4-trifluorobenzene	132	9.34	9.836	0.689	0.002	3
1,2,3-trifluorobenzene	132		10.067			
1,3,5-trifluorobenzene	132	9.51	10.138	0.912	0.006	3
1,2,4,5-tetrafluorobenzene	150	9.36	10.030			
1,2,3,5-tetrafluorobenzene	150	9.56	10.177	0.474	0.005	3
1,2,3,4-tetrafluorobenzene	150	9.58	10.175			
pentafluorobenzene	168	9.77	10.406	0.155	0.002	3
hexafluorobenzene	186	9.99	10.766	0.031	0.001	3

[a] Values taken from ref 16, except the IP of 1,2,4-trifluorobenzene was taken from ref 21. [b] Conditions were an ion source temperature of 250 °C and a source pressure of 0.4 torr using a 10% mixture of methane in argon. All abundances have been corrected for the natural abundance of carbon-13. [c] Standard deviation of an individual measurement. [d] Number of measurements.

which is highly significant ($p < 0.01$). Figure 3 shows a similar trend for a series of substituted benzenes ($r = 0.83$). We conclude that the Hammett equation is valid for (CE/CI)MS conditions. The slopes of the lines seen in Figures 2 and 3 are positive, signifying that electron-withdrawing groups increase the $(M + H)^+/M^+$ ratio.

These observations can be explained in the following manner. The Hammett constant characterizes the ability of various substituents to stabilize or destabilize an ionic state based on the substituent's electron-withdrawing or releasing properties. For example, an amino substituent ($\sigma^+ = -1.3$) strongly releases electron character into the electron cloud of PAH and will stabilize a radical cation. This results in a lowering of the IP; for example, 1-aminonaphthalene has a lower IP relative to naphthalene (7.38 eV vs. 8.15 eV) (*19*). A decrease in the IP increases the rate of charge exchange with argon, which results in a decrease in the $(M + H)^+/M^+$ ratio. On the other hand an electron-withdrawing substituent such as the cyano moiety ($\sigma^+ = 0.66$) destablizes the ionic state; hence, an increase in the IP of 1-cyanonaphthalene relative to naphthalene is seen (8.61 eV vs. 8.15 eV) (*19*). Raising the IP slows the rate of charge exchange although the rate of protonation is not affected (*1*). This results in a relative increase in the rate of protonation; hence, larger $(M + H)^+/M^+$ ratios are observed for electron-withdrawing substituents. No attempt was made to correlate the observed $(M + H)^+/M^+$ behavior with the numerous other modified σ constants (*8*).

Multiple Substituents. We would predict that the addition of more electron-releasing substituents (negative σ^+ values) would further decrease the $(M + H)^+/M^+$ ratio. For example, we observed that as one increases the number of fluorine substituents, the $(M + H)^+/M^+$ ratio decreases (see Table I). However, the addition of more than one fluororine

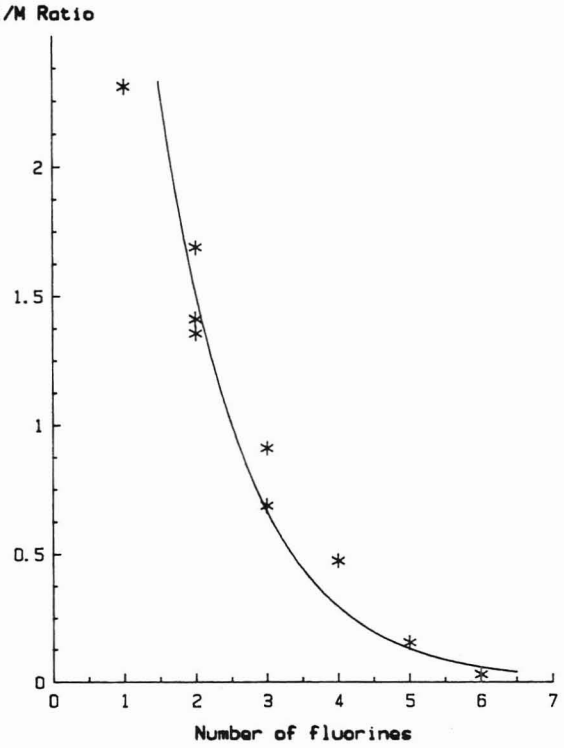

Figure 4. $(M + H)^+/M^+$ ratio vs. the number of fluorines substituted on a benzene ring. Conditions are listed in Table I.

to a benzene ring no longer stabilizes the radical cation as reflected by an *increase* in the experimental IP. We would predict from our CE/CI model that an increase in the IP would result in a corresponding increase in the $(M + H)^+/M^+$ ratio, although the opposite trend is observed (see Figure 4). The reason for this contradicting observation may be the following:

It has been suggested for alkyl and halo substituents that ring protonation occurs in a position para to the site of substituent (*20*). Therefore, by the addition of another fluorine atom in the para position we prevent protonation at that location. We still observe a large amount of $(M + H)^+$ formation, which suggests that protonation occurs at several sites on the molecule. Our model does predict correctly the ordering of the $(M + H)^+$ ratios for the difluoro compounds among themselves. Examination of the trifluorobenzenes reveals the same behavior. A higher IP is observed relative to the less substituted compounds, but a lower $(M + H)^+/M^+$ is observed because less sites are available for protonation. The trifluoro compound with the larger IP also has the higher $(M + H)^+/M^+$ ratio. The extreme case is hexafluorobenzene, which has the highest IP of the fluorobenzenes although it yields the lowest ratio. This is a consequence of the nearly complete blocking of all protonating sites.

Analytical Utility. The resulting EI mass spectra of positional isomers of substituted PAH are, in most cases, indistinguishable. For example, neither 1- or 2-naphthylamine nor 1- or 2-chloronaphthalene are distinguished by EIMS (*22*). Because the (CE/CI)MS technique is sensitive to small differences in molecular structure, similar compounds give different CE/CI mass spectra.

As discussed above, the power of the (CE/CI)MS technique is its ability to predict the (CE/CI)MS behavior of isomers without possessing the compounds in pure form (*1*). All that is necessary are IP's of the isomers in question and a mass spectrometer equipped to do chemical ionization. Because we did not want to limit ourselves to the analysis of compounds for which IP's are available from the literature, we decided to use calculated IP's obtained by the MNDO method of Dewar and Thiel with geometric optimization (*14*). The

Table II. Comparison between Experimental Ionization Potentials and Those Calculated by the MNDO Method for Substituted Aromatic Compounds

compound name	IP, eV lit.[a]	IP, eV MNDO[b]
1-aminonaphthalene	7.38	8.348
1-methoxynaphthalene	7.72	8.292
1-naphthol	7.77	8.345
aniline	7.86	8.209
2-methoxynaphthalene	7.87	8.459
2-naphthol	7.88	8.486
2-methylnaphthalene	7.97	8.569
1-methylnaphthalene	7.98	8.549
fluorenone	8.20	8.757
phenalene-1-one	8.36	8.953
biphenyl	8.37	8.650
1-naphthaldehyde	8.43	8.853
p-xylene	8.46	9.178
o-xylene	8.58	9.235
1-nitronaphthalene	8.60	9.302
1-cyanonaphthalene	8.61	8.937
phenol	8.61	8.889
m-xylene	8.63	9.233
2-nitronaphthalene	8.67	9.299
benzo[*c*]cinnoline	8.69	9.130
toluene	8.85	9.281
chlorobenzene	9.09	9.625
fluorobenzene	9.23	9.468
1,4-difluorobenzene	9.26	9.557
1,2,4-trifluorobenzene	9.34	9.836
1,2,4,5-tetrafluorobenzene	9.36	10.030
1,2-difluorobenzene	9.40	9.688
1,3-difluorobenzene	9.42	9.728
1,3,5-trifluorobenzene	9.51	10.137
1,2,3,5-tetrafluorobenzene	9.56	10.177
1,2,3,4-tetrafluorobenzene	9.58	10.175
cyanobenzene	9.70	9.817
pentafluorobenzene	9.77	10.406
nitrobenzene	9.93	10.311
hexafluorobenzene	9.99	10.766

[a] Values taken from ref 19; IP of 1,2,4-trifluorobenzene taken from ref 21. [b] Calculated using geometric optimization.

MNDO method has been previously demonstrated to yield calculated molecular parameters in accord with experimental results for PAH (*23–25*). Table II compares the calculated IP's for 35 substituted aromatic compounds to literature values. A high linear correlation coefficient was found (r = 0.97, N = 35). Hence, we conclude that the IP's calculated by the MNDO method are reliable for our work and elected to use these values over experimental ones.

Naphthalenes. Table III summarizes the data for the mono-, di-, and trisubstituted naphthalenes. There are only two isomers of each group of monosubstituted naphthalenes. We could not resolve the monomethylnaphthalenes employing only (CE/CI)MS; however, the resolution of these species is easily accomplished by GC. The remaining groups of isomeric monosubstituted naphthalenes are easily distingished using (CE/CI)MS. In all cases, the isomer with the larger calculated IP had the larger $(M + H)^+/M^+$ ratio. For example, the calculated IP for 2-naphthol is greater than the IP for 1-naphthol by 0.141 eV, which is reflected by an increase of 0.317 ratio units. Likewise, 2-methoxynaphthalene has a calculated IP that is 0.167 eV larger than 1-methoxynaphthalene and has a correspondly higher $(M + H)^+/M^+$ ratio (0.255 ratio units).

Notice that as the degree of methyl substitution is increased from zero (naphthalene) to three (2,3,6-trimethylnaphthalene) a corresponding decrease is seen in the $(M + H)^+/M^+$ ratio. We attribute this to a combination of the decrease of the available sites for protonation and the lowering of the IP relative to naphthalene.

Table III. IP and $(M + H)^+/M^+$ Data for Substituted Naphthalenes

compound	mol wt	ionization potential (eV) explt[a]	ionization potential (eV) MNDO	$(M + H)^+/M^+$[b]	std dev[c]	N[d]
naphthalene	128	8.15	8.575	2.080	0.097	20
1-naphthol	144	7.77	8.345	1.497	0.024	4
2-naphthol	144	7.88	8.486	1.814	0.027	4
1-methylnaphthalene	142	7.98	8.549	1.655	0.030	11
2-methylnaphthalene	142	7.97	8.569	1.677	0.023	10
2,3-dimethylnaphthalene	156	7.89	8.556	1.364	0.060	4
2,6-dimethylnaphthalene	156		8.558	1.186	0.041	4
2,3,6-trimethylnaphthalene	170		8.548	0.912	0.010	4
1-naphthaldehyde	156	8.43	8.853	3.223	0.023	4
2-naphthaldehyde	156		8.867	3.464	0.081	4
1-methoxynaphthalene	158	7.72	8.292	1.182	0.036	4
2-methoxynaphthalene	158	7.87	8.459	1.437	0.028	4

[a] Values taken from ref 19. [b] All ratios corrected for natural abundance of carbon-13. [c] Standard deviation of individual measurement. [d] Number of measurements.

Phenanthrenes and Anthracenes. Table IV summarizes the data for the substituted phenanthrenes and anthracenes. The addition of a methyl group lowers the $(M + H)^+/M^+$ ratio relative to the parent PAH for the reasons previously discussed. Particularly interesting is the case of both 9,10-dimethylphenanthrene and 4,5-dimethylphenanthrene. These compounds yield much lower $(M + H)^+/M^+$ ratios (0.382 and 0.545, respectively) than would be expected based on the calculated IP. For the former, we think that the methyl groups block protonation at the K region where protonation would be expected because of the high electron density of this area. The low ratio of the 4,5-isomer also suggests that significant protonation occurs at this region of the molecule.

Although we are not able to predictively distinguish all positionally substituted isomers, we can easily tell if a methyl-substituted PAH with a molecular weight of 192 is a methylanthracene or methylphenanthrene. This cannot be done with EIMS. Note that the methylanthracenes cluster in one group (with an average $(M + H)^+/M^+$ ratio of 0.59) while the methylphenanthrenes cluster in another group (with an average ratio of 1.31). This observation could be used in the petroleum industry where it is generally accepted to report only the total amount of structural isomers present (*26*). (CE/CI)MS provides additional data in a predictive manner.

Amino polycyclic aromatic hydrocarbons (amino-PAH) have been cited as the principal microbial mutagens in coal liquids (*3*). Amino-PAH comprise about 1% of the weight of these liquids while they account for approximately 98% of the mutagenic activity. We have employed (CE/CI)MS for the analysis of two amino-PAH standards: 1-aminoanthracene and 9-aminophenanthrene. These compounds have lower ratios than their unsubstituted homologues because of the amino group's electron-donating character. The (CE/CI)MS technique correctly predicts the ordering of ratios between these compounds (see Table IV). This illustrates that (CE/CI)MS may be suited for difficult to resolve mutagenic amino-PAH.

Table IV. IP and $(M + H)^+/M^+$ Data for Substituted Phenanthrenes and Anthracenes

compound	mol wt	IP-(MNDO), eV	$(M + H)^+/M^+$[a]	std dev[b]	N[c]
anthracene	178	8.049	0.661	0.030	57
phenanthrene	178	8.479	1.518	0.072	68
9-methylanthracene	192	8.026	0.540	0.012	4
1-methylanthracene	192	8.032	0.602	0.011	4
2-methylanthracene	192	8.049	0.627	0.021	4
3-methylphenanthrene	192	8.462	1.258	0.005	3
9-methylphenanthrene	192	8.463	1.231	0.036	4
1-methylphenanthrene	192	8.465	1.364	0.052	4
2-methylphenanthrene	192	8.486	1.406	0.023	3
4,5-dimethylphenanthrene	206	8.417	0.545	0.019	3
1,8-dimethylphenanthrene	206	8.436	0.971	0.030	3
3,6-dimethylphenanthrene	206	8.439	1.193	0.021	3
9,10-dimethylphenanthrene	206	8.441	0.382	0.012	3
1-aminoanthracene	193	7.952	0.468	0.002	2
9-aminophenanthrene	193	8.331	0.617	0.004	2

[a] All ratios corrected for natural abundance of carbon-13. [b] Standard deviation of an individual measurement. [c] Number of measurements.

CONCLUSION

This study examined substituent effects in (CE/CI)MS. We have shown that the Hammett equation was valid under (CE/CI)MS conditions and that the (CE/CI)MS behavior is a function of ionization potential and steric factors for a series of multisubstituted methylated PAH and fluorinated benzenes. We have demonstrated that calculated IP's agree well with experimental IP's for substituted compounds. We were able to predict the correct isomer in the absence of standard compounds for substituted naphthalenes, and we think this could be extrapolated to larger ring systems, particularly the highly mutagenic amino-PAH. Unfortunately, the nitro-PAH fragmented extensively, and we were not able to predict their (CE/CI)MS behavior. Finally, the method was evaluated as a potential predictive method for methylated-PAH. We were able to distinguish groups of methylated isomeric PAH arising from different parent PAH.

ACKNOWLEDGMENT

We are grateful to Indiana University's Bloomington Academic Computing Services for use of their facilities. We also thank Beth Stemmler for helpful discussions and Milos Novotny for furnishing some of the methylated-PAH used in this study.

Registry No. Naphthalene, 91-20-3; 1-naphthol, 90-15-3; 2-naphthol, 135-19-3; 1-methylnaphthalene, 90-12-0; 2-methylnaphthalene, 91-57-6; 2,3-dimethylnaphthalene, 581-40-8; 2,6-dimethylnaphthalene, 581-42-0; 2,3,6-trimethylnaphthalene, 829-26-5; 1-naphthaldehyde, 66-77-3; 2-naphthaldehyde, 66-99-9; 1-methoxynaphthalene, 2216-69-5; 2-methoxynaphthalene, 93-04-9; anthracene, 120-12-7; phenanthrene, 85-01-8; 9-methylanthracene,

779-02-2; 1-methylanthracene, 610-48-0; 2-methylanthracene, 613-12-7; 3-methylphenanthrene, 832-71-3; 9-methylphenanthrene, 883-20-5; 1-methylphenanthrene, 832-69-9; 2-methylphenanthrene, 2531-84-2; 4,5-dimethylphenanthrene, 3674-69-9; 1,8-dimethylphenanthrene, 7372-87-4; 3,6-dimethylphenanthrene, 1576-67-6; 9,10-dimethylphenanthrene, 604-83-1; 1-aminoanthracene, 610-49-1; 9-aminophenanthrene, 947-73-9; fluorobenzene, 462-06-6; 1,4-difluorobenzene, 540-36-3; 1,2-difluorobenzene, 367-11-3; 1,3-difluorobenzene, 372-18-9; 1,2,4-trifluorobenzene, 367-23-7; 1,2,3-trifluorobenzene, 1489-53-8; 1,3,5-trifluorobenzene, 372-38-3; 1,2,4,5-tetrafluorobenzene, 327-54-8; 1,2,3,5-tetrafluorobenzene, 2367-82-0; 1,2,3,4-tetrafluorobenzene, 551-62-2; pentafluorobenzene, 363-72-4; hexafluorobenzene, 392-56-3; 1-cyanonaphthalene, 86-53-3; 1-aminonaphthalene, 134-32-7; aniline, 62-53-3; fluorenone, 486-25-9; phenalen-1-one, 548-39-0; biphenyl, 92-52-4; *p*-xylene, 106-42-3; *o*-xylene, 95-47-6; 1-nitronaphthalene, 86-57-7; phenol, 108-95-2; *m*-xylene, 108-38-3; 2-nitronaphthalene, 581-89-5; benzo[*c*]cinnoline, 230-17-1; toluene, 108-88-3; chlorobenzene, 108-90-7; cyanobenzene, 100-47-0; nitrobenzene, 98-95-3.

LITERATURE CITED

(1) Simonsick, W. J., Jr.; Hites, R. A. *Anal. Chem.* **1984**, *56*, 2749–2754.
(2) Hecht, S. S.; Loy, M.; Hoffman, D. In *Carcinogenesis—A Comprehensive Survey*; Jones, R. W., Freudenthal, R. I., Ed.; Raven Press: New York, 1976; Vol. 1, p 325.
(3) Wilson, B. W.; Pelroy, R.; Cresto, J. T. *Mutagen Res.* **1980**, *79*, 193–202.
(4) Mermelstein, R.; Kirlazides, D. K.; Butler, M.; McCoy, E. C.; Rosenkranz, H. S. *Mutagen Res.* **1981**, *89*, 187–196.
(5) Jennings, K. R. In *Gas Phase Ion Chemistry*; Bowers, M. T., Ed.; Academic Press: New York, 1979; Vol. 2, p 123.
(6) Keough, T. *Anal. Chem.* **1982**, *54*, 2540–2547.
(7) Hammett, L. P. *J. Am. Chem. Soc.* **1937**, *59*, 96–103.
(8) Lowry, T. H.; Richardson, K. S. In *Mechanism and Theory in Organic Chemistry*; 2nd ed.; Harper and row: New York, 1981; pp 113–225.
(9) Bursey, M. M. *Org. Mass Spectrom.* **1968**, *1*, 31–46.
(10) Field, F. H. *J. Am. Chem. Soc.* **1969**, *91*, 6334–6341.
(11) Levsen, K. In *Fundamental Aspects of Organic Mass Spectrometry*; Weinheim: New York, 1978; pp 19–21.
(12) Tembreull, R.; Sin, C. H.; Ping, L.; Pang, H. M.; Lubman, D. M. *Anal. Chem.* **1984**, *57*, 1186–1192.
(13) Jensen, T.; Kaminsky, R.; McVeety, B. D.; Wozniak, T. J.; Hites, R. A. *Anal. Chem.* **1982**, *54*, 2388–2390.
(14) Dewar, M. J. S.; Thiel, W. *J. Am. Chem. Soc.* **1977**, *99*, 4899–4907.
(15) Fletcher, R.; Powell, J. J. D. *Comput. J.* **1963**, *6*, 163–168.
(16) Hunt, D. F.; Gale, P. J. *Anal. Chem.* **1984**, *56*, 1111–1114.
(17) Cox, J. D.; Pilcher, G. In *Thermochemistry of Organic and Organometallic Compounds*; Academic Press: London, 1970.
(18) Brown, H. C.; Okamoto, Y. *J. Am.* Chem. *Soc.* **1958**, *80*, 4979–4987.
(19) Levin, R. D.; Lias, S. G. *Natl. Stand. Ref. Data Ser.* (*U.S. Natl. Bur. Stand.*) **1982**, *No. 71*.
(20) Lau, Y. K.; Kebarle, P. K. *J. Am. Chem. Soc.* **1956**, *98*, 7452–7453.
(21) Rosenstock, H. M.; Herron, J. T.; Draxl, K.; Steiner, B. W. "Energetics of Gaseous Ions", *J. Phys. Chem. Ref. Data Suppl.* **1977**, *6*, I365.
(22) Hites, R. A. *Handbook of Mass Spectra of Environmental Contaminants*; CRC Press: Boca, Raton, FL, 1985; pp 84, 85, 188, 189.
(23) Dewar, M. J. S.; Thiel, W. *J. Am. Chem. Soc.* **1977**, *99*, 4907–4917.
(24) Ford, G. P.; Scribner, J. D. *J. Am. Chem. Soc.* **1981**, *103*, 4281–4291.
(25) Mirek, J.; Buda, A. *Z. Naturforsch.*, A **1984**, *39a*, 386–390.
(26) White, C. M. In *Handbook of Polycyclic Aromatic Hydrocarbons*, Ed., Bjorseth, A., Ed.; Marcel Dekker: New York, 1983; pp 525–616.

RECEIVED for review February 4, 1986. Accepted April 16, 1986. Supported by the U.S. Department of Energy (Grant No. 80EV-10449).

Application of Particle Desorption Mass Spectrometry to the Characterization of Minerals

W. R. Summers and E. A. Schweikert*

Center for Chemical Characterization & Analysis, Texas A&M University, College Station, Texas 77843-3144

Four mineral specimens were analyzed by particle desorption mass spectrometry using californium-252 as the primary ion source. Pollucite, amblygonite, microcline, and lepidolite, chosen for their high alkali metal content, were characterized with no apparent decrease in the extraction field strength even though the samples were thick and insulating. Further, given the very low bombarding ion fluence, no complications due to charge accumulation on the sample were encountered. Qualitative results obtained by PDMS were validated by XPS, EMP, and SIMS. PDMS provides for a rapid, nondestructive determination of alkali metals in complex natural matrices with minimal sample preparation.

Geological materials represent a challenging case for surface characterization methods that employ charged particles as the probe or signal beam, due to their heterogeneity and insulating nature. Techniques currently applied in the analysis of geological specimens include SIMS, LAMMA, and especially EMP (*1*). Each of these techniques has strengths and limitations. EMP can provide quantitative data for elements of $Z \geq 11$ and with detection limits ≥0.1 atom % (*2*, *3*). SIMS and LAMMA both can provide isotopic and molecular information with detection limits as low as 10^{-4} atom % (*4*). For geological specimens, SIMS is semiquantitative because the yield of the secondary ions emitted is strongly matrix dependent (*5*). LAMMA is less prone to charge buildup problems since the probe beam consists of photons and the signal beam is of extremely low current; however, the sample spot addressed is destroyed in the analysis process (*6–8*).

The present study examines the feasibility of applying particle desorption mass spectrometry for examining geological specimens. The method is based on the desorption of atomic and molecular species from surfaces bombarded by fast heavy ions ($Z \geq 20$; $E \geq 0.5$ MeV/amu). This phenomenon was first observed by Macfarlane (*9*). Particle-induced desorption coupled with time-of-flight mass spectrometry (usually referred to as PDMS) has been applied successfully for the characterization of large involatile biomolecules (*10*, *11*). In the realm of materials characterization, the application of PDMS in a microscopic mode has recently been discussed (*12*). The present paper presents the first results of PDMS applied on geological materials.

The strong suits of PDMS are (a) the sample amount consumed is negligible and (b) the primary ion current required for PDMS is low; thus charge buildup and sample damage are avoided.

This study like most PDMS work to date used as the beam of heavy ions the fission fragments from a low-intensity ^{252}Cf source. The discrete nature (in time) of the fission event lends itself conveniently to time-of-flight mass spectrometry. This

0003-2700/86/0358-2126$01.50/0 © 1986 American Chemical Society

mass detection and identification mode allows simultaneous multimass, isotope-specific, elemental and molecular analysis. PDMS is a surface-sensitive technique. The sample depth probed, while varying with the nature of the matrix, appears not to exceed a few hundred Å (*13, 14*). The application of PDMS for bulk analysis requires, then, that surface contamination be controlled and kept to a minimum. Accordingly, this study was carried out in a UHV chamber. The PDMS experiment with a ^{252}Cf source is particularly well suited for UHV conditions. A compact setup can be devised featuring 10^{-9} torr vacuum; a detailed description of this setup is given elsewhere (*15*). A noteworthy characteristic is that the primary and secondary ion optics are positioned so as to address the same side of the sample, i.e., the "reflection" mode; this allows the analysis of thin or thick samples without altering the geometry of the experiment. An added advantage of using a ^{252}Cf source is that its predictable stable output is inherently most suitable for achieving precision in analysis. Conversely, the low-intensity fission fragment output and their varying characteristics (energy, atomic number) preclude microprobe analysis or fundamental studies of the desorption phenomenon.

In the subsequent sections we describe the experimental aspects of PDMS with a ^{252}Cf source and then for the case of minerals examine the performance of this method and compare PDMS with other analysis techniques.

EXPERIMENTAL SECTION

The design and operation of the apparatus used in this study are described elsewhere (*15*); however, a few pertinent details are given here. The drift length used in this series of analyses was 20 cm, which results in flight times on the order of 0.5–3 μs. The 25-μCi Cf source was positioned at 35° relative to the sample normal, and each fission event was registered in a silicon surface barrier detector (Tennelec HI-100-60-30). Desorbed ions were detected in a chevron array of microchannel plates (Galileo FTD 2002) with 1000 V across each plate. Secondary ions were extracted by a potential field of +9 kV/mm in all cases, and all spectra were acquired for 3 h. Pressure during all analyses was 2×10^{-9} mbar. Digital flight times were generated by a multistop time digitizer capable of processing 255 stops per start with 0.5 ns resolution, made at the Institute of Nuclear Physics, Orsay, France (*16, 17*). This module was hard-wired to a ND 66 MCA which was interfaced to a PDP 11/24 for data archiving. The acquisition time chosen for this series of experiments was chosen somewhat arbitrarily and can be readily reduced by 5 to 10 times by using a more intense californium source (i.e., 50 μCi instead of 25 μCi) and by designing a more compact source-sample geometry.

Geological specimens, consisting of pollucite (Bikita, Rhodesia), amblygonite and lepidolite (Keystone, SD), spodumene (Newry, ME), and microcline (Central Texas), were purchased from Ward's Natural Science Establishment, Inc., Rochester, NY. Samples were prepared by National Petrographic Service, Inc., Houston, TX, as highly polished 1 mm thick disks, 1 cm in diameter. The polishing process consisted of sequential polishing of the mineral samples with 15 μm, 6 μm, and 0.25 μm diamond pastes with intermittent washing followed by a final polish with a 0.03-μm alumina slurry. Spodumene could not be successfully prepared and was deleted. Samples were mounted onto standard aluminum SEM mounts (Ted Pella, Inc., Tustin, CA) by silver conducting paint.

SIMS analyses were performed on the Cameca IMS-3F at Texas Instruments, Dallas, TX. Primary ion current was approximately 1 μA of 10-keV O^+, with an arc current of 58 mA and raster size of 500 μm. Secondary ion extraction voltage was +4500 V. Transfer optics were 150 μm with contrast aperture and field aperture of zero. The mass resolving power was set at 300. An electron flood gun was used in the positive ion analyses to compensate for charge buildup.

EMP analysis was performed by use of a JEOL JSM-35CF with a Tracor Northern TN-2000 EDS system at the Texas A&M University Electron Microscopy Center. Samples were coated with 100 Å of carbon and the analysis area was 1 mm^2 (100× integrated area analysis). Primary beam energy was 25 keV.

XPS analyses were performed at the Surface Science Facility at Texas A&M University using the Kratos XSAM-800. Primary excitation was provided by an Al anode biased at 12 kV using 20 mA filament current. Magnification was in the "low" position, while resolution was in the "high" position.

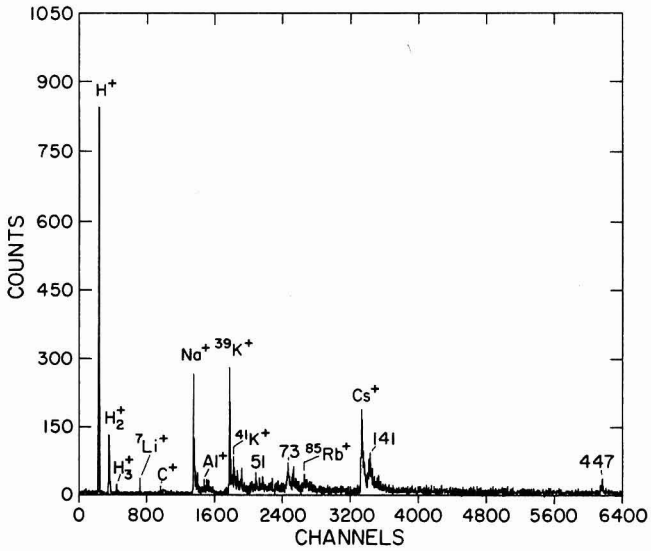

Figure 1. PDMS positive ion spectrum of pollucite, $Cs_4Al_4Si_9O_{26}{\cdot}H_2O$. Acquisition time was 3 h; sample bias was +9 kV.

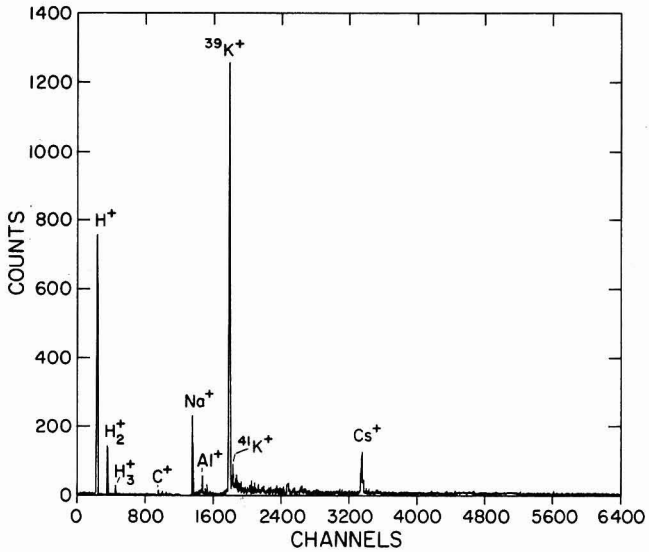

Figure 2. PDMS positive ion spectrum of microcline, $(K, Na)AlSi_3O_8$. Acquisition time was 3 h; sample bias was +9 kV.

RESULTS AND DISCUSSION

Time-of-flight spectra for pollucite, microcline, amblygonite, and lepidolite are presented in Figures 1–4, respectively. All spectra were acquired for 3 h each under identical experimental conditions. The time calibration of the spectra is 0.5 ns per channel; thus the time scale of the spectra is about 3 μs. Common to all spectra are the low mass peaks, e.g., H^+, Na^+, and K^+, which can be used to construct an empirical calibration curve of channel number vs. the square root of the mass-to-charge ratio. Additionally there is a series in all spectra of low-intensity peaks at m/z ratios of 12, 13, 14, and 15, which corresponds to hydrocarbon contaminants. Peaks present in low intensities in all spectra at m/z values of 43, 45, 51, 53, 55, 57, 61, 63, 65, 67, and 73 are attributable to impurities in the sample or contaminants from the vacuum system. The mass peaks register within a few channels (out of 8K channels) of those channel positions predicted on the

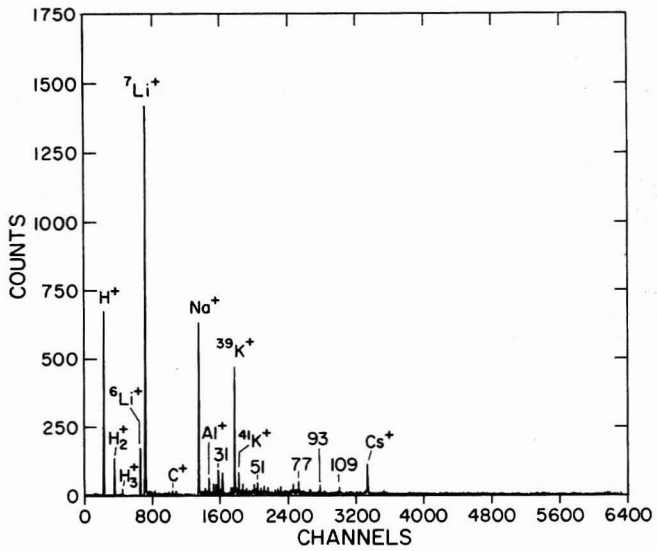

Figure 3. PDMS positive ion spectrum of amblygonite, $LiAlFPO_4$. Acquisition time was 3 h; sample bias was +9 kV.

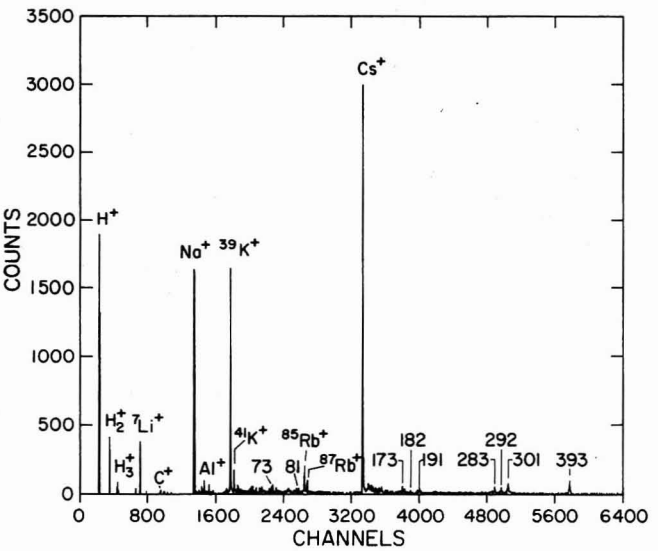

Figure 4. PDMS positive ion spectrum of lepidolite, $K_2Li_3Al_3(AlSi_3O_{10})_2$. Acquisition time was 3 h; sample bias was +9 kV.

basis of analyses of alkali halide vapor deposits, which implies that there is no decrease in extraction field strength which would be indicated by a shift toward longer flight times. This is noteworthy given the insulating nature of the samples as well as the 1 mm thickness through which the potential field must be transmitted. Finally, the occurrence of peaks such as Cs^+ in the spectra of microcline, amblygonite, and lepidolite is not expected on the basis of the mineral formulas of these samples but can be attributed to the natural substitution of alkali metal atoms for each other in the mineral matrix. The presence of these "anomalous" alkali metals was confirmed by SIMS, XPS, and EMP analyses, the results of which are discussed below for the case of lepidolite.

The time-of-flight spectrum of pollucite, a tectosilicate [$Cs_4Al_4Si_9O_{26}\cdot H_2O$], is presented in Figure 1. In addition to the expected Cs^+ peak, Na^+, K^+, Li^+, and Rb^+ peaks are also evident. Peaks at m/z ratios of 141 and 447 may be assigned to $(Al_2O_3)K^+$ and $(Al_2O_3)_4K^+$ (the absence of the dimer and trimer is perhaps attributable to lower stabilities of these species). Peaks corresponding to Mg^+, Al^+, Si^+, and SiH^+ are present in the region between Na^+ and K^+. This spectrum shows high flight time tails, which may be due to a slight decrease in the extraction field strength by the matrix itself or to a kinetic energy spread that is greater for this sample than for the others. The secondary ion yield for this sample as a whole is also markedly lower than for the others.

The time-of-flight spectrum for microcline, a tectosilicate [$(K, Na)AlSi_3O_8$], is presented in Figure 2. The sodium and potassium peaks dominate the spectrum. Cesium is also evidenced, whereas lithium and rubidium are absent. Low-intensity peaks at m/z ratios of 27 and 29 are attributed to Al^+ and SiH^+. The peaks in this spectrum are notably sharper and more intense than those in Figure 1 although both matrices are silicates.

Figure 3 shows the time-of-flight spectrum for amblygonite, a phosphate mineral [$LiAlFPO_4$]. Amblygonite is approximately 10% Li_2O by weight (*18*) and the lithium isotopes at m/z values of 6 and 7 dominate the spectrum. Sodium and potassium are present as always, and a small cesium peak is again conspicuous. A small Al^+ peak is present that is consistent with the empirical formula, while peaks at m/z values of 31 and 32 are attributed to Li^+ (LiOH) and $[Li_2F]^+$, respectively. The peak at m/z 37 is assigned to a lithium attachment molecule of Li_2O, e.g., Li^+ (Li_2O). The series at m/z 77, 93, and 109 progresses in increments of 16 daltons and is attributable to $(Li_xNa_yPO_2]^+$, where x ranges from 2 to 0 while y ranges from 0 to 2.

Figure 4 is the time-of-flight spectrum of lepidolite, a phyllosilicate [$K_2Li_3Al_3(AlSi_3O_{10})_2$], and is unique for the significant levels of all the alkali metal ions and the high secondary ion yield in general. Lepidolite is higher in Li_2O content than is amblygonite (10% vs. 3.3–7%) (*18*) and this trend is reflected in the spectra, although the matrices are dissimilar. The isotope pairs of rubidium, lithium, and potassium are all resolved, while the monoisotopic alkali metals, sodium and cesium, are also present in significant intensities. The sodium and cesium are present in such quantities as to form a series of attachment clusters (*19*) with chlorine and iodine which are also unexpectedly present in the mineral matrix. This series is of the form $[Na_xCs_yCl]^+$, where x ranges from 0 to 2 while y ranges from 2 to 0 (m/z values of 301, 191, 81). The $[Cs_2Cl]^+$ molecule has been previously observed elsewhere (*20*). The iodine series is of the form $[Na_xCs_yI]^+$ where x ranges from 0 to 2 while y ranges from 2 to 0 (m/z values of 393, 283, 173). Peaks at m/z values of 292, 182, and 72 (masked by the m/z 73 contaminant peak) are attributable to the series $(Na_xCs_yCN]^+$, where x ranges from 0 to 2 while y ranges from 2 to 0.

The high level of cesium, which was not expected given the empirical formula of lepidolite, as well as lower levels of cesium in microcline and amblygonite, was attributed at first to cesium contamination on either the extraction grid or sample surface. To clarify the origin of cesium, the samples were analyzed by SIMS, XPS, and EMP. Since the effect was most pronounced in lepidolite, only results from this sample are presented here.

The presence of cesium was confirmed in the lepidolite sample by the observation of the $3d_{3/2}$, $3d_{5/2}$ couplet at 740.1 eV and 726.1 eV, respectively, in the XPS spectrum. Further confirmation came upon the observation of peaks in the SIMS spectrum at m/z values of 133 and 66.5, corresponding to Cs^+ and Cs^{2+}, respectively. Those observations exclude a cesium contamination of the secondary ion extraction grid. To ensure that the cesium was not just a surface contaminant, the lepidolite sample was sputter cleaned for 5 min with 5-keV Ar^+ and then reanalyzed by XPS. The cesium couplet remained unchanged in intensity, while the oxygen 1s peak increased in intensity, indicating liberation of the matrix oxygen. Additionally, EMP analysis demonstrated that the cesium was localized rather than being uniformly distributed over the sample surface. These observations show that the Cs^+ peaks in the desorption mass spectra are true indications of cesium

occurrence not evidenced by the empirical formulas of the mineral samples.

The results of this study demonstrate the feasibility of using ion induced desorption mass spectrometry for characterizing minerals. The method is nondestructive and is free from charging effects, which often complicate the use of charged particle beams for the surface analysis of insulating materials. It is also highly sensitive to the alkali metals and confirms the natural process of substitution of these ion species for each other in mineral matrices. The results presented are not quantitative, due in large part to the pronounced matrix effects that influence secondary ion yields. The desorption process is most efficient for elements with low ionization potentials. This is evidenced by the conspicuous absence of silicon and oxygen, which are present as major components of the sample matrix.

ACKNOWLEDGMENT

The experimental assistance of C. D. McAfee is hereby acknowledged. The XPS and EMP analyses were performed at the Texas A&M University Surface Science Facility. Beam time for the SIMS analyses was graciously provided by J. M. Anthony at Texas Instruments Central Research Labs in Dallas, TX, where W.R.S. participated in a short-term collaboration.

Registry No. ^{252}Cf, 13981-17-4; pollucite, 1308-53-8; amblygonite, 1302-58-5; microline, 12251-43-3; lepidolite, 1317-64-2.

LITERATURE CITED

(1) Moore, C.; Canepa, J. *Anal. Chem.* **1985**, *57*, 88R–94R.
(2) Colby, J. W. In *Practical Scanning Electron Microscopy*; Goldstein, J. I., Yakoitz, H., Eds.; Plenum Press: New York, 1975; pp 529–572.
(3) Benninghoven, A. *Trends Anal. Chem.* **1984**, *3*(5), 112–115.
(4) Turner, N.; Dunlap, B.; Colton, R. *Anal. Chem.* **1984**, *56*, 373R-416R.
(5) Slodzian, G. *SIMS III*; Benninghoven, A., et al., Eds.; Springer-Verlag: Berlin, Heidelberg, New York, Tokyo, 1983; pp 115–123.
(6) Conzemius, R.; Simons, D.; Shankai, Z.; Byrd, G. In *Microbeam Analysis—1983*; Gooley, R., Ed.; San Francisco Press: San Francisco, CA, 1983; pp 301–332.
(7) Simons, D. *Int. J. Mass Spectrom. Ion Processes* **1984** *55*, 15.
(8) Shaeffer, O. A. *ACS Symp. Ser.* **1982**, *No. 176*, 139–148.
(9) Torgerson, D.; Skowronski, R.; Macfarlane, R. *Biochem. Biophys. Res. Commun.* **1974**, *60*, 616–620.
(10) Macfarlane, R. *Acc. Chem. Res.* **1982**, *15*, 268–275.
(11) Macfarlane, R. *Anal. Chem.* **1983**, *55*, 1247A–1263A.
(12) Filpus-Luyckx, P. Ph.D. Dissertation, Texas A&M University, College Station, TX, 1985.
(13) Gunthier, W.; Becker, O.; Della-Negra, S.; Knippelberg, W.; LeBeyec, Y.; Wienhert, U.; Wien, K.; Wiesser, P.; Wurster, R. *Int. J. Mass Spectrom. Ion Processes* **1983**, *53*, 185.
(14) Macfarlane, R. D. *J. Trace Microprobe Tech.* **1985**, *2*(3,4), 267–291.
(15) Summers, W. R.; Schweikert, E. A. *Rev. Sci. Instrum.* **1986**, *57*(4), 692–694.
(16) Festa, E.; Sellem, R. *Nucl. Instrum. Methods* **1981**, *188*, 99–104.
(17) Festa, E.; Sellem, R.; Tassan-Got, L. *Nucl. Instrum. Methods Phys. Res., Sect. A* **1985**, *A234*, 305–314.
(18) Hurlburt, C. S. In *Dana's Manual of Mineralogy*, 18th ed.; Hurlburt, C. S., Ed.; Wiley Interscience: New York, 1971.
(19) Ens, W.; Beavis, R.; Standing, K. G. *Phys. Rev. Lett.* **1983**, *50*(1), 27–29.
(20) Castro, M. E.; Russell, D. H. *Anal. Chem.* **1985**, *57*, 2290–2293.

RECEIVED for review March 10, 1986. Accepted May 12, 1986. The authors gratefully acknowledge the financial support of the National Science Foundation under Grant CHE-8310783.

Multidimensional, Laser-Based Instrument for the Characterization of Environmental Samples for Polycyclic Aromatic Compounds

R. L. M. Dobson, A. P. D'Silva, S. J. Weeks, and V. A. Fassel*

Ames Laboratory—USDOE and Department of Chemistry, Iowa State University, Ames, Iowa 50011

A laser-based multidimensional analytical instrument that provides selective, sensitive, and on-line detection of polycyclic aromatic compounds (PAC) is described. The effluent of a capillary GC is interrogated by a tunable UV laser beam at collision-free pressures. Selective excitation/ionization occurs based primarily on the spectroscopic absorption characteristics of the analyte molecules. The laser–analyte interaction products (cations, electrons, and photons) are simultaneously monitored, permitting all of the analytically useful data to be extracted "on-the-fly". The heart of this multidimensional detection scheme is a time-of-flight mass spectrometer that provides access to an entire photoionization mass spectrum for each laser pulse. This simultaneous measurement capability simplifies the task of PAC characterization, as is qualitatively demonstrated for a synthetic organic mixture and a Paraho shale oil fraction. Absolute detection limits in the low picogram range for 21 PAC and a linear dynamic range of 4 decades are reported.

Of the thousands of chemical compounds that have been deemed mutagenic or carcinogenic it is generally agreed that the polycyclic aromatic compounds (PAC) are among the most potent (*1*). It is for this reason that a premium has been placed on the development of analytical methodology for the identification and quantitation of trace-level PAC in the environment. The many different sources, the variety of matrix compositions, and the overall complexity of most PAC-contaminated environmental samples impose several stringent requirements on methodologies for PAC determinations. Not only must the analytical approach allow detection of trace levels of both polar and nonpolar PAC in complex environmental matrices but also it must provide adequate selectivity so as to distinguish between various geometric and substitutional isomers (*2*, *3*).

Capillary column gas chromatography combined with mass spectrometry (CC/GC-MS) has become the most popular and effective analytical method for characterization of PAC in complex environmental samples (*4–6*). When employed in the conventional manner, the power of this technique is limited by the physical separation capabilities of the CC/GC, in that species that are well-resolved chromatographically are easily identified by the mass spectrometer. To minimize the impact of this limitation, environmental samples must usually undergo an extensive, time-consuming, cleanup and chemical class separation procedure prior to analysis by CC/GC-MS (*6*, *7*). However, for the case of complex samples containing a number of coeluting isomers, it is impossible to provide full

0003-2700/86/0358-2129$01.50/0 © 1986 American Chemical Society

characterization when a conventional, nonselective, ionization technique is employed prior to mass analysis (*7–9*). Therein lies the ultimate limitation of CC/GC-MS for PAC characterization. Recently, novel chemical ionization mass spectrometric techniques (*10, 11*) have been utilized to determine specific "targeted" coeluting isomer pairs; however, these approaches do not represent a general solution to this selectivity problem.

A number of state-of-the-art, laser-based, analytical spectroscopic methodologies have recently been developed to increase the specificity of PAC detection. Generally, these approaches involve prior chromatographic "mixture simplification" and/or low-temperature "spectral simplification". Three cryogenic techniques have been utilized to produce narrow band fluorescence of PAC trapped in appropriate matrices. All of these methods, namely, fluorescence line narrowing spectroscopy (FLNS) (*12*), laser-excited Shpol'skii spectroscopy (LESS) (*13*), and matrix isolation fluorescence spectroscopy (MIFS) (*14*), have demonstrated highly selective PAC determinations in complex mixtures with minimal sample preparation. Although these techniques show promise, each of them has solvent/matrix restrictions and may not provide sufficient spectral resolution for complete PAC characterization in most real samples. Obviously, such fluorescence techniques are not applicable to the determination of "dark" (nonfluorescing) species, and their solid-state nature precludes applications that require on-line monitoring.

Other workers have demonstrated the high spectral selectivity of laser-induced fluorescence (LIF) of molecules seeded in a rotationally cooled (RC) supersonic expansion (*15–19*). However, only two groups have reported the application of RC/LIF to the detection of PAC in environmental samples. Hayes and Small utilized this approach to selectively determine methylnaphthalenes in crude oil (*20*). D'Silva and coworkers demonstrated the feasibility of employing RC/LIF for on-line monitoring of certain PAC in the effluents from a fluidized bed combustor (*21*).

Lubman and co-workers (*22*) have discussed the analytical attributes of detecting rotationally cooled aromatic compounds by resonance enhanced multiphoton ionization (REMPI) mass spectrometry and have demonstrated high spectral selectivity in discriminating among several substituted benzene isomers (*23, 24*). Among the advantages of the REMPI approach are its intrinsically high sensitivity, straightforward interfacing to mass spectrometry, and ability to detect nonfluorescing species (*25*). A primary shortcoming of these gas-phase detection schemes has been the lack of satisfactory techniques for accurate quantitation. However, a promising approach is to incorporate a chromatographic sample inlet system to establish a reproducible means of sample introduction (*20, 26*).

The utilization of gas chromatographic separation prior to detection by gas–phase REMPI greatly relaxes the spectral selectivity requirements for the determination of PAC in complex mixtures. With this "mixture simplification" step, based on a packed column GC separation prior to the interrogation of analyte with a tunable, ultraviolet laser beam, Klimcak and Wessel (*27*) demonstrated spectral differentiation between coeluting PAC isomers. These investigators reported a quadratic relationship between laser power and signal intensity with their atmospheric pressure proportional counter detector (*28*). Rhodes et al. (*29*) have reported on the analytical figures of merit for a photoionization capillary GC/MS system, as related to the detection of PAC. Excellent absolute detection limits, in the sub-picogram range, and a linear dynamic range of greater than 4 decades were established for selected PAC. The excitation source employed in this study was a fixed wavelength (248.5 nm) excimer laser. In general,

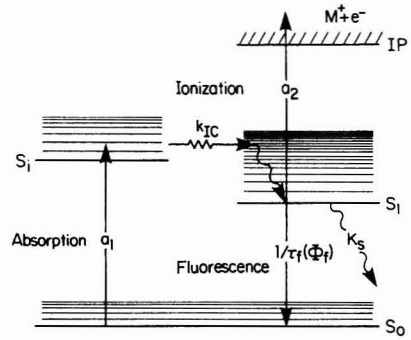

Figure 1. Simplified energy level diagram showing relevant absorption–ionization pathways: radiative transition, absorption (a_1, a_2) and fluorescence ($1/\tau_f$) rates; nonradiative deactivation internal conversion (k_{IC}) and total radiationless first excited singlet (K_s) relaxation rates.

while this approach tended to be class–selective for PAC and other easily ionized species, the lack of tunability of the excitation source precluded spectral differentiation among coeluting isomers.

APPROACH

Although state-of-the-art analytical approaches have provided their own particular advantages, most of them offer little hope in completely solving difficult PAC characterization problems, if used as "stand alone" techniques. In this paper we describe an instrument that utilizes a number of the above gas-phase PAC detection innovations but also incorporates additional dimensions that further contribute to form one very powerful multidimensional analytical system. This polyhyphenated technique is termed capillary column gas chromatography, resonance-enhanced multiphoton ionization, time-of-flight mass spectrometry, laser-induced fluorescence with parallel flame ionization detection (CC/GC-REMPI-TOFMS-LIF-FID). First, CC/GC is used for the high-resolution separation of the individual compounds in the sample and for reproducible controlled sample introduction. Second, a FID serves as a "universal" detector to provide general information on the overall composition of the sample. Finally, a tunable ultraviolet laser provides selective excitation/ionization of chromatographic eluents. All analytically useful products of the laser–analyte interaction are collected and monitored, providing simultaneous access to several types of information, including (a) REMPI via a novel total electron current detector (TECD), (b) photoionization GC/MS utilizing the TOFMS, and (c) LIF via an optical emission probe. This approach and other state-of-the-art techniques that utilize a single excitation source to produce several analytically useful signals, such as the multidimensional laser-based detector for liquid chromatography developed by Voigtman and Winefordner (*30*), could certainly be numbered among "The Hyphen-ated Methods", as described by Hirschfeld (*31*).

The energy level diagram in Figure 1 provides a simplified view of those dynamic processes associated with one-color, resonant, laser–analyte interactions that are relevant to the instrumental detection scheme to be described. Typically, a PAC molecule is excited to an upper vibronic state through the absorption of a resonant photon. This state then undergoes intramolecular conversion to the congested upper level vibronic states of the lowest excited singlet, followed by relaxation to the zero point vibrational level (*32, 33*). The molecule may then absorb a second photon to become ionized (REMPI), should the ionization level be accessible by a one-photon transition. Alternatively, relaxation to a ground vibronic state may occur through the spontaneous release of a photon (LIF) or by a nonradiative decay pathway. The nonresonant MPI contribution is taken to be negligible, as the laser power densities employed in this study are sufficiently low. Also, intermolecular deactivation of excited

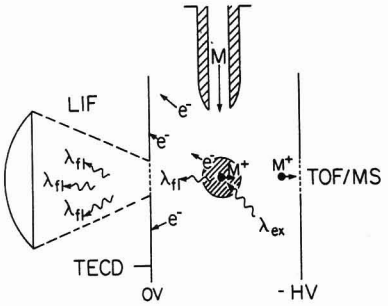

Figure 2. Dynamic gas sample cell showing simultaneous collection of M^+, e^-, and λ_{fl} from laser–analyte interaction volume.

species is essentially nonexistent because the laser-analyte interaction occurs at collision-free pressures of less than 10^{-4} torr. Each molecular species may, therefore, be defined by its own unique fluorescence quantum yield (Φ_f) and set of spectroscopic rate constants (a_1, a_2, k_{IC}, $1/\tau_f$, K_s), for any given excitation wavelength. Many of these values have not yet been determined for most PAC. However, through the simultaneous monitoring of all laser–analyte interaction products, characteristic detector responses may be established for each molecular species, at selected laser wavelengths and intensities. Such responses, which are actually the manifestation of these characteristic spectroscopic constants, may then be utilized in qualitative determinations.

The gas sample cell, shown in Figure 2, schematically illustrates the general arrangement that allows simultaneous monitoring of all analytically useful signals generated by the laser–analyte (M) interaction. This interaction occurs between two properly biased parallel grids, so that electrons (e^-) resulting from molecular ionization are efficiently captured and monitored with TECD. The cations (M^+) are extracted into a TOFMS. A fraction of the photons (λ_{fl}) are also collected with an appropriately positioned quartz lens, providing access to LIF information as well. These laser–analyte interaction products are, therefore, simultaneously collected and monitored on-line for each absorbing chromatographic effluent. Thus, this approach combines the selectivity and sensitivity of two complementary laser-based methods, REMPI and LIF, with a very powerful analytical tool, namely, CC/GC-MS.

In the present sampling configuration, the chromatographic effluent enters the low-pressure sample cell in the form of a thermal, or effusive, expansion. Thus, each analyte species retains broad band spectral features, characteristic of large gas-phase molecules at ambient temperatures. This limits the achievable excitation selectivity for molecules in complex mixtures. However, owing to the high degree of physical separation of mixture components provided by CC/GC, these limitations are minimized. For coeluting compounds, excitation selectivity based on differences in ambient-temperature absorption spectra and/or ionization energies should be possible. Although such selectivity is demonstrated in this paper, it in no way should diminish the potential of utilizing rotational cooling (*15–21*) to provide additional spectral selectivity, if warranted.

In this paper, the viability of this multidimensional analytical technique as a sensitive and selective detection scheme for PAC in complex mixtures is assessed in terms of intrinsic response characteristics and analytical figures of merit of the instrument. Qualitative effects of laser power density on REMPI signals and the extent of fragmentation are explored. The advantage of employing a tunable excitation source is made clear by demonstrating selective ionization for two closely eluting PAC isomers. Linear dynamic range (LDR) and absolute limits of detection (LOD) are reported for a number of PAC. Further, various degrees of chromatogram simplification are demonstrated, through utilization of the

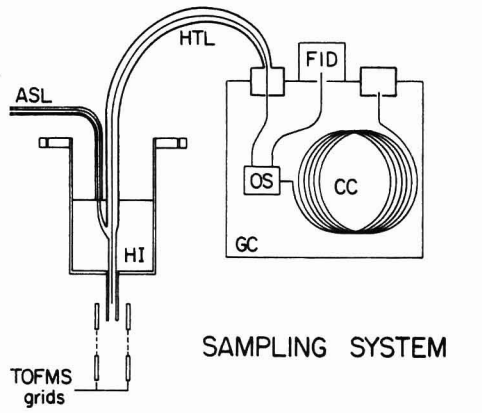

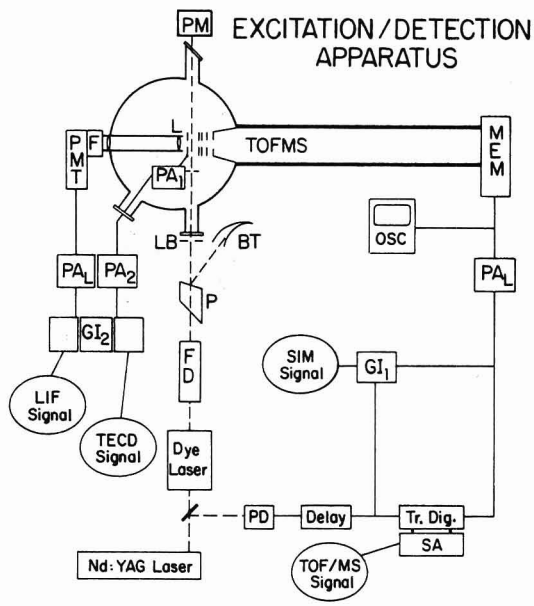

Figure 3. Schematic diagram of CC/GC-REMPI-TOFMS-LIF-FID analytical instrumentation. Components are listed in Table I.

respective dimensions of this analytical system, for a synthetic organic mixture and a PAC fraction of Paraho shale oil.

EXPERIMENTAL SECTION

Table I identifies the components of the analytical instrument shown schematically in Figure 3.

Lasers and Optics. The frequency-doubled output (532 nm) of a 10-Hz Nd:YAG laser was used to pump a tunable dye laser. The dyes used were rhodamine 590, 610, and 640 (Exciton) and oxazine (720) (Interactive Radiation, Inc.). These dyes provided a fundamental lasing range of 565–700 nm. The fundamental output of the tunable dye laser was collimated down to a diameter of approximately 2 mm, utilizing a laboratory-assembled telescope, and was then frequency doubled by KDP crystals. Thus, an ultraviolet tuning range of 282–350 nm was provided. The fundamental (visible) laser beam was then separated from its second harmonic (UV) beam through the use of a Pellin-Broca prism, after which it was trapped by a beam dump. The range of UV pulse energies employed in this study was 0.1–2.6 mJ, with a temporal pulse width of approximately 10–15 ns. The UV laser beam was carefully aligned through the center of the low-pressure, gas-sample cell and entered the vacuum system via a fused silica window and exited on the opposite side through a similar window placed at Brewster's angle. To aid in alignment and to minimize stray and scattered light within the detector, a series of four (6 mm i.d.) apertures were empirically positioned within the vacuum chamber. The UV laser power was monitored beyond the exit window of the vacuum chamber.

A portion of the 532-nm Nd:YAG laser beam illuminated a fast photodiode that provided a reference trigger for the synchronization of all detector electronics.

Table I. Instrumental Components

component	symbol[a]	model no.	manufacturer
A. Laser System			
Nd:YAG laser		YG481	Quantel International,
dye laser		TDL III	Santa Clara, CA
frequency doubler	FD	5-12	INRAD, Northvale, NJ
power meter	PM	36-1002	Scientech, Boulder, CO
B. Detection System			
TOF mass spectrometer	TOFMS	MA-2000[b]	CVC Products, Inc., Rochester, NY
magnetic electron multiplier	MEM		
preamplifier	PA_L	6102	LeCroy Research Syst., Spring Valley, NY
transient digitizer/signal averager	Tr. Dig. SA	3500S-A200	
source preamplifier	PA_1	*c*	
active filter preamplifier	PA_2	*c*	
fast photodiode circuit	PD	*c*	
pulse delay generator	Delay	*c*	
gated integrator	GI_1	162/165/165	EG&G Princeton Applied Research, Princeton, NJ
	GI_2	SR225/250/250	Stanford Research Syst., Palo Alto, CA
oscilloscope	OSC	475A	Tektronix, Inc., Beaverton, OR
photomultiplier tube	PMT	R955	Hamamatsu Co., Middlesex, NJ
C. Sampling System			
gas chromatograph	GC	560	Tracor Instruments, Austin, TX
flame ionization detector	FID		
capillary column	CC	DB-5	J & W Scientific, Inc., Rancho Cordova, CA
outlet splitter	OS	VSOS	SGE, Austin, TX
heated transfer line	HTL	*c*	
heated interface	HI	*c*	
alternate sampling line	ASL	*c*	
D. Vacuum System			
vacuum chamber		*c*	
diffusion stacks with		VH6	Varian, Palo Alto, CA
cryotraps and valves		M4	
mechanical pumps		1397	Sargent-Welch
		1402	Skokie, IL
E. Miscellaneous Components			
optical filters (F); Pellin Broca prism (P); fused silica lenses (L); light baffles (LB); optical beam trap (BT); power supplies; recorders			

[a] Refer to Figure 3. [b] Basic components of this instrument were adapted for photoionization experiments. [c] Constructed at Ames Laboratory.

Capillary Gas Chromatography and Low Pressure Dynamic Gas Sample Cell Interface. A temperature programable gas chromatograph, equipped with a capillary inlet system and a FID detector was utilized in these studies. As emphasis was not placed on high-resolution chromatography, a modest (15 m × 0.32 mm i.d.) DB-5 fused silica capillary column was employed. All chromatographic analyses were conducted at a helium carrier gas linear flow rate of 50 cm/s, measured at 100 °C. Typically, 1.2-μL samples were injected into the capillary GC with a split ratio of approximately 50:1. Various temperature programs were selected to best suit the particular study being conducted. As a result, conditions were commonly chosen to provide adequate chromatographic resolution in the shortest time possible.

A vitreous silica outlet splitter served to split the chromatographic effluent approximately 30:70 for parallel detection by both the FID and the laser-based detectors. A deactivated fused silica transfer line (2 m × 0.20 mm i.d.), as well as a laboratory constructed interface oven (*34*), were heated to a temperature (typically 350 °C) greater than the final GC oven temperature in order to allow efficient transfer of analyte to the low-pressure gas sample cell.

Resonance-Enhanced Multiphoton Ionization (REMPI) Detection. Simultaneous detection of all ionization products was provided by a novel total electron current detector (TECD) and a laboratory-modified TOFMS.

TECD. The stainless steel backing grid assembly was electrically isolated from the other nude ion source components and grounded across a 10-kΩ resistor. This assembly then served as a convenient collector plate for electrons that were produced in the sample interrogation volume. A fast operational-amplifier, current-to-voltage converter, designed and assembled in the Ames Laboratory, was mounted directly on the backing grid assembly to serve as a very sensitive preamplifier (*34*). The output of this preamplifier was connected to an active-filter preamplifier (also designed in the Ames Laboratory). A tunable, twin-T, electronic filter network in the feedback loop of this second preamplifier provided preferential amplification of the signal, while discriminating against higher frequency electronic noise. The output was then processed by a gated integrator. The time constant (1 s) and gate width (200 ns) were empirically adjusted to minimize chromatographic peak distortion and base line noise.

Although the TECD signal was primarily utilized to provide total ionization chromatograms, it also provided a reliable indication of the onset of ion formation and therefore served as a signal to begin collection of mass spectra utilizing the TOFMS data acquisition system.

TOFMS. A time-of-flight mass spectrometer was chosen for use in these pulsed laser excitation studies because of its inherently high ion detection efficiency. In principle, all ions created for each laser pulse may be simultaneously extracted and mass analyzed. The TOFMS, which was assembled in-house, utilized several components of a commercially available instrument that were altered to suit our needs. The spacing between the backing and first ion drawout grids was enlarged from the standard 3 mm to a 15 mm spacing. This enlargement was primarily done to allow for incorporation of a supersonic jet nozzle/rotational cooling sampling system at a later date. Also, the wider spacing somewhat relaxed the ionizing beam diameter restrictions of the instrument and, therefore, allowed variations in mass spectral resolution. The positioning of the drawout grid assembly was adjusted, with respect to the flight tube entrance, so that the ionization region could be precisely centered directly beneath the heated interface oven/sample inlet. The first and second ion drawout grids were held at dc potentials that were empirically optimized to yield maximum ion transmission and highest mass resolution through the 2-m flight tube. The mass spectral resolution achieved, under the experimental parameters employed for these studies, was greater than 300.

A variable-gain, magnetic electron-multiplier (MEM) provided an output signal that was first preamplified and then processed by either a gated integrator, for selective ion monitoring (SIM), or a 200-MHz (5 ns resolution) transient digitizer and microcomputer system (LeCroy 3500 SA 200) for collection, processing, and storage of any mass spectral window of interest during the elution of selected chromatographic peaks. Proper synchronization of all TOFMS detection electronics was achieved through the incorporation of a 1–100 μs variable trigger delay generator, in conjunction with the photodiode trigger system.

Table II. 64-Component Organic Mixture

no.	compound	mol wt	retn time, min	no.	compound	mol wt	retn time, min
1	**p-cresol**[e]	108	0.80		triphenylmethane	244	7.95
	1,6-hexanediol	118	1.02		fluoranthene[a]	202	8.18
	3,4-dimethylphenol	122	1.25		1-octadecanol	270	8.38
2	**naphthalene**[a]	128	1.28	12	**pyrene**[b]	202	8.45
	1-decanol	158	1.80		bis(2-ethoxyethyl) phthalate	310	8.73
3	**biphenyl**	154	2.72		methyl stearate	298	8.77
	acenaphthylene[a]	152	3.05	13	**p-terphenyl**	230	9.07
	m-dinitrobenzene	168	3.33		*n*-docosane[d]	310	9.20
4	**acenaphthene**[b]	154	3.37		*n*-tetracosane[d]	338	10.63
5	**dibenzofuran**	168	3.60	14	**benz[*a*]anthracene**[a]	228	10.77
6	**fluorene**[a]	166	4.23	15	**chrysene**[b]	228	10.80
	n-hexadecane	226	4.38	16	**triphenylene**[a]	228	10.80
	diethyl phthalate	222	4.42		bis(2-ethylhexyl) phthalate	390	11.55
	phenyl benzoate	198	4.98		*n*-hexacosane[d]	366	11.82
	1-tetradecanol	214	5.02	17	**benzo[*b*]fluoranthene**[c]	252	12.68
	hexachlorobenzene	282	5.35		benzo[*j*]fluoranthene[c]	252	12.68
7	***p*-phenylphenol**	178	5.40	18	**benzo[*k*]fluoranthene**[c]	252	12.68
8	**dibenzothiophene**[a]	184	5.68		*n*-octacosane[d]	394	12.97
	pentachlorophenol	264	5.73	19	**benzo[*e*]pyrene**[c]	252	13.07
	benzyl benzoate	212	5.82	20	**benzo[*a*]pyrene**[b]	252	13.17
9	**phenanthrene**[b]	178	5.95	21	**perylene**[b]	252	13.28
10	**anthracene**[b]	178	5.98		*n*-triacontane[d]	422	14.17
	benzil	210	6.10		*n*-hentriacontane[d]	436	14.68
	n-octadecane[d]	254	6.13		cholesterol	386	14.82
11	**carbazole**	167	6.45		indeno[1,2,3-*cd*]pyrene[c]	276	14.83
	1-hexadecanol	242	6.62	22	**dibenz[*a*,*b*]anthracene**[a]	278	14.83
	n-nonadecane	268	6.75	23	**dibenz[*a*,*b*]anthracene**[a]	278	14.90
	phenyl sulfone	232	7.07	24	**benzo[ghi]perylene**[a]	276	15.12
	dibutyl phthalate	278	7.45		*n*-dotriacontane[d]	450	15.30
	9,10-anthraquinone	208	7.52		*n*-tritriacontane[d]	464	15.90
	4,4′-dibromobiphenyl	312	7.58		*n*-tetratriacontane[d]	478	16.50
	n-eicosane[d]	282	7.75		coronene[a]	300	16.97

Chemicals were obtained from Chem Services, West Chester, PA, unless otherwise denoted by lettered superscript: [a] Aldrich Chemical, Milwaukee, WI. [b] Zone refined at Ames Laboratory, Ames, IA. [c] Community Bureau of Reference (CBR), Commission of the European Communities. [d] Alltech, Deerfield, IL. [e] Bold type labels species detected by TECD (λ_{ex} 285 nm).

While the analytical system was in operation, a typical pressure of 6×10^{-6} torr was maintained in the main vacuum chamber (ion source region) by a 6-in. (15.2 cm) diffusion stack backed by a 500 L/min mechanical pump. A pressure of approximately 3×10^{-7} torr was maintained in the 2-m flight tube by an additional 4-in. (10.2 cm) diffusion stack backed by a 160 L/min mechanical pump.

Laser-Induced Fluorescence (LIF). Molecular fluorescence was collected through the backing grid of the mass spectrometer and focused on a fast-response photomultiplier tube (PMT). Appropriate sharp cutoff optical filters allowed detection of a total fluorescence signal while discriminating against scattered laser light. The PMT output signal was processed by a gated integrator (1-s time constant). Compromise gate delay (20 ns) and gate width (40 ns) settings were selected for detection of all fluorescing PAC that were investigated in this study.

Chemicals and Samples. The reference compounds used in this study and their sources are summarized in Table II. Each compound was at least 97% pure, as verified by GC-FID. The phenanthrene-d_{10} used in the wavelength-selective ionization study was obtained from MSD Isotopes (98%+ atom purity). Reference stock solutions (~5 mg/mL) were prepared by dissolving each of these chemicals in pesticide grade methylene chloride. Solutions of various concentrations and compositions were prepared by appropriate dilution with methylene chloride and/or mixing of these reference stock solutions.

Crude Shale Oil A (Paraho shale oil), CRM-2, supplied by DOE Fossil Fuels Research Material Facility (Oak Ridge National Laboratory), was fractionated according to the procedure of Later et al. (*8*). The A-2 fraction (neutral PAC) was chosen for the present studies. Typically, such fractions contain a wide variety of PAH as well as N-, O-, and S-heterocyclic compounds.

RESULTS AND DISCUSSION

Laser Power Density Effects on REMPI Linearity and Fragmentation. With pulse energies of a 2-mm laser beam ranging from 0.1 to 2.6 mJ, at an excitation wavelength of 285 nm, representative PAC chromatographic eluents were ionized while monitoring TECD and TOFMS signals. The TECD responded linearly to power density within the 0.1–2.6 mJ range. For example, the linear correlation coefficients for acenaphthene and carbazole were 0.996 and 0.977, respectively. Precision was limited by the present method of sample introduction (split mode) and laser beam pulse-to-pulse energy density fluctuations. However, this initial study did indicate that the primary ionization mechanism was a stepwise one-photon-limited process for this range of laser power densities. Thus, for a given beam diameter, the analytical signal should be normalized with respect to laser pulse energies to compensate for any drift in laser power.

The effect of laser power density on the degree of cation fragmentation was also investigated. A simple PAC mixture, consisting of approximately 0.5 mg/mL each of acenaphthene, dibenzofuran, fluorene, and carbazole, was used. The temperature program employed was as follows: column temperature held at 130 °C for 1 min and then programmed to 190 °C at a rate of 14 °C/min, where it was held for 1 min. In the same power density range and wavelength that was used in the linearity study, the extent of fragmentation increased slightly with laser pulse energy. However, the parent ion still dominated, even at 2.6 mJ/pulse. This indicated that the PAC analytes largely experienced "soft ionization", absorbing just enough photons (two) to lose an electron.

With an appropriate lens in front of the vacuum chamber entrance window, the beam diameter was reduced by a factor of 4 within the laser-analyte interaction region. A comparison of the TECD and TOFMS data obtained for this focused vs. an unfocused laser beam, both at 2 mJ/pulse, is given in Figure 4. Interestingly, the respective TECD peak heights are similar

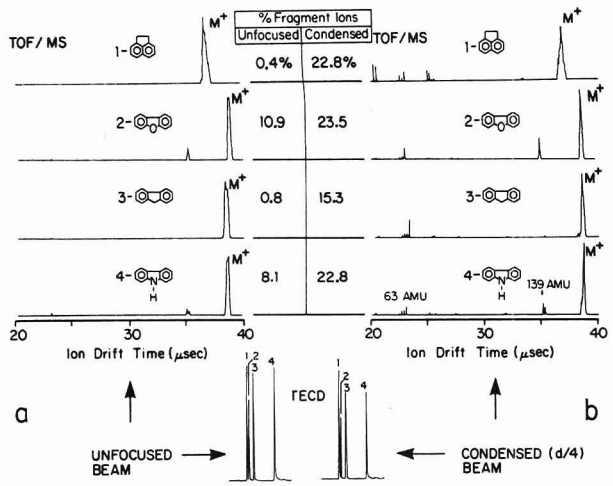

Figure 4. Effect of laser power density on TECD signal and TOFMS fragmentation spectra (5 shots, 0.5 s) for (1) acenaphthene, (2) dibenzofuran, (3) fluorene, and (4) carbazole in an (a) unfocused vs. (b) condensed laser beam.

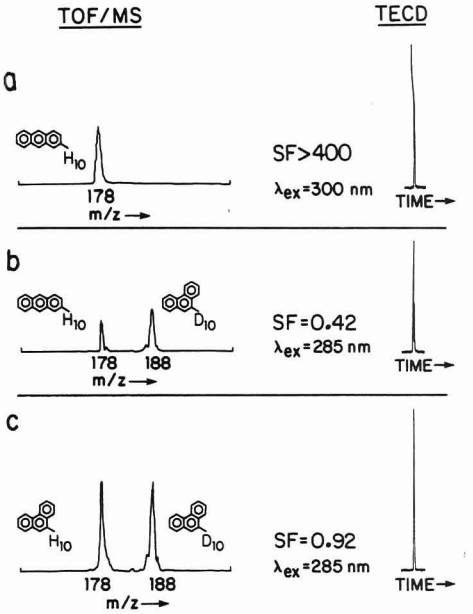

Figure 5. Selective ionization of closely eluting compounds demonstrated by TECD chromatograms and their respective TOFMS spectra for [a] anthracene (A-H_{10}) and deuterated phenanthrene (P-D_{10}), λ_{ex} 300 nm, SF > 400; [b] A-H_{10} and P-D_{10}, λ_{ex} 285 nm, SF = 0.42; and [c] P-H_{10} and P-D_{10}, λ_{ex} 285 nm, SF = 0.92.

in both cases, indicating that approximately the same number of ions are created in both excitation modes. Because the sample volume interrogated was reduced by a factor of 16 while the laser power density was increased by an identical factor, linear response of the TECD with respect to laser power density is implied to still higher power densities. Also, this indicates that the TECD signal observed with an unfocused beam is far from saturation and that the efficiency of the analyte ionization process may be further increased, should a higher power laser source be employed.

The TOFMS data acquisition system was manually triggered, upon the appearance of each TECD chromatographic peak, to sum and store mass spectra from five consecutive laser pulses (0.5 s). The percent of fragment ion formation was determined for each mass spectrum by comparing the total fragment peak area to the total ion peak area. As shown in Figure 4, the extent of fragmentation was significantly increased by condensing the laser beam, although the parent peak continued to dominate for these PAC. The option of obtaining a complete fragmentation pattern for a well-resolved chromatographic peak should prove to be quite valuable for the identification of unknown PAC. However, the simplified mass spectra provided by the "soft ionization" alternative may be more practical when there exists a number of coeluting photoionizable species in complex PAC analyses.

Wavelength-Selective Ionization. Selective ionization of ambient-temperature GC effluents may be achieved, in a number of cases, by exploiting differences in the respective REMPI spectra of various compounds. The TECD chromatographic peak heights represent relative REMPI responses, at a chosen excitation wavelength. Thus, TECD chromatograms of several simple PAC mixtures were accumulated over an excitation wavelength range of 282–350 nm, in 2.5-nm increments, at a constant pulse energy of approximately 1 mJ. Accordingly, these wavelength-dependent relative chromatographic peak heights were assembled into a REMPI spectrum for each of 28 PAC. Such spectra could be referenced for selection of compromise excitation wavelengths for general PAC detection or consulted for choosing selective ionization conditions when coeluting isomers must be distinguished.

The reconstructed REMPI excitation spectra of two closely eluting PAC isomers, anthracene and phenanthrene, suggested that by choosing the laser excitation wavelength to be 300 nm, anthracene could be selectively ionized in the presence of phenanthrene. This prediction was verified by using both TECD and TOFMS to monitor laser-ionization products of a chromatographic eluent consisting of a 1:1 mixture of these two PAC. In this study, the deuterated analogue of phenanthrene was substituted to make obvious the identity of the ionized species. Each of the TOFMS spectra of Figure 5 represents a summation of all ions produced, in a 42 amu mass window, during the elution of both PAC peaks. Spectral selectivity factors (SF) were determined by ratioing mass spectral peak areas of the protonated species to those of phenanthrene-d_{10}. Photoexcitation at 300 nm provided selective ionization of anthracene, as is convincingly shown by the resulting mass spectrum (Figure 5a) and the corresponding SF value of greater than 400.

For comparison, both PAC isomers were detected utilizing 285-nm irradiation, as indicated by the 0.42 SF value (Figure 5b). A 1:1 mixture of phenanthrene and its deuterated analogue was also run, under identical conditions, with the results shown in Figure 5c. A SF value of 0.92 indicates similar responses for both of these species at 285 nm. This, in part, justifies the substitution of a deuterated analogue in these selective ionization studies. Further, these observations imply that deuterated analogues should prove ideal for use as internal reference standards for quantitation, as their physical, chemical, and ambient-temperature spectroscopic properties are nearly identical with those of the parent compound.

Analytical Figures of Merit. The overall analytical figures of merit for the TECD and TOFMS detectors were determined for a number of representative PAC. The measurements were conducted with a compromise laser excitation wavelength of 285 nm. Also, all analytical signals were normalized to a laser pulse energy of about 1 mJ. The LDR study was performed under the same chromatographic conditions as employed in the power density study. The four-component PAC mixture, also used in the power density study, was prepared at 11 different dilutions over a broad range of concentrations. A log–log plot of the TECD chromatographic peak heights as a function of the mass of PAC delivered to the gas sample cell was linear over approximately a 4-decade change in concentration for all four compounds. The linear correlation coefficients were all better than 0.995 in this range. Deviations from linearity were observed above 50 ng because of overloading of the TECD amplifiers. The upper end of the LDR could certainly be extended by attenuating the signal or by changing the operational amplifier circuitry.

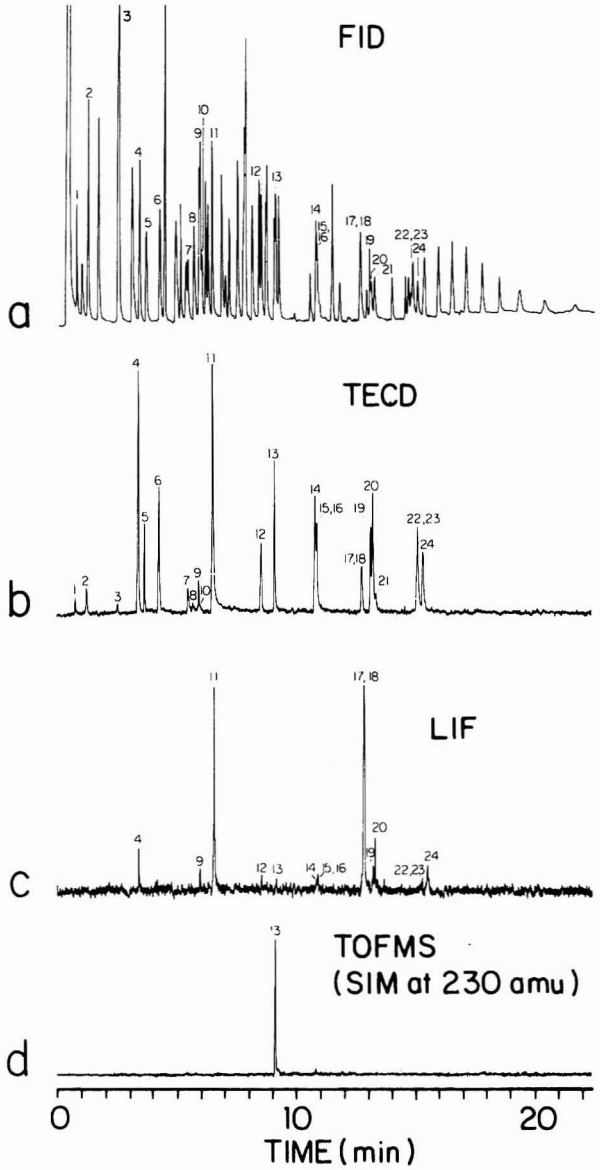

Figure 6. Chromatogram simplification demonstrated for a 64-component mixture by simultaneous (a) FID, (b) TECD, (c) LIF, with WG 320 and WG 335 optical filters, and (d) TOFMS, SIM at 230 amu (1 amu window), λ_{ex} 285 nm. Temperature programmed from 100 °C to 320 °C at 14 °C min with 1-min initial hold and 6-min final hold.

The absolute LOD (S/N = 3) for TECD and TOFMS detection, respectively, are given in Table III for 21 PAC. Under the compromise excitation conditions, the absolute LOD values for most of these species were in the low picogram range. These LOD values were limited by ionization of background molecules (likely residual PAC) within the gas sample cell, as well as stray electronic noise picked up by the preamplifiers. It must be stressed that these LOD values were wavelength and laser power dependent. Therefore 285 nm did not necessarily represent an optimum value for most of these PAC.

Simplification of Chromatograms. One of the more obvious consequences of the inherent selectivity of the multidimensional analytical system is its potential for simplification of chromatographic data. To demonstrate this simplification, a 64-component mixture containing a wide variety of organic compounds, including PAC and other aromatic compounds, aliphatic hydrocarbons, alcohols, sulfones, and esters, was prepared. Table II lists each of these components, in order of retention time, for the chromatographic conditions employed. The numbered compounds (in bold type) label those species for which a measurable REMPI signal was obtained using 1 mJ/pulse laser excitation at 285 nm.

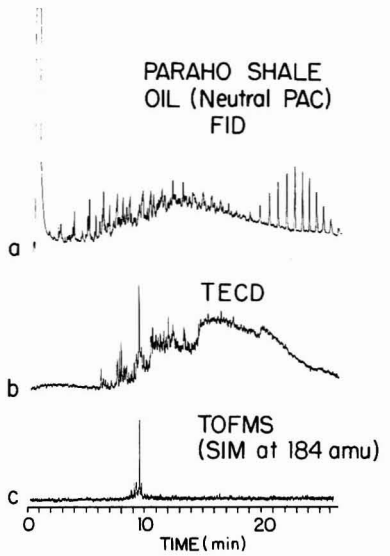

Figure 7. Simultaneous chromatograms of a Paraho shale oil fraction: (a) FID; (b) TECD; and (c) TOFMS, SIM at 184 amu (±1 amu window). Temperature was programmed from 60 °C to 340 °C at 12 °C/min with 1 min initial hold and 2 min final hold.

Graphic demonstration of the various degrees of chromatogram simplification provided by this instrumentation is displayed in Figure 6. The FID chromatogram (Figure 6a) was complex, with many unresolved peaks, including peaks due to septum bleed. The laser-based portion of the detection system provided selective excitation–ionization based largely on characteristic molecular absorption coefficients and ionization cross sections at the excitation wavelength. Hence, at 285 nm, the TECD chromatogram (Figure 6b) indicated that only 24 of these compounds, mostly PAC, were ionized. The LIF chromatogram (Figure 6c) was obtained under compromise detector gate width/delay and emission filtering conditions, all of which effected selectivity and sensitivity for each compound. Again, this LIF mode of detection responded only to a select group of compounds.

The SIM chromatogram (Figure 6d) illustrated, in part, the additional selectivity offered by the incorporation of a mass spectrometer. In this case, only *p*-terphenyl was detected by preselecting only a 1 amu mass window, at 230 amu, for monitoring. When the transient digitizer data processing system is utilized, full advantage of the TOFMS detector may be realized, as an entire mass spectrum may then be collected for each ionizable chromatographic effluent. Thus, all of these chromatograms (FID, TECD, LIF, and TOFMS-SIM or full mass spectra) are simultaneously available for each injection of analyte.

Unfortunately, most real samples are far more complex than this 64-component synthetic mixture. To provide a qualitative indication of the practical level of chromatogram simplification obtainable, the A-2 fraction (neutral PAC) of a crude shale oil (Paraho shale oil), CRM-2, was examined. The complexity of this sample was apparent in the FID chromatogram (Figure 7a). Obviously, most of the components of this fraction were hopelessly unresolved under the given chromatographic operating conditions. Although the TECD provided a somewhat simplified chromatogram (Figure 7b), it was still far too complex for a complete PAC characterization, even under optimized CC/GC conditions. This was not surprising, as this fraction typically contains hundreds of different PAC species. However, as is shown by the SIM chromatogram (Figure 7c), the ability to isolate a narrow (±1 amu) mass window allowed the targeting of a specific PAC for detection. In this case, dibenzothiophene (184 amu) was the targeted molecule. A match of chromatographic retention time, along with REMPI

Table III. Current REMPI Detection Limits[a]

COMPOUND	STRUCTURE	LOD (pg @ 285mm)		COMPOUND	STRUCTURE	LOD (pg @ 285mm)	
		TECD	TOF/MS			TECD	TOF/MS
p-Cresol	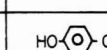	59	7	p-Terphenyl	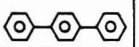	13	2
Naphthalene		130	16	Triphenylene		43	5
Acenaphthylene		N.D.		Benz(a)anthracene	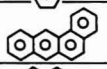	19	2
Acenaphthene		7	1	Chrysene	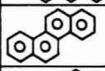	24	3
Dibenzofuran		18	2	Benzo(b)fluoranthene	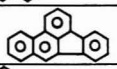	500	63
Fluorene		12	2	Benzo(j)fluoranthene	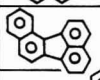	N.D.	
p-Phenylphenol	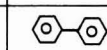	53	7	Benzo(k)fluoranthene	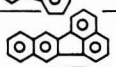	38	5
Dibenzothiophene		260	32	Benzo(e)pyrene		20	3
Pentachlorophenol		N.D.		Benzo(a)pyrene	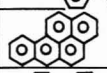	12	2
Phenanthrene		47	6	Perylene		*	*
Anthracene		270	34	Indeno(1,2,3-c,d)pyrene	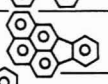	N.D.	
Carbazole		6	1	Dibenz(a,h)anthracene	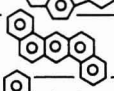	*	*
Fluoranthene		N.D.		Dibenz(a,c)anthracene		37	5
Pyrene		33	4	Benzo(g,h,i)perylene		35	4

[a] N.D., not detected; *, detected, not quantitated.

and mass spectral data verified the identification. Fluorescence data are not presented for this application, as this aspect of the system is not yet sufficiently optimized.

Future Considerations. Although the use of this instrument at ambient temperatures provides for selective excitation/ionization and detection of many coeluting isomers, it is unlikely that this approach will be able to do so as a general rule. This is particularly important when complete characterization of PAC distributions in complex environmental samples is the goal. Even these extremely demanding problems may be completely solved by incorporating a supersonic jet, rotational cooling sampling system to provide an enhancement of selectivity in the excitation/ionization process. To this end, a high temperature, low dead-volume pulsed jet sampling valve is now being tested. It is anticipated that this valve not only will provide efficient cooling of CC/GC effluent but also will result in at least 2 decades gain in sensitivity, in comparison to the continuous flow approach, resulting from a considerable improvement in duty cycle.

Additional reduction in stray light and background electronic noise should greatly improve S/N in LIF detection. Other dimensions of LIF emission information, such as observation of fluorescent lifetime and the characteristic emission spectra, remain to be exploited. With the addition of a spectrometer/photodiode array detection system, an entire fluorescence emission spectrum can be made available on-line, for each fluorescing chromatographic eluent. These spectra would be particularly useful if employed with a rotational cooling sampling system, as the resulting narrow band fluorescence emission spectra would serve as "fingerprints" for the identification of various species.

Presently the most urgent need is to develop a low-pressure, gas-phase PAC excitation/ionization spectral data base, particularly if rotational cooling is to be employed. Sophisticated data acquisition and reduction techniques, including chemometrics, must be incorporated to take full advantage of the available analytical information. Diagnostic and mechanistic studies would also be helpful in the prediction of detector responses for various species and to assist in developing analytical methodologies for specific applications. Such a mechanistic study involving simple halogenated aromatics has recently been reported by Tembreull et al. (*35*).

The studies presented here only begin to describe the analytical utility of the instrument. However, the potential for high selectivity in the excitation/ionization process, coupled with the selectivity and sensitivity of the multidimensional detection scheme, clearly indicate the promise of utilizing CC/GC-REMPI-TOFMS-LIF-FID for a wide variety of analytical applications involving trace PAC characterization in complex mixtures.

ACKNOWLEDGMENT

R.L.M.D. thanks the Standard Oil Co. (Ohio) for support provided through a graduate research fellowship. The authors gratefully acknowledge R. S. Houk for valuable discussions concerning various aspects of instrumental design. The timely contributions of J. L. Hand and C. Burg of the Ames Laboratory Development Shop during the fabrication stage of this work are also acknowledged.

LITERATURE CITED

(1) *Chemical Carcinogens, Vols. 1 and 2*, 2nd ed.; Searle, C. E., Ed.; American Chemical Society: Washington, DC, 1984.
(2) Griest, W. H.; Tomkins, B. A.; Epler, J. L.; Rao, T. K. *Polynuclear Aromatic Hydrocarbons*; Jones, P. W., Leber, P., Eds.; Ann Arbor Science Publishers: Ann Arbor, MI, 1979; p 395.

(3) Jones, D. W.; Mathews, R. S. *Prog. Med. Chem.* **1974**, *10*, 159.
(4) Romanowski, T.; Funcke, W.; Grossmann, I.; Konig, J.; Balfanz, E. *Anal. Chem.* **1983**, *55*, 1030.
(5) Tong, H. Y.; Karasek, F. W. *Anal. Chem.* **1984**, *56*, 2129.
(6) Grimmer, G.; Jacob, J.; Naujack, K.; Dettbarn, G. *Anal. Chem.* **1983**, *55*, 892.
(7) Later, D. W.; Andros, T. G.; Lee, M. L. *Anal. Chem.* **1983**, *55*, 2126.
(8) Later, D. W.; Lee, M. L.; Bartle, K. D.; Kong, R. C.; Vassilaros, D. L. *Anal. Chem.* **1981**, *53*, 1612.
(9) Crowley, R. J.; Siggia, S.; Uden, P. C. *Anal. Chem.* **1980**, *52*, 1224.
(10) Hilpert, L. R.; Byrd, G. D.; Vogt, C. R. *Anal. Chem.* **1984**, *56*, 1842.
(11) Simonsick, W. J., Jr.; Hites, R. A. *Anal. Chem.* **1984**, *56*, 2749.
(12) Brown, J. C.; Duncanson, J. A., Jr.; Small, G. J. *Anal. Chem.* **1980**, *52*, 1711.
(13) D'Silva, A. P.; Fassel, V. A. *Anal. Chem.* **1984**, *56*, 985A.
(14) Perry, M. B.; Wehry, E. L.; Mamantov, G. *Anal. Chem.* **1983**, *55*, 1893.
(15) Amirav, A.; Even, U.; Jortner, J. *Anal. Chem.* **1982**, *54*, 1666.
(16) Imasaka, T.; Fukuoka, H.; Hayashi, T.; Ishibashi, N. *Anal. Chim. Acta* **1984**, *156*, 111.
(17) Johnston, M. V. *Trends Anal. Chem.* **1984**, *3*, 58.
(18) Smalley, R. E.; Wharton, L.; Levy, D. H. *Acc. Chem. Res.* **1977**, *10*, 139.
(19) Hayes, J. M.; Small, G. J. *Anal. Chem.* **1983**, *55*, 565A.
(20) Hayes, J. M.; Small, G. J. *Anal. Chem.* **1982**, *54*, 1202.
(21) D'Silva, A. P.; Iles, M.; Rice, G.; Fassel, V. A. Ames Laboratory Report IS-4556, Ames, IA, April 1984.
(22) Lubman, D. M.; Kronick, M. N. *Anal. Chem.* **1982**, *54*, 660.
(23) Tembreull, R.; Lubman, D. M. *Anal. Chem.* **1984**, *56*, 1962.
(24) Sin, C. H.; Tembreull, R.; Lubman, D. M. *Anal. Chem.* **1984**, *56*, 2776.
(25) Dietz, T. G.; Duncan, M. A.; Liverman, M. G.; Smalley, R. E. *J. Chem. Phys.* **1980**, *73*, 4816.
(26) Imasaka, T.; Shigezumi, T.; Ishibashi, N. *Analyst (London)* **1984**, *109*, 277.
(27) Klimcak, C. M.; Wessel, J. E. *Anal. Chem.* **1980**, *52*, 1233.
(28) Frueholz, R.; Wessel, J.; Wheatley, E. *Anal. Chem.* **1980**, *52*, 281.
(29) Rhodes, G.; Opsal, R. B.; Meek, J. T.; Reilly, J. P. *Anal. Chem.* **1983**, *55*, 280.
(30) Voigtman, E.; Winefordner, J. D. *J. Liq. Chromatogr.* **1983**, *6*, 1275.
(31) Hirschfeld, T. *Anal. Chem.* **1980**, *52*, 297A.
(32) Siebrand, W. *Dynamics Of Molecular Collisions, Part A*; Miller, W., Ed.; Plenum: New York, 1976; Chapter 6.
(33) Kasha, M. *Discuss. Faraday Soc.* **1950**, *9*, 14.
(34) Dobson, R. L. M. Ph.D. Dissertation, Iowa State University, Ames, IA, 1986.
(35) Tembreull, R.; Sin, C. H.; Li, P.; Pang, H. M.; Lubman, D. M. *Anal. Chem.* **1985**, *57*, 1186.

RECEIVED for review February 10, 1986. Accepted May 5, 1986. The Ames Laboratory is operated by Iowa State University for the U.S. Department of Energy under Contract No. W-7405-ENG-82. This research was supported by the U.S. DOE Office of Health and Environmental Research, Physical and Technological Studies.

Detection of Nonvolatile Species by Laser Desorption Atmospheric Pressure Mass Spectrometry

Leonidas Kolaitis and David M. Lubman*

Department of Chemistry, The University of Michigan, Ann Arbor, Michigan 48109

This work examines the use of laser desorption as a means of volatilizing thermally labile compounds for detection in atmospheric pressure mass spectrometry. A number of different classes of compounds have been examined including amino acids, purine and pyrimidine bases and their nucleosides, drugs, vitamins, and catecholamines. The main advantage of this method is that desorption of neutrals and the atmospheric pressure ionization process are performed in two separate steps as compared to LDMS where desorption and ionization occurs in one step. Thus, detection limits reaching down to ~0.3 ng can be achieved in the total process due to the high efficiency of each step where complete desorption of the sample can be achieved and almost 100% efficient ionization of the resulting neutrals is possible using atmospheric pressure ionization in these high proton affinity molecules. The use of this atmospheric pressure technique obviates the need of manipulating samples under vacuum and may prove to be particularly convenient for interfacing HPLC and SFC in mass spectrometry.

The detection and identification of nonvolatile organic species at low concentration levels are important problems in pharmaceutical quality control and clinical analysis. These problems require analysis of a wide range of species including amino acids, peptides, purine and pyrimidine bases, drugs, vitamins, and nerve stimulants. Mass spectrometry is a particularly powerful means of analysis for these species based upon exact mass identification; however, the compounds must first be volatilized into the gas phase and injected into the mass analyzer. Many of the components of real clinical samples though are either nonvolatile or thermally labile so that they rapidly decompose upon heating. Thus, a means of volatilizing these samples has remained an important field in mass spectrometry.

A number of techniques have been developed for volatilization and ionization, among which are field desorption (FD) (*1–4*), secondary ion mass spectrometry (SIMS) (*5–8*), fast atom bombardment (FAB) (*9–11*), laser desorption (LD) (*12–15*) and plasma desorption mass spectrometry (PDMS) (*16, 17*). Each of these methods has found important applications in the analysis and structural elucidation of large nonvolatile molecules. However, it should be noted that in each of these methods desorption and ionization are accomplished in one step so that the sensitivity is ultimately limited to the combined efficiency of the total process. The probability for a sample to be transformed into a parentlike ion is often quite low, ranging generally from <0.01 to 1% (*7, 16, 18*). In addition, each of these methods has their own particular experimental problems which may limit their usefulness such as difficult sample preparation in FD (*4*) and varying sensitivity depending on the background matrix for PDMS (*17*). These techniques also require analysis to be performed under vacuum conditions and thus may not be simple to interface with liquid introduction techniques such as HPLC (*19*). Derivatization of these compounds has traditionally been used as a means of volatilization especially for gas chromatography work; however, this requires extensive sample preparation. Thus, further development of methods to analyze for thermally labile compounds under real analysis conditions is warranted.

The main requirements for an ionization method applicable to organic and biologically important molecules are high sensitivity (10^{-9} g) and mass spectra that are reasonably interpreted. The ionization method must produce a substantial molecular ion peak for identification. Thus, a logical solution

0003-2700/86/0358-2137$01.50/0 © 1986 American Chemical Society

to achieving high sensitivity and soft ionization would be to separate the volatilization and ionization processes into two steps. The method investigated herein combines the laser desorption process with chemical ionization in atmospheric pressure mass spectrometry. In LDMS generally a high-powered laser is used to simultaneously desorb and ionize molecules on a surface. The actual number of ions produced in the desorption process is quite small compared to the large number of neutral species that result at power densities below 10^8 W/cm^2 unless precharged ions of organic salts are formed at the surface (*18*). The ratio of ions to neutrals is described to first approximation by the Saha–Langmuir equation (*20*) where the key parameter is the temperature at the surface. Although this equation applies to an equilibrium condition, which is obviously not the case here, it nevertheless appears that a higher laser power density at the surface will result in a higher transient surface temperature and a greater percentage of ions produced, although at some point extensive fragmentation may also result. Thus, in the experiments described herein a low-powered laser is used to generate mainly neutrals from the surface resulting in a much larger sample available for ionization and subsequent study. The ionization method used is a ^{63}Ni β atmospheric pressure ionization source in which the radioactive ^{63}Ni generates kiloelectronvolt electrons that ionize the components in air resulting in a series of ion/molecule reactions where the charge is transferred to the trace species of interest (*21*, *22*). These ion/molecule reactions depend on the proton affinities of the reactant ions and the molecules to be examined herein should be very effectively ionized by this method since these biological species generally either are N-heterocycles or have amino groups attached to the aromatic ring and thus have relatively high proton affinities. In addition, the enormously large number of collisions that occur at atmospheric pressure may result in nearly 100% efficient ionization for these high proton affinity species although the method does not work well for molecules with low proton affinities. In the case of species with high electron affinities negative ion mass spectrometry may serve as a sensitive means of detection, although in either detection mode the ultimate sensitivity is limited by transmission of the ions produced into the mass spectrometer. This technique is in essence a form of chemical ionization that is accomplished at atmospheric pressure and should thus produce soft ionization with production of molecular ions, M^+, or their protonated counterparts, MH^+, as in CIMS under vacuum conditions. In combination with a soft vaporization method such as LD the production of nonvolatile molecular ions should be easily achieved.

Laser desorption of neutrals followed by chemical ionization (CI) under vacuum conditions has recently been studied and shown to be extremely promising for analysis of nonvolatile drug compounds (*14*, *15*). Laser desorption and subsequent ionization at atmospheric pressure, however, may minimize fragmentation that can occur in either process under vacuum if excessive internal energy is produced in the molecule since the large number of collisions at atmospheric pressure can relax this excess energy. In addition, the API method does not require manipulation of the sample under vacuum and desorption of neutrals at atmospheric pressure should greatly extend the time the sample remains in the ionization region for study using a scanning mass spectrometer as opposed to a relatively low pressure CI source.

McIver et al. (*23*) have separated the desorption and ionization processes in laser desorption using a low-power laser pulse to desorb organic molecules from a Pt surface followed by electron beam ionization in a FTMS. They observed essentially no background ions produced by LD alone at the low laser power used and thus avoided ion/molecule reactions that may occur near the surface as in SIMS. In addition, the KrF excimer laser used for desorption was found to produce laser photoionization for benzene and naphthalene within the 20-ns pulse width so that most of the neutrals have moved away from the surface before ionization occurs and only the molecular ion was obtained. More recently, Tembreull and Lubman (*24*) have explored laser desorption of neutrals by an infrared laser into a supersonic jet followed by laser multiphoton ionization by a second, ultraviolet laser source in a time-of-flight device as a possible technique for volatilizing nonvolatiles for study in laser ionization spectroscopy.

EXPERIMENTAL SECTION

The experimental apparatus consists of an atmospheric pressure source chamber interfaced to a Spectra-EL Extranuclear quadrupole mass spectrometer and has been described previously (*25*). The ionization source is a ^{63}Ni β foil which initiates a series of ion/molecule reactions at atmospheric pressure which in turn ionizes trace organic species in the spectrometer. The device is normally kept at 200 °C and the β source at 270 °C and a countercurrent flow of N_2 gas produced as the boiloff from liquid N_2 at a rate of 650 cm^3/min is continuously swept through the ionization chamber to keep it clean and free from contamination. The atmospheric pressure inlet to the mass spectrometer is a 30-μm orifice which is maintained at a higher temperature than the body in order to prevent clogging. The temperature of the device was lowered to an appropriate value if the melting point of the sample was lower than the normal operating temperature.

Laser desorption was accomplished by use of the second harmonic of a Nd:YAG laser (532 nm). The laser desorption results were also checked in several cases by using the fourth harmonic (266 nm). Although in previous work under vacuum conditions the CO_2 laser is shown to be the preferable desorption source (*24*), the 532-nm source was used due to its availability for this experiment. The typical laser energy used for desorption is on the order of 100 mJ or less, which corresponds to a maximum power of 7×10^6 W/cm^2, although significantly less power was needed to desorb some of the lower melting point compounds. This is in contrast to laser desorption–ionization experiments where energies on the order of 0.5–1 J are used to obtain sufficient ion yields for measurement. However, since we are trying to desorb neutrals, much lower laser power can be used. The laser beam is used unfocused and is collimated with an iris to 4–5 mm in diameter. The beam enters the device through a quartz window and impinges on a metal rod from which the sample is desorbed. In the initial experiments the rod was made of aluminum, but later Teflon and finally ceramic was used. The ceramic was found to work well for these experiments with less interference of the electric field in the cell than the metal rod and was found to provide the best soft desorption–ionization results. The rod enters from the opposite side of the chamber and extends into the guard ring structure where the desorption and subsequent ionization occurs. The guard ring structure provides a homogeneous electric field and the ions produced in the device are kept moving on axis to the mass spectrometer orifice.

The sample is prepared by dissolving it in a solvent such as toluene and applying the paste that results on the end of the rod. The sample is allowed to dry so that a coat, which probably consists of several hundred monolayers, is formed on the surface. The laser power is adjusted to a level high enough to produce a signal but is kept low enough so that the whole sample is not desorbed off the surface in one shot. Generally, the desorption process may take anywhere from 15 s to several minutes at which time all the sample has been removed from the surface depending on the adjusted power level. The ^{63}Ni β source then produces ionization and the ions are injected into the mass spectrometer and mass analyzed. If a grid is biased to prevent ionization from the ^{63}Ni β source, then the signal after desorption becomes negligible and any background is due to leakage of electrons from the β source through the grid. After desorption, the device is slowly cleaned by the N_2 flow through the cell, although a small background memory signal may remain for some time in cases where there is a limited background pressure from the sample that has deposited on the hot walls of the IMS. This memory appears even at low cell temperatures, which means that sput-

Table I. Product Ions Produced by LD-APIMS

	mol wt	obsd ions	rel peak heights	melting point, °C
		I. Purines and Pyrimidines		
adenine	135	136 MH^+		>360
guanine	151	152 MH^+		>300
hypoxanthine	136	137 MH^+		>300
cytosine	111	112 MH^+	70	>300
		111 M^+	25	
		223 M_2H^+	100	
		222 M_2^+	70	
thymine	126	127 MH^+	100	316–317
		252 M_2^+	80	
		253 M_2H^+	60	
creatinine	113	114 MH^+	88	255
		227 M_2H^+	100	
uric acid	168	164 $(M - 4H)^+$		>300
		II. Nucleosides		
adenosine	267	268 MH^+		234–236
cytidine	243	244 MH^+		215–216
thymidine	242	243 MH^+		187–189
inosine	268	269 MH^+		222–223
		III. Amino acids		
arginine	174	175 MH^+		223–224
glutamic acid	147	148 MH^+		205
histidine	155	156 MH^+		273
tryptophan	204	205 MH^+		280–290
tyrosine	181	182 MH^+		300
		IV. Vitamins		
niacin	123	124 MH^+	100	236–239
		245 $(M_2 - H)^+$	27	
pyridoxine hydrochloride	205	169 $(M - HCl)^+$	100	214
		154 $(MH - HCl - CH_4)^+$	24	
riboflavin	376	241 $(M - C_5H_{11}O_4)^+$		290
thiamine hydrochloride	336	266 $(M - 2HCl)^+$		260
		V. Drugs		
iminostilbene	193	193 M^+		199
amitryptyline hydrochloride	313	277 $(M - HCl)^+$		195–197
imipramine hydrochloride	316	280 $(M - HCl)^+$		158–159
desipramine hydrochloride	302	266 $(M - HCl)^+$		217–218
norliptyline hydrochloride	299	263 $(M - HCl)^+$		215–217
chlorpromazine hydrochloride	354	318 $(M - HCl)^+$		194–195
trimeprazine hemitartate salt (X)	373	298 $(M - X)^+$		159–160
		VI. Catecholamines		
tyramine	137	138 MH^+		161–163
Dopa	197	198 MH^+		280
dopamine hydrochloride	189	154 $(MH - HCl)^+$		241–243
epinephrine	183	184 MH^+		204
norepinephrine hydrochloride	205	154 $(MH - HCl - NH_2)^+$		145–147

tering of the sample on the walls from the reactant ions may occur and in essence a background SIMS signal results.

RESULTS AND DISCUSSION

In this work we have investigated the use of laser desorption of neutrals followed by atmospheric pressure ionization for several types of biologically important molecules as shown in Table I. Among the species studied are included the purine and pyrimidine bases and their ribose sugars, amino acids, vitamins, various antidepressant drugs, and catecholamines. The key result here is that in most cases the molecular ion or MH^+ is obtained with little or no fragmentation. Thus, in such cases the desorption process produces intact neutrals and the CI API method softly ionizes these species. In the direct LD method where desorption and ionization are produced together, ionization often occurs by attachment of an alkali cation to the desorbed molecules so that $M + Na^+$ or $M + K^+$ is detected and often a number of fragmentation peaks are observed (*12*). In neutral desorption followed by API rarely are more than one or two fragment peaks observed in the compounds studied thus far. In cases such as cytosine, thymine, and creatinine strong dimer peaks may appear after

desorption since these compounds are known to dimerize readily (*26*), although the dimer peaks will decrease as the concentration becomes lower. Further, there are examples such as pyridoxine and norepinephrine where small molecule elimination cannot be avoided, although it is not clear whether this is due to the desorption or ionization step. Nevertheless, the present technique provides a relatively simple mass spectrum characteristic of each of these compounds. In addition, the compounds that are in the M·HCl form are detected without the HCl, which must be detached in either the desorption or ionization step.

Other methods have been studied for volatilization and ionization of these nonvolatile compounds and each has its own advantages and disadvantages. Electron beam ionization has been used in conjunction with LD vaporization and a number of heating probe and in-beam techniques (*27*); however EI generally results in fairly extensive fragmentation. For example, free amino acids generally provide weak molecular ions due to facile loss of the carboxyl group (*27*). Field ionization (FI) and field desorption (FD) have also been used to ionize the compounds studied herein and often a strong molecular ion peak is present, however, a number of fragmentation peaks generally accompany the mass spectra, which in the case of FD may depend upon sample preparation and emitter conditions (*27*). Benninghoven and co-workers have extensively explored the use of SIMS in a host of drugs and biological species similar to those studied herein (*5*, *6*). This method often yields substantial parentlike secondary ions and the sensitivity reaches down to the nanogram level. Positive cationized molecular ions and fragments often appear and a number of fragments may be observed from almost any of these samples which are useful for structural determination. For example, in the detection of adenosine monophosphate not only do MH^+ and $(M + Ag)^+$ appear but also BH^+, $(B + Ag)^+$, and $(B + H - NH_3)^+$ appear, where B is the free base (*5*). However, ions sputtered from the surface may react rapidly in the gas phase directly above the surface with sputtered neutral species and produce mass spectra that complicate identification of the surface species. Fast atom bombardment (FAB), which uses an energetic beam of fast neutral atoms to desorb and ionize molecules from a solid surface or liquid matrix, can often provide molecular ions or more generally their protonated or cationized counterparts with interpretable fragmentation similar to that of SIMS (*9*, *10*). This method though avoids several of the problems of ion bombardment such as surface charging of insulating samples as well as practical problems of steering the beam into the high voltage regions of ion sources of modern mass spectrometers (*9*). In this process as in SIMS both ions and neutral organic molecules are desorbed and it is believed that the number of desorbed neutral molecular species is significantly larger than the number of secondary molecular ions (*11*). Campana et al. (*11*) have therefore used FAB followed by CI in order to increase the formation of protonated molecular ions with enhancements on the order of 3 orders of magnitude in some cases. In addition by choice of the CI agent and source pressure they were able to change the relative degree of fragmentation and enhance the protonated molecular ion by varying amounts compared to the FAB spectrum obtained by direct sample bombardment. This enhancement may be due to collisional stabilization of excited secondary ions at higher pressure as well as charge exchange to the species of interest. In this method the desorption and ionization steps have been separated in order to increase both the efficiency and selectivity of ion production.

Atmospheric pressure ionization mass spectrometry had been successfully used previously by Kambara and co-workers (*28*, *29*) for analysis of thermally labile biomolecules using

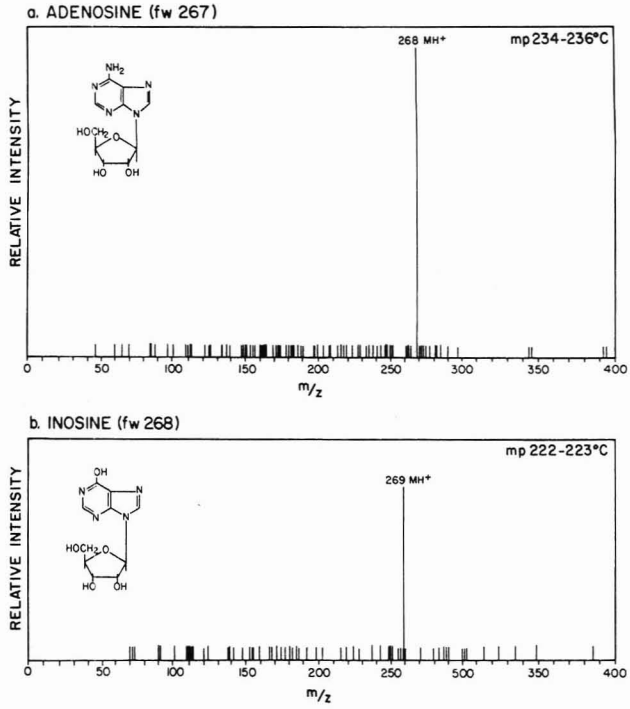

Figure 1. Laser desorption atmospheric pressure ionization mass spectrum (LD-APIMS) of (a) adenosine and (b) inosine where ~0.1 mg was initially deposited on the rod.

HPLC injection with a nebulizing sample introduction system. Chemical ionization was accomplished by use of a corona discharge source where reactant ions used were protonated solvent molecules and their clusters. They examined a number of nonvolatile species similar to those of this study and were generally able to detect large MH^+ signals with minor fragmentation. In the case of glutamic acid for example they observed a significant MH^+ peak; however, fragments were also found at mass 130 $(MH - H_2O)^+$ and mass 113 $(MH - H_2O - NH_3)^+$ (*29*). A peak at mass 55 appears due to water solvent ions, i.e., the protonated water cluster $(H_2O)_3H^+$, and in any spectrum a number of solvent peaks may be present due to acetone solvent including its protonated clusters or clusters with fragment species. In the spectrum of glutamic acid taken herein, we observe only MH^+ with the LD-APIMS method. A mass spectrum taken using thermal evaporation or CI in Kambara's work showed only a minor MH^+ peak and a strong $(MH - H_2O)^+$ peak plus other fragments (*29*). Kambara had also compared this method with SIMS and found significant fragmentation with this latter method as well as cationized species although he also observed MH^+ ions. Several nucleosides were also examined and in the case of inosine Kambara observed MH^+ but also reported a more intense base peak at mass 137 as well as solvent peaks (*28*). The same pattern appeared for adenosine where he observed MH^+ and also a strong base fragment peak at 136 and guanosine where the major peak is due to the base moiety at mass 152 although the MH^+ peak at mass 283 is also present. In our work using LD-APIMS with the ^{63}Ni β source method we observe only the molecular ions for the nucleosides examined (see Figure 1). In addition, Kambara had studied thiamine by nebulization introduction into his APIMS system. He saw a strong MH^+ peak; however, he also observed bond cleavage to produce peaks at mass 122 and 144 (*29*). In our LD-APIMS system we observe only MH^+ at mass 265 for thiamine. Liquid injection into atmospheric pressure mass spectrometry has also been achieved using an ion-evaporation (IE) method, which both volatilizes and ionizes large molecules using a special type of field desorption obtained when ions are present in small aqueous droplets (*30*). It is found that if one produces

a mist of highly charged droplets that are allowed to evaporate, then the field at their surface becomes high enough to produce field emission. This process occurs at atmospheric pressure and was found to be an effective source for producing molecular ions for nonvolatile biological species (*30*). Thus, the LD-APIMS can be considered a method that acts to augment the information obtained by present methods of analysis such as SIMS, CI, EI, FAB, IE, and FD rather than replacing any given technique. However, the LD-APIMS may be quite suitable for interfacing with liquid injection where the LD method used herein obviates the problem of injection of large amounts of solvent into the ionization source. The interface could conceivably be accomplished by use of a moving belt scheme similar to that developed by Vestal et al. (*13*), where the material is desorbed on the belt at atmospheric pressure so that no special differential pumping is required and the setup remains fairly simple.

Catecholamines and their metabolites are a particularly important group of compounds requiring accurate analysis since they are often associated with detection and treatment of such diseases as Parkinson's and neurogenic tumors. Detection of pure catecholamines in clinical samples is often difficult due to their rapid oxidation and decomposition. Using laser desorption followed by ^{63}Ni β source atmospheric pressure ionization we observe a strong MH^+ peak for tyrosine with no fragmentation. Tyrosine acts as the precursor from which the catecholamines are synthesized. DL-Dopa exhibited an intense peak at mass 198, which corresponds to MH^+, whereas dopamine hydrochloride was found to have a peak at mass 153, which corresponds to MH^+ with elimination of HCl. Norepinephrine hydrochloride gave a single characteristic peak at mass 154, which appears to be $(MH - HCl - NH_2)^+$, and epinephrine and tyramine also showed a single peak at mass 184 and 137, respectively, which correspond to the molecular ion, MH^+.

The key to the results reported herein is the desorption process. In LD generally a high-powered (0.5–1 J) pulsed laser is used to rapidly desorb a thin coat of material several monolayers thick from a surface to produce ions for examination in a mass spectrometer. In the desorption process used herein a thick coat of sample, which may consist of >100 monolayers, is desorbed using a low-powered laser where the energy is generally <100 mJ/pulse. Since we are interested in neutrals rather than ions, significantly lower desorption energies can be used. A similar method has been used for laser desorption under vacuum conditions in our previous work (*24*), and although the initial desorption occurs from the surface, this desorption sends a shock wave through the solid causing material to desorb from the sample into the gas phase. Thus, depending on the laser power, a small amount of material can be desorbed on each laser pulse so that the sample may last up to several minutes even at a laser repetition rate of 10 Hz. At high laser power all the material may be desorbed in several laser pulses. The slow desorption method is preferable for sensitive detection since rapid desorption may saturate the reactant ions from the ^{63}Ni β API source and much of the sample is thus lost for sensitivity measurements. In addition, it had been shown in our earlier desorption work that a CO_2 laser was preferable for desorption than the 532 nm from the Nd:YAG laser. The green light may cause fragmentation of ions produced by desorption and can even cause ionization and fragmentation of the neutrals if the power is high enough. However, neither of these processes is detected in these experiments since both processes involved are probably relaxed by the large number of collisions at atmospheric pressure and very few ions appear to be produced by the initial desorption process. The fourth harmonic of the Nd:YAG laser at 266 nm is found to work equally well since the desorption does not appear to be wavelength dependent and subsequent ionization by resonant two-photon ionization (R2PI) does not occur in most of these N-heterocyclic systems since their ionization potentials are too high. There are some cases, however, where R2PI does appear to occur in the gas phase after desorption and with the correct choice of wavelength selectivity could be achieved in the ionization process. A more optimal experiment for the future might be desorption by a visible or infrared beam followed by laser ionization after a delay adjusted to allow the maximum amount of material to be desorbed into the gas phase followed by mass analysis of the laser produced ions.

A measure of the sensitivity was made by accurately preparing several solutions of imipramine (mass 280) in methanol in which the concentration ranged from 40 μg/mL down to 0.6 μg/mL. A microsyringe was used to place 10 μL of solution on the end of the desorption probe and allowed to dry. The highest concentration solution provides about 400 ng on the surface, which corresponds to ~40 monolayers, while the lowest concentration provides about 6 ng, which corresponds to a coverage of ~0.5 monolayers. Laser desorption followed by API was performed and pulse counting was used to record the number of ions detected over a given time interval during which desorption occurred. A plot of the number of counts against the amount of material originally placed on the surface gave a reasonably straight line, which upon extrapolation indicates an ultimate detection limit for this compound of ~0.3 ng of sample above the background ion count in our device. This estimate of the sensitivity has not been absolutely optimized for such parameters as collection efficiency of the ions from the API cell or for background count ionization although only one to three counts were detected over the 80 s over which counting was performed. Our results also show that this sensitivity limit should be comparable or even better for most of the compounds examined in this study. We repeated these results on chlorpromazine (mass 319) over a sample range of 200 ng down to 4 ng and obtained an ultimate detection limit estimated at 0.3–0.4 ng.

Registry No. Adenine, 73-24-5; guanine, 73-40-5; hypoxanthine, 68-94-0; cytosine, 71-30-7; thymine, 65-71-4; creatinine, 60-27-5; uric acid, 69-93-2; adenosine, 58-61-7; cytidine, 65-46-3; thymidine, 50-89-5; inosine, 58-63-9; arginine, 74-79-3; glutamic acid, 56-86-0; histidine, 71-00-1; tryptophan, 73-22-3; tyrosine, 60-18-4; niacin, 59-67-6; pyridoxine hydrochloride, 58-56-0; riboflavin, 83-88-5; thiamine hydrochloride, 67-03-8; iminostilbene, 256-96-2; amitryptyline hydrochloride, 549-18-8; imipramine hydrochloride, 113-52-0; desipramine hydrochloride, 58-28-6; nortriptyline hydrochloride, 894-71-3; chlorpromazine hydrochloride, 69-09-0; trimeprazine hemitartrate salt, 4330-99-8; tyramine, 51-67-2; DOPA, 59-92-7; dopamine hydrochloride, 62-31-7; epinephrine, 51-43-4; norepinephrine hydrochloride, 329-56-6.

LITERATURE CITED

(1) Beckey, H. D. *Int. J. Mass Spectrom. Ion Phys.* **1969**, *2*, 500.
(2) Daves, G. D., Jr. *Acc. Chem. Res.* **1979**, *12*, 359.
(3) Giessman, U.; Rollgen, F. W. *Org. Mass Spectrum.* **1976**, *11*, 1094.
(4) Schulten, H. R. "Advances in Field Desorption Mass Spectrometry". In *Soft Ionization Biological Mass Spectrometry*; Morris, H. R., Ed.; Heyden Press: Philadelphia, PA, 1980.
(5) Eicke, A.; Sichtermann, W.; Benninghoven, A. *Org. Mass Spectrom.* **1980**, *15*, 289.
(6) Benninghoven, A.; Sichtermann, W. *Anal. Chem.* **1978**, *50*, 1180.
(7) Benninghoven, A.; Sichtermann, W. *Int. J. Mass Spectrom. Ion Phys.* **1981**, *38*, 351.
(8) Day, R. J.; Unger, S. E.; Cooks, R. G. *Anal. Chem.* **1980**, *52*, 557A.
(9) Barber, M.; Bordoli, R. S.; Sedgwick, R. D. "Fast Atom Bombardment Mass Spectrometry". In *Soft Ionization Biological Mass Spectrometry*; Morris, H. R., Ed.; Heyden Press: Philadelphia, PA, 1980.
(10) Barber, M.; Bordoli, R. S.; Elliott, G. J.; Sedgwick, R. D.; Tyler, A. N. *Anal. Chem.* **1982**, *54*, 645A.
(11) Campana, J. E.; Freas, R. B. *J. Chem. Soc., Chem. Commun.* **1984**, *21*, 1414.
(12) Posthumus, M. A.; Kistemaker, P. G.; Meuzelaar, H. L. C.; Ten Noever de Brauw, M. C. *Anal. Chem.* **1978**, *50*, 985.
(13) Hardin, E. D.; Fan, T. P.; Blakely, C. R.; Vestal, M. L. *Anal. Chem.* **1984**, *56*, 2.

(14) Perchalski, R. J.; Yost, R. A.; Wilder, B. J. *Anal. Chem.* **1983**, *55*, 2002.
(15) Cotter, R. J. *Anal. Chem.* **1980**, *52*, 1770.
(16) MacFarlane, R. D. *Acc. Chem. Res.* **1982**, *15*, 268.
(17) MacFarlane, R. D.; Vemura, D.; Veda, K.; Hirata, Y. *J. Am. Chem. Soc.* **1980**, *102*, 875.
(18) Conzemius, R. J.; Capellen, J. M. *Int. J. Mass Spectrom. Ion Phys.* **1980**, *34*, 197.
(19) Jungclas, H.; Danigel, H.; Schmidt, L.; Dellbrügge, J. *Org. Mass Spectom.* **1982**, *17*, 499.
(20) Datz, S.; Taylor, E. H. *J. Chem. Phys.* **1956**, *25*, 389.
(21) Carroll, D. J.; Wernlund, R. F.; Cohen, M. J. U.S. Patent 3 639 757 (Feb 1, 1972).
(22) Horning, E. C.; Horning, M. G.; Carroll, D. I.; Dzidic, I.; Stillwell, R. N. *Anal. Chem.* **1973**, *45*, 936.
(23) Sherman, M. G.; Kingsley, J. R.; Hemminger, J. C.; McIver, R. T., Jr. *Anal. Chem. Acta* **1985**, *178*, 79.
(24) Tembreull, R.; Lubman, D. M. *Anal. Chem.* **1986**, *58*, 1299–1300.
(25) Kolaitis, L.; Lubman, D. M. *Anal. Chem.* **1986**, *58*, 1993–2001.
(26) Stryer, L. *Biochemistry* W. H. Freeman: San Francisco, CA, 1975.
(27) Fales, H. M.; Milne, G. W. A.; Winkler, H. V.; Beckey, H. D.; Danice, J. N.; Barron, R. *Anal. Chem.* **1975**, *47*, 207.
(28) Kambara, H. *Anal. Chem.* **1982**, *54*, 143.
(29) Kambara, H. *Mass Spectrom.* **1983**, *31*, 87.
(30) Iribarne, J. V.; Dziedzic, P. J.; Thomson, B. A. *Int. J. Mass Spectrom. Ion Phys.* **1983**, *50*, 331.

RECEIVED for review March 7, 1986. Accepted April 28, 1986. We gratefully acknowledge initial financial support of this research by a Cottrell Research Grant and the donors of the Petroleum Research Fund, administered by the American Chemical Society. We also acknowledge support of this work from the Army Research Office under Grant DAAG29-85-K-1005 and also the Department of Defense through the U.S. Army Research Office under Grant No. DAAG29-85-G-0018 for purchase of the equipment used in this work. We also acknowledge support under NSF Grant CHE83-19383.

Photoionization in Air with Ion Mobility Spectrometry Using a Hydrogen Discharge Lamp

C. S Leasure, M. E. Fleischer, G. K. Anderson, and G. A. Eiceman*

Department of Chemistry, New Mexico State University, Las Cruces, New Mexico 88003

An ion mobility spectrometer (IMS) suitable for operation in air at atmospheric pressure using direct gaseous photoionization (PI) was demonstrated by using an on-axis mounted 10.2-eV hydrogen discharge lamp (λ_{max} 121.5 nm). Penetration of UV photons into air in PI-IMS was determined by using product ion intensity and analyte location as 15 mm from the lamp window. Spectra were obtained for ten organic compounds and were simple with one to three peaks. Detection limits in PI-IMS ranged from 0.1 to 50 ppb directly without any sample preconcentration and working ranges were 1000–10 000. Detection limits were similar to those for conventional chemical ionization but working ranges were improved 100- to 1000-fold. Operation of PI-IMS in nitrogen with on-axis placement of the discharge lamp was complicated by penetration of photons >2 cm through the Bradbury–Nielson shutter leading to analyte ionization in the drift region. Use of nitrogen as a drift gas was possible with the lamp placed perpendicular to gas flow. However, sensitivity and limits of detection were better with the on-axis design in air since ionization volumes were 7.1 cm^3 for the on-axis mount but only 4.0 cm^3 for the side-mount.

Ion mobility spectrometry (IMS) has been used in the separation and detection of organic (*1–5*) and inorganic (*6, 7*) compounds in the gas phase at atmospheric pressure. Separation is achieved through differences in gaseous mobility of molecular or pseudomolecular ions under the influence of an applied electric field and against the flow of a neutral drift gas. Ions are formed from analyte indirectly through ion/molecule collisions with reagent ions (chemical ionization) or directly through photoionization. Attractive features for use of IMS in the detection of atmospheric pollutants include high sensitivity, operation at atmospheric pressure, relatively simple instrumentation, and moderate selectivity. However, extreme memory effects, overloading of response, and, more importantly here, a narrow working range have been associated with and restricted the utility of IMS. Each of these limitations may be attributed to either flow characteristics or principles of ionization in IMS rather than limitations in mobility-based separations.

Historically, the most common ionization method in IMS has been chemical ionization (CI) initiated with reactant ions formed from β emission. While CI provided high sensitivity (sub-part-per-billion levels) and some selectivity in ionization processes, working ranges of analyte response vs. concentration were only 10–100. Selectivity of ionization in mixtures was quantitatively shown recently to be governed in CI-IMS by proton affinities in the positive mode (*5*) and electron affinities in the negative mode (*6*). Unfortunately, selectivity of ionization was controlled mostly by molecular parameters, rather than by the analyst, except for the choice of reagent gas. While lasers have been used in IMS for controllable selectivity through multiphoton ionization (*8*), the high cost and typically large size of lasers presently restrict convenient and economical application of laser-IMS as a routine laboratory tool and especially as an atmospheric sensor. However, a Kr vacuum (vac)-ultraviolet (UV) discharge lamp was proposed (*9*) as an inexpensive and practical alternative to lasers for photoionization (PI) in IMS. While the PI discharge lamp in prior PI-IMS measurements showed sensitivity only 0.1–0.01 of that obtained in CI-IMS, reactant ions that interfere in detection of analytes with short drift times were not observed. Thus, PI-IMS may have promise as a direct atmospheric sensor for contaminant in air.

A serious limitation with vac-UV discharge lamps is the presumed need for a nitrogen atmosphere due to oxygen quenching of photons (*10*). Although this was not important in PI-IMS use as a gas chromatographic detector with nitrogen carrier gas (*9*), direct IMS sensing of atmospheric samples would be facilitated with air as the drift gas. In exploratory studies in this laboratory, an existing PI-IMS design (*11*) showed satisfactory response for aromatic hydrocarbons in nitrogen. However, response for these compounds with the

0003-2700/86/0358-2142$01.50/0 © 1986 American Chemical Society

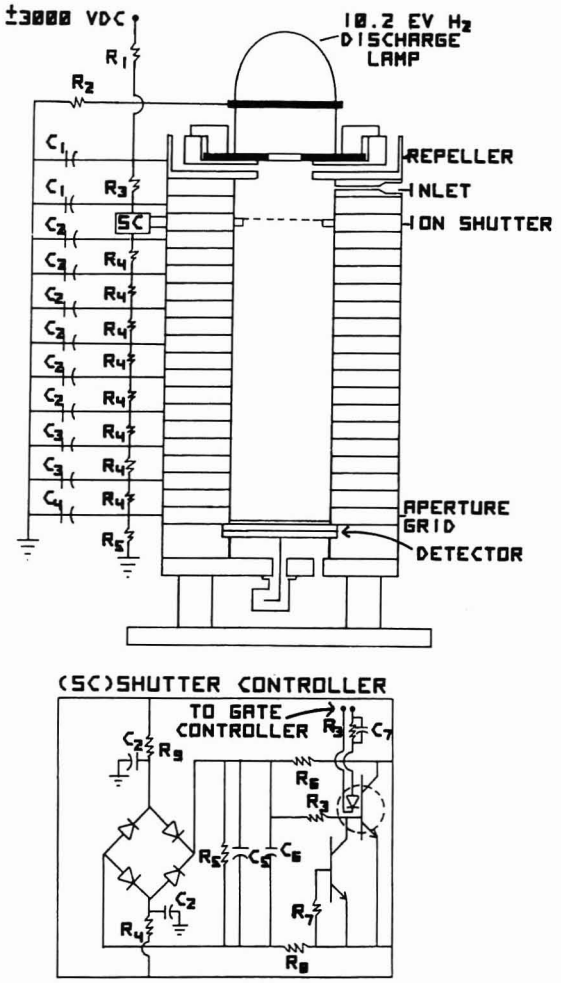

Figure 1. Schematic of ion mobility spectrometer with hydrogen discharge lamp for photoionization in air. Values for resistors and capacitors are as follows: R_1, 59 kΩ; R_2, 1.8 MΩ; R_3, 220 kΩ; R_4, 240 kΩ; R_5, 470 kΩ; R_6, 18 kΩ; R_7, 15 kΩ; R_8, 20 kΩ; R_9, 110 kΩ; C_1, 0.0047 μF, 6 kV; C_2, 0.002 μF, 6 kV; C_3, 0.005 μF, 4 kV; C_4, 0.47 μF, 600 V; C_5, 0.1 mF, 500 V; C_6, 4 mF, 450 V; C_7, 0.047 μF.

same IMS design in air was weak and irregular. In work reported here, a vac-UV hydrogen discharge lamp was incorporated into an PI-IMS with a reconfigured ionization chamber for detection of organic compounds directly in air with high sensitivity. Our objectives were to explore response characteristics of this new PI-IMS design for comparison to existing ionization sources and to describe the PI behavior of selected organic compounds in air at atmospheric pressure. The goal of this study was development of IMS instrumentation that will be suitable for direct atmospheric sensing of hazardous organic compounds without membrane interfaces or radioactive sources.

EXPERIMENTAL SECTION

Instrumentation. An ion mobility spectrometer described previously (*12*) was modified by replacing the ^{63}Ni ionization source ring and repeller with a 10.2-eV hydrogen discharge lamp (HNU Systems, Boston, MA) as shown in Figure 1. A second design was assembled with the lamp mounted perpendicular to flow as described by Hill et al. (*9*). In both arrangements, the drift region was 9.0 cm and the reaction region was 2.0 cm. the IMS drift gas was typically breathing air and was used in unidirectional flow at 300 mL/min. Conditions of operation were as follows (unless otherwise noted): tube temperature, 149 °C; reaction region field, 221 V/cm; drift region field, 244 V/cm; ion shutter pulse width, 0.2 ms; repetition rate, 28 Hz; amplification, 10^9–10^{11} V/A; and barometric pressure, 662.0–668.1 mmHg. Sample was introduced to the IMS using headspace vapors over pure solutes in a small flow (1–10 mL/min) of nitrogen gas as previously described (*5*, *7*, *12*).

Table I. Reduced Mobilities for Selected Compound Determined in Air Using PI-IMS

analyte	K_0, cm²/(V s)	% rel abundance
benzene	2.23 ($C_6H_6^+$)[a]	20
	2.04 ($C_6H_6NO^+$)[a]	100
p-xylene	2.01 ($C_8H_{10}^+$)	100
	1.83 ($C_8H_{10}NO^+$)	20
naphthalene	1.92 ($C_{10}H_8^+$)	100
	1.80 ($C_{10}H_8NO^+$)	20
acetone	2.19 ($C_3H_6O^+$)	100
2-butanone	2.05 ($C_4H_8O^+$)	100
acetophenone	1.82	100
2-propanol	1.87	100
	1.97	20
	2.13	20
	2.46	10
1-butanol	1.88	100
	1.73	50
	1.97	25
aniline	2.09	100
	1.98	25
	1.54	10
n-butylamine	1.95	100
	1.69	100

[a] Mass identified, ref 13.

Reagents. The following compounds were acquired from J. T. Baker Chemical Co. (Phillipsburg, NJ): 2-propanol, 1-butanol, *p*-xylene (all reagent grade), and acetone (HPLC grade). Pesticide grade benzene and reagent grade aniline were acquired from Fisher Scientific Co. (Fair Lawn, NJ); HPLC grade 2-butanone and 99+% naphthalene were acquired from Aldrich Chemical Co. (Milwaukee, WI). All reagents were used without further purification.

Procedures. Characteristics of operation and features of response for PI-IMS in air were determined by use of several studies. These studies were designed generally to measure flow effects, electric field effects, and particulars in the use of air as a drift gas in PI-IMS. Comparisons were made to PI-IMS operation in nitrogen drift gas.

A. Response Curves for On-Axis Mounting. Response of the IMS to concentration for pure compounds was measured in air as ion current for peaks vs. gaseous concentration of neutral analyte in the drift gas. Compounds of environmental importance from several chemical classes were selected for study as shown in Table I.

B. Ion Shutter Field Study. At concentrations of 15, 177, or 1500 ppb for *p*-xylene in air drift gas, dc offset was measured in PI-IMS vs. shutter field with the ion shutter operated in either static open or static closed modes. Identical measurements were made in nitrogen drift gas. Peak heights were also measured for pulsed shutter operation in air at *p*-xylene concentrations of 170–1500 ppb. Measurements were obtained at eight settings of ion shutter field from 260 to 3000 V/cm.

C. Response Curves for Side Mount. Response curves of peak height vs. concentration for benzene, *p*-xylene, and aniline were collected in air drift gas. The PI-IMS ionization chamber was assembled by use of an existing PI source design (*9*). Response curves were also collected with this design using nitrogen drift gas.

D. Measurements of Penetration of Photons in Air. The PI-IMS is on-axis configuration with undirectional flow was altered so that air drift gas was vented from the side of the drift tube. Spacers made from 6 mm i.d., 1 mm thick Teflon O-rings were then used to locate the vent at a fixed distance from the discharge lamp. In ths particular design, clean air was introduced into the IMS at the repeller at 2 L/min and was used simply to oppose drift gas flow for displacing neutrals from the lamp window to the gas vent. Analyte was introduced to the IMS through the ring adjacent (and down-flow) to the shutter. The vent was set at distances of ~0, 0.5, 1.0, and 1.5 cm from the lamp window. In this experimental design, the distance from lamp face to available neutral analyte could be partially controlled to measure distances photons traveled. Response at each distance was

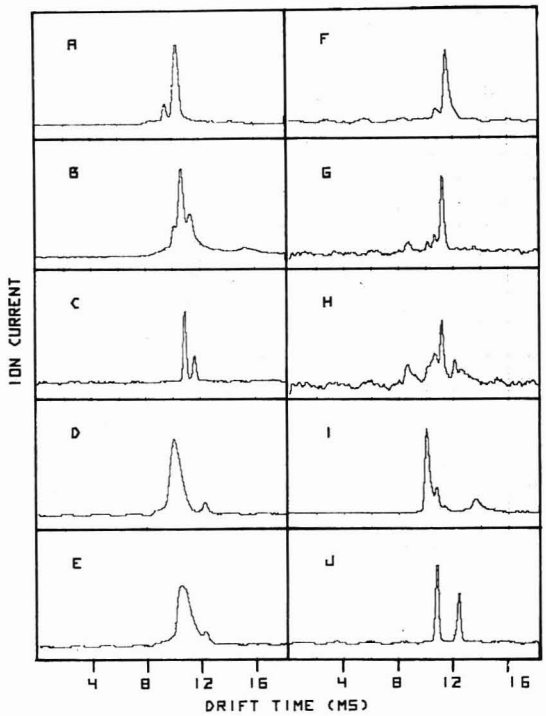

Figure 2. Ion mobility spectra for (A) benzene, (B) *p*-xylene, (C) naphthalene, (D) acetone, (E) 2-butanone, (F) acetophenone, (G) 2-propanol, (H) 1-butanol, (I) aniline, (J) *n*-butylamine.

measured by using ion currents for peak heights with *p*-xylene at 150 ppb in the drift gas.

RESULTS AND DISCUSSION

Ion mobility spectra in air using the on-axis mounting for the hydrogen discharge lamp are shown for ten compounds in Figure 2 and were characterized as simple spectra with limited or no fragmentation. As expected, reactant ions were not observed and thus presented no interference in spectra. Reduced mobilities for these same ten compounds are listed in Table I along with ion identities, some of which were mass identified while others were only posulated. The IMS spectrum for benzene consisted of two peaks at reduced mobilities (K_0) of 2.04 and 2.23 $cm^2/(V\ s)$ while literature values were 2.04 and 2.25 $cm^2/(V\ s)$, respectively, (*13*). The smaller peak at K_0 of 2.23 $cm^2/(V\ s)$ was mass identified previously as the molecular ion and the larger peak at K_0 of 2.04 $cm^2/(V\ s)$ was $C_6H_6NO^+$ (*13*). Similar behavior was also seen in spectra for other aromatic compounds including *p*-xylene and naphthalene. Spectra for ketones showed one product ion which may have been the molecular ion but which was not mass identified. The trend in drift times for acetophenone, 1-butanone, and acetone reflected a size difference consistent with and indicative of molecular ions for each compound. Alcohols typically formed a major ion with three or more minor ions as shown in Table I. One major peak with a reduced mobility of 2.09 $cm^2/(V\ s)$ (literature value 2.01 $cm^2/(V\ s)$ (*14*)) and two minor peaks with reduced mobilities of 1.98 and 1.54 $cm^2/(V\ s)$ were found in the PI-IMS spectrum of aniline. The widths of product ions from molecules with –OH, –NH, and C=O moieties were occasionally 2- to 3-fold larger than those for aromatic compounds. This may have been due to formation of multiple cluster ions or ion–ion repulsions in the PI source. Indeed ion currents in PI-IMS were 100-fold larger than ion currents in CI-IMS. Apart from improvements in peak broadening, a larger ion shutter field for optimum control of ion leakage was anticipated from their greater ion densities. Thus, effects from shutter field on sensitivity and response in PI-IMS were determined. Nonetheless, preliminary results showed that on-axis operation of a PI-IMS was suitable for

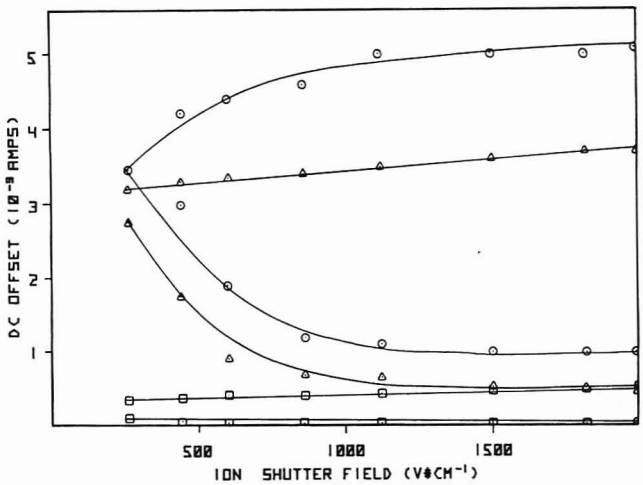

Figure 3. Plots of dc offset vs. ion shutter field for *p*-xylene at static open and static closed ion shutter modes in air for (O) 15 ppb, (△) 177 ppb, and (□) 1500 ppb.

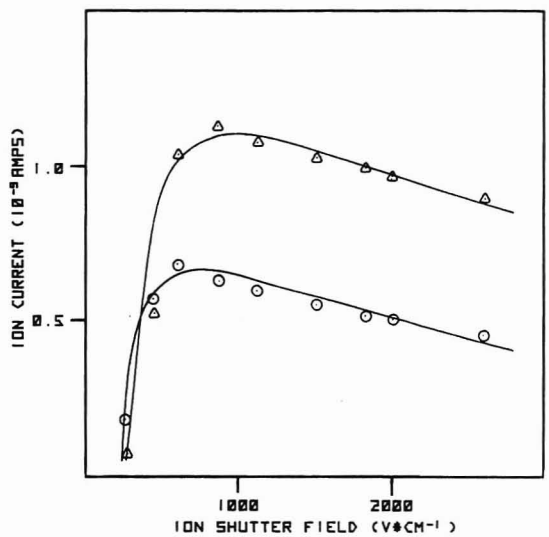

Figure 4. Plots of ion current vs. ion shutter field for *p*-xylene for pulsed ion shutter modes: (O) 177 ppb, (△) 1500 ppb.

air sensing of compounds with a range of moieties and that spectra were simple as described in earlier PI-IMS instruments (*9*).

In Figure 3, a plot of dc offset vs. shutter field in air for three concentrations of *p*-xylene in air (15, 177, and 1500 ppb) are shown for static tests of the ion shutter in fully open and in fully closed modes. With the shutter in the fully open mode, ions passed continuously through the shutter to the drift region while ions were deflected from the drift region with the shutter closed and only ion leakage (or background current) was measured. Ions penetrated through the shutter almost completely at the lowest field for all three concentrations as shown in Figure 3. The difference in offset between the open and closed modes increased initially with higher shutter fields and then became constant and at concentrations of 177 and 1500 ppb the effect from increasing ion shutter fields from 260 to 1000 V/cm was particularly pronounced. On the basis of these results the shutter field of greatest strength should provide highest sensitivity with a low background. However, at increasing shutter fields in the pulsed shutter (normal) operation, the peak heights for *p*-xylene increased rapidly, reached a maximum between 600 to 1000 V/cm, and decreased slightly at higher fields as shown in Figure 4; the maximum was concentration-dependent. This shutter behavior was described previously in CI-IMS and was rationalized by using transverse vs. axial field arguments (*15*).

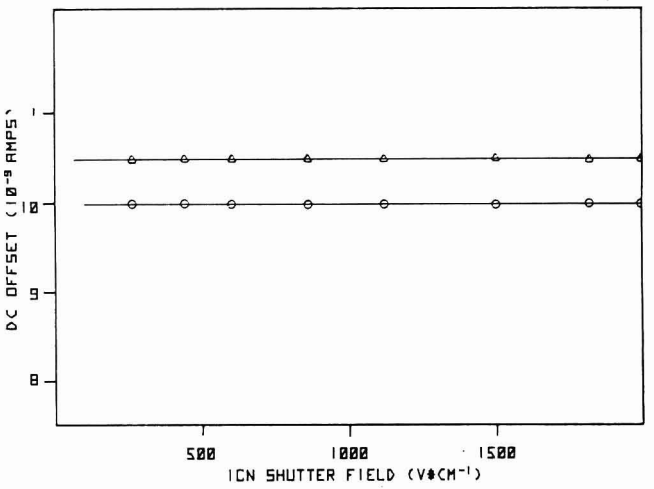

Figure 5. Plots of dc offset vs. ion shutter field for *p*-xylene at static open (O) and static closed (Δ) ion shutter modes in nitrogen with *p*-xylene at 177 ppb.

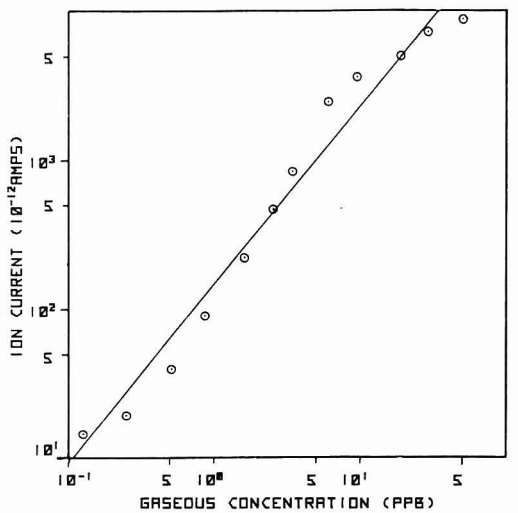

Figure 6. Plot of log ion current vs. log gaseous concentration from PI-IMS with on-axis design for naphthalene in air.

Table II. Summary of Response Curves from PI-IMS Operation in Air

analyte	working range	slope, pA/ppb	LOD, ppb	ionization potential (ref 16)
naphthalene	2×10^3	155	0.1	8.12
benzene	2×10^3	200	2	9.24
p-xylene	1×10^3	6	5	8.44
acetone	5×10^3	10	1	9.69
2-butanone	5×10^3	0.1	1	9.50
acetophenone	1×10^2	20	0.1	9.27
aniline	5×10^3	5	0.2	7.7
n-butylamine	1×10^3	1	10	8.71
2-propanol	1×10^2	4.4	10	10.15
1-butanol	1×10^2	0.15	50	10.04

Regardless of origin of this effect, higher electrical fields in the shutter caused a decrease in sensitivity and 1120 V/cm was chosen for the shutter field in all further studies.

In Figure 5, results from a dc offset study with nitrogen drift gas are shown for static tests with open and closed ion shutter for three concentrations of *p*-xylene in the on axis PI-IMS. As seen in the flat and large dc offset in this figure, the ion shutter was virtually ineffective in deflecting ions at any shutter field. Penetration of UV photons to distances greater than 2 cm in nitrogen and through the shutter caused ionization in the drift region since photons were largely unobstructed by the shutter wires. Consequently, PI-IMS with an on-axis design was made inoperable with nitrogen drift gas and the oxygen quenching of photons in air drift gas was actually advantageous in the on-axis design.

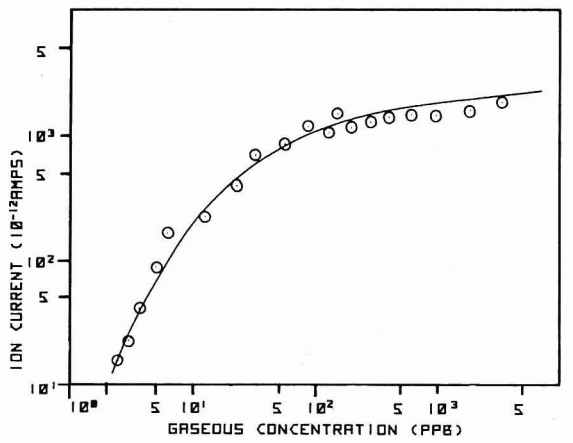

Figure 7. Plot of log ion current vs. log gaseous concentration from PI-IMS with on-axis design for benzene in air.

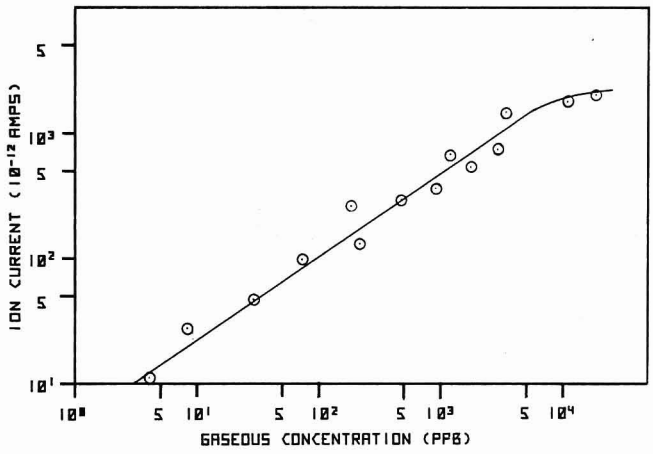

Figure 8. Plot of log ion current vs. log gaseous concentration from PI-IMS with on-axis design for acetone in air.

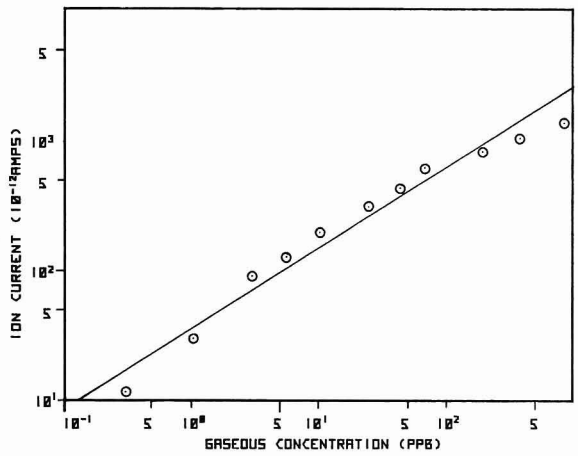

Figure 9. Plot of log ion current vs. log gaseous concentration from PI-IMS with on-axis design for aniline in air.

Response vs. concentration was determined individually for the ten compounds with PI-IMS in air drift gas and plots of ion current (from peak height) vs. gaseous concentrations for four representative compounds are shown in Figures 6–9. Slopes of curves and detection limits for all other compounds are summarized in Table II. Three of the four plots were relatively linear with a working range of between 200 and 100 000. The plot for naphthalene Figure 6 showed a working range of about 2000, a slope of 155 pA/ppb, and a limit de-

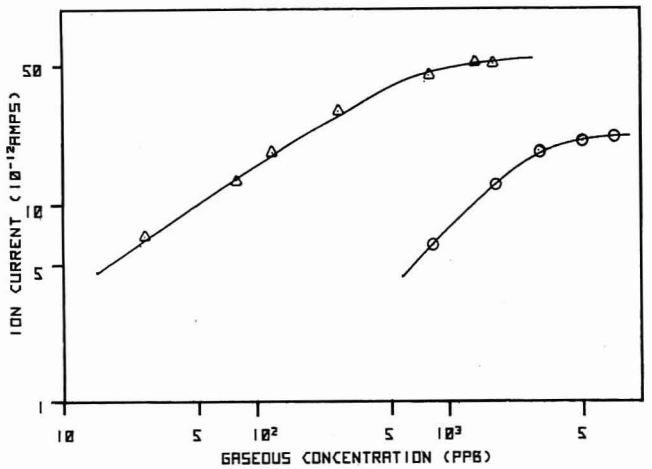

Figure 10. Plot of log ion current vs. log gaseous concentration from PI-IMS with side-mount design for benzene in (O) air and (Δ) nitrogen.

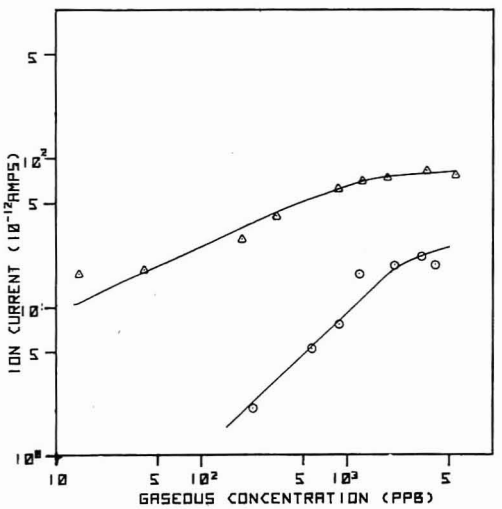

Figure 11. Plot of log ion current vs. log gaseous concentration from PI-IMS with side mount design for *p*-xylene in (O) air and (Δ) nitrogen.

tection (LOD) of 0.1 ppb. In a previous study using CI-IMS, the LOD for naphthalene was approximately 0.1 ppb, the working range was 200, and the slope was 0.2 pA/ppb. In the plot for benzene from the PI-IMS (Figure 7), the LOD was near 2 ppb with a curved working range of about 2000 and a slope of 200 pA/ppb. In comparison, LOD for benzene in CI-IMS was 100 ppb, working range was 20 and the slope was 0.3 pA/ppb. Clearly, PI-IMS had not only the same or better LODs than CI-IMS but also had a greater working range and correspondingly higher ionization efficiency than a 12 mCi ^{63}Ni source. Response of the instrument to acetone showed a working range in Figure 8 of about 5×10^3, a slope of 10 pA/ppb, and a LOD of less than 1 ppb. Similarly, a working range of about 5×10^3 a slope of 5 pA/ppb and a LOD near 0.1 ppb was obtained for aniline. Both 2-propanol and 1-butanol had working ranges of about 1000 with LODs of 10 and 50 ppb, respectively. However, at concentrations higher than 250 ppb for 2-propanol and 500 ppb for 1-butanol, peak widths increased 4-fold and drift times were longer (decreased K_6 values) than at lower concentrations. These shifts were attributed to clustering of these compounds and not mutual repulsion of ions since little or no broadening or shifting of drift time was observed for the other compounds at similar concentrations. Hydrogen bonding of these alcohols should favor cluster formation at higher gaseous concentrations. Not surprisingly, other compounds in which hydrogen bonding should not occur showed no comparable behavior.

In Figures 10–12, response for three compounds, benzene, *p*-xylene, and aniline, in air drift gas are shown for PI-IMS

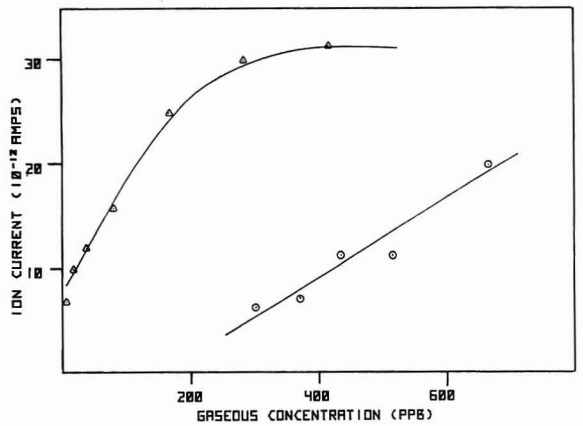

Figure 12. Plot of ion current vs. gaseous concentration from PI-IMS with side-mount design for aniline in (O) air and (Δ) nitrogen.

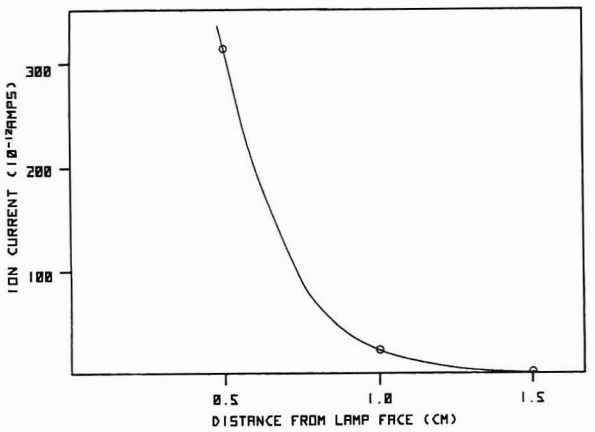

Figure 13. Plot of ion current vs. distance through clean air from PI lamp window for 150 ppb *p*-xylene in air drift gas.

with the side-mounted design of Hill (*9*). In this configuration, photon transmission was perpendicular to the direction of analyte flow in the drift gas. This instrumental configuration was also operated with nitrogen drift gas to evaluate photon adsorption by the air drift gas. In general, the LODs for these compounds were better in nitrogen rather than in air. The approximate LODs for the three compounds (in air and nitrogen, respectively) were as follows: benzene, 500 and 15 ppb; *p*-xylene, 100 and 10 ppb; and aniline, 200 and 10 ppb. The slopes for the response curves were also different in air and nitrogen and were (pA/ppb) as follows: benzene, 4.3×10^{-3} and 5.4×10^{-2}; *p*-xylene, 7.8×10^{-3} and 1×10^{-1}; and aniline, 3.4×10^{-2} and 9.0×10^{-2}, respectively. Since the only difference between the two curves for each plot was the drift gas, poorer PI-IMS response in air with a side-mounted lamp was caused by photons quenched by oxygen through the 3.1 cm distance from lamp to analyte. Although the LODs in nitrogen drift gas were better than LODs in air in the side-mount PI-IMS, even the best LODs were still not as sensitive as those in CI-IMS and in PI-IMS with the on-axis mount. This difference was attributed to the small volume of ionization of 4.0 cm^3 in the side mount configuration vs. 7.1 cm^3 for the on-axis design.

The volume of ionization and distance of photon penetration into the gas for the PI-IMS with on-axis lamp mounting was determined by using an indirect approach. Drift gas was vented through spacers placed in the IMS tube rather than through the repeller. The vent was set initially just below the face of the lamp. The probe analyte in the air drift gas was *p*-xylene at 152 ppb and clean air at 2000 mL/min was introduced at the repeller to ensure that neutral analytes did not diffuse toward the lamp. In this manner, for ionization of *p*-xylene to occur, the radiation had to penetrate a distance

through only clean air. The distance from the lamp face was increased in steps of 0.5 cm until no peak from *p*-xylene was observed. A plot of ion current vs. distance from the lamp face is shown in Figure 13, and ions, were not formed from the *p*-xylene neutrals at 1.5 cm from the face of the lamp. Although not refined, this experiment yielded an approximate distance of photon travel in air and the estimated volume of ionization for on-axis design was 7.1 cm^3, which was 2-fold greater than that for the side mount. The larger volume for ionization in on-axis PI-IMS was believed responsible, in part, for the low LODs and larger working ranges compared to the side-mount configuration.

ACKNOWLEDGMENT

Machining and advice from John Tobin are gratefully acknowledged.

Registry No. Benzene, 71-43-2; *p*-xylene, 106-42-3; naphthalene, 91-20-3; acetone, 67-64-1; 2-butanone, 78-93-3; acetophenone, 98-86-2; 2-propanol, 67-63-0; 1-butanol, 71-36-3; aniline, 62-53-3; *n*-butylamine, 109-73-9.

LITERATURE CITED

(1) Karasek, F. W. *Anal. Chem.* **1971**, *43*, 1982.
(2) Karasek, F. W.; Tatone, O. S.; Kane, D. M. *Anal. Chem.* **1973**, *45*, 1210.
(3) Karasek, F. W.; Denney, D. M. *Anal. Chem.* **1974**, *46*, 1312.
(4) Karasek, F. W.; Kim, S. H.; Rokushika, S. *Anal. Chem.* **1978**, *50*, 2013.
(5) Vandiver, V. J.; Leasure, C. S.; Eiceman, G. A. *Int. J. Mass Spectrom. Ion Proc.* **1985**, *66*, 223.
(6) Eiceman, G. A.; Leasure, C. S.; Vandiver, V. J. *Anal. Chem.* **1986**, *58*, 76.
(7) Leasure, C. S.; Eiceman, G. A. *Anal. Chem.* **1985**, *56*, 1890.
(8) Lubman, D. M.; Kronick, M. N. *Anal. Chem.* **1982**, *54*, 1546.
(9) Baim, M. A.; Eatherton, R. L.; Hill, H. H., Jr. *Anal. Chem.* **1983**, *55*, 1761.
(10) Lubman, D. M.; Kronick, M. N. *Anal. Chem.* **1983**, *55*, 867.
(11) Eiceman, G. A.; Vandiver, V. J. *Anal. Chem.* **1986**, *58*, 2331.
(12) Eiceman, G. A.; Leasure, C. S.; Vandiver, V. J.; Rico, G. *Anal. Chim. Acta* **1985**, *175*, 135.
(13) Kim, S. H.; Betty, K. R.; Karasek, F. W. *Anal. Chem.* **1978**, *50*, 1784.
(14) Lubman, D. M.; Kronick, M. N. *Anal. Chem.* **1983**, *55*, 1486.
(15) Vandiver, V. J.; Eiceman, G. A., submitted for publication in *J. Phys. E*.
(16) *Handbook of Chemistry and Physics*; CRC Press: Cleveland, OH, 1970; pp E80–85.

RECEIVED for review February 18, 1986. Accepted May 5, 1986.

Measurement of the Laser-Induced Ionization Yield for Lithium in an Air–Acetylene Flame

B. W. Smith,[1] L. P. Hart,[2] and Nicoló Omenetto*

Joint Research Centre, Chemistry Division, Ispra (Varese), Italy

Single-step excitation and two-step excitation, followed by collisional ionization, have been used to measure the ionization yield of lithium atoms produced in a separated air–acetylene flame. The excitation is provided by two pulsed, tunable dye lasers, pumped simultaneously by an excimer laser and tuned to two connected transitions of the atom. The ionization signal is taken simultaneously with the fluorescence signal, which is measured with a monochromator and a photomultiplier placed at 90° with respect to the laser beams. The ionization yield for a single-step excitation at 670.784 nm was found to be 0.26%, increasing to 58% for two-step excitation (670.784 + 460.286 nm). By use of these values in a simplified theoretical treatment of the ionization process, it is shown that one can obtain order of magnitude estimates of the effective collisional ionization rate coefficients of the process(es) assumed.

The techique of laser-enhanced ionization or optogalvanic spectroscopy is now well established in atmospheric pressure flames as a very sensitive analytical tool and a most versatile diagnostic method (*1–6*). Several types of lasers have been used to provide the primary excitation step, i.e., flash lamp pumped dye lasers, nitrogen, Nd-YAG, or excimer-pumped dye lasers, and continuous wave lasers. The duration of the interaction between the atoms and the radiation field was therefore widely different, being in the microsecond range for flash lamp pumped lasers, in the nanosecond range for the gas discharge pulsed lasers, and in the millisecond range for the continuous wave (CW) lasers. In the last case, the interaction time is the dwell time of the atoms in the laser beam, which is in turn dictated by the rise velocity of the flame gases. The ability to achieve a significant ionization clearly depends, among other parameters, upon the length of the laser pulse. As it has been shown from simple theoretical considerations (*1–3*), the ionization yield, i.e., the ratio between the number of ions created during the laser pulse and the total number of neutral (ground state) atoms present in the laser volume, will approach unity when an optically saturating laser pulse has a duration that significantly exceeds the reciprocal of the effective ionization rate of the laser populated excited state (see below). The fact that the excitation produced in ~5 ns by a single laser beam to a level lying some electronvolts below the ionization potential would result in a significant ionization yield can then be questioned, since in this case the collisional ionization rate from that level is believed to much lower than the radiative and quenching rates. A second laser can therefore be used to populate in a stepwise manner (*6–9*) excitation levels much closer to the ionization potential of the atom. In this way, the ionization yield should increase appreciably. Although such considerations are clearly stressed in several papers, there appears to be no experimental measurement of the absolute value of the ionization yield in the case of single-step or two-step excitation with pulsed or CW lasers. A neutral depletion of 60% and 75% for sodium atoms and for laser pulses longer than 100 μs was reported in the air–hydrogen and air–acetylene flame, respectively (*10, 11*). However, laser-induced chemistry (*12*) was also considered to be partially responsible for the observed depletion.

The aim of this work is to describe the experimental evaluation of the absolute ionization yield of the lithium atoms in the air–acetylene flame. Single-step and two-step excitation

[1] Permanent address: Department of Chemistry, University of Florida, Gainesville, FL 32611.
[2] Present address: Oregon State University, Department of Chemistry, Corvallis, OR 97331.

0003-2700/86/0358-2147$01.50/0 © 1986 American Chemical Society

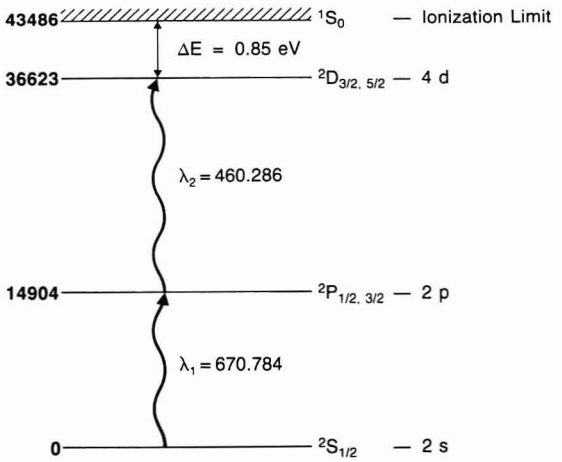

Figure 1. Simplified partial energy level diagram of the lithium atom pertinent to the experiment described in this work. Laser transitions are indicated in nanometers; energies (left) in cm^{-1}.

is provided by two laser beams tuned at appropriate bound transitions of the atoms. The duration of the laser pulses is 4.4 ns. The temporal wave forms of the laser have been experimentally measured and are reported elsewhere (*13*). The total number of lithium atoms in the laser volume has been measured by an absolute absorption method (*14*) and the ionization detection system is calibrated in terms of output voltage per electron produced.

The results obtained have been used in connection with a simplified excitation–ionization model to derive order of magnitude estimates of the effective ionization rate coefficients. Due to the simplified nature of the model, especially regarding the temporal shape of the laser pulses, assumed to be rectangular, quantitative accuracy cannot be claimed nor was this in the scope of the present investigation. It is believed, however, that the absolute measurement of the ionization yield for short laser pulses represents an essential step in any further modeling of the ionization mechanism in flames.

THEORETICAL CONSIDERATIONS

The ionization yield, IY, is defined here as the number of ions (electrons) produced during the laser excitation time divided by the total number of atoms present in the laser volume. When two lasers are used, it is assumed that their pulse duration is strictly the same and that the spatially uniform excitation volumes in the flame overlap perfectly.

If the signal obtained by integrating the electron current pulse is representative of the total charge created by the laser (*15*), the yield is given by

$$\mathrm{IY} \equiv \frac{n_e}{n_T} = \frac{(\text{voltage pulse})/e(\Delta t_p)^{-1}\xi}{n_a b \pi r_l^2} \qquad (1)$$

In this equation, n_e is the number of electrons produced in the ionization process, n_T is the total number of atoms in the laser volume, e is the charge of the electron (coulomb), Δt_p is width of the electron pulse (seconds), ξ is the calibration factor of the detection system ($V\ A^{-1}$), n_a is the number density of the atoms in the flame (cm^{-3}), b is the laser interaction length in the flame (cm), and r_l is the radius of the laser(s) beam(s) in the flame (cm).

The energy level diagram for lithium pertinent to our experiment is shown in Figure 1. In the single-step excitation scheme, one laser is tuned to the resonance transition at 670.784 nm, involving the excited 2p doublet, and subsequent collisional ionization occurs in the flame. With this simple scheme, the fraction of the total number of atoms ionized during an optically saturating laser pulse, i.e., the ionization yield, will be given by (*1–3*, *13*)

$$\frac{n_i}{n_T} = 1 - \exp\left[-\left(\frac{g_2}{g_1 + g_2}\right)k_{2i}\,\Delta t_l\right] \qquad (2)$$

In this equation, g_1 and g_2 are the statistical weights of the ground state (here indicated as level 1) and of the excited doublet (here indicated as level 2), k_{2i} (s^{-1}) is the coefficient describing the *effective* collisional ionization rate (*14*), and Δt_l (s) is the duration of the (rectangular) laser pulse. As stated before, Δt_l must be (much) greater than the ratio $(g_1 + g_2)/(g_2 k_{2i})$ in order to attain unity ionization yield.

In the two-step excitation scheme, the second laser is tuned to 460.286 nm (see Figure 1) and populates the 4d doublet, which lies 0.85 eV below the ionization limit. If this last level is indicated as level 3 and if both transitions are now optically saturated, the ionization yield is given by (*13*)

$$\frac{n_i}{n_T} = 1 - \exp\left[-\left(\frac{g_3}{g_1 + g_2 + g_3}\right)k_{3i}\,\Delta t_l\right] \qquad (3)$$

where now g_3 is the statistical weight of the 4p doublet and k_{3i} becomes the effective ionization rate coefficient.

From these simple considerations it can be deduced that, provided that the ionization yield can be measured experimentally under saturated conditions, order of magnitude estimates can be inferred from eq 2 and 3 for both k_{2i} and k_{3i}.

As seen in eq 1, the number of absorbing atoms in the laser volume needs to be measured. This number can safely be identified with n_T (see eq 2 and 3) since this last number in the air–acetylene flame at 2500 K represents, within less than 0.1%, the lithium ground-state population. In order to accurately evaluate n_T, it was decided to adopt the well-known absorption method (*14–17*). In our case, the laser can be considered to be a quasi-continuum excitation source, since its spectral bandwidth exceeds approximately 10 times the absorption profile of the lithium atoms in the flame.

Finally, to check that the transitions used were optical saturated, atomic fluroescence was simultaneously recorded with a conventional monochromator–photomultiplier setup.

EXPERIMENTAL SECTION

A block diagram of the experimental arrangement is shown in Figure 2. An excimer laser (Model EMG-102, Lambda Physik, Göttingen, FRG) operated with XeCl pumped two dye lasers (Jobin Yvon, Longjumeau, France) that were located on either side of a commercially available flame ionization system (SOPRA, Bois Colombes, France), which was modified for this experiment. A hole was drilled at the rear of the burner housing to allow the observation of fluorescence and the long path burner head normally used for flame ionization was replaced by a homemade capillary-type burner fitted with an argon sheath. This burner, which has been used in our laboratory in several emission and fluorescence experiments (*18*), was mounted on a standard mixing chamber with pneumatic nebulization. Gas flows were accurately measured with calibrated rotameters. As shown in Figures 1 and 2, the first laser provided the excitation of lithium atoms from the ground state (λ_1 670.784 nm) and was adjusted to be temporally coincident with laser 2, tuned at 460.286 nm. With this scheme, the final level was 0.85 eV below the ionization limit. Both laser beams were expanded and then reduced in size with apertures to provide spatially homogeneous beams of about 0.3 cm diameter. Figure 3 shows the geometry of the beams in the flame and their positions with respect to the burner surface and the high-voltage electrode.

The energy of the lasers was measured with a volume absorbing calorimeter (Model 38-0101, Scientech, Boulder, CO). The temporal coincidence of the two beams was ascertained by examining their respective temporal positions with a fast photodiode (Electrooptical Products Division ITT, Fort Wayne, IN, Type F-4000, S-5 response). The high-voltage electrode (molybdenum around a water-cooled glass tube) was biased at −1800 V and the electrons produced via laser excitation were collected at the burner, converted to a voltage, and processed by a boxcar integrator

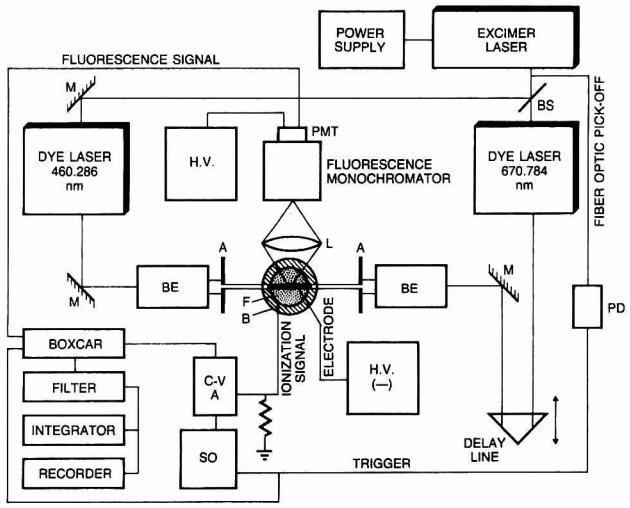

Figure 2. Experimental setup: BS, beam splitter; PMT, photomultiplier tube; PD, photodiode; H.V., high voltage; BE, beam expander; M, mirror; L, Lens; A, aperture; F, flame; B, burner; C-VA, current-to-voltage amplifier; SO, storage oscilloscope. See text for description.

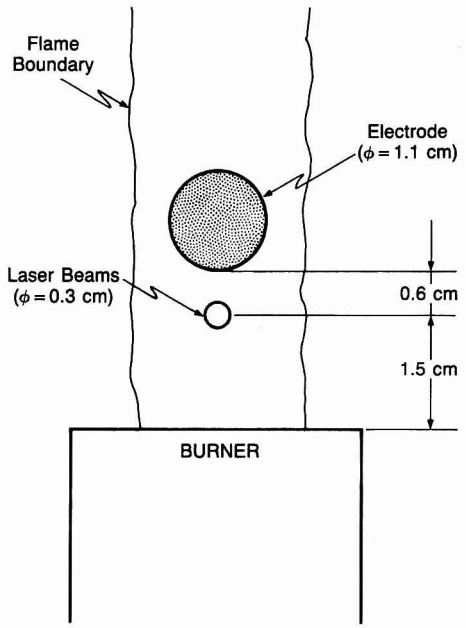

Figure 3. Geometrical arrangement of the exciting laser beams, high voltage electrode and burner for the experiment described.

(Stanford Research Corp., Palo Alto, CA). The dc flame ionization background was blocked by an ac coupling capacitor. Some characteristics of the signal processing electronics have been discussed by Berthoud et al. (*19*). The resonance fluorescence signals are collected at 90° with respect to the excitation axis with a lens and a high luminosity monochromator (Model H-10, Jobin Yvon, Longjumeau, France). The signal from the photomultiplier (Type R928S, Hamamatsu Corp., Japan) is then fed to the boxcar integrator.

RESULTS AND DISCUSSION

As stated before, the calculation of the ionization yield requires the determination of two parameters: the number of electrons produced per laser pulse and the number of ground-state atoms present in the region of excitation. These will be discussed separately.

The electrons collected at the burner head produce a current pulse of approximately 200 ns width (*1*, *19*). In our experiment the pulse is stretched by the current to voltage converter and arrives at the input to the boxcar integrator as a voltage pulse of 800 nm fwhm and full base width of 1.8 μs. In order to determine the number of electrons produced at the burner head, it is necessary to measure the total integrated voltage pulse at the boxcar and to know the gain of the current to voltage preamplifier at the frequency of the measurement. This gain was calibrated by injecting current pulses of the same shape and duration of those produced by the laser ionization in the flame at the burner head and measuring the time integrated input to the current to voltage preamplifier. The response to a current pulse was 2.913×10^5 V A^{-1} ($\pm 3\%$). The dc gain was also measured by injecting signals from a precision dc current source directly at the input at the amplifier. The dc response was 5.4×10^5 V A^{-1}. The output of the current to voltage preamplifier was integrated with a 2.0-μs boxcar gate width. The response of the boxcar and digital readout were also calibrated against known voltage sources.

In the absence of the excimer firing, the limiting noise was that of the boxcar and had a standard deviation of 10 μV (referred to the boxcar input, 20 Hz repetition rate, 30 laser shots), which corresponded to about 500 electrons at the burner. When the excimer laser was firing, the radio frequency noise increased the background noise to a standard deviation of 14 mV, which corresponded to 6×10^5 electrons at the burner. This noise was much larger than that reported when the overall system was optimized for analytical measurements (*9*).

An aqueous solution of 1 μg/mL of lithium was aspirated into the flame. The resulting current pulse, integrated over the 2.0-μs boxcar gate, was measured with laser excitation set at 670.784 nm only and subsequently with the additional excitation at 460.286 nm. The spatial coincidence of the beams was ascertained by visual alignment at the burner head and subsequently by maximizing the ionization signal by a small adjustment of one beam The energy of the lasers was 62 μJ per pulse for the 670.784-nm beam and 51 μJ per pulse for the 460.286-nm beam, corresponding to peak excitation powers close to 200 kW/cm^2.

The number of ground-state atoms present in the beam volume was determined by carrying out several measurements, namely, the measurement of the laser diameter and spectral bandwidth, the total fraction of radiation absorbed, and the absorption interaction length in the flame. The diameters of the laser beams in the flame (after the beam expanders and the apertures) were measured by translating with a stepping motor a photodiode with 0.1 mm × 0.5 mm aperture across the center of the beam and recording the resulting intensity profile. An estimate was also obtained by recording an image of the beams at the burner on the photographic paper. The beam had a nearly rectangular intensity profile with ±20% reproducible fluctations in the maximum intensity. The diameter was taken as that of a perfectly rectangular profile having the same area as the measured profile. The radius determined in this way, 0.129 ± 0.013 cm, agreed with that estimated from the image on photographic paper within 7%.

The spectral width of the laser was measured in three different ways: (i) the beam was directed into a 1.29-m focal length grating monochromator (Model 1269, Spex, Metuchen, NJ) equipped with 10-μm slits whose instrumental function was 0.006 nm; (ii) a fluorescence excitation profile was recorded with the high luminosity fluorescence monochromator by slowly scanning the laser throughout the absorption profile of the atoms; and (iii) the laser output was directly monitored in absorption during a spectral scan with a photodiode with and without lithium atoms in the flame. The procedures followed agreed with each other satisfactorily and a value of 0.0526 ± 0.005 nm was found.

The measurement under (iii) was indeed performed to evaluate the fraction of the incident laser radiation absorbed in the flame. The photodiode (Type PIN 10 DP/58, United Detector Technology, Santa Monica, CA) fitted with a diffuser was positioned to detect the laser after it traversed the flame.

Table I. Parameters Used in the Calculation of the Curve of Growth

parameters	value	source
$\Delta\lambda_l$	0.0526 ± 0.005 nm	measured
a	0.6 ± 0.1	ref 21–23
k_0/n	(3.136 ± 0.094) × 10^{-12} cm^2	ref 24
$\Delta\lambda_D$	0.0090 ± 0.0002 nm	calculated (T = 2450 K)

[a] $(k_0/n) = ((4 \ln 2)^{1/2}e^2\lambda_0^2/mc^2)(f_{abs}/\Delta\lambda_D)$. Here, e is the electronic charge, m is the electron mass, c is the velocity of light in vacuum, and f_{abs} is the absorption oscillator strength.

It was necessary, to avoid saturation effects and to ensure linearity in the photodiode response, to attenuate the laser with a stack of neutral density filters of total (nominal) density 5.3. With these filters, the residual energy of the laser was approximately 300 pJ per pulse. The current pulse from the photodiode was converted to a voltage and measured with the boxcar averager and a 10-s integrator. Five 10-s integrations were taken on each of eight alternating aspirations of water and a 10 μg/mL lithium solution.

From the theory of absorption of radiation with continuum and line sources (*14–17*) the *product* of the absorbing atoms and the absorption path, i.e., ($n_a b$) in eq 1, can be directly evaluated from the *curve of growth* obtained as the double logarithmic plot of the fraction of radiation absorbed α, vs. this product. A curve of growth was calculated for lithium for this particular experiment. The calibration was carried out by numerical integration using the approach of Hui et al. (*20*). Table I lists the necessary parameters used. These parameters either have been directly measured, e.g., the source half width, or were taken from the literature or calculated. Curves of growth were calculated for the range of damping parameter values from 0.5 to 0.7. Because the measured source width, 0.0526 nm, is rather wide compared to the absorption width of the atoms in the flame (~0.01 nm), the curve of growth in the low density region is not sensitive to changes in the damping parameter (*14–17*). The experimental value of α obtained for a 10 μg/mL solution is slightly outside the linear region of the curve of growth and therefore a ±20% variation in the damping parameter introduces a small (±1%) error in the value of the product ($n_a b$) calculated. The absorption coefficient in Table I has been calculated from the absorption oscillator strength given in the literature (*24*) and is believed to be accurate to within ±3%. The Doppler width has been calculated for a temperature of 2450 K and varies by no more than 2% over a range of ±100 K. This particular flame and burner have been well characterized during several years in our laboratory (*18, 25*). A plot of the curves of growth calculated for three values of the damping parameters is shown in Figure 4.

The value of α = 0.215 corresponds to a product ($n_a b$) = (6.34 ± 0.06) × 10^{11} cm^{-2}. From the value of r_l measured (0.129 cm), the number of atoms in the beam volume for the aspiration of a 10 μg/mL solution is therefore 3.31 × 10^{10}. It is safe to assume that a 1.0 μg/mL solution will introduce exactly 10 times fewer atoms into the flame, and as a result, a value of 3.31 × 10^9 atoms was taken for the calculation of the yield.

As said before, simultaneous fluorescence and ionization measurements were performed. Firstly, it was checked that the resonance transition at 670.784 mm was optically saturated. This was done in the usual way, i.e., by attenuating with calibrated filters the laser output and monitoring the resulting fluorescence signal. A typical saturation curve obtained is shown in Figure 5. A simultaneous monitoring of the ionization and fluorescence signals is reported in Figure 6. Here, it is clearly shown that the ionization enhancement obtained when the second laser step is spectrally tuned into

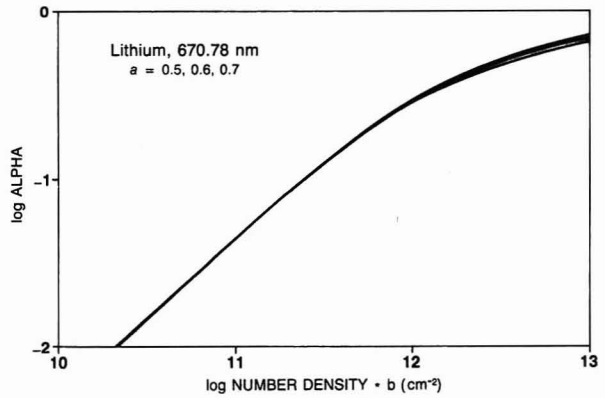

Figure 4. Calculated curves of growth for the fraction of radiation absorbed by increasing values of the product ($n_a b$), for the different values of the damping parameter, a, indicated in the insert: upper curve, a = 0.5; intermediate curve, a = 0.6; lower curve, a = 0.7.

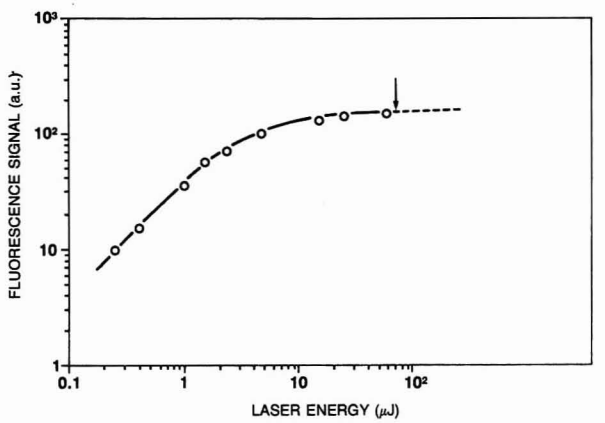

Figure 5. Saturation curve obtained by aspirating 1 μg/mL of lithium in the flame. The arrow indicates the laser energy pertinent to the experiment.

resonance with the 460.286-nm line is accompanied by a decrease in the resonace fluorescence signal at 670.784 nm, indicating the depletion in the population of the 2p doublet.

Table II summarizes all the measured parameters and the values of the ionization yield calculated for single-step and two-step excitation. With the pertinent values in eq 2 and 3, k_{2i} and k_{3i} are calculated as 0.78 × 10^6 s^{-1} and 3.55 × 10^8 s^{-1}, respectively. As repeatedly pointed out, no quantitative accuracy can be claimed for these values, due to the simplifying assumptions of the theory (*15*). However, our values seem to be consistent with those calculated by Smyth et al. (*26*) for their *global* rate constants (s^{-1}) and for principal quantum number n = 4.

CONCLUSION

The results described in this paper can be extrapolated to several other atoms present in a similar flame environment and excitation conditions. If the level excited by a single laser pulse lies several electronvolts below the ionization potential and the pulse duration does not exceed a few nanoseconds, the ionization yield will not be significant. Two interesting observations can then be derived:

(i) A resonance fluorescence measurement obtained under optically saturated conditions can indeed be related to the total number density of the atoms in the two levels connected by the laser excitation. In other words, during the short excitation, no significant losses are expected for the atoms interacting with the laser field. This has important consequences in flame and plasma diagnostics.

(ii) The *analytical* sensitivity and detection limit that can be obtained by the ionization technique under these excitation conditions are still very good, despite the low ionization yield.

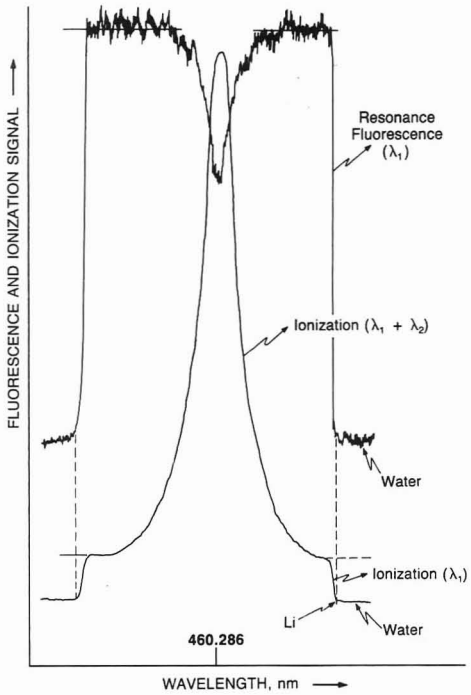

Figure 6. Simultaneous recording of the fluorescence and ionization signals for both single-step and two-step excitation. The wavelength of the second laser, which is spectrally scanned, is indicated in abscissa. Lithium concentration was 0.2 μg/mL. Laser energy was 1 mJ/pulse for both lasers. The explanation of the labeling in the figure is as follows: water, the background level due to the aspiration of water in the flame; Li, the aspiration of the lithium solution into the flame. This results in the ionization signal due only to λ_1 and in the resonance fluorescence signal, also excited at λ_1. Ionization (λ_1 + λ_2) indicates the enhancement in the ionization signal, and the corresponding dip in the fluorescence signal, when λ_2 is tuned to resonance with the second step (460.286 nm). The two-step ionization signal (λ_1 + λ_2) resulted in the saturation of the detection system, and therefore the enhancement cannot be calculated from this figure.

Table II. Parameters Measured and Ionization Yield for Single-Step and Two-Step Laser Excitation

parameters	value	error
$\Delta\lambda_l$ (nm)	0.0526 nm	±0.005
α	0.215	±0.0032
r_1 (cm)	0.129	±0.013
$n_a b$ (cm^{-2}) (10 μg/mL)	6.34×10^{11}	±0.063
ξ (V A^{-1})	2.91×10^5	$\pm 0.087 \times 10^5$
Δt_l (s)	4.4×10^{-9}	$\pm 0.5 \times 10^{-9}$
Δt_p (s)	8×10^{-7}	$\pm 0.2 \times 10^{-7}$
electrons (λ_1) (1 μg/mL)	8.61×10^6	$\pm 2 \times 10^5$
electrons (λ_1 + λ_2) (1 μg/mL)	1.93×10^9	$\pm 2 \times 10^7$
I.Y. (λ_1)	0.0026	±0.0006
I.Y. (λ_1 + λ_2)	0.58	±0.12

This can be easily seen for the lithium case investigated from the following considerations. The number of atoms in the laser volume for a solution of 1 μg/mL was 3.31×10^9. With a 0.26% ionization yield, 8.61×10^6 electrons are formed (see Table II). If the collection efficiency is unity, this number corresponds to a total charge of 1.4×10^{-12} C. For a 800-ns pulse, this will give a current of 1.75×10^{-6} A, or a voltage pulse of 510 mV, by taking into account the calibration of our detection system. If the root-mean-square noise of 1.2 mV is now used (*9*), 1 μg/mL will result in a signal-to-noise ratio of 425 or in a detection limit, for $S/N = 2$, of 4.7 ng/mL. This calculation stresses once again the extremely high sensitivity of the laser-enhanced ionization technique.

When two lasers are used, energy levels close to the ionization limit can be efficiently populated and the ionization yield increases considerably. This scheme is therefore the choice for the best analytical sensitivity. It is recalled that the two-step excitation described here for lithium gave a detection limit of 0.2 pg/mL (*13*).

The errors reported in Table II have been calculated from several repeated measurements of the parameters involved. As far as the accuracy of the values of the ionization yield is concerned, one should take into account the dependence of the current pulse on the position of the laser beam relative to the electrode. In our case, this position was fixed at 0.6 cm (see Figure 3). When the laser beam is aligned near the cathode, the magnitude of the signal should not vary by more than 20% (*15*). However, this correction factor should be kept in mind since the values of the ionization rate coefficients should be modified accordingly. A study of the dependence of the integrated pulse signal on the laser position in the flame is therefore warranted.

Finally, it would be interesting to study the dependence of the ionization yield upon the duration of the laser pulse. For single-step excitation, larger yields (and lower detection limits) should be achieved. It is therefore hoped that similar measurements, along the lines described in this work, will be performed with other types of lasers and for several other elements.

ACKNOWLEDGMENT

The authors are grateful to G. C. Turk for the critical reading of the manuscript and useful suggestions. B. W. Smith and L. P. Hart wish to thank the Joint Research Centre and in particular the Education Training Service of Ispra for the grant of Visiting Scientist Fellowships.

Registry No. Li, 7439-93-2.

LITERATURE CITED

(1) Travis, J. C.; Turk, G. C.; DeVoe, J. R.; Schenck, P. K.; Van Dijk, C. A. *Prog. Anal. At. Spectrosc.* **1984**, *7*, 199–241.
(2) Travis, J. C.; Turk, G. C.; Green, R. B. *Anal. Chem.* **1982**, *54*, 1006A–1018A.
(3) Travis, J. C. *J. Chem. Educ.* **1982**, *59*, 909–914.
(4) Schenck, P. K.; Hastie, J. W. *Opt. Eng.* **1981**, *20*, 522–528.
(5) Camus, P., Ed. *J. Phys.* **1983**, *44*, Suppl. 11.
(6) Turk, G. C.; DeVoe, J. R.; Travis, J. C. *Anal. Chem.* **1982**, *54*, 643–645.
(7) Axner, O.; Lindgren, I.; Magnusson, I.; Rubinsztein-Dunlop, H. *Anal. Chem.* **1985**, *57*, 776–778.
(8) Van Dijk, C. A.; Curran, F. M.; Link, C.; Crouch, S. R. *Anal. Chem.* **1981**, *53*, 1275–1279.
(9) Omenetto, N.; Berthoud, T.; Cavalli, P.; Rossi, G. *Anal. Chem.* **1985**, *57*, 1256–1261.
(10) Schenck, P. K.; Travis, J. C.; Turk, G. C.; O'Haver, T. C. *Appl. Spectrosc.* **1982**, *2*, 168–171.
(11) Schenck, P. K.; Travis, J. C.; Turk, G. C., National Bureau of Standards Washington, DC, unpublished results, 1982.
(12) Muller, C. H., III; Schofield, K.; Steinberg, N. In *Laser Probes for Combustion Chemistry*; Crosley, D. R., Ed.; American Chemical Society: Washington, DC 1960; ACS Symp. Ser. No. 134, pp 189–194.
(13) Omenetto, N.; Smith, B. W.; Hart, L. P. *Fresenius' Z. Anal. Chem.*, in press.
(14) Alkemade, C. Th. J.; Hollander, Tj.; Snelleman, W.; Zeegers, P. J. Th. *Metal Vapours in Flames*; Pergamon Press: New York, 1982; Chapter IX.
(15) Havrilla, G. J.; Schenck, P. K.; Travis, J. C.; Turk, G. C. *Anal. Chem.* **1984**, *56*, 186–193.
(16) Mitchell, A. C. G.; Zemansky, M. W. *Resonance Radiation and Excited Atoms*; Cambridge University Press: London, 1961.
(17) De Galan, L.; McGee, W. W.; Winefordner, J. D. *Anal. Chim. Acta* **1967**, *37*, 436–444.
(18) Rossi, G.; Benetti, P.; Omenetto, N., EUR External Report, (1971) No. 4598e.
(19) Berthoud, T.; Lipinsky, J.; Camus, P.; Stehlé, J. L. *Anal. Chem.* **1983**, *56*, 959–963.
(20) Hui, A. K.; Armstrong, B. H.; Wray, A. A. *J. Quant. Spectrosc. Radiat. Transfer* **1978**, *19*, 509–516.
(21) Hinnov, E.; Kohn, H. *J. Opt. Soc. Am.* **1957**, *47*, 156.
(22) Hofmann, F. W.; Kohn, H. *J. Opt. Soc. Am.* **1961**, *51*, 512.
(23) Lovett, R. J.; Parsons, M. L. *Appl. Spectrosc.* **1977**, *31*, 424.
(24) Wiese, W. L.; Smith, M. W.; Glennon, B. M. *Atomic Transition Probabilities, Vol. 1 Hydrogen through Neon*; National Bureau of Standards: Washington, DC, 1966; NSRDS-NBS-4.
(25) Omenetto, N.; Benetti, P.; Rossi, G. *Spectrochim. Acta, Part B* **1972**, *27B*, 453–461.
(26) Smyth, K. C.; Schenck, P. K.; Mallard, W. G. In *Laser Probes for Combustion Chemistry*; Crosley, O. R., Ed.; American Chemical Society: Washington, DC, 1980; ACS Symp. Ser. No. 134, pp 175–181.

RECEIVED for review February 18, 1986. Accepted May 1, 1986.

High-Temperature Pulsed Nozzle for Supersonic Jet Spectrometry and Its Application to Gas Chromatography

Totaro Imasaka, Takeshi Okamura, and Nobuhiko Ishibashi*

Faculty of Engineering, Kyushu University, Hakozaki, Fukuoka 812, Japan

An electrically controlled pulsed nozzle was constructed, which consisted of a stainless steel body and a solenoid coil. The developed nozzle had a minimum pulse width of 1.3 ms, and it could be operated up to 300 °C. By use of this nozzle, a supersonic jet fluorescence spectrum was measured for perylene. The single components in the mixture of anthracene derivatives were selectively excited by a tunable dye laser, and the sharp fluorescence spectra from those compounds were clearly resolved. The nozzle had a dead volume of 0.2 mL, and it was useful as a detector for gas chromatography. The application to a capillary gas chromatograph combined with a multiphoton ionization detector is also presented.

Supersonic jet spectrometry provides a very simple spectrum, and therefore it has great selectivity in analysis of samples (*1*, *2*). This spectrometric technique has already been used for determination of carcinogenic polycyclic aromatic hydrocarbons (PAHs) such as benzo[*a*]pyrene (*3*, *4*). If a sample molecule with a large molecular weight has a low vapor pressure at a room temperature, then the sample should be heated to maintain a sufficient vapor pressure. In this case a high-temperature nozzle is necessary to expand the sample into a vacuum. A high-temperature continuous-flow nozzle is currently used for this purpose because of its simplicity (*4*, *5*). However, it requires a vacuum system with a large pumping capacity. It is noted that efficient sample cooling is achieved only when the sample gas with sufficient pressure is expanded from a large pinhole. Alternatively, in application of a supersonic jet spectrometric detector to conventional gas chromatography, the flow rate of the expansion gas (~130 mL/min) is larger than the optimum flow rate of the carrier gas (~10 mL/min). In previous studies, the sample is separated under vacuum, and the resolution of the column is degraded (*6*, *7*).

To overcome these problems a high-temperature pulsed nozzle is necessary. It seems to be a key technology of supersonic jet spectrometry especially in the chromatographic determination of less-volatile PAHs. However, commercially available pulsed nozzles are operated below 100 °C (maximum temperature: Quanta Ray, 70 °C; Beam Dynamic, 60 °C; Lasertechniques, 50 °C; General Valve, ?) (*8*), though Lubman et al. have used a commercial nozzle (Quanta Ray) at 80–150 °C (*9*). In our previous study we constructed a pulsed nozzle modified from a fuel injection valve for an automobile (*7*). However, the maximum operating temperature was limited to 150 °C, since it consisted of plastic components and O-ring seals. The sample with a large molecular weight sometimes remained in the nozzle, and the background signal occurring from the sample itself determined the detection limit (*7*, *10*). In the extreme case, the nozzle was completely clogged with sample. In gas chromatography the column is frequently heated to 300 °C, and a high-temperature pulsed nozzle that can be heated to this temperature is required.

A few groups have already constructed high-temperature pulsed nozzles, though their structures have not been clarified in detail. Jortner and co-workers constructed a slit nozzle (0.2 mm wide, 35 mm long, maximum temperature 200 °C), consisting of two concentric cylinders with the inner one rotating (*3*, *11*, *12*). They also constructed a circular pulsed nozzle (0.25–0.6 mm i.d., 400–520 °C) used for measurements of PAHs and porphine compounds (*13*). Chan et al. also used an electrically controlled pulsed nozzle for measurement of fluoranthene (0.25 mm or 0.5 mm i.d., 400 °C) (*14*). Besides, Zewail et al. recorded the spectra for anthracene and its derivatives by using a pulsed nozzle maintained at 140–160 °C (maximum temperature, 200 °C) (*15*, *16*). However, these high-temperature pulsed nozzles were developed only for spectroscopic purposes, and the samples were placed inside the nozzle. Furthermore, its dead volume is not minimized and it is difficult to apply it to the detector for gas chromatography.

In this study we develop a new type of the high-temperature pulsed nozzle with a small dead volume, which can be operated at least to 300 °C. We apply this nozzle to the detector for gas chromatography for selective determination of aromatic hydrocarbons.

EXPERIMENTAL SECTION

Nozzle. The constructed pulsed nozzle is shown in Figure 1. This nozzle is basically identical with the electric fuel injection valve for an automobile produced by Honda (main injection valve, City Turbo). But, it is completely redesigned and reconstructed for operation at a high temperature. The top needle of the plunger for the commercial parts is ground off to form an uniform jet. The commercial orifice (0.8 mm i.d.), which is made of hardened stainless steel, is machined to a cylindrical shape by a cutting tool with a ceramic tip. The orifice is mounted to the stainless steel body by an 8-mm Swagelock. The plunger is attracted by an electromagnet and is pushed back by a spring. The iron core for the electromagnet is machined from the commercial parts and is driven inside the body. The solenoid coil is made by winding a copper wire insulated by Teflon (Junko-sha, 0.32 mm o.d., 15 m, insulator thickness 50 μm) which is heat resistive to 325 °C. The end of the nozzle is machined to a $^1/_4$-in. stainless steel tube. The sample is introduced from a $^1/_{16}$-in. stainless steel tube (0.8 mm i.d.), which is connected by a $^1/_4$-in. to $^1/_{16}$-in. reducing union. The tube is inserted into the spring to reduce the dead volume of the nozzle. The nozzle is mounted to a 6-in. flange by an 18-mm Swagelock. The nozzle is heated by a tape heater or a nichrome wire insulated by a ceramic tube. The electric current is supplied from an power inlet port (Anelva, 954-7227) mounted on the flange. The temperature of the nozzle is monitored by a thermocouple. The nozzle is heated, and the flange is cooled by circulating the tap water. The $^1/_{16}$-in. stainless steel tube for sample introduction was also heated by a tape heater. The temperature was monitored by a thermocouple, which was adjusted to the nozzle temperature.

The electronic circuit for driving the nozzle is shown in Figure 2. The TTL input pulses are amplified by the three-stage transistors, and they control the electromagnet in the nozzle. The pulse width of the jet was determined by the pulse width of the TTL signal, and the sample density was adjusted by the output voltage of the driver.

Apparatus. A block diagram of the supersonic jet spectrometer combined with a gas chromatograph system is shown in Figure 3. The sample is introduced from an injection port of the gas chromatograph (Shimadzu, GC-8A). The separation column for conventional chromatography is 25 cm long (stainless steel, 3 mm i.d.), and is packed with silicone SE-30 (Gas Chromatograph Co.). The sample is separated to two streams by a three-way union.

0003-2700/86/0358-2152$01.50/0 © 1986 American Chemical Society

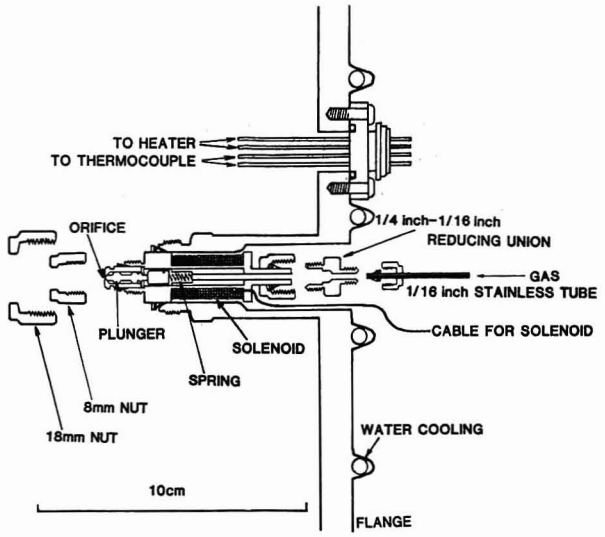

Figure 1. Structure of the high-temperature pulsed nozzle.

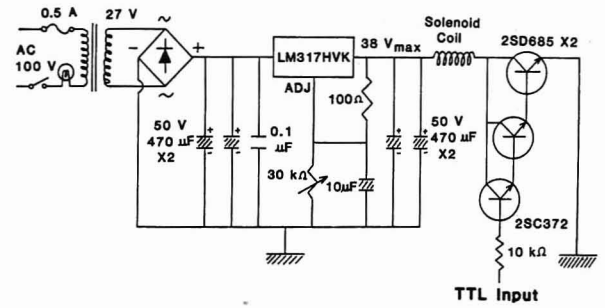

Figure 2. Electronic circuit for driving pulsed nozzle.

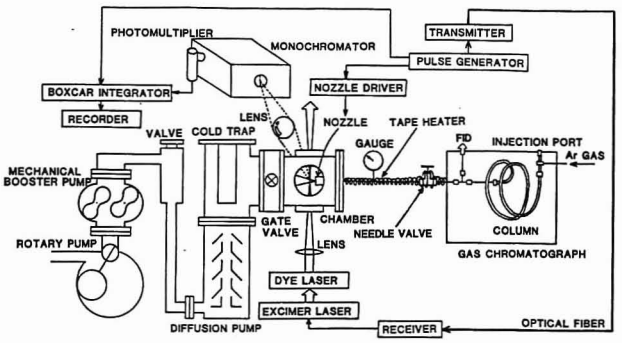

Figure 3. Block diagram of supersonic jet spectrometer combined with gas chromatograph.

The sample is detected by flame ionization and supersonic jet techniques, simultaneously. In the case of capillary chromatography, the fused silica capillary column (Shimadzu, CBP-1-425, 25 m, 0.2 mm i.d., 0.3 mm o.d.) was inserted into the $^1/_{16}$-in. stainless steel tube for sample introduction, and the argon dilution gas flowed between the stainless steel tube and the capillary column. The eluent and diluent gases were mixed just behind the nozzle.

The vaporized sample diluted with argon is expanded into a 6-in. vacuum chamber from the constructed pulsed nozzle. The stagnation pressure was typically adjusted to 200–300 torr. For fluorescence detection the expanded gas is directly evacuated with a 6-in. diffusion pump (Ulvac, ULK-06, 1400 L/s) equipped with a cold trap, which is followed by a mechanical booster pump (Shimadzu, MB-100, 1500 L/min) and a rotary pump (Shimadzu, DK300, 300 L/min). For ion detection the sample molecule should be multiphoton ionized at a sufficiently low background pressure. Then, a differential pumping system was used. The sample gas was expanded in advance into a 6-in. vacuum chamber evacuated by a 4-in. diffusion pump (Ulvac, ULK-04, 650 L/s) and collimated by a homemade skimmer (1 mm i.d.) placed 7 mm away from the nozzle (7). This vacuum chamber was connected with the main vacuum system described above.

The molecule in the supersonic jet is excited by an excimer-laser-pumped dye laser (Lambda Physik, EMG 102MSC, FL2002) at 7 mm away from the nozzle. For excitation of aniline derivatives, the dye laser was converted to the first anti-Stokes emission by a homemade Raman shifter. Fluorescence is collected by a quartz lens (focal length 10 cm, diameter 10 cm) and focused onto a slit of the 1-m monochromator (Jasco, CT-100). Fluorescence is detected by a photomultiplier (Hamamatsu Photonics, R212) and is measured by a boxcar integrator (NF Circuit Design Block, BX-530A). The induced ions by multiphoton ionization were detected by a channeltron detector (Murata, Ceratron EMS-6081B), and the signal was measured by the boxcar integrator. Timing of the signals is controlled by a homemade pulse generator through a data-link system (Mitsubishi Rayon, Eskalink, ED0101).

Reagents. The NO_2 was obtained from Takachiho Chemical Co. and perylene from Aldrich Chemical Co. Anthracene, 9-methylanthracene, and 9,10-dimethylanthracene were purchased from Tokyo Kasei Kogyo, Wako Chemicals, and Aldrich Chemical Co., respectively. Aniline and its derivatives were obtained from Tokyo Kasei Kogyo. The laser dye of phenylbiphenyl-1,3,4-oxadiazole (PBD) and *p*-terphenyl (PTP) were obtained from Nakarai Chemical Co. and Dojindo Lab., respectively.

RESULTS AND DISCUSSION

Performance of Nozzle. For the constructed nozzle the cooling effect was examined by using NO_2 as a sample. The temperature was calculated from the profile of the rotational line structure in the excitation spectrum (*17*). The estimated temperature was 5 K. The jet temperature was also estimated by using aniline in the case of multiphoton ionization spectrometry. From the rotational envelope of the pure electronic transition ($^1A_1 \rightarrow {}^1B_2$, 293.77 nm) in the excitation spectrum the temperature was calculated to be 10 K. These results show that the nozzle has a sufficient performance for sample cooling in the supersonic jet spectrometry.

The maximum temperature for the pulsed nozzle was examined by operating it in a gas chromatograph oven. It was confirmed that the nozzle could be operated at least to 300 °C, though the power of the electromagnet became slightly weak at around 300 °C. The maximum temperature may be limited to 325 °C, at which Teflon used for insulating the solenoid coil decomposes. For operation at higher temperature, other insulating materials such as polyimide might be used. However, the manufacturer informs us that the polyimide film coating is rather poorly bound to copper wire by thermally labile adhesive. Then, it seems to give a poorer performance than Teflon at present.

As an application of this nozzle to supersonic jet spectrometry, we measured the fluorescence spectrum of perylene having five fused aromatic rings. The sample was heated to 175 °C, and the nozzle temprature was maintained at 280 °C. When perylene is excited at 415.3 nm, a jet spectrum was composed of sharp vibrational lines, and the result was identical with the spectrum previously reported using a continuous-flow nozzle (*4*). The constructed nozzle has a small dead volume (0.2 mL), and the sample can be introduced from the outside. Therefore, it can be applied to a gas chromatograph detector, in which a detector temperature should be frequently raised to 300 °C.

The mininum pulse width of the nozzle was measured by recording the fluorescence intensity by changing the delay time of the TTL signal that drives the excimer laser. The nozzle opened within 0.5 ms and closed in 0.8 ms, the minimum pulse width being 1.3 ms. When the shorter TTL pulse was applied to the nozzle driver, it decreased the electromagnet power and the signal intensity decreased. The observed pulse width is similar to the currently used nozzle modified from the fuel injection valve for an automobile (0.5–1.3 ms) (*18*, *19*). In principle, the jet pulse width is shortened by increasing the current of the electromagnet and increasing the strength of

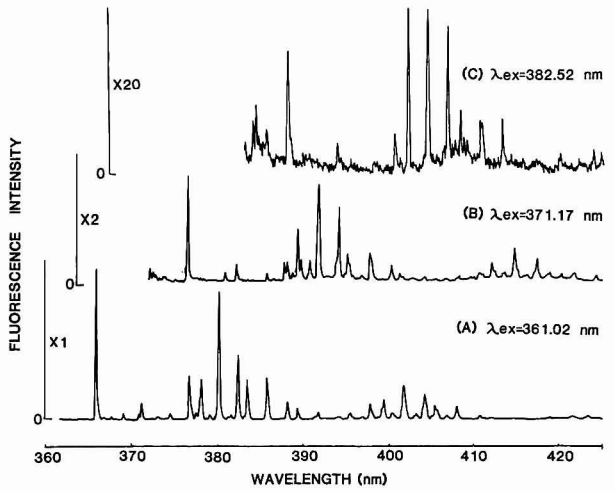

Figure 4. Fluorescence spectra for mixture of anthracene, 9-methylanthracene, and 9,10-dimethylanthracene recorded by exciting at specified wavelengths.

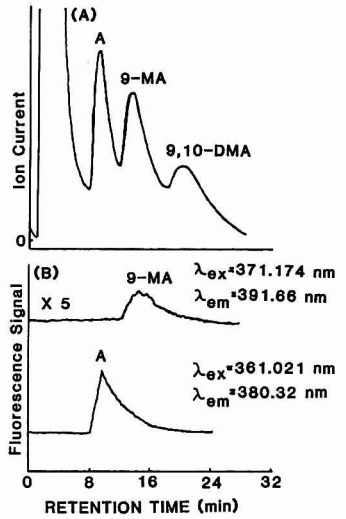

Figure 5. Gas chromatogram for mixture of anthracene, 9-methylanthracene, and 9,10-dimethylanthracene recorded by flame ionization detector (A) and supersonic jet detector (B). The 5-μL sample solution containing 25 nmol of compounds was injected.

the spring. However, the present pulse width is considered to be sufficient for fluorescence measurements. It is noted that a cold spectrum is observed by using only a rotary pump, though the jet temperature is slightly increased by molecular collisions.

In the application to the multiphoton ionization detector, the chamber pressure should be maintained below 1×10^{-5} torr. By use of a differential pumping system, the pressure in the ionization chamber could be reduced to 5×10^{-6} torr when the pulsed nozzle was operated at 20 Hz. The pressure decreased to 1×10^{-6} torr when the nozzle was closed. The background pressure was measured by replacing the nozzle by a blank flange. The pressure decreased to 10^{-7} torr, depending on the conditions of the vacuum system. Thus the present nozzle may have a sufficient performance for use in multiphoton ionization spectrometry.

The nozzle could be operated at least to 100 Hz, and the maximum repetition rate was limited by the capacity of the power supply for the nozzle driver. We usually demonstrate our experiment at 20 Hz, and sometimes at 100 Hz in special cases (*20*). The nozzle temperature increased gradually when it was operated at high repetition rate. Care must be taken when the nozzle is operated at around 300 °C and when a thermally labile sample is measured.

The constructed nozzle is quite reliable, and no damage has been observed in a year. The nozzle is made totally of stainless steel, so that even an oxidative inorganic sample such as NO_2 and a corrosive organic sample such as aniline cause no deterioration in the performance of the nozzle. Unfortunately, sample clogging is not avoided for the molecule with a high boiling point, which sometimes occurs by careless operation of the nozzle. For example, the sample is easily condensed in the nozzle or in the stainless steel tube when the sample reservoir is heated without raising the nozzle temperature. Even in this case, the nozzle can be completely disassembled, so that the nozzle can be easily cleaned and the stainless steel tube can be replaced. This is a great advantage for its practical use. Moreover, the nozzle structure is very simple and does not require great skill for its construction. The diameter of the present orifice is 0.8 mm, but other orifices are also commercially available (0.6 mm or 0.2 mm) and may be chosen depending on the application.

Anthracene Derivatives. Figure 4 shows the fluorescence spectra for the mixture of anthracene, 9-methylanthracene, and 9,10-dimethylanthracene. The sample reservoir was heated to 130 °C, and the nozzle temperature was maintained at 170–200 °C. The spectra were recorded by adjusting the exciting wavelength to 361.02 nm, 371.17 nm, and 382.52 nm, which corresponds to the pure electronic transitions (0–0 transition) for anthracene, 9-methylanthracene, and 9,10-dimethylanthracene, respectively. The observed fluorescence spectra of parts A–C were identical with the standard samples of these compounds, and no appreciable difference could be observed. This fact indicates that the single components of mixture are completely selectively excited.

Similar results have already been published for naphthalene and its derivatives using a continuous-flow nozzle by Warren et al. (*5*) and also for anthracene derivatives using a mechanically rotating planner nozzle by Amirav et al. (*3*). On the other hand Yamada et al. have demonstrated the determination of anthracene derivatives by nonselective excitation using a xenon lamp source (*21*, *22*). The method using the pulsed nozzle is apparently advantageous to forming a cold dense molecular jet under the limited performance of the vacuum system, and therefore it is useful for sensitive detection. Furthermore, the electrically controlled nozzle is convenient to adjust timing of the laser and other electronics.

Application to Conventional Gas Chromatography. Figure 5 A shows a gas chromatogram for the mixture sample detected by flame ionization. Three components are observed, and their integrated intensities are almost identical. A large peak immediately after sample injection is coming from benzene solvent. Figure 5B is obtained by using a supersonic jet detector. The excitation and emission wavelengths in the lower and upper traces are optimized to detect anthracene and 9-methylanthracene, respectively. In these chromatograms single peaks are observed. These results show that the supersonic jet detector has a distinct advantage over flame ionization detector with respect to selectivity. The peak for anthracene in Figure 5B has a long tail, and it implies that the dead volume for the supersonic jet system is not completely negligible. It is mainly coming from the dead volume of the connection tube (0.5 mL) between the gas chromatograph and the jet nozzle. However, the resolution of the chromatogram measured by the supersonic jet detector is similar to that obtained by a flame ionization detector. Then, the resolution is mainly limited by the separation column. It is noted that the low signal intensity for 9-methylanthracene in comparison with that estimated from Figure 4 is due to degradation of the laser dye. The flame ionization detector is universal; therefore it is useful when several components with defferent chemical structures are included in the sample. On the other hand a supersonic jet detector is very specific, and therefore it is useful for the sample containing many

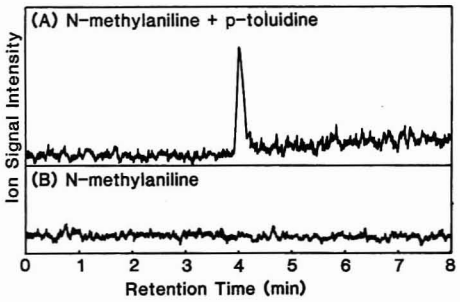

Figure 6. Chromatograms for mixture of *N*-methylaniline and *p*-toluidine (A) and *N*-methylaniline (B). The wavelength is optimized to *p*-toluidine (302.2 nm). The 1-μL sample (1%) dissolved in cyclohexane was injected to the chromatograph.

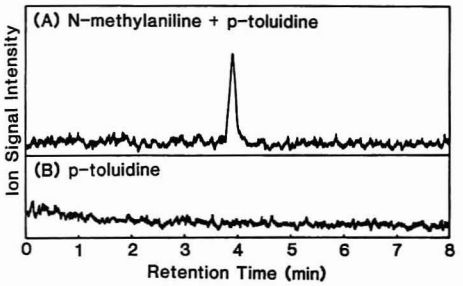

Figure 7. Chromatograms for mixture of *N*-methylaniline and *p*-toluidine (A) and *p*-toluidine (B). The wavelength is optimized to *N*-methylaniline (300.3 nm). Other experimental conditions are identical with those given in Figure 6.

components with similar chemical structures.

Application to Capillary Gas Chromatography. High-performance capillary gas chromatography is advantageously used to improve the separation resolution. In this case a pulsed nozzle with a much smaller dead volume is required. The dead volume of the present nozzle is not sufficiently small when directly applied to the detector for the capillary gas chromatograph. However, if the eluent is mixed with the diluent gas just behind the nozzle to increase the flow rate for use in supersonic jet spectrometry and the effective dead volume can be reduced to 0.2 mL/dilution ratio, then the present nozzle might be used for the detector in capillary gas chromatography.

First, we measured the multiphoton ionization spectrum for aniline, *N*-methylaniline, *m*-toluidine, and *p*-toluidine. The jet spectra were composed of sharp line structures as reported (*10*, *23*, *24*). Second, we measured the capillary gas chromatograms for aniline derivatives. Figure 6 shows the results obtained by adjusting the exciting wavelength for *p*-toluidine (302.2 nm). It is apparent that *p*-toluidine is selectively ionized and determined. The chromatograph resolution was mainly limited by the separation column since the chromatograph conditions are not necessarily optimized. Figure 7 was obtained by adjusting the exciting wavelength for *N*-methylaniline (300.3 nm). When the selective ionization of *N*-methylaniline was achieved, the detection limits were 3 μg for these compounds and were determined by the background noise occurring from the sample itself remaining in the sample introduction line. The present study is performed by using a split injection method, and only several percent of the sample is introduced into the capillary column. An updated cold-on-column technique allows 100% sample introduction, and its use might readily improve the detection limit 1–2 orders of magnitude. We wish to emphasize that time-of-flight mass spectrometry combined with this system provides further information for assignment of the sample species (*24*).

ACKNOWLEDGMENT

The authors wish to thank Ryoichi Shimada of Kyushu University for his helpful suggestion in construction of the nozzle and its driving electronic circuit.

Registry No. Anthracene, 120-12-7; 9-methylanthracene, 779-02-2; 9,10-dimethylanthracene, 781-43-1; *N*-methylaniline, 100-61-8; *p*-toluidine, 106-49-0; perylene, 198-55-0.

LITERATURE CITED

(1) Hayes, J. M.; Small, G. J. *Anal. Chem.* **1983**, *55*, 565A–574A.
(2) Johnston, M. V. *Trends Anal. Chem.* **1984**, *3*, 58–61.
(3) Amirav, A.; Even, U.; Jortner, J. *Anal. Chem.* **1982**, *54*, 1666–1673.
(4) Imaska, T.; Fukuoka, H.; Hayashi, T.; Ishibashi, N. *Anal. Chim. Acta* **1984**, *156*, 111–120.
(5) Warren, J. A.; Hayes, J. M.; Small, G. J. *Anal. Chem.* **1982**, *54*, 138–140.
(6) Hayes, J. M.; Small, G. J. *Anal. Chem.* **1982**, *54*, 1202–1204.
(7) Imaska, T.; Shigezumi, T.; Ishibashi, N. *Analyst (London)* **1984**, *109*, 277–279.
(8) Kronick, M. N. *Chemistry Research at Quanta-Ray*; Quanta-Ray, Inc.: Mountain View, CA, 1981.
(9) Tembreull, R.; Sin, C. H.; Li, P.; Pang, H. M.; Lubman, D. M. *Anal. Chem.* **1985**, *57*, 1186–1192.
(10) Sin, C. H.; Tembreull, R.; Lubman, D. M. *Anal. Chem.* **1984**, *56*, 2776–2781.
(11) Even, U.; Magen, J.; Jortner, J. *Chem. Phys. Lett.* **1982**, *88*, 131–134.
(12) Amirav, A.; Even, U.; Jortner, J. *Chem. Phys. Lett.* **1981**, *83*, 1–4.
(13) Smulevich, G.; Amirav, A.; Even, U.; Jortner, J. *Chem. Phys.* **1982**, *73*, 1–18.
(14) Chan, I. Y.; Dantus, M. J. *Chem. Phys.* **1985**, *82*, 4771–4776.
(15) Syage, J. A.; Felker, P. M.; Semmes, D. H.; Adel, F. Al; Zewail, A. H. *J. Chem. Phys.* **1985**, *82*, 2896–2908.
(16) Keelan, B. W.; Zewail, A. H. *J. Chem. Phys.* **1985**, *82*, 3011–3019.
(17) Smalley, R. E.; Wharton, L.; Levy, D. H. *J. Chem. Phys.* **1975**, *63*, 4977–4989.
(18) Mikami, N. *Oyo Buturi* **1980**, *49*, 802–812.
(19) Otis, C. E.; Johnson, P. M. *Rev. Sci. Instrum.* **1980**, *51*, 1128–1129.
(20) Imasaka, T.; Hirata, K.; Ishibashi, N. *Anal. Chem.* **1985**, *57*, 59–62.
(21) Yamada, S.; Smith, B. W.; Voigtman, E.; Winefordner, J. D. *Analyst (London)* **1985**, *110*, 407–408.
(22) Yamada, S.; Smith, B. W.; Voigtman, E.; Winefordner, J. D. *Appl. Spectrosc.* **1985**, *39*, 513–515.
(23) Lubman, D. M.; Kronick, M. N. *Anal. Chem.* **1982**, *54*, 660–665.
(24) Imasaka, T.; Tashiro, K.; Ishibashi, N., submitted for publication in *Anal. Chem.*

Received for review February 3, 1986. accepted May 14, 1986. This research is supported by the Nissan Science Foundation.

Theoretical Optimization of Parameter Selection in Constant Energy Synchronous Luminescence Spectrometry

Eugene L. Inman,[1] Leigh Ann Files, and James D. Winefordner*

Department of Chemistry, University of Florida, Gainesville, Florida 32611

The spectral parameters of constant energy synchronous luminescence spectrometry (CESLS) have been evaluated for optimization of experimental variables. Mathematical relationships have been derived for peak wavelength maximum, intensity maximum, and peak bandwidth, defining their dependence upon the luminescence excitation and emission spectral characteristics and the selected scan path. Graphical representations of CESLS scans illustrate these relationships, with model compounds used to demonstrate their application. Three special cases are detailed, with experimental design considerations for CESLS applications presented. Finally, translation of these principles to band-narrowing techniques demonstrates their utility.

Synchronous luminescence spectrometry (SLS) implements the simultaneous scanning of both the excitation and emission monochromators, synchronized so that a well-defined relationship is maintained between the wavelengths of the monochromators (*1*). Conventionally, this relationship is a constant wavelength difference, $\Delta\lambda$, which is called constant wavelength synchronous luminescence spectrometry (CWSLS). Alternately, variable-angle synchronous luminescence spectrometry implements different scan speeds between the monochromators, thus providing a variable wavelength difference during the scan (*2*, *3*). Recently, constant energy synchronous luminescence spectrometry (CESLS) has been described where a constant energy difference is maintained between the monochromators (*4*). In this way, the natural energy relationships fundamental to spectroscopic evaluation of fluorescent compounds are instrumentally exploited.

The advantages of synchronous techniques have been discussed, with examples demonstrating qualitative spectral improvements (*5*). These advantages include a reduction in spectral complexity, a reduction in peak bandwidths, a reduction in Rayleigh scatter (*6*), and even a reduction in Raman scatter (*7*). Full realization of these advantages has been limited due to the lack of a thorough theoretical evaluation and subsequent parameter optimization to aid in the routine application of these techniques. The characteristics of the luminescence excitation and emission spectra and their effect on the selection of scan parameters and the resultant synchronous spectral features are considered here.

The prediction of peak wavelength maxima, intensity maxima, and peak bandwidths in conventional constant wavelength synchronous luminescence (CWSL) spectra have been described (*8*, *9*). However, these have included approximations due to the complexity of the mathematical manipulations necessary when assuming excitation and emission peaks to be Gaussian in frequency and determining their response in terms of constant wavelength scanning (i.e., the reciprocal relationship between wavelength and frequency). The calculations are less formidable for CESLS and exact relationships can be obtained. Thus, the spectral advantages of CESLS can be quantitated and utilized for scan selection, providing for systematic parameter optimization. These will be presented, along with a discussion of the experimental consequences of these relationships.

[1] Present address: Lilly Research Laboratories, Eli Lilly and Co., Indianapolis, IN 46285.

THEORY

The fundamental spectral parameters of interest in CESLS include the location of the synchronous peak maximum, its relative intensity, and its bandwidth as functions of luminescence excitation band characteristics, emission band characteristics, and scan parameters. Lloyd and Evett (*8*) obtained the following relationship for the synchronous peak wavelength maximum in CWSLS:

$$\lambda_{s_0} = 2\lambda_{i_0}\lambda_{j_0}(\lambda_{i_0} + \lambda_{j_0} - \Delta\lambda)^{-1} \quad (1)$$

where λ_{s_0} is the wavelength of maximum luminescence intensity in the synchronous spectrum, λ_{i_0} is the wavelength of maximum intensity in the luminescence excitation spectrum, λ_{j_0} is the wavelength of maximum intensity in the luminescence emission spectrum, and $\Delta\lambda$ is the wavelength difference in the conventional synchronous (CWSLS) scan mode. An assumption is made in their treatment that the bandwidths of the excitation and emission peaks are equivalent when expressed in energy terms. Satisfactory agreement was observed with experimental data for a number of compounds over a range of $\Delta\lambda$ values. From the experimental data, an empirical relationship was derived for the synchronous bandwidth

$$\delta\lambda_s \cong 0.364(\delta\lambda_i + \delta\lambda_j) - 3.309 \quad (2)$$

where $\delta\lambda_s$ is the synchronous bandwidth, $\delta\lambda_i$ is the luminescence excitation bandwidth, and $\delta\lambda_j$ is the luminescence emission bandwidth. Andre et al. (*10*) approximated the bandwidths of synchronous peaks as

$$\delta\lambda_s \cong \delta\lambda_i + \delta\lambda_j - (\delta\lambda_i^2 + \delta\lambda_j^2)^{1/2} \quad (3)$$

While no derivation was provided for this expression, it seemed to agree with observed experimental data. It was noted that $\delta\lambda_s$ was always less than $\delta\lambda_j$, confirming the bandwidth reduction observed for synchronous techniques. Thus, experimental data have suggested the direction for parameter optimization for synchronous techniques.

For the discussion to follow, luminescence excitation and emission peaks are represented as single Gaussian functions of frequency (wavenumbers) or reciprocal wavelength. A range of energy differences ($\Delta\bar{\nu}$) are considered where the scan path does not cross the excitation–emission peak maxima. The peak location and the bandwidth of the CESLS peak, $\bar{\nu}_{js_0}$ and $\delta\bar{\nu}_s$, respectively, are derived in the discussion to follow. Appropriate modification is necessary when the derived expressions are used with other SLS scanning techniques.

Peak Maximum Location and Relative Intensity. To obtain equations that will define the location, $\bar{\nu}_{js_0}$, and intensity, M_{ijs_0}, of peak maxima in constant energy scans, it is necessary to establish functions that describe the intensity of these scans. To determine these functions in terms of the excitation and emission spectra assuming peaks which are Gaussian in fre-

0003-2700/86/0358-2156$01.50/0 © 1986 American Chemical Society

quency, the following definitions and substitutions were required.

The terms used throughout this discussion were selected in an attempt to maintain consistency throughout the literature and are defined in a Glossary. The general equation defining a Gaussian distribution can be written as

$$y = \frac{1}{\sigma(2\pi)^{1/2}} \exp[-(x-\mu)^2/2\sigma^2] \quad (4)$$

where y is the normalized peak intensity, σ is the standard deviation of the peak, x is an independent variable, and μ is the average value of x over the peak. If the luminescence excitation and emission spectral band shapes are Gaussian functions, then

$$x_i = x_{i_0} \exp[-(\bar{\nu}_i - \bar{\nu}_{i_0})^2/2\sigma_i^2] \quad (5)$$

and

$$y_j = y_{j_0} \exp[-(\bar{\nu}_j - \bar{\nu}_{j_0})^2/2\sigma_j^2] \quad (6)$$

The relative luminescence measured for a single-component sample can be written as

$$M_{ij} = \alpha x_i y_j \quad (7)$$

where α is the product of wavelength-independent terms, x_i is the product of excitation wavelength-dependent terms, and y_j is the product of emission wavelength dependent terms (*11*). The conversion from wavelength (nm) to frequency (cm^{-1}) is written as

$$\bar{\nu} = 10^7/\lambda \quad (8)$$

Substitution of eq 5 and 6 into eq 7 yields

$$M_{ij} = \alpha x_{i_0} y_{j_0} \exp[-(\bar{\nu}_i - \bar{\nu}_{i_0})^2/2\sigma_i^2 - (\bar{\nu}_j - \bar{\nu}_{j_0})^2/2\sigma_j^2] \quad (9)$$

Equation 9 defines the intensity at any excitation ($\bar{\nu}_i$) and emission ($\bar{\nu}_j$) wavelength relative to the maximum peak wavelengths. The wavenumber difference between the excitation and emission monochromators in a CESLS scan is defined as

$$\Delta\bar{\nu} = \bar{\nu}_i - \bar{\nu}_j \quad (10)$$

where $\Delta\bar{\nu}$ is the constant frequency difference maintained between the excitation and emission monochromators during the CESLS spectral measurements. Placing this restriction on eq 9 gives

$$M_{ijs} = \alpha x_{i_0} y_{j_0} \exp[-(\bar{\nu}_j + \Delta\bar{\nu} - \bar{\nu}_{i_0})^2/2\sigma_i^2 - (\bar{\nu}_j - \bar{\nu}_{j_0})^2/2\sigma_j^2] \quad (11)$$

This equation defines the synchronous spectrum as a function of only the emission wavenumber, $\bar{\nu}_j$, at a selected energy difference, $\Delta\bar{\nu}$.

To determine the location of the intensity maximum of the CESLS scan, M_{ijs_0}, the CESLS intensity function is differentiated with respect to emission frequency and set equal to zero. Therefore

$$dM_{ijs}/d\bar{\nu}_j = 0 \quad (12)$$

This results in a peak wavenumber maximum, $\bar{\nu}_{js_0}$ of

$$\bar{\nu}_{js_0} = (\bar{\nu}_{j_0}(\sigma_i^2/\sigma_j^2) + \bar{\nu}_{i_0} - \Delta\bar{\nu})/(1 + \sigma_i^2/\sigma_j^2) \quad (13)$$

Because $\delta\bar{\nu}$ by definition is related to σ by

$$\delta\bar{\nu} = (8 \ln 2)^{1/2}\sigma \quad (14)$$

eq 13 can be rewritten as

$$\bar{\nu}_{js_0} = (\bar{\nu}_{j_0}(\delta\bar{\nu}_i^2/\delta\bar{\nu}_j^2) + \bar{\nu}_{i_0} - \Delta\bar{\nu})/(1 + \delta\bar{\nu}_i^2/\delta\bar{\nu}_j^2) \quad (15)$$

Equation 15 defines the location of the peak maximum in a given constant energy scan in terms of the emission wavenumber. Therefore, the intensity of the CESLS maximum in a specific constant energy scan is given from eq 11 by

$$M_{ijs_0} = \alpha x_{i_0} y_{j_0} \exp[-(\bar{\nu}_{js_0} + \Delta\bar{\nu} - \bar{\nu}_{i_0})^2/2\sigma_i^2 - (\bar{\nu}_{js_0} - \bar{\nu}_{j_0})^2/2\sigma_j^2] \quad (16)$$

CESLS Bandwidths. To calculate the bandwidth of a constant energy peak, $\delta\bar{\nu}_s$, one can determine the location of the peak maximum at $\bar{\nu}_{js_0}$ and the location at which the intensity is half the maximum value. The difference in these two locations is equal to half the CESLS bandwidth. This goal is accomplished through the use of eq 16 and an analogous equation for the relative intensity at half the maximum intensity

$$M_{ijs_h} = \alpha x_{i_0} y_{j_0} \exp[-(\bar{\nu}_{js_h} + \Delta\bar{\nu} - \bar{\nu}_{i_0})^2/2\sigma_i^2 - (\bar{\nu}_{js_h} - \bar{\nu}_{j_0})^2/2\sigma_j^2] \quad (17)$$

Under these conditions

$$M_{ijs_0}/M_{ijs_h} = 2 \quad (18)$$

Substitution and simplification result in

$$0 = (\bar{\nu}_{js_h}^2 - \bar{\nu}_{js_0}^2)(\sigma_i^2 + \sigma_j^2) + (\bar{\nu}_{js_h} - \bar{\nu}_{js_0})(2\sigma_j^2\Delta\bar{\nu} - 2\sigma_j^2\bar{\nu}_{i_0} - 2\sigma_i^2\bar{\nu}_{j_0}) - 2\sigma_i^2\sigma_j^2 \ln 2 \quad (19)$$

The bandwidth, $\delta\bar{\nu}_s$, is introduced and defined as

$$\delta\bar{\nu}_s = 2|\bar{\nu}_{js_h} - \bar{\nu}_{js_0}| \quad (20)$$

Solving eq 19 for $\delta\bar{\nu}_s$ gives the CESLS bandwidth

$$\delta\bar{\nu}_s = (8 \ln 2)^{1/2}(\sigma_i\sigma_j/(\sigma_i^2 + \sigma_j^2)^{1/2}) \quad (21)$$

and so

$$\delta\bar{\nu}_s = \delta\bar{\nu}_i\delta\bar{\nu}_j/(\delta\bar{\nu}_i^2 + \delta\bar{\nu}_j^2)^{1/2} \quad (22)$$

Geometric Representation. The total luminescence spectrum provides a clear picture of the CESLS scanning procedure. This spectrum includes the relative luminescence intensity contours measured as a function of excitation and emission wavelengths (*12*). For this discussion, this spectrum can be plotted in frequency units, maintaining spectral symmetry (*4*). For simplicity, Figure 1 illustrates the total luminescence spectrum of a single peak, where the ellipse defines the contour equivalent to half the maximum peak intensity. The following terms are used for this model:

$$x = \bar{\nu}_i - \bar{\nu}_{i_0} \quad (23)$$

$$y = \bar{\nu}_j - \bar{\nu}_{j_0} \quad (24)$$

$$2a = \delta\bar{\nu}_i \quad (25)$$

$$2b = \delta\bar{\nu}_j \quad (26)$$

The dashed line represents the CESLS scan path for the special case

$$\Delta\bar{\nu} = \bar{\nu}_{i_0} - \bar{\nu}_{j_0} \quad (27)$$

The ellipse can be expressed as

$$x^2/a^2 + y^2/b^2 = 1 \quad (28)$$

or

$$x^2b^2 + y^2a^2 = a^2b^2 \quad (29)$$

As $\Delta\bar{\nu}$ is varied, a number of scan paths are defined as shown in Figure 2, each with a slope of 1, or

$$dy/dx = 1 \quad (30)$$

These definitions can be used to determine the intensity maximum for each CESLS spectrum. The maxima fall on a line that runs through the origin in Figure 1. The equation for this line can be established by using two points, one of these being the origin and the other being determined by

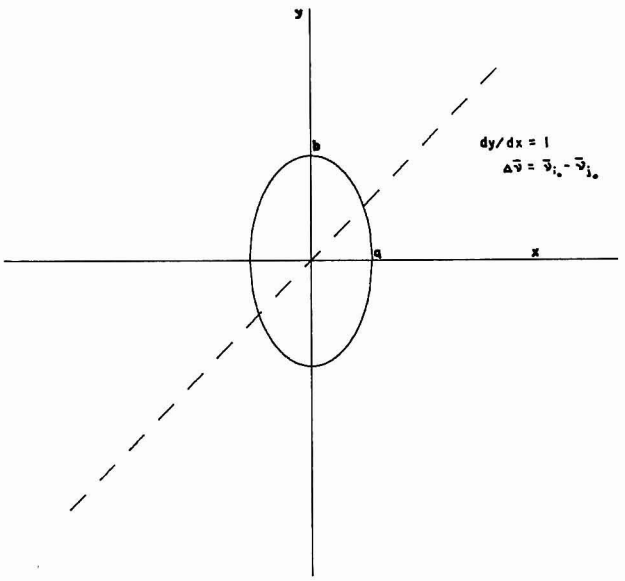

Figure 1. Geometric model for CESLS. The ellipse defines the contour equivalent to half the maximum peak intensity. The dashed line defines a CESLS scan with $\Delta\bar{\nu} = \bar{\nu}_{i_0} - \bar{\nu}_{j_0}$.

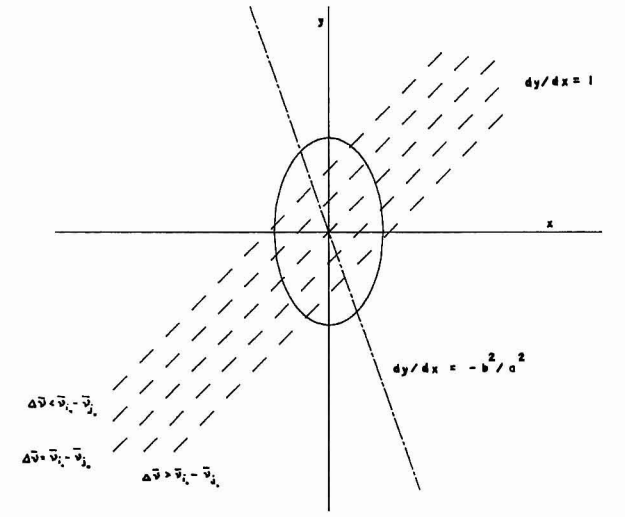

Figure 2. Graphical representation of various values of $\Delta\bar{\nu}$ (– –) and the line (– – –) defining the position of the CESLS maxima for this scan.

finding one of the two points on the ellipse where the scan path intersects the ellipse at a single point. While this might not seem intuitively obvious, the addition of a number of contour lines will verify this conclusion. Differentiating eq 29 yields

$$y = -(b^2/a^2)x \tag{31}$$

Equation 31 represents the line defining the intensity maxima for CESLS scans. Substituting the appropriate CESLS terms into eq 31 and solving for $\bar{\nu}_{js_0}$ gives

$$\bar{\nu}_{js_0} = (\bar{\nu}_{j_0}(\delta\bar{\nu}_i^2/\delta\bar{\nu}_j^2) + \bar{\nu}_{i_0} - \Delta\bar{\nu})/(1 + \delta\bar{\nu}_i^2/\delta\bar{\nu}_j^2) \tag{32}$$

Equation 32 represents the location of the CESLS peak maximum in terms of the emission wavenumber, $\bar{\nu}_{j_0}$. Note that this agrees with eq 15.

DISCUSSION

From these expressions, a number of observations can be made concerning CESLS spectral characteristics. For illustration, a number of hypothetical compounds were evaluated. These observations will provide guidelines for experimental design of CESLS applications.

Peak Wavelength and Intensity Maxima. The shape and location of each CESLS peak are a function of the intensity maxima of the excitation and emission bands and the selected $\Delta\bar{\nu}$. Thus, for a specific compound, the synchronous spectrum intensity maximum and location vary only with the scan parameter, $\Delta\bar{\nu}$. The peak characteristics of three hypothetical compounds are shown in Table II. For each compound, $\Delta\bar{\nu}$ is varied to compare the peak maximum locations, relative intensities, and peak bandwidths. The values of $\Delta\bar{\nu}$ were selected to coincide with $\bar{\nu}_{i_0} - \bar{\nu}_{j_0}$ and reasonable variation around this value. Equation 15 suggests that if $\Delta\bar{\nu}$ is chosen to coincide with $\bar{\nu}_{i_0} - \bar{\nu}_{js_0}$, then $\bar{\nu}_{js_0}$ is equivalent to $\bar{\nu}_{j_0}$. That is, if the scan path passes through the peak maximum, the synchronous and emission peak maxima are identical. If $\Delta\bar{\nu}$ is less than $\bar{\nu}_{i_0} - \bar{\nu}_{j_0}$, then $\bar{\nu}_{js_0}$ is greater than $\bar{\nu}_{j_0}$ (thus shorter in wavelength terms), and the scan crosses the x axis in Figure 2 to the left of the origin. If $\Delta\bar{\nu}$ is greater than $\bar{\nu}_{i_0} - \bar{\nu}_{j_0}$, then $\bar{\nu}_{js_0}$ is less than $\bar{\nu}_{j_0}$ and the scan crosses the x axis in Figure 2 to the right of the origin. If eq 13 is differentiated, then

$$d\bar{\nu}_{js_0}/d\Delta\bar{\nu} = -1/(1 + \sigma_i^2/\sigma_j^2) \tag{33}$$

This defines the slope of the line of CESLS maxima.

The three compounds in Table I represent three cases for relative values of σ_i and σ_j. These are

1. $\sigma_i = \sigma_j$
2. $\sigma_i << \sigma_j$
3. $\sigma_i >> \sigma_j$

The total luminescence spectra for these cases are illustrated in Figure 3. Case 1 is representative of the solution fluorescence spectra of the majority of common fluorescent compounds. If $\sigma_i = \sigma_j$, then eq 13 reduces to

$$\bar{\nu}_{js_0} = (\bar{\nu}_{j_0} + \bar{\nu}_{i_0} - \Delta\bar{\nu})/2 \tag{34}$$

From eq 33, $d\bar{\nu}_{js_0}/d\Delta\bar{\nu}$ reduces to $-1/2$. The data for compound A in Table II confirms these relationships. For case 2, $\bar{\nu}_{js_0}$ approaches $\bar{\nu}_{i_0} - \Delta\bar{\nu}$. That is, the synchronous maximum is proportional to $\Delta\bar{\nu}$, representing the conditions for maximum change in $\bar{\nu}_{js_0}$ as $\Delta\bar{\nu}$ is varied; also from eq 33, $d\bar{\nu}_{js_0}/d\Delta\bar{\nu}$ ap-

Table I. Spectral Data for Three Model Compounds

$\Delta\bar{\nu}$, cm^{-1}	$\bar{\nu}_{js_0}$, cm^{-1}	$\delta\bar{\nu}_s$, cm^{-1}	M_{ijs_0}/M_0
	Compound A		
13 000	28 500	1061	0.641
14 000	28 000	1061	0.895
15 000	27 500	1061	1.000
16 000	27 000	1061	0.895
17 000	26 500	1061	0.641
	Compound B		
13 000	29 100	671	0.491
14 000	28 300	671	0.837
15 000	27 500	671	1.000
16 000	26 700	671	0.837
17 000	25 900	671	0.491
	Compound C		
13 000	27 900	671	0.491
14 000	27 700	671	0.837
15 000	27 500	671	1.000
16 000	27 300	671	0.837
17 000	27 100	671	0.491

	compound A	compound B	compound C
$\bar{\nu}_{i_0}$, cm^{-1}	42 500	42 500	42 500
$\bar{\nu}_{j_0}$, cm^{-1}	27 500	27 500	27 500
σ_i, cm^{-1}	1 500	750	1 500
σ_j, cm^{-1}	1 500	1 500	750

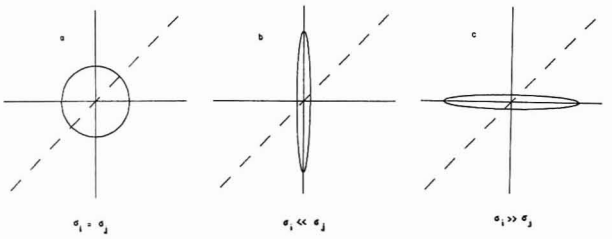

Figure 3. Graphical representation of three special cases for (a) $\sigma_i = \sigma_j$, (b) $\sigma_i << \sigma_j$, and (c) $\sigma_i >> \sigma_j$.

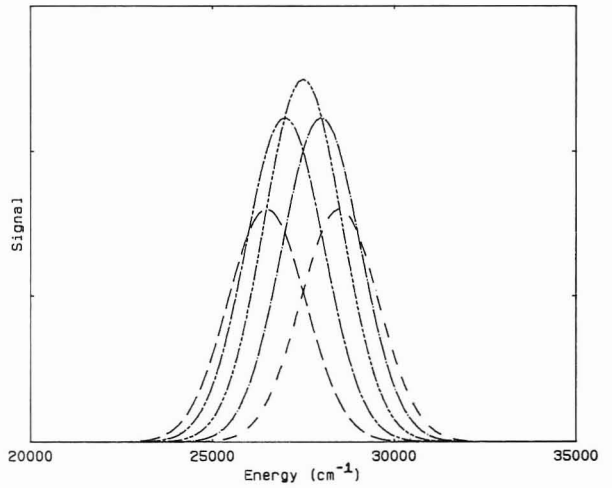

Figure 4. Comparison of peaks generated by using a variety of $\Delta\bar{\nu}$ values for model compound A. See Table II. $\Delta\bar{\nu}$ = 15 000 cm^{-1} (----), 14 000 cm^{-1} (---), 13 000 cm^{-1} (--), 16 000 cm^{-1} (-·-), and 17 000 cm^{-1} (---).

Table II. Limiting Cases

	case 1 ($\sigma_i = \sigma_j$)	case 2 ($\sigma_i << \sigma_j$)	case 3 ($\sigma_i >> \sigma_j$)
$d\bar{\nu}_{js_0}/d\Delta\bar{\nu}$	−1/2	−1	0
$\bar{\nu}_{js_0}$	$(\bar{\nu}_{j_0} + \bar{\nu}_{i_0} - \Delta\bar{\nu})/2$	$\bar{\nu}_{i_0} - \Delta\bar{\nu}$	$\bar{\nu}_{j_0}$
σ_s	$\sigma_j/2^{1/2}$	σ_i	σ_j
$\delta\bar{\nu}_s$	$\delta\bar{\nu}_j/2^{1/2}$	$\delta\bar{\nu}_i$	$\delta\bar{\nu}_j$

proaches −1. For case 3, $\bar{\nu}_{js_0}$ approaches $\bar{\nu}_{j_0}$. That is, the synchronous maximum does not deviate significantly from the emission maximum as $\Delta\bar{\nu}$ is varied. This is readily apparent from Figure 3C and is further proven by eq 33, since $d\bar{\nu}_{js_0}/d\Delta\bar{\nu}$ approaches 0. These three cases are summarized in Table II.

CESLS Bandwidths. Several observations can be made about CESLS bandwidths. Note that from eq 22, $\delta\bar{\nu}_s$ is independent of $\Delta\bar{\nu}$. This is also confirmed by the data in Table I. This is graphically illustrated in Figure 4 where five CESLS spectra are shown with varying values of $\Delta\bar{\nu}$. The bandwidth at half maximum is identical for each peak. In conventional synchronous (CWSLS) techniques, it has been observed that $\delta\lambda_s$ is dependent upon $\Delta\lambda$ (*8*). The three cases previously described are also important in this discussion. For case 1, $\sigma_i = \sigma_j$ and $\delta\bar{\nu}_s$ is equivalent to $\delta\bar{\nu}_j/2$. This effect is clearly seen in the example shown in Figure 5. For case 2, $\sigma_i << \sigma_j$ and $\delta\bar{\nu}_s$ approaches $\delta\bar{\nu}_i$ as this difference increases. An example of this is shown in Figure 6 where $\sigma_i = \sigma_j/2$. Correspondingly for case 3, $\sigma_i >> \sigma_j$ and $\delta\bar{\nu}_s$ approaches $\delta\bar{\nu}_j$. An example of this is shown in Figure 7 where $\sigma_i = 2\sigma_j$. These two cases have significant experimental consequences. This suggests that the CESLS bandwidth corresponds to the narrower of the excitation and emission bandwidths as one becomes much larger than the other. Therefore, $\delta\bar{\nu}_s$ is theoretically always less than or equal to $\delta\bar{\nu}_j$.

Experimental Design. Room temperature fluorescence and phosphorescence spectra generally fall within the case 1

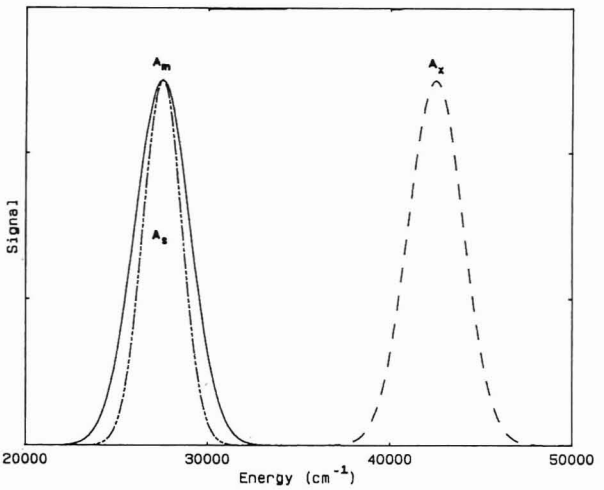

Figure 5. Excitation, A_x (--), and emission, A_m (——), peaks for model compound A. $\sigma_i = \sigma_j$. The CESLS spectra A_s (----) for compound is shown for the scan path $\Delta\nu = \bar{\nu}_{i_0} - \bar{\nu}_{j_0}$.

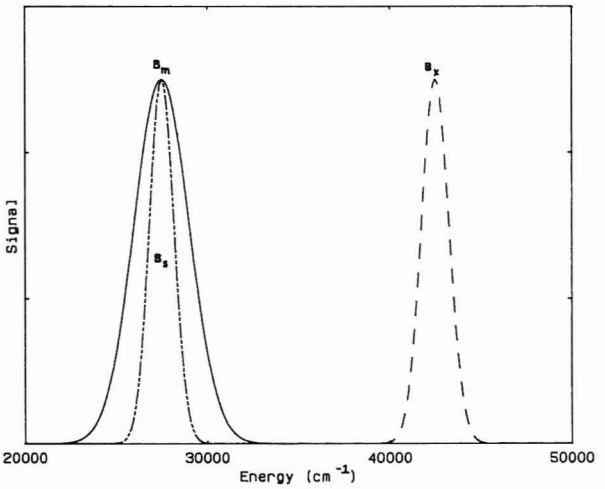

Figure 6. Excitation, B_x (--), and emission, B_m (——), peaks for model compound B, where $\sigma_i = \sigma_j/2$. The CESLS spectrum, B_s (----), is shown for the scan path $\Delta\bar{\nu} = \bar{\nu}_{i_0} - \bar{\nu}_{j_0}$.

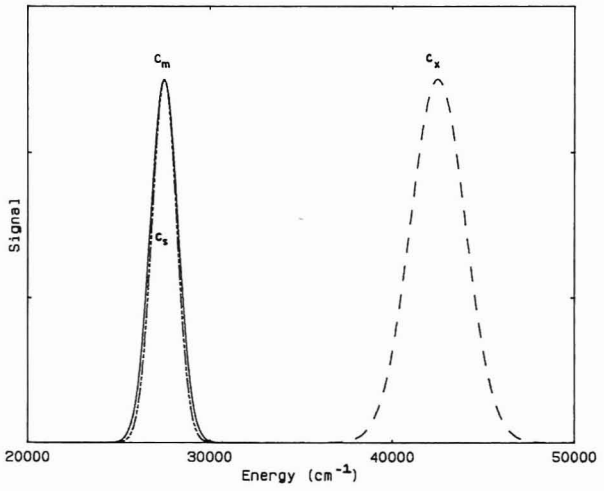

Figure 7. Excitation, C_x (--), and emission, C_m (——), peaks for model compound C where $\sigma_i = 2\sigma_j$. The CESLS spectrum, C_s (----), is shown for the scan path $\Delta\bar{\nu} = \bar{\nu}_{i_0} - \bar{\nu}_{j_0}$.

category where $\sigma_i \cong \sigma_j$. For these spectra, monochromator band-passes are selected to limit instrumental broadening of the luminescence bands. A reduction of the spectral bandwidth by a factor of $2^{1/2}$ can be advantageous. Cases 2 and 3 describe those systems where significant band narrowing is observed in the luminescence excitation and emission

spectra, such as the fluorescence observed at reduced temperaures (*13*, *14*). The combination of low-temperature spectral band narrowing techniques with synchronous scanning provides extensive application of the selectivity advantages described for synchronous techniques. Experimental parameter selection for these combinations requires a careful evaluation of the fundamental relationships as they have been presented above.

The major considerations for synchronous scanning of narrow peaks include ensuring that the scan path crosses the peak of interest, providing sufficient light throughput for detection, and maintaining the spectral features provided by the band-narrowing technique. All three objectives are met by maintaining the band-pass of one monochromator at a level where the bandwidth is not instrumentally broadened and by increasing the band-pass of the other monochromator to a significantly larger value. The narrow band-pass is maintained on the monochromator where narrower bands are observed in the excitation and emission spectra. While a thorough evaluation of experimental parameters was not available at the time, ref 13 demonstrated the effectiveness of this approach. If the excitation and emission spectra are comparable in bandwidth, increasing the excitation monochromator band-pass is recommended, forcing the system into the case 3 category. Case 3 offers several advantages for this application. The CESLS maximum approaches the emission peak maximum, providing a means of peak comparison for identification. Note that the CESLS maximum is independent of $\Delta\bar{\nu}$. Also $\delta\bar{\nu}_s$ is then approximately equal to $\delta\bar{\nu}_j$. With an increase in the excitation monochromator band-pass, sensitivity is increased for adequate detection. Finally, the luminescence intensity of the synchronous peak relative to the maximum peak intensity is maintained over a wide range of scan values for $\Delta\bar{\nu}$ using these experimental conditions. Figure 3 demonstrates that a case 3 peak has a greater probability of being included in a synchronous scan than a case 1 peak without instrumental broadening.

CONCLUSIONS

The CESLS parameters of peak wavelength maximum, intensity maximum, and peak bandwidth have been evaluated, with mathematical relationships derived for each parameter as it is affected by the luminescence excitation and emission spectral characteristics and the scan path. These relationships are solved without approximation based on the initial assumption of single Gaussian peak shapes. Graphical representations of CESLS scans confirm these relationships, with hypothetical compounds used to demonstrate their application. Calculations are significantly influenced by the ratio of the excitation and emission bandwidths, resulting in three special cases used for detailed discussion. Observations from three cases were translated into experimental design considerations for CESLS applications. This provides a parameter optimization strategy based on fundamental spectral characteristics rather than empirical determinations. As a result, the combination of synchronous scanning with other luminescence techniques should implement the selectivity advantages.

GLOSSARY

λ_i	excitation wavelength (nm)
λ_j	emission wavelength (nm)
λ_{i_0}	peak excitation wavelength (nm)
λ_{j_0}	peak emission wavelength (nm)
$\bar{\nu}_i$	energy equivalent to λ_i (cm^{-1})
$\bar{\nu}_j$	energy equivalent to λ_j (cm^{-1})
$\bar{\nu}_{i_0}$	energy equivalent to λ_{i_0} (cm^{-1})
$\bar{\nu}_{j_0}$	energy equivalent to λ_{j_0} (cm^{-1})
x_i	excitation intensity at λ_i or $\bar{\nu}_i$
x_{i_0}	excitation intensity at λ_{i_0} or $\bar{\nu}_{i_0}$
y_j	emission intensity at λ_j or $\bar{\nu}_j$
y_{j_0}	emission intensity at λ_{j_0} or $\bar{\nu}_{j_0}$
M_{i_4}	luminescence intensity at λ_i, λ_j or $\bar{\nu}_i$, $\bar{\nu}_j$
M_{ijs}	luminescence intensity of synchronous scan at λ_i, λ_j
M_{ijs_0}	luminescence intensity maximum of synchronous scan
M_0	luminescence intensity at λ_{i_0}, λ_{j_0}
σ_i	standard deviation of excitation peak (cm^{-1})
σ_j	standard deviation of emission peak (cm^{-1})
σ_s	standard deviation of synchronous peak (cm^{-1})
$\Delta\lambda$	wavelength difference in conventional synchronous scan (nm)
$\Delta\bar{\nu}$	energy difference in CESLS scan (cm^{-1})
λ_{s_0}	wavelength of synchronous maximum (nm)
$\bar{\nu}_{s_0}$	energy equivalent to λ_{s_0} (cm^{-1})
$\delta\lambda_i$	luminescence excitation bandwidth (nm)
$\delta\lambda_j$	luminescence emission bandwidth (nm)
$\delta\lambda_s$	synchronous luminescence bandwidth (nm)
$\delta\bar{\nu}_i$	luminescence excitation bandwidth (cm^{-1})
$\delta\bar{\nu}_j$	luminescence emission bandwidth (cm^{-1})
$\delta\bar{\nu}_s$	synchronous luminescence bandwidth (cm^{-1})

For Geometric Model

x	$\bar{\nu}_i - \bar{\nu}_{i_0}$ (cm^{-1})
y	$y = \bar{\nu}_j - \bar{\nu}_{j_0}$
a	$\delta\bar{\nu}_i/2$ (cm^{-1})
b	$\delta\bar{\nu}_j/2$ (cm^{-1})

LITERATURE CITED

(1) Vo-Dinh, T. In *Modern Fluorescence Spectroscopy*; Wehry, E. L., Ed.; Plenum: New York, 1981; Vol. 4.
(2) Miller, J. N. *Analyst (London)* **1984**, *109*, 191–198.
(3) Clark, B. J.; Fell, A. F.; Milne, K. T.; Pattie, D. M. G.; Williams, M. H. *Anal. Chim. Acta* **1985**, *170*, 35–44.
(4) Inman, E. L.; Winefordner, J. D. *Anal. Chem.* **1982**, *54*, 2018–2022.
(5) Vo-Dinh, T. *Anal. Chem.* **1978**, *50*, 396–401.
(6) Andre, A. C.; Bouchy, M.; Viriot, M. L. *Anal. Chim. Acta* **1979**, *105*, 297–310.
(7) Inman, E. L.; Winefordner, J. D. *Anal. Chim. Acta* **1982**, *138*, 245–252.
(8) Lloyd, J. B. F.; Evett, I. W. *Anal. Chem.* **1977**, *49*, 1710–1715.
(9) Andre, J. C.; Bouchy, M.; Niclause, M.; Baudot, Ph. *Anal. Chim. Acta* **1977**, *92*, 369–378.
(10) Andre, J. C.; Baudot, Ph.; Niclause, M. *Clin. Chim. Acta* **1977**, *76*, 55–66.
(11) Warner, I. M.; Christian, G. D.; Davidson, E. R.; Callis, J. B. *Anal. Chem.* **1977**, *49*, 564–573.
(12) Johnson, D. W.; Callis, J. B.; Christian, G. D. *Anal. Chem.* **1977**, *49*, 747A–757A.
(13) Inman, E. L.; Winefordner, J. D. *Anal. Chim. Acta* **1982**, *141*, 241–251.
(14) Kerkhoff, M. J.; Files, L. A.; Winefordner, J. D. *Anal. Chem.* **1985**, *85*, 1673–1676.

RECEIVED for review February 24, 1986. Accepted May 12, 1986. This work has been supported by NIH-GM-11373-23.

Metal Chelate Fluorescence Enhancement by Nonionic Micelles: Surfactant and Auxiliary Ligand Nature Influence on the Niobium–Lumogallion Complex

Alfredo Sanz-Medel* and M. M. Fernandez Perez

Department of Analytical Chemistry, Faculty of Chemistry, University of Oviedo, Oviedo, Spain

Miguel De La Guardia Cirugeda and J. L. Carrion Dominguez

Department of Analytical Chemistry, Faculty of Chemistry, University of Valencia, Valencia, Spain

The effect of the chemical nature and degree of condensation of nonionic micelle-forming agents on the fluorescence intensities of the chelate niobium–lumogallion are investigated. The observed micellar enhancement factor (MEF) of the fluorescence depends on the chemical type of the surfactant (an MEF of 19.3–25.5 was observed for Nemols, 14.7–19.5 for Tritons, and 3.5–5.6 for Genapols). The surfactant chain length did not influence the MEF. The influence on the observed MEF of the micellar charge and of the nature of the auxiliary ligand used to maintain Nb(V) in solution is studied as well, from parallel absorptiometric and fluorometric measurements. A new analytical method for the fluorometric determination of Nb(V) is proposed (detection limit 0.007 ppm) based on the ternary complex Nb(V)–tartaric acid–lumogallion formed at pH 1 in micelles of Triton X-100. A discussion on the role of surfactants in the micellar fluorescent reaction is presented.

It is well established today that the local microenvironment in a micellar aggregate is dramatically different from that in the homogeneous aqueous bulk solution. This microenvironment in micellar media may lead to significant increases in photoluminescence (*1*) and in chemiluminescence (*2*) quantum yields. Therefore it is clear now that better limits of detection can be achieved in the fluorometric (*3*, *4*), phosphorimetric (*5*), and chemiluminescent (*2*) methods by analytically exploiting photophysical and/or photochemical phenomena taking place in micellar systems. By now it appears that the enhanced fluorescence method is more effective and convenient than the current phosphorescence method (*6*).

Since the early work by Ishibashi and Kina (*7–9*) at the beginning of the last decade, interest on the fluorescence enhancement by surfactants is steadily increasing over the last few years (*4*, *10*, and references therein) in order to establish fluorescent determinations of metal ions more sensitive and convenient. At present, a lot more of fundamental work is needed in order to be able to predict which type of surfactant will enhance the fluorescence of a particular metal-chelate system. Were such basic knowledge established, an intelligent search for new micellar fluorometric methods would be encouraged.

We have reported previously on some trends observed in the fluorescence enhancement of metal chelates in cationic micelles (*3*, *10*, *11*): first of all a lumophoric organic reagent should be selected to produce a highly fluorescent binary compound able to interact strongly with the micellar aggregates. Unfortunately, very few reagents have been studied so far in this context (*4*, *10*). Once a given metal–chelate compound has been selected, the most important factor governing the observed fluorescence enhancements is the nature of the surfactant used: charge type and chemical structure of the surfactant, besides formation of true homomicelles (*10*), are the leading properties determing the final degree of interaction lumophor–micelles. We have shown how in the "organized" medium, i.e., the micellar medium, hydrophobic solvatation of the chelate and stabilization of its singlet excited state would account for many of the interactions and effects observed. Most of our studies, however, have concentrated on positively charged micelles: in such cases it seems clear that the electrostatic interactions are the driving force that facilitates the closer approaches of the negative complex to the positively charged micellar surface.

There, even very close to the surface (*11*, *12*), hydrophobic interactions between hydrocarbon parts of the complex and of the micelle would be operative. In other words, if a charge type effect can combine with the more typical hydrophobic interactions at the micellar level, both kinds of interactions seem to act concurrently bringing about the largest enhancements observed of the fluorescence intensity.

Nonionic micelles are also known to produce fluorescence enhancements of certain metal–chelates (*4*, *7*, *8*, *13*). In fact, the practical importance of these reactions is rocketing today due to their enormous potential in fluoroimmunoassay (*14*). The use of europium labels and time-resolved fluorescence is becoming today a new powerful tool not only in research but in routine clinical analysis. The principle of such technique is based on the use of nonionic micelles to improve the fluorometric determination of rare-earth metals with β-diketones and tri-*n*-octylphosphine oxide as a mixed ligand (*14–16*).

In spite of such importance, the absence of any charge-type effect in nonionic micelles and the lack of knowledge on the effect of chemical nature of these surfactants on fluorescence enhancement make it virtually impossible at present to explain why some nonionic surfactants increase the fluorescence while others, very similar, are quenchers for the same fluorescent complex (*13*).

In the course of study of the trends existing in the fluorescence enhancement of metal–chelates by micelles (*10*), the present communication describes some fundamental studies on the effect of the chemical nature and degree of condensation of several nonionic micelle forming agents on the fluorescence of the complex niobium–lumogallion (*10*). At the same time the effect of the micellar charge and especially the nature of the auxiliary or "mixed" ligand used in this fluorescent system are also discussed.

EXPERIMENTAL SECTION

Reagents. A 100 ppm stock solution of Nb(V) was prepared from Nb_2O_5 (Scharlau) as described in the literature (*17*).

A 1.016×10^{-3} M solution of lumogallion (ICN Pharmaceuticals) was prepared fresh in water.

Stock solutions (15% w/v) of the following nonionic surfactants were prepared by dissolving the surfactant in water:

(a) Nonylphenol–ethylene oxide condensates. Nemol K-36, K-1032, K-1035, K-2030, and K-3030 (Masso and Carol) with an

0003-2700/86/0358-2161$01.50/0 © 1986 American Chemical Society

average number of ethylene oxide moles of 7.2, 13.4, 17.8, 25.8, and 36.4, respectively, were used.

(b) *tert*-Octylphenol–ethylene oxide condensates. Triton X-114, X-100, and X-405 (Fluka) with an average condensation degree of 7.8, 10.3, and 44.2, respectively, were essayed.

(c) Ethylene oxide–propylene oxide condensates. Genapol PF-10, PF-20, and PF-40 (Hoechst), with average molecular weights of 2080, 2040, and 2840, respectively, and with ethylene oxide–propylene oxide mole ratios of 0.23, 0.57, and 1.01, respectively, were studied. Genapol PF-80, with an 80% of ethylene oxide and average molecular weight of 6600–9300 according to manufacturer specifications, was also tested.

(d) Poly(ethylene glycols) (ICI) with average molecular weights of 190–210, 380–420, 570–630, and 5800–6800, respectively, according to manufacturer specifications, were tested.

Those surfactants were characterized by NMR (*18*), UV (*19*), and IR (*20*) spectroscopies. In the case of the ethylene oxide–propylene oxide condensates, the ISO norme was used for the determination of the molecular weight from the hydroxyl group (*21*) and NMR spectroscopy was used for the determination of the ethylene oxide/propylene oxide mole ratio (*22*).

Stock solutions of the "auxiliary ligands" were prepared 1 M in all cases.

Apparatus. Fluorescence intensity measurements were initially made on a Perkin-Elmer MPF-44 spectrofluorometer, with a high-pressure xenon tube and 1.0-cm quartz cells. A Shimadzu difference spectrofluorometer, Model RF-520, equipped with a xenon lamp and a U-135 s recorder, was eventually used for the nonionic surfactant chemical nature studies. Absorbance measurements were made on a Perkin-Elmer, Model 124, spectrophotometer. A Julabo (Paratherm III) thermostat with temperature control to ±0.2 °C was employed to hold constant the sample compartment temperature; pH measurements were made with a WTW pH meter, Model 139. A simple, conventional, stalagmometer was used for surface tension measurements.

General Procedure. Aliquots (0.5 mL) of a 10 ppm Nb(V) solution are transferred to a 25-mL volumetric flask. Then the following reagents are added: tartrate solution (0.25 mL of 10^{-2} M), HCl solution to fix the acidity (1 mL of 3.6 M), lumogallion solution (1 mL of 10^{-3} M), and finally 2.5 mL of a 15% solution of Triton X-100. Alternatively, for study of the influence of the chemical nature and condensation degree of other nonionic surfactants on the fluorescence of the complex, 2.5 mL of a 15% (w/v) solution of each surfactant to be tested is added at optimum experimental conditions to form the Nb(V) complex in Triton X-100 (between brackets). For every set of experiments the apparatus is adjusted with a ternary complex solution containing 200 ppb of Nb(V) and 1.5% of Triton X-100.

The fluorescence measurements were obtained 4 h after the preparation of solutions containing Triton, Nemol, and poly(ethylene glycol) and 5 h later for solutions containing, Genapol (using in all cases water as a blank) to ensure reaching of the equilibrium.

In order to determine the break point or critical micelle concentrations (cmc), aqueous solutions of the different surfactants assayed were prepared at concentrations ranging from 4×10^{-3} to 1% (w/v) and their surface tension was measured with the stalagmometer.

All the surface tension measurements in each series are carried out in a single session, in order to prevent changes in the experimental conditions, and 24 h after the preparation of the solutions so that the dynamic monomer–micelle equilibrium has been totally reached.

RESULTS AND DISCUSSION

Previous work (*10*) demonstrated that the addition of micelles of Triton X-100 to the fluorescent complex of Nb(V) with the azo dye lumogallion produced a dramatic enhancement of the fluorescence (specially at pH 1). It is also known that the fluorescence of this complex is very sensitive to the presence of "auxiliary" ligands (*23*), used to prevent Nb(V) hydrolysis and precipitation via mixed ligand complex formation, and this behavior could be modified by a micellar medium. For both reasons, this system appears as an adequate probe to study fluorescent nonionic micellar effects and the influence of mixed ligand formation on the measured fluorescence intensity in a micellar medium.

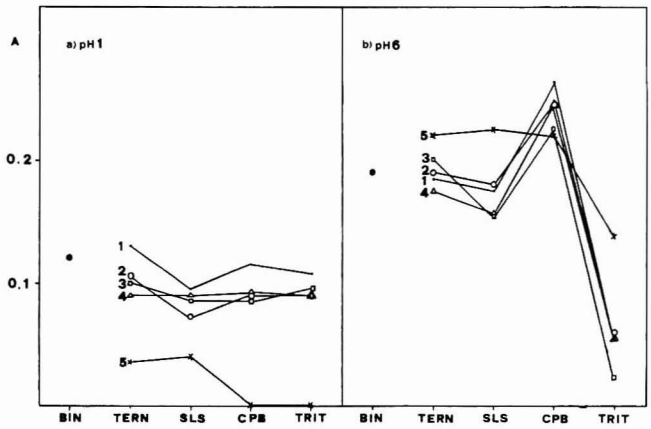

Figure 1. Effect on absorbance of Nb(V–lumogallion complex (BIN) of mixed ligand nature (TERN) and micelle charge type: (1) tartaric acid, (2) fluoride, (3) oxalic acid, (4) citric acid, (5) hydrogen peroxide; [Nb] = 1.07×10^{-5} M; [Lum] = 5.14×10^{-5} M; [oxalic acid] = 0.5×10^{-5} M; [fluoride] = [tartaric] = 10×10^{-5} M; [hydrogen peroxide] = [citric acid] = 5×10^{-5} M; [surfactant] > cmc and maximum wavelength used in each case.

In order to get a deeper insight into the nature of the micellar reactions, parallel absorptiometric measurements were carried out.

Mixed-Ligand Nature and Micelle Charge Influence. Spectrophotometric measurements of solutions of the Nb(V)–lumogallion complex, carried out to study the influence of common Nb(V) auxiliary ligands (hydrogen peroxide, fluoride, tartaric, oxalic or citric acids), demonstrated that "ternary (mixed ligands)" complex formation seems to take place at any pH (from 1 to 6 were tested) in the aqueous solution. The change in absorbance depends on the nature of the ligand and on the pH but is most notorious when hydrogen peroxide is added (see Figure 1 "bin" and "tern", where only the extreme pH values studied are illustrated). The addition of tensoactives of different charge at pH 3 did not alter significantly the spectra (a slight red shift of 5–15 nm in the presence of the surfactants) or the sensitivity of the corresponding ternary complexes. At higher pH (Figure 1b) the positively charged micelles seem to "sensitize" slightly the absorbance of the ternary complexes while the nonionic micelles produced the reverse effect. In any case it is clear from the absorptometric results that the ternary (or mixed ligand) complexes do interact with the micellar media. This interaction depends on the nature of the auxiliary ligand (H_2O_2 always showed an anomalous behavior) and on the charge type of the micelle (anionic micelles of SLS hardly modified the spectral characteristics of any ternary complex at any pH).

Spectrofluorometric results (Figure 2) showed that the slight fluorescence of the Nb–lumogallion complex increases due to ternary complex formation with any of the studied auxiliary ligands, provided that pH >2. The enhancement due just to auxiliary ligand addition is more noticiable the higher the pH, being maximum at pH 6 in the sequence: hydrogen peroxide > fluoride > oxalic > tartaric > citric.

The addition of different charge type micelles to these ternary complexes at different pH values produced dramatic changes on their fluorescence intensity (I_F) depending on the charge of the micelle; while the anionic SLS only brings about very small increases in I_F at any pH, the cationic surfactant BCP originates dramatic enhancements of I_F at any pH and for any ternary complex. Maximum I_F occurs at pH 6 using tartaric acid as auxiliary ligand as shown by Figure 2b. It is interesting to note how at low pH (pH 1), the nonionic surfactant Triton X-100 produces an enhancement of I_F even

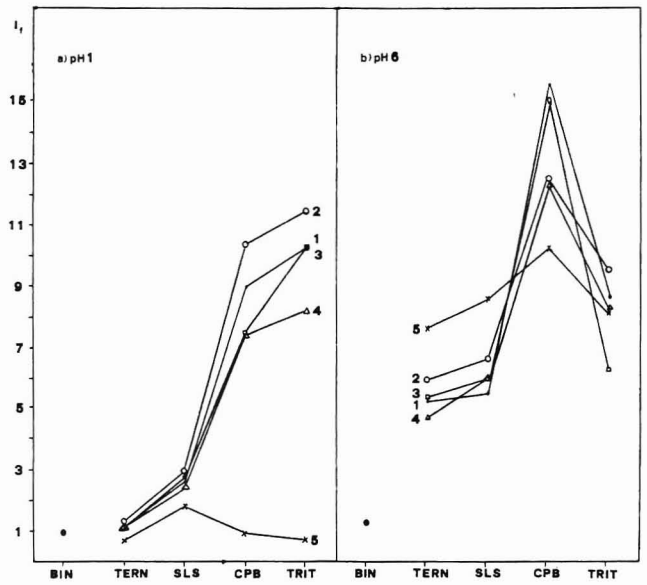

Figure 2. Effect of mixed ligand nature and micelle charge type on fluorescence intensity (at maximum emission wavelength for each system and all conditions as in Figure 1).

Table I. Excitation and Emission Maxima of the Ternary Complexes at pH 1 in the Absence and Presence of Surfactants of Different Charge

system	surfactant	micelle	λ_{ex}	λ_{em}
Nb–lum–tartaric acid			490	630
	Triton	nonionic	495	610
	BCP	positive	515	615
	SLS	negative	495	618
Nb–lum–oxalic acid			490	630
	Triton	nonionic	495	610
	BCP	positive	505	620
	SLS	negative	490	615
Nb–lum–citric acid			490	630
	Triton	nonionic	495	610
	BCP	positive	495	620
	SLS	negative	490	620
Nb–lum–H_2O_2			495	620
	Triton	nonionic	495	600
	BCP	positive	519	625
	SLS	negative	490	615
Nb–lum–fluoride			490	630
	Triton	nonionic	495	610
	BCP	positive	505	615
	SLS	negative	490	615

higher than that produced by BCP. For higher pH values, this nonionic micellar effect decreases very sharply as illustrated comparing Figure 2, parts a and b. In fact all the graphs at intermediate pH were less pronounced but similar in shape to those at pH 6.

Table I shows the effect upon other relevant spectral characteristics at pH 1 (excitation and fluorescence maxima of the corresponding ternary complexes) of the addition of different charge-type micelles. A comparison of the spectrophotometric and the corresponding fluorometric results (compare Figure 1a and 2a) shows how to observe micellar fluorometric enhancement; it is not necessary that micellar spectrophotometric sensitization occurs; i.e., the nature of the fluorescence enhancement by micelles appears different from the enhancement in "sensitized" spectrophotometric reactions. Rather than an increase in the apparent probability of the electronic transition involved (molar extinction coefficient), a sheltering or protection of the lowest singlet excited state by the micelles to avoid its radiationless deactivation (increase of quantum efficiency) seems to be the most probable mechanism in micellar fluorescence.

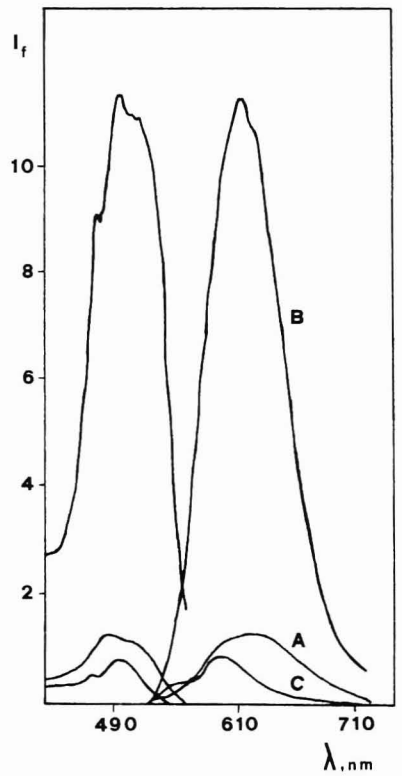

Figure 3. Excitation and emission spectra at pH 1 of: (A) the ternary Nb(V)–lumogallion–tartrate system, [Nb] = 1.07×10^{-5} M, [Lum] = 5.14×10^{-5} M, [tartaric acid] = 10^{-4} M; (B) the above system with 0.5% of Triton X-100; (C) the above solution without niobium (blank).

Optimization of the System Nb(V)–Lumogallion–Triton X-100. From all the above results, it is clear that at pH 1 the fluorescence of the ternary systems Nb(V)–Y–lumogallion (Y being fluoride or oxalic, tartaric, or citric acid) is strongly enhanced by nonionic micelles of Triton X-100 (Figure 2a). The low pH and the high fluorescence of these reactions could offer the basis for a selective and sensitive determination of the metal, apart from constituting an adequate probe to study micellar enhancements of the metal chelates. Therefore, all the reaction variables were carefully optimized.

Figure 3 shows the uncorrected excitation and fluorescence spectra of the ternary complex Nb–lumogallion–tartaric acid alone and in the presence of Triton X-100 at pH 1 (as obtained in the MPF-44A). Tartaric acid was eventually selected as the mixed ligand, Y, because it is the most common auxiliary agent used for dissolution and stabilization of Nb(V) solutions and because a relatively high concentration of tartaric acid ($\leq$3%) can be tolerated without virtual loss in the analytical signal. The rest of the auxiliary ligands studied produced sharp decreases in the fluorescence observed even when small excesses of the ligand, over the molar Nb(V) content, were added.

Addition of Triton X-100 micelles to this ternary system causes not only a dramatic increase in fluorescence intensity but also a 5-nm red shift in the excitation and a 20-nm blue shift in the emission maximum (see Table I).

The influence of the pH on the fluorescence intensity (I_F) of the ternary complex alone and in the presence of nonionic micelles is given in Figure 4. As can be seen, the ternary complex reaches its maximum fluorescence between pH 4 and 6, while the micellar medium shifts the optimum pH for complex formation to pH 1. At higher acidities the observed I_F decreases. HCl acid turned out to produce higher fluorescent signals than HNO_3 or H_2SO_4 acids.

Although temperature of the measurement in the cuvette was not very critical around 20 °C, some photodecomposition

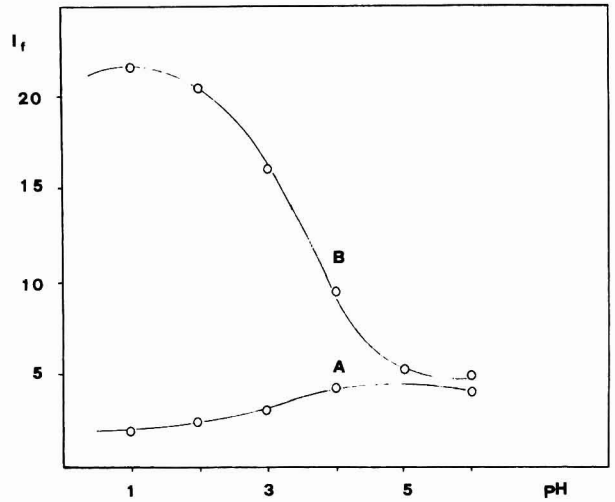

Figure 4. Influence of pH on fluorescence intensity of: (A) the ternary Nb(V)–lumogallion–tartrate system, [Nb] = 1.07×10^{-5} M; [Lum] = 7.34×10^{-3} M; [tartaric acid] = 2×10^{-2} M; (B) the above system in the presence of Triton X-100.

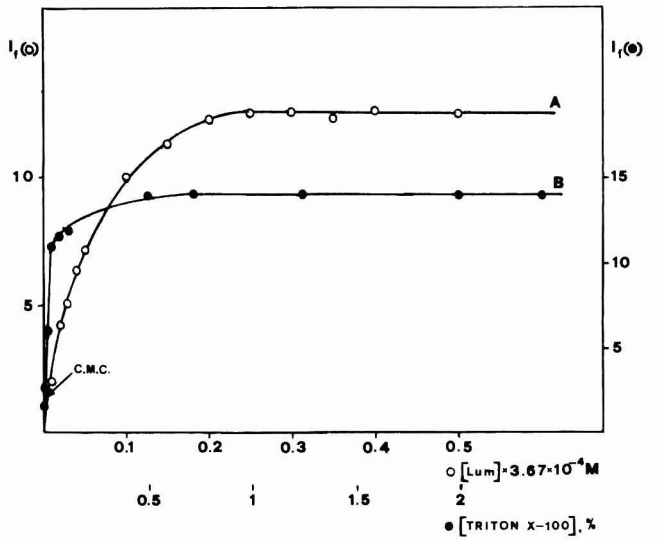

Figure 5. Lumophor reagent (A, where [Triton] = 0.5%) and Triton X-100 (B, [Lum] = 7.34×10^{-5} M) influence on the fluorescence. Metal and tartaric acid concentrations are given in Figure 4.

and kinetic effects were noticed when studying the influence of standing time. The observed I_F increases steadily with standing time of solutions in the flasks at room temperature. If the ternary complex is heated for 20 min at 40–50 °C in a water bath and allowed to cool before final addition of the surfactant, a stable signal is obtained after about 1 h of standing time (otherwise 4 h are necessary to obtain the same signal without heating).

The influences of surfactant and lumogallion concentrations have been plotted in Figure 5. The observed effect of increasing concentration of Triton X-100 (curve 5B) shows clearly that fluorescence enhancement starts only after the cmc of this surfactant has been reached (0.014% w/v final concentration, in 0.1 M HCl acid). The fluorescence only levels off after surfactant concentration is high enough (>0.5%). These facts demonstrate the micellar nature of the observed fluorescence enhancement: only when the "organized" medium is established can the ternary complex be accommodated in the surface of the micelles and so fluorescence is favored. The effect of the lumophoric reagent is illustrated in Figure 5A. The intensity increases with concentration of Lumogallion until a plateau is reached at around 10^{-4} M final concentration of the reagent (above 7-fold molar excess over the Nb(V) concentration tested).

The detection limit of the fluorometric niobium determination ($3\sigma_b$ criterium, σ_b being the standard deviation of the blank) was 0.007 ppm and the calibration graph was linear up to 0.6 ppm of the metal.

Effect of Chemical Nature and Degree of Condensation of the Nonionic Surfactant. In order to investigate the influence of the nature of the nonionic micelle, we measured the fluorescence enhancement in solutions of the ternary complex of the same concentration and at pH 1 prepared as described for Triton X-100, but adding in each case a final concentration of 1.5% (w/v) of the different nonionic surfactants assayed.

At the same time, we have tested the effect of the addition of poly(ethylene glycols) of different molecular weight (i.e., condensation degree) for comparative purposes, as these reagents do not exhibit amphiphilic character.

For every surfactant we obtained the corresponding calibration graph, in the linear response interval, in order to be able to compare the sensitivity in each case. The standard deviation of the corresponding blanks, σ_b, was also worked out from ten independently prepared blank solutions without niobium.

The instrumental sensitivity was adjusted in all cases by using a reference solution and fluorescence measurements were made consistent every day by comparing with the observed I_F of the freshly prepared ternary complex in Triton X-100. The kinetic character of these reactions was again evidenced because a stable signal was only obtained after 4 h of standing time for nonylphenols, *tert*-octylphenols, and poly(ethylene glycols); 5 h had to be allowed when using ethylene oxide–propylene oxide condensates to get a reproducible value of I_F.

The results obtained have been summarized in Table II in terms of equations of the linear calibration graphs (with the correlation coefficients observed), detection limits, and observed micellar "enhancement factor", MEF (ratio between the slope observed in a given surfactant and that characteristic of the ternary system alone). It is evident from these results that all the amphiphilic surfactants (nonylphenols, *tert*-octylphenols, and propylene oxide–ethylene oxide condensates) enhanced the fluorescence intensity much more than the nonsurfactant poly(ethylene glycols). Moreover, for each family of nonionic surfactants, a certain homogeneous "enhancement factor" is noticed: Nemols producing the highest enhancement, followed by Tritons and Genapols. In other words, the chemical structure of the monomers of the tensoactive, which will eventually form the nonionic micelle, really matters on the final fluorescence observed. Within a given family of surfactants, however, our results do not indicate any significant trend of I_F enhancement with molecular weight (degree of condensation). It has to be pointed out here that although we used in all cases a 1.5% concentration of the surfactants, regardless of its chemical nature or molecular weight, such concentration is well above the cmc of any of the surfactants studied (see Figures 6 and 7). For ethylene oxide–propylene oxide condensates, a much higher surfactant concentration is needed to get saturation of I_F; in any case, with a saturation concentration (15%) the value of I_F is only twice that observed for 1.5% as shown by Figure 7. In other words, these kinds of compounds should still exhibit much worse "enhancement factor" even at high concentrations.

As the detection limit depends also on the absolute value of the fluorescence of the blanks, given by the first term of the analytical curves, it is worth noting that with some exceptions the order of magnitude of the intercept with the I_F axis, depends again mainly on the surfactant chemical family considered. Surfactants for which the emission of the complex was noticed slightly more red shifted than usual (at 605 nm

Table II. Characteristics of the Fluorescence of the Niobium–Lumogallion–Tartrate System Enhanced by Nonionic Surfactans

surfactant	λ_{ex}, nm	λ_{em}, nm	linear calibration equation	DL, ppb	MEF
	490	595	$I_F = 0.912 + (6.68 \times 10^{-3})c$ $r^2 = 0.999$	23.15	1
Triton X-114	490	605	$I_F = 45.77 + 0.107c$ $r^2 = 0.99$	7.77	16.0
Triton X-100	495	600	$I_F = 25.16 + 0.130c$ $r^2 = 0.999$	7.41	19.5
Triton X-405	505	595	$I_F = 29.03 + 0.098c$ $r^2 = 0.99$	6.16	14.7
Nemol K-36	490	605	$I_F = 354.9 + 0.129c$ $r^2 = 0.9999$	16.7	19.3
Nemol K-1032	490	600	$I_F = 25.72 + 0.129c$ $r^2 = 0.999$	2.4	19.3
Nemol K-1035	490	595	$I_F = 17.73 + 0.128c$ $r^2 = 0.9999$	2.1	19.2
Nemol K-2030	495	590	$I_F = 18.92 + 0.170c$ $r^2 = 0.9999$	2.17	25.5
Nemol K-3030	495	595	$I_F = 16.02 + 0.161c$ $r^2 = 0.999$	2.06	24.1
Genapol PF-10	485	605	$I_F = 10.88 + 0.033c$ $r^2 = 0.99$	13.68	4.9
Genapol PF-20	490	605	$I_F = 18.33 + 0.026c$ $r^2 = 0.99$	22.73	3.9
Genapol PF-40	490	590	$I_F = 2.53 + 0.037c$ $r^2 = 0.999$	4.09	5.5
Genapol PF-80	490	590	$I_F = 1.96 + 0.022c$ $r^2 = 0.999$	5.27	3.3
PEG 200	490	590	$I_F = 0.38 + 0.0095c$ $r^2 = 0.9$	14.21	1.4
PEG 400	485	590	$I_F = 1.84 + 0.0081c$ $r^2 = 0.999$	18.19	1.2
PEG 600	485	590	$I_F = 1.49 + 0.0094c$ $r^2 = 0.999$	16.59	1.4
PEG 6000	490	590	$I_F = 1.63 + 0.015c$ $r^2 = 0.999$	11.39	2.2

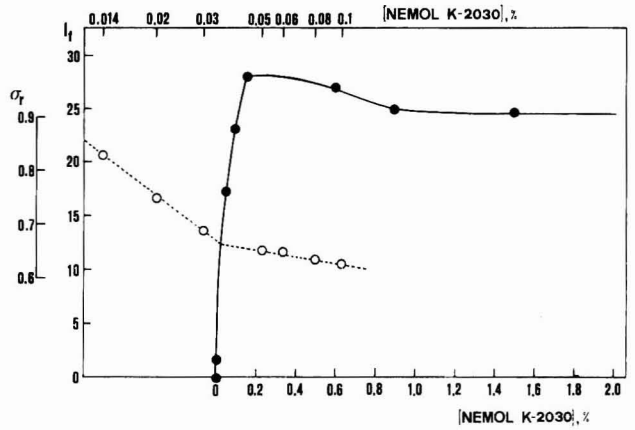

Figure 6. Effect of the concentration of Nemol K-2030 on the fluorescence intensity of the niobium–lumogallion–tartrate system at pH 1.

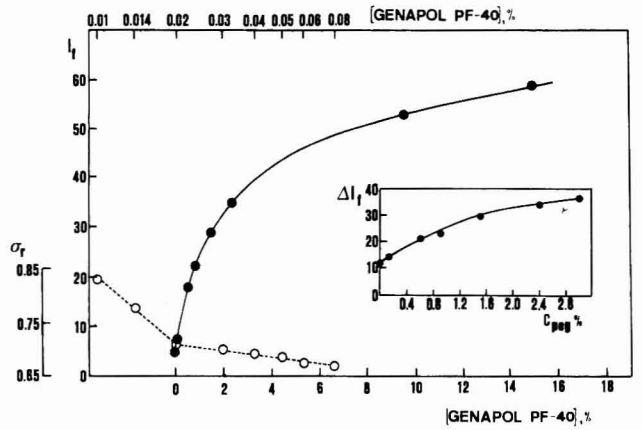

Figure 7. Effect of the concentration of Genapol PF-40 (A) and poly(ethylene glycol) (PEG-6000) (B) on the fluorescence intensity of the niobium–lumogallion–tartrate system at pH 1.

Table II) showed anomalously high values of the blanks. This could be attributed to the presence of impurities in the commercial surfactants used. Such impurities would not virtually disturb the MEF but would increase the blank fluorescence (see the data for the case of Nemol K-36).

In conclusion, the addition of a 1.5% (w/v) final concentration of nonionic surfactant to the ternary complex Nb(V)–lumogallion–tartaric acid, at pH 1, produced an enhancement of the I_F that depends on the chemical type of surfactant used: an MEF of 19.3–25.5 for the condensates of ethylene oxide and nonylphenol, from 14.7 to 19.5 for the condensates of ethylene oxide and *tert*-octylphenol, and finally an enhancement of 3.3–5.6 times for the condensates of ethylene oxide and propylene oxide (better enhancements can be obtained in the last case by increasing ten times the concentration of the tensoactive agent). Finally, the poly(ethylene glycols) (PEG), which are lacking the tensoactive character, can modify the I_F observed, but only slightly when compared with those having surfactant properties (Figure 7).

Role of the Surfactant in the Micellar Fluorescent Reaction. With surfactant "sensitized" spectrophotometric determinations, at least two different basic metal chelate–surfactant interactions have been demonstrated: formation of unusual ion-association complexes (*11*, *12*, *24*) or formation of true micelles where the chromophoric metal–chelate is solubilized and "organized" (*5*). In both cases, the microenvironment experienced by the chromophore is different from that for bulk water. All the information available so far on metal chelate fluorescence enhancement by surfactants indicates (*4*, *10*, *12*) that the phenomenon of enhancement of fluorescence is not observed unless a minimum concentration of true micelles (charged or uncharged) is secured in the solution. In other words, with surfactant-enhanced fluorometric determinations, only the solubilizing–organizing mechanism, characteristic of true micelles, seems to be operative. Of course this claim should be specially true with nonionic surfactants where the absence of charge prevents any ion-association or electrostatic interaction with the chelate.

On the other hand, it has been stated (*10*) that one of the most important factors, governing the metal chelate fluorescence enhancement by surfactants, is the charge type of the micelle. Present work results (Figure 2) confirm how the decisive factor is the charge of the micelles but relative to the *actual charge* of the metal chelate. Let us consider first our results at low pH. At pH 1 the ternary complex could be thought of as consisting of two moieties, a more hydrophobic one (the phenolic ring with the –OH group protonated at such pH) and the hydrophilic one having the dissociated sulfonic group (see Figure 8). Then, this ternary complex could be solubilized–organized by the Triton X-100 nonionic micelles in the following manner: the –OH group of the complex would form hydrogen bonds with oxygen of the ethylene oxide chains (Figure 8) or/and van der Waals attractions would take place between the hydrophobic benzene ring of the complex and those rings of the surfactant chains exposed, through dynamic bending and disorder (*25*), to external water and counterions existing in the micellar surface. A more rigid and ordered environment results in this way where the fluorophor would be sheltered from collisional deactivations. As shown by Figure 8, however, even at pH

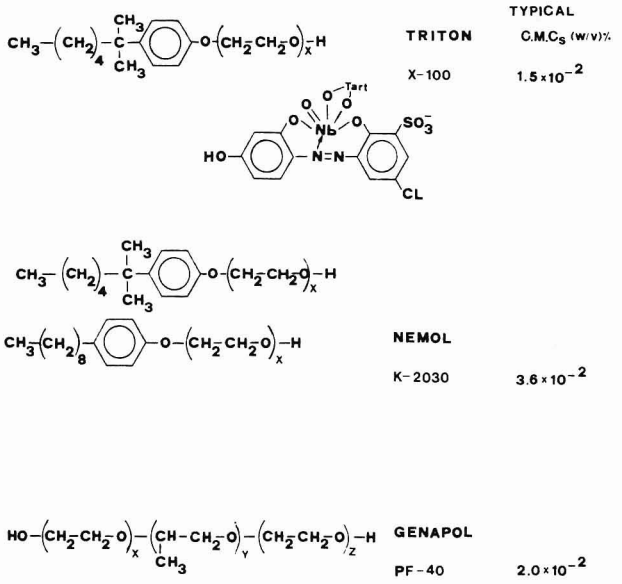

Figure 8. Chemical formulas of the different families of nonionic surfactants used and speculative formula of the Nb(V)–lumogallion–tartrate system.

1 there is another charged (much more polar) moiety in the complex which through the $-SO_3^-$ group holds the posibility of electrostatic interaction with positively charged micelles. This would explain why cationic surfactants also enhance the fluorescence while anionic ones do not (see Figure 2a). At such a low pH, however, the chemical interaction ("ordering or penetration") of the ternary complex with the positive micelles (CTAB showed analogous behavior to that of CPB) seems to be weaker than the interaction observed with nonionic Triton X-100 micelles.

If the negative charge of the chelate is too high (e.g., at pH 6 in Figure 2b) electrostatic interactions should be favored against hydrophobic ones. Then, in such cases, positively charged micelles would interact more strongly with the chelate, i.e., cationic surfactants would be more effective than nonionic ones to enhance the fluorescence at such pH (Figure 2b). In any case, it is interesting to note that, for the rest of the conditions being the same, the "micellar enhancement factor" of CPB at pH 1 (MEF $\simeq$ 10) is clearly superior to the MEF of the same surfactant at pH 6 (MEF $\simeq$ 3). We verified that the corresponding MEF at pH 3 was around 6 for all the ternary complexes. These facts seem to support the general idea that the maximum fluorescence *enhancements* are observed when electrostatic and hydrophobic interactions can act concurrently (*10*, *12*).

In the case of nonionic micelles the leading force of the interaction must be hydrophobic attraction. Therefore, the chemical nature of the monomers of the surfactant and their particular affinity to the metal chelate considered should be expected to play the fundamental role. Our results indicate that the micellar enhancement factor for the fluorescence of the ternary system with different nonionic surfactants actually depends on the chemical nature of the tensoactives. It seems like the presence of an aromatic ring (*25*) in the surfactant molecule (i.e., nonylphenols and *tert*-octylphenols) would favor the interaction of the micelles with the more hydrophobic aromatic ring of the Nb(V) complex (Figure 8). With ethylene oxide–propylene oxide condensate surfactants (Genapols) such aromatic chemical affinity cannot operate. An additional factor to consider is that the presence of branched methyl groups in the chain of genapols could hinder a "good packing" of the molecules of the ternary Nb(V) complex.

It is interesting to note that the reverse behavior was noticed for Al(III)–morine (*13*): ethylene oxide–propylene oxide condensate surfactants allowed appreciable fluorescence enhancement, whereas fluorescence quenching occurred in the presence of nonylphenol and *tert*-octylphenol ethylene oxide condensate surfactants.

The effect of increasing the surfactant concentration on the fluorescence of the ternary complex differs from one type of nonionic surfactant to another suggesting the existence of an optimum concentration of micelles in each case to get saturation fluorescence (Figures 6 and 7). Curiously enough we have not experienced the expected influence of the surfactant chain length on the sensitization of the Nb(V) ternary system. In fact, for nonylphenols an increase in the condensation degree from 7 to 37 mol yields only an increase in the MEF from 19.2 to 25.0 whereas for *tert*-octylphenols an increase in the condensation degree from 8 to 44 mol only gives rise to a slight decrease in the MEF value, having obtained the maximum MEF for a compound with an intermediate condensation degree.

LITERATURE CITED

(1) Turro, N. J.; Gratzel, M.; Braun, A. M. *Angew. Chem., Int. Ed. Engl.* **1980**, *19*, 675.
(2) Yamada, M.; Suzuki, S. *Anal. Lett.* **1984**, *17*(4A), 251.
(3) Sanz-Medel, A.; Garcia Alonso, J. I. *Anal. Chim. Acta* **1984**, *165*, 159.
(4) Hinze, W. L.; Singh, H. N.; Baba, Y.; Harvey, N. G. *Trends Anal. Chem.* **1984**, *3*, 193.
(5) Cline Love, L. J.; Habarta, J. G.; Dorsey, J. G. *Anal. Chem.* **1984**, *56*, 1133A.
(6) Armstrong, D. W.; Hinze, W. L.; Bui, K. H.; Singh, H. N. *Anal. Lett.* **1981**, *14*(A19), 1659.
(7) Ishibashi, N.; Kina, K. *Anal. Lett.* **1972**, *5*, 637.
(8) Ishibashi, N.; Kina, K. *Microchem. J.* **1974**, *19*, 26.
(9) Kina, K.; Tamura, K.; Ishibashi, N. *Jpn. Anal.* **1974**, *23*, 1404.
(10) Sanz-Medel, A.; Garcia Alonso, J. I. *Anal. Chem.* **1985**, *57*, 1681.
(11) Garcia Alonso, J. I.; Diaz Garcia, M. E.; Sanz-Medel, A. *Talanta* **1984**, *31*, 361.
(12) Diaz Garcia, M. E.; Sanz-Medel, A. *Talanta* **1986**, *33*, 255.
(13) Medina, J.; de la Guardia Cirugeda, M.; Hernandez Hernandez, F. *Analyst (London)* **1983**, *108*, 1386.
(14) Lovgren, T.; Hemmila, I.; Petterson, K.; Eskola, J. U.; Bertoft, E. *Talanta* **1984**, *31*, 909.
(15) Hemmila, I. *Anal. Chem.* **1985**, *57*, 1676.
(16) Taketatsu, T. *Talanta* **1982**, *29*, 397.
(17) Sanz-Medel, A.; Camara, C.; Perez Bustamante, J. A. *Anal. Chem.* **1980**, *52*, 1035.
(18) Carrion, J. L.; de la Guardia, M.; Medina, J. *Quim. Anal. (Barcelona)* **1983**, *2*(4), 271.
(19) de la Guardia, M.; Carrion, J. L.; Medina, J. *Anal. Chim. Acta* **1983**, *155*, 113.
(20) de la Guardia, M.; Carrion, J. L.; Medina, J. *Analyst (London)* **1984**, *109*, 157.
(21) ISO 4327–1979. International Organization for Standardization, Geneva, 1979.
(22) Carrion, J. L.; de la Guardia, M. XX Bienal R. S. Esp. Quim. Castellon, Sept. 1984.
(23) Pilipenko, A. T.; Volkova, A. I.; Zhebentyaev, A. I. *Zh. Anal. Khim.* **1971**, *26*, 2048.
(24) Blanco, E.; Diaz Garcia, M. E.; Sanz-Medel, A. *Quim. Anal. (Barcelona)* **1985**, *4*(4), 408.
(25) Dill, K. A.; Koppel, D. E.; Cantor, R. S.; Dill, J. D.; Bendedouch, D.; Chen, S. *Nature (London)* **1984**, *309*, 42.

RECEIVED for review February 11, 1986. Accepted May 5, 1986.

Synchrotron X-ray Fluorescence: Diffraction Interference

S. R. Sutton,*[1] M. L. Rivers,[1] and J. V. Smith

Department of the Geophysical Sciences, University of Chicago, Chicago, Illinois 60637

Synchrotron X-ray fluorescence (SXRF) is valuable for rapid, nondestructive trace element analysis of geological and biological specimens with minimum detection limits of 10–100 parts per billion weight for 20-μm spots. X-ray diffraction is a significant interference in SXRF analysis of well-ordered specimens. It depends on excitation source (continuum or monochromatic), detection system (energy or wavelength dispersive), and specimen orientation. The most pronounced effects occur for synchrotron continuum and energy-dispersive detectors: thus, the probability of observing diffraction peaks from a randomly oriented quartz crystal is near unity. Diffraction peaks were observed in X-ray fluorescence spectra from silicon, quartz, and deep sea particles at the National Synchrotron Light Source (Brookhaven National Laboratory, Upton, NY). Scattering peaks were observed from silica glass. Identification of diffraction effects is best accomplished by changing the specimen orientation since diffraction features are modified while fluorescence lines remain unaltered.

Synchrotron X-ray fluorescence (SXRF) permits rapid, nondestructive trace-element analysis of geological and biological specimens with minimum detection limits of 10–100 parts per billion weight (ppbw) for 20-μm spots (ref 1–3 and references therein). High sensitivity results from the special nature of the synchrotron radiation. For a bending magnet of a dedicated X-ray storage ring, the small source size (<1 mm) and natural collimation (vertical divergence < 0.2 mrad) produce a natural radiation intensity $\sim 10^5$ times that of a conventional X-ray tube over the continuum and $\sim 10^2$ times greater at a characteristic X-ray energy (*4*). Second, the natural collimation allows focusing of the photons into small spots. Third, a strong polarization of the X-rays exists within the plane of the storage ring, and backgrounds from scattered radiation can be minimized by placing the X-ray detector within the polarization plane and normal to the photon beam (e.g., ref 5). Fourth, the synchrotron continuum is sufficiently intense to allow tuning of the incident energy using a monochromator to just above the absorption edge of an element of interest.

X-ray spectra obtained for ordered specimens irradiated with a continuous source contain characteristic fluorescence lines and diffraction peaks (*6*). Fluorescence interference in diffraction studies has been treated previously (*7*, *8*). This paper discusses the complementary situation of diffraction interference in fluorescence spectra using synchrotron radiation as the excitation source. The theory of synchrotron radiation diffraction under various excitation and detection conditions is presented as well as observations using white, unfocused synchrotron radiation produced by the X-ray ring at the National Synchrotron Light Source (NSLS) of Brookhaven National Laboratory. The diffraction effects depend on the excitation source (continuous or monochromatic), detection system (energy or wavelength dispersive), and specimen orientation. Diffraction peaks are more likely for excitation with continuum radiation rather than monochromatized X-rays since each crystal plane selects from the incident spectrum X-rays of appropriate energy to satisfy the Laue equations (*9*).

[1] Current address: Department of Applied Science, Building 901A, Brookhaven National Laboratory, Upton, NY 11973.

EXPERIMENTAL SECTION

General. Specimens are mounted vertically on a Klinger "x-y-z" stepping motor stage and viewed by a MTI TV camera attached to a horizontally mounted Nikon SMZ-10 stereozoom binocular microscope (Figure 1). For maximum discrimination against scattered radiation, the X-ray detector (Nuclear Semiconductor Autotrace Si(Li)) is placed in the storage ring plane normal to the primary beam. An aperture/collimator is placed in front of the detector to eliminate detection of "off-axis" scattered radiation. Data acquisition and stepper motor control are performed with a programmable LeCroy System 3500M.

X-radiation of wavelength λ striking parallel lattice planes of spacing d at some arbitrary orientation is diffracted only at the Bragg reflection condition, $n\lambda = 2d \sin \theta$ (e.g., ref 9), where n is an integer. The diffraction angle θ lies within the plane containing the normal vector to the lattice plane and the incident beam (Figure 2). The diffraction direction will, in general, be out of the plane containing the incident beam and the detector. Unlike incoherently scattered X-rays, diffraction X-rays possess narrow energy distributions, which produce sharp peaks.

The detection system is constrained geometrically to accept only diffracted X-rays with mean $2\theta = 90°$. The finite size of the detector allows some deviation from this value. For example, the angular acceptance of a 30-mm^2 detector at a sample-to-detector distance of 40 mm is 8.8°, which corresponds to $\theta = 42.8$–$47.2°$.

Continuum Excitation: General. The unfocused continuous synchrotron radiation, or "white light", from the bending magnets is sufficiently intense for SXRF microanalysis. The beam size is adjusted with motor-driven slits to optimize the photon flux and/or excitation volume for particular applications. Lattice planes effectively filter the source by diffracting only X-rays possessing wavelengths that satisfy the range of Bragg angles for the detector aperture. Photographic film exposed at the detector position reveals a typical Laue pattern of diffraction spots (Figure 3), each spot produced by a different wavelength subset of the incident spectrum. Each set of crystal planes diffracts in a unique direction and the X-rays in each diffraction direction possess a unique set of energies. For a well-ordered sample, the resulting Laue spots are approximately the same size as the incident beam, typically tens of micrometers, due to the small divergence of the latter. Intrinsic broadening due to the finite dimension t of the excitation volume is negligible for a single crystal since $\delta\theta \approx \lambda/t \simeq 10^{-5}$ for a 10-μm beam and 1-Å X-rays.

Continuum Excitation: Energy-Dispersive Detector. Diffraction interference in white light fluorescence spectra is most pronounced with an energy dispersive detector (e.g., Si(Li)) for three reasons. First, the simultaneous detection at a wide range of energies increases the probability of observing diffraction features. Second, the low-energy resolution (100–200 eV) increases the likelihood of diffraction features overlapping fluorescence peaks. Third, acceptance solid angles are 10^2–10^3 larger than for wavelength dispersive detectors.

Diffraction features in EDS spectra can usually be identified by using three criteria: energy, shape, and the occurrence of companion peaks. The first indication that a spectral peak results from diffraction is failure to correspond to the energy of a fluorescence transition; this is common since diffraction and fluorescence energies rarely coincide. Second, diffraction peaks exhibit non-Gaussian shapes typically characterized by extended

0003-2700/86/0358-2167$01.50/0 © 1986 American Chemical Society

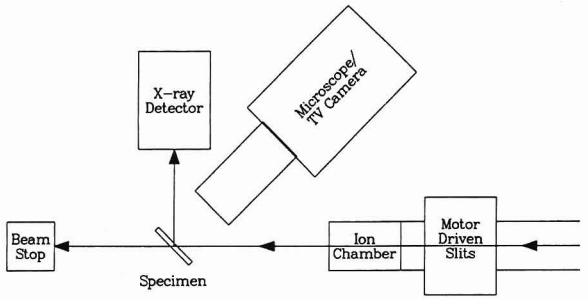

Figure 1. Schematic of SXRF apparatus at NSLS used for white light excitation of geological and biological specimens.

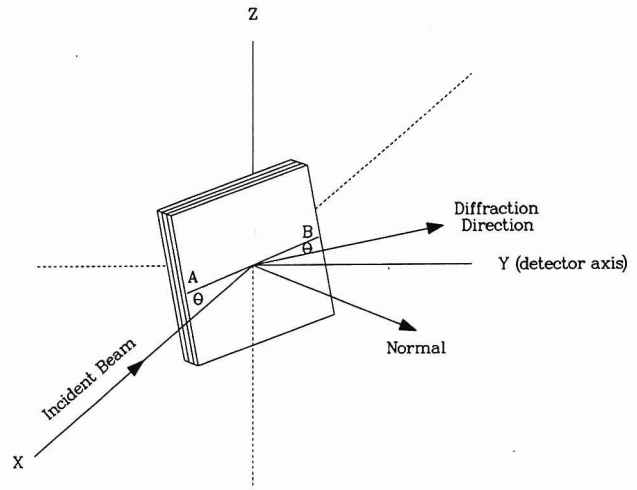

Figure 2. Diagram of diffraction geometry from a randomly oriented crystal plane. The line AB is the intersection of the crystal plane and the plane containing its normal vector and the incident beam. The diffraction angle is that between AB and the incident beam. In general, the diffraction vector lies out of the beam line/detector plane.

tails. Third, a peak that lies near a fluorescence energy but lacks appropriate companion fluorescence peak(s) is also likely to be due to diffraction (e.g., a peak with energy close to that for Kα which lacks a Kβ companion). A suite of peaks occurring at regularly spaced energies indicates harmonic diffractions.

These criteria may be inadequate for peak overlap and low intensity. A diffraction peak that is unresolvable from, and therefore contributes to, a more intense fluorescence peak results in an erroneous "fluorescence" intensity. Low intensity peaks are ill-shaped, and companion lines are likely to be undetectable.

Hence, definitive identification can best be obtained through a comparison of spectra taken under different collection geometries. Whereas diffraction exhibits a strong angular dependence, fluorescence is unaltered by geometrical modifications, except for trivial variation in self-absorption.

The two obvious ways to modify the geometry, reorient the specimen or use a second "off-axis" detector, have advantages and disadvantages. The latter is faster but the "off-axis" detector receives a higher scattered background, and a weak peak observed in the "on-axis" spectrum might be lost in the background of the "off-axis" detector. The former avoids this complication, but accurate repositioning of the sample after reorientation is required to ensure that similar volumes are excited.

The principal effect of reorientation is to move particular diffraction spots, either out of or into the collection solid angle of the detector. Three principal rotation axes exist for the geometry in Figure 1: (a) the vertical axis normal to the storage ring plane, (b) the horizontal axis parallel to the specimen surface, and (c) the horizontal axis normal to the specimen surface. Only rotations about axes (a) and (b) are effective in eliminating the detection of particular spots. Although a small angular change of crystal orientation may be insufficient to prevent the detection of a diffraction spot, it can be large enough to significantly modify its corresponding diffraction angle. As a result, the diffraction peak can experience an energy shift, the maximum value of which is defined by the detector solid angle. For a 30-mm^2 detector,

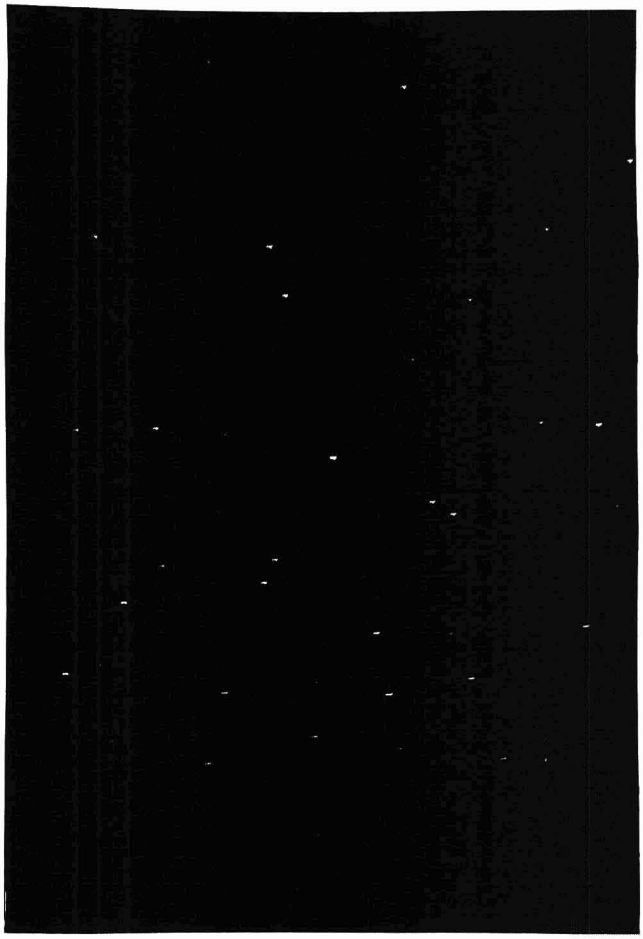

Figure 3. Laue photograph of ultrapure silicon observed from white synchrotron light at a scattering angle of 44° to (111). A Si(Li) detector positioned to accept the central Laue spot produced the SXRF spectrum in Figure 5.

the maximum change of 4.4° in diffraction angle results in a 7% shift of diffraction energy. Thus, a 10-keV peak could shift by as much as 700 eV. The maximum shift will occur only for a perfectly vertical plane which is rotated about a vertical axis causing the diffraction spot to move within the storage ring plane from one side of the detector to the other. Since such alignments are rare, reorientations typically result in energy shifts that are significantly less than the maximum.

An important consideration is the probability of detecting diffraction X-rays from a randomly oriented crystal excited by continuum radiation. If F is the total fractional area of all Laue spots on the spherical surface centered at the specimen and containing the detector, the probability P that at least one Laue spot strikes the detector is

$$P = 1 - (1 - F)^{\gamma} \quad (1)$$

where γ is the number of "Laue spot-sized" areas subtended by the detector. In the limit that Laue spots represent small fractional area, i.e., $F \ll 1$, this expression is approximated by

$$P = 1 - e^{-F\gamma} = 1 - e^{-(na/4\pi r^2)} \quad (2)$$

which depends only on the number of spots n, the specimen-to-detector distance r, and the detector area a. The pertinent value of n is the number of crystal plane sets that can diffract the incident X-rays at a diffraction angle of 45°. For filtered radiation from the NSLS bending magnets (roughly 3–30 keV), appropriate interplanar spacings are constrained by Bragg's law to be in the range $0.293 < d < 2.927$ Å and the distribution is strongly weighted toward lesser d (greater energy). The number of such plane sets depends on the particular crystal's structure and lattice parameters. Crystals with large unit-cell volume, such as feldspar, will generally produce more diffractions than those with small unit cells such as silicon. The probability of detection of a single

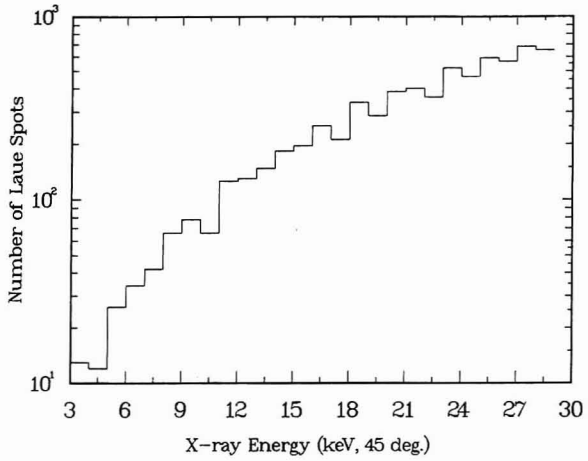

Figure 4. Energy distribution of possible 45° diffractions from interplanar spacings in the range $0.293 \leq d \leq 2.927$ Å for α-quartz (bandwidth = 1 keV).

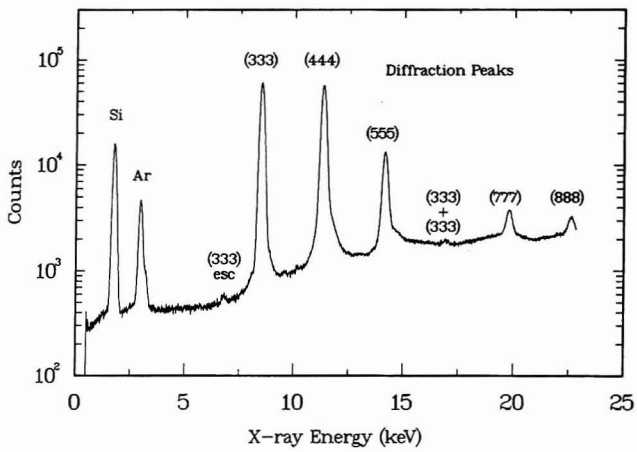

Figure 5. SXRF spectrum of ultrapure silicon wafer oriented with (111) parallel to specimen surface excited with NSLS continuum radiation (beam diameter 100 μm, low-energy filtering by Be and Al windows in the storage ring/beam line vacuum system). X-ray spectrum obtained in air with a Si(Li) detector (5-min measurement time). Si and Ar fluorescence lines are observed as well as (111) diffraction harmonics at integral multiples of 45° (111) diffraction energy of 2.8 keV. Second- and sixth-order reflections are forbidden. The 8.4-keV photons produce escape and sum peaks. (See related photograph—Figure 3.)

diffraction generally increases with increasing cell size and with lowering of symmetry but depends to some degree on the extent of any pseudosymmetry. Intensity generally decreases with increasing energy (decreasing d spacing) and, therefore, high energy diffractions are weakest.

An illustrative example is α-quartz (space group $P3_121(152)$), a mineral of interest in studies of crystallization history (*10*). Interplanar spacings were calculated from $a_0 = 4.9133$ Å and $c_0 = 5.4053$ Å (*11*) and the space group restriction that l must be an integral multiple of 3 in (00l). A total of 7520 unique diffraction directions exist for spacings in the appropriate range. Although the probability of satisfying the diffraction condition is near unity, diffraction of higher energy X-rays is favored (Figure 4). For example, the probability of diffracting X-rays between 4 and 5 keV into the detector (eq 2) is 0.018 (1 chance in 56) compared to 0.59 (1 chance in 2) for 25–26-keV X-rays. Most diffractions that strike the detector are expected to be detectable above the continuous scattered background—based on the observation of a weak 16.68-keV diffraction from α-quartz (Figure 6).

Continuum Excitation: Crystal Spectrometer. At the cost of lower flux, crystal spectrometers offer some advantages over energy dispersive detectors for X-ray fluorescence detection such as high count rate capability, greater energy resolution, and low detector background. From the standpoint of diffraction interference, a wavelength dispersive spectrometer is advantageous over an energy dispersive detector because its low collection angle

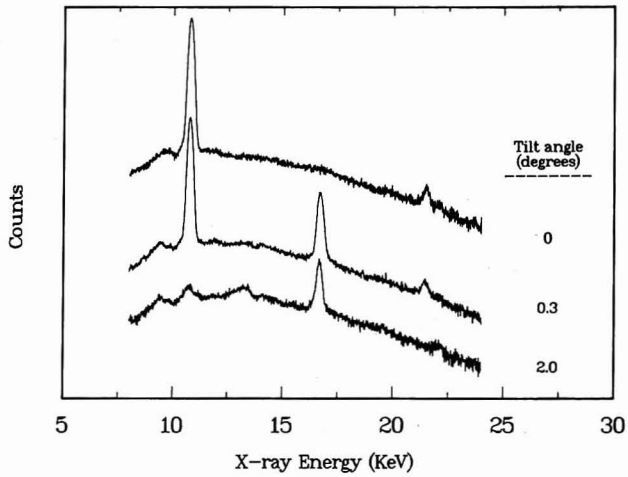

Figure 6. SXRF spectrum between 8 and 24 keV for a natural single quartz crystal (Keith and Tuttle 49-103) at three different tilt angles. Conditions are the same as in Figure 5. Three prominent diffraction features are observed, 10.77, 16.68, and 21.5 keV. At least two diffraction spots are represented, one observed at 0° tilt and producing peaks at 10.77 and 21.5 keV and the other observed at 2.0° and producing the 16.68-keV peak. The 0.3° orientation contains all three peaks.

($\sim 10^{-5}$ steradians) reduces the probability of detecting a diffraction feature about a thousand-fold. In addition, the high-energy resolution ($\sim$5 eV), about 30 times better than EDS, reduces the probability of diffraction features overlapping fluorescence lines. A minor drawback is the difficulty in identifying diffraction peaks. Since detection at all energies is unrealistic, due principally to the analytical time required, it is equally impractical to rely on the observation of peaks at regular energy intervals in verifying diffraction identification. Peak shape and energy provide one test for diffraction interference because of the high resolution available, and another approach is the reorientation technique described above.

Monochromatic Excitation. An important advantage of synchrotron radiation for X-ray studies is that the continuous nature of the energy spectrum allows the energy of the incident beam to be accurately tuned with the use of a monochromator for optimum excitation of a particular element. The significant reduction in photon flux is offset to some extent by the reduction in scattered radiation at the energy of interest.

Using an energy dispersive detection system for fluorescence excited by monochromatic radiation, the probability of a diffraction spot striking the detector is significantly less than for continuum excitation. An appropriate diffracting lattice plane must not only be properly oriented (θ = 43 to 47°) but also have an interplanar spacing $d = \lambda_{incident}/(2 \sin \theta)$. For a 14-keV primary beam incident on α-quartz, d must lie between 0.650 and 0.607 Å. The probability of detecting a diffraction spot from this mineral, calculated using eq 2 (n = 173, determined in an analogous manner to that in the continuum example above), is 0.23, a one-in-four chance. No new X-ray peaks are introduced, however, since diffraction results from constructive interference of elastically scattered radiation. Diffraction simply increases the magnitude of the peak due to Rayleigh scattering, which occurs at the incident energy.

For detection of a narrow range of X-ray energies, a crystal spectrometer is the detector of choice. In this arrangement, the interference from diffraction is negligible since the energy of diffracted X-rays (equivalent to the incident energy) is greater than that of the fluorescence photons. For example, if the iron content of quartz is to be measured, the monochromator would be tuned to pass 7.2-keV X-rays, just above the K absorption edge of 7.111 keV, and the WDS detector would be set at the iron Kα energy, 6.40 keV. Consequently, even if crystal planes of the proper interplanar spacing and orientation diffracted X-rays into the spectrometer, their energies would be 7.2 keV and would not be detected.

Table I. Diffraction Angles for Silicon Diffraction Peaks

index	obsd energy, keV	calcd 2θ angle, deg	calcd energy for 2θ = 88.80, keV	dE,[a] eV
333	8.482	88.73	8.476	−6
444	11.296	88.86	11.302	+6
555	14.133	88.76	14.127	−6
777	19.772	88.84	19.778	+6

mean 2θ: 88.80 ± 0.06°

[a] dE = (observed energy) − (calculated energy for 2θ = 88.80).

RESULTS AND DISCUSSION

Single Crystals. An example of diffraction peak identification is provided by an SXRF spectrum of ultrapure silicon (Figure 5) oriented with (111) vertical and at 45° to the primary beam and detector axes (optimum orientation to observe reflections from (111)) and excited with white light (low-energy X-rays filtered by 250-μm Be and 25-μm Al windows within the storage ring/beamline vacuum system). In addition to fluorescence lines for Si and Ar (measurement performed in air), six peaks (8.4, 11.2, 14.0, 16.8, 19.6, and 22.4 keV) were observed at integral multiples of the (111) diffraction energy in this configuration (2.8 keV for d = 3.136 Å (*12*) and θ = 45°). With the exception of the 16.8-keV feature, these peaks are interpreted as harmonics of the (111) diffraction. Since the diamond structure of silicon forbids (222) and (666) diffraction, the 16.8-keV peak must be the "(333) + (333)" sum peak. Diffraction from (111) is not observed because 2.8-keV X-rays in the incident spectrum are completely absorbed in the Be and Al windows. The small 6.7-keV peak is an escape peak produced in the detector by the abundant 8.4-keV X-rays. The extended tails of the diffraction peaks are easily observable in this spectrum.

The energies of harmonic diffraction peaks also provide an accurate evaluation of the diffraction angle since the interplanar spacing is well-defined by previous work. Diffraction angles calculated for each silicon diffraction peak in Figure 5 are given in Table I. The mean angle, 88.80 ± 0.06° (2θ), demonstrates that (111) lies at 44.4° to the incident beam. The small uncertainty in the mean represents only a 6-eV error in energy (1/2 channel in the EDS spectrum).

Strong diffraction peaks were also observed from individual quartz crystals. The effect of specimen reorientation on diffraction features was studied for one such crystal (specimen 49-103 of the Keith–Tuttle collection, Jemez Mountains rhyolite tuff (*13*)) randomly oriented and mounted on a rotating micrometer stage (Figure 6). Two prominent diffraction peaks were observed, 10.77 and 16.68 keV, in the original orientation of the crystal (tilt = 0.3°). The crystal was rotated about an axis lying within the storage ring plane and parallel to the specimen surface (Figure 1). SXRF spectra taken after various degrees of rotation show that the two peaks behave independently and, therefore, represent two distinct diffraction spots. The spots are sufficiently close together spatially, that in particular orientations (for example, tilt = 0.3°, Figure 6) both enter the detector's aperture. The 10.77- and 16.68-keV peaks are interpreted as first-order diffractions since lower energy harmonics are not observed. Four constraints allow unambiguous identification of the two diffracting planes. First, the detector acceptance angle and peak energies force diffraction angles to be between 43° and 47° and corresponding d spacings for first-order reflections to lie in the ranges 0.79–0.85 and 0.51–0.55 Å for the 10.77- and 16.68-keV peaks, respectively. Second, the simultaneous detection of the two diffractions requires the diffraction angles to differ by ≤4.4°. Third, diffraction energies of 10.77 and 16.68 keV must correspond to diffraction angles that differ by exactly the angle between the normal vectors to the two planes in their crystallographic setting. Finally, the 16.68-keV peak was lost by reducing the tilt angle (Figure 6), indicating that it possesses the greater diffraction angle of the two. Only one pair of quartz planes satisfactorily meets these criteria: (143), d = 0.825 37 Å, θ = 44.3° producing the 10.77-keV peak and (266), d = 0.49361 Å, θ = 48.9° producing the 16.68 keV. The magnitude and difference between the two diffraction angles indicate a detector acceptance angle of 9.2° rather than 8.8° as originally assumed and an angle of 93° between the incident beam and the detector axis. The small 21.5-keV peak follows the 10.77-keV peak and is either a second-order harmonic of the latter or its sum peak.

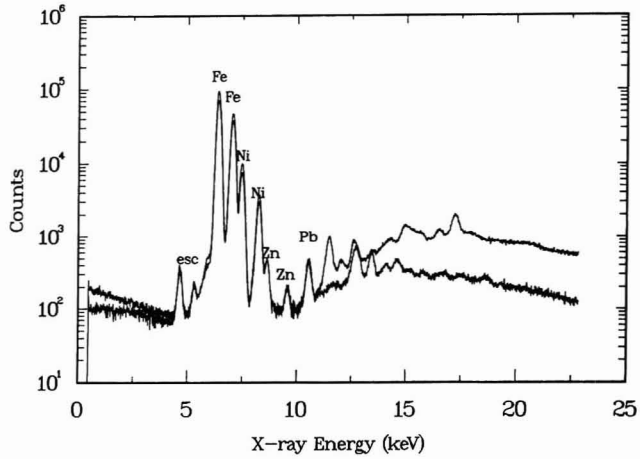

Figure 7. SXRF spectrum of a 100-μm deep sea particle in two different orientations under the same conditions as in Figure 5. Fluorescence peaks (Fe, Ni, Zn, and Pb) remain unaltered by reorientation but the numerous diffraction "bumps" on the high-energy background change position and intensity.

Polycrystalline Aggregates and Amorphous Materials. Broad peaks from polycrystalline aggregates derive from the range of diffraction angles and the finite acceptance angle of the detector while those from amorphous specimens result from short-range order of the atomic components.

An example of polycrystalline scattering behavior was shown by a 100-μm deep sea particle, the product of a micrometeorite which was melted during atmospheric entry, deposited on the ocean floor, and subsequently collected magnetically (*14*). The particle is composed of micrometer-sized crystallites of olivine and magnetite plus glass. Figure 7 shows the SXRF spectrum at two different orientations. The high-energy background contains abundant, broad scattering "bumps" which are modified by reorientation.

An example of amorphous scattering behavior was shown by silica glass (Suprasil). The observed SXRF spectrum after a 12-min exposure possesses scattering features in the energy range 5–14 keV and compares well with a theoretical scattering spectrum (Figure 8) which was calculated by convolution of the incident synchrotron spectrum (e.g., ref 15) and a scattering intensity function I for silica glass (*16*, *17*)

$$I = N\left[f_{\mathrm{Si}} \sum_n f_n \frac{\sin(sr_{\mathrm{Si}-n})}{sr_{\mathrm{Si}-n}} + 2f_0 \sum_n f_n \frac{\sin(sr_{\mathrm{O}-n})}{sr_{\mathrm{O}-n}} \right] \quad (3)$$

where f_n is the atomic scattering factor of atom n, $s = 4\pi \sin(\theta)/\lambda$, r_{m-n} is the distance from atom m to n, and N is the number of molecules in the sample. The observed scattering features are, therefore, satisfactorily explained by the short-range order of silicon and oxygen atoms within a random network of SiO_4 tetrahedra.

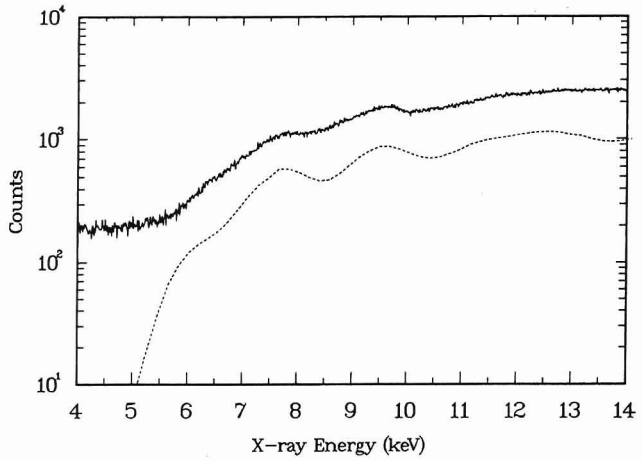

Figure 8. SXRF spectrum (solid line) of synthetic silica glass (Suprasil) obtained under the same conditions as in Figure 5 (12-min measurement time). Prominent scattering features occur at 7.8 and 9.7 keV. The observed spectrum agrees well with a theoretical one (dashed line; normalized to 1000 counts at 14 keV) calculated from the incident synchrotron spectrum and the scattering intensity function adopted by Warren (*16*) (assumed scattering angle of 42° provides best agreement). The experimental spectrum contains detector background at low energies.

ACKNOWLEDGMENT

We are indebted to Keith W. Jones, head of the Atomic and Applied Physics Division, Department of Applied Science, of Brookhaven National Laboratory, who is responsible for development and operation of the SXRF facility and to the NSLS staff for providing beam time for this research. This work benefited from the assistance of Christine Skirius (University of Chicago), and Stuart Stock (Georgia Institute of Technology), and from helpful discussions with Dean Chapman (Purdue University). Gregory Herzog (Rutgers University) kindly supplied the deep sea particle.

Registry No. Si, 7440-21-3; quartz, 14808-60-7; vitreous silica, 60676-86-0.

LITERATURE CITED

(1) Sparks, C. J., Jr. *Synchrotron Radiation Research*; Winick, H., Doniach, S., Ed. Plenum Press: New York, 1980; pp 459–512.
(2) Gordon, B. M. *Nucl. Instrum. Methods* **1982**, *204*, 223–229.
(3) Jones, K. W.; Gordon, B. M.; Hanson, A. L.; Pounds, J. G.; Rivers, M. L.; Schidlovsky, G. *EMSA Bull.* **1985**, *15*, 28–29.
(4) Chen, J. R.; Gordon, B. M.; Hanson, A. L.; Jones, K. W.; Kraner, H. W.; Chao, E. C. T.; Minkin, J. A. *Scanning Electron Microscopy IV*; SEM, Inc.: Chicago, IL, 1984; pp 1483–1500.
(5) Jones, K. W.; Gordon, B. M.; Hanson, A. L.; Hastings, J. B.; Howells, M. R.; Kraner, H. W.; Chen, J. R. *Nucl. Instrum. Methods* **1984**, *231*, 225–231.
(6) Giessen, B. C.; Gordon, G. E. *Science* **1963**, *159*, 973–975.
(7) Sparks, C. J., Jr.; Gedcke, D. A. *Adv. X-ray Anal.* **1971**, *15*, 240–253.
(8) Hastings, J. B.; Thomlinson, W.; Cox, D. E. *J. Appl. Crystallogr.* **1984**, *17*, 85–95.
(9) Nuffield, E. W. *X-ray Diffraction Methods*; Wiley: New York, 1966; pp 1–409.
(10) Smith, J. V.; Skirius, C. M.; Rivers, M. L.; Jones, K. W. *Eos (Madrid)* **1985**, *66*, 1117.
(11) *NBS Monogr. (U.S.)* **1981**, *25*(Sec. 18), 61.
(12) *NBS Monogr. (U.S.)* **1981**, *25*(Sec. 13), 35.
(13) Keith, M. L.; Tuttle, O. F. *Am. J. Sci. Bowen V.* **1952**, 203–280.
(14) Brownlee, D. E. *Annu. Rev. Earth Planet. Sci.* **1985**, *13*, 147–173.
(15) *Synchrotron Radiation Research*; Winick, H., Doniach, S., Eds. Plenum Press: New York, 1980, pp 1–754.
(16) Warren, B. E. *X-Ray Diffraction*; Addison-Wesley: Reading, MA, 1969.
(17) Clark, G. L. *Applied X-rays*; McGraw-Hill: New York, 1955; pp 657–664.

RECEIVED for review December 13, 1985. Accepted April 14, 1986. This work was supported by the National Science Foundation (Grant No. EAR-8313683) and the National Aeronautics and Space Administration (Grant No. NAG 9-106). Research was carried out at the National Synchrotron Light Source, Brookhaven National Laboratory, which is supported by the US Department of Energy, Division of Materials Sciences and Division of Chemical Sciences (Contract No. DE-AC02-76CH00016).

Measurement of $^{13}CO_2/^{12}CO_2$ Abundance by Nondispersive Infrared Heterodyne Ratiometry as an Alternative to Gas Isotope Ratio Mass Spectrometry

Charles S. Irving, Peter D. Klein,* Philip R. Navratil, and Thomas W. Boutton

USDA/ARS Children's Nutrition Research Center, Department of Pediatrics, Baylor College of Medicine, and Texas Children's Hospital, Houston, Texas 77030

We report the performance of a prototype nondispersive infrared heterodyne ratiometer in the analysis of seven reference gas samples containing 3.0% CO_2 in air, and isotopic enrichments from −85 to +329 δ‰ vs. PDB as measured by gas isotope ratio mass spectrometry. The instrument response in volts^{-1} (V^{-1}) varied from −0.51 to 1.22 over the range of −85 to +329‰. A mean instrument response with a 0.0015 standard deviation (0.375‰) required 110 s of signal averaging at a 1-s sampling rate. The calibration curve of instrument response vs. δ‰ was linear over the entire range and had a slope of 0.003 89 ± 0.000 03 (SD), an intercept of −0.168 ± 0.005, and a standard error of 0.009. With this curve, 45 s of data acquisition at a mean instrument response of −0.280 V^{-1} attained a standard deviation of ±1.3‰ at −28.7‰. Nondispersive infrared heterodyne ratiometry can analyze the ^{13}C content of respiratory gas samples with acceptable accuracy and sensitivity for clinical studies.

The gas isotope ratio mass spectrometer is the most widely used means to determine the isotopic composition of carbon dioxide and in particular the abundance of ^{13}C. Such instrumentation has been of fundamental importance in geochemical, environmental, and ecological studies concerned with variations in natural abundance, as well as in biomedical applications employing compounds enriched in ^{13}C (*1*). The latter differ from geochemical measurements in two important respects. First, the precision of the isotope ratio is affected by dietary and physiological processes which result in fluctuations in the basal values of respiratory $^{13}CO_2$ (*2*). Second, the large numbers of samples generated require automated sample isolation, purification, introduction, and analysis (*3*). Even though such instrument capabilities exist, biomedical studies impose further requirements, e.g., high reliability, minimal downtime, low maintenance demands, and facile operation.

In 1973, the National Institute of General Medical Science (NIGMS) learned of a novel method for ^{13}C measurement based on a newly patented technique called nondispersive infrared heterodyne ratiometry (*4*). The rising interest in stable isotope usage and the central role of $^{13}C/^{12}C$ measurements prompted the NIGMS to issue a contract to Andros Analyzers, Inc., of Berkeley, CA, in 1975 to design and fabricate a working model for biomedical applications. In 1981, our laboratory responded to a Request for Applications for analytical and clinical evaluation of this instrument and was awarded its custody upon arrival in July 1983. The effort and cost spent to develop this instrument mandated a stringent assessment of its capability in an environment dedicated to $^{13}CO_2$ determinations. The outcome reported here suggests that nondispersive infrared heterodyne ratiometry is the candidate method for ^{13}C abundance measurements in a clinical setting.

* Address correspondence to this author at Stable Isotope Laboratory, Medical Towers Bldg., 1709 Dryden, Suite 519, Houston, TX 77030.

PRINCIPLE OF OPERATION

Nondispersive infrared heterodyne spectrometry can be used to quantitate components of a gas mixture. Such a spectrometer measures the intensity of a heterodyne signal generated from the partial absorption of amplitude-modulated infrared radiation by a pressure-modulated gas sample. The method does not require monochromatic infrared radiation but does require that the intensity of the radiation transmitted through the sample be selectively modulated at the absorption wavelengths of the gas of interest. This process is accomplished by transmitting radiation through a sample of the gas while the density of the gas is modulated in a sinusoidal manner.

The theory of the successive attenuation of infrared radiation that passes serially through density-modulated gas samples is complex and has not been fully analyzed (*4*). Dimeff (*4*) treated the case in which light of wavelength λ and initial intensity $I_{0\lambda}$ is transmitted serially through two optical cells of length l_1 and l_2 containing gases with mean densities in the light path of ρ_1 and ρ_2 and molecular absorption coefficients of μ_1 and μ_2. The gases are sinusoidally modulated at frequencies ω_1 and ω_2, respectively, to produce density changes of $\Delta\rho_1$ and $\Delta\rho_2$, respectively. The ratio of the intensities of radiation leaving the second cell I_λ compared with the radiation entering the first cell $I_{0\lambda}$ is given by eq 1

$$I_\lambda/I_{0\lambda} = \exp[-(\Delta_0 + \Delta_1 + \Delta_2)] \quad (1)$$

$$\Delta_0 = \mu_1 l_1 \rho_1 + \mu_2 l_2 \rho_2 \quad (2)$$

$$\Delta_1 = \mu_1 l_1 \Delta\rho_1 \cos \omega_1 t \quad (3)$$

$$\Delta_2 = \mu_2 l_2 \Delta\rho_2 \cos \omega_2 t \quad (4)$$

where Δ_0 is the static component defined by eq 2 and Δ_1 and Δ_2 are the dynamic components defined by eq 3 and 4, respectively.

Expansion of eq 1 yields

$$I_\lambda/I_{0\lambda} = [1 - (\Delta_1 + \Delta_2) + (1/2)(\Delta_1^2 + \Delta_2^2 + 2\Delta_1\Delta_2) - \ldots]e^{-\Delta_0} \quad (5)$$

which contains a product term, $\Delta_1\Delta_2$, that corresponds to additional frequency components of the intensity modulation at the heterodyne frequencies, $\omega_1 \pm \omega_2$. The heterodyne signal is denoted by $H_{1,2}$ and is defined at the frequency $\omega_1 - \omega_2$ by

$$(I_\lambda/I_{0\lambda})_{\omega_1-\omega_2} = [(1/2)\mu_1\mu_2 l_1 l_2 \Delta\rho_1\Delta\rho_2 \cos(\omega_1 - \omega_2)t]e^{-\Delta_0} \quad (6)$$

The amplitude of the heterodyne signal is directly proportional to the absorption coefficients of the two gases at wavelength λ. The amplitude of the heterodyne signal is also proportional to the lengths of the two optical cells, λ_1 and λ_2, and to the

0003-2700/86/0358-2172$01.50/0 © 1986 American Chemical Society

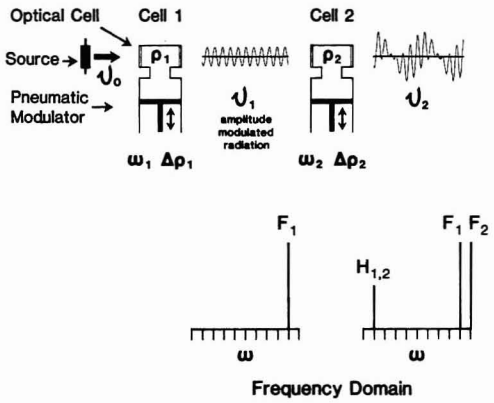

Figure 1. Schematic representation of the generation of fundamental and heterodyne signals. Curves depicting amplitude modulation of transmitted radiation represent the ac component of radiation intensity over approximately 100 ms. Symbol definitions are given in the text.

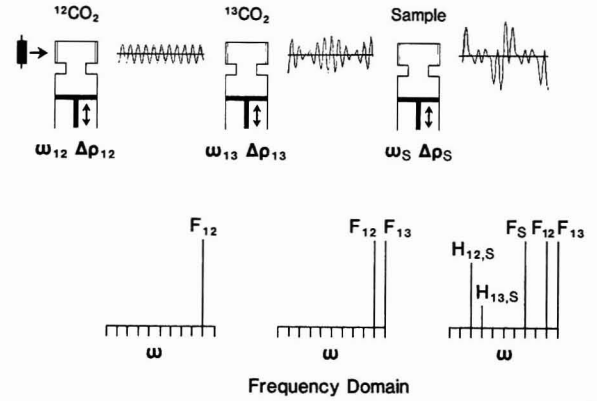

Figure 2. Schematic representation of the simplest use of nondispersive infrared heterodyne spectrometry for the determination of the $^{13}C/^{12}C$ isotopic ratio of CO_2.

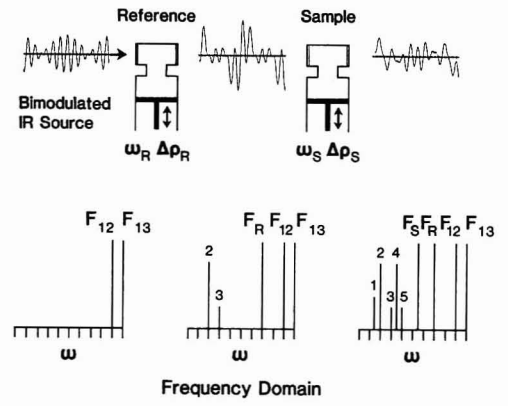

Figure 3. Schematic representation of the use of a reference optical cell in nondispersive infrared heterodyne ratiometric measurement of the $^{13}C/^{12}C$ isotopic enrichment of a sample of CO_2 compared with that of a reference gas. Bimodulated IR radiation is generated by $^{12}CO_2$ and $^{13}CO_2$ optical cells, shown in Figure 2. The heterodyne signals generated by the reference cell and the sample cell have the following origins: (1) $H_{r,s}$, (2) $H_{12,r}$, (3) $H_{13,r}$, (4) $H_{12,s}$, and (5) $H_{13,s}$.

magnitude of the density changes, $\Delta\rho_1$ and $\Delta\rho_2$. For a detectable heterodyne signal to be produced, the individual vibrational–rotational lines of the two gas samples must overlap. The problem of interference by other substances is thus reduced and the method can be used to analyze complex mixtures. In practice, infrared radiation from a nondispersive infrared source is passed through a broad-band interference filter before entering the first optical cell. Therefore, eq 6 must be integrated, as in eq 7, over all wavelengths transmitted through the broad-band interference filter.

$$\frac{I}{I_0} = \int_{\lambda_1}^{\lambda_2} \left(\frac{I_\lambda}{I_{0\lambda}}\right) \tag{7}$$

The principle of nondispersive infrared heterodyne spectrometry is shown schematically in Figure 1. Radiation, ν_0, is modulated to yield ν_1, as it is transmitted through an optical cell containing a gas with a mean density ρ_1 that is density-modulated to $\Delta\rho_1$ at frequency ω_1. The power spectrum in the frequency domain of the transmitted radiation intensity shown in Figure 1 displays a single fundamental line, F_1, at ω_1. The partial absorption of intensity-modulated infrared radiation by a second gas sample with density ρ_2 at ω_2 results not only in the generation of a second fundamental signal, F_2, at ω_2, but also in two heterodyne signals $H_{1,2}$ at $\omega_2 \pm \omega_1$. The signal at $\omega_2 + \omega_1$ is not shown in the figure. The intensity of the $H_{1,2}$ signal is directly proportional to $\Delta\rho_2$, which is the product of the density modulation $\Delta\rho_2$ of the entire gas sample and the concentration of the absorbing gas, C_2. Nondispersive infrared heterodyne spectrometry can be used for trace gas analysis since the concentration of the molecular species that selectively absorbs the modulated radiation in cell 2 can be calculated easily from the intensity of the $H_{1,2}$ signal.

Nondispersive infrared heterodyne spectrometry can be extended to isotope ratio measurements of carbon dioxide because $^{12}CO_2$ and $^{13}CO_2$ behave as two distinct molecular species in their responses to the incident IR beam (*5*). This is due to the absence of significant overlap of individual rotational–vibrational lines in the ν_3 fundamental vibrational bands of $^{13}CO_2$ and $^{12}CO_2$ centered at 4.375 μm (2284.5 cm^{-1}) (*6*) and 4.256 μm (2349.3 cm^{-1}) (*7*), respectively. The simplest form of CO_2 isotopic measurement is shown in Figure 2. Infrared radiation is transmitted through a cell containing $^{12}CO_2$ modulated at ω_{12} and then through a cell containing $^{13}CO_2$ modulated at ω_{13}. This produces amplitude-modulated infrared radiation with two fundamental components, F_{12} and F_{13}, whose amplitudes are given by

$$F_{12} = \mu_{12} l_{12} \Delta\rho_{12} \tag{8}$$

$$F_{13} = \mu_{13} l_{13} \Delta\rho_{13} \tag{9}$$

No $H_{12,13}$ heterodyne signal is generated because the product $\mu_{12}\mu_{13}$ in eq 6 is negligible at all wavelengths in the 4-μm region. When this bimodulated radiation is passed through a CO_2 gas sample modulated at ω_s, heterodyne signals at $\omega_{12} - \omega_s$ and $\omega_{13} - \omega_s$ are produced. Their amplitudes are given by

$$H_{12,s} = \mu_{12}^2 l_{12} l_s \Delta\rho_{12} \Delta P_s C_s^{12} \tag{10}$$

$$H_{13,s} = \mu_{13}^2 l_{13} l_s \Delta\rho_{13} \Delta P_s C_s^{13} \tag{11}$$

$$R_s = C_s^{13}/C_s^{12} = K\, H_{13,s}/H_{12,s} \tag{12}$$

where

$$K = (\mu_{12}^2 l_{12} \Delta\rho_{12})/(\mu_{13}^2 l_{13} \Delta\rho_{13})$$

where ΔP_s is the change in the pressure of the sample gas and C_s^{12} and C_s^{13} are the concentrations of $^{12}CO_2$ and $^{13}CO_2$ in the sample gas. As seen in eq 12, the ratio $H_{13,s}/H_{12,s}$ is proportional to the $^{13}C/^{12}C$ ratio in the gas sample. In practice, however, variations in $\Delta\rho_{12}$ and $\Delta\rho_{13}$ restrict the precision and accuracy of the isotope-ratio measurement.

A four-cell, four-frequency design employing an internal reference has been used to compensate for instabilities in $\Delta\rho_{12}$ and $\Delta\rho_{13}$ (*5*). This method is described schematically in Figure 3. Bimodulated infrared radiation obtained from reference $^{12}CO_2$ and $^{13}CO_2$ cells is passed through a third reference cell containing CO_2 with natural isotopic abundances that is modulated ($\Delta\rho_r$) at a third frequency, ω_r. This process produces two more heterodyne signals, $H_{12,r}$ and $H_{13,r}$, at $\omega_{12} - \omega_r$ and $\omega_{13} - \omega_r$, respectively. These signals monitor $\Delta\rho_{12}$ and $\Delta\rho_{13}$ and thus serve as internal references. Subsequent

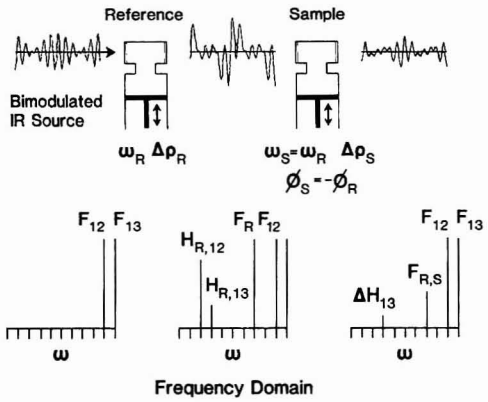

Figure 4. Schematic representation of the pressure servo mode of nondispersive infrared heterodyne ratiometric analysis of the $^{13}C/^{12}C$ isotopic enrichment of a sample of CO_2. ϕ_s and ϕ_r refer to the phase of the density modulations of the sample and reference cells, respectively.

transmission of the beam through the sample cell produces (among others) heterodyne signals $H_{12,s}$ and $H_{13,s}$. In addition, because the sample and reference cells contain $^{12}CO_2$ and $^{13}CO_2$, an $H_{s,r}$ heterodyne signal is generated at $\omega_s - \omega_r$. More importantly, however, the $^{13}C/^{12}C$ ratio of the sample gas, normalized to that of the reference gas, can be derived from the amplitudes of four heterodyne signals as shown in eq 13.

$$\frac{R_s}{R_r} = \frac{H_{13,s}}{H_{12,s}} \frac{H_{12,r}}{H_{13,r}} \tag{13}$$

Initial isotopic analyses of CO_2 carried out by Andros Analyzers, Inc., were based on this method and utilized four phase-sensitive Ithaco Dynatrac-3 signal analyzers to determine the amplitudes of the four heterodyne signals. In practice, the precision of these measurements was found to be limited by differential drifts in the four signal analyzers (*8*).

A novel pressure servo scheme, shown in Figure 4, was used by Andros Analyzers, Inc., to overcome these drift problems. In the pressure servo mode, the sample and reference cells are modulated at the same frequency, $\omega_s = \omega_r$; however, the phase of the pressure modulation in the reference cell is shifted by 180° with respect to the sample cell. Only two heterodyne signals are observed and these represent the difference between reference and sample heterodyne signals. As seen in eq 14 and 15, the signal ΔH_{12} at $\omega_{12} - \omega_{s,r}$ is the difference between the $H_{12,s}$ and $H_{12,r}$ signals, and the signal ΔH_{13} at $\omega_{13} - \omega_{s,r}$ is the difference between the $H_{13,s}$ and $H_{13,r}$ signals. In

$$\Delta H_{12} = H_{12,s} - H_{12,r} = \mu_{12}{}^2 l_{12} \Delta\rho_{12} (\Delta P_s C_s{}^{12} l_s - \Delta P_r C_r{}^{12} l_r) \tag{14}$$

$$\Delta H_{13} = H_{13,s} - H_{13,r} = \mu_{13}{}^2 l_{13} \Delta\rho_{13} (\Delta P_s C_s{}^{13} l_s - \Delta P_r C_r{}^{13} l_r) \tag{15}$$

$$\Delta P_s C_s{}^{12} l_s = \Delta P_r C_r{}^{12} l_r \tag{16}$$

the pressure servo mode, the modulation of the reference cell, ΔP_r, is adjusted continuously to null the ΔH_{12} signal. The isotopic composition of the gas in the sample cell can then be derived from the ΔH_{13} signal. The intensity of the F_{13} signal (eq 9) is substituted in eq 15 to yield eq 17. By substituting in eq 17 the expression for ΔP_s (eq 18), derived from eq 16, and rearranging the terms for gas concentrations, one obtains eq 19. Because ΔP_r is monitored continuously by a pressure

$$\Delta H_{13}/F_{13} = \mu_{13} (\Delta P_s C_s{}^{13} l_s - P_r C_r{}^{13} l_r) \tag{17}$$

$$\Delta P_s = \Delta P_r C_r{}^{12} l_r / C_s{}^{12} l_s \tag{18}$$

$$\Delta H_{13}/F_{13} = \mu_{13} \Delta P_r l_r C_r{}^{12} (R_s - R_r) \tag{19}$$

transducer in the reference cell, it can be combined with the

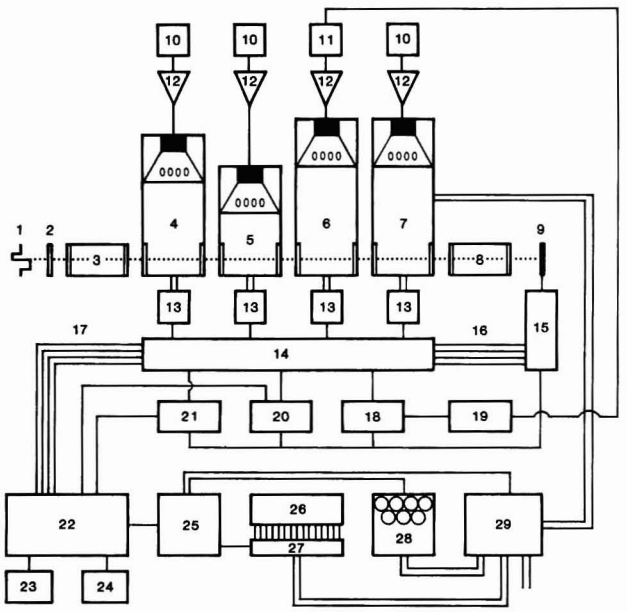

Figure 5. Block diagram of the components of the nondispersive infrared heterodyne ratiometer instrument. See Instrumentation section for a description of components by number.

two other observable parameters, ΔH_{13} and F_{13}, to yield eq 20, which relates the instrument response, $\Delta H_{13}/(F_{13} + \Delta P_r)$, defined in arbitrary units, to the absolute difference between $^{13}C/^{12}C$ isotopic ratios of CO_2 in the reference and sample gases.

The principles of the instrument operated in the pressure servo mode are summarized in eq 20. In practice, the term

$$\text{instrument response} = \Delta H_{13}/F_{13}\Delta P_r = \mu_{13} l_r C_r{}^{12} (R_s - R_r) \tag{20}$$

to express the difference in isotopic content between the sample and reference $(R_s - R_r)$ has been replaced by isotopic enrichment expressed in delta units $(R_s - R_r)/R_r$, which approximates the former term since R_r approximates 1.0×10^{-2}.

In addition to isotope ratio values, the instrument also measures the level of CO_2 in the sample gas. The CO_2 concentration of the sample is determined from the ratio of the pressure modulations in the reference and sample cells given in eq 21, obtained by rearranging eq 16.

$$C_s{}^{12} = C_r{}^{12} \left(\frac{\Delta P_r}{\Delta P_s}\right)\left(\frac{l_r}{l_s}\right) \tag{21}$$

INSTRUMENTATION

The components of the Andros instrument are shown in Figure 5. Infrared radiation obtained from an automobile cigarette lighter, 1, operated at 9 V and 4.5 A passes through a 4.0–4.4 μm interference filter, 2, an optical cell containing 100% natural abundance CO_2, 3, four pressure-modulated optical cells containing 100% ^{12}C CO_2 (^{12}C 99.9%) (Monsanto Mound Laboratory HH-3-77-49), 4, 5% ^{13}C CO_2 (^{13}C 99.3%) (MSD Isotopes, MS-2163) in dry air, 5, 15% CO_2 of natural abundance in dry air, 6, breath sample containing 1.0–4.5% CO_2, 7, and a second nonmodulated optical cell containing 100% CO_2 of natural abundance, 8. The two nonmodulated cells attenuate the ^{12}C signal in relation to the ^{13}C signal. The light path in optical cells 1, 2, and 3 is approximately 2 cm per cell and in 4 is approximately 6 cm. Each cell is fitted with a pair of sapphire windows. The pressure-modulated optical cells act as quarter-wave closed-pipe resonators. In each optical cell, a 10-cm diameter, 10-W full-range speaker (Radio Shack 40-1197) generates an acoustic wave that is channeled through a horn machined in the top of the cell. The four optical cells, whose lengths perpendicular to the light path

have been adjusted to achieve acoustic resonance, are driven at 781, 895, 575, and 575 Hz, respectively. The speakers are driven by a ±9-V signal obtained from four sine wave generators, 10 and 11, and power amplifiers, 12. Pressure modulation in each optical cell is measured by a pressure transducer, 13, whose voltage and frequency are monitored by a pressure signal demodulator/reference signal generator, 14.

To prevent changes in the gas density in the optical cells and consequent effects on the resonance frequency and pressure modulation, the temperature of the optical cells is maintained at 15 ± 0.1 °C by chilled water from a Neslab CFT-33 refrigerated recirculating bath. Infrared radiation is detected by an InSb crystal maintained at −198 °C. In the detector preamplifier 15, the photovoltaic output from the crystal is mixed with four fundamental suppression signals, 16, obtained from the pressure signal demodulator/reference signal generator. These fundamental suppression signals are generated from the pressure transducer outputs and are phase-shifted 180° with respect to the F_{12}, F_{13}, $F_{s,r}$, and $\omega_{13} - \omega_{12}$ signals. After being mixed with the fundamental suppression signals, the detector output is biased, amplified, and fed to three signal demodulators.

The ΔH_{12}-pressure servo system operates in the following manner: a reference signal for ΔH_{12} is generated by 14 from the pressure transducer of the comparison cell. The reference signal is used by an Ithaco Dynatrac-3 signal analyzer, 18, to monitor the in-phase and quadrature components of the ΔH_{12} signal obtained from the preamplifier, 15. The pressure servo circuit, 19, controls the signal that is synthesized in 11 that drives the comparison cell speaker. The amplitude of the speaker drive is adjusted so that the output from the ΔH_{12} demodulator, 18, is minimal. The ΔH_{13} heterodyne signal is monitored by another Ithaco Dynatrac-3 signal analyzer, 20, that receives its reference signal from 14.

The servo system that suppresses the fundamental signal operates as follows: the preamplifier output is fed into custom-designed fundamental signal demodulators, 21. The amplitude of the F_{12}, F_{13}, and $F_{s,r}$ fundamental suppression signals is adjusted by 16 to maintain a low, preset output from the fundamental signal demodulator. Systems 10–21 thus constitute the analog electronics of the original instrument designed by Andros Analyzers, Inc., and operate in the manner described.

The data acquisition and computational components perform three major functions: (1) control the gas manifold system; (2) digitize the analog signals from signal demodulators and calculate and time-average $\Delta H_{13}/(F_{13}\Delta P_r)$, the instrument response; and (3) calculate breath-test parameters, generate reports and graphics, and document test results. The system consists of a Columbia personal computer, 22, equipped with a 12-bit analog and digital I/O system (Data Translation DT2801).

The gas manifold system consists of (1) a microprocessor-based valve-control unit, 25, capable of driving 32 Mini-Mizer 0.5-W air valves (Humphrey M3E1), (2) a 20-port sample-inlet manifold, 27, and a detachable sample-transport unit, 26, consisting of 20 1-L sample collection bags, (3) a manifold of seven cylinders of calibration gases, 28, and (4) a utility manifold and vacuum pump, 29. When the instrument is to be started, the personal computer sends a command via the serial port to the valve-controller unit which, in turn, activates the valves in the utility manifold to evacuate the sample cell, flush with air, and reevacuate the cell. The valve controller then fills the sample cell with 400 mL of calibration gas from the first cylinder in the calibration gas manifold. Upon completion of the first set of calibration measurements, the cell is evacuated, flushed, and reevacuated and the next calibration gas is introduced. Upon completion of the seven-point calibration routine, the instrument is ready to analyze samples from the sample inlet manifold in a similar manner. For on-line breath test analyses, the utility manifold is connected directly to the subject's face mask or to a mixing chamber downstream from the mask. The time required to evacuate, flush, reevacuate, and introduce a sample is less than 1 min.

Digitization and analysis of analog signals obtained from the analog control electronics and demodulators are carried out in the following manner. One set of A/D conversions is performed on the ΔP_{12}, ΔP_{13}, ΔP_s, and ΔP_r signals, 17, obtained from 14, the pressure signal demodulator/reference signal generator. These dc signals are proportional to the amplitude of the ac components of the pressure transducer signals.

The other set of A/D conversions is performed on the quadrature ($Q\Delta H_{13}$) and in-phase ($I\Delta H_{13}$) output voltages from the ΔH_{13} demodulator, 20, and the quadrature (QF_{13}) and in-phase (IF_{13}) output voltages from the F_{13} demodulator, 21. Instrument response (V^{-1}) is calculated as $(Q\Delta H_{13}^2 + I\Delta H_{13}^2)^{1/2}/(\Delta P_c(QF_{13}^2 + IF_{13}^2)^{1/2})$. Measurements were performed at a rate of one per second; during each cycle the running mean and standard deviation of the averaged instrument response were computed.

The standard deviation of the mean is estimated for band-limited Gaussian noise and is given by the square root of the variance divided by $2BT$, where B, the noise bandwidth, is 0.2 for the 1.25-s time constant of the signal demodulator and T is the acquisition time (seconds). This cycle is repeated until a specified precision has been achieved or until the signal time has exceeded 4 min. Diagnostic information on the system operation generated by the analog control electronics in the form of an 8-bit digital signal is monitored by the personal computer. The dc output from a temperature probe in the sample cell is also used to monitor the optical cell temperature.

Breath test curves are displayed graphically on the video display terminal, 23, and reports are generated with an Epson RX-80F/T dot matrix printer, 24. Data are also archived on floppy disks.

METHODS AND MATERIALS

Materials. $^{12}CO_2$ (99.9% ^{12}C) was obtained from Mound Laboratory Monsanto (HH-3-77-49). $^{13}CO_2$ (99.3% ^{13}C) was obtained from MSD Isotopes (MS-2163). Compressed air (UN 1002), 3.06% CO_2 (natural abundance) in 96.94% air (18510784A), and 5.16% CO_2 (natural abundance) in 94.84% air were prepared by Big Three Industries, Houston, TX, from NF- or USP-grade gases. All gas samples were used without further purification.

Calibration Gas Samples. Seven CO_2 concentration gas standards (320 L) ranging from 1 to 5% CO_2 in air were prepared by dilution of a sample of 5.15% CO_2 with air. The composition of the resulting mixture was determined by gas chromatography as previously described (*9*). Seven ^{13}C CO_2 calibration standards (1140 L) with isotopic enrichments ranging from approximately −85 to +329‰ vs. PDB were prepared by the addition of either $^{12}CO_2$ or $^{13}CO_2$ to 3.06% CO_2 (^{13}C, −27‰) in air. The final isotopic enrichments of the standards were determined by triplicate geochemical grade mass spectrometric gas isotope ratio measurements (R. Dunbar, Ph.D., Department of Geology, Rice University, Houston, TX). Aliquots (115 L) were transferred to Luxfer C5 gas cylinders in the calibration gas manifold of the Metabolic Carbon Analyzer. Each instrument calibration curve required a 400-mL sample of each of the $^{13}CO_2$ calibration standards.

$^{13}CO_2$ Calibration Routine. The seven $^{13}CO_2$ standard calibration gases were analyzed in order of increasing enrichment using the following method: the sample cell was evacuated, flushed with air, reevacuated, filled with calibration standard to a pressure of 5 psi, and then vented to atmospheric pressure. Instrument responses ranged from approximately −0.5 to 1 V^{-1}. Signal averaging was continued until a standard deviation of the mean of 0.0015 V^{-1} of the instrument response was achieved or the accumulation time exceeded 240 s. Upon completion of the seven

analyses, linear regression methods were used to determine the standard error, slope, and intercept of the regression line, together with the standard deviations and the uncertainty associated with use of the calibration curve for interpolation of instrument response to obtain the isotopic enrichment of a sample.

CO_2 Concentration Calibration Curve. Nylon sample bags fabricated from 0.002 × 54 in. Wrightlon 4500 (452541.5M International Plastics Products, Carson, CA) were filled with 500-mL aliquots of each of the seven CO_2 concentration standard gas samples, placed on the sample inlet manifold, and analyzed using the method described above. Upon completion of the seven analyses, linear regression analysis of P_c/P_s vs. $\%CO_2$ was carried out on the five samples in the 2–4% CO_2 range and a calibration curve was plotted.

Test of Intra- and Intersample Precision. A sample bag was filled with 30 L of 3.05% CO_2 (^{13}C, −26.7‰) in air and was attached to one of the ports of the sample inlet manifold. The bag was sampled repetitively over 120 min and analyzed following the same procedure used for the calibration test. After each measurement, the time of sampling, instrument response, standard deviation of the mean, calculated ^{13}C abundance as ‰ vs. PDB, CO_2 concentration, and sample cell temperature were recorded and the measured ‰ vs. PDB was plotted against the time of sample analysis. The mean and standard deviation of each value throughout the run were then calculated and compared with the intrasample standard deviation set for individual measurements.

Test of Residual Sample Bias. Two sample bags were filled with 3 L of the −85.5‰ calibration standard and attached to sample ports 1 and 3. Another sample bag was filled with 3 L of the 329‰ calibration standard and attached to sample port 2. Five successive samples from ports 1, 2, and 3 were analyzed as described above.

Test of the Effect of ^{18}O Content on $^{13}CO_2$ Measurements. Standard water samples with ^{18}O enrichments of 25, 100, 200, 500, and 1000‰ above natural abundance were prepared by the addition of $H_2{}^{18}O$ (^{18}O 10 atom % excess) to water samples. Oxygen-18 enriched water standards were equilibrated with natural abundance CO_2, and the resulting ^{18}O enrichment of the CO_2 was determined by using the method described by Schoeller et al. (*10*). Aliquots of the oxygen-enriched CO_2 samples were placed in Wrightlon sample bags and analyzed as described above.

RESULTS

Demonstration of Nondispersive Infrared Heterodyne Spectrometry Using the Pressure Servo System. Figure 6 (top) displays the semilog plot of the fast Fourier transform (FFT) spectrum in the frequency domain from 175 to 975 Hz. This represents the output of the detector preamplifier signal before demodulation. The spectrum was obtained without acoustic modulation in the reference cell and displays the $H_{12,s}$, $H_{13,s}$, F_s, F_{12}, and F_{13} signals at 205, 269, 575, 781, and 845 Hz, respectively. Aside from two minor extraneous signals, the frequency spectrum is pure over a range of 40 dB. Suppression of the F_s, F_{12}, and F_{13} fundamental signals in the detector preamplifier has reduced their intensities to the levels of the heterodyne signals. Operation of the instrument in the pressure servo mode in which the reference cell was driven 180° out of phase with the sample cell (Figure 6, bottom) resulted in the complete nulling of the ΔH_{12} signal at 205 Hz and reduced the intensity of the ΔH_{13} signal at 269 Hz with respect to the $H_{13,s}$ signal in Figure 6A. The additional signals seen in the FFT spectrum have not been assigned, but do not affect the measurement of the ΔH_{13} and F_{13} signals. The F_s signal in Figure 6B arises from modulation in both the sample and reference cells. It is larger and broader than the corresponding signal in Figure 6A, due to the varying pressure modulation in the reference cell that occurs in the pressure-servo mode. These spectra demonstrate that the instrument operates in the pressure servo mode, as described in the Principle of Operation and Instrumentation sections.

$^{13}CO_2$ Calibration Curve. The instrument response, $\Delta H_{13}/(F_{13}\Delta P_c)$, obtained for seven calibration gas standards consisting of 3% CO_2 in air with ^{13}C isotopic enrichments of

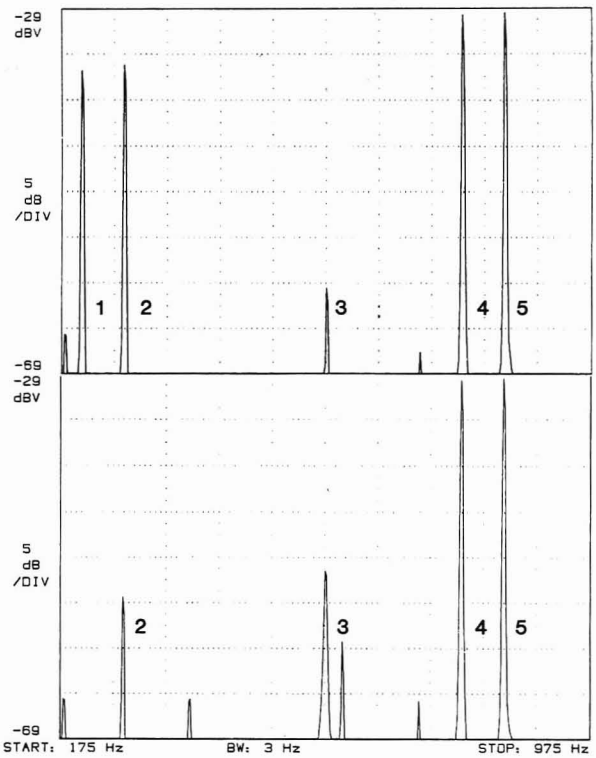

Figure 6. Frequency domain spectra of preamplifier output of the nondispersive infrared heterodyne ratiometer in the pressure servo mode with acoustic drive to the reference cell (top) off and (bottom) on. The signals observed with reference cell drive off (top) are (1) $H_{12,s}$ (205 Hz), (2) $H_{13,s}$ (269 Hz), (3) F_s (575 Hz), (4) F_{12} (781 Hz), and (5) F_{13} (845 Hz). In the pressure servo mode with the reference cell drive on (bottom), note that the ΔH_{12} signal at 205 Hz is nulled and the ΔH_{13} signal (2) at 269 Hz is attenuated with respect to the $H_{13,s}$ signal in A. Spectra were obtained with a Hewlett-Packard 3561A dynamic signal analyzer.

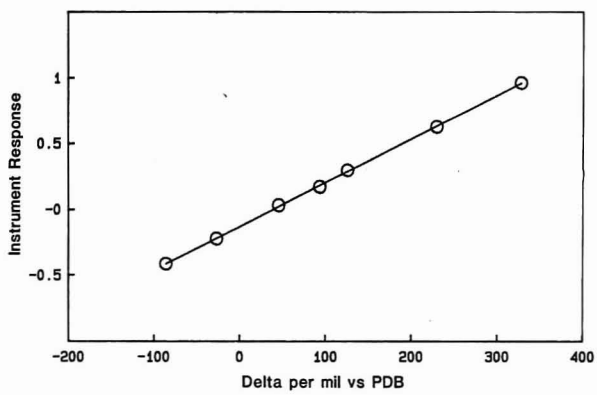

Figure 7. Plot of instrument response vs. the isotopic enrichment of calibration gas standards given in units of δ‰ vs. PDB. Solid line represents the least-squares regression line, whose parameters are given in the text.

−85.5, −26.7, +46.0, +94.1, +124.4, +230.6, and +329.0‰ vs. PDB, respectively, is plotted in Figure 7 against isotopic enrichment. Instrument response was linear over the range of 400‰. The data could be fitted to a regression line with slope and intercept of 0.003 895 ± 0.000 027 (SD) ($V^{-1}\cdot‰^{-1}$) and −0.1681 ± 0.0046 V^{-1}, respectively. Instrument response, which ranged from −0.51 to 1.2, could be determined with a precision of 0.0015 (standard deviation of the mean) within 110 s of data acquisition for all calibration samples. This response was equivalent to a precision of 0.38‰ for less than 2 min of data acquisition of a sample containing approximately 3% CO_2. An additional measure of instrument performance was obtained, when the calibration data were used to estimate the uncertainty of a hypothetical sample at an interpolated re-

Table I. Daily Log of ^{13}C Calibration Curve Parameters

date	slope	intercept	SE[a]	δ‰ vs. PDB[b]
02–20	3895 ± 27[c]	−1681 ± 46	0.0095	−28.7 ± 1.35
02–21	3924 ± 28	−1670 ± 47	0.0098	−28.8 ± 1.39
02–22	3938 ± 29	−1645 ± 48	0.0100	−29.2 ± 1.41
02–25	3312 ± 26	−1376 ± 44	0.0092	−43.0 ± 1.62
02–26	3308 ± 24	−1299 ± 40	0.0086	−45.4 ± 1.48
02–27	3304 ± 26	−1366 ± 44	0.0092	−43.4 ± 1.61
02–28	3323 ± 25	−1404 ± 39	0.0081	−42.0 ± 1.41
03–01	3905 ± 39	−1504 ± 46	0.0113	−33.2 ± 1.40
03–04	3314 ± 29	−1314 ± 49	0.0102	−44.8 ± 1.80
03–05	3293 ± 24	−1440 ± 41	0.0085	−41.3 ± 1.49
03–06	3274 ± 22	−1318 ± 36	0.0076	−45.3 ± 1.36
03–07	3311 ± 27	−1379 ± 46	0.0096	−42.9 ± 1.67
03–08	3271 ± 27	−1317 ± 45	0.0094	−45.3 ± 1.68
03–11	3289 ± 25	−1175 ± 43	0.0089	−49.4 ± 1.61
03–13	3288 ± 31	−1470 ± 36	0.0086	−40.4 ± 1.36
03–14	3253 ± 34	−1439 ± 40	0.0099	−41.8 ± 1.52
03–15	3268 ± 28	−1480 ± 47	0.0099	−40.4 ± 1.74
03–18	3277 ± 25	−1522 ± 41	0.0086	−39.0 ± 1.51
03–20	3275 ± 25	−1363 ± 43	0.0087	−43.9 ± 1.55
03–21	3266 ± 24	−1397 ± 41	0.0085	−43.0 ± 1.51
03–22	3267 ± 31	−1433 ± 52	0.0109	−41.8 ± 1.93
04–08	3180 ± 21	−1758 ± 35	0.0073	−32.8 ± 1.28
04–09	3186 ± 23	−1748 ± 39	0.0081	−33.0 ± 1.43
05–15	3004 ± 17	−1605 ± 20	0.0049	−39.8 ± 0.83

[a] Standard error of the regression line. Lark, P. D.; Craven, B. R.; Bosworth, R. C. L. The Handling of Chemical Data; Pergamon Press: Oxford, 1968; Chapter IV. [b] PDB, Pee Dee belemnite. [c] Standard deviation.

sponse to −0.284 V^{-1}. Forty-five 1-s measurements at this instrument response would result in a standard deviation of ±1.3‰ at an isotopic enrichment of −28.7‰. This point on the calibration curve was selected because it represents the lowest ^{13}C abundance normally encountered in respiratory CO_2. Each time the instrument was turned off after use, it was recalibrated on start up. The effect of powering-up the instrument on the calibration curve parameters as well as the long-term drift in these parameters is seen in Table I. The daily calibration curve parameters obtained over a 1-month period are listed, starting with the calibration curve data displayed in Figure 7. The precision of the slope and intercepts and the standard error of the regression did not vary greatly from day to day over the course of a month. However, slope and intercept did change slightly, which justified automatic recalibration of the instrument on power up. The abrupt change in the slope and intercept from one day to the next is the consequence of operational changes made in the pressure modulation of one of the optical cells.

Precision and Sample Analysis Time. To determine the intra- and intersample variation and average sample analysis time under actual operating conditions, repetitive sampling and ratiometric analysis were carried out on a sample of 3% CO_2 (^{13}C, −26.7‰) in air over 120 min. Data acquisition was carried out for a minimum of 110 s and terminated when the standard deviation of the instrument response reached 0.0015 (0.375‰). Over the course of 120 min, 32 analyses were obtained, with approximately 2 min devoted to data acquisition in each cycle. The ^{13}C enrichments measured are plotted as a function of sampling time in Figure 8. The mean of the 32 measurements was −27.47 ± 0.56‰, which corresponds to the ability to measure a change of 1.68‰ at the 3σ level. The level of precision attainable with 120 s of signal averaging permits the instrument to carry out on-line measurements of breath $^{13}CO_2$ sampled repetitively from a face mask, hood, or mixing chamber.

CO_2 Concentration Calibration Curve. The values of $\Delta P_c/\Delta P_s$ (v/v) obtained from analysis of seven CO_2 concentration standards over a range of 1–5% CO_2 in air. The

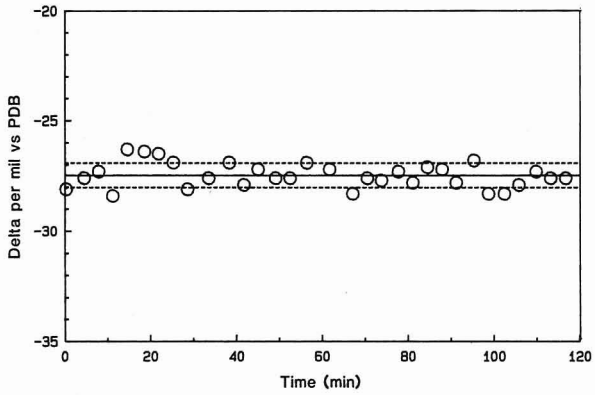

Figure 8. Isotopic enrichments in δ‰ vs. PDB of repetitive samples of 3% CO_2 (^{13}C −26.5‰) in air plotted as a function of the sampling time. The solid line designates the mean of the 32 measurements (−27.47‰), while the standard deviation of ±0.56‰ is designated by the dashed line. This plot demonstrates the rate at which samples can be measured as well as the long-term instrument precision.

Table II. Memory Effect of Low or High ^{13}C Enrichment Alteration on Sequential Measurements

enrichment measd by GIRMS,[a] ‰	‰ measurement 1	2	3	4	5	mean, ‰	std dev, ‰
−85.5	−85.1	−85.6	−85.9	−88.3	−87.5	−86.5	±1.3
329.0	328.1	328.0	331.8	329.0	327.8	328.8	±1.3
−85.5	−86.5	−86.9	−87.5	−88.2	−88.3	−87.5	±0.8

[a] Gas-isotope-ratio mass spectrometry.

response was linear over the range of 2–4% CO_2, in which most breath test samples fall. The regression line through these points had a slope and intercept of 0.3595 ± 0.0027 ($\%^{-1}$) and 0.0275 ± 0.0085, respectively, with r = 0.999 91. Interpolation of a mean value for $\Delta P_c/\Delta P_s$ of 1.0 (obtained from averaging of 42 1-s readings of $\Delta P_c/\Delta P_s$ into the calibration curve yields a CO_2 concentration of 2.8585 ± 0.0058%. The instrument thus not only provides an estimate of the isotopic enrichment of CO_2 but also yields a precise estimate of the CO_2 content of the sample.

Bias Due to Residual Sample Gases. To determine the magnitude of memory effects resulting from residual gases left in the sample cell from previous analyses, five samples of −85.5‰ CO_2 were analyzed followed by five samples of 329‰ CO_2. The analyses were repeated on a second lot of five samples of −85.5‰ CO_2. As seen in Table II, after five determinations of the depleted CO_2, no bias toward lower values was detected in the analyses of the first enriched samples. Although a slight bias to more negative values is seen in the second set of determinations on the depleted samples, a similar trend was seen in the first set of analyses of this sample. For all practical purposes, no memory effects could be detected.

Interference by $C^{18}O_2$. To determine the extent to which $^{12}C^{18}O^{16}O$ is detected as $^{13}C^{16}O^{16}O$ by the instrument, five samples of 3% CO_2 (^{13}C, −26.5‰) in air were equilibrated with a standard of $H_2{}^{18}O$ to obtain standards of CO_2 with ^{18}O enrichments of 33.9, 94.7, 223, 513, and 989‰ vs. SMOW. The apparent ^{13}C enrichments of these samples were −28.7, −25.5, −20.7, −7.9, and +12.7‰, respectively. Linear regression analysis of the apparent ^{13}C enrichment of CO_2 as a function of the actual ^{18}O enrichment of the sample yielded a slope and intercept of 0.043 13 ± 0.000 37 and −29.99 ± 0.19, respectively, and a standard error of 0.291. This slope indicates that on a *mole fraction basis*, the effect of $^{12}C^{18}O^{16}O$ on the instrument response is 24.1% that of the effect of $^{13}C^{16}O^{16}O$. The sensitivity of the instrument to $^{12}C^{18}O^{16}O$ probably arises from an overlap of the spectral lines. In practice, any biological

enrichment of ^{18}O levels in CO_2 would be so small as to have a negligible effect on ^{13}C measurements.

Overall Performance Characteristics. The daily start up of the instrument consists of cooling the optical cells to 15 °C, cooling the InSb detector to liquid N_2 temperature, and turning on power to the instrument and computer. If the optical cells are at room temperature, approximately 1 h is required to achieve operating temperature. Cooling of the IR detector requires approximately 5 min. Once these temperatures are achieved, the calibration program can be initiated. At this stage, the instrument can be restarted immediately after a power failure. Calibration of the instrument is completely automatic and requires only that the operator fill the liquid N_2 Dewar.

DISCUSSION

Measurements of excess $^{13}CO_2$ in breath after the administration of ^{13}C-labeled substances have biomedical applications that range from monitoring energy metabolism and substrate utilization to the assessment of organ function.

Current gas isotope ratio mass spectrometers have the ability to measure isotopic abundances of ^{13}C to within ±0.01‰. In human tracer studies, the excretion of ^{13}C varies with the metabolic fuel being oxidized and this variation has been shown to be ±0.7‰ (standard deviation) over a 6-h period. Thus, analytical precisions greater than 0.3–0.5‰ are of little use in physiological studies with ^{13}C-enriched substrates. Moreover, conventional tracer studies are concerned with relative responses, i.e., changes from base line abundance, so that the requirement for accuracy with which the absolute abundance is determined, typically ±0.5–1.0‰, is less stringent than in other (e.g., geochemical) applications.

Although the development of the original instrument system faltered before completion, use of the principle of nondispersive infrared heterodyne spectrometry to determine $^{13}CO_2/^{12}CO_2$ ratios is clearly established by the present instrument. The instrument is capable of measuring ^{13}C abundance over a range of −100 to 320‰ with a precision of 0.4‰ and an accuracy of 1.3‰ within 120 s on a sample of 3% CO_2. No memory effect is displayed, and following our modifications, the instrument has a sample introduction time of 60 s and an overall sample analysis cycle of 3.75 min. Thus the metabolic carbon analyzer is capable of providing rapid analyses, including on-line measurements of ^{13}C abundance in respiratory CO_2. The instrument now has the capability to conduct an automatic seven-point calibration, requiring less than 30 min and is equipped with a 20-port sample manifold under computer control.

With the experience gained from this assessment, the limitations in the original design that must be overcome have become evident. These include reliance on acoustical resonance and the attendant 400-mL sample requirement, the use of an InSb detector, which must be maintained at liquid N_2 temperatures, and, finally, the use of analog technology to demodulate multicomponent ac signals. All of these limitations can be and are being overcome in the future development of this instrument into a clinically useful system for ^{13}C abundance measurements.

ACKNOWLEDGMENT

K. Williams, Andros Corporation, provided substantive background and perspective on original prototype designs. Manuscript preparation by S. Wahl and S. Perez and editorial review by Y. Garza are also appreciated.

Registry No. $^{13}CO_2$, 1111-72-4; CO_2, 124-38-9.

LITERATURE CITED

(1) Klein, P.; Klein, E. R. *J. Pediatr. Gastroenterol. Nutr.* **1985**, *4*, 9–19.
(2) Schoeller, D. A.; Schneider, J. F.; Solomons, N.; Watkins, J. B.; Klein, P. D. *J. Lab. Clin. Med.* **1977**, *90*, 412–417.
(3) Schoeller, D. A.; Klein, P. D. *Biomed. Mass Spectrom.* **1979**, *6*, 350–355.
(4) Dimeff, J. **1972**, U.S. Patent 3 679 899.
(5) Davies, D. W. **1977**, U.S. Patent 4 027 972.
(6) Herzberg, G. *Molecular Spectra and Molecular Structure*; D. Van Norstrand: Princeton, NJ, 1945; Vol. II, p 274.
(7) Nielsen, A. H. *Phys. Rev.* **1938**, *53*, 983–985.
(8) Williams, K., personal communication, 1983.
(9) Irving, C. S.; Wong, W. W.; Shulman, R. J.; Smith, E. O.; Klein, P. D. *Am. J. Physiol.* **1983**, *245*, R190–R202.
(10) Schoeller, D. A.; van Santen, E.; Peterson, D.; Dietz, W.; Jaspan, J.; Klein, P. D. *Am. J. Clin. Nutr.* **1980**, *33*, 2686–2697.

RECEIVED for review September 30, 1985. Resubmitted January 24, 1986. Accepted May 5, 1986. This work was supported by GM 28783, AM 28129, by the USDA/ARS Children's Nutrition Research Center, Department of Pediatrics, Baylor College of Medicine, and Texas Children's Hospital, and by BCM Technologies, Inc.

Effect of Absorbing Matrices on Diffuse Reflectance Infrared Spectra

Paul J. Brimmer and Peter R. Griffiths*

Department of Chemistry, University of California, Riverside, California 92521

The effects of absorbing matrices on the diffuse reflectance infrared spectra of organic analytes are investigated. The Kubelka–Munk function for compounds dispersed in absorbing matrices varies in a nonlinear manner with concentration, making quantitative analysis difficult. The qualitative behavior of these systems is also different from that of species dispersed in nonabsorbing matrices. For example intense absorption bands may appear as reflection maxima when absorbing matrices are used. Potential causes of this behavior are discussed. The results of this study are important in the interpretation of spectra of adsorbates on absorbing substrates, such as TLC plates and supported catalysts, and carbon-containing materials, such as coals.

The number of applications for which diffuse reflectance (DR) infrared spectrometry has been used has grown substantially since 1978, when Fuller and Griffiths (*1*, *2*) described optics for DR measurements that were readily compatible with rapid scanning Fourier transform infrared (FT-IR) spectrometers. Since that time DR infrared spectrometry has been used in a qualitative manner for a wide variety of samples (*3*, *4*). However DR infrared spectrometry may be described as semiquantitative at best, and then only if characteristics of the sample and dilution matrix adhere to certain criteria. These criteria originate from the assumptions made in the derivation of the Kubelka–Munk equation (*5*, *6*), which is the diffuse reflectance analogue to Beer's law for transmission measurements.

The Kubelka–Munk (K-M) equation is often used to describe the behavior of diffuse reflectance in the mid-infrared region. The K-M function, $F(R_\infty)$ is given by

$$F(R_\infty) = (1 - R_\infty)^2/2R_\infty = k/s \quad (1)$$

where R_∞ is the diffuse reflectance spectrum of an "infinitely thick" sample ratioed to that of a nonabsorbing reference, k is the absorption coefficient, and s is the scattering coefficient. If the sample is mixed with a matrix, the reference spectrum is usually that of the pure diluent. The dilution matrix should be nonabsorbing so that k is related to the absorption of the sample alone. In this case, k is related to the absorptivity, a, and the concentration, c, by (*7*)

$$k = 2.303ac \quad (2)$$

In many applications of DR infrared spectrometry, the characteristics of the sample or the matrix do not follow the assumptions that were made in the derivation of the K-M equation. For example, the K-M equation was derived for weakly absorbing samples. Thus to achieve adherence to K-M behavior for mid-infrared DR spectrometry, samples must often be diluted in a nonabsorbing matrix, such as an alkali halide powder. There are certain applications, however, where the matrix has strong absorption bands in several spectral regions. In these spectral regions, the intensity of the absorption bands of minor components dispersed in the matrix does not usually follow the behavior predicted by the K-M equation. Components of a mixture separated by thin-layer chromatography (TLC) measured in situ (*8*, *9*) and species adsorbed on alumina or silica supported catalysts (*10*, *11*) fall into this category. The reduction in intensity of bands of separated components on silica TLC plates in the region of strong absorption by the silica adsorbent is readily apparent in the spectra reported by Zuber et al. (*9*).

Most organic compounds must be diluted in a nonabsorbing matrix (such as KCl) to avoid the effects of anomalous dispersion (*12*). We have noticed, however, that the DR spectra of coals prepared at various concentrations in a nonabsorbing powdered diluent behave in a quite different manner to the DR spectra of most organic compounds. For example, the spectra of coals of low mineral content are strikingly similar whether or not they are diluted in KCl (see Figure 1), and no evidence of anomalous dispersion may be seen in the DR spectrum of the neat coal. For coals of high mineral content, the absorption bands of minerals (especially clays) are greatly enhanced relative to those of the organic components when the sample is ground with a KCl diluent as opposed to being simply mixed; see Figure 2. The reason for this behavior was initially not readily apparent to us.

In this paper we report the results of several measurements that suggest reasons for behavior of the type described above for coals and species adsorbed on substrates such as silica. A strongly absorbing material, carbon black, was added to a transparent diluent, KCl, to simulate the effect of absorption by the matrix while minimizing the introduction of artifacts due to anomalous dispersion from intense discrete absorption bands in the matrix (as would been seen, for example, in the spectrum of silica). The behavior of absorption bands of organic analytes added to this matrix was then investigated quantitatively.

EXPERIMENTAL SECTION

Diffuse reflectance measurements were performed with a Model 296 interferometer (Digilab Division of Bio-Rad, Cambridge, MA) and the optical layout described by Fuller and Griffiths (*1*, *2*). All measurements were made with an intermediate range mercury cadmium telluride detector (Infrared Associates, New Brunswick, NJ). Interferograms were collected at 4 cm^{-1} resolution and were triangularly apodized. The amplifier gain was adjusted in each case so that the signal triggered the most significant bit of the analog-to-digital converter, and 1000 scans were signal averaged for each spectrum.

Potassium chloride (obtained as "random cuttings", Harshaw Chemical Co., Solon, OH) was ground for 5 min in a Wig-L-Bug ball and mill grinder (Crescent Manufacturing Co., Chicago, IL) and subsequently sieved to less than 100 μm diameter with a sonic sifter (ATM Corp., Milwaukee, WI) and stored in an oven at 120 °C. Carbon black was obtained from Bay Carbon Co. (Bay City, MI) and used as received. The average diameter of the carbon black particles estimated from electron micrographs was less than 10 μm and each particle appeared to be formed from an aggregate of several smaller particles. Coal samples were obtained from the Pennsylvania State University Coal Bank, and were ground for 5 min in a Wig-L-Bug. Carbazole (Eastman Kodak Co., Rochester, NY) was used as a typical organic analyte for most of the experiments reported here; it was ground in a Wig-L-Bug for 5 min and stored in a desiccator. Dilution matrices, which ranged from

0003-2700/86/0358-2179$01.50/0 © 1986 American Chemical Society

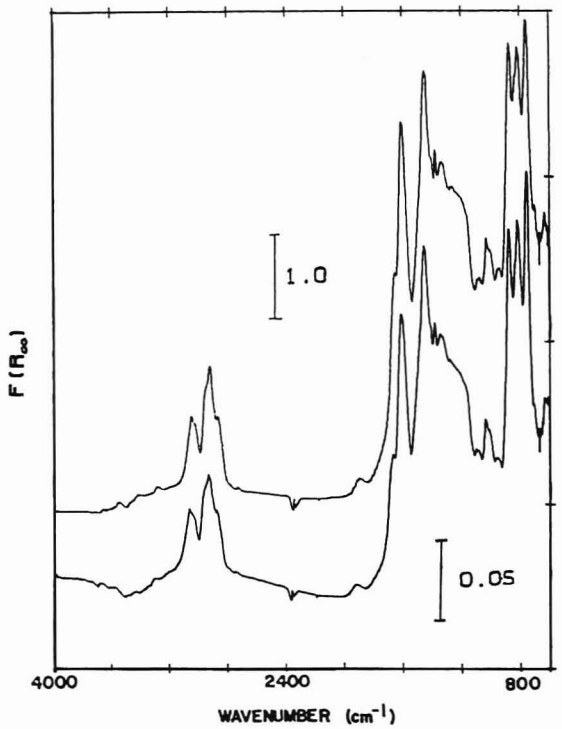

Figure 1. Kubelka–Munk spectra of a low volatile bituminous coal of low mineral content (PSOC 645, 4.32% mineral matter) measured neat (top) and as a 1% mixture (by weight) in KCl powder (bottom).

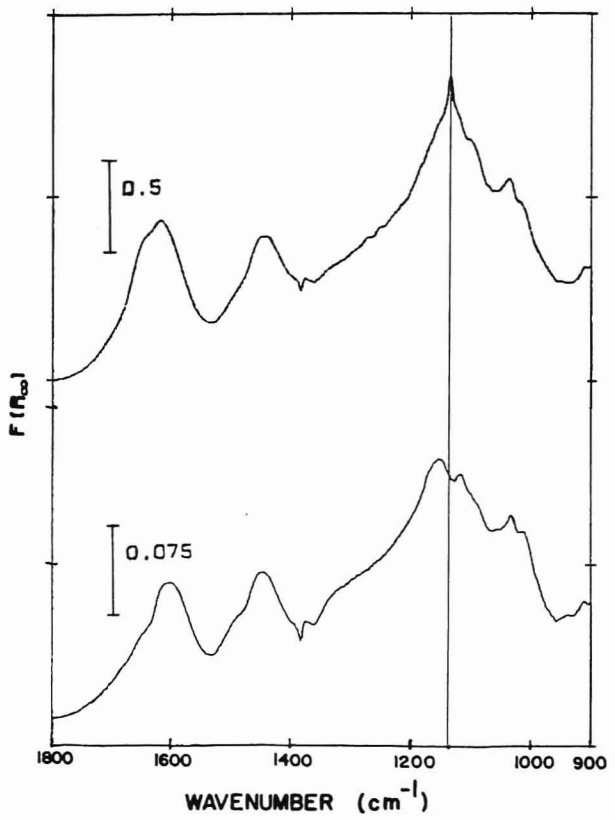

Figure 2. Kubelka–Munk spectra of a high volatile bituminous coal with high mineral content (PSOC 401, 13.13% mineral matter) prepared as a 1% mixture in KCl by simple mixing (bottom) and by grinding together (top).

"totally absorbing" (carbon black) to nonabsorbing (potassium chloride), were made by mixing carbon black and preground KCl in a Wig-L-Bug capsule with no ball bearings in the capsule to prevent further grinding. This method of mixing samples was found to be the most accurate and reproducible for quantitative DR measurements (*13*). Mixtures of carbazole in the prepared

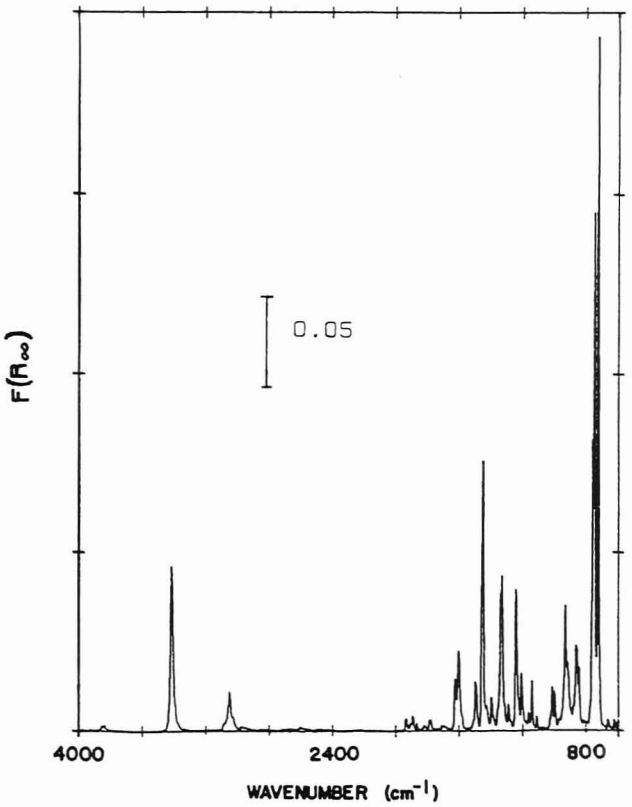

Figure 3. Kubelka–Munk spectrum of 1% carbazole (weight percent) in KCl powder.

matrices, and coal in KCl, were mixed in a similar fashion and stored in a desiccator prior to measurement of the DR spectrum.

Prepared samples were pressed into 4 mm diameter cups by using a modification of a Parr pellet press (A. H. Thomas, Philadelphia, PA). The amount of sample, as well as the amount and duration of applied pressure, was kept constant, since the manner in which the sample is packed can drastically affect the scattering coefficient in the K-M function (*14*). In our laboratory, band intensities of DR spectra of samples prepared in this manner have a relative standard deviation of approximately 3%.

The single beam spectrum of carbazole in the different dilution matrices was always ratioed to the single beam spectrum of the matrix in which the analyte was dispersed. The resulting reflectance spectrum sometimes exceeded 100%. This occurred when using highly absorbing matrices, where addition of carbazole causes an increase in the intensity of the reflected radiation. Therefore, before computing the K-M function, the single-beam spectrum of the reference was scaled so that the base line was just below 100% (at about 98% for the region in which the reflectance was greatest).

RESULTS AND DISCUSSION

When a nonabsorbing powder is used both as a diluent and as a reference for DR measurements, the calculated K-M spectrum appears similar to the absorbance spectrum of the compound dispersed in a KBr pellet. As an example, the K-M spectrum of 1% carbazole (weight percent) in KCl is shown in Figure 3. Quantitative analysis can be performed from plots of the intensity or area of an absorption band from K-M spectra of known concentrations of the compound. A typical K-M plot for a strongly absorbing band of an organic compound is shown in Figure 4, curve A, which shows the change in the intensity of the 3400-cm^{-1} band of carbazole with its weight percent in KCl. The intensity of this band increases linearly at low concentration and exhibits a strong deviation from linearity at higher concentrations. The deviation from linearity occurs in part because absorption by the analyte at high concentration causes the effective penetration depth at the analytical wavenumber to decrease (*13*) and in part because of the effect of anomalous dispersion. Both effects

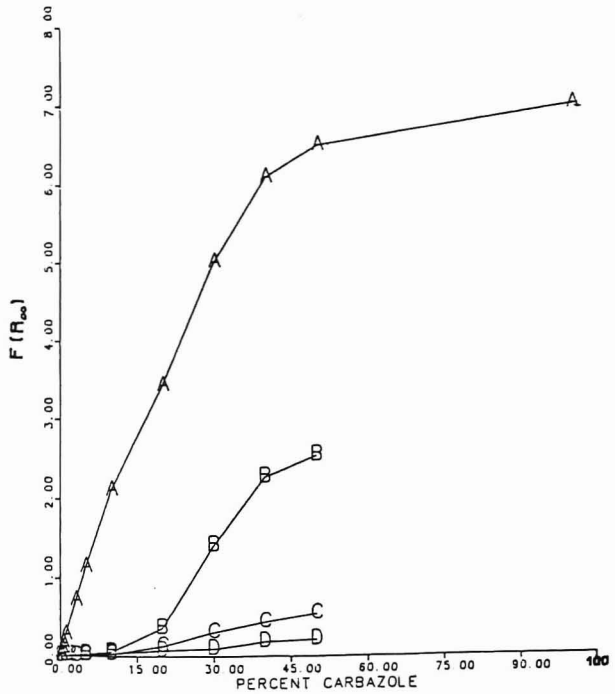

Figure 4. Plot of the change in intensity of the 3400-cm^{-1} band in the spectrum of carbazole with the weight percent carbazole in a dilution matrix of (A) KCl, (B) 99:1 KCl/carbon black, (C) 95:5 KCl/carbon black, (D) 90:10 KCl/carbon black.

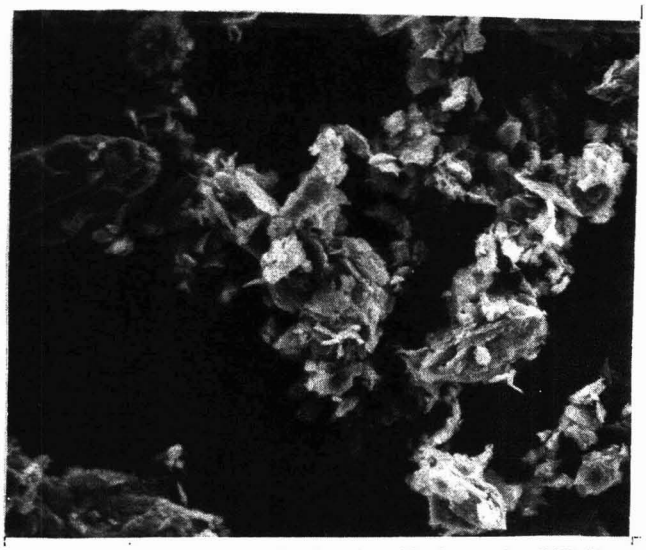

Figure 5. Electron micrograph of carbon black powder (×576).

operate in concert, causing the observed negative deviation from linearity.

The three remaining curves in Figure 4 are plots of the variation in the intensity of the 3400-cm^{-1} band of carbazole with concentration, for carbazole dispersed in dilution matrices composed of 99:1 KCl/carbon black (CB), 95:5 KCl/CB, and 90:10 KCl/CB, respectively. None of the curves for adsorbing matrices follows the behavior predicted by the K-M equation. For a given concentration of the carbazole analyte, the observed intensity of each band decreases as the absorption by the matrix increases (i.e., as the carbon black content increases). As the absorption by the matrix increases, the effective penetration depth decreases. This in turn causes a decrease in the number of analyte (carbazole) particles that can interact with the infrared radiation, with a resultant decrease in the band intensity.

It is also interesting that the shapes of the curves for analytes diluted in absorbing matrices are sigmoidal, which is quite different from the curves obtained for nonabsorbing

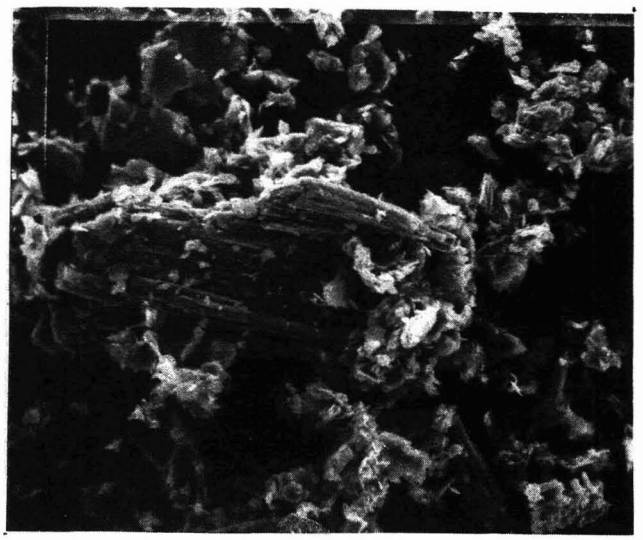

Figure 6. Electron micrograph of a matrix composed of 95:5 carbon black/KCl (×432).

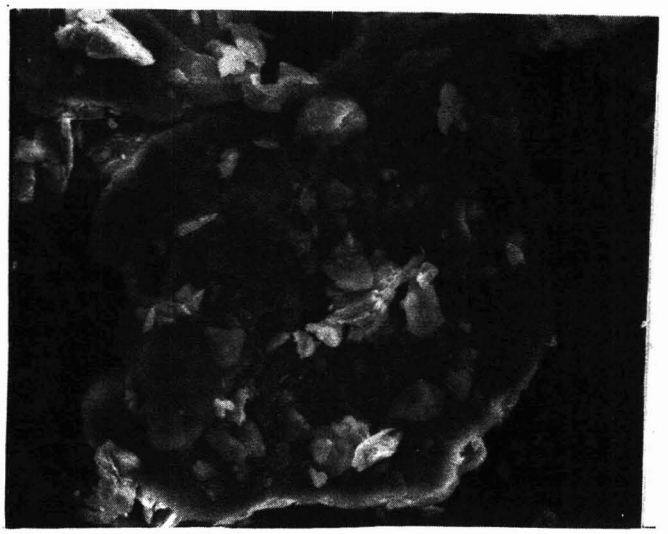

Figure 7. Electron micrograph of 50% carbazole mixed in a matrix composed of 95:5 carbon black/KCl (×576).

matrices. Our rationale for this behavior is that at low analyte concentrations, the surface of the sample is composed mostly of particles of the matrix, which consists of a large number of carbon black particles ($d < 10$ μm, see Figure 5) and a smaller number of larger KCl particles ($d < 100$ μm, see Figure 6). In Figure 6, the large KCl particle near the middle of the electron micrograph is shown to be surrounded by a number of smaller carbon black particles. For compacted samples, the smaller carbon black particles probably coat the larger KCl particles to a greater degree.

The particles of carbazole are much larger than carbon black particles, as can be seen in Figure 7. The large ($d \approx 100$ μm) carbazole particles are again coated with smaller carbon black particles, which strongly absorb infrared radiation and to a large degree prevent it from interacting with the carbazole analyte. This behavior results in greatly reduced intensities for the carbazole bands. Although a fraction of the infrared beam is undoubtedly transmitted through either a KCl or a carbazole particle, these particles are surrounded by carbon black particles. There is therefore a high probability of absorption of the photons which have been transmitted through a given carbazole particle by the particles of carbon black on its surface and a concomitantly low probability of the beam reemerging from the sample and being measured at the detector.

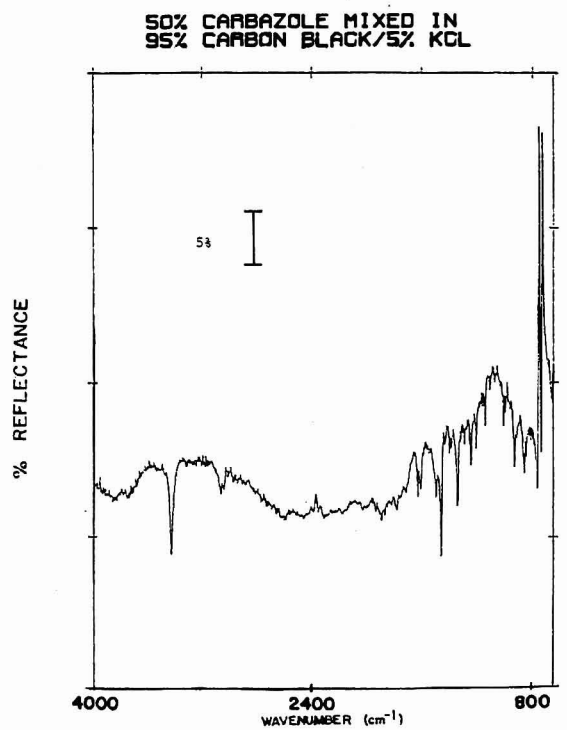

Figure 8. Reflectance spectrum of 50% carbazole mixed in a matrix composed of 95:5 carbon black/KCl.

At higher carbazole concentrations, a greater proportion of analyte is present in the uppermost layer of the sample independent of the nature of the matrix. More carbazole particles therefore interact with the incident infrared radiation, and fewer of the transmitted photons are absorbed by carbon black on the surface of the analyte. Thus more intense absorption bands result. At very high carbazole concentration, the K-M curves deviate toward a horizontal asymptote for the same reason discussed earlier for nonabsorbing matrices.

For high concentrations of the analyte, an unusual behavior is observed when the carbon black content exceeds 10% by weight. In this case reflectance maxima, or *reststrahlen* bands, are observed at intense absorption bands of the analyte. For example, in the DR spectrum of 50% carbazole in a matrix of 95:5 CB/KCl, the bands near 750 cm^{-1} appear as reflectance maxima; see Figure 8. *Reststrahlen* bands are observed for bands of very high absorptivity in the specular reflectance spectra of bulk samples. The reason for this behavior can be understood conceptually by using the simplest form of the Fresnel equations (namely for unpolarized incident radiation at normal incidence), which relates the front surface reflectance, R, to the index of refraction, n, and the index of absorption, κ of pure samples as

$$R = \frac{(n-1)^2 + n^2\kappa^2}{(n+1)^2 + n^2\kappa^2} \tag{3}$$

κ can be related to the absorptivity, a, by

$$a = \ln 10 \frac{4\pi n}{\lambda}\kappa \tag{4}$$

where λ is the wavelength. For bands of low absorptivity, Fresnel (front surface) reflectance is low, and reflection minima result in the DR spectrum of powdered samples as absorptivity maxima. For bands of very high absorptivity, the Fresnel reflectance is greater and reflectance maxima may be observed near absorptivity maxima. For bands of intermediate absorptivity a combination of absorption and front surface reflection gives rise to anomalous dispersion, which can be detected as a small shift of the band maxima to longer wavelength.

The intense doublet near 750 cm^{-1} in the spectrum of carbazole has a different appearance when measured neat than when measured after dilution in KCl. The 750-cm^{-1} bands are slightly shifted to lower wavenumber in the spectrum of the neat sample as anomalous dispersion begins to occur. This behavior is probably not a result of a change in the index of refraction of carbazole, but rather a change in the type of interface the infrared photons must encounter when impinging on a carbazole particle. For the neat sample, the interface is air–carbazole or carbazole–carbazole. For the sample diluted in KCl, the interface is KCl–carbazole. In this case the ratio of the refractive indexes is significantly less than for air–carbazole at all but the most intense carbazole absorption bands. Thus, for the neat sample there is a greater amount of Fresnel reflectance and there is usually indirect evidence of anomalous dispersion for bands of intermediate intensity.

A similar situation exists in the case of the reflectance maxima that occur when using highly absorbing matrices. For example, the surface of the sample discussed earlier (Figure 8), which was composed of 50% carbazole in the matrix of 95:5 CB/KCl, is largely composed of carbon black and carbazole particles. That fraction of the incident radiation that impinges on carbon black particles is totally absorbed. The radiation impinging on a carbazole particle is partially transmitted and partially reflected, according to the Fresnel equations. The radiation that is transmitted through the carbazole particle will be partially absorbed, giving rise to an absorption spectrum. On emerging from the particle, this transmitted radiation has a high probability of subsequently encountering a carbon black particle and being absorbed. Thus most of that fraction of the incident radiation that has been transmitted through an analyte particle, and therefore contains absorption information about the compound, never reaches the detector. Much of the radiation reflected from the surface of the carbazole particles, however, is collected and directed to the detector.

The effect of grinding the analyte and matrix together, as opposed to mixing, was examined by preparing the sample in a manner similar to that described above, except that during mixing of the carbazole in the matrix, two small ball bearings were included in the Wig-L-Bug capsule. The DR spectrum of the same sample discussed above (Figure 8) prepared by grinding in this manner is shown in Figure 9. In this case, the bands near 750 cm^{-1} appears as reflectance minima, with little evidence of anomalous dispersion. The electron micrograph of this sample, shown in Figure 10, indicates that the carbazole particles have been ground much smaller than when the components of the mixture are simply mixed. Thus the alkali halide appears to act as an abrasive during grinding. The sample is also quite possibly more intimately mixed, with particles composed of all of the components ground into each other. Thus, instead of having large particles of carbazole surrounded by smaller carbon black particles, we have an intimate mixture of smaller particles, with more carbazole accessible to the incident infrared radiation. The intensities of the other absorption bands in the spectrum of carbazole are increased as well, which is consistent with this interpretation, since the scattering coefficient, s, decreases when the mixture is ground.

In summary, the DR infrared spectra of samples prepared in absorbing matrices by two different methods appear vastly different. This was observed not only for carbazole but also for most other organic analytes. In all the cases studied, the softer analyte particles had a tendency to agglomerate into larger particles, which were decreased in size when ground in the presence of an abrasive matrix. By preparation of the

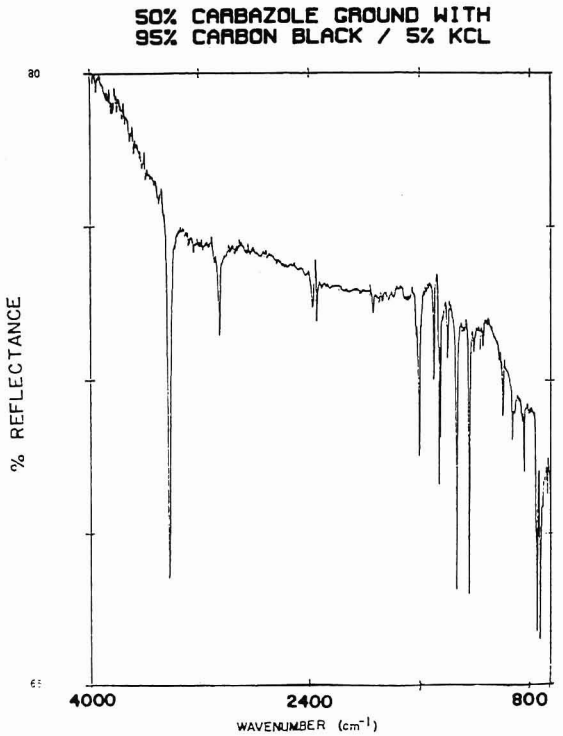

Figure 9. Reflectance spectrum of 50% carbazole ground with a matrix composed of 95:5 carbon black/KCl.

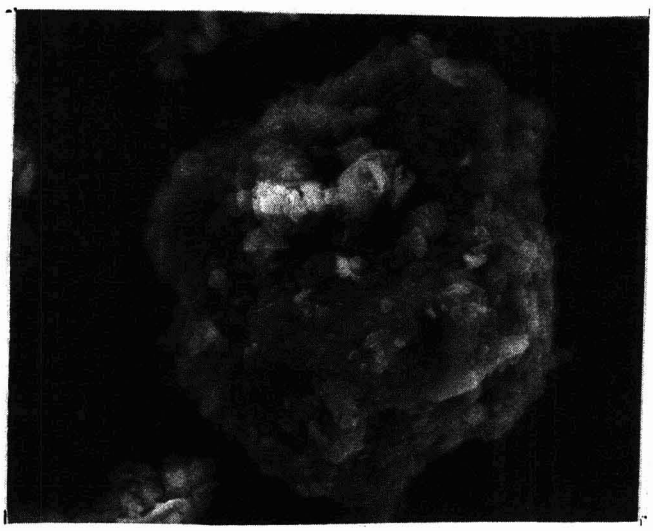

Figure 10. Electron micrograph of 50% carbazole ground with a matrix composed of 95:5 carbon black/KCl (×1440).

sample in this manner, the amount of Fresnel reflectance from the surface of particles was reduced, and the appearance of *reststrahlen* bands was eliminated.

With the knowledge gained in this study, we are in a position to offer explanations for the behavior of DR infrared spectra of material adsorbed on an infrared absorbing substrates and of coals. It can be deduced from Figure 4 that the effective penetration depth near regions of absorption by the matrix (e.g., alumina or silica) is much smaller than in the "window" regions where absorption due to the matrix is much weaker. This results in less intense absorption bands for the analyte than would be observed using a transmitting matrix. In addition, Fresnel reflectance from the substrate in the regions of absorptivity maxima is much greater than the "window" regions, so that less of the incident radiation penetrates into the adsorbent in the first place.

The behavior of DR infrared spectra of coal appears to be due to a very fine dispersion of carbon particles, or another material which has a very high absorptivity across the spectrum, within the organic matrix. The penetration of the infrared beam into the coal is therefore very small because of absorption by the carbon particles. In fact, Fuller has reported that the DR infrared spectrum of a bulk coal can be measured by creating a roughened layer on its upper surface no more than 10 μm in thickness (*15*). This suggests that the effective penetration depth of the infrared beam into a coal sample is not much greater than this. The effect of the strongly absorbing carbon particles is a reduction in band intensity well below the value that would have been measured if the organic molecules were dispersed in a transmitting matrix (see Figure 4).

If a coal is simply physically mixed in a nonabsorbing powder, such as KCl, the spectrum appears very similar to the spectrum of the neat coal, but of lower intensity, as shown in Figure 1. If the coal is ground together with KCl, several spectral differences result, which may be observed in Figure 2. After the coal is ground with KCl, all absorption bands in the spectrum are of greater intensity than if the coal were only mixed with the same quantity of the matrix. As in the case of carbazole in an absorbing matrix, this band intensification is the result of producing smaller products. As a result the scattering coefficient, s, in the K-M equation is decreased. Since a more intimate mixture also results, some of the organic molecules are released from the absorbing matrix and are made more accessible to the incident IR beam.

The absorption band at 1135 cm^{-1}, which is largely due to the mineral kaolinite present in the coal, is enhanced to an even greater degree by grinding with KCl. The absorptivity of this band is much greater than that of typical organic compounds, and therefore a greater amount of Fresnel reflectance would be expected near 1135 cm^{-1} (see eq 3). After the coal is ground with KCl, the amount of Fresnel reflectance from the surface of mineral particles is decreased. This behavior may be compared to the differences observed in the 750-cm^{-1} band of carbazole, which appear as *reststrahlen* bands when the analyte is simply mixed with an absorbing matrix and as absorption bands when it is ground with the absorbing matrix. With a decrease of the amount of Fresnel reflectance, the transmission through mineral particles increases, resulting in enhanced absorption bands. This enhancement, along with that gained by liberation from the carbon matrix during grinding with KCl, combines to increase the relative intensity of the mineral band at 1135 cm^{-1}.

CONCLUSIONS

This study has shown that a quantitative description of DR infrared spectra using absorbing matrices will be very difficult unless the samples are prepared in an exceptionally reproducible manner. Qualitative analysis of such systems can be performed, but great differences in the infrared spectrum can appear as a consequence of different methods of sample preparation. The differences that occur, specifically the appearance of anomalous dispersion or *reststrahlen* features, should not be confused with chemical changes in the compound of interest.

Registry No. KCl, 7447-40-7; carbazole, 86-74-8.

LITERATURE CITED

(1) Fuller, Michael, P.; Griffiths, Peter R. *Anal. Chem.* **1978**, *50*, 1906–1910.
(2) Fuller, Michael P.; Griffiths, Peter R. *Am. Lab. (Fairfield, Conn.)* **1978**, *10*(10), 69–82.
(3) Chalmers, J. M.; Mackenzie, M. W. *Appl. Spectrosc.* **1985**, *39*(4), 634–641.
(4) Griffiths, Peter R.; Fuller, Michael P. *Adv. Infrared Raman Spectrosc.* **1983**, *9*, 277.
(5) Kubelka, P.; Munk, F. *Z. Tech. Phys.* **1931**, *12*, 593–601.
(6) Kubelka, P. *J. Opt. Soc. Am.* **1948**, *38*, 448–457.
(7) Frei, Roland, W.; MacNeil, J. D. *Diffuse Reflectance Spectroscopy in Environmental Problem Solving*; CRC Press: Cleveland, OH, 1973.
(8) Fuller, Michael P.; Griffiths, Peter R. *Appl. Spectrosc.* **1980**, *34*, 533–539.

(9) Zuber, Gary E.; Warren, Richard J.; Begosh, Peter P.; O'Donnell, Ellen L. *Anal. Chem.* **1984**, *56*, 2935–2939.
(10) Hamadeh, Issam M.; King, Dewey; Griffiths, Peter R. *J. Catal.* **1984**, *88*, 264–272.
(11) Van Every, Kenneth W.; Griffiths, Peter R. *Proc. Soc. Photo-Opt. Instrum. Eng.* **1985**, *553*, 509.
(12) Brimmer, Paul J.; Griffiths, Peter R. *Appl. Spectrosc.*, in press.
(13) Hamadeh, Issam M.; Yeboah, Samuel A.; Trumbull, Kathy A.; Griffiths, Peter R. *Appl. Spectrosc.* **1984**, *38*(4), 486–491.
(14) Yeboah, S. Agyare; Wang, Shih-Hsien; Griffiths, Peter R. *Appl. Spectrosc.* **1984**, *38*(2), 259–264.
(15) Fuller, E. L. Martin Marietta Energy Systems, Inc., Oak Ridge, TN, personal communication, 1984.

RECEIVED for review February 4, 1986. Accepted April 28, 1986.

Continuous Recording of Reflection–Absorbance Fourier Transform Infrared Spectra of the Effluent of a Microbore Liquid Chromatograph

John J. Gagel and Klaus Biemann*

Department of Chemistry, Massachusetts Institute of Technology, Cambridge, Massachusetts 02139

A new method for the recording of the infrared spectra of components separated by high-performance liquid chromatography is demonstrated. In this scheme, chromatographic effluent is continuously sprayed onto a rotating disk that has a reflective surface. After deposition the solutes are analyzed by again rotating the disk in the sample compartment of a Fourier transform infrared spectrometer equipped with a beam condenser while reflectance–absorbance spectra are continuously collected. By this method, spectra that compare well with conventional KBr data over the entire mid-infrared region may be obtained at sensitivities in the hundred nanogram range for anthracene and lower for more strongly absorbing compounds. The continuous record of the chromatographic separation allows display of the data as Gram–Schmidt plots, spectra, or wavelength chromatograms, which all aid in the interpretation. Since this record is permanent, spectra may be enhanced by signal averaging many scans while the mirror is stopped at a position corresponding to the component of interest.

The high scan speed and sensitivity of Fourier transform infrared (FTIR) spectroscopy have made it possible to record infrared spectra of the individual components of mixtures separated by chromatographic techniques (*1–22*). To date this concept has been successful for gas chromatography coupled with FTIR (GC/FTIR) (*2–6*). However, many compounds of interest are not sufficiently volatile for GC separation and the sensitivity of the popular lightpipe method of GC/FTIR is reduced for less volatile compounds due to higher lightpipe temperatures (*4*, *5*). These less volatile and/or more polar compounds can usually be separated by high-performance liquid chromatography (HPLC). The interfacing of an HPLC with FTIR is, however, more difficult because the infrared absorption of the mobile phase must be compensated for by spectral subtraction or eliminated before infrared analysis in order to obtain useful data for a solute present in low concentrations. To achieve this end, two general types of systems have been developed: (1) flow cells, which allow the recording of spectra while HPLC effluent passes by a window transparent in the infrared region (*7–11*), and (2) solvent deposition systems, which involve transfer and elimination of the solvent on a medium compatible with infrared spectroscopy (*12–18*).

The flow cell approach represents the simplest method for obtaining infrared data. Furthermore, it makes the spectrometer a true chromatographic detector by allowing continuous analysis of the chromatographic effluent. Although several applications have been reported (*9*, *10*), the usefulness of the technique is limited because the spectral regimes where the solvent absorbs radiation are opaque result in loss of information or require such short path lengths that sensitivity is drastically decreased.

A more recent innovation in the flow cell type design involves flowing the chromatographic effluent along the outside of an attenuated total reflectance cell (ATR) (*11*). Because of the short path lengths inherent to ATR, even the highly absorbing aqueous solvents may be used with this technique. For the same reason, however, the sensitivity is decreased and the spectra of milligram injections were reported (*11*).

Solvent deposition designs have utilized diffuse reflectance Fourier transform infrared spectroscopy (DR-FTIR) and transmittance spectroscopy. The DR-FTIR interface, pioneered by Kuehl and Griffiths (*12*), involves the depositing of concentrated portions of HPLC effluent into a series of diffuse reflectance cups filled with KBr powder. After the solvent is evaporated, the cup is brought into the beam path of the spectrometer and the diffuse reflectance spectrum is recorded. Although this system has demonstrated good sensitivity, especially with the use of microbore HPLC columns (*13*), it does not allow a continuous analysis of the chromatographic effluent. This is a considerable disadvantage because a component can be missed or more than one component may collect in a single cup. Furthermore, continuous recording of spectra has many advantages in the interpretation of the spectral data such as Gram–Schmidt reconstructions (*19*), wavelength chromatograms, or the plotting of successive spectra to identify closely eluting compounds. Continuous collection with a DR-FTIR interface has been accomplished recently using supercritical fluid chromatography (SFC) (*16*). In these experiments the deposition of the sample onto a strip of KBr powder was facilitated by the easy elimination of the mobile phase (CO_2), which is a gas at atmospheric pressure. However, according to the authors, the same principle appears not to be applicable to conventional HPLC using liquid phases.

A solvent deposition device introduced by Jinno et al. (*17*, *18*) utilizes transmission spectroscopy. In this system, the effluent from a microbore HPLC flows directly onto a moving, rectangular KBr crystal. After evaporation of the solvent, the

0003-2700/86/0358-2184$01.50/0 © 1986 American Chemical Society

crystal is then passed across the spectrometer beam and spectra are collected, thus providing a continuous spectral record of the chromatographic experiment.

The extension of both flow cell (*8*) and DR-FTIR (*14*, *15*) interfaces to reverse-phase chromatography employing aqueous solvents has been reported. To accomplish this, both designs required a solvent change before analysis. For flow cells, an on-line extraction of the solute from aqueous to infrared compatible solvents was employed similar to that originally used in extension of the moving belt HPLC–mass spectrometry interface (LC/MS) (*20*). Unfortunately, the sensitivity of the technique was reduced by at least an order of magnitude (*8*). Water must also be removed for any method employing KBr as the deposition medium. The DR-FTIR interface has been used with a similar solvent extraction apparatus (*14*) or, alternatively, water was removed by reaction with 2,2-dimethoxypropane to produce acetone and methanol (*15*).

Other designs for HPLC/FTIR have been suggested, including a reflectance–absorbance (R–A) device that flows solvent through a lightpipe (*21*) and an ambient temperature emission device (*22*). Griffiths suggested a R–A device designed similarly to a moving belt interface used in LC/MS but because of excessive solvent spreading on the deposition surface, this approach was abandoned in favor of the DR-FTIR interface (*12*).

We have therefore undertaken the design of a different interface between HPLC and the FTIR spectrometer. The main objectives are the capability of continuous recording of infrared spectra, high sensitivity, and independence of the nature of the solvent or solvent mixture used as the mobile phase, including the aqueous phases used in reverse-phase HPLC. The principle involves continuous deposition of the effluent on a rotating reflective surface which is suitable for R–A spectroscopy and inert to all commonly used solvents. Instead of real-time spectral collection—while in principle possible—the FTIR spectra are measured off-line by again rotating the reflective collection medium in the sample compartment of an FTIR while R–A spectra are continuously collected. This paper describes the design of the device and the results of preliminary experiments demonstrating the principle with normal-phase solvents.

EXPERIMENTAL SECTION

Chromatography. A Perkin-Elmer (Norwalk, CT) series 4 HPLC capable of flow rates as low as 10 μL/min was used for these experiments. The system is equipped with a Rheodyne Model 7125 injector and a 6-μL sample loop. Since chromatographic peak widths are dependent on the injection volume, an effort was made to sharpen peaks and enhance solute concentrations by first filling the loop with solvent and then injecting a small sample volume (1–1.2 μL). A Perkin-Elmer Model LC-85B variable wavelength detector was used with a 1.4-μL volume, 6 mm path length flow cell. All separations were performed on an Alltech (Alltech Associates, Deerfield, IL) 1 mm internal diameter (i.d.), 50 cm long microbore HPLC column with 10-μm silica packing. Hexane and dichloromethane were used in the mobile phase and preparation of standard mixtures were "distilled in glass" grade purchased from Caledon (Georgetown, Ontario, Canada). Methanol used in the mobile phase was ChromAR HPLC grade from Mallinckrodt (Paris, KY).

Spectroscopy. Infrared data were obtained with a Digilab (Digilab Division of Bio-Rad Inc., Cambridge, MA) Model 15/90E FTIR. The spectrometer was equipped with a liquid nitrogen cooled wide band mercury/cadmium/telluride (MCT) detector and the interferometer operated at a moving mirror speed of 1.2 cm/s. Continuously collected data were obtained with software intended for GC/FTIR which was set to coadd eight scans at 8-cm^{-1} resolution before transforming to form a scan set. This provided a time resolution of 1.5 s. Gram–Schmidt chromatograms were calculated by using reference vectors from a blank spot on the reflective surface or by reconstructing the data using reference vectors from within the run. The selection of coaddition regions for spectra of components from chromatographic runs was accomplished by using the automatic peak finding software available with the GC/FTIR software package. Wavelength chromatograms are created by Digilab supplied software which monitors absorbance at a user-specified frequency throughout the chromatogram or any portion thereof. For R–A spectra, which showed excessive base line sloping or curvature due to scattering from the sample, a piecewise linear tracing of the base line was generated using Digilab supplied software. Subtraction from the raw spectrum produces a flatter base line and facilitates peak intensity comparison with standard spectra. The spectra in Figures 6–8 and Figure 10 have also been background subtracted. These treatments may shift the base line and make it difficult to assign an absolute absorbance scale. However, the signal to noise ratio is a good measure of the spectral quality and sensitivity.

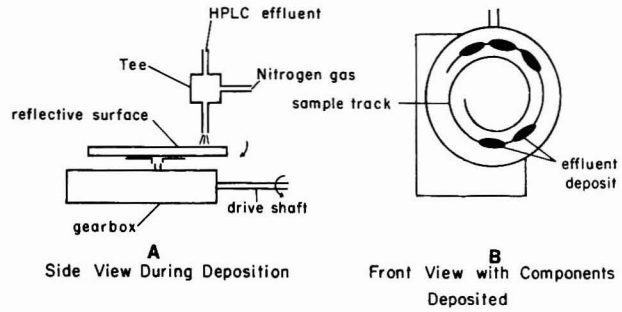

Figure 1. Diagrams of the continuous collection device: (A) deposition of HPLC effluent and (B) view of deposited components.

Standard spectra in KBr pellets were produced by thoroughly grinding small amounts of the compound (about 1% sample) in KBr and pressing a pellet with a 2-bolt Mini Press (Foxboro Co., South Norwalk, CT).

Continuous Collection/Detection Device. The device consists of a right angle gearbox, a 1 mm thick, 60 mm diameter circular front surface aluminum mirror (Edmund Scientific, Barrington, NJ), and a mirror attachment assembly (Figure 1). The gearbox, machined from block aluminum, is 7.5 cm high by 4 cm wide by 1.5 cm thick and bored to provide space for right angle gears to meet 4 cm from its base. A vertical shaft $^1/_8$ in. outer diameter (o.d.) extends 12 cm above the box and a horizontal shaft ($^1/_8$ in. o.d.) extends 0.5 cm beyond the box. The mirror attachment assembly is a 4 cm diameter aluminum piece with three raised pods on one side to which the glass face of the mirror is cemented and a drilled protrusion which fits over the horizontal shaft of the gearbox on the opposite side to the mirror. The protrusion has a tapped hole perpendicular to the shaft opening that allows the assembly to be secured to the shaft by means of a setscrew. The HPLC effluent is sprayed onto the mirror surface which is rotated by a stepper motor (HSI, Waterbury, CT) capable of 2000 steps per revolution (Figure 1). For a typical sample track with a radius of 2.5 cm, each step corresponds to 0.08 mm.

Chromatographic effluent is sprayed onto the mirror with a nebulizer fashioned from an HPLC mixing tee designed for use with SSI high-pressure fittings (Alltech Association, Deerfield, IL) that has an internal volume of 0.62 μL. HPLC effluent is brought from the UV detector by a short length of (0.004 in. i.d., $^1/_{16}$ in. o.d.) stainless steel tubing to one of the tee ports where it is mixed with and pressurized by nitrogen gas which is introduced from a short length of the same tubing attached to another tee port. Thus nebulized, the effluent is then directed to the reflective surface through a syringe tip fitted to the third tee port and emerges as a fine spray. Fitting the syringe tip to the tee port was accomplished by forcing Teflon tubing over the tip to give the proper external diameter and make a gas-tight, liquid-tight seal. A gentle stream of nitrogen may be passed over the nebulized solvent after contacting the mirror to rapidly evaporate any remaining solvent. The tip of the syringe was held about 3 mm above the mirror surface and resulted in a 1–2 mm wide solute deposit track.

After deposition of the chromatographic effluent, the device is fastened to a Barnes Model 126 reflectance accessory (Barnes Analytical Division, Spectra Tech, Inc., Stamford, CT) with 3× beam condensing optics which has been modified by removal of

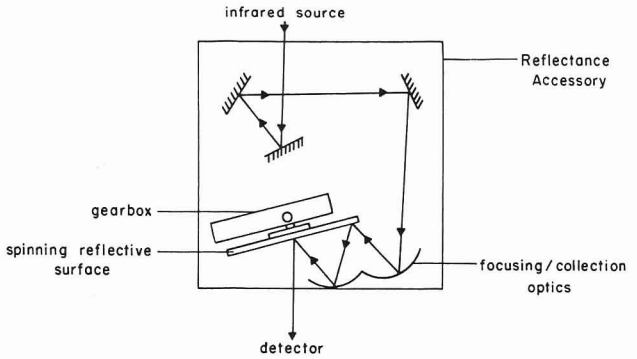

Figure 2. Top view of device with reflectance accessory in the sample compartment of an FTIR with ray diagram of infrared radiation.

the sample holder and the final directive plane mirror before the detector. The gearbox and the circular mirror have been designed to take the place of these components by focusing the beam onto the sample near the edge of the circular mirror for analysis of deposits, and after collection of the R-A radiation, the beam is directed to the center of the circular mirror which reflects it on to the detector (Figure 2). In these preliminary experiments, the gearbox was held to the floor of the reflective accessory by means of a C-clamp. Future generations could easily make this device self-aligning by utilizing alignment pegs protruding from the accessory floor and drilling corresponding holes into the base of the gearbox.

The 3× beam condensing optics with 20° incident angle provided about a 2 mm spot size with the spectrometer source aperture set to 6 mm. Under these conditions, the throughput of the reflectance unit with the device installed was just below the maximum dynamic range of the 15 bit analog to digital converter. When the unit is in the sample compartment, the vertical shaft of the gearbox extends about 5 cm above the spectrometer bonnet at which point a 1/30 rmp dc motor is fastened by means of a shaft coupler. In the recording mode the mirror is rotated once again by a motor drive and spectral data are continuously obtained by using the GC/FTIR software (Figure 2).

Test Mixtures. A mixture of 0.46 μg/μL anthracene (Chem Service, West Chester, PA), 0.64 μg/μL *N*-ethylcarbazole (Aldrich Chemical, Milwaukee, WI), 0.18 μg/μL 9-nitroanthracene (Aldrich Chemical), 0.42 μg/μL 1-nitropyrene (ICN Pharmaceuticals, Plainview, NY), and 0.16 μg/μL carbazole (Chem Service) was prepared in methylene chloride. About 1.2 μL with a 10-μL syringe was injected for the separation experiment discussed below. For the sensitivity experiment (Figure 5), a standard solution of anthracene in methylene chloride was prepared at a concentration of 1.00 μg/μL and diluted to produce solutions of 0.5 μg/μL, 0.25 μg/μL, 0.125 μg/μL, and 0.068 μg/μL. A 1-μL volume of each dilution was injected at 3-min intervals.

RESULTS AND DISCUSSION

The objective of these experiments was to determine whether a device of the design described could provide useful spectra in a continuous collection/detection mode. In Figure 3 the separation of a synthetic five-component mixture of polycyclic aromatic compounds (PAC) is shown using a UV detector placed before the nebulizer. The corresponding Gram–Schmidt chromatogram is shown in Figure 4. These data clearly demonstrate that this deposition method is capable of continuous collection and detection and that the resolution of the chromatographic separation is maintained. In this experiment, the effluent was collected at about 5 mm from the edge of the rotating mirror at a deposition speed of 4 mm/min. Under these conditions, a 40-min chromatogram could be collected in a single track. The high signal to noise ratio of the Gram–Schmidt chromatogram indicates that the limit of detection by this method is considerably below the amounts injected. To gauge the sensitivity of the device, decreasing sample weights of anthracene were successively injected and deposited and the resulting wavelength chromatograms are plotted in Figure 5. These data indicate that detection of spectral peaks of this compound is possible below 125 ng but no spectrum was obtained from the injection of 68 ng. This is a severe test because anthracene is a poor absorber and is also relatively volatile. For small samples of volatile compounds, loss by sublimation from the deposition surface would adversely effect the sensitivity of the method (*13*). However, these compounds are therefore sufficiently volatile to be analyzed by GC/FTIR.

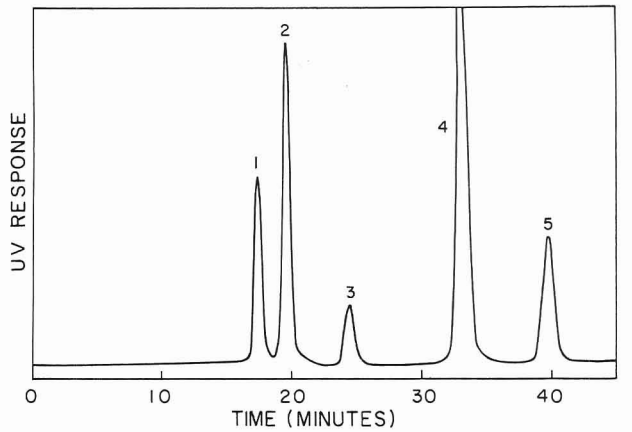

Figure 3. Microbore HPLC separation of a five-component mixture using 75:25 hexane–dichloromethane as the mobile phase at 30 μL/min and UV absorbance detection at 315 nm: (1) anthracene, (2) *N*-ethylcarbazole, (3) 9-nitroanthracene, (4) 1-nitropyrene, and (5) carbazole.

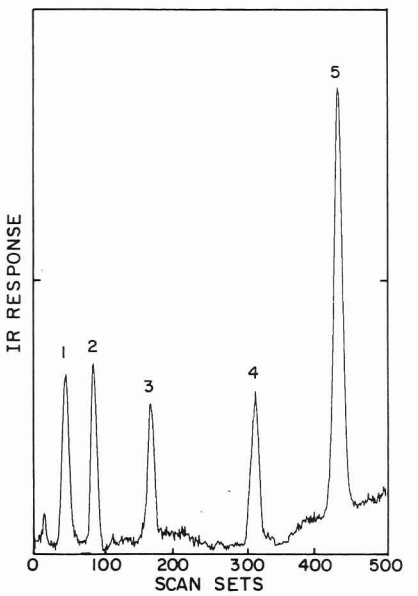

Figure 4. Gram–Schmidt infrared chromatogram of the five-component mixture in Figure 2 produced after deposition onto the reflective surface. The identities and the weight of each compound injected are as follows: (1) anthracene, 550 ng; (2) *N*-ethylcarbazole, 770 ng; (3) 9-nitroanthracene, 220 ng; (4) 1-nitropyrene, 500 ng; (5) carbazole, 190 ng.

Figures 6–8 compare the spectra of three of the compounds obtained with the device to the spectra of standards taken by conventional transmission spectroscopy in a KBr pellet. The R–A spectra show some base line fluctuations due to Christiansen scattering (*23*), which is often characterized by a sudden rise on one side of an aborption band and a tailing on the other side. This effect is dependent on the particle size and the refractive index changes of the sample in the neighborhood of an absorption band and is particularly evident in the aromatic C–H stretching region of the anthracene spectrum (Figure 6). Some variations in the relative intensity of bands may also be noted between the two methods of

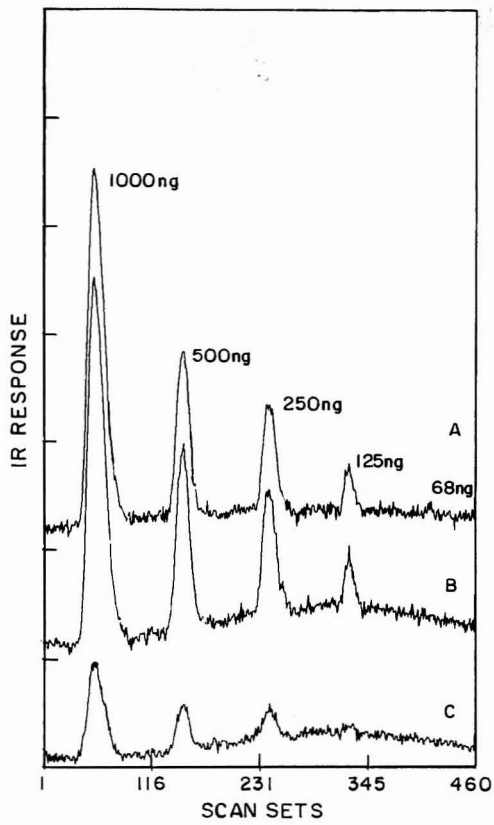

Figure 5. Wavelength chromatograms of successive injections of anthracene at reduced sample weights. The compound was eluted with 98% dichloromethane and 2% methanol at 30 μL/min. Deposition speed was about 6 mm/min. The chromatograms represent absorbance at (A) 879 cm^{-1}, (B) 721 cm^{-1}, and (C) 956 cm^{-1}. Weights shown are amount injected.

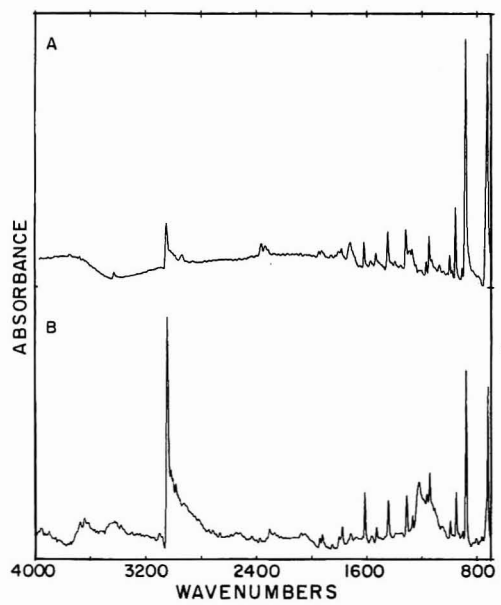

Figure 6. Infrared spectra of anthracene: (A) transmission spectrum taken in a KBr pellet and (B) continuously collected R–A spectrum from peak 1 in Figure 4.

infrared analysis. Despite these characteristics, the R–A spectra compare well qualitatively with those recorded in the conventional way in KBr and cover the entire mid-infrared range which could be used for compound identification. Furthermore, the high signal to noise ratio of the spectra of the deposited samples indicates that the identification limits should be below the amounts injected in this experiment. Even for poor absorbers such as anthracene, identifiable spectra of 125 ng have been obtained after deposition. These

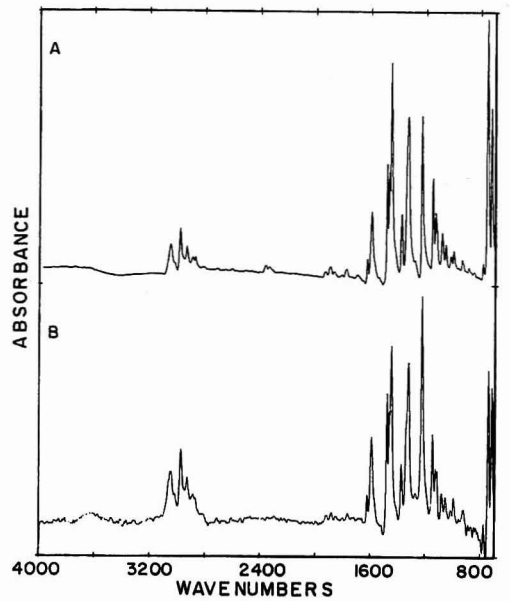

Figure 7. Infrared spectra of *N*-ethylcarbazole: (A) transmission spectrum taken in a KBr pellet and (B) continuously collected R–A spectrum from peak 2 in Figure 4.

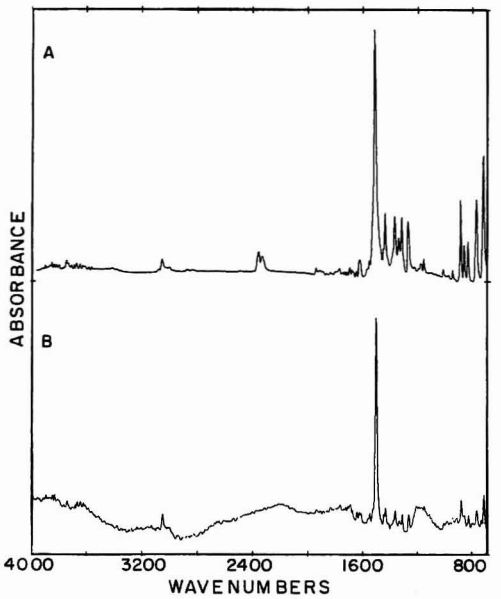

Figure 8. Infrared spectrum of 9-nitroanthracene: (A) transmission spectrum taken in a KBr pellet and (B) continuously collected R–A spectrum from peak 3 in Figure 4.

data should be compared to the sensitivity of previous designs with microbore HPLC. Using the noncontinuous DR-FTIR interface, Griffiths obtained a good spectrum of 10 ng of the much stronger absorbing 4-chloronitrobenzene (*13*), while Taylor et al. reported spectra of several hydroxy- or methoxy-substituted compounds in the 5-μg range using a flow cell (*7*). Extrapolated detection limits for the flow cell, defined by the visibility of the hydroxy stretching bond of 2,6-di-*tert*-butylphenol were found to be about 50 ng (*7*). Using the peak heights of infrared chromatograms, Jinno calculated the detection limit of the transmission device to around 100 ng (*18*). In Figure 5 we have shown values as good as these for the weakly absorbing anthracene. For more nonvolatile compounds that exhibit prominent peaks in their infrared spectra, even lower detection limit values would be expected. In fact, by comparison of the peak heights of anthracene to carbazole in Figure 4, the detection limit for carbazole should be about 7 times lower than for anthracene. Although the monitoring of a single band, especially in the form of a

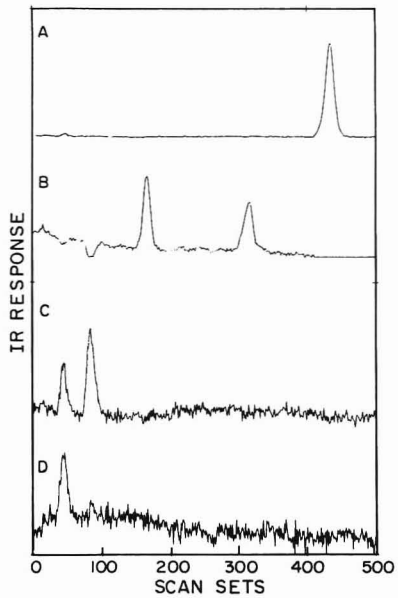

Figure 9. Wavelength chromatogram analysis of five-component separation: (A) N–H stretching frequency at 3417 (cm^{-1}, (B) N=O stretching frequency at 1510 cm^{-1}, (C) aliphatic C—H stretching frequency at 2974 cm^{-1}, and (D) aromatic out-of-plane bending frequency at 956 cm^{-1}.

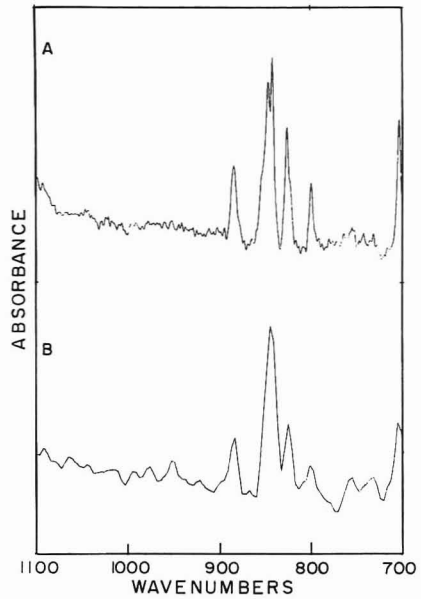

Figure 10. R–A spectra of the fingerprint region of 1-nitropyrene: (A) disk stopped with 512 scans coadded at 2-cm^{-1} resolution and (B) continuously collected spectrum with 56 scans coadded at 8-cm^{-1} resolution while the disk rotates at 4 mm/min.

wavelength chromatogram, provides important information, we believe using it to determine detection limits may be misleading. Components detected in this manner may not yield spectra containing enough information to allow identification of the compound (*6*). The sensitivity of the method presented here would be increased by depositing the material over the smallest possible surface area and the ability to focus the beam onto this small area. Determination of the ultimate sensitivity limits therefore will require further experimentation in deposition methods and improved beam condensing power in the reflectance accessory.

The ability to analyze the chromatographic run in a continuous fashion allows the use of the Gram–Schmidt reconstruction to indicate the presence of a deposited component as shown and the use of wavelength chromatograms to further interrogate the data for the presence of certain important absorption bands. The Figure 9, the wavelength chromatograms for several characteristic frequencies are plotted, simplifying the original chromatogram. The wavelength chromatogram in Figure 9c is characteristic of an aliphatic C–H stretching frequency and the major peak is due to *N*-ethylcarbazole. The presence of a peak where anthracene elutes is due to the strong absorbance of the aromatic C–H stretching band which, due to the Christiansen effect, trails into the aliphatic region.

An important advantage of FTIR over conventional grating instruments is the ability to enhance spectral data by signal averaging many scans. The design of this device provides a record of the chromatographic separation that may be analyzed noncontinuously and may thus take advantage of these signal averaging capabilities. In Figure 10, the aromatic C–H out-of-plane bending region for 1-nitropyrene is shown for the continuously collected spectrum at a resolution of 8 cm^{-1} with 56 scans coadded (Figure 10b) and, for the same compound with the mirror stopped at a resolution of 2 cm^{-1} with 512 scans coadded (Figure 10a). The improved spectral quality of the latter is evident. For continuous collection, as in GC/FTIR experiments, lower resolution spectra are collected to increase time resolution and to save computer storage space. For noncontinuous analysis of selected components there are no such concerns. Enhancement of minor separated components also could be accomplished in this way.

This design has other inherent advantages. During the collection step, the mirror speed may be reduced to enhance sensitivity by concentrating more material in a smaller track area or enhance the infrared chromatographic resolution by using a faster speed. With a computer-controlled motor drive, the rotation of the mirror could be programmed to vary the speed during the chromatographic run to maximize the resolution.

The circular shape of the deposition surface allows modification of the operating mode by concurrent rotation and translation of the mirror. This would generate a spiral deposition track to accommodate more and/or longer chromatographic runs. A nondestructive collection of the chromatographic effluent also allows further analysis by other methods (*18*).

Although this device could be developed for use on line with the deposition step carried on inside the spectrometer, in the authors' opinion this serves no advantage and, in fact, would complicate the experiment with provisions required to extract solvent vapors. The time saved in the on-line experiment is small compared to the time required for sample preparations and analysis of the infrared data.

Preliminary experiments indicate that extension of this device to reverse-phase HPLC by direct deposition of aqueous solvent mixtures is possible with greater provision for eliminating this less volatile mobile phase. This result represents an improvement over the transmission device of Jinno which, although capable of providing a continuous chromatographic record, precludes the direct deposition of aqueous solvents because it employs KBr as the deposition medium. Improvements of the critical deposition and solvent elimination steps for reverse phase are in progress. Extension of this device to SFC should be equally possible.

ACKNOWLEDGMENT

The authors thank Arthur Lafleur of the MIT Energy Laboratory Chemical Analysis Facility for the use of the HPLC and K. Krishnan of the Digilab Division of Bio-Rad for the loan of the reflectance accessory used in these experiments.

LITERATURE CITED

(1) Zuber, G. E.; Warren, R. J.; Begosh, P. P.; O'Donnell, E. L. *Anal. Chem.* **1984**, *56*, 2935.

(2) Griffiths, P. R.; de Haseth, J. A.; Azarraga, L. V. *Anal. Chem.* **1983**, *55*, 1361A.
(3) Bourne, S.; Reedy, G.; Coffey, P.; Mattson, D. *Am. Lab.* (*Fairfield Conn.*) **1984**, June.
(4) Gurka, D. F.; Hiatt, M.; Titus, R. *Anal. Chem.* **1984**, *56*, 1102.
(5) Brown, R. S.; Cooper, J. R.; Wilkins, C. L. *Anal. Chem.* **1985**, *57*, 2275.
(6) Cooper, J. R.; Taylor, L. T. *Anal. Chem.* **1984**, *56*, 1989.
(7) Johnson, C. C.; Taylor, L. T. *Anal. Chem.* **1984**, *56*, 2642.
(8) Johnson, C. C.; Hellgeth, J. W.; Taylor, L. T. *Anal. Chem.* **1985**, *57*, 610.
(9) Brown, R. S.; Taylor, L. T. *Anal. Chem.* **1981**, *53*, 197.
(10) Brown, R. S.; Taylor, L. T. *Anal. Chem.* **1983**, *55*, 723.
(11) Sabo, M.; Gross, J.; Wang, J. S.; Rosenberg, I. E. *Anal. Chem.* **1985**, *57*, 1822.
(12) Kuehl, D.; Griffiths, P. R. *J. Chromatogr. Sci.* **1979**, *17*, 471.
(13) Conroy, C. M.; Griffiths, P. R.; Jinno, K. *Anal. Chem.* **1985**, *57*, 822.
(14) Conroy, C. M.; Griffiths, P. R.; Duff, P. J.; Azarraga, L. V. *Anal. Chem.* **1984**, *56*, 2636.
(15) Kalasinsky, K. S.; Smith, J. A. S.; Kalasinsky, V. F. *Anal. Chem.* **1985**, *57*, 1969.
(16) Shafer, K. H.; Pentoney, S. L., Jr.; Griffiths, P. R. *Anal. Chem.* **1986**, *58*, 58.
(17) Jinno, K.; Fujimoto, C.; Hirata, Y. *Appl. Spectrosc.* **1982**, *36*, 67.
(18) Fujimoto, C.; Jinno, K.; Hirata, Y. *J. Chromtogr.* **1983**, *258*, 81.
(19) Hanna, D. A.; Hangac, G.; Hohne, B. A.; Small, W. G.; Wieboldt, R. C.; Isenhour, T. L. *J. Chromatogr. Sci.* **1979**, *17*, 423.
(20) Karger, B. L.; Kirby, D. P.; Vouros, P.; Foltz, R. L.; Hidy, B. *Anal. Chem.* **1979**, *51*, 2324.
(21) Castles, M. A.; Azarraga, L. V.; Carreira, L. A. Presented at the Pittsburgh Conference, Atlantic City, NJ, March 1984; paper 655.
(22) Azarraga, L. V.; Castles, M. A.; Brackett, J. M.; Rogers, L. B. Presented at the Pittsburgh Conference, Atlantic City, NJ, March 1984; paper 656.
(23) De Faubert Maunder, M. J. *Practical Hints on Infrared Spectrometry*; Adam Hilger: London, 1971; p 147.

RECEIVED for review February 18, 1986. Accepted May 12, 1986. The work reported here was supported by Grants from the National Institutes of Health (ESO-1640 and ESO-2109).

Rapid Nontarget Screening of Environmental Extracts by Directly Linked Gas Chromatography/Fourier Transform Infrared/Mass Spectrometry

Donald F. Gurka*

U.S. Environmental Protection Agency, Office of Research and Development, Environmental Monitoring Systems Laboratory, Las Vegas, Nevada 89114

Richard Titus

Chemistry Department, University of Nevada at Las Vegas, Las Vegas, Nevada 89109

A directly linked gas chromatography/Fourier transform infrared/mass spectrometry (GC/FT-IR/MS) system was constructed and evaluated for its capability to provide *rapid*, on-line identification and compound class confirmations. The validity of the forward on-line library search results for each detector was evaluated with 50 organic standards. From the standard solution experience, forward search criteria were proposed for *rapid* GC/FT-IR/MS identification and compound class screening. Six complex environmental extracts were analyzed with this system leading to 20 confirmed identifications and 24 confirmed compound class assignments. Since 106 analytes were jointly detected, this meant that 41% of the joint detections resulted in confirmed structural information. As *independent* detectors, each provided approximately the same amount of *tentative* structural information.

Currently the U.S. Environmental Protection Agency (EPA) screens the gas chromatographicable portion of sample extracts for a few hundred target organic compounds (*1*, *2*). Since over 6×10^4 manufactured chemicals are currently regulated under the Toxic Substance Control Act (TSCA) and thus may be found in the environment, and since the major portion of sample extract contaminants are not expected to be sufficiently volatile (*3*) to pass through a gas chromatograph (GC), this target compound approach clearly wastes most of the chemical information contained in such extracts. This is particularly disturbing since much of the total sample costs (in-the-field sampling, chain of custody, laboratory subaliquoting, and sample workup) have already been expended. The target compound approach is designed to minimize false positives in regulatory situations and results in part from the general perception that there is a lack of sufficiently sensitive and selective detectors, other than mass spectrometers, for application to environmental organic analytical situations.

The situation is further complicated by the necessity for confirmed environmental identifications (*4–7*), which has led to the current EPA GC retention time approach to confirming MS identifications. This confirmation approach presumes the availability of suitable pure organic standards and their GC resolution, a situation not always obtainable, especially for isomeric compounds. For example, the 22 isomeric tetrachlorodibenzodioxins cannot be resolved on a single GC column (*8*, *9*). In addition the utilization of GC retention time standards for confirmation would be extremely awkward and expensive for a target compound approach encompassing more than a few hundred compounds.

The recent availability of hyphenated techniques (see ref 10 for a recent review) allows the construction of linked detector systems providing an increased amount of on-line chemical information. A directly linked gas chromatography/Fourier transform infrared/mass spectrometry (GC/FT-IR/MS) system has been reported by several laboratories (*11–13*) and although one of these laboratories (*11*) has reported several multicomponent sample analyses, no environmental analyses have to date been reported for such a direct-linked system. However, Gurka et al. (*14*, *15*) and Shafer et al. (*16*) have reported the usefulness of independent GC/MS and GC/FT-IR analyses on hazardous waste extracts. These independent analyses suffer from an inexact correspondence between the FT-IR and MS reconstructed chromatogram peaks and possible analyte degradation before the confirmatory analysis. In addition a direct-linked system evaluation

0003-2700/86/0358-2189$01.50/0 © 1986 American Chemical Society

is required prior to the preparation of suitable GC/FT-IR/MS computer software.

The availability of a viable GC/FT-IR/MS system should greatly increase the chemical information obtained from environmental samples thereby allowing better risk assessment. This, in turn, should lead to more efficient cleanup and disposal measures at the nation's uncontrolled chemical waste sites. In addition, on-line identification, chemical class, and quantitation confirmations will become available. The on-line identification confirmations would only be limited by the number of reference spectra that are common to both the MS and FT-IR search libraries. This number is currently estimated at 1535 common entries for the 2300-member EPA library (*17*).

Prior to the initiation of a GC/FT-IR/MS screening program, an attempt was made to assess previous GC/MS screening results which had been carried out on large numbers of environmental samples. Shackelford et al. reported the results of the U.S. EPA's survey of wastewaters by GC/MS spectrum matching. Approximately 30% of 225 000 GC/MS detections in 4000 samples led to 30% tentative identifications (*18*). Lucas et al. reported that 46% of 2383 GC/MS detections in 15 drinking water samples and 46% of 2097 detections in advanced treatment works (ATW) samples led to tentative identifications (*19*). Lucas' samples, however, received extensive pretreatment prior to GC/MS analysis. In a survey of wastewater GC/MS analyses Bursey et al. reported that use of other techniques, when GC/MS spectrum matching failed, did not usually lead to additional structural assignments (*20*). Bursey did point out that use of GC/FT-IR was extremely useful in some cases but that the FT-IR system employed was generally too insensitive. Since the system employed was an old packed column GC/FT-IR it may be supposed that this system was at least an order of magnitude less sensitive than modern capillary column GC/FT-IR systems (*15*). On the basis of these earlier studies, it appeared that GC/MS screening, in conjunction with GC/MS spectrum matching, would lead to no better than 30–50% tentative identifications.

EXPERIMENTAL SECTION

GC/FT-IR Instrumentation and Software. The FT-IR system consisted of a Digilab (Cambridge, MA) FTS-20B spectrometer equipped with a medium-band, 1-mm^2 focal chip mercury–cadmium–telluride detector (MCT). The data system included a Data General (Southboro, MA) Nova/4 computer, a 16-bit A/D converter, Digilab (Cambridge, MA) HI-COMP 32 high-speed array processor, and a Control Data Lark Model 50 megabyte disk system. With the Digilab GC/S software, four scans per second were collected to magnetic disk. The U.S. EPA 2300 vapor-phase FT-IR search library was used. Chromatography was performed with a Hewlett-Packard (Palo Alto, CA) Model 5880A with a J and W Scientific, Inc. (Rancho Cordova, CA), 1.0-μm DB-5 film, fused silica capillary column (FSCC) GC column (30 m × 0.32 mm) at a flow rate of 1 mL/min of helium. The end of the FSCC column was interfaced to a nominal 10:1 effluent splitter which sent the major portion of the GC effluent to the FT-IR lightpipe and the lesser effluent stream to the mass spectral detector. The FT-IR transfer lines were maintained at 280 °C. The sensitivity and quality control requirements for the FT-IR system have been described elsewhere (*21*). A diagram of the GC/FT-IR/MS system is shown in Figure 1.

After an initial hold time of 1 min, the GC oven was ramped from 40 to 280 °C at 10 °C/min and was held at 280 °C for 20 min. All GC injections were 2 μL and the FT-IR spectra were referenced against a 60-scan file of the chromatogram base line.

GC/MS Instrumentation and Software. The mass spectrometer was a Hewlett-Packard 5970A mass selective detector (MSD) utilizing a 15-megabyte Winchester disk drive and a Hewlett-Packard 9816 desk top computer. The Hewlett-Packard Quicksilver Software and the 38 000 NBS mass spectral library were used. The MSD was utilized in the full-scan mode (50–800 amu) collecting one scan/1.2 s at a nominal 1 amu resolution. Each day the spectrometer was calibrated with perfluorotributylamine.

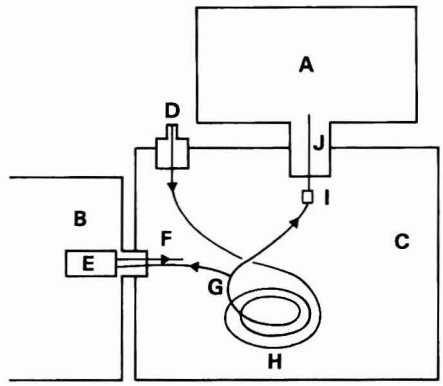

Figure 1. GC/FT-IR/MS interface: (A) MSD, (B) FT-IR interface, (C) GC oven, (D) on-column injector, (E) light pipe assembly, (F) Effluent vent, (G) splitter, (H) 30 m × 0.32 mm DB5 column, (I) 0.3 m × 0.23 mm DB5 coated line, (J) MSD interface.

GC/MS and GC/FT-IR Structural Assignments. The appropriate library (38 000 NBS or 2300 FT-IR spectra) was searched for the first five library hits. If these hits indicated close similarity indexes, additional hits were examined until significant mathematical differences appeared between sucessive library hits. Such hit differences have been shown to reveal the most valid search library selections for GC/MS and GC/FT-IR (*14, 15*). It was assumed, a priori, that GC/MS could only determine the compound class of aromatic isomers and GC/FT-IR could only determine the compound class of homologous series members. All GC/MS and GC/FT-IR hits were hand checked except when the GC/MS similarity index was below 7500 (best index = 10 000) and the GC/FT-IR similarity index was greater than 0.90 (best index = 0.00) or when the GC/MS integrated area counts were less than 10 000. If these three criteria were not met, the detection data received no further consideration. All FT-IR and MS analyte spectra that satisfied these criteria were hand checked against the library hit spectra. The GC/MS analyte molecular ion was compared to the molecular weight of each search kit. (Molecular ions were assigned by selecting the highest mass fragment which was at least 10% of the base peak intensity and which was also consistent with the FT-IR and MSD structural information.) The criterion for compound class assignment was at least one functional group plus a differentiation between aromaticity or aliphaticity. The GC/MS search algorithm reduces each library and unknown mass spectrum to 10 peaks. The criterion for peak selection is mass times abundance. The mass spectral similarity index (SI) is defined as (*22*)

$$SI = \frac{\sum_{m=1}^{1000} Am\ am}{(\sum_{m=1}^{1000} (Am)^2 \cdot \sum_{m=1}^{1000} (am)^2)^{1/2}} \quad (1)$$

where Am is the abundance of the ion at mass m in the unknown spectrum and am is the abundance of the ion at mass m in the library spectrum.

Environmental Extracts. Each of the sample extracts was received from EPA contractors and used as is. All samples were carefully dried methylene chloride extracts that did not receive extensive purification (the chlorinated hydrocarbon contaminated soil had been steam distilled).

Standard Solutions. Solutions of organic compounds were purchased from Applied Sciences Corp. (State College, PA). The nine solutions contained C_4–C_7 aliphatic alcohols, C_9–C_{13} 1-alkenes, C_{12}–C_{22} alkanes, C_5–C_9 ketones, C_1–C_4 alkylbenzenes, methyl esters of C_{10}–C_{18} acids, ethyl esters of C_3–C_6 acids, propyl esters of C_2–C_6 acids, and butyl esters of C_3–C_7 acids. Twelve standard solutions containing four to six components each, were prepared containing about 300 ng/μL of each component. Each standard solution was injected separately into the GC/FT-IR/MS system to minimize chromatographic coelution.

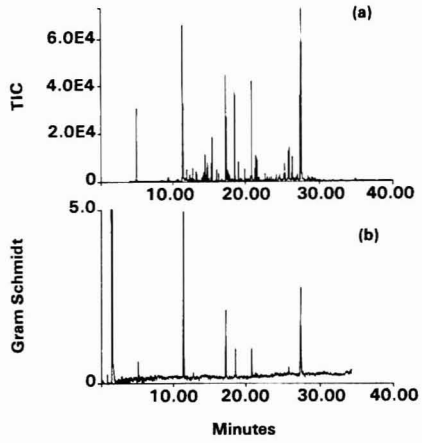

Figure 2. Total ion chromatogram (a) and infrared reconstructed chromatogram (b) of herbicide still bottom extract.

RESULTS AND DISCUSSION

Evaluation of the Directly Linked System for Rapid, Nontarget Screening, by Use of Standard Solutions. Standard solutions of alkanes, alkenes, alcohols, ketones, alkylbenzenes, and esters were used to evaluate the rapid screening capability of the directly linked system. A forward-search approach, using the first five MSD and FT-IR library search fits, was employed to determine to what extent spectral hand checking could be minimized. Spectral hand checking employs highly experienced spectroscopists and currently costs the EPA 50–80 dollars per hour. If the analyte's spectrum is contained in both data bases, such hand checking under certain circumstances may be eliminated. If the analyte's spectrum is not in either data base, the best one can expect is to determine the analyte's compound class (functionality). The MSD and FT-IR on-line library search results for 50 standard compounds are summarized in Table I. Fifty-eight percent of the standards were identified by FT-IR and 18% by MSD, within the first five on-line library search hits. Seventy-two percent of the standards were contained within the FT-IR library while 98% were in the MSD library. In those cases where the standard was not in the FT-IR library, and the compound was not an alkene or an alkane, the FT-IR library search provided convincing proof of the molecular class by yielding a high percentage of search hits with the proper functionality. For compound class assignment (without hand checking) by the forward-search technique the FT-IR detector was superior for alcohols, ketones, ethyl esters, propyl esters, and butyl esters. The MSD detector was superior for alkanes and alkenes, and the two detectors were equally successful for alkylbenzenes and methyl esters. Fifty percent (52 of 103) of the correct MSD class hits were for the biologically inert class of alkanes and alkenes, while only 4% (7 of 179) of the correct FT-IR hits were for this class.

MSD and FT-IR Structural Assignments. After evaluation of the interface with standard solutions, extracts of dye and manufacturing wastes and soils contaminated by organophosphorus pesticides and chlorinated hydrocarbons were analyzed by fused silica capillary column GC/FT-IR/MS. These results are summarized in Table II. FT-IR detections ranged from 15% to 137% of MSD detections but averaged about 33%. Figure 2 shows the real-time, simultaneously displayed, infrared reconstructed and total ion chromatograms of the herbicide still bottom. The herbicide still bottom was a chlorinated phenol waste residue and provided the greatest test for both detectors. In particular, the MSD detected 47 compounds of which the chromatogram peak intensity for most can be observed from Figure 2 to be well above the base line signal noise (S/N). By use of the criteria outlined in the Experimental Section, 23% of these MSD detections led to compound class information. FT-IR and MS retention times for corresponding chromatogram peaks generally agreed to within ±0.01 min.

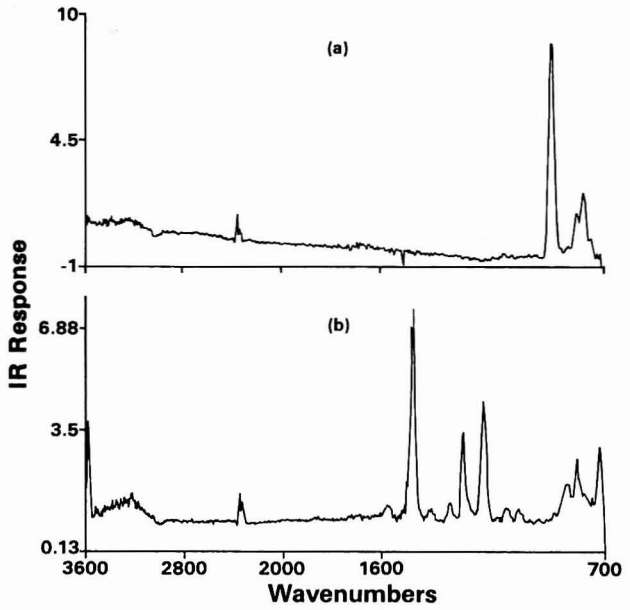

Figure 3. FT-IR herbicide still bottom identifications: (a) tetrachloroethylene, (b) 2,4-dichlorophenol.

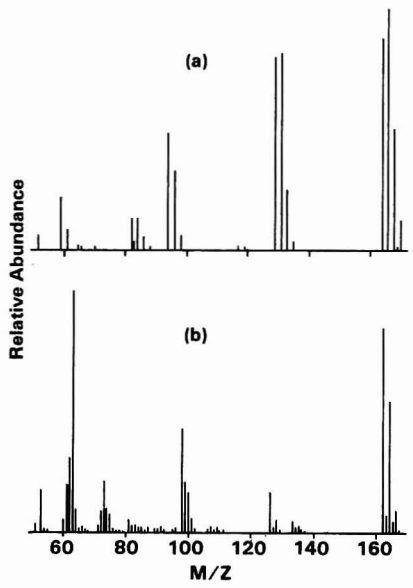

Figure 4. MSD still bottom identifications: (a) tetrachloroethylene, (b) 2,4-dichlorophenol.

After an examination of the FT-IR and MSD library search fits and integration counts, those spectra exhibiting sufficiently high S/N, fits, and counts were visually examined for characteristic vapor-phase group frequencies (*23*, *24*) or fragment masses (*25*). The analyte mass spectral molecular weights are compared to those for analytes on the search-library lists. In addition the library search hits for both detectors were examined for chemical structural consistencies. It was found that the two detectors provided almost equal amounts of unique and common structural information. Figures 3 and 4 show the FT-IR and MS spectra of two peaks in the still bottom extract. Each detector identified these compounds as tetrachlorethylene and 2,4-dichlorophenol within the first five library hits. Thus, real-time identification confirmation was achieved without the extra data acquisition cost of standard GC retention time determinations. Figures 5 and 6 show the mass spectrum and FT-IR spectrum of a major

Table I. FT-IR and MSD On-Line Search Results for Standards

compound	library[a]		search fits[b]		identification[b]		class hits[c]	
	FT-IR	MSD	FT-IR	MSD	FT-IR	MSD	FT-IR	MSD
2-methyl-1-propanol			0.20–0.24	8800–8400	+		5	1
1-butanol			0.16–0.20	9300–8800	+		5	0
2-ethyl-1-butanol			0.18–0.23	8400–8300	+		5	0
1-hexanol			0.13–0.20	9500–9100	+		5	0
cyclohexanol			0.16–0.28	9300–9200	+		5	1
1-heptanol			0.13–0.18	9100–8800	+		5	0
1-decene			0.18–0.20	9300–9100	+		2	4
1-dodecene			0.14–0.17	9300–9200	+		1	2
1-undecene	–		0.14–0.16	9400–9300			1	2
1-tridecene			0.15–0.17	9300–9250			2	3
1-tetradecene			0.15–0.17	9400–9100		+	0	1
n-dodecane			0.09–0.13	9100–8900			0	5
n-tridecane			0.09–0.13	9000–8900			0	5
n-tetradecane			0.10–0.13	9000–8800			0	5
n-hexadecane			0.13–0.15	9100–9000			0	5
n-octadecane			0.49–0.50	9200–9000			0	5
n-nonadecane			0.23–0.24	9200–9000	+		0	5
n-heneicosane	–		0.21–0.23	9300–9000		+	0	5
n-docosane	–		0.26–0.28	9300–9000			1	5
3-pentanone	–		0.32–0.42	9200–9100			5	0
4-methyl-2-pentanone			0.19–0.28	8100–7700	+		5	1
5-methyl-2-hexanone			0.21–0.26	9200–9100	+		5	0
4-heptanone	–		0.23–0.27	9600–9300			5	0
2-heptanone			0.22–0.28	9700–9400	+		5	0
5-methyl-3-heptanone	–		0.25–0.28	8300–8100			5	0
2,6-dimethyl-4-heptanone			0.20–0.31	9300–9000	+			
benzene			0.17–0.76	8800–8600	+		4	0
toluene			0.17–0.49	9800–9700	+	+	3	1
ethylbenzene			0.15–0.46	9800–9600	+	+	3	4
m-xylene			0.17–0.57	9900–9500	+	+	4	4
o-xylene			0.12–0.52	9700–9600	+	+	3	4
p-cymene			0.17–0.35	9800–9400	+	+	5	5
methyl decanoate	–		0.19–0.26	9200–9000			5	4
methyl dodecanoate			0.59–0.60	9600–9500	+	+	5	4
methyl tetradecanoate			0.22–0.24	9600–9400	+	+	5	4
methyl hexadecanoate	–		0.22–0.24	9600–9400			5	4
methyl octadecanoate			0.18–0.20	9600–9400	+		5	5
ethyl propionate			0.32–0.38	9400–9300	+		5	1
ethyl butyrate			0.18–0.33	7800–6800	+		5	0
ethyl valerate	–		0.22–0.29	6800–6600			5	2
ethyl caproate			0.17–0.26	8600–8400	+		5	0
propyl acetate			0.21–0.29	8000–6300	+		5	0
propyl propionate			0.18–0.24	8600–7800	+		5	1
propyl butyrate	–		0.22–0.31	8300–8100			5	0
propyl valerate	–		0.21–0.31	8100–7700			5	1
propyl caproate		–	0.19–0.28	7600–6100	+		5	1
butyl propionate			0.18–0.23	9400–9300	+		5	0
butyl valerate	–		0.17–0.27	7000–6700			5	1
butyl caproate	–		0.19–0.26	9200–9000			5	2
butyl heptanoate	–	–	0.19–0.25	8300–7500			5	0
total	14[d]	2[d]			29	9	179 (250)[e]	103 (250)[e]

[a] A "–" indicates that the standard is not in the search library. [b] First five library search hits. [c] Number of library search hits, within the first five hits, with the proper functionality. [d] Number of standards missing from library. [e] Maximum number of hits.

peak in the pesticide soil extract. Both the FT-IR and MSD searches identified this peak as an organosulfur–phosphorus compound. The FT-IR ν_{max} was at 1038 cm^{-1} and the spectrum was very similar to that of Diazinon, a phosphorothionate (*26*). The mass spectrum contained fragments at m/z 88 (base peak) and m/z 60. These ions correspond to $[CH_2{=}CHSC_2H_5]^+$ and $[CH_2{=}CHSH]^+$ respectively, also suggesting a phosphorothionate (*27*). This was an example of an on-line compound class confirmation.

Since essentially all FT-IR detected analytes were also detected by the MSD, approximately 41% of the *jointly detected* analytes [(20 + 24)/106] led to structural confirmations. This is surprisingly high in light of the general perception that GC/FT-IR is insensitive and that the FT-IR vapor-phase library is too small. Implementation of the GC/FT-IR single-beam sensitivity improvements of Griffiths et al. (*28*, *29*) will dramatically improve the capability of GC/FT-IR/MS by bringing the number of FT-IR detections more in line with that obtainable from the MS detector.

Sample Representativeness. While these samples exhibit a variety of matrix types, it is also important to ascertain that a broad spectrum of analyte types were present. The com-

Table II. Comparison of FT-IR, MSD, and FT-IR/MSD Selectivities

sample	no. detected		meet[a] criteria		compound class (tentative)		no. identified (tentative)		FT-IR/MSD confirmation	
	FT-IR	MSD	FT-IR	MSD	FT-IR	MSD	FT-IR	MSD	ident	class
dye 1	1	3	1	1	1	1	0	1	0	1
dye 2	4	6	1	4	1	1	0	1	0	1
dye 3	4	7	4	7	1	2	1	1	0	2
herbicide still bottom	7	47	7	28	4	11	2	3	2	3
pesticide soil	56	41	51	32	24	13	5	3	3	10
chlorohydrocarbon soil	34	121	33	78	10	31[b]	17	10	15	7
total	106	225	97	150	41 (27)[c]	59 (32)[d]	25 (13)[c]	19 (9)[d]	20	24

[a] Meet the three criteria of the Experimental Section (GC/MS and GC/FT-IR structural assignments). [b] Sample contained many aromatic isomers. MSD used alone can only determine compound class. [c] Unique FT-IR information. [d] Unique MSD information.

Table III. FT-IR and MSD Tentative Structural Assignments

class	dyes			still bottom	pesticide soil	chlorohydrocarbon soil	total
	no. 1	no. 2	no. 3				
acid						2[a] (1, 1)[b]	2
alcohol					4 (2, 2)	3 (1, 2)	7
aldehyde						2 (2, 2)	2
alkane					14 (2, 14)	4 (1, 4)	18
alkene				1 (1, 1)		1 (1, 1)	2
amide	1 (1, 1)	2 (1, 1)	2 (1, 2)		1 (0, 1)		6
amine		1 (1, 0)	1 (1, 0)			1 (0, 1)	3
aromatic hydrocarbon				1 (1, 0)	13 (13, 7)	3 (2, 2)	17
chlorohydrocarbon				3 (3, 2)		14 (13, 14)	17
ester	1 (1, 0)	1 (1, 0)	1 (1, 0)	3 (1, 2)		3 (0, 3)	9
ether				3 (3, 0)		1 (1, 1)	4
fluorohydrocarbons						4 (1, 3)	4
ketone					2 (2, 0)		2
nitro					2 (1, 2)	2 (1, 2)	4
organophosphorus						7 (5, 7)	7
phenol				1 (1, 1)	1 (1, 0)		2
total							106

[a] Total unique FT-IR and unique MSD assignments. [b] FT-IR result, MSD result.

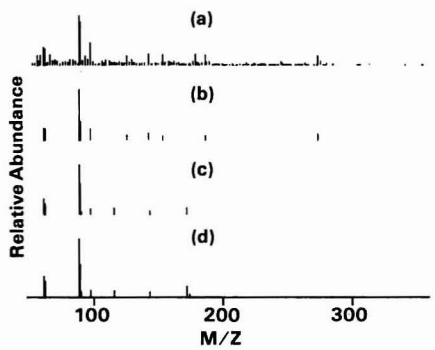

Figure 5. MSD pesticide soil compound class assignment: (a) analyte, (b) substituted phosphorodithioic acid, (c) substituted phosphorothionate, (d) substituted phosphorothionate.

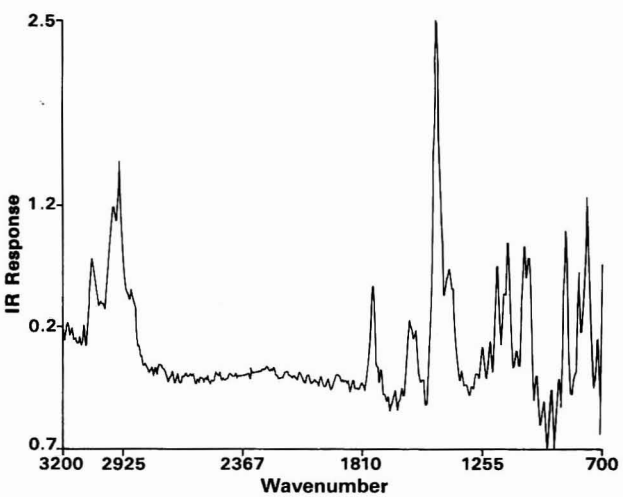

Figure 6. FT-IR pesticide soil compound class assignment. Substituted phosphorothionate.

pound types found by each detector in each sample extract are summarized in Table III. A total of 106 tentative class assignments representing 16 compound classes were made by the directly linked system. The dominant class types were alkanes, aromatic hydrocarbons, chlorinated hydrocarbons, and organophosphorus compounds. As was the case with standards, a high percentage of the MSD class assignments were of the biologically inert class of alkanes and alkenes (20/79 = 0.25). For the 45 oxygen-containing compounds, FT-IR was able to make tentative class assignments on 28 while the MSD provide tentative class information on 30. The MSD provided tentative class information on 25 of 34 aromatic and chlorinated hydrocarbons, while the FT-IR provided 32 assignments. The importance of proper identification of oxygen compounds is to be emphasized since such compounds are polar and the polar fraction of sample extracts has been reported to be mutagenic (*30*). The mass spectral selectivity for the environmentally ubiquitous chlorine-containing compounds is greatly aided by the unique chlorine isotopic clusters (see page 19 of ref 25 and page 59 of ref 27). It should also be pointed out that although the nominal MS search library size is over 38 000 spectra, most of these are not the spectra of compounds likely to be found in the environment. Milne et al. (*31*) have pointed out that less than 6000 of the spectra

in the NBS data base are those of manufactured chemicals registered under TSCA. In addition, the MS reference spectra have been measured by direct probe insertion; thus many of the library reference chemicals may not actually pass through a GC transfer line, in sufficient quantity, to be detected (note that this also may apply to some of the 6000 TSCA chemical mass spectra). For a complete survey of mass spectral data bases, see ref 32. By contrast, most or all of the 2300 FT-IR spectra are those of common manufactured chemicals, were measured in the gas-phase, and were selected because they had been previously observed in the environment (*33*). In addition, Frankel has shown (*34*) that this FT-IR library of 2300 spectra contains all the compound types required to develop a pattern recognition identification algorithm for organic compounds.

CONCLUSIONS

It is understood that more exhaustive spectral hand checking or sample cleanup would improve the performance of this system, but not without a substantial increase in analytical costs. In addition, more sophisticated computer software of the type described by McLafferty (*35*) would greatly improve the MSD capability, which is currently limited by a small desk top computer.

An order of magnitude improvement in FT-IR sensitivity will greatly improve GC/FT-IR/MS for high throughput, nontarget screening of complex environmental, multicomponent samples. Not only will this bring the number of FT-IR detections more in line with those obtained from MS but it will also allow the use of narrow bore capillary columns in the directly linked system, thereby reducing chromatographic coelution. Directly linked GC/FT-IR/MS is demonstrated to be superior to either stand-alone technique for environmental analyses. This superiority can be *routinely* implemented when suitable computer software becomes available to process the large quantities of spectral information that will be generated. Wilkins has reported a preliminary version of such software (*36*). The computer software and the FT-IR sensitivity improvements are being pursued via a grant from this laboratory to the University of California at Riverside (*37*).

In his elegant review of hyphenated techniques (*10*), Hirschfeld noted that the extravagance of such techniques may only be justified by sufficiently high sample demands. Such high sample demands currently exist within the EPA's Superfund Laboratory Contracts Program within which over 20 000 organic samples (this excludes 7000 dioxin samples) were processed in 1984 (*38*). The availability of small, relatively inexpensive, mass spectral detectors such as the MSD and the ion trap (*39*), as well as small FT-IR detectors (*40*) suggests that this "extravagance" may not be as great as formerly anticipated.

ACKNOWLEDGMENT

The authors wish to thank Charles Wilkins of the University of California at Riverside for several helpful discussions.

Registry No. Phenol, 108-95-2; tetrachloroethylene, 127-18-4; 2,4-dichlorophenol, 120-83-2.

LITERATURE CITED

(1) Gurka, D. F.; Meier, E. P.; Beckert, W. F.; Haeberer, A. F. Paper presented at the 3rd National Conference on Management of Uncontrolled Hazardous Waste Sites. Washington, DC, November 1982.
(2) *Fed. Regist.* **1979**, *44*(233), 69464–69558.
(3) National Academy of Sciences–National Research Council *Drinking Water and Health*; Printing and Publishing Office, National Academy of Sciences: Washington, DC, 1977; p 489.
(4) "Improving Analytical Chemical Data Used for Public Purposes" *Chem. Eng. News* **1982**, June 7, 44–48.
(5) ACS Committee on Environmental Improvement *Anal. Chem.* **1980**, *52*, 2242–2249.
(6) ACS Committee on Environmental Improvement *Anal. Chem.* **1983**, *55*, 2210–2218.
(7) Christman, R. F. *Environ. Sci. Technol.* **1982**, *11*, 594A.
(8) Buser, H. R.; Rappe, C. *Anal. Chem.* **1980**, *52*, 2257–2262.
(9) Gurka, D. F.; Billets, S.; Brasch, J. W.; Riggle, C. J. *Anal. Chem.* **1985**, *57*, 1975–1979.
(10) Hirschfeld, T. *Anal. Chem.* **1980**, *52*, 297A–309A.
(11) Wilkins, C. L.; Giss, G. N.; White, R. L.; Brissey, G. M.; Onyiriuka, E. C. *Anal. Chem.* **1982**, *54*, 2260–2264.
(12) Shafer, K. H.; Hayes, T. L.; Tabor, J. E. Paper presented at the 1981 International Conference on Fourier Transform Infrared Spectroscopy.
(13) Crawford, R. W.; Hirschfeld, T.; Sanborn, R. H. Wong, C. M. *Anal. Chem.* **1982**, *54*, 817–820.
(14) Gurka, D. F.; Betowski, L. *Anal. Chem.* **1982**, *54*, 1819–1824.
(15) Gurka, D. F.; Hiatt, M.; Titus, R. *Anal. Chem.* **1984**, *56*, 1102–1110.
(16) Shafer, K. H.; Hayes, T. L.; Brasch, J. W.; Jakobsen, R. J. *Anal. Chem.* **1984**, *56*, 237–240.
(17) Wilkins, Charles, University of California at Riverside, private communication, January 1986.
(18) Shackelford: W. M., Kline; D. M.; Faas, L.; Karth, G. *Anal. Chim. Acta* **1983**, *146*, 15–27.
(19) Lucas, S. V. "GC/MS Analysis of Organics in Drinking Water Concentrates and Advanced Waste Treatment Concentrates"; EPA-600/1-84-020, November 1984.
(20) Bursey, J. T. "Application of an Analysis Protocol to Identify Organic Compounds Not Identified by Spectrum Matching", EPA/600-4-84-072B, August 1984.
(21) Gurka, D. F. *Appl. Spectrosc.* **1985**, *39*, 827–833.
(22) *Hewlett-Packard 59970A Workstation Operators Manual*. November 1984, A-10.
(23) Welti, D. *Infrared Vapor Spectra*; Heyden and Son: London, 1970.
(24) Nyquist, R. A. "The Interpretation of Vapor-Phase Infrared Spectra," *Group Frequency Data*; Sadtler Research Laboratories: Philadelphia, PA, 1984.
(25) McLafferty, F. W. *Interpretation of Mass Spectra*; 2nd ed.; W. A. Benjamin: Reading, MA, 1973.
(26) Gurka, D. F.; Umaña, Pellizari, E. D.; Moseley, A; de Haseth, J. A. *Appl. Spectrosc.* **1985**, *39*, 297–303.
(27) Safe, S.; Hutzinger, O. *Mass Spectrometry of Pesticides and Pollutants*; CRC Press: Boca Raton, FL, 1980; p 194.
(28) Yang, P. W.; Ethridge, E. L.; Lane, J. L.; Griffiths, P. R. *Appl. Spectrosc.* **1984**, *38*, 813–816.
(29) Yang, P. W.; Griffiths, P. R. *Appl. Spectrosc.* **1984**, *38*, 816–821.
(30) Newton, D. L.; Erickson, M. D.; Tomer, K. B.; Pellizzari, E. D.; Gentry, P. *Environ. Sci. Technol.* **1982**, *16*, 206–213.
(31) Milne, G. W. A.; Budde, W. L.; Heller, S. R.; Martinsen, D. P.; Oldham, R. G. *Org. Mass. Spectrom* **1982**, *17*, 547–551.
(32) Martinsen, D. P. *Appl. Spectrosc.* **1981**, *35*, 255–266.
(33) Shackelford, W. M.; Keith, L. H. "Frequency of Organic Compounds Identified in Water"; EPA-600/4-76-062, December, 1976.
(34) Frankel, D. S. *Anal. Chem.* **1984**, *56*, 1011–1014.
(35) McLafferty, F. W.; Stauffer, D. G. *J. Chem. Inf. Comput. Sci.* **1985**, *25*, 245–252.
(36) Laude, Jr., D. A.; Brissey, G. M.; Ijanes, C. F.; Brown, R. S.; Wilkins, C. L. *Anal. Chem.*, **1984**, *56*, 1163–1168.
(37) Cooperative Agreement Number R811730-01-0 between the U.S. EPA/LV and the University of California at Riverside.
(38) Fourth Annual Contract Laboratory Program Conference, U.S. EPA, August 27, 1984, Las Vegas, NV.
(39) Stafford, G. C.; Kelley, P. E.; Bradford, D. C. *Am. Lab.* (*Fairfield, Conn.*) **1983**, (June), 51.
(40) Rossiter, V. *Am. Lab.* (*Fairfield, Conn.*) **1982** (February), 144–152.

RECEIVED for review July 23, 1985. Resubmitted April 21, 1986. Accepted May 12, 1986. Although the research described in this article has been funded wholly or in part by the United States Environmental Protection Agency, it has not been subjected to Agency review and therefore does not necessarily reflect the views of the Agency and no official endorsement should be inferred. Mention of trade names or commercial products does not constitute endorsement or recommendation for use. This work was presented in part at the 24th Eastern Analytical Symposium, November 21, 1985, New York, NY.

Maximum Absorbance Algorithm for Reconstruction of Gas Chromatograms from Gas Chromatography/Infrared Spectrometry Data

Ian C. Bowater,[1] Robert S. Brown, John R. Cooper, and Charles L. Wilkins*

Department of Chemistry, University of California, Riverside, California 92521

A new algorithm for generation of chromatograms in gas chromatography/Fourier transform infrared spectrometry is described. This "maximum absorbance" algorithm is compared with both the integrated absorbance method and the Gram–Schmidt reconstruction technique. Such comparisons establish that maximum absorbance reconstruction is more sensitive than the integrated absorbance method for selective detection reconstructions. For universal (i.e., wide frequency window) reconstructions, the maximum absorbance algorithm is as sensitive as the Gram–Schmidt reconstruction. Because of its simplicity and its ability to create both universal and selective reconstructions with good sensitivities, it is suggested the new algorithm should replace the integrated absorbance method and be considered as an alternative to the Gram–Schmidt method.

The two algorithms most widely used to reconstruct chromatograms in gas chromatography/Fourier transform infrared spectrometry are the Gram–Schmidt (*1*) and the integrated absorbance methods (*2*). The Gram–Schmidt method, which operates on time domain interferograms, is preferred for universal reconstructions (i.e., wide frequency window) because it is computationally faster (*1*) and, when optimized, gives reconstructions with greater signal to noise ratios (S/N) than integrated absorbance reconstructions (*3*, *4*). The integrated absorbance method, however, can be used to create selective chromatograms by integrating over a narrow frequency range, characteristic of a particular functional group. Both methods have been implemented to reconstruct chromatograms in real time.

To use the Gram–Schmidt method, one first collects a series of base line interferograms that contain no sample absorption. These interferograms are then used to construct a set of orthonormal basis vectors (NBV), using a number of consecutive data points (NPT) from each of the original interferograms, starting at some positive or negative displacement (DISP) from the interferogram centerburst. For chromatogram reconstruction, each interferogram collected following the start of chromatography is used to compute a resultant vector orthogonal to the basis vectors. The magnitude of this orthogonal vector increases from the noise level when an absorbing compound elutes from the gas chromatograph. This magnitude is a measure of the total infrared absorbance of the sample. These operations were fully described in the original paper by de Haseth and Isenhour (*1*).

Values, which optimize the S/N of the resulting reconstructions, must be chosen for the parameters NBV, NPT, and DISP. The values of NTP = 100 and NBV = 10–30 were shown to give close to the maximum S/N (*1*, *3*, *4*). However, several studies demonstrated that the optimal value of DISP depends on both the spectral characteristics of the compound (*5*, *6*) and interferometer stability (*4*, *6*). Signal due to sample absorption is greatest at the centerburst and decays with increasing distance from the centerburst, with the rate of decay dependent on the bandwidths of the peaks. Noise behaves in the same manner; however, the magnitude of centerburst noise is smallest for stable interferometers. Brissey et al. (*6*) and Sparks et al. (*4*) suggested that values from +10 to +20 for DISP would be a good compromise for most compounds and interferometers. Sparks et al. (*4*) also concluded that use of double-sided vectors would increase the S/N and reduce the dependence of S/N upon choice of DISP.

The integrated absorbance method calculates the total absorbance in a selected frequency window of the transformed spectra. Universal reconstructions can be formed by selecting a wide frequency window. However, the S/N values thus obtained were shown to be poorer than those obtained using the Gram–Schmidt methoid (*4*, *7*). A major reason for poorer S/N is that the choice of a wide frequency range includes substantial regions of base line containing only noise. More selective reconstructions with improved S/N can be formed by selecting a frequency window characteristic of part of the infrared spectrum. For example, choice of the window 1800–1700 cm^{-1} gives a reconstruction characteristic of compounds in the sample which contain the C=O bonds with absorbances in that frequency range.

This paper describes and evaluates an alternative method of reconstructing chromatograms, which has been previously applied in liquid chromatography/UV spectrometry (*8*). This method, called maximum absorbance reconstruction, is based upon the *magnitude* of frequency-domain data values within a selected frequency window. The frequency window may contain one or several ranges of contiguous points. A similar method that involved monitoring the frequency of a single spectral peak (similar to selected ion monitoring in GC/mass spectrometry) was advocated by Krishnan and co-workers in an early paper (*9*). The maximum absorbance algorithm presented here is a more general implementation of the same fundamental concept. In practice, following the start of chromatography, interferograms are collected and Fourier transformed and the maximum absorbance value within the selected frequency window is used as the Y coordinate value for the corresponding time (X coordinate) value in the reconstruction. For base line regions, this procedure results in low values and, as absorbing compounds elute, the values rise and fall to reflect their absorbance behavior, producing the desired reconstruction. It is shown that this method can be used to create selective reconstructions that are superior to those obtained from the integrated absorbance method and universal reconstructions with similar S/N to those obtained from the Gram–Schmidt method.

EXPERIMENTAL SECTION

Two samples were analyzed with a GC/FTIR system that consisted of a Varian 3700 gas chromatograph coupled to a Nicolet 60SX FT-IR spectrometer. For sample 1, the gas chromatograph

[1] Present address: Department of Chemistry, Swinburne Institute of Technology, Melbourne 3122, Australia.

0003-2700/86/0358-2195$01.50/0 © 1986 American Chemical Society

Table I. Identities of Compounds in Order of Elution

sample 1[a]	sample 2[b]
1 hydrocarbon impurity	1 1,1,2-trichloroethane
2 3-methylpentane	2 *o*-xylene
3 ethyl acetate	3 *o*-dichlorobenzene
4 methylcyclopentane	4 nitrobenzene
5 diethyl ketone	
6 3-heptene	
7 toluene	
8 hydrocarbon impurity	
9 hydrocarbon impurity	
10 *p*-xylene	
11 hydrocarbon impurity	
12 hydrocarbon impurity	
13 isobutyl methacrylate	

[a] Hexane was eluted between peaks 2 and 3. [b] Chloroform was eluted before peak 1.

was equipped with a 25 m × 0.33 mm i.d. capillary column coated with a 1.0 μm thick coating of Carbowax 20M. For sample 2, a 60 m × 0.32 mm i.d. capillary column coated with a 1.0 μm thick coating of DB-5 was used. Each column was connected directly to the light pipe entrance and enclosed in a short transfer line, which was heated to 250 °C. The gold-coated light pipe was 15 cm long with a 1.0 mm i.d. and was heated to 200 °C. For sample 1, a narrow-range MCT detector with a 1 mm^2 element was used (D^* = 42.5 × 10^9 cm $Hz^{1/2}$ W at 10 kHz). For sample 2, a medium-range MCT detector with a 0.5 mm^2 element was used (D^* = 48 × 10^9 cm $Hz^{1/2}$ W at 10 kHz). The low-frequency cutoffs for these detectors were about 750 cm^{-1} and 640 cm^{-1}, respectively.

Sample 1 consisted of 100 μL each of ethyl acetate, isobutyl methacrylate, diethyl ketone, 3-heptene, toluene, and *p*-xylene diluted to about 2 mL with hexanes (predominately *n*-hexane). Sample 2 contained 100 μL each of 1,1,2-trichloroethane, *o*-xylene, *o*-dichlorobenzene, and nitrobenzene diluted to about 1.5 mL with chloroform. About 0.4 μL of each sample was injected onto the column via a split (30:1) injection. In sample 1, two of the three peaks, which eluted near the large *n*-hexane peak, were identified as 3-methylpentane and methylcyclopentane, using the Nicolet search software (*10*) and the EPA Vapor Phase Library. The other peak and the four weak impurity peaks, which eluted near *p*-xylene, could not be identified. However, all the unidentified compounds had their strongest absorbance in the range 3000–2900 cm^{-1}, so they were presumed to be hydrocarbons. These impurities were retained in the analysis, as they showed trends at concentrations near the detection limit. The compounds in both samples are listed in Table I in order of elution.

Data acquisition was controlled by a Nicolet 1280 data system employing standard GC-FTIR software. For sample 1, the physical velocity of the interferometer was 0.733 cm s^{-1}, and 10 scans were coadded and saved to disk every 1.7 s. For sample 2, the physical velocity of the interferometer was 1.626 cm s^{-1}, and 12 scans were coadded and saved to disk every 1.2 s. For both samples, 2048 point interferograms were collected. The 1024-point Fourier transformations were performed in real time, so that the eluents could be monitored by use of a series of selective reconstructions called chemigrams (*2*). The 512-, 1024-, and 2048-point interferograms were transformed with one level of zero filling and Happ–Genzel apodization after data collection, to produce 32, 16, and 8 cm^{-1} resolution infrared spectra, respectively.

All data manipulation programs were written in Fortran. The Gram–Schmidt program provided by Nicolet was altered to allow the value of DISP to be altered and double-sided vectors to be chosen. Programs were written to produce maximum absorbance and integrated absorbance reconstructions and S/N analyses of reconstructions. After a linear least squares fit through sections of the base line where there was no evidence of eluting compounds, the root mean square noise and then S/N for the peaks were calculated. These sections of base line contained 140 points for sample 1 and 123 points for sample 2. This method of calculating the root mean square noise was preferred to the calculation of the local root mean square noise near each peak (*4*), as variations in the local root mean square noise, due to a smaller number of base line points, obscured some trends in S/N values.

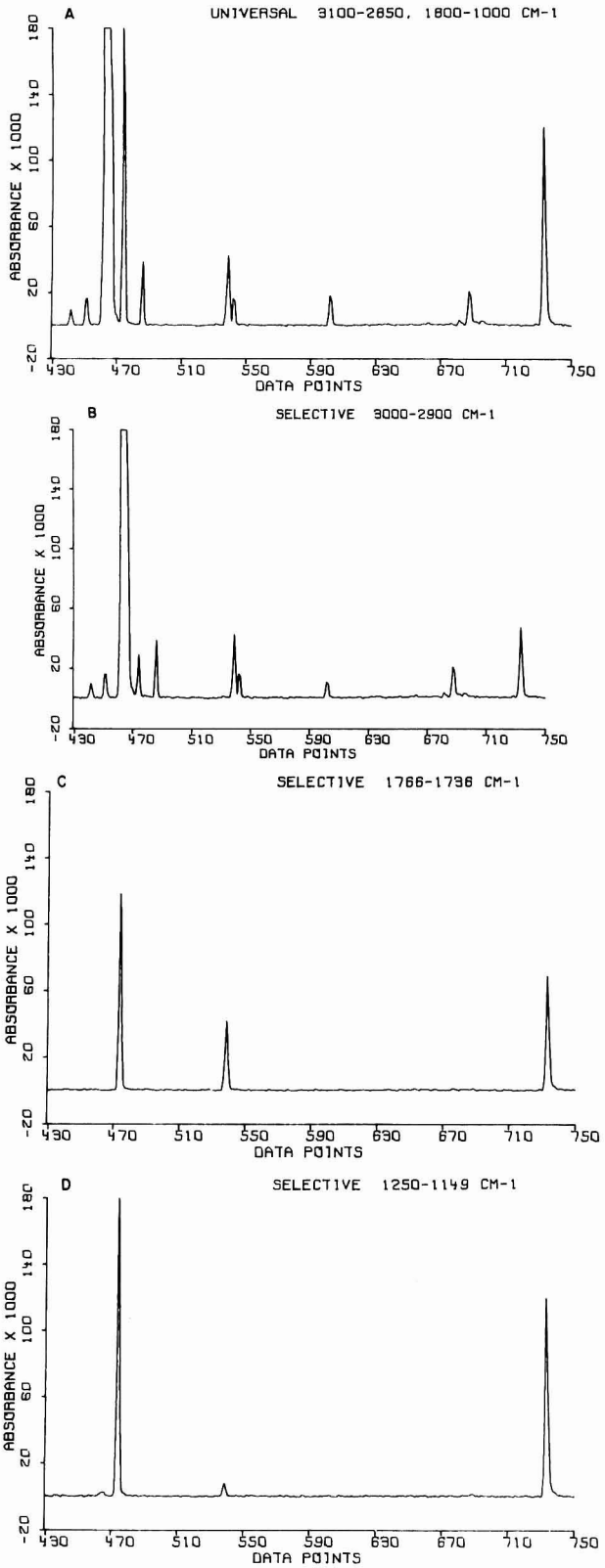

Figure 1. Reconstructions using the maximum absorbance method for sample 1 at 16-cm^{-1} resolution.

RESULTS AND DISCUSSION

The strongest absorbances of the majority of organic compounds are in the frequency ranges 3100–2850 and 1800–1000 cm^{-1}. A universal maximum absorbance reconstruction for sample 1 using this frequency window (3100–2850, 1800–1000 cm^{-1}) is shown in Figure 1A. There are larger noise spikes below 1000 cm^{-1} than in the selected ranges, due to decreased sensitivity of the narrow range MCT detector from 1000 cm^{-1} to 750 cm^{-1}, the low-frequency cutoff. However the S/N is

Table II. Effect of Resolution on S/N of Gas Chromatographic Peaks in the Universal Maximum Absorbance Reconstruction

resolution	rms noise ($A^a \times 10^3$)	S/N for compounds in sample 1[b]												
		1	2	3	4	5	6	7	8	9	10	11	12	13
32 cm^{-1}	0.28	30	49	555	115	138	51	58	6.2	9.5	63	6.6	7.0	322
16 cm^{-1}	0.30	32	52	640	127	140	52	59	6.0	10.6	67	6.4	8.2	395
8 cm^{-1}	0.37	28	47	587	121	119	45	49	5.1	8.4	61	5.5	5.3	375
8 cm^{-1}, 3 points	0.40	25	43	525	108	108	39	46	5.0	7.6	56	5.0	5.1	324
8 cm^{-1}, 5 points	0.41	24	41	502	102	104	38	45	4.8	7.1	53	5.2	5.2	303

resolution	rms noise ($A^a \times 10^3$)	S/N for compounds in sample 2[c]			
		1	2	3	4
32 cm^{-1}	0.17	75	25	27	81
16 cm^{-1}	0.17	124	41	54	127
8 cm^{-1}	0.25	99	41	53	92

[a] Absorbance. [b] Frequency window 3100–2850, 1800–1000 cm^{-1}. [c] Frequency window 3100–2850, 1800–700 cm^{-1}.

only 15% lower when the low frequency end of the window is extended down to 800 cm^{-1}. Selective maximum absorbance reconstructions using the ranges 3000–2900, 1766–1736, and 1250–1149 cm^{-1} are shown in Figure 1, parts B, C, and D, respectively.

For some compounds the strongest absorbance is outside the range 3100–1000 cm^{-1}. Sometimes it is also below 750 cm^{-1}, the low-frequency cutoff of the narrow range MCT detector. For example, many aromatic compounds and halogenated compounds absorb most strongly below 750 cm^{-1}. This will only cause a substantial loss in sensitivity for compounds where the most intense infrared peak is much greater than those in the selected frequency window (e.g., polyhalogenated compounds).

Each compound in sample 2 was chosen because it has a strong infrared absorbance below 750 cm^{-1}, but above 640 cm^{-1}, the low-frequency cutoff of the medium range MCT detector. A universal maximum absorbance reconstruction for sample 2 using the frequency window 3100–2850, 1800–700 cm^{-1} is shown in Figure 2A. A representative selective maximum absorbance reconstruction using the range 771–677 cm^{-1} is shown in Figure 2B. The corresponding integrated absorbance reconstruction for this region is shown in Figure 2C.

As the resolution of the infrared spectrum was improved from 32 cm^{-1} to 8 cm^{-1}, both the maximum absorbance of the peak, and the noise in the reconstruction increased. Although the S/N was relatively insensitive to the resolution, the S/N was best at 16 cm^{-1} for both samples. Averaging the absorbance value at the selected maximum point with the absorbance value of the points on either side of the maximum did not improve the S/N. These changes in the S/N of the universal reconstructions are shown in Table II.

Selective reconstructions for sample 1, using both the maximum absorbance and the integrated absorbance methods, were compared over the ranges 3000–2900, 1766–1736, and 1250–1149 cm^{-1}. The S/N values at 16 cm^{-1} resolution are listed in Table IIIA. The S/N values, using the maximum absorbance method, are slightly better in the range 3000–2900 cm^{-1}, and much superior in the other two ranges. The integrated absorbance method is at its best in the 3000–2900 cm^{-1} range because the position of the band in this range is relatively constant, and the band is sufficiently broad to occupy most of the range. However, in the other ranges, the characteristic bands are narrower and their frequencies less constant. The frequency windows used for these two ranges in Table IIIA were selected to give the maximum values of the S/N for the integrated absorbance method. If the windows had been larger, the S/N would have been worse, as shown in Figure 3. On the other band, the S/N obtained by using the maximum absorbance method is relatively independent

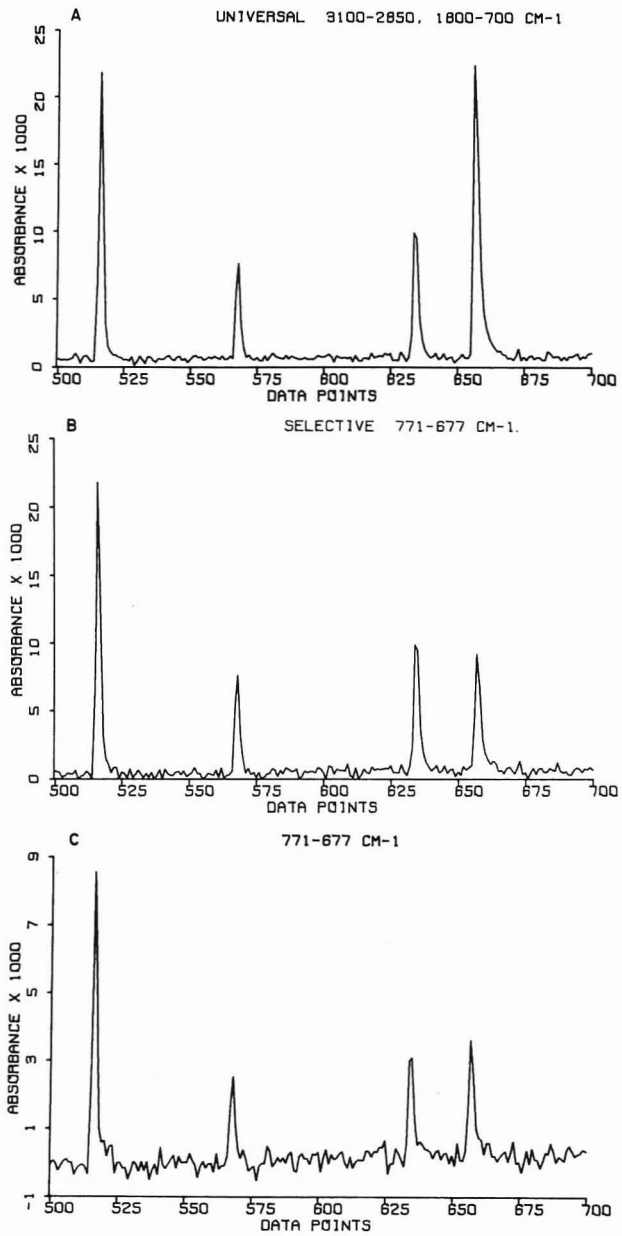

Figure 2. Reconstructions using the maximum absorbance and integrated absorbance methods for sample 2 at 16-cm^{-1} resolution.

of the size of the window, provided that the tops of all the selected infrared absorptions are included in the window. For sample 2, selective windows using both methods were com-

Table III. Comparison of S/N for Sample 1

algorithm	frequency range, cm^{-1}	rms noise ($A^a \times 10^3$)	S/N for compounds 1	2	3	4	5	6	7	8	9	10	11	12	13
A. Comparison of S/N for the Selective Maximum Absorbance and Selective Integrated Absorbance Reconstructions for Sample 1 at 16-cm^{-1} Resolution															
maximum	3000–2900	0.35	29	46	83	111	121	45	30	5.3	9.3	58	5.7	7.2	134
integrated	3000–2900	0.27	23	39	65	77	120	39	24	5.0	7.4	48	7.1	5.7	96
maximum	1766–1736	0.26			464		162								268
integrated	1766–1736	0.27			325		93								155
maximum	1250–1149	0.30			649		27								402
integrated	1250–1149	0.28			238		14								161
B. Comparison of S/N for Sample 1 Using Real Time Transforms with 1024 Points															
maximum	3000–2900	0.50	23	32	63	95	91	31	21	4.7	6.0	47	6.3	5.6	107
integrated	3000–2900	0.31	21	36	57	70	109	34	20	4.9	7.0	42	7.4	5.4	85

[a] Absorbance.

Table IV. Comparison of S/N for the Selective Maximum Absorbance and Selective Integrated Absorbance Reconstructions for Sample 2 at 16-cm^{-1} Resolution

algorithm	frequency range, cm^{-1}	rms noise ($A^a \times 10^3$)	S/N for compounds 1	2	3	4
maximum	3000–2900	0.19		24		
integrated	3000–2900	0.18		20		
maximum	1600–1500	0.13		18	5	172
integrated	1600–1500	0.12		5	4	72
maximum	1500–1400	0.13	9	19	53	17
integrated	1500–1400	0.12	3	12	21	7
maximum	1400–1300	0.11	10			156
integrated	1400–1300	0.11	2			54
maximum	771–677	0.25	86	29	37	34
integrated	771–677	0.20	43	13	14	17

[a] Absorbance.

pared over the ranges 3000–2900, 1600–1500, 1500–1400, 1400–1300, and 771–677 cm^{-1}. The S/N values are listed in Table IV. The maximum absorbance method is again superior for all frequency windows.

When 1024-point real-time transforms are used instead of the 16-cm^{-1} postrun transforms, noise is greater, and S/N is lower for both maximum absorbance and integrated absorbance reconstructions, as shown in Table III. This is because with the real-time transforms, time is saved by using boxcar apodization, no zero-filling, and magnitude-mode phase correction. However, computer advances, such as the use of array processors or coprocessors, should make these compromises unnecessary in the near future. When these compromise real time transforms are used, the maximum absorbance method still gives similar S/N to the integrated absorbance method over the range 3000–2900 cm^{-1}, and better S/N over the other ranges.

Universal reconstructions using the Gram–Schmidt method were optimized prior to comparison with the results from the maximum absorbance method. With NPT = 100 and NBV = 10, DISP was altered by using both single-sided and double-sided vectors to select the parameters that give the best S/N, under the prevailing interferometer conditions. All the hydrocarbons in sample 1 gave the best S/N using single-sided vectors across the centerburst (DISP = −50), whereas the esters and the ketone gave the best S/N using double-sided vectors with DISP = +20. Each of these values of DISP agree with a recommendation in the literature (*3*, *4*) and suggest that the spectrometer used has a stable interferometer. In Table V, the S/N of the gas chromatographic reconstruction peaks obtained by using the Gram–Schmidt method with these two sets of parameters are compared with those obtained by using the maximum absorbance method at 16-cm^{-1} reso-

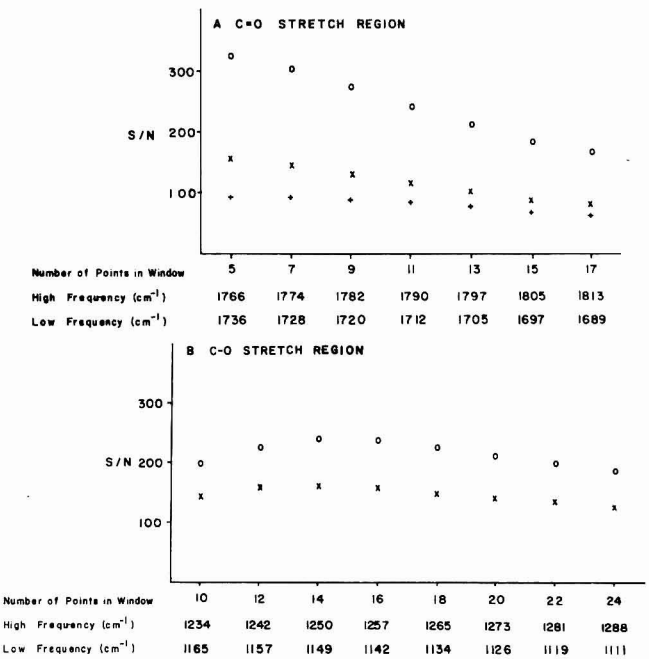

Figure 3. Variation of S/N with the number of points in the window for the integrated absorbance method for sample 1 at 16-cm^{-1} resolution. All windows include the top of each band in Figure 4: (O) ethyl acetate, (X) isobutyl methacrylate, (+) diethyl ketone.

lution. The maximum absorbance method gives a better S/N for GC peaks 1, 2, 4, 6, 8, and 9 (all hydrocarbons) and a poorer S/N for GC peaks 5 (diethyl ketone) and 10 (*p*-xylene). These differences reflect variations in the relative maximum absorbance when compared to the total integrated area of these compounds. At the extremes, the maximum absorbance method should be better for a compound with one narrow absorption, and the Gram–Schmidt method should be better for a compound with many broad absorptions of equal intensity. For the four solvent impurity peaks near the detection limit, the maximum absorbance method gives a similar S/N for peaks 11 and 12, but a much larger S/N for peaks 8 and 9.

The compounds in sample 2 gave the best S/N using double-sided vectors with NBV = 10, NPT = 100, and DISP in the range +40 to +80. Increasing NBV to 20 and 30 did not increase the S/N values. The compounds in sample 2 were expected to have an optimum value of DISP further from the centerburst, because their major bands are narrower than the major bands of the compounds in sample 1. However, these optimum values of DISP may also result from the interferometer being less stable at the higher velocities employed for sample 2. The universal maximum absorbance and optimized

Table V. Comparison of S/N for Universal Maximum Absorbance and Gram–Schmidt Reconstructions

	S/N for compounds in sample 1												
reconstruction method	1	2	3	4	5	6	7	8	9	10	11	12	13
G.S.,[a] DISP = −50, single sided	20	39	434	79	157	44	58	3.0	4.6	82	8.2	7.1	243
GS.,[a] DISP = +20, double sided	14.5	32	652	75	191	32	41	2.1	1.9	57	3.6	2.8	400
M.A.,[b] 16 cm^{-1}	32	52	640	127	140	52	59	6.0	10.6	67	6.4	8.2	395

	S/N for compounds in sample 2			
	1	2	3	4
M.A.,[c] 16 cm^{-1}	124	41	54	127
G.S.,[a] DISP = +60, double sided	68	35	55	193
G.S.,[a] DISP = +10, double sided	33	24	23	89

[a] NTP = 100, NBV = 10. [b] Frequency window 3100–2850 cm^{-1}, 1800–1000 cm^{-1}. [c] Frequency window 3100–2850 cm^{-1}, 1800–700 cm^{-1}.

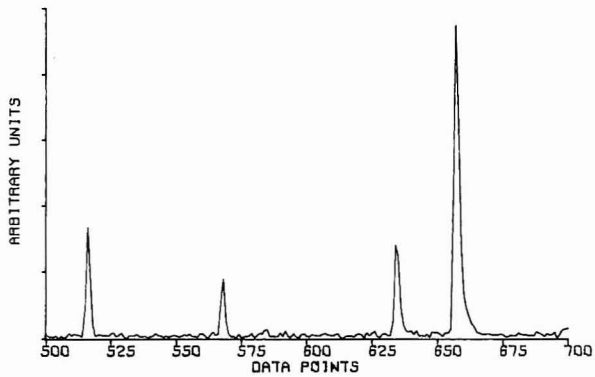

Figure 4. Universal Gram–Schmidt reconstruction for sample 2 using double-sided vectors and DISP = +60.

Gram–Schmidt reconstructions are shown in Figures 2A and 4, respectively. The S/N of the GC peaks obtained by using the Gram–Schmidt method are compared with those obtained with the maximum absorbance method in Table V. The results at DISP = +10 have been included to show how sensitive the Gram–Schmidt method is to the value of DISP. Again, the S/N is better using the maximum absorbance method for some compounds and worse for others. However, the selection of the optimum values of parameters was easier using the maximum absorbance method than the Gram–Schmidt method. From the Gram–Schmidt results obtained in this study, it appears that any universal compromise set of parameters could involve a loss in sensitivity of up to a factor of 2 for some compounds.

CONCLUSIONS

The maximum absorbance algorithm can be used to create both universal and selective reconstructions. The best sensitivity is obtained at a resolution of 16 cm^{-1} for most compounds. At present, the full sensitivity is not available in real time, due to compromises used in the calculations. However, improvements in computer speed and structure should make the full sensitivity available in the near future. The maximum absorbance method should replace the integrated absorbance method of creating chemigrams, because it is more sensitive, even in real time with the current reduction in sensitivity. In contrast to the integrated absorbance method, the sensitivity does not decrease when the size of the frequency window is increased to include sections of base line. This results because the maximum absorbance method employs an extremely narrow window, which can move within a larger window to find the peak maximum, and ignore the rest of the larger window. Thus, the maximum absorbance method is substantially more sensitive than the integrated absorbance method for universal reconstructions and selective reconstructions where the frequency window is much larger than the bandwidth of the peak within the window. With the maximum absorbance method, it is possible to select a wide window to include infrared peaks at different frequencies without the penalty of a loss of S/N. This will often be necessary, because many characteristic frequencies vary significantly from compound to compound.

The best senstivity obtained by using the maximum absorbance method for universal reconstructions is better than that obtained by using the *optimized* Gram–Schmidt for some compounds, and worse for others. This variation arises because the maximum absorbance method utilizes peak height, whereas the Gram–Schmidt method uses the total integrated area. When the full sensitivity for the maximum absorbance method is available in real-time, it should be considered an alternative or supplement to the Gram–Schmidt method. The Gram–Schmidt method has the advantage that it involves fewer computations, although advances in computer technology should render this aspect less important in the future. The maximum absorbance method has the advantage that it is easier to understand, less sensitive to the values of parameters, and can be used to create both universal and selective reconstructions with good sensitivities.

ACKNOWLEDGMENT

We wish to thank P. R. Griffiths for the loan of the medium-range MCT detector.

LITERATURE CITED

(1) de Haseth, J. A.; Isenhour, T. L. *Anal. Chem.* **1977**, *49*, 1977–1981.
(2) Coffey, P. J.; Mattson, D. R.; Wright, J. C. *Am. Lab. (Fairfield, Conn.)* **1978**, *10*, 126–129.
(3) Hanna, D. A.; Hangac, G.; Hohne, B. A.; Small, G. W.; Wiebolt, R. C.; Isenhour, T. L. *J. Chromatogr. Sci.* **1979**, *17*, 423–427.
(4) Sparks, D. T.; Owens, P. M.; Williams, S. S.; Wang, C. P.; Isenhour, T. L. *J. Chromatogr. Sci.* **1985**, *39*, 288–296.
(5) White, R. L.; Giss, G. N.; Brissey, G. M.; Wilkins, C. L. *Anal. Chem.* **1983**, *55*, 998–1001.
(6) Brissey, G. M.; Henry, D. E.; Giss, G. N.; Yang, P. W.; Griffiths, P. R.; Wilkins, C. L. *Anal. Chem.* **1984**, *56*, 2002–2006.
(7) White, R. L.; Giss, G. N.; Brissey, G. M.; Wilkins, C. L. *Anal. Chem.* **1981**, *53*, 1778–1782.
(8) Drouen, A. C. J. H.; Billiet, H. A. H.; De Galan, L. *Anal. Chem.* **1985**, *57*, 962–968.
(9) Krishnan, K.; Curbelo, R.; Chiha, P.; Noonan, R. C. *J. Chromatogr. Sci.* **1979**, *17*, 413–416.
(10) Lowry, S. L.; Huppler, D. A. *Anal. Chem.* **1981**, *53*, 889–893.

RECEIVED for review December 30, 1985. Resubmitted March 31, 1986. Accepted May 20, 1986. Support of this research under National Science Foundation Grant CHE-82-08073 is gratefully acknowledged.

Probability Distributions of the Number of Chromatographically Resolved Peaks and Resolvable Components in Mixtures

Michel Martin,* David P. Herman, and Georges Guiochon

Ecole Polytechnique, Laboratoire de Chimie Analytique Physique, 91128 Palaiseau, France

A theoretical model of peak overlapping is developed on the basis that sample components are randomly distributed along the retention axis. This model overcomes some limitations of previous models, in that it takes into account the variation of the probability of interferences near the extremities of the retention interval, it does not require that the number of sample components be large, and it gives directly the probability distribution of the number of resolvable peaks for a known number of sample components rather than just simple averages. More importantly, the theory allows a prediction of the probability distribution of the number of components in a sample when the number of resolved peaks is known. Finally, the adherence of real-world chromatograms to the retention randomness assumption of the theory is tested by using retention data of 20 arbitrarily selected compounds with different chemical functionalities on 65 gas chromatographic stationary phases. The normalized cumulative frequency distributions of relative consecutive distances calculated for their specific retention volumes indicate agreement with the general hypothesis that component retentions of complex mixtures are free energy random.

The analyst generally recognizes that the peaks observed in a chromatogram may not necessarily correspond to pure individual components of a sample, especially when it is complex. In the past, the severity of the component overlapping problem has been generally overlooked. Only recently have statistical models addressing this problem in quantitative terms been reported in the literature. Rosenthal developed a model of the balls-in-a-box type, based on combinatorial analysis to describe the number of occurrences of singlets, doublets, ..., multiplets in a chromatogram (*1*). His experimental results were in excellent agreement with the predicted values for the number of overlap occurrences. The Rosenthal model, however, applies only to discrete chromatograms such as those provided by GC/MS with finite time scans.

More recently, Davis and Giddings developed a model of component overlap in multicomponent chromatograms based on Poisson statistics (*2*) which applies to continuous chromatograms. They derived a relationship that allows one to predict the probable number of components in the sample from a knowledge of the number of separated peaks in a chromatogram and the peak capacity of the system. Using the analogy between the depolymerization and separation processes, Martin and Guiochon derived an expression of the probable number of sample components in terms of the areas of the peaks observed in the chromatogram (*3*). These models allow an estimation of the average probable number of components in the sample mixture to be made, where the relative accuracy of the estimation is expected to increase with increasing component number. In addition, computer simulations of random chromatograms have shown that the Davis and Giddings model is strictly followed only when the system peak capacity exceeds the number of sample components (*4-6*).

The objective of the present work is therefore to provide a new model of the peak overlapping problem that can be applied equally well to chromatograms exhibiting both large and small component numbers. For this reason, the model must take into account the boundary effects, which have been neglected in the previous works. Indeed, the probability of interferences between component zones decreases in the vicinity of the extremities of the separation domain, because no zone can be present on either side of the extremities. This effect is negligible for large system peak capacities. Most importantly, this work intends to extend the previous models by predicting not only the average values of the number of peaks or of the number of components but also the probability distribution of these numbers.

THEORY

In this model, one first considers that the number of components, m, is known. It represents the total number of detectable sample components eluting within an interval X. In order to take into account the boundary effects, it is assumed that two components are located at the extremities of the retention interval, X, expressed in units of time, volume, length, retention index, or any other appropriate thermodynamic scale. In addition, the $m - 2$ other sample components are assumed to arrange themselves randomly within the interval X. Discussion about the validity of this assumption will be addressed later in this paper.

As in the previous models (*2*, *3*), a given component is represented by a point located at the zone maximum or, if desired, at its center of gravity. In order for two adjacent components to appear as two separated peaks in a chromatogram, the distance between their representative points must be larger or equal to some constant value, x_0. The assumption of the constancy of x_0 implies that the width of each individual component zone is constant. In fact, this equal peak width assumption is generally considered to be valid only over limited retention time ranges in gas chromatography with linear temperature programming as well as in reverse-phase liquid chromatography with proper linear programming of the mobile phase composition (*7*, *8*). For this reason, it is best to determine the total number of components in a sample by breaking a long chromatogram up into several smaller intervals where the individual peak widths within the subintervals can be assumed to be constant. The value of x_0 depends on the means used to scrutinize real chromatograms and to count the number of separated peaks. As previously discussed, it will be close to 6σ, where σ is the standard deviation of the zones, when base line separation is required between two peaks, or close to 2σ when a peak is counted each time a maximum appears in the chromatogram. While the effect of individual peak height variations on the value of x_0 is not explicitly accounted for in the model, it is felt that this might be done by considering x_0 as an average value resulting from these variations. It seems, however, that this effect is relatively minor (*4*). This value can be related to commonly used parameters reflecting the efficiency of the separation system, such as the peak capacity, n, defined on the basis of a x_0, rather than of a 4σ separation as originally described (*9*)

0003-2700/86/0358-2200$01.50/0 © 1986 American Chemical Society

$$n = 1 + X/x_0 \tag{1}$$

With the model described above, the problem of determining the probability, $P_{m,n}(p)$, that p separated peaks are observed in a separation system with a fixed peak capacity, n, when analyzing a sample with a known number of components, m, becomes the problem of estimating the probability that $(p - 1)$ intervals between adjacent points are larger than or equal to x_0 when $(m - 2)$ points are randomly distributed in the interval X. The solution to this classical probability problem has been known since the beginning of this century (*9*) and is given by (*9*, *10*)

$$P_{m,n}(p) = \frac{(m-1)!}{(p-1)!}\sum_{i=0}^{h}\frac{(-1)^i}{(m-p-i)!i!}\left(1 - \frac{p-1+i}{n-1}\right)^{m-2} \tag{2}$$

In this equation, the summation is terminated when i becomes larger than the smaller of the two values $(m - p)$ or the integer part of $(n - p)$.

Simple expressions for the average number of peaks, $\bar{p}$, and for the variance of the probability distribution of the number of peaks, σ_p^2, can be obtained

$$\bar{p} = 1 + (m-1)\left(1 - \frac{1}{n-1}\right)^{m-2} \tag{3}$$

and

$$\sigma_p^2 = (\bar{p} - 1)\left[1 + (m-2)\left(1 - \frac{1}{n-1}\right)^{m-2} - (\bar{p} - 1)\right] \tag{4}$$

The major steps in the derivation of these expressions are indicated in the Appendix.

Equations 2–4 thus provide a solution to the problem stated above; i.e., what is the probability of observing p peaks for a given number of components, m, and at fixed peak capacity, n? The analyst, however, does not always know the number of components in the sample but can only count the number of peaks separated in the chromatogram. The problem becomes consequently the following: After having observed p peaks at a given known peak capacity, n, what is the probability distribution of the number of components in the sample, $P_{p,n}(m)$? The answer is provided by Bayes' theorem on the probability of the hypotheses

$$P_{p,n}(m) = \frac{P_0(m)\, P_{m,n}(p)}{\sum_{m'=p}^{\infty} P_0(m')\, P_{m',n}(p)} \tag{5}$$

In this equation, $P_0(m)$ represents the a priori probability that the sample mixture contains m components, such that

$$\sum_{m'=p}^{\infty} P_0(m') = 1 \tag{6}$$

The analyst has usually no reason to suspect that the mixture is more likely to contain m_1 than m_2 components ($m_1 \neq m_2$) unless m_1 and m_2 differ greatly. Consequently, we will assume that $P_0(m')$ is essentially constant for all reasonable values of m. Equation 5 then becomes

$$P_{p,n}(m) = \frac{P_{m,n}(p)}{\sum_{m'=p}^{\infty} P_{m',n}(p)} \tag{7}$$

Therefore, the desired probability that p observed peaks originate from a mixture of m components is equal to the one given by eq 2 divided by a normalization constant. In order to calculate this constant, the infinite sum in eq 7 can conveniently be replaced by a finite one, which is given in the Appendix.

RESULTS AND DISCUSSION

Examples of the Probability Distribution of the Number of Peaks Obtained with a Known Number of Components. The calculation of the probability given by eq 2 for each value of p between 1 and $\inf(m,I(n))$ when m and n are fixed leads to a histogram of the probability distribution of the number of x_0-resolved peaks. Representative histograms are plotted in Figure 1 for the singular case where $m = 20$ at four different values of the peak capacity, i.e., $n = 10$, 20, 50, and 100. In all cases the distributions appear approximately symmetric about some mean value. It is interesting to compare them with a Gaussian probability density distribution, P', having the same mean value and variance as the true one

$$P' = \frac{1}{\sigma_p(2\pi)^{1/2}}\exp\left[-\frac{(p-\bar{p})^2}{2\sigma_p^2}\right] \tag{8}$$

with $\bar{p}$ and σ_p^2 given by eq 3 and 4. The corresponding curves are also plotted in Figure 1. They are seen to closely approximate the true distributions, especially for intermediate values of the peak capacity when they are not truncated near the extremities of the range of p values, i.e., where neither $m/n << 1$ nor $m/n >> 1$.

The probability distributions shown in Figure 1 give some complementary insight to previous works as to the seriousness of the peak overlapping problem. The most interesting feature of these distributions is the information contained in their breadth and more specifically their limits. For example, we see that for the case where $m = 20$, $n = 50$, if we were to perform a single chromatographic experiment, we could not (even with good luck) reasonably expect to observe more than about 18 resolved peaks in the resulting chromatogram. Conversely, we realize from these data that there is also a small yet distinct possibility that we may be so unfortunate as to obtain as little as 10 resolved peaks. It is exactly this information on the breadth of the probability distribution that distinguishes the current model from all previous models in that they only yield estimates of the average number of expected peaks and hence contain no inherent information as to practical limits.

Probability That All the Components in a Mixture Are Separated. A common objective of the analyst is to resolve all the components of a sample. The theory developed above allows one to estimate what the probability is that this objective will be satisfied. The application of eq 2 to the case where $p = m$ gives the probability, $P_{m,n}(m)$, that all the sample components are separated. Obviously, this can occur only when $m < n$, in which case one has

$$P_{m,n}(m) = \left(1 - \frac{m-1}{n-1}\right)^{m-2} \tag{9}$$

The variation of this probability is plotted in Figure 2 as a function of the peak capacity for four values of m. One notes that only under the most favorable of conditions (i.e., relatively long analysis times and/or use of highly efficient columns operated under programming conditions) can peak capacities based on a 2σ separation definition be larger than approximately 1000 in capillary GC or 200 in packed column gradient elution LC. Hence we see from Figure 2 that one has only a marginal hope (less than 1% chance) of fully separating all the components of a sample from a single-shot, arbitrarily chosen, nonoptimized chromatogram in LC and GC when their component numbers exceed about 30 and 70, respectively. We

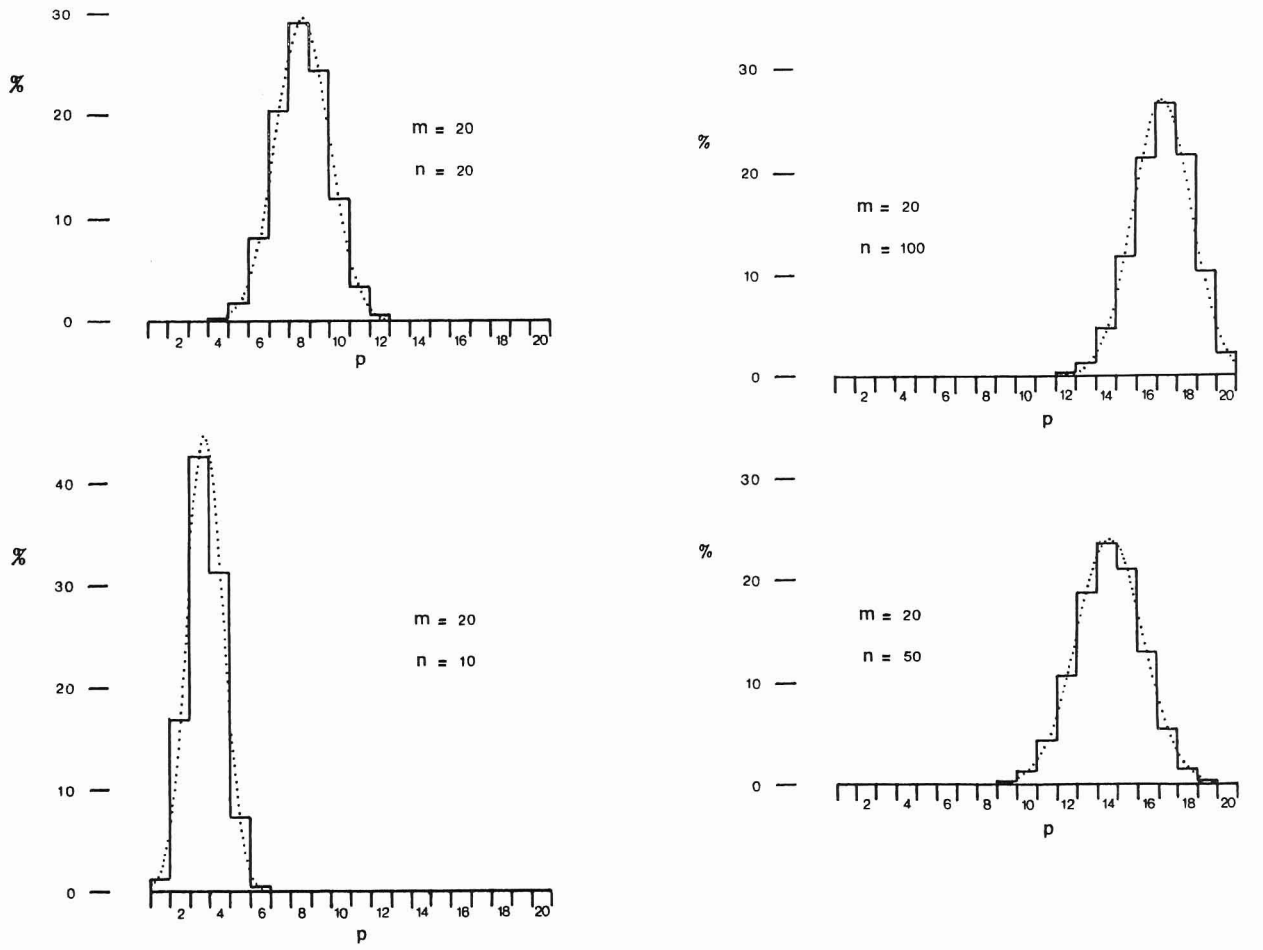

Figure 1. Probability distributions of the number of (p) peaks observed in chromatograms containing m = 20 components at peak capacities (n) of 10, 20, 50, and 100. The dotted curves represent the Gaussian approximations.

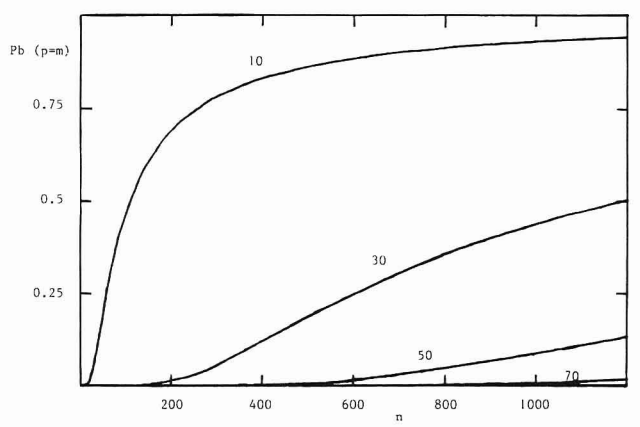

Figure 2. Plots of the probability that all (m) sample components will be separated, Pb(p = m), as a function of the system peak capacity, n, for the representative cases where m = 10, 30, 50, and 70.

realize that eluent optimization procedures are directed toward making more efficient use of the separation space than those where chromatographic conditions are chosen at random. Hence, complete separation of mixtures of greater complexities than those indicated above may be frequently possible when eluent compositions are optimized. One should not conclude however that the process of optimization somehow invalidates the randomness hypothesis of the model, but rather optimization can be viewed as simply being the process whereby one searches for those sets of conditions where the probability distribution, $P_{m,n}(p)$, is at an extreme limit, i.e., where p = m.

In Figure 3, the minimum value of the peak capacity, n_{min}, required to separate all sample components with a given probability, P_x, is plotted vs. the number of components for three values of P_x.

According to eq 9, it is equal to

$$n_{min} = 1 + (m - 1)/(1 - P_x^{1/(m-2)}) \qquad (10)$$

and is seen to increase dramatically with small increases in component numbers. Indeed, when this number is large, n_{min} increases as $m^2/[\ln (1/P_x)]$. Figure 3 shows that for a single trial-and-error chromatogram, one has little hope to separate all the sample components in a mixture with good probability, for instance 90%, unless one makes use of separation systems with very large peak capacities and associated very long analysis times for analyzing samples of low or moderate complexities. If however the operator were to take a trial-and-error approach where after an unsuccessful initial run several independent phase systems of differing selectivity were sequentially tried, the probability that the sample mixture can be totally resolved on at least one of the phase systems increases dramatically in accordance with the multiplication theorem for stochastically independent events. For example, let us assume that one has k mutually independent chromatographic systems or columns on which the sample components are randomly retained as described above. The probability Pb(k) that the mixture is totally resolved on at least one column is the complement of the probability that the separation is incomplete on all columns. Since this latter event must occur for all independent columns, one has according to the multiplication theorem for stochastically independent events

$$\mathrm{Pb}(k) = 1 - \prod_{i=1}^{k}[1 - P_{m,n_i}(m)] \qquad (11)$$

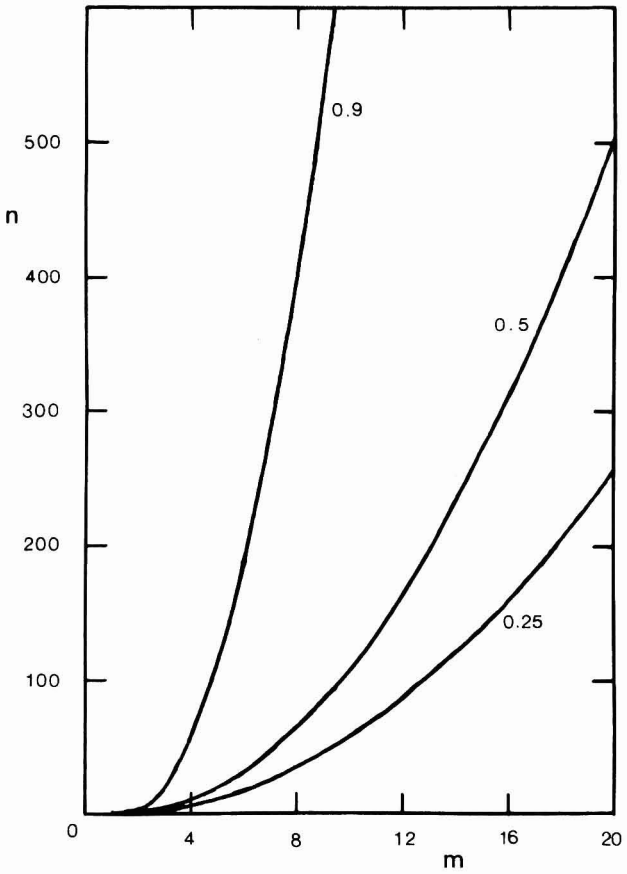

Figure 3. Plot of the peak capacity required to ensure with a given probability that all (m) sample components will be x_0 separated vs. the number of such sample components at the three probability levels of 0.9, 0.5, and 0.25.

If the k columns have the same peak capacity, n, one has, from equations 9 and 11

$$\mathrm{Pb}(k) = 1 - \left[1 - \left(1 - \frac{m-1}{n-1}\right)^{m-2}\right]^k \qquad (12)$$

It can easily be calculated that for a 10-component mixture analyzed on a column with a peak capacity of 50, the probability of complete resolution of the mixture from a single experiment is only 20%. If now the mixture is injected on 10 independent noncorrelated columns of similar peak capacity (n = 50), there is an 89% probability that the mixture will be totally resolved on at least one column.

Probability Distribution of the Number of Sample Components When the Number of Separated Peaks and the Peak Capacity Are Known. The determination of the probability distribution of the number of sample components is of direct interest to the analyst who has enumerated the number of x_0-separated peaks in a mixture chromatogram and can determine the peak capacity of the chromatographic system by appropriate peak broadening measurements on pure standard compounds with a chemical structure similar to that of the sample components. This probability distribution is computed from eq 7 in combination with eq 2. More simply, a nonnormalized distribution is directly calculable from eq 2, by neglecting the normalization constant in the denominator of eq 7.

Figure 4 shows the histogram of such a probability distribution when 10 peaks are observed with a chromatographic system having a peak capacity of 20. The calculation of the probability $P_{p,n}(m)$ can be simplified as shown above by using the Gaussian approximation expressed in eq 8, combined with eq 3 and 4. The approximation curve so obtained is also plotted in Figure 4 and is seen to be in close agreement with

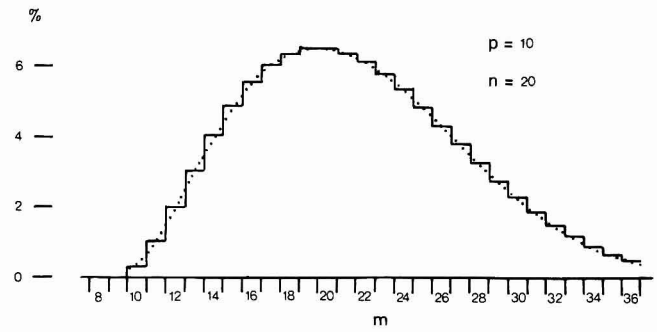

Figure 4. Probability distribution of the number of (m) possible sample components responsible for producing a chromatogram exhibiting p = 10 peaks when the system peak capacity is measured to be n = 20, $P_{p,n}(m)$. The dotted curve represents the "Gaussian approximation" (see text).

the exact histogram. Although it is referred to as a "Gaussian approximation", this curve is obviously no longer Gaussian since the variable in eq 9 is now m rather than p, where p is now assumed to be known and hence fixed. Although the most probable value of the number of components is 19–20, the calculated probability distribution clearly indicates that there is a small yet real chance that a chromatogram exhibiting 10 peaks within an interval of peak capacity 20 could have originated from a mixture containing as little as 10 or 11 components or as many as 36 or 37. The importance of the current model is thus due to its ability to calculate this range of "possible" component numbers at any specified probability level from experimentally determined p and n values, rather than simply $\bar{m}$, the average expected component numbers.

Depending upon the relative values of the number of resolved peaks and of the system peak capacity, uni- or bimodal distributions of $P_{p,n}(m)$ can be obtained. In Figure 5 a histogram of the component number distribution, when p is still equal to 10 but where n is now equal to 50, is plotted. An expanded scale plot at relatively small values of m is also shown along with its Gaussian approximation.

It is an interesting feature of the present model that its single probability expression (eq 7) or its Gaussian approximation provides the component number probability distribution of either one or two modes whenever they are present. Moreover, the theory allows any prior knowledge about the number of sample components to be included in the calculations. For instance, if it is known before performing the chromatographic analysis that the component number does not exceed, let us say, 50, then $P_0(m')$ will be set equal to 0 in eq 6 for every value of $m > 50$ and the distribution will have only the first mode shown in Figure 5. The results from the separation process, such as those shown in Figure 5, which constitute an a posteriori probability distribution of the number of components, can be used as an a priori distribution, $P_0(m')$, to be entered into eq 5 when a further independent analysis of the sample is to be performed. The outcome from such a pair of analyses should lead to the virtual disappearance of one of the two initial apparent modes and to a significant sharpening of the remaining principal mode.

Adherence of Real-World Chromatograms to the Theory. In a previous publication the underlying assumption of component retention time randomness was demonstrated for a limited set of real samples chromatographed by TLC and GLC methods (*4*). We now wish to choose a much larger set of data (multiple independent chromatograms for which we know the actual number of components in the mixture) and address ourselves to the question of which of the retention parameters, e.g., interaction energies, capacity factors, etc., in GC and HPLC are most nearly random.

In one of the earlier publications by Davis and Giddings (*2*) an argument was made that the components of truly

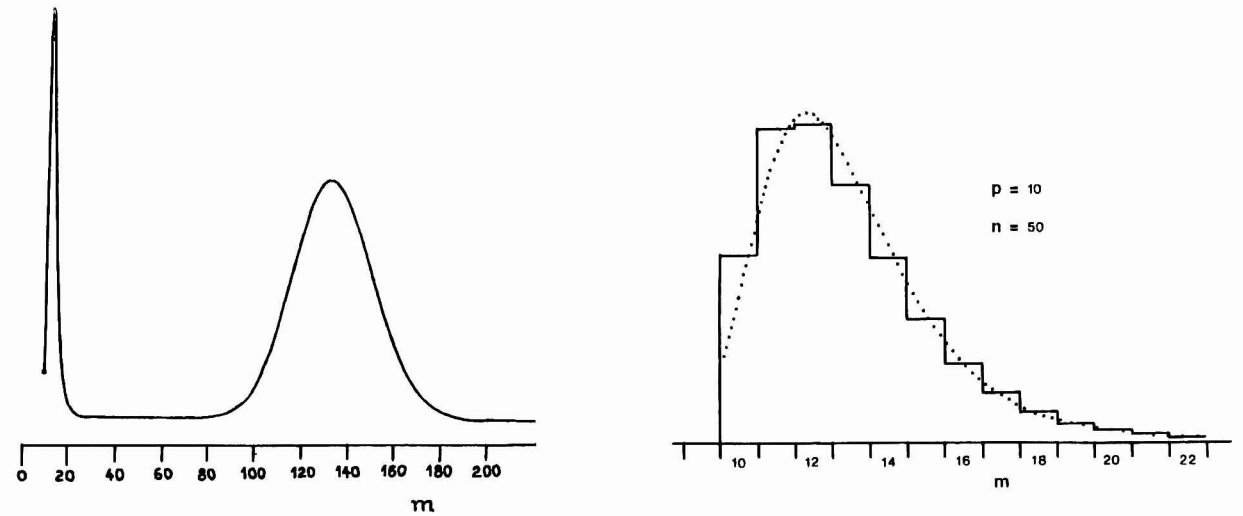

Figure 5. Total probability distribution of the component number, $P_{p,n}(m)$ for $p = 10$ and $n = 50$. The first mode is also shown on an expanded scale. The y axis is in arbitrary units and is therefore not indicated.

complex mixtures when chromatographed should distribute themselves randomly along the standard chemical potential scale, $\Delta\mu°$. If generally true, one would thus expect component retentions to be ln k' rather than k' random under isocratic and isothermal conditions in HPLC and GC, respectively. To date, no direct evidence in support of this hypothesis has been advanced in the literature. We should stress that such a conclusion will only remain valid when utilizing nonprogramming techniques in GC and HPLC for it has previously been demonstrated in the literature that the apparent k' of a sample component under typical programming conditions becomes nearly proportional to its interaction free energy at the beginning of the gradient program and hence proportional to ln k_0' (*7*, *8*). Thus, if the hypothesis of random standard chemical potentials is to be accepted as a general phenomenon in the chromatography of complex mixtures, large volumes of data must be scrutinized and shown to be ln k' and apparent k' random under nonprogramming and programming conditions, respectively. The subsequent data and discussion below should be viewed by the reader as only a start in that ongoing process.

A literature search was begun for the largest possible set of chromatographic retention data of pure compounds possessing diverse polarities, functional groups, shapes, etc., such that when artificially mixed they could be representative of the elution spectrum of a "typical" complex mixture. A rather large set of such data can be found in the handbook of Mc Reynolds (*12*). Therein the specific retention volumes, V_g, of approximately 340 compounds on 79 distinct stationary phases at two different isothermal temperatures are tabulated. From these data we have chosen to use a much smaller subset of 20 compounds on 65 stationary phases to test the above hypothesis of free energy randomness for one of several reasons. First, the data are not complete for all compounds on all stationary phases at a common analysis temperature. Second, many of the compounds tabularized are a member of the same homologous series as other entries in the handbook and are thus clearly not randomly spaced or hence assumed present in abundance in our hypothetical complex mixture. For this reason, all structural homologues that are known to be nearly equally spaced on the ln k' scale were eliminated from consideration. Beyond these requirements and restrictions an attempt was made to include at least one of each functional group type compound in the working subset of 20 and to choose compounds having approximately the same number of carbon atoms. Had the data set been much larger in size, i.e., had it contained many more compounds from among numerous additional functional groups, inclusion of all components (inclusive of homologues) could have been justified. However, when forced to use a limited subset of data to arrive at some conclusion as to the inherent distribution of a larger parent population, obvious outliers at the extremes of the distribution as well as consecutive data points having obvious correlation need be excluded from the limited subset. A list of the 20 eluites and 65 stationary phases selected can be found in Table I.

We have chosen to determine which of the two retention parameters, ln V_g or V_g of the 20 compounds, is most nearly Poisson distributed on each of the 65 stationary phases by attempting to fit the data to the following normalized cumulative Poisson probability function:

$$\ln\left(1 - \frac{N'}{m-1}\right) \Big/ (-m) = x_0/X \qquad (13)$$

Hence a plot of the cumulative integer number of points, N', separated from their nearest neighbors by less than the relative distance x_0/X when plotted as ln $(1 - N'/(m-1))/(-m)$ vs. x_0/X will yield a straight line with a slope of 1.0 and intercept equal to zero.

In Figure 6 the normalized cumulative distributions of relative consecutive distances in units of V_g and ln V_g for the 20 eluites of Table I are plotted for each of the 65 stationary phases and shown superimposed on single plots of ln $(1 - N'/(m-1))/(-m)$ vs. x_0/X. Note that each point in these plots represents one consecutive distance on one of the 65 chosen stationary phases. The equation line of slope 1.0 and intercept equal zero predicted for ideally random data are also drawn. It is easily seen that the GLC retention data of the 65 stationary phases, when expressed on the ln V_g retention scale, are on average more equally centered about the predicted line for ideally random data than when scrutinized as specific volumes, V_g. On the V_g retention scale the consecutive distances are clearly consistently lower than that predicted for randomly displaced components on nearly all the stationary phases studied. Also shown in the figure are the normalized cumulative Poisson distributions for 20 data points generated by using the random number generator function of the Commodore 3032 computer and repeated 65 times so as to closely simulate the GLC retention data but where the data are now known to be a finite subset of an infinite random number population. As anticipated there are in all instances large degrees of scatter about the predicted lines owing to the finiteness of the data sets.

Via comparisons to the normalized cumulative frequency distribution of the random number generator data, it is

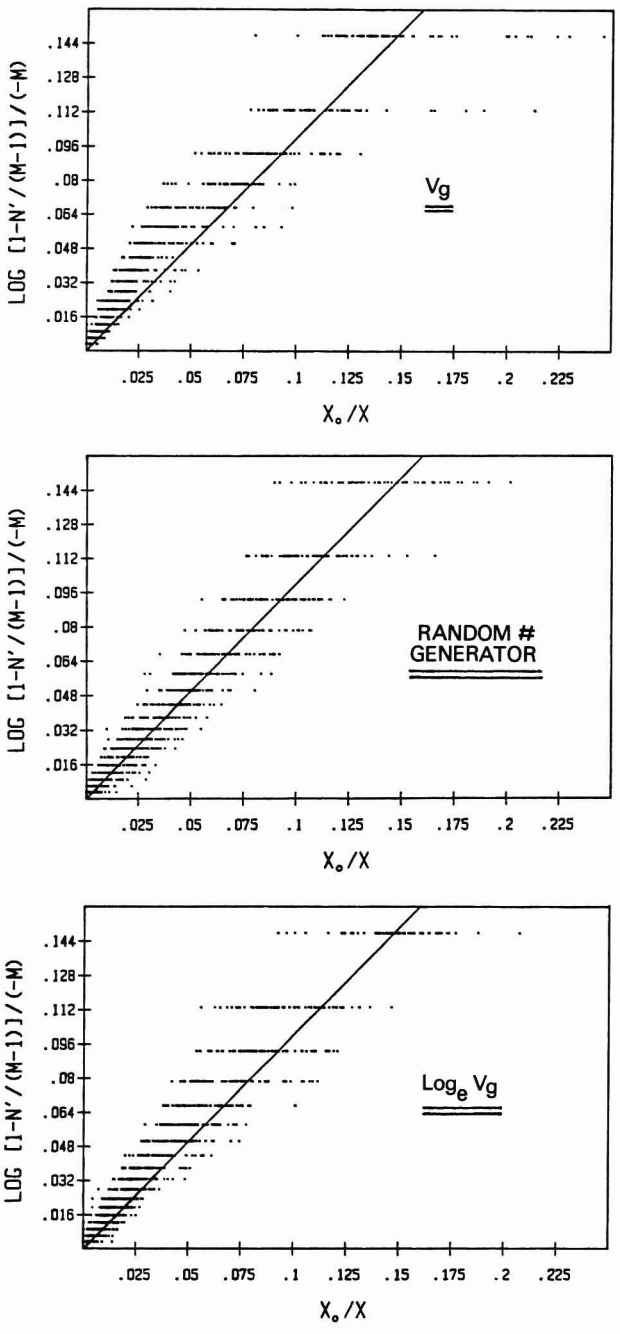

Figure 6. Normalized cumulative frequency distributions of relative consecutive distances, x_0/X. Comparisons between the V_g (upper plot) and the ln V_g (lower plot) data for the 20 eluites on the 65 GC stationary phases listed in Table I. The cumulative distributions calculated for 65 repetitions of a subset of 20 data from a random number generator are also shown (middle plot).

possible to obtain a numerical qualitative measure of the extent to which the finite V_g and ln V_g data are Poisson distributed. Owing to the fact that all the data presented above must fall along the same universal line according to eq 13, a simple sum of squares of deviations between the observed data points of Figure 6 for each stationary phase and the predicted ideal line will be an adequate numerical measure of apparent randomness of the finite data population. Defining y_i and x_i to be equivalent to the left-hand and right-hand sides of eq 13, respectively, we calculate the sum of squares deviations for the $i = m - 2$ consecutive intervals of each stationary phase as

$$r^2 = \sum_{i=1}^{m-2} (y_i - x_i)^2/y_i \qquad (14)$$

We divide the observed squared deviation by y_i in eq 14 owing to the fact that the deviations are observed to increase nearly linearly with increasing y_i and hence choose to weight the residuals accordingly. The r^2 values of the 65 stationary phases were averaged for the V_g, ln V_g, and random number generator data of Figure 6 and were calculated to be 4.7×10^{-3}, 2.7×10^{-3}, and 2.6×10^{-3}, respectively. The corresponding standard deviations in r^2 were 3.1×10^{-3}, 1.4×10^{-3}, and 1.9×10^{-3}, respectively. We note that there is sizable overlap in these distributions such that on 12 of the 65 stationary phases the V_g data of the chosen 20 compounds are more random according to the criteria of eq 13 than when expressed on the ln V_g scale. However, on the greater majority of the stationary phases studied, ln V_g values are observed to be considerably more randomly spaced than when expressed as V_g data as evidenced by the high correlation between the cumulative frequency distribution of the ln V_g and the random number generated data. Hence we conclude that our finding are in general agreement with the hypothesis of Davis and Giddings; i.e., component retention of complex mixtures in chromatographic systems is free energy random.

APPENDIX

Average and Standard Deviation of the Probability Distribution of the Number of Peaks when *m* and *n* Are Fixed. Let r be the number of intervals between adjacent points larger than or equal to x_0. One has

$$r = p - 1 \qquad (A\text{-}1)$$

and

$$P''_{m,n}(r) = \frac{(m-1)!}{r!} \sum_{i=0}^{\inf(m-1-r,n-1-r)} \frac{(-1)^i}{(m-1-r-i)!i!}\left(1 - \frac{r+i}{n-1}\right)^{m-2} \qquad (A\text{-}2)$$

From eq A-1, one has

$$\bar{p} = 1 + \bar{r} \qquad (A\text{-}3)$$

with

$$\bar{r} = \sum_{j=0}^{\inf(m-1,n-2)} jP''_{m,n}(j) \qquad (A\text{-}4)$$

Developing the sum in eq A-4 for each value of j with the help of eq A-2 and rearranging the result by grouping terms with constant value of $j + i$, one gets

$$\bar{r} = \sum_{k=1}^{\inf(m-1,n-2)} \left(1 - \frac{k}{n-1}\right)^{m-2} \frac{(m-1)!}{(m-1-k)!} \sum_{i=1}^{k} (-1)^{k-i} \frac{1}{(i-1)!(k-i)!} \qquad (A\text{-}5)$$

For all values of k except 1, one can write

$$\sum_{i=1}^{k} (-1)^{k-i} \frac{1}{(i-1)!(k-i)!} = \frac{(-1)^{k-1}}{(k-1)!} \sum_{j=0}^{k-1} (-1)^j \frac{(k-1)!}{j!(k-1-j)!} \qquad (A\text{-}6)$$

The sum in the right-hand term of eq A-6 is easily recognized as equal to $[1 + (-1)]^{k-1}$, which is zero, according to the binomial theorem. Therefore, the double sum in equation A-5 is reduced to only the $k = 1$ term, which gives

$$\bar{r} = (m-1)\left(1 - \frac{1}{n-1}\right)^{m-2} \qquad (A\text{-}7)$$

From eq A-3, one gets the average value of p given in eq 3.

Table I. Eluites and Stationary Phases Selected from Reference 12 To Test Random Interaction Energy Hypothesis

eluites	GLC stationary phases		
isobutyl alcohol	Apiezon J	Apiezon L	Apiezon M
sec-butyl alcohol	Apiezon N	bis(2-ethoxy) phthalate	Carbowax 300
tert-butyl alcohol	Carbowax 400	Carbowax 600	Carbowax 1000
3-buten-1-ol	Carbowax 1540	Carbowax 4000	Carbowax 6000
3-buten-2-ol	Carbowax 20M	Castorwax	Citroflex A-4
butyraldehyde	dibutyl tetrachlorophthalate	di-2-ethylhexyl adipate	di-2-ethylhexyl sebacate
isobutyraldehyde	diisodecyl phthalate	dioctyl phthalate	dioctyl sebacate
2-butanone	docosanol	Dow Corning 550 Fluid	Dow Corning FS 1265 Fluid
3-buten-2-one	Ethofat 60-25	Flexol 8N8	Hallcomid M18
propyl formate	Hallcomid M18 OL	Igepal CO 880	isooctyl decyl adipate
isopropyl formate	neopentyl glycol adipate	neopentyl glycol adipate terminated	neopentyl glycol succinate
ethyl acetate	Oronite NIW	Pluronic F68	Pluronic F77
methyl propionate	Pluronic F88	Pluronic L42	Pluronic L44
methyl acrylate	Pluronic L63	Pluronic L72	Pluronic P46
ethyl methyl formal	Pluronic P65	Pluronic P84	Pluronic P85
ethylene glycol acetal	polyphenyl ether-5 rings	polyphenyl ether-6 rings	Quadrol
propyl methyl ether	SE 30	SE 30 polyester NPGA terminated	SE 31
1,2-butylene oxide	SE 52	squalane	sucrose acetate isobutyrate
trans-2,3-butylene oxide	sucrose octaacetate	Tergitol NPX	TMP tripelargonate
tetrahydrofuran	tricresyl phosphate	triethylene glycol succinate	Triton X 305
	Ucon LB-1715	Ucon 50 HB-2000	Versilube F-50
	XF 1150	Zonyl E7	

The variance of the p distribution is equal to the variance of the r distribution and is given by

$$\sigma_p^2 = \sum_{i=0}^{\inf(m-1,n-2)} i^2 P''_{m,n}(i) - \bar{r}^2 = S - \bar{r}^2 \qquad \text{(A-8)}$$

The double sum S can be rearranged similarly to what has been done above to give

$$S = \sum_{i=0}^{\inf(m-1,n-2)} \left(1 - \frac{k}{n-1}\right)^{m-2} \frac{(m-1)!}{(m-1-k)!} \sum_{i=1}^{k} \frac{i(-1)^{k-i}}{(i-1)!(k-i)!} \qquad \text{(A-9)}$$

One can write

$$S' = \sum_{i=1}^{k} \frac{i(-1)^{k-i}}{(i-1)!(k-i)!} = \frac{(-1)^k}{(k-1)!}\left[\sum_{i=1}^{k}(-1)^i \frac{(i-1)(k-1)!}{(i-1)!(k-i)!} + \sum_{i=1}^{k}(-1)^i \frac{(k-1)!}{(i-1)!(k-i)!}\right] \qquad \text{(A-10)}$$

S' can be rearranged in order to make apparent the binomial coefficients in the two sums of eq A-10. One gets

$$S' = \frac{(-1)^k}{(k-1)!}\left[(k-1)\sum_{j=0}^{k-2}(-1)^j \frac{(k-2)!}{j!(k-2-j)!} - \sum_{j=0}^{k-1}(-1)^j \frac{(k-1)!}{j!(k-1-j)!}\right] \qquad \text{(A-11)}$$

According to the binomial theorem, the two sums in eq A-11 are reduced to their first $j = 0$ terms, which gives for S

$$S = (m-1)\left(1 - \frac{1}{n-1}\right)^{m-2} + (m-1)(m-2)\left(1 - \frac{2}{n-1}\right)^{m-2} \qquad \text{(A-12)}$$

After rearrangement of S and combination with eq A-8, one gets the desired expression for σ_p^2 given in eq 4.

Normalization Constant of the Probability Distribution of the Component Number When p and n Are Fixed. This normalization constant, C, is equal to

$$C = \sum_{m'=p}^{\infty} P_{m',n}(p) \qquad \text{(A-13)}$$

where $P_{m',n}(p)$ is given by eq 2. Developing the sum for each value of m' and grouping terms with constant value of $m' + i$, it becomes

$$C = \sum_{i=0}^{n-p-1}\left(1 - \frac{p-1+i}{n-1}\right)^{p-2+i} \frac{(-1)^i}{(p-1)!i!} \sum_{j=0}^{\infty} \frac{(p-1+i+j)!}{j!}\left(1 - \frac{p-1+j}{n-1}\right)^j \qquad \text{(A-14)}$$

It is easy to show that the function

$$S_k(x) = \sum_{j=0}^{\infty} \frac{(k+j)!}{j!} x^j \qquad \text{(A-15)}$$

obeys to the following recurrence relationship:

$$S_k(x) = \frac{dS_{k-1}(x)}{dx} \qquad \text{(A-16)}$$

Since $S_0(x)$ represents the serial development of $1/(1-x)$, one gets

$$S_k = \frac{d^k S_0(x)}{dx^k} = \frac{k!}{(1-x)^{k+1}} \qquad \text{(A-17)}$$

If one replaces k by $(p-1+i)$ and x by $[1-(p-1+i)/(n-1)]$ in eq A-17 and combines the results with eq A-14, it becomes

$$C = \sum_{i=0}^{n-p-1}\left(1 - \frac{p-1+i}{n-1}\right)^{p-2+i} \frac{(-1)^i}{(p-1)!i!} \frac{(p-1+i)!}{\left(\frac{p-1+i}{n-1}\right)^{p+i}} \qquad \text{(A-18)}$$

After rearrangement, one obtains

$$\left(1 - \frac{p-1+i}{n-1}\right)^{p-2+i} \Big/ \left(\frac{p-1+i}{n-1}\right)^{p+i} = \left(\frac{n-1}{p-1+i}\right)^2 \left(\frac{n-p-i}{p-1+i}\right)^{p-2+i} \qquad \text{(A-19)}$$

Combining eq A-18 and A-19 and noting that

$$\frac{(p-1+i)!}{(p-1)!} = \prod_{j=1}^{i}(p-1+j) \qquad \text{(A-20)}$$

with the convention that $\prod = 1$ if $i = 0$, one obtains the final expression for C

$$C = \sum_{i=0}^{n-p-1} \frac{(-1)^i}{i!}\left(\frac{n-p-i}{p-1+i}\right)^{p-2+i}\left(\frac{n-1}{p-1+i}\right)^{2}\prod_{j=1}^{i}(p-1+j) \qquad \text{(A-21)}$$

For practical computational purposes, one can note that

$$T_i = \frac{(-1)^i}{i!}\prod_{j=1}^{i}(p-1+j) = -T_{i-1}\frac{p-1+i}{i} \qquad \text{(A-22)}$$

with $T_0 = 1$. Although still expressed as a sum, eq A-21 is much more convenient for practical purposes than eq A-13 or A-14, since its sum contains only $n - p$ terms while the latter equations are made of an infinite number of terms.

ACKNOWLEDGMENT

Fruitful discussions with Joseph Gril and Jean-Baptiste Leblond of the Laboratoire de Mécanique des Solides, Ecole Polytechnique, are greatly acknowledged.

LITERATURE CITED

(1) Rosenthal, D. *Anal. Chem.* **1982**, *54*, 63–66.
(2) Davis, J. M.; Giddings, J. C. *Anal. Chem.* **1983**, *55*, 418–424.
(3) Martin, M.; Guiochon, G. *Anal. Chem.* **1985**, *57*, 289–295.
(4) Herman, D. P.; Gonnord, M. F.; Guiochon, G. *Anal. Chem.* **1984**, *56*, 995–1003.
(5) Davis, J. M.; Giddings, J. C. *J. Chromatogr.* **1984**, *289*, 277–298.
(6) Giddings, J. C.; Davis, J. M.; Schure, M. R. *Ultrahigh Resolution Chromatography*; Ahuja, S., Ed.; American Chemical Society: Washington, DC, 1984; ACS Symposium Series 250, pp 9–26.
(7) Habgood, H. W.; Harris, W. E. *Anal. Chem.* **1960**, *32*, 450–453.
(8) Snyder, L. R. *High-Performance Liquid Chromatography—Advances and Perspectives*; Horváth, C., Ed.; Academic Press: New York, 1980; Vol. 1, pp 207–316.
(9) Giddings, J. C. *Anal. Chem.* **1967**, *39*, 1027–1028.
(10) Kendall, M. G.; Moran, P. A. P. *Geometrical Probability*; Charles Griffin & Co. Ltd.: London, 1963; Chapter 2.
(11) Santalo, L. A. *Integral Geometry and Geometric Probability*; Encyclopedia of Mathematics and Its Applications; Addison-Wesley: London, 1976; Vol. 1, Chapter 2.
(12) Mc Reynolds, W. O. *Gas Chromatographic Retention Data*; Preston Technical Abstracts: Evanston, IL, 1966.

RECEIVED for review October 19, 1984. Resubmitted May 5, 1986. Accepted May 5, 1986. Part of this paper was presented at the 15th International Symposium on Chromatography, Nürnberg, Germany, October 1–5, 1984.

Physical Model for Gas–Solid Chromatography with Volatile and Nonvolatile Modifiers

Jon F. Parcher,* Ping J. Lin, and David M. Johnson

Chemistry Department, University of Mississippi, University, Mississippi 38677

The two-dimensional (adsorption) version of the scaled particle solution theory has been used to interpret the single-component isotherms of propane, butane, and acetone on a graphitized carbon black adsorbent over a range of temperatures. In addition, the multicomponent adsorption model has been used to develop an equation to describe the retention volume of an infinite dilution solute as a function of surface coverage by a volatile modifier as well as to interpret the experimental results from previous investigations of such quasi-binary chromatographic systems. Several sets of binary chromatographic data in the form of the retention volume of one solute as a function of the surface coverage by a different solute were regressed to the proposed retention volume equation. The adsorption coefficients of each solute obtained from the binary isotherm data (propane + butane and acetone + butane) agreed with those determined from the single-component isotherms as well as those calculated from specific retention volumes of the infinite dilution solutes with no modifier present. The retention volume equation provides the first quantitative description for the retention of one solute as a function of the surface coverage by a second component.

Volatile "modifiers" are commonly used in gas, liquid, and supercritical fluid chromatography (SFC) to decrease the retention and improve the peak shape of eluted samples. The modifiers are usually low molecular weight, polar materials, such as water, alcohols, or amines, which are usually added to the inert gas mobile phase in relatively low concentrations. Nonvolatile modifiers have been used as well to improve the efficiency of gas–solid chromatographic systems. In particular, the graphitized carbon black adsorbents, such as the Carbopacks, are commonly coated with a low percentage of a polar liquid phase. Although the use of these modifiers is common, they introduce a certain "black-magic" aspect to chromatography because there is no theoretical model for the prediction of the effect of a given modifier in any chromatographic system. Most of the current applications involving volatile or nonvolatile modifiers have been developed empirically by experienced chromatographers. Thus, there is a tremendous need for a sound theoretical model that will allow the design of a system for a particular separation that requires the use of some type of modifier.

Recently supercritical fluid chromatography has emerged as a viable separation method to bridge the gap between GC and HPLC. Many studies (*1–5*) have shown that volatile modifiers added to the supercritical mobile phase improved the chromatographic separations in SFC. The most common interpretation of the effect of polar modifiers, such as ethanol, was that the modifiers interacted with the stationary phase to block residual, active sites, usually silanol groups, on the solid support. However, Hirata (*4*) has shown that the mechanisms are probably more complex because in some cases the modifier, especially at high concentrations, can cause an *increase* in the retention of some solutes. This enhancement has been attributed to either decreased solubility of the solute in the mobile phase or increased adsorption on, or absorption in, the stationary phase (*3, 4*). However, the exact mechanisms are uncertain. In addition, the physical properties, such as

0003-2700/86/0358-2207$01.50/0 © 1986 American Chemical Society

solubility, viscosity, diffusion coefficients, and critical properties, of supercritical systems, which are mixtures of a supercritical fluid and a subcritical modifier, have not been measured for most of the applicable systems.

The effects of volatile modifiers in gas–liquid and gas–solid chromatography have been investigated to a greater extent than in the case of SFC. Modifiers, such as steam, ammonia, and formic acid, have been used to eliminate the deleterious effects of solid support adsorption or to change the properties of the stationary liquid phase (*6*). In the case of gas–solid chromatography, very complex patterns were observed when the retention of an infinite dilution solute was measured as a function of the pressure or mole fraction of a volatile modifier in the mobile phase (*6–11*). In most cases, a maximum in the retention volume was observed at intermediate pressures. Later more quantitative studies (*9–11*) showed that the maximum occurred at surface coverages close to the point of formation of about one-half of a monolayer. That is, at low surface coverages, the retention volume of most elution samples increased with surface coverage. This cooperativity was attributed to the influence of lateral interactions between the eluted solute and preadsorbed modifier. At higher surface coverages, i.e., greater than 50% monolayer coverage, increased surface coverage resulted in decreased retention due to the loss of available surface area. Similar maxima have been observed at higher liquid loadings for porous supports (*12, 13*), although liquid surface adsorption and liquid distribution (wetting) effects were invoked to explain the experimental results.

Nonvolatile modifiers, i.e., low percentages of polar stationary liquid phases, have been used extensively, especially with the GCB adsorbents. Several reviews (*14, 15*) have been written on the effect of these modifiers; however, the experimental results are strikingly similar to those observed for volatile modifiers. The nonvolatile modifiers simply represent one extreme of an adsorption system with an adsorbate with very low equilibrium pressure. Di Corcia et al. (*14*) have discussed this subject and pointed out the similarities between the effects of volatile and nonvolatile modifiers.

The influence of both volatile and nonvolatile modifiers in the diverse forms of chromatography could theoretically be interpreted and ultimately predicted by a model for adsorption of multicomponent systems on heterogeneous, or at least quasi-homogeneous, adsorbents such as silica, alumina, or graphitized carbon black. The model would have to incorporate both specific and nonspecific solute–solute and solute–solid interactions as well as localized and mobile adsorption processes. No such theoretical model is currently available, although there are several models that have been developed for, or extended to, multicomponent adsorption systems. These models include the two-dimensional van der Waals equation (*8, 16*), ideal adsorbed solution model (*17*), vacancy theory (*18, 19*), and the potential theory method (*20, 21*).

An additional model has been developed by extension of a bulk solution model to a two-dimensional adsorbed state (*22, 23*). This scaled particle adsorption model is relatively simple, it is easily extended to multicomponent systems, and it was recently shown to be accurate for adsorption of mixtures of propane and propene on GCB (*23, 24*). The model was also adequate for the interpretation of chromatographic data for binary systems involving several infinite dilution solutes with benzene (*10*) and acetone (*11*) as modifiers on GCB over a range of pressures and temperatures *above the melting point of the modifier*. At temperatures close to or below the melting point of the modifier, the model was not accurate, presumably because of the strong, localized adsorption observed at the lower temperatures.

In the present investigation, a retention volume equation is derived from the multicomponent version of the scaled particle theory, and the model is evaluated for the interpretation of existing chromatographic data for binary systems comprised of mixtures of acetone, propane, and butane on GCB.

EXPERIMENTAL SECTION

The experimental procedure used for all of the investigations was mass spectrometric tracer pulse chromatography (MSTPC) (*25, 26*). This method involves the use of heavy, stable isotopes of the modifiers to measure the amount of modifier adsorbed on the stationary phase. A small sample of the isotopically labeled modifier was injected into the carrier composed of different amounts of natural modifier diluted with helium. The plug of labeled modifier as well as the other foreign solutes could be detected in the presence of natural modifier by a mass spectrometer operated in the selected ion monitoring mode without interference from a high background. The retention time of the labeled modifier was directly related to the amount of modifier adsorbed. This method gives the adsorption data directly and does not require an assumed isotherm equation or an integration sequence like all of the other chromatographic methods for measuring equilibrium isotherms (*8, 27*).

Only the adsorption isotherm of acetone at 20 °C was determined directly in the present investigation. The remainder of the experimental data were taken from previously published investigations (*28–30*). All of the experiments involved one type of graphitized carbon black, i.e., Carbopack C. However, the original data were reported on the assumption of a surface area of 12 m^2/g as reported by the manufacturer. In order to check the accuracy of the data for this investigation, the surface area of the adsorbent was determined from the adsorption isotherm of propane. Several authors (*26, 31, 32*) have reported a specific area of 30.1 $Å^2$ for propane adsorbed on GCB at ambient temperatures. All of the propane isotherms fit the BET isotherm equation with a calculated monolayer capacity of 43.9 $\mu mol/g$. This determination allowed a correct calculation of the surface area of the original adsorbent as 8.0 m^2/g, rather than the assumed 12.0 m^2/g. All of the experimental data (*28–30*) were corrected for this error in the originally reported surface area.

The parameters of the isotherm and retention volume equations were determined from the experimental data by using either Simplex optimization or nonlinear least squares. The minimization function in all cases was the square of the sum of errors between the calculated and observed pressures or retention volumes at fixed surface coverages. All of the calculations were limited to experimental data representing less than monolayer surface coverage because of the form of the isotherm model.

RESULTS AND DISCUSSION

The scaled particle adsorption model (*22*) was derived with the assumption that the adsorbates occupied "hard-core" areas, β_i, which usually correspond to about half the values obtained from the BET monolayer capacity. The surface coverage by component i was then represented as a "reduced" coverage, η_i, given by $\eta_i = \beta_i n_i^{ads}$, where n_i^{ads} corresponds to the amount ($\mu mol/m^2$) of component i adsorbed on the stationary phase. The single-component isotherm equation is (*22, 23*)

$$P_i = \frac{1}{K_i\beta_i}\frac{\eta}{1-\eta}\exp\left(\frac{(3-2\eta)\eta}{(1-\eta)^2} - \frac{2\alpha_i\eta}{\beta_i RT}\right) \qquad (1)$$

where P_i is the equilibrium pressure, K_i is the adsorption coefficient (reciprocal of Henry's constant) of component i, and α_i is a term representing the interaction energy of the adsorbate molecules, i.e., the lateral, solute–solute interactions in the two-dimensional condensed phase.

The major objective of this study was to interpret experimental chromatographic data for systems involving concurrent adsorption of two or more components. One of the major advantages of the scaled particle model is that it easily extended to binary systems of components i and j with the

appropriate definitions for α_m and β_m for the mixture, i.e., $\beta_m = x_i\beta_i + x_j\beta_j$ and $\alpha_m = x_i^2\alpha_i + 2x_ix_j\alpha_{ij} + x_j^2\alpha_j$ where x is the mole fraction in the condensed phase and α_{ij} is the interaction term for unlike pairs i–j. The binary isotherm equation is

$$P_i = \frac{1}{K_i}\left(\frac{X_i\eta}{\beta_m(1-\eta)}\right)\exp\left(\frac{\beta_m + 2\beta_i}{\beta_m}\frac{\eta}{1-\eta} + \frac{\beta_i}{\beta_m} - \left(\frac{\eta}{1-\eta}\right)^2 - \frac{2\eta}{\beta_m RT}(\alpha_i X_i + \alpha_{ij}X_j)\right) \quad (2)$$

The theoretical link between chromatography and thermodynamics is the concept of the specific retention volume, $V°_{g,i}$. This parameter is directly proportional to the limiting slope of the adsorption isotherm of one component

$$V°_{g,i} = 273R \lim_{P\to 0}(n_i^{ads}/P_i) \quad (3)$$

If there is no modifier present and the carrier gas is not adsorbed on the stationary phase, the specific retention volume can be related directly to the adsorption coefficient by the equation

$$K_i = V°_{g,i}/(273R) \quad (4)$$

The primary experimental retention volume data were in the form of specific retention volumes of one solute with various pressures of a volatile modifier in the mobile phase. The isotherm data were used to convert the retention volume data from a function of a mobile phase property (pressure or mole fraction) to a stationary phase property (surface coverage). This type of data is far more practical for modeling purposes because the retention of the solutes was determined almost exclusively by the properties of the stationary phase in these studies (*28–30*). Vapor-phase interactions were minimal because of the low mole fractions (<0.03) of the solutes and modifier in the inert (helium) carrier gas.

These unique systems represent binary or quasi-binary systems with one compontne, i, present at infinite dilution with the other component present at finite concentrations. In order to derive a retention volume equation for these quasi-binary systems, the limit of $P_i \to 0$ in eq 3 must be taken at a fixed surface coverage by component j, η. Thus eq 3 becomes

$$V°_{g,i}(\eta) = 273R \lim_{P\to 0}(n_i^{ads}/P_i)_\eta \quad (5)$$

The required retention volume equation for binary systems can be derived from eq 2 and 5 to give

$$V°_{g,i}(\eta) = K_i 273R(1-\eta)\exp\left(\frac{2\alpha_{ij}\eta}{\beta_j RT} - \left(1 + 2\frac{\beta_i}{\beta_j}\right)\frac{\eta}{1-\eta} - \frac{\beta_i}{\beta_j}\left(\frac{\eta}{1-\eta}\right)^2\right) \quad (6)$$

Equation 6 gives a quantitative relationship for the retention volume of an infinite dilution solute, i, as a function of the surface coverage by a second adsorbate, j. The adsorption coefficient, K_i, in this equation represents the limiting value of the ratio n_i^{ads}/P_i only in the limit of $P_i \to 0$ *and* $P_j \to 0$.

SINGLE-COMPONENT SYSTEMS

In order to determine the pure-component α, β, and K parameters for each adsorbate (modifier), the single-component isotherm data were fit to eq 1. The results along with literature values are given in Table I, and the fit of the equation for one isotherm is shown in Figure 1. Although several other isotherm equations were as accurate, the scaled particle isotherm equation fit the data satisfactorily, and the derived parameters, K, α, and β, agreed well with the literature data for the propane (*23*). The literature data (*23*) were determined by a classical volumetric method, and the chromatographic data (*28, 29*) agreed satisfactorily with the static data. The calculated adsorption coefficients varied linearly with $1/T$ and were comparable to the values determined from the specific retention volumes of the solutes measured with no modifier in the carrier gas (eq 4) as shown in Figure 2. The calculated values of the size parameter, β, and interaction term, α, did not show any systematic variation with temperature over the limited range used in these studies. Thus, the linear form of the data in Figure 2 and the temperature invariance of the other parameters allowed interpolation of isotherms at other temperatures.

Figure 3 illustrates the adsorption isotherm of butane at 10 °C, and Figure 4 shows the calculated adsorption coefficients for butane over a range of temperatures from 10 to 100

Table I. Measured Parameters for the Single-Component Isotherms of Propane, Butane, and Acetone on Carbopack C for the Scaled Particle Adsorption Model, Equation 1

temp, °C	10^2K_i, mol/(m² torr)	$10^{-8}\alpha_i$, J m²/mol²	β_i, Å²	lit. ref
		Propane		
0	4.16	5.6	14.4	23
10	2.39	5.6	14.3	23
10	2.60	5.6	14.1	28, 29
25	1.63	5.9	14.6	23
40	1.17	5.2	13.8	23
40	0.95	4.7	13.3	28, 29
70	0.44	5.5	13.9	29
		5.4 ± 0.4[a]	14.1 ± 0.4[a]	
		Butane		
10	27.1	5.3	15.2	28
40	7.71	5.1	14.6	28
100	1.06	5.8	*b*	28
		5.4 ± 0.4[a]	14.9	
		Acetone		
20	16.6	5.4	10.4	*c*
30	8.87	6.3	10.3	30
45	5.87	5.9	10.2	30
60	3.15	5.9	*b*	30
75	2.06	5.3	*b*	30
		5.8 ± 0.4[a]	10.3	

[a] Average ± 1 standard deviation. [b] At high temperatures, there were not enough data for a reliable regression of all three parameters. In such cases, the β term was fixed to the average value determined at the lower temperatures. [c] This work.

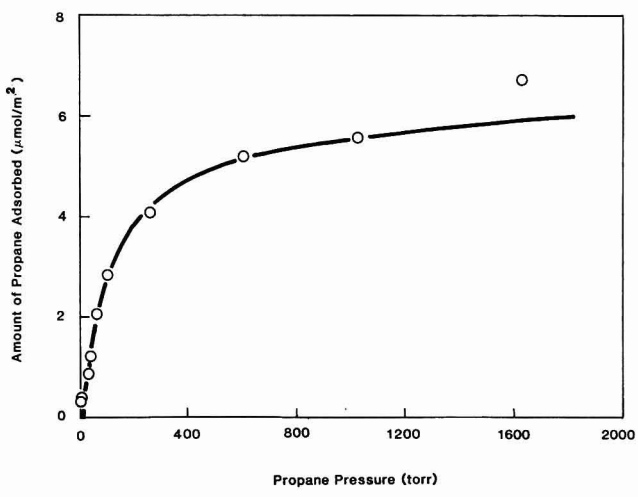

Figure 1. Adsorption isotherm of propane on Carbopack C at 10 °C (*28, 29*). The line was calculated from eq 1 with the parameters given in Table I.

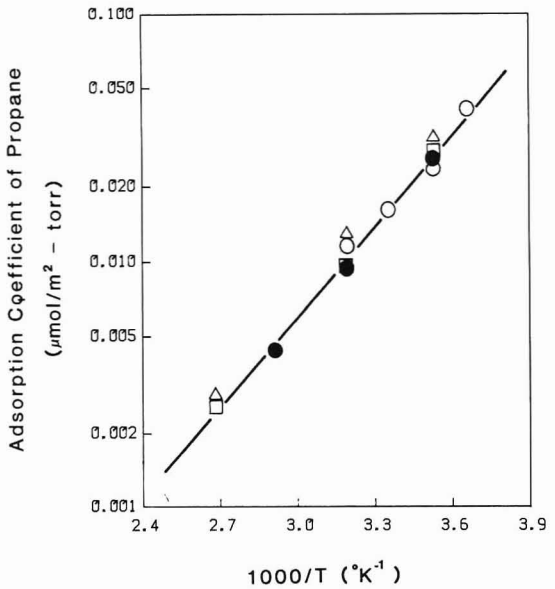

Figure 2. Calculated adsorption coefficients of propane on Carbopack C as a function of $1/T$: (●) calculated from single-component isotherm data (Table I); (○) volumetric isotherm data (*23*); (△) measured from specific retention volume data (*28*, *29*); (□) calculated from binary-component retention volume data with eq 6.

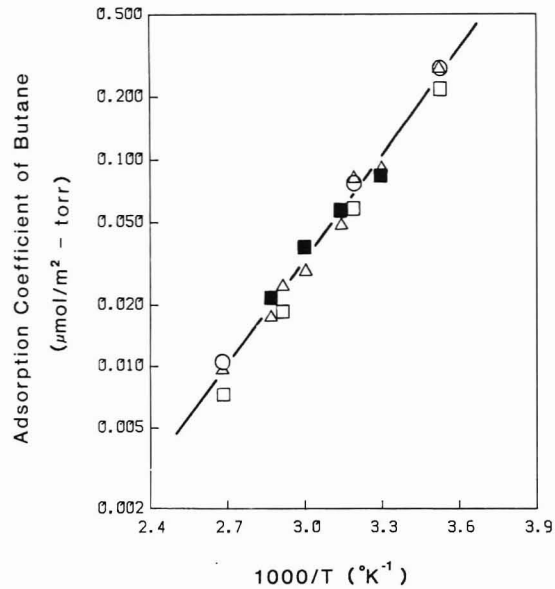

Figure 4. Calculated adsorption coefficients of *n*-butane on Carbopack C as a function of $1/T$: (○) calculated from single-component isotherm data (Table I); (△) measured from specific retention volume data (*28*, *29*); calculated from binary-component retention volume data with eq 6; (□) butane + propane; (■) butane + acetone.

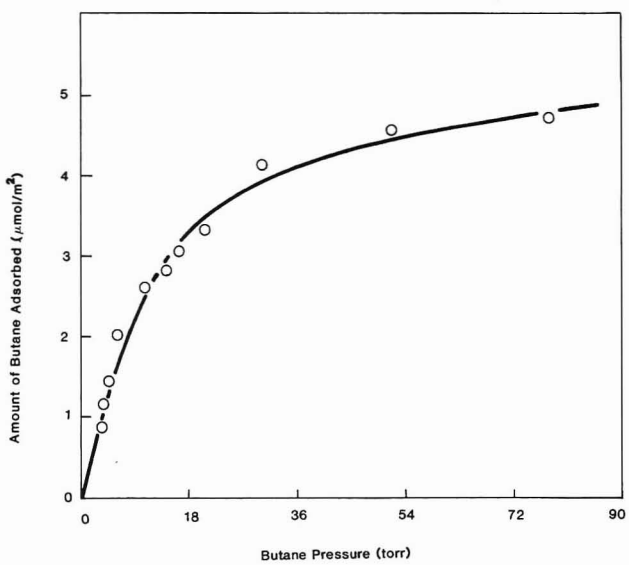

Figure 3. Adsorption isotherm of *n*-butane on Carbopack C at 10 °C (*28*).

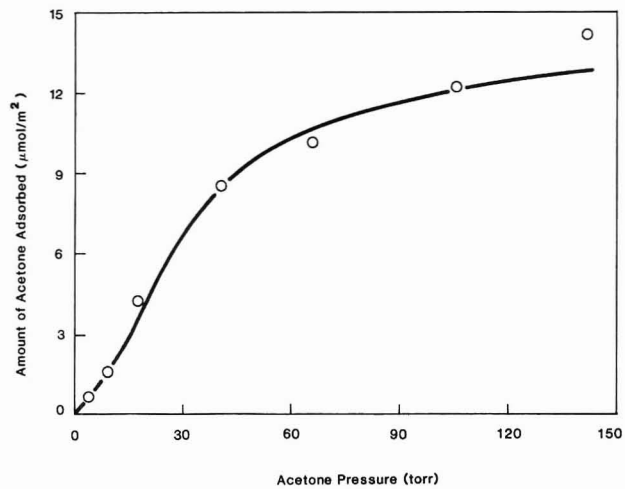

Figure 5. Adsorption isotherm of acetone on Carbopack C at 30 °C (*30*).

°C for the two different experiments, i.e., single-component isotherm data fit to eq 1 and retention volume (no modifier) (eq 4). The agreement is satisfactory although the values calculated from the binary data (retention volumes with acetone or propane as the modifier) appear to be consistently low.

Isotherm data for acetone are shown in Figure 5 and the calculated K values are plotted in Figure 6. In this case, the adsorption constants calculated from specific retention volumes were scattered due to the difficulty of accurately measuring the retention parameters of a polar solute such as acetone. The parameters obtained from the single-component isotherms were more consistent than the elution data, and the values agreed with the average of the retention volume data.

BINARY SYSTEMS

In the original studies (*28–30*) the specific retention volumes of infinite dilution samples of each adsorbate were measured as a function of surface coverage by a second adsorbate. These retention volume data were fit to eq 6 with the size parameters given in Table I in order to determine the other two parameters, i.e., the unlike-pair interaction term, α_{ij}, and the adsorption coefficient, K_i, of component i. The calculated values of these two parameters are given in Table II, and the calculated adsorption coefficients are shown as squares in Figures 2 and 4. The adsorption coefficients determined from (i) single-component isotherm data, (ii) retention volume data for a solute without a gas-phase modifier, and (iii) the same type of data with a modifier present should all be equivalent *if the infinite dilution retention volumes are not distorted by preferential adsorption of the solutes on the high-energy adsorption sites*. That is, the K values obtained from eq 1, 4, and 6 should all be equivalent for any given solute even though three completely different types of experimental measurements are involved.

The slopes of the lines in Figures 2, 4, and 6 are directly proportional to the heats of adsorption of the solutes on Carbopack C. The values of the isosteric heats of adsorption calculated from *all* of the data points shown in each figure are given in Table III along with previously published values. Again, the data agree well with previously measured values.

Figures 7 and 8 show the fit of some representative systems to the proposed retention volume equation. The lines in these

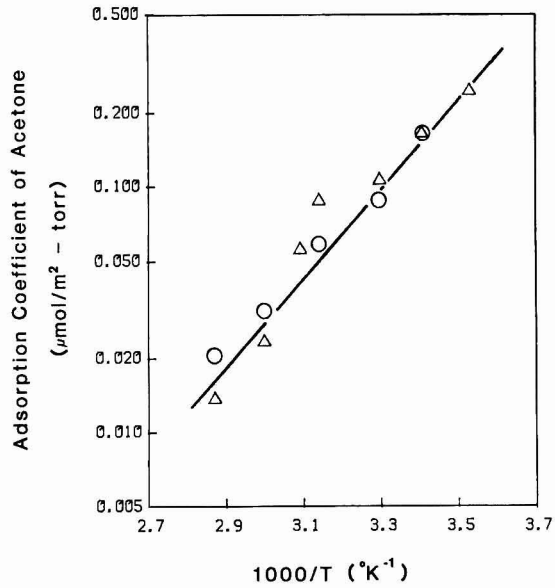

Figure 6. Calculated adsorption coefficients of acetone on Carbopack C as a function of $1/T$: (O) calculated from single-component isotherm data (Table I); (△) measured from specific retention volume data (*30*).

Table II. Nonlinear Least Squares Regression Parameters for the Specific Retention Volumes of Small Samples of Each Adsorbate, *i*, as a Function of Surface Coverage by a Coadsorbate, *j*

infinite dilution solute, *i*	finite concn modifier, *j*	temp, °C	10^2K_i, mol/(m² torr)	$10^{-8}\alpha_{ij}$, J m²/mol²
propane	butane	10	2.78	5.5
		40	0.98	7.1
		100	0.26	6.5
butane	propane	10	21.6	5.1
		40	5.77	4.7
		70	1.86	5.7
		100	0.73	6.8
				5.9 ± 0.9[a]
butane	acetone	30	8.26	6.0
		45	5.64	4.8
		60	3.75	4.4
		75	2.14	5.6
				5.2 ± 0.7[a]

[a] Average ± 1 standard deviation.

Table III. Limiting Isosteric Heats of Adsorption of the Adsorbates on Graphitized Carbon Black (Carbopack C)

adsorbate	isosteric heat of adsorption, kJ/mol: this work	lit. value
propane	−23.4	−24.5 (32)
		−23.4 (24)
		−22.1 (33)
n-butane	−32.2	−27.6 (33)
		−31.1 (32)
		−32.9 (34)
acetone	−31.4	−34.7 (35)

figures were calculated from eq 6 with the size parameters given in Table I and the K and α model parameters given in Table II. The theoretical model was generally adequate except at very low surface coverages where the experimental retention volumes are significantly increased by preferential adsorption of the solute, in this case butane, on the high-energy sites on the surface of the GCB adsorbent. There are very few of these sites on the GCB, so their effect is eliminated by even very small amounts of any modifier. Thus, all of the experimental data for binary systems were measured under conditions where the active sites were blocked by adsorbed modifier. That is the reason the theoretical equation does not accurately extrapolate to zero surface coverage. Thus, the data points obtained with no modifier (closed circles in Figures 7 and 8) were consistently greater than the values extrapolated from eq 6. The model used to develop the binary adsorption isotherm and retention volume equations is based on the assumption of a homogeneous surface. Thus, it cannot describe the effect of high-energy sites that influence the retention volumes with no modifier present.

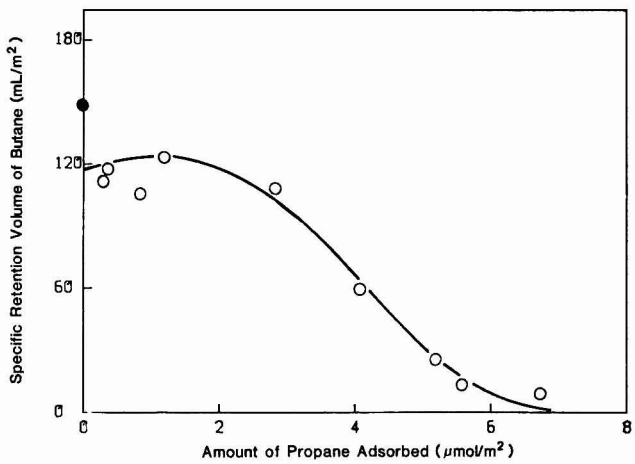

Figure 7. Specific retention volume of *n*-butane as a function of the amount of propane modifier adsorbed on Carbopack C at 10 °C (*28*).

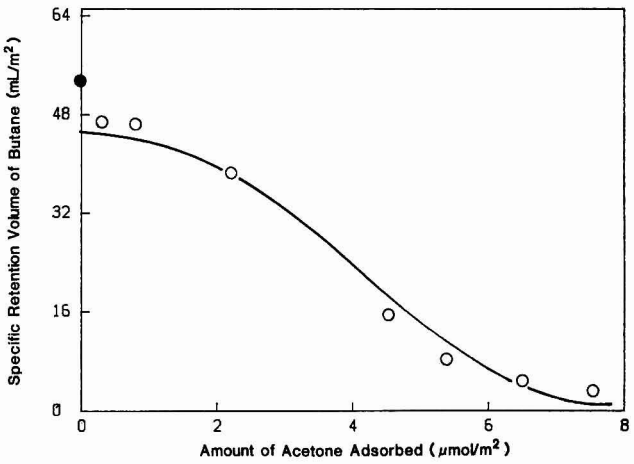

Figure 8. Specific retention volume of *n*-butane as a function of the amount of acetone modifier adsorbed on Carbopack C at 30 °C (*30*).

The fit of the theoretical line to the experimental data is not precise in most cases; however, the general shape of the plot is correct. In particular, the cooperativity effect at low surface coverages is substantiated. The magnitude of this effect is determined by the value of α_{ij}, which is a measure of the strength of the lateral interactions between unlike adsorbates in the two-dimensional adsorbed phase. The influence of this model parameter on the shape of the retention volume plot is illustrated in Figure 9 for butane + propane. The maximum in the retention volume plot is enhanced at high values of the interaction parameter α, and this correlation provides the first quantitative explanation of such experimentally observed maxima.

CONCLUSIONS

MSTPC has proven to be an accurate, dependable method for the determination of phase distribution equilibria. The

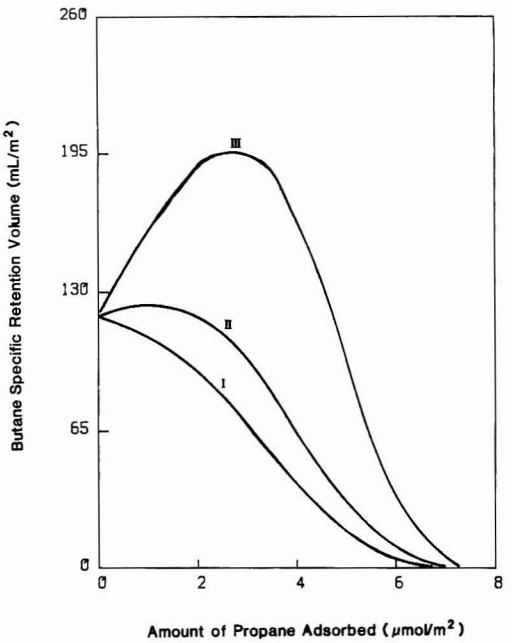

Figure 9. Calculated theoretical plots of the specific retention volume of butane as a function of the amount of propane adsorbed on Carbopack C at 10 °C using the size parameters and adsorption coefficients given in Table I and the following interaction parameters: (I) $\alpha_{ij} = 4.0 \times 10^8$ J m²/mol²; (II) $\alpha_{ij} = 5.3 \times 10^8$ J m²/mol²; (III) $\alpha_{ij} = 8.0 \times 10^8$ J m²/mol².

method is particularly valuable for multicomponent systems that are for all practical purposes beyond the range of classical static experimental procedures. The quasi-binary systems used in this study form an intermediate class of systems that are particularly easy to investigate and are very similar to many of the practical systems encountered in separation technology, as well as, catalysis, corrosion, and adhesion research.

The scaled particle adsorption theory for multicomponent systems is sufficiently accurate to allow a quantitative description of binary chromatographic retention data, such as the retention of one solute as a function of the amount of a second component adsorbed, in certain cases, that is when the experimental system conforms to the assumptions used in the derivation of the original equation-of-state (22). The primary restrictions are the assumption of nonspecific, mobile adsorption on a Gaussian (homogeneous) adsorbent. This particular model would thus be expected to fail for nonvolatile modifiers because of the localized, strong adsorption of the liquids, although the concept of a retention volume equation derived from a suitable model for the adsorption of multicomponent systems is valid.

Equation 6 is the first quantitative model for the description of the effect of surface coverage on the retention of infinite dilution solutes in gas–liquid–solid chromatography. The model provides a qualitative explanation of the maxima observed in many previous studies of retention volume vs. surface coverage or liquid loading. The magnitude of the interaction parameter, α, determines the shape of the curve and the position of the maximum. The size parameter determines the point of completion of a monolayer and provides an alternative to the BET method for the determination of the surface area of solid adsorbents.

One significant application of this model would be the development of optimization methods for the selection of the type and quantity of volatile or nonvolatile modifier required to produce a desired separation in a chromatographic scheme whether SFC, GSC, or GLSC. The experimental data obtained in these studies is unique because of the quasi-binary character of the systems, i.e., one solute present at limitingly low pressure. In addition, the easily measured chromatographic data for binary or more complex systems could provide a much-needed data base for the development of more accurate multicomponent adsorption models without the need for the arduous measurement of binary isotherms.

In addition to the development of chromatographic systems, the study of interactional phenomenon at the molecular level in a two-dimensional condensed phase is of interest in a wide range of fields. As Phillips has suggested (*36*), the use of molecular probes for the characterization of surfaces and two-dimensional condensed phases is an excellent supplement to the more popular spectroscopic methods, which use other probes such as photons, electrons, or charged particles. In particular, the selective poisoning or enhancement of catalysts by volatile modifiers involves processes exactly analogous to those observed with the present chromatographic systems.

Registry No. Propane, 74-98-6; butane, 106-97-8; acetone, 67-64-1.

LITERATURE CITED

(1) Wright, B. W.; Kalinoski, H. T.; Smith, R. D. *Anal. Chem.* **1985**, *57*, 2823–2829.
(2) Mourier, P. A.; Eliot, E.; Caude, M. H.; Rosset, R. H.; Tambute, A. G. *Anal. Chem.* **1985**, *57*, 2819–2823.
(3) Blilie, A. L.; Greibrokk, T. *Anal. Chem.* **1985**, *57*, 2239–2242.
(4) Hirata, Y. *J. Chromatogr.* **1984**, *315*, 31–37.
(5) Hirata, Y. *J. Chromatogr.* **1984**, *315*, 39–44.
(6) Parcher, J. F. *J. Chromatogr. Sci.* **1983**, *21*, 346–351.
(7) von Rybinski, W.; Findenegg, G. H. *Ber. Bunsenges. Phys. Chem.* **1979**, *83*, 1127–1130.
(8) von Rybinski, W.; Albrecht, M.; Findenegg, G. H. In *Faraday Symp. Chem. Soc.* **1980**, *No. 15*, 25–37.
(9) Parcher, J. F.; Hyver, K. J. *J. Chromatogr. Sci.* **1983**, *21*, 304–309.
(10) Hyver, K. J.; Parcher, J. F. *Anal. Chem.* **1984**, *56*, 274–278.
(11) Lin, P. J.; Parcher, J. F. *Anal. Chem.* **1985**, *57*, 2085–2091.
(12) Mathiasson, L.; Jonsson, J. J. *J. Chromatogr.* **1979**, *179*, 7–17.
(13) Conder, J. R.; Ibrahim, N. K.; Rees, G. J.; Oweimreen, G. A. *J. Phys. Chem.* **1985**, *89*, 2571–2576.
(14) Di Corcia, A.; Liberti, A. In *Advances in Chromatography*; Giddings, J. C., et al., Eds.; Marcel Dekker: New York, 1976; Chapter 7.
(15) Naito, K.; Takei, S. *J. Chromatogr.* **1980**, *190*, 21–34.
(16) Ross, S.; Oliver, J. P. *On Physical Adsorption*; Interscience: New York, 1964.
(17) Meyers, A. L.; Prausnitz, J. M. *AIChE J.* **1965**, *11*, 121–127.
(18) Suwanayuen, S.; Danner, R. P. *AIChE J.* **1980**, *26*, 76–83.
(19) Cochran, T. W.; Kabel, R. L.; Danner, R. P. *AIChE J.* **1985**, *31*, 268–277.
(20) Sicar, S.; Meyers, A. L. *Chem. Eng. Sci.* **1973**, *28*, 489–499.
(21) Mehta, S. D.; Danner, R. P. *Ind. Eng. Chem. Fundam.* **1985**, *24*, 325–330.
(22) Steele, W. A. *The Interaction of Gases with Solid Surfaces*; Pergamon Press: Oxford, 1974; Chapter 4.
(23) Glanz, P.; Korner, B.; Findenegg, G. H. *Adsorpt. Sci. Technol.* **1984**, *1*, 183–193.
(24) Glanz, P.; Findenegg, G. H. *Adsorpt. Sci. Technol.* **1984**, *1*, 41–50.
(25) Parcher, J. F.; Selim, M. I. *Anal. Chem.* **1979**, *51*, 2154–2156.
(26) Parcher, J. F. *J. Chromatogr.* **1982**, *251*, 281–288.
(27) Hyun, S. H.; Danner, R. P. *Ind. Eng. Chem. Fundam.* **1985**, *24*, 95–101.
(28) Lin, P. J.; Parcher, J. F. *J. Colloid Interface Sci.* **1983**, *91*, 76–86.
(29) Parcher, J. F.; Lin, P. J. *Anal. Chem.* **1981**, *53*, 1889–1894.
(30) Parcher, J. F.; Lin, P. J. *J. Chromatogr.* **1982**, *250*, 21–34.
(31) Mangani, F.; Bruner, F. *J. Chromatogr.* **1984**, *289*, 85–94.
(32) Hoory, S. E.; Prausnitz, J. M. *Trans. Faraday Soc.* **1967**, *63*, 455–460.
(33) Krawiec, Z.; Gonnord, M. F.; Guiochon, G. *Anal. Chem.* **1979**, *51*, 1655–1660.
(34) Chirnside, G. C.; Pope, C. G. *J. Phys. Chem.* **1964**, *68*, 2377–2379.
(35) Avgul, N. N.; Kiselev, A. V. *Chemistry and Physics of Carbon*; Walker, P. L., Ed.; Marcel Dekker: New York, 1970; Vol. 6.
(36) Phillips, C. S. G. *J. Chromatogr. Libr.* **1985**, *32*, 332–346.

RECEIVED for review February 3, 1986. Accepted May 12, 1986. Acknowledgement is made to the National Science Foundation and to the donors of the Petroleum Research Fund, administered by the American Chemical Society, for support of this research.

Carbon Hollow Tubes as Collectors in Thermal Desorption/Gas Chromatographic Analysis of Atmospheric Organic Compounds

George P. Cobb and Robert S. Braman*

Department of Chemistry, University of South Florida, Tampa, Florida 33610

Ke Min Hua

Southwest Institute for National Minorities, Chengdu, The People's Republic of China

Carbon hollow tubes are introduced as preconcentrators for atmospheric organic compounds. The technique has a demonstrated range of applicability for stable compounds having boiling points between 90 and 235 °C. Studies indicate a linear response from 3 to 770 ng/sample. The collector's capacity was found to range from 0.4 to 2.6 μmol depending on the compound being adsorbed. The method has been used to determine diffusion coefficients of organic air analytes and to record organic component patterns.

Atmospheric organic compounds are analyzed by a multitude of methods. Probably the oldest method of collection involves impingers to remove components of interest from air (*1–4*). Many methods accepted today utilize filters. Filters are generally made of fiberglass or polyeurethane (*4, 5*) and may be impregnated with various adsorbants (*4*). A series of filters arranged in order of decreasing pore size has been used to achieve size discrimination (*4*). Charcoal (*6–12*), diatomaceous earth (*13*), and commercial adsorbants such as XAD's (*14–17*) and Tenax (*4, 17–22*) are popular collection tube packings for preconcentration of atmospheric organics. The newest additions to the list of packings are metal chelates that selectively preconcentrate polar organics (*23*).

Complications accompany most of the above preconcentration methods used before finishing analyses—gas chromatography (GC) (*4, 24*), gas chromatography/mass spectrometry (*12, 20, 21*), or high-performance liquid chromatography (*4, 25*). Many recoveries from filters and packed collectors require lengthy extractions before chromatographic analysis (*9, 11, 17, 21*). Thermal desorption has been presented as an effective means of sample introduction for GC analysis (*17, 18 21, 22, 26*). Analyte decomposition has been observed during adsorption/thermal desorption on Tenax. Although no mechanism for this decomposition has been proved, it likely occurs during the desorption process (*10, 21*). At elevated temperatures, the natural atmospheric oxidants, O_3 and NO_2, react with sorbed analytes. Under normal experimental conditions in the presence of oxidants, the Tenax adsorbant decomposes to produce various byproducts (*10, 21*).

Interior-coated hollow tubes (HTs) have been used as thermally reversible chemisorbers (*27, 28*). Many atmospheric nitrogen containing compounds, including amines, have been collected on HTs coated with thin metal oxide layers. A logical extention of this research is a preconcentration and analysis method for atmospheric organic compounds. The thermal desorption characteristics of the carbon hollow tube (CHT) system eliminates many of the problems encountered with various other systems for sampling atmospheric organics. First, the surface is sufficiently shallow for easy thermal desorption of the organic molecules, a fact that may aid in minimizing decomposition of trapped analytes. The analytes tested did not decompose during the desorption process. In addition, the rapid speed of desorption makes direct interfacing into a GC feasible without requiring an intermediate trapping step.

Finally, the tubular design of the CHT provides a high degree of separation of gases and particles. The basis of the size discrimination is the large difference in diffusion coefficients. Only gases (D_a = 0.2–0.01 cm^2/s) are removed by CHTs. Particles, 0.1 μm in diameter and larger, have D_a values on the order of 10^{-5} cm^2/s. Particle D_as are not large enough to allow these analytes to collide with the CHT walls with the frequency necessary to allow collection. Diffusion coefficients are of importance in speciation of atmospheric components (*28*). Knowledge of the D_a of a compound analyte provides valuable information concerning possible dimerization, hydration, or large agglomerates formed.

EXPERIMENTAL SECTION

Tube Preparation and Coating Depth. The carbon surface was deposited on the interior of a 6 mm. o.d. Vicor glass tube. The tube was first soaked in 10% aqueous NaOH for 1 h and then thoroughly washed with deionized water. After the glass ends were fire polished and the entire tube was flame dried, the coating procedure began. Soot from the smoke of a benzene or toluene fire was drawn into the HT by means of a Neptune Dyna pump (Universal Electric; Owosso, MI) or a pipet bulb. The procedure was carried out on both ends of the tube to create a more uniform coating. The layer deposited was estimated by weighing to be on the order of 100 nm in depth.

With helium passing through the CHT, it was then heated to 270 °C for 30 min. A moderate amount of smoke and yellow oil was produced in this step. Finally the coating on the CHT ends was removed with a hot flame while passing oxygen through the tube. One inch was left uncoated on each tube's ends. Active coating lengths can vary. Tubes with 20–40 cm coatings were used to allow good adsorption efficiency of analytes at sampling rates of 0.5–1.0 L/min.

After 1 month of intermittant use (200 or more cycles), deterioration in the CHT surface became apparent. Spaces barren of the carbon surface began to appear. Analyte capacities and measured collection efficiencies decreased. At this point, the coating procedure was repeated from the surface deposition step.

Carbon coating depths were estimated by using CHTs prepared as described above. After a CHT's mass was recorded, the entire carbon surface was removed by use of a flame as in the final preparation step. The difference in coated and uncoated masses provided coating masses. By use of the density of amorphous carbon, 2 g/mL (*29*), the coating depth was easily calculated.

Collectors packed with carbon-coated sand (60/80 mesh, precoated) were made in the following manner. A 6 mm o.d. Vicor glass collection bed (*27, 28*) was packed with the HCl-washed sea sand (*28*). The sane was carbon coated as were the CHTs. The preanalysis heat treating was done at 270 °C, and the duration was 1 h. The tube was then repacked to ensure clean glass wool in the collector.

CHT–GC Interface. The inlet of an HP-3890 GC required modification to accomodate the CHT. The septum and retaining nut were replaced with a system capable of holding the CHT. The first step in the modification of the injection port (Figure 1)

0003-2700/86/0358-2213$01.50/0 © 1986 American Chemical Society

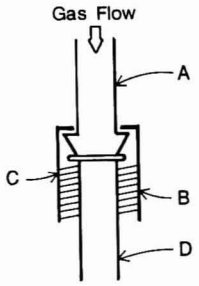

Figure 1. Injection port modification: (A) port connector; (B) Swagelok nut; (C) Teflon O-ring; (D) injection port.

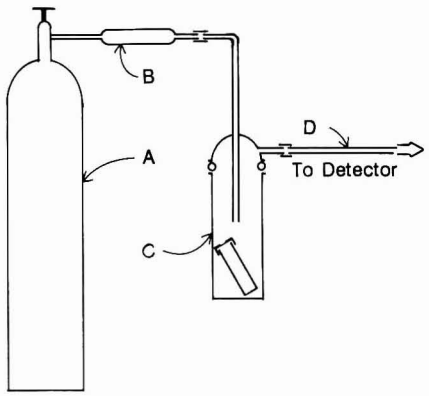

Figure 2. Experimental design for breakthrough capacities: (A) helium gas cylinder; (B) charcoal scrubber; (C) permeator in permeation chamber; (D) carbon hollow tube.

consisted of cutting 4.5 mm from the ferruled end of a port connector and filing the ends to smoothness. The reduction in ferrule length allowed the 0.25 in. Swagelok nut to reach the threads on the top of the injection port. The modification left a flat metal/metal interface that will not seal. A Teflon O-ring solved this problem although it required periodical replacement. A 0.25-in. Swagelok tee connector was used to attach the CHT to the new inlet in a verticle position (Figure 3). The first of two carrier gas lines was connected to the CHT with a 0.25 in.–0.125 in. reducing union. The other was connected to the remaining fitting of the tee connector.

Sample Preparation. All standards were 99% mol purity or redistilled over a range of not more than 1 °C. The permeation devices were one of two types: a screw top vial with a 0.125-in. hole drilled in the top and a Teflon diaphragm inside the cap serving as a permeation membrane or a Pasteur pipet with the large end sealed and the small end formed into a capillary. After addition of the standards to the permeators, they were placed in glass chambers (Figure 2c) and 100 mL/min of air was passed through the apparatus. Permeator masses were recorded periodically, usually daily, with a Mettler H20T balance until a constant permeation rate, ±10%/day, was achieved. Thereafter masses were taken periodically when in use.

Samples from the permeators generally consisted of the entire effluent from the permeation chamber although occasional use of a glass tee and a Dyna-Pump allowed sampling of only a fraction of the total effluent (i.e., 100 mL/min of 1.0 L/min. All permeation flow rates were monitored with a calibrated Matheson Model 8160 flowmeter.

Experimental Procedure. *Hollow Tube Capacity.* Hollow tube capacity was determined by using either a direct current discharge (DCD) (*30*) or a Bendix NOx analyzer. Nitrogen-containing compounds were analyzed by the NO_x analyzer, and the remaining compounds were analyzed on the DCD. The total effluent from a permeation chamber was passed over a CHT and into the analyzer (Figure 2) at a rate of less than 100 mL/min.

Molecular Stability Experiments. The stability of analytes undergoing adsorption/thermal desorption was studied by using two CHTs. Analytes from an air stream were first adsorbed onto one of the tubes. Analytes on this tube were then thermally desorbed directly into the analyzer. In a second experiment, the same amount of analyte was first adsorbed onto one CHT and

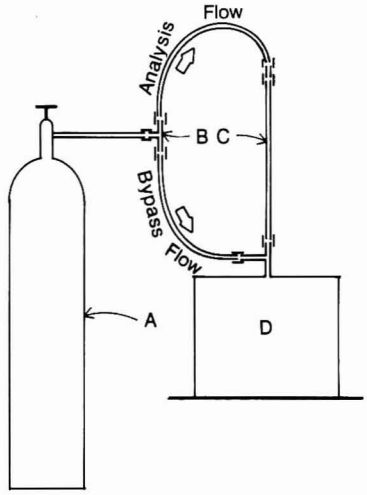

Figure 3. GC carrier gas flows: (A) helium gas cylinder; (B) three-way valve; (C) carbon hollow tube; (D) gas chromatograph.

then transferred by thermal desorption onto the a second CHT. This second tube was then analyzed by GC, NO_x analyzer, or DCD.

Calibration curve comparisons utilized GC responses of a component injected as a solution standard and those of the same component adsorbed on CHT. The solutions for injection were 65.0 ppm toluene in H_2O along with 7 ppth and 0.7 ppth 1-decanol in benzene. A range of sample sizes were analyzed. A gas sampling rate of less than 100 mL/min was used in all CHT analyte sampling to ensure quantitative adsorption.

Chromatography Effect. In the chromatography effect experiments, a breathing air flow of 40 mL/min was passed through the permeation chamber and through a CHT. For each analyte, direct analysis was performed as in the molecular stability experiments. Next the compound was collected on a CHT and then 600 mL/min of clean breathing air was passed through the CHT. The duration of exposure of the air flow was varied during compound testing. All samples were subsequently analyzed by GC. Sampling rates of less than 100 mL/min were used to ensure quantitative adsorption of the analytes on the CHTs.

Diffusion Coefficients. Diffusion coefficient determinations required a known flow rate of breathing air, a permeation chamber, and two CHTs of known length. Optimal air flow rates ranged from 1 to 2 L/min for many atmospheric organic organic compounds, whose D_as generally range from 0.05 to 0.1 cm^2/s. Tube lengths may vary but the best results were obtained when the first tube was at least 17 cm long and the second was 35–40 cm in length. Air was passed through the permeation chamber. Analytes were collected by passing the permeation chamber effluent through a pair of CHT in series. The quantity of analyte on each CHT was then determined by GC. Data analysis using a computer program allowed calculation of the best D_a according to the Gormley–Kennedy equation (*28*).

Organic Component GC Patterns. With a single CHT, organic components evolved from solid natural substances were preconcentrated from the effluent of a permeation chamber containing them. Indoor and outdoor air samples were taken by using a CHT(s) followed by a collection tube packed with carbon-coated sand (CPT). All sampling rates were 0.5 L/min. Each sample was analyzed by GC.

GC Analysis. The GC used was an HP-3890 with a flame ionization detector (FID). An HP-3390A integrator and an HP-19400A sampler/event controller module, which controlled a three-way Delta solenoid value (Fluorocarbon, Inc.; Aneheim, CA), were also used in combination with the GC. Separations were achieved by use of a 1 m × 0.125 in. stainless steel 5% OV-101 column and a carrier gas flow rate of 22–24 mL/min. During GC analyses, typical temperature programs began at 30 °C and ramped to a maximum of 250 °C. The injection port was held at 250 °C. The FID was held at 270 °C.

Samples were desorbed into the GC at 270 °C for 2.5 min, with the carrier gas flowing along the analysis path (Figure 3). After heating, the carrier gas was switched to the bypass path where it remained until the next desorption began.

Table I. Hollow Tube Capacity

compound	capacities, μg	capacities, μmol	bp, °C	vapor pressure, mmHg at 23 °C	N
acetonitrile	16.38	0.397	81.6	68.2	1
benzene	31.1 (±2.2%)	0.398 (±2.2%)	80.1	61.6	2
hexylamine	59.6 (±4.4%)	0.589 (±4.4%)	130	6.0	3
chlorobenzene	140 (±2.8%)	1.25 (±2.8%)	132	9.0	2
nitrobenzene	181 (±2.4%)	1.47 (±2.4%)	210.8	0.46	4
pyridine	181 (±17%)	2.30 (±17%)	115.5	14.5	4
pyrrole	197 (±1.7%)	2.93 (±1.7%)	130	6.8	2
m-nitrotoluene	257 (±10%)	1.87 (±10%)	232.6	0.34	2
nicotine	436 (±9.9%)	2.62 (±9.9%)	242.3	0.20	3

Table II. Analyte Transfer

compound	desorptions prior to detection: single CHT	desorptions prior to detection: CHT1 → CHT2	% recovery	N	detector
1-butanol	96.0 (±2.9%)	99.48 (±5.5%)	103	3	DCD
2,4-pentanedione	55.3 (±7.0%)	53.75 (±4.6%)	97.2	2	DCD
chlorobenzene	25.5 (±9.5%)	24.7 (±13.8%)	97.2	5	DCD
pyridine	78.5	79.0 (±16.4%)	101	3	NO_x
benzene	2.74	2.77	101	1	GC
nitrobenzene	18.7	18.2	97.4	1	GC

Blanks. Helium gas was passed through CHT overnight at 40 mL/min to determine blanks. Repeated GC analyzes showed no measurable organics. When left opened overnight, CHTs did show substantial blanks as would be expected from inboard diffusion of organics from laboratory air.

RESULTS AND DISCUSSION

CHT analyte capacities were measured via DCD or NO_x analyzer. Capacities ranged from 16 to 440 μg depending on the analyte (Table I). CHT analyte capacity vs. analyte vapor pressure was fit to an exponential. The resulting correlation coefficient was 0.90. This dependence illustrates the importance of analyte vapor pressure as a collection parameter.

The fact that the carbon surface of the CHTs slowly degraded upon repeated use points to the possibility that species adsorbed on the surface may also decompose. Reported evidence of analyte decomposition on Tenax increased this concern. Tests of a few compounds adsorbed onto a CHT and desorbed for analysis showed no decomposition losses as indicated by the data in Table II. Analytes produce the same response whether desorbed from one CHT into the detector or from one CHT to a second CHT then into the detector. The quantitative readsorption of components transferred from one tube to the next illustrates the retention of components' integrity throughout the adsorption/thermal desorption process. If the analytes had fragmented, the products would likely have been too volatile to be readsorbed by the second CHT.

In a similar experiment (Table II) benzene and nitrotoluene were collected on CHTs and analyzed by GC. Virtually identical GC retention times (±0.05 min) and area responses were observed whether desorbed through one or two CHT's. The combination of reproducible retention times and peak areas reinforces the assertion that compounds are unchanged in the adsorption/thermal desorption process.

The final molecular stability study involved comparing chromatograms of injected samples to those of samples desorbed from CHTs. Table III shows the linear regression parameters for integration vs. analyte mass. This experiment showed that polar and nonpolar analytes, injected or adsorbed onto and then desorbed from CHTs, produce the same response. Calibration curves derived from injected and desorbed standards of toluene and 1-decanol, respectively, were linear at least over the range 10–770 ng. Slopes for the injected and desorbed toluene samples do not differ statistically. The

Table III. Calibration Curves

compound	GC introduction	slope (×10⁴)	ordinate intercept (×10⁴)
toluene	injection	1.42 ± 0.057	−4.05 ± 13
	TD[a]	1.26 ± 0.13	44.7 ± 8.2
1-decanol	injection	1.12 ± 0.086	3.93 ± 3.7
	TD[a]	1.61 ± 0.066	−18.3 ± 13

[a] Thermal desorption.

difference in the 1-decanol slopes is 30%. Poor integration of broad decanol peaks and incomplete volatilization of decanol from the injection needle are possible reasons for the difference in decanol slopes. Most of the error is likely manifested in the 10% day to day variation in permeation rate.

Retention times for the desorbed samples are found to be up to 0.2 min longer than those for the injected standards. This time lag is due to the delay in maximum heating during the desorption process. Thus all retention times for desorbed samples should be longer than those for the respective injection samples.

The smallest sample from the toluene calibration curve was 23.7 ng. Decanol samples of 2.84 ng were analyzed and found to be near the detection limit. The calibration curve indicates a lower limit of detection at 10.5 ± 7.5 ng. A more precise determination of the limit of detection will require a standard with a slower permeation rate, near 100 ng/min. This rate is necessary to ensure precision both in permeator weight loss and in sampling time.

A study of the extent to which various species chromatograph from the carbon surface at room temperature provided interesting results. Figure 4 depicts the movement of organics sorbed on the surface of a CHT as a function of air volume passed through a loaded CHT. The chromatography effect seems to disappear above a boiling point of approximately 85–90 °C. Cyclohexane had little quantitative retention as seen by the loss of analyte after only 150 mL of air flow. Benzene retention was a bit better. Approximately 12 L of air was required to remove 10% of the benzene from the surface. Toluene and nitrotoluene (not shown) were not moved even after 65 min of air flow. This chromatography effect supports a view that strong physisorption is the mechanism of collection at the carbon surface. If there are

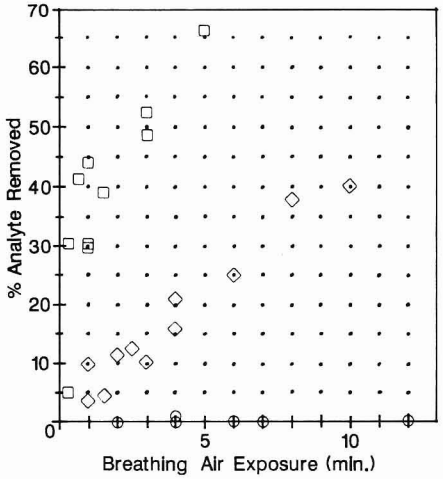

Figure 4. Chromatography effect: circle, toluene; diamond, benzene; square, cyclohexane.

no bonds formed in the adsorption process, as in physisorption, the more volatile analytes should slowly chromatograph through a HT during sampling.

One useful application demonstrated for this method is the determination of D_as. Gromley and Kennedy have described the adsorption of species, individual molecules or agglomerations, from a gas stream onto the surface of a HT through which the stream is passing. Their mathematical expression (*28*) is

$$C_n/C_0 = 0.819 \exp(-3.6568\pi DL_n/F) + 0.0976 \exp(-22.3\pi DL_n/F) + \ldots \quad (1)$$

where C_0 is the analyte concentration entering the hollow tube, C_n is the concentration exiting hollow tube n, D is the diffusion coefficient of the compound in question, L_n is the length of tube n, and F is the flow rate. Utilizing the definition

$$C_1 = C_0 - S_1 \quad (2)$$

eq 1 may be written in the form

$$S_1/C_0 = 1 - 0.819 \exp(-3.6568\pi DL_n/F) + \ldots$$

where S_1 is the amount of analyte adsorbed on tube 1.

Utilizing the facts that C_0 is the total amount of a component arriving at the head of tube 1 and that S_1 may be treated as a fraction of that total, eq 1 reduces to

$$S_1 = 1 - \sum a_i \exp\{b_i DL_n/F\} \quad (3)$$

$$= 1 - R(D,L_1,F) \quad (4)$$

where $R(D,L_n,F)$—a function of D, L_n, and F—is the summation portion from the left site of eq 3. For the second tube in the set

$$S_2/C_1 = 1 - R(D,L_2,F) \quad (5)$$

Using eq 2, 4, and 5

$$S_2 = [1 - R(D,L_2,F)] \times R(D,L_1,F) \quad (6)$$

The iterative computer calculation of a D_a began by assuming a D_a of 0.1 cm^2/s. The calculation of S_1/S_2 values was done using eq 4 and 6. This calculated value was then compared to the S_1/S_2 ratio from the experimental data. This comparison provided an index of precision of the two values. The iteration was complete when the difference in the ratios is below the selected precision threshold.

Experimental diffusion coefficients were in good agreement with those calculated from physical properties using the Arnold method (Table IV) (*31*). It should be noted that this method of calculating theoretical D_a values has a standard deviation of ±8.4% when compared to experimental data (*31*). This fact shows the experimentally determined D_a values to be within the error range of the theoretical values. The average standard deviation of all D_a experimental values was ±12.1%, and the average absolute deviation between the experimental and theoretical was ±6.91%. These data indicate CHT performance is in agreement with theoretical predictions.

Table IV. Diffusion Coefficients

compound	theoretical value, cm^2/s	exptl value, cm^2/s	N
pyridine	0.095 24	0.109 (±3.85%)	2
chlorobenzene	0.081 46	0.0789 (±9.64%)	3
toluene	0.085 07	0.0802 (±1.50%)	12
1,2-dichloroethane	0.093 12	0.0931 (±32.9%)	5
1,2-dibromoethane	0.083 81	0.0744 (±12.8%)	4

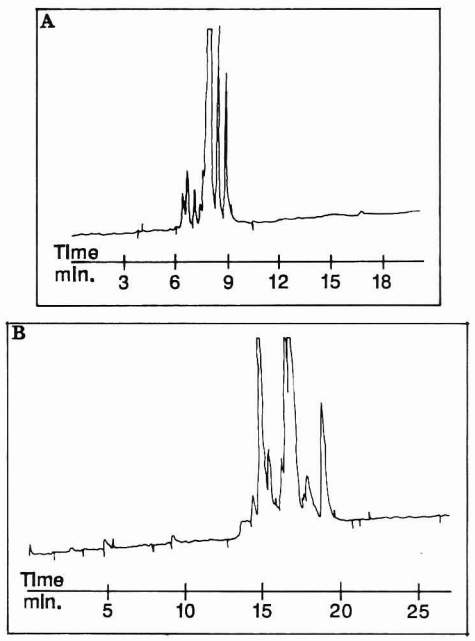

Figure 5. Spice odor patterns: (A) nutmeg; (B) cinnamon. Both samples separated with He flow of 32 mL/min, temperature program hold 40 °C, 1 min ramp at 10 °C/min to 210 °C for cinnamon and 250 °C for nutmeg, both held at their maximum temperature for 5 min.

Chemical patterns of volatile organics evolved from fresh citrus and spices were obtained by use of a single CHT and subsequent GC analysis. Representative chromatograms are shown in Figure 5. These chemical patterns are readily distinguished from one another. With computer aid, sources of such patterns should be easily accessible.

Figures 6 and 7 contain indoor and outdoor patterns, respectively. Inspection of indoor organic component patterns desorbed from the three collection surfaces points out the normal performance of this collection system. The components with medium volatility are collected on the CHTs. The higher volatility components chromatograph through the CHTs and thus show up on the CPT. The low volatility components are usually associated with particulates. The low D_a of a particle is insufficient to allow efficient collision with the CHT collection surface.

Of the components collected on the CHTs, those with higher D_a values are collected more efficiently. Tubes with the same lengths have equal efficiencies. Thus, for a pair of CHTs, the amount of analyte(s) collected by the first CHT will be greater than that collected by the second. The only exception to this rule is the case where the CHT has been overloaded with analyte. The CPT collects the analytes not collected by CHT(s). The majority of these are of low and high volatility. The patterns from Figure 6 illustrate these properties. The patterns of Figures 6A and 6B are very similar; the main

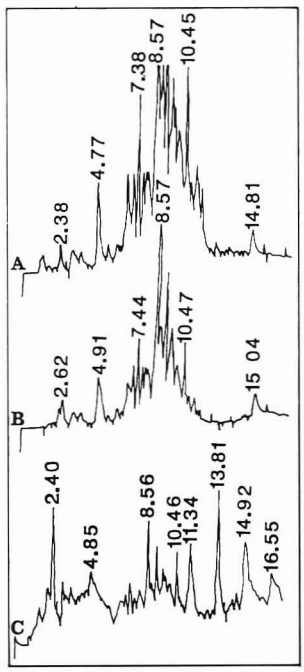

Figure 6. Chromatograms of an indoor air sample: (A) first CHT; (B) second CHT; (C) CPT. All retention times are in minutes.

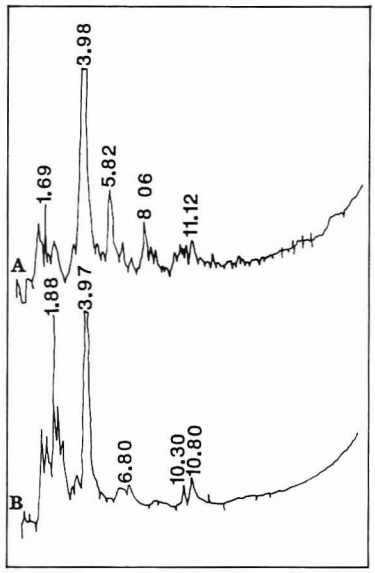

Figure 7. Chromatograms of an outdoor air sample: (A) CHT; (B) CPT. All retention times are in minutes.

difference is in peak area. A comparison of components collected by a CPT to those collected by a CHT shows the low and high volatility analytes to be concentrated most heavily on the CPT. Analytes with retention times less than 4 min and greater than 11 min are of little importance in CHT analyzes. However, in the CPT analysis, the peak at 13.81 min is the largest and the peak at 2.4 min is the second largest.

The same type patterns are observed by the outdoor chromatograms in Figure 7. The large amount of low volatility components is not present in the CPT analysis. One explanation is that the samples were collected on board ship in the Gulf of Mexico. The high humidity in the atmosphere above these waters may have removed particulates, generally associated with anthropogenic sources of organic pollutants.

CONCLUSIONS

The chromatography effect data shows that components with boiling points below 85–90 °C are not quantitatively retained by the CHTs. Molecular stability and calibration curve data indicate an upper limit of boiling point usefulness at 235 °C or more. The calibration curves also indicate a linear response over at least 2 orders of magnitude. Experimental D_a values are within the error range for calculated theoretical values. And finally organic component patterns from different sources are readily discernible. These facts illustrate the potential of the CHT–GC method for analysis of diversified atmospheric organics.

Registry No. Acetonitrile, 75-05-8; benzene, 71-43-2; hexylamine, 111-26-2; chlorobenzene, 108-90-7; nitrobenzene, 98-95-3; pyridine, 110-86-1; pyrrole, 109-97-7; *m*-nitrotoluene, 99-08-1; nicotine, 54-11-5; 1-butanol, 71-36-3; 2,4-pentadione, 123-54-6; toluene, 108-88-3; 1-decanol, 112-30-1.

LITERATURE CITED

(1) Audunsson, G.; Mathiasson, L. *J. Chromatogr.* **1983**, *261*, 253–264.
(2) Matthews, T. B. *Am. Ind. Hyg. Assoc. J.* **1982**, *43*, 547–552.
(3) DePascale, A.; Cobelli, L.; Paladino, R.; Pastorello, L.; Frigerio, A.; Sala, C. *J. Chromatogr.* **1983**, *256*, 352–358.
(4) Hertz, H. S.; Chesler, S. N. *Trace Organic Analysis: A New Frontier in Analytical Chemistry* NBS Press: Washington, DC, 1979; pp 478–500.
(5) Grimmer, G.; Jacob, J.; Naujack, K.; Dettbarn, G. *Anal. Chem.* **1983**, *55*, 892–900.
(6) Nowicka, K. *Anal. Abstr.* **1983**, *45*(5), H42.
(7) Torres, L. *Int. J. Environ. Anal. Chem.* **1973**, *3* (2), 155–164.
(8) Van de Wal, J. F.; Moerkerken, A. *Ann. Occup. Hyg.* **1984**, *28*, 39–47.
(9) Coutant, R. W.; Scott, D. R. *Environ. Sci. Technol.* **1982**, *16*, 410–413.
(10) Raymond, A.; Guiochon, G. *Environ. Sci. Technol.* **1974**, *8*, 143–148.
(11) Simoneit, B. R. T. *Atmos. Environ.* **1984**, *18*, 51–67.
(12) Isadorov, V. A.; Zenkevich, I. G.; Ioff, B. V. *Atmos. Environ.* **1983**, *17*, 1347–1353.
(13) Kdesnik, M. I.; Bukovskii, M. I.; Zhukov, V. I.; Sedei, M. M. *Anal. Abstr.* **1983**, *45*(5), H29.
(14) Anderssen, K.; Levin, J.; Lindahl, R.; Nilsson, C. *Chemosphere* **1982**, *11*, 1115–1119.
(15) Anderssen, K.; Levin, J.; Nilsson, C. *Chemosphere* **1983**, *12*, 197–203.
(16) Anderssen, K.; Levin, J.; Nilsson, C. *Chemosphere* **1983**, *12*, 821–826.
(17) Billings, W. N.; Bibleman, T. F. *Atmos. Environ.* **1983**, *17*, 383–391.
(18) Brookes, B. I.; Young, P. J. *Talanta* **1983**, *30*, 665–676.
(19) Stump, F. D.; Dropkin, D. L. *Anal. Chem.* **1985**, *57*, 2629–2634.
(20) Yokoucki, Y.; Onaniwa M.; Ambe, Y.; Fuwa, K. *Atmos. Environ.* **1983**, *17*, 743–750.
(21) Ligocki, M. P.; Pankow, J. F. *Anal. Chem.* **1985**, *57*, 1138–1144.
(22) Lawrence, A. H.; Elias, L. *Anal. Chem.* **1985**, *57*, 1485–1488.
(23) Williams, E. J.; Seivers, R. E. *Anal. Chem.* **1984**, *56*, 2523–2528.
(24) Kodama, Y.; Arashidani, K.; Yoshikawa, M. *J. Chromatogr.* **1983**, *261*, 103–110.
(25) Kuwata, K.; Uebori, M.; Yamasaki, H.; Kuge, Y. *Anal. Chem.* **1983**, *55*, pp 2013–2016.
(26) Pellizzari, E.; Demain, B.; Krost, K. *Anal. Chem.* **1984**, *56*, 793.
(27) Braman, R. S.; Trindade, M.; Han, Q. X. "A Sequential and Specific Hollow Tube System for Trace Nitrogen Compounds in Air"; Third National Symposium on Recent Advances in Pollution Monitoring of Ambient Air and Stationary Sources, May 3–6, 1983.
(28) Braman, R. S.; Shelley, T. J.; McClenny, W. A. *Anal. Chem.* **1982**, *54*, 358–364.
(29) *CRC Handbook of Chemistry and Physics*, 60th ed.; Weast, R. C., Ed.; CRC Press: Boca Raton, FL, 1980.
(30) Braman, R. S.; Dynako, A. *Anal. Chem.* **1968**, *40*, 95.
(31) Wilkie, C. R.; Lee, C. Y. *Ind. Eng. Chem.* *47*, 1253–1257.

RECEIVED for review November 18, 1985. Resubmitted May 8, 1986. Accepted May 8, 1986.

Determination of Nicotine *N*-Oxide by Gas Chromatography following Thermal Conversion to 2-Methyl-6-(3-pyridyl)tetrahydro-1,2-oxazine

Peyton Jacob, III,* Neal L. Benowitz, Lisa Yu, and Alexander T. Shulgin

Division of Clinical Pharmacology of the Department of Medicine, University of California, Building 100, Room 235, San Francisco General Hospital Medical Center, San Francisco, California 94110

Nicotine *N*-oxide is extracted from urine by use of silica gel columns and eluted with methanolic ammonia. The eluate is evaporated and then heated at 150–160 °C in anisole, which results in conversion to the ring-expansion product 2-methyl-6-(3-pyridyl)tetrahydro-1,2-oxazine. The oxazine derivative is readily extracted from aqueous solution with organic solvents and has good chromatographic properties. A method for determination of nicotine *N*-oxide in smokers' urine, using 5-methylnicotine *N*-oxide as an internal standard, is described.

The mammalian metabolism of tertiary amines generally involves α-carbon oxidation and N oxidation (*1*). The tobacco alkaloid nicotine is metabolized primarily by oxidation at the 5′ carbon, which leads to the lactam cotinine (*2*, *3*). The other major route of metabolism appears to be oxidation of the pyrrolidine nitrogen to give the diasteriomeric 1′-*N*-oxides (Figure 1), although relatively little data on the quantitative importance of this pathway (*2*, *4*, *5*) has been published.

In order to evaluate the quantitative importance of the N-oxidation pathway in humans, we required a reliable method for the determination of nicotine *N*-oxide in biologic fluids. Determination of low concentrations of *N*-oxides in biologic samples presents a challenge to analytical chemists because the polarity of this functional group makes extraction difficult (*6*). Recently, a procedure was described for solid-phase extraction of radiolabeled nicotine *N*-oxide from urine, HPLC separation, and determination by liquid scintillation counting (*5*). We attempted to adapt this method for determination of nicotine *N*-oxide in urine using HPLC with UV detection but were unsuccessful owing to the presence of substances in the urine extract that gave peaks coeluting with nicotine *N*-oxide.

Most *N*-oxides are thermally labile (*7–9*) and, as a result, it is often not possible to analyze them directly with techniques that require vaporization, such as gas chromatography or mass spectrometry. Determination of *N*-oxides by these methods has generally involved reduction back to the parent tertiary amine using titanium trichloride (*2*, *9*, *10*). If the parent amine is present in relatively high concentrations, it must be removed prior to determination of the *N*-oxide. In smokers' urine, nicotine concentrations are generally higher than nicotine *N*-oxide concentrations (ref 2, Table III) and, consequently, several extractions are necessary to remove nicotine prior to the reduction step (*2*). Such procedures are prone to errors due to residual nicotine and/or losses of the *N*-oxide during nicotine extraction.

The determination of polar compounds by gas chromatography is often facilitated by conversion to derivatives that are less polar and more volatile. On thermal treatment, nicotine *N*-oxide undergoes a Meisenheimer rearrangement to the ring-expansion product 2-methyl-6-(3-pyridyl)tetrahydro-1,2-oxazine in high yield (*11*). We have found that the thermal rearrangement occurs smoothly with nanogram quantities of nicotine *N*-oxide in anisole at 150–160 °C. The oxazine derivative is easily extracted from aqueous solutions with organic solvents and has good chromatographic properties. This paper describes a new method for determination of nicotine *N*-oxide in urine based on its conversion to the oxazine derivative and gas chromatography with nitrogen–phosphorus detection.

EXPERIMENTAL SECTION

Instrumentation. Gas chromatographic analyses were carried out by use of a Hewlett-Packard Model 5880A chromatograph with a nitrogen–phosphorus detector, a Level IV computing integrator, Model 7672A automatic liquid sampler, a packed column injection port, and a split–splitless capillary injection port. A 2 m × 2 mm i.d. glass column packed with 2% Carbowax 20 M and 2% KOH on 100/120 mesh Chromosorb W (Alltech Associates), configured for on-column injection, was used for packed column determinations, at an oven temperature of 160 °C. A 25 m × 0.31 mm cross-linked 5% phenylmethylsilicone, 0.52-μm film thickness, fused silica column (Hewlett-Packard) was used for the capillary GC determinations. The carrier gas (nitrogen) flow rate was 30 mL/min for packed column analyses, and 2 mL/min (helium) for capillary column analyses; detector air and hydrogen flow rates were 50 mL/min and 5 mL/min, respectively. The N/P detector bead voltage was adjusted to give a background current of 12–20 pA. Mass spectral analyses were carried out with a Hewlett-Packard 5970B mass selective detector interfaced with a Hewlett-Packard 5890A gas chromatograph, or with a Kratos MS-25S mass spectrometer.

Chemicals and Reagents. Toluene and isopropyl alcohol were from Burdick and Jackson, distilled in glass. All other solvents and chemicals were reagent grade. Solid-phase extraction of urine was carried out by using 3-mL disposable columns packed with 40-μm silica gel (BondElute Si, Analytichem, or Baker-10 SPE). Nicotine *N*-oxide, 5-methylnicotine *N*-oxide, and 2-methyl-6-(3-pyridyl)tetrahydro-1,2-oxazine were synthesized as described below. Microanalyses of new compounds were carried out by Galbraith Laboratories, Knoxville, TN.

Synthesis of 5-Methylnicotine *N*-Oxide. (*A*) *Synthesis of 5-Methylmyosmine.* Condensation of ethyl 5-methylnicotinate (15 g, 91 mmol) (*12*) with *N*-vinylpyrrolidinone (11 g, 100 mmol) was carried out in a manner analogous to the reported method for the synthesis of 5-bromomyosmine (*13*). The crude product was purified by a bulb-to-bulb distillation (Kugelrohr oven) at 110–120 °C (0.1 mmHg), giving 10.4 g (71% yield) of white solid. The analytical sample was recrystallized from methylcyclohexane, mp 69.5–71 °C. Anal. Calcd for $C_{10}H_{12}N_2$: C, 74.96; H, 7.55; N, 17.49. Found: C, 74.79; H, 7.59; N, 17.47.

(*B*) *Synthesis of 5-Methylnicotine.* To a suspension of 3 g of 5-methylmyosmine in 150 mL of H_2O was added 1 g of sodium cyanoborohydride. Concentrated hydrochloric acid was added dropwise with stirring over 30 min, during which the pH of the solution was reduced to 1.7. The solution was stirred for an additional 15 min, and then enough solid sodium acetate was added to bring the pH to 6. Formaldehyde (2 mL of 40% aqueous) was added, followed by 1 g of sodium cyanoborohydride. After being stirred for 15 min, the solution was made basic with sodium hydroxide and was extracted twice with 100-mL portions of methylene chloride. The organic phase was extracted with two

0003-2700/86/0358-2218$01.50/0 © 1986 American Chemical Society

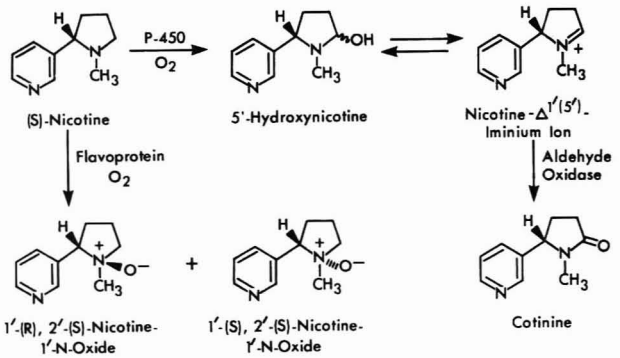

Figure 1. Oxidative metabolism of nicotine.

50-mL portions 1 N H_2SO_4, which were combined, and the methylene chloride layer was discarded. The acidic aqueous phase containing the product was made basic with sodium hydroxide and then was extracted with methylene chloride (2 × 50 mL). Evaporation of the methylene chloride using a rotary evaporator followed by bulb-to-bulb distillation (Kugelrohr oven, 110–120 °C, 0.1 mmHg) provided 2.1 g (70% yield) of light yellow mobile liquid. The bis(oxalate) was prepared by combining 0.29 g of the base with 0.42 g of oxalic acid dihydrate in methanol. Evaporation of the methanol (rotary evaporator) followed by recrystallization from methanol yielded 0.28 g of white crystalline powder, mp 131.5–133 °C. Anal. Calcd for $C_{15}H_{20}N_2O_8$: C, 50.56; H, 5.66; N, 7.86. Found: C, 50.87, H, 5.72; N, 7.89.

(C) Preparation of 5-Methylnicotine N-Oxide Bis(picrate). Hydrogen peroxide (0.1 mL of 35%) was added to 0.16 g of 5-methylnicotine in 10 mL of water. The solution was allowed to stand at room temperature for 3 days, after which it was extracted twice with 50-mL portions of ether to remove unreacted 5-methylnicotine. The ether extracts were discarded, and the aqueous phase was evaporated on a rotary evaporator to give an oil, which was combined with a solution of 0.4 g of picric acid in methanol. A gum separated which, on scratching with a glass rod, crystallized. Recrystallization from 30 mL of boiling 75% aqueous ethanol provided 0.25 g of bright yellow crystalline solid, mp 200–201 °C dec. Anal. Calcd for $C_{23}H_{22}N_8O_{15}$: C, 42.46; H, 3.41; N, 17.23. Found: C, 42.41; H, 3.36; N, 17.00.

Synthesis of Nicotine *N*-Oxide Bis(picrate). The sample of nicotine *N*-oxide used as the analytical standard was prepared from commercial nicotine by the method of Taylor and Boyer (*14*) and converted to the bis(picrate) in a manner analogous to the preparation of the 5-methyl analogue described above. The product was obtained as yellow needles from 65% ethanol, mp 170–171 °C (lit. mp 168–169 °C). Anal. Calcd for $C_{22}H_{20}N_8O_{15}$: C, 41.51; H, 3.17; N, 17.61. Found: C, 41.21; H, 3.20; N, 17.58.

Synthesis of 2-Methyl-6-(3-pyridyl)tetrahydro-1,2-oxazine (11). Nicotine *N*-oxide, prepared from 8.1 g (50 mmol) of nicotine, was heated at 150–160 °C under 25 mmHg using a Kugelrohr oven, and 6.4 g of light yellow liquid distilled. The electron impact mass spectrum (Kratos MS-25S) displayed prominent peaks at *m/z* 178 (9%, molecular ion), 119 (78%), 118 (44%), and 60 (100%), consistent with reported (*15*) mass spectral data for this compound. A small portion was converted to the bis(perchlorate) salt, which was recrystallized from ethanol as white needles, mp 155.5–156.5 °C. Anal. Calcd for $C_{10}H_{16}N_2Cl_2O_9$: C, 31.68; H, 4.25; N, 7.39. Found: C, 31.78; H, 4.23; N, 7.26.

Standards and Controls. Nicotine *N*-oxide bis(picrate) was dissolved in 75% aqueous ethanol to make a stock solution containing 1.0 mg/mL nicotine *N*-oxide base. The stock solution was diluted with water to prepare aqueous working standards or to spike nonsmokers' urine to concentrations over the range of 50–2000 ng/mL.

Sample Preparation and Gas Chromatographic Determination. Urine samples were acidified to a pH of 2–3 with HCl and stored frozen until the day of the analysis. Disposable 3-mL silica extraction columns were washed with 2 mL of methanol–57% ammonia (10:1) followed by 2 mL of water and then sucked dry. To 2-mL aliquots of urine were added 100 μL of internal standard (20 μg/mL aqueous 5-methylnicotine *N*-oxide) and 0.2 mL of saturated aqueous sodium acetate. The samples were vortex-mixed and applied to the columns under slight vacuum—enough to produce a flow of about 1 mL/min. By use of a homemade manifold constructed from copper tubing, up to 20 samples can be processed simultaneously. The columns were then washed successively with 2 mL of water and 2 mL of isopropyl alcohol to remove extraneous urinary constituents. Elution of nicotine *N*-oxide and internal standard was accomplished by passing 4 mL of methanol–57% ammonia (10:1) through the columns by gravity. The eluates were evaporated to dryness at about 50 °C with a current of nitrogen in 13 × 100 mm Pyrex culture tubes. Anisole (0.5 mL) was added to each tube and the tubes were capped and then heated at 150–160 °C for 30 min in a heating block. After the tubes were cooled to room temperature, 0.5 mL of 0.5 M sulfuric acid and 2 mL of toluene–isoamyl alcohol (95:5) were added to all tubes, which were then vortex-mixed for 5 min and centrifuged. The aqueous layers were frozen by placing the tubes in a dry ice–acetone bath, and the organic layers were poured off and discarded. Aqueous 3 M sodium hydroxide (0.5 mL) and toluene–isoamyl alcohol (95:5, 0.5 mL) were added, the tubes were vortex-mixed, centrifuged, and placed in a dry ice–acetone bath to freeze the aqueous layers. The organic layers were poured into autosampler vials for GC analysis. For packed column analyses, the autosampler parameters were two prewashes, two pumps, and 3-μL injection volume. At a column oven temperature of 160 °C, the retention times for 2-methyl-6-(3-pyridyl)tetrahydro-1,2-oxazine and the 5-methyl analogue were 1.50 and 2.22 min, respectively (Figure 4). For capillary column analyses (Figure 5), injections (1 μL) were made in the splitless mode, and the oven temperature was programmed from 90 to 275 °C at 25 deg/min after a 0.5-min initial hold. Retention times for the tetrahydro-1,2-oxazines derived from nicotine *N*-oxide and internal standard were 6.09 and 6.74 min, respectively. For both packed and capillary column analyses, the computing integrator was calibrated on a 1000 ng/mL standard using the internal standard method and peak height ratios. Standard curves were linear from 10 to 4000 ng/mL.

GC–MS Analysis of Urine Extract Containing Oxazine Derivatives. A smoker's urine specimen containing 1100 ng/mL nicotine *N*-oxide and 1000 ng/mL 5-methylnicotine *N*-oxide was carried through the extraction and thermal rearrangement procedure described above. A 1-μL aliquot was analyzed by GC–MS on a 12 m × 0.21 mm cross-linked methylsilicone column with a capillary direct interface to the mass spectrometer (Hewlett-Packard 5970B). The GC separation was carried out with a temperature program of 70–200 °C at 20 deg/min following a 3-min initial hold. The mass spectral analysis was carried out by using electron impact ionization at 70 eV and scanning from 35 to 210 amu. The mass spectrum of the oxazine derivative of nicotine *N*-oxide, which had a retention time of 8.7 min, displayed major ions at *m/z* 178 (8%, molecular ion), 119 (92%), 118 (68%), and 60 (100%), which is in good agreement with the mass spectral data obtained from the synthetic tetrahydro-1,2-oxazine described above. The oxazine derivative of 5-methylnicotine *N*-oxide, which had a retention time of 9.7 min, had a mass spectrum that was consistent with the proposed structure: *m/z* 192 (7%, molecular ion), 133 (100%), 132 (95%), and 60 (98%).

Determination of Efficiency of Extraction and Thermal Conversion to the Oxazine Derivative. Nonsmokers' urine was spiked with nicotine *N*-oxide to a concentration of 500 ng/mL, extracted, and analyzed as described above. The peak area of the thermal rearrangement product was compared to the area obtained by injecting a solution of synthetic oxazine derivative. For four replicate determinations, the yield ranged from 92 to 97%.

RESULTS AND DISCUSSION

Thermal rearrangement of nicotine *N*-oxide on an analytical scale was first attempted by directly injecting solutions into the gas chromatograph. At injection port temperatures ranging from 150 to 350 °C, we observed roughly equal amounts of reduction back to the nicotine and oxazine formation, as well as the formation of several minor products. This is consistent with a report (*16*) that nicotine *N*-oxide undergoes deoxygenation and dehydration as well as rearrangement to the oxazine when heated in the ion source of a mass spectrometer. When we injected extracts of urine

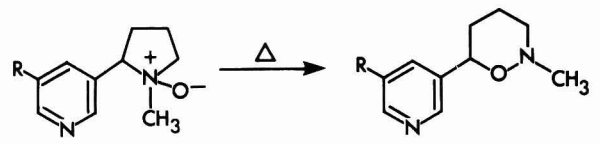

Nicotine N-Oxide, R = H

Internal Standard, R = CH_3

Figure 2. Thermal rearrangement of nicotine *N*-oxide and internal standard.

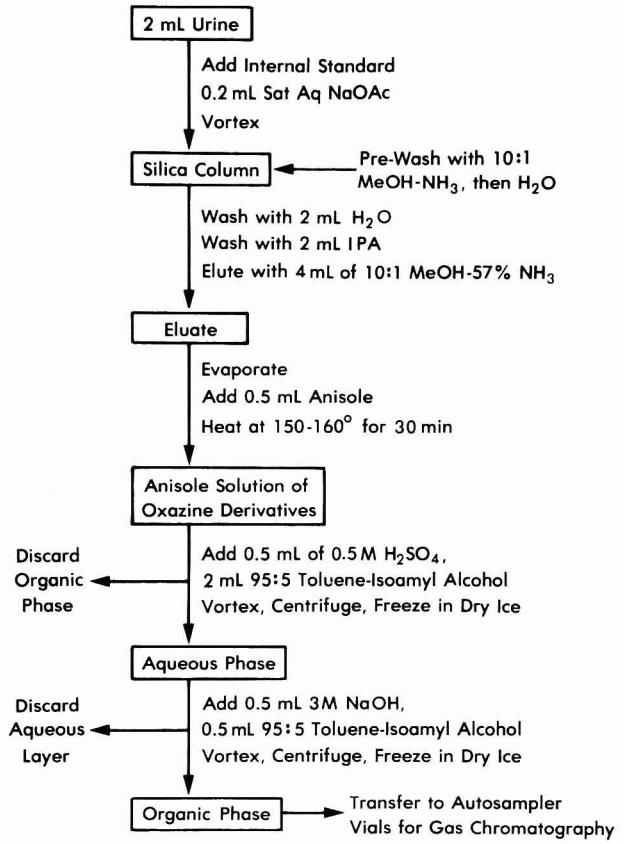

Figure 3. Flow diagram of the extraction procedure.

containing nicotine *N*-oxide, the oxazine was not resolved from other urinary constituents on either packed or capillary columns. Consequently, we turned our attention to methods for effecting the ring-expansion reaction prior to injection into the gas chromatograph in order to include cleanup steps in the extraction procedure.

Heating nicotine *N*-oxide neat or in various solvents at temperatures ranging from 100 to 200 °C resulted in varying amounts of reduction and oxazine formation. Aromatic ethers such as anisole, veratrole, and diphenyl ether gave the best results. With anisole as the solvent, the conversion to oxazine was 90% complete in less than 15 min at 160 °C with negligible reduction and was successful for quantities as little as 20 ng. The identity of the rearrangement product was confirmed by comparison of its retention time to that of material synthesized by the method of Rayburn et al. (*11*) and by its mass spectrum (*15*). In order to correct for losses of nicotine *N*-oxide occurring during extraction, thermal rearrangement and chromatography, we utilized a structural analogue, 5-methylnicotine *N*-oxide (Figure 2) as an internal standard. On thermal treatment, this compound was converted to a derivative which, based on its mass spectrum, is the Meisenheimer rearrangement product 2-methyl-6-(5-methyl-3-pyridyl)tetrahydro-1,2-oxazine.

The procedure developed for analysis of urine samples is shown in Figure 3 and described in detail in the Experimental

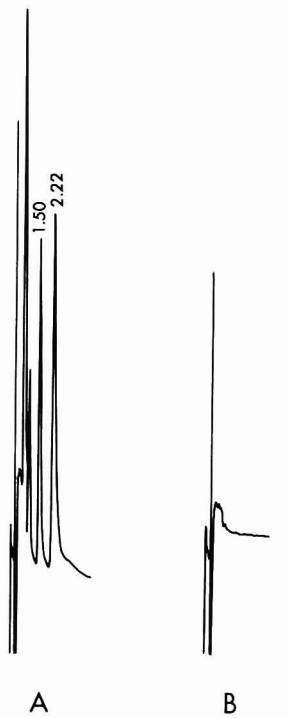

Figure 4. Chromatograms of urine extracts on Carbowax-KOH packed column. Numbers above peaks are retention times in min: tetrahydro-1,2-oxazine derived from nicotine *N*-oxide, 1.50 min; internal standard, 2.22 min. A, smoker's urine containing 540 ng/mL nicotine *N*-oxide. B, nonsmoker's urine.

Table I. Precision (%) of the Method for Spiked Urine Samples

	100 ng/mL	500 ng/mL	1000 ng/mL
within-run rel std dev (n = 6)	3.5	3.7	4.3
between-run rel std dev (n = 3)	9.0	1.0	5.6

Section. Following extraction from urine with silica columns and elution with methanolic ammonia, the eluates were evaporated to dryness with a current of nitrogen and heated in anisole at 150–160 °C to effect the ring-expansion reactions. After cooling to room temperature, the samples were cleaned up using standard acid–base partitioning steps. Unlike the *N*-oxides, the tetrahydro-1,2-oxazine derivatives are lipophilic and may be easily extracted from aqueous solutions into organic solvents. The final extracts were transferred to autosampler vials for gas chromatographic analysis. The analyses were carried out using either packed (2% Carbowax 20 M, 2% KOH) or capillary (25-m 5% phenylmethylsilicone fused silica) columns. Chromatograms obtained from extracts of nonsmokers' urines were free of peaks at retention times corresponding to the oxazine derivatives of both nicotine *N*-oxide and internal standard (Figures 4 and 5). We are now carrying out all of our analyses using capillary GC due to the high resolution and stability of modern cross-linked fused silica capillary columns. This requires temperature programming and a longer chromatographic run time but using an automatic sampler over 90 samples can be analyzed during a 24-h period.

The precision of the method is good. By use of packed column analysis, within-run relative standard deviations were between 3 and 5% at concentrations found in smokers' urine (Table I). A good correlation (r = 0.99) was obtained for a set of samples analyzed by both capillary and packed column GC. Twelve representative smokers' urine specimens which had originally been analyzed by packed column GC were reextracted and analyzed by capillary GC 2 years later (Table

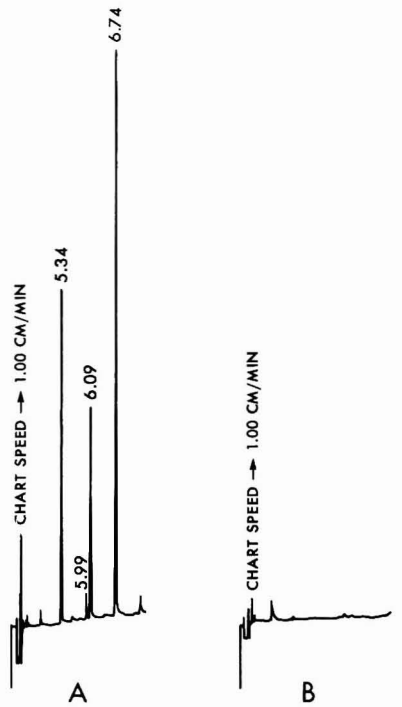

Figure 5. Chromatograms of urine extracts on 25 m × 0.31 mm 5% phenylmethylsilicone capillary column. Numbers above peaks are retention times in min: tetrahydro-1,2-oxazine derived from nicotine *N*-oxide, 6.09 min; internal standard, 6.74 min. A, smoker's urine containing 244 ng/mL nicotine *N*-oxide. B, nonsmoker's urine.

Table II. Concentration of Nicotine *N*-Oxide in Urine of 12 Smokers Determined on Packed and Capillary Columns[a]

	nicotine *N*-oxide concn,[a] ng/mL	
sample	packed column[b]	capillary column[c]
HB	410	445
MJ	1090	1260
LD	1040	1190
SS	909	1090
SK	242	236
JD	282	395
DM	363	300
ND	113	98
AL	86	81
JM	304	364
EB	370	335
SC	990	963
mean	525	562

[a] Correlation coefficient $r = 0.99$. [b] Extraction and GC determination carried out in January 1984, using a 2-m Carbowax-KOH column. [c] Extraction and GC determination carried out in March 1986, using a 25 m × 0.132 mm 5% phenylmethylsilicone column.

II). Values obtained by capillary GC averaged 7% higher, but the difference was not statistically significant by paired *t* test.

This method has been used in our laboratory for the analysis of approximately 250 urine specimens obtained from smokers. Urinary excretion of nicotine *N*-oxide in 26 smokers averaged 0.56 mg per 24 hr, which is similar to published data (*2*, *17*, *18*). Nicotine and cotinine excretion were also determined (*19*) in these subjects and was found to be 2- to 3-fold greater than nicotine *N*-oxide (Table III).

The previously reported gas chromatographic methods (*2*, *20*) for determining nicotine *N*-oxide in smoker's urine require reduction of the *N*-oxide to nicotine. In these procedures nicotine, present in much higher concentrations than the

Table III. Urinary Excretion[a] of Nicotine and Metabolites by 26 Smokers

	mean	std dev	range
nicotine concn, ng/mL	2230	1800	159–6540
nicotine excretion, mg/24 h	1.12	0.88	0.076–3.18
cotinine concn, ng/mL	2800	1600	438–6170
cotinine excretion, mg/24 h	1.39	0.66	0.174–2.78
nicotine *N*-oxide concn, ng/mL	1060	665	102–3120
nicotine *N*-oxide excretion, mg/24	0.56	0.37	0.041–1.59

[a] Urine was collected in 24-h blocks on a research ward.

N-oxide in most biological samples, must be removed first by several extractions. Our method, which utilizes the Meisenheimer rearrangement of nicotine *N*-oxide to the tetrahydro-1,2-oxazine derivative, does not require prior removal of nicotine. We have not yet explored the generality of the method, but it appears that analogous procedures would be applicable for the determination of other tertiary amine *N*-oxides.

ACKNOWLEDGMENT

The authors are grateful to Kaye Welch, Beverly Busa, and Guy Flores for their assistance in this research and to Lisa Peterson for providing some of the mass spectral data.

Registry No. Nicotine *N*-oxide, 2820-55-5; 2-methyl-6-(3-pyridyl)tetrahydro-1,2-oxazine, 15769-88-7; ethyl 5-methylnicotinate, 20826-02-2; *N*-vinylpyrrolidin-2-one, 88-12-0; 5-methylmyosmine, 102780-52-9; 5-methylnicotine, 77629-31-3; 5-methylnicotine *N*-oxide bis(picrate), 102780-54-1; nicotine *N*-oxide bis(picrate), 102780-55-2.

LITERATURE CITED

(1) Rose, J.; Castagnoli, N., Jr. *Med. Res. Rev.* **1983**, *3*, 73–88.
(2) Beckett, A. H.; Gorrod, J. W.; Jenner, P. *J. Pharm. Pharmacol.* **1971**, *23*, 55S–61S.
(3) Benowitz, N. L.; Kuyt, F.; Jacob, P., III; Jones, R. T.; Osman, A.-L. *Clin. Pharmacol. Ther. (St. Louis)* **1983**, *34*, 604–611.
(4) Booth, J.; Boyland, E. *Biochem. Pharmacol.* **1970**, *19*, 733–742.
(5) Kyerematen, G. A.; Damiano, M. D.; Dvorchek. B. H.; Vesell, E. S. *Clin. Pharmacol. Ther. (St. Louis)* **1982**, *32*, 769–780.
(6) Thompson, J. A.; Norris, K. J.; Petersen, D. R. *J. Chromatogr.* **1985**, *341*, 349–359.
(7) Castagnoli, N., Jr.; Craig, J. C.; Melikian, A. P.; Ray, S. K. *Tetrahedron* **1970**, *26*, 4319–4327.
(8) Cowan, D. A. In *Biological Oxidation of Nitrogen*; Gorrod, J. W., Ed.; Elsevier/North Holland Biomedical Press: Amsterdam, 1978; pp 263–268.
(9) Hallstrom, G.; Nguyen, C. H.; Cho, A. K. *Acta Pharm. Suec.* **1983**, *20*, 181–192.
(10) Chan, K.; Kendall, M. J.; Mitchard, M. *J. Chromatogr.* **1974**, *89*, 169–176.
(11) Rayburn, C. H.; Harlan, W. R.; Hanmer, H. R. *J. Am. Chem. Soc.* **1950**, *72*, 1721–1723.
(12) Deady, L. W.; Shanks, R. A.; Campbell, A. D.; Chooi, S. Y. *Aust. J. Chem.* **1971**, *24*, 385.
(13) Jacob, P., III *J. Org. Chem.* **1982**, *47*, 4165–4167.
(14) Taylor, E. C.; Boyer, N. E. *J. Org. Chem.* **1959**, *24*, 275–277.
(15) Phillipson, J. D.; Handa, S. S. *Phytochemistry* **1975**, *14*, 2683–2690.
(16) Shuller, D.; Harker, H.-P. *Org. Mass Spectrom.* **1973**, *7*, 839–843.
(17) Gorrod, J. W.; Jenner, P.; Keyrell, G. R.; Mikhael, B. R. *J. Natl. Cancer Inst. (U.S.)* **1974**, *52*, 1421–1424.
(18) Klein, A. E.; Gorrod, J. W. *Eur. J. Drug Metab. Pharmacokinet.* **1978**, 87–93.
(19) Jacob, P., III; Wilson, M.; Benowitz, N. L. *J. Chromatogr.* **1981**, *222*, 61–70.
(20) Stehlik, G.; Kainzbauer, J.; Tausch, H.; Richter, O. *J. Chromatogr.* **1982**, *232*, 295–303.

RECEIVED for review June 10, 1985. Resubmitted April 21, 1986. Accepted April 21, 1986. This research was supported in part by Public Health Service Grants DA02277, DA01696, CA32389, and HL29476. The clinical studies were carried out at the San Francisco General Hospital Clinical Research Center (RR-00083) with support from the Division of Research Resources, National Institutes of Health.

Dynamic Chromatographic Systems for the Determination of Rare Earths and Thorium in Samples from Uranium Ore Refining Processes

D. J. Barkley* and Marcia Blanchette[1]

Mineral Sciences Laboratories, Canada Centre for Mineral and Energy Technology, Ottawa, Ontario, Canada K1A 0G1

R. M. Cassidy and Steve Elchuk

General Chemistry Branch, Chalk River Nuclear Laboratories, Atomic Energy of Canada Limited, Chalk River, Ontario, Canada K0J 1J0

Dynamic ion exchange has been used for the rapid separation (16 min) and determination of rare earths and Y in samples from hydrometallurgical processes used to recover U, Th, Y, and the rare earths from uranium ore. Optimization of the effective capacity of the dynamic ion exchanger and the selectivity of postcolumn reaction detection permitted analysis down to 0.1 $\mu g \cdot mL^{-1}$ of the rare earths and yttrium in the presence of U, Th, and a number of other metal ions. A comparison with X-ray fluorescence results showed good agreement, and the chromatographic procedure offered considerable savings in analysis time. Studies with Th(IV) and U(VI) showed that both metal ions exhibited selective sorption of their α-hydroxyisobutyric complexes, formed in situ in the eluent, onto reversed phases. The analytical results obtained showed that this dynamic separation process could be used for the determination of Th, and its potential for the determination of U was demonstrated.

The Canada Centre for Mineral and Energy Technology is concerned with the development of new and improved refining processes to maximize the recovery of uranium and valuable byproducts, including Th and the rare earths, from low-grade and complex ores. Ion exchange and solvent-extraction processes are used to separate, concentrate, and purify the metals. In a typical process the ore is leached with an acid, and the resulting uranium leach liquid containing U, Th, rare earths, and other metals dissolved from the ore is passed through an ion exchange system to remove U. The uranium–barren solution is used as a feed for a solvent-extraction process to remove Th, and rare earths are then separated from the uranium–thorium–barren solution.

In solvent extraction processing, the metal or metals of interest are selectively complex from the feed solution by an organic extractant and are then acid stripped from the organic phase. These procedures have been described in more detail elsewhere (*1*). To optimize these processes, the determination of rare earths, Y, and Th is required. Analytical methods used previously have included X-ray fluorescence, multichemical separation schemes, and classical ion-exchange techniques. A problem common to these analytical techniques is the separation step, or steps, used to isolate rare earths and Th from extraneous metals. Chemical separations, e.g., fluoride, oxalate, and hydroxide precipitations, are time-consuming, require careful attention, and have the possibility of rare earth losses (*2*). Sufficient sample size is important for chemical separation techniques, and in the development of new refining processes, sample quantity can be limited. Classical ion exchange separations are also time-consuming and have poor resolution and poor reproducibility.

Small-particle styrene–divinylbenzene resins (*3*, *4*) and bonded-phase exchangers (*5*, *6*) have been used to give improved resolution of the rare earths. However, column stability and resolution were not equivalent to that expected for modern high-performance liquid chromatography (HPLC), and the application of these techniques to samples required preliminary separations to obtain adequate resolution of the rare earths. Recent studies of dynamic ion exchangers (*7*) have shown that this technique in combination with postcolumn-reaction detection can be used for the sensitive and reproducible determination of rare earths in thorium and uranium fuels (*8*, *9*) and for the determination of uranium (*8*). Dynamic ion exchangers are formed when hydrophobic ions, which are present in the mobile phase, are sorbed onto the hydrophobic surface of a reversed-phase to produce a charged double layer at the surface where ion exchange can occur. These exchangers gave improved column efficiency for metal ions, and greater flexibility with regard to choice of separation conditions. Consequently the application of these dynamic ion exchangers was studied for the determination of rare earths, Y, and Th in samples from different circuits of a refining process for uranium ore. This paper presents the results of this study and compares these results with X-ray fluorescence analyses.

EXPERIMENTAL SECTION

Reagents and Materials. Water used for solutions and eluents was freshly prepared distilled water that had been purified in a Milli-Q deionizing unit (Millipore, Bedford, MA). Stock solutions of α-hydroxyisobutyric acid (HIBA) and sodium *n*-octylsulfonate ($C_8SO_3^-$) were purified by cation ion exchange; the H^+ form was used for HIBA and the NH_4^+ form for $C_8SO_3^-$. All other chemicals were reagent grade. The columns used were 4.6 × 150 mm 5-μm Supelcosil LC-18 (Spelco, Bellefonte, PA), 4.6 × 100 mm 3-μm Hypersil C-18 (chromatographic Sciences Co., Montreal, PQ), and 4.6 × 150 mm 5-μm and 10-μm PRP-1 (Hamilton, Reno, NV). Standards were obtained from SPEX Industries (Metuchen, NJ).

Apparatus. A variety of HPLC apparatus was used for these studies. It consisted of a Spectra Physics SP-8100 system (Spectra Physics, Santa Clara, CA), a Spectra Physics M8700 pump, Rheodyne (M7125, Berkley, CA) and Valco (Model CV-6-UNPa-N60, Valco Instruments, Houston, TX) sample valves, Kratos SF770 and SF773 variable wavelength detectors (Kratos Analytical Instruments, Westwood, NJ), and Spectra Physics SP-4270 computing integrators. The X-ray fluorescence measurements were made with a Philips 1220 X-ray spectrometer.

Procedures. For HPLC analysis the 5-μm C_{18} reversed phase was equilibrated with an aqueous mobile phase containing 2.5 × 10^{-4} to 3.0 × 10^{-2} $mol \cdot L^{-1}$ ammonium *n*-octylsulfonate, 0.05 $mol \cdot L^{-1}$ HIBA at pH 4.2 (adjusted with NH_4OH), and 7.5% (v/v) methanol. A 25-μL sample was injected and separated via a gradient from 0.05 to 0.4 $mol \cdot mL^{-1}$ HIBA over 10 min at 1 $mL \cdot min^{-1}$ and then held at 0.4 $mol \cdot L^{-1}$ for 5 min. The eluted metal ions were monitored at 658 nm after a postcolumn reaction with

[1]Present address: University of Ottawa, Ottawa, Ontario, Canada.

0003-2700/86/0358-2222$01.50/0 Published 1986 by the American Chemical Society

Table I. Expected Concentrations of Metals in Samples and Detection Limits for Arsenzao III

metal	concn of metal ion,[a] $\mu g \cdot mL^{-1}$	detection limits,[b] $\mu g \cdot mL^{-1}$
Ni(II)	0.64	>10
Zn(II)	5.3	>10
Mn(II)	3.2	>10
Cu(II)	1.78	2
Pb(II)	0.40	2
CO(II)	0.36	>10
Fe(III)	230	*c*
Fe(II)		2.5
rare earths	0.1–6	0.08
Y(III)	5–7	0.08
Th	40–30	0.2

[a] Concentrations given for 10-fold dilution of sample. [b] Detection limits are 3× peak-to-peak noise. [c] Elutes at solvent front.

Arsenazo III (3,6-bis[(*o*-arsenophenyl)azo]-4,5-dihydroxy-2,7-naphthalenedisulfonic acid). The postcolumn reagent (1.2 $mol \cdot L^{-1}$ in Arsenazo III and 0.5 $mol \cdot L^{-1}$ in acetic acid) was added to the eluent with a syringe pump (M314, ISCO, Lincoln, NE) via a low dead-volume mixer (*6*) at 1.2 $mL \cdot min^{-1}$. Quantitation was done by comparison of sample peak heights with the peak heights for a series of standards. Aqueous samples from the solvent extraction process were analyzed by direct injection of a 10- to 30-fold dilution of the process samples. Aliquots of the organic phase, which consisted of a kerosene solvent and the extractant, were evaporated on a steam bath and treated repeatedly with HNO_3 and $HClO_4$ to oxidize all remaining organic material. The samples were then taken to incipient dryness and dissolved in the eluent.

The X-ray fluorescence procedure consisted of chemical separations, preparation of fused glass disks with lithium tetraborate, and a subsequent measurement with a Philips PW 1220 semiautomatic X-ray fluorescence spectrometer. The chemical separations consisted of double precipitations (ammonium hydroxide followed by fluoride) and the fluoride precipitate was used for preparation of the fused-glass disks. Two disks were prepared for each sample as the calibration technique used was a double-dilution technique with one aliquot being twice the quantity of the other. The spectral corrections and details of the calculations have been published (*10*).

The reagent Thorin was used for the spectrophotometric determinations of thorium. Samples were first precipitated with NaOH, dissolved in HCl, and then separated on a cation exchange resin. Details of the procedure are given elsewhere (*11*).

RESULTS AND DISCUSSION

Detection. In preliminary work to apply HPLC to the separation and determination of rare earths, 4-(2-pyridylazo)resorcinol (PAR) was used as a postcolumn reagent. Satisfactory detection limits were obtained for the rare earths, but it could not be used with direct injection of process samples because of the interference from other metals. Metals present in the samples included Fe(II) and Fe(III), Mn(II), Co(II), Cu(II), Ni(II), Zn(II), and Pb(II); the concentrations expected in the samples are given in Table I. Tests with Arsenazo III showed that it was more selective for the rare earths than PAR and gave better detection limits (~2 ng, 3× peak-to-peak base line noise); detection limits observed in this work are given in Table I. These data show that the extraneous metals should not interfere and that the detection limits for the metals were sufficient to permit their determination at the required levels. During these studies it was observed that bacteria in the water collected on the column and caused large disruptions in the background (*8*, *9*) which could interfere with the detection of small amounts of metal ions. To prevent the buildup of bacteria, particularly during summer months, mobile phases were filtered through a 0.2-μm membrane; the addition of methanol to the mobile phase also helped to reduce this problem.

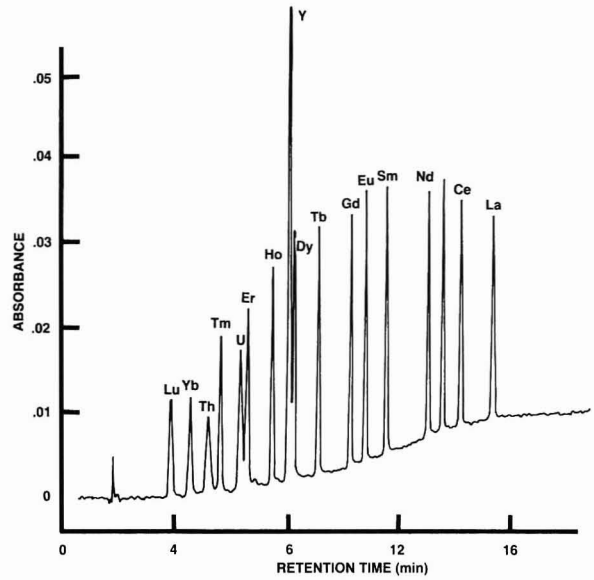

Figure 1. Separation of rare earths, yttrium, thorium, and uranium. Experimental conditions: column, 4.6 × 150 mm 5-μm Supelcosil LC-18; gradient separation at 1 $mL \cdot min^{-1}$ from 0.05–0.4 $mol \cdot L^{-1}$ HIBA at pH 4.2 over 10 min and held at 0.4 $mol \cdot L^{-1}$ for 5 min; modifiers, 0.03 $mol \cdot L^{-1}$ $C_8SO_3^-$ and 7.5% (v/v) methanol; sample, 25 μL containing 25 ng of each rare earth and 50 ng of Y(III), Th(IV), and U(VI); detection at 658 nm after a postcolumn reaction with Arsenazo III.

Determination of Rare Earths and Yttrium. The dynamic ion exchange and postcolumn reaction system gave efficient separation and sensitive detection of the rare earths and Y(III) as shown in Figure 1. The sharp peaks reflect the rapid mass transfer characteristics of the dynamic ion exchanger, and the ability to quickly adjust the effective ion exchange capacity was an important factor in being able to optimize separation from Th(IV) and U(VI). With appropriate adjustments in the concentration of the $C_8SO_3^-$ and methanol, which changed the effective ion exchange capacity, and in the pH of the eluent, it was thus possible to optimize the eluant composition to place the Th(IV) and U(VI) peaks between Yb(III)/Tm(III) and Tn(III)/Er(III), rather than in the middle or end of the rare earth separation where the peaks were broad and overlapped rare-earth peaks. The Th(IV) peak was placed near Tm(III) because the concentration of Tm(III) in the samples was low and thus of minor importance. Except for the uranium-leach liquor, the concentration of U(VI) was generally low enough that it did not interfere with Er(III) determinations.

Figure 2 shows the chromatogram obtained for a uranium-leach liquor. This chromatogram shows that good peak shape was observed for the rare earths and that this system should also be applicable to the determination of U(VI) in these samples. Although these samples were analyzed by HPLC, no data from X-ray fluorescence measurements were available for comparison. Figure 3 shows the separation of a uranium–barren sample, and as can be seen uranium has been removed by the process. To give perspective to the peak heights in Figure 3, the peak for Gd(III) was equivalent to 33 ng in the injected 25-μL sample. Ytterbium(III) and Er(III) were well-separated from Th(IV), but Tm(III) was on the side of the Th(IV) peak. There was some band broadening of the Th(IV) peak, which made quantitation of the Th(IV) difficult. The results obtained for this sample are compared with results from XRF analysis in Table II. The HPLC data were obtained from the average of five duplicate determinations over a 2-week period, and good reproducibility was obtained for all the rare earths. The relative precision (1σ) obtained for the determination of Ce, Nd, and Ho in a U–Th–barren sample with five different calibrations over a 2-week period

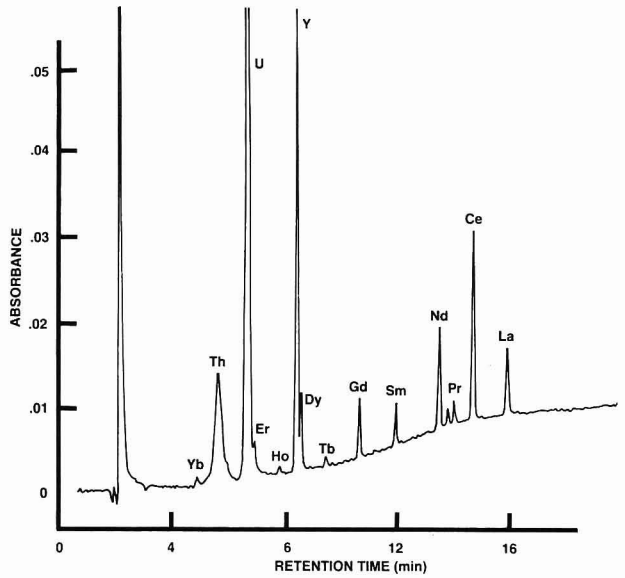

Figure 2. Separation of uranium leach liquor. Experimental conditions are given in Figure 1.

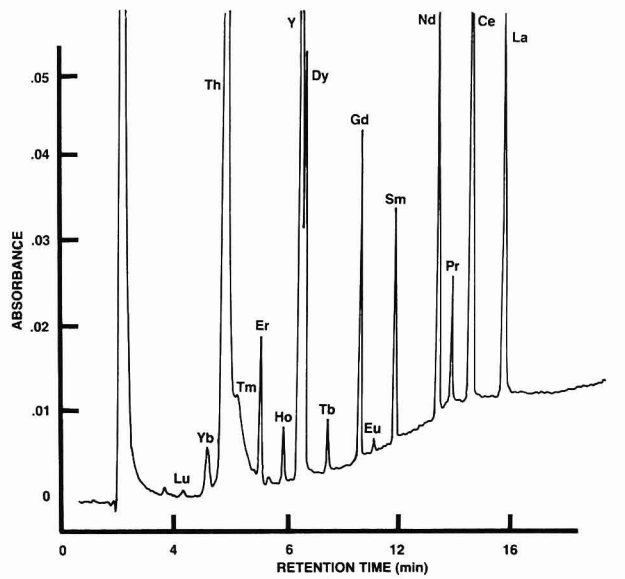

Figure 3. Separation of uranium–barren liquor. Experimental conditions are given in Figure 1.

was 1.9%, 1.6%, and 12%, respectively; the weights of Ce, Nd, and Ho in the injected samples were 47.5 ng, 12.5 ng, and 3.2 ng, respectively. The average of the ratio of HPLC/X-ray results was 1.16 (Table II), which suggests a bias of 16% between the two methods. However, this bias is not statistically significant at the 95% confidence level for this set of data where $\sigma = 0.3$.

Overall there was good agreement between the procedures for the majority of the rare earths; however, significant discrepancies existed for Er(III), Pr(III), and Dy(III). HPLC results obtained by standard addition analysis for Er(III) and Dy(III) were 8.0 and 18 mg·L^{-1}, respectively, and were in agreement with those calculated from direct injection, but the value for Pr(III), 4.2 mg·L^{-1}, was lower and not in agreement with the X-ray results. The results for Er(III) and Dy(III) were low relative to the X-ray fluorescence results, but the most obvious source of interference that could affect only two of the rare earths was coelution with another component, which should cause high results. Although the determination of Dy(III) was susceptible to interference from Y (see Figure 3), it was uncertain whether the errors for Dy(III) and Er(III) were associated with the HPLC or the X-ray fluorescence

Table II. Comparison of HPLC and X-ray Results for Uranium–Barren Sample

	analysis results		
rare earth	HPLC,[a] mg·L^{-1}	HPLC std dev 1σ	X-ray, mg·L^{-1}
Lu	<1		<2
Yb	6.2	0.6	5
Tm	2.1		<2
Er	8.8	0.3	14
Ho	3.6	0.3	2
Dy	18	0.2	12
Tb	3.3	0.5	2
Gd	14	0.2	12
Eu	<2	0.5	<2
Sm	9.9	0.4	7.8
Nd	24	0.2	20
Pr	6.7	0.8	4
Ce	46	1.1	45
La	21	0.5	21

mean of HPLC/X-ray results = 1.16

$1\sigma = 0.30$

[a] Average of results for sample that had been analyzed five times in duplicate in 2 weeks. Three different sample dilutions were used.

procedure. It is known that the double dilution X-ray fluorescence calibrations technique has a high theoretical error at low concentrations (*10*). As the detection limit is ~3 mg·L^{-1} this could account for some of the discrepancies, especially in the lower concentration range. The decrease in the analyzed value for Pr(III) for standard addition quantitation was unexpected because it suggested the presence of a significant matrix effect for only one of the rare earths. A possible source of the error in the Pr(III) results was from effects of equilibria (system peaks) that are present in dynamic ion exchange systems (*12*). If a sample peak partially overlaps a system peak, it will experience a gradient in eluent strength or effective ion exchange capacity either of which can change peak shape. Thus for quantitation from peak-height calibration curves, analyses would be sensitive to these effects, but not for quantitation by standard addition. Another potential source of error was from the effects of bacteria in the eluents (see Detection) which caused a base line shift (mainly due to Fe(II)) near Pr(III)). The magnitude of this shift is also dependent on the nature of the sample injected. To help ensure that these effects do not occur, all samples should be diluted with the mobile phase, and bacteria should be eliminated (see Detection).

The separation of uranium–thorium–barren samples gave a chromatogram similar to Figure 2 except that the majority of the Th(IV) and almost all the U(VI) had been removed. The HPLC results for this sample are compared with the X-ray fluorescence results in Table III. As for the previous comparison (Table II) the agreement was good except for Pr(III). Reanalysis by standard addition gave essentially the same results for Er(III) and Dy(III), but the result for Pr(III) was lowered to 3.4 mg·L^{-1}, now in agreement with the X-ray results (Table III). The error in the Dy(III) value may be the result of an interference from the large amounts of Y(III) in this sample (see Figure 2) and the error in the Pr analyses may be caused by the effects discussed above for uranium–barren samples. The mean of the HPLC/X-ray results, 1.17, is similar to that found for the uranium–barren samples (Table II). The bias between the two sets of data, 17%, was close to being significant at the 95% confidence level because of the small value of σ relative to that of the data in Table II. When the results in Tables II and III were pooled to increase

Table III. Comparison of HPLC and X-ray Results for Uranium–Thorium–Barren Sample

	analysis results		
rare earth	HPLC,[a] mg·L^{-1}	HPLC std dev 1σ	X-ray, mg·L^{-1}
Lu	<1		<2
Yb	4.1	0.5	3
Tm			<2
Er	6.5	0.5	4
Ho	2.6	0.4	<2
Dy	12	0.1	7.8
Tb	2.6	0.4	2
Gd	10	0.2	9.5
Eu	1.8	0.4	<2
Sm	8.1	0.5	6.9
Nd	21	0.2	18
Pr	5.9	0.7	3
Ce	38	0.9	38
La	17	0.2	17

mean of HPLC/X-ray results = 1.17

1σ = 0.22

[a] Average of results for sample that had been analyzed five times in duplicate in 2 weeks. Three different sample dilutions were used.

Table IV. Determination of Th in U–Barren and U–Th–Barren Samples[a]

	thorium concn, g·L^{-1}		
sample	HPLC	colorimetric	X-ray
U–barren	0.29	0.28	0.28
U–Th–barren	0.038	0.040	0.040

[a] Experimental conditions: 0.25 mol·L^{-1} HIBA, 2.5 × 10^{-4} mol·L^{-1} $C_8SO_3^-$, 10% (v/v) methanol, pH 4.6, flow rate = 1 mL·min^{-1}.

the size of the data base, the overall bias was also close to being significant at the 95% level, and thus was of some concern. One possible reason for this bias is the fact that the X-ray method was being applied at or near its detection limit for many of the samples. This bias will be given additional consideration during future applications of the HPLC method.

This HPLC method has also been applied to monitoring the performance of new processes developed to recover Fe and Th and Y plus the rare earths and to the analysis of organic extracts containing lanthanide concentrations down to levels of 1 μg·g^{-1}. With this method it was possible to quickly quantify the metal ions of interest as well as identify and determine other metal ions that were coextracted in both aqueous and organic phases.

Determination of Uranium and Thorium. Th(IV) and, to a lesser extent, U(VI) exhibited broad peaks under the conditions used for the determination of the rare earths, and their determination at low concentrations in the presence of the rare earths was difficult. Experiments with columns of different exchange capacity (different concentrations of $C_8SO_3^-$) showed that selective separation of Th(IV) and U(VI) was possible. This separation was optimized for Th(IV) and the results obtained for Th(IV) in a uranium–barren and a uranium–thorium–barren sample were compared with results from X-ray and colorimetric methods. Table IV shows that excellent agreement was obtained.

Under the conditions used to obtain the HPLC data in Table IV it was unlikely that the $C_8SO_3^-$ had any appreciable effect on the separation. Consequently the mechanism of this separation was examined in more detail. These studies showed that the $C_8SO_3^-$ modifier was not required for sorption and

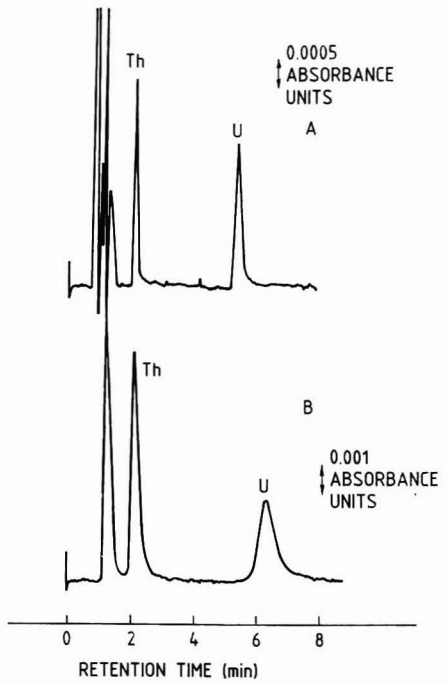

Figure 4. Separation of uranium and thorium on reversed-phase columns. Curve A, 3-μm C_{18} column; 0.15 mol·L^{-1} HIBA at pH 3.8 with 10% (v/v) methanol; flow rate, 1.5 mL·min^{-1}; sample, 100 μL containing 3.5 ng of each rare earth, 5 ng of Th(IV) and U(VI). Curve B, 5-μm PRP-1 column; 0.25 mol·L^{-1} HIBA at pH 3.8; flow rate, 1.0 mL·min^{-1}; sample, 100 μL containing 14 ng of each rare earth, 20 ng of Th(IV) and U(VI). Detection was the same as that given in Figure 1.

Table V. Change in k' with Acetonitrile Concentration[a]

	capacity factor (k')	
% (v/v) acetonitrile	Th(IV)	U(VI)
0	4.6	17
5	0.74	6.9
15	0.50	2.5

[a] Experimental conditions: PRP-1 column, 0.1 mol·L^{-1} HIBA at pH 4.5.

that Th(IV) and U(VI) were selectively sorbed onto reversed phases in the presence of only HIBA. Figure 4 shows chromatograms obtained on a PRP-1 and a C_{18} reversed phase. The C_{18} phase gave a higher resolution separation, and detection limits were <1 ng for Th(IV) and U(VI). The rare earths eluted at the solvent frot as did the transition metal ions Cu(II), Zn(II), Fe(II), Fe(III), Mn(II), Co(II), Pb(II), and Ni(II).

Addition of organic solvent to the HIBA eluent decreased retention times of U(VI) and Th(IV) as shown in Table V. The U(VI) peak exhibited considerable fronting in the absence of organic solvents but was symmetrical at compositions above 5% for acetonitrile or methanol (see Figure 4). Increases in the concentration of HIBA had only a slight effect (increased) on the retention time of U(VI) and Th(IV), but decreases in pH caused large decreases in retention time. Changes in pH from 4.8 to <3 caused protonation of the HIBA, and U(VI) and Th(IV) were essentially unretained below pH 3.

Sample pH also affected the retention and analysis of U(VI) and Th(IV). For sample pH values between 4.5 and 2.4 quantitative recovery was obtained even though a slight shift to lower retention times was observed. Below pH 2.4, however, losses were observed, primarily for U(VI), and part of the samples eluted with the low pH solvent front. At a sample pH of 1.6, approximately 75% of the U(VI) was eluted at the solvent front. Calibration curves for U(VI) separations on a

PRP-1 column (0.1–1.0 $\mu g \cdot mL^{-1}$) and on a C_{18} reversed phase (18–58 $\mu g \cdot mL^{-1}$) were linear with a negative Y axis intercept equivalent to 0.05 and 0.04 $\mu g \cdot mL^{-1}$ U(VI) respectively. Silica-based supports used for this analysis must have a minimum of free silanol sites. Both U(VI) and Th(IV) interact strongly with bare silica surfaces and this interaction can cause peak tailing. The excellent sensitivity and selectivity of this interaction with HIBA make this approach attractive for the determination of trace concentrations of U(VI) and Th(IV) after trace enrichment, and this approach is being studied. This technique is also being studied for the selective determination of U(VI) in solutions of irradiated fuel.

ACKNOWLEDGMENT

The authors wish to thank J. L. Dalton (CANMET) for the X-ray fluorescence results and helpful discussions and F. M. B. Pontes (University of Waterloo, Ontario) for technical assistance during parts of this work.

Registry No. La, 7439-91-0; Ce, 7440-45-1; Nd, 7440-00-8; Sm, 7440-19-9; Eu, 7440-53-1; Gd, 7440-54-2; Tb, 7440-27-9; Dy, 7429-91-6; Ho, 7440-60-0; Er, 7440-52-0; U, 7440-61-1; Tm, 7440-30-4; Th, 7440-29-1; Yb, 7440-64-4; Lu, 7439-94-3; Y, 7440-65-5; Pr, 7440-10-0; Arsenazo III, 1668-00-4.

LITERATURE CITED

(1) Ritcey, G. M. *Sep. Sci. Technol.* **1983**, *18*, 1617–1646.
(2) Barkley, D. J. *Tech. Bull. TB125*; Energy Mines and Resources Canada: Ottawa, July 1970.
(3) Takata, Y.; Arikawa, Y. *Bungeski Kagaku* **1975**, *24*, 762–767.
(4) Dubuquoy, C.; Metzer, G. *Analysis* **1977**, *5*, 314–320.
(5) Larsen, N. R. *J. Radioanal. Chem.* **1979**, *52*, 85–91.
(6) Elchuk, S.; Cassidy, R. M. *Anal. Chem.* **1979**, *51*, 1434–1438.
(7) Cassidy, R. M.; Elchuk, S. *Anal. Chem.* **1982**, *54*, 1558–1563.
(8) Knight, C. H.; Cassidy, R. M.; Recoskie, B. M.; Green, L. W. *Anal. Chem.* **1984**, *56*, 474–478.
(9) Cassidy, R. M.; Elchuk, S.; Elliot, N. L.; Green, L. W.; Knight, C. H.; Recoskie, B. M. *Anal. Chem.* **1986**, *58*, 1181–1186.
(10) Lalonde, C. R.; Dalton, J. L. *Can. J. Spectrosc.* **1982**, *27*, 163–170.
(11) Hunt, G. A.; Guest, R. J.; Ingles, J. C.; Hitchen, A.; Barkley, D. J. *A Manual of Analytical Methods Used by the Canadian Mining Industry*; Energy, Mines and Resources Canada: Ottawa, 1974; p 196.
(12) Cassidy, R. M.; Fraser, M. *Chromatographia* **1984**, *18*, 369–373.

RECEIVED for review January 28, 1986. Accepted April 30, 1986.

Liquid Chromatographic Separation and Indirect Detection of Inorganic Anions Using Iron(II) 1,10-Phenanthroline as a Mobile Phase Additive

Pantelis G. Rigas and Donald J. Pietrzyk*

Chemistry Department, The University of Iowa, Iowa City, Iowa 52242

Iron(II) 1,10-phenanthroline [$Fe(phen)_3^{2+}$] salts are used as a mobile phase additive for the liquid chromatographic separation of inorganic analyte anions on a reverse stationary phase. The retention appears to be consistent with an ion interaction type retention. Major variables evaluated are the type of reverse stationary phase, $Fe(phen)_3^{2+}$ retention and mobile phase concentration, organic modifier effects, pH, buffer components, type and concentration of counteranion, ionic strength, and anion selectivity. Indirect detection is used to detect analyte anions by monitoring the effluent at 510 nm where $Fe(phen)_3^{2+}$ absorbs. Several separations of multicomponent mixtures illustrating excellent resolution and efficiency are shown. A detection limit under favorable conditions approaches about 1 ng. Linear detector response with analyte anion (Cl^-, Br^-) concentration was found from 10 ng to over 10 000 ng of injected analyte.

A successful strategy used in the liquid chromatographic (LC) separation of ionic analytes is to use a hydrophobic ion as a mobile phase additive and take advantage of the interactions that occur between the analyte ion, hydrophobic ion, and the stationary phase. In general, the result is increased retention, improved selectivity, more favorable resolution, and more mobile–stationary phase parameters that can be adjusted for optimization of the factors. This technique, which was first applied to the separation of organic analyte ions, is most often referred to as "ion pair chromatography" (IPC) and the hydrophobic ion is called the pairing reagent. IPC and its applications in organic separations have been reviewed extensively (*1–4*).

This same strategy has been shown to be applicable to the separation of inorganic analyte ions (*5–12*); for example, to separate inorganic anions, a tetraalkylammonium (R_4N^+) salt can be used as the mobile phase additive (*5–9*) while for cations an alkylsulfonate (RSO_3^-) salt can be used (*9–12*).

Several studies have focused on the nature of the interactions in IPC; these are reviewed elsewhere in detail (*1–4*, *11–16*, and references within). Clearly, no single interpretation of the interactions accounts for all observations and it is conclusive that the experimental conditions must be carefully accounted for. For example, appreciable association (ion pair formation) is indicated when both the analyte ion and the pairing reagent have extensive hydrophobic centers, when mobile phase organic modifier concentration is high, or when the stationary phase is modified by the presence of a immiscible, liquid stationary phase. In contrast, no or little association is indicated when using hydrophobic ions with modest hydrophobic centers, inorganic analyte ions, organic analyte ions that contain weak hydrophobic centers, and predominately aqueous mobile phases. Because of the lack of ion pair formation under the latter conditions, this type of retention and separation is often referred to as "ion interaction chromatography" (IIC) and involves a double layer type interaction at the stationary phase surface (*5*, *12*, *13*).

Several types of hydrophobic ions have been employed in IPC and IIC. In this report the use of iron(II) 1,10-phenathroline [$Fe(phen)_3^{2+}$] salts as the hydrophobic cation mobile phase additive for the separation of inorganic analyte anions

0003-2700/86/0358-2226$01.50/0 © 1986 American Chemical Society

is discussed. $Fe(phen)_3^{2+}$ offers several advantages. (1) $Fe(phen)_3^{2+}$ is highly retained on a reverse stationary phase because of the contribution of the three phenanthroline rings in the complex to its hydrophobicity; thus, the mobile phase concentration of $Fe(phen)_3^{2+}$ needed to establish an equilibrium amount of $Fe(phen)_3^{2+}$ retained on the stationary phase is small. (2) $Fe(phen)_3^{2+}$ is a divalent cation; thus, its apparent anion exchange capacity is twice the amount retained on the stationary phase. (3) $Fe(phen)_3^{2+}$ in the mobile phase provides a way to indirectly detect analyte anions in the column effluent by monitoring absorbance at the wavelength at which $Fe(phen)_3^{2+}$ absorbs. (4) Several mobile phase variables can be manipulated to alter inorganic analyte anion retention, selectivity, and resolution. (5) This approach coupled with indirect detection by absorbance change provides a useful alternative to double and single column ion exchange chromatography (ion chromatography) (*17*), which are widely used for the separation and determination of inorganic anions.

EXPERIMENTAL SECTION

Reagents. Sulfate and ClO_4^- salts of $Fe(phen)_3^{2+}$ and 1,10-phenanthroline were purchased from GFS Chemical Co. Initially, the Cl^- salt was prepared by reaction of $FeCl_3$ with $NH_2OH{\cdot}HCl$ and 1,10-phenanthroline or by reaction of $FeCl_2$ with the ligand (*18*). Subsequently, the F^- and Cl^- salts of $Fe(phen)_3^{2+}$ were prepared by passing a solution of the SO_4^{2-} salt through a strong base anion exchanger charged in the F^- or Cl^- form, respectively. Inorganic and organic salts used for buffers, ionic strength adjustment, or analytes were analytical reagent grade when possible. Organic solvents were LC quality. LC quality water was obtained by passing distilled water through a Sybron/Barnstead purification unit.

Prepacked columns were obtained from Hamilton Co., PRP-1, and Du Pont Co., Zorbax C_{18}. PRP-1 is a polystyrene divinylbenzene, 10 μm, spherical, reverse phase adsorbent in a 150 mm × 4.1 mm i.d. column. Zorbax C_{18} is a reverse phase, 6 μm, spherical, octadecylsilica in a 150 mm × 4.6 mm i.d. column.

Instrumentation. The LC instrumentation consisted of a Waters 6000A pump and U6K injector and a Spectra Physics 770 or Kratos 773 variable wavelength detector. Column temperature was maintained at 30 °C with a Bioanalytical Instrument temperature controller. A Spectra Physics M4100 computing integrator was used for peak area measurements.

Procedures. Analyte anions were prepared as aqueous solutions of 1–2 mg/5 mL of Na or K salts. Sample aliquots of 1–10 μL were introduced by syringe. Mixed mobile phase solvents are percent by volume. Weighed amounts of ionic strength salts, $NaClO_4$, NaCl, or Na_2SO_4, and buffer salts, which were prepared by adding weighed amounts of the acid, usually acetic, citric, or succinic acid and adjustment to the desired pH with NaOH solution, were added to the mobile phase prior to dilution to volume. Buffer concentrations were usually 1.0×10^{-4} M; when necessary ionic strength accounts for buffer concentration.

Column breakthrough volumes were determined by passing a $Fe(phen)_3^{2+}$ mobile phase of known concentration through a column that is free of $Fe(phen)_3^{2+}$ at a constant flow rate until the $Fe(phen)_3^{2+}$ appeared in the column effluent. This was determined by monitoring the effluent at 510 nm where $Fe(phen)_3^{2+}$ absorbs. The breakthrough profile appears as a very sharp rise in detector response which reaches a maximum value. The breakthrough volume was taken as the inflection point of the profile. The amount of retained $Fe(phen)_3^{2+}$ is calculated from the breakthrough volume (the volume was always >20 mL; thus column void volume is negligible) flow rate, and $Fe(phen)_3^{2+}$ mobile phase concentration.

Columns were conditioned prior to use with the desired mobile phase by passing at least 100 mL (1 mL/min) of mobile phase beyond that required to reach the breakthrough. The retained $Fe(phen)_3^{2+}$ salt was rapidly removed from the PRP-1 column with 9:1 $CH_3CN:H_2O$, usually 500 mL was sufficient, while for the Zorbax C_{18} several liters were required for removal of the $Fe(phen)_3^{2+}$ salt from the column. Flow rate was usually 1.0 mL/min and inlet pressure depending on the mobile phase was 800–1500 psi. Analyte detection was at 510 nm. Capacity factors, k', were calculated in the usual way; column void volume, V_0, which was determined by using analytes that were not retained at the conditions being studied, were 1.0–1.3 mL.

RESULTS AND DISCUSSION

Studies (*5*, *9*, *11–13*, *19*) with R_4N^+ and RSO_3^- salts as mobile phase additives and inorganic analyte anions and cations, respectively, indicate that in IIC two major simultaneously occurring equilibria are responsible for analyte ion retention on a reverse stationary phase. One describes retention of the hydrophobic ion and its counterion as a surface double layer on the stationary phase. The primary layer is due to hydrophobic ion retention via its hydrophobic center producing a surface charge. The secondary diffuse layer is composed of inert ions of opposite charge. The second equilibrium defines an ion exchange like selectivity between ions in the diffuse secondary layer and analyte ions of the same charge. Thus, analyte ion retention, selectivity, and resolution are influenced by how the hydrophobic ion used and its properties and the stationary-mobile phase parameters and their optimization affect these two equilibria.

$Fe(phen)_3^{2+}$ is a dication that also has a significant hydrophobic center. Since it is a water soluble, inexpensive, stable complex, like a R_4N^+ salt, it should be useful as a mobile phase additive for the separation of analyte anions. Thus, for the system composed of a reverse stationary phase, A, and an aqueous mobile phase containing a $Fe(phen)_3^{2+}$ salt, a buffer within the pH range of $Fe(phen)_3^{2+}$ stability, a known counteranion, C^-, provided by the buffer, inert electrolyte which also provides a known counteranion as well as a fixed ionic strength, perhaps a small amount of organic modifier, and the analyte anion, X^-, the two major equilibria, if IIC is followed, are

$$A + Fe(phen)_3^{2+} + 2C^- \rightleftarrows A\cdots Fe(phen)_3^{2+}2C^- \quad (1)$$

$$A\cdots Fe(phen)_3^{2+}2C^- + 2X^- \rightleftarrows A\cdots Fe(phen)_3^{2+}2X^- + 2C^- \quad (2)$$

The parameters are, therefore, the reverse stationary phase (influences the equilibrium in eq 1 and column performance), the mobile phase $Fe(phen)_3^{2+}$ concentration (determines the number of apparent anion exchange sites by controlling the direction of eq 1 and determines the counteranion and analyte selectivity defined in eq 2), mobile phase solvent composition (since retention of $Fe(phen)_3^{2+}$ is consistent with reverse phase retention, mobile phase solvent composition determines the direction of eq 1; a lesser effect is on selectivity in eq 2 assuming the solvent change is a modest one), type and concentration of counteranion in the mobile phase (the type influences eq 1 while its concentration through mass action shifts eq 2), mobile phase pH and buffer (provides a counteranion, influences stability of $Fe(phen)_3^{2+}$, and affects the charge of the analyte anion if it is derived from a weak acid).

To follow IIC, it is assumed that $Fe(phen)_3^{2+}$ salts are appreciably dissociated in an aqueous medium. Extraction data suggest that this might not be the case for salts of certain simple counteranions. For example, the distribution ratio values for nitrobenzene/H_2O extraction of $Fe(phen)_3^{2+}(C^-)_2$ salts is highly dependent on the counteranion; for $C^- = ClO_4^-$, SCN^-, I^-, Br^-, and Cl^- the values are 13.5, 1.7, 0.8, 0.03, 0.003, respectively (*20*). The favorable nonpolar solvent solubility relative to the other anions suggests a partial dissociation of the ClO_4^- salt and because of this ClO_4^- should be a strong eluent counteranion.

Stationary Phase. Two reverse stationary phases, PRP-1 and Zorbax C_{18}, were evaluated. The studies reported here deal primarily with PRP-1 as the stationary phase. Several reasons favored this decision. (1) Retention of $Fe(phen)_3^{2+}$ appeared to be more reversible on PRP-1. That is, the column could be repeatedly equilibrated with a $Fe(phen)_3^{2+}$ mobile

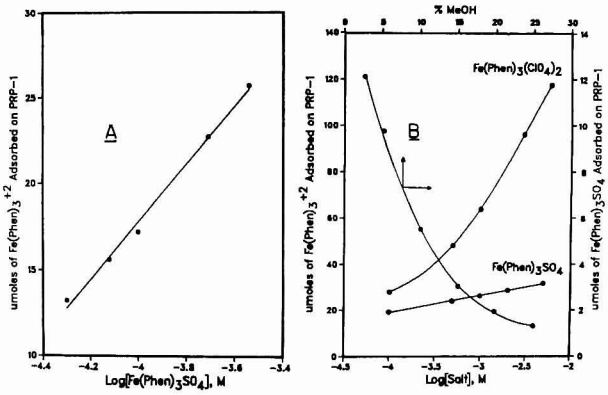

Figure 1. Retention of $Fe(phen)_3^{2+}$ salts on PRP-1 as a function of the mobile phase variables: (A) a 4.1 × 150 mm, 10 μm PRP-1 column and an aqueous $Fe(phen)_3SO_4$, 5.0×10^{-4} M acetate, pH 6.2, mobile phase at 1.0 mL/min and 30 °C; (B) conditions are the same as A except an aqueous 1.0×10^{-4} M $Fe(phen)_3^{2+}$ perchlorate or sulfate salt, $NaClO_4$ or Na_2SO_4 mobile phase or a MeOH:H_2O, 1.0×10^{-4} M $Fe(phen)_3SO_4$ mobile phase.

phase; the $Fe(phen)_3^{2+}$ salt removed from the stationary phase and then recharged in the $Fe(phen)_3^{2+}$ salt form. Each time the $Fe(phen)_3^{2+}$ loaded column still provided reproducible chromatography. In contrast large volumes of CH_3CN:H_2O were required to remove the $Fe(phen)_3^{2+}$ salt from the Zorbax C_{18}. Repeated cycling leads to nonreproducible results. Also, inspection of the C_{18} particles indicated that not all the $Fe(phen)_3^{2+}$ salt was removed. Other studies (*9*) have indicated that free silanol sites within the Zorbax C_{18} can participate in cation exchange and it is possible that part of the $Fe(phen)_3^{2+}$ is retained as a cation, thus eliminating it as a source for anion exchange. (2) PRP-1 being stable throughout the pH range, unlike the C_{18}, allows chromatography at a basic pH. (3) PRP-1 gave favorable column efficiencies even though a 10-μm particle was used. (4) PRP-1 column life was significantly longer. (5) Retention of a $Fe(phen)_3^{2+}$ salt at a given condition was greater on PRP-1; this contributes to better analyte anion selectivity and resolution. All PRP-1 columns used were of similar hydrophobicity according to a phenol (3.2 min) and benzene (5.4 min) test sample using a 9:1 CH_3CN:H_2O mobile phase at 0.5 mL/min. Significant departure from this will alter retention times because of a subsequent effect of $Fe(phen)_3^{2+}$ retention.

Retention of $Fe(phen)_3^{2+}$. $Fe(phen)_3^{2+}$ salt retention on PRP-1 and C_{18} is high and counteranion-dependent. A mobile phase rich in organic modifier is required to elute the $Fe(phen)_3^{2+}$ salts in a reasonable time period. The equilibrium amount of $Fe(phen)_3^{2+}$ salt retained on PRP-1 for a given mobile phase $Fe(phen)_3^{2+}$ concentration was calculated from column breakthrough volumes. These experiments are summarized in Figure 1A. As the mobile phase $Fe(phen)_3^{2+}$ salt concentration increases, the amount retained on the PRP-1 column, which is also a measure of the apparent anion exchange capacity, appears to increase over the concentration range studied. Since the $Fe(phen)_3^{2+}$ is hydrophobic due to the three phenanthroline rings, it is highly retained. Thus, a significant surface anion exchange capacity is produced even at low mobile phase $Fe(phen)_3^{2+}$ concentrations. For example, at a mobile phase concentration of 1.0×10^{-4} M $Fe(phen)_3^{2+}$, which was used in most subsequent studies, there are 17.2 μmol of $Fe(phen)_3^{2+}$ distributed throughout and in equilibrium with the stationary phase surface provided within the 15-cm PRP-1 column. Since $Fe(phen)_3^{2+}$ is divalent this represents 34.4 μequiv/column of anion exchange sites. This is typical of the apparent anion and cation exchange capacities generated when using R_4N^+ salts (*5*, *9*) and RSO_3^- salts (*9*, *11*) as mobile phase additives for inorganic analyte anion and cation separations, respectively, and the lower end of exchange capacities used in single column ion chromatography (*17*). If the mobile phase organic modifier concentration for a given $Fe(phen)_3^{2+}$ concentration is increased, the equilibrium amount of the $Fe(phen)_3^{2+}$ salt retained on the PRP-1, and subsequently the apparent anion exchange capacity, decreases. In contrast increasing the mobile phase ionic strength for a given $Fe(phen)_3^{2+}$ mobile phase concentration causes the equilibrium amount of the $Fe(phen)_3^{2+}$ salt retained on the PRP-1 and the apparent anion exchange capacity to increase. As shown in Figure 1B a modest change in either of these variables significantly alters the amount of retained $Fe(phen)_3^{2+}$ salt per column. The amount of retained $Fe(phen)_3^{2+}$ salt and the subsequent number of anion exchange sites are also counteranion-dependent. In Figure 1B not only the amount of $Fe(phen)_3^{2+}$ salt retained on PRP-1 from an aqueous $NaClO_4$ medium is significantly higher but the rate at which the number of sites increases with increased salt concentration is greater than that from the Na_2SO_4 medium. Over the $NaClO_4$ and Na_2SO_4 salt concentration studied (Figure 1B) the number of sites in the SO_4^{2-} mobile phases even at its most favorable condition is still below the least favorable ClO_4^- condition. This is consistent with eluent strength and inorganic analyte anion elution order which became apparent in subsequent studies. That is the ClO_4^- salt provides greater surface coverage and is a stronger eluent counteranion than the SO_4^{2-} salt. Therefore, for a given column the major variables that determine the number of apparent anion exchange sites due to retention of the $Fe(phen)_3^{2+}$ salt are the $Fe(phen)_3^{2+}$ salt mobile phase concentration, the organic modifier and its concentration (at a given percent the amount of $Fe(phen)_3^{2+}$ salt retained decreases in the order MeOH < EtOH < CH_3CN), and the mobile phase ionic strength.

The surface coverage for the $Fe(phen)_3^{2+}$ sorption isotherm shown in Figure 1A was calculated by using a PRP-1 surface area of 415 m^2/g and column weight of 1 g. Thus, from 5×10^{-5} to 2.86×10^{-4} M $Fe(phen)_3SO_4$ the equilibrium coverage due to retained $Fe(phen)_3SO_4$ changes from 0.040 to 0.077 μmol/m^2, respectively. The isotherm in Figure 1A follows $C_s = kC_m^{1/x}$, where C_s and C_m are the amount of $Fe(phen)_3SO_4$ in the stationary and mobile phase, respectively, and fits the equation log [μmol of $Fe(phen)_3^{2+}/m^2$] = 0.38 log [$Fe(phen)_3^{2+}$] + 0.26 with a correlation of 0.9992 and a $1/x$ value of 0.38. When compared to $C_7SO_3^-Li^+$ retention on PRP-1 (*9*) the coverage of the $Fe(phen)_3SO_4$ for a given mobile phase concentration is greater but the rate at which it increases in surface coverage with increased mobile phase concentration is much less. For example, at 0.0003 M $Fe(phen)_3SO_4$, 27 μmol of $Fe(phen)_3SO_4$ is retained per column while the amount of $C_7SO_3^-Li^+$ retained per column is estimated (*9*) to be about 2.5 μmol. From Figure 1A a 10-fold increase in $Fe(phen)_3SO_4$ concentration increases the amount retained by about 15 μmol while for $C_7SO_3^-Li^+$ (*9*) the increase is about 50 μmol. This difference is probably due to (1) $Fe(phen)_3^{2+}$ has higher retention on PRP-1 due to increased hydrophobicity, (2) $Fe(phen)_3^{2+}$ is larger in size, and (3) since $Fe(phen)_3^{2+}$ is a dication, it builds up surface charge in the primary layer at a much greater rate, thus, repelling additional $Fe(phen)_3^{2+}$.

Detection. A common detection technique in IPC and IIC is UV absorption providing the analyte ion is chromophoric. This detection can also be used for analyte ions that are UV-transparent by using a hydrophobic ion mobile phase additive that is chromophoric itself. For example, cetylpyridinium chloride can be used as the pairing and chromophoric reagent for the detection of separated alkylsulfonates (*21*), *p*-ethyl benzenesulfonate for octylammonium detection (*22*), and aryltrialkylammonium salts for inorganic anion detection (*6*, *7*). This type of indirect UV–vis detection has

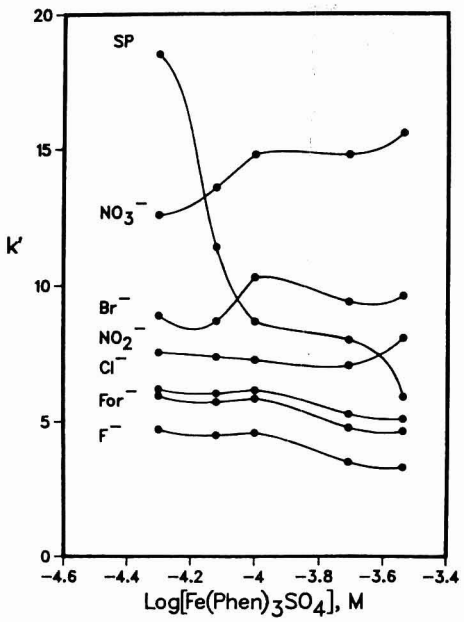

Figure 2. Retention of inorganic analyte anions as a function of mobile phase $Fe(phen)^{2+}$ salt concentration. Conditions are the same as Figure 1A with indirect detection at 510 nm; SP is the system peak for OAc^-.

been the subject of several studies and has been employed in both normal- and reverse-phase chromatography (see for example ref 6, 7, 21–25, and references within).

In the indirect UV–vis detection strategy the small amount of chromophoric hydrophobic ion in the mobile phase contributes to the background absorbance. Since the detector is set at the wavelength at which the hydrophobic ion absorbs its contribution to the detector, response is electronically offset. Movement of the analyte band through the column alters the concentration of the hydrophobic ion within the band relative to the mobile phase concentration. Thus, when the analyte band reaches the detector, absorbance must change because of the hydrophobic ion concentration difference. In the studies reported here, indirect detection is done in the visible at 510 nm where the $Fe(phen)_3^{2+}$ salt absorbs. Since the $Fe(phen)_3^{2+}$ salt is highly retained and a significant number of anion exchange sites are obtained on the stationary phase at low $Fe(phen)_3^{2+}$ salt mobile phase concentrations, the required offset is modest even though the $Fe(phen)_3^{2+}$ salt has a very high molar absorptivity.

Although several parameters will influence indirect retention (*6*, *7*, *20–23*), the major one appears to be mobile phase ionic strength. Both analyte retention time and peak area are influenced by ionic strength. Previous studies (*20*, *23*) have suggested that a high salt containing mobile phase is preferred. A second feature of indirect detection is the appearance of system peaks that result from counterions used in the mobile phase. When a mobile phase containing a $Fe(phen)_3^{2+}$ salt as the chromophoric hydrophobic ion, buffer salts for pH control, and inert salt for ionic strength is used, the counteranions provided by these components will produce these peaks. The key mobile phase parameters that determine the location of the system peak(s) and how these can be optimized to prevent their interference in the analyte peaks are discussed elsewhere (*6*, *7*, *21–25*).

Mobile Phase $Fe(phen)_3^{2+}$ Concentration. Figure 2 shows that monovalent inorganic analyte anion retention on PRP-1 changes slightly over the $Fe(phen)_3^{2+}$ mobile phase concentration of 5.0×10^{-5} M to 3.0×10^{-4} M. Each analyte anion was detected by indirect detection at 510 nm. While higher $Fe(phen)_3^{2+}$ concentrations should provide a greater number of anion exchange sites and subsequently higher analyte anion retention, a higher concentration is not recommended because the higher background absorbance that results cannot be easily offset and analyte peak heights and areas are reduced (*25*). Because of this, a 10^{-4} M $Fe(phen)_3^{2+}$ concentration is optimum and, in general, was used throughout the study. Figure 2 also demonstrates that retention difference between inorganic analyte anions and resulting selectivities are favorable.

The OAc^- system peak due to the buffer salt is shown in Figure 2 as a function of $Fe(phen)_3SO_4$ concentration. A second system peak due to SO_4^{2-} is also present but it is not easily detected because it is a very broad, poorly defined peak at high retention time. As the $Fe(phen)_3SO_4$ concentration increases, the OAc^- system peak shifts to a lower retention time.

Analyte Anion Concentration. Retention isotherms were determined for Cl^- and Br^- by using an aqueous 1.0×10^{-4} M $Fe(phen)_3(ClO_4)_2$, 1.0×10^{-4} M succinate, pH 6.1 mobile phase. For these conditions 30 μmol of $Fe(phen)_3^{2+}$ salt are retained per column, which represents 60 μequiv of anion exchange sites. As the Cl^- or Br^- amount injected exceeds approximately 0.5% of the available exchange capacity, retention of the analyte starts to change significantly. Below this loading limit, which is analyte and mobile phase dependent, the change in k' with analyte concentration is small. For example, for Cl^- and Br^- analytes over the injected weight range of 0.010–10 μg (0.5% loading), retention time increases from 8.07 to 8.86 min and 10.2 to 11.4 min, respectively. If the mobile phase ionic strength is modestly increased, k' is nearly constant for this concentration range. For example, when studying the retention of NO_2^- and Br^- over an injected range of 0.8–118 μg of anion from a 1.0×10^{-4} M $Fe(phen)_3SO_4$, 2.0×10^{-3} M Na_2SO_4 mobile phase, analyte anion retention was constant up to about 10 μg (0.5% loading) of injected anion. In general, for all other studies reported here, the injected weight of analyte anion was 1 μg and only at mobile phase conditions that favor a low amount of retained $Fe(phen)_3^{2+}$ salt on the PRP-1 was the 0.5% analyte loading approached.

Mobile Phase pH. The effect of mobile phase pH on inorganic analyte anion retention was studied over the range of pH 4–7. $Fe(phen)_3^{2+}$ salt pH stability is within the range of pH 3–9 (*18*). The mobile phase consisted of 1.0×10^{-4} M $Fe(phen)_3SO_4$, 1.0×10^{-3} M Na_2SO_4, and 1.0×10^{-4} M succinate buffer, which was adjusted with NaOH to provide the desired pH. From pH 4 to 7 k' values for retention on PRP-1 decreased by about 10%. For example, for the analytes NO_3^-, Br^-, and Cl^- the k' change between pH 4 and 7 was 6.59 to 5.80, 3.90 to 3.53, and 2.12 to 1.92, respectively. Measurements indicated that the amount of $Fe(phen)_3^{2+}$ salt retained on the PRP-1 also increased modestly from 26 to 28 μmol/column from pH 4 to 7. Column experiments were reproducible and favorable mobile phase stability was obtained within this pH range. Subsequently, several separations were carried out at pH 9 and reproducibility and stability still appeared to be favorable.

Mobile phase pH will affect peak area and k' for analyte anions derived from weak acids. As the pH decreases, dissociation is suppressed, which causes the peak area to decrease and k' to change.

Temperature. The retention of several inorganic analyte anions on PRP-1 was studied for a column temperature of 25–40 °C. A 1:9 MeOH:H_2O, 1.0×10^{-4} M $Fe(phen)_3SO_4$, pH 5.3 mobile phase was used. As column temperature increased analyte anion retention decreased; for example, for NO_3^- k' = 6.17 at 25 °C and 4.92 at 40 °C. Although the changes were small, selectivity was more favorable at a lower temperature. In all experiments reported here column temperature was 30 °C.

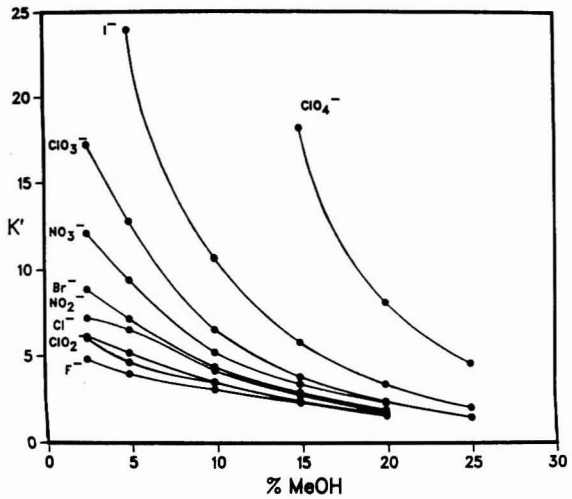

Figure 3. Effect of mobile phase MeOH–H_2O composition on inorganic analyte retention. Conditions are the same as Figure 2 except the mobile phase is MeOH:H_2O, 1.0 × 10^{-4} M $Fe(phen)_3SO_4$, unbuffered, pH 5.3–5.5.

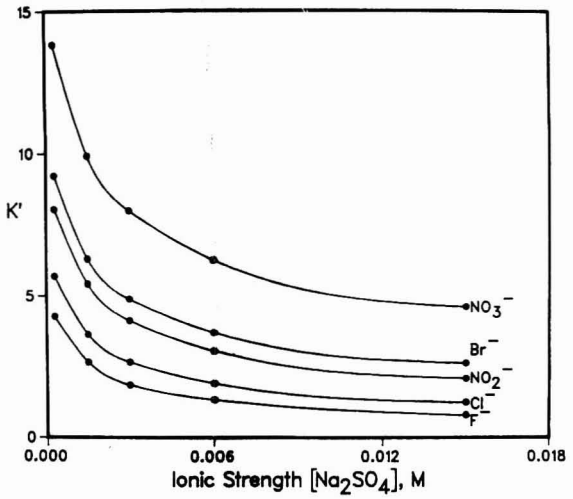

Figure 4. Effect of mobile phase ionic strength (Na_2SO_4) concentration on inorganic analyte anion retention. Conditions are the same as Figure 2 except the mobile phase is aqueous 1.0 × 10^{-4} M $Fe(phen)_3SO_4$, Na_2SO_4, unbuffered, pH 5.3–5.5.

Organic Modifier. Figure 1B indicates that the number of anion exchange sites on the column due to the retained $Fe(phen)_3^{2+}$ salt decreases as organic modifier increases. If the number of anion sites is significantly reduced, analyte anion retention will decrease. This is demonstrated in Figure 3 where analyte anion retention on PRP-1 from a 1.0 × 10^{-4} M $Fe(phen)_3SO_4$ solution is shown as a function of MeOH–H_2O solvent composition. While the anion elution order is maintained at all MeOH–H_2O ratios studied, the more favorable selectivity ratio is obtained in the absence of MeOH. The effect of organic solvent on analyte anion retention is consistent with its effect on $Fe(phen)_3^{2+}$ salt retention. That is for a given organic modifier:H_2O ratio analyte anion retention decreases in the order MeOH < EtOH < CH_3CN. A system peak, due to the SO_4^{2-} counteranion, occurs as a broad peak at a high retention time. As the MeOH modifier concentration increases in Figure 3 the system peak retention time drops sharply, for example, in Figure 3 the k' for the system peak at 15, 20, and 25% MeOH is 13.3, 7.0, and 4.0, respectively.

Ionic Strength–Counteranion Selectivity. Mobile phase ionic strength will have several competing major effects on analyte anion retention. (1) Retention of $Fe(phen)_3^{2+}$ salt on the stationary phase increases (see Figure 1B) with an increase in ionic strength. For example, for an ionic strength increase from 3.0 × 10^{-4} M to 1.5 × 10^{-2} M, which corresponds to a 1.0 × 10^{-4} M to 5.0 × 10^{-3} M increase in Na_2SO_4, in a 1.0 × 10^{-4} M $Fe(phen)_3SO_4$ mobile phase the amount of retained $Fe(phen)_3^{2+}$ salt changes from 19 to 32 μmol per column; this corresponds to an anion exchange capacity increase from 38 to 64 μequiv per column, respectively, and should cause analyte anion retention to increase. (2) Increase in the counteranion concentration provided by the increase in the ionic strength salt reduces analyte anion retention by mass action by competing more favorably with the analyte anion for the exchange site. (3) For a given ionic strength analyte anion retention will depend on the counteranion and its respective ion exchange selectivity. (4) If the counteranion is one that favors association with $Fe(phen)_3^{2+}$, an increase in the counteranion concentration suppresses its dissociation and thus reduces analyte anion retention. (5) Analyte peak position and area are affected by a change in ionic strength since indirect detection is used.

Figure 4 shows how retention for several analyte anions decreases as mobile phase ionic strength increases; the ionic strength corresponds to a Na_2SO_4 concentration range of 1.0 × 10^{-4} M to 5.0 × 10^{-3} M. A similar change was obtained when using $Fe(phen)_3(ClO_4)_2$ and $NaClO_4$ with the difference being that retention is less in a $NaClO_4$ solution of equal ionic strength. Even though the number of anion exchange sites in the column increases with ionic strength due to increased $Fe(phen)_3^{2+}$ salt retention (see Figure 1B for $Fe(phen)_3SO_4$ retention from a SO_4^{2-} solution), the mass action effect of the counteranion to reduce retention is much greater. As shown in Figure 4 the analyte anion retention order stays constant over the ionic strength range studied.

Table I. Effect of Counteranion on Analyte Anion Retention

analyte	k', $Fe(phen)_3^{2+}X$ mobile phases[a]			
	X = SO_4^{2-}	X = ClO_4^-	X = Cl^-	X = F^-
F^-	4.22	5.38	5.46	
IO_3^-	4.31	5.41	6.05	8.23
Cl^-	6.25	7.36		8.39
NO_2^-	8.78	9.49	10.9	11.3
BrO_3^-	9.15	9.61	11.3	11.7
Br^-	10.2	10.8	12.5	12.8
NO_3^-	15.3	14.5	18.1	18.3
ClO_3^-	24	20	28	29
I^-	51	37	65	56
SP[b] (X)	>>61	>>70	9.37	6.64
SP[b] (succinate)	61	68	85	84

[a] A 150 mm × 4.1 mm, 10 μm, PRP-1 column and an aqueous 1.0 × 10^{-4} M $Fe(phen)_3^{2+}X$ (where X = SO_4^{2-}, ClO_4^-, Cl^-, or F^-), 1.0 × 10^{-4} M sodium succinate buffer, pH 6.10 mobile phase at 1.0 mL/min. [b] System peak.

A comparison of four common eluent counteranions at 1.0 × 10^{-4} M $Fe(phen)_3^{2+}$ salt mobile phase concentration is shown in Table I. Counteranion eluent strength follows the order $SO_4^{2-} \geq ClO_4^- > Cl^- > F^-$, which is similar to the order observed when using typical quaternary ammonium type anion exchangers (*26*). The mobile phase used in Table I contains two counteranions, one from the $Fe(phen)_3^{2+}$ salt and succinate from the buffer. Even though succinate is a divalent anion at the mobile phase pH of 6.1 and is a strong eluent counteranion, the effect of the second counteranion on analyte anion retention is still observed. If NaOAc is used as a buffer, its concentration would have to be about five times the succinate concentration used in Table I to obtain similar k' values. Thus, the mass action effect of an increased concentration of the monovalent acetate anion is used to compensate for the greater eluent strength of the divalent succinate anion. Both mobile phase counteranions produce system peaks. The

Table II. Effects of Different Mobile Phases on Analyte Anion Retention

	k' for mobile phases A to F[a]					
analyte	A	B	C	D	E	F
F^-	5.38	3.06	0.80	4.59	1.31	1.10
IO_3^-	5.41				1.18	
Cl^-	7.36	3.50	1.24	6.15	1.93	1.61
NO_2^-	9.49	4.16	2.07	7.26	2.68	2.29
BrO_3^-	9.61				2.64	
Br^-	10.8	4.38	2.62	10.3	3.25	2.82
NO_3^-	14.5	5.23	4.62	14.8	4.88	4.23
ClO_3^-	20.3				7.28	6.46
SO_4^{2-}					8.92	6.44
I^-	36.6	10.7			15.0	14.9
BF_4^-	44.8				23.4	21.4
SCN^-	>120				63	

[a] A 150 mm × 4.1 mm, 10 μm, PRP-1 column and (A) aqueous 1.0×10^{-4} M $Fe(phen)_3(ClO_4)_2$, 1.0×10^{-4} sodium succinate, pH 6.1; (B) 1:9 MeOH:H_2O, 1.0×10^{-4} M $Fe(phen)_3SO_4$, pH 5.30; (C) aqueous 1.0×10^{-4} M $Fe(phen)_3SO_4$, 5.0×10^{-3} M Na_2SO_4, pH 5.50; (D) aqueous 1.0×10^{-4} M $Fe(phen)_3SO_4$, 5.0×10^{-4} M NaOAc, pH 6.2; (E) aqueous 1.0×10^{-4} M $Fe(phen)_3(ClO_4)_2$, 1.0×10^{-4} M sodium citrate, pH 7.25; (F) aqueous 1.0×10^{-4} M $Fe(phen)_3(ClO_4)_2$, 1.0×10^{-4} M sodium 1,3,5-benzenetricarboxylate, pH 5.8 mobile phases at 1.0 mL/min.

stronger the eluent counteranion is, the higher the retention volume for its system peak. Thus, in Table I the stronger eluent counteranions, which are also highly retained analyte anions, such as succinate, ClO_4^-, and SO_4^{2-}, yield system peaks that do not interfere in the chromatogram. The weaker ones both in eluent strength and retention as analytes, such as Cl^- and F^-, yield system peaks early in the chromatogram and may interfere depending on the analyte anion.

Comparison of the data for the retention of different anions as analytes establishes the analyte selectivity order. For PRP-1 and $Fe(phen)_3^{2+}$ salt as the additive at a pH 6.1 the retention of inorganic monovalent anions follows the order

$$ClO_4^- > I^- > ClO_3^- > NO_3^- > \text{propionate} > CNO^- > IO_4^- > IO_3^- > Br^- > BrO_3^- > NO_2^- > Cl^- > ClO_2^- > \text{formate} > \text{acetate} > F^- \quad (3)$$

Since several analytes are weak acid anions retention order will be altered depending on pK_a by using a mobile phase pH that suppresses ionization. At these conditions elution will be earlier, since the equilibrium shown in eq 2 is shifted to the left. Also, since indirect detection is used, the more ionization is suppressed the smaller the analyte peak area becomes (*25*). The elution order in eq 3 is similar to the order observed when using quaternary ammonium type anion exchangers (*26*).

A quantitative comparison of retention data for monovalent anions for several mobile phase conditions is shown in Table II. Adding MeOH or other organic modifier (see Figure 3 and compare eluent A to B in Table II) and increasing ionic strength (see Figure 4 and compare eluent A to C) decreases analyte anion retention. Changing $Fe(phen)_3^{2+}$ concentration will also affect analyte retention; however, a large change is required (see Figure 2) before a noticeable effect on analyte anion retention is obtained. The variable offering the most versatility in influencing analyte anion retention is the counteranion that can be supplied by the $Fe(phen)_3^{2+}$ salt, the buffer, and/or ionic strength salt. Table I illustrates the effect of counteranion due to an ionic strength salt while mobile phases A, D, E, and F in Table II focus on the buffer as the counteranion source. At the mobile phase pH used the buffer anions, acetate, succinate, citrate, and 1,3,5-benzenetricarboxylate are predominately −1, −2, −3, and −3, respectively. As the charge or the concentration (note that acetate in mobile phase D is 5 times as concentrated as the others) of these buffer anions increases, analyte anion retention decreases. Table II also lists retention data for SO_4^{2-}. Clearly, in order to separate multivalent anion mixtures and/or the more highly retained monovalent anions, the strong eluent strength offered by multivalent buffer anions (mobile phases A, E, and F in Table II) are required for more favorable separation times.

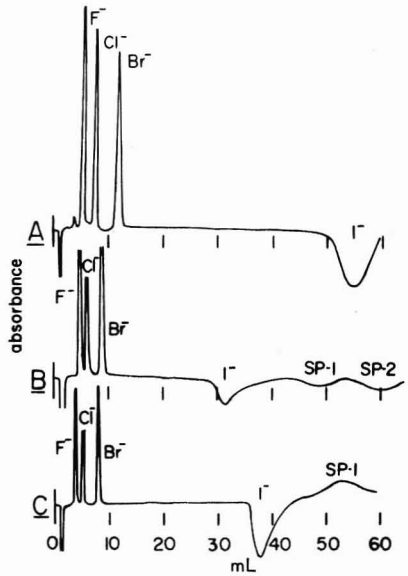

Figure 5. Effect of mobile phase variables on the separation of the halides: a 4.1 × 150 mm, 10 μm, PRP-1 column and an aqueous (A) 1.0×10^{-4} M $Fe(phen)_3SO_4$, 1.0×10^{-4} M succinate, pH 6.1; (B) same as (A) except 1:95 MeOH:H_2O, pH 6.1; (C) same as (A) plus 4.0×10^{-4} M Na_2SO_4, pH 6.1, mobile phase at 1.0 mL/min, 30 °C, and indirect detection at 510 nm.

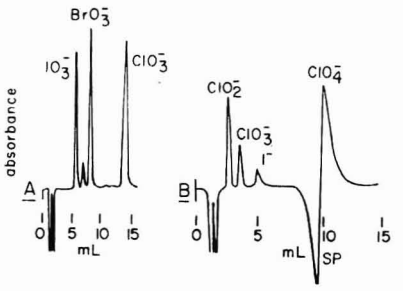

Figure 6. Separation of highly retained inorganic monovalent anions. Conditions are the same as in Figure 5A except in (A) 5:95 MeOH:H_2O and in (B) no buffer (pH 5.5) and 1:5 MeOH:H_2O.

Separations. Several mobile phase parameters can be manipulated to optimize retention time, selectivity, and resolution when attempting to separate mixtures of inorganic analyte anions. If indirect absorption detection is used, a high $Fe(phen)_3^{2+}$ salt mobile phase concentration, which increases the apparent anion exchange capacity on the PRP-1 surface due to retention of the $Fe(phen)_3^{2+}$ salt, is not recommended to increase analyte retention time because of the need to offset background absorbance with the detector. If conductivity is used, more flexibility is available with $Fe(phen)_3^{2+}$ salt concentration providing the mobile phase conductivity is not excessive. Altering mobile phase ionic strength, organic modifier concentration, and type and concentration of counteranion used for the inert ionic strength salt and/or buffer can be readily done to optimize separations. Mobile phase pH is a useful variable to alter elution order only if the analytes are anions of weak acids or to determine buffer anion charge. Retention data from the previous figures and tables indicate that selectivity and resolution are favorable for the separation of complex mixtures of inorganic anions. Several

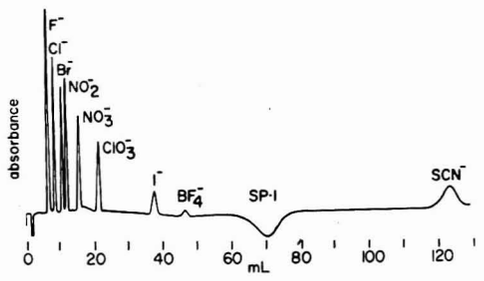

Figure 7. Separation of a multicomponent mixture of inorganic monovalent anions. Conditions are the same as Figure 5A except $Fe(phen)_3(ClO_4)_2$ is used.

examples illustrating this are shown in Figures 5–7. Also, these separations focus on how the mobile phase parameters can be adjusted to change retention time, selectivity, and resolution.

Figure 5 shows the separation of a halide mixture on PRP-1 using several different mobile phase conditions and indirect detection at 510 nm. Each halide was injected at about 1 μg calculated as the anion. For all examples in Figure 5 the $Fe(phen)_3^{2+}$ mobile phase concentration is 1.0×10^{-4} M, a divalent counteranion is used, and the pH is 6.1; thus, the change in retention is the result of altering other variables. In Figure 5A, an aqueous $Fe(phen)_3SO_4$, succinate buffer mobile phase is used. Although not shown, a succinate system peak occurs at about 67 mL and a broad SO_4^{2-} system peak appears at about 90 mL. All chromatographic peaks are well-defined and indicate favorable column efficiency. For example, the Cl^- peak in Figure 5A corresponds to 21 000 plates/m using a width at half-height calculation. If a ClO_4^- salt is used with the succinate buffer, a base line resolution is still obtained even though halide retention decreases; for example, I^- retention drops to about 38 mL. Figure 5B shows how adding MeOH to the mobile phase can be used to effectively decrease retention; in this case the column equilibrium anion exchange capacity is decreased. System peaks 1 and 2, which are also shifted to a slower retention time, are due to succinate and SO_4^{2-}, respectively. Increasing the counteranion concentration will reduce halide analyte retention. This can be done in two ways. As shown in Figure 5C, adding Na_2SO_4 (4.0×10^{-4} M), which provides a strong divalent counteranion, reduces halide and the system peaks (only succinate system peak is shown) retention. When only the buffer was increased to 5.0×10^{-4} M, which provides the strong divalent succinate counteranion, a similar decrease in retention was obtained but was not as large as shown in Figure 5C; for example, I^- retention appeared at 42 mL. The amount of $Fe(phen)_3^{2+}$ salt retained in Figure 5A corresponds to about 30 μmol/column or 60 μequiv of exchange sites column.

Separations of highly retained monovalent anions are shown in Figure 6. In Figure 6A a small MeOH concentration and a strong counteranion, ClO_4^-, is used to reduce retention where the halide oxygenated anions follow a reversed elution order when compared to the halide anions. In Figure 6B a large MeOH concentration is used to reduce analyte anion retention time. Figure 7 illustrates a separation of a nine-component mixture of monovalent anions covering a wide range of analyte retention. The ClO_4^-–succinate combination provides a stronger eluent than the SO_4^{2-}–succinate combination used in Figure 5; its major effect on reducing retention occurs with the more highly retained anions. Two system peaks are observed, one shown in Figure 7 at 71 mL due to succinate and one not shown due to ClO_4^- at >>120 mL. A discussion of how to adjust mobile phase components so that system peaks are at a more favorable retention time will be reported later (*25*).

Calibration–Detection Limits. Calibration curves were prepared over the range of 10–10000ng of Cl^- and 7–15000 ng of Br^- calculated as the anion and injected by a 20-μL fixed loop. Peaks shapes were Gaussian and well-defined over the entire weight range and k' increased by about 10% from the lower to the upper end. If the mobile phase ionic strength is modestly increased, this change is reduced; however, the detection limit is less favorable. A 1.0×10^{-4} M $Fe(phen)_3(ClO_4)_2$, 1.0×10^{-4} M succinate, pH 6.1 mobile phase (aqueous for Cl^- and 1:95 MeOH:H_2O for Br^-) and a PRP-1 column was used with a Micrometrics M725 autoinjector, Kratos SF773 or Spectra Physics 770 detector (510 nm), and a Spectra Physics M4100 data analysis center. Linear curves for indirect detection of peak area vs. weight injected were obtained for both analyte anions indicating a very favorable dynamic range. No attempt was made to determine the upper limit for linearity; however, for the mobile phase conditions used, 10 000 ng is approaching about 0.5% of the available anion exchange capacity provided by the retained $Fe(phen)_3^{2+}$ salt on the PRP-1 stationary phase surface. For Cl^- the equation defining the calibration curve using the Spectra Physics 770 detector is given by (peak area $\times 10^{-3}$) = 0.866 (ng of Cl^-) + 7.035 with a correlation factor of 0.9999 while for Br^- using the Kratos SF773 detector it is (peak area $\times 10^{-3}$) = 2.406 (ng of Br^-) – 230.9 with a correlation factor of 0.9997. At 1 ng of injected analyte, anion peak height signal was still about 6 times background signal indicating that additional optimization of the injector, detector, and data analysis would permit even a lower detection limit. Because indirect detection is used, analyte anion calibration is very dependent on mobile phase ionic strength (*20*, *23*). Both peak area and location are affected by ionic strength. A discussion of the effects of ionic strength and other parameters on indirect detection will be reported later (*25*).

Conductivity detection can also be used since the $Fe(phen)_3^{2+}$ mobile phases, in general, do not provide excessive background conductance. No attempt was made to determine the limits for conductivity detection. However, for an aqueous 1.0×10^{-4} M $Fe(phen)_3(ClO_4)_2$, 6.0×10^{-3} M $NaClO_4$, 5.0×10^{-4} M NaOAc, pH 5.29 mobile phase, 1 μg of NO_2^- was easily detected. Reducing and/or eliminating the ionic strength and the buffer salt will improve the detection.

Registry No. F^-, 16984-48-8; Cl^-, 16887-00-6; Br^-, 24959-67-9; NO_2^-, 14797-65-0; NO_3^-, 14797-55-8; ClO_3^-, 14866-68-3; I^-, 20461-54-5; BF_4^-, 14874-70-5; SCN^-, 302-04-5; IO_3^-, 15454-31-6; BrO_3^-, 15541-45-4; ClO_2^-, 14998-27-7; ClO_4^-, 14797-73-0; SO_4^{2-}, 14808-79-8; $Fe(phen)_3SO_4$, 14634-91-4; $Fe(phen)_3(ClO_4)_2$, 14586-54-0; $Fe(phen)_3(Cl)_2$, 14978-15-5; $Fe(phen)_3(F)_2$, 103190-67-6.

LITERATURE CITED

(1) Tomlinson, E.; Jefferies, T. M.; Riley, C. M. *J. Chromatogr.* **1978**, *159*, 315–358.
(2) Gloor, R.; Johnson, J. *J. Chromatogr. Sci.* **1977**, *15*, 413–423.
(3) Majors, R. E.; Barth, H. G.; Lochmüller, C. H. *Anal. Chem.* **1984**, *56*, 300R–349R.
(4) *Ion-Pair Chromatography*; Hearn, M. T. W., Ed.; Chromatographic Science Series; Marcel Dekker: New York, 1985; Vol. 31, pp 1, 27, 77, 141, 207, 259.
(5) Iskandarani, Z.; Pietrzyk, D. J. *Anal. Chem.* **1982**, *54*, 2427–2431.
(6) Barber, W. E.; Carr, P. W. *J. Chromatogr.* **1983**, *260*, 89–96.
(7) Barber, W. E.; Carr, P. W. *J. Chromatogr.* **1984**, *301*, 25–38.
(8) Dasgupta, P. K. *Anal. Chem.* **1984**, *56*, 769–772.
(9) Smith, R. L.; Iskandarani, Z.; Pietrzyk, D. J. *J. Liq. Chromatogr.* **1984**, *7*, 1935–1959.
(10) Knight, C. H.; Cassidy, R. M.; Recoskie, B. M.; Green, L. W. *Anal. Chem.* **1984**, *56*, 474–478.
(11) Smith, R. L.; Pietrzyk, D. J. *Anal. Chem.* **1984**, *56*, 1572–1577.
(12) Iskandarani, Z.; Pietrzyk, D. J. *Anal. Chem.* **1982**, *54*, 1065–1071.
(13) Bidlingmeyer, B. A.; Deming, S. N.; Price, W. P.; Sachok, B.; Petrusek, M. *J. Chromatogr.* **1979**, *186*, 419–434.
(14) Deelder, R. S.; Van Den Berg, J. H. M. *J. Chromatogr.* **1979**, *186*, 419–434.
(15) Knox, J. N.; Hartwick, R. A. *J. Chromatogr.* **1981**, *204*, 3–21.
(16) Sorel, R. H. A.; Hulshoff, A. *Advances in Chromatography*; Giddings, J. C., Grushka, E., Cazes, J., Brown, P. R., Eds.; Marcel Dekker: New York, 1983; Vol. 21, pp 87–129.
(17) Fritz, J. S.; Gjerde, D. T.; Pohlandt, C. *Ion Chromatography*; Huthig Verlag: Heidelberg, 1982.

(18) Schilt, A. A. *Analytical Applications of 1,10-Phenanthroline and Related Compounds*; Pergamon Press: Oxford, 1969.
(19) Cantwell, F. F.; Puon, S. *Anal. Chem.* **1979**, *51*, 623–632.
(20) Yammamoto, Y.; Tarumoto, T.; Iwamto, E. *Chem. Lett.* **1972**, 255–258.
(21) Bidlingmeyer, B. A.; Warren, F. V., Jr. *Anal. Chem.* **1982**, *54*, 2351–2356.
(22) Sachok, B.; Deming, S. N. *J. Liq. Chromatogr.* **1982**, *5*, 389–402.
(23) Denkert, M.; Hackzell, L.; Schill, G.; Sjogren, E. *J. Chromatogr.* **1981**, *218*, 31–43.
(24) Warren, F. V., Jr.; Bidlingmeyer, B. A. *Anal. Chem.* **1984**, *56*, 478–491.
(25) Rigas, P. G.; Pietrzyk, D. J., to be submitted for publication in *Anal. Chem.*
(26) Helfferich, F. *Ion Exchange*; McGraw-Hill: New York, 1962; p 95.

RECEIVED for review January 27, 1986. Accepted May 7, 1986. Part of this work was supported by Grant AM 28077 awarded by the National Institute of Arthritis, Diabetes, Digestive, and Kidney Diseases and was presented in part at the 1984 International Chemical Congress of Pacific Basin Societies, Honolulu, HI, December, 1984, paper 0-1047 and at the 190th American Chemical Society National Meeting, Chicago, IL, September 1985, paper 111.

Liquid Chromatography of Alkali and Alkaline-Earth Metal Ions Using Octadecylsilanized Silica Columns Modified in Situ with Lipophilic Crown Ethers

Keiichi Kimura,* Hiroya Harino, Eiji Hayata, and Toshiyuki Shono*

Department of Applied Chemistry, Faculty of Engineering, Osaka University, Yamada-oka, Suita, Osaka 565, Japan

Octadecylsilanized silica (ODS) was coated with highly lipophilic crown ethers to obtain novel crown ether containing stationary phases for ion chromatography. The in situ modified ODS columns proved convenient and efficient for chromatographic separation of alkali and alkaline-earth metal ions. The retention times of alkali metal ions on the crown ether coated ODS are increased in the order $Li^+ < Na^+ < Cs^+ < Rb^+ < K^+$ for the 18-crown-6 and 15-crown-5 derivatives and in the order $Li^+ < Cs^+ < Rb^+ < K^+ < Na^+$ for the 12-crown-4 derivatives, being reflected in the cation-complexing properties of the crown ether rings. Simultaneous coating of more than one crown ether on ODS is possible as well, which permits easy control of the chromatographic behavior of the crown ether stationary phases. The stability (durability) of the crown ether modified ODS columns is also described.

Extensive studies about use of crown ethers in liquid chromatography of cationic species, especially, alkali and alkaline-earth metal ions, have been made so far. In most cases polymeric crown ether resins (*1–6*) and silica gels on which crown ether moieties are immobilized through covalent bonding (*7–10*) or which are coated with polymeric crown ether (*11*, *12*) have been applied to the stationary phases for the ion chromatography. The crown ether stationary phases are quite different in chromatographic behavior from conventional "ionic" cation exchangers. For instance, the elution order of alkali metal ions in the "ionic" cation exchangers follows the ionic size ($Li^+ < Na^+ < K^+ < Rb^+ < Cs^+$ in the retention time), not being varied from one cation exchanger to another. In contrast, the retention behavior of the crown ether stationary phases depends on the type of the immobilized crown ether moiety. This variable elution order on the crown ether stationary phases is attractive for chromatographic analyses of the cationic species. Hence, various cation-specific stationary phases may be designed for liquid chromatography of ionic species by selecting the immobilized crown ether moiety. The crown ether immobilized stationary phases, however, might not be easily available for most analytical chemists due to some difficulty with the syntheses.

During synthesis and purification of crown ether derivatives incorporating long aliphatic chain(s), we have found that the highly lipophilic crown ethers are retained strongly on octadecylsilanized silica (ODS) by powerful hydrophobic interaction. Some of them could not be eluted out from ODS columns even by using pure methanol as the mobile phase. This incident induced us to test ODS coated with highly lipophilic crown ethers for usefulness as stationary phases for liquid chromatography of ionic species. For convenience we attempted in situ coating of lipophilic crown ethers on ODS by passing coating solutions through commercially available, high-performance ODS-packed columns. We recently communicated the preliminary results concerning the use of crown ether coated ODS for chromatography (*13*). In this publication we wish to report in detail the liquid chromatography of alkali and alkaline-earth metal ions on ODS columns modified with lipophilic crown ethers and their analogues, **1** through **7** (Figure 1).

EXPERIMENTAL SECTION

Materials. Dodecyl-18-crown-6, -15-crown-5, and -12-crown-4, **1** through **3**, were synthesized by modification of the procedure in the literature (*14*). Dodecanoyloxymethyl crown ethers **4** and **5** were prepared by the reaction of dodecyl chloride with the corresponding hydroxymethyl crown ethers (*15*) in refluxing chloroform in the presence of triethylamine for 20 h. A similar reaction of chlorocarbonylbenzo-18-crown-6 (*16*) and dioctylamine afforded *N,N'*-dioctylcarbamoylbenzo-18-crown-6, **6**. All of the lipophilic crown ether derivatives were isolated as oil or wax after purification by preparative reversed-phase liquid chromatography (ODS, $CHCl_3$/MeOH). They were identified by ^1H NMR and mass spectroscopy and elemental analysis. The data for the elemental analysis are as follows: Calcd for **1**, $C_{24}H_{48}O_6$: C, 66.63; H, 11.18. Found: C, 66.70; H, 11.32. Calcd for **2**, $C_{22}H_{44}O_5$: C, 68.00; H, 11.41. Found: C, 67.69; H, 11.66. Calcd for **3**, $C_{20}H_{40}O_4$: C, 69.72; H, 11.70. Found: C, 70.05; H, 11.98. Calcd for **4**, $C_{25}H_{48}O_8$: C, 63.00; H, 10.15. Found: C, 62.73; H, 10.27. Calcd for **5**, $C_{23}H_{44}O_7$: C, 63.86; H, 10.25. Found: C, 64.56; H, 10.53. Calcd for **6**, $C_{33}H_{57}NO_7$: C, 68.36; H, 9.91; N, 2.42. Found: C, 68.01; H, 10.34; N, 2.51. Oligo(oxyethylene) mono-*p*-nonylphenyl ether **7** (average polymerization degree of 18, Tokyo Kasei) is commerically available and was employed as received. The metal salts are of analytical grade. Water was distilled and deionized. Methanol was purified by double distillation.

Chromatography. The high-performance liquid chromatograph system employed here consists of a pumping system (Milton Roy 0369-57 or Waters Associates 6000A), a sample injector (Kyowa Seimitsu KHP-UI-130A or Waters Associates U6K), and

0003-2700/86/0358-2233$01.50/0 © 1986 American Chemical Society

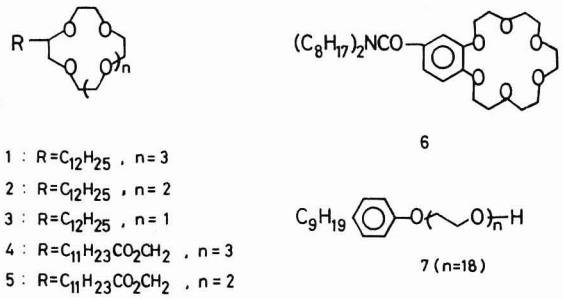

1 : R=$C_{12}H_{25}$, n=3
2 : R=$C_{12}H_{25}$, n=2
3 : R=$C_{12}H_{25}$, n=1
4 : R=$C_{11}H_{23}CO_2CH_2$, n=3
5 : R=$C_{11}H_{23}CO_2CH_2$, n=2

Figure 1. Lipophilic crown ethers employed for this study.

a conductivity detector (LDC Conductomonitor). Chromatograms were processed with a computing integrator (Shimadzu Chromatopac-E1A). Chromatography was carried out at a flow rate of 1 mL min^{-1} unless otherwise specified. The sample size was generally 50 μL and the concentrations were 0.04 mol L^{-1} for each alkali metal salt and 0.02 mol L^{-1} for each alkaline-earth metal salt. Thin-layer chromatography was run with reversed-phase TLC plates (Merck HPTLC RP-18, 10 × 10 cm) and methanol/water developing solvent.

Coating of Crown Ethers on ODS. The coating was performed by passing an appropriate coating solution of crown ether through a ODS-packed column at a flow rate of 1 mL min^{-1} (*17*). Commercially available packed columns (6 mm i.d. × 10 cm column length, 5 μm spherical ODS, YMC-Pack A-311) were employed throughout this study. Appropriate amounts of crown ethers were dissolved in methanol/water mixtures (about 200 mL), the compositions of which were 60/40 (v/v) for **3**, **4**, **5**, and **7**, 50/50 (v/v) for **1**, **2**, and **6**, and 1/3 mixture. The coating solutions were filtered with membrane filters (Teflon, 0.5 μm pore size) and then degassed by sonication. After the coating of ODS the solvent of the effluent was evaporated and the residual crown ether was weighed. The coating amount of crown ether on ODS was calculated by subtracting the residual crown ether weight from the initial one.

RESULTS AND DISCUSSION

Coating of Lipophilic 18-Crown-6 Derivatives. High lipophilicities of crown ethers are required for stable coating on ODS through hydrophobic interaction. Highly lipophilic 18-crown-6 derivatives employed here are the crown ethers carrying one or two long aliphatic chains, **1**, **4**, and **6**. As the solvent of the coating solution, methanol/water mixtures in which the crown ethers are barely soluble were chosen for effective coating. Under these coating conditions almost all of the crown ether molecules in the coating solution were retained on ODS. Higher methanol content of the coating solvent was also attempted, which was expected to allow the more homogeneous coating of crown ether on ODS. Moreover, circulation of the coating solution through the packed column was carried out for the coating. Nevertheless, these attempts did not improve the efficiency of the resulted crown ether modified ODS columns.

Liquid chromatography of alkali and alkaline-earth metal ions was performed using the ODS column modified in situ with dodecyl-18-crown-6 **1** and methanol/water mixtures as the mobile phase. Selection of the mobile phase for the liquid chromatography is very important since high methanol content in the mobile phase may cause severe stripping of the crown ether from ODS. An examination of the mobile phase by reversed-phase thin-layer chromatography indicated that the use of higher than 60% methanol content in the mobile phase leads to easy removal of the crown ether from ODS (Figure 2). Less than 60% methanol content, therefore, was adopted as the mobile phase for the ion chromatography. The results for the chromatography of alkali metal halides and thiocyanates on a ODS column loaded with 0.12 mmol of **1** are given as retention times in Table I. Use of pure water as the mobile phase allowed only slight separation of the alkali metal ions. Increasing methanol content in the mobile phase generally enhances the retention of the metal ions on the stationary phase and improves the chromatographic separation. The **1**-coated ODS possesses high affinity for K^+, the retention time decreasing in the order $K^+ > Rb^+ > Cs^+ > Na^+ > Li^+$. This retention behavior is definitely reflected in the cation-complexing property of the 18-crown-6 ring (*18*). The chromatographic retention of the metal ions is also affected by the kind of the counteranion. High polarizability of the counteranion generally augments the cation complexation of the crown ether, in turn increasing the retention times as is the case for ion chromatography using the previous covalently bonded crown ether stationary phases. Alkaline-earth metal ions were also chromatographed on the crown ether coated ODS and the retention time was increased in the order $Mg^{2+} \leq Ca^{2+} < Sr^{2+} < Ba^{2+}$. Typical chromatograms for the ion chromatography using the **1**-modified column are given in Figure 3, which shows excellent separation of five alkali metal ions. Also, Mg^{2+}/Ca^{2+} group, Sr^{2+}, and Ba^{2+} can be separated on this column, although Mg^{2+} and Ca^{2+} are hard to separate under these chromatographic conditions. The lower coating amounts of **1** (less than 0.1 mmol) suppressed the chromatographic retention on the resulting stationary phases. The much higher coating amount did not afford remarkable im-

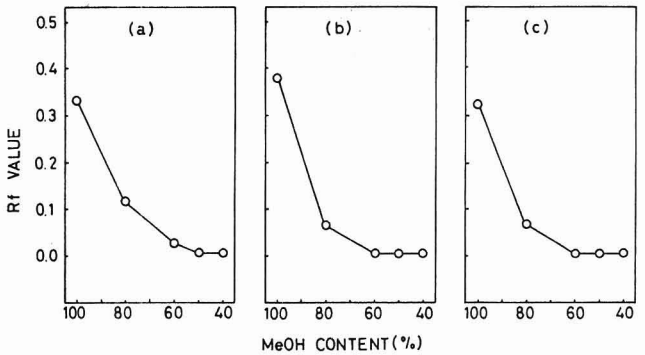

Figure 2. Correlation between R_f value and methanol/water composition in developing solvent for reversed-phase thin-layer chromatography of lipophilic crown ethers **1** (a), **2** (b), and **3** (c). For details see Experimental Section.

Table I. Retention Times of Alkali Metal Salts in Liquid Chromatography on ODS Column Modified with Dodecyl-18-crown-6 1[a]

		retention time, min, for following MeOH/H_2O			
cation	counteranion	20/80	30/70	40/60	50/50
Li^+	Cl^-	1.8	1.8	1.8	1.8
	Br^-	1.8	1.8	1.8	1.9
	I^-	1.9	1.9	2.0	2.0
	SCN^-	2.0	2.0	2.0	2.0
Na^+	Cl^-	1.9	1.9	2.0	2.1
	Br^-	1.9	1.9	2.0	2.2
	I^-	2.0	2.0	2.2	2.3
	SCN^-	2.2	2.2	2.4	2.5
K^+	Cl^-	2.2	2.4	3.0	4.5
	Br^-	2.4	2.6	3.2	4.8
	I^-	2.8	3.2	4.3	5.7
	SCN^-	3.7	4.1	5.2	6.7
Rb^+	Cl^-	2.0	2.0	2.4	3.1
	Br^-	2.1	2.2	2.5	3.1
	I^-	2.4	2.6	3.1	3.7
Cs^+	Cl^-	2.0	2.0	2.1	2.5
	Br^-	2.0	2.0	2.2	2.5
	I^-	2.3	2.3	2.7	2.8

[a] Coating amount of crown ether: 0.12 mmol. For other details see Experimental Section.

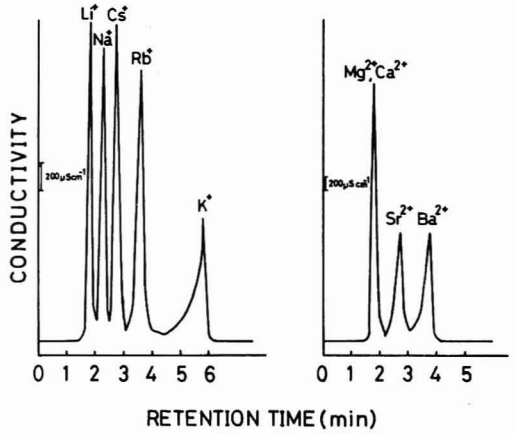

Figure 3. Liquid chromatography of alkali and alkaline-earth metal halides on ODS coated with dodecyl-18-crown-6, **1**: coating amount of crown ether, 0.12 mmol; mobile phase, MeOH/H_2O (50/50); counteranion, iodide for alkali metal ions and bromide for alkaline-earth metal ions.

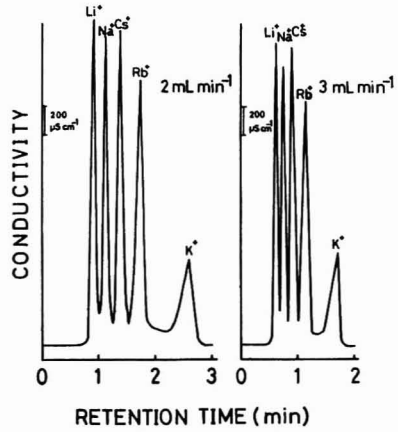

Figure 4. Effect of flow rate on liquid chromatography of alkali metal iodides using **1**-coated ODS.

provement on the chromatography. Distinct peak broadening was even observed in the chromatograms on the heavily coated ODS columns, thus resulting in diminution of the column efficiency.

The same retention order of the metal ions was found for liquid chromatography using ODS columns modified with the other 18-crown-6 derivatives, **4** and **6**. The crown ether, **6**, should be more favorable than **1** for the coating with regard to column stability due to the higher lipophilicity. The use of **4** and **6**, however, did not give any better result than **1** in the liquid chromatography of the metal ions on the modified ODS column. For example, serious peak broadening was observed on the stationary phases with the 18-crown-6 derivatives except **1**. The reason for the difference in the column efficiency between **1** and the other 18-crown-6 derivatives is not yet understood.

Rapid, but still excellent chromatographic separation of alkali metal ions on the **1**-coated ODS was realized with higher flow rates than 1 mL min^{-1} as shown in Figure 4. Even with a flow rate of 3 mL min^{-1}, five alkali metal ions can be separated almost completely within 2 min.

Coating of Lipophilic 15-Crown-5 and 12-Crown-4 Derivatives. ODS columns were similarly modified with lipophilic 15-crown-5 and 12-crown-4 derivatives, **2**, **3**, and **5**. The results for the liquid chromatography of alkali metal ions on the **2**- or **3**-coated ODS using methanol/water (50/50) as the mobile phase are presented in Table II and Figure 5. The retention times are in the order $K^+ > Rb^+ > Cs^+ \geq Na^+ > Li^+$ for the 15-crown-5 system and $Na^+ > K^+ > Rb^+ \geq Cs^+ \geq Li^+$ for the 12-crown-4 system. The elution orders generally

Table II. Retention Times of Alkali Metal Salts in Liquid Chromatography on ODS Columns Modified with Dodecyl-15-crown-5 and -12-crown-4[a]

crown ether	counter-anion	retention time, min Li^+	Na^+	K^+	Rb^+	Cs^+
2	Cl^-	2.0	2.3	4.8	4.2	2.3
	Br^-	2.0	2.4	5.2	4.5	2.4
	I^-	2.0	2.5	5.7	4.9	2.5
	SCN^-	2.1	2.9	8.2		
3	Cl^-	1.9	2.4	2.0	2.0	1.9
	Br^-	2.0	2.5	2.0	2.0	2.0
	I^-	2.0	3.0	2.3	2.2	2.1
	SCN^-	2.0	3.5	2.5		

[a] Coating amount of crown ether: 0.18 mmol for **2**, 0.43 mmol for **3**; mobile phase, MeOH/H_2O (50/50).

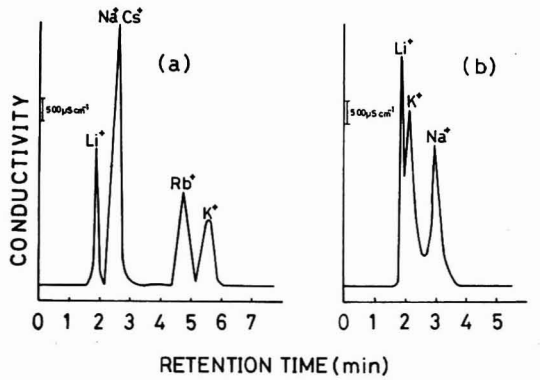

Figure 5. Liquid chromatography of alkali metal iodides on ODS coated with dodecyl-15-crown-5, **2** (a), or dodecyl-12-crown-4, **3** (b). The chromatographic conditions are as given in Table II.

seem to be governed by the cation-complexing properties of the respective crown ether rings (*18*). On the **3**-coated ODS, K^+ is eluted faster than Na^+, although the former ion is equivalent to or slightly greater than the latter one in the stability constant for the 12-crown-4 complexes. The Na^+ selectivity over K^+ of the **3**-coated ODS might be explained by formation of 2:1 (crown ether/cation) complexes as expected in the ion chromatography on the poly(12-crown-4)-modified silica (*9*). On the **2**- coated ODS, Na^+ and Cs^+ were hard to separate from each other under our chromatographic conditions. This is also the case for the separation of Li^+, Rb^+, and Cs^+ on the **3**-coated ODS. On the liquid chromatography of alkaline-earth metal ions on either of the **2**- or **3**-coated ODS, the retention times followed the order of the ionic size as observed in the 18-crown-6 chromatographic system. Since 12-crown-4 derivatives generally possess weak cation-complexing abilities as compared to 15-crown-5 and 18-crown-6 derivatives, a high coating amount of crown ether (0.43 mmol) was required in the **3**-coated ODS to obtain such chromatographic separation as shown in Figure 5. The higher coating amount did not improve the chromatographic separation of the metal ions any more. The **3**-coated ODS, however, is specific for Na^+ on chromatography. In this respect this crown ether stationary phase is distinct from the 18-crown-6 and 15-crown-5 systems. An ODS column modified with the other 15-crown-5 derivative, **5**, was quite similar to that with **2** in chromatographic behavior.

Coating of Lipophilic Oligo(oxyethylene). Lipophilic oligo(oxyethylene) derivatives such as **7**, which are inexpensive nonionic surfactants, are considered as noncyclic crown ether derivatives. Cross-linked polystyrene resins on which oligo(oxyethylene)s are immobilized through covalent bonding have been applied to stationary phases for liquid chromatography of alkali metal ions (*19*). Mixtures of thiocyanates of Li^+, Na^+,

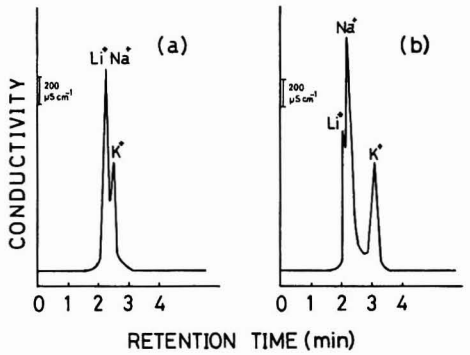

Figure 6. Liquid chromatography of alkali metal thiocyanates using lipophilic oligo(oxyethylene), **7**: (a) ODS column modified with **7** (0.12 mmol), mobile phase MeOH/H_2O (40/60); (b) unmodified ODS column, mobile phase MeOH/H_2O (40/60) containing **7** of 5.2 mmol L^{-1}.

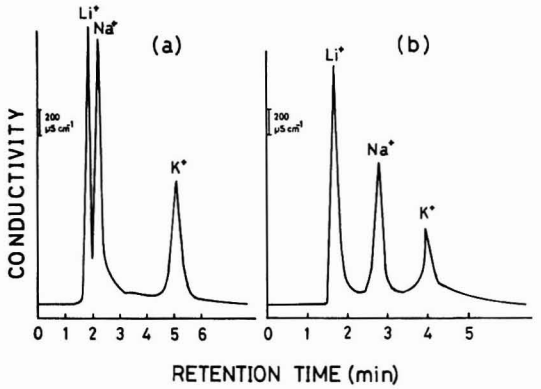

Figure 7. Comparison of liquid chromatographic separations of alkali metal iodides between single and binary coating of lipophilic crown ethers on ODS: (a) ODS column with **1** (0.12 mmol); (b) ODS column with **1** (0.12 mmol) and **3** (0.43 mmol); mobile phase, MeOH/H_2O (50/50).

and K^+ seem separable on the oligo(oxyethylene)-immobilized resins. This opens up a possibility of use of the lipophilic oligo(oxyethylene)s as the coating reagent on ODS for liquid chromatography of metal ions. However, since the noncyclic crown ethers have low cation-complexing abilities as compared to the "cyclic" ones, the ODS with oligo(oxyethylene) **7** afforded only poor separation of even alkali metal thiocyanates on the chromatography (Figure 6). The higher coating amount hardly promotes the retention of the metal ions on the resulting stationary phases. Another problem in the oligo(oxyethylene) system is rather high water solubility of the coating reagent. The lipophilic oligo(oxyethylene), **7**, is easily removed from ODS during chromatography.

We also tried liquid chromatography of the alkali metal thiocyanates on unmodified ODS using methanol/water solutions of **7** as the mobile phase. As a result some improvement on the chromatography separation of the metal ions was found with the oligo(oxyethylene)-containing mobile phase, as also illustrated in Figure 6. Better separation between Li^+ and Na^+ could not be attained by changing the composition of methanol/water or the oligo(oxyethylene) concentration in the mobile phase. ODS columns with higher theoretical plates or greater column length might bring about improvement of the chromatographic separation by the oligo(oxyethylene)–ODS system.

Simultaneous Coating of Different Crown Ethers. One of the advantages for this in situ coating of ODS is ease of coating and removal of the crown ethers. The crown ethers on ODS can be flushed out readily with methanol or methanol/chloroform mixtures from the ODS column, which is usually reused without any other special treatment. Another is simultaneous coating of more than one crown ether derivative, which thereby enables us to regulate the separation on the liquid chromatography of ionic species.

We attempted simultaneous coating of dodecyl-18-crown-6 and -12-crown-4, **1** and **3**, which are quite different in the cation-complexing property as already mentioned. Let us think about chromatographic separation of Li^+, Na^+, and K^+, which are likely to coexist in environmental and biological systems, on a crown ether modified ODS column. On the chromatography of samples containing the same concentrations of Li^+, Na^+, and K^+ on the **1**-coated ODS, the peaks for Li^+ and Na^+ are too close to each other and K^+ is eluted too slowly (Figure 7). If a larger quantity of Li^+ than Na^+ is contained in the samples or vice verse, the two ions are hard to separate on this modified column. Additional coating of the 12-crown-4 derivative, which possesses high affinity for Na^+, are expected to improve the separation among the three alkali metal ions. Actually, a more favorable chromatographic separation was realized by the simultaneous coating of **1** (0.12 mmol) and **3** (0.43 mmol) on ODS (Figure 7). In comparison with the chromatogram on ODS with only **1**, Li^+ and Na^+ are

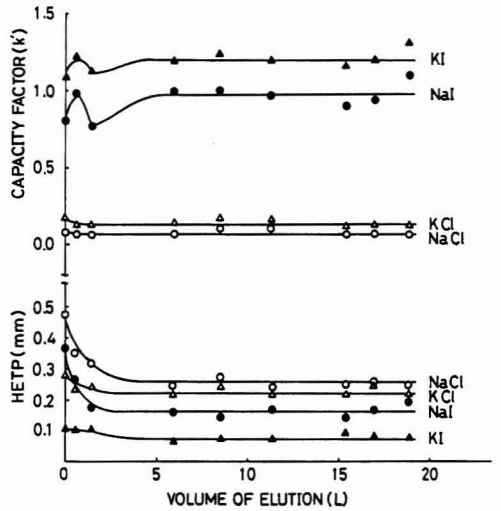

Figure 8. Stability of ODS column modified with dodecyl-18-crown-6 on liquid chromatography of Na^+ and K^+: coating amount, 0.12 mmol of **1**; mobile phase, MeOH/H_2O (40/60).

well-separated and K^+ is eluted a little faster in the binary coating system. This example indicates that the simultaneous coating of lipophilic crown ethers is a convenient, promising way to improve separation in the ion chromatography on crown ether stationary phases. Ternary systems of lipophilic crown ethers for the ODS coating would be also possible.

Column Stability. A most important factor in ion chromatography with crown ether–ODS columns is stability or durability of the columns, since the lipophilic crown ethers are adsorbed mainly by hydrophobic interaction. Definitely, the stability of the modified ODS columns depends on lipophilicities of the crown ethers and the methanol content in the mobile phase. We followed changes in the capacity factor and the height of theoretical plate (HETP) with volume of eluent, in the chromatography of Na^+ and K^+ salts using the **1** (0.12 mmol)-coated ODS column and methanol/water (40/60) as the mobile phase. Figure 8 shows that except in the early stages there is no significant change in the factors even after elution with 20 L of the eluent, which takes more than 330 h in a flow rate of 1 mL min^{-1}. The initial changes, especially decrease in HETP, might be due to rearrangement of the crown ethers adsorbed on ODS. The phenomenon, however, does not seem to be a serious problem on the chromatographic analysis of the metal ions. The crown ether coated ODS is, therefore, considered rather stable under this chromatographic condition. We tried to draw calibration curves (correlation between the peak area and ion concentration) for Na^+ and K^+ determination by chromatography

under identical condition as a stability check. The calibration curves exhibited good linearity in a wide concentration range from about 0.5 to 1000 $\mu g\ mL^{-1}$ at both of the ions. Thus, the coating of lipophilic crown ethers on ODS is quite promising for high-performance liquid chromatography of ionic species.

Registry No. 1, 83255-15-6; 2, 74649-89-1; 3, 102725-12-2; 4, 102725-13-3; 5, 102725-14-4; 6, 102725-15-5; 7, 26027-38-3; Li, 7439-93-2; Na, 7440-23-5; Cs, 7440-46-2; Rb, 7440-17-7; K, 7440-09-7; Ba, 7440-39-3; Mg, 7439-95-4; Sr, 7440-24-6; Ca, 7440-70-2.

LITERATURE CITED

(1) Blasius, E.; Janzen, K.-P.; Adrian, W.; Klautke, G.; Lorscheider, R.; Maurer, P.-G.; Nguyen, V. B.; Nguyen-Tien, T.; Scholten, G.; Stockemer, J. *Z. Anal. Chem.* **1977**, *284*, 337–360.
(2) Blasius, E.; Janzen, K.-P.; Klein, W.; Klotz, H.; Nguyen, V. B.; Nguyen-Tien, T.; Pfeiffer, R.; Scholten, G.; Simon, H.; Stockemer, H.; Toussaint, A. *J. Chromatogr.* **1980**, *201*, 147–166.
(3) Blasius, E.; Janzen, K.-P.; Keller, M.; Lander, H.; Nguyen-Tien, T.; Scholten, G. *Talanta* **1980**, *27*, 107–126.
(4) Kutchukov, P.; Ricard, A.; Quivoron, C. *Eur. Polym. J.* **1980**, *16*, 753–758.
(5) Yagi, K.; Sanchez, M. C. *Makromol. Chem., Rapid Commun.* **1981**, *2*, 311–315.
(6) Frere, Y.; Gramain, P. *Makromol. Chem.* **1982**, *183*, 2163–2172.
(7) Nakajima, M.; Kimura, K.; Shono, T. *Anal. Chem.* **1983**, *55*, 463–467.
(8) Nakajima, M.; Kimura, K.; Shono, T. *Bull. Chem. Soc. Jpn.* **1983**, *56*, 3052–3056.
(9) Nakajima, M.; Kimura, K.; Hayata, E.; Shono, T. *J. Liq. Chromatogr.* **1984**, *7*, 2115–2125.
(10) Blasius, E.; Janzen, K.-P.; Simon, H.; Zender, J. *Fresenius' Z. Anal. Chem.* **1985**, *320*, 435–438.
(11) Igawa, M.; Saito, K.; Tsukamoto, J.; Tanaka, M. *Anal. Chem.* **1981**, *53*, 1942–1944.
(12) Igawa, M.; Saito, K.; Tanaka, M.; Yamabe, T. *Bunseki Kagaku* **1983**, *32*, E137–E141.
(13) Kimura, K.; Hayata, E.; Shono, T. *J. Chem. Soc., Chem. Commun.* **1984**, 271–272.
(14) Bowsher, B. R.; Rest, A. J.; Main, B. G. *J. Chem. Soc., Dalton Trans.* **1984**, 1421–1425.
(15) Czech, B. *Tetrahedron Lett.* **1980**, *21*, 4197–4198.
(16) Bourgoin, M.; Wong, K. H.; Hui, J. Y.; Smid, J *J. Am. Chem. Soc.* **1975**, *97*, 3462–3467.
(17) Cassidy, R. M.; Elchuk, S. *Anal. Chem.* **1982**, *54*, 1558–1563.
(18) Izatt, R. M.; Bradshaw, J. S.; Nielsen, S. A.; Lamb, J. D.; Christensen, J. J.; Sen, D. *Chem. Rev.* **1985**, *85*, 271–339.
(19) Fujita, H.; Yanagida, S.; Okahara, M. *Anal. Chem.* **1980**, *52*, 869–875.

RECEIVED for review February 18, 1986. Accepted April 17, 1986.

Mechanism of the Reversed-Phase High-Performance Liquid Chromatographic Separation of D- and L-Valine Using Copper(II) and L-Aspartyl-L-phenylalanine Methyl Ester

J. M. Broge[1] and D. L. Leussing*

Department of Chemistry, The Ohio State University, Columbus, Ohio 43210

Mobile and stationary phase interactions existing in the reverse-phase separation of D- and L-valine with an eluant containing Cu(II) and aspartame have been studied in depth. Diastereomeric mixed ligand complexes formed in the solution phase have a negligible influence on the separation. Enantiomeric discrimination occurs solely on the stationary phase. The number of moles of Cu(II) and aspartame adsorbed onto the C_{18} packing are described by Langmuir isotherms in which HA, $Cu(A)^+$, and $Cu(A)_2$ compete for a given number of sites (A^- = aspartame$^-$). Observed retention times are well-reproduced by a model assuming the reactions $HVal_{aq} + Cu(A)_s \rightleftharpoons Cu(A)(Val)_s + H^+$, $HVal_{aq} + Cu(A)_{2s} \rightleftharpoons Cu(A)_2(Val)_s + H^+$, and $Cu(Val)_{aq} + Cu(A)_{2s} \rightleftharpoons Cu(A)_2Cu(Val)_s$.

The use of complexes formed between chiral ligands and metal ions to perform chromatographic separations and analyses of amino acid enantiomers has attracted considerable attention in recent years (*1*). One approach has been to covalently bond a chiral ligand to the solid support of the chromatographic column (*2–5*). Another has been to add a chiral ligand and metal ion to the eluant phase (*6–18*). This latter method is particularly attractive because the eluant is easily prepared by mixing solutions containing the metal ion and ligand and adjusting the pH to an appropriate value. A conventional column, usually reverse phase, may be used.

Two limiting mechanisms have been invoked to account for the separations obtained by using chiral eluant phases. At one limit the chiral complex is considered to be adsorbed onto the solid support with separation occurring entirely on the stationary phase via a ligand exchange mechanism (*1*, *6*, *11*, *19*). Along this line, Karger (*6*, *10*, *13*) and Davankov (*11*) and their co-workers have designed ligands with long alkyl side chains that have been successfully used to effect separations of amino acid enantiomers and their derivatives. At the other limit, separation is thought to occur mainly in the eluant phase through the formation of diastereomeric mixed ligand complexes which have different stabilities (*20*). Mixed ligand complex formation perturbs partition between moving and stationary phases resulting in different rates of movement of the enantiomers through the column. Separations effected by using small chiral ligands that contain relatively low proportions of hydrocarbon, such as proline and histidine, are generally considered to operate through this second limiting mechanism. Recently Zare has employed solution phases containing Cu(II) and L-histidine to separate amino acid enantiomers using zone electrophoresis (*21*).

An intriguing reagent, which may operate through both mechanisms, is the Cu(II) complex of L-aspartyl-L-phenylalanine methyl ester (aspartame) (*7*). Originally this reagent was thought to operate via mobile phase interactions (*7*), but later experiments using analogous L-aspartyl-c-hexylamine derivatives led to the conclusion that stationary phase reactions were important (*15*). We report here the results of an in-depth study of the separation of D- and L-valine using mobile phase solutions of Cu(II) and aspartame. Stability constants of solution species have been determined as well as the amounts of Cu(II) and aspartame adsorbed on to an octadecylsilane stationary phase as a function of solution composition. A relationship between solution and stationary

[1] Present address: General Mills, Inc., James Ford Bell Technical Center, 9000 Plymouth Ave. N, Golden Valley, MN 55427.

0003-2700/86/0358-2237$01.50/0 © 1986 American Chemical Society

Table I. Valine Retention Times and Moles of Adsorbed Cu(II) and Aspartame as a Function of Overall Eluent Composition (pH 4.0, I = 0.02)

expt no.	10^3C_{Cu},[a] M	10^3C_A,[a] M	n[b]	Cu_{ads}, mol × 10^3	A_{ads}, mol × 10^3	t_0, min	t_L, min obsd	t_L, min calcd	t_D, min obsd	t_D, min calcd
1	0	0.199	2	0	0.123 (4)					
2	0	0.398	2	0	0.175 (6)					
3	0	0.601	2	0	0.220 (8)					
4	0	0.800	2	0	0.268 (10)					
5	0	1.000	2	0	0.279 (10)					
6	0.243	0.200	3	0.0933 (5)	0.261 (9)	1.79	5.95	5.65	8.40	7.88
7	0.487	0.200	2	0.1217 (1)	0.285 (10)	1.86	7.76	7.52	11.17	10.7
8	0.730	0.200	2	0.1412 (1)	0.302 (11)	1.82	8.70	8.70	12.60	12.6
9	0.974	0.200	2	0.1511 (3)	0.321 (11)	1.76	9.25	9.33	13.42	13.5
10	1.22	0.200	2	0.1590 (5)	0.323 (12)	1.72	9.72	9.75	14.18	14.1
11	0.243	0.400	4	0.1429 (14)	0.397 (14)	1.78	5.98	6.04	8.25	8.44
12	0.487	0.400	4	0.1776 (16)	0.417 (15)	1.77	7.47	7.70	10.51	10.9
13	0.730	0.400	3	0.2196 (2)	0.476 (17)	1.75	8.58	8.68	12.16	12.4
14	0.974	0.400	2	0.2023 (1)	0.421 (15)	1.72	9.10	9.27	12.97	13.2
15	1.22	0.400	3	0.2279 (41)	0.456 (16)	1.69	9.66	9.74	13.78	13.9
16	0.100	0.800	3	0.1378 (4)		1.79	4.41	4.20	5.74	5.56
17	0.300	0.800	4	0.2092 (4)		1.77	6.04	6.01	8.27	8.29
18	0.464	0.802	3	0.2374 (1)		1.69	6.54	6.71	9.03	9.33
19	0.500	0.798	3	0.2404 (1)		1.71	6.98	6.89	9.65	9.54
20	0.695	0.803	3	0.2590 (3)		4.69	7.28	7.48	9.97	10.4
21	0.700	0.806	3	0.2633 (17)		1.73	7.48	7.52	10.33	10.4
22	0.898	0.803	3	0.2743 (1)		1.68	8.13	7.93	11.30	11.0
23	1.16	0.804	2	0.2819 (6)		1.62	8.05	8.34	11.20	11.5
24	0.243	1.20	3	0.2072 (11)	0.498 (18)	1.77	5.10	5.23	6.75	7.08
25	0.487	1.20	2	0.2546 (4)	0.548 (20)	1.74	6.49	6.76	8.83	8.41
26	0.730	1.20	2	0.2973 (2)	0.600 (21)	1.72	7.19	6.81	9.84	9.28
27	0.974	1.20	3	0.3146 (7)	0.593 (21)	1.69	7.48	7.27	10.19	9.87
28	1.22	1.20	2	0.3333 (96)	0.601 (21)	1.68	7.97	7.70	10.49	10.43

[a] Total solution phase concentration. A = aspartame. [b] Number of determinations.

phase compositions and retention times is proposed.

EXPERIMENTAL SECTION

$CU(ClO_4)_2$ was obtained from the G. Frederick Smith Chemical Co. A stock solution was standardized by titration with edta following the method of Flaschka (22). L-Aspartyl-L-phenylalanine methyl ester (aspartame) was obtained in part from the Sigma Chemical Co. and as a gift from G. D. Searle and Co. D,L-Valine was obtained from Calbiochem Co., and L-valine and D-valine were obtained from Sigma Chemical Co. $NaClO_4$ was obtained from the G. Frederick Smith Chemical Co.

Complex formation constants and ligand protonation constants were determined by pH titration. A Radiometer ABU 12 Autoburet was used to deliver titrant (either standard NaOH or $HClO_4$) into the probe solution which was maintained at 25 ± 0.1 °C and adjusted to an ionic strength of 0.02 with $NaClO_4$. The acid dissociation constants of aspartame and valine were determined in separate experiments. The Cu–ligand complex formation constants were then determined for aspartame and L-valine separately, and finally the mixed ligand complex formation constants were determined for both valine enantiomers. Measured hydrogen ion activities were converted to hydrogen ion concentration by means of a calibration curve obtained by titrating 0.02 M $NaClO_4$ with standard $HClO_4$. Equilibrium constants reported here are expressed entirely in concentration units.

The effect of pressure on the Cu–aspartame equilibria was assessed by determining the absorption spectra at different pressures. Two sets of solutions were prepared, one containing monoprotonated aspartame, HA, and $Cu(A)^+$ in equal concentrations and the other containing $Cu(A)^+$ and $Cu(A)_2$ at equal concentrations (A^- = aspartame$^-$). These mixtures give the highest sensitivities to changes in the stepwise formation constants, Q_{CuA} and Q_{CuA_2}. The solutions were placed in a high-pressure optical cell and spectra were scanned in the range 600–800 nm where Cu(II) d–d electronic transitions are sensitive to the replacement of oxygen donor atoms by nitrogen donor atoms in the primary coordination sphere of the metal ion. Spectra were measured at atmospheric pressure, 1500 psi and 3000 psi. The positions of the band maxima were found to be invariant over this pressure range and relative changes in their intensities were less than 0.5%.

Chromatograms and column adsorption data were collected by use of a Beckman Model 330 HPLC with an Altex octadecylsilane reverse-phase packing having a particle size of 5 μm. The column, thermostated at 25 °C, was equilibrated with a mobile phase containing Cu(II), aspartame, and sufficient $NaClO_4$ to bring the ionic strength to 0.02. All solutions were adjusted to pH 4.00. The eluant flow rate was 1.5 mL/min for all of the final runs. Equilibration was indicated by a constant base line following a marked absorbance increase due to breakthrough of the complex. Simultaneously, the pH of the effluent attained the same value as that of the solution entering the column, and retention times for trial chromatograms of valine became constant.

Valine retention times, adsorbed Cu(II), and adsorbed aspartame were determined in replicate for 28 different compositions of the mobile phase. Adsorbed aspartame and Cu(II) were determined after valine chromatograms had been obtained for a given eluant. The Cu(II)–aspartame eluant was flushed from the pump and detector with methanol and then methanol was passed through the column at 0.5 mL/min. A clear solution having only a faint blue color (void volume effluent) emerged from the column for several minutes and was discarded. A deep blue solution then emerged and was collected until the detector showed very little absorbance. The collected eluant was diluted to 50.0 mL in a volumetric flask. After a further 10-fold dilution separate aliquots were analyzed for Cu and aspartame.

Cu(II) was determined by potentiometric titration with a standard edta solution and using an Orion Cu ion selective electrode to monitor Cu(II) activity. Aspartame was determined spectrophotometrically at pH 2 in solutions to which an excess of $Cu(ClO_4)_2$ was added, bringing the Cu concentration to 0.0025 M, in order to mitigate the minor influence on aspartame absorbance of variations in the effluent Cu(II) concentration. Absorption intensities were measured at the phenylalanine absorption maxima, 263, 257, and 253 nm, and compared with the intensities of known solutions of aspartame measured under the same conditions. The results are presented in Table I.

Nonlinear curve fitting was performed by use of the program MINUIT developed at CERN (23). Important sections of this program are SIMPLEX and polynomial fitting routines. Solution equilibrium constants were obtained by fitting calculated pH–

Table II. Equilibrium Constants for Cu(II)/Valine/Aspartame (25 °C, I = 0.02, A = aspartame, Val = valine)

reaction	log K or pK_a	n^a
$H_2A^+ \rightleftharpoons H^+ + HA$	pK_{1a}^A = 2.92 (2)	12
$HA \rightleftharpoons H^+ + A^-$	pK_{2a}^A = 7.51 (4)	11
$H_2Val^+ \rightleftharpoons H^+ + HVal$	pK_{1a}^V = 2.32 (8)	6
$HVal \rightleftharpoons H^+ + Val^-$	pK_{2a}^V = 9.35 (2)	6
$Cu^{2+} + A^- \rightleftharpoons Cu(A)^+$	log Q_{CuA} = 6.26 (2)	7
$Cu(A)^+ + A^- \rightleftharpoons Cu(A)_2$	log Q_{CuA_2} = 5.27 (4)	12
$Cu^{2+} + Val^- \rightleftharpoons Cu(Val)^+$	log Q_{CuV} = 8.00 (2)	12
$Cu(Val)^+ + Val^- \rightleftharpoons Cu(Val)_2$	log Q_{CuV_2} = 6.71 (0.04)	11
$Cu(A)^+ + L\text{-}Val^- \rightleftharpoons Cu(A)(L\text{-}Val)$	log Q_{CuAVL} = 7.18 (8)	14
$Cu(A)^+ + D\text{-}Val \rightleftharpoons Cu(A)(D\text{-}Val)$	log Q_{CuAVD} = 7.13 (0.13)	14

[a] Number of determinations.

titrant volume curves to observe data points using a subroutine developed and used in our laboratory for many years. This subroutine employs the Newton–Raphson method to solve the mass balance and equilibrium constraints pertaining to a given equilibrium system for which total species concentrations and equilibrium constants are specified. To obtain unknown equilibrium constants, this subroutine was incorporated into a program which called MINUIT to perform the fitting process. In other applications this subroutine was used to obtain species distributions once the equilibrium constants were known.

RESULTS AND DISCUSSION

The equilibrium constants calculated from replicate potentiometric titrations are presented in Table II. Both pK_{1a} (2.92) and pK_{2a} (7.51) of aspartame are assigned to the proton ionization occurring at the aspartyl residue, the former to the carboxylic acid of the monocation and the latter to the ammonium group of the zwitterion. Due to the proximity of the α-amide linkage the amine group of aspartame has a substantially lower basicity than the amine group of the unsubstituted analogue, β-alanine (pK_{2a} = 10.1). Reflecting both the lower amine basicity and the lower stability of a six-membered ring relative to a five-membered ring, the stability constant of $Cu(A)^+$, $10^{6.26}$ M^{-1}, is seen to be substantially lower than that for $Cu(Val)^+$, $10^{8.00}$ M^{-1}. For comparison, the stability constant of $Cu(\beta\text{-Ala})^+$ is intermediate at $10^{7.0}$ M^{-1} (*24*).

Stability differences between diastereomeric Cu(II) complexes principally arise from steric interactions between the bound ligands. Within the experimental uncertainties the stepwise constants for the formation of Cu(A)(D-Val) and Cu(A)(L-Val) are seen to be essentially identical, indicating little selective interaction between the isopropyl side chain of valine and the amide chain of aspartame. Even the stabilities of the individual binary bis complexes relative to the stabilities of the mono complexes show little effect of this kind of interaction. After correcting for the statistical effects that with tetragonal Cu(II) the 1:1 complexes may be formed four ways and dissociate by only one, while the bis complexes may be formed only one way from the mono complexes but dissociate by two, the logs of the stepwise constants are 5.66 for the formation of $Cu(A)^+$ and 5.57 for $Cu(A)_2$. The corresponding values for $Cu(Val)^+$ and $Cu(Val)_2$ are 7.40 and 7.00. As a comparison, for the unhindered glycinate complexes the logs of the corrected stepwise formation constants are 7.6 and 7.2 showing the intrinsic electronic effect of basic ligands on the stepwise values. In the absence of interligand steric hindrance the log of the stepwise constant for the reaction, $CuA)^+ + D\text{- or } L\text{-}Val^- \rightleftharpoons Cu(A)(D\text{- or } L\text{-Val})$, is expected to lie within the range 7.4–7.0. The observed values of $\simeq$7.1–7.2 provide further evidence of negligible contact between the bound ligands in the solution phase complexes.

More importantly, even if the diastereomers had significantly different stabilities, the absolute magnitudes of their formation constants are such that under the experimental conditions employed to effect the separation of the enantiomers, very little of the valine is present in the solution phase as the mixed ligand complex. Table III gives the calculated concentrations of the Cu–aspartame species and the fractions of valine present in various forms under the experimental conditions investigated. It is seen that at best less than 1.7% of the valine is bound as the mixed ligand complex. The high pressure within the HPLC column may induce some changes in the distributions from those shown in Table III, but the differences are expected to be small as inferred from the slight effects of pressure on the spectra of solutions contaiing Cu–aspartame complexes and by the observed independence of valine capacity factors on eluant flow rate, which is determined by pump pressure.

The values presented in Table III underscore the importance of calculating species distribution in a separation system

Table III. Solution Phase Distributions of Species in Experiments 6–28

expt no.	$10^3[Cu^{2+}]$, M	$10^6[A^-]$, M	$10^3[HA]$, M	$10^3[H_2A^+]$, M	$10^3 \cdot [CuA^+]$, M	$10^5[Cu(A)_2]$, M	fraction of Val present as HVal	$CuVal^+$	Cu(A)(Val)
6	0.223	0.051	0.165	0.014	0.021	0.020	0.89	0.09	0.0012
7	0.449	0.046	0.149	0.013	0.037	0.032	0.82	0.16	0.0021
8	0.678	0.042	0.136	0.011	0.052	0.040	0.75	0.23	0.0026
9	0.909	0.039	0.125	0.010	0.064	0.046	0.70	0.28	0.0030
10	1.143	0.036	0.115	0.010	0.074	0.049	0.65	0.33	0.0033
11	0.205	0.101	0.332	0.028	0.038	0.071	0.90	0.08	0.0023
12	0.415	0.093	0.303	0.025	0.070	0.122	0.83	0.15	0.0039
13	0.630	0.086	0.277	0.023	0.098	0.156	0.76	0.22	0.0051
14	0.852	0.078	0.257	0.022	0.120	0.174	0.71	0.27	0.0058
15	1.073	0.073	0.236	0.020	0.142	0.191	0.66	0.32	0.0064
16	0.071	0.218	0.710	0.059	0.028	0.114	0.95	0.03	0.0018
17	0.217	0.203	0.659	0.055	0.080	0.303	0.89	0.09	0.0048
18	0.341	0.192	0.623	0.052	0.119	0.424	0.85	0.13	0.0068
19	0.369	0.188	0.611	0.051	0.126	0.441	0.84	0.14	0.0072
20	0.528	0.169	0.579	0.051	0.162	0.509	0.79	0.18	0.0090
21	0.532	0.169	0.581	0.051	0.163	0.513	0.79	0.18	0.0091
22	0.687	0.164	0.540	0.046	0.205	0.626	0.75	0.23	0.010
23	0.898	0.155	0.496	0.041	0.253	0.731	0.69	0.28	0.012
24	0.152	0.312	1.019	0.086	0.086	0.501	0.91	0.06	0.0054
25	0.314	0.286	0.940	0.079	0.164	0.871	0.85	0.12	0.0095
26	0.484	0.267	0.870	0.073	0.235	1.167	0.80	0.17	0.013
27	0.660	0.250	0.807	0.067	0.300	1.396	0.75	0.22	0.015
28	0.848	0.229	0.751	0.063	0.354	1.513	0.70	0.27	0.017

before attributing any observed results to the influence of solution phase complexes.

Adsorption Isotherms. Aspartame in the absence of Cu(II) is adsrobed onto the octadecylsilane support, presumably in the form of the neutral acid

$$HA_{aq} \overset{K_{HA}}{\rightleftharpoons} HA_s \quad (1)$$

The relationship between the number of moles adsorbed and the solution phase concentration was found to be described by the equation for the Langmuir isotherm (eq 2) with K_{HA} equal to 2.2×10^3 M^{-1} and n, the number of moles adsorbed at saturation, equal to 0.000 42 mol. Agreement between observed and calculated moles of adsorbed aspartame yielded a linear correlation coefficient, r, equal to 0.991 and a standard deviation, s, equal to ±0.000 010 mol.

$$K_{HA} = x_{HA}/[HA](1 - x_{HA}) \quad (2)$$

$$x_{HA} = \text{mol of adsorbed aspartame}/n$$

The addition of Cu(II) to the mobile phase results in the adsorption of substantial amounts of Cu(II) onto the ODS phase and an increase in the moles of adsorbed aspartame. At low mobile phase concentrations of aspartame (expt 6–15, Table I) the observed ratio of bound aspartame to bound Cu(II) is greater than 2:1 at low concentrations of Cu(II) but approaches 2.0 as the Cu(II) concentration is increased. While similar behavior is found at higher solution concentrations of aspartame (expt 24–28), the observed A/Cu ratio falls below 2.0 at the highest Cu(II) concentration investigated, 1.22 mM Cu(II). These results suggest that Cu(II) is bound to the solid phase predominantly as $Cu(A)_2$, but some adsorption as a lower complex also occurs. Further evidence for the binding of a second complex was also provided by an unsatisfactory fit of the calculated to the observed data points assuming a model in which only the adsorption of two species, HA (eq 1) and $Cu(A)_2$ (eq 4) was assumed. Inclusion of $Cu(A)^+$ (eq 3) into the model greatly improved the fit. $Cu(A)^+$ adsorption

$$Cu(A)_{aq}^+ \overset{K_{CuA}}{\rightleftharpoons} Cu(A)_s^+ \quad (3)$$

$$Cu(A)_{2(aq)} \overset{K_{CuA2}}{\rightleftharpoons} Cu(A)_{2(s)} \quad (4)$$

must be accompanied by a counterion, in this case ClO_4^-. Because the ClO_4^- concentration was maintained essentially constant at 0.02 M and the effect of a variation in ClO_4^- was not tested, we have chosen to express K_{CuA} for eq 3 as a unitless conditional constant.

Equations 2 through 4 lead to competitive equilibrium adsorption expressions of the form

$$K_i = x_i/[i](1 - \sum_{j=1}^{J} x_j) \quad (5)$$

In eq 5 x_i is the ratio of the number of moles of adsorbed i to n, the number of moles bound at saturation, and J is the total number of adsorbed forms of aspartame. The values found from the nonlinear curve fitting process are 4.1×10^3 M^{-1} (K_{HA}), 6.8×10^3 M^{-1} (K_{CuA}), 2.1×10^6 M^{-1} (K_{CuA_2}), and 0.000 33 mol (n).

The excellent agreement attained between the observed and calculated values for Cu and aspartame is shown in Figure 1. For the Cu(II) data points $r = 0.980$ and $s = \pm 0.000\,14$ mol, while for the aspartame data points $r = 0.987$ and $s = \pm 0.000\,020$ mol. Points 26–28 show a tendency for the observed Cu(II) adsorption data points to be higher than those calculated by the model. If these points are omitted from the correlation analysis, then the agreement between observed and calculated values for Cu(II) adsorption corresponds to $r = 0.988$, $s = \pm 0.000\,09$ mol. Attempts to modify the model by

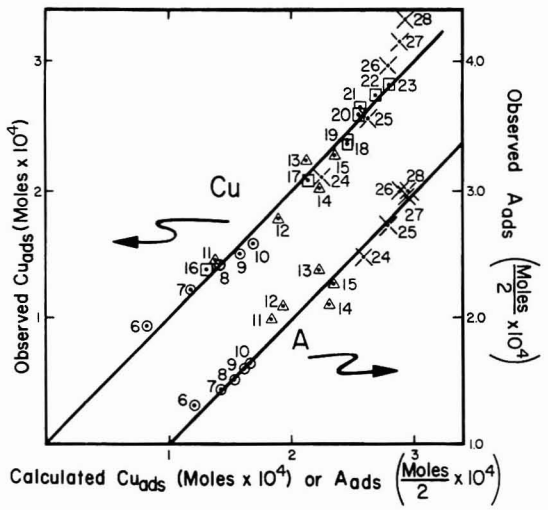

Figure 1. Agreement between observed and calculated moles of Cu(II) and aspartame adsorbed onto the octadecylsilane packing: A = aspartame; (O) experiments 6–10, (△) experiments 11–15, (□) experiments 16–23, (×) experiments 24–28.

incorporating an equilibrium expression which accounts for the deviations of points 26–28 were unsuccessful. Tentatively, we propose that this trend arises from a tendency for $Cu(A)^+$ to associate with $Cu(A)_2$ at higher column loadings. Another indication of intermolecular association is shown by the increase in K_{HA} which is necessary to account for HA adsorption in the presence of adsorbed $Cu(A)_2$. It is not surprising that at high column loading deviations from ideal behavior are observed. Nevertheless, except for these data points, 26–28, the model very satisfactorily accounts for both aspartame and Cu(II) adsorption.

The value of K_{CuA} has the same order of magnitude as that of K_{HA} suggesting that it is the phenylalanine methyl ester residue of the dipeptide which is primarily responsible for the adsorption process. Consistent with this conclusion, K_{CuA_2} is seen to be about equal to $(K_{HA})^2$; the free energy of adsorption of $Cu(A)_2$ is about twice that for the adsorption of HA. The decrease in n that occurs when $Cu(A)_2$ replaces HA on the solid support is also consistent with the displacement of one molecule by a larger one. The decrease is less than a factor of 2, however, indicating that the free area on the solid occupied by $Cu(A)_2$ is less than twice that occupied by HA.

Retention Times. A reaction model that quite satisfactorily accounts for the observed retention times ($r = 0.991$, $s = \pm 0.20$ min for L-valine, $r = 0.991$, $s = \pm 0.31$ min for D-valine) is based on the following processes:

$$HVal_{aq} + Cu(A)_s^+ \overset{K_{CuAV}}{\rightleftharpoons} Cu(A)(Val)_s \quad (6)$$

$$HVal_{aq} + Cu(A)_{2(s)} \overset{K_{CuA_2V}}{\rightleftharpoons} Cu(A)_2{\cdot}(Val)_s \quad (7)$$

$$Cu(Val)_{aq}^+ + Cu(A)_{2(s)} \overset{K_{CuA_2CuV}}{\rightleftharpoons} Cu(A)_2{\cdot}Cu(Val)_s^+ \quad (8)$$

Reactions 6 and 7 define the conditional equilibrium expressions as used here. Presumably a proton is liberated, but because the pH was not varied in these experiments, proton release was not verified.

The capacity factor for valine, k', is equal to moles of adsorbed valine/moles of valine in solution phase

$$k' = (m_{CuAV} + m_{CuA_2V} + m_{CuA_2CuV})/([HVal] + [Cu(Val)])V_0 \quad (9)$$

V_0 is the void volume of the column.

Only the two principal solution phase forms of valine are included in the denominator of eq 9 because the sum of all

the other forms comprises less than 3% of the total valine in the solution phase. See Table III. Here again, because the pH and ClO_4^- concentrations were held constant, the equilibrium constants involving these species are expressed as conditional constants omitting H^+ and ClO_4^- concentrations.

Invoking equilibrium between solution and solid components as expressed in eq 6–8 and the relationship $m_1 = x_1 n$; expressing the concentration of $Cu(Val)_{aq}^+$ in terms of HVal, Cu^{2+}, and H^+, and canceling [HVal] from the numerator and denominator of the resulting equation yields eq 10.

$$k' = \frac{K_{CuAV} m_{CuA} + K_{CuA_2V} m_{CuA_2} + K_{CuA_2CuV} Y m_{CuA_2}}{(1 + Y)V_0} \quad (10)$$

$$Y = Q_{CuV} 10^{-pK_{2a}V} [Cu^{2+}]/[H^+]$$

Since $k' = (t_r - t_0)/t_0$ and $V_0 = Rt_0$ (R is the flow rate of eluant), eq 10 leads to a relationship between retention times and solution and stationary phase compositions.

$$t_r = \frac{K_{CuAV} m_{CuA} + K_{CuA_2V} m_{CuA_2} + K_{CuA_2CuV} Y m_{CuA_2}}{(1 + Y)R} + t_0 \quad (11)$$

For a each set of experimental conditions, solution distributions and stationary phase values of m_{CuA} and m_{CuA_2} were calculated. MINUIT was then used to find the values of K_{CuAV}, K_{CuA_2V}, and K_{CuA_2CuV} that give the best least-squares fit of eq 11 to the observed retention times. The results are as follows: $K_{CuAV} = 4.2\ M^{-1}$, $K_{CuA_2V} = 0.12\ M^{-1}$, $K_{CuA_2CuV} = 0.008\ M^{-1}$, (D-Val); $K_{CuAV} = 2.7\ M^{-1}$, $K_{CuA_2V} = 0.082\ M^{-1}$, $K_{CuA_2CuV} = 0.006\ M^{-1}$ (L-Val). The very good agreement between observed and calculated retention times can be seen in the values given in Table I.

For each of the binding modes expressed in eq 6–8, the D isomer of valine is found to favor the stationary phase more than the L isomer. For both isomers the strength of the bonding follows the expected order: interaction of uncomplexed valine is strongest with $Cu(A)_s^+$, which has two equatorial Cu(II) positions available, followed by bonding to $Cu(A)_{2(s)}$ for which only axial sites are free. The bonding of $Cu(Val)_{aq}^+$ to $Cu(A)_{2(s)}$ possibly involves the formation of weak dimers in which two Cu(II) atoms are bridged by carboxylate groups. Similar structures are known to be formed in solid and nonaqueous phases (25).

It is interesting to note that the constant for the formation of the mixed ligand complex on the stationary phase (eq 7) is much smaller than it is in the solution phase. From the results obtained here the stepwise constant for the reaction, $Val_{aq}^- + Cu(A)_{2(s)} \rightleftharpoons Cu(A)_2(Val)_s$, is calculated to have an upper limit of $1.4 \times 10^4\ M^{-1}$ for D-valine and $9 \times 10^3\ M^{-1}$ for the L isomer. These values are about 1/25 as large as those for the corresponding solution phase constants. In contrast to the negligible formation of mixed ligand complexes in solution, the fact that the enantiomers are actually retained by the stationary phase must be attributed to the presence of large amounts of adsorbed complexed aspartame which tends to drive reactions 6–8 to the right. In addition, this high concentration of chiral ligand together with the orientation entailed by adsorption plausibly accounts for the discrimination between the valine enantiomers by the solid support.

Registry No. D-HVal, 640-68-6; L-HVal, 72-18-4; Cu^{2+}, 15158-11-9; HA, 22839-47-0; DL-HVal, 516-06-3; $Cu(A)_2$, 103004-21-3; $Cu(L\text{-}Val)_2$, 14267-13-1; Cu(A)(L-Val), 103004-22-4; Cu(A)(D-Val), 103066-77-9.

LITERATURE CITED

(1) Davankov, V. A.; Kurganov, A. A.; Bochkov, A. A. *Advances in Chromatography*; Giddings, J. C., Grushka, E., Cazes, J., Brown, P. R., Eds.; Marcel Dekker: New York, 1983; Vol. 22, pp 71–116.
(2) Snyder, R. V.; Angelici, R. J.; Meck, R. B. *J. Am. Chem. Soc.* **1972**, *94*, 2660.
(3) Kurganov, A. A.; Zhuchkova, L. Y.; Davankov, V. A. *Makromol. Chem.* **1979**, *180*, 2101.
(4) Tsuchida, E.; Nishikawa, H.; Terada, E. *Eur. Polym. J.* **1976**, *12*, 611.
(5) Jozefonvicz, J.; Petit, M. A.; Szubarga, A. *J. Chromatogr.* **1978**, *147*, 177.
(6) LePage, J. N.; Lindner, W.; Davies, G.; Seitz, D. E.; Karger, B. L. *Anal. Chem.* **1979**, *51*, 433.
(7) Gilon, C.; Leshem, R.; Tapuhi, Y.; Grushka, E. *J. Am. Chem. Soc.* **1979**, *101*, 7612.
(8) Hare, P. E.; Gil-Av, E. *Science* **1979**, *204*, 1226.
(9) Gil-Av, E.; Tishbee, A.; Hare, P. E. *J. Am. Chem. Soc.* **1980**, *102*, 5115.
(10) Lindner, W.; LePage, J. N.; Davies, G.; Seitz, D. E.; Karger, B. L. *J. Chromatogr.* **1979**, *185*, 323.
(11) Davankov, V. A.; Bochkov, A. S.; Kurganov, A. A.; Roumetliotis, P.; Unger, K. K. *Chromatographia* **1980**, *13*, 677.
(12) Gilon, C.; Leshem, R.; Grushka, E. *Anal. Chem.* **1980**, *52*, 1206.
(13) Tapuhi, Y.; Miller, N.; Karger, B. L. *J. Chromatogr.* **1981**, *205*, 325.
(14) Nimura, N.; Suzuki, T.; Kasahara, Y.; Kinoshita, T. *Anal. Chem.* **1981**, *53*, 1380.
(15) Grushka, E.; Leshem, R.; Gilon, C. *J. Chromatogr.* **1983**, *255*, 41.
(16) Dobashi, A.; Hara, S. *Anal. Chem.* **1983**, *55*, 1805.
(17) Engel, M. H.; Macko, S. A. *Anal. Chem.* **1984**, *56*, 2598.
(18) Wernicke, R. *J. Chromatogr. Sci.* **1985**, *23*, 39.
(19) Davankov, V. A.; Kurganov, A. A. *Chromatographia* **1983**, *17*, 686.
(20) Lam, S. *J. Chromatogr. Sci.* **1984**, *22*, 416.
(21) Gassman, E.; Kuo, J. E.; Zare, R. N. *Science* **1985**, *230*, 813.
(22) Flaschka, H. A. *EDTA Titrations*; Pergamon Press: New York, 1964.
(23) James, F.; Roos, M. *Comput. Phys. Commun.* **1975**, *10*, 343.
(24) Martell, A. E.; Smith, Robert M. *Critical Stability Constants*; Plenum Press: New York, 1974; Vol. 1, p 20.
(25) Doedens, R. J. *Prog. Inorg. Chem.* **1976**, *21*, 209.

RECEIVED for review January 21, 1986. Accepted May 1, 1986.

Determination of Nonionic and Partially Hydrolyzed Polyacrylamide Molecular Weight Distributions Using Hydrodynamic Chromatography

Martin A. Langhorst,*[1] Frederick W. Stanley, Jr.,[1] Sergio S. Cutié,[1] Jeffrey H. Sugarman,[2] Larry R. Wilson,[1] David A. Hoagland,[3] and Robert K. Prud'homme[2]

The Dow Chemical Company, Midland, Michigan 48667, and Department of Chemical Engineering, Princeton University, Princeton, New Jersey 08544

Polyacrylamide and its copolymers of acrylic acid have wide application as flocculants and mobility control fluids in enhanced oil recovery. Detailed knowledge of the molecular weight and molecular weight distribution has not been available for these polymers because their exceptionally high molecular weight exceeds the capabilities of traditional techniques, such as size exclusion chromatography (SEC). The combination of hydrodynamic chromatography (HDC) and low-angle laser light scattering (LALLS) detection can be used to measure the molecular weight distribution of this group of polymers. Chromatographic conditions can be chosen so that the elution of the polymer is primarily a function of molecular weight and independent of the composition of the polymer. Weight-average molecular weights determined by this technique agree well with those calculated from intrinsic viscosity measurements.

Polyacrylamide and its copolymers of acrylic acid have wide commercial application as flocculants and mobility control fluids in enhanced oil recovery. The key to understanding their behavior in solution is a detailed knowledge of their molecular weight and molecular weight distribution. In general, this information has not been available for these polymers because of their exceptionally high molecular weight.

SEC, the most common method for obtaining distribution information, has an exclusion limit below the range of commercial poly(acrylamide acrylic acid) copolymers ((8–10) × 10^6). Seright et al. (*1*) employed ultracentrifugation with fluorescence detection to measure the molecular weight distribution of commercially available polyacrylamides. They observed that these polymers contain fractions having molecular weights in excess of 50 × 10^6. Light scattering techniques have been used to obtain weight-average molecular weights of these polymers. However, no distribution information is available, and the presence of "gels" requires extensive sample filtration with the potential of molecular weight degradation. Intrinsic viscosity is the most commonly used method to measure the molecular weight, but again with no distribution information available. Routine measurement of molecular weight distribution could be used to optimize polymerization kinetics of products with improved end-use performance, as well as contribute to a fundamental understanding of the behavior of these polymers in solution. Hydrodynamic chromatography (HDC) is a technique originally developed for sizing latex particles. The separation in HDC arises from the spacial variation of fluid velocity in a packed column. Large particles (or polymers) are sterically excluded from slow moving fluid near the packing material and are thus convected through the column faster than small particles (or molecules). In an HDC experiment, one measures the location of the particle peak and compares it to the location of low molecular weight marker species. A retention factor, R_f, is defined as the marker elution volume divided by the particle elution volume. The R_f is always greater than unity.

Recently, Prud'homme and co-workers have shown that hydrodynamic chromatography (HDC) offers considerable promise for the analysis of a variety of high molecular weight water-soluble macromolecules (*2*), including three important polymer conformations: rigid rod (xanthan polysaccharides), flexibile linear-chain coil (partially hydrolyzed polyacrylamides), and flexible branched-chain coil (dextrans). This technique has been extended to biological polymers, e.g., tobacco mosaic virus, linear DNA, and superhelical DNA (*3*). These previous characterizations of water-soluble polymers by HDC have related the elution position of the polymer to an effective diameter determined using a calibration obtained with latex spheres. In the work described in this paper, the molecular weight of the polymer that elutes from the HDC column will be measured using a low-angle laser light scattering (LALLS) detector.

EXPERIMENTAL SECTION

A schematic of the chromatographic system used in this work is illustrated in Figure 1. Note the presence of a sub-micrometer filter present between the column outlet and detector system inlet. This filter was necessary to reduce the amount of particulate material in the eluent, since particulates cause a large light scattering signal as they pass through the LALLS detector. The polymer concentration was detected with a Kratos 773 variable wavelength UV detector at 200 nm.

The eluent used in these experiments was 0.1 M NaH_2PO_4, 0.1% Brij 35 (nonionic surfactant), and 0.1% HCHO (preservative) at pH 4 except where noted. The columns used in this work were 10 mm i.d. × 25 cm length packed with nominal 15-μm styrene/divinylbenzene beads. Eluent was delivered to the system by use of a Waters M-45 pump with a microflow controller. Injection and switching valves were manufactured by Valco Instruments Co, Inc. (Houston, TX). A delayed marker injection technique was used to deliver the polymer and marker solutions to the column and has been previously discussed (*4*). The polymer concentration injected onto the column ranged from 75 to 100 ppm. The injection volume was 100 μL. A Nelson Analytical Model 761 A/D converter, using an HP-IB interface to an HP-85 computer was used to collect data from the detectors as well as control the valve operation. Concentration and scattering intensity measurements were taken every 10 s, resulting in a total of 800 pairs of data points for each experiment.

The PUSHER 500, 700, and 1000 samples analyzed in this study are commercially available partially hydrolyzed polyacrylamides with nominal weight average molecular weights of 5 × 10^6, 7 × 10^6, and 9 × 10^6, respectively. Also analyzed were polymers A and B, which were prepared in the laboratory. These nonionic polymers have nominal weight average molecular weights of 9 × 10^6 and 7 × 10^6, respectively, and were hydrolyzed by using known amounts of NaOH. Polymer SF-210 was also analyzed, which is ~10% hydrolyzed and has a nominal weight average molecular weight of (12–15) × 10^6.

[1] The Dow Chemical Co.
[2] Princeton University.
[3] University of Massachusetts at Amherst.

0003-2700/86/0358-2242$01.50/0 © 1986 American Chemical Society

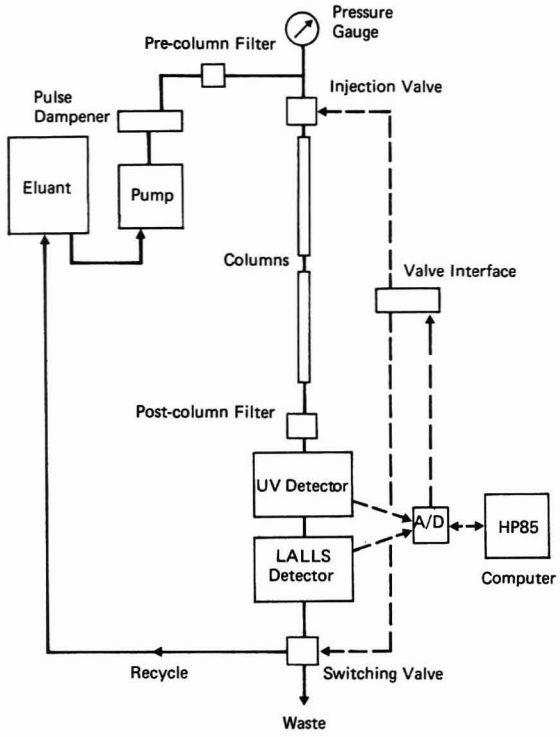

Figure 1. Schematic of the hydrodynamic chromatograph with low angle laser light scattering (LALLS) detection

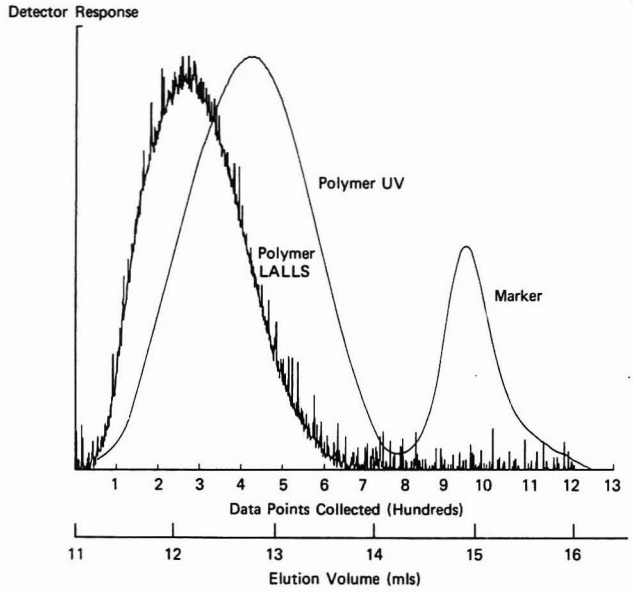

Figure 2. Typical composite chromatogram illustrating UV and LALLS responses for a nonionic polyacrylamide on the HDC.

The intensity of scattered light was measured in a Chromatix KMX-6 laser photometer. From the measured intensity of scattered light and the concentration (as measured by the UV detector), the molecular weight of a particular fraction was calculated. The UV response–concentration relationship was linear up to at least 50 ppm solution concentration and was observed to be independent of the degree of hydrolysis and molecular weight of the polymer at 200–210 nm. For these calculations, it is necessary to know the refractive index increment (dn/dc), and second virial coefficient of the polymer solution, and the eluent refractive index. The dn/dc value of 0.163 was determined with a KMX-16 laser photometer and was not found to be a function of the composition of the copolymer up to 30% acrylic acid.

For an accurate dn/dc measurement, it is necessary that the polymer solution be in dialytic equilibrium with the eluent used in the reference cell. In addition, the polymer concentration must be known in order to determine dn/dc. For dialysis, a known volume of a polymer solution was placed in dialysis tubing

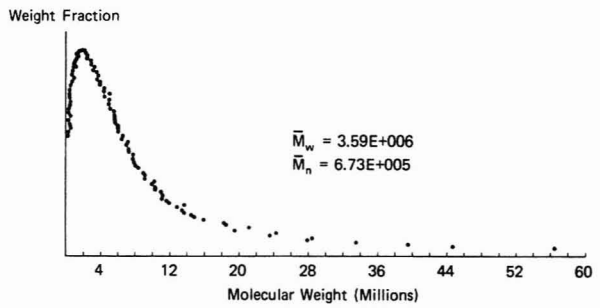

Figure 3. Typical molecular weight distribution of a partially hydrolyzed polyacrylamide (PUSHER 700) calculated from the HDC/LALLS experiment.

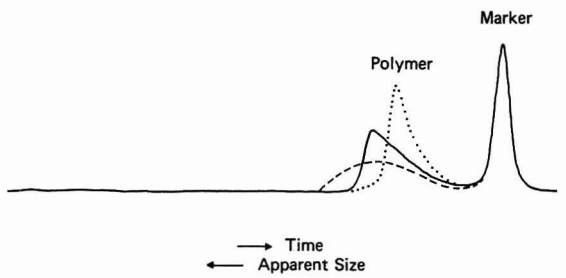

Figure 4. Composite chromatograms of a typical ultrahigh molecular weight partially hydrolyzed polyacrylamide (polymer A) at three different flow rates: 500 μL/min (•••), 100 μL/min (——), and 25 μL/min (– – –); 0.1 M NaH_2PO_4 pH 4 eluant containing 0.1% Brij 35.

(Spectrum 12000–14000 molecular weight cutoff) and then placed overnight in a stirred beaker of pure eluent. This "batch" dialysis permits complete recovery of the polymer solution from the bag.

In Figure 2, a typical composite chromatogram is shown. The smooth curve is the UV detector response, displaying two peaks, the smaller of which is a low molecular weight marker ($Cr_2O_7^{2-}$). The jagged curve is the laser photometer output, which has been offset by the time delay between the two detectors. Note that the light scattering peak precedes the concentration peak. This is due to the fact that the intensity of scattered light is a function of the product of molecular weight and concentration. In HDC, as in SEC, higher molecular weight material always elutes faster than lower molecular weight material. From this collection of data, the molecular weight distribution can be calculated (*5*) and plotted, as shown in Figure 3.

RESULTS

Influence of Flow Rate on Elution Position. The flow rate dependence on the elution position of a given polymer is illustrated in Figure 4. The peak maximum shifts to larger apparent diameter as a flow rate is decreased from ~0.5 mL/min to 0.1 mL/min, while the peak shape remains basically unchanged. Further reduction in flow rate from 0.1 mL/min to 0.025 mL/min does not substantially alter the peak maximum but significantly alters the peak shape of the eluting polymer.

While there appears to be a distinctive flow-rate dependence for the ultrahigh molecular weight polymers, this same dependence does not appear for lower molecular weight polyacrylamides. Figure 5 illustrates the chromatograms of a 2×10^6 molecular weight standard at 0.5 and 0.1 mL/min. The elution positions and peak shape are almost identical.

The change in the elution position of these ultrahigh molecular weight water-soluble polymers as a function of flow rate can be explained by deformation of the polymer during the chromatographic analysis (*6*). If a polymer molecule is deformed (stretched out in the direction of flow) during passage through a porous bed, we would expect the apparent size of the molecule to be smaller than an undeformed molecule, since in HDC it is the dimension transverse to the direction of flow that is measured. The deformed molecules, as compared to undeformed molecules, have a slower average

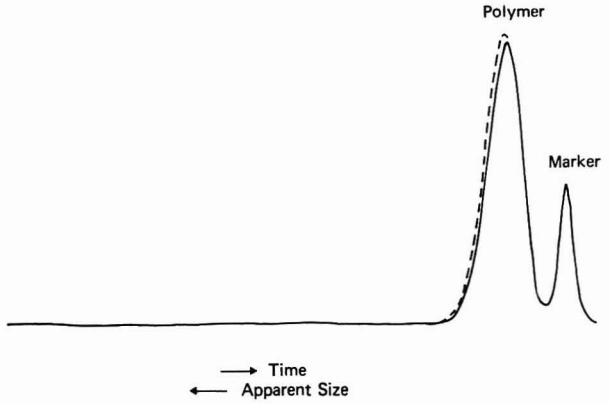

Figure 5. Composite chromatograms of a 2×10^6 nonionic polyacrylamide standard at two different flow rates: 500 μL/min (——) and 100 μL/min (– –); 0.1 M NaH_2PO_4 pH 4 eluant containing 0.1% Brij 35.

velocity due to their ability to sample a wide range of transverse locations (and flow velocities) within the bed. As a result, high molecular weight deformed molecules may elute at the same velocity as lower molecular weight undeformed molecules, and the chromatogram will not accurately reflect the "actual" molecular weight distribution of the polymer.

Durst and co-workers (*7*, *8*) in their investigations of the flow behavior of ultrahigh molecular weight partially hydrolyzed polyacrylamides found that highly dilute (50–200 ppm) solutions of these polymers possess only slightly higher shear viscosity than pure solvents; but in porous media flow, they can exhibit extensional viscosities that are dramatically higher than those of pure solvents. Specifically, at low Reynolds number (Re) (<0.1) the pressure drop across a porous media test section for a polymer solution is essentially identical with that of the solvent. Above a critical Re however, the pressure drop increases relative to that observed with pure solvent. The onset of this behavior is a function of molecular weight, diameter of packing in porous media, polymer chain flexibility, polyelectrolyte effects, and temperature. This phenomenon is attributed to the transition of the polymer molecules from a random coil conformation to an elongated coil conformation due to the elongational stress applied to the molecule during passage through the porous bed.

Using kinetic theory arguments, Durst has related this transition to the dimensionless Deborah number (De), which is the longitudinal velocity gradient multiplied by the relaxation time of the molecule. If De >0.5, the polymer will be deformed in the flow from its equilibrium (relaxed) random coil shape. If De <0.5, the molecule is not deformed.

The changes in chromatographic peak shape and position of polyacrylamide that accompany changes in flow rate may be explained by the observations of Durst. For the polymers analyzed in this study (molecular weight $(7–9) \times 10^6$), the Deborah number for flow through an HDC column packed with 15 μm cation-exchange resin, using a water-based eluent at 0.5 mL/min, is approximately 6.5. Reduction in flow rate to 0.1 mL/min decreases the De to 1.34 and further reduction to 0.025 mL/min decreases the De proportionately to 0.34. From this approximate calculation, one can predict that characterization of these polymers by HDC at flow rates on the order of 0.025 mL/min more nearly reflects the true molecular weight distribution than that determined at higher flow rates, at which molecules are deformed. It is important to note that the analysis of higher molecular weight polymers (with correspondingly longer relaxation times) require even lower flow rates to ensure no deformation.

Polymer Degradation. At high Deborah number, the elongational stresses in the chromatography column can cause not only polymer deformation but also polymer degradation.

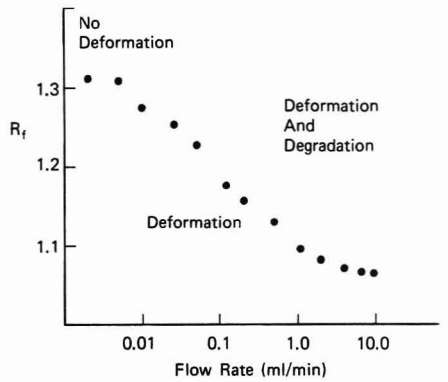

Figure 6. Flow rate dependence of an ultrahigh molecular weight polyacrylamide (SF-210). The R_f or effective size of the polymer molecules decrease as flow rate through the column increases. At low flow rates (<0.01 mL/min) the equilibrium size is measured. At intermediate flow rates (~0.1 mL/min) the polymer is deformed during chromatographic analysis but not degraded. At high flow rates (>5 mL/min) the polymer is degraded during the passage through the column.

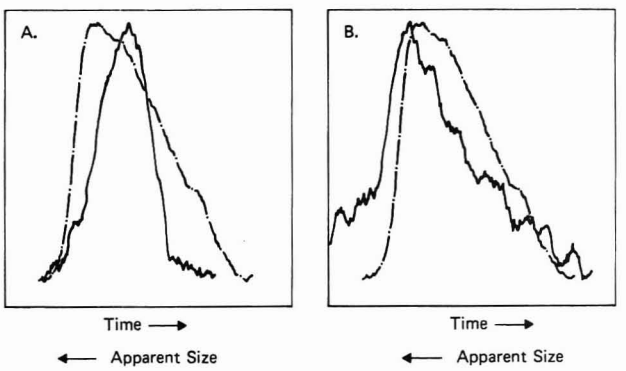

Figure 7. Detection of degradation. An ultrahigh molecular weight polyacrylamide (SF-210) was passed through the HDC column and then reinjected onto the column. Part A compares the R_f of the native plymer (–·–, $R_f = 1.274$) and the R_f of the reinjected polymer (——, $R_f = 1.189$) after passage through the column at 8.5 mL/min. Part B compares the R_f of the native polymer and the R_f of the reinjected polymer (——, $R_f = 1.296$) after passage through the column at 0.1 mL/min. Native polymer R_f was determined at 0.01 mL/min. Eluant was 0.1 M NaH_2PO_4 pH 4 containing 0.1% Brij 35.

The results of a series of flow rate experiments are shown in Figure 6. In these experiments, the polymer was of extremely high molecular weight $((12–15) \times 10^6)$, and the eluent was of low ionic strength (0.002 M NaN_3). As explained in the last section, high flow rates cause deformation and orientation that reduce the polymer's R_f—the apparent molecular size decreases. This decrease could also be attributed to polymer degradation. In order to test when degradation was significant, polymer solutions were eluted at each of the flow rates in Figure 6 and the polymer was collected from the exit of the column. These solutions were then reinjected and analyzed at a low flow rate (0.01 mL/min) where no significant deformation or degradation occurs (*6*). The low flow rate R_f of each of the reinjected samples was then compared to the low flow rate R_f of a "native" sample (one that had not been preflowed through the column).

If the R_f of a reinjected sample is the same as that of the "native" polymer, then degradation could be considered insignificant. Such was the case for the polymer samples that were preflowed at flow rates below 0.1 mL/min. Figure 7B shows the polymer peaks and R_f's for such an experiment. Samples that were preflowed above 0.1 mL/min exhibited low flow rate R_f's lower then that of the "native" polymer (Figure 7A). Degradation for these samples was considered to be significant. In Figure 6, the approximate flow rates that can

Table I. Viscosity of Polymer B Partially Hydrolyzed Polyacrylamide

	viscosity, cP	
% hydrolysis	0.1 M NaH_2PO_4 pH 4	0.04 M Na_2HPO_4 pH 8.4
10	28.4	48
20	29.9	185
30	30.0	199

cause deformation and degradation for this polymer have been indicated.

The particular flow rate at which degradation will begin to occur in dilute solutions is dependent on the molecular weight of the polymer at a given ionic strength. Low molecular weight polymers with correspondingly fast relaxation times, for instance, will require higher flow rates for degradation. Degradation will also be dependent on the backbone structure of the polymer. For a single polymer composition, however, the dimensionless strain rate or Deborah number is the important parameter for degradation as it is for deformation (*9*). More complete data on flow rate effects and degradation of water-soluble polymers in porous media flow will be published separately.

Influence of Eluent pH on Elution Position. Researchers have previously observed that the viscosity of a solution of pure polyacrylamide is independent of pH, while that of a given solution of partially hydrolyzed polyacrylamide increases in a sigmoidal fashion as the pH is increased from pH 3 to pH 10. This change in viscosity is caused by the transition of the hydrolyzed side groups from uncharged carboxylic acid at pH 3 to charged carboxylate ion at pH 7. The force of repulsion between adjacent ionic charges uncoils and expands the polymer, which results in an increase in viscosity of the polymer solution. One might expect the viscosity of a given partially hydrolyzed polyacrylamide to increase with increasing hydrolysis when measured at pH >4 but to be constant when measured at pH ~4. Viscosities of a partially hydrolyzed polyacrylamide dissolved in 0.04 M pH 8.4 Na_2HPO_4 and 0.1 M pH 4 NaH_2PO_4 are indicated in Table I. Each of these polymer solutions were prepared from the same polymer, so that the molecular weight of the three are the same. Also, both of the solvents have approximately the same ionic strength.

As expected, the viscosities of the pH 4 solutions are essentially independent of the extent of hydrolysis and the viscosities of the pH 8.4 solutions increase dramatically with the extent of hydrolysis.

Based on these observations, the apparent size of a given partially hydrolyzed polyacrylamide at pH >4 as measured by HDC should be dependent upon both the composition and molecular weight of the polymer, while at pH ~4, the apparent size should be dependent upon molecular weight and essentially independent of the degree of hydrolysis.

HDC analysis at pH 4 of a given polyacrylamide, which has been hydrolyzed to several different levels, indicates the molecules are approximately the same size based on their elution positions (Figure 8). Calculations of molecular weight based on size will not be significantly influenced by the extent of hydrolysis of the polymer. More quantitatively the LALLS data were used to measure the weight average molecular weights of this series of polymers. As Table II indicates the molecular weights of the these polymers are essentially identical as expected. At constant ionic strength, analysis of this polymer series by HDC at pH 8.4 indicates that the size of the polymer increases with increasing hydrolysis (Figure 9). Therefore the elution position reflects both the molecular weight of the polymer and its degree of hydrolysis.

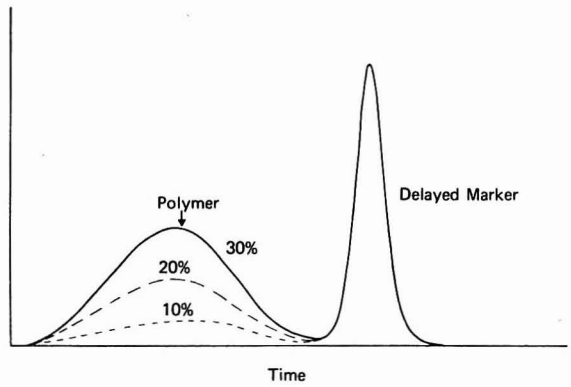

Figure 8. Composite chromatograms of an ultrahigh molecular weight plyacrylamide (polymer B) 10%, 20%, and 30% hydrolyzed: eluant composition, 0.1 M NaH_2PO_4 pH 4; flow rate, 25 μL/min.

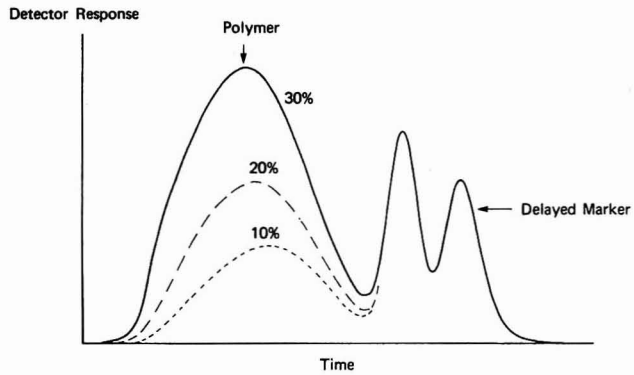

Figure 9. Composite chromatograms of an ultrahigh molecular weight polyacrylamide (polymer B) 10%, 20%, and 30% hydrolyzed: eluant composition, 0.04 M Na_2HPO_4 pH 8.4; flow rate, 25 μL/min.

Table II. Calculated M_w of Polymer B by HDC/LALLS

% hydrolysis	$\bar{M}_w$
0	6.7×10^6
10	7.14×10^6
20	6.68×10^6
30	6.45×10^6
av	6.7×10^6

From Figures 8 and 9 it can also be seen that the relative apparent size of a polymer molecule of a given extent of hydrolysis is larger in 8.4 pH eluent than in pH 4 eluent. This provides the basis for a multidimensional chromatography experiment wherein the polymer molecules can be sorted by molecular weight or size, independent of the extent of hydrolysis, as well as by the extent of hydrolysis.

Influence of Sample Filter Pore Size. When a LALLS detector is used to determine the weight-average molecular weight of a polymer in solution, either in a static mode or when coupled to a chromatograph, particles should not be present in the cell due to their large light scattering signal relative to that of polymer. Therefore, it is customary to filter the sample being delivered to the light scattering cell with a 0.1 or 0.2 μm pore size membrane. Normally, the membrane pore size is not of critical importance because the molecules being analyzed are much smaller than the particles that must be removed. In the present application however, care must be taken in choosing the most appropriate filter pore size in view of the size of these molecules in solution. Analysis of these water-soluble polymers without a filter present between the column outlet and detector inlet would be preferred. However, the frequency and intensity of spikes due to the passage of particles through the light scattering cell significantly increase in the absence of a filter.

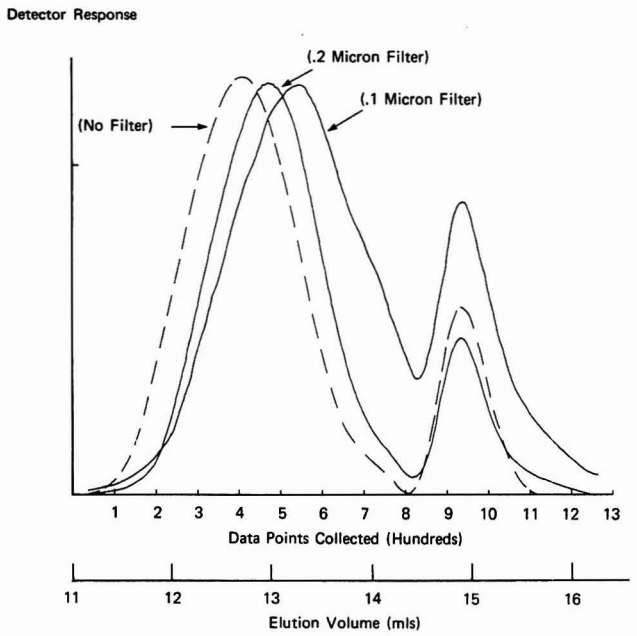

Figure 10. Influence of membrane pore size on the elution position of an ultrahigh molecular weight polyacrylamide (polymer B) 10% hydrolyzed: eluant composition, 0.1 M NaH_2PO_4 pH 4 containing 0.1% Brij 35; flow rate, 25 μL/min.

Table III. Calculated M_w of PUSHER Polymers Using HDC/LALLS

	$\bar{M}_w$
PUSHER 500	5.6×10^6
PUSHER 700	7.5×10^6
PUSHER 1000	9.0×10^6

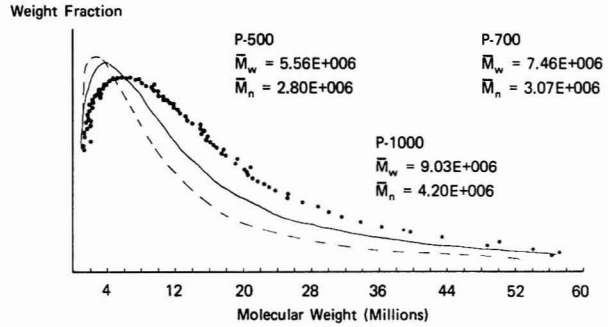

Figure 11. Molecular weight distribution of PUSHER 500, 700, and 1000 determined by using HDC/LALLS: P-500 (– –), P-700 (——), and P-1000 (* * *).

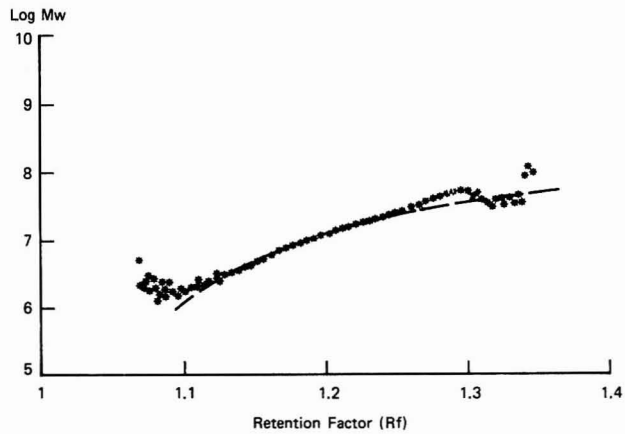

Figure 12. Calibration comparison. Plotted points were determined from HDC/LALLS experiment. Dashed line is the relationship based on polyacrylamide standards extrapolated to 60×10^6.

To illustrate the influence of membrane pore size on the elution of a typical partially hydrolyzed polyacrylamide from an HDC column, a sample was chromatographed first with a 0.1-μm porosity membrane placed between the column outlet and detector inlet. The analysis was repeated with a 0.22-μm membrane. Figure 10 illustrates the UV detector output for these two analyses. Note that the marker retention times for both runs are approximately the same while the elution position of the sample analyzed with the 0.1-μm membrane in place indicates smaller relative size in general compared to the same sample analyzed with a 0.22-μm membrane. The area of the LALLS peak obtained with and without a 0.22-μm membrane between the column and detectors is quite similar, which suggests that a fraction of the polymer is not being retained on the membrane and that the polymer is not being significantly degraded upon passage through the membrane. Rather, it appears that the polymer is simply being retarded by the membrane, and as such, does not significantly influence the analysis. With the extended use of the 0.22-μm membrane (~25 injections), the elution position of the polymer sample moves toward smaller relative size. Therefore, the molecular weight distributions reported here were obtained with a 0.22-μm membrane.

Molecular Weight Distributions and Calibration. The absolute molecular weight distributions of PUSHER 500, 700, and 1000 samples were determined by use of the HDC/LALLS system, and are illustrated in Figure 11. The calculated weight-average molecular weights are indicated in Table III. The major differences in the molecular weight distributions are in the higher molecular weight regions, >10 $\times 10^6$. In all three samples, the distribution extends to ~60 $\times 10^6$.

In an effort to verify that the data collection and software calculations were performing as anticipated, one of the largest molecular weight polyacrylamide standards that are commercially available was analyzed by HDC/LALLS. The value reported by Polysciences for this standard is 1×10^6. The value determined by static light scattering was 1.1×10^6 and by HDC/LALLS was 1.3×10^6.

The intrinsic viscosity of one sample of polyacrylamide was determined to be 1300 cm^3/g, which can be used to calculate a weight-average molecular weight for the polymer using the appropriate Mark–Houwink coefficients (*10*). The weight-average molecular weight based on the intrinsic viscosity is 6.65×10^6, which is in excellent agreement with the value of 6.7×10^6 based on the HDC/LALLS experiments (Table II).

Since the HDC/LALLS system can be used to measure the absolute molecular weight and distribution of a given polymer sample, a calibration relationship between molecular weight and elution position of the eluting fractions can be determined. Figure 12 illustrates such a calibration relationship for the columns used in this work. The calibration relationship determined in this work is quite specific to those water-soluble polymers composed of polyacrylamide and copolymers of acrylamide and acrylic acid. It is not necessarily appropriate for other comonomer systems. Each system must be evaluated separately.

Due to the expense of a LALLS detector, it would be preferred if the calibration relationship could be defined by using narrow fraction polyacrylamide standards. Commercially available standards are available to only 2×10^6. To accommodate the observed elution positions of several commercially available polymers, the elution position/molecular weight relationship must be extrapolated to $\sim 60 \times 10^6$. This extrapolated relationship is illustrated as a dotted line in Figure 12. The agreement between these relationships is surprisingly good in view of the extrapolation from 2×10^6 to 60×10^6 molecular weight. In view of this correlation,

molecular weight distributions can be calculated on the basis of the the combination LALLS and UV data and also on the basis of the UV chromatogram only.

Registry No. PUSHER 500, 54182-67-1; PUSHER 700, 39341-25-8; PUSHER 1000, 54174-00-4.

LITERATURE CITED

(1) Seright, R. S.; Maerker, J. M.; Holzworth, G. *Polym. Repr. Am. Chem. Soc., Div. Polym. Chem.* **1981**, *22* (2), 30. Paper presented at the National ACS Meeting, Division of Polymer Chemistry, New York, August 1981.
(2) Hoagland, D. A.; Larson, K. A.; Prud'homme, R. K.; In *Modern Methods of Particle Size Analysis*; Barth, H. G., Ed.; Wiley: New York, 1984; p 277.
(3) Larson, K. A.; Prud'homme, R. K. *J. Colloid Interface Sci.*, in press.
(4) McGowan, G. R.; Langhorst, M. A. *J. Colloid Interface Sci.* **1982**, *89*, 94.
(5) "Determination of Molecular Weight Distributions by Combining Low Angle Light Scattering with Gel Permeation Chromatography"; Applications Note LS-2, Chromatix, 1977.
(6) Hoagland, D. A. Ph.D. Thesis, Princeton University, 1985.
(7) Haas, R.; Durst, F. *Rheol. Acta 1982*, *21*, 566.
(8) Durst, F.; Haas, R.; Kaczmar, B. U. *J. Appl. Polym. Sci.* **1981**, *26*, 3125.
(9) Farinato, R. S.; Yen, W. S. *J. Appl. Polym. Sci.*, in press.
(10) Klein, J.; Conrad, K. D. *Makromol. Chem.* **1978**, *179*, 1635.

RECEIVED for review January 27, 1986. Accepted May 12, 1986. A patent has been issued to The Dow Chemical Company covering this method of analysis.

Supercritical Fluid Fractionation of Petroleum- and Coal-Derived Mixtures

Robert M. Campbell and Milton L. Lee*

Department of Chemistry, Brigham Young University, Provo, Utah 84602

A supercritical fluid chromatographic system was constructed to provide separations and fraction collection on a semipreparative scale. Columns packed with silica materials of intermediate particle sizes (30–70 μm) were used to allow dynamic pressure programming with minimum pressure drop of the CO_2 mobile phase along the length of the column. A variety of complex coal- and petroleum-derived polycyclic aromatic compound mixtures were fractionated according to the number of aromatic rings using columns packed with an NH_2-modified stationary phase bonded on silica particles. The CO_2 mobile phase was programmed with an alternating series of linear pressure ramps and isobaric intervals to effect even peak spacing and near base line resolution of compounds of differing ring number in a coal tar. A solvent refined coal heavy distillate and a crude oil were similarly fractionated. Effluents were monitored with an ultraviolet spectrophotometer at 254 nm and a flame ionization detector while fractions were collected in pressurized vessels for subsequent analysis by capillary gas chromatography. Sample capacities of up to 20 mg were possible with this system.

Supercritical fluids have been used with considerable success both as mobile phases in chromatography and as solvents in extraction processes. While reduced analysis time is the major advantage of supercritical fluid chromatography (SFC) with packed columns (*1*), ease of solvent removal has been one of the major benefits of extractions with supercritical CO_2 (*2*). The supercritical fluid extraction of caffeine from coffee and of nicotine from tobacco are only two of the many uses of supercritical fluids for separations which have been reported. An extensive review of this topic is available (*2*).

In 1977, Wise et al. (*3*) reported the liquid chromatographic (LC) separation of polycyclic aromatic hydrocarbons (PAH) according to the number of aromatic carbon atoms using a chemically bonded aminosilane stationary phase. Each of the ring-number cuts could then be further resolved using reversed phase LC or capillary column gas chromatography (GC). While the LC ring number separation has proven to be extremely useful, the method suffers from several drawbacks. Fractions collected from the NH_2 column are concentrated by carefully directing a stream of nitrogen gas onto the sample until it is near dryness. Then the sample is dissolved in a solvent that is appropriate for reversed phase LC analysis. In addition to being slow and tedious, this process can result in sample losses and contamination. Quantitation can also be difficult with this procedure if the solutes of interest are volatile, photolytically unstable, or subject to air oxidation. Finally, the complex environmental samples that are frequently analyzed by this technique invariably, regardless of how carefully pretreated, contain material that is irreversibly adsorbed on the NH_2 column. These columns are usually of the small-particle preparative scale variety and can be very expensive. After a number of fractionations, the columns tend to degrade due to these adsorbed materials, despite backflushing with strong solvents.

An on-line multidimensional supercritical fluid chromatographic system was recently reported (*4*) which utilized both an aminosilane column in the normal phase and an octadecylsilane column in the reversed phase mode. This system used supercritical CO_2 as the mobile phase for both columns and, by appropriate valving, eliminated the need for solvent removal after the NH_2 column. However, the system was designed for analytical purposes and did not provide for sample collection.

It was the objective of this study to utilize the selectivity that can be obtained by programming the density of a supercritical fluid in conjunction with columns packed with larger, less expensive particles to achieve separations similar to those that can be obtained with microparticulate HPLC columns. In several previous studies, packed columns were used with supercritical fluid mobile phases to improve the separation of closely related compounds over that which could be obtained by supercritical fluid extraction. For example, supercritical fluid fractionation (SFF) methods were used to isolate several PAH in an automobile exhaust extract (*5*). In another case, pressure programming of the mobile phase was used with packed columns to facilitate the separation of a series of polystyrene oligomers (*6*). In a study with capillary columns in SFC, where pressure drops across the column are minimal, nonlinear density programming yielded regular spacing of components of a polystyrene oligomer mixture (*7*).

0003-2700/86/0358-2247$01.50/0 © 1986 American Chemical Society

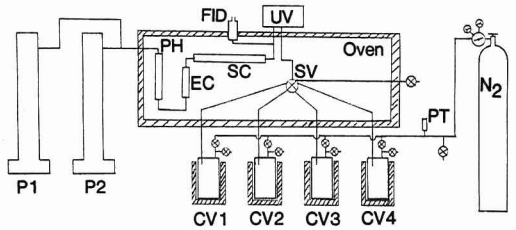

Figure 1. Schematic diagram of the supercritical fluid extraction/fractionation system: P1 and P2, syringe pumps 1 and 2; PH, solvent preheater/equilibrator; EC, extraction column; SC, separation column; SV, six-port switching valve; FID, flame ionization detector; PT, pressure transducer; N_2, high-pressure cylinder of nitrogen gas; CV1–4, pressurized fraction collection vessels equipped with cooling jackets.

These studies have shown that the ability to instantaneously vary the solvating power of a supercritical fluid by changing its pressure (or density) can be used to great advantage. With the selectivity of the mobile phase, compounds were resolved in SFC which would have required many more theoretical plates to resolve in gas chromatographic systems (*8*). This mobile phase selectivity can only be preserved by avoiding large pressure drops across the column, which can occur in columns packed with very small particles or in systems operated at very high flow rates (*9*). In the present study, columns packed with silica materials of intermediate particle sizes (30–70 μm) were used to prevent large pressure drops and to allow dynamic pressure programming for semipreparative-scale separations.

EXPERIMENTAL SECTION

Sample Origin. The coal tar used in this study was a medium-crude coke oven tar and was obtained from the National Bureau of Standards, Washington, DC. This tar is a proposed standard reference material. The coal tar extract was obtained by eluting the crude coal tar with *n*-pentane after it had been adsorbed on silica gel. A solvent refined coal heavy distillate (SRC II HD), boiling point range 260–450 °C, was collected during the processing of a West Virginia coal from the Pittsburgh Seam, and obtained from the Fort Lewis, WA, pilot plant, which was operated by the Pittsburgh & Midway Coal Mining Co. This material is of pilot plant origin and should not necessarily be considered as representative of products that may eventually be produced on a commercial scale. The PAH fraction (*10*) of the SRC II HD and a Wyoming Recluse Crude oil were also subjected to the SFF procedure.

Instrumentation. A supercritical fluid extraction/fractionation system was constructed as diagrammed in Figure 1. The system included a 375-mL syringe pump (Isco, Lincoln, NE) and a 250-mL syringe pump (Varian 8500, Walnut Creek, CA), each modified for pressure control at flow rates of up to 8 mL min^{-1} (liquid), a chromatographic oven (Varian Series 2100, Walnut Creek, CA), and four 125-mL stainless steel fraction collection vessels that were fitted with cooling jackets. During fraction collection, the vessels were cooled to 3 ± 2 °C via a circulating cooling bath (Grant Science/Electronics, Dayton, OH). A six-port switching valve (Valco Instrument Co., Houston, TX) was used to effect collection of successive fractions in different collection vessels. The collection vessels were pressurized with nitrogen gas from a high-pressure tank with appropriate valving. A micrometering valve (Autoclave Engineering, Erie, PA) was used to control the flow when the effluent was vented directly to atmospheric pressure.

The fractions containing the more volatile compounds were collected either by bubbling the effluent through methylene chloride or by venting the effluent through a 60-cm length of $^1/_{16}$ in. i.d. Teflon tubing which was immersed in a dry ice/isopropyl alcohol bath (−78 °C). To recover the collected materials, the Teflon tubing was removed from the bath and rinsed with a small amount of an appropriate solvent. An extraction column (10 cm × 4.6 mm i.d.) and a separation column (25 cm × 4.6 mm i.d.) were placed in the oven, and effluents were monitored with a UV-absorbance detector (Hitachi Model 100-10, Toykyo, Japan) equipped with a high-pressure flow cell (Hewlett-Packard, Avondale, PA). A small fraction of the column effluent was split into a flame ionization detector (FID) through a 15 cm length of tapered 25 μm i.d. fused silica tubing. The FID block was shortened by half and heated to 400 °C with heat tape. All parts of the extraction/fractionation apparatus were constructed of stainless steel. Fractions were analyzed by capillary column gas chromatography using an HP 5880 gas chromatograph equipped with a 20 m × 0.2 mm i.d. fused silica capillary column coated with SE-54 (0.25 μm film thickness).

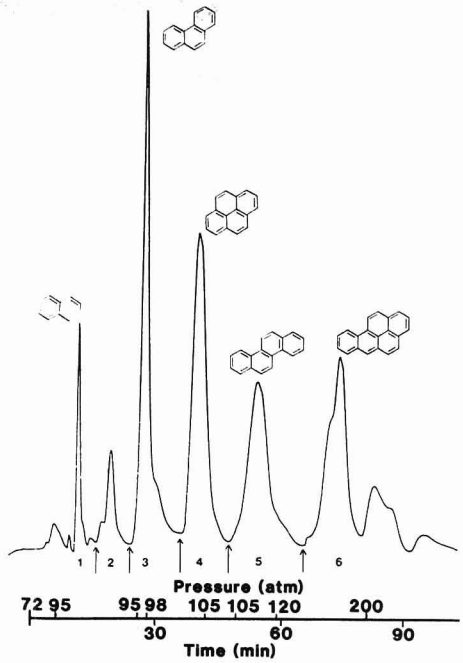

Figure 2. Supercritical fluid fractionation of a coal tar with UV detection at 254 nm. Numbers refer to fractions that were collected.

Procedure. A coal tar was fractionated by adding 1 mg of tar in 50 μL of methylene chloride to the top of the extraction column, which had been dry-packed with 40–63 μm silica (Sigma No. S-0507, St. Louis, MO). The column end fittings (equipped with 2-μm frits) were tightened and the column was installed in the oven by tightening the appropriate fittings. The separation column was dry-packed with NH_2-Adsorbosil (30–70 μm, Applied Science, State College, PA). The oven temperature was raised to 40 °C and held there for the duration of the fractionation. The pressure of the CO_2 mobile phase (SFC Grade, Scott Specialty Gases, Plumsteadville, PA) was brought to 72 atm and then raised to 95 atm at 8 atm min^{-1}. The pressure was held at 95 atm until phenanthrene began to elute (fraction 3), whereupon it was raised at 1.5 atm min^{-1} to 98 atm. As soon as the fluoranthene/pyrene peak (fraction 4) started eluting, the pressure was again programmed at 1.5 atm min^{-1} to 130 atm. At this point, as the chrysene peak (fraction 5) was finishing, the pressure was programmed at 5 atm min^{-1} to 198 atm and held for about 10 min. Fractions were collected as marked on the chromatogram in Figure 2. The other materials were similarly fractionated. After the CO_2 was removed from the collection vessels by venting to atmospheric pressure, the solutes were removed from the vessels by rinsing with a small amount of solvent.

RESULTS AND DISCUSSION

Detailed analyses of complex mixtures of polycyclic aromatic compounds (PAC) are important for several reasons. Many PAC have been shown to be mutagenic or carcinogenic and while some members of a closely related group of isomers may be biologically active, other members of the series may be inactive. Resolution of these isomers is therefore necessary, especially since selective detection methods for closely related isomers are extremely rare. Detailed structural information is also important for evaluation of products and process conditions of liquefaction, thermal cracking, and other processes. Many mixtures of PAC exhibit a wide molecular weight range and almost all are extremely complex. Some type

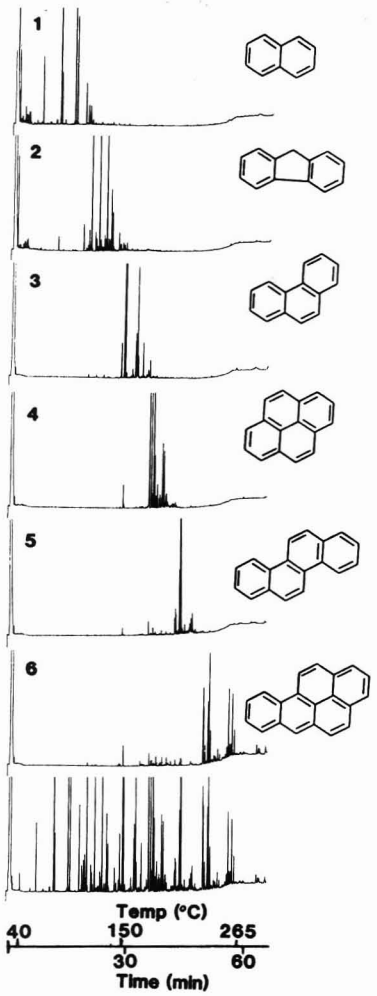

Figure 3. Capillary gas chromatograms of the fractions obtained during the supercritical fluid fractionation of a coal tar. Numbers refer to fractions shown in Figure 2.

of fractionation is important for simplification of the mixture prior to analysis by high-resolution separation techniques such as capillary GC and capillary GC/mass spectrometry (GC/MS). For example, ring-number fractions of complex mixtures of PAH have recently been obtained for analysis by GC with a liquid crystalline stationary phase which exhibits excellent selectivity for the separation of geometric isomers (*11–13*).

Figure 2 shows a UV chromatogram of the coal tar sample. Figure 3 shows capillary gas chromatograms of the fractions of the coal tar extract obtained on the SFF system. The polar amino bonded phase in conjunction with supercritical fluid pressure programming provided good selectivity for separation according to ring number. Alkylated species eluted at or near the same times as their parent compounds, while compounds of different ring numbers were widely separated.

A UV chromatogram of a supercritical fluid fractionation of the aromatic fraction of an SRC II HD is shown in Figure 4. GC chromatograms of these fractions are displayed in Figure 5. Again, while a higher degree of alkylation was present in this sample as compared to the coal tar, excellent separation according to number of aromatic rings was obtained. Fraction 1 contained the two- and three-ring compounds such as naphthalene and phenanthrene. Fraction 2 was composed of the peri-condensed four-ring compounds such as fluoranthene and pyrene. Fraction 3 included the cata-condensed four-ring compounds such as chrysene, and fraction 4 contained the five-ring peri-condensed compounds (e.g., benzopyrenes).

To demonstrate the applicability of the SFF system to samples containing materials other than PAC, a crude petroleum oil was fractionated. In this case, the separation was mainly by boiling point, since the aliphatic materials had little interaction with the polar NH_2 stationary phase. Boiling point fractionations are useful because the narrow molecular weight fractions obtained can then be easily further fractionated into chemical classes. A flame ionization detector was used in addition to the UV detector in this fractionation to monitor the effluents as shown in Figure 6. The gas chromatograms of the resolved fractions (Figure 7) demonstrate the exactness of the separation; little overlap of isolated fractions was obtained.

Standard compounds were used to study the effects of mobile phase density on resolution of closely related com-

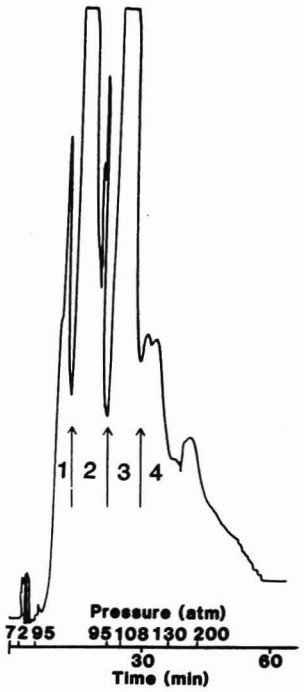

Figure 4. Supercritical fluid fractionation of the aromatic fraction of an SRC II HD. Numbers refer to fractions that were collected.

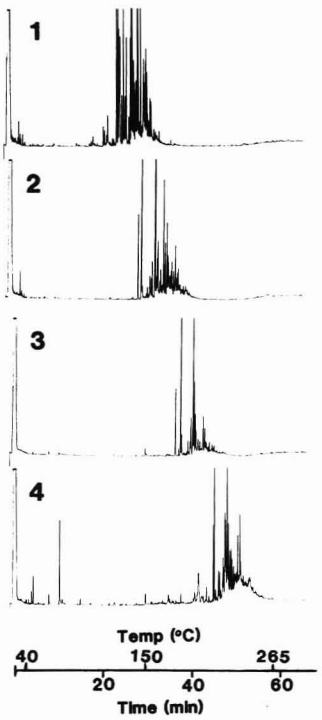

Figure 5. Capillary gas chromatograms of the fractions obtained during the supercritical fluid fractionation of an SRC II HD sample. Numbers refer to fractions shown in Figure 4.

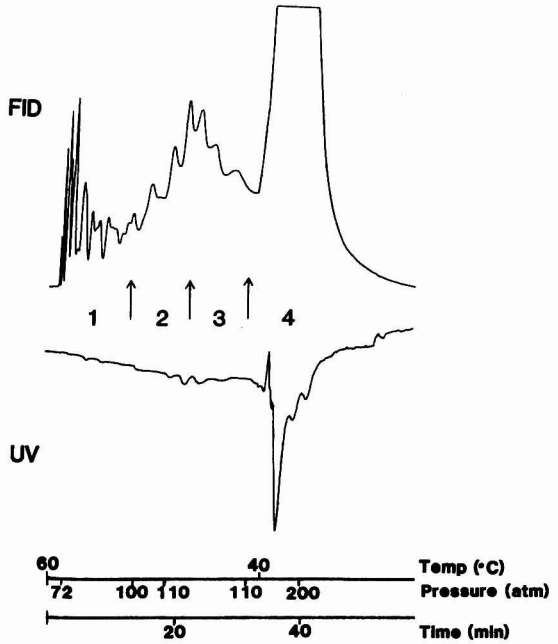

Figure 6. Supercritical fluid fractionation of a Wyoming Recluse crude oil. Numbers refer to fractions that were collected.

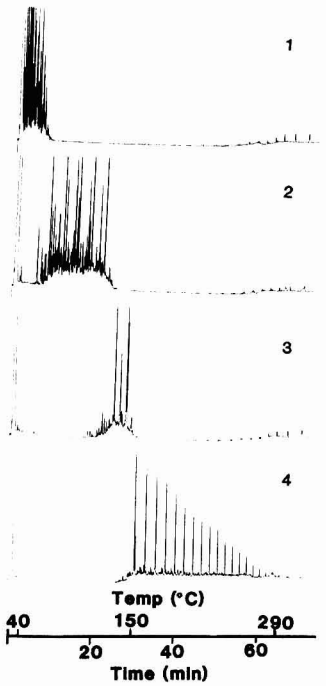

Figure 7. Capillary gas chromatograms of fractions obtained during the supercritical fluid fractionation of a Wyoming Recluse crude oil. Numbers refer to fractions shown in Figure 6.

Table I. Resolution of Acenaphthalene and Biphenyl at Various Pressures of CO_2 at 40 °C and Using a 30–70 μm NH_2-Silica Column

pressure, atm	resolution	pressure, atm	resolution
85	1.1	140	0.9
90	1.1	160	0.9
100	0.8	180	0.7
120	0.9	198	0.5

pounds. The resolution of biphenyl and acenaphthylene was measured at a number of different mobile phase densities, and these data are listed in Table I. It was found that, in general, the resolution of a pair of closely related isomers could be improved by as much as 100% by decreasing the mobile phase pressure at constant temperature on a given column. However, it should be noted that the particle size of the packing in the column has a large effect on resolution as well. Column efficiency, which is dependent on the particle size of the column packing material, may have a greater effect on resolution than the selectivity of the mobile phase in supercritical fluid systems as well as in liquid chromatography. Furthermore, analysis times can be shortened by going to smaller particle diameter column packings. Although large presssure drops across columns packed with very small particles can cause significant selectivity losses, the gain in efficiency in many cases may offset the loss in selectivity.

One additional factor that should be considered when choosing an optimum particle size for column packings in SFF is that large pressure drops across columns packed with small particles can reduce the molecular weight range of the solutes that can be eluted from the column. The maximum column pressure obtainable in a given system is equal to the maximum pressure rating of the pump minus the pressure drop across the column. Therefore, the use of columns with low pressure drops increases the maximum solvent strength of the mobile phase on the column and the maximum molecular weight of solutes that can be eluted from the column without adding a modifier. Particles in the 30–70 μm range were chosen for the separations that were studied here. The trade-off between column efficiency and pressure drop was at or near optimum with this particle size. Smaller particles resulted in large pressure drops, while larger particles resulted in poor efficiency (*1*, *6*, *9*). While LC with microparticulate columns provides higher resolution for PAC mixtures than SFF with 30–70 μm diameter particles, the advantages of lower cost and higher sample capacity make the 30–70 μm packing an attractive alternative for many separations.

Samples were best introduced into the SFF system by applying them in a small amount of solvent to the head of the extraction column with a syringe. This method resulted in narrower bands than were obtained when the sample was distributed over the entire extraction column. An external sample loop injection valve was not used in the system because at the lower pressures used at the beginning of a fractionation run, all sample components were not dissolved, resulting in plugging of the frit at the head of the separation column.

UV monitoring of the column effluents was essential to enable precise cuts during fractionation on a routine basis as well as during development. Solutes in the fractions were best collected by cooling the collection vessels to 3 ± 2 °C. This created a two-phase (gas/liquid) region in the collection vessels, causing the solutes to collect in the CO_2 liquid phase. The collection of fractions by use of pressurized vessels was not sufficient to contain very volatile solutes such as naphthalene. Therefore, fractions containing very volatile components were collected by bubbling the effluent through methylene chloride or *n*-pentane. As mentioned in the Experimental Section, very volatile hydrocarbons were also trapped by venting the effluent through a piece of Teflon tubing which was immersed in a dry ice/isopropyl alcohol bath. Typical analysis times for separations of components ranging from two to five rings were between 1 and 1.5 h.

With this pumping system, the sample capacity appears to be about 10 to 20 mg per run on a 6.2 mm i.d. column. Sample capacity was double or triple that which could be obtained on a microparticulate column of equal dimensions. This can be explained by the fact that with larger particle size packings, efficiency is lower and the peaks are broader. This means that the solutes are in contact with more stationary phase, resulting in greater sample capacity. This phenomenon is discussed by Snyder (*14*).

A number of advantages were realized with this SFF system. The use of CO_2 allowed an FID to be used to monitor the fractionations and to provide quantitative information, while

CO_2 was easy to remove from the fractions that were collected. The selectivity produced by varying the density of the supercritical fluid enabled the use of larger particle packings. The lower cost of these packings eliminated the need for extensive sample cleanup prior to analysis by SFF. In addition, this procedure may be used to fractionate thermally labile materials, since CO_2 has a very low critical temperature. Overall, it was found during this study that semipreparative SFF shows great potential for high-quality separations with easy solvent removal.

LITERATURE CITED

(1) Gere, D. R.; Board, R.; McManigill, D. *Anal. Chem.* **1982**, *54*, 736–740.
(2) Randall, L. G. *Sep. Sci. Technol.* **1982**, *17*, 1–118.
(3) Wise, S. A.; Chesler, S. N.; Hertz, H. S.; Hilpert, L. R.; May, W. E. *Anal. Chem.* **1977**, *49*, 2306–2310.
(4) Christensen, R. G. *HRC CC. J. High Resolut. Chromatogr. Chromatogr. Commun.* **1985**, *8*, 824–828.
(5) Jentoft, R. E.; Gouw, T. H. *Anal. Chem.* **1976**, *48*, 2195–2200.
(6) Graham, J. A.; Rogers, L. B. *J. Chromatogr. Sci.* **1980**, *18*, 75–84.
(7) Fjeldsted, J. C.; Jackson, W. P.; Peaden, P. A.; Lee, M. L. *J. Chromatogr. Sci.* **1983**, *21*, 222–225.
(8) Sie, S. T.; Rijnders, W. A. *Sep. Sci.* **1967**, *2*, 755–777.
(9) Peaden, P. A.; Lee, M. L. *J. Liq. Chromatogr.* **1982**, *5* (*Suppl. 2*), 179–221.
(10) Later, D. W.; Lee, M. L.; Bartle, K. D.; Kong, R. C.; Vassilaros, D. L. *Anal. Chem.* **1981**, *53*, 1612–1620.
(11) Nishioka, M.; Chang, H.-C.; Lee, M. L. submitted for publication in *Environ. Sci. Technol.*
(12) Markides, K. E.; Nishioka, M.; Tarbet, B. J.; Bradshaw, J. S.; Lee, M. L. *Anal. Chem.* **1985**, *57*, 1296–1299.
(13) Nishioka, M.; Whiting, D. G.; Campbell, R. M.; Lee, M. L. *Anal. Chem.* **1986**, *58*, 2251–2255.
(14) Snyder, L. R. *Principles of Adsorption Chromatography*; Marcel Dekker: New York, 1968.

RECEIVED for review February 3, 1986. Accepted April 17, 1986. This work was supported by the Department of Energy, Office of Health and Environmental Research, Contract No. DE-AC02-79EV10237, and the Department of Energy, Fossil Energy Program, Contract No. DE-FG22-83PC60807.

Supercritical Fluid Fractionation and Detailed Characterization of the Sulfur Heterocycles in a Catalytically Cracked Petroleum Vacuum Residue

Masaharu Nishioka, David G. Whiting, Robert M. Campbell, and Milton L. Lee*

Department of Chemistry, Brigham Young University, Provo, Utah 84602

The sulfur heterocycles in a catalytically cracked vacuum residue were isolated by use of a newly developed ligand exchange chromatographic procedure, and they were then fractionated according to the number of aromatic rings by using a supercritical fluid fractionation system with supercritical CO_2 as the fractionation solvent. Compounds in each fraction were identified by capillary column gas chromatography and gas chromatography/mass spectrometry. Characteristic mass spectral fragmentation patterns were used to confirm identifications, particularly for the alkyl-substituted compounds. The sulfur heterocycles in this sample were annellated on both sides of the thiophene ring and were highly alkylated; the most abundant compounds contained alkyl chains with three carbon atoms. Several four-ring compounds containing two sulfur heteroatoms were also detected. This example illustrates the effectiveness of supercritical fluid fractionation according to the number of aromatic rings for highly alkylated samples.

The petroleum industry has continually been troubled with various problems related to sulfur in petroleum, such as product odor and storage stability, corrosion of processing equipment, and pollution during usage. With regard to pollution, sulfur oxides produced during fossil fuel combustion are major contributors to air pollution (*1*) and can lead to acid rain damage to forests (*2*). For these reasons, hydrodesulfurization during refining is important. It is essential to identify the structures of sulfur compounds in crude oils and petroleum-derived products in order to more effectively optimize these desulfurization processes.

Desulfurization of heavy oils is more difficult than that of light oils. This is because highly aromatized polycyclic aromatic sulfur heterocycles (PASH) in heavy oils decrease the reactivity of desulfurization (*3–5*). These compounds are also known to poison catalysts used in catalytic desulfurization processes (*6*). High-molecular-weight sulfur compounds in high-boiling-point fractions and heavy residues are difficult to determine and have not yet been adequately characterized. This is primarily because they are highly alkylated and their identification in such complex mixtures is difficult, even when using high-resolution mass spectrometry.

The structures of sulfur compounds found in petroleum and the analytical methods for different types of sulfur compounds were reviewed by Drushel (*7*) and Dean et al. (*8*). Isolation or concentration of sulfur-rich fractions is essential for accomplishing the required detailed analysis. Although a totally nondiscriminating separation method for sulfur heterocycles has not been found, a new isolation method for compounds with two to six annellated rings, based on ligand exchange chromatography, was recently developed by us (*9, 10*). Further subfractionation based on molecular weight or number of aromatic rings is necessary in order to further simplify complex PASH fractions for final characterization (*11*).

In this study, PASH in a catalytically cracked petroleum vacuum residue were isolated by ligand exchange chromatography, followed by ring-number separation using a new supercritical CO_2 fractionation system. The resultant PASH fractions were then analyzed using capillary column gas chromatography (GC) and gas chromatography/mass spectrometry (GC/MS) in order to provide detailed structural information.

0003-2700/86/0358-2251$01.50/0 © 1986 American Chemical Society

Table I. Elemental Analysis of an FCC VR Crude and Its P-1 and P-2 Fractions

element	concentration, wt %		
	FCC VR crude	P-1	P-2
C	90.7	91.8	77.2
H	8.0	7.1	5.7
S	1.7	1.4	9.7
N	0.2	*a*	*a*

[a] Trace.

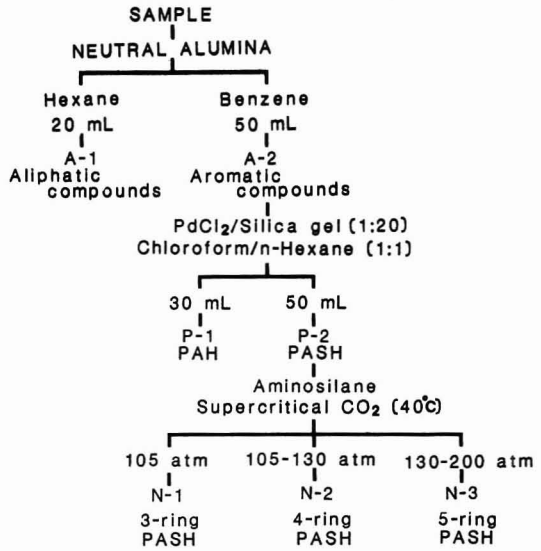

Figure 1. Isolation and fractionation scheme for sulfur heterocycles.

EXPERIMENTAL SECTION

A catalytically cracked petroleum vacuum residue (FCC VR) was obtained from Exxon Research and Engineering Co., Linden, NJ. A 0.3-g sample was fractionated into chemical classes by column adsorption chromatography on neutral alumina (*12*). The PASH fraction (P-2, approximately 10 mg) was isolated from the second fraction (A-2, 0.2 g) by ligand exchange chromatography as previously described (*9*). Silica gel impregnated with $PdCl_2$, which was stored in an oven at 160 °C after activation at 200 °C, was used. The elemental analyses of the crude sample, the P-1 (polycyclic aromatic hydrocarbon) fraction, and the P-2 (PASH) fraction are given in Table I.

The supercritical fluid extraction/fractionation (SFF) system used in this study was recently reported by Campbell and Lee (*13*). About 5 mg of the P-2 fraction in 50 μL of methylene chloride was fractionated. The separation column was dry-packed with NH_2-Adsorbosil (30–70 μm, Applied Science, State College, PA). The oven temperature was raised to 40 °C and held there for the duration of the fractionation. The pressure of the CO_2 mobile phase was initially brought to 105 atm and held there until the first fraction (N-1) was eluted, whereupon it was raised at 1.5 atm min^{-1} to 130 atm. As soon as the second fraction (N-2) eluted, the pressure was again programmed at 8 atm min^{-1} to 200 atm and held there for about 10 min while the third fraction (N-3) eluted. The above fractionation scheme is summarized in Figure 1. Approximately 100 μL of diethylamine was added to each fraction before analysis by GC (*9*).

A Hewlett-Packard Model 5880 gas chromatograph equipped with a flame ionization detector (FID) and flame photometric detector (FPD) was used for all gas chromatographic analyses in this study. Sample injection was made in the splitless mode, and hydrogen carrier gas was set at a linear velocity of 100 cm s^{-1}. The capillary column used in this study was prepared by statically coating fused silica capillary tubing (20 m × 0.3 mm i.d., Hewlett-Packard, Avondale, PA) with SE-54 (film thickness of 0.25 μm), cross-linking using azo-*t*-butane (*14*), and conditioning overnight at 300 °C under nitrogen gas flow. Semiquantitation of the PASH in the samples was accomplished by comparing FID areas of the resolved components with the average peak areas of a standard injection of dibenzothiophene and phenanthrene.

A Hewlett-Packard 5982A GC/MS system was used for obtaining mass spectral information on the isolated fractions and standard samples. The mass spectrometer was operated in the electron impact mode at 70 eV.

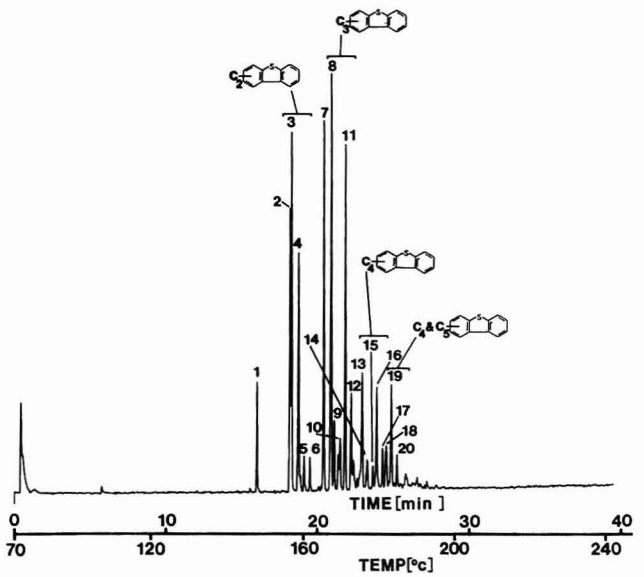

Figure 2. FPD gas chromatogram of the N-1 fraction of an FCC VR P-2 fraction. Conditions were as follows: 70–120 °C at 10 °C min^{-1} and 120–240 °C at 4 °C min^{-1} after an initial 2-min isothermal period; hydrogen carrier gas at a linear velocity of 100 cm s^{-1}. Peak assignments are listed in Table II.

RESULTS AND DISCUSSION

The elemental analysis data (Table I) support the isolation of the PASH from other aromatic compounds using the ligand exchange chromatographic procedure. FPD chromatograms of the three PASH fractions (N-1 to N-3) fractionated by SFF with CO_2 are shown in Figures 2–4, respectively. Although FPD chromatograms are shown in order to clearly distinguish PASH and residual polycyclic aromatic hydrocarbons (PAH) in the PASH (P-2) fraction, these low amounts of PAH did not interfere with the GC/MS analysis. The compounds identified, their molecular masses, and their approximate concentrations are listed in Table II. It was found previously that Pd in the $PdCl_2$/PASH complexes, which eluted from the ligand exchange chromatographic column, catalyzed desulfurization in the column or injection port of the gas chromatograph if the sulfur atom in the compounds analyzed was not in an interior ring of the molecule (*9*). Therefore, diethylamine-treated P-2 fractions were analyzed by gas chromatography. The gas chromatograms of the diethylamine-treated and nontreated FCC VR P-2 fractions were compared. Since both chromatograms were exactly the same, PASH with fusion on only one side of the thiophene ring were not present in this sample.

A chemically bonded aminosilane stationary phase has become popular in liquid chromatography for the separation of PAH according to the number of aromatic rings (*15*). Recently, this aminosilane phase was similarly applied to the ring-number separation of PAH using SFF (*13*). However, the application of this SFF technique to highly alkylated samples had not been investigated until this study. The ring-number separation of alkylated PASH by SFF on the aminosilane phase was very effective as is shown in Figures 2–4. The C_4- and C_5-benzonaphthothiophenes were collected in the second fraction (N-2), while the C_1- and C_2-chrysenothiophenes, which have lower molecular masses, were collected in the third fraction (N-3) according to the number of aromatic rings. Gas chromatographic retention temperatures were

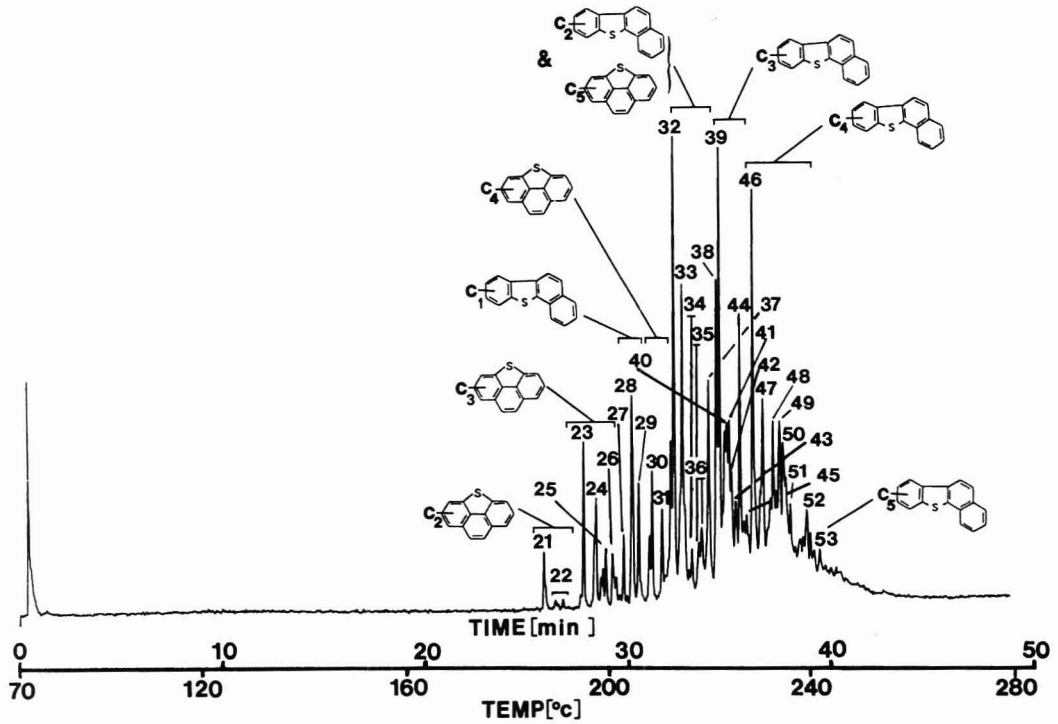

Figure 3. FPD gas chromatogram of the N-2 fraction of an FCC VR P-2 fraction. Conditions were as follows: 70–120 °C at 10 °C min^{-1} and 120–280 °C at 4 °C min^{-1} after an initial 2-min isothermal period; hydrogen carrier gas at a linear velocity of 100 cm s^{-1}. Peak assignments are listed in Table II.

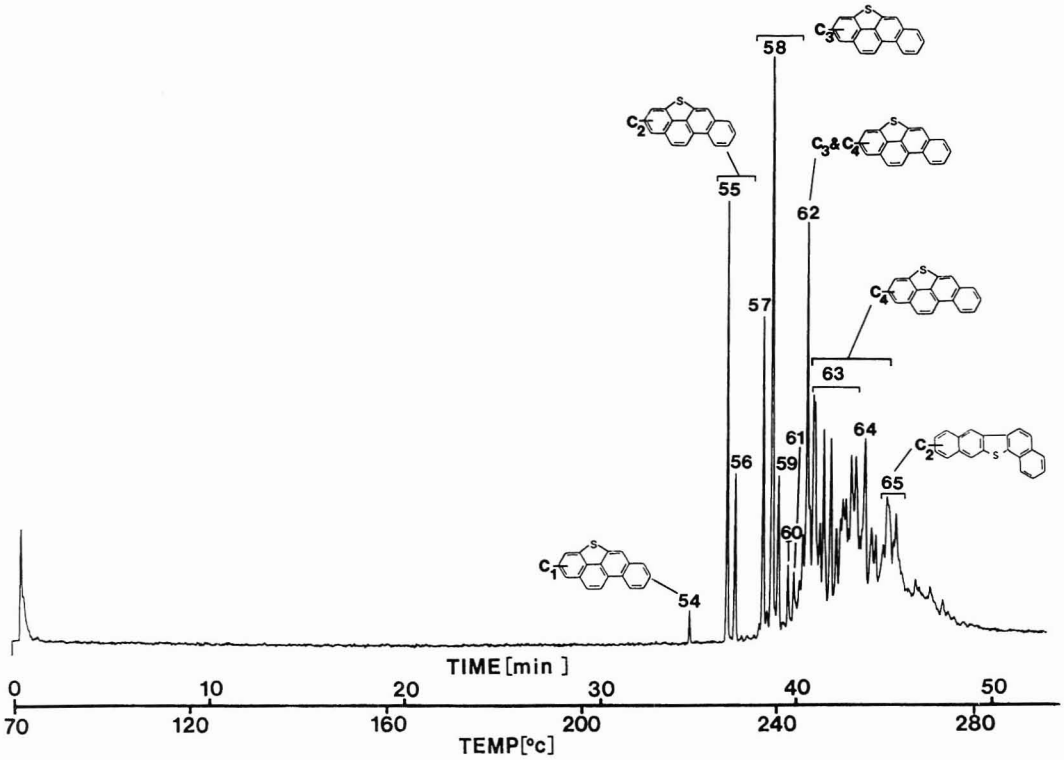

Figure 4. FPD gas chromatogram of the N-3 fraction of an FCC VR P-2 fraction. Conditions are as in Figure 2. Peak assignments are listed in Table II.

higher for the former than for the latter. This ring-size separation was essential for the detailed analysis of such highly alkylated compounds.

Representative mass spectra for several of the PASH identified are shown in Figure 5. Although the molecular ion (M^+) is generally the most abundant ion in PAH mass spectra, methyl-substituted PAH show strong $(M - 1)^+$ ions because of the stability of the tropylium ion (*16*, *17*). Furthermore, $(M - 15)^+$ ions are also observed for the alkylated PAH; the $(M - 15)^+$ ion of ethylnaphthalene is more abundant than the M^+ ion (*17*). Similarly, these mass spectral fragmentation patterns are expected for the PASH.

Figure 5A shows a mass spectrum of a C_1-chrysenothiophene. The absence of the $(M - 15)^+$ ion and the high abundance of the $(M - 1)^+$ ion are characteristic of the formation of the tropylium ion. The mass spectrum of a C_3-chrysenothiophene (Figure 5B) illustrates a typical spectrum of a compound with higher alkylation than methyl substitution. In this case, one observes a strong $(M - 15)^+$ ion and an $(M - 29)^+$ ion. The mass spectra of alkylated compounds

Table II. Sulfur Heterocycles Identified and Quantified in an FCC VR

peak no.	molecular ion[a]	proposed identification	concn,[b] μg/g
1	198	2- and/or 3-methyldibenzothiophene	30
2	212, 204	C_2-dibenzothiophene, unknown	80
3	204, 212	unknown, C_2-dibenzothiophene	100
4	204, 212	unknown, C_2-dibenzothiophene	70
5	204, 212	unknown, C_2-dibenzothiophene	10
6	204, 212, 226	unknown, C_2-dibenzothiophene, C_3-dibenzothiophene	10
7	226, 212	C_3-dibenzothiophene, C_2-dibenzothiophene	100
8	226, 212	C_3-dibenzothiophene, C_2-dibenzothiophene	140
9	226	C_3-dibenzothiophene	20
10	226	C_3-dibenzothiophene	20
11	226	C_3-dibenzothiophene	90
12	226, 240	C_3-dibenzothiophene, C_4-dibenzothiophene	20
13	240, 226	C_4-dibenzothiophene, C_3-dibenzothiophene	30
14	240, 226	C_4-dibenzothiophene, C_3-dibenzothiophene	30
15	240	C_4-dibenzothiophene	30
16	240	C_4-dibenzothiophene	20
17	240, 254	C_4-dibenzothiophene, C_5-dibenzothiophene	10
18	240, 254	C_4-dibenzothiophene, C_5-dibenzothiophene	10
19	240, 254	C_4-dibenzothiophene, C_5-dibenzothiophene	20
20	240, 254	C_4-dibenzothiophene, C_5-dibenzothiophene	10
21	236	C_2-phenanthrothiophene	30
22	236	C_2-phenanthrothiophene	2
23	250, 236	C_3-phenanthrothiophene, C_2-phenanthrothiophene	50
24	250	C_3-phenanthrothiophene	40
25	250	C_3-phenanthrothiophene	20
26	250, 264	C_3-phenanthrothiophene, C_4-phenanthrothiophene	20
27	248, 264	C_1-naphthobenzothiophene, C_4-phenanthrothiophene	20
28	248, 264	C_1-naphthobenzothiophene, C_4-phenanthrothiophene	60
29	248, 264	C_1-naphthobenzothiophene, C_4-phenanthrothiophene	40
30	264	C_4-phenanthrothiophene	40
31	264, 278	C_4-phenanthrothiophene, C_5-phenanthrothiophene	20
32	262, 278	C_2-naphthobenzothiophene, C_5-phenanthrothiophene	150
33	262	C_2-naphthobenzothiophene	100
34	262, 278, 276, 282, 292	C_2-naphthobenzothiophene, C_5-phenanthrothiophene, C_3-naphthobenzothiophene, C_3-bis(benzothiophene), C_6-phenanthrothiophene	10
35	262, 276, 282	C_2-naphthobenzothiophene, C_3-naphthobenzothiophane, C_3-bis(benzothiophene)	10
36	262, 278, 282, 292	C_2-naphthobenzothiophene, C_5-phenanthrothiophene, C_3-bis(benzothiophene), C_6-phenanthrothiophene	20
37	276, 282	C_3-naphthobenzothiophene, C_3-bis(benzothiophene)	70
38	276	C_3-naphthobenzothiophene	100
39	276	C_3-naphthobenzothiophene	150
40	276	C_3-naphthobenzothiophene	50
41	276	C_3-naphthobenzothiophene	50
42	276	C_3-naphthobenzothiophene	30
43	276, 290	C_3-naphthobenzothiophene, C_4-naphthobenzothiophene	20
44	276, 290	C_3-naphthobenzothiophene, C_4-naphthobenzothiophene	80
45	290, 276, 296	C_4-naphthobenzothiophene, C_3-naphthobenzothiophene, C_4-bis(benzothiophene)	30
46	290, 276	C_4-naphthobenzothiophene, C_3-naphthobenzothiophene	130
47	290, 276	C_4-naphthobenzothiophene, C_3-naphthobenzothiophene	60
48	290	C_4-naphthobenzothiophene	50
49	290	C_4-naphthobenzothiophene	50
50	290	C_4-naphthobenzothiophene	50
51	290	C_4-naphthobenzothiophene	20
52	290	C_4-naphthobenzothiophene	20
53	304, 290	C_5-naphthobenzothiophene, C_4-naphthobenzothiophene	10
54	272	C_1-chrysenothiophene	10
55	286	C_2-chrysenothiophene	200
56	286	C_2-chrysenothiophene	90
57	300	C_3-chrysenothiophene	130
58	300	C_3-chrysenothiophene	240
59	300	C_3-chrysenothiophene	80
60	300	C_3-chrysenothiophene	30
61	300	C_3-chrysenothiophene	20
62	300, 314	C_3-chrysenothiophene, C_4-chrysenothiophene	180
63	314, 300	C_4-chrysenothiophene, C_3-chrysenothiophene	
64	314	C_4-chrysenothiophene	110
65	312	C_2-dinaphthothiophene	

[a] Molecular ions are listed in order of decreasing abundance. [b] Approximate concentration in μg/g of original material.

in this sample reflect extended chain alkylation instead of multi-methyl substitution. Figure 5C is a composite mass spectrum of two coeluting compounds, a C_3-benzonaphthothiophene and a C_3-substituted four-ring compound containing two thiophene rings. Although a C_7-dibenzothiophene has the same molecular mass as the latter compound, it is not expected to be in the four-ring fraction. Since the thiophene compounds found in this sample are annellated on more than one side,

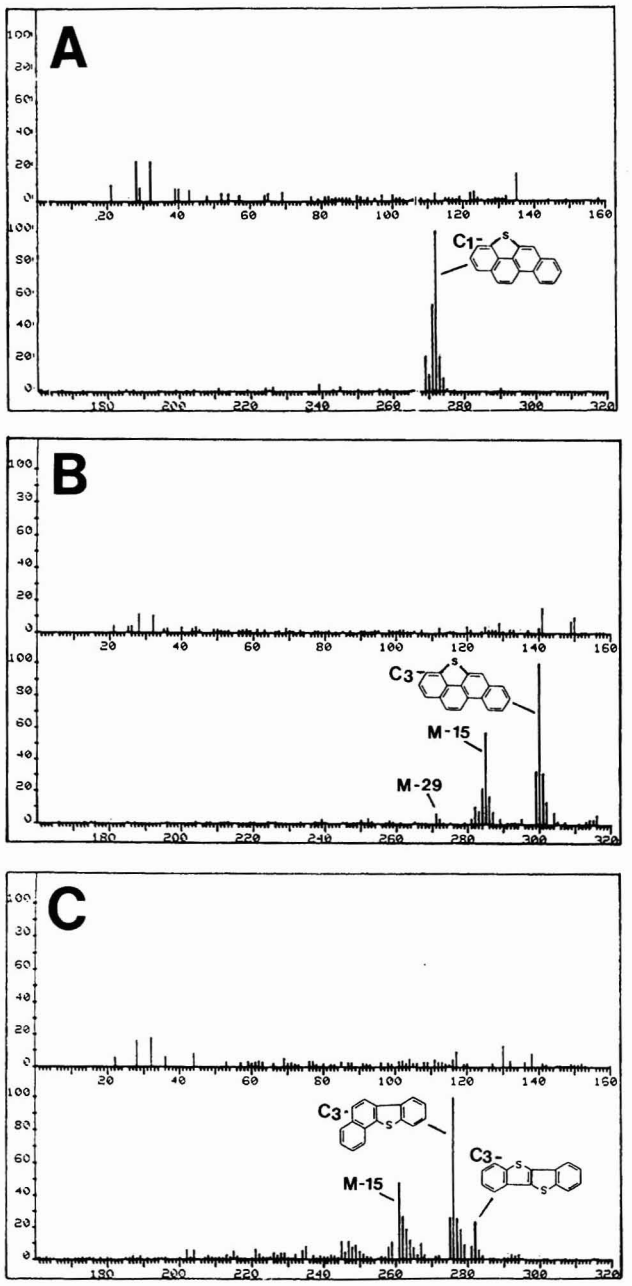

Figure 5. Mass spectra of peak 54 (A), peak 58 (B), and peak 37 (C).

compounds with two thiophene rings must have at least four rings total. Lower molecular weight compounds containing two thiophene rings were not detected. Compounds such as these were previously proposed (*3*, *18*, *19*).

In conclusion, the structural characteristics of the PASH in this FCC VR are summarized as follows:

(1) The empirical formula of the P-2 fraction determined by elemental analysis is $C_{21}H_{19}S$ and is consistent with the average structure, C_3-chrysenothiophene ($C_{21}H_{17}S$), as determined by GC/MS.

(2) PASH with fusion on only one side of the thiophene ring were not found. Since this type of PASH is easily desulfurized by a catalyst (*3*, *10*), it is believed that they were removed in the catalytic cracking process.

(3) The PASH in this sample were highly alkylated, and the average degree of alkylation was three carbons.

(4) Linear chain alkylation was predominant over multimethyl substitution.

ACKNOWLEDGMENT

We thank W. K. Robbins (Exxon Research and Engineering Co., Clinton, NJ) for supplying the catalytically cracked vacuum residue.

LITERATURE CITED

(1) Horne, R. A. In *The Chemistry of Our Environment*; Wiley: New York, 1978; p 178.
(2) Kraushaar, J. J.; Ristinen, R. A. In *Energy and Problems of a Technical Society*; Wiley: New York, 1984; pp 425–428.
(3) Drushel, H. V.; Sommers, A. L. *Anal. Chem.* **1967**, *39*, 1819–1829.
(4) Frye, C. G.; Mosby, J. F. *Chem. Eng. Prog.* **1967**, *63*(9), 66–70.
(5) Kushiyama, A. *Petrotech (Tokyo)* **1978**, *1*, 705–711.
(6) Kamiya, Y.; Sanada, Y.; Tomita, A. In *Coal and Heavy Oils: Chemistry and Applications*; Kodansha: Tokyo, 1979; p 79 (Japanese).
(7) Drushel, H. V. *Prepr.—Am. Chem. Soc., Div. Pet. Chem.* **1970**, *15*(2), C13–C42.
(8) Dean, R. A.; Whitehead, E. V. *Proc. World Pet. Congr., 7th* **1967**, *9*, 165–175.
(9) Nishioka, M.; Campbell, R. M.; Lee, M. L.; Castle, R. N. *Fuel* **1986**, *65*, 270–273.
(10) Nishioka, M.; Lee, M. L.; Castle, R. N. *Fuel* **1986**, *65*, 390–396.
(11) Kong, R. C.; Lee, M. L.; Tominaga, Y.; Pratap, R.; Iwao, M.; Castle, R. N.; Wise, S. A. *J. Chromatogr. Sci.* **1982**, *20*, 502–510.
(12) Later, D. W.; Lee, M. L.; Bartle, K. D.; Kong, R. C.; Vassilaros, D. L. *Anal. Chem.* **1981**, *53*, 1612–1620.
(13) Campbell, R. M.; Lee, M. L. *Anal. Chem.* **1986**, *58*, 2247–2251.
(14) Wright, B. W.; Peaden, P. A.; Lee, M. L.; Stark, T. *J. Chromatogr.* **1982**, *248*, 17–34.
(15) Wise, S. A.; Chesler, S. N.; Hertz, H. S.; Hilpert, L. R.; May, W. E. *Anal. Chem.* **1977**, *49*, 2306–2310.
(16) Safe, S.; Hutzinger, O. In *Mass Spectrometry of Pesticides and Pollutants*; CRC Press: Cleveland, OH, 1973; Chapter 6.
(17) Lee, M. L.; Novotny, M.; Bartle, K. D. In *Analytical Chemistry of Polycyclic Aromatic Compounds*; Academic Press: New York, 1981; p 242.
(18) Coleman, H. J.; Dooley, J. E.; Hirsch, D. E.; Thompson, C. J. *Anal. Chem.* **1973**, *45*, 1724–1737.
(19) Ruiz, J.-M.; Carden, B. M.; Lena, L. J.; Vincent, E.-J.; Escalier, J.-C. *Anal. Chem.* **1982**, *54*, 688–691.

RECEIVED for review February 3, 1986. Accepted April 17, 1986. This work was supported by the Department of Energy, Office of Health and Environmental Research, Contract No. DE-AC02-79EV10237.

Reaction Monitoring in Supercritical Fluids by Flow Injection Analysis with Fourier Transform Infrared Spectrometric Detection

S. V. Olesik,[1] S. B. French, and M. Novotny*

Department of Chemistry, Indiana University, Bloomington, Indiana 47405

The advantages of direct reaction monitoring using supercritical fluids as solvents in conjunction with Fourier transform infrared spectrometry (FTIR) are illustrated. A capillary system was used in the "flow-injection analysis" mode for the study of the decomposition of allyldiisopropylamine oxide. The solvation effects of supercritical carbon dioxide were monitored as a function of solvent density.

Owing to certain unique physical properties of supercritical fluids (systems above their critical temperatures and near critical pressures), numerous benefits may be found in their use as solvent media. The possible uses of supercritical fluids in organic chemistry were recently discussed by Squires et al (*1*). The mass transfer processes in supercritical fluids are approximately 2 orders of magnitude faster than those in liquids; this fact translates itself into advantages for certain (mass-transfer limited) reactions, extraction processes, and fast chromatography. The solvating power of supercritical fluids, being a sensitive function of pressure, can be easily controlled during such processes. For example, Liphard and Schneider (*2*) showed that the solubility of squalane in supercritical carbon dioxide varies by a factor of 10^{10} when the pressure is increased from 0 to 395 atm. Significant changes in the solvation properties of supercritical fluids with increasing pressure are also indicated by appreciable changes in the dielectric constant. At 50 °C, the static dielectric constant of CO_2 varies from 1 to 1.8 over the pressure range of 0 to 1700 atm (*3*). By use of supercritical fluids as solvents, a wide range of interactions can be studied without changing the chemical nature of a solvent or temperature.

Advantages to be gained from Fourier transform infrared spectrometry (FTIR) in studying various chemical processes are well-known: (1) excellent sensitivity at fast spectral acquisition; (2) the capability to simultaneously monitor the variation of absorption bands. Since certain supercritical fluids (e.g., carbon dioxide or xenon) are relatively transparent in FTIR, they can serve as convenient solvents while a great variety of other organic molecules are monitored in such media.

In the first communication on capillary supercritical fluid chromatography (SFC), a suggestion was made (*4*) that appropriate mobile phases could facilitate solute measurements in the infrared spectral region. The following experiments have demonstrated that supercritical carbon dioxide (*5*, *6*) and xenon (*7*) permit an effective combination of capillary SFC and FTIR spectrometry. The purpose of this communication is yet another demonstration of the advantages of the capillary flow systems, this time for direct reaction monitoring. In this capacity, an earlier described (*6*) capillary supercritical-fluid chromatographic system was used in a "flow injection analysis" mode (*8*) for kinetic measurements on a model reaction.

Just as with capillary SFC (*6*), a capillary flow apparatus with a short, uncoated fused silica column provides a convenient addition to high-pressure FTIR spectrometry, since high pressures are easily contained at extremely small volumes (of the order of microliters) and the flow rates used (microliters per minute). The combined use of supercritical fluids as solvents and FTIR for detection, therefore, may provide a powerful means for studying closely various kinetic and structural parameters. Alternatively, reaction product separation and analysis could be accomplished by capillary SFC/FTIR. As an example presented here, the unimolecular conversion of allyldiisopropylamine oxide (I) to *O*-allyl-*N*,*N*-diisopropylhydroxylamine (II) was monitored using supercritical carbon dioxide as the solvent.

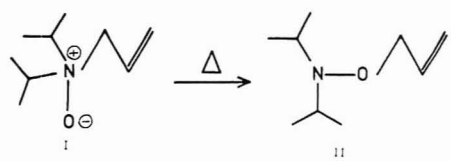

I II

EXPERIMENTAL SECTION

A schematic of the experimental setup is shown in Figure 1. While the system pressure was controlled by a Varian 8500 high-pressure pump, a Varian 1200 gas chromatographic oven controlled the capillary temperature. Details of the high-pressure flow cell have been described in a previous publication (*6*).

A 0.2-μL plug of reactant (sample obtained through courtesy of J. J. Gajewski of our department) was injected, without dilution, into a 1-m section of a 250 μm, i.d., fused silica capillary. The capillary was maintained at 50 ± 0.5 °C with a gas chromatographic oven, which served as the inlet to the high-pressure IR flow cell (nominal volume of 2 μL, optical path length of 1 mm, and cross sectional area of 2 mm^2). The flow cell was also maintained at 50 ± 1 °C. The outlet of the flow cell was a section of 250 μm, i.d., capillary. A shut-off valve (used to trap sample in the IR flow cell) was placed between the outlet fused silica and a 20-m section of 50 μm, i.d., glass capillary restrictor (flow controlling device). The infrared spectrometer used in these experiments was an IBM IR/85 instrument (IBM Instruments, Inc., Danbury, CT) equipped with a narrow bandwidth (4000–669 cm^{-1}) mercury cadmium telluride (MCT) detector with $D^* = 5.96 \times 10^9$ cm $Hz^{1/2}$ W^{-1}. (The D^* is a figure of merit associated with the detector. The larger the value of D^*, the more sensitive the detector. A detailed comparison of detectors may be found elsewhere (*9*).) Because the reaction was thermally induced, the sample was maintained at −77 °C until injection time. The sample was then warmed to liquid state (by allowing it contact with the ambient temperature) and injected neat into the Valco high-pressure valve. The large heat transfer rate across the small capillary ensured a quick rise in the sample temperature from −77 °C to the reaction temperature. Total time from −77 °C bath to reaction temperature was typically less than 2 min.

During the kinetic experiments, the reactant (N-oxide) was passed into the high-pressure flow cell, and trapped there by stopping the flow. Approximately 40 interferograms were accumulated at a rate of 2.5 interferograms/s, every 3 min, over the total run times of typically 4–6 h. Each set of 40 interferograms

[1] Present address: Department of Chemistry, The Ohio State University, Columbus, OH 43210.

0003-2700/86/0358-2256$01.50/0 © 1986 American Chemical Society

Table I. Variation of Rate Constant as a Function of Solvation

solvent	solubility parameter	pressure, atm	temp, °C	density,[c] g/cm³	k + std,[d] s⁻¹ pathway I	k + std,[d] s⁻¹ pathway II
CO_2	2.62[a]	68.0	50	0.18	$(8.2 + 0.4) \times 10^{-5}$	
	4.88[a]	98.67	50	0.45		$(1.8 + 0.2) \times 10^{-4}$
	6.42[a]	115.7	50	0.68		$(1.1 + 0.1) \times 10^{-4}$
$CDCl_3$	9.3[b]		17.2	liquid	1.12×10^{-4}	

[a] Reference 10. [b] Reference 11. [c] Reference 12. [d] Standard deviation.

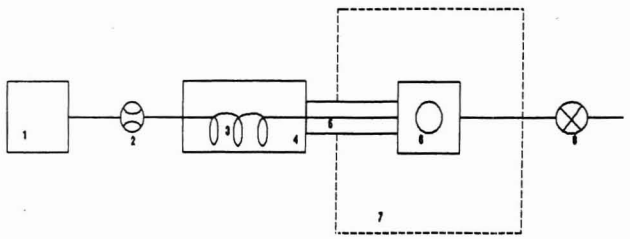

Figure 1. Schematic of the flow injection analysis system with high-pressure FTIR: (1) Varian 8500 syringe pump; (2) Valco injection valve with 0.2-μL loop; (3) 1-m section of fused silica capillary; (4) Varian 1200 gas chromatographic oven; (5) heated transfer line; (6) a heated high-pressure flow cell; (7) IBM Model IR-85 spectrometer; (8) on–off valve.

was coadded before the transform was taken to produce the 4-cm⁻¹ IR spectrum. A spectrum of supercritical carbon dioxide was used as the measure of the incident light intensity. No data manipulation such as spectral subtraction or base line correction was used in this study.

RESULTS AND DISCUSSION

Solvation effects may broadly be classified in terms of chemical forces (complex formation, hydrogen bonding, etc.) and weak physical forces of the van der Waals type. An intent of this study was to evaluate the effect of increasing physical forces on the model reaction by increasing the density of supercritical carbon dioxide. This solvent medium was chosen because carbon dioxide is relatively transparent to mid-IR radiation over an appreciable density range (*6*).

Substantial solvent effects were observed as a function of pressure and, therefore, density variation. Table I provides a summary of experiments included in this study. Initially, at a carbon dioxide density of 0.18 g/cm³, the measured spectra showed an absorbance band at 1218 cm⁻¹, forming and increasing in intensity as a function of time. The intensity of the 1218-cm⁻¹ band [due to C–O stretching of the reaction product (II)] was plotted against the intensity of the 2978-cm⁻¹ band (C–H stretching) to compensate for changes in concentration of the reacting mixture in the cell as a function of time. From the slope of a plot of the log (absorbance at 1218-cm⁻¹ band/absorbance at 2978-cm⁻¹ band) vs. time, the reaction rate constant was determined to be $(8.2 \pm 0.4) \times 10^{-5}$ (rate constant ± standard error).

When the density of carbon dioxide was increased to 0.45 g/cm³, no absorbance band formed at 1218 cm⁻¹; instead, two bands appeared and increased as a function of time at 1728 cm⁻¹ and 1610 cm⁻¹. These bands correspond to the C=O stretching and C=C stretching of a conjugated aldehyde and alkene system. With the increased density of solvent, no further *O*-allyl-*N*,*N*-diisopropylhydroxylamine was detected. The absorbance bands listed above are those of acrolein when solvated by supercritical carbon dioxide, as found in a separate experiment. The formation of an aldehyde as a product in the decomposition of an N-oxide was unexpected. To our knowledge, there is only one other report of this type of reaction, that for the decomposition of benzyldiethylamine oxide (*13*). The rate constant determined by monitoring the increase in the 1610-cm⁻¹ band $[(1.8 \pm 0.2) \times 10^{-4}\ s^{-1}]$ was approximately equal but opposite in sign to the rate constant determined by monitoring the decrease in the 920-cm⁻¹ band (N–O stretching of allydiisopropylamine oxide).

The final solvent conditions studied were 115.7 atm (P_R = 1.59) and 50 °C (T_R = 1.06) corresponding to a carbon dioxide density of 0.68 g/cm³. At these conditions two bands, 1728 cm⁻¹ and 1610 cm⁻¹, increase with increasing time. Under these circumstances, acrolein was the primary product with a rate constant of $(1.1 \pm 0.1) \times 10^{-4}\ s^{-1}$.

The solvation effects of supercritical carbon dioxide on the thermal decomposition of allyldiisopropylamine oxide seem complex in that both rearrangement and elimination reactions occur as a function of solvent density variation. When liquid deuterated chloroform was the solvent, only the rearrangement pathway was observed using proton NMR detection (*14*). The rate constant (*14*) for the rearrangement reaction in deuterated chloroform (T = 17.2 °C) is also shown in Table I. Additionally, Table I lists the Hildebrand (or one-component) solubility parameters (*10*, *11*, *15*, *16*) for the solvents studied. The solubility parameter is a measure of the cohesive forces holding a liquid together. It is primarily a measure of "physical" forces and therefore does not include solvation effects such as solvent–solute interactions. As the density of carbon dioxide increases, its solubility parameter also increases and begins to approach that of chloroform. Roughly speaking then, if the physical forces of solvation (the molecular cohesive energy) dominate, then the high-pressure carbon dioxide experiment should compare favorably with the experiment in which deuterated chloroform was used. This was not the case, as only for the lowest density of carbon dioxide was the rearrangement reaction dominant. This seems to imply that "chemical" forces such as more intimate solute–solvent interactions significantly affect the thermal decomposition of allyldiisopropylamine oxide in supercritical carbon dioxide.

The most likely explanation for the kinetic data is that the reaction follows two pathways.

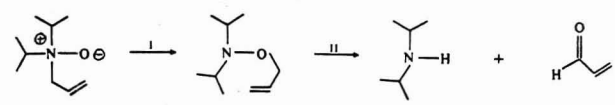

At low carbon dioxide pressures (below its critical pressure) pathway I dominates. Pathway II proceeds so slowly at this pressure that over the time scale studied (approximately 3 h) no elimination occurs. When the pressure of carbon dioxide is increased above the critical point, pathway I becomes much faster, but the elimination reaction rate is increased to a much greater extent to the point that no *N*,*N*-diisopropyl(allyloxy)amine is detected. If this proposed mechanism is true, then the measured rate constants would be due primarily to the rearrangement reaction because the rearrangement is the rate-limiting step in the high-pressure reactions. The transition state for the rearrangement reaction (pathway I) is believed to involve charge separation (*14*) and, therefore, an increase in reaction rate is predicted for increasing solvent density. A consistent trend in rate constant variation with increasing solvent density was not discernible. It may be of interest to compare the course of this reaction in more nonpolar supercritical fluids, such as xenon.

While further studies are necessary to identify the exact mechanism for the decomposition of allyldiisopropylamine oxide, the present study has shown the value of combining a capillary flow system with high-pressure FTIR spectrometry for reaction monitoring. Other spectroscopic techniques may be adaptable to similar measurements, as indicated by the recently reported combinations of capillary SFC with a mass spectrometer (*17*) or a photodiode array system (*18*). In addition, the setup described in this communication may represent the smallest flow injection analysis (*8*) system reported to date.

ACKNOWLEDGMENT

The authors acknowledge Jahangir Emrani and Joseph Gajewski of this department for helpful discussions and the samples of allyldiisopropylamine oxide. We also thank Sharon Smith and Dennis Gerson of IBM Instruments, Danbury, CT, for helpful discussions and technical assistance.

Registry No. I, 102725-56-4.

LITERATURE CITED

(1) Squires, T. G.; Renier, C. G.; Aida, T. *Fluid Phase Equilib.* **1983**, *10*, 261–268.
(2) Liphard, K. G.; Schneider, G. M. *J. Chem. Thermodyn.* **1975**, *7*, 805–814.
(3) Michels, A.; Kleerkoper, L. *Physica (Amsterdam)* **1939**, *6*, 586–590.
(4) Novotny, M.; Springston, S. R.; Peaden, P. A.; Fjeldsted, J. C.; Lee, M. L. *Anal. Chem.* **1981**, *53*, 407A–414A.
(5) Shafer, K. H.; Griffiths, P. R. *Anal. Chem.* **1983**, *55*, 1939–1942.
(6) Olesik, S. V.; French, S. B.; Novotny, M. *Chromatographia* **1984**, *18*, 489–495.
(7) French, S. B.; Novotny, M. *Anal. Chem.* **1986**, *58*, 164–166.
(8) Ruzicka, J.; Hansen, E. L. "Flow Injection Analysis", in *Chemical Analysis*; Elving, P. J., Winefordner, J. D., Eds.; Wiley: New York, 1981; Vol. 62.
(9) *Optical and Infrared Detectors*; Keys, R. J., Ed.; Springer-Verlag: Berlin, 1977.
(10) Schoenmakers, P. J. *J. Chromatogr.* **1984**, *315*, 1–18.
(11) Barbon, A. F. M. *Chem. Rev.* **1975**, *75*, 731–753.
(12) IUPAC *International Thermodynamic Tables of the Fluid State, Carbon Dioxide*; Pergamon Press: Oxford, 1976.
(13) Culvenor, C. C. J. *Rev. Pure Appl. Chem.* **1953**, *3*, 83–114.
(14) Emrani, J.; Gajewski, J. J., Department of Chemistry, Indiana University, private communication, September 1984.
(15) Dack, M. R. J. *J. Chem. Educ.* **1974**, *51*, 231–234.
(16) Schoenmakers, P. J.; Billiet, H. A. H.; de Galan, L. *Chromatographia* **1982**, *15*, 205–214.
(17) Smith, R. D.; Felix, W. D.; Fjelsted, J. C.; Lee, M. L. *Anal. Chem.* **1982**, *54*, 1883–1885.
(18) Gluckman, J.; Shelly, D.; Novotny, M. *Anal. Chem.* **1985**, *57*, 1546–1552.

RECEIVED for review November 27, 1985. Accepted April 14, 1986. These investigations were supported by Grants N14-82-K-0561 from the Office of Naval Research and NSF CHE 82-00034 from the National Science Foundation.

Versatile Automatic Development System for Flow Injection Analysis

D. Betteridge,*[1] Timothy J. Sly, and Adrian P. Wade[1]

Department of Chemistry, University College of Swansea, Singleton Park, Swansea SA2 8PP, United Kingdom

Derrick G. Porter

Department of Trade and Industry, Laboratory of the Government Chemist, Cornwall House, Stamford Street, London SE1 9NQ, United Kingdom

A computer-controlled automatic analyzer has been developed to facilitate the rapid development of novel analytical methods based on flow injection analysis (FIA) through the use of mathematical techniques such as modified simplex optimization. The apparatus allows variation of flow rates, pH, and reagent concentration in one or more sample or carrier streams and can accommodate spectrophotometric or electrochemical detectors. The system software, written in BASIC, is menu-driven and interactive. It includes a modified simplex optimization procedure that has permitted automated optimization of analytical methods, yielding an improvement in sensitivity equal to that obtained in earlier manual experiments. The results obtained are discussed, as are the design and execution of the apparatus and software.

One of the crucial problems of automatic analysis is how to speed up or automate the development of an automated method or system. The difficulty is especially acute if one has such diversity of workload that an automatic method needs to be up and running quickly and is subsequently discarded after a month or so of intensive use.

Flow injection analysis (FIA) systems (*1–3*) afford a means of studying the general problem in a concrete way; they are versatile, easy to configure, have a rapid response, and can simulate many other systems. However, in developing a method based on even a simple FIA system, one may need to adjust five or more variables in order to establish optimum conditions for the analysis. This can be very time-consuming if a conventional univariate optimization is undertaken manually, and indeed where interactions exist between the variables, one is unlikely to find the true optimum (*4*).

One solution to this problem would lie in the use of an automated instrument, in which the experimental conditions of concentration, flow rate, pH, etc. may be varied according to a preprogrammed pattern under computer control. The ability to control the system parameters in this way would allow a conventional univariate optimization to be performed much more quickly than is possible by manual means.

In this approach, however, the number of experiments to be performed is still extremely large (*4*). A more economical scheme would be to use the automatic control facilities to carry out a modified-simplex optimization (*5, 6*). This optimization

[1] Present address: BP Research Centre, Chertsey Rd, Sunbury-on-Thames TW16 7LM, UK.

0003-2700/86/0358-2258$01.50/0 © 1986 American Chemical Society

procedure is faster and more reliable than a univariate approach and has been applied successfully to the development of several new analytical methods based chemiluminescence (*6*) FIA (*4*, *7*, *8*). When performed manually, a significant proportion of the experimental time for any optimization procedure is spent in preparing solutions and adjusting the apparatus, and this can be greatly reduced by automation, with the added advantage that the operator is freed for other work.

The aim of this study was to develop a versatile, general purpose FIA instrument under full computer control that could be used in conjunction with a suitable simplex optimization program in order to develop new FIA methods reliably, in the minimum time, and with a minimum of manual intervention—in other words, an automated development system. Methods developed using such an instrument could be either implemented directly on the development system itself, where the method was to be used for a limited period only, or transferred to standard FIA apparatus for long-term routine use.

The design strategy adopted for the whole system was based upon the use of separate, versatile items of hardware and software that could be quickly and easily rearranged to cope with a wide range of applications, rather than a dedicated automatic analyzer, which could only be used for one particular type of method development (such as the system used by Stieg and Nieman (*6*)). There is no reason, for instance, why the system could not be used for the development of methods based on air-segmented continuous flow analysis, with a suitable manifold, or indeed any type of analytical procedure involving the use of flowing liquids at low pressure (<3 bar), which can be monitored with a spectrophotometric or electrochemical detector.

With these criteria in mind, and with a limited equipment budget, it was decided to design and construct most of the apparatus required, rather than adapt a complete commercially built FIA system.

In addition to varying the reaction conditions between each experiment in an optimization procedure, the control facilities may also be used to vary the reaction conditions while an analysis is in progress, i.e., change conditions along the length of a sample plug. By adjustment of the concentrations of different species in this way, accurate, linear concentration gradients and sharp concentration steps may be constructed which open up the possibility of new forms of dynamic analysis. The computer facilities may also be used to acquire and process data from the experiment.

It was decided to control the experimental parameters of reagent concentration, pH, and flow rate with a set of five peristaltic pumps. Pumping speeds were individually controlled by microcomputer. Each component of a stream was pumped separately, and thus by varying the relative speeds of the various pumps, it was possible to vary the concentration of each of the components of the stream, as well as the total flow rate. Control of pH was achieved by pumping solutions of a universal buffer and sodium hydroxide in varying proportions, while a diluent stream of distilled water was pumped to reconcile the desired concentration levels with the required flow rate.

The system has so far been used in two applications, the first was a straightforward application of the control principles described above, while the second system incorporated a modified simplex algorithm for experimental optimization.

The applications are as follows: (a) automatic generation of a series of complex peaks obtained by the reaction of mixtures of Co(II) and Mn(II) with a color-forming reagent in a pH gradient; (b) simplex optimization of an FIA method for the determination of isoprenaline, to enable comparison with a simplex optimization undertaken previously using manual apparatus.

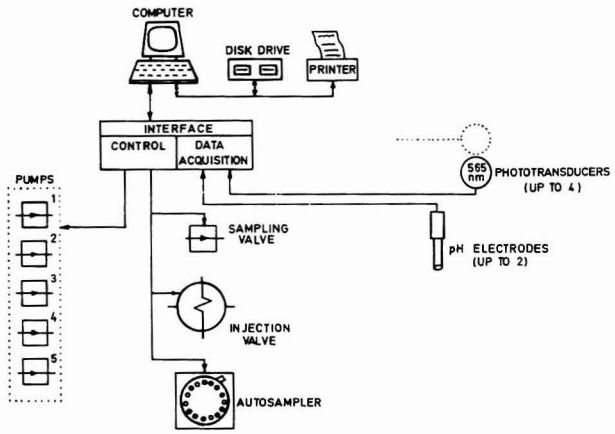

Figure 1. Schematic view of apparatus.

EXPERIMENTAL SECTION

Apparatus. The system is shown in schematic form in Figure 1 and consisted of the following units:

Pumps. Five independent peristaltic pumps (Ismatec type mini-micro 2/6, UK) were housed in a 19 in. rack. The standard fixed-speed synchronous motors were removed from the pumps and replaced with stepper motors (Impex type) driven from driver boards incorporating the necessary phasing and current forcing circuits (McLennan type EM127). The unit was powered by an integral 12 V dc, 120 V ac power supply.

Control of pumping speeds was effected by varying the frequency of digital pulse trains applied to the inputs of the driver circuits; each square-wave pulse applied at an input resulted in a 7.5° rotation of the corresponding pump rollers.

Sampling Pump. Masterflex type 7544-20 with pump head type 7015 (CO Laboratories, Ltd., UK).

Injection Valve. Rheodyne Model 5020 (Rheodyne, Inc., Cotati, CA) driven by an electrical actuator consisting of a geared reversible dc motor fitted with an end slip-clutch (McLennan type P576 DC050 G19 102C) to ensure the valve was driven fully to the end of its travel. The motor was controlled by an electronic timing circuit that could be triggered either manually or remotely to take up a "fill" or "inject" position.

The unit was powered from an integral 12 V dc, 50 A power supply and housed in a small metal box.

Spectrophotometric Detector. The spectrophotometric detector was a flow-through LED phototransducer, details of which have been reported elsewhere (*9*). Two different types of flow cells were used: (a) UV–visible spectrophotometer flow cell (Cecil Instruments, Ltd., Cambridge, UK) modified by fitting a green, high intensity LED to one end and a silicon phototransistor to the other, with a path length of 10 mm and an internal diameter of 2 mm; (b) noninstrusive encapsulated Kel-F flow cell, described elsewhere (*9*).

Analytical Manifold. The analytical manifold was constructed from 0.8 mm i.d. PTFE tubing, configuration dependent upon analytical method (see text). All connections were made by means of Altex flared-end zero dead volume tube fittings with the exception of connections to the pump tubing and Kel-F flow cells, which were made by push-fit connections.

Recorder. A Servoscribe chart recorder (type RE511.20) was used to record peaks. A Solartron digital voltmeter (type A200) was connected in parallel with the chart recorder to measure base line drift and to facilitate calibration of the detectors.

Power Supply. Power supply was sufficient to provide +5 V at 3 A and ±15 V at 1 A to power the interface circuits, as well as power for the phototransducers.

ADC Board. The ADC board was used to provide an interface to the computer together with a 16-channel, 12-bit analog to digital converter capable of conversion rates up to 20 kHz. The circuit accepted input voltages in the range ±5 V from the various detectors via suitable signal conditioning amplifiers.

Phototransducer Board. The phototransducer board was used to accept inputs from up to four phototransducers, which were

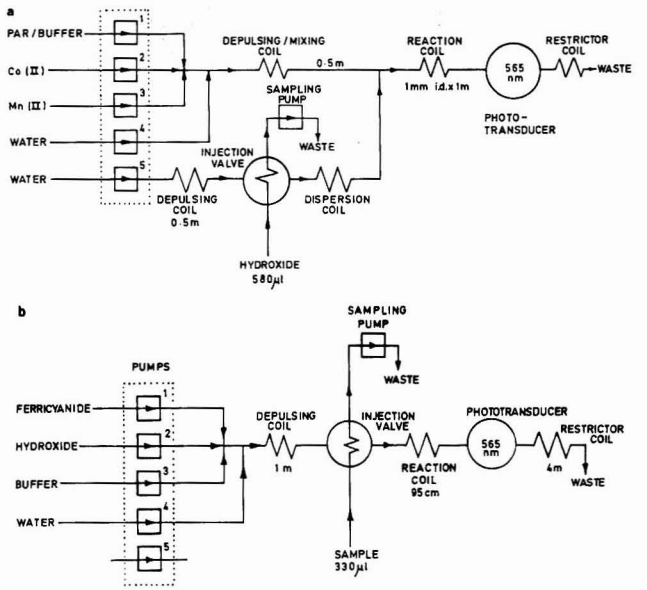

Figure 2. Arrangement of apparatus for (a) simultaneous multielement analysis by pH gradient and (b) automatic simplex optimization of the determination of isoprenaline.

buffered and amplified to suitable levels before being fed to the ADC. An 8-bit digital to analog converter mounted on the board provided the facility to adjust the base line settings of the phototransducers directly from the computer, if required.

Decoder/Frequency Synthesizer. Five phase-locked loop frequency synthesizers generated frequencies in the range 0–122 Hz in 0.477-Hz increments (255 steps = 8-bit resolution) under computer control. The signals were fed to the five driver circuits in the pump unit to control the speed and direction of each of the pumps.

Computer. A Commodore PET computer, type 3032, was used to control the experiment and acquire and process data. The computer was modified to provide a bidirectional parallel interface to the experiment, via a 15-way ribbon cable. Eight additional ports were located within the ROM expansion area of system memory, at addresses 9800–9807 hexadecimal. A dual floppy disk drive (Commodore type 4040) was used for program and data storage, while a TRS-80 daisywheel printer and a TRS-80 four color plotter, type CGP-115 (Tandy Corp, Walsall, UK), were used to produce hard copy. Connection to the computer was via an IEEE-488 to centronics interface (Aculab, Ltd., UK).

Software. A general purpose menu-driven software package was written in BASIC, consisting of groups of dedicated routines arranged in a tree structure which could be called from the menu. The details of the various operating programs are discussed in the text. A group of support programs performed calibration, priming, and purging of the apparatus and allowed incoming raw data to be viewed in real time, to allow easy adjustment of the detectors.

Reagents. Reagents used were as follows: Britton & Robinson's universal buffer solution (*10*); sodium hydroxide stock solution (0.500 M); potassium hexacyanoferrate(III) stock solution (0.243 M) (AnalaR); isoprenaline sulfate dihydrate stock solution (0.05 g·dm^{-3}) (Fisons); 4-(2-pyridylazo)resorcinol (0.001 M) (Aldrich); cobalt(II) nitrate stock solution (0.01 M) (BDH); manganese(II) sulfate stock solution (0.01 M).

Method. *Automatic Control of pH and Concentration (Multielement Analysis).* The apparatus was set up as shown in Figure 2a. A 0.5 mL sample loop was employed. The phototransducer was fitted with a cross-beam Kel-F flow cell (type b) with a path length of 1.25 mm, and fitted with an LED with an emission wavelength of 565 nm. The conditions were chosen to closely reproduce those used by Betteridge and Fields (*11*, *12*).

The controlling software required that the five peristaltic pumps be designated as two sections (Figure 2a). In the first, pumps 1–4 were used to give one resulting stream of controlled flow rate in which the PAR reagent reacts with Co(II) + Mn(II) samples. The second section was comprised of just one pump (pump 5), which propelled a water stream. A slug of 0.5 M sodium hydroxide was injected into this and subsequent dispersion in the mixing coil caused a controlled uniform hydroxide concentration gradient to be formed. The two streams were then combined, the hydroxide reacting with the universal buffer present in the sample/reagent/buffer stream to form a pH gradient. The combined stream then passed through a 1 m × 1 mm i.d. reaction coil to the phototransducer, where the output obtained was in the form of a complex peak resulting from the reaction of the Co(II) and Mn(II) present in the stream with PAR at different pH. The shape of such peaks contained information about the concentration of each of the two sample components present.

The apparatus was programmed to repeat this procedure 3 times at concentration levels for each of the two sample components of 2–10 ppm in increments of 2 ppm, a total of 25 different sample combinations. The resulting peaks were collected, subjected to a nine-point Savitzky–Golay smooth, and stored on disk.

Simplex Optimization. The apparatus was arranged as shown in Figure 2b. A 0.25 mL sample loop was used, giving in total sample volume of 0.33 mL, and the phototransducer was fitted with a 10 mm path length spectrophotometer flow cell (type a), fitted with high-intensity LED with an emission wavelength of 565 nm. The various reagents, and water as diluent, were pumped individually under computer control, and streamed together to give a reagent solution with the desired combination of concentrations, pH, and flow rate.

The starting conditions for the optimization were chosen to coincide with those used in the earlier manual simplex optimization of this method (*4*), in order to enable a true comparison of results to be made.

Each optimization was allowed to proceed through approximately 25 points of the simplex, or until it stopped. Each point was repeated three times, and the response calculated as the mean amplitude of the two most consistent peaks of the three. The entire procedures were repeated for different sizes of factor space and for two different response functions.

In all experiments, the pump tubing was recalibrated once per day, after allowing the tubing to condition by operating the system for approximately 45 min. Before and after experiments, an aqueous solution containing 20% propan-2-ol and 1% Brij-35 was pumped through the system to remove any accumulated debris or precipitates. All reagent and sample solutions were degassed in an ultrasonic bath prior to use.

RESULTS AND DISCUSSION

Consideration of the Apparatus. *Control of Concentration and Flow Rate.* Concentration, pH, and flow rate of the carrier streams were controlled by a set of peristaltic pumps operating under microcomputer control. In the general case of a system of n pumps, each pumping one component of a combined stream, the total flow rate of the combined stream is given by

$$U_T = \sum_{i=1}^{n} U_i \qquad (1)$$

where U_1–U_n are the flow rates of the individual streams and U_T is the flow rate of the combined stream for individual pumps

$$U_i = k_i f_i \qquad (2)$$

where k_i is the calibration factor for the pump and f_i is the pump speed setting. The concentration, C_i, of any component of the combined stream is given by

$$C_i = C_{s_i} U_i / U_T \qquad (3)$$

where C_{s_i} is the concentration of i, i.e., that in the individually pumped reagent stream before combination. Substitution of eq 2 into 3 and rearrangement give

$$f_i = U_T C_i / C_{s_i} K_i \qquad (4)$$

Equation 4 thus describes the pump speed settings required to give a desired concentration of each component at a certain overall flow rate. If the nth stream is used to pump distilled water as a diluent

$$U_n = U_T - \sum_{i=1}^{n-1} U_i \quad (5)$$

and

$$f_n = \frac{U_T - \sum_{i=1}^{n-1} U_i}{K_n} \quad (6)$$

Thus, the overall flow rate required can be reconciled with the concentration levels set for each component. In practice, the controlling program kept a check to ensure $U_n > 0$ and where necessary adjusted the concentrations of the other components to take account of this. Control of pH was effected by pumping a solution of Britton and Robinson's universal buffer as a fixed proportion of the total flow rate (to ensure consistent buffering action in all experiments), and pumping varying amounts of sodium hydroxide to produce varying pH values in the combined stream. This may be illustrated by considering a typical system of four streams, such as that used for the simplex optimization of isoprenaline.

In this case, the pumps were allotted as follows: 1, potassium ferricyanide 0.243 M; 2, sodium hydroxide 0.200 M; 3, Britton and Robinson's buffer; 4, water.

The flow rate of buffer was held constant at 40% of that of the total stream; thus

$$U_3 = 0.4U_T \quad (8)$$

The pH of a solution of Britton and Robinson's buffer is given by

$$\text{pH} = 3.91 + 0.0853V \quad (9)$$

where V is the volume of 0.2 M NaOH solution added to 100 mL of buffer solution.

This expression is equivalent to

$$U_2 = (\text{pH} - 3.91)U_3/8.53 \quad (9)$$

for a flowing stream of buffer with a flow rate of U_3 mL·min^{-1}.

Equation 3 gives U_1 and

$$U_4 = U_T - (U_1 + U_2 + U_3) \quad (10)$$

The corresponding pump speed settings are obtained by applying the appropriate factors (eq 2).

It was thus possible to control the concentration, pH and flow rate of the carrier stream. The alternative method of using fixed speed pumps and a number of manifolds of different bore tubing would have been less elegant and more difficult to automate.

Pump Control. Phase-locked loop frequency synthesis was used to generate pulses to control operation of the stepper motors. This method has the advantage of extreme stability, as the frequencies generated are exact multiples of a stable reference frequency—in this case the 1 MHz clock from the microprocessor bus, which is crystal-controlled. The resultant signals had a frequency of $n \times (10^6/2^{21})$ Hz, where n is a number in the range 0–255 specified by the control program. It was thus possible to control the speed of each pump to better than 0.5% resolution.

The alternative method of frequency synthesis—a digital to analog converter driving a voltage-controlled oscillator—would have been more costly and would have involved the use of analog circuitry with the attendant problems of noise and drift.

Injection Valve. The automatic injection valve was chosen for its suitability as a general purpose unit, suitable for use independently of the complete analyzer, and was based on a Rheodyne 5020 Teflon injection valve. The pneumatic actuator produced commercially for the Rheodyne valve was rejected in favor of a motor-driven actuator, thus obviating the requirement for a compressed air supply to power the unit. By use of interfacing facilities inside the unit for a sampling pump and a Chemlab CS40 autosampler, it was hoped to cater for a wide range of operating requirements.

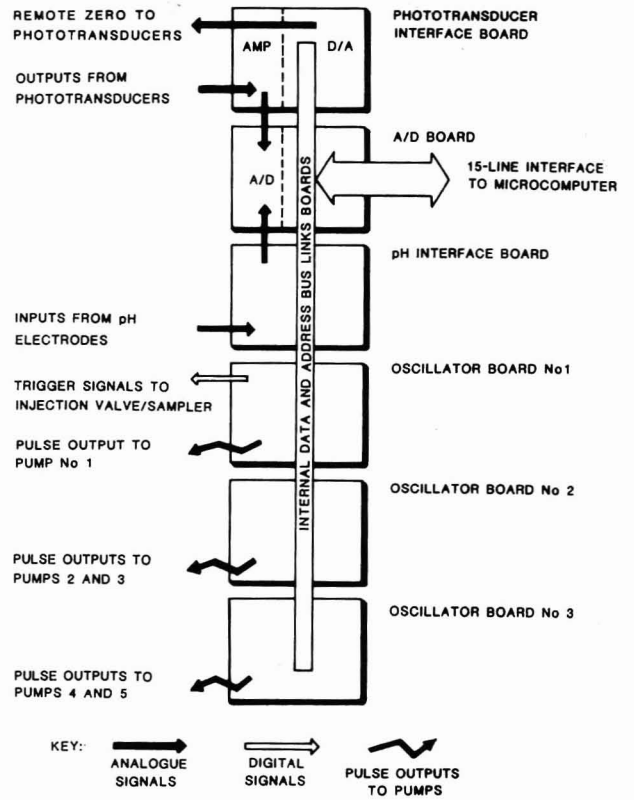

Figure 3. Arrangement of interfacing, control, and data acquisition circuits.

Detectors. The flow-through phototransducer (*9*) was chosen as a detector since it is reliable, simple, cheap, and well-suited to the requirements of FIA experiments, and was specifically designed to be used with a computer data acquisition system. They can also be used in series (*13*, *14*) for variable tube length experiments.

Facilities were also included to collect data from pH or selective-ion electrodes, both as an alternative means of peak detection for methods where colorimetric detection was not feasible and also as a means of following pH gradient experiments through the use of a flow-through pH electrode of low internal volume (*13*). However, these facilities have not so far been used.

Data Acquisition System. The computer interface and data acquisition system were designed to meet a number of criteria. The data acquisition system had to be capable of collecting data at medium speed with 12-bit resolution, from several different detectors. A circuit was developed based on Analog Devices' AD364 chip set, a 12-bit design that has a total of 16 inputs. One of these input channels was permanently connected to analogue ground as a check on the correct operation of the system. Six were connected to signal conditioning circuits, four accepted inputs from phototransducers, and two accepted inputs from pH or selective ion electrodes, while the remaining nine inputs are available for future expansion of the system. Were it necessary to use all 15 available inputs for a single application, perhaps for the multiple detector system described above, the signal conditioning boards could easily be removed and replaced, since all the circuits are housed on pull-out cards in a 19-in. rack. The arrangement of the control and data acquisition circuits is shown in Figure 3.

Interfacing between the computer and the data acquisition and control circuits was provided via a 15-line parallel in-

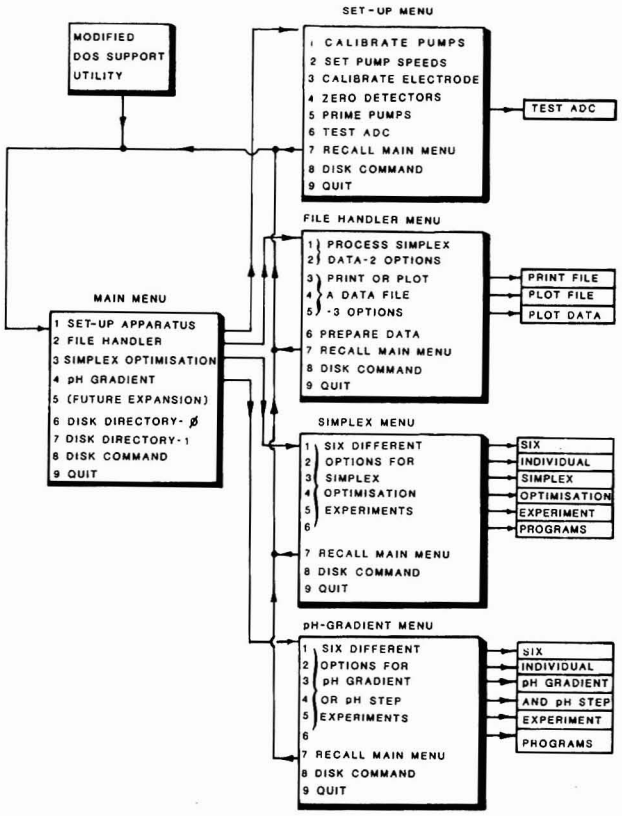

Figure 4. Schematic representation of software. Boxes indicate separate programs; items within a box indicate functions available from that program's menu. Arrows indicate calls possible between programs.

terface, consisting of 8 data lines, 3 address lines, a read/write select line, an enable line, the 1 MHz system clock, and digital ground.

The interface to the PET is achieved by use of one of the three expansion ROM sockets provided in the machine. Although each ROM socket occupies a 4K block of memory, only the lower 2K of this is available to a ROM placed in the socket. By combination of the chip select line from the ROM socket with an extra address line (A_{11}) to discriminate between the upper and lower 2K sections, it was possible to use the upper 2K for the interface with the experiment while retaining the lower 2K for use with an expansion ROM, if required. The remaining data, address, and control lines were merely buffered from the microprocessor bus.

The decision to directly memory-map the experimental interface in this way was based largely upon the simplicity of this arrangement, combined with extremely simple programming required to transfer data to and from the experiment via this route, particularly useful where assembly language programming is used for rapid data acquisition or pump control.

Software. The structure of the software is shown in Figure 4. Each routine was called from a menu of up to nine items displayed on the screen, simply by entering the number of the desired operation. The main system menu allowed the user to select the broad type of operation to be performed, which then caused the appropriate program to be loaded and run, which in turn offered the user a menu of the different options available within that area of operation, plus the option of returning to the main system menu in order to select another area of operation. The automatic calling of program and subroutines from the menu was achieved by using a method described by Hampshire (*15*), which allows direct commands (such as "load", "run", etc.) to be embedded within a program statement. Such an arrangement obviated the need for the user to remember the name of each of the several programs comprising the software suite or the location within each program of the various subroutines. Instead, an appropriate command was automatically generated by entering the menu number of the desired item.

Table I. Noise Levels and Precision of Isoprenaline Analysis[a]

FIA system		
manual	automated	
		Precision
1.4%	1.7%	with 1.25 mm path length flow cell
0.62%	0.53%	with 1.0 mm path length flow cell
		Noise Level
2.38%	2.38%	with 1.25 mm path length flow cell
0.31%	0.31%	with 1.0 mm path length flow cell

[a] Conditions: flow rate, 1.2 mL·min^{-1}; ferricyanide concentration, 3.41 mM; pH, 7.54; coil length, 95 cm.

The operating routines fell into several broad categories: (1) data acquisition/smoothing; (2) pump/valve control; (3) support programs (priming/calibration of apparatus, etc.); (4) experiment "master" programs—simplex optimization, pH gradient, etc. The software was structured so that as far as possible the data acquisition, pump control, and simplex optimization routines acted as software "black boxes", which could be linked together or with other routines to provide a complete operating program for a particular experiment with the minimum of reprogramming, as opposed to writing an entirely new operating program for each experiment. This modular approach to the software, coupled with the screen menu system, added greatly to the flexibility of the system as a whole, while simplifying its use.

Performance Criteria. One of the aims in creating a fully automated instrument was to improve upon the repeatabilty and precision of results obtainable by manual methods. At the outset of the project a target of 1% was set as the minimum acceptable precision for the automated analyzer, and experiments were subsequently undertaken to determine the precision and signal-to-noise ratio for the automatic system and for an equivalent manual system under identical conditions; the results are given in Table I. Figures were obtained for a series of ten identical samples; the mean peak height and sample standard deviation were calculated and the precision was expressed as twice the percentage relative standard deviation. Before and after the series of injections, the maximum variation in base line level was estimated and used to calculate a figure for noise level as a percentage of the mean peak height.

These results indicate that the target figure of 1% precision was easily met with a 10 mm path length flow cell (type a). In this case, the precision attained by the automated instrument bettered the figure obtained by manual experiments. Given the increased resolution and peak smoothing facilities embodied in the peak collection routine used in the automated system, this is perhaps to be expected. However, where the base line is comparatively poor, as was the case where the 1.25 mm path length flow cell was used, the precision obtained by the automatic analyzer was inferior to that gained by manual experiments, because the computational procedure was less effective than the human eye in discriminating the starting point of a peak against a noisy background.

Interestingly, however, even the automated system managed to determine peak heights to a precision better than the inherent base line noise level for the shorter path length detector, reflecting a basic soundness in the peak collection algorithm selected. The fact that the precision in the case of the longer path length cell was inferior to the detector noise level

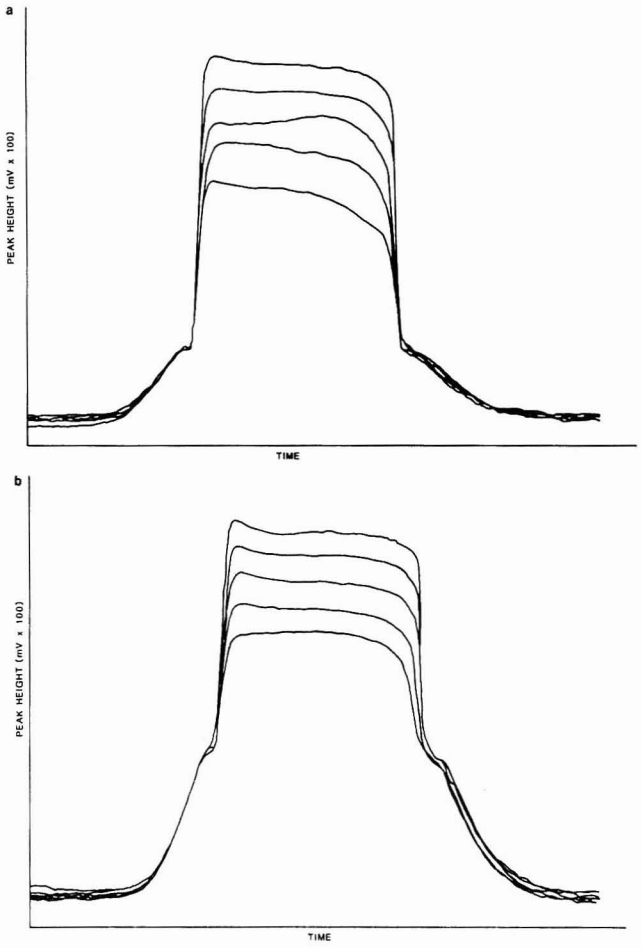

Figure 5. Successive peaks obtained for the simultaneous determination of mixtures containing (a) 2 ppm Co(II) and (b) 4 ppm Co(II), each with 2, 4, 6, 8, and 10 ppm Mn(II), respectively. Peaks have been superimposed to show more clearly the effect of changing concentration upon peak shape.

probably results from other sources of imprecision in the system, in the sample injection, control of flow rate, etc.

pH Gradient Experiment (Control of pH and Concentration). Similar peaks to those obtained by Betteridge and Fields (*11*, *12*) were obtained when experimental conditions were comparable. Figure 5 shows a number of representative peaks obtained under these conditions for various different concentrations of the Co(II) and Mn(II) samples. In all, 25 different sample combinations were used to produce composite peaks; only a small number are shown here, but the changes to peak shape with differing sample concentrations are clearly visible.

This experiment confirmed the capability of the apparatus to perform controlled chemical experiments. This was confirmed by the performance of automatic simplex optimization.

Automated Simplex Optimization. The system selected for optimization was the flow-injection analysis of isoprenaline, which has been thoroughly studied in our laboratory (*4*). The simplex algorithm was the same as that used previously; but the variables and the ranges were not identical. Then a four-variable and a five-variable optimization were carried out with pH, reagent concentration, flow rate, and tube length being variables to both sets of experiments and sample size being added to give the fifth. For the automated optimization only the first three were taken as variables. This meant that, with a fixed length of tubing between the points of injection and detection, the time dependency was concentrated in the flow rate variation.

Three sets of experiments were performed. The first was identical with the manual experiments. The improvement

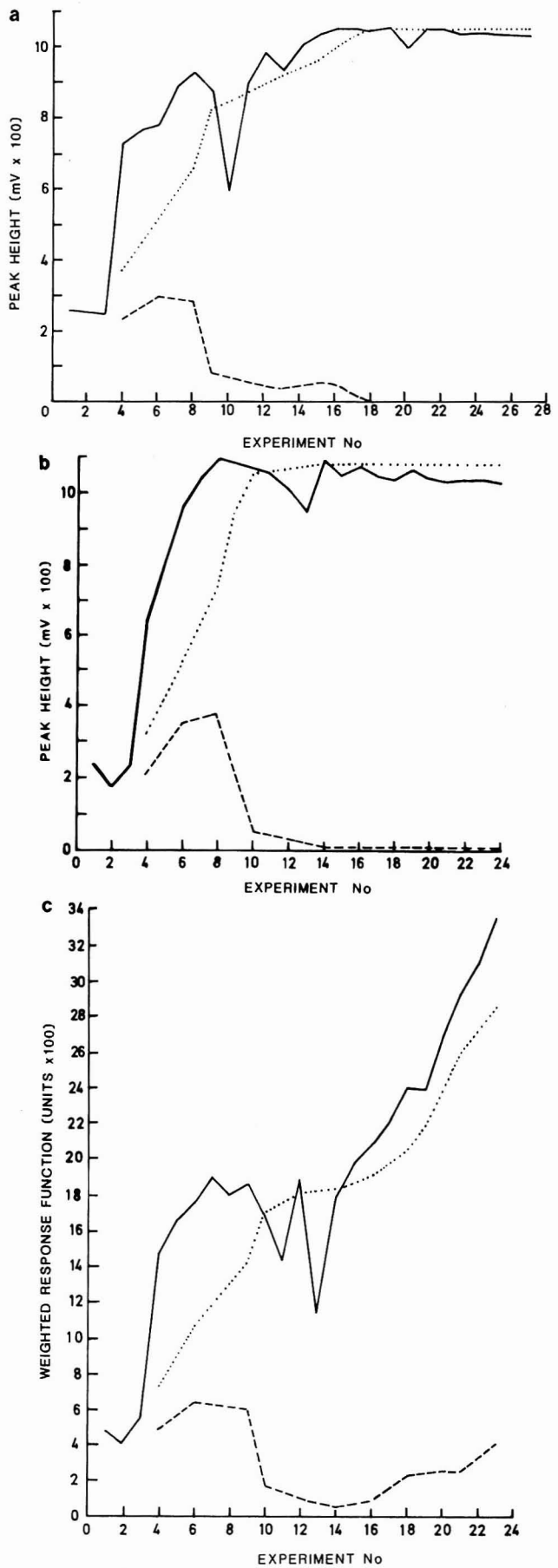

Figure 6. Graphs showing variation in response (solid line), mean response of points in simplex (dotted line), and standard deviation of responses of points in simplex (dashed line) for (a) initial simplex experiment, (b) repeat experiment using larger factor space, and (c) repeat experiment using larger factor space and weighted response function.

in sensitivity was rapid (Figure 6a) but there was a loss of dimensionality, since the simplex veered toward very slow flow rates. Possibly the loss of a time-sharing variable, i.e., coil length, contributes to this. Another optimization was carried out with a larger factor space and a satisfactory convergence was obtained (Figure 6b). The relative improvement in sensitivity obtained with the automated simplex optimization was identical with that from the manual method (4.56), but the optimum settings of the variables differed appreciably.

The coil length for the automated system was set to be the same as the optimum found in the manual experiments, 95 cm. The optimum settings for flow rate, pH, and reagent concentration were, respectively, 0.63 mL·min^{-1}, 7.40, and 7.36 mM for the automated method compared with 1.20, 7.54, and 3.41 for the manual. Thus the automated simplex arrived at settings of about half the flow rate and twice the reagent concentration. Given the nature of the response surface (*4*), which has a large plateau, these results are not inconsistent. However the sample throughput at the lower flow rate corresponds to 25 h^{-1}, which is well below normal FIA rates. Accordingly, a fresh optimization was carried out using an optimizing function which favored sample throughput and sensitivity. This was

$$R = H + 0.5(H + U_T) \quad (11)$$

where H is the peak height and U_T the flow rate. The response, R, is enhanced by increased sensitivity and flow rate.

The results of the 23 experiments carried out are shown in Table II. The last point gave a peak height 3.57 times greater than the initial starting conditions at a flow rate equivalent to 150 samples per hour. Thus although the objective function was crude, it was experimentally effective. Comparison of this with the optimization for sensitivity alone showed that for a trade-off in sensitivity of ca. 20%, a gain in sample throughput of 600% had been possible.

The automated apparatus carried out 15 simplex experiments per hour, whereas manually, only 3–4 had been possible.

The function used here was a suitable choice for this system since the absolute maximum value of U_T and likely maximum of H were known. It would not, however, be applicable to some other systems as increasing the flow rate for an experiment with zero sensitivity would still give a response "improvement". In such cases an equation of the form

$$R = H/(A + B(U_T - U_{T(ideal)})^2)$$

could be used, where A and B are constants that reflect the relative importance of H and U_T, and $U_{T(ideal)}$ is the objective flow rate. Further terms could be added to take sample size into account.

Table II. Sequential Simplex Opotimization Experiments[a]

	values used				
pt no.	flow rate	pH	reagent concn	rel improv	weighted response
1	3.22	6.88	0.29	1.00	485
2	2.94	6.86	0.21	0.72	410
3	2.51	7.37	0.24	1.04	555
4	2.52	7.05	1.33	2.77	1475
5	1.99	7.29	1.84	3.54	1665
6	1.53	7.44	2.8	4.22	1760
7	1.64	7.9	4.09	4.42	1900
8	1.4	8.14	5.89	4.49	1805
9	1.56	7.89	4.68	4.44	1865
10	1.1	7.87	6.12	4.59	1680
11	0.49	8.24	7.45	4.72	1425
12	2.01	7.43	2.74	3.99	1890
13	2.31	7.42	0.79	2.25	1145
14	1.41	7.76	4.75	4.46	1795
15	1.83	8.09	5.01	4.38	1980
16	1.96	8.3	6.21	2.90	2040
17	2.38	8.24	4.99	4.29	2215
18	2.86	8.47	5.12	4.18	2400
19	2.76	9.02	7.52	4.25	2390
20	3.61	0.039	7.85	4.06	2685
21	4.52	9.02	8.03	3.81	2930
22	5.09	8.74	7.13	3.69	3095
23	5.99	8.67	6.97	3.57	3365
1	3.22	6.88	0.29	1.00	485
2	2.94	6.86	0.21	0.72	410
3	2.51	7.37	0.24	1.04	555
4	2.52	7.05	1.33	2.77	1475
5	1.99	7.29	1.84	3.54	1665
6	1.53	7.44	2.8	4.22	1760
7	1.64	7.9	4.09	4.42	1900
8	1.4	8.14	5.89	4.49	1805
9	1.56	7.89	4.68	4.44	1865
10	1.1	7.87	6.12	4.59	1680
11	0.49	8.24	7.45	4.72	1425
12	2.01	7.43	2.74	3.99	1890
13	2.31	7.42	0.79	2.25	1145
14	1.41	7.76	4.75	4.46	1795
15	1.83	8.09	5.01	4.38	1980
16	1.96	8.3	6.21	2.90	2040
17	2.38	8.24	4.99	4.29	2215
18	2.86	8.47	5.12	4.18	2400
19	2.76	9.02	7.52	4.25	2390
20	3.61	0.039	7.85	4.06	2685
21	4.52	9.02	8.03	3.81	2930
22	5.09	8.74	7.13	3.69	3095
23	5.99	8.67	6.97	3.57	3365

[a] Weighted response = peak height + (1/2)(peak height, flow rate. Rel improv = improvement in peak height relative to starting conditions. Boundaries for variables were as follows: flow rate, 1.0 – 5.0 mL·min^{-1}; pH, 5–8; reagent concentration, 0.1–8.0 mM.

CONCLUSIONS

A number of conclusions can be drawn from these experiments. First the automated optimization procedure worked. Second, there is advantage in having an interactive optimization procedure. Third, the selection of response function is critical. Fourth, the automated system is faster and much less labor intensive.

Thus, overall the automated optimization procedure is advantageous, but, blind acceptance of its results is not desirable.

Future work will concentrate upon using the apparatus to optimize other analytical methods based on FIA, including further developments of the pH-gradient techniques described above, and the use of multiple detection systems for kinetic analyses and the automatic variation of effective reaction coil length. The optimization of continuous flow titration techniques is another area where this system may usefully be applied. Automatic optimizations including continuously variable sample size and reaction coil length have already been carried out (references to FACCS and unpublished work), and will be reported elsewhere.

LITERATURE CITED

(1) Ruzicka, J.; Hansen, E. H. *Flow Injection Analysis*; Wiley: New York, 1981.
(2) Betteridge, D. *Anal. Chem.* **1978**, *50*, 832A.
(3) Stewart, K. K.; Beecher, G. R.; Hare, P. E.; *Fed. Proc., Fed. Am. Soc. Exp. Biol.* **1974**, *33*, 1439.
(4) Betteridge, D.; Sly, T. J.; Wade, A. P.; Tillman, J. E. W. *Anal. Chem.* **1983**, *55*, 1292.
(5) Morgan, S. L., Deming, S. N. *Anal. Chem.* **1974**, *46*, 1170.
(6) Stieg, S.; Nieman, T. A. *Anal. Chem.* **1980**, *52*, 800.
(7) Janse, T. A. H. M.; Van der Wiel, P. F. A.; Kateman, G. *Anal. Chim. Acta* **1983**, *155*, 89.
(8) Stedman, G.; Bourke, G. C. M.; Wade, A. P. *Anal. Chim. Acta* **1983**, *153*, 277.
(9) Sly, T. J.; Betteridge, D.; Wibberley, D.; Porter, D. G. *J. Autom. Chem.* **1982**, *4*(4), 186.
(10) Britton, H. T. S.; Robinson, R. A. *J. Chem. Soc.* **1983**, 1456.
(11) Fields, B. Ph.D. Thesis, University of Wales, 1981.
(12) Betteridge, D.; Fields, B. *Anal. Chim. Acta* **1981**, *132*, 139–155.
(13) Betteridge, D.; Cheng, W. C.; Dagless, E. L.; David, P.; Goad, T. B.; Deans, D. R.; Newton, D. A.; Pierce, T. B. *Analyst (London)* **1983**, *108*, 1.

(14) Hooley, D. J.; Dessy, R. E. *Anal. Chem.* **1983**, *55*, 313.
(15) Hampshire, N. *The PET Revealed*; Hampshire Commodore Publications.

RECEIVED for review May 6, 1985. Resubmitted March 10, 1986. Accepted April 21, 1986. The authors are grateful to the Department of Trade & Industry for provision of a Studentship to T.J.S. and to the British Petroleum Co., Plc, for provision of a Studentship to A.P.W. and an extramural research award to T.J.S.

Indirect Atomic Absorption Determination of Anionic Surfactants in Wastewaters by Flow Injection Continuous Liquid–Liquid Extraction

Mercedes Gallego, Manuel Silva, and Miguel Valcárcel*

Department of Analytical Chemistry, Faculty of Sciences, University of Córdoba, Córdoba, Spain

A determination of anionic surfactants with an automatic continuous liquid–liquid extractor is reported in this paper. The method involves the formation of the detergent–[1,10-phenanthroline–copper(II)] ion pair and extraction into methyl isobutyl ketone. The overall concentration of anionic surfactants can be determined indirectly by measurement of copper present in the organic layer by atomic absorption spectrometry. A phase separator fitted with a PTFE porous membrane was specially designed for the determination. The optimum experimental conditions for determining detergents in the concentration range 0.1–5.0 μg/mL are described. The relative standard deviation found was 0.8%. The method is highly selective and free from the interference of nonionic surfactants and has been applied to the determination of anionic surfactants in wastewaters. The results show good agreement with those obtained by the classical methylene blue method.

The determination of anionic surfactants in water by atomic absorption spectrometry (AAS) has been reported by several authors (*1–7*). The methods applied for this purpose are based on the ion-pair extraction of anionic surfactants with a cationic complex such as ethylenediamine–copper(II), 1,10-phenanthroline–copper(II), thiourea–copper(I), and so on.

The flow injection analysis (FIA) technique constitutes a major alternative to manual methods of analysis as it is a simple, inexpensive, versatile, and easy to manipulate continuous-flow analysis mode (*8, 9*). Continuous liquid–liquid extraction based on the flow-injection principle was simultaneously introduced by Karlberg et al. (*10*) and Bergamin et al. (*11*). Over 30 papers have been published on this topic up to now (*9*). Kina et al. (*12*) have determined anionic surfactants by FIA based on the fluorescence-diminishing reaction of acridine orange–10-dodecyl bromide in an aqueous solution. Other authors have carried out this determination by an extraction spectrophotometric method with a flow injection system. These methods are based on the ion-pair extraction of anionic surfactants and methylene blue (*13*) or on the ion-pair formation between anionic surfactants and the cationic dye ethyl violet, followed by extraction into toluene (*14*).

The advantages of the AAS-FIA association have been recently praised by several authors (*15–18*). We have recently made use of the association AAS-FIA in conjunction with liquid–liquid extraction as a separation technique for the indirect determination of perchlorate in human urine and serum samples (*19*) and nitrate and nitrite in meats (*20, 21*).

This paper describes a simple and accurate method for determination of anionic surfactants in wastewaters which involves continuous extraction of the compound formed between the detergent and the sulfate of the 1,10-phenanthroline–copper(II) complex into isobutyl methyl ketone and determination of copper in the extract by AAS.

EXPERIMENTAL SECTION

Apparatus and Procedure. A schematic diagram of the flow injection system used is shown in Figure 1. A four-channel peristaltic pump (Gilson Minipuls-2) was fitted with Tygon pump tubes for aqueous or organic solutions. For the latter, this pump was coupled on-line with two displacement bottles as shown in Figure 1. Another peristaltic pump was used to transport the organic extract injected as an undispersed plug to the nebulizer of the atomic-absorption spectrometer (AAS). A Rheodyne 5301 diverting valve was used to change the sample solution in order to avoid the introduction of air into the system. A variable-volume Tecator L100-1 injection valve (I), an A-10T solvent segmentor (S Sg) (Bifok) and an extraction coil (EC) were also used.

The membrane phase separator (PS) (Figure 2) was designed as follows: the Teflon body consists of an inlet and two outlets (bore 0.5 mm i.d.) and a separating chamber (approximate volume 60 μL). The three-threaded hole accepted the standard polypropylene end pieces and flaired Teflon tubing. During operation, the two blocks were pressed together with six screws and aluminum end plates. Alignment was achieved with the aid of two stainless steel pins. Two layers of Fluoropore membranes (1.0 μm pore size, FALP 04700, Millipore) permeable to methyl isobutyl ketone (MIBK) but impermeable to the aqueous solution were sandwiched between the two main body pieces. Both porous membranes were wetted with methyl alcohol prior to use according to the manufacturer's instructions.

A Perkin-Elmer 380 atomic absorption spectrometer equipped with a copper hollow cathode lamp working at 324.7 nm (spectral band-pass 0.7 nm) and using air–acetylene flame was employed in combination with a multirange Radiometer REC 80 recorder.

With the manifold described above and under the optimum instrumental conditions, a sodium dodecyl sulfate sample solution (0.1–5.0 μg/mL) of pH 2.8–10.0 was pumped continuously into the system and mixed with the carrier solution. A stream of MIBK obtained by pumping water into a displacement bottle B_1 filled with MIBK as well as the mixed sample–carrier solution stream were segmented in the solvent segmentor, resulting in a regular pattern of alternative aqueous and MIBK segments. The extraction process took place in the extraction coil and a fraction of the extract, controlled by bottle B_2, was separated in the membrane phase separator. The determination was affected by

0003-2700/86/0358-2265$01.50/0 © 1986 American Chemical Society

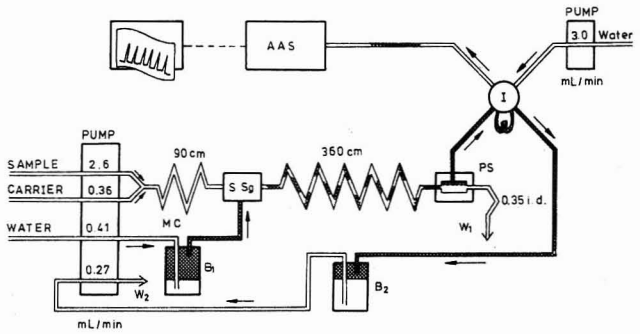

Figure 1. Flow diagram for the determination of anionic surfactants. All tubes are made of Teflon (0.5 mm i.d., except where specified).

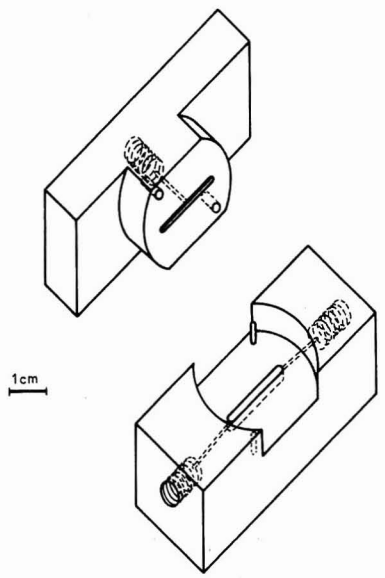

Figure 2. Drawing of the membrane phase separator. For details, see text.

injecting a 135-μL organic extract with injector I into the water stream from the Ismatec peristaltic pump, which was subsequently introduced into the atomic absorption spectrometer. The signal from extracted copper yielded the FIA peaks, the height of which was proportional to the detergent concentration. The calibration curve was obtained by linear regression analysis.

Reagents and Chemicals. All chemicals were reagent grade. A 0.01 M 1,10-phenanthroline–copper(II) complex solution was prepared by dissolving 1.760 g of 1,10-phenanthroline chloride monohydrate and 0.624 g of copper sulfate pentahydrate in 250 mL of distilled water. This solution remained stable for at least 1 month. Sodium dodecyl sulfate (LAS, 99%, Sigma) and sodium dioctyl sulfosuccinate (Manoxol O.T., 96%, Aldrich-Chemie) stock solutions (1.000 g/L) were prepared in distilled water. All these solutions were stored in a refrigerator to minimize biodegradation.

The carrier solution was prepared by mixing 10 mL of 0.01 M complex reagent and 10 mL of 1 M acetic acid/1 M sodium acetate buffer (pH 4.75) and diluting to 100 mL with distilled water.

RESULTS AND DISCUSSION

The automation of the batch procedure for the indirect determination of anionic surfactants by AAS (*22*, *23*) associated to a flow injection technique is linked to factors such as the flow injection and chemical variables, which must be fixed and studied in order to obtain more accurate and reproducible results.

Influence of Chemical Variables. The plots of absorbance vs. pH for LAS and carrier solutions show a plateau over the ranges 2.8–10.0 and 4.0–9.1, respectively (Figure 3). Hence, 10 mL of 1 M acetic acid/1 M sodium acetate buffer (pH 4.75) was added to 100 mL of carrier solution.

The concentration of the 1,10-phenanthroline–copper(II) complex in the carrier solution was varied from (0.1 to 5.0)

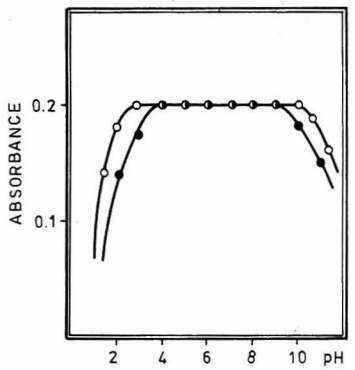

Figure 3. Influence of the pH on the absorbance (O) of the sample solution (pH of the carrier is kept constant at 5.6) and (●) of the carrier solution (pH of the sample is kept constant at 4.9). In both experiments the LAS concentration was 2.0 μg/mL.

$\times 10^{-3}$ M while the LAS concentration was kept constant at 2.0 μg/mL. Peak height increased rapidly until a constant value was obtained at about 0.5×10^{-3} M. At concentrations higher than 2.0×10^{-3} M the peak height increased owing to the increase in the blank signal, owing to the appreciable extraction of carrier anion (acetate). However, with this or smaller concentrations of the 1,10-phenanthroline–copper(II) complex, the effect of the blank was negligible and its measurement could therefore be avoided in the experimental procedure. Thus, a concentration of 1.0×10^{-3} M of this variable was selected for use in the determination of surfactant traces.

The influence of the chloride ion on the extractability of the ion pair was also studied. In the bath procedure, this variable shows a stronger influence on the extraction of the anionic surfactant. Thus, the chloride concentration in the samples must be above 2.5×10^{-2} M when the copper(II) complex concentration is 1.5×10^{-3} M in order to obtain an extraction efficiency of about 95% (*22*, *23*). The effect of chloride ion in this bath procedure can be attributed to its breaking effect on the emulsions originated during the manual extraction process. In the FIA technique, the chloride ion does not affect the extraction efficiency even at 0.25 M concentrations and its addition to the samples is therefore unnecessary. When the surfactant distribution process is carried out by this technique, no emulsions are probably originated between the two phases in the extraction coil since mixing was more gentle.

Selection of Flow Injection Variables. The number of possible flow rate combinations in the extraction system is quite large since several of the flows can be varied individually. Thus, a systematic investigation was necessary in order to find the optimum conditions for the extraction so that a high concentration ratio of the sample could be achieved without detracting from precision.

In this study, the carrier flow rate was kept at 0.14 of the sample flow rate in order to avoid excessive dilution of the continuously pumped sample. Thus, the liquid–liquid extraction process was only linked to the flow rates of the sample and organic phase. Figure 4A shows the effect of varying the sample flow rate while keeping the flow rate of the organic phase constant. This study was carried out by using a membrane phase separator as well as T-shaped separator (A4T-connector, Technicon, Tarrytown, NY) in order to compare their performance in this distribution process. The absorbance increased as the flow ratio of sample to organic phase increased up to a value of 10 for the membrane phase separator and 7.8 for the T-shaped one and decreased at higher values. Figure 4B shows the dependence of the absorbance on the flow ratio (aqueous/organic phase) when the aqueous flow rate is kept constant. The absorbance increases as the flow rate of the

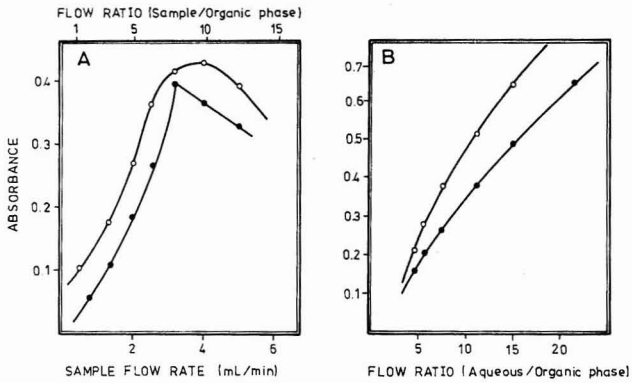

Figure 4. Flow rates in the extraction system and comparison between phase separators: (O) present membrane phase separator; (●) T-shaped phase separator. (A) Organic phase flow rate: 0.41 mL/min; the carrier flow rate is kept at 0.14 × sample. (B) Sample flow rate: 2.6 mL/min; carrier flow rate 0.36 mL/min. (Extraction coil, 360 cm long, 0.5 mm i.d., coil diameter 4 cm).

organic phase decreases. This decrease is limited by the dissolution of MIBK in the aqueous phase. We chose a sample flow rate of 2.6 mL/min and an organic-phase flow rate of 0.41 mL/min, taking into account the mutual influence of three factors: reproducibility, concentration ratio, and sampling frequency.

Finally, the performance of both phase separators used in this work was compared and the following conclusions can be drawn. (a) Both approaches showed a similar dependence on the flow rates although the separation efficiency was higher when the separation of the phases was carried out with the membrane phase separator (79% for T-shaped with regard to the membrane separator). (b) The introduction of air into the extraction system, for example, when a sample was changed, did not affect the performance of the T-shaped phase separator. However, the performance of the membrane phase separator was greatly affected by this factor. Thus, air goes through the membrane and occupies dead volumes in the joints, injection valve, etc., which results in irreproducible measurement until its complete removal from the system, which in turn redounds to decreased sampling rate. This problem could be easily avoided by using a diverting valve. (c) The total lifetime of the Teflon porous membrane was such that its aging originated a break in the continuous liquid–liquid extraction process and therefore had to be changed. In this work two 1.0 μm pore size Fluoropore membranes (total lifetime between 2 and 3 h) were selected instead of two 0.5 μm pore size PTFE membranes (total lifetime between 1 and 2 h) because of their longer lifetime. When a single membrane was used, the total lifetime is decreased by one-third in both cases.

The influences of other variables related to the solvent extraction process were also investigated: mixing coil and extraction coil characteristics and injected sample volume. In all studies the sample solution used contained 1.0 μg/mL LAS.

The tube length between the mixing point for the sample and the carrier stream and the solvent segmentor did not affect the FIA peak at values above 40 cm for an inner diameter between 0.35 and 0.70 mm.

The extraction coil length was varied from 40 to 750 cm while the flow rate ratio was maintained constant. A plot of the peak height vs. the extraction coil length showed that the height of the FIA peak increased with increasing extraction coil length up to 250 cm; in the range 250–500 cm, the peak height was not affected by the length of the extraction coil, whereas at larger values the FIA peak started to decreased slightly. In order to keep precision as high as possible, an extraction coil length of 360 cm was selected. Several other characteristics of the extraction coil are also worth mentioning:

Table I. Features of the Calibration Graphs for the Determination of LAS Using T-Shaped and Membrane Phase Separators

phase separator	range, μg/mL	slope, A mL/μg	intercept, A	corr coeff (n = 7)
T-shaped	0.1–5.0	0.0743	1.73×10^{-3}	0.998
membrane	0.1–7.0	0.1019	2.17×10^{-3}	0.999

(a) Inner diameters between 0.35 and 0.70 mm did not affect the absorbance when the volume of the extraction coil was kept constant at 700 μL. An inner diameter of 0.5 mm was selected. (b) Coil diameters up to 60 mm had no influence on the absorbance. A coil diameter of 40 mm was chosen for further investigations.

The extracted sample volume injected into the water line exerted a significant effect on the absorbance. The signal increased with increasing injected sample volume up to 90 μL and remained constant for larger volumes, up to 360 μL. An injection volume of 135 μL was chosen for all subsequent studies. Neither back-extraction nor dispersion of the organic plug occurred since identical results were obtained when the organic phase was aspirated continuously in other experiments.

Determination of Trace Levels of Anionic Surfactants. The features of the calibration graphs (absorbance vs. μg/mL) run for several surfactant standards (LAS and Manoxol O.T.) assayed with the proposed flow injection system and using the T-shaped and membrane phase separators are shown in Table I. The lesser sensitivity obtained with the T-shaped separator is in agreement with the results obtained in the study of the flow rate ratio and depends on its separation efficiency.

The extraction efficiency was calculated by means of a series of experiments in which the flow-injection method was compared with the batch method, in which, under the same experimental conditions as in the flow method, both phases (aqueous/organic phase volume ratio = 7.2) were brought to equilibrium in a funnel for 5 min, and the organic extract was aspirated into an air–acetylene flame. The value found was 95% with regard to the batch method.

Some other characteristics related to the determination of surfactants were also studied. (a) The detection and quantification limits (45 and 150 ng/mL, respectively) were calculated as 3-fold or 10-fold, respectively, the standard deviation of the peak height for 30 injections of the same sample (*24*). (b) The precision of the method was checked on 11 samples containing 1.0 μg/mL each. The relative standard deviation was 0.8%. (c) The sampling frequency was 40 ± 5 h^{-1}.

Finally, it is noteworthy that the proposed method is suitable for the determination of the overall concentration of unknown anionic surfactant mixtures which is corroborated by two facts: (a) the slopes of their calibration curves for LAS and Manoxol O.T. are identical when both are plotted as absorbance vs. molar concentration; and (b) good agreement is found between the methylene blue method and the one proposed herein when the flow injection method is applied to the determination of anionic surfactants in wastewaters.

The effect of many common species associated with anionic surfactants in real samples was examined to find possible interferences. The tolerances to the species investigated are given in Table II. Foreign species were added at a maximum level of 1000 μg/mL (tolerated ratio to LAS, 1000). The tolerance ratio of each foreign species was taken as the largest amount yielding an error less than ±3% in the peak height for 1.0 μg/mL of LAS.

The substances assayed in this study of interferences can be classified in four groups: (a) ionizable organic compounds such as glutamic acid, succinic acid, phenol, etc., which can

Table II. Tolerance Limits for Foreign Ions in the Determination of 1.0 μg/mL of Anionic Surfactant

tolerance limit of ion to LAS	foreign ion
1000	Na(I), K(I), Ca(II), Mg(II), Co(II), Pb(II),[a] Al(III),[a] SO_4^{2-}, SO_3^{2-}, $S_2O_3^{2-}$, PO_4^{3-}, $P_2O_7^{4-}$, $P_3O_{10}^{5-}$, CO_3^{2-}, $C_2O_4^{2-}$, NO_3^-, F^-, Cl^-, Br^-, $B_4O_7^{2-}$, ClO_3^-, BrO_3^-, IO_3^-, AsO_4^{3-}, S^{2-},[b] citrate, tartrate, glutamic acid, succinic acid, phthalic acid, phenol
500	benzoic acid
250	Ni(II), Triton X-100
100	Brij
25	Zn(II), Fe(III), I^-, ClO_4^-

[a] Using a microfilter. [b] With 3 mL of 30% (v/v) hydrogen peroxide.

Table III. Comparison of Interferences between the FIA Technique and the Batch Procedure Using the Copper–Phenanthroline Method

	tolerance ratio of ion to LAS	
foreign ion	FIA method	batch method
PO_4^{3-}, SO_4^{2-}	1000	1000
NO_3^-	1000	<5
Br^-	1000	50
Co(II)	1000	<50
phthalic acid	1000	50
succinic acid	1000	50
glutamic acid	1000	50
benzoic acid	500	50
Ni(II)	250	<50
Triton X-100	250	5
I^-	25	10
ClO_4^-	25	<5

form ion pairs with 1,10-phenanthroline–copper(II) complex; (b) inorganic cations such as Co(II), Ni(II), Zn(II), and Fe(III), which can replace copper(II) in the complex; (c) inorganic anions (ClO_4^-, I^-, NO_3^-, etc.) that can originate a positive interference through extraction as ion pairs with the copper complex, and (d) inorganic anions such as oxalate and thiosulfate, which can form soluble copper complexes and therefore destroy the 1,10-phenanthroline–copper(II). In general, these species can be tolerated at higher concentrations in the flow injection method (1000 μg/mL) and only Zn(II), Fe(III), iodide, and perchlorate cause serious interferences, although at a high level (tolerance ratio to LAS, 25).

As can be observed in Table III the FIA method offers better selectivity with respect to the batch method for LAS both using phenanthroline method. This is probably due to the fact that the experimental conditions are optimized for a given analyte, LAS, and the effect of other species is less apparent as their interference is lessened by the short time over which both phases remain in contact. Thus, the increase in selectivity can be attributed to a kinetic factor. Thus, in the flow injection method, nitrate, bromide, iodide, perchlorate, and organic compounds can be tolerated at higher ratios. Furthermore, it is noteworthy the high level of tolerance to nonionic surfactants in the flow injection method, which will permit the resolution of anionic/nonionic surfactant mixtures in further experiments.

Application to Wastewater Samples. The flow injection method was satisfactorily applied to the determination of total anionic surfactant in wastewaters. The pH of the samples must be fixed between 2.8 and 10.0 and if appreciable amounts of suspended matter are present in sample, they should be removed by filtering through glass wool. On the other hand, in order to prevent the possible interference from sulfur compounds, 3 mL of 30% (v/v) hydrogen peroxide was added to 1–40 mL of wastewater sample in all cases in a final volume of 50 mL. These solutions were analyzed as described above.

Table IV. Determination of Total Anionic Surfactants in Wastewaters by the Proposed FIA Method and the Methylene Blue Method

sample no.	FIA method,[a] μg/mL	methylene blue method,[a] μg/mL
1	6.04 ± 0.04	6.5 ± 0.6
2	17.23 ± 0.03	18 ± 2
3	21.6 ± 0.1	22 ± 2
4	10.52 ± 0.02	9.5 ± 0.9
5	1.61 ± 0.02	1.4 ± 0.2
6	5.02 ± 0.03	4.9 ± 0.5
7	57.0 ± 0.5	61 ± 5
8	2.90 ± 0.03	3.7 ± 0.4
9	26.3 ± 0.4	27 ± 3
10	2.39 ± 0.01	2.2 ± 0.3
11	6.26 ± 0.02	7.0 ± 0.6
12	4.08 ± 0.07	4.4 ± 0.4
13	3.15 ± 0.07	3.1 ± 0.4

[a] ± standard deviation.

Table IV shows the results found by the proposed method compared with those obtained by the standard methylene blue method (*25*). It can be concluded that the flow injection method is simple and more rapid (the methylene blue method requires three extraction steps per sample) and precise than the standard methylene blue method.

Advantages of the FIA Method over the Batch Procedure Using the Copper(II)–1,10-Phenanthroline Method. It has been shown that total anionic surfactant concentrations in the μg/mL range can be determined by continuous flow extraction using a flow injection atomic absorption detection system. The method compares favorably with the batch one and has the following advantages, which can be classified in two groups:

(1) Inherent in the FIA technique: (a) small sample volume and low sample and reagent consumption; (b) ease of automation; (c) higher sampling frequency (two extraction steps are necessary in the batch method) and (d) low cost per determination.

(2) Specific advantages: (a) wide pH range; (b) the addition of chloride ion is unnecessary; (c) no blank is required; (d) higher sensitivity (0.1 mL/μg for the FIA technique and 0.06 mL/μg for the batch procedure); (e) higher selectivity and precision (RSD).

Registry No. 1,10-Phenanthroline, 66-71-7; water, 7732-18-5.

LITERATURE CITED

(1) Gagnou, M. J. *Water Res.* **1978**, *13*, 53.
(2) Matsueda, T.; Marimoto, M. *Bunseki Kagaku* **1980**, *29*, 769.
(3) Matsueda, T. *Bunseki Kagaku* **1981**, *30*, 375.
(4) Benoit, O.; Lamathe, J. *Bull. Liaison Lab. Ponts Chausses* **1981**, *115*, 25.
(5) Adachi, A.; Kobayashi, T. *Eisei Kagaku* **1982**, *28*, 43 and 99.
(6) Nakamura, E.; Fujisawa, I.; Namiki, H. *Bunseki Kagaku* **1983**, *32*, 332.
(7) Sourova, J.; Suchanova, V. *Vodni Hospod. B* **1983**, *33*, 82.
(8) Ruzicka, J.; Hansen, E. H. *Flow Injection Analysis*; Wiley: New York, 1981.
(9) Valcárcel, M.; Luque de Castro, M.D. *Flow Injection Analysis. Principles and Applications*; Ellis Horwood: Chichester, in press.
(10) Karlberg, B.; Thelander, S. *Anal. Chim. Acta* **1978**, *98*, 1.
(11) Bergamin, F. H.; Medeiros, J. X.; Reis, B. F.; Zagatto, E. A. G. *Anal. Chim. Acta* **1978**, *101*, 9.
(12) Kina, K.; Ichisima, S.; Ishibashi, N. *Abstr. 37th Annu. Meeting Chem. Soc. Jpn. Proc.* **1978**, *14*, 3A35.
(13) Kawase, J.; Nakae, A.; Yamanaka, M. *Anal. Chem.* **1979**, *51*, 1640.
(14) Hirai, Y.; Tomokuni, K. *Anal. Chim. Acta* **1985**, *167*, 409.
(15) Gallego, M.; Luque de Castro, M. D.; Valcárcel, M. *At. Spectrosc.* **1985**, *6*, 16.
(16) Tyson, J. F.; Adeeyinwo, C. E.; Appleton, J. M. H.; Bysouth, S. R.; Idris, A. B.; Sarkissian, L. L. *Analyst (London)* **1985**, *110*, 487.
(17) Sweileh, J. A.; Cantwell, F. F. *Can. J. Chem.* **1985**, *63*, 2559.

(18) Sweileh, J. A.; Cantwell, F. F. *Anal. Chem.* **1985**, *57*, 420.
(19) Gallego, M.; Valcárcel, M. *Anal. Chim. Acta* **1985**, *169*, 161.
(20) Gallego, M.; Silva, M.; Valcárcel, M. *Fresenius' Z. Anal. Chem.* **1986**, *323*, 50.
(21) Silva, M.; Gallego, M.; Valcárcel, M. *Anal. Chim. Acta* **1986**, *179*, 341.
(22) Le Bihan, A.; Courtot-Coupez, J. *Bull. Soc. Chim. Fr.* **1970**, *1*, 406.
(23) Le Bihan, A.; Courtot-Coupez, Analusis **1973–1974**, *2*, 695.
(24) Wolf, W. R.; Stewart, K. K. *Anal. Chem.* **1979**, *51*, 1201.
(25) *Standard Methods for Examination of Water and Waste Waters*, 15th ed.; American Public Health Association: Washington, DC, 1980; pp 530–532.

RECEIVED for review September 25, 1985. Resubmitted February 4, 1986. Accepted April 15, 1986.

Solvent Extraction Studies of Lanthanum(III) and Neodymium(III) with Ionizable Macrocyclic Ligands and Thenoyltrifluoroacetone

V. K. Manchanda[1] and C. Allen Chang*

Department of Chemistry, University of Texas at El Paso, El Paso, Texas 79968-0513

Extraction behavior of La(III) and Nd(III) has been investigated by using thenoyltrifluoroacetone (TTA) as extractant in the presence of 1,7-diaza-4,10,13-trioxacyclopentadecane-*N*,*N*′-diacetic acid (DAPDA) and 1,10-diaza-4,7,13,16-tetraoxacyclooctadecane-*N*,*N*′-diacetic acid (DACDA) as macrocyclic ionophores. DAPDA and DACDA were chosen in this work in view of their unique complexation toward lanthanides. Ultraviolet spectra were adduced for the formation of ternary complex La(DAPDA)TTA in the aqueous phase. It was observed that $Ln(TTA)_3$ is the dominating species extracted at pH ≤5.0 and Ln(DAPDA/DACDA)TTA is the dominating species at pH ∼7.5. Extraction of ternary complex of La(III) was found to be greater in the case of DAPDA and smaller in the case of DACDA as compared to the extraction of the corresponding ternary complex of Nd(III). By use of the stoichiometric concentration of DAPDA/DACDA and following distribution as a function of pH, lanthanide extraction maxima were observed at pH 7.5–8.0. Finally, the analytical significance of the work is discussed.

Development of suitable separation procedures of trivalent lanthanides from actinides has drawn the attention of analytical chemists since the advent of nuclear industry (*1*, *2*). Their role in the disposal of nuclear waste to the environment was recognized during the early years of nuclear power production (*3*, *4*). Subsequently, this area received further impetus with the increasing application of transuranium elements in industry and research (*5*). On the other hand, continued studies on the properties of lanthanide compounds have revealed their interesting applications as laser materials (*6*), as catalysts (*7*), and as shift reagents in nuclear magnetic resonance spectroscopy (*8*) and in magnetohydrodynamics (*9*).

Multistage extraction is usually necessary for the separation of adjacent lanthanides in solvent extraction methods employing neutral phosphorus reagents, monoacidic orthophosphates, β-diketones, and tertiary/quaternary ammonium ion species. One of the most common extractants employed at present for the separation of lanthanides from each other as well as from actinides is bis(2-ethylhexyl)phosphoric acid (HDEHP), which suffers from another drawback due to its limited solubility in the organic phase (*10*).

During the last few years interest has been focused in our laboratory on the development of ionizable macrocyclic ionophores selective toward lanthanides. It was found that both 1,7-diaza-4,10,13-trioxacyclopentadecane-*N*,*N*′-diacetic acid (K21DA or DAPDA) and 1,10-diaza-4,7,13,16-tetraoxacyclooctadecane-*N*,*N*′-diacetic acid (K22DA or DACDA) shown in Figure 1 form stronger lighter lanthanide complexes with the former being slightly selective toward the Eu(III) ion (*11*, *12*). These reagents form monovalent cationic complexes with trivalent lanthanides, and in a recent communication (*13*) we have demonstrated the possibility of ternary complex formation involving these cationic species and the acetylacetonate anion. It is therefore of particular interest to develop extraction procedures employing ion-specific macrocyclic compounds capable of selective complexation of lanthanides.

Due to the favorable partition coefficient and dissociation constant, thenoyltrifluoroacetone (TTA) was used as the more suitable extracting agent instead of acetylacetone (*14*). La(III) and Nd(III) were chosen as metal ions in this work as typical representatives of early members of the lanthanide series. Apart from using macrocyclic ionophores as selective complexing agents, ethylenediamine-*N*,*N*′-diacetic acid (EDDA), a noncyclic polyaminopolycarboxylic acid with similar functional groups, was also included in the present study for comparison purposes.

EXPERIMENTAL SECTION

Reagents. DAPDA and DACDA were synthesized and purified in our laboratory by the procedure reported earlier (*11*). Analytical reagent grade EDDA and EDTA were purchased from Spectrum Chemical Manufacturing Corp. and Mallinckrodt, Inc., respectively. Nitrates of lanthanum and neodymium used were supplied by Aldrich Chemical Co. and Alfa Products, respectively. Standard metal salt solutions (0.01 M) were prepared by titrating them against standard EDTA solution using xylenol orange as indicator. Thenoyltrifluoroacetone (TTA, laboratory reagent grade) was obtained from Aldrich Chemical Co. and its purity was confirmed by melting point determination and measurement of acid dissociation constant. Spectroscopic grade benzene was used as organic diluent.

Distribution Studies. The aqueous phase contained 1.6×10^{-4} M metal ion, 1.6×10^{-4} M DAPDA/DACDA and the ionic strength was adjusted to 0.2 M with tris(hydroxymethyl)aminomethane (Tris) buffer and tetramethylammonium chloride. Varying proportions of tris(hydroxymethyl)aminomethane and hydrochloric acid were used to form buffers in the pH range 6.5–9.0. It was required to adjust the ionic strength of Tris buffer

[1] On leave from Radiochemistry Division, B.A.R.C., Bombay, India.

0003-2700/86/0358-2269$01.50/0 © 1986 American Chemical Society

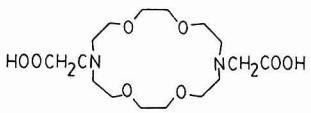

1. dacda (K22DA)

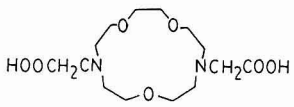

2. dapda (K21DA)

Figure 1. Structures of DAPDA and DACDA.

to at least 0.2 M, in view of its low buffer capacity particularly in the region below pH 7.5 and above pH 8.5. Acetic acid/tetramethylammonium hydroxide buffer was employed for adjusting the pH of aqueous phase in the range 4.7–6.0 (acetate concentration of ~0.01 M and ionic strength of 0.1 M, adjusted with $(CH_3)_4N^+Cl^-$ was used). The organic phase contained varying concentrations of TTA in the range 8.3×10^{-4} M to 1.0×10^{-2} M in benzene. A volume of each phase was maintained at 6.0 mL. Equilibration was carried out for 10–12 h on a Burrell wrist shaker followed by settling of the two phases for 1 h. Two phases were separated thereafter avoiding carefully any cross contamination. Prolonged shaking was done for the purpose of convenience though equilibrium was reached much earlier, and the equilibrium distribution ratio obtained did not decrease with additional time allowed. The pH of the aqueous phase was measured by using a Fisher combination pH electrode and a Fisher Model 825 MP pH meter. Acidity of the aqueous phase was adjusted to ~0.1 M by adding 0.05 mL of concentrated HCl to approximately 5.0 mL of the aqueous phase.

Concentration of lanthanide ion in the aqueous phase was measured by dc plasma emission spectroscopic technique, using a Beckman Spectrospan VI spectrometer equipped with an instrument computer and a dataspan computer. The spectrometer combines a high-energy dc plasma excitation source with a high-resolution echelle grating. Liquid samples were converted to aerosol form and introduced into the excitation region. The echelle grating and prism in the optics module separate the emitted light into its component wavelengths. In the present work, intensites of emitted light at 408.672 nm and 406.109 nm were measured for the determination of lanthanum and neodymium concentrations, respectively.

The dc plasma emission instrument was calibrated using five standards of the lanthanide ion in 0.1 M HCl medium covering the concentration range of most of the samples analyzed (0.1–30 ppm). Acetate was found to interfere seriously with La (408.672 nm) as well as with Nd (406.109 nm) peaks. When the total lanthanide concentration in the aqueous phase was 1.8×10^{-3} M, the EDTA titration method was used to determine the remaining lanthanide concentration after the distribution experiment using xylenol orange as the indicator.

Occasionally, the organic phase was equilibrated with 1 M HCl and the concentration of stripped lanthanide ion was obtained by the dc plasma emission technique. Material balance within ±5% was obtained in all experiments carried out at pH 7.5 in the presence of DAPDA/DACDA.

Distribution ratio (D) is defined as

$$D = \frac{[\mathrm{Ln}]_t - [\mathrm{Ln}]_a}{[\mathrm{Ln}]_a}$$

where $[Ln]_t$ is the total initial concentration of Ln in the aqueous phase and $[Ln]_a$ is the concentration of Ln in the aqueous phase at equilibrium. $[Ln]_t$ was obtained experimentally by equilibrating the benzene phase in the absence of TTA with the aqueous phase at a particular pH.

Spectrophotometric Studies. A Perkin-Elmer 552 spectrophotometer equipped with a microcomputer was used for ultraviolet absorption studies. Aqueous phase spectra of 5×10^{-5} M TTA were measured at different pH values. UV spectra of the binary system (La–TTA) in the presence of 4×10^{-4} M La(III) and those of ternary systems (La–DAPDA/DACDA–TTA) in the presence of 4×10^{-4} M La(III) + 4×10^{-4} M DAPDA/DACDA were measured at pH 7.5 (Tris buffer) against appropriate reference solutions, respectively.

Organic phase spectra were measured after equilibrating 1.66×10^{-3} M TTA/benzene solutions with aqueous phases containing 1.66×10^{-3} M La(III) or 1.66×10^{-3} M La(III) + 1.66×10^{-3} M DAPDA, at pH 7.5 (Tris buffer). After equilibration, benzene solutions were always diluted with heptane (50 times).

Calculations. The neutral form of TTA is designated as HA and the fully protonated form of DAPDA/DACDA as H_4L^{2+}.

(*a*) *Determination of Extraction Constant* (K_{ex}) *for Binary Species* LnA_3. The equilibrium and the expression for K_{ex} are given as follows:

$$\mathrm{Ln}^{3+}(a) + 3\mathrm{HA}(o) \overset{K_{ex}}{\rightleftharpoons} \mathrm{LnA_3}(o) + 3\mathrm{H}^+(a) \quad (1)$$

$$K_{ex} = [\mathrm{LnA_3}]_o[\mathrm{H}^+]_a^3/[\mathrm{Ln}^{3+}]_a[\mathrm{HA}]_o^3 \quad (2)$$

where subscripts o and a indicate organic and aqueous phases, respectively. The experimentally observed distribution ratio, D, is defined as

$$D = \frac{\text{total metal in organic phase}}{\text{total metal in aqueous phase}} \quad (3)$$

Assuming (i) only mononuclear species are present in the two phases and (ii) complexation of Ln^{3+} with A^- and OH^- can be neglected at pH ≤5.0, eq 3 can be written in a simplified manner as

$$D = [\mathrm{LnA_3}]_o/([\mathrm{Ln}^{3+}]_a + \sum_i [\mathrm{LnAc}_i^{(3-i)+}]_a) \quad (4)$$

The second term in the denominator refers to the complexation of lanthanide ion with acetate in aqueous phase. From eq 2 and 4 it is obtained

$$K_{ex} = D(1 + \sum_i \beta_i[\mathrm{Ac}^-]^i)[\mathrm{H}^+]_a^3/[\mathrm{HA}]_o^3 \quad (5)$$

where β_i is the overall stability constant for complex $\mathrm{LnAc}_i^{(3-i)+}$ and $[Ac^-]$ is the free acetate ion concentration at equilibrium. $[HA]_o$ in eq 2 and 5 refers to the concentration of HA in the organic phase at equilibrium, which is related to $[HA]_{total}$ and $[HA]_o'$ as follows:

$$[\mathrm{HA}]_o' = [\mathrm{HA}]_{total} - n[\mathrm{LnAn}]_o;\ [\mathrm{LnAn}]_o = [\mathrm{Ln}]_{total}D/(D+1)$$

$$[\mathrm{HA}]_o = [\mathrm{HA}]_o'P_{HA}/(P_{HA} + 1 + K_{HA}/[\mathrm{H}^+]) \quad (6)$$

where n is the number of ligands A^- on Ln^{3+}, P_{HA} is the partition coefficient of HA = $[HA]_o/[HA]_a$ (40, in the present case), and K_{HA} is the acid dissociation constant of HA ($-\log K_{TTA} = 5.87$).

(*b*) *Determination of Extraction Constant* (K_{ex}') *for Ternary Species LnLA.*

$$\mathrm{LnL}^+(a) + \mathrm{HA}(o) \overset{K_{ex}'}{\rightleftharpoons} \mathrm{LnLA}(o) + \mathrm{H}^+(a) \quad (7)$$

$$K_{ex}' = [\mathrm{LnLA}]_o[\mathrm{H}^+]_a/[\mathrm{LnL}^+]_a[\mathrm{HA}]_o \quad (8)$$

Assuming (i) only mononuclear species are present in two phases and (ii) lanthanide is present only as LnL^+ in aqueous phase at pH ~7.0, as suggested by the nature of potentiometric titration curves in our previous work (*11*, *12*), eq 3 can be written in a simplified manner for the extraction of ternary species

$$D_1 = [\mathrm{LnLA}]_o/[\mathrm{LnL}^+]_a \quad (9)$$

From eq 8 and 9

$$K_{ex}' = D_1[\mathrm{H}^+]_a/[\mathrm{HA}]_o \quad (10)$$

or

$$\log D_1 = \log [\mathrm{HA}]_o + \log K_{ex}' + \mathrm{pH} \quad (11)$$

(*c*) *Determination of Two-Phase Stability Constants* (P_mK) *for Ternary Species LnLA.* Considering the presence of LnLA

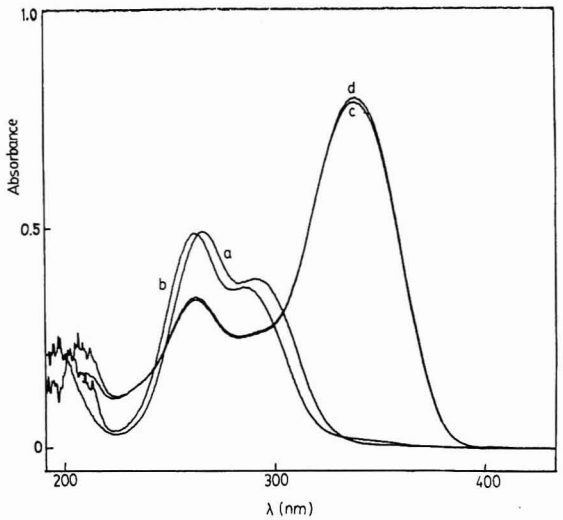

Figure 2. UV spectra of 5×10^{-5} M theonyltrifluoroacetone at different pH: (a) at pH 1.0; (b) at pH 12.0; (c) at pH 7.5 (Tris buffer); (d) at pH 8.0 (Tris buffer).

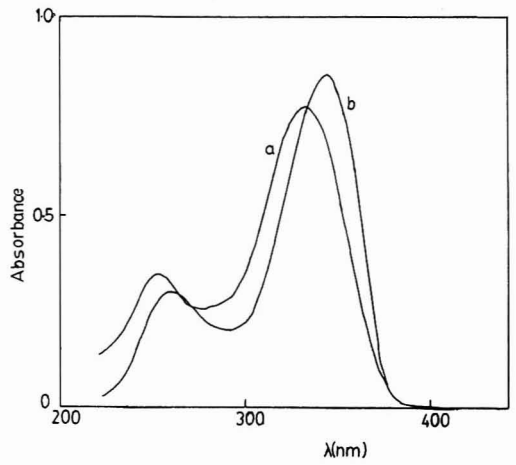

Figure 3. UV spectra of 5×10^{-5} M thenoyltrifluoroacetone at pH 7.5 (Tris buffer) under different complexing conditions: (a) only TTA; (b) TTA + 4×10^{-4} M La(III) + 4×10^{-4} M DAPDA.

species in aqueous phase along with LnL^+, eq 9 can be written as

$$D_2 = [LnLA]_o/([LnL^+]_a + [LnLA]_a)$$

or

$$D_2 = [LnLA]_o/[LnL^+]_a(1 + K[A^-]_a) \quad (12)$$

Defining P_m as the partition coefficient of ternary complex (LnLA), $P_m = [LnLA]_o/[LnLA]_a$, and K as the adduct formation constant of ternary complex (LnLA), $K = [LnLA]_a/([LnL^+]_a[A^-]_a)$, eq 12 is transformed into

$$D_2 = P_mK[A^-]_a/(1 + K[A^-]_a)$$

or

$$\frac{1}{D_2} = \frac{1}{P_mK[A^-]_a} + \frac{1}{P_m} \quad (13)$$

Thus, a plot of $1/D_2$ vs. $1/[A^-]_a$ gives a slope value $1/(P_mK)$ and an intercept $1/P_m$ where $[A^-]_a$ is calculated from $[HA]_o'$ employing the relation

$$[A^-]_a = [HA]_o'K_{HA}/\{(1 + P_{HA})[H^+] + K_{HA}\} \quad (14)$$

(concentration of A^- in LnLA present in aqueous phase has been neglected).

(d) Determination of Equilibrium Constant (K_2) for the Formation of LnL_2^-. Considering the presence of LnL_2^- species along with LnL^+ in aqueous phase, eq 9 can be written as

$$D_3 = [LnLA]_o/([LnL^+]_a + [LnL_2^-]_a)$$

or

$$D_3 = [LnLA]_o/\{[LnL^+]_a(1 + K_2[L^{2-}]_a)\} \quad (15)$$

From eq 9 and 15

$$D_3 = D_1/(1 + K_2[L^{2-}]_a)$$

or

$$K_2 = [(D_1/D_3) - 1]/[L^{2-}]_a \quad (16)$$

where $[L^{2-}]_a$ is the concentration of L present in the anion form at equilibrium.

RESULTS AND DISCUSSION

Spectrophotometric Studies. *UV Spectroscopy of TTA in Aqueous Phase.* Figure 2 shows the ultraviolet spectra of TTA under different pH conditions. Curve a obtained at pH 1.0 refers to the ketohydrate form of TTA (*15*) and curve b obtained at pH 12.0 refers to the decomposition products of TTA, i.e., acetylthiophene and sodium trifluoroacetate (*16*). Curves c and d measured at pH 7.5 and 8.0, respectively, correspond to the enolate anion (*16*). As expected on the basis of the pK_a value of TTA (5.87), enolate anion concentration at pH 8.0 (curve d) is nearly the same as that at pH 7.5 (curve c).

Figure 3 shows the spectra of TTA at pH 7.5 (Tris buffer) in the uncomplexed form as well as in the presence of La(III) and macrocyclic ionophore, DAPDA. It is clear that peak maxima at 338 nm as well as 262 nm corresponding to uncoordinated TTA anion at pH 7.5 (curve a) are shifted toward longer wavelengths on complexation (curve b). Similar shifts have been observed in various systems which follow the order La–DAPDA (11 nm) > La–H_2O (8 nm) > La–DACDA (4 nm). Similar order has also been observed when La(III) was replaced by Nd(III). These shifts have been proposed to be related to the relative complexation of β-diketonate anion to the lanthanide cation in our earlier studies on similar systems (*13*).

Spectra corresponding to enolate anion of TTA at pH 7.5 as well as at pH 8.0 were found slowly transforming to the spectrum corresponding to acetylthiophene and sodium trifluoroacetate. The rate of hydrolytic cleavage has been reported (*16*) to be a function of pH and ionic strength of buffer medium. Similar transformation has also been seen in the present work even for coordinated TTA in the systems La–H_2O, La–DAPDA, and La–DACDA. Though a significant decrease in the intensities of all spectra given in Figure 3 has been observed as a function of time, there was little shift observed in the peak maxima over a period of few days. A typical spectral change of ternary system, La–DAPDA–TTA, is shown in Figure 4 where the spectrum was scanned every hour for the same solution. Nevertheless, spectra recorded after 500 h in all the cases (in Figure 3) at pH 7.5 resembled acetylthiophene and sodium trifluoroacetate spectrum measured at pH 12.0 in every respect. It is obvious from these studies that in the aqueous phase at pH 7.5, TTA anion is in the coordinated form as La(DAPDA)TTA species in equilibrium with decomposition products of TTA.

UV Spectroscopy of TTA in Organic Phase. Figure 5 shows the spectra of benzene solutions of TTA diluted in heptane, after equilibrating the benzene solutions for about 12 h with aqueous phases adjusted at pH 1.0 (b), pH 7.5 (c), and pH 12.0 (d) in three separate experiments. The spectrum of unequilibrated solution of TTA is also shown in Figure 5a for comparison purpose. As suggested by King and Reas (*15*), these organic-phase spectra appear predominantly to be due to the enol form of TTA. Decrease in concentration of TTA in the organic phase at pH 7.5 and at 12.0 is expected in view of its dissociation and decomposition, respectively, in the aqueous phase.

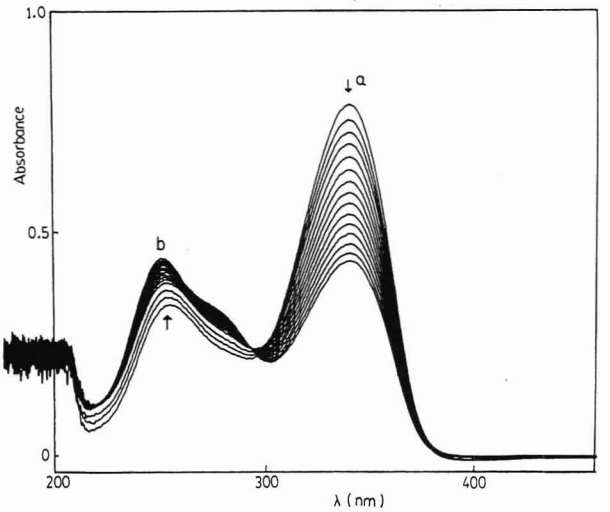

Figure 4. UV spectra of La–DAPDA–TTA (Figure 3b) as a function of time: (a) spectrum obtained 2 h after adjusting pH at 7.5 (Tris buffer); (b) spectrum obtained 17 h after adjusting pH at 7.5 (Tris buffer).

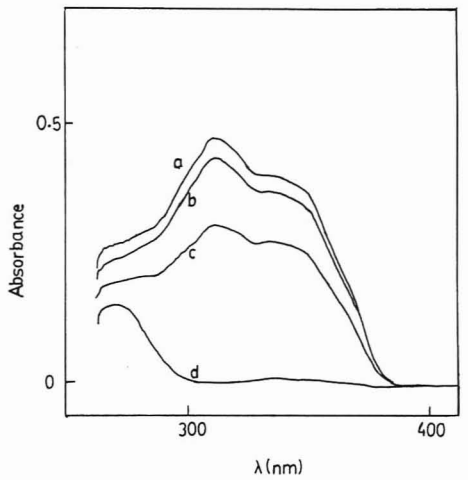

Figure 5. UV spectra of 1.66×10^{-3} M theonyltrifluoroacetone in organic phase under different conditions: (a) TTA in benzene, diluted 50 times in heptane; (b) TTA in benzene equilibrated with aqueous phase at pH 1.0, diluted 50 times in heptane; (c) TTA in benzene equilibrated with aqueous phase at pH 7.5, diluted 50 times in heptane; (d) TTA in benzene equilibrated with aqueous phase at pH 12.0, diluted 50 times in heptane.

Figure 6 shows the spectra of benzene solutions of TTA diluted in heptane, after equilibrating the TTA/benzene solutions for about 12 h with aqueous phases containing La(III) (b), La(III) with DAPDA (c), and a blank experiment corresponding to pH 7.5 (Tris buffer) alone (a). Figure 6 parts b and c clearly suggest that TTA is present in these two cases in a different form (complexed) than in the case of Figure 6a (uncomplexed). Analogous to what was observed in the aqueous phase (Figure 3), organic phase spectra are also similar for both La–TTA and La–DAPDA–TTA systems in terms of peak maxima though spectral intensities of the latter are much smaller than those of the former. Relative intensities of the peaks corresponding to La–TTA (λ_{max} 346 nm) and La–DAPDA–TTA (λ_{max} 349 nm) in the spectra of aqueous phases corresponding to the organic phases included in Figure 6 have been reversed as compared to their organic phase intensities. This reversal suggests the lower extraction of La(DAPDA)TTA compared to $La(TTA)_3$ toward the organic phase.

Identical distribution experiments carried out with Nd(III) in place of La(III) revealed similar peak maxima for coordinated TTA in binary as well as ternary systems in both aqueous and organic phases. It was rather interesting to

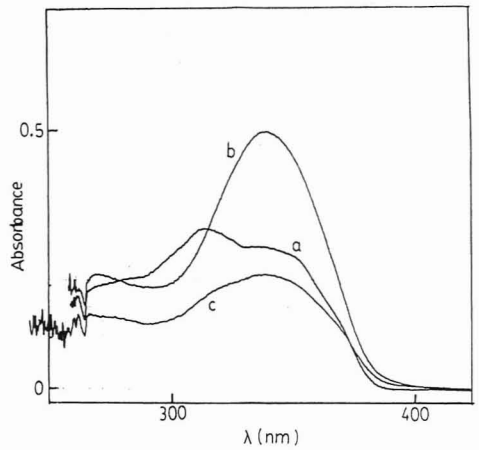

Figure 6. UV spectra of 1.66×10^{-3} M theonyltrifluoroacetone in organic phhse on complexation: (a) TTA in benzene equilibrated with aqueous phase at pH 7.5, diluted 50 times in heptane; (b) TTA in benzene equilibrated with aqueous phase containing 1.66×10^{-3} M La(III) at pH 7.5, diluted 50 times in heptane; (c) TTA in benzene equilibrated with aqueous phase containing 1.66×10^{-3} M La(III) + 1.66×10^{-3} M DAPDA at pH 7.5, diluted 50 times in heptane.

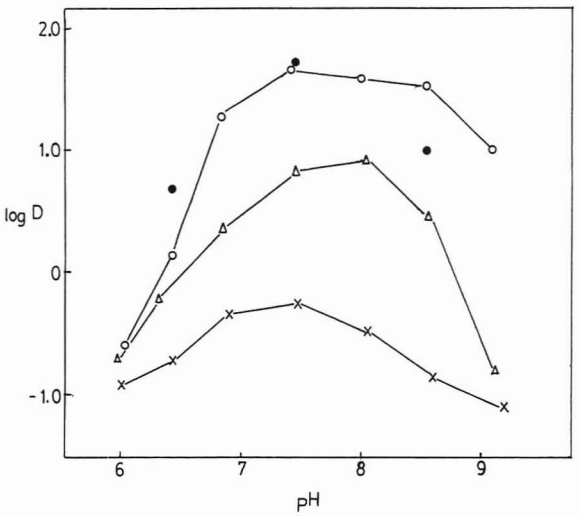

Figure 7. Distribution of La(III) as a function of pH in the presence of different complexing agents, $[TTA]_{total} = 3.3 \times 10^{-3}$ M, $I = 0.13$: (●) 1.6×10^{-4} M La(III); (○) 1.6×10^{-4} M La(III) + 1.6×10^{-3} M EDDA; (△) 1.6×10^{-4} M La(III) + 1.6×10^{-4} M DAPDA; (×) 1.6×10^{-4} M La(III) + 1.6×10^{-4} M DACDA.

observe that in the binary system the intensity of Nd–TTA peak is larger in the organic phase and smaller in the aqueous phase compared to the corresponding La–TTA peaks. On the other hand, in the ternary system, intensity of the La–DAPDA–TTA peak is larger in the organic phase and smaller in the aqueous phase compared to the corresponding Nd–DAPDA–TTA peak. These studies suggest that whereas neodymium extracts more than lanthanum in the binary system, Ln–TTA, lanthanum extracts more than neodymium in the ternary system, Ln–DAPDA–TTA.

A similar reversal in the distribution ratios measured by the dc plasma emission spectroscopic technique has been observed for lanthanum and neodymium in binary and ternary systems as discussed in Distribution Studies.

No changes in intensities of the organic-phase spectra were observed with time indicating the stability of the extracted species. This is in contrast to the behavior of species in the aqueous phase, which were found quite susceptible to decomposition in basic media.

Distribution Studies. *Effect of pH.* Variation of distribution ratio (D) for the extraction of La(III) and Nd(III) ions was investigated as a function of pH in the range 6.0–9.0.

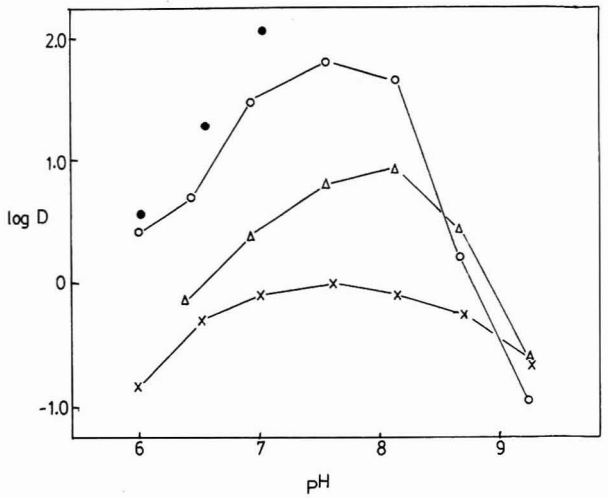

Figure 8. Distribution of Nd(III) as a function of pH in the presence of different complexing agents, $[TTA]_{total} = 3.3 \times 10^{-3}$ M; $I = 0.13$: (●) 1.6×10^{-4} M Nd(III); (○) 1.6×10^{-4} M Nd(III) + 1.6×10^{-3} M EDDA; (△) 1.6×10^{-4} M Nd(III) + 1.6×10^{-4} M DAPDA; (×) 1.6×10^{-4} M Nd(III) + 1.6×10^{-4} M DACDA.

It is seen from Figures 7 and 8 that the distribution ratio increases with pH up to 7.5 and decreases thereafter presumably due to hydrolysis of the species LnL^+ (where L = EDDA, DAPDA, or DACDA). This decrease may also be partly due to the decomposition of TTA in the aqueous phase which is accelerated at high pH as discussed in the previous section under Spectrophotometric Studies. Similar variation of distribution ratio with pH was observed by Zolotov et al. (*17*) while investigating the extraction of mixed complexes of In(III) with 1-(2-pyridylazo)-2-naphthol and acetate at different pH values. Extraction maximum was observed at lower pH for In(III) (6.0–6.5) compared to that of lanthanides in the present studies (7.5–8.0). This may be principally due to the ease of hydrolysis of In^{3+} compared to that of La^{3+} or Nd^{3+} (*14*).

At a particular pH, the D value decreased for various extraction systems in the order (Ln–H_2O) > (Ln–EDDA) > (Ln–DAPDA) > (Ln–DACDA). This can be explained on the basis of the availability of uncomplexed trivalent lanthanide ion as well as the relative complexation of TTA anion (A^-) with the central metal cation. Due to stronger complexation of DACDA with Ln^{3+}, a relatively less amount of uncomplexed Ln^{3+} is available for the formation of species of the type LnA_3. Extraction systems involving larger proportion of LnA_3 species are expected to result in higher distribution ratio values due to larger partition coefficients of these species compared to the ternary LnLA species (*18*). It was also observed that D decreased in the case of DAPDA after pH 8.0 whereas for DACDA, it started decreasing at about pH 7.5. This is also possibly due to the stronger complexation of A^- with Ln(DAPDA)$^+$ cation compared to that with Ln(DACDA)$^+$ cation.

Concentration of EDDA was maintained at 10 times the stoichiometric amount of the metal ion since the experiments with an equal stoichiometric amount revealed the tendency of metal ion to hydrolyze at pH >7.0. On comparison of the curves in Figures 7 and 8, it was further observed that generally extraction of Nd(III) is larger in all cases except with DAPDA where La(III) extracts more up to pH 8.0.

Due to the varying amount of $[TTA]_o$ at different pH, slope of log D – pH curve for Ln^{3+} as well as LnL^+ species changes continuously. This is due to the fact that pH values are high which makes $[HA]_o$ change drastically as a function of pH. In addition, the change in relative proportion of Ln^{3+} and LnL^+ species with pH may affect the slope of these curves.

Effect of TTA Concentration. Extraction of Nd(III) at a concentration of 1.8×10^{-3} M was studied as a function of

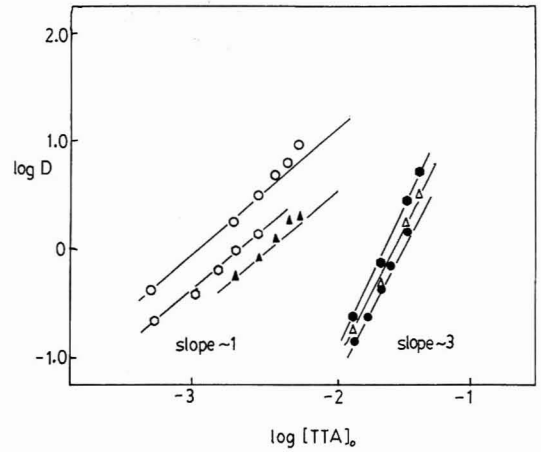

Figure 9. Variation of log D as a function of log $[TTA]_o$: (○) Ln = La (1.6×10^{-4} M), L = DAPDA (1.6×10^{-4} M), pH 7.5, $I = 0.2$; (○) Ln = Nd (1.6×10^{-4} M), L = DACDA (1.6×10^{-4} M), pH 7.5, $I = 0.2$; (▲) Ln = La (1.6×10^{-4} M), L = DACDA (1.6×10^{-4} M), pH 7.5, $I = 0.2$; (△) Ln = Nd (1.8×10^{-3} M), pH 4.7, $I = 0.1$; (●) Ln = Nd (1.8×10^{-3} M), L = EDDA (5×10^{-3} M), pH 5.1, $I = 0.1$; (●) Ln = Nd (1.8×10^{-3} M), L = DAPDA (2×10^{-3} M), pH 5.1, $I = 0.1$.

Table I. Equilibrium Constants for the Extraction of Ternary Complexes (I = 0.2 M)

system	log k_{ex}'	log $(P_m K)$	log K_1[a]
La(DAPDA)TTA	−4.31 ± 0.07	2.95 ± 0.02	10.11
La(DACDA)TTA	−4.86 ± 0.06	2.46 ± 0.03	12.21
Nd(DAPDA)TTA	−4.59 ± 0.02	2.78 ± 0.03	11.6
Nd(DACDA)TTA	−4.71 ± 0.04	2.72 ± 0.04	12.21

[a] Data taken from ref 11 and 12.

TTA concentration, varying in the range 1.4×10^{-2} M to 4.8×10^{-2} M at pH 4.7, using acetate buffer ($I = 0.1$ M). Figure 9 shows that linear plot of log D vs. log $[TTA]_o$ results in a slope of ~3.0 confirming that the extracted species is Nd(TTA)$_3$. On addition of 5×10^{-3} M EDDA to the aqueous phase, a similar log–log plot was obtained at pH 4.7 and 5.1 except that distribution ratio values were marginally decreased for a particular combination of TTA concentration and H^+ concentration. Slope of ~3.0 in the presence of EDDA suggests that the dominating species extracted at pH 5.1 is still Nd(TTA)$_3$. Lowering of the extraction constant value from −8.54 ± 0.12 (log K_{ex}) for Nd–TTA at pH 4.7 to −9.54 ± 0.10 (log K_{ex}) for Nd–EDDA–TTA at pH 5.1 indicated aqueous complexation of Nd^{3+} with EDDA. Note that the values for log K_{ex} were calculated by using eq 4 and 5 with the consideration of acetate complexation which is significant in the present case.

Distribution experiments carried out at pH 5.1 in the presence of 2×10^{-3} M DAPDA showed further decrease in the distribution ratio values. Slopes of log D vs. log $[TTA]_o$ plots for NdLA system in the pH range 5.9 to 7.3 were found to vary between 2.0 and 1.0 suggesting that both binary, NdA_3, as well as ternary, NdLA, species were coextracted into the organic phase. Figure 9 also shows plots of log D vs. log $[TTA]_o$ at pH 7.5 for La(DAPDA)TTA, La(DACDA)TTA, and Nd(DACDA)TTA systems. Marginal deviation from unity slope was observed in one case with increasing value of $[TTA]_o$, suggesting the presence of species of the type LnA_3 or LnLA·HA along with ternary species LnLA. Binding of chelating extractant as neutral molecule as well as in the anionic form has been observed by Kawashima et al. (*19*) in their study of lanthanide extraction and by Tamhina et al. (*20*) in their investigation on thorium extraction.

Points falling on lines of unit slope in Figure 9 were further considered for the calculation of extraction constants (K_{ex}')

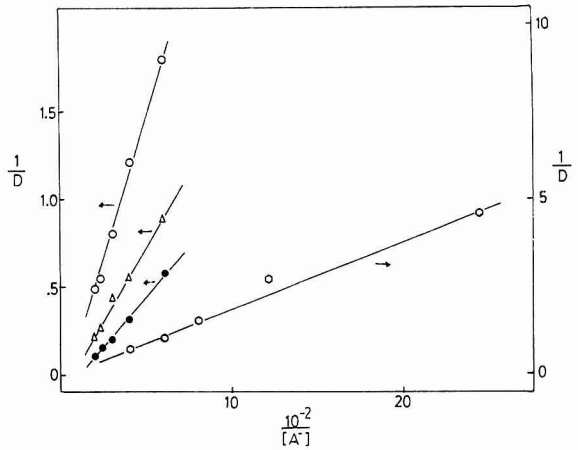

Figure 10. Variation of $1/D$ as a function of $1/[A^-]$ at pH 7.5 to determine log (P_mK): (○) La(III)–DACDA–TTA; (●) La(III)–DAPDA–TTA; (△) Nd(III)–DAPDA–TTA; (○) Nd(III)–DACDA–TTA.

Table II. Observed Separation Factors between Nd(III) and La(III) with Different Complexing Agents at pH 7.5, [Ln] = 1.6×10^{-4} M

complexing agent	ligand:metal ratio	separation factor $[D(\text{Nd})/D(\text{La})]$
DAPDA[a]	1:1	0.55 ± 0.08
DACDA[a]	1:1	1.7 ± 0.05
EDDA[b]	10:1	2.08 ± 0.20

[a] $[\text{TTA}]_{\text{total}}$ varied between 3.3×10^{-3} M and 1.0×10^{-2} M. [b] $[\text{TTA}]_{\text{total}}$ varied between 3.3×10^{-4} M and 1.6×10^{-3} M.

of the ternary complexes using eq 10. Table I shows the K_{ex}' values obtained for various extraction systems investigated in this work. An attempt was made to calculate log (P_mK) values from the slopes of linear plots of $1/D$ vs. $1/[A^-]_a$ (Figure 10) as given in eq 13 (Table I).

It should be noted that the P_m values could not be obtained from the values of intercepts of plots $1/D$ vs. $1/[A^-]_a$ due to large errors. Also, log K_1 values listed in Table I have been obtained earlier in our laboratory by the potentiometric technique (*11*, *12*).

The highest value of log (P_mK) for La(DAPDA)TTA appears to be due to the stronger binding of TTA with the relatively weaker complex La(DAPDA)$^+$. Similarly, the lowest value of log (P_mK) is observed for the stronger La(DACDA)$^+$ complex. The higher value obtained for the Nd(DACDA)$^+$ complex, in spite of its similar stability with La(DACDA)$^+$, could possibly be explained on the basis of a favorable partition coefficient of Nd(DACDA)TTA compared to the corresponding lanthanum complex.

Macrocyclic ionophores employed in the present study offer interesting possibilities of extracting La(III) more in the case of DAPDA and less in the case of DACDA compared to Nd(III). Table II summarizes the mean separation factors $[D(\text{Nd})/D(\text{La})]$ obtained by varying $[\text{TTA}]_{\text{total}}$ in the range 3.3×10^{-3} M to 1.0×10^{-2} M at pH 7.5. Extraction of La(III) was about 1.8 times that of Nd(III) in the case of DAPDA whereas in other cases of DACDA and EDDA, simple TTA extraction behavior of Nd(III) extracting more than La(III) was observed (*14*). Also in the latter two cases, separation factor decreased significantly from the one observed with TTA alone as the extractant. The separation factor (~100) reported in the literature for binary systems (*14*) in favor of Nd(III) at low pH (~5.0) could not be reproduced in the present studies at pH 7.5. Though an exact value could not be assigned due to the complex nature of extraction, i.e., hydrolysis, it appeared to decrease by at least more than an order of magnitude

Table III. Distribution Ratios of La(III) and Nd(III) with Varying Concentration of TTA in the Presence of EDDA at pH 7.5, [Ln] = 1.66×10^{-4} M, [EDDA] = 1.66×10^{-3} M

$10^4[\text{TTA}]_{\text{total}}$, M	D(La)	D(Nd)
3.33	0.19	0.37
6.66	0.34	0.72
10.0	1.05	2.31
13.32	1.36	2.99
16.66	3.35	6.72

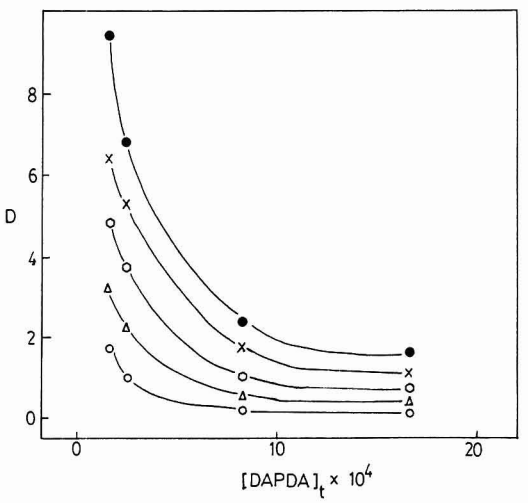

Figure 11. Variation of D with $[\text{DAPDA}]_{\text{total}}$, [La] = 1.6×10^{-4} M, pH 7.5, and I = 0.2 M: (○) $[\text{TTA}]_{\text{total}} = 3.33 \times 10^{-3}$ M; (△) $[\text{TTA}]_{\text{total}} = 5.0 \times 10^{-3}$ M; (○) $[\text{TTA}]_{\text{total}} = 6.66 \times 10^{-3}$ M; (×) $[\text{TTA}]_{\text{total}} = 8.33 \times 10^{-3}$ M; (●) $[\text{TTA}]_{\text{total}} = 1.0 \times 10^{-2}$ M.

(separation factor 5.0) in this work. It should be noted that there is no report available on the role of ionizable macrocyclic ionophores on the extraction of lanthanides by organic extractant.

No attempt was made to calculate extraction constant with EDDA as primary ligand in the present work for the following reasons: (i) concentration of EDDA was 10 times the stoichiometric requirement, thus there was some possibility of formation of anionic species of the type Ln(EDDA)_2^-, and (ii) $[\text{TTA}]_0$ dependency on the distribution ratio (D) was ~1.7 (from the slope of log D–log $[\text{TTA}]_0$ plot) suggesting significant contribution of Ln(TTA)_3 species even at pH 7.5. Distribution ratio data for varying concentrations of TTA are given in Table III.

Effect of DAPDA Concentration. Distribution experiments were also carried out on La(III) at fixed TTA concentration, fixed pH, and various concentrations of DAPDA. Figure 11 shows the exponential decrease of distribution ratio (D) with increase of DAPDA concentration for several fixed $[\text{TTA}]_{\text{total}}$ values. This decrease suggests the presence of an additional equilibrium involving the species LnL^+. It appears that on adding increasing amounts of DAPDA, anionic species of the type LnL_2^- are formed. A second molecule of L may bind only through acetate anionic groups. Employing eq 16, log K_2 was obtained as 3.66 ± 0.08 in the present work for La(DAPDA)_2^-, which is consistent with what would be expected using acetate as a model.

Analytical Significance. During the distribution of lighter lanthanides with thenoyltrifluoroacetone in the presence of macrocyclic ionophores, i.e., DAPDA and DACDA, ternary complexes of the type Ln(DAPDA)TTA appear to be the dominant extracting species at pH 7.5. The distribution ratio of lanthanides in the ternary system decreases significantly compared to simple TTA extraction, presumably due to the lower partition coefficient of ternary complexes compared to that of binary complexes. Nevertheless, it has been found

possible to extract quantitatively lanthanides from the ternary system by adjusting reagent concentration. Extraction of ternary complexes with DACDA as a macrocyclic ionophore was always lower compared to that with DAPDA. Selective extraction of Nd(III) over La(III) reported for simple TTA extraction was though maintained in the case of DACDA; it was reversed in the case of DAPDA.

These extraction results have very significant implications. Two common procedures are followed to extract lanthanide species at low pH (i.e., 3 or 4). With extractant such as TTA, the heavier lanthanide complexes are extracted more because they form stronger TTA complexes due to their greater charge density. The lanthanide species can also be extracted in the presence of a strong complexing agent such as EDTA. The results are that the lighter lanthanide ions are extracted more because the heavier lanthanides are all tied up in the aqueous solution with EDTA and are less available for extraction. The ternary complexes of lanthanides with open-chained, flexible primary ligands such as EDTA and secondary extractants are not found in the organic phase. Thus the presence of ternary macrocyclic lanthanide complexes in the organic phase indicates their improved hydrophobicity. Because of the various possibilities of forming ternary macrocyclic complexes with extractants of different sizes and steric requirements, one can further tune the selectivity for the extraction. Certainly, the subtle differences in solubility of the resulting ternary species are also significant for determining the final selectivity.

Registry No. TTA, 14529-33-0; DAPDA, 81963-61-3; DACDA, 72912-01-7; La, 7439-91-0; Nd, 7440-00-8.

LITERATURE CITED

(1) Surls, J. P.; Choppin, G. R. *J. Inorg. Nucl. Chem.* **1957**, *4*, 62.
(2) Leuze, R. E.; Lloyd, M. H. *Process Chem.* **1970**, *4*, 597.
(3) Weaver, B.; Kappelmann, F. A. ORNL-3559, 1964.
(4) Bilal, B. A.; Herrmann, F.; Metscher, K.; Mühlig, B.; Reichmuth, Ch.; Schwarz, B. *Actinide Separations*; Navratil, J. D., Schulz, W. W., Eds.; American Chemical Society: Washington, DC, 1979; ACS Symp. Ser. No. 117, pp 561–569.
(5) Seaborg, G. *Man made Transuranium Elements*; Prentice-Hall: Englewood Cliffs, NJ, 1963; p 58.
(6) Chinn, S. R.; Hong, H. Y.-P.; Pierce, J. W. *Laser Focus Electro-Opt. Mag.* **1976**, *12*, 64.
(7) Elattar, A.; Wallace, W. E.; Craig, R. S. *The Rare Earths in Modern Science and Technology*; McCarthy, J. G., Rhyne, J. J., Eds.; Plenum Press: New York, 1977; Vol I, p 87.
(8) Reuben, J.; Elgavish, G. A. *Handbook on the Physics and Chemistry of Rare Earths*; Gschneidner, K. A., Jr., Eyring, L., Eds.; North-Holland: Amsterdam, 1979; Vol 4, p 483.
(9) Marchant, D. D.; Bates, J. L. *The Rare Earths in Modern Science and Technology*; McCarthy, J. G., Rhyme, J. J., Silben, B. H., Eds.; Plenum Press: New York, 1977; Vol II, p 553.
(10) Cecille, L.; Dworschak, H.; Girardi, F.; Hunt, B. A.; Mannore, F.; Mousty, F. "*Actinide Separations*"; Navratil, J. D., Schulz, W. W., Eds.; American Chemical Society: Washington, DC, 1979; ACS Symp. Ser. No. 117, pp 427–440.
(11) Chang, C. A.; Rowland, M. E. *Inorg. Chem.* **1983**, *22*, 3866–3869.
(12) Chang, C. A.; Ochaya, V. O. *Inorg. Chem.* **1986**, *25*, 355–358.
(13) Chang, C. A.; Garg, B. S.; Manchanda, V. K.; Ochaya, V. O.; Sekhar, V. C. *Inorg. Chim. Acta* **1986**, *115*, 101–106.
(14) Marcus, Y.; Kertes, A. S. *Ion Exchange and Solvent Extraction of Metal Complexes*; Wiley-Interscience: New York, 1969; Chapters 3 and 8.
(15) King, E. L.; Reas, W. H. *J. Am. Chem. Soc.* **1951**, *73*, 1806–1808.
(16) Cook, E. H.; Taft, R. W. *J. Am. Chem. Soc.* **1952**, *79*, 6103–6104.
(17) Zolotov, Y. A.; Seryakova, I. V.; Vorobyeva, G. A. *Talanta* **1967**, *14*, 737–743.
(18) Zolotov, Y. A. *Extraction of Chelate Compounds*; Ann-Arbor Humphrey Science Publishers: Ann Arbor, MI, 1970; p 36.
(19) Kawashima, M.; Freiser, H. *Anal. Chem.* **1981**, *53*, 284–286.
(20) Tamhina, B.; Gojmerac, A.; Herak, M. J. *J. Inorg. Nucl. Chem.* **1978**, *40*, 335–338.

RECEIVED for review December 2, 1985. Accepted May 12, 1986. This material was prepared with the support of U.S. Department of Energy Grant No. DE-FG05-84ER12392; however, any opinions, findings, conclusions, or recommendations expressed herein are those of the authors and do not necessarily reflect the views of the DOE.

Determination of Sub-Part-per-Trillion Amounts of Cobalt by Extraction and Photoacoustic Spectroscopy

Takehiko Kitamori,*[1] Kazumichi Suzuki,[1] Tsuguo Sawada,[2] Yohichi Gohshi,[2] and Kenji Motojima[1,3]

Energy Research Laboratory, Hitachi, Ltd., 1168 Moriyama, Hitachi, Ibaraki 316, Japan, and Department of Industrial Chemistry, Faculty of Engineering, University of Tokyo, 7-3-1 Hongo, Bunkyo, Tokyo 113, Japan

Ultratrace amounts of cobalt at parts-per-trillion (ppt) levels were extracted into *m*-xylene from aqueous solution as nitrosonaphthol chelates, and colorimetric determination of the *m*-xylene phase was carried out with photoacoustic spectroscopy (PAS). Coexistent metals and excessive reagents were completely eliminated by acidic and alkaline washings of the *m*-xylene phase, and the background level became constant and low enough for ultrasensitive PAS determination. Concentrations of foreign heavy metals, such as iron, nickel, chromium, and copper, 10^5 times more than cobalt caused no interference. The determination limit was obtained as 0.64 ppt based on twice the standard deviation. The reagent 2-nitroso-1-naphthol was more suitable than 1-nitroso-2-naphthol from the viewpoint of stability.

In recent years, water and reagents used in technical fields, such as semiconductor, biochemical, and nuclear engineering, are being highly purified, and some kinds of impurities are demanding part-per-trillion (ppt) (pg/mL) level analyses. For example, the amounts of cobalt that are neutron activated in nuclear power reactor coolant and cause an increase of radiation dose rate around the coolant system have been reduced to extremely low levels and are estimated to be on the order of parts per trillion (*1*). Hence a determination method for ultratrace cobalt is required to clarify the species behavior in the coolant.

Photoacoustic spectroscopy (PAS) for liquid samples using a piezoelectric transducer as an acoustic signal detector has been shown to be quite sensitive, and the detection limit absorbance of the equipment (S/N = 2; N, noise of the equipment) has reached the order of 10^{-8} cm^{-1} when employing an optimized photoacoustic (PA) cell (*2*, *3*). Therefore, determination with PAS seems to be suited to ultratrace analysis, and indeed its potentiality has been shown experimentally

[1] Hitachi, Ltd.
[2] University of Tokyo.
[3] Present address: Laboratory of Analytical Chemistry, Kaken Co., Ltd., Shinden 1044 Hori, Mito, Ibaraki 310, Japan.

0003-2700/86/0358-2275$01.50/0 © 1986 American Chemical Society

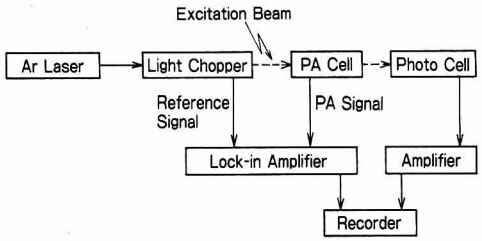

Figure 1. Block diagram of the photoacoustic spectrometer for liquid samples.

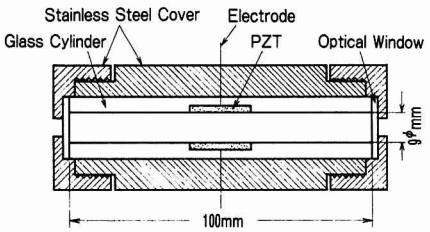

Figure 2. Longitudinal section of optimized cylindrical PA cell for *m*-xylene solutions. The samples were poured into the cylinder by removing the stainless steel cover and the optical window.

(*4*, *5*). These experiments demonstrated the determination of solute at 10–20 ppt, for example, determination limits (2σ; σ, standard deviation) of 12 ppt for β-carotene (*4*) and 14 ppt for cadmium dithizonate (*5*), both in chloroform, have been achieved. The measurements were done by using a series of solutions prepared not by extraction but by stepwise dilution. However, generally, a solvent extraction is included in procedures for colorimetric determination, and various trace impurities, such as unreacted reagents, remain in the extracted phase. In some cases, these trace impurities cause a high background level in ultrasensitive measurements with PAS and are considered to obstruct the determination at part-per-trillion levels. Thus, ultratrace determinations using extraction and PAS measurements have not been done yet.

In the present paper, the determination of ultratrace amounts of cobalt was carried out by extraction and PAS. Cobalt in aqueous solution is extracted in *m*-xylene as chelate with nitrosonaphthol (nitroso-N). This reagent is known to be specific for cobalt (*6*–*8*), and the chelate is not destroyed by concentrated hydrochloric acid or sodium hydroxide solutions (*9*). Therefore, coexistent metals and excess reagent can be removed by washing the *m*-xylene phase with concentrated hydrochloric acid and sodium hydroxide solutions. In this paper, suitable washing conditions to reduce the background are proposed experimentally, and determination of sub-part-per-trillion levels of cobalt in water is shown. The effects of coexistent metals and structual isomerism of the reagent are also discussed.

EXPERIMENTAL SECTION

Apparatus. The apparatus used in the present experiments was an optimized PAS system designed on the basis of our optimization methods (*2*). A block diagram of the PAS system and a longitudinal section of a cylindrical photoacoustic (PA) cell are shown in Figures 1 and 2, respectively. The radius and the length of the PA cell were optimized with material constants of *m*-xylene, which was used as solvent, and with the following parameters for the excitation beam: wavelength, 488 nm; beam power, 1.6 W; and beam radius, 2.0 mm (*3*). The excitation beam was modulated as a rectangular form with a rotating blade light chopper, for which the duty cycle was 50%. The lock-in amplifier was an autophase type, used to adjust its phase with that of the PA signals.

A spectrophotometer with 1-cm cuvette was used for the measurement of chelate absorption curves.

Reagents. All reagents were ultrapure grade or spectral grade. Water was subjected to the following ultrapurification measures: distillation in a glass apparatus, two demineralizations with a resin ion exchanger, and filteration with an activated carbon filter and a membrane filter. It should be noted that water distilled in a stainless steel apparatus contains 10^1–10^2 ppt of cobalt. The resistivity of the obtained water was about 18 MΩ/cm, and particulate impurities above 0.2 μm were completely removed.

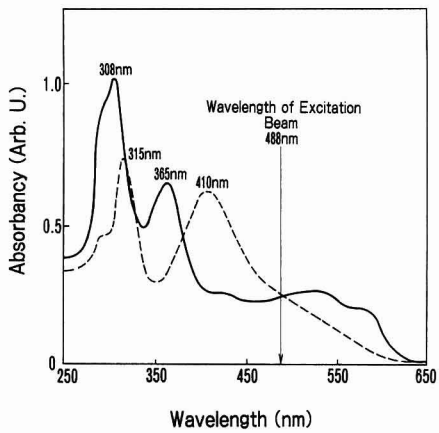

Figure 3. Absorption spectra of cobalt chelates in *m*-xylene. The concentration of both chelate solutions was 1 ppm. The solid line indicates the spectrum of the chelate with 2-nitroso-1-naphthol, and the dashed line shows the spectrum of the chelate with 1-nitroso-2-naphthol.

2-Nitroso-1-naphthol (2-nitroso-N) was purified by recrystallization from benzene, and a sodium hydroxide solution of the reagent was obtained with the following procedure. A 2.5-g sample of recrystallized 2-nitroso-N was dissolved in 250 mL of *m*-xylene while heating at about 100 °C. The solution was filtered through a paper filter, and the eluent was transferred to a separatory funnel containing 500 mL of 0.2 M sodium hydroxide solution. The reagent was extracted into the aqueous phase by shaking for about 3 min, and the obtained 2-nitroso-N sodium hydroxide solution was removed. A sodium hydroxide solution of 1-nitroso-2-naphthol (1-nitroso-N) was obtained by using the same procedure.

Reference cobalt aqueous solution containing 1.0 ng/mL of cobalt was prepared by stepwise dilution of the stock solution, for which concentration was 1.0 mg/mL, obtained by dissolving pure cobalt metal (99.99%) in hydrochloric acid. The reference cobalt solution was kept acidic with 0.05 M hydrochloric acid.

Analytical Procedure. Trace amounts of cobalt at the parts-per-trillion level were extracted in 10 mL of *m*-xylene as a nitroso-N chelate by the following procedure. A 1-L portion of cobalt aqueous solution was placed in a separatory funnel. Then 1 mL of 2 M citric acid solution, for masking, and 2 mL of nitroso-N solution were added. The pH was adjusted to within 4–5 by adding 2 mL of 2 M sodium acetate solution. Then exactly 10 mL of *m*-xylene was added. After the funnel was shaken for 30 min with a mechanical shaker, the mixture was allowed to stand for 20 min, after which the aqueous phase was discarded.

The obtained *m*-xylene phase was washed by shaking in the separatory funnel with 15 mL of concentrated hydrochloric acid (3 times), 50 mL of water (2 times), 50 mL of 0.2 M sodium hydroxide (4 times), and again with 50 mL of water (2 times), to remove the metal impurities and excess nitroso-N. The *m*-xylene phase was collected in an Erlenmeyer flask by filteration after dehydration with 3 g of anhydrous sodium sulfate. The same procedure was carried out for the blank solution.

The PA signal magnitude for each sample was measured. Calibration curves were obtained by the least-squares method.

RESULTS AND DISCUSSION

Absorption spectra of cobalt 1- and 2-nitroso-N chelates in *m*-xylene, obtained with the spectrophotometer, are shown in Figure 3. While the chelates have absorption peaks in the spectral region from 308 nm to 410 nm, a 488-nm lasing line was chosen in the present experiments, because the sensitivity of PAS is proportional to the beam power, and the beam power at this line is several orders higher than other lasing lines near the absorption peaks. Furthermore, both chelates have about the same molar absorptivity at 488 nm, and this value is 1.4 $\times 10^4$ (L mol^{-1} cm^{-1}).

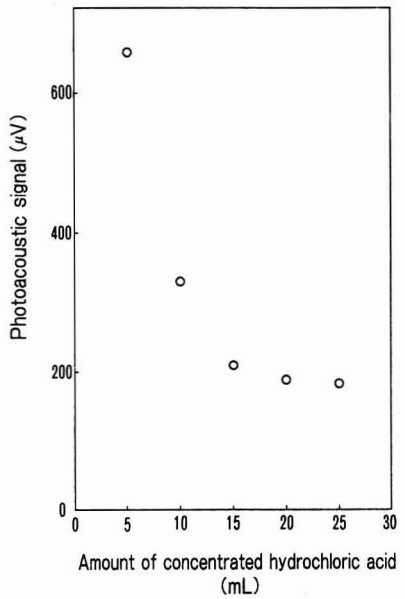

Figure 4. Dependence of background level on the amount of concentrated hydrochloric acid used for washing the *m*-xylene phase. The amounts of cobalt-free water and *m*-xylene were 1 L and 10 mL, respectively, for two acidic washings.

A nitroso-N chelate with metals other than cobalt can be readily destroyed by concentrated hydrochloric acid, and the destroyed chelates can be extracted in the concentrated hydrochloric acid phase. As PAS is ultrasensitive, remaining chelates with other metals produce a background and obstruct the exact determination of trace cobalt; hence complete washing of the *m*-xylene phase with concentrated hydrochloric acid is required. First, the background PA signal was measured for the *m*-xylene phase extracted with 2-nitroso-N from a blank solution while changing the amount of concentrated hydrochloric acid used for washing from 5 to 25 mL. The results are plotted in Figure 4. The background decreased on increasing the amount of concentrated hydrochloric acid and reached a nearly constant value at more than 15 mL. The background also depended on the number of washings and became constant after more than three washes. Therefore, suitable washing conditions for concentrated hydrochloric acid were three 15-mL portions.

The remaining 2-nitroso-N reagents in *m*-xylene phase also caused a background increase. The excess reagents were removed by 0.2 M sodium hydroxide solution, and suitable washing conditions were obtained with the same procedure that determined the acidic washing conditions, which was found to be four 50-mL portions.

As the remaining trace quantity of excess 2-nitroso-N reagent was proportional to the added quantity of the reagent, the background was proportional to the added quantity of the reagent. Hence the quantity of the reagent should be minimized. However, quantitative extraction of 100 ng of cobalt in 1 L of aqueous solution was obtained by the addition of more than 2 mL of 0.5% 2-nitroso-N 0.2 M sodium hydroxide solution. Therefore, the optimum quantity of the reagent was 2 mL.

With these obtained conditions, the background was the lowest, and the value was about 75 μV for 1–100 ng of cobalt extraction with the present analytical procedure. When the quantity of reagent exceeded 2 mL and the acidic and alkaline washings were not sufficient in comparison with the present optimized conditions, the background varied on the order of 10^1–10^2 μV due to the residual impurities.

Ultratrace amounts of cobalt of 1, 2, 5, and 10 ng in 1 L of water were extracted in 10 mL of *m*-xylene with 2-nitroso-N, and PA signal magnitude for each *m*-xylene phase was measured. This magnitude was proportional to the cobalt concentration, and the determination limit of cobalt in aqueous solution was calculated on the basis of twice the standard deviation of the measured values. This value was 0.64 ng/L, or 0.64 ppt, and was at least 3 orders lower than conventional colorimetric analyses using spectrophotometers. The sensitivity of this analytical method, that is the slope of the calibration curve, was 3.80 μV/ppt. Hence a change in PA signals at the 10^{-1}–10^0 μV order for the determination of 10^{-1} ppt levels of cobalt would not be identified, if the background varied on the 10^1–10^2 μV order. Therefore, it was noted that careful washing of the extracted phase to obtain a sufficiently constant and low background is a prerequisite for ultrasensitive analysis with PAS.

Table I. Parameters of the Calibration Curves

sample no.	foreign metal	slope, μV/ng of Co	blank level, μV
1	–	3.75	74.8
2	iron	3.85	118.0
3	nickel	3.87	126.9
4	chromium	3.80	131.3
5	copper	3.88	168.0

Furthermore, the effect of excessive amounts of foreign metals, iron, nickel, chromium, and copper, was investigated. Except for copper, these heavy metals are main constituents of stainless steel as is cobalt. Copper has a strong chelate forming property. One of these heavy metals (1 mg) was added to the 5, 10, 15, and 20 ng of cobalt solutions and the blank. Four calibration curves with coexisting metals were obtained with the present analytical method, and the parameters of the calibration curves, slope and blank level, are listed in Table I. As the slope variation was within 1.3%, no significant interference from these heavy metals at amounts 10^5 times those of cobalt could be found. The shift of the blank level originated in the cobalt impurity included in these heavy metals, and the amounts were 11.5, 13.9, 15.1, and 24.9 ppm for iron, nickel, chromium, and copper, respectively. These values could be easily confirmed by atomic absorption spectrometry.

By use of results of ten extractions of cobalt at 5 ppt, precision of the present analytical procedure was calculated to be within 2.8%. Furthermore, although it is hard to obtain an exact loss of cobalt after extraction at part-per-trillion levels of concentration, no significant differences could be found between the slopes of the calibration curves obtained by dilution and extraction within the variation of 1.3% for the chelate concentration range of 5–20 ng/(10 mL of *m*-xylene); that is, 5–20 ppt of cobalt in aqueous solutions. Hence, loss of cobalt in the extraction procedure was negligible within the precision of the present analytical procedure. This seems to be due to the high stability of the cobalt chelate in *m*-xylene, although the washing procedure involved 11 steps.

Nearly the same results were obtained with 1-nitroso-N. However, pure 1-nitroso-N is difficult to obtain, and it is less stable in comparison with 2-nitroso-N. For example, when 1-nitroso-N prepared several weeks before was used, sometimes the *m*-xylene phases that extracted parts-per-trillion levels of cobalt were colored red, although the absorption coefficients of the *m*-xylene phases for this cobalt concentration range were typically 10^{-4} cm^{-1}, which appeared as colorless. Consequently, the determination of ultratrace cobalt became impossible due to the background increment and fluctuation in 10^2–10^3 μV order. This instability of 1-nitroso-N was not further examined in the present study. However, 2-nitroso-N did not show such instability and is recommended for this cobalt analytical method.

Ultrasensitive determination with PAS is applicable to various kinds of liquid samples. However, when PAS is combined with an extraction technique, the background due to impurities, excess reagents, and instability of reagents should be low and constant as shown in this paper. When a suitable extraction method, which can highly enrich the chelate and reduce the background, is applied, various materials should be determined at sub-part-per-trillion to parts-per-trillion levels using PAS.

ACKNOWLEDGMENT

We are greatly indebted to Junko Fujita of the Laboratory of Analytical Chemistry, Kaken Co., Ltd., for skillful preparation of the reagents and samples and her useful advise regarding technical aspects of the extraction.

Registry No. 2-Nitroso-N, 132-53-6; cobalt, 7440-48-4.

LITERATURE CITED

(1) Kitamura, M.; Ibe, E.; Uchida, S.; Honda, T.; Romeo, G.; Cowan, R. L. *Nucl. Sci. Eng.* **1985**, *89*, 61.
(2) Kitamori, T.; Fujii, M.; Sawada, T.; Gohshi, Y. *J. Appl. Phys.* **1985**, *58*, 268.
(3) Kitamori, T.; Fujii, M.; Sawada, T.; Gohshi, Y. *J. Spectrosc. Soc. Jpn.* **1985**, *34*, 359.
(4) Lahmann, W.; Ludewig, H.; Welling, H. *Anal. Chem.* **1977**, *49*, 549.
(5) Oda, S.; Sawada, T.; Kamada, H. *Anal. Chem.* **1978**, *50*, 865.
(6) Boyland, E. *Analyst (London)* **1946**, *71*, 230.
(7) Almond, H. *Anal. Chem.* **1953**, *25*, 166.
(8) Needleman, M. *Anal. Chem.* **1966**, *38*, 915.
(9) Motojima, K., unpublished work.

RECEIVED for review February 27, 1986. Accepted May 5, 1986.

Electrochemistry in the Gas Phase. Use of Ultramicroelectrodes for the Analysis of Electroactive Species in Gas Mixtures

Jamal Ghoroghchian, Fereshteh Sarfarazi, Timothy Dibble, John Cassidy, Jerry J. Smith, Andrea Russell, Gordon Dunmore,[1] Martin Fleischmann,[2] and Stanley Pons*

Department of Chemistry, University of Utah, Salt Lake City, Utah 84112

It is demonstrated that ultramicroelectrodes can be used as sensitive electrochemical detectors and sensors in the gas phase. The sensitivity of these devices depends on the electrochemical properties of the analyte and on the properties of the surface separating the ultramicroelectrode from the counter electrode. The devices are demonstrated in this work as gas-phase chromatographic detectors.

New and interesting applications of very small electrodes (ultramicroelectrodes) have been the subject several researchers in the recent literature. High rates of mass transport to, and reduced ohmic and capacitative effects at these devices allow electrochemical measurements under conditions that avoid the need for traditional electrode system environments, such as highly conducting electrolyte solutions. Electrochemical experiments in liquid- and gas-phase solvents with little or no purposely added supporting electrolyte have been reported (*1–6*). The electrochemical potential window is generally extended in the experiments: acetonitrile can be used in simple redox reactions to about 4 V vs. a silver reference, and under special circumstances can be used to almost 6 V. Under these conditions, it has been possible to study the voltammetry of species with very high oxidation potentials, such as short chain alkanes (*7*) and oxygen and the rare gases (*8*). Electrochemistry in low-temperature solution solid eutectic mixtures and glasses of nonaqueous solvents has also been reported (*9*); electrochemistry in these media permits studies of thermally stabilized reactive intermediates that may be generated subsequent to the electron transfer. Each of the above examples makes use of the advantage of greatly reduced ohmic losses at ultramicroelectrodes.

Very small electrodes require only a small number of ion dipoles to charge the electrical double layer. The required number may easily be supplied from the free carrier population present in solutions as impurities or from the autoionization of the solvent. Likewise, some of the aforementioned examples make use of this property. We report in this work the novel use of ultramicroelectrodes in the gas phase and demonstrate their use as an electrochemical detector in gas-phase chromatography, as well as a sensitive electrochemical gas sensor. In these experiments, the charge required for the double layer is supplied from the free carrier charge at the surface of an "insulator" in contact with the ultramicroelectrode. Limiting currents measured are typically on the order of 10^{-10} to 10^{-16} A, in contrast to those measured at conventional macroelectrodes (>10^{-9} A). Since the resistivity of the insulators used to mount the electrodes are on the order of 10^9 Ω, adequate carriers are present for double layer charging. We will show that the conductivity is also sufficiently high to allow measurement of faradaic currents in the gas phase. These experiments must be distinguished from those that have been previously described where macroelectrodes in solid electrolytes have been used. In the present case, a true flux steady state is reached in short times. Ohmic potential losses are small, and the current response can be described in a manner similar to that in conventional electroanalysis (*10*).

EXPERIMENTAL SECTION

A schematic diagram of a ring ultramicroelectrode gas phase detector assembly is shown in Figure 1. Gold was plated onto a 5-μm quartz fiber by first painting a diluted solution (1:1 benzene:ethyl acetate) of Hanovia Liquid Bright Gold (Englehard Industries, Inc.) onto the fiber with subsequent firing at 625 °C

[1] Present address: Dow Chemical Canada, Inc., Research Laboratories, Fort Saskatchewan, Alberta, Canada.
[2] Department of Chemistry, The University, Southampton, Hants S09 5NH, England.

0003-2700/86/0358-2278$01.50/0 © 1986 American Chemical Society

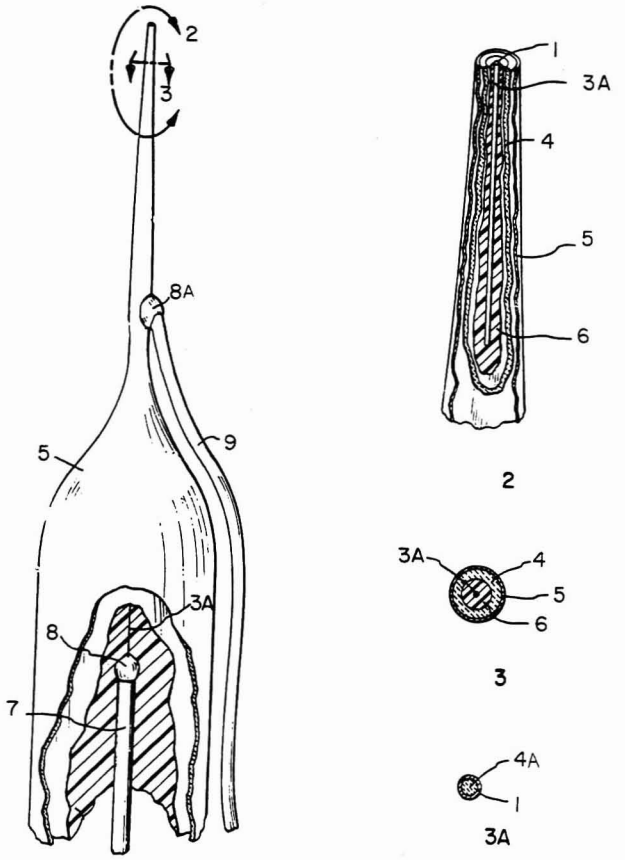

Figure 1. Ultramicroelectrode (gold ring) gas phase detector assembly. The microelectrode assembly (3A) in this case is constructed of a thin gold film (1) on a glass fiber (4A). The tip cross section (3) consists of the assembly (3A) sealed in a glass tube (4) coated with a thick metal film (5) with epoxy resin (6). The working electrode ring (1) is thus separated from the auxiliary electrode (5) by a thin ring of glass and epoxy resin. (2) details the side view of the tip. A fine copper wire (9) is soldered to the metal film for external contact to the auxiliary/reference electrode with lead solder (8A), while a similar connection is made to the microelectrode with another copper wire (7) with silver epoxy (8).

for 1 h in a tube furnace. The procedure is more easily performed by treating a bundle of the fibers simultaneously and extracting a single fiber later under a microscope for the mounting. A quartz tube (0.5–0.7 mm i.d. at the tip) is used for the outer housing and auxiliary electrode mount. Undiluted Liquid Bright Platinum or Palladium was painted onto the outside surface of the tube for a distance of about 2 cm from the tip. The tube was then fired in the tube furnace as were the fibers. A piece of insulated fine copper wire was soldered to the resulting thick film of palladium metal near the end furthest from the tip of the tube. The wire was epoxied to the glass barrel so as to prevent breakage of the connection at the solder joint.

Electrical contact was made to the gold ultramicroelectrode by attaching another fine insulated copper wire with silver loaded epoxy resin (Epoxy Technology, Inc.). The fiber was then inserted into the palladium-coated tube until it just protruded from the tip. This procedure is best performed with a mechanical manipulator under a magnifying glass or microscope. Epoxy resin was then forced into the tube from the large end with a large bore hypodermic needle and syringe so that retraction of the fiber into the tube was prevented by the outward flow of the epoxy from the tip.

When the entire assembly was dry, the tip was cut perpendicularly to the axis of the tube so that a gold ring ultramicroelectrode was exposed. The average thickness of the ring used in this work was about 1 μm.

Carbon disk ultramicroelectrodes (5 μm diameter) were constructed similarly. The carbon fiber (Hercules Corp.) was cut into 2 cm lengths. These were attached to the tip of insulated copper wire leads with conducting epoxy as described above for the rings and mounted in appropriate auxiliary electrode tube assemblies

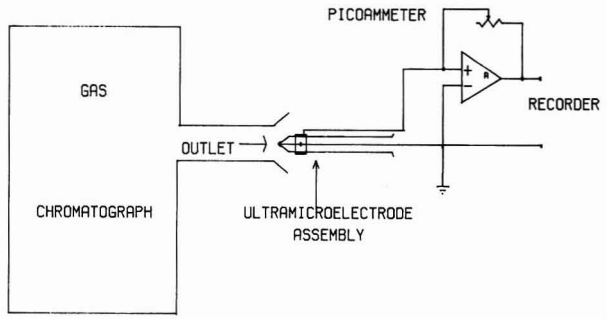

Figure 2. Schematic diagram of the GC system used.

in the same manner. All electrodes were polished on balsa wood bases with varying grades of polishing alumina before use.

The potential difference between the inner and outer electrodes was controlled with a wave form generator (Hi Tek Instruments, Model PPR1). Currents were measured with a digital picoammeter (Keithley Model 619) which was placed in series with the wave form generator and electrochemical cell. We point out that the use of relatively high impedance output devices, like the wave form generator, as current sources is justified in the light of the magnitude of the currents drawn by an ultramicroelectrode system.

The finished ultramicroelectrode assembly was mounted in a Faraday cage to reduce the capacitatively coupled noise. A gas chromatograph (Hewlett-Packard Model 700) was set up adjacent to the cage so that the gas outlet port extended inside the Faraday cage. The tip of the ultramicroelectrode was inserted inside the outlet port so that the dead volume between the column and the detector was minimized (Figure 2). When chromatograms were recorded in this manner and the peaks from the electrochemical detector and a commercial thermal conductivity detector compared after normalizing to a common peak intensity, there were no observed differences in the dispersions of the two peaks. A simultaneous record was maintained on a dual pen strip chart recorder (Houston Instruments, Inc., Omniscribe) of the response of the ultramicroelectrode and the commercially supplied thermal conductivity detector.

Experimental details of specific sets of measurements are given in the results and discussion section.

Ultramicroelectrodes can be designed that, depending on the size, will support steady-state currents in both electrolyte and resistive solutions. All very small conductive microstructures imbedded in a relatively large insulating plane will develop essentially spherical diffusion characteristics during an electrochemical reaction. Diffusion to microspheres can be shown to give rise to a steady-state flux; for instance the relaxation time for this process at a microsphere electrode is given by

$$\tau \approx r^2/4D$$

where r is the radius of the sphere and D is the diffusion coefficient of the electroactive species. This time can be made short ($<10^{-6}$ s) by the simple construction techniques described above. Currents at these structures, typically in the picoampere range, give rise to only small errors in the applied electrode potential; values in highly resistive media result in corrections typically in the millivolt region.

The electrode assembly used in this work consisted of a working ultramicroelectrode separated by a few tenths of a millimeter from the auxiliary electrode by epoxy resin and a thin glass tube. The auxiliary/pseudoreference electrode was made relatively large ($>10^6$) in area. Polarization of the reference system does not occur due to the small currents that are dissipated over the entire surface of the large reference electrode. The total resistance of the resin/glass boundary, although high in absolute terms, still is low enough for the required small currents. The typical leakage current in the system when polarized at +3 V polarization was about 600 fA when using the gold ring electrode. The electroactive analyte, dissolved in the dry nitrogen carrier gas of the chromatograph, is delivered directly to the microelectrode detector at the outlet port. (We point out here that the same assembly can be used as conveniently in a liquid chromatographic or flow injection apparatus. In these cases, supporting electrolyte is not

Table I. Response–Concentration Results for a Platinum Ring Ultramicroelectrode: Water in Ethanol

corr coeff r	slope, nA/% H_2O	injected concn c_0, % H_2O (v/v)	detected concn C_m, ppm	equiv current injected h_0, μA	equiv current detected h_m, nA
0.9998	4.41	0.1	0.5	0.8	2.0
		1	5.3	8.2	4.3
		2	11.2	16.4	8.7
		5	27.7	41.0	22.0
		8	44.1	65.6	36.1
		10	55.5	82.0	43.8
		13	72.0	106.6	57.1
		15	83.1	123.0	66.2

required, and conventional HPLC grade solvents may be used.)

RESULTS AND DISCUSSION

Dilute water samples were prepared in dry ethyl alcohol by volumetric addition and dilution. The chromatographic column in these experiments was Carbowax 20M 3% on Chromasorb W. The dry nitrogen carrier flow rate was maintained at 60 cm^3/min; the injection port temperature was 110 °C, and the column temperature was 50 °C. One-microliter injections of the water alcohol samples were made, and the response of a 1 μm thick 100 μm diameter platinum ring ultramicroelectrode with a platinum auxiliary electrode was measured. Harris (*11*) has provided a discussion of the relation between peak dispersion, injected concentration, and detected concentration, useful in the description of detection limits in systems where Gaussian peak shapes are present.

The concentration C_m detected at the peak maximum is given by

$$C_m = C_0/D_i$$

where D_i is the dispersion and C_0 is the injected concentration. For a detector that has a response h linear with concentration

$$C_m = C_0 h_m/h_0$$

where h_m and h_0 are the responses for the concentration at the maximum of the peak and at a concentration equal to C_0, respectively. h_0 is given by

$$h_0 = (Q/V_s) \int h(t)\, dt$$

where $h(t)$ is the time-dependent response (the peak profile), Q is the gas flow rate (assumed to be constant here), and V_s is the volume of the sample injected. Using this method, C_m was calculated for each of the injected samples. Linearity of the ultramicroelectrode detector was checked by comparing the area of the $h(t)$ response with the injected mass of material. Results for these comparisons are given in Table I, with the correlation coefficient and slope of the response/injected concentration plot. Although a detailed analysis of the detection limits of these detectors has not yet been completed, we can offer some preliminary comments. The background dc noise level for the Pt/Pt electrode system examined has a value of +1.2 pA, and a ripple fluctuation typically of 0.9 pA peak to peak. These values varied as much as 50% depending on the care taken in producing the electrode, its handling, cleanliness of the test solutions, and quality of electrical shielding employed when using. Using these noise figures and the slope from Table I, we calculate the detection limits for water in ethanol to be 6.1×10^{-4}%, if we define detection limits to be the concentration that gives a signal strength three times larger than the background noise level. The dynamic range is limited on the less sensitive end by the fact that at very high mass transport rates, the electrochemical reaction will be pushed into kinetic control; we then expect nonlinear behavior of concentration and current. In this case, the appropriate modifications to the theory must be made in order to obtain quantitative results (*7*).

Scope of Usefulness: Comparison to Thermal Conductivity Detectors. The experiments described in this section were performed to compare the specific detectivity of the ultramicroelectrode with respect to a thermal conductivity detector (Hewlett-Packard Model 4-4188 for their Model 700 gas chromatograph). When the detector amplifier was set to maximum gain, the absolute noise level indicated on the chart recorder was about 100 μV peak to peak.

Experiments were performed with the 5-μm carbon disk electrode. The auxiliary pseudoreference was a 100 μm thick palladium film. The response of the electrode system was checked initially by performing voltammetry of a 5.0 mM hexacyanoferrite solution in 0.06 M KOH and 0.70 mM diphenylanthracene in acetonitrile solution to verify the electrode dimensions and reproducibility of results. Limiting currents for each of 10 successive experiments did not vary by more than 1% in either solution.

The column of the gas chromatograph was maintained at 80 °C. The column was Carbowax 20M 3% on Chromabsorb W. Injector temperature on the chromatograph was maintained at 90 °C. The carrier gas was nitrogen, and the flow rate was 30 mL/min. The effluent was first detected by the same thermal conductivity detector as mentioned above and was then detected by the ultramicroelectrode which was located about 1 mm further down the gas line from the thermal conductivity detector. In the first experiments the electrode was maintained at a potential of +3.0 V with reference to the palladium auxiliary electrode.

The response of the carbon ultramicroelectrode prepared as described in the Experimental Section could be progressively increased by appropriate conditioning. Pulsing the potential of the ultramicroelectrode from +3.0 V to −3.0 V for 5-s intervals for 30 s electrochemically reduces surface impurities and increases the sensitivity of the ultramicroelectrode markedly. This procedure was repeated once every 30 injections to maximize the response. The background noise fluctuation level of the thermal conductivity detector was about 200 μV peak to peak. Table II illustrates relative responses (ultramicroelectrode/thermal conductivity detector) observed under these conditions. The sample injection was 1.0 μL. Figure 3 shows a typical result for aniline at the two detectors at a relative concentration of 10000:1.

The potential of the detector was subsequently adjusted to −3.0 V. Virtually identical responses were observed for the same compounds, except the observed signals were inverted in sign. It is perfectly feasible to perform voltammetry "on the fly" during elution of the peaks, and thus detect the half-wave potential(s) for a component(s) in a chromatographic peak by virtue of the shape of the voltammetric response (*12*).

N-Methylamine was used to study the potential dependence of the response between 0 and +3.0 V. A polarization curve is obtained as expected, except the response is observed to fall at potentials greater than about +2.5 V. This decrease

Table II. Relative Response of Carbon Ultramicroelectrode Detector to Thermal Conductivity Detector

compound	rel response[a]
n-hexane	10
1-hexene	10
acetone	20
acetic acid	10
0.1 M ammonium hydroxide	13000
isopropylamine	10000
N-methylacetamide	10
vinyl chloride (10 ppm in air)	2000
nitrobenzene	500
aniline	1000000
ethanol	12000
methylamine (40% in H_2O)	125000
formic acid	7500
triethylamine	100000
N,*N*-dimethylacetamide	100
carbon monoxide 1.03% in air)	10000
ethyl acetate	10
ethylene dichloride	24000
benzonitrile	172000
ethylbenzene	6000
acetonitrile	16000
trichlorotrifluoromethane	0
toluene	4000
cyclohexanone	10000
water	12000
3-bromothiophene	10

[a] Average of five runs (at +3.0 V). Ratio of calculated detection limits (ultramicroelectrode/thermal conductivity). The detection limits for each detector were obtained from extrapolated values calculated by the method described in section a. The ultramicroelectrode was maintained at +3 V with respect to the auxiliary reference.

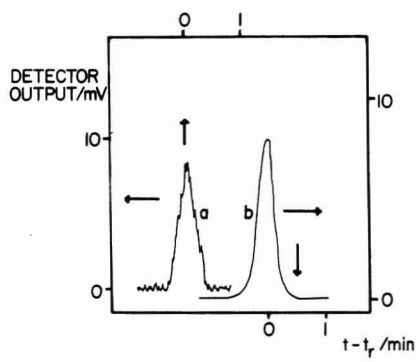

Figure 3. Response of aniline (a) at the thermal conductivity (1.0 μL, neat aniline) detector and (b) at the ultramicroelectrode (1.0 μL, 0.1 mM aniline in diethyl ether) detector.

is most likely due to passivation of the electrode due to polymerization of electroactive species or depletion of electrolyte in the epoxy surface by electrochemical oxidation. Degradation of the response was always accelerated by operation at higher potentials. The surface could be regenerated to the same initial response after cathodic pulse treatment as described earlier. Other compounds show similar behavior at high potentials indicating that the reaction responsible for the degradation in response is most likely due to reaction in the epoxy sealer.

Two standard gas mixtures were analyzed: carbon monoxide (1.03% in air) and pure vinyl chloride. The relative responses to those of a thermal conductivity detector were 10^4 and 2×10^3, respectively.

If the electrode is subjected to 0.1 M NaOH solution for 30 s before use, sensitivity for most compounds is increased by a factor of 2–5. This enhancement fades after a few minutes of exposure to the gas stream. This observation is probably due to several effects. One is the evaporation of the water present at the surface of the epoxy surface, which will increase the resistance. A second possibility is that since electrooxidations for most compounds will proceed easier in the presence of base, there will be an increased response at any fixed high potential. In this case, a fall in the current will be expected after continued oxidation due to a depletion of base. The enhancement returns if the electrode is subsequently subjected to a 5-s submersion in water. Again the response will fade after a few runs. This procedure can be repeated a few times with less enhancement observed on each subsequent treatment. Eventually no enhancement is observed, and we assume that all of the excess KOH electrolyte trapped near the epoxy surface has either been leached out by the excess water, or reacted away, or both. Enhancement can be regenerated by treating the assembly again with the KOH solution. It is clear that permanent increases in ionic conductivity of the surface of the epoxy sealer will provide higher sensitivities, and work is in progress in this area.

Table III. Relative Response of a Gold Ring Ultramicroelectrode Detector to a Thermal Conductivity Detector

compound	rel response[a]
ethanol	1000
ethylene dichloride	80
n-propylamine	50
triethylamine	50
water	3600
methylamine (40%)	6270
aniline	>1000000
acetonitrile	750
toluene	220
ethylbenzene	150
benzonitrile	30000
ethyl acetate	300
acetone	120
hexene	10
carbon tetrachloride	10
cyclohexanone	3800
tert-butylbenzene	<10

[a] Measured as described in Table II.

Table III gives the results for a gold ring ultramicroelectrode using a platinum auxiliary pseudoreference electrode. The diameter of the ring was 50 μm, and the average ring thickness was 1 μm. The potential maintained between the two electrodes was +3.0 V (working vs. auxiliary).

Although there is general similarity in the responses of the carbon and gold ultramicroelectrode detectors, there are some distinct differences. Some of the differences can be explained in terms of relative activation overpotentials of the substrate on the two different surfaces, while some are not easily explained. This area is under continued investigation.

CONCLUSIONS

The results presented show that ultramicroelectrode assemblies can be used to monitor species present in the gas phase as high sensitivity. Such measurements open up a new field of electrochemistry; namely, the reaction of gas-phase species at the microelectrode; these reactions being coupled to current flow over the surface of the "insulator" used to separate the microelectrode and the counter electrode. The reactions may take place on the microelectrode or at the edge of the microelectrode; furthermore the response may be modified by incorporating catalysts at the ultramicroelectrode surface or in the "insulator", as well as by membrane coatings (*12*).

Therefore, topics receiving current attention include: kinetic measurements, the rates of the processes on the surface and the edge of the ultramicroelectrode, the effect of catalysts and membrane coatings.

ACKNOWLEDGMENT

The authors thank Joel Harris for his helpful comments regarding the treatment of the data. This paper is dedicated to Cheves Walling on the occasion of his 70th birthday.

LITERATURE CITED

(1) Pons, S.; Ghoroghchian, J.; Fleischmann, M., patents pending.
(2) Ghoroghchian, J.; Fleischmann, M.; and Pons, S., in preparation.
(3) Bond, A.; Fleischmann, M.; Robinson, J. *J. Electroanal. Chem.* **1984**, *11*, 172.
(4) Howell J. O.; Wightman, R. M. *Anal. Chem.* **1984**, *56*, 524.
(5) Bond, A. M.; Fleischmann, M.; Robinson, J. *J. Electroanal. Chem.* **1984**, *168*, 299.
(6) Bond, A. M.; Fleischmann, M.; Khoo, S. B.; Pons, S.; Robinson, J., submitted for publication in *J. Electrochem. Soc.*
(7) Cassidy, J., Khoo, S. B., Pons, S., and Fleischmann, M., *J. Phys. Chem.* **1985**, *89*, 3933.
(8) Dibble, T.; Bandyopadhyay, S.; Ghoroghchian, J.; Smith, J. J.; Sarfarazi, F.; Fleischmann, M.; Pons, S., submitted for publication in *J. Phys. Chem.*
(9) Bond, A. M.; Fleischmann, M.; Robinson, J. *J. Electroanal. Chem.* **1984**, *180*, 257.
(10) Fleischmann, M.; Bandyopadhyay, S.; Pons, S. *J. Phys. Chem.* **1985**, *89*, 5537.
(11) Harris, J. M. *Anal. Chem.* **1982**, *54*, 2337.
(12) Ghoroghchian, J.; Fleischmann, M.; Pons, S., in preparation.

RECEIVED for review February 27, 1986. Accepted May 12, 1986. We thank the Office of Naval Research and Dow Chemical Co. for support of this work.

Neutral Carrier Based Ca^{2+}-Selective Electrode with Detection Limit in the Sub-Nanomolar Range

Urs Schefer, Daniel Ammann, Ernö Pretsch, Urs Oesch, and Wilhelm Simon*

Department of Organic Chemistry, Swiss Federal Institute of Technology (ETH), Universitätstrasse 16, CH-8092 Zürich, Switzerland

In a 1:3 cation/ligand complex the ionophore *N,N,N′,N′*-tetracyclohexyl-3-oxapentanediamide forms an almost ideal coordination sphere of nine oxygen atoms for the uptake of Ca^{2+}. By use of this ionophore and current membrane technology, solvent polymeric membranes with extremely high Ca^{2+} selectivities are obtained. Na^+ and K^+ are rejected by a factor of $10^{7.4}$ and 10^8, respectively, and the detection limit of the Ca^{2+} electrode response function in an intracellular ion background is at about 100 pM Ca^{2+}.

Considerable effort is invested in the design of calcium ion selective electrodes with improved selectivity and detection limits (*1–5*). The most attractive sensors in this respect are based on the neutral carrier (–)-(*R,R*)-*N,N′*-bis[11-(ethoxycarbonyl)undecyl]-*N,N′*-4,5-tetramethyl-3,6-dioxaoctanediamide (ETH 1001) (*2*) introduced in 1975 (*6*). These sensors have been widely accepted for clinical and electrophysiological Ca^{2+}-activity measurements (*7*). Studies of resting and changing intracellular Ca^{2+} levels are however performed close to the sensor's detection limit, which is dictated by K^+ interference (*8*). Similarly, it has been claimed that the usefulness of these sensors in soil sciences is limited by cation interferences (*9*, *10*).

The neutral carrier *N,N,N′,N′*-tetracyclohexyl-3-oxapentanediamide (ETH 129) (*11*) was shown to form extremely lipophilic 1:3 cation/ionophore complexes with Ca^{2+} and 1:2 complexes with Mg^{2+} (*12*). It is therefore not surprising that the corresponding solvent polymeric membranes show a high rejection of Mg^{2+} relative to Ca^{2+}. A high selectivity for calcium over monovalent cations may be obtained through the incorporation of lipophilic anionic sites into the membrane phase of neutral carrier based liquid membranes for divalent cations (*13*). Thus, with adequate membrane technology, a further improvement of the selectivity of Ca^{2+} electrodes should be feasible. Here we report on a sensing system involving ETH 129 with clearly improved selectivities and detection limits, which was obtained through such interventions.

EXPERIMENTAL SECTION

Reagents. For all experiments, doubly quartz distilled water and chemicals of puriss. or p.a. grade were used.

Membranes. The solvent polymeric membranes were prepared according to ref. 14 using 1 wt % ETH 129 or ETH 1001 carrier, 66 wt % *o*-nitrophenyl octyl ether (*o*-NPOE; puriss. p.a., Fluka AG, Buchs, Switzerland), and 33 wt % poly(vinyl chloride) (PVC high molecular; purum p.a., Fluka AG). As lipophilic anionic site, potassium tetrakis(*p*-chlorophenyl)borate (KTpClPB; purum p.a., Fluka AG) was used (for concentration see below). The syntheses of the carriers ETH 1001 and ETH 129 are described in detail in ref 15 and 11, respectively.

Electrode System. Cell assemblies of the following type were used:

Hg; Hg_2Cl_2, KCl (satd)|3 M KCl|sample solution||
membrane||0.01 M $CaCl_2$, AgCl; Ag

The external half cell was a free flowing free diffusion liquid-junction calomel reference electrode (*16*). The solvent polymeric membranes were mounted in electrode bodies Philips IS-561 (N.V. Philips Gloeilampenfabrieken, Eindhoven, Holland).

Emf Measurements (General). The emf values were measured at 20 ± 1 °C unless otherwise specified. The 16-channel electrode monitor used was equipped with FET operational amplifiers AD 515 KH (input impedance 10^{13} Ω/2 pF; bias current < 150 fA; capacity neutralization; Analog Devices, Norwood, MA). The signal was digitized by a 14-bit analog-to-digital converter DT 1744 (successive approximation, full scale ± 500 mV, Data Translation, Natick, MA). Data were acquired with a single board computer (SBC 80/20-4; SBC 116A; Intel Corp., Santa Clara, CA) programmed in assembly language, using an AMC 95/6011 arithmetic processor (Advanced Micro Computers, Santa Clara, CA). Further processing of the data was performed off-line on a HP-85 calculator (Hewlett-Packard, Palo Alto, CA), programmed in BASIC. The measured emf values were corrected for changes in the liquid-junction potential according to Henderson (*17*, *18*). Using the Debye–Hückel theory, single-ion activities were calculated with the coefficients given in ref 19.

Selectivity Determinations. *Separate Solution Method.* The selectivity factors, log K^{Pot}_{CaM}, were obtained in 0.1 M unbuffered solutions of the corresponding chloride salts.

Fixed Interference Method. The selectivity factors were evaluated from the electrode response functions for the primary

0003-2700/86/0358-2282$01.50/0 © 1986 American Chemical Society

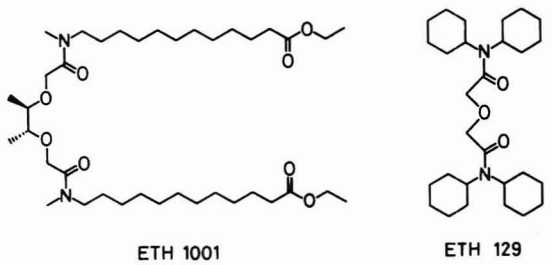

Figure 1. Constitutions of the Ca^{2+} carriers discussed.

ion containing a fixed concentration of the respective interfering ion. The solutions were buffered with pH buffers and Ca^{2+} buffers, using 94 mM Na^+ and 125 mM K^+ as background electrolytes, respectively. The preparation of the buffer solutions is described in ref 20 (Na^+) and 21 (K^+). The solutions with pCa = 9 and pCa = 10 containing 125 mM K^+ were prepared according to ref 21. The compositions of the solutions are given in Table I. The accuracy of the Ca^{2+} activity in the buffer with pCa = 10 is limited by the buffer range of EGTA.

The differences between the measured emf and values corrected for liquid-junction potentials amount, e.g., to −1.39 mV for pCa = ∞, −1.39 mV for pCa = 6 and −1.36 mV for pCa = 3.

Interference by Hydrogen Ions. About 50 mL of a $CaCl_2$ solution of a given concentration (10^{-3}, 10^{-2}, or 10^{-1} M) was used for the measurements. By stepwise addition of small amounts of NaOH and HCl solutions, the pH was gradually changed to about 13 and 1, respectively. The emf values were corrected for changes in the liquid-junction potential and in the activity of Ca^{2+} due to the ionic strength. For example, the differences between the measured emf's and the values corrected for liquid-junction potentials are 1.94 mV for 10^{-1} M $CaCl_2$, −3.83 mV for 10^{-2} M $CaCl_2$, and −4.51 mV for 10^{-3} M $CaCl_2$ (worst case).

Practical Response Time. The electrodes were conditioned in 40 mL of 3×10^{-3} M $CaCl_2$ solution for 1–2 min. Then 1 mL of 0.3 M $CaCl_2$ solution was added and a magnetic stirrer was turned on for approximately 2 s. Emf values were taken at 100-ms intervals.

Stability/Drift. Emf stabilities and emf drift were examined by use of a cell assembly in a thermostated open beaker at 21 ± 1 °C (room temperature) containing a 10^{-3} M $CaCl_2$ solution. The total measuring time was 48 h.

RESULTS AND DISCUSSION

Results of the analysis of the crystal structures of $Mg(NCS)_2$ and of $Ca(NCS)_2$ complexes with ETH 129 (Figure 1) are shown in raster graphics in Figure 2 (*12*). These pictures corroborate the high lipophilicity of the 1:3 Ca^{2+}/ETH 129 complex relative to the 1:2 Mg^{2+}/ETH 129 complex. Indeed, an almost ideal fit with a cavity radius of 102 pm is obtained for Ca^{2+} (radius, 106 pm (*22*)), if nine oxygen atoms (radius

Table I. Composition of Ca^{2+} Buffer Solutions

components	pCa = 9 (125 mM K^+)	pCa = 10 (125 mM K^+)
pH	8.34	8.97
HEPES[a] ($g \cdot L^{-1}$)	2.3831	2.3831
EGTA[b] ($g \cdot L^{-1}$)	3.8035	3.8035
$CaCl_2 \cdot 2H_2O$ ($g \cdot L^{-1}$)	0.7351	0.7351
KOH 1 M ($mL \cdot L^{-1}$)	45.8	48.95
KCl 2 M ($mL \cdot L^{-1}$)	39.6	38.03

[a] HEPES: 4-(2-hydroxyethyl)piperazine-1-ethane-2-sulfonic acid. [b] EGTA: ethylene glycol bis(2-aminoethyl ether)tetraacetic acid.

Table II. Influence of the Concentration of Lipophilic Anionic Sites in ETH 129 Based Membranes[a] on the Ca^{2+} Selectivity

	KTpClPB[b]					
log K^{Pot}_{CaM}	0%	23%	37%	61%	93%	107%
M = Na^+	−3.0	−3.3	−3.5	−3.7	−0.9	−0.9
M = K^+	−3.3	−3.6	−3.9	−4.0	+1.8	+2.1

[a] Membrane composition: 1 wt % ETH 129, 66 wt % *o*-NPOE, 33 wt % PVC. [b] Additions of KTpClPB in mol % relative to the Ca^{2+} carrier concentration.

140 pm) are brought together with a local symmetry of D_{3h} (*23*). This is very close to the observed fit (see Figure 2) with a Ca^{2+}–oxygen distance of 238–263 pm (mean distance amide oxygen to Ca^{2+}, 242 pm; mean distance ether oxygen to Ca^{2+}, 258 pm) formed by three nonmacrocyclic ligands (*12*). Since Mg^{2+} is not located in an optimal, octahedral array of coordinating atoms, a high rejection relative to Ca^{2+} has to be expected in ETH 129 based ion-selective electrodes (*11*).

A high preference of divalent relative to monovalent cations in neutral carrier based potentiometric sensors is observed, if the ionophore is used in a membrane with plasticizers of high dielectric constant in the presence of lipophilic anionic sites (e.g., potassium tetrakis(*p*-chlorophenyl)borate (KTpClPB)). The highest possible carrier-induced selectivity for divalent cations is expected at concentrations of anionic sites of 162, 73, and 46 mol % with respect to the total carrier concentration and 1:1, 1:2, and 1:3 cation/ionophore stoichiometries, respectively (*13*). This trend can be recognized from the data in Table II. In agreement with the 1:3 Ca^{2+}/ETH 129 stoichiometry an optimal rejection of Na^+ as well as of K^+ is observed at around 50 mol % site addition. Since the selectivity data in Table II have been assessed by

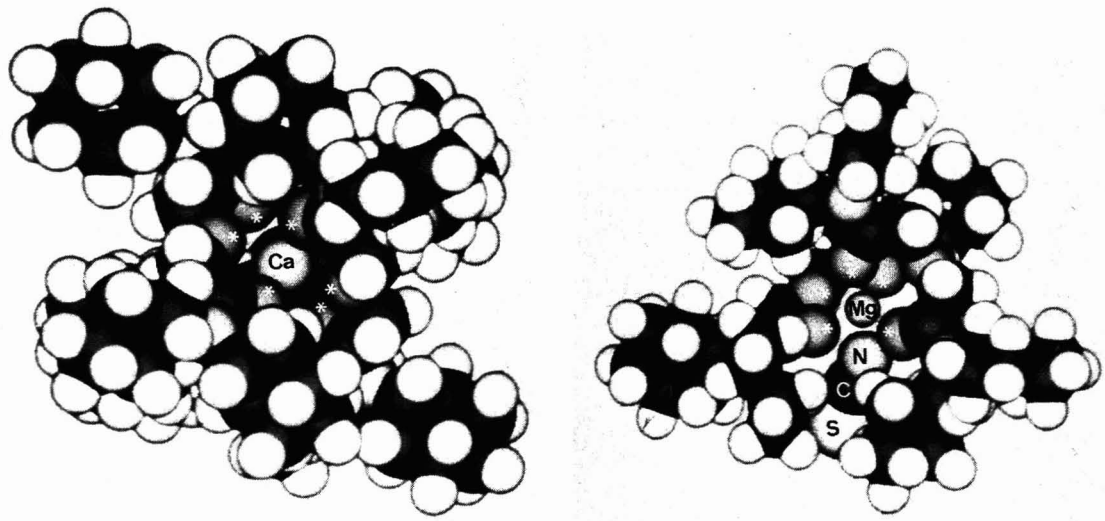

Figure 2. Raster display of the structure of the Ca^{2+} (left) and Mg^{2+} complex (right) of the ligand ETH 129. Oxygen atoms in contact with Ca^{2+} and Mg^{2+} are marked with asterisks (for clarity, pictures show 60% of the van der Waals radii).

Table III. Selectivity Factors, log K^{Pot}_{CaM}, for Solvent Polymeric Membrane Electrodes Based on the Ca^{2+} Carriers ETH 1001 and ETH 129

log K^{Pot}_{CaM}	1.0 wt % ETH 1001 0.5 wt % KTpClPB (69 mol %) 64.0 wt % *o*-NPOE 34.5 wt % PVC	1.0 wt % ETH 129 0.6 wt % KTpClPB (53 mol %) 65.6 wt % *o*-NPOE 32.8 wt % PVC
$M = H^+$	−4.4[a] −0.1[b]	−1.6[a]
$M = Li^+$	−2.8[a]	−3.3[a]
$M = Na^+$	−3.4[a] −6.1[c]	−3.7[a] −7.4[c]
$M = K^+$	−3.8[a] −6.6[d]	−4.0[a] −8.0[d]
$M = Mg^{2+}$	−4.4[a] −5.1[e]	−4.9[a]

[a] Separate solution method using 0.1 M unbuffered metal chloride solutions. [b] Fixed interference method (pH 2), no Ca^{2+} buffers. [c] Fixed interference method (c_{Na} = 94 mM) using Ca^{2+}-buffered solutions. [d] Fixed interference method (c_K = 125 mM) using Ca^{2+}-buffered solutions. [e] Fixed interference method (c_{Mg} = 0.33 M), no Ca^{2+} buffers.

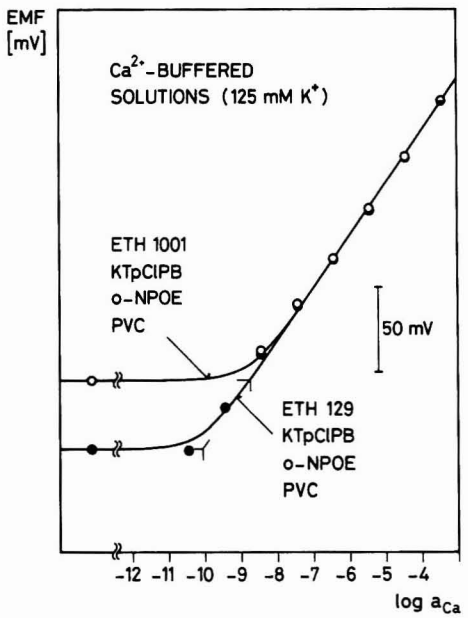

Figure 3. Electrode response of membrane electrode cell assemblies based on the carriers ETH 1001 and ETH 129 in Ca^{2+}-buffered solutions containing 125 mM K^+. The detection limits are at −8.7 (ETH 1001) and −10.1 (ETH 129) log *a* units.

the separate solution method, they may be biased by the presence of alkaline-earth metal cation impurities in the alkali metal solutions. The data therefore may mimic selectivities that are too poor.

A comparison of the selectivities of membranes based on the Ca^{2+} carriers ETH 1001 and ETH 129 (Figure 1) is given in Table III. In both membranes, the addition of a well-defined concentration of lipophilic anionic sites has led to a considerable increase of the Ca^{2+} selectivity. These extremely high Ca^{2+} selectivities can only be measured reliably when using Ca^{2+}-buffered solutions with a high background of interfering ions.

In Ca^{2+}-unbuffered systems the emf measured for the 0.1 M interfering ion solutions is determined by the Ca^{2+} impurities within the reagents used, e.g., an impurity of 10^{-6} M Ca^{2+} determines the emf to the same extent as 10^{-1} M Na^+ for a $K^{Pot}_{CaNa} = 10^{-4}$. This explains the drastically different selectivities observed in Ca^{2+}-buffered and Ca^{2+}-unbuffered systems. Figures 3 and 4 show Ca^{2+} electrode response

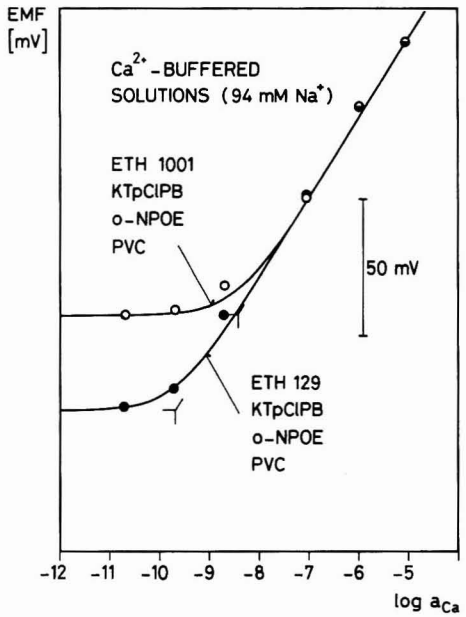

Figure 4. Electrode response of membrane electrode cell assemblies based on the carriers ETH 1001 and ETH 129 in Ca^{2+}-buffered solutions containing 94 mM Na^+. The detection limits are at −8.4 (ETH 1001) and −9.7 (ETH 129) log *a* units.

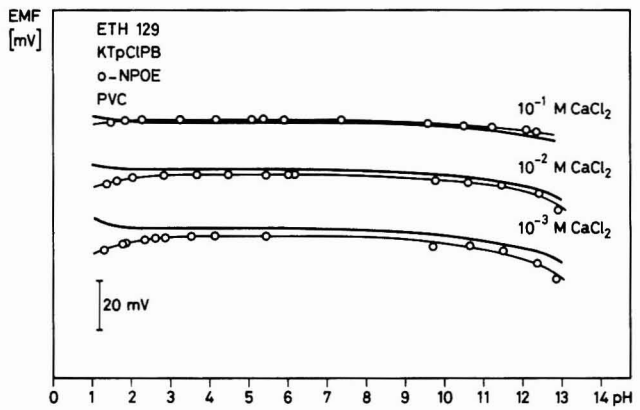

Figure 5. Dependence of the emf of the Ca^{2+} electrode cell assembly based on ETH 129 on the pH of the sample solution for different $CaCl_2$ concentrations: points, experimental values (uncorrected); thick line, emf response after corrections for changes in liquid-junction potentials and Ca^{2+} activity coefficients.

functions obtained in Ca^{2+}-buffered solutions containing a constant typical intracellular K^+ concentration of 125 mM or a relatively high Na^+ background (94 mM). Membranes based on ETH 129 exhibit clearly improved detection limits at pCa = 10.1 (K^+ background) and pCa = 9.7 (Na^+ background), respectively.

The optimum pH working range of the Ca^{2+} electrodes with ETH 129 was evaluated by the fixed primary ion method (Figure 5). The data, which have been corrected for changes in the liquid-junction potential and in the activity coefficients, clearly show that even in millimolar Ca^{2+} solutions no relevant H^+ interference is present at pH values of about 2.

For a stepwise change in the Ca^{2+} concentration from 3×10^{-3} M to 10^{-2} M, the response time is 2.5 s ($t_{90\%}$, Figure 6). Stability measurements using thermostated, unstirred 10^{-3} M $CaCl_2$ solutions in an open beaker yielded emf drifts of ≤50 μV/h. According to its lipophilicity (log P_{TLC} = 7.2 (*24*)) the Ca^{2+} carrier ETH 129 should be a suitable component for the design of membrane electrodes with high lifetime.

The results presented here clearly demonstrate that very high selectivities may be induced with nonmacrocyclic ligands. As predicted earlier (*25*), macrocyclic systems such as cryptands (*26, 27*) and crown ethers (*28, 29*) are not a prerequisite

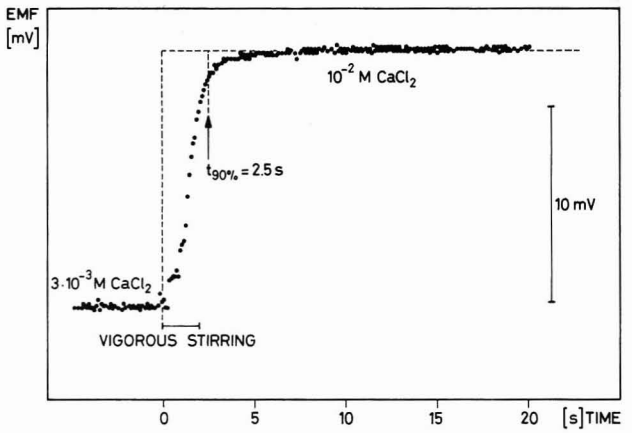

Figure 6. Emf response of a cell assembly based on ETH 129 to a change in concentration from 3×10^{-3} M to 10^{-2} M $CaCl_2$.

for a high selectivity. Using the nonmacrocyclic neutral carrier ETH 129 and current membrane technology, solvent polymeric membranes exhibiting the highest so far reported membrane selectivities for metal cations have been realized. The extreme ion selectivity (10^8) and low detection limit (100 pM Ca^{2+}) open several new aspects in Ca^{2+} analysis. If these properties can be taken advantage of in microelectrodes, intracellular studies of sub-micromolar Ca^{2+} activities will become more reliable and versatile. Furthermore, the sensor is especially suited for other low-level Ca^{2+} measurements, e.g., the detection of $\leq 10^{-4}$ M Ca^{2+} concentrations at pH ≤ 4 in soil chemistry.

Registry No. ETH 129, 74267-27-9; Ca, 7440-70-2.

LITERATURE CITED

(1) Thomas, J. D. R. *Anal. Proc. (London)* **1985**, *22*, 356.
(2) Simon, W.; Ammann, D.; Oehme, M.; Morf, W. E. *Ann. N. Y. Acad. Sci.* **1978**, *307*, 52.
(3) Moody, G. J.; Thomas, J. D. R. *Ion-Sel. Electrode Rev.* **1979**, *1*, 3.
(4) Petranek, J.; Ryba, O. *Anal. Chim. Acta* **1981**, *128*, 129.
(5) Kimura, K.; Kumami, K.; Kitazawa, S.; Shono, T. *J. Chem. Soc., Chem. Commun.* **1984**, 442.
(6) Ammann, D.; Güggi, M.; Pretsch, E.; Simon, W. *Anal. Lett.* **1975**, *8*, 709.
(7) Ammann, D.; Morf, W. E.; Anker, P.; Meier, P. C.; Pretsch, E.; Simon, W. *Ion-Sel. Electrode Rev.* **1983**, *5*, 3.
(8) Meier, P. C.; Lanter, F.; Ammann, D.; Steiner, R. A.; Simon, W. *Pflügers Arch.* **1982**, *393*, 23.
(9) Yu, T. R., private communication.
(10) Yu, T. R. *Ion-Sel. Electrode Rev.* **1985**, *7*, 165.
(11) Pretsch, E.; Ammann, D.; Osswald, H. F.; Güggi, M.; Simon, W. *Helv. Chim. Acta* **1980**, *63*, 191.
(12) Neupert-Laves, K.; Dobler, M. *J. Crystallogr. Spectrosc. Res.* **1982**, *12*, 287.
(13) Meier, P. C.; Morf, W. E.; Läubli, M.; Simon, W. *Anal. Chim. Acta* **1984**, *156*, 1.
(14) Anker, P.; Wieland, E.; Ammann, D.; Dohner, R. E.; Asper, R.; Simon, W. *Anal. Chem.* **1981**, *53*, 1970.
(15) Ammann, D.; Bissig, R.; Güggi, M.; Pretsch, E.; Simon, W.; Borowitz, I. J.; Weiss, L. *Helv. Chim. Acta* **1975**, *58*, 1535.
(16) Dohner, R. E.; Wegmann, D.; Morf, W. E.; Simon, W. *Anal. Chem.*, in press.
(17) Henderson, P. *Z. Phys. Chem.* **1907**, *59*, 118.
(18) Henderson, P. *Z. Phys. Chem.* **1908**, *63*, 325.
(19) Meier, P. C. *Anal. Chim. Acta* **1982**, *136*, 363.
(20) Růžička, J.; Hansen, E. H.; Tjell, J. C. *Anal. Chim. Acta* **1973**, *67*, 155.
(21) Tsien, R. Y.; Rink, T. J. *J. Neurosci. Methods* **1981**, *4*, 73.
(22) Goldschmidt, V. M. *Skr. Nor. Vidensk.-Akad., [Kl.] 1: Mat.-Naturvidensk. Kl.* **1926**.
(23) Morf, W. E.; Simon, W. *Helv. Chim. Acta* **1971**, *54*, 2683.
(24) Simon, W.; Ammann, D.; Pretsch, E.; Morf, W. E.; Oesch, U.; Huser, M.; Schulthess, P. Proceedings of the International Symposium on Ion Transport Through Membranes, Nagoya, Japan, 1986, in press.
(25) Simon, W.; Morf, W. E.; Meier, P. C. *Struct. Bonding (Berlin)* **1973**, *16*, 113.
(26) Dietrich, B.; Lehn, J.-M.; Sauvage, J. P. *Tetrahedron Lett.* **1969**, *34*, 2885.
(27) Lehn, J.-M. *Pure Appl. Chem.* **1980**, *52*, 2441.
(28) Pedersen, C. J. *J. Am. Chem. Soc.* **1967**, *89*, 2495.
(29) Vögtle, F.; Weber, E.; Elben, U. *Kontakte (Darmstadt)* **1980**, *2*, 36.

RECEIVED for review February 18, 1986. Accepted April 28, 1986. This work was partly supported by the Swiss National Science Foundation, by Nova Biomedical Corp., and by Orion Research, Inc.

Design of Neutral Hydrogen Ion Carriers for Solvent Polymeric Membrane Electrodes of Selected pH Range

Urs Oesch, Zbigniew Brzózka,[1] Aiping Xu,[2] Bruno Rusterholz, Gabriela Suter, Hùng Viet Pham, Dieter H. Welti, Daniel Ammann, Ernö Pretsch, and Wilhelm Simon*

Department of Organic Chemistry, Swiss Federal Institute of Technology (ETH), Universitätstrasse 16, CH-8092 Zürich, Switzerland

A series of new neutral carriers for hydrogen ions are used in solvent polymeric membrane (SPM) pH electrodes. Their dynamic pH range is directly related to the acidity constant of the active site of the ionophore. Further features for designing a SPM based pH electrode of broad and selected dynamic range are discussed. On this basis a neutral carrier based membrane electrode for hydrogen ions with a dynamic pH range from 8 to 0 is introduced.

[1] On leave from the Department of Chemistry, Technical University of Warsaw, Ul. Noakowskiego 3, PL-00-664 Warsaw, Poland.
[2] On leave from the Hygiene Department of Nanjing Medical College, Nanjing, People's Republic of China.

In view of ease of preparation, low electrical resistance, and handling safety, there is a considerable interest in nonglass systems for clinical pH measurements for intravascular and intraluminal applications. For this purpose, classical electrically charged ion carriers have been introduced for use in solvent polymeric membranes (*1–4*). Neutral carriers such as tri-*n*-dodecylamine induce much higher selectivities (*5*) and have therefore found wide application in microelectrodes for intracellular studies (*6*, *7*), in solvent polymeric membranes for blood pH measurement (*8*), and in sensors for a variety of other assays (*9–13*). Although the obtained sensor selectivities are very impressive ($\log K^{Pot}_{HNa} = -10.4$, $\log K^{Pot}_{HK} = -9.8$, $K^{Pot}_{HCa} < -11.1$ (*5*)), they are still inferior as compared to glass

0003-2700/86/0358-2285$01.50/0 © 1986 American Chemical Society

electrodes. The cation interference imposes limitations in their use at high pH values and the anion interference sets a limit at the lower end of the pH scale. Since the extent of loading of a neutral carrier with the transported ion is relevant for its behavior in ion-selective electrodes (*14*), it can be assumed that the pH range for the application of a hydrogen ion selective sensor will depend on the acidity constant (pK) of the incorporated ionophore (*5*).

Here we report on the design of neutral hydrogen ionophores for ion-selective electrodes applicable in a distinct pH range. The constitutions of the new ionophores have been selected to cover a wide pK range as well as to exhibit high lipophilicities in view of a high sensor lifetime (*15*). We report further about the design features of such solvent polymeric membrane pH electrodes for an improvement, i.e., an extension, of the applicable pH range.

EXPERIMENTAL SECTION

Membrane Materials. High molecular weight poly(vinyl chloride) (PVC), potassium tetrakis(*p*-chlorophenyl)borate (KTpClPB), tridodecylamine (TDDA, ionophore **1** (Figure 1)), *o*-nitrophenyl octyl ether (*o*-NPOE), dibutyl phthalate (DBP), bis(2-ethylhexyl) sebacate (DEHS), decane-1,10-diyl bis(1-butylpentyl)glutarate (ETH 469 (*16*)) and tris(2-ethylhexyl) phosphate (TEHP) have been obtained from Fluka, Buchs, Switzerland. Tritetradecylamine (TTDA, ionophore **2**) and trihexadecylamine (THDA, ionophore **3**) were purchased from ICN Pharmaceuticals Inc., Plainview, NY. 2-Octadecyloxyaniline (ODA) originates from Alfred Bader Library of Rare Chemicals, Aldrich Co., Inc., Milwaukee, WI. The synthesis of the plasticizer 3,3′,4,4′-benzophenonetetracarboxylic acid tetra-*n*-undecyl ester (BTCU) will be reported elsewhere (*17*). The syntheses of ionophores **4**–**6** are described in ref 13.

Syntheses of Ionophores 7–9 and 11. Ionophore **8** (1-octadecanoyl-4-methylpiperazine) was obtained by the reaction (1 h, 0 °C) of equimolar amounts of 1-methylpiperazine (Fluka) with freshly distilled stearoyl chloride (Fluka) in dry tetrahydrofuran (THF) in the presence of an equimolar amount of triethylamine. The solution was filtered and evaporated. The residual crude product was redissolved in chloroform. This solution was first washed with 0.1 N aqueous sodium hydroxide and then dried with solid anhydrous magnesium sulfate. Purification by flash chromatography (silica gel, acetone) gave pure ionophore **8** (mp 52 °C; 25% yield). Anal. Calcd for **8**: C, 75.35; H, 12.65; N, 7.64. Found: C, 75.21; H, 12.54; N, 7.51.

The synthesis of ionophore **9** (1-octadecanoyl-4-(2-pyridyl)-piperazine) was done as for ionophore **8** using 1-(2-pyridyl)-piperazine (EGA Chemie, Steinheim, GFR) as starting material. Purification was performed by recrystallization from ethyl acetate (mp 77 °C; 64% yield). Anal. Calcd for **9**: C, 75.47; H, 11.03; N, 9.78. Found: C, 75.68; H, 11.37; N, 9.58.

Ionophore **7** (*N*-octadecylmorpholine) was prepared by a two-step reaction over *N*-octadecanoylmorpholine, which was prepared from morpholine (Fluka) according the description for ionophore **8**. *N*-Octadecanoylmorpholine was then reduced (30 min at 0–5 °C and additional 2 h at room temperature) with an equimolar amount of $LiAlH_4$ in dry diethyl ether. After the addition of water and 1 N aqueous sodium hydroxide the suspension was filtered and evaporated. The crude product was purified by flash chromatography (silica gel, ethyl acetate) and distillation (160–170 °C, 0.07 mmHg) to yield pure ionophore **7** (mp 39–40 °C; 34% yield). Anal. Calcd for **7**: C, 77.81; H, 13.36; N, 4.12. Found: C, 77.60; H, 13.18; N, 4.08.

Ionophore **11** (octadecyl isonicotinate) was obtained by reaction of equimolar amounts of isonicotinoyl chloride (crude product from reaction of isonicotinic acid (Fluka) and freshly distilled thionyl chloride in toluene (6 h, 120 °C reflux)) and 1-octadecanol and triethylamine in toluene (16 h, room temperature). After addition of diethyl ether the solution was filtered and evaporated. The residue was redissolved in diethyl ether and three times washed with water. Recrystallization from ethyl acetate/hexane (4:1) yielded pure ionophore **11** (mp 57.5 °C; 15% yield). Anal. Calcd for **11**: C, 76.75; H, 11.00; N, 3.73. Found: C, 76.70; H, 11.10; N, 3.71.

The constitutions of all synthesized ionophores have been confirmed by ^1H NMR (300 MHz, $CDCl_3$), ^{13}C NMR (25 MHz, $CDCl_3$), IR ($CHCl_3$), and MS and the purities have been determined by HPLC (PL gel 100, THF, RI detection).

Lipophilicities. The lipophilicities P of the ionophores have been determined by thin-layer chromatography (TLC) using reverse phase silica plates (KC 18 F, Whatman, Clifton, NJ) and ethanol/water (90:10) as eluent. The retention/lipophilicity correlation has been calibrated with a set of components of known lipophilicities (*18*). Due to the extreme extrapolation on the basis of the calibration components ($0 < \log P < 6$), the uncertainties of the determined $\log P_{TLC}$ values amount from ±1.4 (ionophore **9**, $\log P_{TLC} = 10.8$) up to ±9 (THDA, $\log P_{TLC} \approx 43$).

Membrane Preparation. The membrane components (1 wt % ionophore, 30 wt % PVC, ~70 mol % KTpClPB (with respect to the ionophore), and ~69 wt % plasticizer) totaling 200 mg were dissolved in 2 mL of freshly distilled THF. This solution has been cast into a 24 mm i.d. glass ring resting on a glass plate. After overnight solvent evaporation, the resulting membrane was peeled off from the glass mold and disks of 7 mm diameter were cut out. The membrane disks were mounted in electrode bodies (type IS 561, Philips, Eindhoven, The Netherlands) for emf measurements.

Emf Measurements. All measurements were carried out at 20 °C with cells of the type Hg, Hg_2Cl_2; KCl (satd)|3 M KCl|-sample||membrane||internal filling solution; AgCl, Ag. A citrate buffer of pH 5.6 (1 M citric acid, 2.73 M NaOH, 0.01 M NaCl) has been used as internal filling solution throughout. The potentials have been recorded by a custom made 16-channel electrode monitor (resolution ~120 μV) equipped with one FET operational amplifier AD 515 KH per channel (Analog Devices, Norwood, MA; input impedance 10^{13} Ω/2 pF; input bias current <150 fA; capacity neutralization). The data acquisition was performed with an Intel Data System (Intel Corp., Santa Clara, CA) in combination with a display terminal, ADDS Regent 20 (Applied Digital Data Systems, Inc., Hauppauge, NY), and a Wenger Print Swiss Matrix Printer (Wenger Datentechnik, Basel, Switzerland), and our own software. Off-line processing was performed on a Hewlett-Packard HP-9830 calculator system.

The membrane electrode function as well as that of a pH glass electrode (Philips GA 110, Eindhoven, The Netherlands) has been determined by adding stepwise 4 N hydrochloric acid into the sample buffer (see below). For the presentation of the electrode response, the emf of the membrane electrode is plotted against the pH of the buffer solution measured by the glass electrode. The emf of the membrane electrode is not corrected for the diffusion potential of the liquid junction of the reference electrode, since the measured emf of the glass electrode is influenced in the same manner, thus canceling out by a direct comparison. The pH glass electrode has been calibrated with standard buffers of pH 4.00 and 6.88 (*19*). The *electrical membrane resistance* was determined by use of the method of potential attenuation by known shunt (*15*).

Buffers. The buffer solutions for the determination of the electrode functions have been (a) a citrate/borate buffer with a cationic background of 60 mM Li^+ (60 mM LiOH, 6.6 mM citric acid, and 11.4 mM boric acid), (b) a Tris buffer with 140 mM of Na^+ (10 mM NaOH, 130 mM NaCl, and 10 mM of tris(hydroxymethyl)aminomethane (Tris)), and (c) a Tris buffer with 200 mM K^+ (190 mM KCl, 10 mM KOH, and 10 mM of Tris).

pK Determinations. The pK of the short-chain homologues of the ionophores (Figure 1) have been determined by aqueous titration (Titroprocessor 636/Dosimat E 635, Metrohm, Herisau, Switzerland) at constant ionic strength (I = 0.1 M) (sample, 0.1 M NaCl and 0.01 M amine; titrant, 0.1 M HCl). The used short chain homologues have been triethylamine (Fluka) for ionophores **1**–**3**, 2-(dimethylamino)ethanol (Fluka) for ionophore **4**, (−)-*N*-methylephedrine (Fluka) for ionophore **5**, *N*,*N*,*N*′,*N*′-tetramethylethylenediamine (Fluka) for ionophore **6**, *N*-ethylmorpholine (Fluka) for ionophore **7**, *o*-phenetidine (Fluka) for ionophore **10**, methyl isonicotinate (Fluka) for ionophore **11**, 1-acetyl-4-methylpiperazine for ionophore **8**, and 1-acetyl-4-(2-pyridyl)piperazine for ionophore **9**. The latter two homologues have been synthesized analogously to the descriptions given above.

NMR Experiments. Four milliliters of $CDCl_3$ containing 2.5 wt % dissolved ionophore was shaken vigorously with 4 mL of water containing a varying amount of HCl. After 4 h the pH of

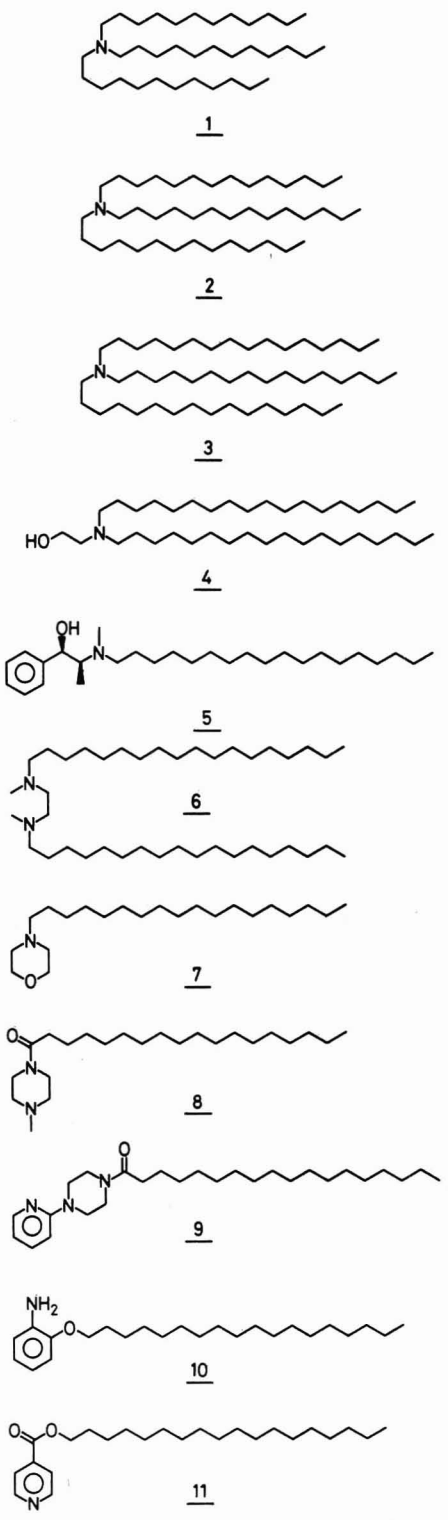

Figure 1. Constitutions of the ionophores discussed.

the water phase was measured with a pH glass electrode. The initial amount of HCl was selected to achieve equilibrium pH values between 6 and 0. The $CDCl_3$ phase was transferred into a 10 mm o.d. NMR tube for recording a ^{13}C NMR spectrum (50.32 MHz, Bruker WP 200 SY FT spectrometer, Fällanden, Switzerland).

The chemical shifts (δ [ppm] relative to Me_4Si as internal standard) of the α-CH_2 to N (ionophore 1), of the β-CH_3 to N (ionophore 5), of the α-CH_2 to O (ionophore 7), and of the γ-C to N (ionophore 11), were measured as a function of the pH of the water phase. The fraction α of the protonated ionophore in $CDCl_3$ was then calculated by

$$\alpha = \frac{\delta - \delta_B}{\delta_{HB} - \delta_B}$$

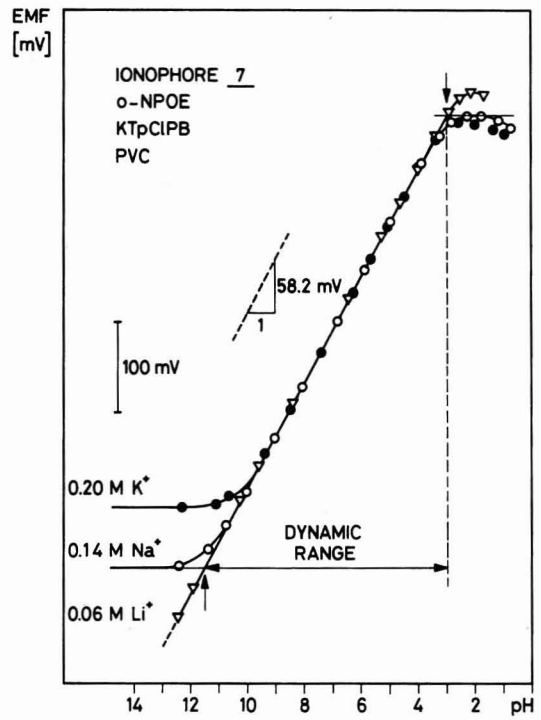

Figure 2. Emf response of a solvent polymeric membrane electrode containing ionophore **7** to the pH of three buffers with different cation backgrounds as indicated (see Experimental Section for detailed buffer compositions). The pH of the buffer is determined by a pH glass electrode. The definition used here for the dynamic range of the electrode is illustrated for the buffer with Na^+ background (circles).

where δ_{HB} and δ_B denote the chemical shifts of the protonated ionophore and the unprotonated ionophore, respectively, and δ denotes the chemical shift of a mixture of them.

RESULTS AND DISCUSSION

A typical electrode response of a solvent polymeric membrane based on a hydrogen ion ionophore to the pH of a sample solution is given in Figure 2. Here we define the dynamic range of the membrane electrode as the pH range extending from the lower to the upper detection limit as it is illustrated for the 0.14 M Na^+/Tris buffer background in Figure 2. The lower detection limit (at high pH) is given by the cation interference and therefore varies depending on the cation background used in the buffered samples. The upper detection limit (at low pH) is controlled by anion interference (*4*).

As expected, a more lipophilic cation M leads to a more severe interference, which is equivalent to a larger potentiometric selectivity factor K^{Pot}_{HM}. The selectivity factors log K^{Pot}_{HM} can be calculated from the electrode functions as depicted in Figure 2 (fixed interference method (*20*)). For the cell assembly described therein log K^{Pot}_{HM} amounts to −9.4, −10.5, and <−11.2 for M = K^+, Na^+, and Li^+, respectively.

Electrode functions as given in Figure 2 for ionophore **7** have been determined for all the ionophores presented in Figure 1. The dynamic ranges of the corresponding membrane electrodes in the three buffers used are displayed in Figure 3 in dependence of the pK of the employed ionophore (Table I). Ionophores **2** and **3** show dynamic ranges only marginally deviating from ionophore **1** as anticipated on the basis of their constitutions. They are therefore not displayed.

The slopes of the linear part of the dynamic ranges have been found to be in all cases between 56.6 mV and 58.7 mV. The electrical resistance of all the electrodes used have been measured to be the range of 30 kΩ to 1 mΩ. The response time (t_{90}%) of the electrodes upon addition of hydrochloric acid to the stirred and buffered sample has been typically a few seconds in all cases. Due to the limited water solubility of

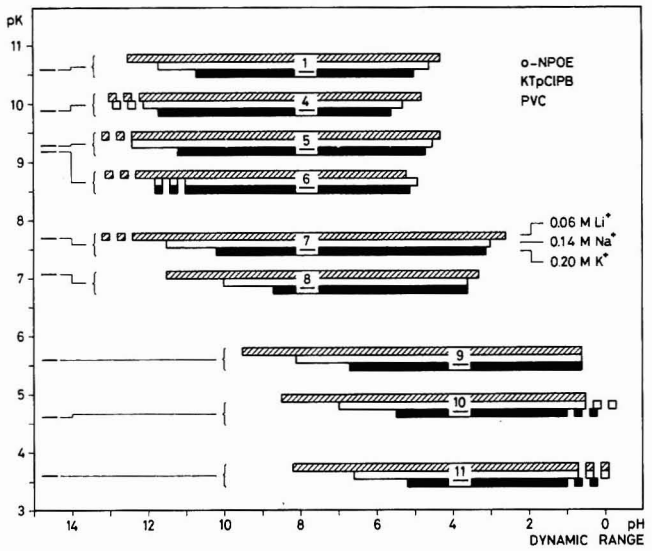

Figure 3. Dynamic pH range of solvent polymeric membrane electrodes containing different hydrogen ion ionophores in three buffers with different but constant cation background in relation to the pK of the corresponding short-chain homologue of the ionophore. In cases where the last or first point of the experimental electrode function is still or already, respectively, on its linear portion, the uncertainty of the end of the dynamic range is indicated by a broken bar (cf. Figure 2). Membrane composition: 30 wt % PVC, ~69 wt % o-NPOE, 1 wt % ionophore, 70 mol % KTpClPB. See Experimental Section for the detailed composition of the background of the three buffers used.

Table I. Physicochemical Properties of the Ionophores Discussed

ionophore	lipophilicity log P_{TLC}[a]	pK[c]	acronym
1	~31[b]	10.6	TDDA
2	~36	10.6	TTDA
3	~43	10.6	THDA
4	23.3	9.9	ETH 1548
5	16.1	9.3	ETH 595
6	15.7	9.2	ETH 1566
7	13.8	7.7	ETH 1859
8	15.3	7.1	ETH 2043
9	10.8	5.6	ETH 2003
10	15.4	4.6	ODA
11	15.2	3.6	ETH 1778

[a] Logarithm of the partition coefficient between water and octan-1-ol as determined by thin-layer chromatography (TLC). [b] A value of 11.6 has been reported in our earlier papers (*21*, *22*). More extensive investigations in the frame of this work revealed that it is originated in an impurity in the batch of TDDA used at that time. [c] Dissociation constant of the protonated short-chain homologue of the ionophore (see Experimental Section) in water.

the highly lipophilic ionophores used in this work, the pK determinations were carried out on short-chain homologues. It can be assumed that the basicity of the nitrogen atom of the carrier involved in the acid/base equilibrium is barely influenced by an elongation of the alkyl chain. The dynamic ranges steadily shift to higher pH values as the pK of the ionophore is increased (Figure 3). The increase of the basicity of the ionophore leads to an increase in the degree of the protonation of the ionophore within the membrane at a given pH of the sample, since the aqueous acid/base equilibrium (pK) of the ionophore is part of the overall extraction equilibrium

$$L(m) + H^+(aq) + X^-(aq) \rightleftharpoons LH^+(m) + X^-(m)$$

This is confirmed by a determination of the degree of protonation of the ionophore within an organic solvent in equilibrium with an aqueous phase of different pH values by ^{13}C NMR (Figure 4). These titration curves shift in the same way along the pH scale as the potentiometric dynamic ranges of the corresponding membrane electrodes. The use of $CDCl_3$ instead of a solvent polymeric membrane as the organic phase does not change the relative hydrogen ion extraction significantly (*23*).

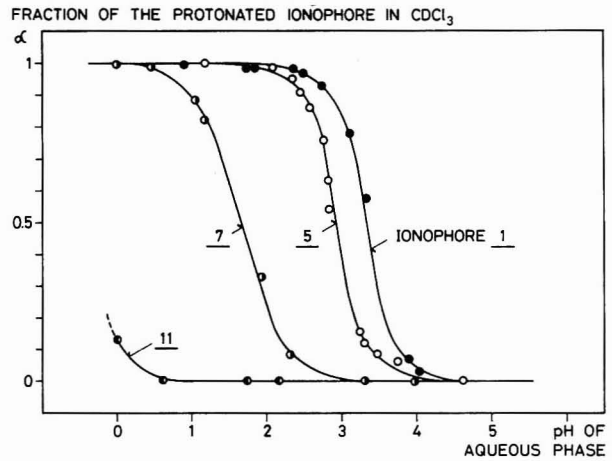

Figure 4. Fraction α of the protonated ionophore in $CDCl_3$ as a function of the pH of an aqueous phase in equilibrium with the organic phase. α has been determined on the basis of the ^{13}C chemical shift of selected carbon atoms of the ionophore (cf. Experimental Section). The chemical shift for the completely protonated ionophore **11**, has been assessed by adding an equimolar amount of KTpClPB into the organic phase and equilibrating it with 4 N hydrochloric acid.

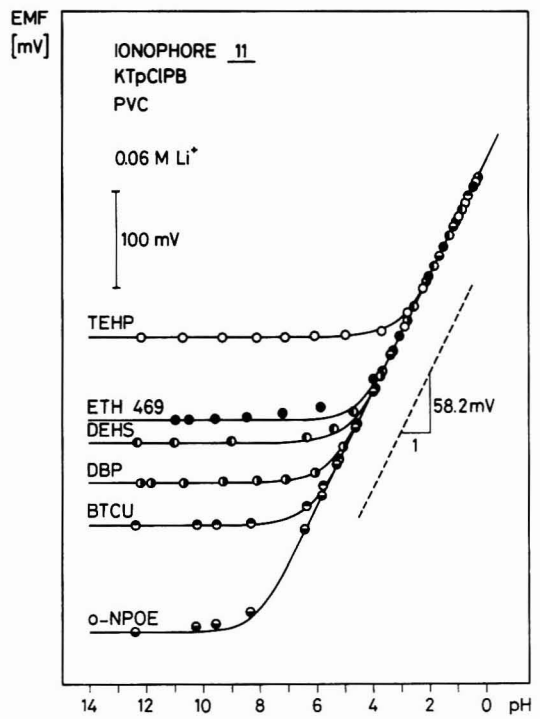

Figure 5. Influence of the plasticizer used in the membrane on the electrode function. Membrane: ~1.0 wt % ionophore **11**, ~1.0 wt % KTpClPB, ~30 wt % PVC, ~68 wt % plasticizer as indicated. Buffer: 60 mM LiOH, 6.6 mM citric acid, 11.0 mM boric acid. The pH adjustment was done by adding stepwise 4 N hydrochloric acid. The pH is determined by a pH glass electrode.

Since different plasticizers extract a given cation to a different extent, the lower detection limit will depend on the nature of the plasticizer used to form the membrane. Indeed, Figure 5 shows that TEHP leads to a poor detection limit at a Li^+ background (*24*), while the use of o-NPOE yields electrodes with a drastically increased dynamic range for the same cation background. Therefore, membranes based on o-NPOE will be most suitable candidates for certain sensor applications.

Such sensors are of particular interest in gastrology, where a dynamic pH range between 0.5 and 7 has to be envisaged (*25*). Yet the electrode shown in Figure 5 satisfies this requirement only partly. Since the selectivity toward Na^+ is poorer than for Li^+ (Figure 3, log $K^{Pot}_{HLi} = -6.9$, log $K^{Pot}_{HNa} = -5.6$), the detection limit will strongly depend on the Na^+ background found in the gastric sample.

The ionophores presented here have been designed to exhibit a high lipophilicity (see Table I). This is necessary to cope with the high lipophilic character of biological samples which will promote the extraction of low molecular weight components (*21*).

The rather low electrical resistance of solvent polymeric membranes (e.g., 2×10^5 Ω cm for the membrane plasticized with *o*-NPOE depicted in Figure 5) as well as the versatility of the membrane fabrication make a miniaturization of a pH sensor easily feasible. The applicability of the membrane system using ionophore **11** in *o*-NPOE plasticized PVC in a miniaturized pH sensor for gastroenterological applications will be reported elsewhere (*26*).

Preliminary in vitro comparison measurements of electrodes using this membrane with glass electrodes show a residual standard deviation of the correlation of 0.15 pH units (n = 23, pH 0 to 6 sample range). Interestingly, the self-correlation between two identical polymeric membrane electrodes leads to a residual standard deviation of 0.02 pH units for the same sample set. Further work for the elucidation of this behavior is in progress.

CONCLUSION

Neutral ionophores for hydrogen ion selective membrane electrodes can be designed by obeying the following points. The ionophore has to contain a basic nitrogen atom. The pK of the nitrogen atom will determine the position of the dynamic range of the electrode. A small pK will shift the dynamic range to small pH values and vice versa. For gastrological applications a pK between 4 and 5 seems to be preferable. To reduce cation interferences, i.e., to broaden the dynamic range, the ionophore should contain neither additional coordination centers as, e.g., amide, ester, or ether functions, nor structural groups that might form chelate rings upon coordination with a cation (e.g., ionophore **10**). The choice of a low metal cation extracting membrane solvent has to be considered with respect to the cation interference as well. Last, the ionophore should be of high lipophilicity and electrically neutral in the unprotonated form. Therefore, simple lipophilic, aromatic heterocycles are promising compounds in this view. Work using such compounds is in progress to create further improved hydrogen ion ionophores of selected and wider pH ranges.

ACKNOWLEDGMENT

Samples of gastric juice were obtained and measured in collaboration with C. Emde and A. L. Blum, Stadtspital Triemli, Zurich.

LITERATURE CITED

(1) Coon, R. L.; Lai, N. C. J. *J. Appl. Physiol.* **1976**, *40*, 625–629.
(2) LeBlanc, O. H.; Brown, J. F.; Klebe, J. F.; Niederach, L. W.; Slusarczuk, G. M. J.; Stoddard, W. H. *J. Appl. Physiol.* **1976**, *40*, 644–647.
(3) Erne, D.; Ammann, D.; Simon, W. *Chimia* **1979**, *33*, 88–90.
(4) Erne, D.; Schenker, K. V.; Ammann, D.; Pretsch, E.; Simon, W. *Chimia* **1981**, *35*, 178–179.
(5) Schulthess, P.; Shijo, Y.; Pham, H. V.; Pretsch, E.; Ammann, D.; Simon, W. *Anal. Chim. Acta* **1981**, *131*, 111–116.
(6) Ammann, D.; Lanter, F.; Steiner, R. A.; Schulthess, P.; Shijo, Y.; Simon, W. *Anal. Chem.* **1981**, *53*, 2267–2269.
(7) Schlue, W. R.; Thomas, R. C. *J. Physiol.* **1985**, *364*, 327–338.
(8) Anker, P.; Ammann, D.; Simon, W. *Mikrochim. Acta* **1983**, *I*, 237–242.
(9) Opdycke, W. N.; Parks, S. J.; Meyerhoff, M. E. *Anal. Chim. Acta* **1983**, *155*, 11–20.
(10) Růžička, J.; Hansen, E. H. *Anal. Chim. Acta* **1984**, *161*, 1–25.
(11) Hongbo, C.; Hansen, E. H.; Růžička, J. *Anal. Chim. Acta* **1985**, *169*, 209–220.
(12) Kessler, M.; Höper, J.; Volkholz, H.-J.; Sailer, D.; Demling, L. *Hepatogastroenterology* **1984**, *31*, 285–287.
(13) Funck, R. J. J.; Morf, W. E.; Schulthess, P.; Ammann, D.; Simon, W. *Anal. Chem.* **1982**, *54*, 423–429.
(14) Büchi, R.; Pretsch, E.; Morf, W. E.; Simon, W. *Helv. Chim. Acta* **1976**, *59*, 2407–2416.
(15) Oesch, U.; Simon, W. *Anal. Chem.* **1980**, *52*, 692–700.
(16) Oesch, U.; Brzőzka, Z.; Simon, W., unpublished work, 1984.
(17) Oesch, U.; Simon, W., unpublished work, 1986.
(18) Ellgehausen, H.; D'Hondt, Ch.; Fuerer, R. *Pestic. Sci.* **1981**, *12*, 219–227.
(19) *Handbook of Chemistry and Physics*, 56th ed.; CRC Press: Cleveland, OH, 1975; p D-135.
(20) Guilbault, G. G.; Durst, R. A.; Frant, M. S.; Freiser, H.; Hansen, E. H.; Light, T. S.; Pungor, E.; Rechnitz, G.; Rice, N. M.; Rohm, T. J.; Simon, W.; Thomas, J. D. R. *Pure Appl. Chem.* **1976**, *48*, 127–132.
(21) Oesch, U.; Dinten, O.; Ammann, D.; Simon, W. *Ion Measurements in Physiology and Medicine*; Kessler, M., Harrison, D. K., Höper, J., Eds.; Springer-Verlag: Berlin, Heidelberg, 1985; pp 42–47.
(22) Oesch, U.; Anker, P.; Ammann, D.; Simon, W. *Ion-Selective Electrodes*; Pungor, E., Buzás, I., Eds.; Akadémiai Kiadó: Budapest, 1985; pp 81–101.
(23) Erne, D. PhD Thesis ETH 6889, Zürich, 1981.
(24) Oesch, U. Diploma thesis ETH Zürich, Zürich, 1974.
(25) Fimmel, C. J.; Etienne, A.; Cilluffo, T.; Ritter, Ch.; Gasser, Th.; Rey, J.-P.; Caradonna-Moscatelli, P.; Sabbatini, F.; Pace, F.; Bühler, H. W.; Bauerfeind, P.; Blum, A. L. *Gastroenterology* **1985**, *88*, 1842–1851.
(26) Oesch, U.; Brzőzka, Z.; Xu, A.; Simon, W., submitted for publication in *Med. Biol. Eng. Comput.*

RECEIVED for review February 26, 1986. Accepted May 6, 1986. This work was partly supported by the Swiss National Science Foundation and by Orion Research, Inc. Z.B. and A.X. thank the Exchange Service of ETH and the Ministry of Education of the People's Republic of China, respectively, for grants.

Predicting Standard pH Values for Reference Buffer Solutions in Solvent Mixtures with Water

Paolo Longhi, Torquato Mussini,* and Sandra Rondinini

Department of Physical Chemistry and Electrochemistry, University of Milan, Via Golgi 19, I-20133 Milano, Italy

Analysis of available data of reference value standards, pH_S, for pH measurements in different binary mixtures of nonaqueous solvents with water shows that these values are satisfactorily accounted for in terms of such determinable physicochemical variables as solvent composition, dielectric constant, and temperature, together with the transfer activity coefficient upon the basic cell for the determination of the above pH_S standards. A procedure is described, based on a multilinear regression analysis, that permits reliable pH_S values to be predicted for other solvents or solvent mixtures from knowledge of the relevant values of the above variables.

According to the procedure recently endorsed by IUPAC (*1*, *2*), the standard values, pH_S, for the reference buffer solution (potassium hydrogen phthalate, KHPh, of molality 0.05 mol/kg in the appropriate solvent–water or aqueous-organic binary solvent mixture) are to be determined experimentally from the electromotive force (emf), E, of the reversible cell

$$\mathrm{Pt|H_2\ (1\ atm)|KHPh}\ (m_S) + \mathrm{KCl}\ (m_{Cl})\mathrm{|AgCl|Ag|Pt} \quad (1)$$

at fixed molality $m_S = 0.05$ and various molalities m_{Cl} of KCl added to KHPh. In fact the functional expression for E is

$$(E - E^\circ)/k = \mathrm{p}(a_H a_{Cl}) = \mathrm{p}(a_H\gamma_{Cl}) + \mathrm{p}m_{Cl} = \mathrm{pH} + \mathrm{p}\gamma_{Cl} + \mathrm{p}m_{Cl} \quad (2)$$

where $k = (RT/F)\ \ln 10$, a, and γ are ionic activities and activity coefficients, respectively (the ions are indicated without charge signs), E° is the standard emf of cell (1), p = −log, and pH is the currently compacted symbol for pa_H. Hence it is evident that the quantity

$$\mathrm{p}(a_H\gamma_{Cl}) = \mathrm{pH} + \mathrm{p}\gamma_{Cl} = (E - E^\circ)/k - \mathrm{p}m_{Cl} \quad (3)$$

is determinable in thermodynamically exact terms, but an extrathermodynamic convention, e.g., a form of the Debye–Hückel equation

$$\mathrm{p}\gamma_{Cl} = AI^{1/2}/(1 + a_0BI^{1/2}) \quad (4)$$

is necessary for obtaining pH from $\mathrm{p}(a_H\gamma_{Cl})$ for the KHPh + KCl mixed electrolyte. This requires determining the ionic strength $I = I_S + m_{Cl}$ (where $I_S \neq m_X$ and $I \leq 0.1$ mol/kg), which in turn requires preliminary knowledge of the ionization constants of the *o*-phthalic acid in the appropriate solvents considered: an iterative calculation scheme described in the literature (*2*–*6*) provides the sought I values, and $\mathrm{p}\gamma_{Cl}$ can therefore be calculated from eq 4 for subsequent insertion into eq 3. Thus a distinct pH value is obtained *for each* m_{Cl} in the KHPh + KCl mixed electrolyte. The required value for KHPh *alone* at $m = 0.05$ mol/kg, i.e., the standard pH_S value, can finally be obtained as intercept at $m_{Cl} = 0$ from the pH vs. m_{Cl} linear regression. It was ascertained that in pure water the same results for pH_S were obtained by the reverse scheme of regression of $\mathrm{p}(a_H\gamma_{Cl})$ values vs. m_{Cl} and use of eq 4 for the I_S ($m_{Cl} = 0$) value only; instead, in nonaqueous or mixed solvents, discrepancies of the order of several 0.001 may ensue. For this reason, all original pH_S results for KHPh in solvent mixtures published prior to 1985 have here been revised to make all of them in line with the former, direct scheme; they are quoted in Table I. It is worthwhile to recall that each standard pH_S so determined is *only* valid for pH measurements in the *same* solvent used in cell 1.

It was shown recently (*3*, *5*, *7*–*9*) that E of cell 1—either as such or with HCl as working electrolyte—as well as $\mathrm{p}(a_H\gamma_{Cl})$ of eq 3 can be analyzed to critically check the internal consistency of results in various series of solvent mixtures and to determine such relevant standard thermodynamic functions as E° of the cell (plus the related ΔG°, ΔH°, and ΔS°) and $\mathrm{p}(a_H\gamma_{Cl})^\circ$—together with the respective estimated errors—by a single-stage multilinear regression method based on three independent variables. The latter are, typically mole fraction x of the nonaqueous component of the solvent mixture, molality m_{Cl} of KCl in admixture with KHPh, and temperature T as articulated into the following definitions: $z = (T - \Theta)/\Theta$ (where $\Theta = 298.15$ K is an arbitrary reference temperature), $u_1 = z/(1 + z)$ and $u_2 = [\ln (1 + z) - u_1]$.

This multiregression scheme can also be fitted to such an extrathermodynamic quantity as pH and leads to functional expressions that can accurately reproduce the pH values determined experimentally in each series of water + nonaqueous solvent mixtures investigated. It was invariably observed that, in all series of aqueous organic solvent mixtures investigated, pH varies linearly with m_{Cl} (which allows straightforward extrapolation to $m_{Cl} = 0$ to obtain pH_S as intercept); thus the m_{Cl} dependence in the multiregression equations is articulated on the first-power term in m_{Cl}. Actually, for methanol/water mixtures we have ($n = 264$; $s_f = 0.010$, $s_{max} = 0.0039$)

$$\mathrm{pH} = 4.0103 + 4.194x - 4.34x^2 + 3.60x^3 - 1.734m_{Cl} + 8.5xm_{Cl} - 31.2x^2m_{Cl} + 24.3x^3m_{Cl} + 0.340u_1 - 5.87xu_1 + 16.6x^2u_1 - 12.8x^3u_1 + 10.1u_2 \quad (5)$$

for 1,4-dioxane/water mixtures ($n = 227$; $s_f = 0.0051$, $s_{max} = 0.0019$)

$$\mathrm{pH} = 4.0040 + 15.54x - 43.6x^2 + 81.0x^3 - 1.05m_{Cl} - 6.53xm_{Cl} + 0.279u_1 - 5.6xu_1 - 86x^2u_1 + 660x^3u_1 + 9.46u_2 - 2210u_2x^3 \quad (6)$$

and for acetonitrile/water mixtures ($n = 159$; $s_f = 0.0097$, $s_{max} = 0.0034$)

$$\mathrm{pH} = 4.0003 + 7.14x + 10.0x^2 - 99x^3 - 0.861m_{Cl} + 3.6xm_{Cl} - 170x^3m_{Cl} + 0.321u_1 - 9.30xu_1 + 14.5u_2 \quad (7)$$

where s_f is the standard deviation of fit, s_{max} is the maximum standard error observed for a single calculated pH value, and n is the number of pH data processed.

Therefore, each of these pH expressions may be safely and conveniently used for standardization purposes, i.e., to interpolate operational pH_S values (obviously zeroing all m_{Cl} terms) at any desired solvent composition and temperature within the ranges explored for each solvent pair in mixture,

0003-2700/86/0358-2290$01.50/0 © 1986 American Chemical Society

Table I. Comparison of pH_S Standard Values (with Estimated Standard Errors) in Different Aqueous Organic Solvent Mixtures at Various Temperatures, T, and Compositions (Mole Fraction x, and Weight Percentages, of Organic Cosolvent in the Mixtures)

organic cosolvent	x	% (w/w)	T/K	a	b	c
methanol	0.0	0.0	283.15	3.994 ± 0.001	4.006 ± 0.003	3.993 ± 0.008
	0.0	0.0	298.15	4.007 ± 0.001	4.010 ± 0.002	4.016 ± 0.005
	0.0	0.0	313.15	4.038 ± 0.001	4.039 ± 0.002	4.037 ± 0.007
	0.0588	10.0	283.15	4.229 ± 0.003	4.254 ± 0.002	4.251 ± 0.008
	0.0588	10.0	298.15	4.220 ± 0.004	4.243 ± 0.002	4.256 ± 0.005
	0.0588	10.0	313.15	4.240 ± 0.003	4.257 ± 0.002	4.265 ± 0.007
	0.1232	20.0	283.15	4.475 ± 0.005	4.490 ± 0.003	4.492 ± 0.012
	0.1232	20.0	298.15	4.465 ± 0.006	4.468 ± 0.003	4.487 ± 0.008
	0.1232	20.0	313.15	4.472 ± 0.005	4.472 ± 0.003	4.486 ± 0.011
	0.3599	50.0	283.15	5.175 ± 0.002	5.151 ± 0.003	5.151 ± 0.011
	0.3599	50.0	298.15	5.146 ± 0.002	5.125 ± 0.003	5.137 ± 0.007
	0.3599	50.0	313.15	5.139 ± 0.003	5.127 ± 0.003	5.130 ± 0.011
	0.4999	64.0	283.15	5.470 ± 0.004	5.488 ± 0.004	5.482 ± 0.014
	0.4999	64.0	298.15	5.458 ± 0.005	5.472 ± 0.004	5.474 ± 0.009
	0.4999	64.0	313.15	5.476 ± 0.006	5.482 ± 0.004	5.472 ± 0.014
	0.7497	84.2	283.15	6.257 ± 0.004	6.254 ± 0.003	6.251 ± 0.017
	0.7497	84.2	298.15	6.227 ± 0.006	6.232 ± 0.003	6.240 ± 0.010
	0.7497	84.2	313.15	6.242 ± 0.004	6.237 ± 0.003	6.235 ± 0.016
1,4-dioxane	0.0	0.0	288.15	3.999 ± 0.001	4.000 ± 0.001	4.001 ± 0.007
	0.0	0.0	298.15	4.007 ± 0.001	4.004 ± 0.001	4.016 ± 0.005
	0.0	0.0	308.15	4.025 ± 0.002	4.018 ± 0.001	4.030 ± 0.006
	0.0	0.0	318.15	4.049 ± 0.002	4.041 ± 0.001	4.043 ± 0.008
	0.0222	10.0	288.15	4.318 ± 0.003	4.330 ± 0.002	4.335 ± 0.006
	0.0222	10.0	298.15	4.322 ± 0.003	4.329 ± 0.002	4.338 ± 0.005
	0.0222	10.0	308.15	4.330 ± 0.003	4.337 ± 0.002	4.340 ± 0.005
	0.0222	10.0	318.15	4.351 ± 0.003	4.355 ± 0.002	4.348 ± 0.007
	0.0806	30.0	288.15	5.038 ± 0.002	5.034 ± 0.002	5.035 ± 0.010
	0.0806	30.0	298.15	5.018 ± 0.003	5.015 ± 0.001	5.021 ± 0.008
	0.0806	30.0	308.15	5.009 ± 0.003	5.007 ± 0.001	5.014 ± 0.008
	0.0806	30.0	318.15	5.014 ± 0.003	5.008 ± 0.002	5.008 ± 0.010
	0.1697	50.0	288.15	5.777 ± 0.004	5.779 ± 0.002	5.775 ± 0.014
	0.1697	50.0	298.15	5.781 ± 0.004	5.782 ± 0.002	5.787 ± 0.010
	0.1697	50.0	308.15	5.784 ± 0.004	5.783 ± 0.002	5.789 ± 0.010
	0.1697	50.0	318.15	5.782 ± 0.003	5.783 ± 0.002	5.780 ± 0.014
acetonitrile	0.0	0.0	288.15	3.999 ± 0.001	3.988 ± 0.002	4.001 ± 0.007
	0.0	0.0	298.15	4.007 ± 0.001	4.000 ± 0.002	4.016 ± 0.005
	0.0	0.0	308.15	4.025 ± 0.002	4.019 ± 0.002	4.030 ± 0.006
	0.0226	5.0	288.15	4.162 ± 0.004	4.170 ± 0.003	4.191 ± 0.006
	0.0226	5.0	298.15	4.163 ± 0.007	4.165 ± 0.003	4.195 ± 0.004
	0.0226	5.0	308.15	4.175 ± 0.007	4.177 ± 0.003	4.194 ± 0.005
	0.0719	15.0	288.15	4.550 ± 0.007	4.548 ± 0.003	4.542 ± 0.008
	0.0719	15.0	298.15	4.527 ± 0.007	4.528 ± 0.003	4.527 ± 0.005
	0.0719	15.0	308.15	4.527 ± 0.005	4.524 ± 0.003	4.509 ± 0.008
	0.1583	30.0	288.15	5.030 ± 0.006	5.034 ± 0.003	5.037 ± 0.014
	0.1583	30.0	298.15	4.985 ± 0.006	4.985 ± 0.003	4.995 ± 0.009
	0.1583	30.0	308.15	4.959 ± 0.005	4.956 ± 0.003	4.951 ± 0.013
isopropyl alcohol	0.0322	10.0	288.15	4.235 ± 0.005		4.187 ± 0.007
	0.032	10.0	298.15	4.247 ± 0.004		4.203 ± 0.005
	0.0322	10.0	308.15	4.260 ± 0.003		4.224 ± 0.006
	0.0322	10.0	318.15	4.285 ± 0.004		4.253 ± 0.009
	0.4114	70.0	288.15	5.662 ± 0.007		5.661 ± 0.015
	0.4114	70.0	298.15	5.637 ± 0.011		5.635 ± 0.010
	0.4114	70.0	308.15	5.646 ± 0.011		5.648 ± 0.010
	0.4114	70.0	318.15	5.966 ± 0.008		5.694 ± 0.015
dimethyl sulfoxide	0.0545	20.0	298.15	4.471		4.488 ± 0.010
	0.0899	30.0	298.15	4.761		4.719 ± 0.014

[a] Observed values, recalculated from ref 3, 5, and 9–11. [b] From eq 5, 6, and 7 for each single series of solvent mixtures. [c] From the all-solvent multiregression equation (8).

thus saving many and expensive experiments.

RESULTS AND DISCUSSION

An overall survey of the pH_S vs. x vs. T courses for KHPh in the five series of water-rich binary solvent mixtures hitherto available (methanol/water (*3*), 1,4-dioxane/water (*5*), acetonitrile/water (*9*), dimethyl sulfoxide/water (*10*), and isopropyl alcohol/water (*11*)) suggests that, at dielectric constants ϵ greater than ≈25 (say, with negligible ion association), the corresponding series of observed pH_S data can well be fitted all together in *one* such multiregression analysis with important functional results, provided that there is introduced some new appropriate variable as an identity marker of the features of the organic component of the solvent mixture. To this purpose, the dielectric constant ϵ and the transfer activity coefficient γ_t (*12*) (which are implicit functions of T and solvent composition) have much to recommend them. It is to be remarked that ϵ values are more easily available for 100%

pure solvents than for binary mixtures, whereas the contrary occurs for γ_t values. Following these lines, the equation of *overall* multiregression comes out as (n = 56; s_f = 0.018, s_{max} = 0.016)

$$pH_S = 4.0159 + 7.61x - 31.7x^2 - 1.28x^3 - 0.664x\epsilon + 0.01464x\epsilon^2 + 2.46x^2\epsilon - 0.0463x^2\epsilon^2 - 1.244 \log \gamma_t + 0.44u_1 - 24.7u_1x + 3.88u_1x\epsilon - 0.091u_1x\epsilon^2 - 6.2u_1x^2\epsilon + 0.164u_1x^2\epsilon^2 + 0.63u_1x^3\epsilon \quad (8)$$

where ϵ is the dielectric constant at 298.15 K of the 100% pure nonaqueous component of the solvent mixture, and the transfer activity coefficient is γ_t = antilog $({}^wE° - {}^sE°)/2k$ where ${}^wE°$ and ${}^sE°$ are the standard emf's of the cell (1) (here γ_t concerns the transfer of the pair of ions H^+ and Cl^-) in pure water and in the aqueous organic mixture, respectively, at the working temperature T. The results are shown in Table I where in column A are quoted the original pH_S values recalculated to make all of them consistent with the same scheme of data elaboration, as mentioned in the introductory section; column B gives pH_S values obtained by putting m_{Cl} = 0 in the multiregression eq 5, 6, and 7 coming out from each separate series of mixtures of the indicated nonaqueous solvent with water; and column C shows the pH_S values given by the *overall* multiregression equation (8). It is evident that this latter equation reproduces the whole of the observed pH_S values with a typical accuracy of ≈0.02 in pH, which complies with the pH standardization requirements in aqueous organic solvent mixtures, even if those observed pH_S values reflect quite different nonaqueous components of those solvent mixtures (methanol and isopropyl alcohol, dipolar amphiprotic; 1,4-dioxane, nonpolar aprotic; acetonitrile and dimethyl sulfoxide, dipolar aprotic). The appropriateness of including ϵ and γ_t in the multiregression as specific variables accounting for the characterizing features of the nonaqueous component of the solvent mixture is quite clear and, since accurate ϵ and γ_t values are now available in the literature (*13*, *14*) for the important case of ethanol/water solvent mixtures, even at temperatures lower than 273 K, eq 8 can be reliably used as a guide to predicting pH_S for the reference value 0.05 m KHPh buffer solution in the latter mixtures. In fact, such pH_S values, which are long overdue, did not hitherto find experimental determination, in spite of the popularity of ethanol as organic cosolvent in admixtures with water for use in chemistry and electrochemistry. Thus, at T = 298.15 K, the following pH_S values can be predicted for the relevant weight percentages (and mole fractions) of ethanol: 4.19 at 10% (x = 0.0417), 4.34 at 20% (x = 0.0891), and 4.65 at 40% (x = 0.2069), respectively.

Continuous accumulation of experimental pH_S data for new and diverse organic cosolvents in admixture with water and their aggregation to the present ones for overall processing will, of course, allow continuous improvement of the constants in the operational equation (8) together with increase of the pH_S-predicting reliability of the latter.

CONCLUSIONS

The present multiregression treatment for interpretation of pH_S based on four variables (temperature, mole fraction of organic cosolvent in admixture with water, dielectric constant, and transfer activity coefficient) can be reliably applied to predict pH_S values for the reference value 0.05 m KHPh buffer solution in other aqueous organic solvent mixtures of dielectric constants greater than ≈25 (provided that the relevant, reliable values of dielectric constant and transfer activity coefficient are available), with a typical accuracy of ≈0.02 in pH, which is compatible with the pH standardization requirements in aqueous organic solutions. This, of course, holds especially for the families of organic cosolvents (alcohols and glycols, ethers, sulfoxides, nitriles) akin to those for which experimental pH_S data were available for the analysis leading to the multiregression equation (8). Acquisition of experimental pH_S values for new and dissimilar solvents will likely improve the pH_S-predicting reliability and extend the area of solvent families of safe applicability, which will be useful for electroanalysis, electrochemistry, and corrosion studies.

This treatment is, evidently, applicable also to standard buffer materials other than KHPh (the reference value standard), e.g., the acetate, phosphate, succinate and oxalate buffers. Hitherto, however, the available data for these buffers are, unfortunately, limited (*2*) to methanol/water, ethanol/water, and dimethyl sulfoxide/water mixtures at 298.15 K, with the only exception of the acetate and succinate buffers in 50% w/w methanol/water, which impairs the treatment basis and curtails its reliability and applicability to other temperatures and other solvents. Clearly, accumulation of data is awaited for the multiregression predicting treatment to be applicable to these subsidiary buffers.

Considering conditions of the aqueous organic mixtures where significant ion association might be expected to occur (i.e., at dielectric constants ϵ < 25), this treatment could be extended by taking into account the appropriate association constants, which are functions of ϵ and can be estimated according to Bjerrum's theory of ion association (*15–19*) as recently extended by Justice (*20*, *21*). However, experimental pH_S data in the domain of low dielectric constants are completely lacking so far, and thus no test is possible.

LITERATURE CITED

(1) Covington, A. K. *Pure Appl. Chem.* **1985**, *57*, 531.
(2) Mussini, T.; Covington, A. K.; Longhi, P.; Rondinini, R. *Pure Appl. Chem.* **1985**, *57*, 865.
(3) Mussini, T.; Covington, A. K.; Dal Pozzo, F.; Longhi, P.; Rondinini, S.; Zi-Ya Zou *Electrochim. Acta* **1983**, *28*, 1593.
(4) Mussini, T.; Covington, A. K.; Cicognini, M.; Longhi, P.; Rondinini, S. *Ann. Chim. (Rome)* **1982**, *72*, 639.
(5) Mussini, T.; Cicognini, M.; Longhi, P.; Rondinini, S.; Covington, A. K. *Anal. Chim. Acta* **1984**, *162*, 103.
(6) Mussini, T.; Covington, A. K.; Longhi, P.; Rondinini, S. *Ann. Chim. (Rome)* **1983**, *73*, 675.
(7) Covington, A. K.; Zi-Ya Zou *Electrochim. Acta* **1983**, *28*, 1587.
(8) Longhi, P.; Mussini, T.; Penotti, F.; Rondinini, S. *J. Chem. Thermodyn.* **1985**, *17*, 355.
(9) Mussini, T.; Longhi, P.; Rondinini, S.; Tettamanti, M.; Covington, A. K. *Anal. Chim. Acta* **1985**, *174*, 331.
(10) Taylor, M. J. *J. Chem. Eng. Data* **1979**, *24*, 230.
(11) Pozzi, M. Thesis, University of Milan, 1985.
(12) Owen, B. B. *J. Am. Chem. Soc.* **1932**, *54*, 1758.
(13) Covington, A. K.; Dickinson, T. *Physical Chemistry of Organic Solvent Systems*; Plenum Press: London, 1973; p 5.
(14) Sankar, M.; Macaskill, J. B.; Bates, R. G. *J. Solution Chem.* **1979**, *8*, 887.
(15) Bjerrum, N. *K. Dan. Vidensk. Selsk.* **1926**, *7*, No. 9.
(16) Bjerrum, N. *Selected Papers*; Einar Munksgaard: Copenhagen, 1949; p 108.
(17) Robinson, R. A.; Stokes, R. H. *Electrolyte Solutions*, 2nd rev. ed.; Butterworths: London, 1965; pp 392–429.
(18) Harned, H. S.; Owen, B. B. *The Physical Chemistry of Electrolytic Solutions*; 3rd ed.; Reinhold: New York, 1958; pp 70–76, 170, 171, 291–294.
(19) Bockris, J. O'M.; Reddy, A. K. N. *Modern Electrochemistry*; Plenum Press: New York, 1970; Vol. I, pp 253–261.
(20) Justice, J. C. *J. Phys. Chem.* **1975**, *79*, 454.
(21) Justice, J. C.; Justice, M. C.; Micheletti, C. *Pure Appl Chem.* **1981**, *53*, 1291.

RECEIVED for review February 25, 1986. Accepted May 12, 1986. This work was carried out with a financial support granted by the National Research Council of Italy (CNR).

On-Line Differential Pulse Polarographic Detection of Carboplatin in Biological Samples after Chromatographic Separation

Frits Elferink,* Wim J. F. van der Vijgh, and Herbert M. Pinedo

Free University Hospital, Department of Oncology, De Boelelaan 1117, 1081 HV Amsterdam, The Netherlands

A method for the determination of the antitumor platinum(II) complex carboplatin has been developed that uses high-performance liquid chromatography with differential pulse polarographic (DPP) detection. Carboplatin is reduced at −1.77 V vs. Ag/AgCl. DPP detection was used because of its sensitivity and selectivity. The influence of differential pulse polarographic parameters on detector performance was investigated. By use of a pulse amplitude of −250 mV at a potential of −1.6 V, with a 0.5-s drop time and a 50-ms memory time constant, detection limits of 0.1 μM carboplatin in plasma ultrafiltrate and 1 μM in urine were achieved. With an injection volume of 50 μL precision was 1.5% and 4.7%, respectively. As an example, the pharmacokinetic profile of carboplatin has been determined in a patient after an intravenous bolus injection.

Carboplatin (diammine(1,1-cyclobutanedicarboxylato)-platinum(II), CBDCA, Figure 1) is a promising analogue of the antitumor platinum complex cisplatin (*cis*-diamminedichloroplatinum(II)) (*1*). It is in an advanced stage of clinical investigation and for this reason its pharmacokinetic profile needs to be elucidated in detail. Therefore, a sensitive assay of carboplatin in body fluids is required. Since pharmacokinetics of platinum compounds is usually compared with pharmacokinetics of platinum determined by atomic absorption spectrophotometry (AAS), the method to be developed for carboplatin should be at least as sensitive as AAS.

Assays of carboplatin have been described using normal-phase (*2*, *3*) as well as reversed-phase (*4–6*) HPLC systems. Selective and sensitive on-line detection of the eluted carboplatin appeared to be the critical step in determining low concentrations. The only method used for pharmacokinetic investigations was based on normal-phase HPLC and UV detection at 225 nm (*3*). Because of the low molar absorptivity of carboplatin at this wavelength (λ_{max} 210 nm, ϵ = 4300 L/(mol cm)) the detection limit in plasma ultrafiltrate was 10 μM, which limits pharmacokinetic and metabolic studies of carboplatin in patients. Other spectrophotometric techniques used to detect carboplatin are quenched phosphorescence detection (*4*) and postcolumn reaction detection (*5*). However, these methods did not provide the desired sensitivity either.

Platinum compounds can be determined by electrochemical reduction or oxidation. Although the polarographic reduction of platinum(II) complexes has been the subject of investigation for years, its electrode reaction mechanism is still not completely understood (*7–10*). Recently, differential pulse polarography (DPP) has been used for the determination of total platinum in inorganic and biological media (*11–13*). Liquid chromatography with electrochemical detection (LC-EC) has been proven to provide a sensitive and selective determination of cisplatin (*14–16*), iproplatin (*cis*-dichloro-*trans*-dihydroxo-*cis*-bis(isopropylamine)platinum(IV)) (*14*, *15*) and spiroplatin (aqua(1,1-bis(aminomethyl)cyclohexane)[sulfato]platinum(II)) (*17*, *18*). Until now, electrochemical detection of carboplatin was only explored in the oxidative mode with a relatively poor detection limit of 14 μM in aqueous solution (*14*), while in the reductive mode no signal was observed at polarographic (*15*) as well as gold/mercury (*14*) electrodes. The present paper describes a sensitive detection of carboplatin by means of reductive DPP.

EXPERIMENTAL SECTION

Instrumentation. The chromatographic system consisted of a Waters Model 590 pump (Etten-Leur, The Netherlands), a Valco air-actuated injection valve provided with a 50-μL injection loop (Chrompack, Milddelburg, The Netherlands), and a Phase Sep Spherisorb S5 ODS2 column (4.6 × 150 mm, particle size 5 μm, ATS Chromatography, Waddinxveen, The Netherlands) combined with an Alltech direct-connect guard column (2.1 × 30 mm, Amstelveen, The Netherlands) filled with Serva octadecyl = Si 100 Polyol 0.03 mm (Brunswich, Amsterdam, The Netherlands). The HPLC pump was provided with an extra pulse dampner (Waters) to eliminate flow noise.

Electrochemical detection and polarographic measurements were performed with a PAR Model 310/303 static mercury drop electrode (SMDE) (EG&G Instruments, Nieuwegein, The Netherlands) provided with a saturated Ag/AgCl reference electrode and a platinum counter electrode. Type G171 capillaries (PAR) were used to prevent mercury drop fall at potentials beyond −1.2 V. The medium mercury drop size (1.57 mm^2) was used. Potential control and current sampling of the SMDE were made by a PAR Model 174A polarographic analyzer. The electronic circuit of the DPP mode was modified as follows: (i) the range of pulse amplitudes was extended with values of 250 and 500 mV by changing the resistors R43–R47 to 800, 100, 60, 20, and 20 kΩ, respectively (*19*), (ii) the sample width was changed from 16.5 to 20 ms to suppress noise from the the 50-Hz line frequency by changing resistor R271 from 165 to 200 kΩ (*19*), and (iii) the memory time constant and (iv) the pulse width were made adjustable both according to ref 20. The actual pulse width was measured by a Hewlett-Packard Universal Counter HP 5325A (Amsterdam, The Netherlands). UV absorption detection was performed with an LDC/Milton Roy UV-III Model 1203 detector with a fixed wavelength of 214 nm (Charles Goffin, De Bilt, The Netherlands). Signals were recorded by a BD 100 strip chart or BD 91 XYY′ recorder (Kipp & Zonen, Delft, The Netherlands). Platinum concentrations in eluent fractions, collected by an LKB 2112 RediRac fraction collector (Zoetermeer, The Netherlands), were determined by a Perkin-Elmer Model 5000 atomic absorption spectrophotometer (Gouda, The Netherlands) as described previously (*21*).

Chemicals. Carboplatin was from Johnson Matthey (Reading, Berkshire, U.K.) and cisplatin was provided by Bristol Meyers (Brussels, Belgium). Distilled demineralized water was used throughout. Mercury of polarographic quality was obtained from Merck (Amsterdam, The Netherlands). All other chemicals were of analytical grade. The mobile phase consisted of 0.05 M $NaClO_4$ and was deoxygenized as described previously (*17*). Blank urine and plasma samples were pooled from healthy volunteers.

Procedures. The plasma ultrafiltrate pool for in vitro experiments was prepared with Amicon Centriflow CF 50A ultrafiltration cones (Oosterhout, The Netherlands). Patient plasma samples (1 mL) were ultrafiltrated by the Amicon MPS-1 system

0003-2700/86/0358-2293$01.50/0 © 1986 American Chemical Society

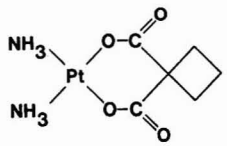

Figure 1. Structural formula of carboplatin.

provided with YMT filters (*22*). Recovery of carboplatin after this ultrafiltration step was tested in duplicate by spiking plasma to obtain concentrations of 5, 50, and 100 μM. Each solution was ultrafiltrated immediately after constitution. Peak heights in the first 200 μL of ultrafiltrate were compared with those from the same concentrations in spiked plasma ultrafiltrate. Plasma ultrafiltrate and urine samples were immediately frozen, stored at −25 °C, and thawed just before injection of 50 μL into the HPLC system without any further pretreatment. Separation and detection were performed at ambient temperature. Calibration curves of carboplatin in spiked plasma ultrafiltrate and urine samples were prepared daily. The guard column was repacked after every 100 samples. Peak heights were recorded rather than peak areas.

RESULTS AND DISCUSSION

Separation. Carboplatin was retained on a C-18 reversed-phase column with a mobile phase of water containing 0.05 M sodium perchlorate as supporting electrolyte. Sodium perchlorate was chosen because it does not form complex bonds with Pt(II) (*23*) and therefore it will not cause degradation of platinum compounds by ligand exchange during separation or detection. The chromatographic separation step could be simple, because of the high selectivity of the applied detection method. A capacity factor (k') of 1.8 appeared to be sufficient to separate carboplatin from detectable endogenous compounds.

Recovery of carboplatin from freshly spiked plasma samples was 97% and independent of the concentration (5–100 μM). Carboplatin injected in aqueous solutions, freshly spiked plasma ultrafiltrate, or urine was totally recovered from the column in one peak as determined by AAS analysis of the fractionated eluent. Possible metabolites or degradation products of carboplatin like *cis*-diamminediaquaplatinum(II), *cis*-diammineaquachloroplatinum(II), and *cis*-diamminedichloroplatinum(II) (cisplatin), which may be formed by exchange of the 1,1-cyclobutanedicarboxylato ligand, eluted at or close to the solvent front. This was expected on account of the high polarity of these molecules. Sodium perchlorate had no influence on retention of carboplatin, as measured by UV detection at 214 nm using the same column and only water as mobile phase. It seems plausible that the hydrophobic cyclobutane group of carboplatin is responsible for its retention on RP-18 columns with purely aqueous mobile phases.

Modification of the Polarographic Analyzer. The polarographic analyzer has been provided with a limited maximum pulse amplitude (−100 mV) and a rather long memory time constant (MTC) of the DPP mode (83 ms). The observed time constants were 2.1 s and 4.2 s with a drop time of 0.5 s and 1 s, respectively (*24*). These long time constants have been reason to reject differential pulse polarographic detection (*15*, *25*). Therefore, a circuit with an adjustable MTC was added, as described by Jackson et al. (*20*). The effect of the MTC on peak height, plate number, and noise is shown in Table I. It can be decided from the ratio between plate number and noise level as well as from the ratio between peak height and noise level that an MTC of 50 ms gives the best results. This effect is even more pronounced with a drop time of 1 s. An MTC of 50 ms and a drop time of 0.5 s were chosen as optimum values to ensure sharp peaks with a reproducible peak height.

The pulse width was also made variable (*20*) to increase sensitivity (*26*). The measured relationship between pulse width and sensitivity (peak height) is shown in Figure 2. An increase in sensitivity of 57% was observed when the pulse width was shortened from the original 40.9 ms to 3.4 ms. The noise level did not change, but the height of the base line was doubled, eliminating the sensitivity advantage in the lower concentration ranges. Therefore, the original pulse width was used for the analysis of carboplatin. Optimization of the pulse amplitude is discussed below.

Table I. Influence of the Memory Time Constant (MTC) on Some Chromatographic Parameters after Injection of 50 μL of 10 μM Carboplatin

MTC, ms	plate no.	peak height, nA	noise level, nA
83	2080	214	0.4
50	3390	255	0.5
20	4230	289	0.7
10	4270	298	1.2

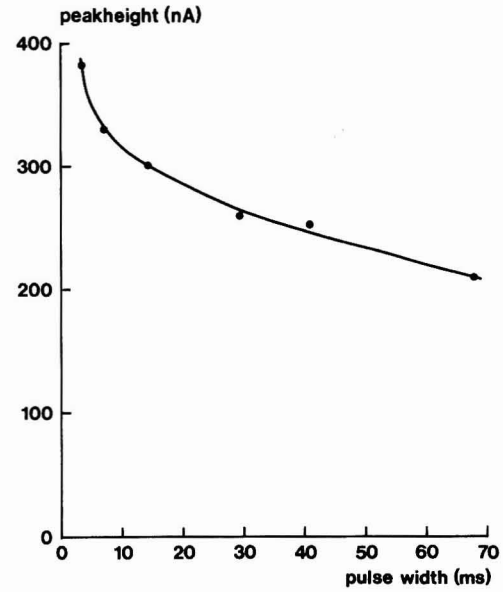

Figure 2. Relationship between the pulse width of DPP detection and the chromatographic peak height of a 50-μL injection of carboplatin 10 μM.

Polarographic Detection. Figure 3a shows a sampled direct current polarogram (SDCP) and backgroud subtracted SDCP and DPP polarorgrams of carboplatin in 0.05 M sodium perchlorate. The reduction wave has a half-wave potential ($E_{1/2}$) of −1.77 V vs. Ag/AgCl. It appeared irreversible according to the Tomeš criterion ($|E_{3/4} - E_{1/4}| = 51.7/n\alpha$) (*27*): from the SDCP curve of Figure 3a it can be calculated that the transfer coefficient $\alpha = 0.32$ when the number of electrons $n = 2$. The limiting current at −1.85 V showed a linear relationship with the carboplatin concentration over the range of 1.0×10^{-6} to 1.7×10^{-4} M suggesting a diffusion-controlled process. Reduction waves of Pt(II) complexes at potentials more negative than −1.3 V have been attributed to catalytic hydrogen evolution (*9–11*). This is in accordance with our observation that the limiting current of the SDCP curve (Figure 3a) is 3 times higher than the value calculated from the Cottrell equation (*27*), which affirms that the observed process is not merely a reduction of $Pt^{2+} \rightarrow Pt^0$. The highly negative reduction potential makes high demands upon the dropping mercury electrode. Nevertheless, the wave was considered to be suited to detect carboplatin in HPLC effluents. Detection at the hanging mercury drop electrode (HMDE) as used for spiroplatin (*18*) was not feasible because of electrode surface contamination by adsorbed species from injected biological samples. Therefore, the static mercury drop electrode (SMDE) was used throughout.

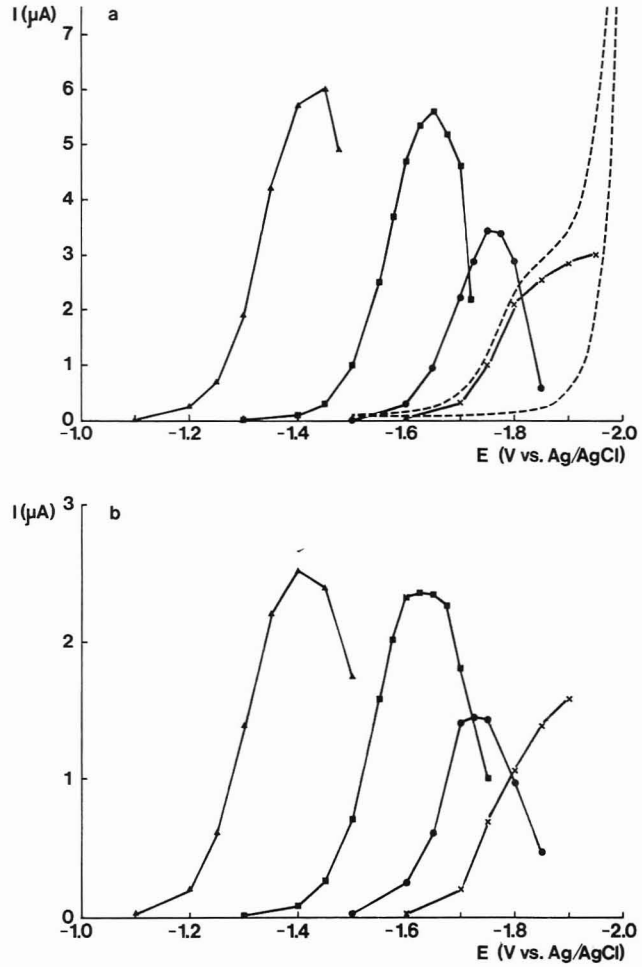

Figure 3. Voltammograms of carboplatin 10^{-4} M: (a) (– – –) sampled direct current polarogram of carboplatin and electrolyte (0.05 M sodium perchlorate), (——) background subtracted SDCP (X) and differential pulse polarograms; (b) hydrodynamic SDC (X) and DP voltammograms. Pulse amplitudes of −100 mV (●), −250 mV (■), and −500 mV (▲), medium drop size, drop time of 0.5 s, and scan rate of 5 mV/s were used.

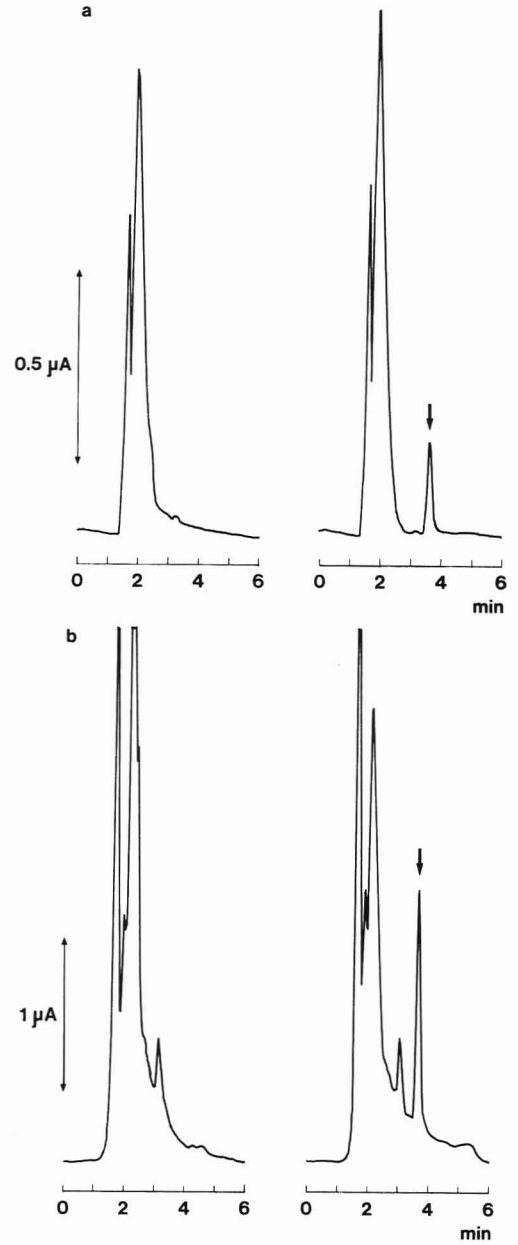

Figure 4. Chromatograms of plasma ultrafiltrate (a) and urine (b) of a patient. Blank samples and samples which contained 10.8 and 60.0 μM carboplatin, respectively. Column, Spherisorb S5 ODS2, 4.6 × 150 mm; mobile phase, 0.05 M $NaClO_4$, 1 mL/min. DPP detection with an initial potential of −1.60 V and a pulse amplitude of −250 mV.

In order to determine optimum detection conditions with the described HPLC system, hydrodynamic voltammograms of carboplatin were recorded with the polarographic detector in the SDCP and DPP mode and with several pulse amplitudes (Figure 3b). The hydrodynamic voltammograms corresponded with the background-subtracted polarograms of Figure 3a. Background subtraction of the batch polarograms was employed to allow comparison with the hydrodynamic voltammograms, which are composed of chromatographic peak heights measured from the base line. Shape, peak potential, and $|E_{3/4} - E_{1/4}|$ of hydrodynamic and batch voltammograms are essentially the same. This means that at the flow rate used, the electrode process has not become rate determining, despite the increased mass transport to the mercury drop.

Maximum sensitivity for carboplatin was reached in the DPP mode with a pulse amplitude of −250 mV. An initial potential of −1.60 V, instead of −1.65 V, was chosen to reduce the contribution from the cathodic background current (Figure 3). The maximum pulse height of −100 mV originally present in the polarographic analyzer produced a lower peak current due to the irreversibility of the reduction wave. A −500 mV pulse did not substantially increase sensitivity; a possible decrease of selectivity led to the choice of −250 mV as the optimal pulse amplitude. The pulse amplitude had no influence on noise levels. Compared to SDCP, DPP detection offered not only an increased sensitivity but also a reduced flow noise. DPP detection is also less susceptible to mercury drop anomalies (e.g., Barker effect) because less negative potentials are applied than with SDCP detection during the main part of drop life. These advantages are of special significance at the applied highly negative potentials.

Determination of Carboplatin in Biological Samples. Carboplatin was determined in human body fluids under the optimized detection conditions. Plasma ultrafiltrate and urine samples were injected without any prepurification or degassing. It can be seen from the chromatograms in Figure 4 that, due to the selectivity of the detection mode, a sufficient separation can be obtained from detectable endogenous compounds in a simple and short chromatographic run. Detection limits were 0.1 and 1 μM in plasma ultrafiltrate and urine, respectively. This is higher than the detection limit of carboplatin in water (0.05 μM), owing to base line irregularities. Nevertheless, the reached value of 1 μM in urine is low enough (because, e.g., 200 mL of urine containing 1 μM of carboplatin represents only 0.013% of a dose of 350 mg/m^2). Linear calibration lines could be obtained up to 150 μM ($r > 0.999$) in both body fluids. A small increase of electronic

noise due to a shorter MTC (Table I) is not significant because of the base line irregularities and, therefore, the increased sensitivity is pure benefit.

The within-day coefficient of variation (CV) of five measurements of carboplatin in plasma ultrafiltrate (0.9 μM) and in urine (9 μM) was 1.5% and 4.7%, respectively. The between-day CV in water was 2.5% ($n = 4$). The short retention time of carboplatin and the absence of detectable peaks with longer retention times allowed the analysis of 10–12 samples per hour.

The developed procedure was used to determine the stability of carboplatin in plasma ultrafiltrate and urine at ambient temperature. Degradation half-lives of 20 and 7 days were found in plasma ultrafiltrate and urine, respectively. After an intravenous bolus injection of 350 mg/m^2 to one patient, a peak plasma concentrtion of 126 μM carboplatin was reached. A biphasic decay in plasma was observed with half-lives of 19 and 132 min. Cumulative urine excretion of carboplatin reached 40% of the administered dose within 6 h. Due to the low detection limit of 0.1 μM, carboplatin could be determined in plasma up to 24 h after administration. Therefore, our procedure is very well suited for pharmacokinetic and metabolism studies. In summary, our developed detection procedure for the determination of carboplatin in body fluids has a comparable or higher sensitivity than that with AAS, can be performed on-line, and is specific for the original compound.

ACKNOWLEDGMENT

The authors acknowledge N. V. Metgod for modifying the electronic circuits, M. B. van Hennik for the patient samples, and I. Klein for AAS measurements.

Registry No. Carboplatin, 41575-94-4.

LITERATURE CITED

(1) Booth, B. W.; Weiss, R. B.; Korzun, A. H.; Wood, W. C.,; Carey, R. W.; Panasci, L. C. *Cancer Treat. Rep.* **1985**, *69*, 919–920.
(2) Newell, D. R.; Siddik, Z. H.; Harrap, K. R. In *Drug Determination in Therapeutic and Forensic Contexts*; Reid, E., Wilson, I. D., Ed.; Plenum Press: New York, 1985; pp 145–153.
(3) Harland, S. J.; Newell, D. R.; Siddik, Z. H.; Chadwick, R.; Calvert, A. H.; Harrap, K. R. *Cancer Res.* **1984**, *44*, 1693–1697.
(4) Gooijer, C.; Veltkamp, A. C.; Baumann, R. A.; Velthorst, N. H.; Frei, R. W. *J. Chromatogr.* **1984**, *312*, 337–344.
(5) Marsh, K. C.; Sternson, L. A.; Repta, A. J. *Anal. Chem.* **1984**, *56*, 491–497.
(6) Elferink, F.; van der Vijgh, W. J. F.; Klein, I.; Pinedo, H. M. *Clin. Chem. (Winston-Salem, N.C.)* **1986**, *32*, 641–645.
(7) Šlendyk, I.; Herasymenko, P. *Z. Phys. Chem. Abt.* **1932**, *162*, 223–240.
(8) Kivalo, P.; Laitinen, H. A. *J. Am. Chem. Soc.* **1955**, *77*, 5205–5211.
(9) Sundholm, G. *Commun. Math. Phys.* **1968**, *34*, 39–46.
(10) Ezerskaya, N. A.; Konstantinova, K. K.; Stetsenko, A. I.; Kazakevich, I. L.; Mitkinova, N. D. *Russ. J. Inorg. Chem. (Engl. Transl.)* **1980**, *25*, 878–881.
(11) Alexander, P. W.; Hoh, R.; Smythe, L. E. *Talanta* **1977**, *24*, 543–548.
(12) Brabec, V.; Vrâna, O.; Kleinwächter, V. *Collect. Czech. Chem. Commun.* **1983**, *48*, 2903–2908.
(13) Bartošek, I.; Cattaneo, M. T.; Grasselli, G.; Guaitani, A.; Urso, R.; Zucca, E.; Libretti, A.; Garattini, S. *Tumori* **1983**, *69*, 395–402.
(14) Krull, I. S.; Ding, X-D.; Braverman, S.; Selavka, C.; Hochberg, F.; Sternson, L. A. *J. Chromatogr. Sci.* **1983**, *21*, 166–173.
(15) Bannister, S. J.; Sternson, L. A.; Repta, A. J. *J. Chromatogr.* **1983**, *273*, 301–318.
(16) Richmond, W. N.; Baldwin, R. P. *Anal. Chim. Acta* **1983**, *154*, 133–142.
(17) van der Vijgh, W. J. F.; van der Lee, H. B. J.; Postma, G. J.; Pinedo, H. M. *Chromatographia* **1983**, *17*, 333–336.
(18) Elferink, F.; van der Vijgh, W. J. F.; Pinedo, H. M. *J. Chromatogr.* **1985**, *320*, 379–392.
(19) *Model 174A Polarographic Analyzer: Instruction Manual*: EG&G Princeton Applied Research: Princeton, NJ, 1974.
(20) Jackson, L. L.; Yarnitzky, Ch.; Osteryoung, R. A.; Osteryoung, J. G. *Chem. Biomed. Environ. Instrum.* **1980**, *10*, 175–180.
(21) van der Vijgh, W. J. F.; Verbeek, P. C. M.; Klein, I.; Pinedo, H. M. *Cancer Lett.* **1985**, *28*, 103–109.
(22) van der Vijgh, W. J. F.; Klein, I. *Cancer Chemother. Pharmacol.*, in press.
(23) Howe-Grant, M. E.; Lippard, S. J. In *Metal Ions in Biological Systems Vol. 11. Metal Complexes as Anticancer Agents*; Sigel, H., Ed.; Marcel Dekker: New York, 1980: pp 63–125.
(24) *Model 310 Polarographic Detector: Operating and Service Manual*: EG&G Princeton Applied Research: Princeton, NJ, 1978.
(25) Palmisano, F.; Zambonin, P. G. *Ann. Chim. (Rome)* **1984**, *74*, 633–671.
(26) Abel, R. H.; Christie, J. H.; Jackson, L. L.; Osteryoung, J. G.; Osteryoung, R. A. *Chem. Instrum.* **1976**, *7*, 123–138.
(27) Bard, A. J.; Faulkner, L. R. *Electrochemical Methods*: Wiley: New York, 1980; Chapter 5.

RECEIVED for review February 5, 1986. Accepted May 19, 1986. This research was supported by a grant from the Netherlands Cancer Foundation (K.W.F.) No. AUKC VU 83-7.

Convolution: A General Electrochemical Procedure Implemented by a Universal Algorithm

Keith B. Oldham

Department of Chemistry, Trent University, Peterborough, Ontario K9J 7B8, Canada

The convolution of the faradaic current with an appropriate "convolution function" can generate surface concentration data in a variety of electrochemical situations. Eight circumstances are discussed, differing in geometry and with or without homogeneous reaction complications, and the corresponding convolution functions are presented. A convolution algorithm is derived that applies equally to all situations.

During the last 15 years, electroanalytical chemists have made increasing use of convolution techniques to process voltammetric current data (*1*). Though these techniques may be applied in investigations having analytical, kinetic, thermodynamic, or mechanistic goals, their fundamental purpose is always the determination of the instantaneous concentration of an electroactive species at the surface of an electrode from the faradaic current.

Consider an electrode reaction that generates a species into a phase initially devoid of that species. Diffusion then occurs away from the electrode surface with diffusion coefficient D. If the current density is $i(t)/A$ and the electrode reaction involves n electrons, then the surface concentration of the electrogenerated species has frequently been shown to be of the form

$$c^s(t) = \frac{i(t)*g(t)}{nAFD^{1/2}} \quad (1)$$

0003-2700/86/0358-2296$01.50/0 © 1986 American Chemical Society

Table I. Forms Adopted by the Convolution Function

geometry	homogeneous reactions	convolution function g(t)
semiinfinite, planar electrode	none	$\frac{1}{\pi^{1/2}t^{1/2}}$
semiinfinite, planar electrode	first order, rate constant k	$\frac{\exp(-kt)}{\pi^{1/2}t^{1/2}}$
semiinfinite, convex spherical electrode, radius r	none	$\frac{1}{\pi^{1/2}t^{1/2}} - \frac{D^{1/2}}{r}\exp\left[\frac{Dt}{r^2}\right]\mathrm{erfc}\left[\frac{D^{1/2}t^{1/2}}{r}\right]$
semiinfinite, convex spherical electrode, radius r	first order, rate constant k	$\frac{1}{t^{1/2}}\exp\left[\left(\frac{D}{r^2}-k\right)t\right]\mathrm{ierfc}\left[\frac{D^{1/2}t^{1/2}}{r}\right]$
finite, within concave sphere of radius r	none	$\frac{D^{1/2}}{r}\mathrm{fa}\left[\frac{Dt}{r^2}\right]$; see text
finite, planar layer of thickness L; impermeable outer boundary of layer	none	$\frac{D^{1/2}}{L}\theta_3\left[0;\frac{Dt}{L^2}\right]$; see text
finite, planar layer of thickness L	none within layer, infinite at outer boundary	$\frac{D^{1/2}}{L}\theta_2\left[0;\frac{Dt}{L^2}\right]$; see text
semiinfinite, planar electrode	pseudo-first-order catalytic regeneration	$\frac{1}{\pi^{1/2}t^{1/2}} + \left[\frac{kD}{d-D}\right]^{1/2}\exp\left(\frac{kDt}{d-D}\right)\left[\mathrm{erf}\left(\frac{kDt}{d-D}\right)^{1/2} - \frac{D}{d}\mathrm{erf}\left(\frac{kdt}{d-D}\right)^{1/2}\right]$

where F is Faraday's constant and g(t) is a "convolution function" that is discussed later. The asterisk indicates the operation of convolution defined by the integral

$$\mathrm{i}(t)*\mathrm{g}(t) = \int_0^t \mathrm{i}(\tau)\mathrm{g}(t-\tau)\,\mathrm{d}\tau = \int_0^t \mathrm{i}(t-\tau)\mathrm{g}(\tau)\,\mathrm{d}\tau \qquad (2)$$

For a species that is *consumed* at an electrode, eq 1 is to be replaced by

$$c^{\mathrm{s}}(t) = c^{\mathrm{b}} - \frac{\mathrm{i}(t)*\mathrm{g}(t)}{nFAD^{1/2}} \qquad (3)$$

where c^{b} is the initially uniform concentration of the electroactive species. Of course, the diffusion coefficient D that appears in eq 1 and 3, and sometimes also as part of the g(t) function, is always that of the species in question. Apart from this minor distinction, the g(t) functions in eq 1 and 3 are identical.

The remainder of this article will focus on species produced by the electrode reaction, rather than on those consumed by it. Thus, eq 1 will be developed and eq 3 will be neglected. However, the modification needed to adapt the results of this article to electroconsumed species is evident from a comparison of the two equations: the sign of the convolution term must be changed and a bulk concentration term must be added.

It should be emphasized that eq 1 applies irrespective of the kinetics of the electron-transfer reaction and is independent of the nature of the potential perturbation applied during the voltammetric experiment. To be concrete, it may be advantageous to think in terms of cyclic voltammetry, but none of the development that follows is restricted to that experimental technique.

EXAMPLES OF CONVOLUTION FUNCTIONS

The function g(t) that appears in eq 1 is a continuous function of time having dimensions of (time)$^{-1/2}$. Its form depends on the geometry of the region into which the electrogenerated species diffuses and on whether or not that species is involved in a homogeneous chemical reaction. Table I is a catalog of a number of important geometries, with the corresponding g(t) functions. Some of these entries are taken from the literature (*2–5*), others are original.

The simplest case is that of planar semiinfinite geometry, for which g(t) is simply $\pi^{-1/2}t^{-1/2}$. The convolution then reduces to the simpler operation of semiintegration (*2*)

$$\mathrm{i}(t)*\mathrm{g}(t) = \frac{1}{\pi^{1/2}}\int_0^t \frac{\mathrm{i}(\tau)\,\mathrm{d}\tau}{(t-\tau)^{1/2}} = \frac{\mathrm{d}^{-1/2}i}{\mathrm{d}t^{-1/2}} = \mathrm{m}(t) \qquad (4)$$

This particular convolution has been extensively used (*6*), under such names as "semiintegral electroanalysis", "convolution voltammetry", and "neopolarography".

When the semiinfinite diffusion geometry has spherical, rather than planar, symmetry, the g(t) function must be modified as shown in the third tabular entry. This so-called "spherical convolution" (*3*) makes allowance for the more rapid diffusion possible from a convex sphere.

If the diffusing species undergoes an irreversible first-order (or pseudo-first-order) reaction with some component of the medium surrounding the electrode, then the convoluting function is to be modified by multiplication by exp(–kt). This procedure was demonstrated for planar diffusion in a recent publication (*4, 5*) under the name "kinetic convolution". The fourth tabular entry gives the corresponding convolution function for spherical out-diffusion coupled to an $\mathrm{EC_{ir}}$ mechanism: again multiplication by exp(–kt) serves to correct g(t) for the kinetic effect. The ierfc notation refers to the integral of the error function complement (*7*).

The fifth entry in Table I is applicable to electrode reactions at a mercury sphere in which the electrogenerated species is a metal that dissolves as an amalgam and diffuses into the mercury drop. The fa function used in the table is defined by (*3*)

$$\frac{D^{1/2}}{r}\mathrm{fa}\left(\frac{Dt}{r^2}\right) = \begin{cases} \dfrac{1}{\pi^{1/2}t^{1/2}} + \dfrac{D^{1/2}}{r}\exp\left(\dfrac{Dt}{r^2}\right)\times \\ \qquad \mathrm{erfc}\left(\dfrac{-D^{1/2}t^{1/2}}{r}\right) \quad \text{(small } t\text{)} \\ \dfrac{D^{1/2}}{r}\left[3 + 2\sum_{p=1}^{\infty}\exp\left(\dfrac{-y_pDt}{r^2}\right)\right] \text{(large } t\text{)} \end{cases} \qquad (5)$$

where y_p denotes the pth positive root of the equation $y =$

tan y. Notice that in the long time limit $g(t \rightarrow \infty)$ is the constant $3D^{1/2}/r$ so that

$$c^s(t) \simeq \frac{3}{nAFr}\int_0^t i(\tau)\,d\tau = \frac{q(t)}{nFV} \qquad (t \rightarrow \infty) \qquad (6)$$

in this limit, where V is the drop volume and $q(t)$ is the total charge. Equation 6 corresponds to a slow electrolysis in which the amalgam concentration is almost uniform and calculable by Faraday's law.

The next two entries in the table could be applied to electrodes modified by a thin film. The sixth entry applies when the electrogenerated species is soluble in the film but not in the medium beyond, whereas the seventh entry relates to cases in which the concentration of the diffusant is maintained at zero (by reaction or extraction) at the outer boundary of the film. The θ functions are defined by

$$\theta_3(0;T) = \begin{cases} \dfrac{1}{\pi^{1/2}T^{1/2}}\left[1 + 2\sum_{p=1}^{\infty} \exp(-p^2/T)\right] & \text{(small } T\text{)} \\ 1 + 2\sum_{p=1}^{\infty} \exp(-p^2\pi^2 T) & \text{(large } T\text{)} \end{cases} \qquad (7)$$

and

$$\theta_2(0;T) = \begin{cases} \dfrac{1}{\pi^{1/2}T^{1/2}}\left[1 + 2\sum_{p=1}^{\infty} (-)^p \exp(-p^2/T)\right] & \text{(small } T\text{)} \\ 2\sum_{p=0}^{\infty} \exp[-(2p+1)^2\pi^2 T/4] & \text{(large } T\text{)} \end{cases} \qquad (8)$$

The series in (7) and (8) all converge extremely rapidly.

The final tabular entry deals with the important case in which the electrogenerated species reacts homogeneously with a catalyst to regenerate the original electroactive species. The catalyst is assumed present in excess, so that the catalysis is effectively first order with a rate constant k. In this entry d denotes the diffusion coefficient of the electrogenerated species. Of course, when the object of the convolution is to determine the surface concentration of the electrogenerated species, i.e., when equation 1 is being exploited, then $d = D$. In this event, the $g(t)$ function reduces to $\pi^{-1/2}t^{-1/2}\exp(-kt)$, identical with the noncatalytic homogeneous reaction case, as is to be expected. This simplification will not normally apply when the $g(t)$ function is needed for use in eq 3.

CONVOLUTION METHODS

Modern voltammetric instrumentation provides digital current data as a set of values $i_0, i_1, i_2, \cdots, i_j, \cdots, i_J$ at equally spaced times. We let Δ represent the time interval between data points and select time = Δ as the first point at which the faradaic current is perceptibly different from zero. Thus $i_0 = 0$ and $i_j = i(j\Delta)$. If $J\Delta = t$, then the data set $i_0, i_1, i_2, \cdots, i_j, \cdots, i_J$ represents the current for times $0 \leq \tau \leq t$ and is to be convolved with $g(t)$ to produce $c^s(t)$.

Convolution may be effected via Laplace transformation (*8*) or Fourier transformation (*9, 10*). However, these indirect methods have no advantages over the straightforward algorithm that is advocated here.

Recognize that whereas the $i(t)$ function is known only at isolated points, the $g(t)$ function has known values over the entire time span. Advantage will be taken of this knowledge in designing the algorithm that follows. The algorithm employs the current data set without manipulation of any sort. In this respect it contrasts with the algorithm adopted by Woodard and co-workers (*4, 5*) who numerically differentiated their current data prior to convolution. Numerical differentiation is notorious as a noise-enhancing procedure.

The convolution integral may be split into J units

$$i(t) * g(t) = \int_0^{J\Delta} i(J\Delta - \tau)g(\tau)\,d\tau = \sum_{j=0}^{J-1}\int_{j\Delta}^{\Delta+j\Delta} i(J\Delta - \tau)g(\tau)\,d\tau \qquad (9)$$

We next make a trapezoidal approximation by assuming that, in the interval $j\Delta \leq \tau \leq \Delta + j\Delta$, the current may be described by the linear relationship

$$i(\tau) \simeq \left(j + 1 - \frac{\tau}{\Delta}\right)i_j + \left(\frac{\tau}{\Delta} - j\right)i_{j+1} \qquad (10)$$

Similarly

$$i(J\Delta - \tau) \simeq \left(\frac{\tau}{\Delta} - j\right)i_{J-j-1} + \left(1 + j - \frac{\tau}{\Delta}\right)i_{J-j} \qquad (11)$$

and this enables expression 9 to be recast as a difference of two sums of integrals

$$i(t) * g(t) = \sum_{j=0}^{J-1}[(j+1)i_{J-j} - ji_{J-j-1}]\int_{j\Delta}^{\Delta+j\Delta} g(\tau)\,d\tau - \sum_{j=0}^{J-1}\frac{i_{J-j} - i_{J-j-1}}{\Delta}\int_{j\Delta}^{\Delta+j\Delta} \tau g(\tau)\,d\tau \qquad (12)$$

Each integral in the first summation may be evaluated in terms of a function ig defined as the indefinite integral $ig(t) = \int_0^t g(\tau)\,d\tau$ of the function g

$$\int_{j\Delta}^{\Delta+j\Delta} g(\tau)\,d\tau = ig(\Delta + j\Delta) - ig(j\Delta) \qquad (13)$$

Likewise, by exploiting parts integration, each integral in the second summation of (12) may be evaluated in terms of ig and of its indefinite integral $iig(t) = \int_0^t ig(\tau)\,d\tau$

$$\int_{j\Delta}^{\Delta+j\Delta} \tau g(\tau)\,d\tau = (\Delta + j\Delta)ig(\Delta + j\Delta) - j\Delta ig(j\Delta) - iig(\Delta + j\Delta) + iig(j\Delta) \qquad (14)$$

When expressions 13 and 14 are inserted into 12, considerable cancellation occurs and the residual terms may be simplified to

$$i(t) * g(t) = \frac{1}{\Delta}\{i_J iig(\Delta) + \sum_{j=1}^{J-1} i_{J-j}[iig(j\Delta - \Delta) - 2iig(j\Delta) + iig(j\Delta + \Delta)]\} \qquad (15)$$

Equation 15 provides a simple and efficient convolution algorithm. Notice that the only function that occurs is iig, the g and ig functions having disappeared during the derivation. Table II lists the iig function corresponding to all of the g functions that are listed in Table I. Each iig function has the dimensions $(\text{time})^{3/2}$. All the functions appearing in Table II are easily calculable via published algorithms (*3, 11*).

Reference 3 may be consulted for examples of the application of eq 15. In that article, currents generated by cyclic voltammetry at a hanging mercury drop electrode are convolved, using the appropriate $g(t)$ functions, to produce numerical values of concentration at the electrode surface during the progress of the voltammetry. Examples from the third and fifth entries of Table I are illustrated there.

An algorithm based on eq 15 may be applied in a wide variety of experimental circumstances. However, other algorithms may be more satisfactory in the case of step experiments, because a trapezoidal approximation is not particularly appropriate for a current response that displays a discontinuity. Reference 12 may be consulted for an example of how special algorithms may be designed to cater to a step perturbation of potential.

Table II. Some Convolution Functions and Their Double Integrals

g(t)	iig(t)
$\frac{1}{\pi^{1/2}t^{1/2}}$	$\frac{4t^{3/2}}{3\pi^{1/2}}$
$\frac{\exp(-kt)}{\pi^{1/2}t^{1/2}}$	$\frac{t^{1/2}\exp(-kt)}{\pi^{1/2}k} + \frac{(2kt-1)\,\mathrm{erf}(k^{1/2}t^{1/2})}{2k^{3/2}}$
$\frac{1}{\pi^{1/2}t^{1/2}} - \frac{D^{1/2}}{r}\exp(T)\,\mathrm{erfc}(T^{1/2})$ where $T = Dt/r^2$	$\frac{r^3}{D^{3/2}}\left[1 - \frac{2T^{1/2}}{\pi^{1/2}} + T - \exp(T)\,\mathrm{erfc}(T^{1/2})\right]$
$\frac{1}{t^{1/2}}\exp(Bt)\,\mathrm{ierfc}\left[\frac{D^{1/2}t^{1/2}}{r}\right]$ where $B = \frac{D}{r^2} - k \neq 0$	$\frac{D^{1/2}}{rB^2}\left[1 + Bt - \exp(Bt)\,\mathrm{erfc}\left(\frac{D^{1/2}t^{1/2}}{r}\right)\right] - \frac{t^{1/2}}{\pi^{1/2}B}\exp(-kt) - \frac{1}{k^{1/2}B}\left[kt - \frac{1}{2} + \frac{D}{rB}\right]\mathrm{erf}(k^{1/2}t^{1/2})$
$\frac{D^{1/2}}{r}\,\mathrm{fa}(T)$ where $T = Dt/r^2$	$\frac{r^3}{D^{3/2}}\left[\exp(T)\,\mathrm{erfc}(-T^{1/2}) - 1 - \frac{2T^{1/2}}{\pi^{1/2}} - T\right]$ small T $\frac{r^3}{D^{3/2}}\left[3T - 2\sum_{p=1}^{\infty}\frac{1 - y_p{}^2T - \exp(-y_p{}^2T)}{y_p{}^2}\right]$ large T
$\frac{D^{1/2}}{L}\theta_3(0;T)$ where $T = Dt/L^2$	$\frac{8t^{3/2}}{3\pi^{1/2}}\left[\frac{1}{2} + \sum_{p=1}^{\infty}\left[1 - \frac{p^2}{T}\right]\exp\left(\frac{-p^2}{T}\right) - \frac{\pi^{1/2}p^3}{T^{3/2}}\,\mathrm{erfc}\left(\frac{p}{T^{1/2}}\right)\right]$ small T $\frac{L^3}{D^{3/2}}\left[\frac{T^2}{2} + \frac{2}{\pi^4}\sum_{p=1}^{\infty}\frac{1}{p^4}\exp(-p^2\pi^2T)\right]$ large T
$\frac{D^{1/2}}{L}\theta_2(0;T)$ where $T = Dt/L^2$	$\frac{8t^{3/2}}{3\pi^{1/2}}\left[\frac{1}{2} + \sum_{p=1}^{\infty}(-)^p\left\{\left[1 - \frac{p^2}{T}\right]\exp\left(\frac{-p^2}{T}\right) - \frac{\pi^{1/2}p^3}{T^{3/2}}\,\mathrm{erfc}\left(\frac{p}{T^{1/2}}\right)\right\}\right]$ small T $\frac{2L^3}{\pi^4D^{3/2}}\sum_{p=0}^{\infty}\left[\frac{2}{2p+1}\right]^4\exp\{-(2p+1)^2\pi^2T/4\}$ large T
$\frac{T^{1/2}}{t^{1/2}}\exp(T)\left[\mathrm{erf}(T^{1/2}) - \frac{D}{d}\,\mathrm{erf}\left(\frac{T^{1/2}d^{1/2}}{D^{1/2}}\right)\right] + \frac{1}{\pi^{1/2}t^{1/2}}$ where $T = \frac{kDt}{d-D}$	$\left[\frac{t}{T}\right]^{3/2}\exp(T)\left[\mathrm{erf}\left(\frac{T^{1/2}d^{1/2}}{D^{1/2}}\right) - \mathrm{erf}(T^{1/2})\right] + \frac{d^{1/2}}{k^{1/2}D^{1/2}}\left[t - \frac{1}{2k} - \frac{t}{T}\right]\mathrm{erf}(k^{1/2}t^{1/2}) + \frac{2t^{1/2}}{\pi^{1/2}k}\left[\frac{d}{D} - 1 + \frac{d^{1/2}}{2D^{1/2}}\exp(-kt)\right]$

SUMMARY

A single universal expression, formed by combining eq 1 and 15 into

$$c^s(t) = \frac{i_J\mathrm{iig}(\Delta) + \sum_{j=1}^{J-1} i_{J-j}[\mathrm{iig}(j\Delta - \Delta) - 2\mathrm{iig}(j\Delta) + \mathrm{iig}(j\Delta + \Delta)]}{nAFD^{1/2}\Delta} \quad (16)$$

provides a means of calculating the time-dependent concentration of an electrogenerated species at the surface of an electrode. The faradaic current values $i_1, i_2, i_3, \cdots, i_J$ used by expression 16 are those determined at the instants $\Delta, 2\Delta, 3\Delta, \cdots, J\Delta$ where $J\Delta = t$ and the current at zero time, i_0, is zero. The iig function, to be selected from Table II, is the double integral of the convolution function appropriate to the particular geometric and kinetic circumstances, as detailed in Table I.

For a sufficiently brief experiment, all iig(t) functions reduce to $4t^{3/2}/3\pi^{1/2}$. Equation 16 then becomes

$$c^s(t) = \frac{4\Delta^{1/2}}{3\pi^{1/2}nAFD^{1/2}}\{i_J + \sum_{j=1}^{J-1} i_{J-j}[(j-1)^{3/2} - 2j^{3/2} + (j+1)^{3/2}]\} \quad (17)$$

which is the so-called RL algorithm (*13*) for semiintegration.

LITERATURE CITED

(1) Oldham, K. B. *J. Chem. Soc., Faraday Trans.*, in press.
(2) Oldham, K. B.; Spanier, J. *J. Electroanal. Chem.* **1970**, *26*, 331.
(3) Myland, J. C.; Oldham, K. B.; Zoski, C. G. *J. Electroanal. Chem.* **1985**, *193*, 3.

(4) Woodard, F. E.; Goodin, R. D.; Kinlen, P. J. *Anal. Chem.* **1984**, *56*, 1920.
(5) Blagg, B.; Carr, S. W.; Cooper, G. R.; Dobson, I. D.; Gill, J. B.; Goodall, D. C.; Shaw, B. L.; Taylor, N.; Boddington, T. *J. Chem. Soc., Dalton Trans.* **1985**, 1213.
(6) Bard, A. J.; Faulkner, L. R. *Electrochemical Methods*; Wiley: New York, 1980; pp 236–242.
(7) Abramowitz, M.; Stegun, I. A. *Handbook of Mathematical Functions*; U.S. Government Printing Office: Washington, DC, 1964; section 7.2.
(8) Pilla, A. *J. Electrochem. Soc.* **1970**, *117*, 467.
(9) Smith, D. E. *Anal. Chem.* **1976**, *48*, 517A.
(10) Suprenant, H. L.; Ridgway, T. H.; Reilley, C. N. *J. Electroanal. Chem.* **1977**, *75*, 125.
(11) Oldham, K. B. *J. Electroanal. Chem.* **1982**, *136*, 175.
(12) Anderson, J. E.; Myland, J. C.; Oldham, K. B., submitted for publication in *J. Electroanal. Chem.*
(13) Oldham, K. B.; Spanier, J. *The Fractional Calculus*; Academic Press: New York, 1974; pp 136–148.

RECEIVED for review March 5, 1985. Resubmitted April 24, 1986. Accepted April 24, 1986. The generous financial support of the Natural Sciences and Engineering Research Council of Canada is acknowledged with gratitude.

Ion Intensity and Image Resolution in Secondary Ion Mass Spectrometry

Margaret E. Kargacin and Bruce R. Kowalski*

Laboratory for Chemometrics, Department of Chemistry, BG-10, University of Washington, Seattle, Washington 98195

With secondary ion mass spectrometry (SIMS), mass spectra can be generated as a function of the sample surface spatial coordinates. Often in a sample analysis, however, the number of surface components, their characteristic mass spectra, and the extent of beam damage are unknown. Relying on single peak intensities to represent individual components can lead to error in the qualitative and quantitative interpretation of SIMS spectra or ion images. The methods of cross-validation and factor analysis are presented as a means for estimating the true number of components in a multicomponent sample. A multivariate curve resolution procedure is used in the analysis of SIMS data from two and three component mixture samples to estimate the pure component spectra and the relative intensity contribution of each component in the mixture spectra. These methods are then applied to the resolution of individual components over the surface of a sample using SIMS ion images and image processing.

Secondary ion mass spectrometry (SIMS) is a widely accepted method for the characterization of surfaces and is often used in the analysis of thermally labile or nonvolatile organic compounds. The low detection limits obtainable with SIMS and the ability to analyze for all elements and isotopes have contributed to the importance of SIMS as an analytical method. Secondary ion mass spectra, containing monatomic and molecular ion peaks, yield information about the elemental composition of a surface and can give chemical information as well. Additionally, mass spectral information can be collected as a function of sample spatial dimensions. A depth profile analysis is an example with one spatial dimension. A two-dimensional description of a sample can be obtained by measuring series of ion images of different m/e values. Here an ion image consists of the secondary ion intensity for a particular m/e value peak at each lateral point (pixel) sampled (*1*, *2*).

In practice the complete analysis of SIMS spectra collected over a surface involves three steps. First, the number of surface components is determined, where a component is defined as an element, compound, or mixture that gives a distinct unchanging mass spectrum over the surface. Second, the components are identified using the spectra of the components determined to be present. Third, the spatial distribution of the components over the sample surface is estimated.

The SIMS spectra contain the information needed to determine the number of distinct surface components and their spectra. However, this information may not be easily extracted. A single component spectrum may contain monatomic and molecular ion peaks. Often more than one component is sampled at one time resulting in spectral interference between components (*3*, *4*) making the determination of the number of components and their identification difficult.

Components that have spectral peaks at the same m/e values, when present in a multicomponent sample, will give extreme spectral overlap. An example of such overlap has been reported for the negative secondary ion mass spectra measured for the inorganic salts Li_2SO_4, Na_2SO_3, Na_2SO_4, and $Na_2S_2O_3$ (*5*). The same m/e value peaks appear in the negative ion spectra of each salt. None of the four salts, when analyzed alone, give spectra containing a unique signal that can serve to distinguish it. The different salts and their anion stoichiometry are distinguishable only by their relative peak intensities in the negative ion spectra. Other such examples include the SIMS analysis of poly(alkyl methacrylates) (*6*) and the SIMS analysis of different oxides of Cr (*7*).

Existing empirical and semitheoretical methods (*1*, *8*) for quantitation in SIMS can yield acceptable results but involve calculations in which an individual component is represented by a single mass spectral peak. Best results are achieved only if the peaks chosen are representative of the pure component and free from spectral interference. Proper peak selection then depends on prior knowledge of the pure component spectrum. Additionally, even if a unique mass is used for quantitation, the information contained in the other masses is wasted.

Multivariate statistical methods, customized for the analysis of multicomponent spectral data, have been applied in analytical chemistry for interpretation of spectra from methods such as GC–MS, LC–UV, and fluorescence spectroscopy (*9*–*12*). These multivariate methods address some of the same problems often encountered in the analysis of SIMS spectra, namely, lack of knowledge of pure component spectra and/or presence of spectral interferences, and may therefore be useful in interpreting SIMS spectra. With one exception involving

0003-2700/86/0358-2300$01.50/0 © 1986 American Chemical Society

the solution of simultaneous equations (*13*), multivariate methods have yet to be applied in SIMS spectral analysis. Since a series of SIMS ion images can be viewed as a spectral data set, with one mass spectrum per pixel, the multivariate methods of spectral analysis that hold promise for analysis of SIMS data sets with only one spatial dimension may also be applied in SIMS image analysis.

A measured SIMS spectrum can be related to the surface component concentrations as described in the following formulation where a measured mass spectrum is represented by a column vector $\mathbf{x}_i$

$$\mathbf{x}_i = (x_1, x_2, \cdots, x_j, \cdots, x_P)^T \quad (1)$$

and x_j is the intensity of the jth m/e value peak and P is the total number of peaks monitored in the mass spectrum. A mixture mass spectrum, $\mathbf{x}_i$ can be expressed as the sum of the spectra of the pure components according to

$$x_j = \sum_{k=1}^{NC} i_p \eta t S_k I^+_k x_k c_{i,k} \quad (2)$$

where i_p is the primary ion current with units of ions per second, t is the count time in seconds, and η is the collection efficiency equal to the (number of ions detected)/(number of ions sputtered). S_k, the sputtering yield, is equal to the number of sputtered particles per incident ion. I^+_k is the ionization yield or the degree of ionization for component k. x_k is the jth peak from the kth component spectrum, normalized to unit area, and $c_{i,k}$ is the mole fraction of component k in mixture spectrum i. NC is the total number of components. In gas-phase mass spectrometry the spectra of individual components in a multicomponent sample add linearly to give a mixture mass spectrum. In SIMS, matrix effects, or interactions between components, may lead to additional terms in the model (*14*). In sample systems where such interactions are absent, the mixture spectra can be considered to be linear superpositions of the component spectra and eq 2 is valid. It is necessary to test the validity of eq 2 for the sample under investigation because in SIMS eq 2 is often not true. This can be done by comparing the results of a cross validation with information obtained about the sample composition from sample preparation, visual examination, or complementary analytical methods.

In this paper the results of the analysis of two SIMS data sets, varying in degree of spectral interference, in the number of components, and in the number of spatial dimensions are used to illustrate the use of a cross-validation method (*15*) involving factor analysis for estimating the number of components in the mixture spectra. A multivariate curve resolution procedure (*9*, *10*), applicable when eq 2 is valid, is then tested as a method for finding pure component spectra and for estimating the relative spectral intensity of each component in mixture spectra.

THEORY

In factor analysis a data matrix of ion intensities, $\mathbf{X}_{N\times P}$, consisting of N mass spectra with P different m/e values, can be represented as the product of two matrices $\mathbf{U}$ and $\mathbf{V}$

$$\mathbf{X} = \mathbf{UV} \quad (3)$$

Where the matrix $\mathbf{V}$, of "loadings", is composed of P rows, each row being one eigenvector of the data scatter matrix, $\mathbf{X}^T\mathbf{X}/N$. The matrix $\mathbf{U}$, of "scores", consists of the projections of the N experimental mass spectra onto the P eigenvectors.

The goal of cross-validation, as used here, is to determine the number of eigenvectors that are representative of systematic variation in the data set (i.e., associated with changes in the relative amounts of the components, and not representative of random variation due to noise). The number of sample components is then estimated as the number of eigenvectors associated with systematic variation in the spectra. The cross-validation method involves the deletion of one or more of the experimental spectra followed by calculation of the eigenvectors using the reduced data set. The spectral intensities deleted are then predicted as a function of the number of eignevectors used in the following:

$$x'(k)_{i,j} = \sum_{k=1}^{P} u_{i,k} v_{k,j} \text{ for } i = 1, N' \text{ and } j = 1, P \quad (4)$$

The term $x'(k)_{i,j}$ denotes the prediction of the jth mass spectral intensity in the ith held out spectrum when calculated using the first k eigenvectors. $u_{i,k}$ is the score of the ith spectrum on the kth eigenvector, $v_{k,j}$ is the jth element of eigenvector k. N' is the number of held out samples. Prediction error is then calculated as a function of the number of eigenvectors used in the calculation of $x'(k)_{i,j}$. This quantity, the prediction residual error sum of squares, designated as PRESS(k), is given by

$$\text{PRESS}(k) = \sum_{i=1}^{N'} (\sum_{j=1}^{P} (x_{i,j} - x'(k)_{i,j})^2)^{1/2} \quad (5)$$

The procedure is repeated with the deletion of a different portion of the full data set until each spectrum has been held out one time only. The PRESS(k) values are summed in each cycle. From a plot of PRESS(k) for the entire data set vs. k, the number of components is estimated to be equal to the value of k at which the plotted PRESS(k) curve drops to a level of steady but slow decline. Relatively large decreases in the value of PRESS(k) are seen as eigenvectors that account for compositional variance in the data are included in the calculation of PRESS(k). But, when eigenvectors representing noise contributions to the data are included, the PRESS(k) value declines very slowly because the noise present in the group of spectra, for which the eigenvectors are found, are not useful for modeling the noise in the spectra held out.

Recently Borgen and Kowalski (*16*) generalized multivariate curve resolution and developed algorithms for the three component case to allow determination of pure component spectra and estimation of the component signal contributions in mixture samples.

In both the two and three component curve resolution procedures each mixture mass spectrum, $\mathbf{x}_i$, is expressed as a linear combination of the pure component spectra

$$\mathbf{x}_i = \sum_{k=1}^{NC} a_{i,k} \mathbf{x}^*_k \qquad i = 1, n \quad (6)$$

where NC indicates the total number of components and $\mathbf{x}^*_k$ is a vector representing the kth pure component mass spectrum. $a_{i,k}$ is the relative contribution of the kth component in $\mathbf{x}_i$ and

$$\sum_{k=1}^{NC} a_{i,k} = 1.0 \quad (7)$$

The measured spectra and pure component spectra can each be expressed as a linear combination of the first NC eigenvectors of the data scatter matrix, $\mathbf{X}^T\mathbf{X}/N$

$$\mathbf{x}_i = \sum_{k=1}^{NC} u_{i,k} \mathbf{v}_k \qquad i = 1, N \quad (8)$$

$$\mathbf{x}^*_i = \sum_{k=1}^{NC} u^*_{i,k} \mathbf{v}_k \quad i = 1, \text{NC} \quad (9)$$

where $u_{i,k}$ are scores or projections of the ith spectrum onto the kth eigenvector, $\mathbf{v}_k$. The asterisk indicates pure component spectra and scores. To estimate the unknown pure component spectra, the scores, $u^*_{i,k}$, must be found.

Table I. Operating Conditions[a]

parameter	
beam current (μA)	0.220
beam voltage (kV)	2.0
energy prefilter:	
E_1 (V)	−6.36
E_2 (V)	2.55
E_3 (V)	−38.2
sample bias (V)	8.50

[a] 30 000 μs/pixel; 64 × 64 pixels; images collected at 46, 48, 49, 50, 55, 56, 57, 62, 63, 64, 65, and 66 amu.

For both the two and three component cases three restrictions enable estimates of these scores to be made. The first restriction arises from the fact that in mass spectra the peak intensity at each m/e value must be nonnegative. The second restriction states that each measured spectrum be a linear combination of nonnegative amounts of the pure components; thus all $a_{i,k}$ are ≥0. The third restriction results from normalization of each spectrum to unit area.

In the two component case the spectra can be represented in a two-dimensional plot by their score pairs $u_{i,1}$ and $u_{i,2}$. These score pairs are found by projection of the measured spectra onto the first and second eigenvectors. In this plot the three restrictions confine the location of the pure component score pairs to the normalization line segments. Possible pure component spectra can be calculated from score pairs located on the normalization line, one score pair from each of the solution bands (*9*, *10*). The normalization line, with the pure component spectra located at the two ends, constitutes a line analogous to a mole fraction line. The distance between a mixture point and the pure component points indicates the relative intensity associated with each component in the mixture spectra.

In the three component case the spectra, represented by their scores on the three major eigenvectors (eq 8 and 9), will fall on a plane in a three-dimensional space. This plane can be viewed as a projection onto the plane defined by the second and third eigenvectors. By use of the three restrictions as before and algorithms developed by Borgen and Kowalski (*16*), allowed regions in this plane can be found for the score values in eq 9. Use of one score triplet from each of the allowed areas enables estimates of the pure component spectra to be calculated (eq 9). The three allowed regions form a triangle, analogous to a mole fraction triangle, from which the relative intensity of any of the three components in a mixture spectrum can be calculated.

EXPERIMENTAL SECTION

In this paper sets of mass spectra are analyzed. The spectra in the first set were taken from the literature (*13*) and the pure component spectra of CrO_2, CrO_3, Cr_2O_3, CrO, and vacuum melted Cr were obtained from H. Werner, Phillips Research Laboratories.

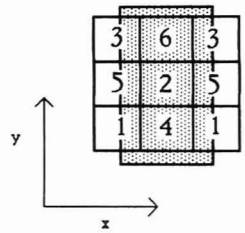

Figure 1. Diagram of iron oxide brown and titanium white sample. Area 1 samples are titanium white paint alone, areas 2 through 5 are mixtures containing progressively more Fe brown paint. Area 6 is Fe brown alone.

A 2.5-h depth profile analysis was performed on the sample as described (*13*) using a Cameca IMS-300 spectrometer with 5.5-keV Ar primary ion beam. The metal and pure oxide spectra were obtained under the same conditions.

Spectra for the second data set were collected from samples of a titanium white paint, an iron oxide brown acrylic paint (M. Grumbacher, Inc., New York), and four mixture samples which were painted onto a silver support in a checkered pattern as shown in Figure 1. Each area in the figure is numbered according to its composition. Ion images were collected with an $^{40}Ar^+$ beam at 46, 48, 49, 50, 55, 56, 57, 62, 63, 64, 65, and 66 amu with a modified 3M (KRATOS) 535-BX secondary ion and ion scattering spectrometer (minor peaks, for example, the Fe isotope peaks at 54 and 58 amu, were not imaged because they were of much lower intensity). Each image consisted of a grid of 64 × 64 pixels. The area of the sample analyzed is shown as shaded in Figure 1. The analyzed area measures 4.0 mm along the sample axis designated as the x axis and 6.5 mm along the y axis. Operating conditions for the spectrometer are given in Table I.

RESULTS AND DISCUSSIONS

Oxidized Chromium Metal, Depth Profile. The object of this experiment was to determine the number of oxides formed on the surface, to identify the oxide(s), and to calculate a concentration profile of the oxide with depth. The depth profile data present a difficult situation for spectral resolution because the possible pure components have very similar spectra and none have unique mass peaks. In the course of the depth profile, peak intensities for the positive ions Cr^+, CrO^+, Cr_2^+, Cr_2O^+, Cr_3^+, Cr_3O^+, and $Cr_3O_2^+$ were recorded (*13*). The ion intensities for the same mass ions for Cr metal and the four pure oxides were also obtained for comparison with the curve resolution estimates of the pure components. In the data analysis the intensity of the Cr_3O^+ peak is not included because its value was much higher in the depth profile than in any of the pure oxide spectra.

In Table II normalized spectra are listed for the metal and oxides. Inspection of the spectra shows that differences exist between the individual samples. All oxides vary from the metal especially in ion intensity for the Cr^+ ion and the cluster ions Cr_2^+ and Cr_3^+. The differences between the individual oxide spectra are not as great but they can be distinguished

Table II. Spectra Normalized to Unit Area

	peak intensity					
sample	Cr^+	CrO^+	Cr_2^+	Cr_2O^+	Cr_3^+	$Cr_3O_2^+$
Cr metal	0.587	0.012	0.176	0.035	0.188	0.003
CrO	0.960	0.015	0.009	0.015	9.6×10^{-5}	3.6×10^{-4}
Cr_2O_3	0.939	0.020	0.013	0.027	5.6×10^{-5}	7.8×10^{-4}
CrO_2	0.975	0.013	0.003	0.010	9.7×10^{-6}	1.6×10^{-4}
CrO_3	0.901	0.089	0.001	0.009	4.5×10^{-5}	2.5×10^{-4}
	Curve Resolution Results					
component one	0.939	0.018	0.013	0.031	0.000	0.002
component two	0.551	0.004	0.178	0.084	0.171	0.016

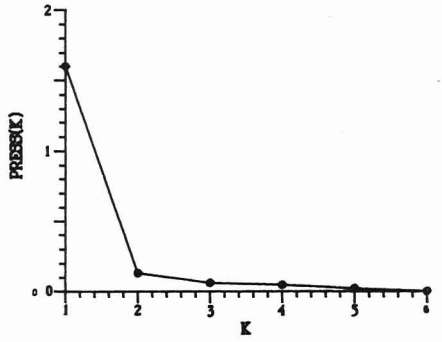

Figure 2. PRESS(K) vs. K calculated for the depth profile of oxidized Cr metal. This plot indicates that two components are present.

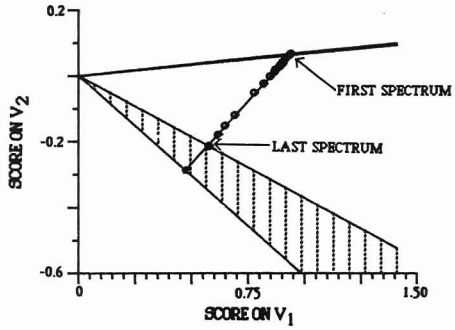

Figure 3. Two-dimensional spectra representation of Cr oxide–Cr metal spectra as projections onto the first two eigenvectors of the covariance matrix. Spectra points are represented by the open circles. The narrow, upper solution band corresponds to component one, the oxide. The wider, lower band corresponds to Cr metal, component two.

from one another. (In ref 13 it was noted that the presence of chromium–oxygen cluster ions indicates that the chromium metal sample was slightly oxidized.)

Eigenanalysis of the normalized depth profile spectra resulted in two major eigenvectors, the first accounting for 98.8% of the total data variance and the second for 1.17%. The plot of PRESS vs. the number of components, Figure 2, suggests that only two components are present. In the curve resolution two dimensional score plot for the experimental spectra, Figure 3, the locations of the first and last spectra are labeled. The spectra fall in order on the normalization line and deviations from the line are small. This is further evidence that only two components are present and that rather good experimental techniques were employed. The solution band is narrow for the component most like the first measured spectrum and arbitrarily called the first component. This indicates that the first measured spectrum is close to the outer bound spectrum for component one. The solution band is wider for the second component.

The solution spectra for both components calculated at the inner bounds of the solution bands are also listed in Table II. On the basis of values calculated for the root mean square error between the solution spectra and those measured for pure oxides and Cr metal (Table III), the two components can be identified. The first component is seen to be most like that of Cr_2O_3 while the second component spectrum is most like that of Cr metal.

The relative intensities of the oxide and metal at each point in the depth profile are shown in Figure 4. The first six spectra in the depth profile are essentially due to the Cr_2O_3 with the relative contribution from the metal steadily increasing in the remaining spectra.

Werner and co-workers (*13*) concluded that three components were present and that CrO was the third. The curve resolution result presented here is different but required fewer assumptions about the experimental spectra to be made. The

Table III. Root Mean Squared Error[a] for Comparison of Curve Resolution Estimator of Pure Component Spectra and Spectra of Pure Cr Oxides and Cr Metal

comparison spectra	root mean squared error	
	component 1	component 2
Cr	0.176	0.026
CrO	0.011	0.196
Cr_2O_3	0.004	0.184
CrO_2	0.018	0.202
CrO_3	0.034	0.180

[a] RMS error = $\sum_{j=1}^{n} (\hat{x}_j - x_j)^{1/2}/n$, where $n = 6$, $\hat{x}_j$ = curve resolution estimate of peak intensity at $m/e = j$. x_j = peak intensity at m/e j measured from pure oxide or pure metal sample.

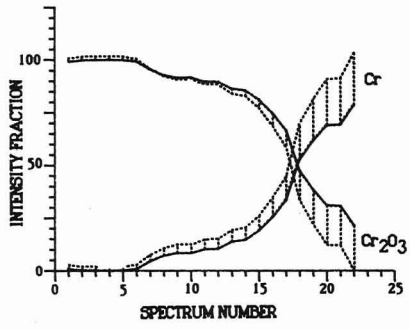

Figure 4. Depth profile plot of Cr and Cr_2O_3. The relative intensity of each component, plotted vs. spectrum number, shows the oxide contribution decreasing with depth. Bands are used instead of lines in order to represent the ambiguity present in the resolution of the pure spectra (*9–11*).

author, using only the peak intensities for Cr^+, Cr_2^+, and Cr_3^+, assumed that the first spectrum was due solely to Cr_2O_3 and the last was from Cr metal only. In the curve resolution no assumptions were made about the composition or identity of the first or last spectra. Also, CrO gives rise to a spectrum very similar to Cr_2O_3.

Studies of the oxidation of metals and formation of oxide layers are common applications of SIMS. The identification of a metal oxide is possible only when its spectrum is resolved from the metal spectrum and those of other oxides. The use of higher mass spectral resolution would not improve the spectral resolution in such a case as presented here but instead would only lower the signal intensities. However, in this experiment curve resolution was used successfully to achieve spectral resolution, allowing calculation of component spatial profiles.

Image Sample. In this experiment, images were collected for 12 different ions measured on a silver support painted with white and brown acrylic paints. Peaks due to Ti^+ and TiO^+ with main isotopes at 48 and 64 amu, respectively, were expected from the titanium white paint. From analysis of samples of the brown paint, a peak at 56 amu from Fe and peaks at 55 and 57 amu were expected. The latter two peaks are presumably from organic compounds in the paint. At least two components, one for each paint, were expected to be found in the curve resolution analysis (the inorganic and organic compounds making up a single paint are expected, if homogeneously distributed, to comprise one component).

The ion images (64 × 64 pixels) for 48, 56, and 64 amu are shown in Figure 5. The expected checkerboard pattern is not observed in any of the ion images. The ion images do not reflect the sample composition for three possible reasons. First, low spectral resolution obscures the differences between compositionally different areas. Second, the ion collection efficiency is lower for ions sputtered away from the center of the imaged area. Third, the use of a beam with a diameter of 1000 μm in imaging the 4.0 × 6.5 mm area causes consid-

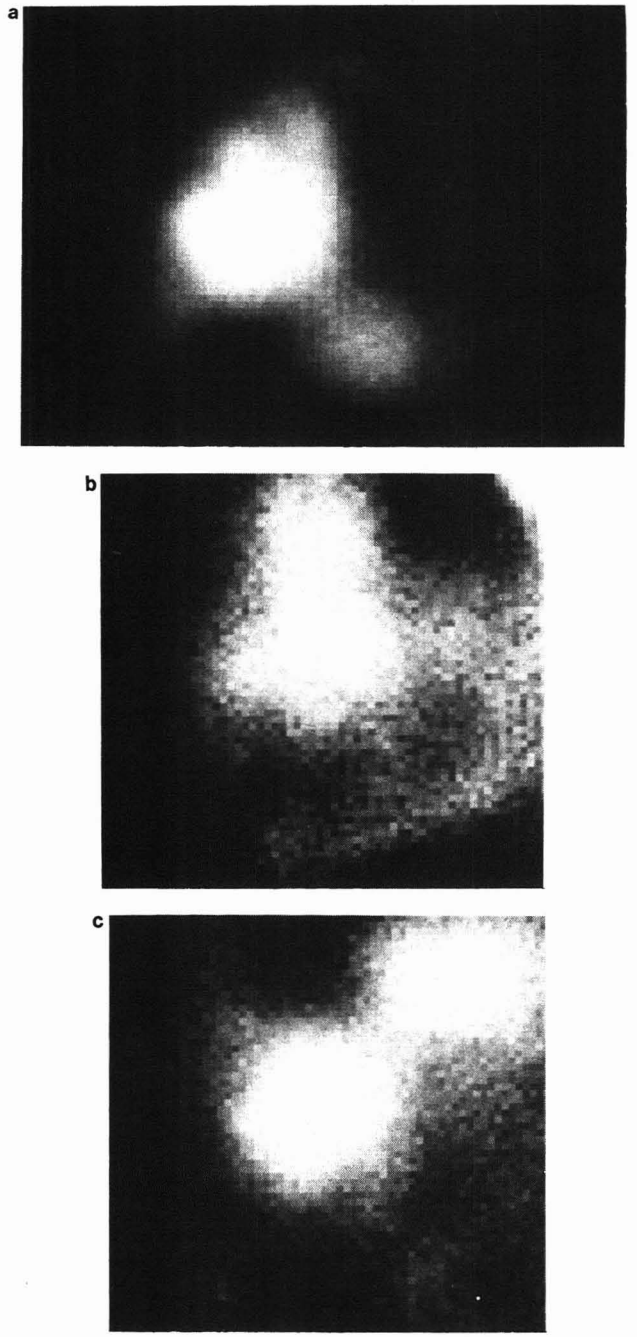

Figure 5. Raw ion images collected for 48 amu (a), 56 amu (b), and 64 amu (c). Each image is 64 × 64 pixels and is scaled to 256 gray levels. The pixel intensity is proportioned to the recorded signal intensity. Brighter areas correspond to higher measured signal.

erable blurring of the image in both spatial directions. Use of a smaller beam size would give sharper images but in this case lowered the signal level so much that peaks with intensity lower than $^{48}Ti^+$ and $^{56}Fe^+$ could not be measured.

Since each of the 12 ion images consisted of 4096 pixels, it is possible to construct 4096 separate spectra (only 12 mass peaks each) from this series of images. For curve resolution analysis a subset of 50 representative spectra was chosen to determine the number of components and to find the eigenvectors spanning the mass spectral space. The spectral set was chosen so that each area of the sample would be represented by multiple spectra. Every sixth spectrum along the image x axis was chosen at the 15th, 22nd, 30th, 37th, and 45th y axis positions.

Eigenanalysis of the 50 spectra, after normalization to unit area, resulted in eigenvectors accounting for 97.87%, 1.78%, and 0.24% of the total data variance. Calculation of the

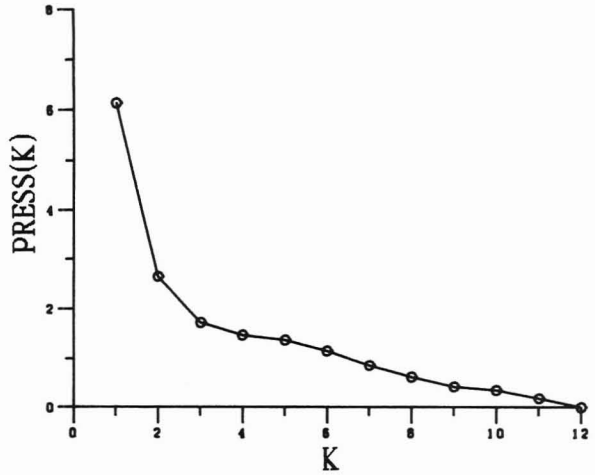

Figure 6. PRESS(K) vs. K plot calculated for iron oxide brown–titanium white sample. The presence of three components is indicated.

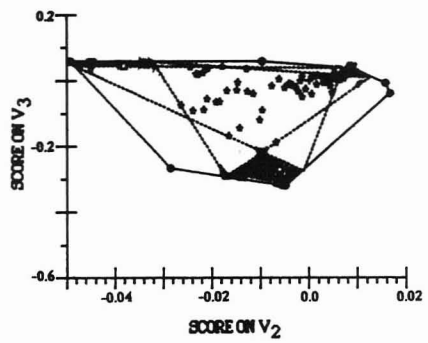

Figure 7. Two-dimensional spectra representation for the three-component case. The iron oxide–titanium white mixture spectra are represented by their scores on the second and third eigenvectors. Stars mark the location of the measured spectra and squares mark the locations of points chosen as representative of the three pure component spectra. The solid line is the outer bound line, all points inside the outer bound satisfy the first curve resolution restriction. The dotted line defines an inner bound region surrounding all the measured spectra. Shaded areas are allowed regions for the three pure components.

PRESS values indicates three components are present and that the three-component curve resolution procedure can be applied. Figure 6 shows the plot of PRESS vs. the number of components.

In the three-component curve resolution analysis the spectra are represented by their scores on the second and third eigenvectors (Figure 7). The score on the second eigenvector is the x axis value. The y axis value is the score on the third eigenvector. In the figure, stars mark the location of data points (spectra). The outer bound resulting from the nonnegativity constraint is shown as the solid line. The dotted line is the inner bound line that surrounds the data points. The shaded areas are the areas where possible pure component spectra must lie. From the figure it can be seen that sample spectra were measured close to the allowed regions for the pure spectra of components one and two.

Locations of the estimated spectral points of the pure components were arbitrarily chosen near inner bounds of the allowed regions. In Figure 7 these are marked with square points. By use of the scores corresponding to these points pure component spectra can be calculated (Table IV).

Examination of the pure component spectra allows the first two components to be identified. Component one is seen to correspond to the Ti-white paint with highest intensity at 48 amu. The peak pattern for m/e ions 46, 48, 49, and 50 is close to the Ti isotope pattern and the peak pattern for the 62–66 mass range is close to that expected for TiO isotopes. The

Table IV. Calculated Pure Component Spectra, Normalized to Unit Area

	peak intensity		
m/e	component one	component two	component three
46	0.084	0.031	0.307
48	0.719	0.334	0.192
49	0.046	0.086	0.187
50	0.021	0.085	0.129
55	0.005	0.139	0.015
56	0.022	0.249	0.007
57	0.002	0.041	0.027
62	0.013	0.021	0.020
63	0.013	0.018	0.027
64	0.058	0.010	0.046
65	0.088	0.019	0.011
66	0.002	0.013	0.007

intensities at 55, 56, and 57 amu are much lower in comparison.

The spectrum for component two is most noticeably different in having a much higher intensity for m/e value ions at 55, 56, and 57. This component is identified as the Fe brown paint.

The third component has its largest peak at 46 amu, with high intensities at m/e 48, 49, and 50. Increased ratios for 46/48 amu, 49/48 amu, and 50/48 amu are seen in the spectra measured from Ti-white paint after continued ion beam bombardment. This could possibly be due to different sputtering rates between the inorganic and organic components in this paint. While appearance of components arising from beam damage to the sample might be expected, this third component is not identified by us as a beam degradation product. Degradation of the sample would be expected to occur to a higher degree in the center of the imaged area where the ion beam is in better focus (with greater number of primary ions/unit area). This component, however, is found in greater amount away from the center of the sample area; thus it cannot be positively identified as a degradation product, but it is spatially resolved from components 1 and 2.

The relative signal contribution of the three components to all 4096 spectra can be calculated allowing a 64 × 64 pixel image to be created for each component of interest (Figure 8). In the first and second component images the expected checkerboard pattern is now apparent. Thus, the spatial resolution of the components has been improved by eliminating spectral interference from the unidentified component. In the Ti white image the intensity in the center area is higher than in the two areas composed of Ti white paint alone. This is due to a higher collection efficiency at the center and, also, more spectra from regions 2, 4, and 6 were analyzed than from regions 1, 3, and 5. In the Fe brown component image the checkerboard pattern is more visible. Component three shows no checkered pattern but has highest intensity away from the center of the imaged area. The resolution of the third component from the first two allows the spatial distribution of the first and second components to be represented more accurately than any of the raw ion images.

In these examples the cross-validation procedure gave good indications of the number of components. Often the intensities of some peaks in a SIMS spectrum will be much greater than zero and may vary by orders of magnitude from other peaks in the spectrum. This is true for the chromium oxides and the metallic chromium. This, combined with high similarity between the component spectra, makes it difficult to determine the number of components based on the percent of total data variance accounted for by each eigenvector. For SIMS data the first eigenvector of the covariance matrix is similar to the mean vector of the data set in mass spectral space and often accounts for greater than 95% of the total

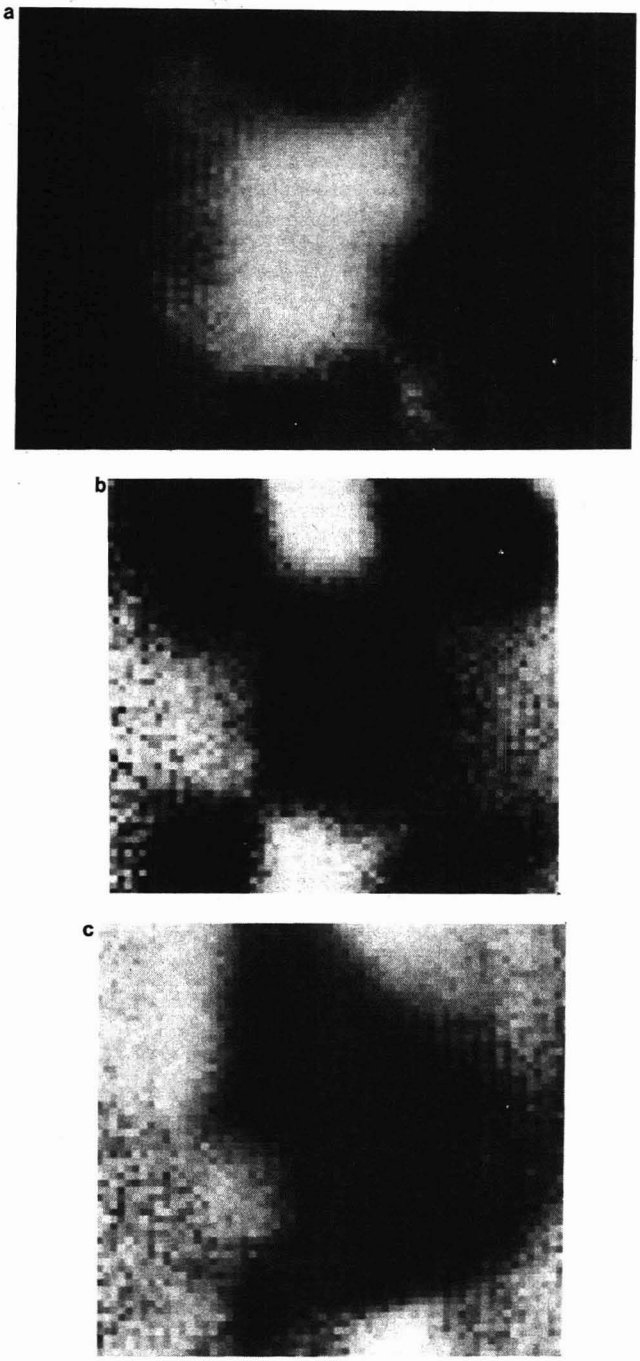

Figure 8. Estimated pure component images for component one, Ti white paint (a); for component two, Fe brown paint (b); and for the unidentified third component (c). The third component shows highest intensity away from the center of the imaged area. Each image is scaled to 256 gray levels.

variance. With a noise level generally around 5–10% this may lead one to conclude incorrectly that no more than one component is present. Calculation of the PRESS value for different numbers of components was a better indicator of the actual number.

Multivariate curve resolution allows spectra for pure components to be estimated for two and three component cases when eq 2 is valid. As mentioned above, eq 2 may be found not to be true for many multicomponent samples. However, in cases where eq 2 is valid, the curve resolution analysis is a useful method for the determination of the component spectra and in these cases the curve resolution estimates of the component spatial distributions are more accurate than those found by relying on a single peak to represent a component. This was especially obvious for the image example. Our results for the first two components agree with what is

known about the spatial distribution of the components from the sample preparation. Their component spectra also make chemical sense. Thus, it appears that, even when eq 2 is not valid, multivariate curve resolution can still yield useful results.

In mixture samples where component spectra add linearly, the curve resolution estimate of a component's relative signal intensity does not usually equal that component's relative concentration because different components generally do not have equal sputter and ion yields. By comparison of eq 2 and 6 the curve resolution estimate, $a_{i,k}$, of the relative spectral intensity of component k, in sample i, can be expressed as

$$a_{i,k} = i_p n t S_k I^+_k c_{i,k} \quad (10)$$

where i_p, n, and t are constants. The calculated $a_{i,k}$ values correspond to relative concentration only if the sputter and ionization yields are equal for all components. This is usually not the case; thus the concentration profiles and component images can only be considered qualitatively correct. Calibration samples are required in order to estimate actual component concentration.

ACKNOWLEDGMENT

The authors thank H. W. Werner of Philips Research Laboratories, Eindhoven, The Netherlands, for providing spectra of Cr metal and Cr oxides.

LITERATURE CITED

(1) Turner, N. H.; Dunlap, B. I.; Colton, R. J. *Anal. Chem.* **1984**, *56*, 373R–416R.
(2) *Secondary Ion Mass Spectrometry SIMS IV*; Benninghoven, A., Okano, J., Shimizu, R., Werner, H. W., Eds.; Springer-Verlag: Berlin, Heidelberg, New York, Tokyo, 1984.
(3) Slodzian, G. *Surf. Sci.* **1975**, *48*, 161–186.
(4) Colby, B. N.; Evans, C. A., Jr. *Appl. Spectrosc.* **1973**, *27*, 274–279.
(5) Ganjei, J. D.; Colton, R. J.; Murday, J. S. *Int. J. Mass Spectrom. Ion Phys.* **1981**, *37*, 49–65.
(6) Gardella, J. A.; Hercules, D. M. *Anal. Chem.* **1980**, *52*, 226–232.
(7) Werner, H. W. *Surf. Sci.* **1975**, *47*, 301–323.
(8) Heinrich, K. F. J., Newbury, D. E., Eds. *Secondary Ion Mass Spectrometry*; National Bureau of Standards: Washington, DC, 1975; NBS Spec. Publ. No. 427, pp 79–127.
(9) Sharaf, M. A.; Kowalski, B. R. *Anal. Chem.* **1981**, *53*, 518–522.
(10) Sharaf, M. A.; Kowalski, B. R. *Anal. Chem.* **1982**, *54*, 1291–1296.
(11) Osten, D.; Kowalski, B. R. *Anal. Chem.* **1984**, *56*, 991–995.
(12) Warner, I. M.; Davidson, E. R.; Christian, G. D. *Anal. Chem.* **1977**, *49*, 2155–2159.
(13) Werner, H. W.; deGrefte, H. A. M.; Van den Berg, J. In *Advances in Mass Spectrometry*; West, A. R., Ed.; Applied Science Publishers: Chichester, England, 1974; Vol. 6.
(14) Blaise, G.; Lyon, O.; Roques-Carmes, C. *Surf. Sci.* **1978**, *71*, 630–656.
(15) Eastmont, H. T.; Krzanowski, W. J. *Technometrics* **1982**, *24*, 73–77.
(16) Borgen, O.; Kowalski, B. R. *Anal. Chim. Acta* **1985**, *174*, 1–26.

RECEIVED for review December 26, 1984. Resubmitted November 18, 1985. Accepted May 6, 1986. This work was supported in part by the Department of Energy under Contract DE-AT06-83ER60108.

Evaluation of Multipoint Kinetic Methods for Immunoassays: Kinetic Quantitation of Immunoglobulin G

John W. Skoug and Harry L. Pardue*

Department of Chemistry, Purdue University, West Lafayette, Indiana 47906

This paper describes results of a study of the kinetic behavior of the reactions between the immunoglobulin, IgG, and antibodies to the protein. Stopped-flow mixing with nephelometric measurements is used to monitor the time course of the reaction and a variety of kinetic parameters is evaluated for the quantitation of IgG. Although several options can be used to quantify IgG, it is concluded that maximum rates are most useful in ranges of excess antibody and excess antigen and that the pseudo-zero-order rate coefficient is most useful for differentiating between these regions and for quantifying IgG at the maximum in the calibration plot of rate vs. concentration. It is shown that these options can be used to quantify IgG throughout the range of clinical interest from a single response curve for each concentration. For IgG concentrations between 0 and 73 mg/dL, a least-squares fit of determined (y) vs. prepared (x) concentrations yielded $y = 1.04x - 0.54$ mg/dL.

Because of the high selectivity associated with immunochemical reactions, immunoassay methods are becoming increasingly important. To date, most immunoassay procedures are based on measurements made after immunochemical reactions have approached equilibrium. Although these procedures are effective, it is possible that kinetic-based methods could offer complementary capabilities as has been the case with more conventional reactions.

Examples of kinetic-based immunoassays reported to date include procedures for immunoglobulins (*1–4*) and drugs (*5, 6*). Most of these procedures are based on single-point measurements analogous of those used with more conventional reactions (*7*).

In recent years we have developed and evaluated a variety of multipoint procedures for kinetic methods (*8–10*). An objective of this study was to evaluate the potential utility of these multipoint-kinetic methods for immunochemical reactions. The determination of the immunoglobulin, IgG, was chosen as a model system because this is an important but difficult assay, because it is representative of a group of similar assays, and because substantial amounts of kinetic data are already available for the reactions (*11–14*).

Reactions of the immunoglobulins with antibodies produce precipitates that are monitored with light-scattering methods (*15*). All procedures reported to date produce calibration plots that pass through maxima such that sensitivities drop to zero at the peaks and there are regions in which two different concentrations given the same measured response. Procedures reported to date usually require special features such as restricted concentration range or consecutive additions of antibody or antigen to overcome these problems. The objectives of this study were to determine if the kinetic characteristics of the antigen/antibody reaction could be used to differentiate unambiguously among the three regions of the so-called immunoprecipitin curve (*12*) and to quantify IgG over the full concentration range of clinical interest. These objectives have been achieved for measurements of purified IgG in synthetic samples. It was found that a kinetic parameter, an apparent zero-order rate coefficient, can be used not only to differentiate among the three regions in the calibration curve but also to

0003-2700/86/0358-2306$01.50/0 © 1986 American Chemical Society

quantify IgG in the region of the maximum in the curve. In addition, it is shown that a variety of data-processing options can be used to quantify IgG on the ascending and descending regions of the curve. The proposed approach is to use the sign of the apparent zero-order rate coefficient to identify the region of the calibration plot that should be used for any sample, to use either the maximum velocity or parameters computed with a curve-fitting method to quantify IgG concentrations in the regions of excess antibody or antigen, and to use the zero-order rate coefficient to quantify IgG concentration in the region of equivalence.

EXPERIMENTAL SECTION

All solutions were prepared with water that had been deionized, distilled, and filtered with a 0.22 μm Nylon-66 membrane filter (Rainin Instrument Co., Woburn, MA). Storage vials for antisera and standard antigen solutions were purged of dust with a stream of filtered nitrogen and capped until use.

Reagents. Poly(ethylene glycol) (PEG) was incorporated into the reaction medium to increase the rate of the aggregation phase of the antigen/antibody reaction (*16*). The diluent contained 40 g of PEG (Fisher Scientific, average molecular weight 8000 g/mol) per liter, 0.15 M NaCl and 10 mM phosphate buffer adjusted to pH 7.95. This solution was filtered with a 0.22-μm filter prior to use.

Human immunoglobulin G (IgG, mol wt = 1.5×10^5) was obtained from Miles Scientific (Naperville, IL) and used without further purification. The standard IgG solutions used to prepare calibration curves were prepared by serial dilution of a saturated protein stock solution that contained approximately 200 mg of IgG in 100 mL of PEG/buffer. Synthetic unknowns used to test the quantitative capabilities of the data-processing options described below were prepared in the same manner as the standards. These solutions were filtered with a 0.22-μm Millex-GV filter unit (Millipore Corp., Bedford, MA) and IgG concentration was calculated from the measured absorbance at 280 nm assuming the absorptivity of IgG to be 1.40 mL mg^{-1} cm^{-1}. The range of IgG concentrations used in this work (0.02–7.5 μ M, 0.30–106 mg/dL) is slightly wider than expected in real samples (0–60 mg/dL), based on a 1:200 dilution of serum (*2*).

Monospecific goat antiserum to human IgG (aIgG) was obtained from International Immunology Corp. (lot no. 100-00-B04, 100-00-B06, Murrieta, CA). This antiserum contains 71 mg/mL total protein and its titer, a measure of the total number of reactive antibodies (*17*), is 10–12 mg of antigen/mL of antiserum as determined by a reverse plate method. Because of the high protein content of the antiserum and the relatively high organic content of the diluent, the antiserum dilution was prepared and allowed to stand at least 24 h at 4 °C before use. On the day experiments were performed, the antiserum solution was filtered with a 0.22-μm filter; this solution was found to be stable for at least 12 h at room temperature.

Instrumentation and Software. All measurements of scattered light were made at 90° to the incident beam with a stopped-flow spectrophotometer (Model D-110 Dionex Corp., Sunnyvale, CA). A brass aperture with a diameter of 6.5 mm was constructed to reduce the effects of spurious stray light from the stopped-flow observation cell (2-cm path length). All measurements were made at 500 nm (1 nm band-pass) with a 50-W tungsten/halogen lamp used as the excitation source.

The stopped-flow instrument is interfaced to a microprocessor (PC-6300, AT&T Information Systems) equipped with 256K bytes of random access memory (RAM), an 8087 math-coprocessor chip, and a 10 Mbyte disk. The interface board used for data acquisition is the LAB Master (Scientific Products Corp., Cleveland, OH), which consists of a "mother" board that plugs into the PC expansion bus and a "daughter" board on which the analog-to-digital conversions are performed. The software for programming the LAB Master board and for on-line data processing was written in the C programming language.

Typically, data acquired on any given day were stored on the disk and later transferred via RS-232C serial lines to a more powerful computer (MCS-510 workstation, Massachusetts Computer Corp., Westford, MA) for further processing, graphics output, and long-term storage. We have translated the data-processing programs reported previously (*8*, *9*) from FORTRAN IV into C language and have modified them to provide autoranging and automatic determination of initial estimates used in fitting data to a combined first-order/zero-order model described in detail below. In addition, a small data-base program has been written to store kinetic data from several different laboratory instruments in a unified format. This generalized approach provides a lot of flexibility in data handling and minimizes duplication of software development efforts (*18*).

Any of the above mentioned programs for data acquisition or data processing are available from the authors on request.

A diode-array-based spectrophotometer (Model 8450 A, Hewlett-Packard, Palo Alto, CA) was used for determination of protein concentrations.

Data Processing. Three modes of data processing were evaluated in this study. First, the rate nephelometric approach described by Sternberg (*3*) was used as a comparison method. The rate of change of intensity with time was computed as the derivative of the response curve by the method of Savitzky and Golay (*19*). Second, the maximum scattering value in each response curve and the average of the last 30 data points collected were used to compute relative intensity changes denoted as ΔI_{max} and ΔI_t, respectively. This method, similar to that described by Hills and Tiffany (*4*), is identified herein as a two-point method. Third, a nonlinear-regression-kinetic method was used to compute relative intensity changes and rate parameters that represent the best fit of intensity vs. time data. Models evaluated included, first-order, parallel first-order/zero-order, and combined first-order/zero-order/quadratic. Parameters computed with the first-order model are the initial intensity, $\hat{I}_0$, the intensity at infinite time, $\hat{I}_\infty$, and the apparent first-order rate coefficient, $\hat{k}_1$. In addition to these first-order parameters, an apparent zero-order rate coefficient, $\hat{k}_0$, is computed for the other models, and a quadratic term is computed with the combined first-order/zero-order/quadratic model. The models used to fit the data are empirical and no physical interpretation of the parameters is possible; hence the term "coefficient" is used to describe the rate parameters throughout this work.

Procedure. Equal volumes (0.25 mL) of each reagent were mixed in the stopped-flow observation cell and 250 data points corresponding to eight to nine reaction half-lives were collected. Data rates ranged from 2 to 20 Hz depending on the IgG/aIgG ratio, defined here as the weight concentration of IgG divided by the product of the titer of the antiserum and its dilution factor. In a typical calibration experiment with a 1:20 aIgG dilution, this ratio varied from 0.07 to 20 for the lowest to highest IgG concentrations (0.3–106 mg/dL). All concentrations are reported prior to a 1:2 dilution in the stopped-flow cuvette.

To prevent bubbles from interfering with light scattering measurements, the IgG standards, synthetic samples, and anti-IgG solution were degassed by stirring under reduced pressure. The temperature was maintained at 25.0 °C.

RESULTS AND DISCUSSION

Response Curves. Figure 1 includes typical time-dependent response curves. Data in Figure 1A correspond to the situation in which antibody is either in excess of or near equivalent to antigen concentration and data in Figure 1B correspond to the situation in which antigen concentration is either near equivalent to or in excess of antibody concentration. After an initial induction period, each response passes through a region of maximum slope and then either approaches a maximum signal value asymptotically (excess antibody) or passes through a maximum and then decreases gradually (excess antigen). It is the reversal in the response curves which occurs when antigen and antibody are nearly equivalent that yields the maximum in the calibration plot and the dual-valued calibration values that were mentioned earlier. An objective of this study was to determine if an empirical model could be used to fit these responses and yield information that could be used to quantify antigen concentration over a wide range.

In each case, data during the induction period were fit to a quadratic model to facilitate computation of the intensity,

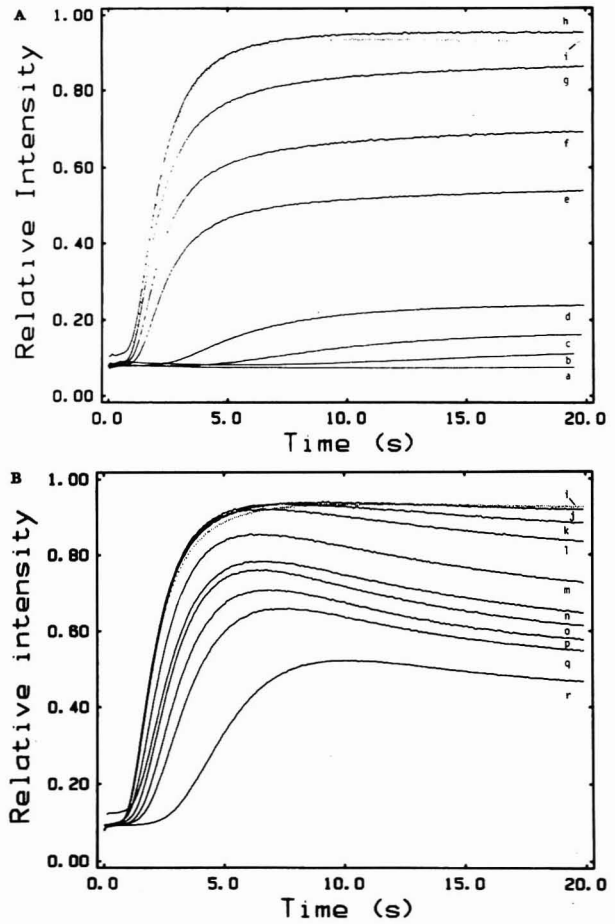

Figure 1. Progress curves for fixed antibody concentration and IgG concentration from large excess of antibody to large excess of antigen. Conditions: 40 g/L PEG, 0.15 M NaCl, 10 mM phosphate buffer, pH 7.95, 1:20 antibody dilution. IgG concentrations (mg/dL): A (a–i), 0.31, 0.46, 0.87, 1.44, 5.38, 8.23, 11.8, 16.2, 17.3; B (j–r), 18.5, 20.8, 23.2, 29.2, 39.0, 48.7, 57.8, 67.4, 106, respectively.

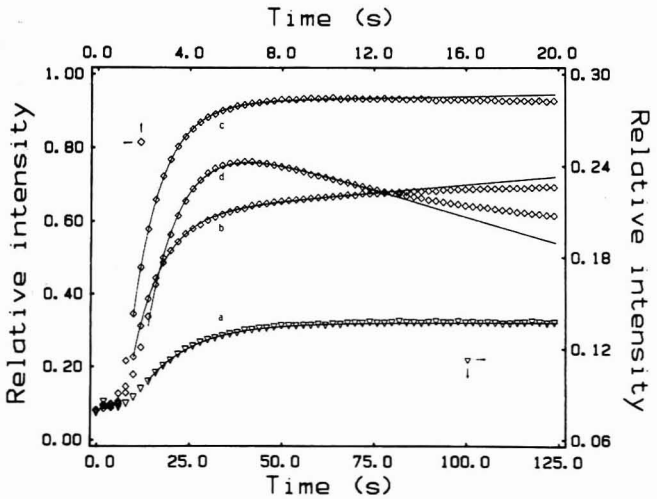

Figure 2. Experimental (◊ and ∇) and fitted (——, first-order/zero-order model) data for selected response curves. C_{IgG} (mg/dL): (a) 0.46, (b) 8.23, (c) 16.2, and (d) 48.7. The last point in the fitting range for curves b–d is 12.5 s.

I_0, at the mixing point ($t = 0$). Slopes of response curves were computed (*19*) and the maximum slope was used to identify the inflection (maximum velocity) in each response curve. Other models mentioned earlier were evaluated for the region beyond the inflection point of each curve.

Figure 2 shows a group of curves fit with a combined first-order/zero-order model. Although the model does not fit the full data range for most curves, it helps to identify four

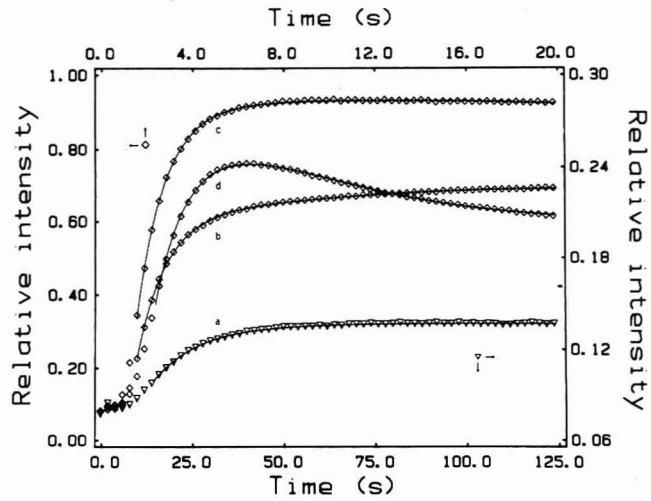

Figure 3. Experimental (◊ and ∇) and fitted (——, first-order/zero-order/quadratic model) data for selected response curves (see Figure 2). The last point in the fitting range for curves b–d is 20 s.

distinctly different and important types of responses. When antibody is in large excess (curve a), the plot at longer times has a very small slope, resulting in a very small value of the apparent zero-order rate coefficient, $\hat{k}_0$, generated by the fitting process. When antibody concentration is in modest excess (curve b), the slope at longer times is more steeply positive, resulting in a finite, positive value of the computed zero-order rate coefficient. When near-equivalent amounts of antibody and antigen are present (curve c), the slope at longer times again approaches zero, resulting in a computed value of the zero-order rate coefficient near zero. When antigen is in excess (curve d), the slope at longer times is distinctly negative, resulting in a finite negative value of the zero-order rate constant. It is shown later that these features of the computed value of the zero-order rate coefficient permit one to differentiate between the so-called antibody-excess and antigen-excess regions of the immunoprecipitin calibration curve and to quantify antigen concentration near the maxima in the usual calibration plots.

Attempts to fit these data with a model for two consecutive first-order processes were unsuccessful. However, as shown in Figure 3, use of a combined first-order/zero-order/quadratic model ($S_t = S_\infty - (S_\infty - S_0)e^{-k_1 t} + k_0 t + k_2 t^2$, where S is scattered intensity) yielded quite good fits throughout the time range monitored for the concentrations represented in Figure 1. Although this model yields the better fits, it does not appear to offer any significant advantages for the quantitation of IgG. Therefore, because the first-order/zero-order model is simpler, rate parameters reported below were obtained with this model unless stated otherwise. It is emphasized that these fitting options are strictly empirical, intended only to aid in the quantitation of IgG, and that no mechanistic information is implied.

Concentration Ratio of Antibody and Antigen. Effects of antibody concentration on the computed first-order rate parameter, $\hat{k}_1$, are illustrated in Figure 4 for three different antigen concentrations. For large excess of antibody relative to antigen (curve a), the first-order rate parameter is relatively independent of antibody concentration. However, for near-equivalent amounts of antibody and antigen and for excesses of antigen, the first-order rate parameter increases with antibody concentration (cures b and c). All time-dependent responses were similar to those in Figures 1 and 2 except that for the largest ratio of antigen to antibody (C_{IgG} = 79.4 mg/dL and 1:50 dilution of antibody); the response curve for this solution had no induction period and exhibited a second exponential rise after about 100 s. Because this is not a situation expected in practice, it was not examined further.

Table I. Least-Squares Statistics for Determined vs. Prepared Concentration of IgG.

row	region	slope ± std dev	intercept ± std dev (mg/dL)	std error of est, mg/dL	corr coeff	quantitative parameters
			Rate Method			
1	excess Ab[a]	0.99 ± 0.01	−0.37 ± 0.20	0.55	0.998	V_m[h]
2	excess IgG[b]	1.02 ± 0.02	0.36 ± 1.23	2.17	0.994	V_m
3	equivalence[c]	0.49 ± 0.06	1.22 ± 1.24	0.77	0.890	V_m
			Two-Point Method			
4	excess Ab[a]	1.16 ± 0.03	−1.50 ± 0.51	1.31	0.992	ΔI_{max}
5	excess Ag[b,d]	1.10 ± 0.03	2.42 ± 1.48	2.61	0.992	ΔI_t
6	equivalence[c,d]	0.97 ± 0.04	0.95 ± 0.71	0.30	0.991	ΔI_t
			Regression-Kinetic Method			
7	excess Ab[a]	1.01 ± 0.01	−0.40 ± 0.12	0.32	0.999	$\Delta\hat{I}$
8	excess IgG[b]	1.12 ± 0.04	−2.59 ± 2.35	4.14	0.982	$\Delta\hat{I}$
9	excess IgG[b]	1.01 ± 0.03	0.40 ± 1.48	2.61	0.991	$\hat{k}_1$
10	equivalence[c]	1.02 ± 0.02	−0.11 ± 0.40	0.25	0.997	$\hat{k}_0$
			Combined Methods			
11	total[a–c,e]	1.04 ± 0.01	−0.54 ± 0.31	1.44	0.998	V_m, $\hat{k}_0$
12	total[a–c,f]	1.08 ± 0.01	−0.85 ± 0.42	1.96	0.997	ΔI_t, $\hat{k}_0$, ΔI_t
13	total[a–c,g]	1.03 ± 0.01	−0.50 ± 0.34	1.57	0.998	$\Delta\hat{I}$, $\hat{k}_0$, $\hat{k}_1$

[a] Four to five replicates on five samples with concentrations between 0 and 25 mg/dL with 1:20 dilution of antibody. [b] Four to five replicates on five samples with concentration between 24 and 70 mg/dL with 1:30 dilution of antibody. [c] Four to five replicates on four samples with concentrations between 16 and 24 mg/dL with 1:30 dilution of antibody. [d] The parameters from a cubic calibration equation were used to compute IgG concentration. [e] Rate and regression-kinetic options. Combination of data from rows 1, 2, and 10. [f] Two-point and regression-kinetic option. Combination of data from rows 4, 5, and 10. [g] Regression-kinetic methods. Combination of data from rows 7, 9, and 10. [h] Maximum velocity.

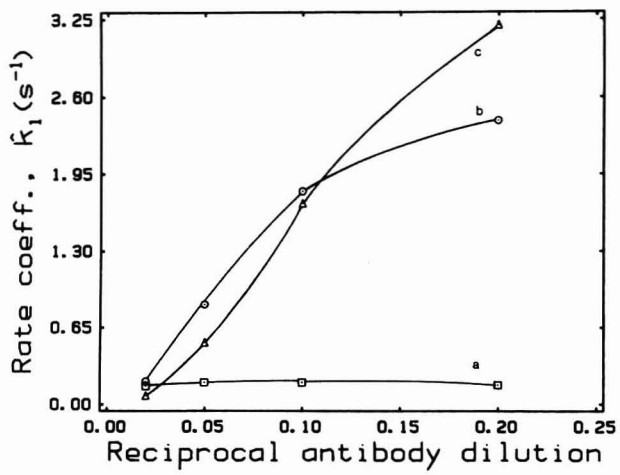

Figure 4. Effect of varying antibody concentration on the observed rate coefficients computed with a first-order/zero-order model. C_{IgG} (mg/dL): (a) 0.66, (b) 20.7, and (c) 79.4.

Mixing Order. Effects of mixing order were examined briefly in an attempt to reduce or eliminate the induction period. In one set of experiments, antigen and antibody were premixed before mixing with PEG. When antibody was in excess, a visually turbid solution resulted when PEG was absent; with antigen in excess, there was no apparent turbidity in the premixed solution and, when mixed with PEG, the resulting solution yielded a smooth response curve with no induction period. Although the absence of an induction period is attractive, the behavior with excess antibody is unsatisfactory and this premixing option was not considered further.

Data-Processing Options. Several data-processing options are discussed here. In each case, one set of serial dilutions of IgG was used to establish calibration curves and equations, and the resulting equations were used to compute concentrations of IgG in a set of synthetic samples prepared to contain known relative concentrations of IgG. Least-squares statistics of computed vs. prepared concentrations were then computed for each data-processing option. Unless noted otherwise, all calibration plots presented below were fit satisfactorily with quadratic equations.

Rate Method. This method, commonly called rate nephelometry (*3*), involves the use of the maximum velocity of the response curve (Figure 1) to compute concentration. In this study, a seven-point quadratic derivative of the response curve was computed (*19*) and the maximum velocity was selected and plotted vs. concentration. As expected, the plot (Figure 5A) passes through a maximum in a region assumed to represent equivalent amounts of antigen and antibody. Each point on the curve is the average of three to seven replicates with relative standard deviations (RSD's) of 0.5–4% except at the lowest concentrations (<1 mg/dL) at which RSD's ranged up to 8%. The solid curves in the plot are the least-squares fits of the data to a quadratic equation. Coefficients obtained from the fits were used to compute concentrations in a set of synthetic samples. Least-squares statistics for fits of computed vs. prepared concentrations are presented in the first three rows of Table I for the three regions of the rate vs. concentration calibration curve. These statistics confirm good correlation between computed and prepared concentrations for the regions of excess antigen and excess antibody, but poor correlation (as expected) in the region of the maximum in the rate vs. concentration calibration plot.

Two-Point Methods. Two approaches identified here as two-point methods were evaluated. In these methods, the intensity changes

$$\Delta I_{max} = I_{max} - I_0 \quad (1)$$

and

$$\Delta I_t = I_t - I_0 \quad (2)$$

were computed and related to concentration. In both equations, I_0 is the intensity at $t = 0$ computed by fitting the first ten data points (during the induction period) to a quadratic equation. In eq 1, I_{max} is the maximum intensity measured and in eq 2, I_t is the intensity at some arbitrary time after mixing, computed as the average of 30 data points equally

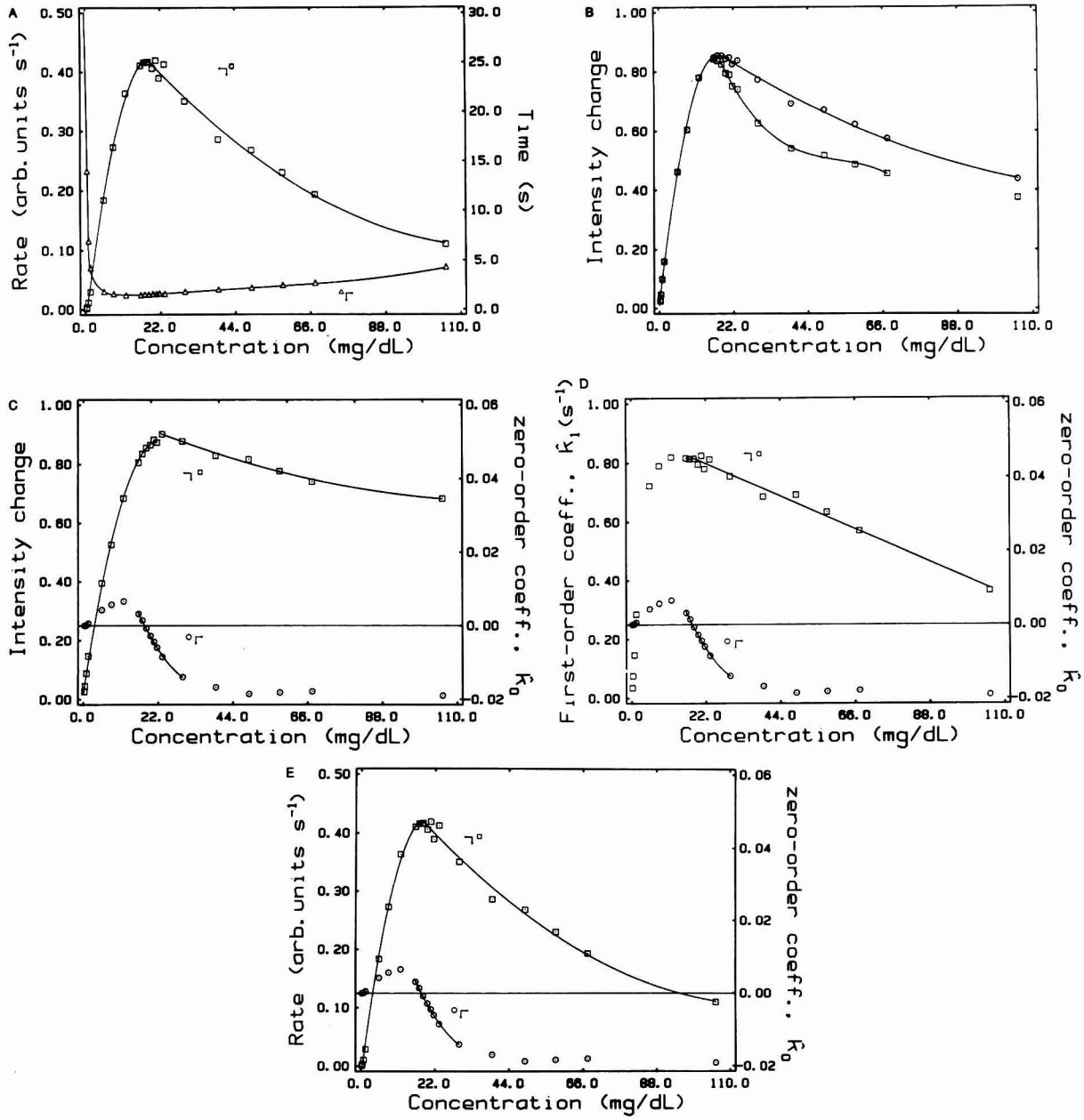

Figure 5. Representative calibration curves for three kinetic options: (A) rate method, maximum reaction rate (□) and time to reach maximum rate (△) vs. C_{IgG}; (B) two-point methods, computed intensity changes ΔI_{max} (○) and ΔI_t (□) vs. C_{IgG}; (C) regression-kinetic method, ΔI (□) and $\hat{k}_0$ (○) vs. C_{IgG}; (D) regression-kinetic method, $\hat{k}_1$ (□) and $\hat{k}_0$ (○) vs. C_{IgG}; (E) combined rate and regression-kinetic methods, maximum reaction rate (□) and $\hat{k}_0$ (○) vs. C_{IgG}.

spaced on either side of the reference point. The time chosen was 31.1 s for concentrations above 1 mg/dL and a longer time (132.5 s) was used for lower concentrations. Results are summarized in Figure 5B. Each point is the average of four to five replicates and RSD's are less than 1.5% in all cases. The two approaches yield near identical results when antibody is in excess but, as expected, yielded different results when antigen is in excess. The solid curve in the region of excess antibody for both methods is the least-squares fit to a quadratic equation as is the solid curve in the region of excess antigen for ΔI_{max} vs. concentration. The solid curve in the region of excess antigen for ΔI_t vs. concentration is the least-squares fit to a cubic equation; the data were not fit satisfactorily with a quadratic equation.

Because the ΔI_t values give higher sensitivity in the region of excess antigen, they were used to quantify IgG in the synthetic samples. Least-squares statistics for computed vs. prepared concentration are presented in rows 4–6 of Table I. Although the statistics show reasonably good correlation between computed and prepared concentrations in the regions of excess antigen and excess antibody (rows 4–5), slopes, intercepts, and standard errors of the estimate are degraded relative to those for the maximum rate data. Correlation statistics presented in the sixth row of Table I for the region of equivalence indicate good agreement between computed and prepared concentrations. This rather surprising result is due to the narrowness of the peak in the calibration curve and steep descent of the ΔI_t vs. concentration plot just into the antigen excess region.

The two-point methods could be used to differentiate between the regions of excess antibody and antigen. In the region of excess antibody, the intensity of scattered light increases throughout the period monitored (see Figure 1A) while for the region of excess antigen, the intensity decreases at longer times (see Figure 1B). Thus, the magnitude of the differences between intensities at two preselected times could be used to differentiate between the ascending and descending regions of the calibration curves.

Regression-Kinetic Methods. As was mentioned earlier, two empirical models (combined first-order/zero-order and

first-order/zero-order/quadratic) were used to fit intensity vs. time data with different degrees of success. Each of these fitting processes generates a variety of parameters, including apparent first-order and zero-order rate coefficients ($\hat{k}_1$ and $\hat{k}_0$), a quadratic coefficient, intensity at $t = 0$ ($\hat{I}_0$), and intensity at $t = \infty$ ($\hat{I}_\infty$) for the first-order component of the reaction. Any of these parameters that varies in a systematic manner with antigen concentration can, in principle, be used to quantitate the antigen. Use of the zero-order rate coefficient, $\hat{k}_0$, is discussed later; some other parameters are discussed here.

Although the combined first-order/zero-order/quadratic model gave a better fit to I vs. t data, no parameters generated with this fitting option offered any advantage relative to the simpler first-order/zero-order model, and results obtained with the latter are discussed here.

Using the intensity at $t = \infty$, $\hat{I}_\infty$ computed with the first-order/zero-order model and the intensity at $t = 0$, I_0, computed with a quadratic fit of data during the induction period, one can compute an intensity difference, $\Delta\hat{I} = \hat{I}_\infty - I_0$, and relate this to concentration. The upper curve in Figure 5C presents the relationship between $\Delta\hat{I}$ and concentrations of IgG. Each point on the curve is the average of three to seven replicates and the relative standard deviation is less than 3% for all concentrations. For all concentrations except the lowest four, the last point included in the fitting process was at 12.5 s; for the lowest four concentrations, it was necessary to fit data over longer times (20–125 s) to obtain reproducibility consistent with that for the higher concentrations.

Least-squares statistics for computed (using $\Delta\hat{I}$) vs. prepared concentrations in the synthetic samples are summarized in the seventh and eighth rows of Table I for the regions of excess antibody and antigen. Results for the region of excess antibody are similar to those for the rate data in the first row but results for the region of excess antigen are degraded relative to the rate data.

It was also observed that the apparent first-order rate coefficient varied with antigen concentration (Figure 5D). In the region of excess antibody, this parameter increased rapidly to a maximum value where it became independent of antigen concentration. For the region of excess antigen, the apparent rate coefficient decreased linearly with antigen concentration. Although the first-order rate coefficient is highly sensitive for very low antigen concentrations, its useful range is limited in the region of excess antibody and cannot be recommended for the quantitation of IgG except at very low concentrations and for the region of excess antigen, where a linear calibration plot is obtained. Least-squares statistics for computed vs. prepared concentrations based on the use of $\hat{k}_1$ in the region of excess antigen are presented in the ninth row of Table I. These statistics compare favorably with those obtained with rate data (row 2).

If the regression-kinetic method were to be used, the best option would be to use $\Delta\hat{I}$ in the region of excess antibody and $\hat{k}_1$ in the region of excess antigen.

It was mentioned earlier (see Figure 2 and related discussion) that the apparent zero-order rate coefficient, $\hat{k}_0$, obtained with the regression-kinetic approach can be used to differentiate between the regions of excess antibody and antigen and to quantify antigen concentration in the regions of the maxima in the calibration curves. Data for $\hat{k}_0$ vs. IgG concentration are included in Figure 5C–E (right-hand ordinate in each case). It is apparent that $\hat{k}_0$ is positive for the region of excess antibody and negative for the region of excess antigen. Also, in the equivalence region in which the slopes of the conventional calibration plots are zero, the zero-order rate coefficient changes steeply and smoothly with antigen concentration. Thus, the sign of $\hat{k}_0$ can be used to identify the region of the calibration response and the magnitude can be used to quantify antigen concentration near the maxima in the calibration plots.

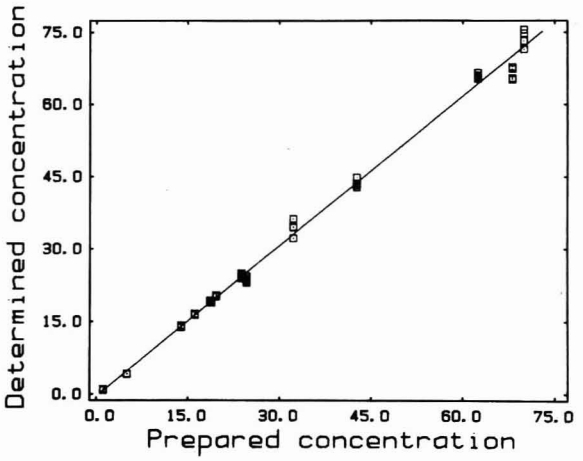

Figure 6. Correlation plot for IgG concentration in synthetic samples using combined rate and regression-kinetic options.

Concentrations of IgG in synthetic samples in the region of the maxima in Figure 5A–C were computed with a quadratic function ($\hat{k}_0$ vs. C_{IgG}) obtained with standards in this range. Linear least-squares statistics for fits of computed vs. prepared concentrations are presented in the tenth row of Table I. These statistics represent good correlation between computed and prepared concentration. Thus, by use of $\hat{k}_0$ to quantify antigen in the region of equivalence and to determine (via sign) whether antibody or antigen is in excess, and by use of selected options from above to quantify antigen in the regions of excess antibody and antigen, it should be possible to quantify IgG throughout the range of clinical interest with a single set of measurements on each sample.

Combined Options. Typical correlation data of computed vs. prepared concentration for the full concentration range examined here are presented in Figure 6 for one combination of options (rate and regression kinetic methods). Least-squares statistics for these and other data are summarized in rows 11–13 of Table I. There is good correlation between computed and prepared concentrations in all cases, confirming the ability to quantify IgG over the full range of clinical interest using different options.

It is difficult to say with certainty which is the best data processing option or combination of options. However, because results by the two-point methods are slightly degraded relative to the rate and regression-kinetic methods, it is our opinion that the best approach is to use the rate method (maximum rates) combined with the zero-order rate coefficient. The rate method is less dependent on the data range used in the fitting process than is the regression-kinetic method and this method appears to have better sensitivity well into the region of excess antigen than does either two-point method. Although it has been suggested that the time required to reach maximum velocity might be used to differentiate the regions of excess antibody and antigen, it is our experience (see Figure 5A) that this time drops off rapidly to a minimum value before the region of equivalence is reached and is not useful for this purpose. Accordingly, we suggest the use of the sign of the zero-order rate coefficient for this purpose with data available from the two-point method being a viable option as indicated above. A relatively simple logical sequence can be devised to differentiate automatically among the different regions via computer.

Work is continuing in this laboratory to fully evaluate the potential merits of each method and combination of methods as described above for use with real samples and with different proteins such as C-reactive protein (*1*) which have very wide physiological ranges. In addition, we are investigating the

potential applicability of these methods to turbidimetric data obtained with multichannel instruments such as centrifugal mixing systems (*19*).

LITERATURE CITED

(1) Buffone, G. J.; Savory, J.; Hermans, J. *Clin. Chem.* (*Winston-Salem, N.C.*) **1975**, *21*, 1735–1746.
(2) Anderson, R. J.; Sternberg, J. C. *Automated Immunoanalysis*; Richie, R. F.; Ed.; Marcel Dekker: New York, 1978; Part 2, Chapter 19.
(3) Sternberg, J. C. *Clin. Chem.* (*Winston-Salem, N.C.*) **1977**, *23*, 1456–1464.
(4) Tiffany, T. O.; Parella, J. M.; Johnson, W. F.; Burtis, C. A. *Clin. Chem.* (*Winston-Salem, N.C.*) **1974**, *20*, 1055–1061.
(5) Wu, J. W.; Bunyagidj, C.; Et al. *Clin. Chem.* (*Winston-Salem, N.C.*) **1983**, *29*, 1540–1542.
(6) Lin, J. D.; Pardue, H. L. *Clin. Chem.* (*Winston-Salem, N.C.*) **1982**, *28*, 2081–2087.
(7) Pardue, H. L. *Clin. Chem.* (*Winston-Salem, N.C.*) **1977**, *23*, 2189–201.
(8) Mieling, F. E.; Pardue, H. L. *Anal. Chem.* **1978**, *50*, 1611–1618.
(9) Harner, R. S.; Pardue, H. L. *Anal. Chim. Acta* **1981**, *127*, 23–38.
(10) Hamilton, S. D.; Pardue, H. L. *Clin. Chem.* (*Winston-Salem, N.C.*) **1982**, *28*, 2359–2365.
(11) Tengerdy, R. P. *J. Immunol.* **1967**, *99*, 126–132.
(12) Marrack, J. R.; Richards, C. B. *Immunology* **1971**, *20*, 1019–1039.
(13) Killingsworth, L. M.; Savory, J. *Clin. Chem.* (*Winston-Salem, N.C.*) **1973**, *19*, 403–407.
(14) Savory, J.; Buffone, G.; Reich, R. *Clin. Chem.* (*Winston-Salem, N.C.*) **1974**, *20*, 1071–1075.
(15) Whicher, J. T.; Perry, D. E. In *Practical Immunoassay, The State of the Art; Clinical Biochemistry Series*; Marcel Dekker: New York, 1984; Vol. 14, Chapter 6.
(16) Hellsing, K. *Automated Immunoanalysis*; Richie, R. F., Ed.; Mercel Dekker: New York, 1978; Part 1, Chapter 3.
(17) Hudson, G. A.; Ritchie, R. F.; Haddow, J. E. *Clin. Chem.* (*Winston-Salem, N.C.*) **1981**, *27*, 1838–1844.
(18) Skoug, J. W.; Weiser, W. E.; Cyliax, I.; Pardue, H. L. *Trends Anal. Chem.*, in press.
(19) Savitzky, A.; Golay, M. J. E. *Anal. Chem.* **1964**, *36*, 1627–1639.

RECEIVED for review January 28, 1986. Accepted May 12, 1986. This work was supported by Grant No. CHE 8319014 from the National Science Foundation. John W. Skoug expresses gratitude to the American Chemical Society—Division of Analytical Chemistry for a summer fellowship.

Two-Method Verification of Hydrogen Peroxide Determinations in Natural Waters

R. J. Kieber* and G. R. Helz

Department of Chemistry and Biochemistry, University of Maryland, College Park, Maryland 20742

An iodometric titration method is investigated for verifying H_2O_2 determinations in natural water matrices. Hydrogen peroxide oxidizes iodide to iodine at pH 4 in the presence of $(NH_4)_6Mo_7O_{24}\cdot 4H_2O$. The I_2 that is generated reacts with an added spike of phenylarsine oxide, the excess of which is titrated with a standardized iodine titrant to an amperometrically determined end point. The difference between titrations with and without the enzyme catalase is proportional to the H_2O_2 concentration. The detection limit is estimated to be 0.02 μM. A previously described independent fluorometric method is in excellent agreement with this method when applied to fresh and saline natural waters containing 0.05–5.00 μM H_2O_2. Demonstration of such agreement can be used for verification purposes in the absence of certified standards.

For unstable analytes in natural waters, verification of analytical results is not easily performed in the usual way, through use of round robins or certified reference materials. Verification is therefore most readily achieved by demonstrating in each laboratory that consistent analytical results can be obtained with two completely independent methods. In this paper we report the development of an iodometric procedure for determining H_2O_2 at concentrations found in natural waters and the use of this method to confirm results obtained by a fluorometric method developed by others (*1–3*).

Hydrogen peroxide is a byproduct of atmospheric and aquatic photochemistry. Its measurement in natural waters has attracted interest in part because of its recently recognized role in converting SO_2 to H_2SO_4 in aqueous aerosols (*4, 5*). A variety of analytical approaches are available for H_2O_2, including chemiluminescence methods (*6–11*), spectrophotometric methods (*12, 13*), and fluorometric methods (*1–3, 14, 15*). A major concern in the development of these methods has been achievement of sub-micromolar detection limits without interference from the numerous other oxidizing substances found in natural waters.

In choosing to develop an iodometric method rather than one of the alternatives, we were influenced by the fact that iodometry is usually the ultimate calibration method for H_2O_2 standards in the laboratory (*16–18*). Furthermore, the equipment needed is reasonably portable and also often available in water analysis laboratories because of its use in the determination of chlorine. Of the methods cited above, the spectrophotometric and fluorometric methods are not independent of one another, since both depend on the use of a peroxidase enzyme to catalyze a reaction between H_2O_2 and a chromophore or fluorophore. Thus, they cannot be used for cross verification. While the chemiluminescence methods are independent of the spectrofluorometric methods, they require special equipment and are prone to interferences.

EXPERIMENTAL SECTION

General. Iodide can be oxidized quantitatively to iodine by aqueous hydrogen peroxide in acidic solutions (*17*)

$$2H^+ + H_2O_2 + 2I^- \rightarrow I_2 + 2H_2O \qquad (1)$$

At pH 2 or lower, oxygen also oxidizes I^-, creating an interference. To avoid this, we buffer the solution at pH 4. However, at pH 4 reaction 1 needs the assistance of a molybdate catalyst (*19, 20*). An excess of phenylarsine oxide is added to the sample to consume I_2 as it is generated. The analytical result is obtained by titrating the remaining phenylarsine oxide to an amperometric end point with I_2

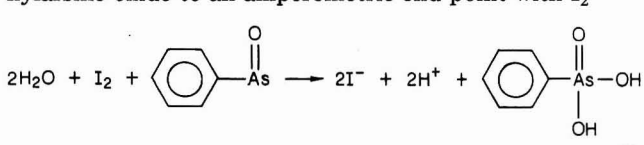

(2)

0003-2700/86/0358-2312$01.50/0 © 1986 American Chemical Society

Phenylarsine oxide was chosen as the iodine scavenger for several reasons: (a) it is readily available commercially; (b) a standardized solution is stable over long periods of time; (c) it reacts extremely rapidly with aqueous halogens (*21*) and thus should be able to compete effectively with any iodine-reactive substances in the sample.

Because a variety of naturally occurring oxidants are capable of converting aqueous iodide to iodine, it is necessary to use the enzyme catalase to gain specificity for H_2O_2. The sample is split and half is treated with catalase. Both are then titrated and the concentration of hydrogen peroxide is determined by difference.

Several assumptions are made in this procedure. First, any iodine demand in the sample (exerted by natural reducing agents after the excess PAO is consumed) is the same in the untreated and catalase-treated aliquots of the same sample. This was found to be true in the samples we studied provided the catalase concentration was kept at moderate levels (catalase itself consumes some I_2). Second, the iodine generated by the oxidants in solution is assumed to react exclusively with the excess phenylarsine oxide spike. Finally, it must be assumed that no loss of phenylarsine oxide occurs except by reaction with iodine during the analysis. Tests conducted during this study as well as past experience in our laboratory indicate that phenylarsine oxide itself is quite stable in natural waters.

Reagents. Water from a deionization/activated carbon absorption system (Milli-Q System, Millipore Corp.) was further purified by a slow redistillation from potassium permanganate. It was stored in either amber glass bottles or Nalgene polyethylene bottles for periods up to several weeks. A 10^{-3} M H_2O_2 solution prepared in the purified water showed no change in peroxide concentration over the course of 1 week.

All chemicals and reagents were used without additional purification. A saturated aqueous solution of $(NH_4)_6Mo_7O_{24}\cdot 4H_2O$ (Fisher Certified ACS) served as the molybdate catalyst. A 0.1 M KI solution was prepared by dissolving 0.83 g of Baker Analyzed reagent grade KI in 50 mL of the purified water. It was prepared fresh daily and stored in a 50-mL amber glass bottle. The 5.64×10^{-3} N phenylarsine oxide solution was purchased from Hach Co. and was standardized with iodate upon arrival. Bovine liver catalase (2800 units/mg solid), horseradish peroxidase (type II, 200 units/mg solid) and scopoletin (6-methyl-7-hydroxyl-1,2-benzopyrone) were all obtained from Sigma Chemical Co. The catalase stock solution (1.0 mg/mL) was made fresh every 7–10 days. The 4 mg/mL horseradish peroxidase stock solution used in the fluorometric procedure was buffered with 0.01 M phosphate at pH 7 and contained 1×10^{-3} M phenol.

The iodine used as a titrant was made from a dilution of a 0.1 N I_2 stock solution. It was stored in the Brinkmann amber glass titrating apparatus and was standardized several times daily against the phenylarsine oxide.

Hydrogen peroxide, 30%, used in the preparation of H_2O_2 stock solutions and standards was obtained from Baker Chemical Co. (Reagent Grade).

Equipment. Amperometric titrations were carried out with a Brinkmann Potentiograph, Model E436. The instrument is equipped with a stationary platinum anode and a rotating spiral platinum cathode. The potential between the electrodes is kept at a constant 200 mV. Fluorescence measurements were made on a Turner Designs Model 10 fluorometer with an excitation wavelength of 365 nm and an emission wavelength of 490 nm.

Iodometric Procedure. Add 1 mL of acetate buffer (0.1 M, pH 4) to 100 mL of sample. Next add a known spike of phenylarsine oxide solution. The exact amount of this reagent will depend on the concentration of hydrogen peroxide in the sample. Preliminary experiments may be needed to find the optimum amount. Next add 3 mL of the freshly prepared 0.1 M KI along with 100 μL of the saturated Mo catalyst solution. The sample is stirred for 15 min during which time iodine is generated by hydrogen peroxide (eq 1) and possibly by other oxidants in the solution. The generated I_2 is destroyed by the added phenylarsine oxide, the excess of which is subsequently titrated with the standardized iodine to an amperometrically determined end point.

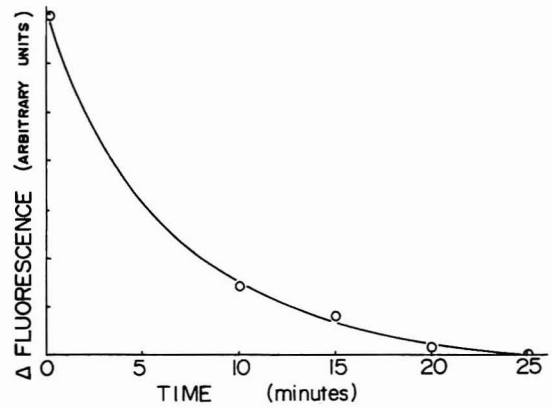

Figure 1. Decay of hydrogen peroxide in a 20-mL natural water sample with time in the presence of 5 μL of 1.0 mg/mL catalase.

A second titration is performed in an analogous manner except that the hydrogen peroxide in the sample is first destroyed by the enzyme catalase. This is accomplished by adding 25 μL of a 1.0 mg/mL catalase solution per 100 mL of sample and stirring for 25 min.

Fluorometric Procedure. One hundred microliters of pH 7 phosphate buffer (0.1 M) is added to 20 mL of sample and inserted into the fluorometer. The instrument is set to 0% transmission. To this a known quantity of the fluorophore scopoletin (typically 5×10^{-5} M) is added and the instrument scale is set to its maximum. The hydrogen peroxide in the sample oxidizes the scopoletin upon addition of 20 μL of the horseradish peroxidase stock solution, resulting in an immediate decrease in fluorescence. The hydrogen peroxide concentration is determined from the difference in fluorescence before and after addition of the catalyst. Calibration curves are obtained by recording the decrease in fluorescence upon addition of a H_2O_2 stock solution to the sample. Reagents are mixed continuously by means of a magnetic stirring device located at the bottom of the fluorescence cell. The reported detection limit is 2×10^{-9} M hydrogen peroxide and the precision is 2% (*22*).

RESULTS

Experimental Conditions for the Iodometric Method. The amount of catalase needed to completely destroy the ambient hydrogen peroxide is sample dependent. It should be sufficient to destroy all the hydrogen peroxide in a reasonable amount of time, yet exert no iodine demand. The catalase concentration chosen was based on the results of the following two experiments. The first was designed to determine the time required for the enzyme to destroy all the hydrogen peroxide in a natural water matrix at a fairly high H_2O_2 concentration. Four liters of water from Paint Branch (a stream on the University of Maryland campus) was collected in an amber glass bottle. This sample was brought back to the lab and H_2O_2 was added until the final concentration exceeded 8×10^{-7} M. Five micrograms of catalase was added to a 20-mL aliquot of the sample and the hydrogen peroxide concentration was monitored by the fluorescence decay technique. The decay of the H_2O_2 (indicated by a decreasing fluorescence change) is presented in Figure 1. The fluorescence change recorded at time = 0 reflects the magnitude of

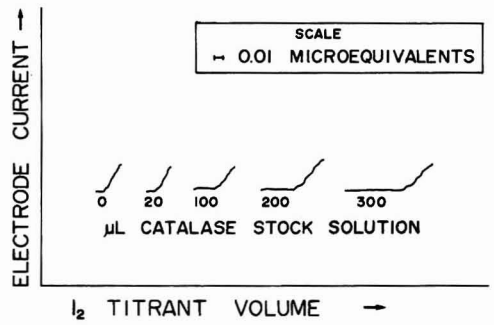

Figure 2. Recorder traces of electrode current vs. titrant volume for five samples containing different amounts of catalase stock solution (volumes shown were added to 100 mL of distilled water). The end point is reached when there is an abrupt rise in current. This experiment demonstrates that catalase exerts I_2 demand.

Table I. Recovery of Hydrogen Peroxide in Permanganate Distilled Water and Paint Branch River Water by Two Independent Methods[a]

H_2O_2 added	H_2O_2 found by fluorescence	H_2O_2 found iodometrically
	A. Distilled Water	
3.1	3.1	3.0
0.31	0.31	0.31
	B. Paint Branch Water	
2.7	2.5	2.6
0.31	0.32	0.31

[a] Concentrations in micromolar units.

the signal before catalase was added to the natural water. After six half-lives (the decay being approximately first order) or 25 min the hydrogen peroxide signal in the spiked Paint Branch water had fallen to an undetectably low level.

Figure 2 is a presentation of the results of some tests to determine the iodine demand of catalase. Various concentrations (0, 0.2, 1, 2, 3 mg/L) of the enzyme were added to permanganate-distilled water and then titrated with iodine. Appearance of free iodine in the solution at the titration end point is marked by a sudden rise in electrode current. Dead time, related to the rate of mixing of I_2 in the titration vessel, results in a finite volume of titrant being added before a current response is observed even in the absence of I_2-consuming components. As seen in Figure 2, a 20-μL addition of catalase, representing a concentration of 0.2 mg/L, produces an iodine demand too small to be distinguished from zero. Higher concentrations of catalase, however, produce a demand that could cause significant error in the determination of H_2O_2 below 10^{-7} M. Based on the results presented in Figures 1 and 2, we chose a catalase dose of 0.25 mg/L and a reaction time of 25 min for subsequent work.

To test recovery, a known quantity of hydrogen peroxide was added to 1-L of the permanganate-distilled water. This sample was analyzed by both the fluorescence decay and the iodine techniques. The amount of hydrogen peroxide found by each analysis and the added H_2O_2 level are presented in Table IA. The I_2 method was able to recover quantitatively the hydrogen peroxide spike at micromolar and sub-micromolar levels. It also produced results that were identical, within analytical precision, with the fluorescence decay technique.

In a similar experiment, river water from Paint Branch was spiked with a known quantity of hydrogen peroxide. The concentration of H_2O_2 in the sample resulting from the spike exceeded, by over an order of magnitude, the ambient concentration of the oxidant. The dosed water was analyzed by

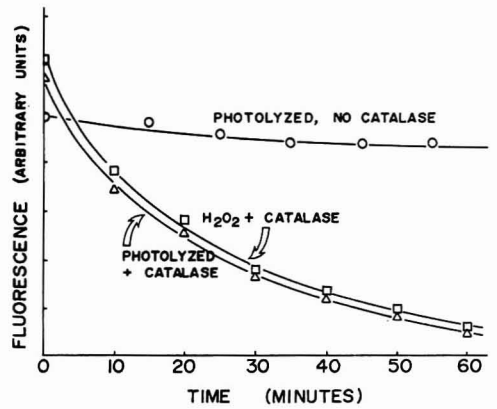

Figure 3. Decay of hydrogen peroxide, as measured by fluorescence change, with time in Patuxent River water. The upper curve demonstrates that the scopoletin reactive oxidant generated by solar photolysis is moderately stable in the absence of added catalase. The identical decay rates of the solar photolysis oxidant and H_2O_2 in the presence of catalase (lower curves) suggests that the photolysis product is indeed H_2O_2.

both the iodine and fluorescence methods. The comparisons are presented in Table IB. Again, the spike was quantatively recovered, within error, by the I_2 analysis. Also, within the normal limits of error, the fluorescence and iodine methods produced analytically equivalent hydrogen peroxide results.

Organic peroxides potentially interfere in both methods employed in this study. The horseradish peroxidase enzyme used in the fluorescence method reacts with low molecular weight organic peroxides (*3*) as does the enzyme catalase used in the iodometric technique (*23*). However, it is known that catalase decomposes hydrogen peroxide more readily than organic peroxides (*23*). This preferential H_2O_2 degradation was used to evaluate the possibility of interference caused by organic peroxides. Several liters of Patuxent River water were collected at Benedict, MD, and were refrigerated. On the next clear day, two aliquots were withdrawn and placed in 500-mL quartz round-bottom flasks. These were placed on the building roof for a total of 3 h of sunlight exposure (10.00 a.m. to 1.00 p.m.), during which time peroxides were generated photochemically. A third aliquot was kept in the dark. The irradiated samples were taken back to our laboratory and the peroxide level was determined by the fluorescence technique to be 3.8×10^{-7} M. Hydrogen peroxide was then added to the nonirradiated flask to give a final level of 3.8×10^{-7} M H_2O_2. Sixty microliters of catalase (0.5 mg/mL) was added to one of the irradiated flasks and to the H_2O_2 spiked flask. The decay in the peroxide signal was followed in all three samples by the fluorescence technique. Figure 3 shows the results. The rate of peroxide decay is very similar in the sample containing authentic H_2O_2 and in the sample containing photochemically generated peroxides. The indicates that very little, if any, organic peroxide was contributing to the analytical results in the photolyzed sample. This result is in agreement with others who found in a variety of natural waters that the organic peroxide content was negligible compared to that of H_2O_2 (*3*, *24*).

Field Measurements. The concentration of hydrogen peroxide in Paint Branch water was determined by the iodometric and fluorometric methods throughout the summer of 1985. Surface samples were collected by immersion of 4-L amber glass bottle. Analyses were begun within 5 min of sampling. The results are presented in Figure 4. In almost all cases the disparity between the fluorescence and iodine methods is less than a few percent (even at 10^{-8} M H_2O_2), well within the analytical uncertainty.

Hydrogen peroxide analyses were also conducted on September 17 and 18, 1985, on the Patuxent River at the Benedict

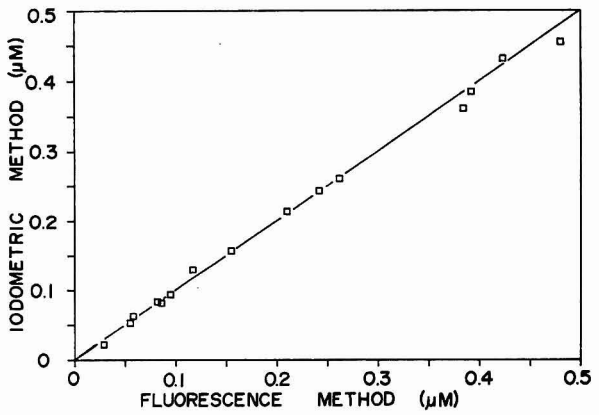

Figure 4. Intercomparison between the iodometric method and the fluorescence decay method on Paint Branch water collected throughout the summer of 1985. The line represents perfect agreement between results, not a statistical fit to the data.

Table II. Concentration of Hydrogen Peroxide (Micromolar) Found in Patuxent Estuarine Water by the Iodine and Fluorescence Methods

fluorescence method	iodine method
A. Natural Concentrations (September 1985)[a]	
0.054	0.056
0.084	0.086
0.075	0.050
B. Variably Spiked Samples Collected in April, 1986	
0.060	0.058
0.094	0.089
0.096	0.099
0.110	0.102
0.115	0.107
0.147	0.150
0.181	0.180
0.233	0.235
0.572	0.590

[a] Fluorescence analyses performed by Philip Kijak.

Estuarine Laboratory. This is a saline estuarine water in contrast to the fresh samples from Paint Branch. The hydrogen peroxide values obtained are presented in Table IIA. In the first two cases the agreement between the results obtained by the iodine and fluorescence methods is excellent. The reasons behind the relatively poor agreement in the last reading are not known, but may involve operator error.

Additional saline samples were collected at Benedict, MD, in April of 1986. Each was refrigerated in the dark until use. In order to obtain a measurable signal (the ambient H_2O_2 had decayed to an undetectably low level between the time of collection and analysis) stock hydrogen peroxide was added to each sample prior to analysis. The H_2O_2 determined in these Benedict samples are presented in Table IIB. The agreement between the results was again well within analytical error, as was the case with the fresh Paint Branch water. Because the H_2O_2 decay rate was greater in the saline samples than in the freshwater samples, special care had to be taken to make the two measurements at the same time after the H_2O_2 spike had been added.

DISCUSSION

The precision of a single iodometric titration is controlled by the precision of three measurements, the volume of sample, the volume of phenylarsine oxide added, and the volume of I_2 titrant. With use of standard glassware, the uncertainty in the first two measurements can be ±1%. The precision of the third measurement is instrumentation dependent. For our system, we estimate it to be ±0.005 μequiv. However, three titrations are required for a given H_2O_2 determination: one to calibrate the I_2 titrant against phenylarsine oxide and two to quantify the oxidants in the sample before and after addition of the catalase. The total uncertainty is consequently larger than the uncertainty of a single titration. At low concentrations, the determination of titrant volume will control the uncertainty so the total uncertainty in a H_2O_2 determination will be about ±0.015 μequiv. With a conventional definition of detection limit as three times the uncertainty, this limit would be 0.045 μequiv or 0.02 μmol.

The key to use of the iodometric method for H_2O_2 is the availability of sensitive instrumentation for determining I_2 or phenylarsine oxide. We used a research grade amperometric titrator; however, other possibilities exist. Phenylarsine oxide may be determined directly by polarography (*25*). Alternatively, the end point of an iodometric titration can be determined with good sensitivity by potentiometric (*26*) and spectrophotometric (*27*) methods. Furthermore, inexpensive, portable amperometric titators are available which have been shown to yield very good results down to about 0.8 μM (*28*). This versatility with regard to instrumentation requirements makes the iodometric technique attractive.

ACKNOWLEDGMENT

The authors are grateful for advice and support recieved from William Barger at Naval Research Laboratory, James Sanders at the Philadelphia Acadamy of Sciences, and Rod Zika at the University of Miami. Field assistance from Philip Kijak is also greatly appreciated.

Registry No. H_2O_2, 7722-84-1; H_2O, 7732-18-5.

LITERATURE CITED

(1) Perschke, H.; Broda, E. *Nature (London)* **1961**, *190*, 257–258.
(2) Van Baalen, C.; Marler, J. E. *Nature (London)* **1966**, *211*, 951.
(3) Zika, R. G.; Moffett, J. W.; Petasne, R. G.; Cooper, W. J.; Saltzman, E. S. *Geochim. Cosmochim. Acta* **1985**, *49*, 1173–1184.
(4) Penkett, S. A.; Jones, B. M.; Brice, K. A.; Eggleton, A. E. *Atmos. Environ.* **1979**, *13*, 123–137.
(5) Calvert, J. G.; Lazrus, A.; Kok, G. L.; Heikes, B. G.; Walega, J. G.; Lind, J.; Cantrell, C. A. *Nature (London)* **1985**, *317*(5), 27–35.
(6) Sinel'nikov, V. Ye. *J. Hydrobiol.* **1971**, *7*, 96–99.
(7) Kok, G. L.; Holler, T. P.; Lopez, M. B.; Nachtrieb, H. A.; Yuan, M. *Environ. Sci. Technol.* **1978**, *12*, 1072–1076.
(8) Kok, G. L. *Atmos. Environ.* **1980**, *14*, 653–655.
(9) Das, T. N.; Moorthy, P. N.; Rao, K. N. *Atmos. Environ.* **1983**, *17*, 79–82.
(10) Ibusuki, T. *Atmos. Environ.* **1983**, *17*, 393–396.
(11) Neftel, A.; Jacob, P.; Klockow, D. *Nature (London)* **1984**, *311*, 43–45.
(12) Mottola, H. A.; Simpson, B. E.; Gorin, G. *Anal. Chem.* **1970**, *42*, 410–411.
(13) Draper, W. M.; Crosby, D. G. *Arch. Environ. Contam. Toxicol.* **1983**, *12*, 121–126.
(14) Lazrus, A. L.; Kok, G. L.; Gitlin, S. N.; Lind, J. A. *Anal. Chem.* **1985**, *57*, 917–922.
(15) Helz, G. R.; Kieber, R. J. *Water Chlorination*; Lewis Publishers: Chelsea, MI, 1985; Vol. 5, pp 1033–1040.
(16) Ricciuti, C.; Coleman, J. E.; Willits, C. O. *Anal. Chem.* **1955**, *27*, 405–407.
(17) Kolthoff, I. M.; Belcher, R. *Volumetric Analysis*; Interscience Publishers: New York, 1957.
(18) Johnson, R. M.; Siddiqi, I. W. *The Determination of Organic Peroxides*; Pergammon Press: London, 1970.
(19) Smith, R. H.; Kilford, J. *Int. J. Chem. Kinet.* **1976**, *8*, 1–10.
(20) Kosak-Channing, L. F. Ph.D. Thesis, Chemistry Department, University of Maryland, 1981.
(21) Jaworske, D. A.; Helz, G. R. *Int. J. Environ. Anal. Chem.* **1985**, *19*, 189–202.
(22) Zika, R. G.; Saltzman, E. S.; Chameides, W. L.; Davis, D. D. *J. Geophys. Res.* **1982**, *87*, 5015–5017.
(23) Chance, B. *J. Biol. Chem.* **1949**, *179*, 1311–1330.
(24) Cooper, W. J.; Zika, R. G. *Science* **1983**, *220*, 711–712.
(25) Lowry, J. H.; Smart, R. B.; Maney, K. H. *Anal. Chem.* **1978**, *50*, 1303–1309.
(26) Rigdon, L. P.; Moody, G. J.; Frazer, J. W. *Anal. Chem.* **1978**, *50*, 465–469.
(27) Wong, G. T. F.; Brewer, P. G. *J. Mar. Res.* **1974**, *32*, 25–36.
(28) Sugam, R. *Water Chlorination*; Ann Arbor Science: Ann Arbor, MI, 1983; Vol. 4, pp 653–666.

RECEIVED for review February 10, 1986. Accepted May 1, 1986. This work is from the Ph.D. Dissertation of the senior author.

Unattended, Robotic Drug-Release Testing of Enterically Coated Aspirin

R. J. Eckstein and G. D. Owens*

The Procter and Gamble Company, Miami Valley Labs, P.O. Box 39175, Cincinnati, Ohio 45247

M. A. Baim and D. A. Hudson

The Procter and Gamble Company, Sharon Woods Technical Center, 11511 Reed Hartman Highway, Cincinnati, Ohio 45241

An automated drug-release testing system capable of performing multiple, unattended dissolution runs has been developed. The flexible combination of a general-purpose microcomputer and a five-axis robot forms the heart of the system, which also contains a six-vessel dissolution tester, an electronic balance, a solution-handling subsystem, an aspirator, and a diode-array spectrophotometer. The system is able to dispense and weigh samples; fill, empty, and clean dissolution vessels; automatically sample and spectrophotometrically analyze dissolution media; and print calculated results. It produces percent release values on enterically coated aspirin with good accuracy and generally better precision in only a fraction of the man hours/analysis time as compared to manual testing. The performance of the system has been validated by comparison with an HPLC method, drug-release manual data, and the analysis of "United States Pharmacopeia" (USP) calibrator tablets.

Dissolution testing is the measurement of the rate and extent of drug release of a pharmaceutical product in an in vitro system. For 3 decades the importance of this technique has increased steadily (*1*). It has been touted as one of the most important members of the quality assurance family and an excellent predictor of in vivo drug performance (*2*). Although recent reports question the use of dissolution as a predictor of clinical performance, its value as a monitor of batch-to-batch consistency and as a screening tool for formulation development is well established (*3*).

One of the driving forces behind the increased industrial usage of this technique has been the economic potential of a variety of new dosage forms (*4*). One of these new dosage forms, enteric coating, decreases the risk of gastric and duodenal mucosa damage by aspirin (*5*). Enteric coatings resist acid attack in the low pH environment of the stomach and dissolve readily in the higher pH environment of the intestine.

The "United States Pharmacopeia" (USP) method for drug-release testing of enterically coated products (*6*) simulates passage through the gastrointestinal tract. The first dissolution period is in 0.1 N HCl and lasts 2 h. The USP guidelines require that enterically coated products release less than 10% of their aspirin during this first period. This first dissolution period is then followed by a second dissolution period of 45 min in a pH 6.8, phosphate buffer. The 4–4.5 man hours/run requirement of this test coupled with its multiple sampling and UV spectrophotometric determinations make it tedious. The tedium is compounded by a need for careful attention to experimental detail. Complicating factors, like the slow hydrolysis of aspirin to acetic and salicylic acids, can degrade precision if all absorbance determinations are not made at the same time. Hence, drug-release testing of enterically coated aspirin products is a good candidate for a high degree of automation.

A number of different approaches to automating single dissolution runs have been published in recent years (*7–9*). The goal of our work has been to assemble a system capable of multiple, unattended dissolution runs. In the achievement of this goal, a number of additional problems had to be solved besides the automated sampling and analysis barriers addressed by earlier workers. The system had to be able to dispense and weigh enterically coated micrograins. It also had to be able to automatically fill and clean out dissolution vessels. These design requirements suggested the need for a high level of flexible automation. This need was met by the powerful combination of a general-purpose laboratory microcomputer and a light-duty industrial robot. In this paper we present this system's architecture and the validation of its performance.

EXPERIMENTAL SECTION

Figure 1 shows a top view of the robotic drug-release testing system. The combination of a microcomputer and a five-axis robot forms the nucleus of this system. A 4-ft translation base gives the robot access to an electronic top-loading balance, sample storage racks, a container for used dissolution baskets, an aspirator tip, and a six-vessel dissolution tester. Other system components not directly accessed by the robot include an aspirator, a solution-handling system, thermostated reservoirs, and a diode array spectrophotometer.

The general-purpose microcomputer is the driving force behind the entire system. Its responsibilities include the following: (1) communication with the robot and the generation of individual robot movement commands; (2) data acquisition from the electronic balance; (3) control of the up/down motion of the dissolution tester spindle housing and the rotation of the spindles; (4) control of solution flow to and from the six dissolution vessels, three reservoirs, and spectrophotometer via the solution-handling subsystem; (5) data acquisition from the spectrophotometer; (6) control of the aspirator; (7) system timing and event scheduling; (8) calculations and report generation.

The five-axis robot provides the microcomputer with a means of changing its physical environment. It performs the following activities: (1) transfer dissolution baskets from their storage racks to the balance; (2) move sample vials from the storage rack to a position above the balance; (3) dispense vial contents into the basket on the balance; (4) transfer sample vials back to the storage rack after weighing is completed; (5) move dissolution baskets from the balance to the dissolution tester and attach the baskets to the end of the spindles; (6) remove baskets from the dissolution tester spindles and transfer them to the used baskets container at the completion of each run; (7) move aspirator tip to each of the dissolution tester vessels for aspiration of spent media and wash water.

Microcomputer. Table I summarizes the interface cards that enable the microcomputer (Model IIe, Apple Computer, Inc., Cupertino, CA) to communicate with the rest of the system

0003-2700/86/0358-2316$01.50/0 © 1986 American Chemical Society

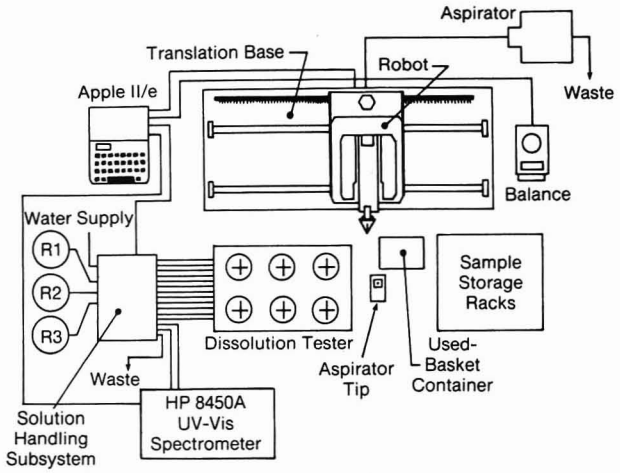

Figure 1. Top view of the robotic dissolution testing system.

Table I. Microcomputer Interface Summary

input/output channel	interface type	device
slot 1	Centronics parallel	printer
slot 2	32-bit parallel	solution-handling valves
slot 3	80 column card	
slot 4	multifunction-serial & clock	robot
slot 5	Softweigh	balance
slot 6	Disk II	disk drives
slot 7	Serial	spectrometer

components. Communication with a line printer (Model MX-100, Epson, Torrance, CA) is accomplished with a Centronics-compatible parallel interface (Grappler +, Orange Micro, Inc., Anaheim, CA). The solenoid valves in the solution-handling subsystem are controlled by a 32-bit parallel interface (Model DI09, Interactive Structures, Inc., Bala Cynwyd, PA) through optically isolated relays (Model UI 16 I/O Chassis, Interactive Structures). A multifunctional interface card (Model CPS, Mountain Computer, Scotts Valley, CA) provides serial communication with the robot and a real-time clock for event scheduling. Automatic taring of and data acquisition from the electronic balance (Model PC180, Mettler Instrument Corp., Hightstown, NJ) occurs through a dedicated interface (Softweigh, Microsystems Research Corp., Cranbury, NJ). Absorbance data and spectrophotometer commands flow to-and-from the microcomputer via a serial interface (Model AIO, SSM Microcomputer Products, San Jose, CA). The microcomputer also contains the standard 80-column card and diskette interfaces provided by the manufacturer.

Robot and Translation Base. The five-axis, revolute-geometry robot (Model Alpha I, Microbot, Inc., Mountain View, CA) has been modified in two ways to facilitate interaction with the aspirator and aspirator tip. First, the standard mechanical gripper was removed and replaced by a more rugged gripper (from a Model Alpha II Robot, Microbot) with removable fingertips. The standard fingertips on the new gripper were replaced with longer, $2^1/_2$ in. fingertips. Second, the two small air lines that are routed through the arm by the manufacturer were replaced with a single, larger tube. This larger tube carries solution out through the robot to the aspirator during cleanup procedures. The aspirator, aspirator tip, and aspiration process are described in more detail below.

The robot's system control enclosure provides a set of eight optically isolated relays that can be accessed by the microcomputer and used to turn off/on devices that the robot must interact with. Table II summarizes how these relays are used to provide control of the dissolution tester, solution-handling pumps, and aspirator.

The translation base allows the robot to move across a 4-ft linear path expanding its work envelope to over 6 ft in length. The robot rides on an aluminum plate that is slightly larger than its base. A stepper motor, its associated drive electronics, and an optical sensor (auxilary motor driver, Microbot) are mounted on the rear

Table II. Summary of Otpically Isolated Relay Outputs from the Robot Controller

output relay no.	destination	
0	spindle housing down	dissolution tester
1	spindle housing up	dissolution tester
2	spindle rotation	
3	media pump	
4	solution pump	
5	aspirator	

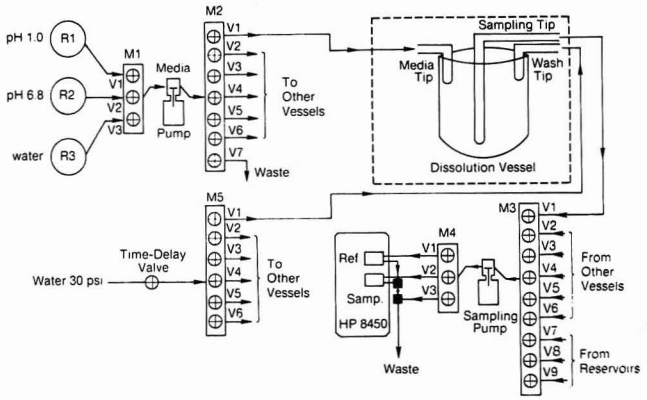

Figure 2. Solution-handling subsystem.

of the plate. A pinion gear (Model G254, Queen City Supply, Cincinnati, OH) is attached to the shaft of the stepper motor and engages a 3.5 ft length of brass rack (Model G579-4, Queen City Supply). The brass rack is mounted on a 2-in. aluminum angle that is bolted to a 4-ft aluminum base plate. The small plate holding the robot and stepper motor is mounted on two, twin ball bushing pillow blocks (Model TWN-16 Thompson, Bearings, Inc., Cincinnati, OH). The pillow blocks ride on two stainless steel shafts (Model 550 C-Rockwell, Bearings, Inc.), which are held up by four support blocks (Model SB-16 Thompson, Bearings, Inc.).

Solution-Handling Subsystem. The solution-handling components of the robotic dissolution tester can be broken down into two main groups of components. The first group of components, diagrammed in Figure 2, perform several functions: they allow fresh dissolution media to be introduced into the vessels; they provide a means of sampling the contents of the vessel by UV–visible spectrophotometry; and, they make it possible to rinse the dissolution vessel with distilled water at the conclusion of each run.

Dissolution medium is prepared and stored in two, 56-L polyethylene containers, R1 and R2 (Model K6725-50, Cole-Parmer, Chicago, IL). Temperature control of these reservoirs is accomplished by use of Teflon-coated immersion heaters and sensors (heater no. GTFL-2209R18, controller no. BCT-801TEF, Chromalox, Inc., Pittsburgh, PA). Thorough agitation of these reservoirs is provided by laboratory stirrers with polypropylene-coated paddles (stirrer no. K-4320-00, paddle no. K-6370-00 LPE, Cole-Parmer).

Thirty solenoid valves (Model A2025, Brunswick Corp., New Britain, CT) control the flow of solutions to and from the dissolution tester. Twenty-nine of these valves are housed in five different stainless steel manifolds, M1–M5 (M1, 3A2015SX; M2 and M4, 7A2015SX; M3, 9A2015SX; M5 6A2015SX, Brunswick Corp.), that allow subsets of the valves to share a common inlet or outlet. These valves and manifolds are automatically flushed with water from R3 after each use of 0.1 N HCl to prolong their period of service.

Solutions are moved to and from the dissolution tester by two piston pumps (Model RP-D-2CKC, Fluid Metering, Inc., Oyster Bay, NY). Short lengths of $^1/_4$ in. Tygon tubing are used on the pump inlets and outlets to decrease pump noise and provide some pulse dampening.

All other solution-handling tubing and connections (tubing, Model K-6400-31; connectors, Model K-6385-10; Cole-Parmer) are made of high-density polypropylene. The tubing lines, which run to and from each vessel, are mounted on a Lucite plate that

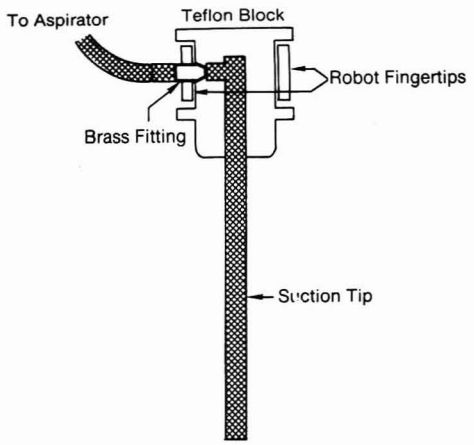

Figure 3. Cutaway view of the aspirator tip.

sits on top of the dissolution vessels. Polypropylene elbows (Model K-6383-10, Cole-Parmer) terminate the media inlet tubing at the edge of the dissolution vessels. The same polypropylene elbows and 3 in. lengths of polypropylene tubing terminate the sampling inlets. The vessel-wash inlets terminate in a polypropylene elbow and tee (elbow, K-6387-10; tee, K-6389-10; Cole-Parmer). The tee has been heated and bent to conform to the inside radius of curvature of the dissolution vessel.

A normally closed, solenoid safety valve has been installed in the low-pressure water line that supplies wash water to M5. This valve is driven by a time-delay relay (Model T3K 600-461, National Controls Corp., Lombard, IL), which is energized each time one of the other valves in M5 is opened. This relay causes the safety valve to shut off automatically after 1 min. This arrangement averts the possibility of flooding if the computer is inadvertently interrupted in the midst of a wash cycle.

Absorbance determinations are made under computer control by a diode-array spectrophotometer (Model 8450A, Hewlett-Packard, Palo Alto, CA). Rectangular, flow-through cells (Model 14-385-926A, Fisher Scientific, Pittsburgh, PA) are located in both the reference and sample compartments of the spectrophotometer. Connection of these cells to the solution-handling system is accomplished via a short length of $^3/_{16}$ i.d. Tygon tubing and polypropylene reducing connectors (Model R-6458-10, Cole-Parmer).

Part of the second main group of solution-handling components are shown in Figure 3. These components provide the robot with a means of removing solutions from the vessels by aspiration. An aspirator (Model 24-7049-00, Cole-Parmer) has been connected to an 8 ft length of $^1/_4$ in. o.d. Tygon tubing. The last 2–3 ft of this tubing has been installed inside the robot as described above. Installation of this tubing inside the arm removes the possibility of entanglements. This aspiration tube terminates in a brass fitting that is mounted near the base of one of the robot's gripper fingers. When the robot grasps a Teflon block, which contains a stainless steel suction tip, the brass fitting makes a vacuum-tight seal with the Teflon block. This arrangement provides a continuous solution path from the suction tip, through the aspirator tubing, and into the aspirator.

When not in use, the aspirator suction tip is located in a Lucite rack. The rack consists of a square hole with beveled edges cut into a $^1/_2$ in. thick Lucite plate. The plate is mounted above the work surface in a location near the dissolution tester where the robot can access it conveniently.

Sample Containers and Storage Racks. Polystyrene snap-cap sample vials (Model K-6102-10, Cole-Parmer) are used as containers for enterically coated micrograins of aspirin. These vials were chosen because they are disposble, can hold up to 5 g of sample, and are small enough to allow 18 samples to be located in only a small fraction of the robot's work envelope. The inside diameter and orifice shape of these vials also facilitates dispensing the free-flowing micrograins of aspirin into the dissolution baskets. The algorithm used for this dispensing and weighing process has been described previously (*10*).

Two Lucite racks have been constructed to hold 18 sample vials and 18 clean dissolution baskets. Each rack consists of three tiers of six vials or baskets. The vials and baskets are located 2 in. apart in $^1/_2$ in. deep holes with beveled edges. The three tiers are located so that the robot can pick up and replace any of the sample vials or baskets without obstruction.

Dissolution Tester. The six-vessel dissolution tester (Vanderkamp 600, Van-Kel Industries, Edison, NJ) has been modified in two ways. The first modification consists of the addition of two relays (Model KA11AG, Potter & Brumfield, Princeton, IN) inside the spindle housing. These relays are connected in parallel with existing front panel switches and allow the spindle housing to be moved up/down under computer control. Spindle rotation is controlled by the computer by paralleling the appropriate front-panel switch with one of the robot's optically isolated relays (see Table II).

The second modification provides a convenient means for the robot to attach the dissolution baskets (Model T-1045-30, Van-Kel Industries) to the rotating spindles. Ceramic ring magnets (Model 5856K5, McMaster-Carr Supply, Chicago, IL) have been cemented to the top of the baskets and to the end of the spindles. A polyvinyl dip coating (Vikem Dip no. 52706-125, Bel-Art Products, Pequannock, NJ) was used as both a cement and a protective coating for the magnets. After almost 1 year of exposure this coating has shown no evidence of chemical attack.

Software. This system is driven by a structured Applesoft BASIC program approximately 32K bytes in length. The program provides on-screen, real-time display of the status of the pumps, valves, spindle housing, spindle rotation, aspirator, and time remaining in the current program step. The operator can interrupt the execution of the program at any time from the keyboard and the program will reset the pumps and valves so that the solution-handling system is not damaged. The USP method (*6*) for enterically coated products is incorporated in the program. Hence, method changes can be accommodated easily by changing the program.

Reagents and Procedures. Drug-release procedures were carried out on a type I apparatus at a rotation speed of 100 rpm as specified by the USP (*6*), method B. All the solutions used for drug-release studies reported in this work were prepared from ACS reagent-grade chemicals. Manual dissolution tests were performed with an identical dissolution tester and a single-beam diode-array spectrophotometer (Model 8451, Hewlett-Packard). Salicyclic acid and prednisone calibrator tablets were obtained from the USP. Enterically coated aspirin microgranules were obtained from naturally aged lots of Encaprin. Since this product contains no binders, filtering of the dissolution media prior to performing spectrophotometry was not necessary. However, to analyze the USP calibrator tablets, it was necessary to interrupt the robotic system at the end of a single 30-min dissolution period and manually filter the solutions. The dissolution media was then returned to the vessel before allowing the automated equipment to proceed with the spectrophotometric determinations.

HPLC analyses were performed on some of the same lots of Encaprin used in the drug-release tests. The Encaprin was dissolved in acetonitrile containing 12 ppm of citric acid. Isocratic, reverse-phase LC analyses were conducted using a 30:70 acetonitrile/0.5 M acetic acid mobile phase and a Model 5000 pump (Varian Instrument Group, Palo Alto, CA). This allowed the separation of aspirin and salicylic acid on a C_{18} column (C_{18} μBondapak, 27324, Waters Associates, Milford, MA). Levels of aspirin and salicylic acid were quantitated, with a UV detector (Model UV-100, Varian) at 300 nm, using external standards.

RESULTS AND DISCUSSION

System Operation and Reliability. The process of preparing this automated equipment for a series of three unattended drug-release runs is straightforward and requires about 1.5 h. Most of this time is consumed by preparation of the two different media and their equilibration to 37 ± 0.5 °C. The various components of the automated system are then turned on and initialized, and the BASIC program is loaded from the microcomputer's floppy disk into memory. Once the execution of the program commences, it prompts the operator to enter 12 different operating parameters and product specifications. An identification code is then entered for each sample. Next, the storage racks are loaded with samples and clean dissolution baskets, and a final keyboard

entry commences sample processing. At the end of each run, a printed report of the concentration and percent release of aspirin in each media is automatically generated.

The reliability of the system has been evaluated over a 2-month period in which 60 runs of six samples each were performed. Four error conditions were encountered during this time period resulting in the loss of 14 samples. Of these 14 samples, six were lost because the operator failed to fill the distilled water reservoir (R3, Figure 1), six were lost due to a power outage during a thunderstorm, one was lost when the robot apparently dropped a basket, and one was lost when the robot dispensed too much material into a basket. Hence, two samples out of 360 were not correctly processed due to robot malfunctions. This corresponds to a processing error rate of <1%. After the dropped-basket incident occurred, the program was changed causing the robot to grip the baskets more tightly. The robot has not dropped a basket since that change was made. Because the processing error rate is so low, no verification sensors have been installed in the system.

Validation of HPLC Method. The HPLC method used to determine the aspirin content of some of the product lots examined in this study was validated in the following manner. Four different lots of commercially available aspirin capsules were analyzed by both the USP aspirin method (*6*) and the HPLC method. Six replicates of each lot were examined yielding an overall average for the USP procedure of 774 ± 11 mg of aspirin/gram and for the HPLC procedure of 767 ± 5 mg of aspirin/gram. A *t* test on these values indicates that their is no statistically significant difference between these values at the 95% confidence level. Nine different samples from the same lot of Encaprin were examined in the same comparative fashion. The HPLC method accounted for an average of 99.2 ± 1.4% of the aspirin found by the USP method. Hence, within experimental error the HPLC method provides the same aspirin content values as the accepted USP method.

Calibration, Aspirin Recovery, and Precision. Before drug-release runs were performed, the response of the spectrophotometer to aspirin in the two different media was determined. In the 0.1 N HCl phase, the absorbance of aspirin standards was measured at 276 nm. Plots of the individual absorbance values as a function of concentration were fit with a linear-least-squares routine and found to exhibit correlation coefficients >0.999 and zero intercepts within experimental error. A similar procedure was followed in the pH 6.8, phosphate buffer media, at both 266 and 290 nm. The absorbance values of the standards were measured after a 45-min delay. This time delay provides a good representation of the actual conditions during the dissolution test and accounts for the slow hydrolysis of aspirin. Once again, the absorbance vs. concentration plots were linear with zero intercept within experimental error.

Prior to undertaking the aspirin recovery and precision studies outlined below, the apparatus was checked for bias between individual vessels. Solution pumping volumes, delivery of solutions to the spectrophotometer, and removal of solutions with the suction-cleanup procedure were found to vary less than ±1% between individual vessels.

The following procedure was used to verify that micrograins were not escaping the dissolution baskets during the 2-h dissolution period at pH 1.0. At the end of this acidic dissolution period, dissolution vessels were removed from the tester and their contents were filtered. Microscopic examination of the filter paper revealed no evidence of micrograins or other particulates that might interfere with the absorbance determinations.

Table III. Aspirin Recovery and Within-a-Day Precision

no. of samples	type	% found (% rel std dev) pH 1.0	pH 6.8
6	blank	0.3 ± 0.1	0.04 ± 0.09
6	enteric coating	0.5 ± 0.1	−0.5 ± 0.3
18	encaprin	2.6 ± 0.2 (8)	94.7 ± 1.5 (1.6)
	total recovery	97.3	

Table IV. Percent Aspirin Released from Three Different Lots of Encaprin, Manual vs. Robot

lot	pH 1.0 manual[a]	pH 1.0 robot[a]	pH 1.0 *F*	pH 6.8 manual[a]	pH 6.8 robot[a]	pH 6.8 *F*
A	3.9 (0.7)	3.6 (0.3)	5.4	92 (3)	93.9 (1.5)	4
B	4.9 (0.5)	4.5 (0.2)	6.2	93 (3)	93.7 (1.1)	7.4
C	5.7 (0.5)	5.1 (0.3)	2.8	92 (3)	92.0 (2.2)	1.9

[a] Values in parentheses are relative standard deviation.

Table III summarizes the results of the aspirin recovery and single-day precision studies. In the first test, blanks were analyzed for aspirin assuming an artibrary sample weight of 500 mg for calculations. The average percent found in both phases was much less than 1%. The slightly elevated value for the blank in the acidic phase is probably due to the extraction of a small amount of residual aspirin from the apparatus during the 2-h test phase.

In the second experiment, a set of six placebos, consisting only of an appropriate amount of enteric coating material, were analyzed. Once again, a sample weight of 500 mg was assumed and the percent aspirin found was negligibly small.

In the final experiment summarized in Table III, three separate runs of six samples of a single lot of Encaprin were analyzed to assess precision within a single day. The relative standard deviation values in the pH 6.8 media are comparable with literature values for aspirin release from baskets at pH 4.5 (*11*). The precision of the acid results is somewhat poorer due to the small absorbance values on which the pH 1.0 phase calculations are based.

The same lot of Encaprin, used for the drug-release tests in Table III, was analyzed by HPLC and found to contain 900 ± 17 mg/g aspirin. The average total of the aspirin released in the drug-release runs was 875 ± 25 mg/g. A *t* test indicates that the difference between these values is not statistically significant at the 95% confidence level. This is good agreement between two quite different techniques and indicates that the automated drug-release tester is efficiently recovering the aspirin from the product.

The out-of-day precision of the robotic drug-release tester was examined by obtaining drug-release results on a different lot of Encaprin. Three different six-sample batches from this lot of Encaprin were analyzed on different days. At pH 1.0 the average amount of aspirin released was 3.9 ± 0.3% and at pH 6.8 it was 94.8 ± 1.6%. The precision of these determinations is comparable with the precision obtained for multiple determinations in a single day. This level of precision has remained constant over many months of operation.

Comparison with Manual Results. Twelve replicate samples from three different lots of Encaprin were analyzed both by manual means and by the robot. The results from these determinations are presented in Table IV. A *t* test at the 95% confidence level indicates no statistically significant difference between the manual and robotic results for all the pH 6.8 results and the pH 1.0 results for lot A. The *t* test does indicate that a slight bias exists between the robotic and manual means for lots B and C at pH 1.0. However, this small bias is inconsequential in light of the generally poor precision

Table V. USP Dissolution Apparatus Suitability Test Results

		USP specificiation		automated system	
sample	media	% released	std dev	% released	std dev
prednisone (log G)	water	49–81	*a*	76	3
salicylic acid (lot F)	pH 7.4 phosphate buffer	23–30	≤4	25.3	1.4

[a] No standard deviation for prednisone is cited by the USP.

of both the manual and robotic values at pH 1.0.

Table IV also shows the appropriate variance ratios comparing the precision of the manual and robotic values with a one-tailed F test (*12*). For 11 degrees of freedom, at the 95% confidence level, the critical value of F is 2.8. Hence, for lots A ad B, where all the values of F are greater than 2.8, the robot produced data that are statistically more precise than the manual data. For lot C the robotic equipment produced comparable data. The robotic data are probably more precise because the automated equipment makes the absorbance determinations at exactly the same time interval in each run. Some of the difference in precision may also be due to the fact that a double-beam spectrophotometer was used in the robotic system and the manual determinations were made on a single-beam instrument. This contribution to the total variance for the manual results is probably small compared to the contribution from absorbance measurement timing differences.

USP Apparatus Suitability Tests. Two different USP apparatus suitability tests were performed on the automated equipment to determine if the modifications made to the dissolution tester were affecting its performance. The results of these tests are summarized in Table V. USP calibrator prednisone tablets were used as an example of a disintegrating sample, and USP calibrator salicylic acid tablets were used as an example of a nondisintegrating sample. The applicable USP specifications for the extent of dissolution of tablets are also presented the Table V. In both cases the results obtained from the modified dissolution tester fall within the acceptable range with good precision for 12 replicate samples. These values indicate that the minor modifications made to the dissolution tester to allow it to be automatically controlled, sampled, cleaned, and loaded by the robot have not adversely affected its performance.

CONCLUSION

Unattended, automated drug-release testing of multiple sets of enterically coated aspirin samples represents a clearly superior alternative to manual testing. The automated apparatus requires only 1/9, or 0.5 h/run, of the dedicated man time. It expands the throughput of a single apparatus via continuous operation. It can provide more precise analytical information by exercising tighter control over experimental parameters like the timing between absorbance determinations.

Registry No. Aspirin, 50-78-2.

LITERATURE CITED

(1) Miller, James A. *Pharm. Technol.* **1977**, *1*(2), 19–42.
(2) Knapp, Gene *Pharm. Technol.* **1977**, *1*(4), 12–13.
(3) PMA's Joint Committee on Bioavailability *Pharm. Technol.* **1985**, *9*(6), 62–66.
(4) Leeson, L. J.; Peterson, R. V.; Robinson, J. R. *Pharm. Forum* **1984**, *10*, 4103.
(5) Lanza, Frank L.; Royer, George L., Jr.; Nelson, Robert S. *N. Engl. J. Med.* **1980**, *303*, 136–138.
(6) "U. S. Pharmacopeia", 21st rev.; U.S. Pharmacopeial Convention: Rockville, MD, 1985; pp 77 and 1245–1246.
(7) Herzfeldt, C. D. *Pharm. Technol.* **1984**, *8*(9), 70–76.
(8) Carrie, T. R.; Sanders, G. A. *J. Pharm. Sci.* **1983**, *72*, 976–978.
(9) Papas, Andrew N.; Alpert, Maurice Y.; Marchese, Salvatore M.; Fitzgerald, James W.; Delaney, Michael F. *Anal. Chem.* **1985**, *57*, 1408–1411.
(10) Owens, G. D.; Eckstein, R. J. *Anal. Chem.* **1982**, *54*, 2347.
(11) Juhl, W. E.; Kirchoefer, R. D. *J. Pharm. Sci.* **1980**, *69*, 967–970.
(12) Miller, J. C.; Miller, J. N. *Statistics for Analytical Chemistry*; Wiley: New York, 1984; pp 58, 192.

RECEIVED for review December 16, 1985. Accepted May 1, 1986.

Digital Simulation of the Measured Electrochemical Response of Reversible Redox Couples at Microelectrode Arrays: Consequences Arising from Closely Spaced Ultramicroelectrodes

Allen J. Bard,*[1] Joseph A. Crayston,[2] Gregg P. Kittlesen,[2] Theresa Varco Shea,[1] and Mark S. Wrighton*[2]

Department of Chemistry, Massachusetts Institute of Technology, Cambridge, Massachusetts 02139, and Department of Chemistry, University of Texas, Austin, Texas 78712

Diffusion to arrays of closely spaced (1.2–0.2 μm) ultramicroelectrodes (50 μm × 2.3 μm) was studied by digital simulation and by examining the redox behavior of $Ru(NH_3)_6^{3+}$ in H_2O. Cylindrical diffusion of solution species resulted in quasi-steady-state currents at the microband electrodes. Generation–collection experiments, analogous to rotating ring–disk collection experiments, resulted in larger generator currents than those observed at a single microelectrode due to the back diffusion of products to the neighboring microelectrode. A collection efficiency of 93% was observed for the reoxidation of $Ru(NH_3)_6^{2+}$ generated at a central microelectrode 0.2 μm from two flanking collector microelectrodes. This experiment as well as generator–single collector electrode pairs was simulated at a two-dimensional rectangular expanding grid and yielded results in good agreement with the experiment. Predictions of the model that the collection efficiency principally depends on the gap size, rather than electrode width, were tested experimentally. The novel application of microelectrode arrays to the study of the follow-up reactions of electrogenerated intermediates is demonstrated.

The digital simulation of electrochemistry of ultramicroelectrode arrays is shown here to be successful in predicting the effect of variations in electrode geometry on the current response. Our results on the properties of arrays of closely spaced microelectrodes represent the most complete study where theory can be tested with experiment.

Already, *single* ultramicroelectrodes have attracted a great deal of interest for analytical applications (*1*). Apart from their obvious compactness, they exhibit: (1) enhanced diffusion to achieve steady-state or quasi-steady-state, diffusion-controlled currents; (2) low charging currents (*2*); and (3) reduced solution resistance effects (*3*). The enhanced diffusion has led to their use in studies of charge transfer kinetics (*4*, *5*).

Recently it has been shown that it is possible to fabricate *arrays* of more than one ultramicroelectrode, each of which is individually addressable (*6–10*). Such arrays consist of microband electrodes, ca. 50 μm long and 2-3 μm wide, with an interelectrode spacing of the order of one to several micrometers (*6–13*). The photolithographic techniques used in the manufacturing process permit a very small spacing (1.2 μm) between electrodes. This makes them suited for use as charge flow control devices based on molecular materials (6–8, *11–13*), in which charge transport is usually very slow. Such devices may find applications as chemical sensors with built-in signal amplification (*14*). Previously described devices includes those that mimic transistor (*6–8*) and diode (*11*, *12*) characteristics with a spacing of 1.2 μm. Recently, a transistor-like device consisting of a poly(3-methylthiophene) film covering two microelectrodes has been exploited as a sensor for H_2 and O_2 (*13*).

The close electrode spacing (1.2 μm) has a profound effect on the solution amperometric response, as will be fully described in the Experimental Section of this paper (part II). Essentially, each microelectrode displays a sigmoidal current response in linear potential sweep voltammetry. This type of response arises from the enhanced mass transport due to nonlinear diffusion (*1–3*). Radial diffusion to the edges of microelectrodes contributes significantly to the overall diffusion and results in quasi-steady-state currents for moderate sweep rates with reversible redox couples. This diffusional flux affects various properties, but the most striking effect of an array of closely spaced electrodes where the diffusion layers overlap is that it becomes possible to detect the electrogenerated products at the adjacent electrodes. For example, the reduced form of a solution species generated at one microelectrode may be "collected" at adjacent microelectrodes, which are held at a potential where oxidation can occur (as indicated by an anodic current). The situation is analogous to collection experiments using conventional rotating ring–disk electrodes (RRDE) of macroscopic dimension (*15*, *16*). Thus, one can define a *collection efficiency* representing the ratio of currents at the generator and collector electrodes. However, as opposed to RRDE experiments, where the current at the disk is unaffected by the ring, for closely spaced stationary electrodes products at the collector can diffuse back to the generator electrode and be electrolyzed there. Thus, an additional *feedback current* at the generator can be observed. Finally, the current at one electrode can affect that at its neighbor when both are at the same potential, because the diffusion layers overlap. This is analogous to *shielding* at the RRDE. For a deeper understanding of the effects of electrode width and interelectrode gap spacing on the collection efficiency, feedback, and shielding, we used digital simulation techniques to model the microelectrode arrays. As described in part I, this model predicts a collection efficiency that is in agreement with experiment.

Finally, we show how it is possible to apply such a digital simulation in the future to a more complex situation, namely, a catalytic follow-up (or EC′) reaction (*17*) represented by eq 1 and 2. Catalytic currents have already been observed at

$$A^{m+} + ne \rightleftarrows A^{(m-n)+} \quad (1)$$

$$A^{(m-n)+} + B \rightarrow A^{m+} + B^{n-} \quad (2)$$

a *single* ultramicroelectrode (*18*, *19*), but not at an array of several electrodes, each of which may be individually potentiostated so that, in principle at least, all of the species in reactions 1 and 2 may be determined separately, provided that their electrode potentials are sufficiently different. Thus, the array of ultramicroelectrodes could function not merely as a

[1] University of Texas.
[2] Massachusetts Institute of Technology.

0003-2700/86/0358-2321$01.50/0 © 1986 American Chemical Society

rotating ring–disk electrode but also as a split ring–disk electrode (*20*), capable of detecting up to seven intermediates.

EXPERIMENTAL SECTION

Ultramicroelectrode Arrays. In the arrays of eight Au microelectrodes, each was 50 μm long, 2.3 μm wide, 0.1 μm thick, and spaced 1.3 μm apart. Complete details of the fabrication of arrays on p-Si/SiO_2/Si_3N_4 substrates are given in earlier reports (*6–8, 11–13*). The arrays of two Au microelectrodes were designed with the aim of reducing the width and spacing dimensions for the particular application of decreasing the amount of polymer necessary to make the type of diode described in previous work (*11, 12*). The fabricated microelectrodes were 50 μm long, 1.2 μm wide, 0.1 μm thick, and interspaced by 0.9 μm. These geometries approach the practical limits imposed by the GCA Mann 4800 Wafer Stepper and positive photoresist. The M.I.T. Microelectronics Laboratory Wafer Stepper has successfully patterned 0.6 μm lines and spaces in MacDermid Ultramac PR-914 positive photoresist.

Prior to use, the electrode surfaces were cleaned by an rf O_2 plasma etch to remove residual photoresist, followed by cycling the potential at each electrode between −1.6 V and −2.0 V vs. SCE in 0.1 M aqueous K_2HPO_4, ca. 5 cycles at 200 mV/s to evolve H_2. Other conventional and more stringent chemical and electrochemical cleaning led to electrode damage. Pt was deposited on each electrode from 2 mM K_2PtCl_4 in 0.1 M aqueous K_2HPO_4. At each electrode, 0.2 μC was passed. The resulting platinized electrodes of an eight-wire array were 2.5 μm wide and interspersed by 1.0 μm. The dimensions were determined by scanning electron microscopy using a Cambridge Mark 2A Stereoscan with a resolution of 20 nm, after first coating the array with ca. 200 Å of Au to minimize problems from surface charging. The platinized electrodes of a two-wire array were 1.5 μm wide and interspaced by 0.8 μm. The interelectrode spacing was significantly reduced by depositing more Pt from solution. Upon passing a total charge of 2.5 μC at each of two adjacent electrodes of an eight-wire array, the electrodes were 3.1 μm wide and separated by 0.3 μm. Another strategy was to platinize the electrode lightly by passing 0.2 μC, and then to platinize the neighboring electrode more heavily by passing 4.0 μC. The heavily platinized electrode was 4.1 μm wide and separated from the lightly platinized one by 0.3 μm. Two-wire arrays were similarly lightly/heavily platinized by passing 0.2 μC and 1.75–2.0 μC, respectively.

Platinization of the Au electrodes was desirable in the Ru^{3+} generation–collection experiments for reasons of: (1) greater lifetime of the quasi-steady-state current for Ru^{3+} reduction—presumably adsorption of impurities with time led to a decreased current and a "flattening" of the sigmoidal i–V curve, and (2) providing a means of reducing the interelectrode spacing. However, the quinone experiments were conducted at the unplatinized Au electrodes so that there was less interference from direct O_2 reduction at the electrode. The Au electrodes were cleaned (as described above) prior to each measurement to obtain reproducible currents.

Gold electrodes were deliberately removed by electrochemically cycling between 0.0 V and +1.8 V vs. SCE in 0.1 M KCl solution until the current at 1.8 V decayed to zero. Alternatively, the electrode was potentiostated at +1.8 V vs. SCE. This removed both the ca. 0.1 μm thick Au electrode and the ca. 60 Å layer of Cr, so that zero current was observed in response to 5 mM $Ru(NH_3)_6Cl_3$. This lift off procedure was also attempted in a 0.1 M NaCN solution and cycling between 0.0 V and +0.5 V. However, preliminary optical microscopic and electrochemical examination suggested that the Au layer was removed, but the Cr layer was not affected.

Chemicals. Triply distilled H_2O (EM Science) was used for all solutions with various supporting electrolytes: KCl, LiCl, $LiClO_4$, and $LiNO_3$ were used as received. $Ru(NH_3)_6Cl_3$ (Strem) was also used as received. 2,5-Dichloro-3,6-bis[[2-(dimethylpropylamino)ethyl]amino]benzoquinone was prepared (*21*) by similar methods to those previously published for naphthoquinone derivatives (*22, 23*).

Electrochemical Equipment. Electrochemical plating of Pt onto the Au microelectrodes was accomplished with a Princeton Applied Research Model 173 potentiostat/galvanostat, Model 179 digital coulometer, and Model 175 Universal Programmer. The remaining electrochemical experiments were performed with a Pine Model RDE4 bipotentiostat and recorded on a Kipp and Zonen BD91 XYY't recorder. All potentials were controlled relative to an aqueous saturated calomel electrode (SCE). Electrochemical measurements were carried under N_2 or Ar at 22 °C, unless otherwise stated.

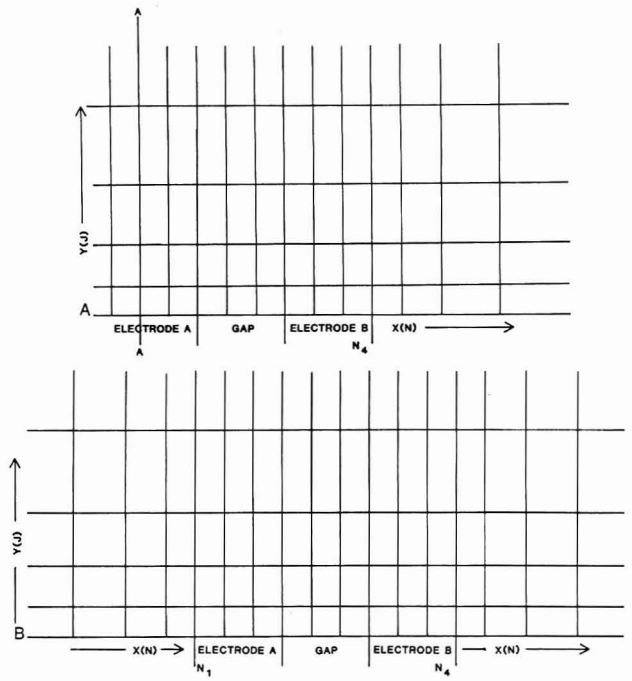

Figure 1. (A) Two-dimensional space grid used for the simulation of the three microelectrode array. The grid begins expanding after element N4, the last uniform element in the *N* direction. The grid expands also from the substrate in the *J* direction. The axis of symmetry through electrode A permits the simulation of half of the array. (B) Space grid used for the simulation of two-electrode pairs. To the right of N4 and in the *J* direction, the grid is the same as A. However, to the left of N1, the grid also expands exponentially.

Digital Simulations. All computations were carried out on the UT-CDC 6000 dual cyber computer (Control Data Corp.)

PART I. SIMULATION OF PATTERNED ARRAY ELECTRODES FOR ELECTROCHEMISTRY

Model and Tests of the Model. Digital simulation of a single microband electrode and arrays of electrodes generally followed previous practice (*24, 25*). To simulate the ultramicroelectrode array, a two-dimensional space grid was set up, Figure 1A, where the two electrodes A and B, the generator and collector, were separated by a gap. Because of the small height to width ratio, 1 to 23, of the experimental arrays, the top of the electrode was assumed to lie in the plane of the substrate, i.e., the height of the electrode in the *J* direction was taken to be zero. The width of the electrodes in the *N* direction, as well as the gap width, was varied by varying the number of boxes corresponding to the electrodes and the interelectrode spacing. In addition, the axis of symmetry through electrode A permitted the simulation of half of the three-electrode array as well as the single band electrode and reduced the amount of computer time and storage space needed. Figure 1B shows the grid configuration adopted for the simulation of generator–single collector pairs.

To further conserve computation time and extend the simulated times to correspond to the rather long experimental times required to attain quasi-steady-state behavior, an exponentially expanding space grid (*26–28*) was added in the *J* direction, perpendicular to the electrode surface, parallel to the substrate (Figure 1). However, the solution boxes above the electrodes and gap in the *N* direction were represented by a uniform space grid and were treated in the usual way (*24, 25*). Details of the mathematical treatment of the digital

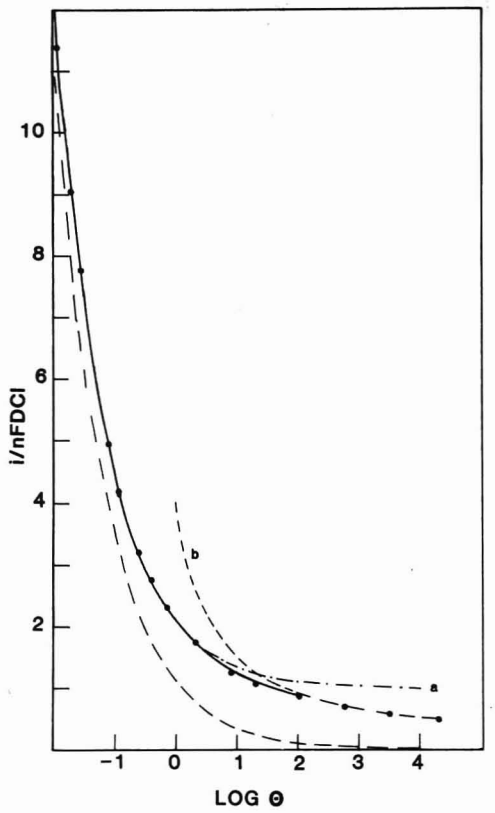

Figure 2. Normalized current, $i/nFDCl$ vs. log ($4Dt/W^2$). The solid line is the theoretical curve calculated in ref 29. The dashed curve (– – –) is the theoretical Cottrell behavior. Curve a was calculated by eq A17 and curve b by eq A16. The circles are simulated results.

simulation are given in the Appendix.

The validity of the model was demonstrated by applying the simulation to a single band electrode. In the test case, we consider a potential step to electrode A while electrode B was missing, i.e., the grid begins expanding at the edge of electrode A in the N direction and the solution contained only species Ox. We assumed total mass-transport-controlled conditions, with the concentration of Ox at the electrode surface going instantaneously to zero and the mass transport solely by diffusion. A typical simulated current–time (i–t) response compared to the numerical solution for a potential step at a microband electrode recently reported by Tallman et al. (*29*) is shown in Figure 2. The i–t response can be described in terms of three time domains that are dependent upon the magnitude of the dimensionless parameter $\theta = 4Dt/W^2$ (eq A15) where D is the diffusion coefficient, t is the time, and W is the electrode width. At very short times, $\theta < 3 \times 10^{-5}$ (corresponding to ca. 65 ns when $W \sim 1$ μm), the flux to the electrode surface is approximated by semiinfinite linear diffusion and the current decays as a function of $t^{-1/2}$ (Cottrell conditions) shown by the dashed line in Figure 2. This time regime was not observed in the digital simulation where the earliest simulation times correspond to real times of the order of microseconds.

In the limit of long times, $\theta <$ ca. 30, the current approaches that expected for a hemicylinder and decays as $(\ln t)^{-1}$ (Figure 2, curve b) (*29*). For the time domain of $0.01 \leq \theta \leq 1$, the current can be approximated by eq A17 (Figure 2, curve a) (*29*). Over the range of θ from 0.01 to 10000 simulated currents agreed with Coen, Cope, and Tallman's (*29*) numerical solution for a microband electrode within 3%, demonstrating the validity of the simulation model for a microband electrode over 6 orders of magnitude of θ thus providing confidence that the digital simulation could be applied to microelectrode arrays and determination of collection efficiencies, feedback, and shielding effects.

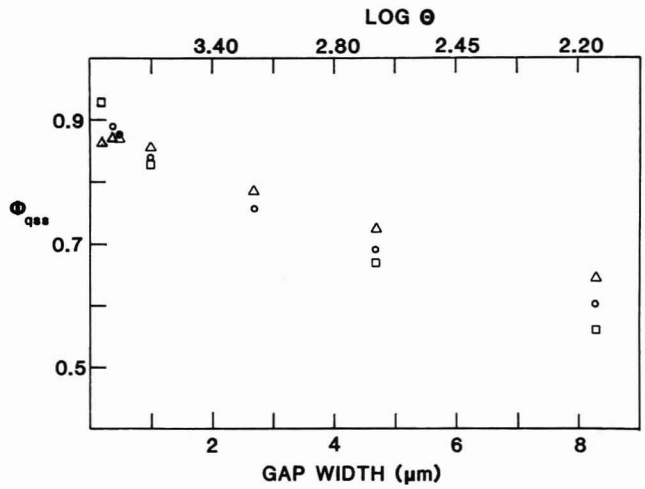

Figure 3. Collection efficiency, ϕ_{ss}, as a function of the interelectrode gap for a single generator, and a pair of flanking collector electrodes ($W_G = W_C = 1$ μm). Squares are experimental points (part II). The circles are simulation results at the same value of log $\theta_{GAP} = 4$ as the experimental points. Triangles are theoretical values calculated by eq 4.

Note that the microband electrode (in common with the cylindrical or hemicylindrical electrode) does not attain a true steady-state current; spherical and embedded disk electrodes do. However, at sufficiently long θ values ($\theta \geq 100$), the rate of decay of current is small; we call this the "quasi-steady-state" region. Feedback from the collector electrode tends to decrease even more the rate of decay, and the onset of natural convection can produce steady-state currents. For electrodes with W = ca. 1 μm, the quasi-steady-state region is attained after about 0.1 s. The quoted quasi-steady-state efficiencies here correspond to log $\theta \sim 3.3$, or experimental times of the order of t ca. 3.5 s. In this region the normalized currents change less than 5% for a 10-fold change in θ.

Simulation of an Array and Dependence of Collection Efficiency on Electrode Geometry. Half of the array is shown in Figure 1A, and results that apply to a central generator electrode and a pair of flanking collector electrodes will be discussed first. Because of the large width at height ratio, 23 to 1, the electrodes were considered to be in the plane of the substrate, so the height in the J direction was zero. At electrode A the reduction reaction $Ox + e^- \rightarrow Red$ occurs, as described in the previous section. However, now a potential is applied to electrode B such that the Red produced at electrode A is reoxidized, $Red \rightarrow Ox + e^-$. This type of experiment is similar to that at a rotating ring–disk electrode (*15*, *16*) with the exception that now diffusion, not convection, is the primary means of mass transport. The geometric considerations necessary to maximize the amount of Red reaching electrode B will be discussed in the remainder of this paper.

To determine the effect of changing a geometric parameter, such as the gap or electrode width, the collection efficiency was studied. The collection efficiency, ϕ_{ss}, is the ratio of the quasi-steady-state current for Ox produced at the collector electrode, B, divided by the current for reduction of Ox at the generator electrode, A; see eq 3.

$$\phi_{ss} = (Z_B/Z_A)_{ss} \quad (3)$$

Simulated collection efficiencies for a generator and a pair of flanking collector electrodes of equal width (W_G and W_C = 1–4 μm) are shown by the circles in Figure 3. These are plotted in terms of the convenient dimensionless parameter $\theta_{GAP} = 4Dt/W_{GAP}^2$, where W_{GAP} is the gap width. The simulated points could be fit by the empirical equation

$$\phi_{ss} = 0.095 + 0.33 \log \theta_{GAP} - 0.035(\log \theta_{GAP})^2 \quad (4)$$

Table I Comparison of Collection Efficiencies for Various Electrode Sizes

electrode width,[a] μm	ϕ^b
1.0	0.85
1.7	0.87
2.0	0.87
3.3	0.88

[a] For $W_G = W_C$; $W_{GAP} = 1$ μm. [b] ϕ calculated at log $\theta_{GAP} = 4.3$ corresponding to $D = 7.1 \times 10^{-6}$ cm²/s, $t = 7$ s.

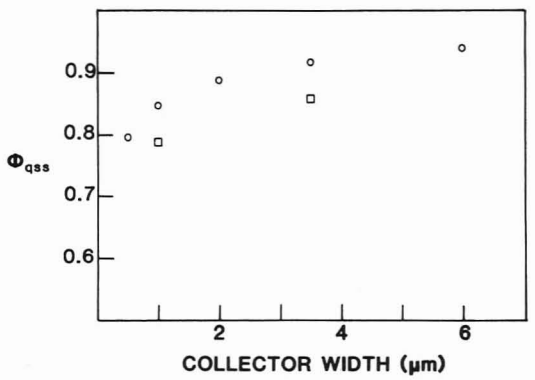

Figure 4. Collection efficiency, ϕ_{ss}, vs. the collector electrode width. The simulated collector widths were varied from 0.5 to 6 μm (circles) while the experimental widths were varied from 1 to 3.5 μm (squares) for the single generator, double collector electrode configuration. $W_G = 1$ μm, $W_{GAP} = 1$ μm, log $\theta_{GAP} = 4$.

The experimental results shown in Figure 3 will be discussed in part II. The results in Figure 3 and eq 4 indicate that, as intuitively expected, the collection efficiency is maximized as the gap width is decreased.

Another consideration in the construction of interdigitized ultramicroelectrode arrays concerns the width of the generator (W_G) and collector (W_C) electrodes, since the quasi-steady-state current (eq A16 and A17) is a function of the width. To maximize the current, a large width is desirable. However, a large width provides a greater lateral surface area from which the species Red can escape into the bulk. Therefore, a compromise between larger, more easily measured currents and minimizing loss due to diffusion out into the bulk must be made. However, for the electrode widths shown in Table I, where $W_G = W_C$ was varied from 1 to 3.3 μm with a 1-μm gap width, the collection efficiency ϕ_{ss} is the same within the error of the simulation (3%). While there is no discernible difference in ϕ_{ss} when the ratio of generator and collector is unity, when the ratio is not unity, the collection efficiency is found to depend on the collector electrode width. In Figure 4, ϕ_{ss} is plotted as a function of collector width for a generator electrode with two flanking collector electrodes, where the generator electrode width, the interelectrode gap, and θ are held constant. The squares are experimental points, discussed in part II. As expected, the collection efficiency increased as the collector electrode width increased from 0.5 to 6 μm with $W_G = 1$ μm and $W_{GAP} = 1$ μm. The increase in ϕ_{ss} is largest for $W_C \sim W_G$ and becomes less important for $W_C \geq 4$ μm. Thus, both the gap size and the ratio of the collector and generator electrode widths must be considered in the design of microelectrode arrays. One gains efficiency by minimizing the gap width while the ratio of the collector to generator widths should be greater than unity to maximize collection.

The digital simulation model could also be used to model a pair of microband electrodes (generator and single collector) of interest in experiments described in part II. The simulation grid used is shown in Figure 1B and the mathematical details are discussed in the Appendix. Simulated results of the collection efficiency, ϕ_{ss}, as a function of the interelectrode gap width, W_{GAP}, are given in Figure 5. The collection efficiency can be approximated by eq 5 (with a coefficient of correlation of 0.997). Equation 5 is useful for estimation of

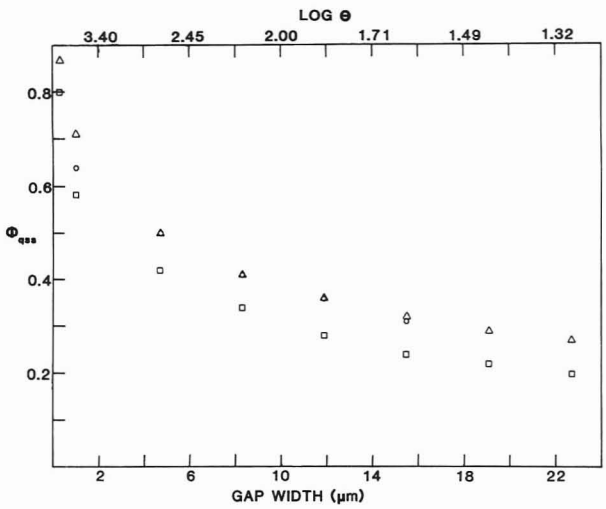

Figure 5. Collection efficiency, ϕ_{ss}, as a function of gap width for the generator–single collector pair. Simulated results (circles) correspond to gap widths of 1 to 15.5 μm while experimental results (squares) are for gaps of 0.5–22.7 μm. Theoretical results (triangles) were calculated by eq 5 for $D = 7.1 \times 10^{-6}$ cm²/s, $t = 3.5$ s, $W_G = 1$ μm.

$$\phi_{ss} = 0.033 + 0.21 \log \theta_{GAP} - 0.016(\log \theta_{GAP})^2 \quad (5)$$

the observed experimental collection efficiencies for gaps of 0.5–23 μm. As expected, the ϕ_{ss} values for a pair of electrodes are smaller than those for flanking collectors (compare Figures 3 and 5).

Effect of Shielding and Feedback. When the array of ultramicroelectrodes was operated in the generator–collector electrode mode, the current response mimicked the steady-state behavior observed at the RRDE as previously demonstrated. As noted, the primary means of mass transport was by diffusion, which is responsible for the closely related shielding and feedback effects.

For the RRDE, the shielding experiment involves reducing the amount of Ox that reaches the ring, where the ring reaction is Ox + e^- → Red, by applying a potential to the disk (e.g., $E_D = E_R$) to cause the same reduction reaction to occur. In the corresponding experiment with the array, the adjacent electrodes were held at the same potential, $E_G = E_C$, where E_G and E_C are the potentials of the generator and collector electrodes, respectively. As the electrolysis proceeds, the diffusion layers overlap, shielding each electrode. This shielding effect reduced the quasi-steady-state current at three electrodes in the array when compared to the sum of the currents expected at three independent electrodes. We define this reduction in current as the *shielding factor*, S_F, given by eq 6 for equal sized electrodes, where Z_i is the current at each

$$S_F = 1 - \frac{\sum_{i=1}^{q} Z_i}{qZ} \quad (6)$$

of the q electrodes in the array and Z is the current observed for a single electrode, with all other electrodes at open circuit. The shielding factor is a measure of the degree of overlap of the diffusion layers and approaches zero in the absence of shielding (e.g., for electrodes widely spaced apart). The simulation results for the quasi-steady-state currents at three electrode arrays are given in Table II. The shielding effect is more pronounced on the inner (generator) electrode than on the flanking (collector) electrodes, because the inner electrode is blocked from nonlinear diffusion paths from both sides while the outer electrodes are only blocked from one side.

Table II. Simulation of Effects of Feedback and Shielding[a]

gap width, μm	electrode width, μm: generator	electrode width, μm: collector	normalized currents: with feedback Z_G	with feedback Z_C	with feedback ϕ_{ss}	without feedback $Z_{G,0}$	without feedback Z_C	without feedback ϕ_{ss}	shielding Z_G	shielding Z_C	shielding Z_{tot}	shielding factor	feedback factor
1.0	1.0	0.5	1.09	0.87	0.80	0.50	0.40	0.80	0.22	0.42	0.64	0.56	0.54
1.0	1.0	1.0	1.14	0.97	0.85	0.50	0.43	0.85	0.18	0.50	0.68	0.57	0.56
1.0	1.0	6.0	1.20	1.13	0.94	0.50	0.47	0.94	0.07	0.83	0.90	0.57	0.58
2.7	1.0	1.0	0.88	0.67	0.77	0.50	0.39	0.77					0.43
0.5	1.0	1.0	1.37	1.21	0.88	0.50	0.44	0.88					0.64

[a] Z_G and Z_c are normalized generator and collector electrode currents, respectively, ϕ_{ss} is the quasi-steady-state collection efficiency (eq 3); the shielding and feedback factors are defined in eq 6 and 7, respectively. For a single generator and two flanking collector electrodes.

A phenomenon related to shielding but not possible at the RRDE is feedback. When the reduced species reaches the collector electrode, it is reoxidized to Ox that can diffuse back to the generator electrode. Thus, the collector electrodes act as a source and increase the flux of Ox to the generator. The effect of feedback was observed in the increased magnitude of the quasi-steady-state generator currents (see Table II). In generator–collector experiments where the reactions were all reversible, the generator currents were increased by the feedback factor, F_B, given in eq 7, where $Z_{G,0}$ is the steady-state

$$F_B = 1 - (Z_{G,0}/Z_{G,C}) \quad (7)$$

current without feedback and $Z_{G,C}$ is the steady state generator current with feedback. Typical effects of feedback with three electrode arrays are given in Table II. It should be noted that at the same log $\theta = 4.3$, the collection efficiencies are the same with and without feedback, although the magnitudes of the generator and collector currents are smaller without feedback.

In summary, the predictions of the digital simulation are as follows: (1) the collection efficiency is strongly dependent on gap size and to a lesser extent on the collector electrode width; (2) by use of eq 4 for a three-electrode array or eq 5 for a two-electrode pair, the collection efficiency can be calculated for a known diffusion constant, time, and interelectrode gap (i.e., θ_{GAP}); (3) shielding and feedback are shown to be important at electrodes of these dimensions; (4) agreement between the simulation predictions and experiment are within 10% and agreement between the simulation and theory is better than 3% for a single microelectrode.

PART II. EXPERIMENTAL RESULTS AND DISCUSSION

Electrochemical Characterization of Microelectrode Arrays. Each Au electrode of an array was individually addressable. Generally, a small amount of Pt (0.2 μC corresponding to a coverage of 0.86 μmol/cm^2) was electrochemically deposited onto each microelectrode to yield a consistently fresh electroactive surface prior to electrochemical experimentation. Figure 6 shows linear potential sweep cyclic voltammograms for the reduction of $Ru(NH_3)_6^{3+}$ at each microelectrode of an eight-electrode array. The solution was not stirred during the measurement. That there was no cathodic current peak is a consequence of the narrow width of the microelectrode. At a larger electrode at the same sweep rate, a cathodic current peak would be observed due to the depletion of $Ru(NH_3)_6^{3+}$ near the electrode surface. On the return scan an anodic current peak would also be observed due to the oxidation of $Ru(NH_3)_6^{2+}$ generated in the negative sweep. At the microelectrode radial diffusion to the edges of the microelectrode was significant and combined with diffusion normal to the microelectrode surface to deliver the redox species to the microelectrode at a rate approximately equal to the electrolysis rate. Hence, a steady-state current was observed at slow sweep rates and low redox reagent concentrations. As shown in part I, it was not necessary for non-

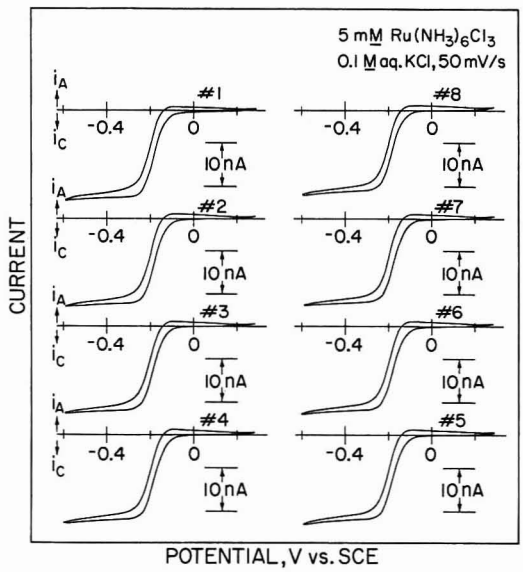

Figure 6. Cyclic voltammetry, 50 mV/s, of an array of eight microelectrodes in a 0.1 mM LiCl solution containing 5 mM $Ru(NH_3)_6^{3+}$.

diffusional hydrodynamic flow to be invoked. The quasi-steady-state cathodic currents in Figure 6 are all nearly identical, demonstrating the success of the encapsulation and Pt deposition techniques used in the array fabrication. The magnitude of the current can be calculated from eq 8 (*29*) for the mass transport limited current at a microband electrode,

$$i = nFDCl[5.553/(\ln \theta) - 6.791/(\ln \theta)^2],\ \theta = 4Dt/W^2 \quad (8)$$

where l is the length of the electrode, W is the width of the electrode, and t is the characteristic time. Typically θ was about 215 for our electrodes, so that for the experiment in Figure 6, eq 8 predicts a current of 13.7 nA compared to ca. 19 nA observed. At a θ of 215, the simulation and theory are in very good agreement. The normalized current function, Z (see eq A16), for the experiment in Figure 6 is 1.11 compared with 0.80 calculated by eq 8 and 0.78 calculated by the simulation.

The results of a generation–collection experiment analogous to a rotating ring–disk electrode collection experiment are given in Figure 7. The potentials of two adjacent microelectrodes were independently controlled by a bipotentiostat. Again, forced convection was not necessary in order to observe quasi-steady-state currents. In the experiment summarized by Figure 7, the potential of one electrode, the generator electrode, was swept in a negative direction linearly in time through the formal potential of $Ru(NH_3)_6^{3+/2+}$. Simultaneously, the potential of the adjacent electrode, the collector electrode, was held fixed at a value such that the $Ru(NH_3)_6^{2+}$ generated was oxidized to $Ru(NH_3)_6^{3+}$. A larger steady-state current (42% greater) was observed at the generator electrode

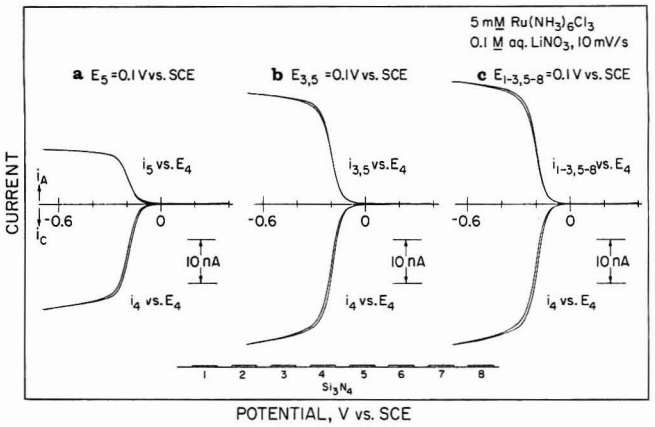

Figure 7. Generation/collection experiment in 5 mM $Ru(NH_3)_6Cl_3$ in 0.1 M aqueous $LiNO_3$ as a function of the number of collector electrodes. Microelectrode no. 4 was the generator electrode in each case. The potential of the generator electrode was swept between +0.4 and −0.7 V vs. SCE at 10 mV/s while the potential of the collector electrodes was held at +0.1 V vs. SCE. Collector electrodes: (a) single adjacent electrode no. 5; (b) microelectrodes no. 3 and no. 5; (c) electrodes no. 1–3 and no. 5–8.

Table III. Distance Dependence of Observed Collection Efficiency Using One Generator Electrode and Two Symmetrically Disposed Collector Electrodes[a]

generator electrode current, nA		collector electrode current, nA		separation,[b] μm	collection efficiency, %
no. 4	36.8	no. 3, 5	30.4	1.0	83
no. 4	25.6	no. 2, 6	17.2	4.7	67
no. 4	22.8	no. 1, 7	12.8	8.3	56

[a] Mean values determined from several different lightly platinized microelectrode arrays. Errors: separation (SEM photographs), ±0.1 μm; collection efficiencies, ±3%. [b] Separation between generator and collector nearest edges.

than when no collector electrode was used. This is the manifestation of feedback associated with closely spaced electrodes discussed in part I. The point is that the collector electrode was an additional source of $Ru(NH_3)_6^{3+}$ to the generator electrode. A total of 51% of the generated $Ru(NH_3)_6^{2+}$ was collected at one adjacent microelectrode, Figure 7. Collection efficiencies were typically 51–60% between adjacent lightly platinized microelectrodes with a 1.0-μm separation between nearest edges. The significant finding is that more than 50% of the generated $Ru(NH_3)_6^{2+}$ can be collected on only one side of the generator electrode. The collection efficiency was the same when the electrode on the other side of the generator was used as a collector. In other words, there is a symmetry of the system in the sense that any pair of adjacent electrodes in a generation–collection experiment will give rise to the same collection efficiency.

Now we examine the first situation investigated in the digital simulation. For two collector electrodes, one on either side of a centrally positioned generator electrode, the collection efficiency was dramatically increased to 79%, Figure 7b. Here, the limiting current observed at the generator electrode was 88% greater than when no collector electrodes were used, F_B = 0.47, demonstrating significant consequence from feedback. Simulation results predict F_B = 0.44 for this electrode geometry at log θ = 3.1. By connecting seven microelectrodes as collector electrodes the collection efficiency only increased to 86%, Figure 7c. Clearly, inclusion of those electrodes lying farther away from the central generator electrode did little to increase the collection efficiency beyond 79%. This result is consistent with part I as shown in Figure 4.

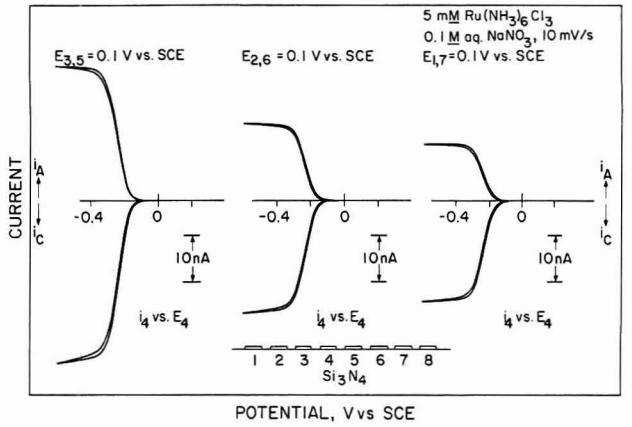

Figure 8. Generation/collection experiment in 5 mM $Ru(NH_3)_6Cl_3$ in 0.1 M aqueous $NaNO_3$ using a central generator microelectrode no. 4 and symmetrical pairs of collector electrodes. (L–R: no. 3, 5; no. 2, 6; no. 1, 7).

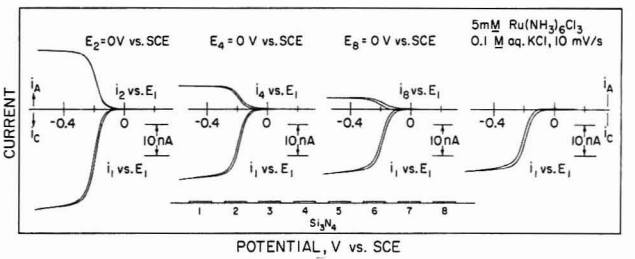

Figure 9. Generation/collection experiment in 5 mM $Ru(NH_3)_6Cl_3$ in 0.1 M aqueous KCl as a function of distance between collector and generator electrode. Electrodes no. 2, 4, and 8 were used as collector electrodes.

By use of a central electrode of the eight as the generator, there were three possible symmetrically disposed collector electrode pairs that could be used to test the predicted dependence of efficiencies on gap size displayed in Figure 3. Figure 8 shows the results from one such set of experiments and Table III summarizes several such determinations. The experimental results and the simulation are in quite good agreement (Figure 3), at the same θ value with the experimental values consistently slightly lower (ca. 7–10%) than the simulated ones. A possible reason for the discrepancy between the simulation and experiment is that the model does not take into account the effect of intervening nonpotentiostated electrodes. Thus, when using electrode no. 4 as a generator and electrodes no. 2 and 6 as collectors, the presence of electrodes no. 3 and 5 may contribute in some way to the observed collection efficiency. To test this, experiments were carried out to measure collection efficiencies before and after electrochemical removal of the intervening electrodes (see Experimental Section). The collection efficiency in an experiment with generator electrode no. 4 and collector electrodes no. 2 and 6 increased from 49% to 57% after removal of electrodes no. 3 and 5. This suggested that intervening electrodes act to diminish currents.

The dependence of collection efficiency on the distance between the generator and only *one* collector electrode is presented in Table IV and Figures 5 and 9. A collection efficiency of 58% between adjacent electrodes was observed. Upon use of electrode no. 4 as the collector and electrode no. 1 as the generator, the collection efficiency dropped by less than a factor of 2 to 34%. For the no. 1/no. 4 generator–collector pair the electrodes were separated by 8.3 μm between adjacent edges. The generator electrode current amplitude for this pair and all pairs at greater separation was identical with the current amplitude observed with no collector electrode, indicating that there was negligible feedback for the

Table IV. Distance Dependence of Observed Collection Efficiency for a Generator–Single Collector Electrode Pair

generator electrode current, nA		collector electrode current, nA		separation,[a] μm	collection efficiency,[b] %
no. 1	32.0	no. 2	24.0	1.0	58
no. 1	24.0	no. 3	10.0	4.7	42
no. 1	22.0	no. 4	7.5	8.3	34
no. 1	21.5	no. 5	6.0	11.9	28
no. 1	21.0	no. 6	5.0	15.5	24
no. 1	20.5	no. 7	4.5	19.1	22
no. 1	20.5	no. 8	4.0	22.7	20

[a] Separation between nearest edges of a single generator and a single collector electrode (±0.1 μm). [b] The standard deviation in absolute collection efficiency from array to array is ±4%. However, each array shows a smooth decrease in collection efficiency as the collector electrode is farther from the generator electrode.

large separations. For the greatest separation, the no. 1/no. 8 pairing, the collection efficiency was 20%. These results agree well with the symmetrical generator–collector experiments and the simulated results in that the collection efficiency falls off slowly with distance.

The collection efficiency vs. gap size (separation between generator and collector) was further investigated by using two-electrode arrays. The smaller interelectrode spacing of the two-electrode arrays, 0.8 μm, compared to 1.0 μm for the eight-electrode arrays, resulted in a larger collection efficiency for the reduction and reoxidation of $Ru(NH_3)_6^{3+}$: 68% compared to 58%. There are two possible geometric factors at work here that can be considered to affect collection efficiency, i.e., collector electrode area and interelectrode spacing. The improved collection efficiency was caused by the smaller spacing, since results above show that collector area is not a big factor in collection efficiency, Figure 7b vs. Figure 7c. Moreover, the electrodes of the two-wire arrays had smaller areas than did the electrodes of the eight-wire arrays that gave the 58% collection efficiency, Figure 9. It appears that collector area does not have as great an effect on the collection efficiency as the interelectrode spacing, as predicted in part I.

Effect of Increased Platinization of Microelectrodes on the Collection Efficiencies. The strong dependence of collection efficiency on gap size (generator separation from *one* collector) was further investigated by electrochemically depositing relatively large amounts of Pt onto the electrodes to close the gap between adjacent microelectrodes by a significant amount. Two different strategies were employed to minimize the interelectrode spacing. Either large amounts of Pt were deposited on each electrode or one electrode was lightly platinized and the other heavily platinized. Large Pt deposits generally resulted in rough edges along the electrodes. Projections of Pt along the rough edge occasionally led to shorted electrode pairs. The light/heavy deposition strategy preserves one straight edge. Clearly, Pt deposition reduces the gap size, but it also increases the height and width of the electrodes.

Large amounts of Pt were deposited on six of eight electrodes in an array by reduction of $PtCl_4^{2-}$ in 0.1 M K_2HPO_4. Amounts of Pt deposited and resulting dimensions of the electrodes (determined by scanning electron microscopy) are detailed in Table V. Figure 10 displays the large increase in limiting currents and collection efficiency as the gap between adjacent electrodes is decreased to 0.2 μm. At a 1.0 μm separation between lightly platinized electrodes, a collection efficiency of 53% was obtained. For heavily platinized microelectrodes with a spacing of 0.2 μm, a collection efficiency of 83% was observed.

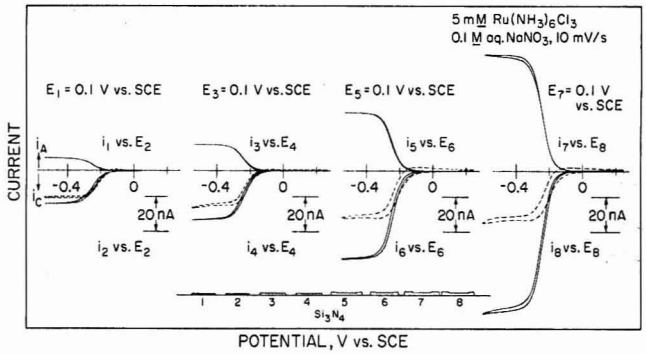

Figure 10. Generation/collection cyclic voltammetry at a series of heavily platinized electrodes in 5 mM $Ru(NH_3)_6Cl_3$ in 0.1 M aqueous $NaNO_3$. Electrode geometries are presented in Table II. Dashed curves represent collectors at open circuit.

Table V. Observed Collection Efficiencies at Heavily Platinized Arrays

electrode	charge passed during $Pt^{2+} \rightarrow Pt^0$, μC	width of electrode, μm	gap size, μm	collection efficiency, %
no. 1	0.0	2.2	1.3	40
no. 2	0.0	2.2		
no. 3	0.25	2.4	1.0	53
no. 4	0.25	2.4		
no. 5	1.25	3.0	0.7	66
no. 6	1.25	2.7		
no. 7	2.00	3.3	0.2	83
no. 8	2.00	3.0		

In another experiment, one electrode was lightly platinized by passing 0.2 μC and the adjacent electrode was heavily platinized by passing 4.0 μC. The heavily platinized electrode was 4.1 μm wide and separated from the lightly platinized electrode by 0.3 μm. The heavily platinized electrodes displayed large nonfaradaic currents and significant cathodic currents for the reduction of H_2O. The lightly platinized electrode situated next to the heavily platinized electrode showed a slight voltammetric cathodic current peak for the reduction of 2 mM $Ru(NH_3)_6^{3+}$. The heavily platinized electrode may impair radial diffusion to the adjacent lightly platinized electrode. A collection efficiency of 80% was obtained when the lightly platinized electrode was connected as the generator electrode and the heavily platinized electrode is connected as the collector electrode. By connection of a lightly platinized electrode as the generator electrode between two heavily platinized collector electrodes, a maximum of 93% collection efficiency was observed. This high collection efficiency was a consequence of the small separation (Figure 3).

The gap between two-electrode arrays was similarly narrowed. For example, one electrode can be plated with 0.2 μC of Pt from $PtCl_4^{2-}$ in solution, and the other electrode can be plated with 1.75–2.0 μC of Pt. The resulting widths were 1.5 μm and 2.2 μm, respectively, separated by 0.3–0.4 μm, which was very similar to that in the analogous electrodes of an eight-electrode array. An 80% collection efficiency for the reoxidation of $Ru(NH_3)_6^{2+}$ was observed, identical with that observed at the eight-electrode array. This experiment confirmed the suggestion that interelectrode spacing is the dominant factor controlling collection efficiencies, and not collector widths, since the widths in the two-electrode arrays are different than those in the eight-electrode arrays.

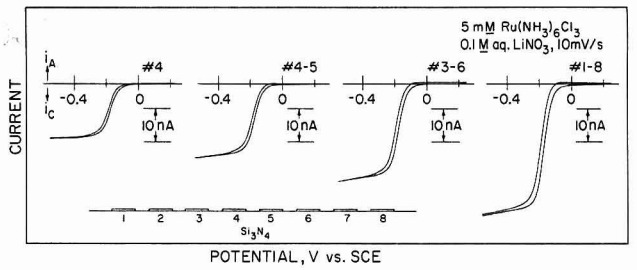

Figure 11. Slow scan rate cyclic voltammetry in 5 mM $Ru(NH_3)_6Cl_3$ in 0.1 M aqueous $LiNO_3$ at one, two adjacent, four adjacent, and eight adjacent electrodes.

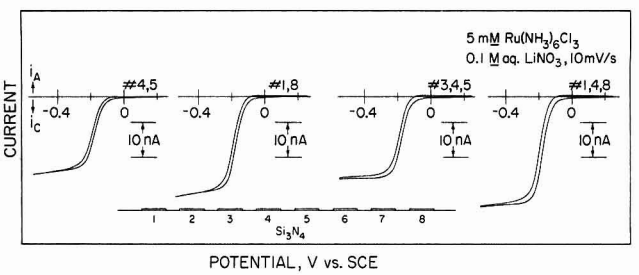

Figure 12. Slow scan rate cyclic voltammetry in 5 mM $Ru(NH_3)_6Cl_3$ in 0.1 M aqueous $LiNO_3$ at adjacent vs. interspaced electrodes.

Shielding Effects at Microelectrode Arrays. To demonstrate shielding in the sense developed in part I, various combinations of the eight electrodes were driven together as the working electrode in a conventional three-electrode linear potential sweep voltammetry configuration for the reduction of 5 mM $Ru(NH_3)_6Cl_3$ in 0.1 M $LiNO_3$. The basic finding was that quasi-steady-state cathodic current amplitudes were not directly proportional to the combined areas of the closely spaced electrodes. Figure 11 presents the results of linear potential sweep voltammetry at one, two adjacent, four adjacent, and all eight electrodes. Two adjacent electrodes displayed 61% of the limiting cathodic current expected by simply doubling the current observed at a single electrode. Driving more adjacent electrodes incrementally decreased the percentage of observed current relative to that expected by simply multiplying the current at a single electrode by the number of electrodes driven together. Driving all eight electrodes together resulted in a limiting cathodic current that was only 28% of 8 times the limiting current at a single electrode. Figure 12 demonstrates the effects of driving a group of electrodes spread out across the array in contrast to driving the same number of adjacent electrodes. The current at two adjacent electrodes was 61% of 2 times the current at a single microelectrode ($S_F = 0.39$). A total of 89% of 2 times the current at a single electrode was observed ($S_F = 0.11$) by driving electrodes no. 1 and no. 8, separated by 23 μm between nearest edges across the microelectrode array. At three adjacent electrodes, 46% of 3 times the current at a single electrode was observed in good agreement with the simulated result at $\log \theta = 4.3$ of $S_F = 0.56$. With a spread of the three electrodes across the array, the limiting cathodic current observed increased to 64% of 3 times the current at a single electrode. The importance of radial diffusion of redox species to the electrodes is clear. The effective radial diffusion to the combined electrode area was reduced by driving the closely spaced electrodes together.

Collection Efficiency of the Intermediate in an EC′ Reaction. So far we have described experiments investigating the generation and collection of a stable redox reagent $Ru(NH_3)_6^{2+}$. Now we describe preliminary results for an intermediate that is unstable in the presence of dissolved O_2 and follows the EC′ mechanism in eq 1 and 2. The type of reaction that we have chosen for study is the reduction ($2e^-/2H^+$) of

Table VI. Grid Parameters for the Digital Simulation

		J direction (perpendicular to the electrodes)			
		N direction (parallel to the electrodes)			
limits[a]	element width	inner boundary	outer boundary	concentration	
all *J*	$\Delta y(J) = \Delta y \exp[\beta(J-1)]$	$y'(J) = \Delta y \dfrac{\exp[\beta(J-1)]-1}{\exp[\beta]-1}$	$y''(J) = \Delta y \dfrac{\exp[\beta J]-1}{\exp[\beta]-1}$	$\bar{y}(J) = \Delta y \dfrac{\exp[\beta(J-1/2)]-1}{\exp[\beta]-1}$	
$N1 \le N \le N4$[b]	$\Delta x(N) = \Delta x$	$x'(N) = (N-1)\Delta x$	$x''(N) = N\Delta x$	$\bar{x}(N) = (N-1/2)\Delta x$	
$N > N4$[b,c]	$\Delta x(N) = \Delta x \exp[\beta(N-\mathrm{N4}-1)]$	$x'(N) = \Delta x \dfrac{\exp[\beta(N-N4-1)]-1}{\exp[\beta]-1}$	$x''(N) = \Delta x \dfrac{\exp[\beta(N-N4)]-1}{\exp[\beta]-1}$	$\bar{x}(N) = \Delta x \dfrac{\exp[\beta(N-N4-1/2)]-1}{\exp[\beta]-1}$	

[a] $\Delta x = \Delta y$ in all cases. [b] $N4$ is the last uniform element corresponding to the electrode edge. [c] For the grid in Figure 1B, these equations were further modified to account for the expanding grid to the left of the generator electrode, $N < N1$, where $N1$ is the first uniform element of the electrode surface.

Table VII. Summary of Simulation Diffusion Constants

limits[a]	inner boundary	outer boundary
$J \geq 2$	$D'(J) = \dfrac{D_M}{\exp[2\beta(J - 5/4)]}$	$D''(J) = \dfrac{D_M}{\exp[2\beta(J - 3/4)]}$
$J = 1$	$D'(1) = D_M \dfrac{\exp[\beta] - 1}{\exp[\beta/2] - 1}$	$D''(1) = \dfrac{D_M}{\exp[2\beta(J - 3/4)]}$
$N < N4$[b,c]	D_M	D_M
$N > N4 + 1$[b,c]	$D'(N) = \dfrac{D_M}{\exp[2\beta(N - N4 - 5/4)]}$	$D''(N) = \dfrac{D_M}{\exp[2\beta(N - N4 - 3/4)]}$
$N = N4 + 1$[b,c]	D_M	$D''(N) = \dfrac{D_M}{\exp[2\beta(N - N4 - 3/4)]}$

[a] In all cases $\Delta x = \Delta y$. [b] $N4$ corresponds to the last element of the electrode surface. [c] For the grid in Figure 1B, the equations were modified to account for the grid expanding to the left of electrode A, i.e., for $N < N1$.

the water-soluble benzoquinone (Q) to QH_2, which undergoes a rapid follow-up reaction with dissolved O_2, eq 9 and 10.

$$Q + 2e^- + 2H^+ \rightleftarrows QH_2 \quad (9)$$

$$QH_2 + O_2 \rightarrow Q + H_2O_2 \quad (10)$$

Q = 2,5-dichloro-3,5-bis[[2-(dimethylpropylamino)-ethyl]amino]benzoquinone

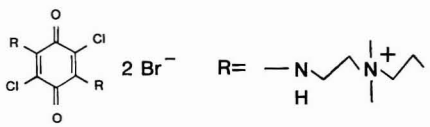

The rate constant, k, was estimated from rotating disk data for immobilized quinone, Q, on a W electrode to be $\geq 0.65 \times 10^5$ M^{-1} s^{-1} (*20*). We now describe experiments aimed at a direct measurement of this rate constant from the electrochemistry of Q at an ultramicroelectrode array. Figure 13a shows the generation and collection of QH_2 at adjacent electrodes after the aqueous Q solution (5 mM, pH 7.2 Tris buffered) was thoroughly deoxygenated by purging with N_2. The generator electrode was swept from 0.0 to −0.8 V to reduce Q ($E°$ = −0.34 V vs. SCE) (*21*) and the collector was held at 0.0 V, a potential sufficiently positive to redoxidize the generated QH_2. The collection efficiency of 57% was close to that observed at the same two electrodes with Ru^{3+} (58%). This indicated that no follow-up reaction of QH_2 occurred in the absence of O_2. For a single electrode with the collector turned off (not shown), the observed generator current was used to estimate a diffusion coefficient based on the observed currents for Ru^{3+} reduction (diffusion coefficient for Ru^{3+} taken as 0.71×10^{-5} cm^2 s^{-1} (*30*)) and assuming that the reaction remained a simple $2e^-/2H^+$ reduction at Au, as it was at W electrodes (*21*, *22*). We know that the current is proportional to the number of electrons and the diffusion coefficients from eq 8. Thus, we calculated a diffusion coefficient, $D_Q = 0.35 \times 10^{-5}$ cm^2 s^{-1}, for Q.

Figure 13 also shows the changes that occur when the same solution was purged with air (Figure 13b) and pure O_2 (Figure 13c). We observed the following: (1) the generator current was increased as expected for the catalytic regeneration of Q (eq 10); (2) the magnitude of the collection current was decreased, indicating the consumption of the intermediate QH_2 as it diffuses to the collector electrode. The increase in the generator current (obtained by subtracting the diffusion limited current in the absence of O_2 from the total current) can be used to calculate a value for the rate constant for the reaction of QH_2 with O_2 by substituting in the following expression for the catalytic current, i_{cat}, eq 11. This equation

$$i_{cat} = nFAD_QC_Q(kC_{O_2}/D_{O_2})^{1/2} \quad (11)$$

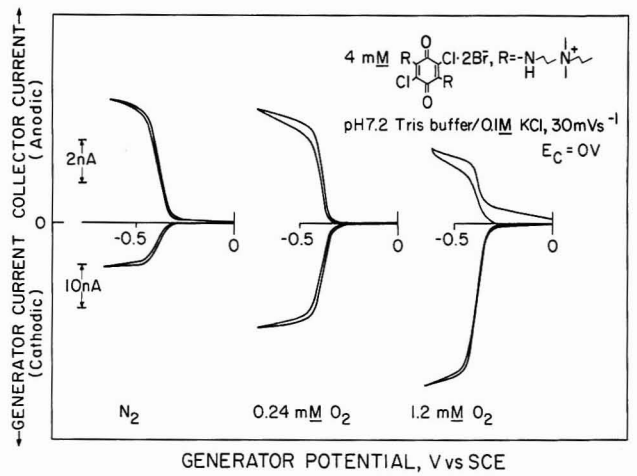

Figure 13. Generation/collection curves at Au microelectrodes for the reduction of 5 mM quinone (Q) in pH 7.2 buffered (Tris/KCl) aqueous solution with (left to right) N_2, air, and O_2 purge.

was derived in a similar fashion to that given in ref 18 for pseudo-first-order reaction of Q. Taking the concentration of O_2 in air-saturated aqueous solution as 0.24 mM (*31*), using the value of D_Q calculated earlier and taking D_{O_2} (*30*) to be 2.6×10^{-5} cm^2 s^{-1}, we obtained a rate constant of $7 (\pm 5) \times 10^6$ M^{-1} s^{-1}, which was an average value taken from several experiments at different Q and O_2 concentrations. (The error stems from the error in measuring the current and the approximation involved in calculating the area of the entire surface of the electrode, including contributions from the walls of the electrode.) This value compares with the lower limit of 0.65×10^5 M^{-1} s^{-1} calculated previously for similar surfaced-confined quinones. As a check that the pseudo-first-order conditions necessary to apply eq 8, i.e., diffusive flux of O_2 >> flux required to sustain reaction with QH_2 are operating, one can derive eq 12 (*18*). This condition was amply

$$(D_{O_2}C_{O_2}/W)[5.553/(\ln \theta) - 6.791/(\ln \theta)^2] >> D_QC_Q(kC_{O_2}/D_{O_2})^{1/2} \quad (12)$$

satisfied in the case of purging the solution with pure O_2. There was direct evidence for an excess of O_2, since a "tail" was seen at the most negative part of the sweep for the direct reduction of O_2 at the Au surface.

Turning our attention once again to the collection currents shown in Figure 13 we see that the current for QH_2 reoxidation was approximately halved in the presence of 1.2 mM O_2. While a quantitative description of this must await a full digital simulation, the decrease in collection current may be qualitatively explained on the basis of transit time arguments

similar to those used in the rotating ring–disk experiment (*32*). From a random walk model the distance, x, traveled by the diffusing quinone in time t is $x^2 \approx (2D_Q t)$. Hence, the transit time to cross the 1.2 μm interelectrode spacing was 1 ms, which was the same order as the half-life of the quinone in the pseudo-first-order reaction with 1.2 mM O_2 ($t_{1/2}(kC_{O_2}) = 2$ ms).

In the recent literature on the electrocatalytic reduction of O_2 by both soluble (*33*, *34*) and insoluble (*31*) catalysts, there has been disagreement concerning the relative importance of the contributions from heterogeneous reactions of supposed soluble catalysts. Shigehara and Anson (*31*) have pointed out that the ratio of the catalytic currents from the adsorbed and dissolved catalysts is given by eq 13, where Γ_{cat} is the surface

$$i_{ads}/i_{sol} = k^{1/2}\Gamma_{cat}/(D_{O_2}{}^{1/2}C_{cat}{}^{1/2}) \quad (13)$$

excess of the adsorbed catalyst. Even with submonolayer coverage (barely detectable by rotating disk techniques), say 10^{-11} mol cm^{-2}, and a rate constant of $k = 4 \times 10^{10}$ M^{-1} s^{-1}, the adsorbed catalyst would have a comparable turnover rate to the dissolved catalyst present in millimolar concentration. In the context of the quinone experiment described in this paper, the absence of such complications was ensured by cleaning the electrodes prior to each measurement. Furthermore, the collection currents for the dissolved QH_2 species were decreased in accordance with the half-life calculated assuming a solution reaction with O_2.

CONCLUSIONS

Steady-state currents are observed for linear potential sweep voltammetry of solution redox species at microelectrodes. The significant contribution of radial diffusion of redox species to and from the microelectrode obviates the need for forced hydrodynamics otherwise necessary to obtain steady current behavior. Moreover, the collection efficiencies attainable at microelectrode arrays are significantly larger than those usually obtained at RRDEs. The observation that the limiting current for the redox reaction of a solution species at two closely spaced microelectrodes is significantly less than the sum of the currents observed at each microelectrode separately provides evidence for shielding and the importance of radial diffusion.

From the digital simulation of microelectrode arrays and the use of these arrays as RRDE-type probes, we can draw several conclusions. One of the key factors allowing these systems to work is the small gap size. As the interelectrode spacing is reduced by Pt deposition, larger collection efficiencies are obtained in generation–collection experiments. In this paper, we report efficiencies of ca. 80% for gap sizes of ca. 0.2 μm. Although it may be possible to reduce the gap further, the gain in efficiency will probably not be sufficient to justify the efforts. In addition, with smaller and smaller gaps, migration may become important. The effect of migration may be useful for the study of intermediates.

The digital simulations reported here are useful for simulating current–time behavior for single microband electrodes as well as for predicting the collection efficiency of RRDE-type experiments at arrays. In future work, we hope to simulate in detail the experiments of homogeneous follow-up reactions briefly outlined in this paper.

ACKNOWLEDGMENT

We thank Diane K. Smith for the sample of the quinone compound and S. W. Feldberg for his assistance and comments on the digital simulations.

APPENDIX: DIGITAL SIMULATION MODEL

The digital simulation methods follow those used previously in electrochemical problems combining the uniform (*24*, *25*) and exponentially expanding space grids (*26*, *28*), Figure 1. The distance in the N direction across the electrode surface, NELE, and the interelectrode gap, NGAP, is divided by a uniform space grid while in the J direction, perpendicular to the substrate and beyond the outer electrode edge in the parallel, N direction, the grid expands exponentially. Each part of the problem will be treated separately beginning with the expanding portions of the simulation. The mathematical treatment generally applies to simulations of a single band and to arrays of band electrodes.

The development of the equations describing the expanding grid elements follows that in ref 26. The width of the expanding box, $\Delta y(J)$ is given by eq A1, which reduces to the uniform grid size when $\beta = 0$. β is the exponential grid factor

$$\Delta y(J) = \Delta y \exp[\beta(J - 1)] \quad (A1)$$

and $\beta = 0.5$ (*26*) for all expanding portions of the grid. The outer boundary of the box is at $y''(J)$, eq A2, while the inner boundary is at $y'(J)$, eq A3. The concentration within each

$$y''(J) = \Delta y(\exp[\beta J] - 1)/(\exp[\beta] - 1) \quad (A2)$$

$$y'(J) = \Delta y(\exp[\beta(J - 1)] - 1)/(\exp[\beta] - 1) \quad (A3)$$

expanded volume element is taken at the position given in eq A4. In the limit as $\beta \to 0$, eq A2–A4 reduce to

$$\bar{y}(J) = \Delta y(\exp[\beta(J - 1/2)] - 1)/(\exp[\beta] - 1) \quad (A4)$$

those for a uniform grid where the concentration is taken at the midpoint of each box. A summary of the grid parameters is presented in Table VI.

The finite difference form of Fick's second law, eq A5, in

$$\partial C/\partial t = D[(\partial^2 C/\partial x^2) + (\partial^2 C/\partial y^2)] \quad (A5)$$

two dimensions is given by eq A6 and can be used to calculated

$$[C(x,y,t+\Delta t) - C(x,y,t)]/\Delta t = D[(C(x+\Delta x,y,t) - C(x,y,t))/\Delta\bar{x}^2 - (C(x,y,t) - C(x-\Delta x,y,t))/\Delta\bar{x}^2 + (C(x,y+\Delta y,t) - C(x,y,t))/\Delta\bar{y}^2 - (C(x,y,t) - C(x,y-\Delta y,t))/\Delta\bar{y}^2] \quad (A6)$$

the change in concentration due to diffusion in a *uniform space grid* where $\Delta x = \Delta y$ for all N and J. The diffusion coefficient, D, the time increment, Δt, and the space increment, Δx, can be gathered into dimensionless simulation diffusion constant, D_m, eq A7. For our simulations, we assume

$$D_m = D\Delta t/\Delta x^2 = D\Delta t/\Delta y^2 \leq 0.25 \quad (A7)$$

that $D_{Ox} = D_{Red}$ and a value of $D_m = 0.24$ is used throughout.

The flux, f, in each of the volume elements is calculated by substituting the values of $\Delta x(N)$, $\Delta y(J)$, $\bar{x}(N)$, and $\bar{y}(J)$ from Table VI into eq A6 which results in eq A8. The flux

$$f = D\Delta t/\Delta y(J)[[C(N,J+1) - C(N,J)]/[\bar{y}(J+1) - \bar{y}(J)] - [C(N,J) - C(N,J-1)]/[\bar{y}(J) - \bar{y}(J-1)]] + D\Delta t/\Delta x(N)[[C(N+1,J) - C(N,J)]/[\bar{x}(N+1) - \bar{x}(N)] - [C(N,J) - C(N-1,J)]/[\bar{x}(N) - \bar{x}(N-1)]], \text{ for } N,J \geq 2 \quad (A8)$$

equation, eq A8 can be simplified by redefining the dimensionless diffusion constant taking into account the modified boundaries so that now the simulation diffusion coefficients are a function of distance. At the outer boundary, $y''(J)$, of the expanded elements, $D''(J)$ is given by eq A9, while eq A10

$$D''(J) = D_M/\exp[2\beta(J - 3/4)] \quad (A9)$$

$$D'(J) = D_M/\exp[2\beta(J - 5/4)], J \geq 2 \quad (A10)$$

is the expression for the diffusion constant at the inner boundary. A summary of the diffusion constants is presented in Table VII.

To calculate the current, the flux at the electrode surface must be calculated. The electrode width, W, is divided by

the number of boxes corresponding to the electrode, NELE, such that eq A11 holds. During a simulation time iteration,

$$\Delta x = \Delta y = W/\mathrm{NELE} \qquad \text{(A11)}$$

K, the flux in each of the NELE boxes representing the electrode is calculated and the individual fluxes, $f_K(N)$, are then summed to yield the total flux, f_K. The average flux in the box N at the electrode is given by eq A12. Since eq A12

$$f_K(N) = D'(1)(C(N,1) - C(N,0)) \qquad \text{(A12)}$$

is the average flux during the time increment, K, the flux at $t = K\Delta t$ is given by the average of the fluxes, $f_K(N) + f_{K+1}(N)$ and the total dimensionless flux, F_K, is calculated by eq A13.

$$F_K = \sum_{N=1}^{\mathrm{NELE}} (f_K(N) + f_{K+1}(N))/(2D_m) \qquad \text{(A13)}$$

The total flux, F_K, is related to the corresponding dimensionless current, $Z(K)$, by eq A14. $Z(K)$ can be expressed for

$$F_K/\mathrm{NELE} = i/nFDCl = Z(K) \qquad \text{(A14)}$$

various time domains which depend on the dimensionless parameter θ defined in eq A15. In eq A15 D is the real

$$\theta = 4Dt/W^2 = 4D_mK/(\mathrm{NELE})^2 \qquad \text{(A15)}$$

diffusion coefficient (cm^2/s), t is the real time in (s), W is the electrode width (cm), while D_m, K, and NELE are the corresponding dimensionless simulation parameters. As shown by Tallman et al. (*29*), in the limit of long times, $\log \theta >$ ca. 2.5, the total dimensionless flux is given by eq. A16. For short

$$Z(K) = i/nFDCl = 5.553/(\ln \theta) - 6.791/(\ln \theta)^2 \qquad \text{(A16)}$$

times, i.e., $\log \theta <$ ca. 1.0, the flux can be calculated by eq A17 (see Figure 2) (*29*, *35*) where eq A16 derives from the long time

$$Z(K) = i/nFDCl = 2/(\pi\theta)^{1/2} + 1 \qquad \text{(A17)}$$

expression for the current at a band electrode (*29*) and eq. A17 follows from eq 40 in ref 35.

Registry No. Q, 103190-68-7; QH_2, 103190-69-8; $Ru(NH_3)_6^{3+}$, 18943-33-4; $Ru(NH_3)_6^{2+}$, 19052-44-9; $Ru(NH_3)_6Cl_3$, 14282-91-8; LiCl, 7447-41-8; $LiNO_3$, 7790-69-4; $NaNO_3$, 7631-99-4; KCl, 7447-40-7; O_2, 7782-44-7; Au, 7440-57-5; Pt, 7440-06-4.

LITERATURE CITED

(1) Wightman, R. M. *Anal. Chem.* **1981**, *53*, 1125A, and references therein.
(2) Bond, A. M.; Fleischmann, M.; Robinson, J. *J. Electroanal. Chem.* **1984**, *168*, 299.
(3) Bond, A. M.; Fleischmann, M.; Robinson, J. *J. Electroanal. Chem.* **1984**, *172*, 11.
(4) Bindra, P.; Brown, A. P. Fleischmann, M.; Pletcher, D. *J. Electroanal. Chem.* **1975**, *58*, 31.
(5) Mallouk, T. E.; Cammarata, V. C.; Crayston, J. A.; Wrighton, M. S., submitted for publication in *J. Phys. Chem.*
(6) White, H. S.; Kittlesen, G. P.; Wrighton, M. S. *J. Am. Chem. Soc.* **1984**, *106*, 5375.
(7) Kittlesen, G. P.; White, H. S.; Wrighton, M. S. *J. Am. Chem. Soc.* **1984**, *106*, 7389.
(8) Paul, E. W.; Ricco, A. J.; Wrighton, M. S. *J. Phys. Chem.* **1985**, *89*, 1441.
(9) Thormann, W.; van den Bech, P.; Bond, A. M. *Anal. Chem.* **1985**, *57*, 2764.
(10) Chidsey, C. E.; Feldman, B. J.; Lundgren, C.; Murray, R. W. *Anal. Chem.* **1986**, *58*, 601.
(11) Kittlesen, G. P.; White, H. S.; Wrighton, M. S. *J. Am. Chem. Soc.* **1985**, *107*, 7373.
(12) Kittlesen, G. P.; Wrighton, M. S. *J. Mol. Electron.*, in press.
(13) Thackeray, J. W.; White, H. S.; Wrighton, M. S. *J. Phys. Chem.* **1985**, *89*, 5133.
(14) Wrighton, M. S. *Comments Inorg. Chem.*, in press.
(15) Albery, W. J.; Hitchman, M. L. In *Ring-Disk Electrodes*; Clarendon Press: Oxford, 1971.
(16) Bruckenstein, S.; Miller, B. *Acc. Chem. Res.* **1977**, *10*, 54.
(17) Bard, A. J.; Faulkner, L. R. In *Electrochemical Methods*; Wiley: New York, 1980; p 429.
(18) Fleischmann, M.; Lassere, F.; Robinson, J.; Swan, D. *J. Electroanal. Chem.* **1984**, *177*, 97.
(19) Dayton, M. A.; Ewing, A. G.; Wightman, R. M. *Anal. Chem.* **1980**, *52*, 2392.
(20) Miller, B.; Visco, R. E. *J. Electrochem. Soc.* **1968**, *115*, 251.
(21) Smith, D. K.; Calabrese, G. S.; Wrighton, M. S., unpublished results.
(22) Calabrese, G. S.; Buchanan, R. M.; Wrighton, M. S. *J. Am. Chem. Soc.* **1982**, *104*, 5786.
(23) Calabrese, G. S.; Buchanan, R. M.; Wrighton, M. S. *J. Am. Chem. Soc.* **1983**, *105*, 5594.
(24) Feldberg, W. S. In *Electroanalytical Chemistry*; Bard, A. J., Ed.; Marcel Dekker: New York, 1979; Vol. 3.
(25) Maloy, J. T. In *Laboratory Techniques in Electroanalytical Chemistry*; Kissinger, P. T., Ed., Marcel Dekker: New York, 1984.
(26) Feldberg, W. S. *J. Electroanal. Chem.* **1981**, *127*, 1.
(27) Reller, H.; Kirowa-Eisner, E.; Gileadi, E. *J. Electroanal. Chem.* **1984**, *161*, 247.
(28) Joslin, T.; Pletcher, D. *J. Electroanal. Chem.* **1974**, *49*, 171.
(29) Coen, S.; Cope, D. K.; Tallman, D. E., submitted for publication in *J. Electroanal. Chem.*
(30) Kovach, P. M.; Caudill, W. L.; Peters, D. G.; Wightman, R. M. *J. Electroanal. Chem.* **1982**, *185*, 285.
(31) Shigehara, K.; Anson, F. C. *J. Phys. Chem.* **1982**, *86*, 2776.
(32) Bruckenstein, S. B.; Feldman, G. A. *J. Electroanal. Chem.* **1965**, *9*, 395.
(33) Kobayashi, N.; Fujihara, M.; Osa, T.; Kuwana, T. *Bull. Chem. Soc. Jpn.* **1980**, *53*, 2195.
(34) Forshey, P. A.; Kuwana, T. *Inorg. Chem.* **1983**, *22*, 699.
(35) Oldham, K. B. *J. Electroanal. Chem.* **1981**, *122*, 1.

RECEIVED for review January 24, 1986. Accepted May 5, 1986. We thank the following agencies for support of this research: National Science Foundation (CHE 8402135), the Office of Naval Research, and the Defense Advanced Research Projects Agencies.

CORRESPONDENCE

Charge Exchange in Binary Mixtures of Polycyclic Aromatic Hydrocarbons Using Photoionization–Ion Mobility Spectrometry

Sir: Ion mobility spectrometry (IMS) has been limited in convenience of operation and breadth of application by complications in processes used to create product ions from gaseous analyte. While chemical ionization (CI) may provide sensitivities directly in the low-parts-per-billion or sub-parts-per-billion ranges without sample enrichment (*1–3*), analytical response with mixtures is governed by competitive ionization reactions (*4–6*). Consequently, analysts typically have limited or no external control (apart from choice of reagent gas) over IMS selectivity or interferences. Indeed, some early reports on poor resolution of binary mixtures in IMS (*7*) may have been due to preferential ionization rather than fundamental limitations in separations based on ion mobility. Although competitive ionization reactions were recognized by some workers early in IMS development (*8*, *9*), selectivity in competitive CI reactions, including proton af-

0003-2700/86/0358-2331$01.50/0 © 1986 American Chemical Society

Table I. Summary of IMS Spectra for Aromatic Hydrocarbons

compound	mol wt, amu	IP, eV	drift time,[a] ms		reduced mobilities, $cm^2/(V\ s)$			ref
			CI	PI	CI	PI	reported	
benzene	78	9.23	6.8, 7.8	7.1	2.28, 1.98	2.32	CI: 2.48, 2.33, 2.08	22
							PI: 2.61, 2.45	22
naphthalene	128	8.13	8.4	8.8	1.84	1.87	CI: 1.84	23
							PI: 2.21, 2.09, 1.90	22
anthracene	178	7.43	9.5	10.2	1.63	1.61	CI: 1.77	23
							PI: 1.73	23
pyrene	202	7.43	10.2	10.9	1.52	1.51	CI: n/a	
							PI: n/a	

[a] Differences in drift times were due largely to differences in total electrical fields of 287 V/m for CI-IMS and of 270 V/m for PI-IMS. This difference was due to particular total current and total tube lengths from separate IMS configurations.

finity and electron capture (*4–6*), was quantified for binary and ternary mixtures in IMS only recently. This was accomplished by using a unidirectional flow, closed-tube IMS with low residence time of analyte in the CI source.

A measure of user-control in IMS ionization was attempted through use of alternate reagent gases (*10*) and use of wavelength selectivity in photoionization (*11–14*). Lasers and inexpensive discharge lamps were adapted to IMS instrumentation for ionization of aromatic hydrocarbons in the presence of alkanes, aromatic amines, and other aromatic hydrocarbons. Although photoionization (PI) has been used successfully in other ion separation techniques including laser–mass spectrometry (*15, 16*), ion–molecule collisions in IMS occur at a rate of $10^{10}\ s^{-1}$. One consequence of these collisions may be charge-transfer reactions which are known and used elsewhere in mass spectrometry at 10^{-3} torr to atmospheric pressure (*17–20*). However, charge-transfer reactions between photon-created ions and neutral molecules at low density and atmospheric pressure have not been reported and the possibility for such reactions is unknown. One practical consequence, should charge-transfer reactions occur in IMS, is that improved methods for selective ionization of analytes such as laser ionization may still be more general than expected with a concurrent loss in selectivity.

The objective of this report was to (a) determine if charge-transfer reactions occurred in IMS, (b) explore trends in charge-transfer selectivity in binary mixtures of aromatic hydrocarbons, (c) quantify behavior of photoionization–IMS response curves, and (d) compare these events to CI selectivity of the same compounds. Aromatic hydrocarbons were chosen for convenient comparison of results with prior findings in PI–IMS.

EXPERIMENTAL SECTION

Instrumentation. An ion mobility spectrometer, designed and constructed at NMSU, has been described in detail (*21*) and was used without charge except for replacement of the radioactive ion source with a PI source and mount. A 10.2 eV hydrogen discharge lamp (HNU Corp., Boston, MA) was used for PI–IMS with a mount similar to one described by Hill et al. (*22*). The drift region in this IMS was 9 cm and the drift gas was nitrogen (99.5% grade). In addition, a small flow of nitrogen gas at 50 mL/min was forced against the face of the lamp and through the lamp mount to prevent diffusion of air into the ionization chamber and subsequent quenching of photons. Conditions for analysis were as follows: tube temperature, 211 °C; reaction region field, 133 V/cm; drift region field, 287 V/cm; drift gas flow, 300 mL/min; shutter time and speed, 0.1 ms pulse at 28 Hz; amplification, 10^{-11} to 10^{-12} A/V; and barometric pressure, 660–670 torr.

Procedures. Two sets of studies completed here were (a) determination of response curves for aromatic compounds using CI- and PI-MIS and (b) measurement of PI–IMS response for binary mixtures of test compounds with one component at a fixed concentration while second component was varied in concentration. Sample was introduced into the IMS through sampling

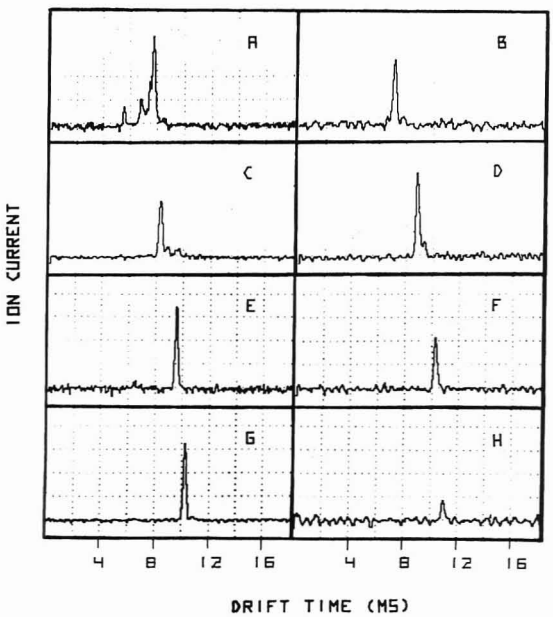

Figure 1. Ion mobility spectra (A) benzene–^{63}Ni, (B) benzene–PI, (C) naphthalene–^{63}Ni, (D) naphthalene–PI, (E) anthracene–^{63}Ni, (F) anthracene–PI, (G) pyrene–^{63}Ni, and (H) pyrene–PI.

headspace vapors over pure solid or liquid samples at controlled temperatures with a small flow of nitrogen gas. Vapor pressures and dilution from drift gas flows were used to calculate concentrations. Concentrations actually delivered to the IMS were calibrated independently by use of gas chromatography. Purity of pyrene (PYR), naphthalene (NAP), and anthracene (ANT) was 99.9% and benzene (BEN) was pesticide grade. Flows of gases were controlled with Nupro fine metering values. In binary mixture studies, two independent sample inlet systems were used to separately control concentrations of each compound delivered to the IMS.

RESULTS AND DISCUSSION

IMS Response to Pure Compounds. Spectra from chemical ionization and photoionization of benzene and selected PAH are shown in Figure 1 and were consistent with prior CI- and PI–IMS studies. Drift times and reduced mobilities are summarized in Table I. The predominant reactant ion in CI–IMS here was $H(H_2O)_2^+$, but small amounts of NO^+ and NH_4^+ were also detected. Except for benzene, which showed three product ion peaks, CI-generated product ions were intense single peaks. All product ions in PI–IMS spectra were also single components. Product ions for aromatic compounds in CI–IMS were mass identified elsewhere as MH^+ (*9*) while product ions in PI–IMS were proposed to be M^+ (*11*). Other product ions based on the minor reactant ions were also observed at very low intensities, were considered minor complications, and were neglected in treatment of results. Response curves for PI–IMS and CI–IMS of benzene, naphthalene, anthracene, and pyrene are shown in Figures

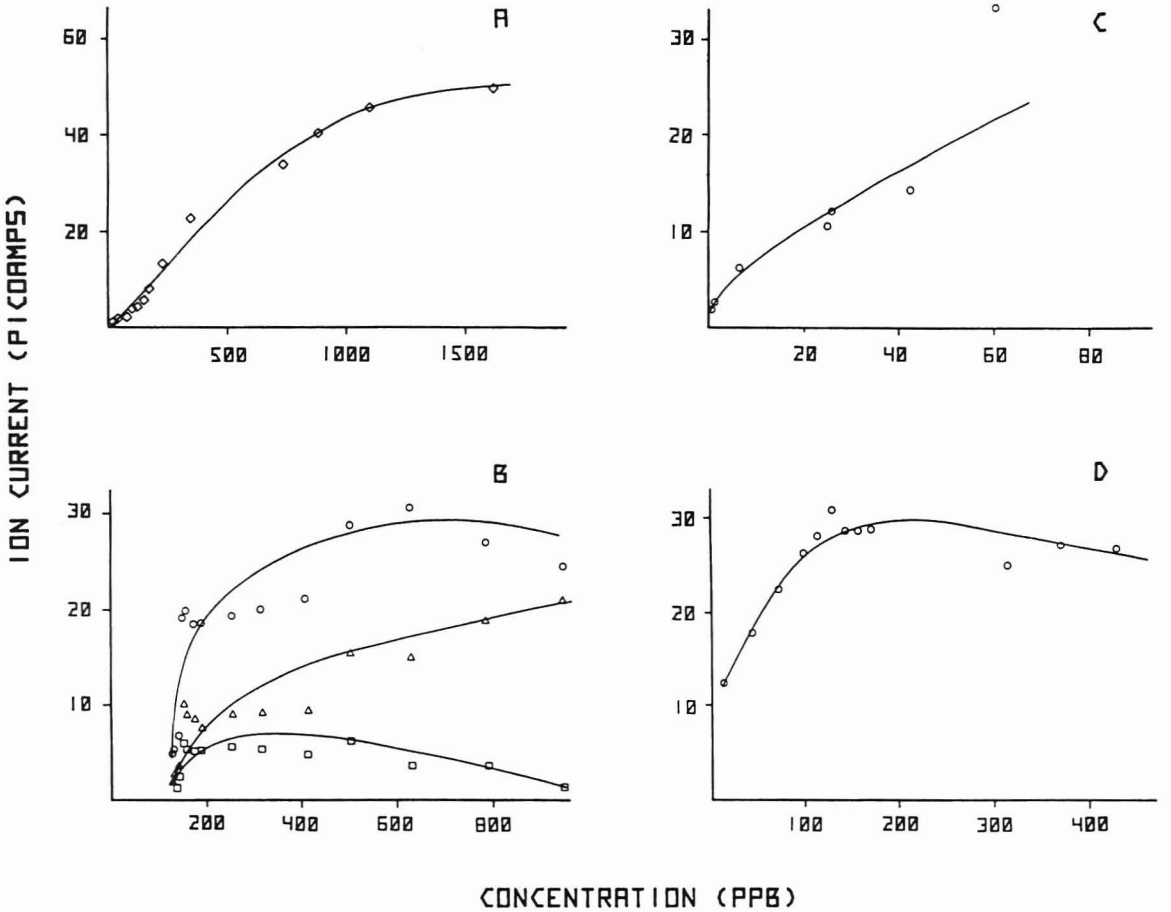

Figure 2. Response curves for individual compounds (A) benzene–PI, (B) benzene–^{63}Ni, (C) naphthalene–PI, and (D) naphthalene–^{63}Ni.

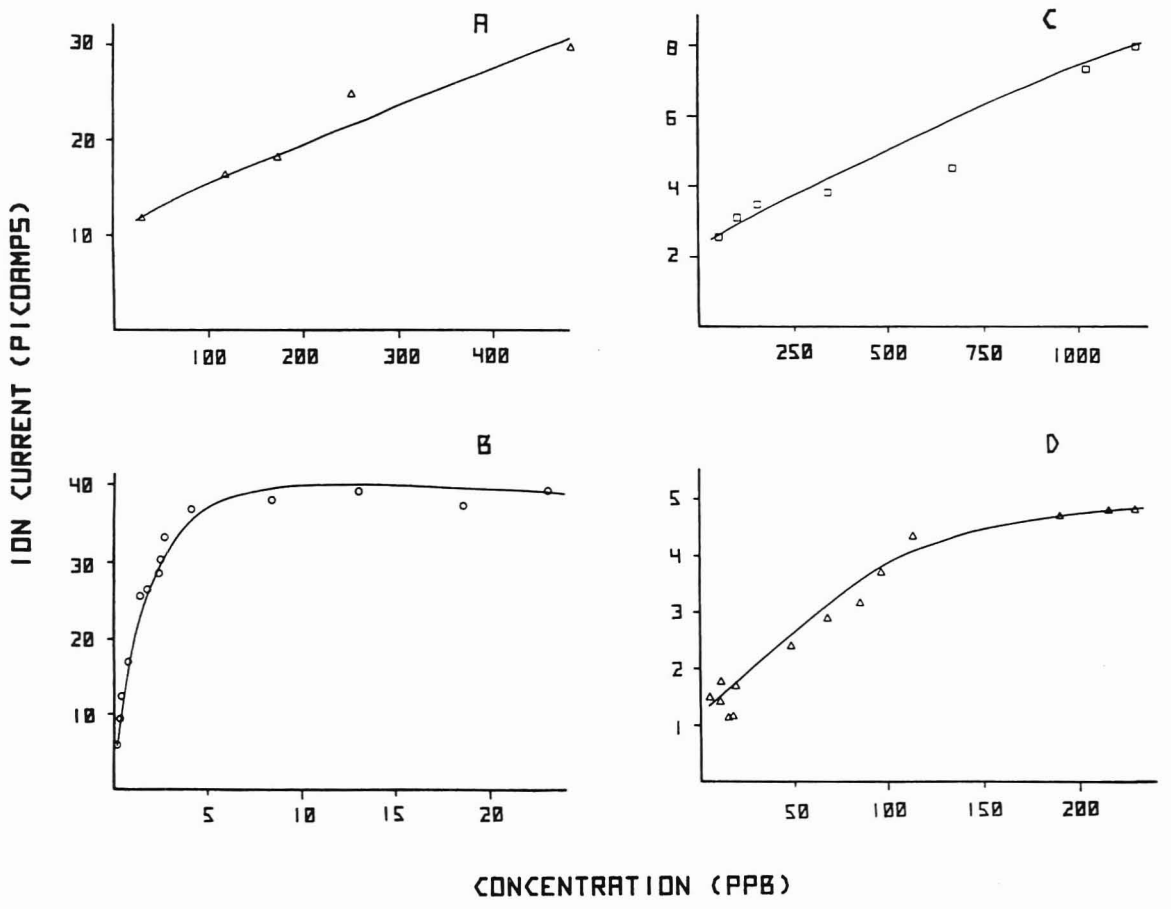

Figure 3. Response curves for (A) anthracene–PI, (B) anthracene–^{63}Ni, (C) pyrene–PI, and (D) pyrene–^{63}Ni.

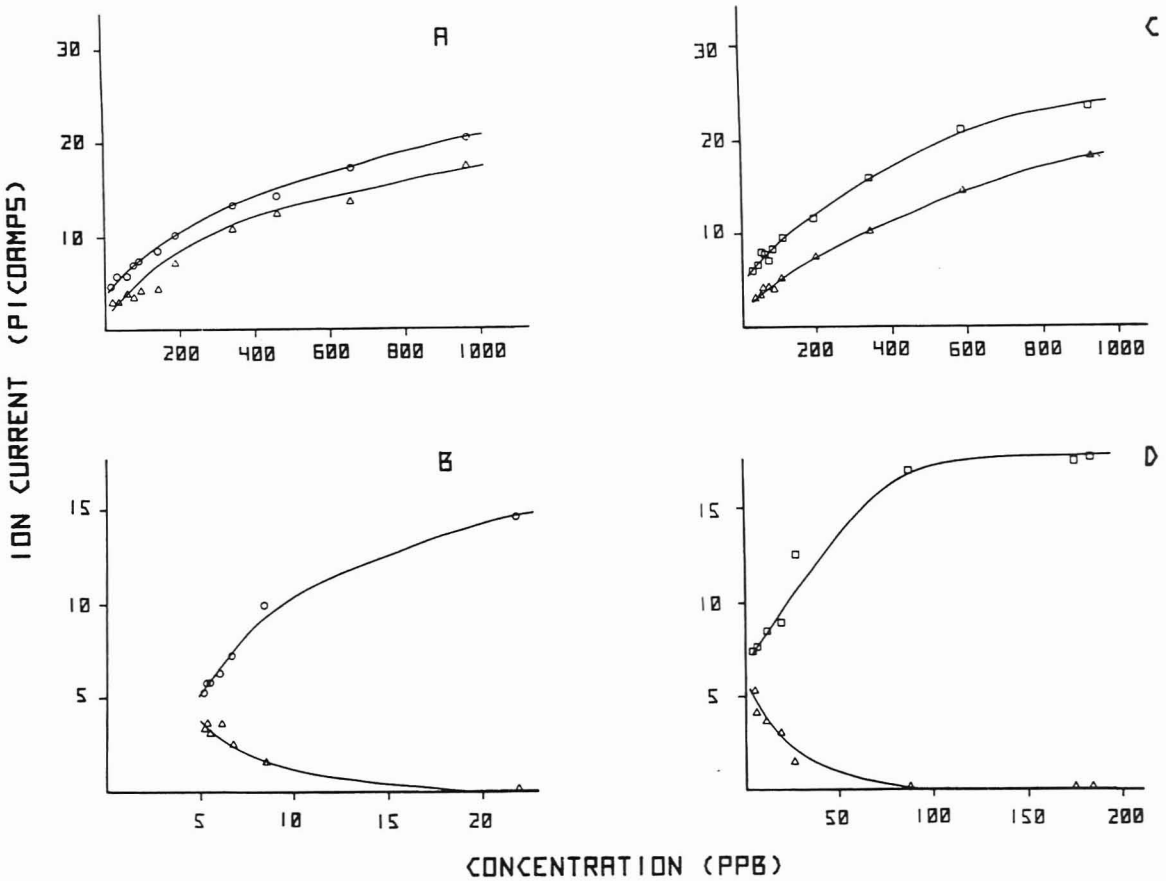

Figure 4. Plots of ion current vs. concentration for binary mixtures. A and B benzene/naphthalene (A and B); C and D benzene/anthracene (C and D). In A benzene was incremented while naphthalene concentration was fixed at 5.19 ppb. Samples are Δ, benzene, and O, naphthalene. In B, naphthalene was incremented while benzene concentration was fixed at 17.2 ppb; symbols are Δ, benzene, and O, naphthalene. In C, benzene was incremented and anthracene concentration was fixed at 4.26 ppb; symbols are Δ, benzene, and O, anthracene. In D, anthracene was incremented and benzene concentration was fixed at 17.2 ppb; symbols are Δ, benzene, and O, anthracene.

2 and 3. Plots for CI–IMS were included, in part, for describing PI behavior as referenced to more common CI methods. In CI response curves for every aromatic hydrocarbon, plots become level to some degree within a 1.5- to 10-fold range of the detection limit. This behavior agreed favorably with charge conservation in existing IMS ionization theory in that the number of product ions is limited by the initial number of available reactant ions (*23*). Although reactant ion intensity from CI response curves was not shown in Figures 2 and 3, increased product ion intensity was accompanied by decreased reactant ion intensity in a regular even fashion for each aromatic hydrocarbon. Detection limits in PI–IMS were 10-fold less sensitive than those for CI-IMS, but the linear range for PI-IMS was 3- to 100-fold improved over CI–IMS. While CI response was limited by available reactant ions, PI response should be limited only by photon density and by quenching at high analyte concentrations. These findings agreed favorably with a linear range of 10^2 for dc-mode electron capture detectors (*24*) and of 10^6 for photoionization detectors (*25*). Curvature in the PI response was possibly due to photon quenching by oxygen which diffused against the purge gas into the region between lamp window and analyte flow. Despite relatively poor limits of detection PI showed promise for ionization in IMS and may be more suitable than CI for quantitative analysis of mixtures.

PI–IMS Response with Binary Mixtures. Results from addition of two aromatic hydrocarbons to the PI–IMS are shown in Figure 4. Response curves are shown for BEN/NAP mixtures in frames A and B and for BEN/ANT in frames C and D. In frame A, NAP concentration was set at 5.19 ppb and the concentration for BEN was increased from 10 to 1000 ppb. These values were within the linear ranges for both compounds. On the basis of response curves for single analytes, the peak height for NAP should have remained level at 5 pA if NAP was independent of product ions from BEN. Moreover, the peak height for BEN should have increased from 23 pA (at 500 ppb) to 39 pA (at 1000 ppb). This behavior was not observed experimentally with binary mixtures since, as the concentration of BEN was increased, peak height for BEN increased from 12 pA (at 500 ppb) to only 18 pA (at 1000 ppb). Also, the peak height for NAP (still at fixed concentration) increased from 15 pA (at 500 ppb for BEN) to 20 pA (at 1000 ppb for BEN). While direct ionization efficiencies should not be expected to vary significantly with such small changes in gas matrix, this behavior may be rationalized as a collisional charge-transfer reaction from BEN to NAP. This was further supported through summation of charge intensity for all product ions in which charge was conserved regardless of charge location. For example, peak height for BEN alone should have been 39 pA at 1000 ppb BEN in the binary mixture study whereas the summed product ion peak heights for BEN and NAP was 38 pA at an intensity ratio of 1.1:1 for BEN:NAP. These results are unsurprising since benzene has been proposed as a charge-transfer reagent gas for CI–IMS and was demonstrated to have reaction properties superior to nitrogen oxide or methane (*17*). Fenselau also showed that charge transfer will occur when ionization potentials (IP) for analyte are less than IP (9.3 eV) for BEN; no charge-transfer ionization occurred for compounds with IP > 9.3 eV. These principles were also noted by Carroll et al. (*18*) and by Hites (*19*). Thus, the trends seen the BEN/NAP mixture study can be explained as enhancement of M^+ for NAP (IP = 8.15 eV) through charge-transfer from BEN. Although neutral densities were very low at $\sim 10^8$ mol/cm^3, collisional rates of 10^{10}

s^{-1} must have been sufficient over an 0.1-s lifetime in the ion source to permit ion/molecule charge-transfer reactions. The parallel behavior for BEN and NAP curves suggested a 1:1 exchange ratio.

In contrast to behavior described above, when the BEN concentration was fixed at 17.2 ppb and NAP was metered into the ion source, increased concentrations of NAP lead to decreased intensity of M^+ for BEN. Since charge will reside on the compound with lower IP (NAP), curves in Figure 4b were consistent with a competitive collisional acquisition of charge. The creation of M^+ for BEN through charge transfer from NAP should not occur and was not observed. Results from binary mixture studies with PI–IMS for BEN/ANT are shown in Figure 4C,D and behavior paralleled results from the BEN/NAP study. At fixed concentration of 4.26 ppb for ANT (IP = 7.43 eV), increased concentration of BEN caused an enhanced intensity in M^+ for ANT. While peak heights for ANT should have remained constant at 2 pA with no charge transfer the actual measured values were 5, 18, and 23 pA at BEN concentrations of 10, 500, and 1000 ppb, respectively. The difference in peak current for BEN from 500 to 1000 ppb should have been 16 pA but was only 10 pA. However, peak heights for benzene were 13 pA at 500 ppb and 18 pA at 1000 ppb rather than expected values of 23 and 39 pA, respectively. Conservation of charge was generally obeyed. Results from BEN/NAP and BEN/ANT studies differed in that the distance between curves for individual product ions in BEN/ANT was larger than that for BEN/NAP. This difference may be related to ΔIP values of 1.88 for BEN/ANT but only 1.15 for BEN/NAP. As observed with NAP/BEN studies, increased concentration of ANT caused nearly complete elimination of BEN at fixed concentration. Clearly, molecular properties in the form of ionization potentials govern the final observed IMS response for binary mixtures even when compounds are photoionized. Similar results should also be expected with mixtures of BEN and other aromatic hydrocarbons including PYR (IP = 7.43 eV) as well as with combinations of NAP/ANT, PYR/NAP, and PYR/ANT. Other combinations of PAH were studied and such investigations would be better suited for IMS/mass spectrometry.

CONCLUSION

The importance of these results is that analytical utility of photoionization as a means of tunable selectivity in analysis by IMS can be severely complicated by charge-transfer reactions. Generally, this means that the analyst is again at a disadvantage when working with samples of unknown matrix, especially when the IP for the analyte of interest is greater than IP values for interferences. While photoionization does add a measure of class selectivity in ionization, ion–molecule chemistry will still govern quantitative response within a chemical class. Preseparation of these compounds on a capillary GC (*22*) may afford fewer complications than are found with direct analysis of a mixture. Alternatively, extensive ionization of all components to M^+ ions in a mixture may eliminate complications from change-exchange selectivity; however, this would negate the inherent advantages of selective ionizations.

Registry No. Benzene, 71-43-2; naphthalene, 91-20-3; anthracene, 120-12-7; pyrene, 129-00-0.

LITERATURE CITED

(1) Karasek, F. W. *Int. J. Environ. Anal. Chem.* **1972**, *2*, 157.
(2) Karasek, F. W.; Cohen, M. J.; Carroll, D. L. *J. Chromatogr. Sci.* **1971**, *9*.
(3) Karasek, F. W. *Res./Dev.* **1970**, *21*(3), 34.
(4) Vandiver, V. J.; Leasure, C. S.; Eiceman, G. A. *Int. J. Mass Spectrom. Ion Processes*, in press.
(5) Vandiver, V. J.; Eiceman, G. A., submitted for publication in *J. Chem. Phys.*
(6) Vandiver, V. J.; Eiceman, G. A., in preparation.
(7) Keller, R. A.; Metro, M. M. *Sep. Purif. Methods* **1974**, *3*, 207.
(8) Karasek, F. W.; Spangler, G. E. *J. Chromatogr. Lib.* **1981**, *20*, 377.
(9) Carroll, D. I.; Dzidic, I.; Stillwell, R. N.; Horning, M. G.; Horning, E. C. *Anal. Chem.* **1974**, *46*, 6.
(10) Proctor, C. J.; Todd, J. F. J. *Anal. Chem.* **1984**, *56*, 1794.
(11) Lubman, D. M.; Kronick, M. N. *Anal. Chem.* **1982**, *54*, 1546.
(12) Lubman, D. M.; Kronick, M. N. *Anal. Chem.* **1983**, *55*, 867.
(13) Lubman, D. M.; Kronick, M. N. *Anal. Chem.* **1983**, *55*, 1486.
(14) Eiceman, G. A., Anderson, G.; Leasure, C. S.; Vandiver, V. J.; Tiee, J.; Danen, W. *Anal. Chem.* **1986**, *58*, 1690.
(15) Mattern, D. E.; Lin, F.; Hercules, D. M. *Anal. Chem.* **1984**, *56*, 2762.
(16) Tabet, J.; Cotter, R. J. *Anal. Chem.* **1984**, *56*, 1662.
(17) Subra Rao, S. C.; Fenselau, C. *Anal. Chem.* **1973**, *50*, 511.
(18) Simonsick, W. J.; Hites, R. A. *Anal. Chem.* **1984**, *56*, 2749.
(19) Lane, D.; Sakuma, T.; Kuan, E. *Polynuclear Aromatic Hydrocarbons*; International Symposium on Chemical and Biological Effects, 4th ed.; Batelle Press: Columbus, OH, 1980, p 199.
(20) Horning, E. C.; Carroll, D. I.; Dzidic, I.; Haegale, K. D.; Horning, M. G.; Stillwell, R. N. *Adv. Mass Spectrom. Biochem. Med.* **1976**, *1*, 1.
(21) Eiceman, G. A.; Leasure, C. S.; Vandiver, V. J.; Rico, G. *Anal. Chim. Acta*, in press.
(22) Baim, M. A.; Eatherton, R. L.; Hill, H. H. *Anal. Chem.* **1983**, *55*, 1761.
(23) Lubman, D. *Anal. Chem.* **1984**, *56*, 1298.
(24) Poole, C. S.; Zlatkis, A. *J. Chromatogr. Lib.* **1981**, *20*, 23.
(25) Driscoll, J. N. *J. Chromatogr.* **1977**, *134*, 49.

G. A. Eiceman*
V. J. Vandiver

Department of Chemistry
New Mexico State University
Las Cruces, New Mexico 88003

RECEIVED for review November 21, 1985. Accepted April 22, 1986.

Excited Triplet State Infrared Spectrometry as an Analytical Technique

Sir: Fourier transform infrared spectrometry (FTIR) has been used extensively in the analytical laboratory for the identification of compounds. FTIR, as well as dispersive infrared, has been limited when identification of a single compound from a complex mixture of compounds is required, due to the numerous vibrational bands present. Although FTIR has the capability to perform intricate subtraction routines, it would be helpful to simplify IR spectra for some analytical applications. For a new IR method to be advantageous, it would have to limit the number of absorption bands to a handful. A new method, which we have labeled as excited triplet state infrared spectrometry (ETSIR), simplifies complex IR spectra so that only a few bands appear, allowing for unequivocal identification of components within a mixture.

The method relies on creating a steady-state population of molecules in their triplet state. Upon continuous wave (CW) excitation of a frozen, dilute solution, intramolecular photophysical processes (in which the excitation rate and the triplet decay rate constitute the critical dynamics) establish a substantial fraction of excited triplet molecules, relative to those

0003-2700/86/0358-2335$01.50/0 © 1986 American Chemical Society

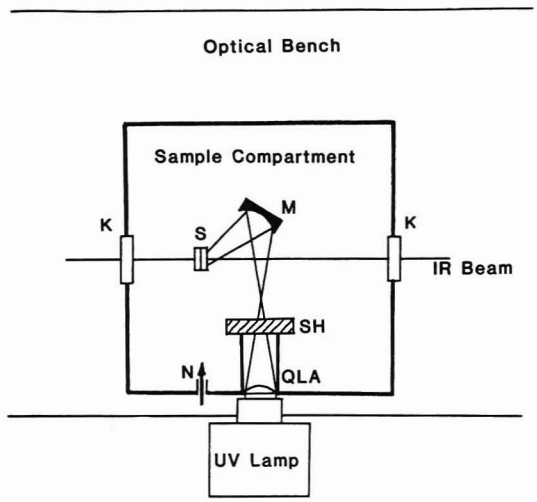

Figure 1. Schematic diagram of the optical bench for the ETSIR experiment. Abbreviations are as follows: M, reflective mirror; K, potassium bromide optical windows; S, sample cell; SH, shutter; QLA, quartz lens assembly; N, nitrogen inlet.

in the ground state. The vibrational potential energy when excited may be different from that in the ground state, leading to possible shifts in vibrational energy absorptions. To the best of our knowledge, ETSIR has not been used as an analytical tool. Investigators have identified new infrared bands in the excited triplet state for a number of molecules: naphthalene (*1*), naphthalene-d_8 (*2*), phenazine (*3*), acridine (*3*), and triphenylene (*4*). Only one of these (*4*) has put to use the advantages of FTIR. In this paper we report utilization of the increased sensitivity and capacity for data massaging provided by FTIR to identify a mixture of naphthalene and its deuterated analogue. The resultant ETSIR spectrum contains only one paired set (a positive and negative) of vibrational bands per compound. This spectrum is obtained by ratioing the ground state spectrum of the naphthalene mixture against the excited triplet state spectrum for the same.

EXPERIMENTAL SECTION

Naphthalene and naphthalene-d_8 were obtained from Aldrich Chemicals. The deuterated sample (>98% deuteration) was used without further purification. Naphthalene was subjected to more than 200 passes through a zone refiner to remove an impurity detected via the emission spectrum (phosphorescence spectra were used as a final check for purity). Nujol (Aldrich) was used without further purification.

The naphthalene-h_8–d_8 mixture was a combination of two separate 0.1 M solutions in Nujol. The sample solution was pipetted into a KBr infrared cell with a path length of 0.2 mm provided by a lead spacer. This assembly was then attached to a cold finger of a conduction type cryostat and cooled down to ~90 K with liquid nitrogen. The sample cell was positioned in the infrared beam of a Nicolet 6000 series Fourier transform infrared spectrophotometer. Ultraviolet (UV) irradiation was provided by an air-cooled 200-W Hg arc lamp (Oriel Model 6143). The UV radiation was filtered with a $CoSO_4$ solution (10 cm path length) and controlled by an electromechanical shutter (ILEX No. 5 Synchro electronic shutter). The UV lamp was positioned perpendicular to the IR beam; UV radiation was then focused, by reflection from a mirror, onto the sample cell. Multiple scans (256) were taken at 0.5 cm^{-1} resolution with the UV source on, as well as shuttered. The sample compartment in the spectrophotometer was constantly purged with nitrogen gas, as well as isolated, in order to minimize frosting of the KBr windows. A quartz lens assembly was attached to the Nicolet optical bench to focus the ultraviolet radiation and contain the nitrogen atmosphere. (See Figure 1.)

RESULTS AND DISCUSSION

In order for ETSIR to be utilized in the analytical laboratory, an appreciable steady-state population in the triplet

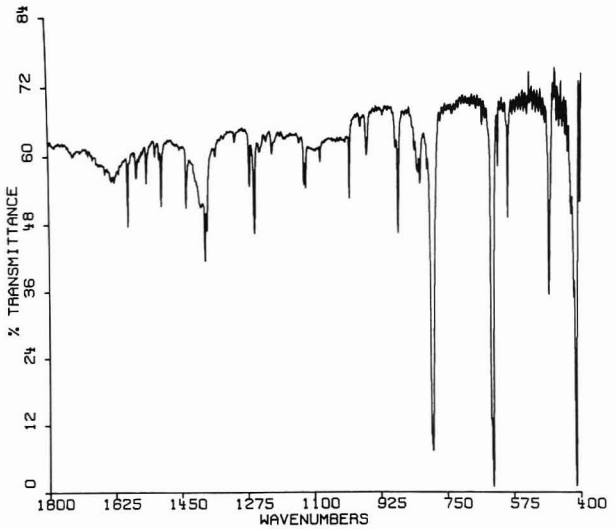

Figure 2. Infrared spectrum of a naphthalene/naphthalene-d_8 mixture in a KBr pellet at 1.0-cm^{-1} resolution.

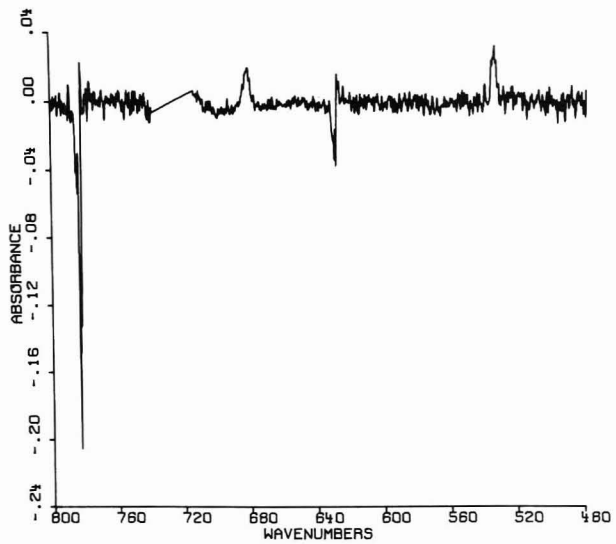

Figure 3. ETSIR spectrum of a naphthalene/naphthalene-d_8 mixture in a Nujol solution at 0.5-cm^{-1} resolution. The 740–715 cm^{-1} region is blanked because of over absorption of Nujol.

state must exist for the particular molecule of interest. This population determines the absorption value of the new vibrational band; therefore an efficient pumping system is necessary to maximize this value. The triplet state lifetime also indirectly affects the ETSIR signal; in our case, naphthalene and naphthalene-d_8 exhibited fairly long lifetimes of 2.2 and 18.0 s, respectively (*5*).

For reference purposes, the 1800–400 cm^{-1} region for a mixture of naphthalene and naphthalene-d_8 in a KBr pellet is shown in Figure 2. Due to the numerous bands, it is difficult to identify one specific compound from this spectrum, even with subtraction and library search routines. Ground-state bands at 958, 782, and 481 cm^{-1} have been assigned to naphthalene (*6*). Prominent naphthalene-d_8 bands are present at 877, 790, and 630 cm^{-1} (*6*, *7*).

Figure 3 displays the triplet state spectrum ratioed against the ground state spectrum of the mixture in a Nujol solution. The 740–715 cm^{-1} region of the spectrum has been omitted because upon ratioing, the over-absorption of Nujol at ~720 cm^{-1} results in an inconsistent line shape. The upward peaks are due to the appearance of new vibrations when molecules are excited into their triplet state. The modes whose frequencies have shifted show downward peaks since a small fraction of the overall collection of molecules has been pro-

moted out of the ground state. The peak at 681 cm^{-1} represents a new vibration produced by the triplet state of naphthalene and corresponds to Nishikida's results (*1*). The upward peak at 535 cm^{-1} arises from the triplet state of naphthalene-d_8 and correlates with Clarke's work (*2*). The downward peaks at 782 and 630 cm^{-1} can be assigned to the b_{3u} out-of-plane mode for naphthalene and naphthalene-d_8, respectively (*6*, *7*), and reflect the origins of the newly created absorptions at 681 and 535 cm^{-1}. The ratioed spectrum then leads to the unambiguous assignment that naphthalene and naphthalene-d_8 are present in the mixture. Clearly this simplified spectrum presents an advantage over that shown in Figure 2.

The absorbance of the exicted triplet state bands depends upon the steady-state population of the molecules in the triplet state. To obtain a spectrum, usually files are ratioed against a background and then converted to an absorbance spectrum. However, due to the capabilities of our FTIR, we may obtain a final absorption spectrum by ratioing the triplet state file against the ground state file. This produces an absorbance spectrum with upward and downward peaks as seen in Figure 3. The ratioing and subtraction methods produce the same absorbance values for specific vibrational peaks (assuming the cell path length and molar absorptivity are constant). This is as expected since

Subtraction:

$$A = [-\log 10^{-(T_1)}] - [-\log 10^{-(S_0)}] \quad (1)$$

Ratioing:

$$A = -\log 10^{(T_1/S_0)} = [-\log 10^{-(T_1)}] - [-\log 10^{-(S_0)}] \quad (2)$$

While the absorbance values are the same, the ratioing technique is preferred. This method eliminates ratioing data files against a background file, and the accompanying time-consuming FT processing. A single beam instrument, such as the Nicolet 6000 FTIR, lends itself better to this form of spectrometry. For dual beam instruments, precision matched cells and dual cryogenic apparatus would be necessary for properly attained ETSIR spectra.

The relative concentrations of molecules in the triplet state with our particular excitation conditions may be calculated from the ETSIR and ground state spectra using the following equation:

$$\% \text{ triplet concn} = (\text{area } T_1 \text{ band})/(\text{area } S_0 \text{ band}) \times 100 \quad (3)$$

with the ground-state peak area being measured when the UV radiation is shuttered. Since the ground state and triplet state peaks differ in line width ($\Delta\nu$ = 2.0 cm^{-1} for S_0; $\Delta\nu$ = 4.5 cm^{-1} for T_1), the integrated intensities are used for this calculation instead of the absorbance at the peak maximum. With our results, this leads to a relative triplet state concentration of approximately 2% for both the d_8 and h_8 naphthalene isomers.

In summary, once triplet-accessible aromatic systems have been assigned triplet state infrared bands, ETSIR may be used to identify these specific molecules from mixtures of unknown composition with increased simplicity. The method lends itself particularly well to single-beam FTIR instruments because computer capabilities allow for ratioing of data files instead of subtraction, leading to shorter experimental time. Future work involves assignment of triplet state peaks for additional organic molecules and quantum mechanical calculations to correlate shifts of the triplet state infrared bands.

Registry No. Naphthalene, 91-20-3; naphthalene-d_8, 1146-65-2.

LITERATURE CITED

(1) Nishikida, K.; Kamura, Y.; Seki, K.; Iwasaki, N.; Kinoshita, M. *Mol. Phys.* **1983**, *49*, 1505–1507.
(2) Clarke, R. H.; Kosen, P. A.; Lowe, M. A.; Mann, R. H.; Mushlin, R. *J. Chem. Soc., Chem. Commun.* **1973**, 528–529.
(3) Mitchell, M. B.; Smith, G. R.; Guillory, W. A. *J. Chem. Phys.* **1981**, *75*, 44–48.
(4) Balardo, J.; Mukherjee, R.; Vala, M. *J. Mol. Struct.* **1982**, *80*, 109–112.
(5) de Groot, M. S.; van der Waals, J. H. *Mol. Phys.* **1961**, *4*, 189–190.
(6) Scully, D. B.; Whiffen, D. H. *Spectrochim. Acta* **1960**, *16*, 1409–1415.
(7) Bree, A.; Kydd, R. A. *Spectrochim. Acta, Part A* **1969**, *26A*, 1791–1803.

David E. Bugay
Willem R. Leenstra*

Department of Chemistry
University of Vermont
Burlington, Vermont 05405

RECEIVED for review November 22, 1985. Accepted April 28, 1986. This work was supported by grants from the Research Corporation (9326), the donors of the Petroleum Research Fund, administered by the American Chemical Society (13295-G6), and the University of Vermont (UVM PS-11).

Indirect Electrochemical Detection in Liquid Chromatography

Sir: Considerable interest has recently been given to the development of so-called indirect detection approaches for use in liquid chromatography (*1–5*). In these systems, a suitable concentration of a species that can be readily monitored by a conventional detection scheme such as UV–visible absorption or fluorescence is intentionally added to the mobile phase to generate a constant background signal. If the elution of sample components is accompanied by a displacement of the additive from the mobile phase as observed at the detector, a transitory decrease in the background level is thereby produced. The analyte species is thus monitored indirectly as a negative peak or trough in the steady-state absorbance or fluorescence signal. The primary advantage of this approach lies in the capability that it affords for the detection and quantitation of species which themselves possess no strongly absorbing chromophore or other group readily lending itself to direct monitoring by one of the usual detection modes.

Refractive index detection, utilizing measurement of the change in refractive index of the eluent plus analyte compared to that of the eluent alone, represents a familiar example of the indirect detection approach. Recently, schemes utilizing absorbance (*1*), polarimetry (*2*, *3*), and fluorescence (*4*) have also been successfully demonstrated. However, the possibility of indirect amperometric detection of nonelectroactive analytes in an eluent containing an easily oxidizable additive has not yet been seriously considered for liquid chromatography. (Very recently, the use of such an approach for the determination of volatile hydrocarbons following gas chromatography (*6*) has been described.) Although direct electrochemical detection of analytes following liquid chromatography (LCEC)

0003-2700/86/0358-2337$01.50/0 © 1986 American Chemical Society

has been shown to produce analyses of extremely high sensitivity, its utility is clearly hampered by the paucity of compounds that undergo electrooxidation or -reduction at accessible potentials. Thus, it is of some interest to investigate the possibility of indirect LCEC for quantitation of nonelectroactive species. In this communication, we demonstrate the feasibility of this technique for detection and quantitation of simple, nonabsorbing organics following reverse-phase chromatography and characterize some of the principal experimental parameters governing its performance.

EXPERIMENTAL SECTION

Instrumentation. The liquid chromatography system consisted of a Perkin-Elmer Series 10 pump, a Rheodyne (Berkeley, CA) Model 7125 injector with a 20-μL sample loop, and an IBM Model EC/230 amperometric detector. The LCEC electrode was a Bioanalytical Systems Model TL-5 thin-layer glassy carbon electrode assembly. The reference electrode was a Ag/AgCl electrode. Chromatography was performed with a 15-cm Econosphere C-8 5-μm column. The mobile phase consisted of 40:60 CH_3OH/pH 3.0 buffer that was 0.12 M in phosphate and 0.083 M in KNO_3; in addition, a specified concentration of *p*-hydroquinone was also present. The flow rate was always 1.0 mL/min.

RESULTS AND DISCUSSION

The first consideration in designing an indirect electrochemical detection scheme is the selection of an electroactive species for addition to the chromatographic mobile phase and generation of a steady-state background current. The choice for most of this work was *p*-hydroquinone, whose redox behavior consists primarily of a chemically reversible, pH-dependent oxidation to the corresponding benzoquinone. With this mobile phase additive, a steady anodic background was generated by the application of a modest positive potential. The analytes chosen for study consisted of mixtures of simple carboxylic acids and aliphatic alcohols for which the best available detection approach has usually been refractive index monitoring (*7*). These compounds were selected primarily because they lack a strongly absorbing chromophore and consequently are not well suited to detection via the usual spectroscopic methods. In addition, none of these compounds is oxidizable or reducible at a sufficiently low potential to make direct electrochemical monitoring a workable possibility.

As expected, addition of hydroquinone to the chromatographic mobile phase produced an anodic background current that was dependent on the applied potential and the concentration of hydroquinone. Chromatograms obtained by recording the decrease in this otherwise steady-state background following injection and elution of the test mixtures are shown in Figure 1. In all cases, the sample mixtures injected were dissolved directly in the mobile phase solution (without hydroquinone) and were reasonably well resolved under the reverse-phase conditions employed. For both the alcohol (curves A) and the fatty acid (curves B) mixtures, distinct concentration-dependent troughs or inverse peaks were observed for all analytes. (Also shown for comparison are the identical chromatograms recorded by conventional UV absorption with no hydroquinone present in the mobile phase. No response was observed with absorption detection at 210 nm even though relatively high alcohol and acid concentrations and the most sensitive instrumental settings permitted by the system noise level were employed.) The slightly different level of response that was obtained for each compound by indirect LCEC could not be accounted for simply by the concentration or retention differences in effect. Rather, each analyte appeared to be able to displace the hydroquinone from the mobile phase to a slightly different degree. The reasons for these differences are currently under investigation.

It was natural to expect that changes in detector potential would directly affect the indirect LCEC response observed. The effect of such changes as typified by the indirect peak observed for isopropyl alcohol (peak 1 in Figure 1a) is shown in the hydrodynamic voltammogram (HDV) in Figure 2. Also shown for comparison is the HDV obtained conventionally for hydroquinone itself by direct LCEC. Clearly, the magnitude of the isopropyl alcohol signal—actually, the extent of the background current decrease—had exactly the same potential dependence as the background current generated by the hydroquinone oxidation. Thus, the potential dependence of the indirect LCEC signal was essentially the same as that of the oxidation/reduction of the electroactive species added to the mobile phase. This observation was further confirmed by the fact that alteration of the current-potential behavior of the background signal by changing the mobile phase pH or by switching to a different mobile phase additive (such as uric acid in place of hydroquinone) produced exactly equivalent changes in the potential dependence seen for the indirect response toward the alcohol and acid mixtures. Note that behavior similar to that described for isopropyl alcohol was observed for nearly all of the nonelectroactive analytes examined.

The results shown in Figure 2 indicate that larger indirect LCEC peaks were obtained at high potentials where the background current due to the mobile phase additive was larger. This was confirmed by chromatograms a and b in Figure 3, which were obtained at different applied potentials for injection of three different isopropyl alcohol concentrations. Changing the detector potential from +0.26 V vs. Ag/AgCl to midway up the hydroquinone oxidation wave at +0.38 V produced a corresponding increase in both the steady-state background level and the indirect response for isopropyl alcohol. An alternative means of increasing the background current (i.e., instead of increasing the applied potential) was simply to increase the hydroquinone concentration in the mobile phase while keeping the detector potential constant. This possibility is illustrated in curve c where increasing the hydroquinone concentration to 1.0×10^{-4} M generated the identical response as in curve b but at a potential of only +0.26 V. In fact, chromatograms obtained for hydroquinone concentrations between 1.0×10^{-3} and 1.0×10^{-6} M showed that the magnitude of the indirect LCEC response for all analytes examined was determined only by the magnitude of the background current. Any combination of applied potential and hydroquinone concentration that produced a given background current level always produced exactly the same analyte response.

Unlike with conventional LCEC, selection of optimum conditions for performing quantitation by the indirect electrochemical approach involved more than just the selection of a potential that produced maximum electrolysis current for the desired analyte. Rather, for indirect detection, maximum signal levels could be generated by a variety of applied potential/additive concentration combinations; and selection of conditions that minimized the system noise level became the limiting factor. In the present case, periodic current fluctuations related to pump pulsation often represented the dominant noise contribution—especially at high potentials in the mass transfer limited regions for the hydroquinone oxidation. Accordingly, optimum sensitivity for indirect LCEC was usually obtained by operation at relatively low potentials in the activation controlled region at the foot of the hydroquinone HDV where pump pulsations exercised virtually no effect on the observed currents. Of course, operation at these low potentials required the use of a very high hydroquinone concentration for the generation of a correspondingly high background current. Thus, lowest detection limits were obtained here by a judicious selection of low applied potential and high hydroquinone concentration. Under these conditions

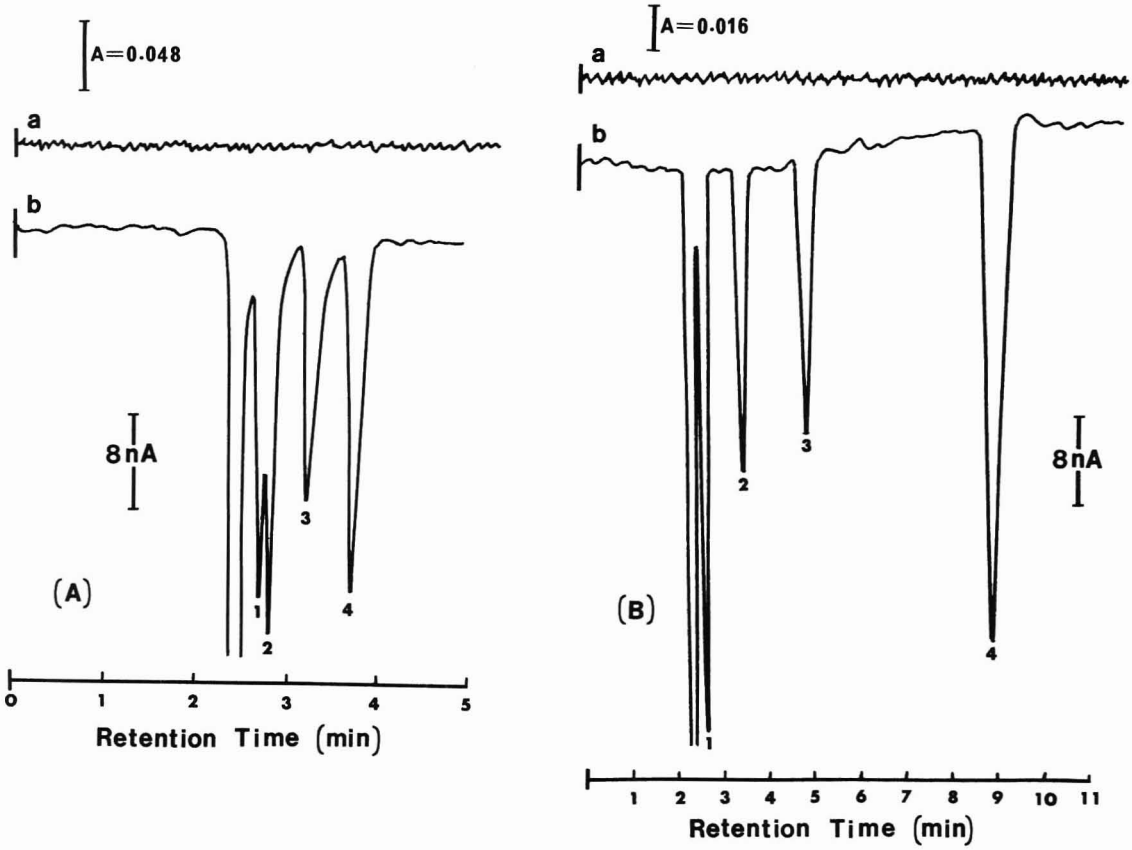

Figure 1. Chromatograms of mixtures of (A) alcohols and (B) aliphatic carboxylic acids. Lower traces were obtained by indirect LCEC at E = +0.27 V vs. Ag/AgCl with a mobile phase hydroquinone concentration of 1.0×10^{-3} M; upper traces were obtained by UV absorbance at 210 nm with no hydroquinone added. The alcohol mixture contained (1) isopropyl alcohol, (2) 1-propyl alcohol, (3) 1-butyl alcohol, and (4) isobutyl alcohol; the acid mixture contained (1) propionic acid, (2) 1-butyric acid, (3) isovaleric acid, and (4) 1-hexanoic acid. All concentrations were 1.0% by volume.

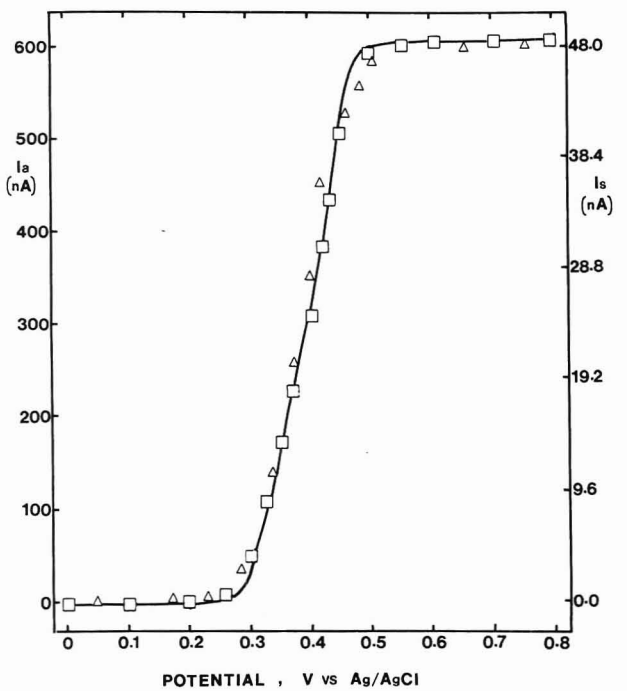

Figure 2. Hydrodynamic voltammograms obtained for isopropyl alcohol by the indirect approach (△) and for hydroquinone by direct LCEC (□). Chromatographic conditions were similar to those in Figure 1 except that the hydroquinone response was obtained directly with no electroactive additive in the mobile phase. Current scale on left applies to the hydroquinone signal (i_a) while that on the right corresponds to isopropyl alcohol (i_s).

(which were essentially those employed to generate the chromatograms in Figure 1), limits of detection observed for

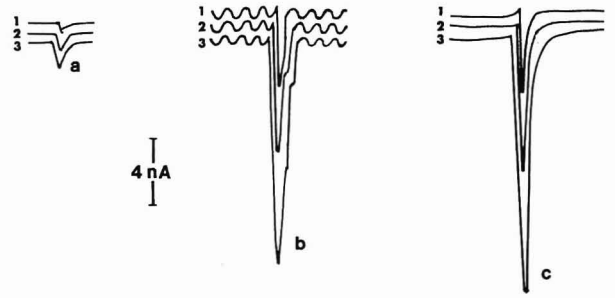

Figure 3. Indirect LCEC of isopropyl alcohol for (a) E = +0.26 V vs. Ag/AgCl and 5.0×10^{-6} M hydroquinone in mobile phase, (b) E = +0.38 V and 5.0×10^{-6} M hydroquinone, and (c) E = +0.26 V and 1.0×10^{-4} M hydroquinone. Isopropyl alcohol concentrations injected were (1) 0.25%, (2) 0.50%, and (3) 1.0% by volume.

both the aliphatic alcohols and fatty acids were uniformly in the 0.01% range (or a few micrograms for the 20-μL injection volume used here). Furthermore, response was linear for concentrations up to at least 2 orders of magnitude higher.

The analytical capabilities demonstrated here for indirect LCEC detection do not rival in sensitivity the results usually obtained by direct amperometric detection. However, for compounds not possessing an electroactive group or a strongly absorbing chromophore, indirect LCEC may represent an attractive detection approach. In particular, for applications currently carried out with refractive index detection, this approach would appear to offer distinct advantages. For the families of compounds examined in this study, the indirect LCEC technique provides a detectability that compares well with that typically seen for refractive index monitoring (7). In addition, the instrumentation required and its ease of operation are far simpler. Further characterization and ap-

plication of indirect LCEC are continuing in this laboratory.

Registry No. Isopropyl alcohol, 67-63-0; 1-propyl alcohol, 71-23-8; 1-butyl alcohol, 71-36-3; isobutyl alcohol, 78-83-1; propionic acid, 79-09-4; 1-butyric acid, 107-92-6; isovaleric acid, 503-74-2; 1-hexanoic acid, 142-62-1; *p*-hydroquinone, 123-31-9.

LITERATURE CITED

(1) Small, H.; Miller, T. E., Jr. *Anal. Chem.* **1982**, *54*, 462.
(2) Bobbitt, D. R.; Yeung, E. S. *Anal. Chem.* **1984**, *56*, 1577.
(3) Bobbitt, D. R.; Yeung, E. S. *Anal. Chem.* **1985**, *57*, 271.
(4) Mho, S.-I.; Yeung, E. S. *Anal. Chem.* **1985**, *57*, 2253.
(5) Banerjee, S. *Anal. Chem.* **1985**, *57*, 2590.
(6) Mills, A.; Giddings, S. L. *Anal. Chem.* **1986**, *58*, 153.
(7) Snyder, L. R.; Kirkland, J. J. *Introduction to Modern Liquid Chromatography*, 2nd ed.; Wiley: New York, 1979; pp 140–145.

Jiannong Ye
Richard P. Baldwin*

Department of Chemistry
University of Louisville
Louisville, Kentucky 40292

K. Ravichandran

Department of Chemsitry
University of Georgia
Athens, Georgia 30602

RECEIVED for review January 27, 1986. Accepted May 1, 1986.

AIDS FOR ANALYTICAL CHEMISTS

Digestion of Biological Materials for Mineral Analyses Using a Combination of Wet and Dry Ashing

A. D. Hill,* K. Y. Patterson, C. Veillon, and E. R. Morris

U.S. Department of Agriculture, Agricultural Research Service, Beltsville Human Nutrition Research Center, Beltsville, Maryland 20705

Periodically in our laboratory, it is necessary to analyze large numbers of diet samples and other biological materials from human studies for a wide variety of essential minerals. Atomic absorption spectrometry is accepted as the preferred method (*1*). Atomic absorption analysis requires the sample be in an aqueous form and this usually requires the destruction of the organic material.

Some common procedures for digestion are low-temperature dry ashing in an oxygen plasma (*2–6*), high-temperature dry ashing (*6–13*), and low-temperature wet ashing in an acid solution (*13–19*). None of these methods is without problems.

The equipment for low-temperature ashing in an oxygen plasma is expensive. Most ashers can handle only a few small samples at one time. Low-temperature ashing can be very time-consuming when high concentrations of salts are present.

Some minerals have been reported to be lost during high-temperature ashing through either volatilization or adsorption onto the walls of the container (*20–22*). Contamination from the ashing vessel has also been reported (*23*).

Wet ashing with perchloric acid is widely used but potentially explosive conditions are needed to totally digest the lipid portion of the sample. Large volumes of acids are sometimes needed and constant operator attention is required. Sulfuric acid, which is used extensively in wet ashing procedures, has been shown to interfere in atomic absorption analysis (*24*) particularly with calcium.

The procedure described in this paper utilizes dry ashing at 375 °C in a muffle furnace for 24–48 h. This temperature will char the sample and burn off the major portion of the organic matrix including the lipid material without causing loss of the seven biologically important minerals investigated in this study.

The ash is suspended in small amounts of deionized water and nitric acid. The samples in borosilicate tubes are then placed in a heating block and hydrogen peroxide is added to complete the digestion. Very little operator time is required. Only small amounts of reagents are used lowering the chance of contamination and resulting in low blanks and allowing for more accurate analysis at low concentrations in samples.

Table I. Recovery of Added Metals

	amt added, μg	amt recovered,[a] μg	rel std dev, %	% recovery
Cu	1.0	0.99	6.5	99
	2.0	2.03	5.4	102
	4.0	4.01	2.8	100
Mn	2.0	2.07	7.2	104
	4.0	4.07	2.0	102
	8.0	8.52	2.8	107
Fe	10.0	9.80	9.4	98
	20.0	19.5	4.4	98
	40.0	40.3	2.1	101
Zn	5.0	4.96	6.5	99
	10.0	10.2	2.8	102
	20.0	19.9	1.6	99
Ca	35	36.7	12.7	105
	70	70.8	6.9	101
Mg	75	81	8.4	108
	150	155	9.3	103

[a] Amount recovered is the average of triplicate determinations.

EXPERIMENTAL SECTION

Procedure. Homogenized, dried samples of about 1 g are weighed into 20 × 150 mm borosilicate test tubes. The tubes are placed in 1000-mL glass beakers, covered with a watch glass, and placed in a muffle furnace. Furnace temperature is increased 50 deg/h to 375 °C and held at that temperature for 48 h. After cooling, samples are removed from the furnace and 0.20 mL of deionized water and 0.20 mL of Ultrex nitric acid (Baker, Phillipsburg, NJ) are added to each. Tubes are placed in heating blocks (Thermolyne Dri-Bath, Dubuque, IA) and the temperature is raised to 90 °C. Hydrogen peroxide (50%) is added in 0.1-mL aliquots at 10–15 min intervals until all black carbon particles are digested. Samples are allowed to evaporate to dryness and

This article not subject to U.S. Copyright. Published 1986 by the American Chemical Society

Table II. Percent Recoveries of ^{65}Zn, ^{54}Mn, ^{59}Fe, and ^{51}Cr in Rat Tissues after Endogenous Labeling[a]

	^{65}Zn	^{54}Mn	^{59}Fe	^{51}Cr
liver	102	98	94	95
heart	97	100	103	102
muscle	96	101	107	104
kidney	100	102	97	103
serum	99	96	108	101
retained in tube wall	0	1	2	1

[a] Values given are the mean of three replicates.

cooled and 2 mL of deionized water and 1 mL of Ultrex HCl are added to each (presumably one could use HNO_3 in situations where chloride ion is undesirable). Samples are reheated at 90 °C for 15 min to dissolve the residue, cooled, transferred quantitatively to 10-mL volumetric flasks, and adjusted to volume with deionized water. After mixing, samples are transferred to polypropylene storage tubes. Standards (1000 ppm, Baker, Phillipsburg, NJ) are diluted with 10% HCl to cover the linear range for each element. Sample solutions can be aspirated directly and diluted when necessary with 10% HCl solution. Standards and samples to be analyzed for calcium should be diluted with lanthanum solution (0.5% La).

Recovery of Added Minerals. One-gram samples from a homogenized, freeze-dried diet composite were spiked with three levels of a solution containing an inorganic form of copper, manganese, iron, and zinc made from the 1000 ppm standards. The solution contained copper at 2 μg/mL, manganese at 4 μg/mL, iron at 20 μg/mL, and zinc at 10 μg/mL. Calcium and magnesium recoveries were from individual additions to samples of U.S. National Bureau of Standards materials Rice Flour (SRM 1568) and Bovine Liver (SRM 1577a), respectively. The samples were digested by use of the procedures described in this paper and analyzed by flame atomic absorption spectrometry (Model 5000, Perkin-Elmer Corp., Norwalk, CT).

RESULTS AND DISCUSSION

The problems with this type of recovery experiment have been discussed by Gorsuch (*21*). Specifically, the additions are made with an inorganic form of the element which could differ from that found natively in the organic matrix. Losses by volatilization or adsorption can be offset with contamination from reagents or equipment because the oxidation step cannot be isolated from other steps necessary for the final analysis. These problems can be avoided by using radioisotopes. Rat tissues were endogenously labeled by intraperitoneal injections with zinc, iron, manganese, and chromium radiotracer solutions and the tissues were removed and digested as described. The radiotracers were "carrier-free", so the total dosage for each is well below physiological levels. The results are given in Table II. Geometry differences between ashed and unashed samples contribute to the variation in the results. Volumes of ashed sample solutions were adjusted to approximately match the unashed tissue sample volume.

The U.S. National Bureau of Standards (NBS) certifies plant and animal materials for a large number of elements. The results of analysis using the described procedure and the certified values are given in Table III. The NBS certified value is the mean determined by using at least two independent methods of analysis ± the estimated uncertainty.

The results given in Tables I and II show no significant losses of minerals during the digestion procedure. The recovery of minerals added to a diet composite averaged 100% for copper, 104% for manganese, 99% for iron, 100% for zinc, 102% for calcium, and 106% for magnesium. Recovery for rat tissues endogenously labeled with radioisotopes averaged 99% for zinc, 99% for manganese, 102% for iron, and 101% for chromium.

Table III shows the results of analysis of NBS reference materials. The results are within the certified range for both plant material and animal tissue. The relative standard deviations show acceptable reproducibility for all analyses. This procedure may be applicable to other elements; however, quartz test tubes may be necessary in some cases where contamination from borosilicate tubes is a problem.

Table III. Analysis of NBS Reference Materials[a] (μg/g)

	Wheat Flour (1567)	Rice Flour (1568)	Bovine Liver (1577a)	Citrus Leaves (1572)
copper				
certified	2.0 ± 0.3	2.2 ± 0.3	158 ± 7	16.5 ± 1.0
determined	2.05	2.12	156	16.7
rel std dev	4.2%	2.3%	1.3%	3.4%
manganese				
certified	8.5 ± 0.5	20.1 ± 0.4	9.9 ± 0.8	23.0 ± 2.0
determined	8.38	20.0	10.2	23.5
rel std dev	1.3%	1.3%	0.7%	1.7%
iron				
certified	18.3 ± 1.0	8.7 ± 0.6	194 ± 20	90 ± 10
determined	17.7	8.64	187	89.7
rel std dev	3.3%	2.4%	1.4%	5.7%
zinc				
certified	10.6 ± 1.0	19.4 ± 1.0	123 ± 8	29 ± 2
determined	10.4	20.2	121	31.0
rel std dev	1.5%	2.8%	0.9%	3.1%
magnesium				
certified	n.c.[b]	n.c.	600 ± 15	5800 ± 300
determined	379	419	585	5540
rel std dev	4.1%	1.3%	1.2%	2.5%
calcium				
certified	190 ± 10	140 ± 20	120 ± 7	31500 ± 1000
determined	198	140	118	31100
rel std dev	3.8%	2.1%	1.9%	2.5%
			ng/g	ng/g
chromium				
certified	n.c.	n.c.	88 ± 12[c]	800 ± 200
determined			85	817
rel std dev			14%	6.9%

[a] Analyzed values are the mean of four replicates. [b] Not certified (no value given). [c] SRM 1577; SRM 1577a not certified for Cr.

Registry No. Cu, 7440-50-8; Mn, 7439-96-5; Fe, 7439-89-6; Zn, 7440-66-6; Cr, 7440-47-3; Mg, 7439-95-4; Ca, 7440-70-2.

LITERATURE CITED

(1) Faulkner, W. R. *Lab. Management* **1981**, July, 21.
(2) Gleit, C. E.; Holland, W. D. *Anal. Chem.* **1962**, *34*, 1454–1457.
(3) Lockwood, T. H.; Limitiaco, L. P. *Am. Ind. Hyg. Assoc. J.* **1975**, *36*, 57–62.
(4) Guthrie, B. E.; Wolf, W. R.; Veillon, C. *Anal. Chem.* **1978**, *50*, 1900–1902.
(5) Raptis, S. E.; Knapp, G.; Schalk, A. P. *Z. Anal. Chem.* **1983**, *316*, 482–487.
(6) Locke, J. Anal. *Chim. Acta* **1979**, *104*, 225–231.
(7) Heanes, D. L. *Analyst (London)* **1981**, *106*, 182–187.
(8) Donaldson, J.; St. Pierre, T.; Minnichi, J. L.; Barbeau, A. *Can. J. Biochem.* **1973**, *51*, 87–92.
(9) Baker, A. D. *J. Assoc. Off. Anal. Chem.* **1971**, *54*, 951–952.
(10) Adrian, W. J.; Stevens, M. L. *Analyst (London)* **1977**, *102*, 446–452.
(11) Boline, D. R.; Schrenk, W. G. *J. Assoc. Off. Anal. Chem.* **1977**, *60*, 1170–1174.
(12) Isaac, R. A.; Johnson, W. C. *J. Assoc. Off. Anal. Chem.* **1975**, *58*, 436–440.
(13) Smith, D. L.; Schrenk, W. G. *J. Assoc. Off. Anal. Chem.* **1972**, *55*, 669–675.
(14) Marks, G. E.; Moore, C. E.; Kanabrocki, E. L.; Oester, Y. T.; Kaplan, E. *Appl. Spectrosc.* **1971**, *26*, 523–527.
(15) Evans, W. H.; Dellar, D.; Lucas, B. E.; Jackson, F. J.; Read, J. I. *Analyst (London)* **1980**, *105*, 529–543.
(16) Johnson, C. A. *Anal. Chim. Acta* **1976**, *81*, 69–74.
(17) Arafat, N. M.; Glooschenko, W. A. *Analyst (London)* **1981**, *106*, 1174–1178.
(18) Clegg, M. S.; Keen, C. L.; Lonnerdal, B.; Hurley, L. S. *Biol. Trace Elem. Res.* **1981**, *3*, 107–115.
(19) Ladefoged, K. *Clin. Chim. Acta* **1980**, *100*, 149–153.
(20) Clegg, M. S.; Keen, C. L.; Lonnerdal, B.; Hurley, L. S. *Biol. Trace Elem. Res.* **1981**, *3*, 237–244.
(21) Gorsuch, T. T. *Analyst (London)* **1959**, *84*, 135–173.
(22) Gorsuch, T. T. *Analyst (London)* **1962**, *87*, 112–115.

(23) Wurts, L.; Smeyers-Verbeke; Massary, D. L. Clin. Chim. Acta 1976, 72, 405-407.
(24) Basson, W. D.; Bohmer, R. G. Analyst (London) 1972, 97, 482-489.

RECEIVED for review February 24, 1986. Accepted April 14, 1986. Trade names are included for the benefit of the reader and do not imply any endorsement or preferential treatment of the product listed by the U.S. Department of Agriculture. Other brands of acids of sufficient purity to produce acceptable blanks have also been used.

Generation of a Helium Inductively Coupled Plasma in a Low-Gas-Flow Torch

Shi-Kit Chan, Raymond L. Van Hoven, and Akbar Montaser*

Department of Chemistry, The George Washington University, Washington, D.C. 20052

In an earlier communication (*1*), we reported the generation of three types of helium inductively coupled plasmas (He ICP) at atmospheric pressure by using modified conventional torches: the hollow He ICP, the filament-type He ICP, and the annular He ICP. Preliminary results indicated that the annular He ICP was capable of exciting elements such as Cl and Br, which possess high excitation energies. Atomic emission detection limits measured for aqueous chloride and bromide solutions were improved by more than 1 order of magnitude, as compared to the results obtained from the Ar ICP.

Two impediments to the investigation of the annular He ICP as a new vaporization–atomization–ionization–excitation source for atomic spectrometry were the high gas flow requirement (57 L/min He) and the necessity to follow a relatively complicated procedure for the generation of plasma (*1*). To circumvent such limitations at atmospheric pressure, a number of investigators have recently reported the use of reduced-pressure He ICPs (*2–4*), especially for the determinations of non-metals. The applications of these reduced-pressure He ICPs, however, are limited to gas analysis. Relatedly, introduction of aqueous samples into filament-type He ICPs (*1, 5, 6*), operated at atmospheric pressure, has been extremely difficult.

In the present study, we report on the design and evaluation of a new demountable, low-gas-flow torch for generating an annular He ICP at atmospheric pressure. For the new design, the total He gas flow has been reduced by a factor of 7 as compared to our previous work (*1*), and the procedure for the formation of the plasma has been simplified significantly to a one-step plasma generation. Detection limits of aqueous bromide obtained at Br I 827.24 nm are also reported, using a photodiode array detector.

EXPERIMENTAL SECTION

Except for the He ICP torch and the detection system, the instrumentation for the inductively coupled plasma atomic emission spectrometry (ICP-AES) system has been discussed elsewhere (*1, 7*). Modifications on the induction load coil and the impedance matching network were similar to those previously described (*1*). The schematic diagram of the demountable, low-gas-flow torch is shown in Figure 1. The torch consisted of three components: a torch base, a threaded insert, and a high precision quartz tube (13 mm i.d. and 15 mm o.d., Wilmad, Buena, NJ), which were closely fitted together by means of nitrile O-rings (Catalog no. 2-113 and 2-015, Parker, Lexington, KY) placed in the square-shaped grooves of the base and the insert. The torch base and the threaded insert were made of Macor machinable glass ceramics (Corning Glass Works, Corning, NY). High-purity helium gas (99.997%, MG Industries, Valley Forge, PA) was introduced tangentially as the plasma gas via the torch base while the injector gas was directed through an 0.5 mm orifice at the center of the insert. Aerosol of liquid sample, produced by an ultrasonic nebulizer (*1*), or gaseous sample was transported by the injector gas into the He ICP.

Table I. Generating and Operating Conditions for the He ICP

forward power, W	1500
reflected power, W	5
plasma gas flow, L/min	7
injector gas flow, L/min	1
sample uptake rate, mL/min	2
observation height above the load coil, mm	25

A 1024-element intensified (700 active elements) linear photodiode array detector (Model 1420R, EG&G Princeton Applied Research, Princeton, NJ) with a detector module and a system processor (Models 1463 and 1460) was used to monitor atomic emission of Br I 827.24 nm. The diode array detector was cooled to −5 °C and was scanned repetitively 100 times at a rate of 100 ms/scan for each signal integration. A sharp-cut-off, red filter (Catalog no. CS2-63,2424, Corning Glass Works) was used to eliminate any possible interference from second- or third-order spectra. The entrance slit of the monochromator was set at 50 μm.

RESULTS AND DISCUSSION

A. Design Considerations. Because of its excellent electrical resistivity, thermal shock resistance, zero porosity, chemical resistance, and machinability, Macor machinable glass ceramics was chosen for constructing the torch base and the threaded insert. Other materials such as nylon and Teflon for the torch base and brass and boron nitride for the threaded insert were also tested but were proven to be less satisfactory. For example, when a brass insert was used, an annular He ICP could be generated at about 3 L/min, but the plasma could not be operated at forward power levels greater than 1 kW because of thermal expansion of brass and the subsequent breakage of the outer tube. Since the Macor ceramics could be machined to a very high precision, the demountable torch could be assembled or dissembled within a minute, and no alignment was necessary after the assembly. The most critical parameters in the design were the groove's geometry and dimension of the threaded insert, which determined the flow pattern and total gas flow for sustaining the He ICP. The insert was quadra-threaded at 1.54 pitch per cm and the dimensions of the V-shaped groove were 1.17 and 0.45 mm for the width and the depth, respectively. To ensure proper introduction of the plasma gas into the grooves, the tangential plasma gas inlet was machined to form a 1.5 mm × 9 mm rectangular slot.

The conditions for generation and operation of the annular He ICP formed in the new torch are listed in Table I. At 1500 W forward power, the plasma gas flow and the injector gas flow were 7 and 1 L/min, respectively. The plasma was usually self-ignited to form a very stable annular He ICP, Figure 2A,B. No external cooling was necessary to prevent overheating of the plasma torch. To the best of our knowledge, this is the first annular He ICP generated directly from helium

0003-2700/86/0358-2342$01.50/0 © 1986 American Chemical Society

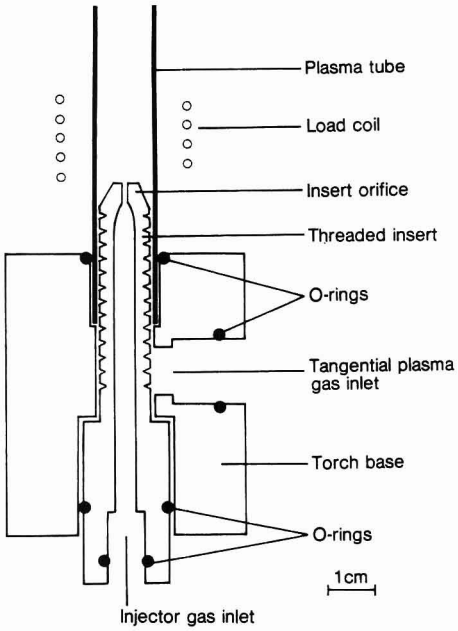

Figure 1. Schematic diagram of the demountable, low-gas-flow torch.

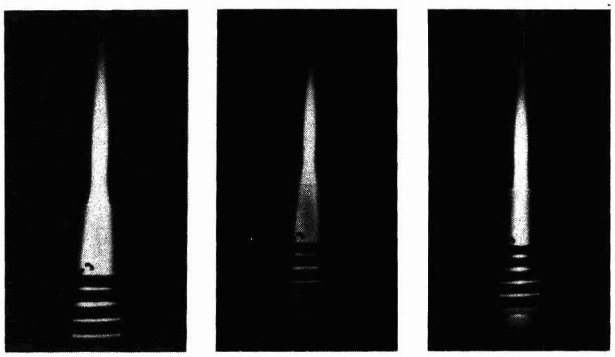

Figure 2. (A,B) Annular He ICP pictured at different exposures and (C) filament-type He ICP generated in the low-gas-flow torch at atmospheric pressure.

gas at atmospheric pressure and at such a low gas flow rate. If no injector gas was used, a filament-type He ICP could be formed, Figure 2C.

Significant differences exist between the He ICP generated in this new torch and the He microwave induced plasmas (MIP) formed in other torches (*8–12*). For example, either the toroidal He MIPs are in contact with the torch outer tube (*8*, *10*), thus causing torch burning, or the torches required a high flow of helium or external cooling (*9*, *11*, *12*). Relatedly, the suspended, filament-type He MIPs (*8–10*) are not satisfactory for introduction of aqueous samples.

B. Analytical Performance. Preliminary analytical performance of the annular He ICP was evaluated in the determination of Br in aqueous solution. The signal-to-background (S/B) ratio, signal-to-noise (S/N) ratio, relative standard deviation (RSD) of the background intensities, and detection limit (DL) of Br at 827.24 nm were measured when 500 μg/mL of aqueous bromide was introduced into the annular He ICP. The highest S/B ratio was obtained at an observation height of 25 mm above the load coil. The results were compared to those obtained from a conventional Ar ICP operated at commonly used conditions (*13*) using the same facility in our laboratory, Table II. These results on the S/B ratios, S/N ratios, and DL suggest that the annular He ICP is a more efficient excitation source for Br than the Ar ICP. Although the percent RSD of the background intensities is relatively poor in the He ICP, it can be improved if the forward power is increased or the water is eliminated totally from the aqueous sample before introducing the aerosol into the plasma. Indeed, data obtained from gaseous sample of Br showed that the RSD of the background intensities could be reduced to less than 1%. These results are presented elsewhere (*14*).

Table II. S/B Ratio, S/N Ratio, % RSD of Background Intensities, and DL[a] (μg/mL) for Annular He and Ar ICPs

	He ICP	Ar ICP
S/B	13	0.2
S/N	323	57
% RSD	4	0.3
DL	5	26

[a] Detection limit is defined as the concentration giving a signal equivalent to 3 times the standard deviation of 11 repetitive measurements of the background intensity. The concentration of the aqueous bromide solution is 500 μg/mL.

In addition to AES, the He ICP is a useful ionization source for mass spectrometry. This application is currently being pursued in our laboratory.

CONCLUSIONS

An annular helium ICP was generated in a demountable, low-gas-flow torch. The total gas consumption was reduced from 57 to 8 L/min, and the procedure for plasma generation was significantly simplified. Preliminary results for aqueous bromide solution indicated that the S/B, S/N, and DL were superior to those obtained with the Ar ICP.

ACKNOWLEDGMENT

Acknowledgment is made to D. W. Golightly, R. W. Werre, and F. L. Harmon at the US Geological Survey for their assistance during the couse of this work.

Registry No. He, 7440-59-7; Br_2, 7726-95-6.

LITERATURE CITED

(1) Chan, S.; Montaser, A. *Spectrochim. Acta, Part B* **1985**, *40B*, 1467–1472.
(2) Seliskar, C. J.; Warner, D. K. *Appl. Spectrosc.* **1985**, *39*, 181–183.
(3) Wolnik, K. A.; Miller, D. C.; Seliskar, C. J.; Fricke, F. L. *Appl. Spectrosc.* **1985**, *39*, 930–935.
(4) Smith, T. R.; Denton, M. B. *Spectrochim. Acta, Part B* **1985**, *40B*, 1227–1237.
(5) Abdallah, M. H.; Mermet, J. M. *Spectrochim. Acta, Part B* **1982**, *37B*, 391–397.
(6) Robin, J. P. *Prog. Anal. At. Spectrosc.* **1982**, *5*, 79–110.
(7) Montaser, A.; Huse, G. R.; Wax, R. A.; Chan, S.; Golightly, D. W.; Kane, J. S.; Dorrzapf, A. F., Jr. *Anal. Chem.* **1984**, *56*, 283–288.
(8) Bollo-Kamara, A.; Codding, E. G. *Spectrochim. Acta, Part B* **1981**, *36B*, 973–982.
(9) Haas, D. L.; Caruso, J. A. *Anal. Chem.* **1984**, *56*, 2014–2019.
(10) Goode, S. R.; Chambers, B.; Buddin, N. P. *Spectrochim. Acta, Part B* **1985**, *40B*, 329–333.
(11) Michlewicz, K. G.; Urh, J. J.; Carnahan, J. W. *Spectrochim Acta, Part B* **1985**, *40B*, 493–499.
(12) Michlewicz, K. G.; Carnahan, J. W. *Anal. Chem.* **1985**, *57*, 1092–1095.
(13) Winge, R. K.; Fassel, V. A.; Peterson, V. J.; Floyd, M. A. *Inductively Coupled Plasma-Atomic Emission Spectroscopy: An Atlas of Spectral Information*; Elsevier: New York, 1985; pp 2–4.
(14) Chan, S.; Montaser, A. submitted to *Spectrochim. Acta* for publication.

RECEIVED for review February 25, 1986. Accepted April 14, 1986. This research was sponsored by the US Department of Energy under Contract No. DE-AS05-84-ER-13172. Patent applications have been filed on the generation of He ICPs in the low-gas-flow torches.

Modifying the Gaussian Peak Shape with More Than One Time Constant

Roland Delley

Central Research, CIBA-GEIGY, Limited, CH-4002 Basel, Switzerland

It is widely accepted that in chromatography the ideal column acts in the long-time approximation as a Gaussian operator; in other words, each element of the input profile is broadened to a Gaussian distribution by passage through the column. The normalized concentration profile $Y(T)$ for an initial concentration pulse is given by

$$Y(T) = h_G e^{-T^2/2} \tag{1}$$

where $T = (t - t_G)/\sigma_G$ and measures the time t in units of the standard deviation σ_G and with zero at the apex t_G of the Gaussian peak. The height of the Gaussian at its maximum is h_G.

The chromatographic process is inevitably disturbed by extracolumn effects. Examples are the volumes within the injector or the detector unit that delay the process. A dead volume acts as a mixing chamber with a characteristic time constant τ (or relaxation time). Time constants are also involved in diffusion chambers and in the amplifier and recorder of the instrumentation. Many of these complex delaying effects have been discussed by Giddings (*1*). Any rate-dependent process delaying the establishment of the chromatographic signal modifies the elution profile more or less.

The modification of any input function $E(T)$ by a single, independent time constant τ results in the output function $Y(T)$ that is governed by the basic differential equation

$$Y(T) + \frac{\tau}{\sigma_G}\frac{dY(T)}{dT} = E(T) \tag{2}$$

given by McWilliam and Bolton (*2*). With normalized time T, the time constant is also expressed in units of σ_G. It is convenient to use the inverse value $S_\tau = \sigma_G/\tau$ in certain expressions.

The differential equation (2) is well-known and can be solved by using an integrating factor. The solution can be expressed in the form of a convolution integral. We use for the convolution integral the convenient shorthand notation of an asterisk (*3*, *4*). Then

$$Y(T) = E(T)*D \tag{3}$$

where D is a truncated exponential (the exponential decay)

$$D = S_\tau e^{-S_\tau T} \qquad 0 < T < \infty \tag{4}$$

is indeed a solution of eq 2.

The fact that convolution is commutative corresponds to the conclusion of Sternberg (*5*) that the effect of a particular modifying process on peak shape is the same whether the modifier be at the inlet, the detector, or some intermediate point.

ONE SINGLE RELAXATION TIME

The peak model adopting solely one single time constant, the exponentially modified Gaussian function (EMG), has been widely used and many actual peaks have been fitted very closely (for a review see ref 6). The success of this simple model, using only four peak parameters, is surprising. Several effects that deform the ideal peak shape cannot be characterized by a time constant, but in practice these effects obviously give the elution curve a similar shape to that of the EMG.

Usually the EMG is described through an equation with the complementary error function as one of the factors. But it is also possible to transform the convolution, eq 3, in such a way as to retain the original Gaussian as a factor (*7*, *8*) and to define a modifying function $f(x)$. It is convenient to formulate the argument of this modifying function as

$$x = S_\tau - T \tag{5}$$

x being itself a simple function of T. The convolution integral, resulting from setting $E(T) = \exp(-T^2/2)$ in eq 2, is transformed (for this combination of functions) to simple multiplication with the function $p(x)$

$$e^{-T^2/2}*(S_\tau e^{-S_\tau T}) = \frac{\sigma_G}{\tau}p(x)e^{-T^2/2} \tag{6}$$

where

$$p(x) = e^{x^2/2}\int_x^\infty e^{-\theta^2/2}\,d\theta \tag{7}$$

The modifying function is

$$f(x) = S_\tau p(x) \tag{8}$$

and the EMG function then reads as follows:

$$Y_1(T) = h_G f(x) e^{-T^2/2} \tag{9}$$

The concentration profile $Y_1(T)$ is proportional to h_G of the parent Gaussian, and the shape is modified by the function $f(x)$. On the leading edge of the peak the modifying function has a value less than 1; on the trailing edge the value is greater than 1. At the maximum of the EMG $f(x)$ equals 1. The area of the peak is not altered by $f(x)$.

Two overlapping series are known for $f(x)$, and with eq 8 also for $p(x)$, which allow the calculation of the value of the functions for the whole range with any desired accuracy (*8*). It is not necessary to use approximations for the integral in eq 7 (that is related to the error function); instead the function $p(x)$ should be regarded as accurately defined by the series (as the exponential function is). Table I gives some values for $p(x)$, a continuous, decreasing function. Values of the function $p(x)$ at negative argument can easily be found with eq 5 of ref 8.

Table I. Function $p(x)$, Calculated with the Two Series of Reference 8

x	$p(x)$	x	$p(x)$
−2.0	18.1002	2.2	0.3919
−1.8	12.2111	2.4	0.3661
−1.6	8.5214	2.6	0.3432
−1.4	6.1394	2.8	0.3228
−1.2	4.5571	3.0	0.3046
−1.0	3.4771	3.2	0.2882
−0.8	2.7206	3.4	0.2734
−0.6	2.1780	3.6	0.2600
−0.4	1.7797	3.8	0.2478
−0.2	1.4813	4.0	0.2367
0.0	1.2533	4.2	0.2264
0.2	1.0759	4.4	0.2170
0.4	0.9357	4.6	0.2083
0.6	0.8230	4.8	0.2003
0.8	0.7313	5.0	0.1928
1.0	0.6557	6.0	0.1624
1.2	0.5926	7.0	0.1401
1.4	0.5394	8.0	0.1231
1.6	0.4940	9.0	0.1098
1.8	0.4551	10.0	0.0990
2.0	0.4214	100.0	0.0100

0003-2700/86/0358-2344$01.50/0 © 1986 American Chemical Society

To prove that eq 9 satisfies the basic eq 2, we need the derivative of $p(x)$; remembering that x is itself a function of T, we get

$$\frac{dp(x)}{dT} = 1 - x\ p(x) \tag{10}$$

By the rules of differentiation it is now easy to prove that with eq 1 as input function the EMG eq 9 is a solution of eq 2.

SECOND-ORDER EMG

In practical situations many cases will occur in which two important time constants have to be considered (*2*, *9*). To modify the (first order) EMG with an independent second time constant τ_2, we again use eq 2, the input function being now the simple EMG. To distinguish the time constants and their related functions, we now use subscripts. Retaining the convolution expression for the first order, we can write the solution for two time constants

$$(e^{-T^2/2}*D_1)*D_2 = e^{-T^2/2}*(D_1*D_2) \tag{11}$$

as convolution is associative (*4*). This rearrangement simplifies the task because the convolution of two exponential decays, eq 4, is well-known (4)

$$D_1*D_2 = \frac{S_1S_2}{S_2 - S_1}(e^{-S_1T} - e^{-S_2T}) \tag{12}$$

neglecting now the original subscript τ of the individual S_τ. The factor $S_1S_2/(S_2 - S_1)$ can be shortened to $\sigma_G/(\tau_1 - \tau_2)$. As convolution is also distributive we get with eq 6

$$e^{-T^2/2}*\left[\frac{\sigma_G}{\tau_1 - \tau_2}(e^{-S_1T} - e^{-S_2T})\right] = \frac{\sigma_G}{\tau_1 - \tau_2}[p(x_1) - p(x_2)]e^{-T^2/2} \tag{13}$$

For the second-order EMG we write therefore

$$Y_2(T) = h_G f(x_1,x_2)e^{-T^2/2} \tag{14}$$

with

$$f(x_1,x_2) = \frac{\sigma_G}{\tau_1 - \tau_2}[p(x_1) - p(x_2)] \tag{15}$$

as the modifying function for the case of two time constants.

Through differentiation it can be shown that eq 14 is a solution of eq 2 if eq 9 is the input function. As can be seen from eq 11, inversion of the sequence of the time constants has no effect on the result.

Since $x_1 - x_2$ is independent of T, the values of $p(x_1)$ and $p(x_2)$ are taken at a constant distance. So the table shows that $f(x_1,x_2)$ is always positive, as $\tau_1 > \tau_2$ means $x_1 < x_2$ and $p(x_1) > p(x_2)$.

If there are two time constants of exactly the same value, then eq 15 becomes the indefinite 0/0. By de l'Hôpital's rule we have to introduce derivatives and after comparison with eq 10 we find

$$f(x_1,x_1) = \left[\frac{\sigma_G}{\tau_1}\right]^2 \frac{dp(x_1)}{dT} \tag{16}$$

Curve c of Figure 1 is a second-order EMG with $\sigma_G = 1$, $\tau_1 = \tau_2 = 1$. By visual inspection the difference between the shape of this curve c and the shape of a superimposed similar first-order EMG with the same variance ($\sigma_G = 1$, $\tau_1 = 2^{1/2}$) would be readily apparent.

As follows from eq 2 the parent curve intersects the second-order EMG at its maximum ($dY_2(T)/dT = 0$).

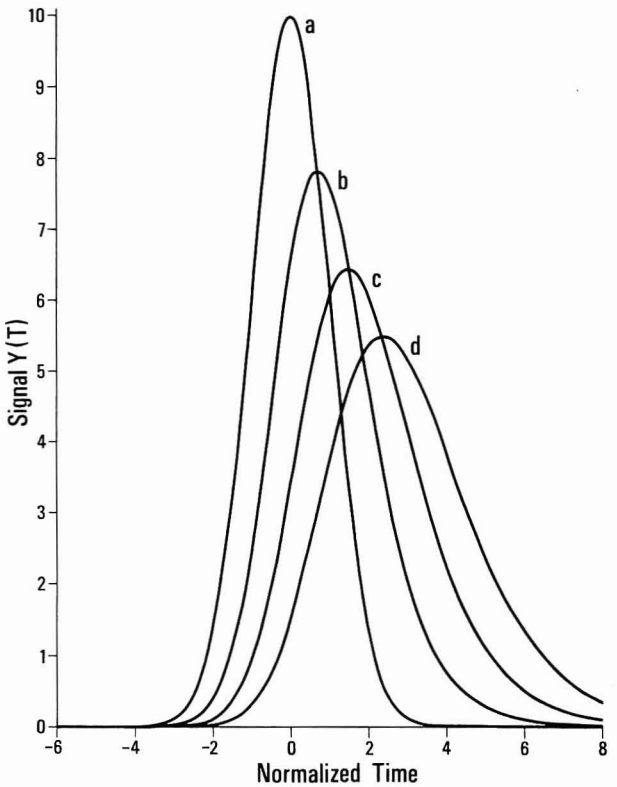

Figure 1. (a) Normalized Gaussian, $\sigma_G = 1$. (b) EMG (first order): $\tau = 1$. (c) Second-order EMG: $\tau_1 = \tau_2 = 1$. (d) Third-order EMG: $\tau_1 = \tau_2 = \tau_3 = 1$.

THIRD-ORDER EMG

A chromatographic system can be described as a mixing chamber followed by a column followed by another mixing chamber and finally by a detector. In some cases the column itself is nonideal, owing to the presence of tail-producing processes. It is therefore useful to consider the effect of three independent time constants.

We follow the same approach as above. For three time constants τ_1, τ_2, and τ_3 we have

$$D_1*D_2*D_3 = \sum_{i=1}^{3}\gamma_i e^{-S_iT} \tag{17}$$

(for instance from ref 4) where

$$\gamma_1 = \frac{\sigma_G\tau_1}{(\tau_2 - \tau_1)(\tau_3 - \tau_1)} \qquad \gamma_2 = \frac{\sigma_G\tau_2}{(\tau_1 - \tau_2)(\tau_3 - \tau_2)} \qquad \gamma_3 = \frac{\sigma_G\tau_3}{(\tau_2 - \tau_3)(\tau_1 - \tau_3)} \tag{18}$$

and therefore the concentration profile of the third-order EMG is

$$Y_3(T) = h_G f(x_1,x_2,x_3)e^{-T^2/2} \tag{19}$$

with the modifying function

$$f(x_1,x_2,x_3) = \sum_{i=1}^{3}\gamma_i p(x_i) \tag{20}$$

The sequence of the time constants is of no importance. If the three time constants are of the same value, τ_1, the modifying function is

$$f(x_1,x_1,x_1) = \frac{1}{2}\left[\frac{\sigma_G}{\tau_1}\right]^3 \frac{d^2p(x_1)}{dT^2} \tag{21}$$

Curve d of Figure 1 is such a third-order EMG; the peak maximum intersects the parent second-order curve. As can be deduced from eq 2, the peak maximum of an nth order

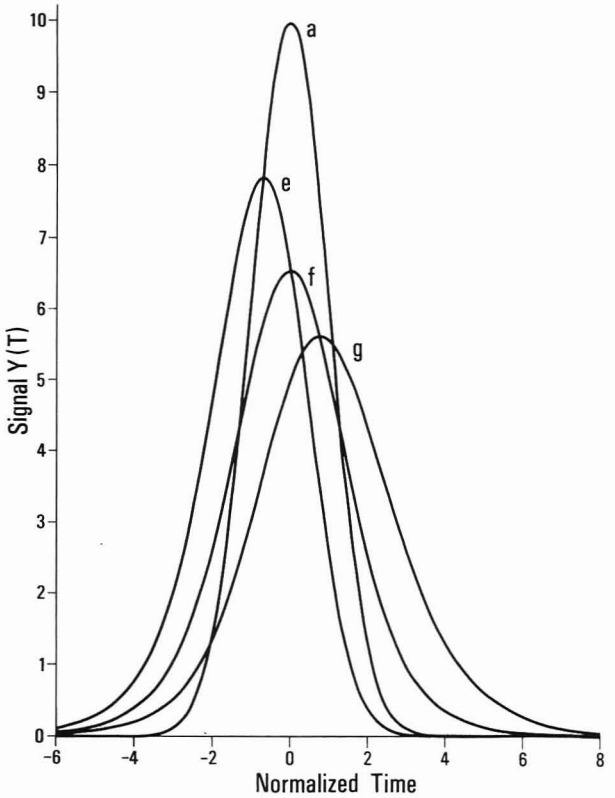

Figure 2. (a) Normalized Gaussian, $\sigma_G = 1$. (e) First-order EMG: $\tau = -1$. (f) Second-order EMG: $\tau_1 = -1$, $\tau_2 = +1$. (g) Third-order EMG: $\tau_1 = -1$, $\tau_2 = \tau_3 = +1$.

EMG function will always intersect the $(n-1)$th order profile.

A special case arises if only two of the time constants coincide, for instance $\tau_2 = \tau_3$. In ref 3 (p 159) $D_1{*}D_2{*}D_2$ is given and we get for the modifying function

$$f(x_1,x_2,x_2) = \frac{1}{\tau_2 - \tau_1}[\tau_2 f(x_2,x_2) - \tau_1 f(x_1,x_2)] \quad (22)$$

FRONTING

Until now we have only considered relaxation times that characterize tailing peaks. To represent fronting peaks, we have to inverse the process and to allow negative τ, as indicated by McWilliam and Bolton (2). Whereas it is easy to find effects with positive time constants, it is more difficult to find effects with negative time constants. (The inverse of exponential decay would be an exponential increasing release from a finite reservoir.) But, as a fact, experimental peaks often manifest fronting that can be fitted with a negative time constant.

To extend the model to fronting, we have to inverse time in eq 7. We introduce formally the sign factor ϵ

$$\epsilon_i = \tau_i/|\tau_i| \quad (23)$$

it is +1 for a positive and −1 for a negative time constant. The generalized argument, eq 5, is

$$x_i = \epsilon_i\left(\frac{\sigma_G}{\tau_i} - T\right) \quad (24)$$

and with this generalized x we have in addition to change eq 7 to

$$p(x_i) = \epsilon_i e^{x_i^2/2}\int_{x_i}^{\infty} e^{-\theta^2/2}\,d\theta \quad (25)$$

Using now the generalized $p(x)$ from eq 25 in eq 8 and 9, we can also manage negative values of τ. With one single negative time constant we get first-order fronting peaks, as curve e of Figure 2. The negative ϵ of eq 25 compensates for the negative sign of S_τ in eq 8 and with the negative ϵ of eq 24 the value of $p(x)$ is altered so that the modifying function $f(x)$ has a value greater than 1 on the leading edge of the peak.

The generalized x and $p(x)$ applied to eq 15 and 19 gives the correct answer for any combination of positive and negative time constants. The derivative, eq 10, is to be altered as follows:

$$\frac{dp(x_i)}{dT} = 1 - \epsilon_i x_i p(x_i) \quad (26)$$

Application of the generalized eq 23 to 26 to the cases of two or three equal time constants gives the correct answer too. Curve f in Figure 2 is an example of a positive and a negative time constant (in the case shown, a symmetrical, non-Gaussian peak); curve g is for one negative and two positive time constants.

LITERATURE CITED

(1) Giddings, J. C. *Dynamics of Chromatography*; Marcel Dekker: New York, 1965.
(2) McWilliam, I. G.; Bolton, H. C. *Anal. Chem.* **1969**, *41*, 1755–1770.
(3) Jenson, V. G.; Jeffreys, G. V. *Mathematical Methods in Chemical Engineering*; Academic Press: London, 1977.
(4) Bracewell, R. *The Fourier Transform and Its Applications*; McGraw-Hill: New York, 1978.
(5) Sternberg, J. C. *Adv. Chromatogr.* **1966**, *2*, 205–270.
(6) Foley, J. P.; Dorsey, J. G. *J. Chromatogr. Sci.* **1984**, *22*, 40–46.
(7) Delley, R. *Chromatographia* **1984**, *18*, 374–382.
(8) Delley, R. *Anal. Chem.* **1985**, *57*, 388.
(9) Niessen, W. M. A.; van Vliet, H. P. M.; Poppe, H. *Chromatographia* **1985**, *20*, 357–363.

RECEIVED for review February 5, 1986. Accepted April 18, 1986.

Mechanical Removal of the Central Sample Zone To Avoid Air Bubbles in Monosegmented Continuous Flow Analysis

Célio Pasquini

Instituto de Química, Universidade Estadual de Campinas, 13081 Campinas, São Paulo, Brazil

The method of monosegmented continuous flow analysis (MCFA) was recently introduced (*1*). In this approach the sample is introduced into the system between two air bubbles that avoid large sample dispersion even for long residence times. For this reason, MCFA can operate at high sample throughput even with spectrophotometric determinations that require slow chemical reactions.

In the first paper about MCFA (*1*), the air bubbles were removed by permeation through a PTFE membrane. The system is very simple and works satisfactorily. However, the

0003-2700/86/0358-2346$01.50/0 © 1986 American Chemical Society

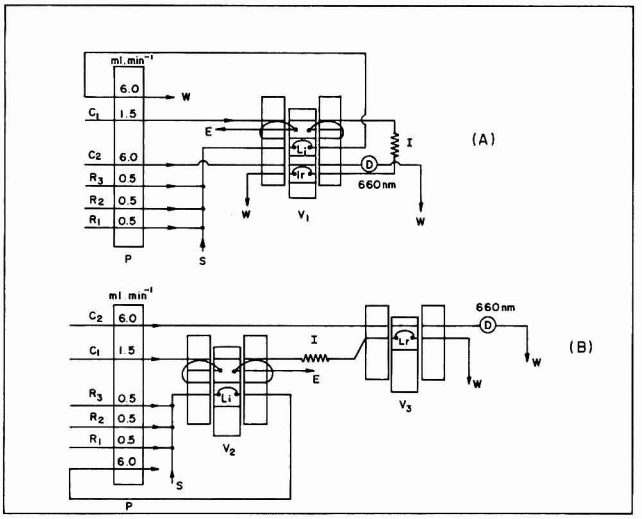

Figure 1. Monosegmented continuous flow analysis manifolds with mechanical removal of central sample zone: A, using only one valve; B, using two valves. Key: P, peristaltic pump; V_1, V_2, and V_3, valves; C_1, carrier stream to incubation coil; C_2, carrier stream to detector; E, to a water aspirator; W, to waste; Li, initial sample loop; Lr, detector sample loop; I, incubation coil; D, detector; S, sample; R_1, R_2, and R_3, reagent streams of sodium hypochlorite, phenol/prussiate, and masking alkaline solution, respectively. Both manifolds are in sampling position.

commercial PTFE tape used lasts only 6–8 h. After this time some small bubbles begin to penetrate into the flow cell, causing imprecise measurements. Further, and more important, this approach suffers from the same kind of limitation observed in other continuous flow systems. The wash time, and thus the analytical rate, is established by the same stream that carries the sample. This seems to be an obstacle to miniaturization of the analyzer since the use of a high carrier flow rate (in order to minimize washing time) requires a larger incubation coil to obtain the desirable sample reaction time. Additionally, much of the washing liquid volume used to reduce the intercontamination to acceptable values is require by the nonsegmented portion existent after the bubbles are removed. This requirement significantly lowers the analytical rate.

In this work a mechanical removal of the central sample zone of MCFA is proposed with the view of substituting the membrane air permeation cell previously used for elimination of air bubbles before detection (*1*). It is also demonstrated how the proposed system can be used both for analyzer miniaturization and for increasing the analysis rate, using the spectrophotometric determination of ammonia as an example.

EXPERIMENTAL SECTION

The fluids were impelled with a peristaltic pump (Ismatec MP 13 GJ4) employing Tygon pumping tubes. The measurements were performed in a photometer, constructed in this laboratory, similar to that previously described (*2*) based on a LED light source (λ_{max} = 660 nm) with a LDR as detector. A flow cell made of acrylic with a 1 cm optical path and about 40 μL total inner volume was used. The signals were registered with a strip chart recorder (ECB, RB 101).

The reagent solutions used for ammonia determination were as follows: R_1, 0.2% (w/v) sodium hypochlorite; R_2, 2% (w/v) phenol and 1% (w/v) sodium prussiate; and R_3, masking solution of 5% (w/v) EDTA and 0.5 M sodium hydroxide. All chemicals were reagent grade except the sodium hypochlorite solution, which was obtained from a commercial bleach. Fresh deionized water was used for all solutions and in the carrier streams.

Figure 1 shows the flow manifolds proposed for mechanical removal of central sample zones from MCFA systems. The air bubble volumes were 25 μL. Both the manifolds work in the same way, removing a fixed volume from the central part of the monosegmented sample at the end of the incubation coil and introducing it into the detector line, while the remainder of the solution and the air bubbles pass to waste. The sample volume originally introduced (Li) was 300 μL and the removed volume (Lr) was 200 μL in both manifolds.

Manifold A uses only one valve operated by means of two solenoids controlled by a single-board microcomputer (Telematic, TSI-1000). With this valve, a new sample is introduced while, simultaneously, a portion of a previously introduced sample, that residing in loop Lr (after the incubation coil), is sent to the detector. The system is programmed so that the segmenting air bubbles are not in loop Lr at the time the valve is moved.

Manifold B employs two valves. One is used for monosegmented sample introduction and is operated automatically as described for manifold A. The other is used to inject an appropriate portion of the liquid into the detector and is operated manually.

The connection of the system to the flow cell was made with a 0.5-nm (i.d.) polyethylene tube 10 cm long in order to avoid undesirable dispersion after sampling the reaction product. The incubation coil I (Figure 1) is made of polyethylene tube (2 mm i.d.) with 150 cm length and wound with 8 cm diameter. Prior mixing of sample and reagents is performed by using six consecutive mixing points constructed as in the literature (*3*). Sample replacement at line S was carried out when the sample valves (V_1 or V_2) were in the injection position.

RESULTS AND DISCUSSION

In MCFA the flow rate (F) that carries the monosegmented sample can be expressed by the equation

$$F = \frac{V_S + V_B + V_W}{t_i + t_a}$$

where V_S (mL) is the sample volume, V_B (mL) is the air bubble sum volume, V_W is the wash liquid volume, t_i (min) is the time necessary to introduce the sample and the two air bubbles into the incubation coil, and t_a (min) is the time required for a new sampling operation when much of the wash fluid is pumped. The analytical rate is determined by the time cycle operation ($t_i + t_a$). The length of incubation coil (L) is defined by

$$L = \frac{tF}{\pi(d/2)^2} \qquad (2)$$

where t (min) is the incubation time interval and d (cm) is the tube diameter.

For a previously defined incubation time, eq 2 shows that a low flow rate is necessary for reduction of the incubation coil length. In the MCFA manifolds described previously (*1*) a typical flow rate of 4 mL·min^{-1} was employed to assure sufficient wash liquid volume with a cycle time of 30 s. For ammonia determination, an incubation coil 3 m long with 2 mm i.d. was necessary.

With the manifolds proposed in this work, a lower flow rate (1.5 mL·min^{-1}) can be employed and the wash volume (V_W) can be reduced because only the segmented part of the analyzer needs to be cleansed. An incubation coil of only 1.50 m, with 2 mm i.d. tube, is then sufficient for obtaining an incubation time of around 210 s. With the reduction of wash volume a increase in analytical rate from 120 to 150 samples per hour was obtained using manifold B (t_i = 16 s and t_a = 8 s). Manifold A operated with a time cycle of t_i = 18 s and t_a = 12 s (allowing 120 samples per hour to be introduced) because syncronism was observed without coil length changes. The reduction of the incubation coil to half its length and the increase in analytical rates demonstrate the advantages of working with incubation times and wash times defined by two independent flow rates in MCFA.

A comparison between the two manifolds proposed here reveals that manifold A is actually simplier than manifold B although it is more difficult to define the necessary synchronous operation when the manifold is first employed. Further, it may be very difficult to connect the valve to the detector in minimum volume when a large detection instru-

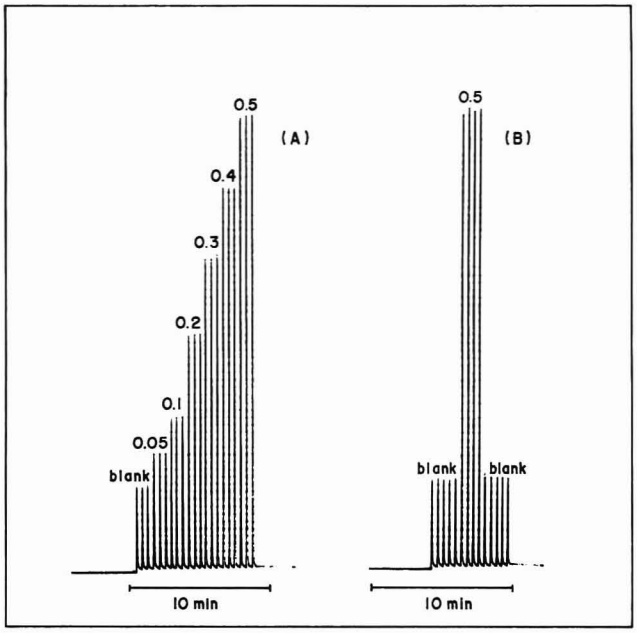

Figure 2. (A) calibration run for ammonia determination with manifold B. The numbers over the peaks are the ammonia concentrations in $\mu g \cdot mL^{-1}$. All measurements were made in triplicate. (B) Signals obtained using the same manifold after 2 h showing the stability and absence of carry-over between blanks and 0.5 $\mu g \cdot mL^{-1}$ ammonia standard solution.

ment is used. On the other hand, the second valve of manifold B (V_3) can easily be placed near the detector and there are no difficulties with synchronism. Additionally, the operation of manifold B can be fully automated by automating the second valve operation. This can be achieved by using a circuit that can detect air bubbles, as previously described (*4*).

Ammonia determinations were made with both manifolds. With the LED/LDR colorimeter a calibration curve linear through 0.7 $\mu g \cdot mL^{-1}$ with a correlation coefficient of 0.9996 was obtained. A detection limit of 5 $ng \cdot mL^{-1}$ was estimated from the blank standard deviation measurements at 99% confidence. Reproducibility is better than 1% and a negligible carry-over exists between samples, as shown in Figure 2.

Another aspect of the system proposed in this work is that it can effectively provide for coupling the technique of MCFA with that of FIA. One application could be when the chemistry required for a determination envolves a slow reaction followed by a rapid one. In this case, the slow reaction would proceed in a MCFA manifold (taking advantage of its low sample dispersion for long residence time) while the second reaction could take place with the resampled volume by introducing it in a carrier reagent fluid (single-line FIA manifold) or in an inert carrier fluid that merges with the reagent, passing through an incubation coil and then through the flow cell.

ACKNOWLEDGMENT

The author is grateful to C. H. Collins for manuscript revision and critical comments.

Registry No. NH_3, 7664-41-7.

LITERATURE CITED

(1) Pasquini, C.; de Oliveira, W. A. *Anal. Chem.* **1985**, *57*, 2575–2579.
(2) Pasquini, C.; Raimundo, I. M., Jr. *Quim. Nova* **1984**, *7*, 24–28.
(3) Ruzicka, J.; Hansen, R. H. *Flow Injection Analysis*; Wiley: New York, 1981.
(4) Patton, C. J.; Rabb, M.; Crouch, S. R. *Anal. Chem.* **1982**, *54*, 1113–1118.

RECEIVED for review January 7, 1986. Accepted April 24, 1986.

Multifunction Valve for Flow Injection Analysis

Jun-ichi Toei* and Nobuyuki Baba

Development Department, Scientific Instrument Division, Toyo Soda Manufacturing Company, Ltd., 2743-1 Hayakawa, Ayase-shi, Kanagawa 252, Japan

The reproducible introduction of a precisely measured volume of sample into a moving carrier or reagent stream is one of the basic factors that must be fulfilled in order to ensure the successful performance of any flow injection analysis (FIA) system (*1*, *2*). Numerous devices for introduction of samples have been proposed (*3–5*) and now hexagonal valves such as the Rheodyne 7125 are popular for the purpose. Though they have brought precise introduction of samples, the trouble is that they have only that function. As Ruzicka had already pointed out, a parallel introduction of sample and reagent is very important in FIA. Mindegaard and Bergamin have proposed injectors that have those two functions (*6*, *7*). They have reduced consumption of expensive reagents and obtained good success with the valves. But they still have a disadvantage in that introduction of samples could not be performed without a separate operation.

In a previous paper (*8*) we have reported a new-type valve by which sample injection and flow change-over of a stream could be performed at the same time. Now we have designed and fabricated a simple and new type of injector that has two functions, that is, introduction of sample or sample and reagent (*9*).

EXPERIMENTAL SECTION

Injector. Figure 1 shows the cross sectional view of the injector, in which 1 is a stator of a circular plate shape and 2 is a rotor. The rotor is made of Teflon and the stator is made of Kel-F which is surrounded by a stainless steel frame in order to stand the high pressure. This valve can operate satisfactorily under 50 kg/cm^2. This valve has three positions and we can select each position with ease by use of a pulse motor that makes the rotor rotate clockwise or counterclockwise. The precise positioning can be performed by use of photosensors as a position indicator. Figure 2 shows the shapes on the surface of the stator and the rotor. The small openings a to j and the grooves a′, a″, a‴, f′, f″, and f‴ are at the stator and the grooves A to G are at the rotor. In the stator the small opening a is connected to a pump and f is connected to reaction tubing. The small openings b,e and g,j are connected to a sample and a reagent loop, respectively. The small openings c,d and h,i are also connected to a circuit of sample and reagent charge.

Arrangement. Figure 3 shows the arrangements of the flow formed by the stator and the rotor, (a) is the load position, (b) is the sample injection position, and (c) is the reagent and sample injection position (after this we call the position "reagent injection position"). In load position, a solution flows f–F‴–A–a‴–a and a sample and a reagent are charged into the loops, respectively.

0003-2700/86/0358-2348$01.50/0 © 1986 American Chemical Society

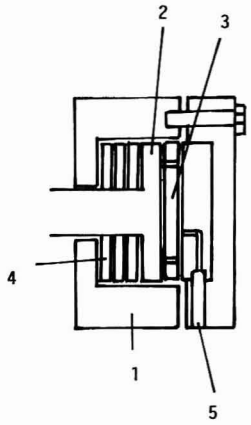

Figure 1. Structure of the valve: 1, stator; 2, rotor; 3, rotor seal; 4, spring; 5, connector.

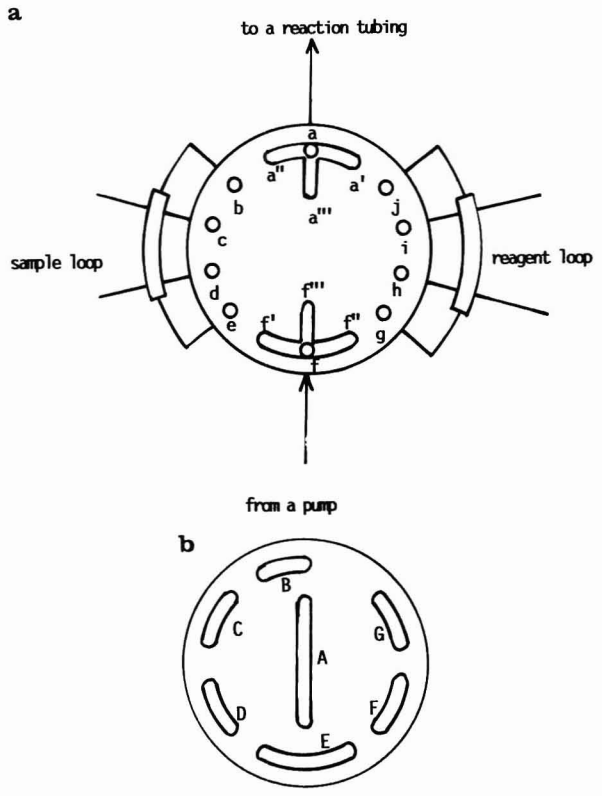

Figure 2. (a) Structure of the stator: a–f small openings connected to tubing; a–a′, a–a″, a–a‴, f–f′, f–f″, f–f‴, grooves. (b) Structure of the rotor: A–G grooves.

Table I. Reproducibility of Injection

flow rate, mL/min	type of injection	measurement	rel std dev (%, n = 7)
0.5	sample	peak height	0.61
		peak area	1.10
	reagent	peak height	0.46
		peak area	1.38
1.0	sample	peak height	0.46
		peak area	0.68
	reagent	peak height	1.09
		peak area	1.38

In sample injection position, to which the rotor is rotated clockwise from the load position, the solution flows f–f′–E–e–sample loop–b–C–a″–a and another path is stopped at j. In reagent injection position, to which the rotor is rotated counterclockwise from the load position, the solution flows f–f″–D–e–sample loop–b–B–a″–a and also f–f″–g reagent loop–j–G–a″–a. So a sample and a reagent are injected into the flow as a parallel plug flow at the same time.

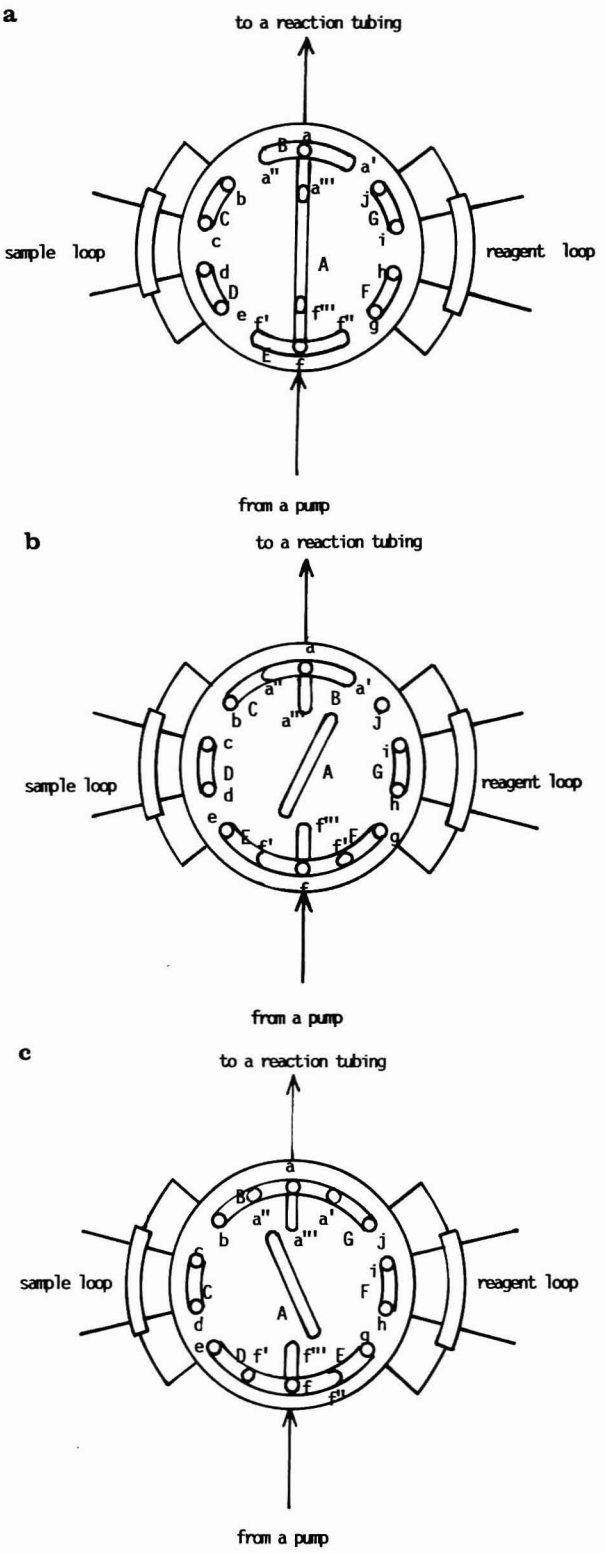

Figure 3. (a) Arrangement of the flow in load position. (b) Arrangement of the flow in sample injection position. (c) Arrangement of the flow in reagent injection position.

Precision Testing. The testing was run using a CCPM pump (metal free Toyo Soda), reaction tubing (0.4 mm i.d. × 50 cm), and a UV–Vis spectrophotomeric detector UV-8000 (Toyo Soda). Results were recorded on a CP-8000 data station (Toyo Soda). The sample loop and the reagent loop were Teflon tubes (0.4 mm i.d. × 79.6 cm) with 100-μL volume.

Flow rate in all tests reported here was 1 or 0.5 mL/min and the absorbance was monitored at 254 nm. The testing solution for injection was 0.1% aqueous acetone solution and deionized

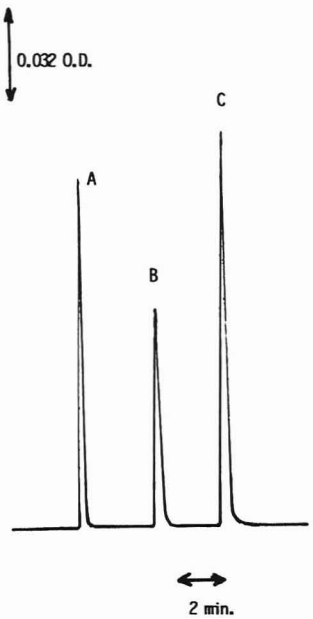

Figure 4. Typical peak shapes of the standard sample with the valve: (A) sample injection in reagent injection position; (B) reagent injection in reagent injection position; (C) sample and reagent injection in reagent injection position; sample volume 100 μL, reagent volume 100 μL.

water was used as a solution of the flow stream. Deionized water was used throughout the testing and acetone was analytical reagent grade and used without further purification.

RESULTS AND DISCUSSION

A typical peak shape when only a sample solution was injected into the flow in reagent injection position (the reagent loop was filled with the deionised water) is shown (A) in Figure 4. Another typical peak shape when only a reagent solution was injected into the flow (the sample loop was filled with deionized water) is shown (B) in Figure 4. Peak C in Figure 4 is a peak shape when the both the reagent and the sample loops were filled with the solution and the solutions were injected into the flow. Though the loop volume and the diameter of the both loops were the same in case (A) and (B), the peak shapes of the two were not in agreement. It could be due to the differences in the shape of grooves and connectors at the rotor or the stator. We are currently investigating the problem.

When flow rate was 0.5 or 1 mL/min, the reproducibilities of the sample injection and the reagent injection were investigated and the results are shown in Table I. The reproducibility of a sample injection only was slightly worse than that with six-port injection valves. In the case of the sample and the reagent injection, the reproducibility was almost twice as bad as that in the case of an only sample injection. The reproducibility may depend upon the number of loops.

As the timing of the slide of the rotor was slightly long (about 1 s), we investigated the reproducibility of the injections at a flow rate of 0.5–1 mL/min. But under these conditions the results were almost the same. So in conclusion, under low pressure (about 1–3 kg/cm^2), which usual FIA is performed, the timing would not affect the injection.

CONCLUSION

We designed and assembled a multifunction valve for flow injection analysis and investigated the properties. On the whole it would be one of the suitable injection devices for flow injection analysis.

LITERATURE CITED

(1) Ruzicka, J.; Hansen, H. *Flow Injection Analysis*; Wiley: New York, 1981.
(2) Tyson, J. F. *Analyst (London)* **1985**, *110*, 419.
(3) Rocks, B. F.; Sherwood, R. A.; Riley, C. *Clin. Chem. (Winston-Salem, N.C.)* **1982**, *28*, 440.
(4) Attiyat, A. S.; Christian, G. D. *Anal. Chem.* **1984**, *56*, 439.
(5) Ruzicka, J.; Hansen, H. *Anal. Chim. Acta* **1983**, *145*, 1.
(6) Mindegaard, J. *Anal. Chim. Acta* **1979**, *104*, 185.
(7) Bergamin, H. F.; Zagatto, G.; Krug, F.; Reis, F. *Anal. Chim. Acta* **1978**, *101*, 17.
(8) Toei, J.; Baba, N. *Bunseki Kagaku* **1986**, *35*, 411.
(9) Toei, J.; Baba, N., Japan patent pending, 1986.

RECEIVED for review March 18, 1986. Accepted May 12, 1986.

Rapid Headspace Analysis in Sealed Drug Vials by Multichannel Raman Spectrometry

Laura Porter Powell*[1]

American Cyanamid Company, Chemical Research Division, 1937 West Main Street, Stamford, Connecticut 06904

Alan Campion

Department of Chemistry, University of Texas, Austin, Texas 78712

Many pharmaceuticals slowly decompose when stored in the presence of oxygen and are therefore packaged in a nitrogen atmosphere. Gas chromatography is frequently used to verify the nitrogen gas purge and check for oxygen leaks. Raman spectrometry can potentially perform this determination more rapidly, reliably, and nondestructively.

Previously reported Raman spectrometric headspace analyses have employed conventional scanning spectrometer systems (*1*, *2*). Residual oxygen content in sealed vials was determined nondestructively by using the nitrogen purge gas as an internal standard. The laser beam was focused inside the sealed vial and the internal Raman scattering was imaged and measured. Both the pure rotational and the pure vibrational Raman peaks have been used; the rotational cross sections are approximately 10-fold larger than the vibrational cross sections (*1*, *2*). The time required for one scan was at least 10 min, plus sample alignment and data analysis time. These techniques are not rapid enough for routine pharmaceutical quality control use.

The well-known analysis speed of multichannel optical detection systems has been demonstrated for Raman spectrometry applications (*3*). This speed advantage was realized by Hug and Surbeck for gas-phase rotational Raman spectra of oxygen and nitrogen, each at atmospheric pressure. The authors suggest that pharmaceutical headspace analyses might be performed if specular reflections from the walls of the sample vials could be reduced by an iodine filter cell (*4*).

[1] Current address: American Cyanamid Co., Medical Research Division, Lederle Laboratories, Pearl River, NY 10965.

0003-2700/86/0358-2350$01.50/0 © 1986 American Chemical Society

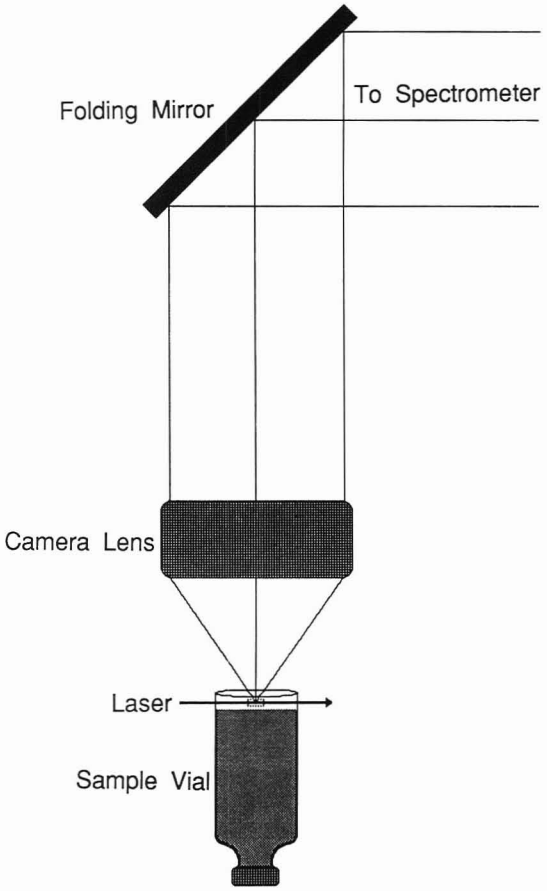

Figure 1. Novel folded beam optical geometry for Raman spectrometric headspace measurements in sealed drug vials (side view; not drawn to scale). The dotted rectangle represents an image of the vertical spectrometer entrance slit inside the vial.

However, sensitive and rapid determinations have not been demonstrated.

In this work the pharmaceutical headspace determination is improved through the use of multichannel Raman detection together with a novel sample imaging technique.

EXPERIMENTAL SECTION

Instrumentation. The Coherent CR-6 argon ion laser was operated at 488.0 nm with 1 W power. The spectrometer was a Spex Triplemate 1877A. In its spectrograph stage a 300 groove/mm grating was used; with an entrance slit width of 300 μm, the spectral bandwidth was 60 cm^{-1}. The spectrometer wavelength was 540.0 nm (so that the central channel of the detector corresponded to 1973 cm^{-1}). The multichannel detector used was a EG&G PARC 1420 reticon diode array with an OMA2 controller. For each spectrum the total data acquisition time was 100 s, and a "dark" background spectrum was subtracted.

Standards. Standards were prepared by evacuating vials to 0.1 torr, and then filling them to 740 torr (at 24 °C) with premixed gases. The gases were purchased from Scott Specialty Gases, Inc., and their oxygen concentrations (in nitrogen) were certified to within 2–5%.

Optical Configuration. A side view of the optical sampling and imaging geometry is depicted in Figure 1. The laser beam was parallel to and directly below the monochromator optic axis, polarized perpendicular to the entrance slit, and focused in the headspace. Some vials had a dimple in the center of the bottom, and were laterally translated to image the Raman scattering through a flat surface. A standard Canon 50-mm $f/1.4$ camera lens collected and collimated the Raman scattered light. The collimated beam was folded by 90° with a 2-in. mirror (larger than the camera lens diameter). It was then focused onto the vertical spectrometer slit with a 2-in. diameter achromatic doublet of 160-mm focal length (not shown). In the figure the dotted rectangle depicts the optical matching of the vertical spectrometer slit wth the horizontal sample image.

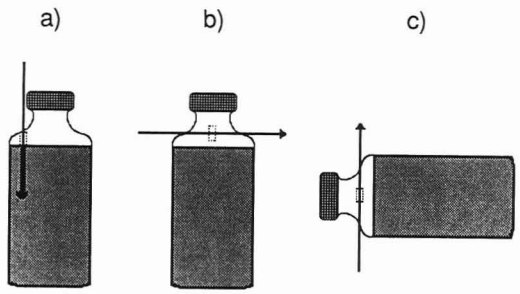

Figure 2. Common optical sampling and imaging geometries for Raman spectrometric pharmaceutical headspace measurements (side view): (a) vertical configuration, (b) horizontal configuration, and (c) configuration for frozen liquid samples. The solid arrows represent the laser beam; the dotted rectangles represent an image of the spectrometer entrance slit.

RESULTS AND DISCUSSION

In this work the pure vibrational oxygen and nitrogen Raman peaks were used instead of the pure rotational peaks, for the following reasons: "Real-world" pharmaceutical vials scatter the laser light (and can emit fluorescence), and the multichannel spectrometer separates the higher-frequency vibrational peaks from this Rayleigh light far more efficiently than at low frequencies. Also, the vibrational peaks can be measured by using wide spectrometer slit widths, providing a rugged method that requires less sample alignment time.

An improved optical geometry was needed for this work because the configurations described in the literature are awkward and time-consuming to use and do not provide the optimal sensitivity. To optimize the light throughput, it is desirable to match optically the entrance slit with a line image of the laser passing through the sample headspace. The dotted rectangles shown in Figure 2 depict how the vertical entrance slit in conventional spectrometers is optically matched within the sample (for three configurations). The vertical configuration normally used (*1*, *5*), shown in Figure 2a, has two major drawbacks: (1) Both the incoming laser beam and the exiting Raman scattering interact with curved glass surfaces which bend the light. Therefore, the image is rotated and incompletely fills the entrance slit and sensitivity is lost. In addition, according to Bailey and Moore, "variability of the ampul wall defocused the laser beam, ...reducing the count rates" (*1*). (2) The laser is sent into the sample and can cause thermal decomposition, especially at the 1-W laser power commonly used (*1*, *5*). Also, for opaque samples there are higher stray light background levels, and fluorescing samples interfere more. This second difficulty is overcome in the horizontal sampling and imaging configuration shown in Figure 2b. However, it provides even less sensitivity than the vertical configuration because the sample image is perpendicular to the entrance slit. An improved geometry for liquid samples is illustrated in Figure 2c. The samples are frozen while standing upright and are then held horizontally with the laser beam directed parallel to the frozen surface (*5*). Freezing the samples adds minutes to hours to the analysis time, and the light must still pass through curved glass surfaces.

The folded beam optical sampling and imaging geometry depicted in Figure 1 provides many advantages. The entrance slit image matches the line image in the sample headspace, so the sensitivity is optimized. With the samples inverted for analysis, the Raman scattered light is collected through the vial bottom, which is the only (relatively) flat glass surface. Small headspace volumes can be analyzed in the inverted vials; the stopper would block the light in the conventional configurations. The laser is directed parallel to the drug surface, so thermal decomposition of the drug is not possible. This optical configuration better discriminates against additional Raman peaks from the drug or the glass; the drug does not

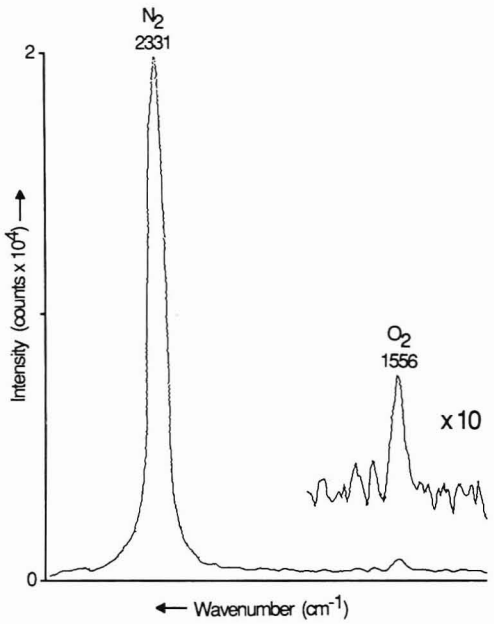

Figure 3. Raman spectrum of the headspace for a standard containing 2.0% O_2 in N_2 (acquired in 100 s, 488.0-nm laser at 1 W). The O_2 peak is scale expanded by a factor of 10.

interact with the laser, and the glass image is much farther from the laser focal spot. Therefore, wide spectrometer slits are used without any peak overlap or interferences. Because of the wide spectrometer slits and the simple technique for imaging the vials through a flat glass surface, *sample alignment is rapid.*

A Raman spectrum of the headspace for a 2.0% O_2 in N_2 standard is illustrated in Figure 3. Longer data acquisition times would yield improved signal-to-noise ratios, but for our quality control applications such 100-s scans are sufficient. Both the limit of detection (roughly 0.6% O_2) and the count rate (200 counts/s at the N_2 peak) were on the order of the results reported by Bailey and Moore (*1*). The optical throughput of the configuration in this work was high because the focused laser beam was properly imaged and the spectrometer entrance slit was properly filled. The high optical throughput probably compensated for the decreased intensity caused by using the vibrational instead of the rotational Raman peaks.

The nitrogen Raman peak was used as an internal standard for quantitation, similar to the method of Bailey and Moore (*1*). The oxygen peak area (or height) was ratioed to the nitrogen peak area (or height). The quantitative results were similar to the literature work (*1*). Changes in the peak shapes were caused by sample alignment differences, but they canceled out in the ratio.

This work is the first demonstration of the advantages of multichannel detection for Raman spectrometric headspace analyses. The data acquisition speed was about *10 times faster* than in the literature work (*1*), even though the spectral range required for the vibrational peak measurement is 100 times larger than that for the rotational peak measurement. Another important advantage is that any changes in experimental conditions such as laser power, sample alignment, detector drift, etc., canceled out because they occurred for both peaks *simultaneously.*

In both this measurement method and the literature method, the largest source of error is the noise associated with the background (*1*). It is difficult to analyze samples in vials that fluoresce or are of poor quality glass. We have successfully measured 2% O_2 Raman peaks against backgrounds 2 orders of magnitude larger. This work probably better discriminates against stray reflected background light (from poor quality glass or from the drug), because the vibrational peak frequencies are far from the Rayleigh line.

This measurement method meets the goals of rapid, noninvasive headspace analysis, with no possibility for sample damage from the laser beam, in "real-world" drug vials. Further work is needed for routine quality control applications. If an interferometric technique for Raman headspace measurements could be developed, the measurement method would be far more rugged and less expensive. An automated (robotic) technique for changing the samples and optimizing their positions would also be highly desirable.

The optical imaging technique described in this work could be extremely useful for general (industrial) Raman spectrometric measurements of solid samples. The samples could be placed on a horizontal surface and translated under the laser beam as on a microscope slide, if the laser entered at an angle instead of parallel to the optic axis. There would be no need for accessories to handle different sample sizes nor for containers to hold powdered samples.

ACKNOWLEDGMENT

The authors wish to thank J. Baldoni and W. Wezel of the Medical Research Division, American Cyanamid Co., for supporting this work. We appreciate the cooperation of D. Hatzenbuhler and R. Chao, The Upjohn Co., who shared information about Raman spectrometric headspace analysis techniques. We also thank W. Haseltine, Chemical Research Division, American Cyanamid Co., for preparing the standard samples.

Registry No. O_2, 7782-44-7; N_2, 7727-37-9.

LITERATURE CITED

(1) Bailey, Glen F.; Moore, Herbert A., Jr. *J. Parenter. Drug Assoc.* **1980**, *34*, 127–133.
(2) DiGregorio, S.; Casper, L. *SPEX Speaker* **1977**, *12*, 8.
(3) Freeman, J. J.; Heaviside, J.; Hendra, P. J.; Prior, J.; Reid, E. S. *Appl. Spectrosc.* **1981**, *35*, 196–202.
(4) Hug, W.; Surbeck, H. *J. Raman Spectrosc.* **1982**, *13*, 38–43.
(5) Hatzenbuhler, Douglas; Chao, Robert, The Upjohn Co., personal communications, Oct 1982 and March 1985.

RECEIVED for review February 3, 1986. Accepted May 2, 1986.

AUTHOR INDEX

Ammann, D., 2282, 2285
Anderson, G. K., 2142

Baba, N., 2348
Baim, M. A., 2316
Baldwin, R. P., 2337
Bard, A. J., 2321
Barkley, D. J., 2222
Benowitz, N. L., 2218
Betteridge, D., 2258
Biemann, K., 2184
Blanchette, M., 2222
Boutton, T. W., 2172
Bowater, I. C., 2195
Braman, R. S., 2213
Brimmer, P. J., 2179
Broge, J. M., 2237
Brown, R. S., 2195
Brzózka, Z., 2285
Bugay, D. E., 2335

Campbell, R. M., 2247, 2251
Campion, A., 2350
Carrion Dominguez, J. L., 2161
Cassidy, J., 2278
Cassidy, R. M., 2222
Chan, S.-K., 2342
Chang, C. A., 2269
Cobb, G. P., 2213
Cooper, J. R., 2195
Crayston, J. A., 2321
Cutié, S. S., 2242

De La Guardia Cirugeda, M., 2161
Delley, R., 2344
Dibble, T., 2278
Dobson, R. L. M., 2129
D'Silva, A. P., 2129
Dunmore, G., 2278

Eckstein, R. J., 2316
Eiceman, G. A., 2142, 2331
Elchuk, S., 2222
Elferink, F., 2293

Fassel, V. A., 2129
Fernandez Perez, M. M., 2161
Files, L. A., 2156
Fleischer, M. E., 2142
Fleischmann, M., 2278
French, S. B., 2256

Gagel, J. J., 2184
Gallego, M., 2265
Ghoroghchian, J., 2278
Gohshi, Y., 2275
Griffiths, P. R., 2179
Guiochon, G., 2200
Gurka, D. F., 2189

Harino, H., 2233
Hart, L. P., 2147
Hayata, E., 2233
Helz, G. R., 2312
Herman, D. P., 2200
Hill, A. D., 2340
Hites, R. A., 2114, 2121
Hoagland, D. A., 2242
Hua, K. M., 2213
Hudson, D. A., 2316

Imasaka, T., 2152
Inman, E. L., 2156
Irving, C. S., 2172
Ishibashi, N., 2152

Jacob, P., III, 2218
Johnson, D. M., 2207

Kargacin, M. E., 2300
Kieber, R. J., 2312
Kimura, K., 2233
Kitamori, T., 2275
Kittlesen, G. P., 2321
Klein, P. D., 2172
Kolaitis, L., 2137
Kowalski, B. R., 2300

Langhorst, M. A., 2242
Leasure, C. S., 2142
Lee, M. L., 2247, 2251
Leenstra, W. R., 2335
Leussing, D. L., 2237
Lin, P. J., 2207
Longhi, P., 2290
Lubman, D. M., 2137

Manchanda, V. K., 2269
Martin, M., 2200
Montaser, A., 2342
Morris, E. R., 2340
Motojima, K., 2275
Mussini, T., 2290

Navratil, P. R., 2172
Nishioka, M., 2251
Novotny, M., 2256

Oesch, U., 2282, 2285
Okamura, T., 2152
Oldham, K. B., 2296
Olesik, S. V., 2256
Omenetto, N., 2147
Owens, G. D., 2316

Parcher, J. F., 2207
Pardue, H. L., 2306
Pasquini, C., 2346
Patterson, K. Y., 2340
Pham, H. V., 2285
Pietrzyk, D. J., 2226
Pinedo, H. M., 2293
Pons, S., 2278
Porter, D. G., 2258
Powell, L. P., 2350
Pretsch, E., 2282, 2285
Prud'homme, R. K., 2242

Ravichandran, K., 2337
Rigas, P. G., 2226
Rivers, M. L., 2167
Rondinini, S., 2290
Russell, A., 2278
Rusterholz, B., 2285

Sanz-Medel, A., 2161
Sarfarazi, F., 2278
Sawada, T., 2275
Schefer, U., 2282
Schweikert, E. A., 2126
Shono, T., 2233
Shulgin, A. T., 2218
Silva, M., 2265
Simon, W., 2282, 2285
Simonsick, W. J., Jr., 2114, 2121
Skoug, J. W., 2306
Sly, T. J., 2258
Smith, B. W., 2147
Smith, J. J., 2278
Smith, J. V., 2167
Stanley, F. W., Jr., 2242
Sugarman, J. H., 2242
Summers, W. R., 2126
Suter, G., 2285
Sutton, S. R., 2167
Suzuki, K., 2275

Titus, R., 2189
Toei, J.-i., 2348

Valcárcel, M., 2265
van der Vijgh, W. J. F., 2293
Vandiver, V. J., 2331
Van Hoven, R. L., 2342
Varco Shea, T., 2321
Veillon, C., 2340

Wade, A. P., 2258
Weeks, S. J., 2129
Welti, D. H., 2285
Whiting, D. G., 2251
Wilkins, C. L., 2195
Wilson, L. R., 2242
Winefordner, J. D., 2156
Wrighton, M. S., 2321

Xu, A., 2285

Ye, J., 2337
Yu, L., 2218

Future Articles

Normal and Resonance Raman Spectroelectrochemistry with Fiber Optic Light Collection
Scott D. Schwab, Richard L. McCreery, and F. Trevor Gamble

Fourier Transform Infrared Surface Electromagnetic Wave Spectroscopy of Polymer Thin Films on Metallic Substrate
Yuichi Ishino and Hatsuo Ishida

Identification and Quantitation of the Impurities in Sodium Pyruvate
S. A. Margolis and Bruce Coxon

High-Speed Liquid Chromatography/Tandem Mass Spectrometry for the Determination of Drugs in Biological Samples
Thomas R. Covey, Edgar D. Lee, and Jack Henion

Fast-Atom Bombardment and Chemical Ionization/Fast-Atom Bombardment Mass Spectrometry of Lubricants
Royal B. Freas and Joseph E. Campana

Solvatochromic Solvent Polarity Measurements and Retention in Reversed-Phase Liquid Chromatography
Bruce P. Johnson, Morteza G. Khaledi, and John G. Dorsey

STANDARDS, CALIBRATION SAMPLES, AND ANALYTICAL SUPPLIES FROM LECO®... THE LEADING SUPPLIER FOR OVER 49 YEARS!



- **Exceptional Quality Control Program Assures Reliable Results Time After Time!**
- **Immediate Worldwide Delivery!**
- **Complete Selection!**

PLEASE SEND THE FOLLOWING CATALOGS:

- ☐ 200-964 Calibration Samples and Reference Materials
- ☐ 200-974 Standard Samples - Coal, Coke and Oil
- ☐ 200-746 Analytical Consumables and Accessories

Name _____

Company _____

Address _____

City _____ State _____ Zip _____

LECO®

LECO CORPORATION
3000 Lakeview Avenue
St. Joseph, MI 49085-2396 U.S.A.
Phone: (616) 983-5531
Telex: 72 9411
Cable: LECO

50 YEARS OF LECO 50th ANNIVERSARY 1936 - 1986 ADVANCED TECHNOLOGY

CIRCLE 126 ON READER SERVICE CARD